

MOLECULAR SIEVES

4 *Science
and
Technology*



CHARACTERIZATION I

H.G. Karge
J. Weitkamp (Eds.)



Springer

Preface to the Series

Following Springer's successful series *Catalysis – Science and Technology*, this series of monographs has been entitled *Molecular Sieves – Science and Technology*. It will cover, in a comprehensive manner, all aspects of the science and application of zeolites and related microporous and mesoporous materials.

After about 50 years of prosperous research, molecular sieves have gained a firm and important position in modern materials science, and we are witnessing an ever increasing number of industrial applications. In addition to the more traditional and still prevailing applications of zeolites as water softeners in laundry detergents, as adsorbents for drying, purification and separation purposes, and as catalysts in the petroleum refining, petrochemical and chemical industries, novel uses of molecular sieves are being sought in numerous laboratories.

By the beginning of 1999, the Structure Commission of the International Zeolite Association had approved approximately 120 different zeolite structures which, altogether, cover the span of pore diameters from about 0.3 nm to 2 nm. The dimensions of virtually all molecules (except macromolecules) chemists are concerned with fall into this same range. It is this coincidence of molecular dimensions and pore widths which makes zeolites so unique in adsorption and catalysis and enables molecular sieving and shape-selective catalysis. Bearing in mind that each zeolite structure can be modified by a plethora of post-synthesis techniques, an almost infinite variety of molecular sieve materials are nowadays at the researcher's and engineer's disposal. In many instances this will allow the properties of a zeolite to be tailored to a desired application. Likewise, remarkable progress has been made in the characterization of molecular sieve materials by spectroscopic and other physico-chemical techniques, and this is particularly true for structure determination. During the last decade, we have seen impressive progress in the application of quantum mechanical *ab initio* and other theoretical methods to zeolite science. The results enable us to obtain a deeper understanding of physical and chemical properties of zeolites and may render possible reliable predictions of their behavior. All in all, the science and application of zeolites is a flourishing and exciting field of interdisciplinary research which has reached a high level of sophistication and a certain degree of maturity.

The editors believe that, at the turn of the century, the time has come to collect and present the huge knowledge on zeolite molecular sieves. *Molecular Sieves – Science and Technology* is meant as a handbook of zeolites, and the term “zeo-

lites” is to be understood in the broadest sense of the word. While, throughout the handbook, some emphasis will be placed on the more traditional aluminosilicate zeolites with eight-, ten- and twelve-membered ring pore openings, materials with other chemical compositions and narrower and larger pores (such as sodalite, clathrasils, $\text{AlPO}_4\text{-8}$, VPI-5 or cloverite) will be covered as well. Also included are microporous forms of silica (e.g., silicalite-1 or -2), aluminophosphates, gallophosphates, silicoaluminophosphates and titaniumsilicalites etc. Finally, zeolite-like amorphous mesoporous materials with ordered pore systems, especially those belonging to the M41S series, will be covered. Among other topics related to the science and application of molecular sieves, the book series will put emphasis on such important items as: the preparation of zeolites by hydrothermal synthesis; zeolite structures and methods for structure determination; post-synthesis modification by, e.g., ion exchange, dealumination or chemical vapor deposition; the characterization by all kinds of physico-chemical and chemical techniques; the acidic and basic properties of molecular sieves; their hydrophilic or hydrophobic surface properties; theory and modelling; sorption and diffusion in microporous and mesoporous materials; host/guest interactions; zeolites as detergent builders; separation and purification processes using molecular sieve adsorbents; zeolites as catalysts in petroleum refining, in petrochemical processes and in the manufacture of organic chemicals; zeolites in environmental protection; novel applications of molecular sieve materials.

The handbook will appear over several years with a total of ten to fifteen volumes. Each volume of the series will be devoted to a specific sub-field of the fundamentals or application of molecular sieve materials and contain five to ten articles authored by renowned experts upon invitation by the editors. These articles are meant to present the state of the art from a scientific and, where applicable, from an industrial point of view, to discuss critical pivotal issues and to outline future directions of research and development in this sub-field. To this end, the series is intended as an up-to-date highly sophisticated collection of information for those who have already been dealing with zeolites in industry or at academic institutions. Moreover, by emphasizing the description and critical assessment of experimental techniques which have been used in molecular sieve science, the series is also meant as a guide for newcomers, enabling them to collect reliable and relevant experimental data.

The editors would like to take this opportunity to express their sincere gratitude to the authors who spent much time and great effort on their chapters. It is our hope that *Molecular Sieves – Science and Technology* turns out to be both a valuable handbook the advanced researcher will regularly consult and a useful guide for newcomers to the fascinating world of microporous and mesoporous materials.

Hellmut G. Karge
Jens Weitkamp

Preface to Volume 4

After synthesis and modification of molecular sieves (cf. Volumes 1 and 3, respectively), the important task arises of appropriately and unambiguously characterizing the materials thus-obtained. Proper characterization is an indispensable prerequisite for judging the reproducibility of the syntheses and modifications of the materials as well as their suitability for application in catalytic and separation processes.

Naturally, a fundamental requirement is the determination of the structure of the molecular sieves under study (cf. Volume 2) through techniques such as X-ray diffraction, neutron scattering, electron microscopy and so on. However, a remarkably broad variety of methods and tools are at our disposal for characterizing the physical and chemical properties of molecular sieves. Volume 4 of the series “Molecular Sieves – Science and Technology” focuses on the most widely used spectroscopic techniques. Thereby, the contributions to this volume not only review important applications of these techniques, but also comprise, to a greater or lesser extent, the basic principles of the methods, aspects of instrumentation, experimental handling, spectra evaluation and simulation, and, finally, employing spectroscopies in situ for the elucidation of processes with molecular sieves, e.g. synthesis, modification, adsorption, diffusion, and catalysis.

Infrared spectroscopy was amongst the first physico-chemical methods applied in zeolite research. Thus, the first Chapter, “Vibrational Spectroscopy”, by *H.G. Karge* and *E. Geidel*, covers the application of IR spectroscopy for molecular sieves characterization with and without probe molecules, including also Raman spectroscopy and inelastic neutron scattering as well as a rather detailed theoretical treatment of vibrational spectroscopy as far as it is employed in zeolite research.

With the advent of solid-state NMR, another powerful tool for the characterization of zeolites and related materials emerged. Similarly and, in many respects, complementarily to infrared spectroscopy, solid-state NMR spectroscopy enabled investigations to be carried out of the zeolite framework, extra-framework cations, hydroxyl groups in zeolites, pore structure, and zeolite/adsorbate systems. The contributions of solid-state NMR to molecular sieves research is reviewed by *M. Hunger* and *E. Brunner* in Chapter 2.

The great potential of electron spin resonance in zeolite science, in particular in the characterization of zeolitic systems containing transition metal cations, paramagnetic clusters, or molecules or metal particles, is demonstrated by *B.M. Weckhuysen*, *R. Heidler* and *R. Schoonheydt*, who co-authored Chapter 3.

Chapter 4 by *H. Förster* is devoted to the potential of and achievements obtained by electron spectroscopy in the field of molecular sieves. This contribution comprises, in a rather detailed manner, the theoretical fundamentals and principles, the experimental techniques, as well as a wealth of applications and results obtained. Results are, e.g., reported on the characterization of zeolites as hosts, guest species contained in zeolite structures, framework and non-framework cations, and zeolitic acidity.

The usefulness of X-ray absorption spectroscopies in zeolite research, i.e. extended X-ray absorption fine structure (EXAFS), X-ray absorption near-edge structure (XANES), as well as electron energy loss spectroscopy and resonant X-ray diffraction is demonstrated by *P. Behrens* (Chapter 5) and illustrated by a number of interesting examples, e.g., the EXAFS of manganese-exchanged A- and Y-type zeolites and guest-containing molecular sieves, or the XANES of oxidation states of non-framework species.

Photoelectron spectroscopy of zeolites is another very interesting technique for zeolite characterization. This is shown by *W. Grünert* and *R. Schlögl* in Chapter 6. The authors carefully describe special aspects of the photoelectron experiments with zeolites, the information obtainable through the spectra, the accuracy and interpretation of the data and, finally, provide a number of illustrative case studies on, e.g., surface composition, isomorphous substitution, host/guest systems, etc.

The last contribution (Chapter 7) dealing with the role of Mössbauer spectroscopy in the science of molecular sieves was provided by *Lovat V.C. Rees*, one of the pioneers in this field. Although Mössbauer spectroscopy is applicable in zeolite research only to a small extent because of the limited number of suitable Mössbauer nuclei, we are indebted to this technique for valuable knowledge of and a deeper insight into some special groups of zeolites and zeolite/guest systems. This is particularly true of molecular sieves, which contain the most important Mössbauer nucleus ^{57}Fe in their framework and/or extra-framework guests (cations, adsorbates, encapsulated complexes, and so on).

Of course, there are many other methods of characterizing zeolites and zeolite-containing systems, in particular non-spectroscopic ones such as chemical analysis, thermal analysis, temperature-programmed desorption of probe molecules, ^{129}Xe NMR, etc. These will be dealt with in one of the subsequent volumes of the series.

November 2003

Hellmut G. Karge
Jens Weitkamp

Contents

Vibrational Spectroscopy	1
<i>H. G. Karge · E. Geidel</i>	
NMR Spectroscopy	201
<i>M. Hunger · E. Brunner</i>	
Electron Spin Resonance Spectroscopy	295
<i>B. M. Weckhuysen · R. Heidler · R. A. Schoonheydt</i>	
UV/VIS Spectroscopy	337
<i>H. Förster</i>	
XANES, EXAFS and Related Techniques	427
<i>P. Behrens</i>	
Photoelectron Spectroscopy of Zeolites	467
<i>W. Grünert · R. Schlögl</i>	
Mössbauer Spectroscopy	517
<i>L. V. C. Rees</i>	
Subject Index	545
Author Index Vols. 1–4	605

Vibrational Spectroscopy

Hellmut G. Karge¹ · Ekkehard Geidel²

¹ Fritz-Haber-Institut der Max-Planck-Gesellschaft, Faradayweg 4–6, 14195 Berlin, Germany
E-mail: karge@fhi-berlin.mpg.de

² Institut für Physikalische Chemie, Universität Hamburg, Bundesstraße 45, 20146 Hamburg, Germany. *E-mail: geidel@chemie.uni-hamburg.de*

1	Introduction	12
2	Theoretical Background	12
2.1	Normal Mode Analysis	13
2.2	Molecular Mechanics	19
2.3	Molecular Dynamics Simulations	21
2.4	Quantum Mechanical Calculations	24
2.5	Some Selected Examples of Modeling Zeolite Vibrational Spectra	28
3	Spectra Evaluation	35
3.1	Qualitative Interpretation	35
3.2	Quantitative Evaluation	35
4	Experimental Techniques	40
4.1	Transmission IR Spectroscopy	40
4.2	Diffuse Reflectance IR (Fourier Transform) Spectroscopy (DRIFT)	42
4.3	Photoacoustic IR Spectroscopy (PAS)	43
4.4	Fourier Transform Infrared Emission Spectroscopy (FT-IRES)	44
4.5	Raman Spectroscopy	45
4.6	Inelastic Neutron Scattering Spectroscopy (INS)	47
5	Information Available from IR, Raman and Inelastic Neutron Scattering Spectroscopy	48
5.1	Introductory Remarks	48
5.2	Framework Modes	49
5.2.1	Pioneering Work	49
5.2.2	More Recent Investigations of Various Molecular Sieves	52
5.2.2.1	Faujasite-Type Zeolites (FAU)	52
5.2.2.2	Zeolite A (LTA)	54
5.2.2.3	Sodalite (SOD)	54
5.2.2.4	Clinoptilolite (Heulandite-Like Structure, HEU)	54
5.2.2.5	Erionite (ERI), Offretite (OFF)	55
5.2.2.6	Zeolite L (LTL)	55

5.2.2.7	Zeolite Beta (BEA)	55
5.2.2.8	Ferrierite (FER)	55
5.2.2.9	Chabazite (CHA)	55
5.2.2.10	ZSM-5 (MFI), ZSM-11 (MEL), MCM-22 (MWW), ZSM-35 (FER), ZSM-57 (MFS)	56
5.2.2.11	AlPO ₄ s, SAPOs, MeAPOs	56
5.2.2.12	Miscellaneous	57
5.2.3	Effect of Cation-Loading on Framework Vibrations	57
5.2.4	Effect of Adsorption on Framework Vibrations	58
5.2.5	Effect of Dealumination and $n_{\text{Si}}/n_{\text{Al}}$ Ratio on Framework Vibrations	58
5.2.6	Effect of Isomorphous Substitution on Framework Vibrations	61
5.3	Cation Vibrations	64
5.3.1	Cation Vibrations in Pure Zeolites	64
5.3.2	Cation Vibrations Affected by Adsorption	71
5.4	Hydroxy Groups	73
5.4.1	Hydroxy Groups of Zeolites Characterized by IR Fundamental Stretching Bands	73
5.4.1.1	Faujasite-Type Zeolites (FAU)	73
5.4.1.1.1	Non-Modified Faujasite-Type Zeolites	74
5.4.1.1.2	Dealuminated Faujasite-Type Zeolites	78
5.4.1.1.3	Cation-Exchanged Faujasite-Type Zeolites	82
5.4.1.2	Other Zeolites	84
5.4.1.2.1	Zeolite A (LTA)	85
5.4.1.2.2	Zeolite L (LTL)	86
5.4.1.2.3	Mordenite (MOR)	86
5.4.1.2.4	Heulandite (HEU) and Clinoptilolite	87
5.4.1.2.5	Erionite (ERI) and Offretite (OFF)	88
5.4.1.2.6	Zeolite Beta (BEA)	88
5.4.1.2.7	Ferrierite (FER)	91
5.4.1.2.8	Zeolites ZSM-5 (MFI) and ZSM-11 (MEL)	91
5.4.1.2.9	Miscellaneous: Zeolites MCM-22 (MWW), Chabazite (CHA), Omega (MAZ), ZSM-20 (EMT/FAU) and ZSM-22 (TON)	93
5.4.1.2.10	Isomorphously Substituted Molecular Sieves	94
5.4.1.2.11	SAPOs, MeAPOs and VPI-5	94
5.4.2	Hydroxy Groups of Zeolites Characterized by Deformation, Overtone and Combination Bands	97
5.4.2.1	Characterization by Transmission IR Spectroscopy	97
5.4.2.2	Characterization by Diffuse Reflectance IR Spectroscopy	98
5.4.2.3	Characterization by Inelastic Neutron Scattering Spectroscopy	102
5.5	Characterization of Zeolite/Adsorbate Systems	103
5.5.1	Introductory Remarks	103
5.5.2	Selected Zeolite/Adsorbate Systems	106
5.5.2.1	Homonuclear Diatomic Molecules (N ₂ , H ₂ , D ₂ , O ₂) as Adsorbates	106
5.5.2.2	Carbon Monoxide (CO) as an Adsorbate	111

5.5.2.3	Linear Triatomic Molecules (N_2O , CO_2) as Adsorbates	119
5.5.2.4	Methane (CH_4) as an Adsorbate	122
5.5.2.5	Bent Triatomic Molecules (SO_2 , H_2S , H_2O) as Adsorbates	124
5.5.2.6	Adsorption of Probe Molecules for the Characterization of Zeolitic Acidity and Basicity	130
5.5.2.6.1	Introductory Remarks	130
5.5.2.6.2	Pyridine, Ammonia and Amines as Probes for Acid Sites	131
5.5.2.6.3	Hydrogen (Deuterium), Light Paraffins and Nitrogen as Probes for Acid Sites	136
5.5.2.6.4	Nitriles as Probes for Acid Sites	138
5.5.2.6.5	Halogenated Hydrocarbons and Phosphines as Probes for Acid Sites	139
5.5.2.6.6	Carbon Monoxide as a Probe for Acid Sites	140
5.5.2.6.7	Nitric Oxide as a Probe for Acid Sites	143
5.5.2.6.8	Benzene and Phenol as Probes for Acid Sites	145
5.5.2.6.9	Acetone and Acetylacetone as Probes for Acid Sites	147
5.5.2.6.10	Probes for Basic Sites	147
5.5.2.7	Adsorption of Methanol, Benzene, Simple Benzene Derivatives, Light Alkanes, Boranes and Silanes	149
5.5.2.8	Adsorption of Large and Complex Molecules	153
5.5.2.9	Infrared Micro-Spectroscopy of Molecules in Single Crystals or Powders of Zeolites	155
5.6	In-situ IR and Raman Spectroscopic Investigation of Processes in Zeolites	156
5.6.1	Introductory Remarks	156
5.6.2	Zeolite Synthesis and Crystallization	156
5.6.3	Chemical Reactions in Zeolites	158
5.6.4	Diffusion in Zeolites	163
5.6.5	Kinetics of Solid-State Ion Exchange in Zeolites	168
6	Concluding Remarks	169
7	References	169

Abbreviations^a

A	zeolite structure (LTA, cf. [235])
A	absorbance of, e.g., OH groups in IR, A(OH), etc.
A	parameter in Eq. (13)
$A, A_{i,j}$	parameter in the Buckingham term of Eq. (16)
$A, A_{i,j}$	parameter in the Lennard-Jones potential of Eq. (18)

^a Unfortunately, many of the above-indicated abbreviations have various meanings (vide supra); in view of the current conventions in the literature, this is hardly avoidable. However, the correct meaning of the abbreviations should follow from the respective context.

A_{initial}	initial absorbance
A_{int}	integrated absorbance
AD	adsorption energy
AN	acetonitrile
$\text{AlPO}_4\text{-}n$	microporous aluminophosphate zeolite-like structure ($n=5, 8, 11, 20, \dots$, cf. [235])
A_{max}	maximal absorbance
A_{treat}	absorbance after treatment
B	Brønsted (e.g., Brønsted acid sites, B-sites, Brønsted acidity)
B	parameter in Eq. (13)
B, $B_{i,j}$	parameter in the Lennard-Jones potential of Eq. (18)
\underline{B}	formation matrix between internal and Cartesian displacement coordinates
B	benzene
BATE	boric acid trimethyl ester
BEA	zeolite structure, acronym for zeolite Beta (cf. [235])
bpy	2,2'-bipyridine
[B]ZSM-5	zeolite structure (MFI, cf. [235]) containing boron in the framework
C	cation (C) site, cation Lewis acid site
C, $C_{i,j}$	parameter in the Buckingham term of Eq. (16)
$C_{i,j}$	parameter in the dispersion term of the potential function Eq. (21)
c	concentration
c_0	velocity of light
C_B	Brodskii constant in Eq. (24)
CA	chemical analysis
CE	conventional ion exchange
CHA	zeolite structure; acronym for chabazite, (cf. [235])
CLIN	abbreviation of clinoptilolite; note: not a three-letter code according to [235]; (clinoptilolite is isostructural with heulandite, HEU)
$\text{CoAPO}\text{-}n$	microporous aluminophosphate zeolite-like structures with cobalt in the $\text{AlPO}_4\text{-}n$ framework (i.e., $\text{MeAPO}\text{-}n$, $\text{Me}=\text{Co}$, $n=5$ (AFT structure), $n=11$ (AEL structure), $n=\text{e.g., } 31, 37,$ $40, \dots$ cf. [235])
D	transport diffusion coefficient
D(B)	diffusion coefficient of benzene
D(T)	diffusion coefficient of toluene
d	thickness (of a zeolite wafer in, e.g., mg cm^{-2})
DAM-1	Dallas amorphous material
DAY	dealuminated Y-type zeolite
DEB	diethylbenzene
DENOX	process for removal of nitrogen oxides
DEXAFS	dispersive extended x-ray absorption fine structure
DFT	density functional theory
DM	dimethylphosphine

D4R	double four-membered ring in, e.g., the structure of zeolite A
D6R	double six-membered ring in, e.g., the structure of zeolites X or Y
D6R	indicates a four-membered ring in the hexagonal prism of Fig. 5
DPPH	2,2-diphenyl-1-picrylhydrazyl, ESR standard
DRIFT	diffuse reflectance IR Fourier transform (spectroscopy)
DRS	diffuse reflectance spectroscopy (in IR or UV-Visible region)
DTG	differential thermogravimetry
ΔH_{ad}	(differential) heat of adsorption
E	total energy
\underline{E}	unit matrix
EB	ethylbenzene
EDAX	energy dispersive x-ray (spectroscopy)
EDS	energy dispersive x-ray spectroscopy
ELAPSO	an MeAPSO material (see below) which contains in addition to the elements of MeAPSO other ones (Li, Be, B, Ga, Ge, As, or Ti) [957]
EM	energy minimization
EMT	zeolite structure; hexagonal faujasite (cf. [235])
EMT/FAU	structural intermediate (cf. ZSM-20, [235])
ERI	zeolite structure; acronym for erionite (cf. [235])
ESR	electron spin resonance (spectroscopy)
Et_3N	triethylamine
ETS-4	zeolite structure related to zorite (cf. [313–316])
ETS-10	zeolite structure (cf. [313–316])
EXAFS	extended x-ray absorption fine structure
F	Schuster-Kubelka-Munk remission function
\underline{F}	force constant matrix
F	force constant
$F_{i,j}$	elements of the force constant matrix
F^r	stretching force constant
F^α	bending force constant
F_x	second derivative of the total energy with respect to Cartesian coordinates
$f_{i,j}^{rr}, f_{i,j}^{\alpha\alpha}, f_{i,j}^{r\alpha}$	interaction force constants related to atomic distances (rr), bond angles ($\alpha\alpha$), simultaneous change of atomic distances and bond angles ($r\alpha$)
F_{TO}	stretching force constants of TO bonds (T=Si, Al; cf. Eq. (13))
F_{SiO}	stretching force constant of the SiO bond
F_{AlO}	stretching force constant of the AlO bond
$f(\nu)$	density of vibrational states
F_R	electric field strength
F_R	second derivative of the total energy with respect to internal coordinates
FAU	zeolite structure; acronym for faujasite (cf. [235])
[Fe]ZSM-5	zeolite structure (MFI, cf. [235]) containing iron in the framework; cf. footnote ^b

[Fe]MCM-41	mesoporous MCM-41 material containing iron in the pore walls, cf. footnote ^b
FER	zeolite structure; acronym for ferrierite (cf. [235])
FIR	far infrared (spectroscopy)
FR	frequency response (spectroscopy)
FKS	Flanigen-Khatami-Szymanski (correlation)
fs	femtosecond ($=10^{-15}$ s)
FT	Fourier transform
FTIR	Fourier transform infrared (spectroscopy)
FT-IRES	Fourier transform infrared emission spectroscopy
FWHH	full-width at half-height (of a band)
\underline{G}^{-1}	kinetic energy matrix
[Ga]BEA	zeolite with Beta (BEA) structure containing gallium in the framework, (cf. [530–534])
[Ga]ZSM-5	zeolite with MFI structure containing gallium in the framework, (cf. [530])
GC	gas chromatography
GF	indicates Wilson's method to solve vibrational problems using the inverse of the kinetic energy matrix and the force constant matrix
GVFF	generalized valence force field
\hat{H}	Hamilton operator
h	Planck's constant
H_0	Hammett value (acidity and basicity scale)
HEU	zeolite structure; acronym for heulandite (cf. [235])
HF	Hartree-Fock (theory)
HF	high frequency (e.g., HF band of OH)
¹ H MAS NMR	proton magic angle spinning nuclear magnetic resonance (spectroscopy)
HMS	hexagonal mesoporous silicate [783]
I	transmitted radiation energy
I_0	incident radiation energy
INS	inelastic neutron scattering
IQNS	incoherent quasielastic neutron scattering
IR	infrared (spectroscopy)
IRES	infrared emission spectroscopy
IVFF	internal valence force field
K	absorption parameter in the Schuster-Kubelka-Munk remission function of Eq. (28)
KED	kinetic energy distribution
K_i	harmonic spring constant between a positively charged mass point and a negatively charged massless shell in Eq. (17)

^b Presenting an element symbol in square brackets should indicate that the respective element is supposed to be incorporated into the framework of the material designated by the subsequent acronym or abbreviation. For instance, “[Ti]SOD” is indicating that titanium is incorporated into the framework of sodalite.

k_{α}	improved angle bending force constant in Eq. (20)
\underline{L}	matrix transforming internal into normal coordinates
L	Lewis (e.g., Lewis acid sites, L-sites, Lewis acidity)
L	zeolite structure (LTL structure, cf. [235])
LF	low-frequency (e.g., LF band of OH)
LO	longitudinal optical (splitting)
LTA	Linde type A zeolite (cf. [235])
LTL	Linde type L zeolite (cf. [235])
\underline{M}	diagonal matrix of atomic masses
M	metal or metal cation
M_1	indicates a metal of sort 1, e.g., Na
M_2	indicates a metal of sort 2, e.g., Ca
m	cation mass (cf., e.g., Eq. (24))
MAS NMR	magic angle spinning nuclear magnetic resonance (spectroscopy)
MAZ	zeolite structure; acronym for mazzite (cf. [235])
MFI	zeolite structure (of, e.g., ZSM-5 or silicalite, cf. [235])
MD	molecular dynamics
MeAPO	microporous metal aluminophosphate zeolite-like structure with metal (Me) in the framework [235, 501, 957]
MAPSO-37	an MeAPO material (see below) with Me=Mg [235, 501, 957]
MeAPO	microporous metal aluminophosphate zeolite-like structures with metal (Me) and additionally silicon in the framework [235, 501, 957]
MCM-22	zeolite structure (acronym or IZA structure code is MWW; cf. [235])
MCM-41	mesoporous material with hexagonal arrangement of the uniform mesopores (cf. Volume 1, Chapter 4 of this series)
MCM-48	mesoporous material with cubic arrangement of the uniform mesopores (cf. Volume 1, Chapter 4 of this series)
MCM-58	zeolite structure (acronym or IZA structure code is IFR)
MIR	mid infrared (spectroscopy)
MM	molecular mechanics
MO	molecular orbital
MOR	zeolite structure; acronym for mordenite (cf. [235])
MP2	Møller-Plesset perturbation theory truncated at second order
MR	membered ring (xMR: x-membered ring, x=3, 4, 5, 6, 8, 10, 12, etc.)
n	vibrational quantum number
n_M/n_{Al}	ratio of metal to aluminum atoms in the framework
n_{Si}/n_{Al}	ratio of silicon to aluminum atoms in the framework
n-Bu ₃ N	tri- <i>n</i> -butylamine
NCA	normal coordinate analysis
NCL-1	high-silica ($n_{Si}/n_{Al}=20$ to infinity) zeolite (cf. [337])
NMA	normal mode analysis
NIR	near infrared (spectroscopy)
NIR-FT	near infrared Fourier transform (spectroscopy)
NU-1	zeolite structure (cf. RUT, RUB-10 [235])
OFF	zeolite structure, acronym for offretite (cf. [235])

O-T-O	angle between adjacent T (T=Si, Al, etc.) and O atoms inside a tetrahedron
OTO	framework fragment, i.e., OSiO or OAlO
P	branch of a vibrational-rotational spectrum (P branch)
P, P_{ij}	parameter in the Buckingham term of Eq. (16)
PAS	photoacoustic (infrared) spectroscopy
Pc	phthalocyanine
PED	potential energy distribution
PES	potential energy surface
n-Pr ₃ N	tri- <i>n</i> -propylamine
PT	proton transfer
PV	pivalonitrile (2,2-dimethylpropionitrile)
p-X	<i>para</i> -xylene
Py	pyridine
Q	branch of a vibrational-rotational spectrum (Q branch)
\underline{Q}	normal coordinate (column vector)
$\dot{\underline{Q}}$	time derivative of the normal coordinate
\underline{Q}^T	transpose of the column vector \underline{Q}
q, q_i, q_j	atomic charges
q	cation charges
QM	quantum mechanical (calculations)
\underline{R}	internal displacement coordinate (column vector)
$\dot{\underline{R}}$	time derivative of an internal displacement coordinate
R	branch of a vibrational-rotational spectrum (R branch)
R_∞	diffuse reflectance of an infinitely (i.e., very) thick sample
R_i	actual distance between the <i>i</i> th core and its shell in Eq. (17)
RR	resonance Raman (spectroscopy)
r	cation radius
r_i, r_j	atomic distances along chemical bonds
r_{TO}	bond length between T and O (T=Si, Al) in Eq. (13)
RE	rare earth metal (cation)
RHO	zeolite structure, acronym for zeolite rho (cf. [235])
S1, S2, S3	cation positions in the structure of zeolite A (adjacent to the single six-membered ring openings to the β -cages, near the center of the eight-membered ring openings to the (large) α -cages and in the center of the (large) α -cages, respectively)
SI, SI', SII, SII', SIII	cation positions in zeolite X or Y, i.e., FAU (cf. [236])
S	scattering parameter in the Schuster-Kubelka-Munk remission function of Eq. (28)
s_i, s_j	ionic radii
SAPO-n	microporous silicoaluminophosphates, n=5, 17, 18, 20, 31, 34, 39 etc. (cf. [235])
SCR	selective catalytic reduction
[Si]MFI	MFI-type zeolite structure containing (exclusively) Si as T-atoms, i.e. silicalite-1; cf. footnote ^b
[Si]SOD	SOD-type zeolite structure containing (exclusively) Si as T-atoms; cf. footnote ^b

[Si,Fe]MFI	MFI-type zeolite structure containing Si and Fe as T-atoms; cf. footnote ^b
[Si,Ti]MFI	MFI-type zeolite structure containing Si and Ti as T-atoms; cf. footnote ^b
[Si,Fe]BEA	zeolite structure of Beta-type (BEA) with small amounts of iron besides silicon in the framework; cf. footnote ^b
[Si,Ti]BEA	zeolite structure of Beta-type (BEA) with small amounts of titanium besides silicon in the framework, [336]; cf. footnote ^b
[Si,V]MFI	MFI-type zeolite structure with small amounts of vanadium besides silicon in the framework; cf. footnote ^b
[Si,Ti]MFE	zeolite structure of ZSM-11 type (MFE) with small amounts of titanium besides silicon in the framework; cf. footnote ^b
[Si,Al]MCM-41	mesoporous MCM-41 material containing both silicon and aluminum in the walls of the pores, [350, 351]; cf. footnote ^b
[Si,Ti]MCM-41	mesoporous MCM-41 material containing both silicon and titanium in the walls of the pores [350, 351]; cf. footnote ^b
[Si,V]MCM-41	mesoporous MCM-41 material containing both silicon and vanadium in the walls of the pores [350, 351]; cf. footnote ^b
SGVFF	simplified generalized valence force field
S _{int}	intermediate Sanderson electronegativity
SOD	zeolite structure, acronym for sodalite (cf. [235])
SOD	four-membered rings in the sodalite structure (particular meaning in Fig. 5)
SQM	scaled quantum mechanical (force field)
SSZ-n	series of zeolite structures; aluminosilicates, e.g., SSZ-24 and SSZ-13, isostructural with corresponding aluminophosphates, AlPO ₄ -5 (AFI) and AlPO ₄ -34 (CHA structure) (cf. [235])
SUZ-4	zeolite structure [877]
T	(tetrahedrally coordinated) framework atom (cation) such as Si, Al, Ti, Fe, V, B
T	absolute temperature, in Kelvin (K)
T	indicating the transpose of a matrix or column vector
T	kinetic energy
T	transmittance (transmission)
T*	transmittance (transmission) of the background (base line)
T	toluene
TAPSO	Ti-containing microporous silicoaluminophosphate of the MeAPSO family [335, 573]
T _E	kinetic energy of electrons
T _N	kinetic energy of nuclei
TEHEAOH	triethyl(2-hydroxyethyl)ammonium hydroxide
[Ti]MMM-1	Ti-containing material with both mesoporous (MCM-41) and microporous (TS-1) constituents [353]; cf. footnote ^b of the table
TO	framework fragment (SiO, AlO, etc.)
TMP	trimethylphosphine
TO	transversal optical (splitting)
TON	zeolite structure; acronym for theta-1 (cf. [235])

T-O-T	angle between adjacent T and O atoms (T=Si, Al, Ti, etc.)
TPA	tetrapropylammonium
TPAOH	tetrapropylammonium hydroxide
TPD	temperature-programmed desorption
TPO	temperature-programmed oxidation
TPR	temperature-programmed reduction
TS-1	ZSM-5 (MFI) structure containing small amounts of titanium besides silicon in the framework
TS-2	ZSM-11 (MFE) structure containing small amounts of titanium besides silicon in the framework
TMS	tetramethylsilane
UV-Vis	ultraviolet-visible (spectroscopy)
US-Y	ultrastable Y-type zeolite
V	potential energy
V	term of the potential function accounting for the electrostatic framework-cation interaction
$V^{\text{core-shell}}$	additional term of the potential function accounting for oxygen anions and extra-framework cations
V_{EE}	potential energy originating from electron-electron repulsion
V_{NN}	potential energy originating from nucleus-nucleus repulsion
V_{EN}	potential energy originating from electron-nucleus attraction
V_{ij}	Lennard-Jones (12-6) potential
ν	vibrational quantum number
VPI-5	microporous aluminophosphate zeolite-like structure (VFI, cf. [235])
VPI-7	zeolite structure (VSV; cf. [235, 279, 280])
VPI-8	microporous all-silica zeolite-like structure (VET, cf. [235])
VS-1	zeolite structure (MFI, cf. [235]) containing vanadium besides silicon in the framework
[V]ZSM-5	zeolite structure (MFI, cf. [235]) containing vanadium in the framework (VS-1); cf. footnote ^b
[V]MCM-41	mesoporous MCM-41 material containing vanadium in the pore walls
X	zeolite structure (faujasite-type structure with $n_{\text{Si}}/n_{\text{Al}} < 2.5$, cf. [235])
X	xylene
XAS	x-ray absorption spectroscopy
XRD	x-ray diffraction
Y	zeolite structure (faujasite-type structure with $n_{\text{Si}}/n_{\text{Al}} \geq 2.5$, cf. [235])
YAG	yttrium aluminum garnet (laser)
Z	frequently used as an abbreviation of “zeolite” or a (charged) “zeolite fragment”
ZBS	zirconium-containing mesoporous material [778]
ZK-4	zeolite structure (LTA, cf. [235])
ZSM-5	zeolite structure (MFI, cf. [235])
ZSM-11	zeolite structure (MFE, cf. [235])

ZSM-18	zeolite structure (MEI, cf. [235])
ZSM-34	zeolite structure (cf., e.g., [275, 276])
ZSM-35	zeolite structure (cf. [235])
ZSM-39	zeolite structure (MTN, cf. [235, 873])
ZSM-57	zeolite structure (MFS, cf. [235])

Greek symbols

α	indicates the large cage in the structure of zeolite A (cf. [235])
α_k, α_l	bond angles
α_{jil}	angle in O-T-O tetrahedron
α^0	equilibrium angle
β	indicates the sodalite cage in, e.g., A-type or faujasite-type structure (cf. [235])
$\gamma(\text{OH})$	out-of-plane bending vibration of an OH group
δ	deformation mode or bending mode
δ_{CH}	deformation mode of a CH_x group in, e.g., methanol
$\delta(\text{OH})$	in-plane bending vibration of an OH group
δ_{OH}	deformation mode of an OH group in, e.g., methanol
$\delta(\text{TMS})$	chemical shift (in NMR spectroscopy) referenced to tetramethylsilane
$\epsilon_{\tilde{\nu}}$	extinction coefficient, depending on the wavenumber
$\Delta = \nabla^2$	Laplace operator, equal to “del squared” or “squared” Nabla (operator)
Λ	diagonal matrix of eigenvalues, λ_k
λ	wavelength (in μm)
λ_k	eigenvalues (related to wavenumber, $\tilde{\nu}_k$)
μ	dipole moment
ν	frequency
$\Delta\nu$	frequency shift
ν_{as}	asymmetric stretching mode
ν_{s}	symmetric stretching mode
$\nu(\text{OH})$	O-H stretching vibration
ν_{OH}	stretching mode of an OH group (e.g., in methanol)
ν_{CH}	stretching mode of a CH group (e.g., in methanol)
$\tilde{\nu}$	wavenumber (in cm^{-1})
$\Delta\tilde{\nu}$	wavenumber shift
$\tilde{\nu}_{\text{min}}$	wavenumber at minimal transmittance
$\tilde{\nu}_{\text{b}}$	wavenumber of the beginning of a band
$\tilde{\nu}_{\text{e}}$	wavenumber of the end of a band
$\tilde{\nu}_0$	wavenumber of the light exciting Raman scattering
$\tilde{\nu}_{\text{Ra}}$	wavenumber of a Raman line
$\tilde{\nu}_{\text{sc}}$	wavenumber resulting from Raman scattering
$\tilde{\nu}_{\text{g}}$	wavenumber of a fundamental stretching mode in gaseous state
θ	angle between the molecular and the symmetry axis
Ψ	many-electron wave function

1 Introduction

Besides the techniques of high-resolution solid-state nuclear magnetic resonance, vibrational spectroscopic methods have proven to belong to the most useful tools in structural research. For the characterization of zeolites and molecular sieves especially infrared (IR) and Raman spectroscopy, and inelastic neutron scattering (INS) are of fundamental interest, of which the infrared transmission technique is the most commonly used. Over the last decades, vibrational spectroscopic investigations of zeolites have provided information about framework structures, active sites, extra-framework ions, and extra-framework phases as well as about adsorbed species. The development of new experimental techniques in IR spectroscopy and Raman spectroscopy as well as INS made available a wealth of valuable information about zeolites and zeolite host/guest systems. The same holds for the amendments of knowledge and understanding obtained through combinations of these techniques with other methods of characterization.

The advantages of IR and Raman spectroscopy and INS lie in the fact that they provide information about microporous materials on a molecular level. However, the utilization of vibrational spectroscopic techniques necessitates the reliable assignment of vibrational transitions to particular forms of normal modes in relation to a given structure. Already in the case of medium-sized molecules studied purely on an empirical basis, this leads to unbridgeable difficulties. Force field and quantum mechanical methods can significantly contribute to obtain this information about the dynamic behavior and allow a more sophisticated interpretation of the experimental data. Thus, besides the development achieved over the last years in the field of experimental techniques, substantial progress in describing vibrational spectra of zeolites and adsorbate/zeolite systems on a theoretical basis has been made.

2 Theoretical Background

Zeolite modeling is a quite diverse field which has grown rapidly during the last two decades. A comprehensive literature survey reveals an enormous number of publications and a variety of simulation techniques ranging from force field calculations employing simplified potential energy functions up to high-level quantum mechanics. Of course, the chosen methodology strongly depends on the particular problem to be solved. Within the scope of this contribution we will focus exclusively on recent developments of theoretical methods for the simulation, interpretation and prediction of vibrational spectra. Selected applications for typical problems in zeolite research will be outlined in more detail.

2.1

Normal Mode Analysis

The basic concept of all force field techniques is that the properties of interest are related to the structure of the system under study. To compute vibrational frequencies, the classical approach is the method of normal coordinate analysis (NCA), often called the GF matrix method (cf. [1] and list of abbreviations). In this case, the structure must be known from experimental data like single-crystal X-ray diffraction (XRD), powder XRD techniques or electron diffraction measurements. The classical approach then is to describe the vibrational behavior of a system of point masses in terms of normal coordinates. The mathematical algorithm of this approach was simultaneously formulated around 1940 by Wilson [1, 2] and Eljasevic [3] and has been extensively treated in several books, e.g., [4–6]. In classical mechanics, the vibrational dynamics of an N-atomic molecule can be described in terms of 3 N-6 normal coordinates (3 N-5 for linear molecules). The corresponding normal modes are evidently dependent on the atomic masses and the geometrical arrangement of the atoms on the one side and on the potential energy surface of the system on the other. If the geometry and the force field are known, it is feasible to predict the vibrational frequencies of any system by solving the classical equations of motion. This case is known as the so-called direct eigenvalue problem. In the reverse case, the so-called inverse eigenvalue problem, experimental spectroscopic data of the system under study are used to derive the force constants. In general, the number of observable absorptions is much smaller than the number of adjustable parameters. Therefore, additional data like vibrational frequencies obtained from isotope-substituted species or from molecules consisting of similar atomic groups can remarkably facilitate the parametrization process and can contribute to an improvement of the reliability and transferability of the force constants. The requirements for solving direct and inverse eigenvalue problems and the results which can be obtained are illustrated schematically in Fig. 1.

In both cases, the first step towards solving the equations of motion consists of deriving expressions for the kinetic (T) and potential energies (V) in terms of appropriate coordinates. In vibrational spectroscopy a set of internal coordinates (R) is usually chosen to describe the molecular structure. Such a set generally includes coordinates for the deviation of bond lengths, bond angles, out-of-plane bendings and torsions from their equilibrium values. This makes the description of the potential energy illustrative and physically meaningful. In terms of internal coordinates the expressions for the kinetic and potential energies are given by

$$2T = \dot{\underline{\underline{R}}}^T \underline{\underline{G}}^{-1} \dot{\underline{\underline{R}}} \quad (1)$$

$$2V = \underline{\underline{R}}^T \underline{\underline{F}} \underline{\underline{R}} \quad (2)$$

where simple underlining represents a vector and double underlining indicates a matrix $\underline{\underline{R}}$ represents the time derivative of the internal displacement coordinate

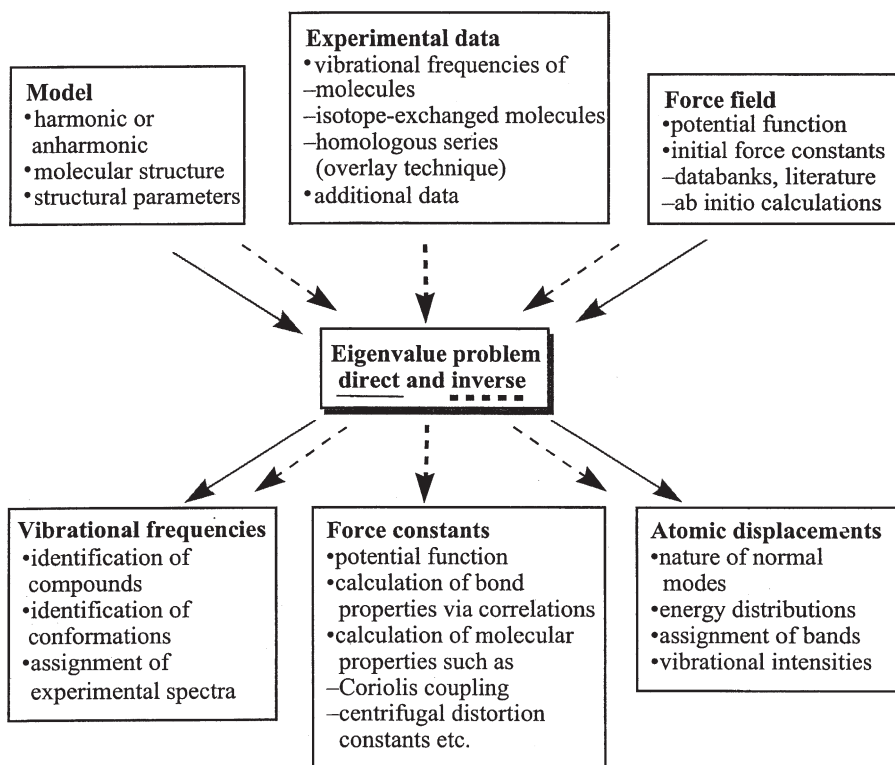


Fig. 1. Input and output for solving the direct and the inverse eigenvalue problem

and the upper index T signifies the transpose of the column vector. The kinetic energy matrix \underline{G}^{-1} depends on the geometry and the atomic masses of the molecule, their inverse can be calculated by

$$\underline{G} = \underline{B}\underline{M}^{-1}\underline{B}^T \quad (3)$$

where the matrix \underline{M} is the diagonal matrix of the atomic masses and \underline{B} is the transformation matrix between internal coordinates and Cartesian displacement coordinates. Setting the potential energy of the equilibrium configuration (eq) equal to zero and taking into account that their first derivatives at the minimum of potential energy are also zero, the potential energy in Eq. (2) has within the frame of the harmonic oscillator approximation a quadratic form. The harmonic force constants are then defined as

$$F_{ij} = \left(\frac{\partial^2 V}{\partial R_i \partial R_j} \right)_{eq} \quad (4)$$

and the force constant matrix \underline{F} in Eq. (2) is symmetric. After transformation of internal into normal coordinates Q via $\underline{R} = \underline{L} Q$ (the crucial transformation matrix

$\underline{\underline{L}}$ yields information about the individual displacements during the normal modes) the kinetic and potential energies assume the form

$$2T = \dot{\underline{\underline{Q}}}^T \dot{\underline{\underline{Q}}} \quad (5)$$

$$2V = \underline{\underline{Q}}^T \underline{\underline{\Lambda}} \underline{\underline{Q}} \quad (6)$$

where $\underline{\underline{\Lambda}}$ in Eq. (6) is a diagonal matrix of the eigenvalues λ_k giving the vibrational frequencies $\tilde{\nu}_k$ in cm^{-1} by

$$\lambda_k = (2\pi c_0 \tilde{\nu}_k)^2. \quad (7)$$

The symbol c_0 in Eq. (7) represents the velocity of light. Substitution of $\underline{\underline{R}} = \underline{\underline{L}}$ into Eqs. (1) and (2) and comparison with Eqs. (5) and (6) then yields

$$\underline{\underline{L}}^T \underline{\underline{G}}^{-1} \underline{\underline{L}} = \underline{\underline{E}} \quad (8)$$

where $\underline{\underline{E}}$ is the unit matrix and

$$\underline{\underline{L}}^T \underline{\underline{F}} \underline{\underline{L}} = \underline{\underline{\Lambda}}. \quad (9)$$

Multiplying Eq. (9) from the left side by $\underline{\underline{L}}$ and taking into account that $\underline{\underline{L}} \underline{\underline{L}}^T = \underline{\underline{G}}$, the classical secular equation can be formulated as

$$\underline{\underline{G}} \underline{\underline{F}} \underline{\underline{L}} = \underline{\underline{L}} \underline{\underline{\Lambda}} \quad (10)$$

which is an eigenvalue equation (the columns of the matrix $\underline{\underline{L}}$ are known as eigenvectors). Non-trivial solutions of Eq. (10) only exist for the condition that the secular determinant vanishes, i.e., if

$$|\underline{\underline{G}} \underline{\underline{F}} - \underline{\underline{E}} \lambda_k| = 0. \quad (11)$$

Although normal mode analyses within the harmonic approximation are nowadays a routine method for most classes of compounds, their application to zeolites is seriously hampered by some special problems making some additional approximations necessary. A brief survey of the major problems and their present solutions is given schematically in Fig. 2.

The first problem originates from the structural complexity of zeolite frameworks which normally contain several hundred atoms per unit cell. This makes studies of the vibrational behavior of the lattice and the search for modes characteristic of special structural units even more difficult. In this case, a usual approximation is to cut out an isolated model cluster from the framework and treat it like a molecule. In comparison with quantum mechanics, in NCA it is not necessary to saturate the dangling bonds of the cluster by terminal pseudoatoms (vide infra). In a first attempt, based on such an assumed decoupling of modes from the surrounding framework, Blackwell [7] predicted vibrational frequencies

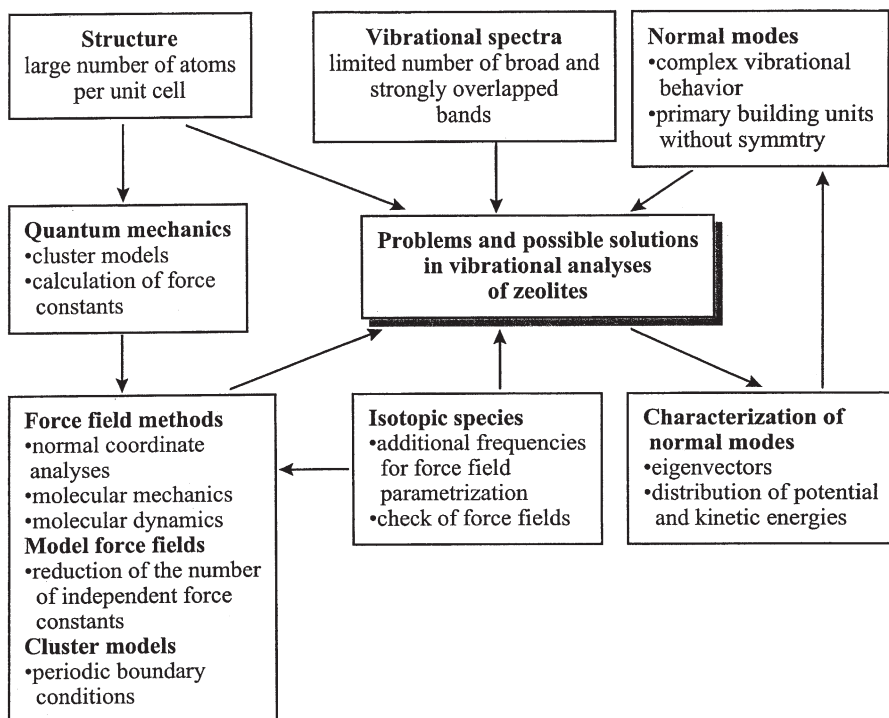


Fig. 2. Survey of problems and their present solutions in normal mode analyses of zeolites

for zeolites A and X by using double-four-ring ($\text{Al}_4\text{Si}_4\text{O}_{12}$) and double-six-ring models ($\text{Al}_6\text{Si}_6\text{O}_{18}$). This basic idea has widely been used for investigations of several zeolites, e.g., [8–10] and was extended to systematically developed clusters of increasing size [11, 12]. Due to the limitations of small, finite models in describing the dynamics of zeolite lattices, calculations have been carried out using the pseudolattice method and the Bethe lattice approximation in order to get closer to the real lattice. Whereas the former utilizes the translational symmetries of atoms instead of the unit cell in setting up a finite pseudolattice model [13, 14], the latter starts with simple SiO oscillators pairwise coupled via common oxygen atoms. Subsequently, these SiOSi oscillators are tetrahedrally connected to one common silicon atom yielding a first shell and in the same way via the second silicon atom to a second shell. This coupling scheme can then be continued ad infinitum. The underlying concept and background symmetry theory have extensively been outlined by van Santen and Vogel [15]. Finally, the exact solution of the eigenvalue problem, i.e., the calculation of the zero-wavevector modes of infinite repeating lattices was presented by de Man and van Santen [16] and by Creighton et al. [17]. To do this, all atoms within a single unit cell must be considered with periodic boundary conditions equating translationally equivalent atoms at opposite faces of the cell. In this way, interaction terms between coordinates in the central unit cell and in next-neighboring cells are replaced

by identical terms on opposite sides of the unit cell under study, and the crystal symmetry is used explicitly to reduce the dynamic matrix. However, it should be noted that, in comparison with the experiment, in the calculations always idealized models are considered taking into account only a single aluminum distribution and a regular cation arrangement. Residual water, template molecules, and aluminum at extra-framework sites, as to be expected in real samples measured under experimental conditions, are normally not taken into consideration.

The second problem is due to the fact that the experimental infrared and Raman spectra of zeolites are characterized by a relatively small number of broad and strongly overlapping bands. Hence, the number of force constants extremely exceeds the number of observable absorptions, and it is impossible to derive the complete force field from experimentally observed vibrational frequencies. In internal coordinates, assuming that the bonds in the lattice are largely covalent, the complete internal valence force field (IVFF) is given by

$$V = \frac{1}{2} \sum_i F_{ii}^r (\Delta r_i)^2 + \frac{1}{2} \sum_k r_0^2 F_{kk}^\alpha (\Delta \alpha_k)^2 + \frac{1}{2} \sum_{i \neq j} f_{ij}^{rr} (\Delta r_i) (\Delta r_j) \quad (12)$$

$$+ \frac{1}{2} \sum_{k \neq l} r_0^2 f_{kl}^{\alpha\alpha} (\Delta \alpha_k) (\Delta \alpha_l) + \frac{1}{2} \sum_{i,k} r_0 f_{ik}^{r\alpha} (\Delta r_i) (\Delta \alpha_k)$$

where the r_i and r_j represent atomic distances along chemical bonds and the α_k and α_l stand for bond angles (in-plane, out-of-plane and torsional ones). F^r are stretching and F^α are bending force constants, whereas the remaining three terms include the interaction force constants. In the past, many systematic attempts have been made to reduce the number of independent parameters in the IVFF for molecules by several model force fields [18]. However, for zeolite frameworks a simple reduction of the number of independent parameters is not sufficient to calculate force constants by a least squares fit. Also, isotope substitution such as H/D exchange [19–22] for Brønsted-acid forms or labeling zeolite frameworks by ^{17}O and ^{18}O isotopes [23, 24] may be fruitful in some particular cases, but cannot completely remove the general problem of missing experimental data to fit the fine structure of valence force fields. In general, the following approaches can be used to get out of this dilemma:

- (i) utilization of empirical rules to estimate force constants [25, 11],
- (ii) transformation of force constants obtained for simpler polymorphs [10, 16, 26–31],
- (iii) taking force constants computed by fitting other experimental data like in molecular mechanics calculations as discussed in the next section, and
- (iv) calculation of force constants by ab initio techniques.

For describing measured zeolite lattice vibrations, the empirical estimation of SiO and AlO stretching force constants from Badger's rule [32] has proven to be one of the most successful tools. It gives a relationship between bond lengths (r) and force constants of the form

$$F_{\text{TO}} = A / (r_{\text{TO}} - B)^3 \quad (13)$$

where A and B are parameters with common values for Si-O and Al-O bonds [7]. In ab initio calculations, this relation has been confirmed [33]. Recently, slight modifications of the empirical parameters A and B were proposed [34]. Taking typical values for crystalline aluminosilicates of $r_{\text{SiO}}=1.62 \text{ \AA}$ and $r_{\text{AlO}}=1.72 \text{ \AA}$ [35], Eq. (13) yields force constants of $F_{\text{SiO}}=4.86 \times 10^2 \text{ N m}^{-1}$ (4.86 mdyne \AA^{-1}) and $F_{\text{AlO}}=3.22 \times 10^2 \text{ N m}^{-1}$ (3.22 mdyne \AA^{-1}). In the reversed case comparing the observed framework spectra of zeolite ZSM-5 with spectra calculated in NCA studies employing Eq. (13) [36], it has been shown that such calculations are useful to restrict the range of bond lengths compared to those obtained from X-ray studies.

The third problem is connected with the asymmetry of the primary building units (allowing no symmetry considerations to factorize the kinetic and potential energy matrices in block form), the large variety of TOT angles (providing a different extent of mode dispersion over the tetrahedra), and the usually low crystal symmetry of zeolite frameworks. This results in normal modes distributed over a wide range of internal coordinates involving a large number of atoms and makes detailed mode analyses and assignments difficult. To get an insight into the individual form of the normal modes, usually the calculated eigenvectors are analyzed. For larger systems it is more appropriate to calculate potential energy distributions (PED) via

$$\text{PED}_{ij}^{(k)} = F_{ij} L_{ik} L_{jk} \lambda_k^{-1} \quad \text{with} \quad \sum_i \sum_j \text{PED}_{ij}^{(k)} = 1 \quad (14)$$

providing information about the relative contribution of each or each kind of force constants F_{ij} to the potential vibrational energy of the normal mode k . Alternatively, the kinetic energy distribution (KED)

$$\text{KED}_{ij}^{(k)} = (G^{-1})_{ij} L_{ik} L_{jk} \quad \text{with} \quad \sum_i \sum_j \text{KED}_{ij}^{(k)} = 1 \quad (15)$$

can be taken into account, advantageously especially in calculations based on Cartesian coordinates. In addition to the characterization of modes, the agreement between experimental and calculated vibrational frequencies is an important criterion for the assignment of bands. However, in direct comparison between observed and calculated wavenumbers, it has to be considered that overtones and hot bands are not accessible in normal coordinate analyses in harmonic approximation.

Having calculated the vibrational frequencies of the system under study, in a second step towards spectra simulation infrared and Raman intensities have to be computed. For infrared spectra of zeolites, the fixed charge approximation is widely used [16, 17]. Intensities are computed from the squares of dipole changes given by the product of atomic charges (normally formal ionic charges or charges taken from ab initio calculations) with the displacements. However, this rather simplified model ignores the charge flux during the vibrational motion. In order to estimate Raman line intensities, an appropriate approximation for aluminosilicates is given by the simplified bond polarizability model [17]. This model is based on the assumption that the total change in polarizability due to the normal mode can be calculated as the sum of contributions due to changes of indi-

vidual bond lengths plus the sum of contributions due to changes in bond orientations. In a more sophisticated model, sets of electro-optical parameters have been derived from small molecules and quantum mechanical considerations [37] which have been transferred very recently to calculate infrared intensities in molecular dynamics simulations of zeolite framework spectra [38].

In a final step of spectral evolution from NCA calculations for each computed transition, an appropriate profile function needs to be chosen. Usually, Gaussian or Lorentzian line shapes with an empirical half band width of 10 cm^{-1} are assumed. The spectra are then generated by plotting the sum of all band intensities against the wavenumbers.

2.2

Molecular Mechanics

The basic goal of the molecular mechanics (MM) method is to relate geometric arrangements of atoms in any system under study to the energy of the system and vice versa. In this way, at minimum energy a good estimation of the preferred geometry of the system can be obtained. Generally, in MM calculations all forces (bonding and non-bonding) between the atoms with electron arrangements fixed on the respective nuclei are taken into account using a mechanical approach. To optimize the geometry, the potential energy of the system is minimized by computational methods. In comparison with NCA this has several advantages. First, as the force field parameters are known, it is possible to sample the potential energy hypersurface and, thus, to locate local and possibly global minima on the surface. This yields information about structures, thermodynamic data, and vibrational spectra. Secondly, in the reversed task even more experimental observables such as structural or elastic constants, thermodynamic data and vibrational frequencies can be used to derive the parameters of the potential energy function. Alternatively, quantum mechanical calculations are a promising way to obtain the force constants for MM calculations. Depending on the method chosen for fitting the force field, diverse potential energy functions with the corresponding parameters have been developed in molecular mechanics.

Several attempts have been undertaken to derive such MM force constants for modeling zeolite frameworks [39]. Typical examples are the rigid ion and the shell model which assume that the character of the bonds in the lattice is largely ionic. Within the rigid ion model developed by Jackson and Catlow [40], the potential energy is given by

$$V = \frac{1}{2} \sum_i \left(\sum_{j \neq i} \frac{q_i q_j}{r_{ij}} + \sum_{j \neq i} \left(A_{ij} e^{-r_{ij}/p_{ij}} - \frac{C_{ij}}{r_{ij}^6} \right) + \sum_{j \neq i; l \neq (i, j)} k_{jil} (\alpha_{jil} - \alpha_{jil}^0)^2 \right) \quad (16)$$

where q are atomic charges, r_{ij} are the distances between atoms i and j , and A , p and C are parameters of the Buckingham term tabulated for a wide range of oxides [41]. The first term in Eq. (16) describes the electrostatic interactions, the second term stands for the short-range interactions and the third one represents the harmonic angle bending potential (α^0 =equilibrium angle, k_{jil} =angle bending

force constant) accounting for the stiffness of O-T-O tetrahedron angles. This term is comparable with the bending term in the IVFF model. The rigid ion model has been used to calculate infrared and Raman active modes of zeolitic silica polymorphs [42] and was slightly modified by reducing the formal ionic charges [43]. Kramer and coworkers derived parameters for the rigid ion potential from ab initio calculations of H_4TO_4 (T=Si, Al, P) clusters and ring structures. With the derived force field the authors were able to reproduce well the structural and elastic properties of silicates, aluminosilicates and aluminophosphates [44, 45].

An extension of the rigid ion model is the shell model taking additional ionic polarizabilities into account [46]. Whereas for silicon and aluminum atoms usually a low polarizability is assumed and they are, therefore, treated as rigid cations in the shell model, for oxygen anions and extra-framework cations an additional term of the form

$$V^{\text{core-shell}} = \frac{1}{2} \sum_i K_i R_i^2 \quad (17)$$

is introduced in the potential function. K_i is a harmonic spring constant between the positively charged point mass (the core) and the negatively charged massless shell, and R_i is the actual distance between the i th core and its shell. Parameters for the shell model potential have been generated both on the basis of experimental data [40, 47, 48] and on the results of ab initio calculations of small silica clusters [49, 50]. Sauer and coworkers parametrized shell model potentials on the basis of ab initio calculations for silica and H-zeolites [51, 52], later extended also to cation-framework interactions of Cu^+ ions in ZSM-5 [53]. The potential not only proved to be successful for predicting crystal structures of silica and H-forms of zeolites [51], but also proved to be well suited for simulating vibrational spectra of faujasite lattices [24].

Another kind of potential model combines potential functions aimed at describing the covalent character of chemical bonds with terms of non-bonding interactions. Such a combination yields force fields as typically used in MM calculations of complex organic molecules and in pharmaceutical research. Nicholas et al. presented an MM force field for silica sodalite and silicates containing bond stretches, bond angle bends, dihedral angles, and cross terms representing the covalent part in the potential function [54]. The non-bonding interactions were expressed via a sum of electrostatic Coulomb interactions and of the Lennard-Jones 12-6 potential of the form

$$V_{ij} = \frac{1}{2} \sum_i \sum_{j \neq i} \left(\frac{A_{ij}}{r_{ij}^{12}} - \frac{B_{ij}}{r_{ij}^6} \right) \quad (18)$$

where r_{ij} is the distance between atoms i and j , and A and B are the Lennard-Jones parameters. The Lennard-Jones potential is characterized by an attractive part that varies as r^{-6} and a repulsive part that varies as r^{-12} . With the parametrization developed by Nicholas et al., the prediction of vibrational spectra for the all-silica frameworks under study succeeded in a fair agreement with experimental data. Another consistent MM force field well-reproducing zeolite infrared spec-

tra was reported by de Vos Burchart et al. for all-silica zeolites [55] and for aluminophosphates [56]. The authors introduced an anharmonic Morse potential instead of the harmonic function for bond stretchings. The angle bending terms of the IVFF were replaced by Urey-Bradley terms representing 1–3 interactions between atoms forming bond angles. Hill and Sauer derived a consistent MM force field for zeolites from results of *ab initio* calculations on molecular models representing typical building units of zeolite structures [57, 58]. After fitting the potential energy surface [computed by *ab initio* calculations of systematically disturbed geometries of selected models (“training set”)] to the consistent force field functional form, the enormous number of 336 force field parameters could be adjusted. The derived parameters were checked for transferability in MM calculations of structures not included in the “training set” and by comparing the results with data of the *ab initio* calculations. Finally, lattice dynamics calculations of periodic structures have been performed. The functional form of the potential energy includes expressions for bond stretchings and angle bendings developed by Taylor expansions up to quartic order, out-of-plane angles, torsions and cross terms. Additionally, non-bonding interactions were considered via Coulomb and Lennard-Jones 9–6 potentials neglecting the dispersive interactions. For the van der Waals interactions, the 9–6 potential gives a less steep curve than the 12–6 power form. The atomic point charges were calculated by a bond increment method yielding topology-dependent charges. The force field developed in this way by Hill and Sauer served excellently for predicting structural features with high accuracy. Moreover, the chosen functional form of interaction potentials has the advantage that for large classes of organic molecules a comprehensive parametrization already exists [59], and, thus, the force field can easily be extended to include interactions of organic molecules with zeolite frameworks in a consistent manner. However, in comparison with the shell model [51], vibrational spectra were only approximately reproduced.

In summary, a high diversity of potential models for molecular mechanics calculations of zeolites hitherto exists. From the theoretical point of view, an appropriate force field should be able to predict structures and vibrations with similar accuracy. On the other hand, the structure of a system under study is determined by the energy minimum, whereas normal modes are dependent on the curvature (second derivative) of the potential energy surface. Consequently, force fields obviously successful in predicting structural features might not automatically be appropriate for simulating vibrational spectra. The only way to overcome this difficulty is to include experimental spectroscopic data into the parametrization process [60]. Alternatively, besides structures and energies a matrix of force constants obtained in quantum mechanical calculations can be included into the quantum mechanical data base used to tune the parameters of the potential function [51].

2.3

Molecular Dynamics Simulations

In molecular dynamics simulations (MD), the time-dependent evolution of a system of atoms interacting via a predefined potential model is recorded. At each

time step the classical equations by Newton of atomic motions are solved and the results are stored in terms of a trajectory in phase space. In principle, each type of force fields evaluated from NCA and MM studies can be employed in MD simulations, too. Necessary conditions for starting an MD run are initial values for atomic coordinates (usually taken from experimental data) and initial velocities (randomly selected from a Maxwell-Boltzmann distribution at the desired temperature). For zeolites, the MD simulation box normally corresponds to one crystallographic unit cell with periodic boundary conditions applied to simulate the translational symmetry of the crystal and to avoid artificial boundary effects. The underlying concept of the molecular dynamics method [61] and its application to zeolite research have extensively been outlined [62–64], so that we can focus here on vibrational studies of microporous materials utilizing the MD technique. A necessary requirement to compute vibrational spectra from the recorded trajectory is that the time step interval to store the trajectory must be considerably shorter than the period of the highest frequency normal mode. For systems with hydrogen atoms this corresponds to approximately 10 fs. Usually, time steps of about 0.5–1 fs are employed to maintain a constant total energy (or temperature), and the simulations are carried out over some hundreds of pico- or nanoseconds. The density of vibrational states $f(\nu)$ can then be calculated from the trajectory data by Fourier transformation of the velocity autocorrelation function [65]

$$f(\nu) = \int_0^{\infty} \langle \mathbf{v}(0) \cdot \mathbf{v}(t) \rangle e^{i\nu t} dt \quad (19)$$

where the angular brackets stand for averaging over all atoms and all time origins. The density of vibrational states is also known as the power spectrum and can directly be compared with experimental spectra recorded by inelastic neutron scattering [66]. Additionally, infrared and Raman spectra can be calculated by Fourier transformation of the dipole and the polarizability tensor autocorrelation functions [67, 68]. This enables the comparison of MD results with a wide range of experimental vibrational spectra.

A first attempt of applying the MD technique to zeolite modeling was published by Demontis et al. [69]. The authors studied water in the cavities of the natural zeolite natrolite. The framework of the zeolite and the cation positions were held fixed during the simulation. The vibrational frequencies calculated for water were found to be somewhat higher compared to the experiment. In subsequent investigations, the authors proposed an empirical atom pair potential (central force field) in MD simulations of natrolite and zeolite A frameworks [70, 71], which has later on been transferred to zeolite Na-Y [72]. In this potential model, the lattice is treated as a network of neutral atoms, and the next-nearest neighbors (Si-O, Al-O and O-O) are connected by harmonic or anharmonic springs. Within this approximation O-T-O (T=Si, Al) angle deformations are described via a spring connecting oxygen atoms jointly to a TO_4 tetrahedron (1–3 interactions). In the anharmonic version, Taylor series were expanded to the third order for intra-framework contacts and to the fifth order for interactions between extra-framework cations and framework atoms. As no charges were included in the potential model, full ionic charges were given to the atoms in order to compute

the dipole moment for the simulation of infrared spectra. Within the chosen approximations, structures of the zeolites under study were reproduced very well, framework frequencies approximately, but infrared intensities only with a high degree of uncertainty. In further developments, the central force field was extended by introducing additional terms for T-T nearest-neighbor interactions modeling T-O-T angles and by adding electrostatic interactions for the framework and between framework and extra-framework cations [73]. The inclusion of the electrostatic interactions was an important step towards a realistic potential to reproduce structural and dynamic properties of aluminosilicates.

Alternatively, Smirnov and Bougeard proposed a simplified generalized valence force field (SGVFF) for MD simulations of siliceous zeolite frameworks [74, 75]. In a first approach, they considered only three terms in the potential energy, namely an Si-O bond stretching, an O-Si-O angle bending, and an Si-O-Si angle bending term. The computed vibrational spectra were in reasonable agreement with the experiment, demonstrating that satisfactory results can be achieved also with relatively simple, but well-tuned force fields. It was shown that the consideration of angle bending terms results in a significantly better description of the vibrational behavior. In later studies, the force field has been improved on the one hand by replacing the Si-O-Si angle bending terms (k_{jil} in Eq. (16)) by cosine harmonic terms of the form

$$V = \frac{1}{2} k_{\alpha} (\cos \alpha - \cos \alpha^0)^2 \quad \text{with} \quad k_{\alpha} = \frac{k_{jil}}{\sin^2 \alpha^0}. \quad (20)$$

This form accounts more appropriately for the high flexibility and permits linearization of Si-O-Si angles. On the other hand, the MD simulations were extended to zeolites A [76–78] and Y [79] which contain aluminum and charge-compensating cations. In these simulations, Al-O stretching and Al-O-Si bending force constants were obtained as 0.75 and 0.875 times of those considering only silicon atoms. The framework-cation interactions were added to the potential function considering electrostatic interactions, a term for core electron repulsion, and a dispersion term expressed by:

$$V = \frac{q_i q_j}{r_{ij}} \left\{ 1 + \left(\frac{\text{sign}(q_i q_j)}{n+1} \right) \left(\frac{s_i + s_j}{r_{ij}} \right)^n \right\} + \frac{C_{ij}}{r_{ij}^6} \quad (21)$$

where q_i , q_j , s_i , and s_j are the atomic charges and ionic radii of the ions i and j , respectively. Sign is the usual sign function, and the parameter n was set equal to 9. The constants C_{ij} in the dispersion term were calculated from polarizabilities and diamagnetic susceptibilities applying the Kirkwood-Müller formula [77]. The complete form of Eq. (21) was assumed for cation-oxygen interactions only, whereas the interactions of Si or Al with the cations and between cations were described by the Coulomb term only. The summation of the long-range interactions was smoothly truncated using a cutoff distance of 10 Å. In MD simulations of cation-exchanged zeolites performed with the mentioned force field, it was shown that the dynamic behavior of such lattices is much more sensitive to the potential function than the structural characteristics. Hence, vibrational spectra

can be used as valuable supplementary experimental material to evaluate the quality of model potentials. The calculated structural parameters and vibrational spectra (in the mid- as well as in the low-frequency region) were found to be in good agreement with experimental data.

In new developments, force field parameters in terms of the SGVFF potential function have been derived for siliceous zeolites [80], aluminosilicates [34], and OH groups in zeolites [81] on the basis of ab initio calculations of small molecular models. The quantum mechanical calculations were performed on cluster models chosen to mimic the basic building units of zeolite frameworks, i.e., TO_4 tetrahedra and $\text{O}_3\text{T-O(H)-TO}_3$ shared tetrahedra with T=Si, Al . In a first step, for these units the matrix of the second derivatives of the total energy with respect to the Cartesian coordinates (F_X) has been calculated. In a second step, the F_X matrix obtained was transformed into the matrix of second derivatives in internal coordinates (F_R) taking into account the redundancies existing between the coordinates. The yielded valence force field has finally been tested in MD simulations of vibrational spectra of zeolites showing a good overall agreement with the experiment. The advantage of the mentioned algorithm is that about forty valence force constants including cross-terms could be derived in a systematic way without any experimental information. Recently, this type of force field has successfully been transferred to spectra simulations of clay minerals following the same strategy and incorporating a new potential for aluminum atoms in octahedral coordination [82].

In summary, the potential models proposed so far for MD simulations of zeolites were able to reproduce quite well structural properties of the frameworks in general, but did not always reach a reliable prediction of the vibrational spectra. The dynamic behavior is obviously much more sensitive to the chosen potential function than structural characteristics. From our point of view, this leads to the conclusion that the accurate reproduction of experimental vibrational spectra should be taken as one of the key criteria in further force field developments.

2.4

Quantum Mechanical Calculations

The methods discussed so far are based on the principles of classical mechanics and necessitate the use of experimental data in the parametrization of the potential model chosen. An alternative approach implies that results of quantum mechanical (QM) calculations are employed as such “experimental” data. Within limits this can allow us to avoid the use of any experimental information other than the values of fundamental physical constants in quantum mechanical ab initio calculations. Alternatively, information about vibrational spectra are also accessible on the direct way from QM calculations.

Any problem concerning the electronic structure of matter is governed by the well-known Schrödinger equation, and for systems without time-dependent interactions the time-independent Schrödinger equation given by

$$\hat{H}\Psi = E\Psi \quad (22)$$

has to be solved. In Eq. (22) E is the total energy, Ψ denotes the many-electronic wave function of the system, and \hat{H} is the Hamiltonian operator determined for molecules by the equation

$$\hat{H} = -\underbrace{\frac{\hbar^2}{2m_e} \sum_i \nabla_i^2}_{T_E} - \underbrace{\sum_A \frac{\hbar^2}{2M_A} \nabla_A^2}_{T_N} + \underbrace{\sum_{A>B} \frac{Z_A Z_B e^2}{r_{AB}}}_{V_{NN}} + \underbrace{\sum_{i>j} \frac{e^2}{r_{ij}}}_{V_{EE}} - \underbrace{\sum_{A,i} \frac{Z_A e^2}{r_{Ai}}}_{V_{EN}} \quad (23)$$

summing up the kinetic energies of electrons and nuclei (T_E and T_N) and the potential energies originating from nucleus-nucleus repulsion (V_{NN}), from electron-electron repulsion (V_{EE}), and from electron-nucleus attraction (V_{EN}), respectively. The symbol \hbar denotes $\hbar = h/2\pi$ and the abbreviation ∇^2 is known as “del-squared”. In contrast to the classical methods mentioned in the previous sections (in which the electronic distribution is hidden behind the potential functions), in almost every QM calculation electronic states are calculated assuming a fixed configuration of the nuclei. Even if the Born-Oppenheimer approximation simplifies the general molecular problem by separating nuclear and electronic motions, in the remaining electronic part of the Hamiltonian some additional approximations are inevitable because of the electron-electron interaction term V_{EE} . Comprehensive surveys of the practicable approximations and their potential and limitations in zeolite research have already been given [33, 83, 84], thus we will pick up here some aspects of quantum chemical studies related to vibrational spectroscopic problems only.

The connecting link between ab initio calculations and vibrational spectra is the concept of the energy surface. In harmonic approximation, usually adopted for large systems, the second derivatives of the energy with respect to the nuclear positions at the equilibrium geometry give the harmonic force constants. For many QM methods such as Hartree-Fock theory (HF), density functional methods (DFT) or second-order Møller-Plesset perturbation theory (MP2), analytical formulas for the computation of the second derivatives are available. However, a common practice is to compute the force constants numerically as finite differences of the analytically obtained gradients for small atomic displacements. Due to recent advances in both software and computer hardware, the theoretical determination of force field parameters by ab initio methods has become one of the most common and successful applications of quantum chemistry. Nowadays, analysis of vibrational spectra of wide classes of molecules by means of ab initio methods is a routine method [85].

Although the harmonic approximation is satisfactory for small displacements from the equilibrium position, ab initio harmonic force constants and vibrational frequencies are known to be typically overestimated as compared with those experimentally found [86]. Sources of this disagreement are the omission or incomplete incorporation of electron correlation, basis set deficiencies, and the neglect of anharmonicity effects. However, as the overestimation is fairly uniform, the application of appropriate scaling procedures becomes feasible. Due to its simplicity, global scaling (using one uniform scale factor determined by a least-squares fit of the calculated to the experimental vibrational frequencies) has widely been used at different levels of theory [87]. However, for most spectro-

scopic investigations a greater accuracy is needed requiring a more sophisticated procedure. Based on the pioneering work of Blom and Altona [88], Pulay and coworkers developed the scaled quantum mechanical (SQM) force field method (cf., e.g., [89–91]). In the SQM method, Cartesian force constants are transformed into internal coordinates and scaling is applied to the internal coordinate force constant matrix (not to the vibrational frequencies), yielding a set of multiple scale factors for different kinds of internal coordinates. This much more systematic procedure has two advantages. First, the obtained scaling factors (slightly smaller than one) are transferable between different molecules [92]. Secondly, the scaling of force constants also affects the nature of the normal modes and hence the computed vibrational intensities. From a spectroscopic point of view, the determination of intrinsic scale factors needs without any doubt a reliable assignment of the bands in the experimental spectra to specific normal modes. Just this is, in addition to the low number of strongly overlapping experimental bands, the key problem for zeolites, making scaling an extremely difficult task. Under these conditions, the apparent perfect matching of observed and calculated spectral curves alone does not seem to be a sufficient criterion to get further information about scaling factors.

Further, the direct comparison with the experiment asks for QM studies avoiding undesirable border effects as occurring in cluster models. Although several QM calculations of periodic zeolite lattices have been reported, e.g., in [93–97], they have, to our best knowledge, never been extended to the determination of force constants and vibrational spectra, probably because of computational expense. As a consequence, to reduce the necessary computer power most QM calculations were performed for finite structural cutouts of the framework by saturating the dangling bonds by terminal atoms (typically hydrogen, fluorine or pseudoatoms). TO_4 tetrahedra and TOT links between two corner-sharing tetrahedra are typical primary building units of zeolite frameworks and, hence, suitable cluster models. Therefore, $\text{T}(\text{OH})_4$ [98–100], $\text{H}_3\text{T-O-TH}_3$ [101–103] and $(\text{OH})_3\text{T-O-T}(\text{OH})_3$ [104] molecules have widely been used to mimic zeolite frameworks in force field studies. Force constants obtained in these calculations considerably varied depending on the chosen theory level and basis set. Since the development of accurate force fields for aluminosilicates requires *ab initio* calculations with extended basis sets and the inclusion of electron correlations, small clusters have the advantage that the influence of increasingly sophisticated methods and basis sets on the results can be verified at moderate computational times. This gives the (rare) possibility to correct force constants for systematic errors by reference calculations [34, 80]. However, the decisive factor in checking different levels of theory and basis sets is not to get “accurate” values for local force constants, but to get an insight into the range of force constant values and into the interatomic interactions in the system, i.e., the structure of the force field. The disadvantages of the use of small clusters for spectroscopic investigations may be summarized as follows:

- (1) They contain a comparatively large number of terminal pseudoatoms. This introduces artificial forms of normal modes leading to artifacts in the vibrational behavior. For instance, in the case of hydrogen as saturating atom the

- OH in-plane bending modes fall into the frequency range of TO stretchings. Therefore, in some studies deuterium or atoms with arbitrary masses are preferred to suppress undue coupling with motions of saturating atoms.
- (2) Due to the flexibility of T-O-T and dihedral angles, the saturating hydrogen atoms sometimes become involved in intramolecular hydrogen bonds, resulting in structures far away from the real zeolite framework. This requires a constraining of selected coordinates during the process of geometry optimization, frequently resulting in negative eigenvalues and vibrational frequencies.
 - (3) The influence of the framework surroundings on the vibrational behavior as well as long-range interactions are neglected. The latter effect can be minimized or avoided by taking into account clusters of increasing size, i.e., to build up systematically the next coordination spheres around a central TO_4 tetrahedron [57, 58, 105–108].

In dependence on adding the next sphere, this algorithm comprises calculations of chains (dimer, trimer, tetramer, and pentamer), ring models of increasing size, double rings, and cage models. Within the scope of the chosen structural models, force field parameters can then be derived and treated as a “test particle setup”. On the other hand, changes in the force field parameters and calculated vibrational frequencies may be followed as a function of the degree of successive dehydration forming the network. From the correlation of the results, the influence of terminating atoms can generally be removed which is an important step towards periodic zeolite structures.

Finally, it should be emphasized that embedded cluster schemes have also been employed to calculate local force constants and vibrational frequencies for bridging hydroxy groups in faujasite-type zeolites [109, 110]. The embedded cluster approach properly accounts for the structure of the periodic lattice. The energy of the whole system is decomposed into contributions of an inner part of interest, e.g., the Brønsted active site, which is treated quantum mechanically, and an outer part (the periodic lattice), which is described by interatomic potential functions. Both parts are connected by an interaction term using a subtraction scheme that approximately eliminates the contribution of terminating atoms of both spheres to the total energy. Using the combined quantum mechanics-interatomic potential functions approach in combination with a crude scaling procedure, Sauer and co-workers [111] were able to predict the splitting between the so-called high-frequency (HF) and low-frequency (LF) O-H stretching bands in faujasites and their dependence on the $n_{\text{Si}}/n_{\text{Al}}$ ratio in excellent agreement with experimental data [109, 111].

In summary, the direct quantum mechanical simulation of zeolite vibrational spectra is evidently a formidable task and is often severely hampered by limited computational resources. Pure ab initio methods are well-suited if local effects or groups with characteristic vibrational frequencies like Brønsted acidic OH groups are under study. In theoretical studies of vibrational spectra of zeolite frameworks and cations on extra-framework sites, QM calculations are of crucial importance in developing force field parameters which can be used in a subsequent step in MM, MD or NMA calculations. Due to the lack of sufficient exper-

imental data, QM calculations seem to be indispensable to shed light upon the fine structure of zeolite force fields.

2.5

Some Selected Examples of Modeling Zeolite Vibrational Spectra

The application of vibrational spectroscopic techniques in zeolite structure research is closely connected with the question as to whether the experimental spectra manifest any structure-specific normal modes. While for organic molecules this question can easily be answered in terms of characteristic group frequencies, the answer for zeolites is not straightforward due to the complexity of zeolitic systems and the variety of framework types with diverse structural features. At first we will focus on some selected problems of framework dynamics.

From the detailed comparison of abundant experimental infrared spectra in the region between 1300 and 200 cm^{-1} , Flanigen, Khatami, and Szymanski derived a correlation between observed bands and structural features of zeolite frameworks, known since that time as the FKS correlation [112].

This correlation has gained significant importance in practice of zeolite research and will, therefore, be described and illustrated in some detail in Sect. 5.2, in spite of serious objections outlined in the following paragraph.

The observed bands were classified by Flanigen et al. [112] into two types, namely internal modes of the TO_4 tetrahedra (“intra-tetrahedral” modes, cf. Sect. 5.2) and external modes (“inter-tetrahedral” modes) of the zeolite framework. Table 1 summarizes the zeolite infrared assignment according to the FKS correlation. The internal vibrations represent structure-insensitive modes, and no distinction has been made between the modes of SiO_4 and AlO_4 tetrahedra. The bands of external modes were observed to be sensitive to the structure, and their positions in the spectra are shifted in dependence on the framework topology and on the $n_{\text{Si}}/n_{\text{Al}}$ ratio. Even though this classification proved to be very successful in many applications, from a theoretical point of view such a division into

Table 1. Zeolite infrared assignments following the FKS correlation [112]

Approximate assignment	Wavenumber range
Internal tetrahedra	
TO_4 antisymmetric stretching, i_1	1250–950
TO_4 symmetric stretching, i_2	720–650
TO_4 bending, i_3	500–420
External linkages	
antisymmetric stretching, e_1	1150–1050
symmetric stretching, e_2	820– 750
double ring mode, e_3	650– 500
pore opening, e_4	420– 300

i: internal (intra-tetrahedral) vibrations.

e: external (inter-tetrahedral) vibrations.

internal and external modes seems to be questionable due to the following reasons:

- (1) Each bond has simultaneously both internal and external character.
- (2) The two stretching force constants in tetrahedra-connecting T-O-T bridges are always of the same order of magnitude which generally forbids isolated internal TO_4 modes.

Therefore, several theoretical attempts have been undertaken to evaluate the assignments of zeolite framework bands. In one of the early studies done to verify the FKS correlation, Geidel et al. [113] performed normal mode analyses for cluster models of X-type zeolites. Starting from simple TO_4 tetrahedra (T=Si, Al), the authors connected the primary building units systematically into increasingly large structures. In the calculations, clusters with one-fold ($\text{O}_3\text{Si-O-AlO}_3$), two-fold ($\text{Si}_2\text{Al}_2\text{O}_{12}$ and $\text{Si}_3\text{Al}_3\text{O}_{18}$ -ring models), three-fold ($\text{Si}_6\text{Al}_6\text{O}_{30}$ double-six-ring model) and four-fold [$\text{TO}_4(\text{TO}_3)_4$ and $\text{TO}_4(\text{TO}_3)(\text{T})_9$, with T alternated Si, Al] bridging of the primary building units were considered. Following the changes in the vibrational behavior by increasing the cluster size in terms of the potential energy distributions and eigenvectors, it was observed that the coupling within Si-O-Al bridges dominates the coupling within the TO_4 tetrahedra. Therefore, it was suggested to distinguish rather between localized and delocalized modes (see also [15]) than between internal and external ones. The second important aim was to obtain information about the role of aluminum in the framework spectra. No modes localized exclusively on bridged Al-O bonds or O-Al-O bond angles could be observed for larger clusters. However, connecting terminal Al-O bonds with adjacent tetrahedra leads (in contrast to Si-O bonds) to red-shifts of the Al-O stretching modes. This shift is accompanied by strong couplings of the Al-O stretchings with the corresponding Si-O stretchings in the Al-O-Si bridges. The frequency is shifted systematically from approximately 830 cm^{-1} (AlO_4) to approximately $790\text{--}760\text{ cm}^{-1}$ [$\text{AlO}_4(\text{SiO}_3)_4$] upon linking the tetrahedra. This result may elucidate the successive disappearance of the infrared band at 850 cm^{-1} observed at progressive crystallization states of sodium aluminosilicates [114]. Furthermore, it can be confirmed by an intense band detected very recently at 885 cm^{-1} in the infrared spectrum of an activated dealuminated zeolite Beta and assigned to Al-O modes at defect sites attached to a hydroxy group [115]. In addition, the loss of intensity of the infrared band at 745 cm^{-1} observed with increasing $n_{\text{Si}}/n_{\text{Al}}$ ratio for H-Y zeolites [116] becomes explicable by this scheme. On the other hand, a reverse trend (i.e., a blue-shift from about 980 cm^{-1} to approximately 1050 cm^{-1}) was calculated on forming the network for Si-O stretching modes. This effect has been used to explain an additional infrared absorption at 900 cm^{-1} (arising upon high-temperature ^{18}O exchange of faujasites) by lattice defects [24]. As the calculations were performed with a simple diagonal valence force field, the reliability of the deduced conclusions were verified by calculations with a force field taking additionally cross terms into account [11]. As expected, slight shifts of the band positions were obtained, but the principal vibrational behavior remained unaltered. Again, no mode could be regarded as exclusively originating from Si-O or Al-O vibrations.

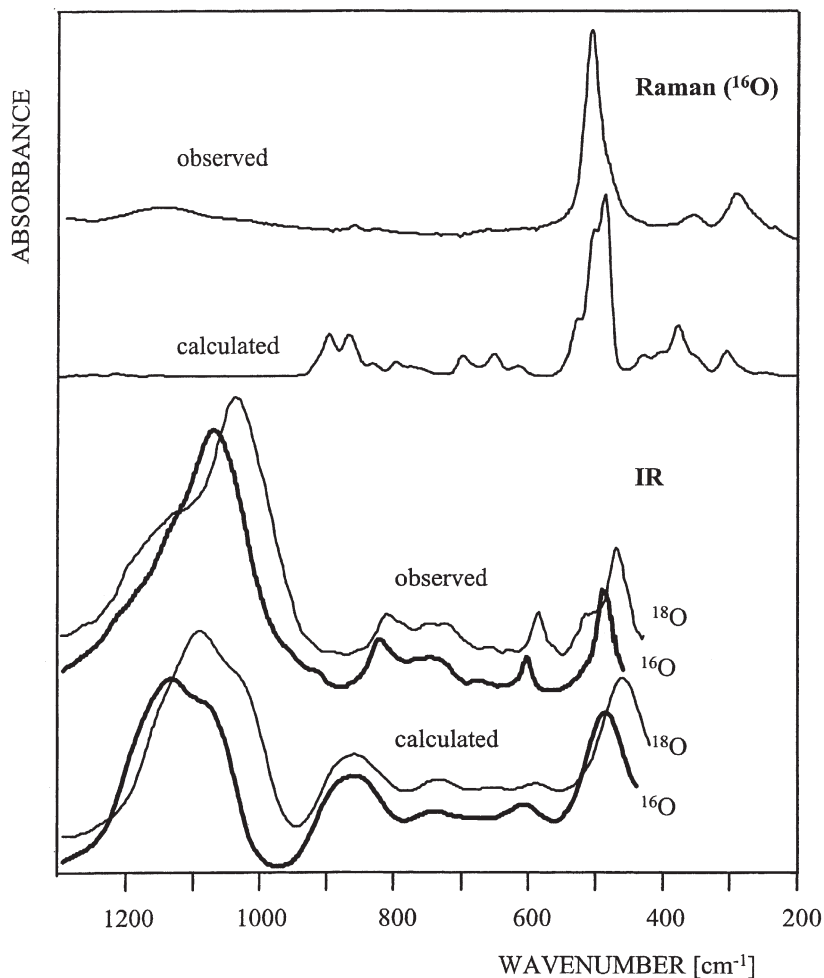


Fig. 3. *Top:* Observed and calculated Raman spectra of ¹⁶O-Na-Y zeolite; *bottom:* observed and calculated infrared spectra of ¹⁶O-Na-Y zeolite in comparison with those of ¹⁸O-Na-Y zeolite [24]. Absorbances are displayed in arbitrary units. Reproduced with permission of the Royal Society of Chemistry

The above conclusions have further been confirmed by Creighton et al. [17] performing NMA calculations with a GVFF for the sodalite lattice. No specific SiO₄ or AlO₄ modes were recognized, but a small preponderance of AlO₄ contributions to the modes in the region 800–600 cm⁻¹ was mentioned. Notably, for the intensity of the infrared-active mode at 750 cm⁻¹ the authors computed a dependence on the T-O-T angle. Similar results were obtained using a shell model and the primitive unit cell under periodic boundary conditions in calculations of the infrared and Raman spectra of zeolite Na-Y [24]. Fig. 3 shows the observed and

calculated infrared and Raman spectra in the framework region together with the IR spectra of ^{18}O -labeled Na-Y ($n_{\text{Si}}/n_{\text{Al}}=2.6$).

It can be seen that no additional bands appeared in the spectra upon isotope exchange, but some bands became slightly more structured. As expected, the bands were shifted to lower wavenumbers due to ^{18}O exchange, but to a different extent in different spectral regions. The largest downward shifts were found in the regions above 950 cm^{-1} (up to 33 cm^{-1}) and below 650 cm^{-1} (about 20 cm^{-1}), whereas bands in the spectral range $900\text{--}700\text{ cm}^{-1}$ were displaced by approximately 10 cm^{-1} only. The shifts observed upon ^{18}O exchange are well-reproduced by the simulation over the whole spectral range. In order to gain more insight into vibrational characteristics, energy distributions were calculated. Since the shell model does not imply the existence of (covalent) chemical bonds, the kinetic energy distribution (KED) was chosen. For each normal mode the participation of all kinds of atoms on the KED was computed. The results are depicted in Fig. 4 as a function of the wavenumber.

The KED of sodium ions (Fig. 4d) shows practically no contribution in the spectral range above 250 cm^{-1} , indicating that a coupling between framework and cation modes can be neglected in this spectral region. This result leads to the important conclusion that shifts in band positions in the mid-infrared upon cation exchange cannot be explained by the coupling with cations. The red-shifts experimentally observed for several framework bands especially upon solid-state ion exchange with cations of large size rather arise from an increase of the lattice parameters [117]. Oxygen atoms (Fig. 4a) generally have a high share in the KED as they represent $2/3$ of the total number of framework atoms. Maxima with more than 80% of the total kinetic energy are clearly perceptible in the range $600\text{--}200\text{ cm}^{-1}$ and above 950 cm^{-1} . This explains the large isotopic shifts observed exactly in these spectral ranges. Also, the minimum in the KED in the $900\text{--}700\text{ cm}^{-1}$ range is in good agreement with the small shift upon ^{18}O exchange in the experiment. Comparison of the kinetic energy distributions of T atoms reveals a dominance of silicon atoms above 800 cm^{-1} and a nearly equal distribution around 700 cm^{-1} . Again, the latter indicates noticeable displacements of aluminum atoms during the modes in the spectral region $800\text{--}600\text{ cm}^{-1}$. The results obtained by the shell model calculations were further compared with those obtained from calculations of potential energy distributions using a valence force field [24], and the following approximate classification of zeolite framework modes was then derived:

region	$1200\text{--}950\text{ cm}^{-1}$	ν_{as} (TOT)	stretching with dominant Si-O displacements,
region	$850\text{--}650\text{ cm}^{-1}$	$\nu_{\text{s,as}}$ (TOT)	stretching with Si-O dominance in the range $850\text{--}750\text{ cm}^{-1}$ and Al-O dominance in the range $750\text{--}650\text{ cm}^{-1}$,
region	$650\text{--}550\text{ cm}^{-1}$	ν_{s} (TOT)	stretching + δ (OTO) bending,
region	$500\text{--}420\text{ cm}^{-1}$	δ (OTO)	bending mostly in-phase with respect to TOT bridges,
region	$420\text{--}300\text{ cm}^{-1}$	δ (OTO)	bending + ν (TO) stretching, and
region	$<300\text{ cm}^{-1}$	δ (TOT)	bending and torsional modes.

The proposed assignment corresponds very well to the classification deduced by Baertsch et al. [10] from investigations of the vibrational spectra of the zeolite A framework. However, it should be noticed that the sharp division into stretch-

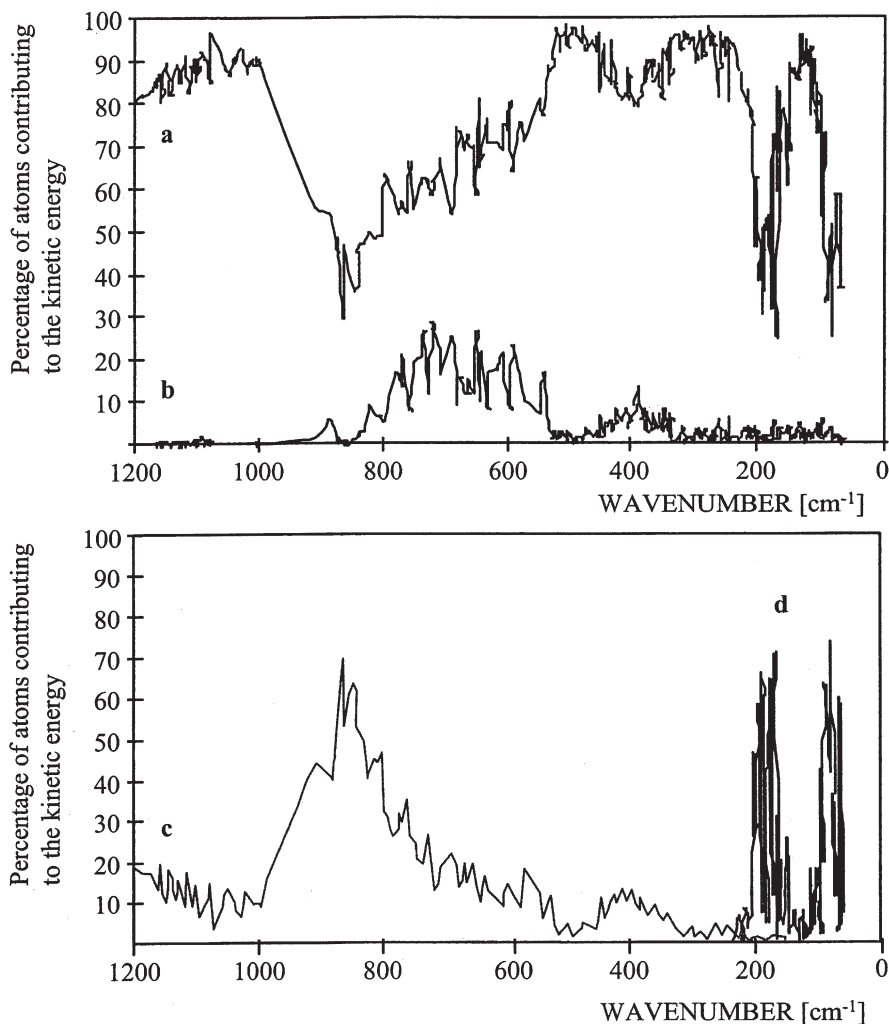


Fig. 4. Kinetic energy distribution of oxygen atoms (a), aluminum atoms (b), silicon atoms (c), and sodium atoms (d) [24]. Reproduced with permission of the Royal Society of Chemistry

ing and bending modes is a rather crude approximation for structures containing cyclic subunits in which both types of internal coordinates are always related to each other. This gives rise to complex couplings within most of the symmetric stretching and bending modes, in particular in the region below 800 cm⁻¹.

The second important aim pursued in theoretical investigations of zeolite framework dynamics was to reveal relations between characteristic spectral features and the presence of specific substructures in the lattices. The results

have recently been reviewed [64]. Therefore, we do not look at them in the same detail, but due to the relevance of this issue for the utilization of vibrational spectroscopic techniques a brief overview will be given. In one of the first studies on this topic de Man and van Santen [16] searched for correlations between ring structures and spectral bands, performing NMA calculations of clusters and periodic models. No clear correspondence between the presence of large structural units and particular bands was found. Creighton et al. [17] introduced local symmetry coordinates for four-rings and six-rings to get information about the localization of vibrations in sodalite frameworks (the ring denotation represents the number of T atoms in the ring). The calculations revealed that most of the modes involve large contributions from only a few of the symmetry coordinates. In particular, a mode at 471 cm^{-1} was characterized as an in-phase bending vibration of the four-ring which can be interpreted as a ring-breathing vibration. Nevertheless, since in the sodalite structure each bond is simultaneously common to one four-ring and two six-rings, no separation into vibrations of four-rings and six-rings was supposed. Comparable assignments of bands at about 450 cm^{-1} to four-ring opening modes were suggested in investigations of spherosiloxanes [12] and of models designed to mimic the double-four-ring unit in zeolite A [10]. The drawn conclusions are also in line with the results yielded by Iyer and Singer in calculations of sodalite [118] and zeolite A [119] using a shell model potential. The authors found that many modes are localized in the four-ring, six-ring, and double-four-ring units of the framework in close resemblance for both types of zeolites. The characteristic four-ring opening mode was calculated for zeolite A at 428 cm^{-1} [119]. In principle, the resulting forms of ring-breathing normal modes in the region around 450 cm^{-1} can also be conceived as (even more localized) $\delta(\text{OTO})$ in-phase bending modes as discussed in the assignment scheme above. Different from the methods considered so far, van de Graaf et al. [64] and Smirnov and Bougeard [120] recently examined pore-opening vibrations of ring structures in zeolites by molecular dynamics simulations. In order to extract information about ring-breathing modes from the trajectory of the unit cell, the authors introduced pore-opening time-dependent vibrational coordinates as fluctuations of the ring diameter (or ring area). The power spectrum of the coordinates was then obtained via Fourier transformation of the corresponding autocorrelation function. The results are presented for all-silica faujasite in comparison with the simulated infrared and Raman spectrum of the whole framework in Fig. 5.

The abbreviations SOD and D6R correspond to the four-rings placed in the sodalite unit and in the hexagonal prism of the faujasite structure, respectively. When looking at contributions of the ring-breathing vibrations, it seems characteristic that they participate in many normal modes in the region below 520 cm^{-1} with maxima around 510 and 100 cm^{-1} . The comparison of the power spectra with the simulated IR and Raman spectra leads to the conclusion that above 150 cm^{-1} no particular band corresponds to the four-ring pore opening mode. The next-nearest band in the IR spectrum is that at 500 cm^{-1} . However, it is well-known that nearly all zeolites show more or less intense bands in their infrared spectra in the region $550\text{--}450\text{ cm}^{-1}$,

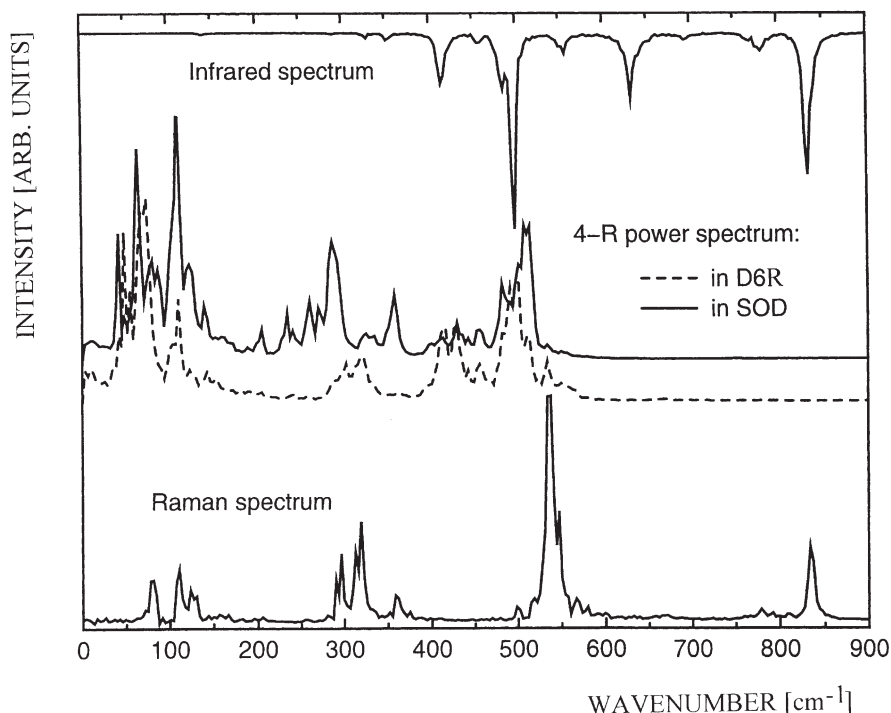


Fig. 5. Calculated power spectrum of the pore-opening vibration of four-rings (4R) in comparison with the simulated infrared and Raman spectrum of all-silica faujasite [64]. For the meaning of D6R and SOD see text

for example, even silicalite-1 and ZSM-5 – zeolites without any four-ring unit.

In summary, the unambiguous assignment of particular bands in zeolite framework spectra to specific ring or double-ring breathing modes remains open for discussion. Even though ring opening vibrations are calculated to have characteristic frequencies (slightly varying dependent on the chosen force field), the proof of the existence of their experimental counterpart is lacking and no general correlation is evident. For a more detailed discussion of this issue comparing the results of MD simulations for various zeolite frameworks with four- and six-membered ring units, the reader is referred to a recently published paper [120].

The third extraordinary challenge to assist vibrational assignments by employing theoretical approaches comprises the dynamics of extra-framework cations. The advance in this field is discussed together with experimental efforts in Sect. 5.3.

3 Spectra Evaluation

3.1 Qualitative Interpretation

In Sect. 2 it was shown that recent progress in theoretical methods and computational techniques enables us, in principle, to compute vibrational spectra of zeolitic systems. In many cases studied so far, the agreement between theoretically and experimentally obtained spectra was rather satisfying (cf., e.g., Sects. 2.5 and 5.4). Computational treatment of zeolitic systems is, however, still an expensive and time-consuming procedure, and particularly for most adsorbate/zeolite systems rarely feasible. Therefore, the qualitative interpretation of IR and Raman spectra for characterization of zeolites and, especially, adsorbate/zeolite samples is still to a large extent based on comparison with safe data obtained from related systems such as other zeolite structures or oxides, pure adsorbates, etc. Further reference is frequently made to the well-known tables of so-called group frequencies, the use of which is very popular in, e.g., spectroscopic analyses of organic compounds (cf. [121–125]). For instance, the stretching vibrations of (zeolitic hydroxy groups) OH, (ammonium) NH, (aromatic) CH, (paraffinic) CH and (carbonylic) CO groups typically give rise to absorption of IR radiation in the ranges of 3800–3500, 3400–3200, 3100–3000, 3000–2800 and 1800–1700 cm^{-1} , respectively. Additional information comes from an inspection of the range of deformation vibrations at lower wavenumbers. Similar assignments are available for many other functional groups. Deviations of the observed spectral features from those used for comparison must then tentatively be explained in view of the specific intrazeolite or adsorbate/zeolite interactions. On the other hand, shifts in the band positions upon adsorption compared to bands of the pure adsorbate frequently provide insight into the nature of host/guest interplay. Examples will be discussed in Sects. 5.5.2.1–5.5.2.8.

3.2 Quantitative Evaluation

From a correct interpretation of the IR or Raman signals one arrives at the identification of the radiation absorbing species (zeolitic OH groups, hydrogen bonds, adsorbate/zeolite complexes, etc.), i.e., one obtains information about their *nature*. However, one also might wish to determine the number of the thus-identified entities per gram or per unit cell, i.e., their *concentration*. This can be achieved through a measurement of the intensity (absorbance, A) of the respective signals. In many cases it may be sufficient to determine the relative concentration, in that one relates the actual absorbance to a standard value. For instance, one might use the ratio, $A_{\text{treat}}/A_{\text{initial}}$, of the actual absorbance of the OH group band of a particularly treated sample to that of the initial absorbance of the parent sample measured prior to the treatment as monitored via IR [126]. Another possibility is the normalization of absorbances by referencing to standard bands. Thus, Jentys et al. [127] used, for instance, the bands of lattice vibrations of

H-ZSM-5 between 2090 and 1740 cm^{-1} for normalizing the absorbances of bands of adsorbed water. If one needs absolute values, one usually uses the Lambert-Beer-Bouguer law (Eq. 24) which relates the absorbance, A , to the concentration, c ,

$$A = \epsilon_{\tilde{\nu}} c d \quad (24)$$

In Eq. (24), A stands for the absorbance, $\epsilon_{\tilde{\nu}}$ for the extinction coefficient (at a given wavenumber), c for the concentration and d for the thickness of the sample). If in transmission spectroscopy (vide infra) the spectrometer does not provide directly the absorbance of the sample but the so-called transmittance, T , then one has to convert T into A according to Eq. (25).

$$A = -\log T = \log(I_0/I)_{\tilde{\nu}} \quad (25)$$

with I_0 being the incident and I the transmitted radiation energy. In principle, Eq. (24) is valid only for dilute systems. For instance, in the case of zeolites populated with OH groups or adsorbate/zeolite systems one has to be aware of the possibility that $\epsilon_{\tilde{\nu}}$ may be dependent on the OH group concentration and adsorbate coverage, respectively.

Frequently, it is sufficient to use as a first approximation the maximal absorbance defined by Eq. (26).

$$A_{\max} = \log T^*(\tilde{\nu}_{\min}) / \log T(\tilde{\nu}_{\min}) \quad (26)$$

where $T^*(\tilde{\nu}_{\min})$ is the background (base line) transmittance and $T(\tilde{\nu}_{\min})$ the actual transmittance, both measured at the wavenumber $\tilde{\nu}_{\min}$ of minimal transmittance (cf. Fig. 6 and [128]).

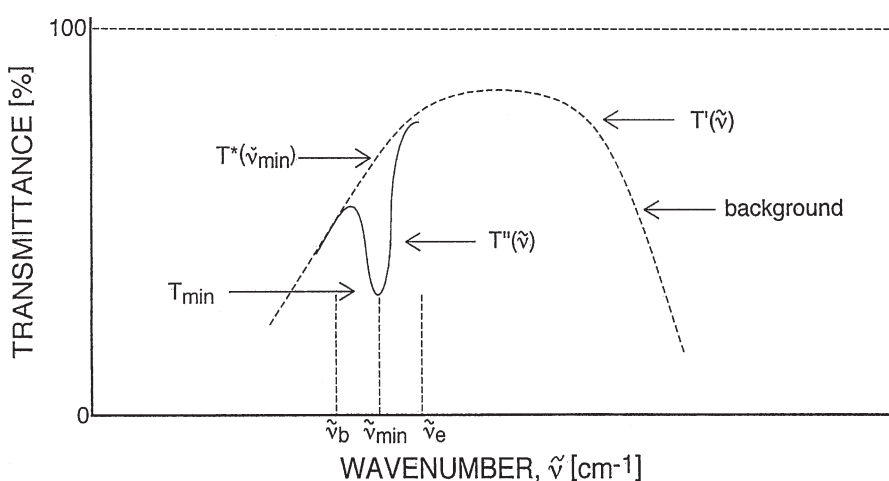


Fig. 6. Scheme for the quantitative evaluation of zeolite spectra using integrated or maximum absorbance [128]

The integral absorbance, as a more precise measure of the concentration of the absorbing species, is presented by Eq. (27).

$$A_{\text{int}} = cd \int_{\tilde{\nu}_b}^{\tilde{\nu}_e} \log [T'(\tilde{\nu})/T''(\tilde{\nu})] d\tilde{\nu} = cd \int_{\tilde{\nu}_b}^{\tilde{\nu}_e} \epsilon_{\tilde{\nu}} d\tilde{\nu} \quad (27)$$

$\tilde{\nu}_b$ and $\tilde{\nu}_e$ stand for the wavenumbers of the beginning and the end of the band, respectively, $T'(\tilde{\nu})$ and $T''(\tilde{\nu})$ for the transmittance along the base line and the band contour, respectively. Modern instrumentation usually allows routine base line determination and band integration to evaluate A_{int} . In IR and Raman spectroscopy of zeolites and adsorbate/zeolite samples, the extinction coefficient, $\epsilon_{\tilde{\nu}}$ or $\epsilon_{\tilde{\nu}}(c)$, is usually unknown. Thus, if knowledge of the absolute concentrations is required, $\epsilon_{\tilde{\nu}}$ has to be determined in separate experiments (cf., e.g., [129–135,]). In such experiments, the absorbance has to be measured of zeolite samples covered with a known number of functional surface groups or loaded with well-defined amounts of adsorbate in order to obtain calibration curves, A_{int} vs. c . An example is shown in Fig. 7.

So far, such determinations of $\epsilon_{\tilde{\nu}}$ were carried out for a limited number of systems (cf., e.g., [130–135, 140, 141, 143, 144]). Examples of results are collected in Table 2. (Note that, as indicated in the table, most of the extinction coefficients

are given as “apparent integrated absorption intensity”, $\int_{\tilde{\nu}_b}^{\tilde{\nu}_e} \epsilon_{\tilde{\nu}} d\tilde{\nu}$, in $\text{cm } \mu\text{mol}^{-1}$

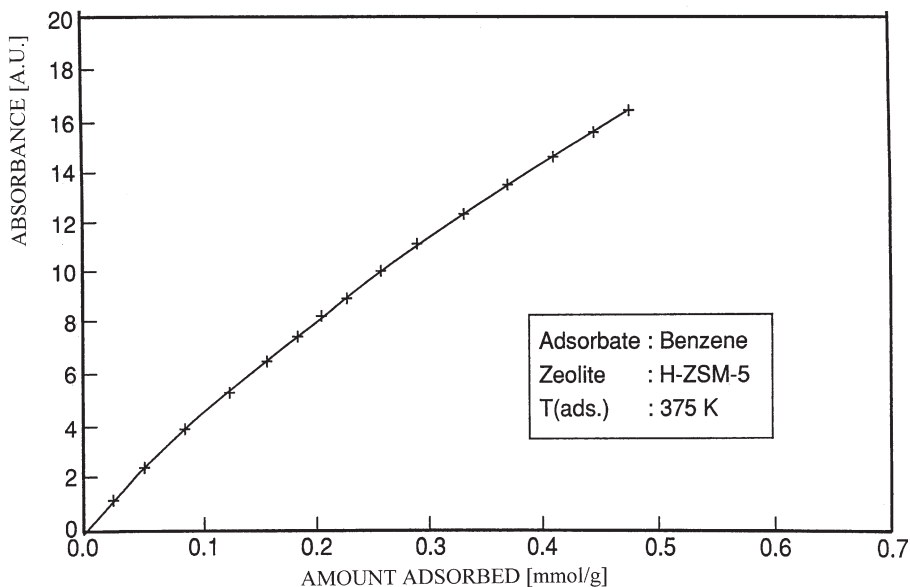


Fig. 7. Calibration curve for the extinction coefficient of benzene sorbed into zeolite H-ZSM-5; integrated absorbance of the typical benzene band at 1478 cm^{-1} vs. the barometrically measured amount adsorbed [132]

Table 2. Experimentally derived IR extinction coefficients^a of surface species of zeolites and adsorbates on zeolites

Species	Zeolite, adsorbent	Extinction coefficients ^{a,b} (cm ² μmol ⁻¹) ^a or (cm ² μmol ⁻¹) ^b	Remarks	Band (cm ⁻¹)	References
Hydroxyl group	H-Y	3.1	HF Brønsted acid site,	3625	[144]
		5.3	Y-type zeolite	3650	[130]
		7.5		3635	[131]
		12.2	HF Brønsted acid site,	3640	[379]
		68.2 ^b	X- and Y-type zeolite	3640	[382]
Hydroxyl group	H-Y	3.1	LF Brønsted acid site,	3550	[144]
		3.5	Y-type zeolite	3550	[130]
		5.6		3547	[131]
		19.9		3550	[379]
		32.6 ^b	Y-type zeolite	3550	[382]
Hydroxyl group	H-Y ^c H-X ^e H-MOR H-MOR H-MOR H-MOR H-FER H-MFI H-Y	40.3 ^b	X-type zeolite	3550	[382]
		8.5	Brønsted acid sites in the main channels	3612	[140]
		4.25 ^c		3605	[144]
		3.5		3602	[134]
		1.55	Brønsted acid sites in the side pockets	3584	[134]
		4.05	Brønsted acid sites	3604	[133]
		3.7	Brønsted acid sites	3605	[144]
		0.147 ^b	Ammonia bound to Brønsted acid sites, NH ₄ ⁺	1460	[141]
		0.022 ^b	Ammonia bound to Lewis acid sites	1622	[141]
		1.47	Ammonia bound to Brønsted acid sites, NH ₄ ⁺	1450	[137]
Ammonia (NH ₃ →L) Ammonia (NH ₃ →B)	H-[Al]MCM-41 H-[Al]MCM-41	1.98	Ammonia bound to Lewis acid sites	1620	[137]
		2.7	Carbon monoxide bound to HF (3612 cm ⁻¹) and LF (3585 cm ⁻¹) hydroxy groups	2177 (HF) 2169 (LF)	[140]

Table 2 (continued)

Species	Zeolite, adsorbent	Extinction coefficients ^{a,b} ($\text{cm}^2 \text{mmol}^{-1}$) ^a or ($\text{cm}^2 \text{mmol}^{-1}$) ^b	Remarks	Band (cm^{-1})	References
Pyridine (Py→B)	H-Y	3.0	Pyridine bound to Brønsted acid sites, (PyH ⁺)	1540	[379]
	H-Y	1.8		1542	[131]
	H-Y	1.3		1540	[135]
	H-Y	0.059 ^b		1545	[707]
	H-MOR	1.8		1540	[140]
	H-MAZ	1.13		1540	[138]
	H-MFI	2–4.3 ^d		1545	[516]
	H-MFI	1.3		1540	[135]
	H-MEL	2.3		1545	[516]
	Alumina	3.3		1450	[379]
Pyridine (Py→L)	Alumina	1.5	Pyridine bound to Lewis acid sites	1450	[135]
	H-Y	1.5		1450	[135]
	H-MFI	1.5		1450	[135]
	H-MOR	1.5		1450	[140]
	H-MAZ	1.28		1450	[138]
	H-ZSM-5	0.3		1478	[132]
	H-ZSM-5	0.4		1496	[132]
	H-FER	2.05		2297	[133]
	H-FER	3.62		($\nu_{\text{C}=\text{N}}$) 2325	[133]
	H-FER			2310	
Coke	H-Y	1.03	$\nu_{\text{as}}[\text{CH}_3]$ $\nu_{\text{s}}[\text{CH}_3]$ $\nu[\text{CH}_2]$	($\nu_{\text{C}=\text{N}}$) 2957	[143]
		0.63		2870	
		0.65		2930	

^a Apparent integrated absorption intensity, $\int \epsilon_{\nu} d\nu$, according to Eq. (27); the respective values are *not* indicated in Table 2 by superscript “a”.

^b note: here, the extinction coefficient (in $\text{cm}^2 \text{mmol}^{-1}$) is defined as according to Eq. (24), $A = \epsilon_{\nu} \cdot c \cdot d$, the slope of the absorbance of the respective band vs. the adsorbate concentration (in $\mu\text{mol cm}^{-2}$); the respective values *are* indicated in Table 2 by superscript “b”.

^c Depending on the temperature of activation and the $n_{\text{Si}}/n_{\text{Al}}$ ratio; band absorbance vs. the adsorbate concentration (in $\mu\text{mol cm}^{-2}$).

^d Depending on the $n_{\text{Si}}/n_{\text{Al}}$ ratio.

^e Various degrees of exchange, X: 40 and 75%; Y: 50 and 90%.

according to Eq. (27); some, however, were determined according to Eq. (24) and are given in $\text{cm}^2 \mu\text{mol}^{-1}$. In some cases, the agreement between the results of different authors is satisfactory, however, more frequently significant deviations occurred. Therefore, it is advisable not to adopt literature data but to rely on one's own data obtained with one's own charge of samples, instrumentation and technique. With respect to quantitative spectroscopic characterization of zeolitic systems, MAS NMR (cf. Chapter 2 of the present volume) is usually in a better situation than IR, because the former technique provides more directly quantitative results in that only a comparison with a standard is required.

4 Experimental Techniques

In this section, experimental techniques for the characterization of zeolites and adsorbate/zeolite samples via IR spectroscopy, Raman scattering and inelastic neutron scattering will be briefly discussed. For more detailed information, the reader is referred to Refs. [145–150].

4.1 Transmission IR Spectroscopy

IR radiation energy transmitted through a zeolite sample is measured by infrared spectrometers as a function of the wavenumber, $\tilde{\nu}$, (in cm^{-1}) or wavelength, λ (in μm), where $\tilde{\nu} = 10^4/\lambda$ and $\tilde{\nu} = c_0 \nu$, with c_0 representing the velocity of light. (Even though not correct in a strict sense, in reports on IR studies, instead of the term “wavenumber, $\tilde{\nu}$,” simply the term “frequency, ν ” is often used; usually, however, this is not misleading, since the meaning is clear from the context).

Two principally different types of IR spectrometers are known, viz., dispersive and non-dispersive (Fourier transform) instruments. The earlier type of dispersive spectrometers uses prisms or gratings which operate as monochromators to select, during a rather slow scan, successively radiation of defined frequencies or frequency intervals from the continuous spectrum emitted from a source such as a globar or Nernst glower. The more recent type of Fourier transform spectrometers, which have apparently completely replaced the dispersive instruments, provides immediately the whole spectrum via a process of interference (cf. Fig. 8). Thus, first a complex interferogram is generated by superimposition of the radiation energies of all partial energy fluxes corresponding to the various wavelengths of the polychromatic IR light transmitted (and partially absorbed) through the sample (cf. the schematic representation in Fig. 8 and more detailed descriptions in Refs. [145, 149, 150]). Using a mathematical procedure called Fourier transformation, the computer of the instrument then derives from the interferogram the spectrum in the traditional form, i.e., a plot of the transmitted intensity as a function of the wavenumber.

The Fourier transform spectrometers have several advantages compared to the dispersive instruments. They (i) exhibit a high signal-to-noise (S/N) ratio (multiplex or Fellgett's advantage); (ii) provide a greater light throughput (Jacquinot's

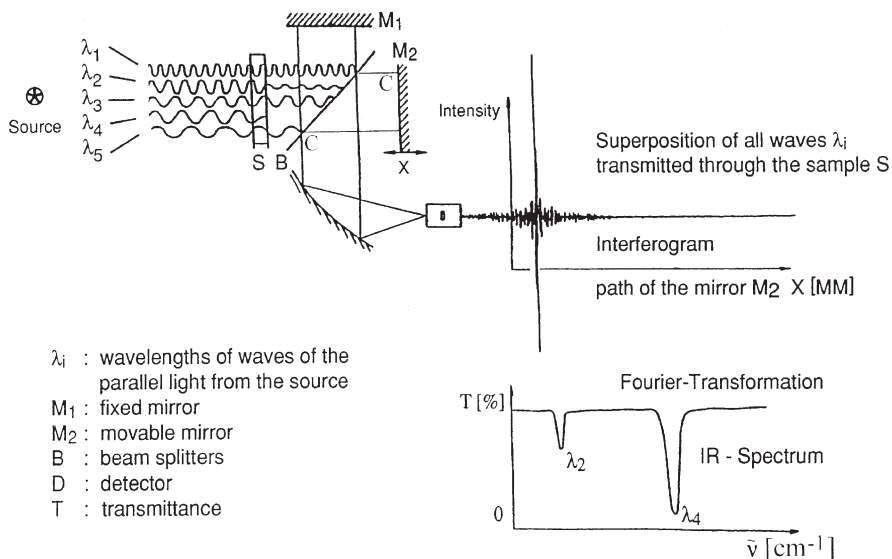


Fig. 8. Scheme of the principal design of a Fourier transform infrared spectrometer (FTIR) [150]

advantage), advantageous especially for measurements in the far-infrared region; (iii) show often a better resolution, (iv) are characterized by a higher wavenumber accuracy (Connes' advantage) and (v) allow a very rapid scanning of the spectra. The latter property is especially valuable for monitoring fast processes via IR (e.g., diffusions, reactions; cf. also Sects. 5.6.3, 5.6.4).

A great variety of cells appropriate for transmission IR spectroscopy on zeolites and related materials has been developed. Some of them are described in Refs. [151–159], among them also flow-through reactor cells suitable for in-situ investigations of diffusion and catalytic processes and low temperature adsorption [153–157]. Here, we reproduce just a scheme of one of them (Fig. 9, cf. [158, 159]), which has been successfully employed in many IR studies by a number of laboratories.

A very interesting modification of the conventional transmission IR spectroscopy technique is the so-called IR microscopy. In fact, it consists of a combination of an FTIR spectrometer with a light microscope, which renders possible the adjustment of a very small area of the sample with respect to the IR beam, so that IR spectra can be obtained from single crystals or very small powdered (polycrystalline) samples. In fact, for experiments with the "IR microscope" a particular cell is required with appropriately small dimensions and a heating device. Moreover, it should be possible to operate the cell under high vacuum and especially as a flow-through microreactor. The spatial resolution is, however, diffraction-limited. Diffraction effects are particularly large if the size of the area under study is approximately equal to the IR wavelength employed. This is known as the optical limit of "IR microscopy". A suitable cell was designed by Mueller et al. and described in Ref. [157] (see also Sects. 5.6.3 and 5.6.4).

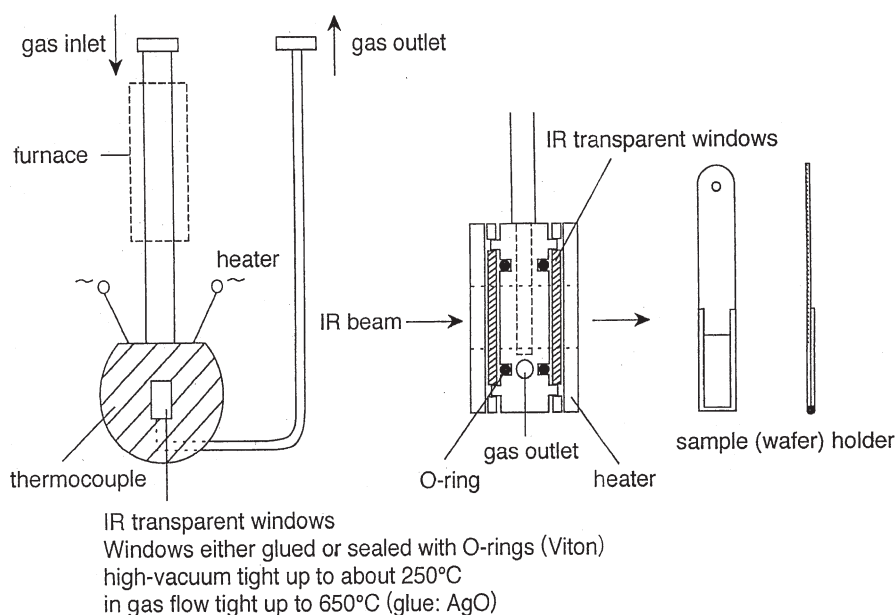


Fig. 9. Infrared flow-reactor cell for in-situ measurements of, e.g., activation, reaction and diffusion [149, 158]

In transmission IR experiments, single crystals, pressed powder wafers or small powder samples embedded in pressed KBr or CsI pellets are used. For a possible detrimental effect of the pressure required to prepare thin IR transparent wafers or KBr pellets etc. compare the following Sect. 4.2.

Transmission FTIR spectroscopy may be combined with a number of other experimental techniques such as, e.g., temperature-programmed reduction (TPR), oxidation (TPO) or desorption (TPD) of probes monitored by, e.g., frequency response (FR) spectroscopy (see also Sect. 4.2), electron spin resonance (ESR) spectroscopy, etc.

4.2

Diffuse Reflectance IR (Fourier Transform) Spectroscopy (DRIFT)

Diffuse reflectance spectroscopy (DRS) has been frequently employed in UV-Vis spectroscopy of zeolites (cf. Volume 4, Chapter 4 of the present series). More recently, it became also popular in IR investigations (cf., e.g., [160, 161]). The DRIFT technique is advantageous because it is successfully applicable not only in the mid infrared but also in the near infrared (NIR) region of $4000\text{--}10,000\text{ cm}^{-1}$, where the transmission technique usually fails because of severe scattering through the absorbent particles. The NIR range, however, is very important with respect to the study of overtone and combination modes of vibrations. Moreover, diffuse reflectance IR experiments can be carried out not only with pressed wafers as in transmission spectroscopy, but also with zeolite pow-

ders. This is an important advantage, not only since thin wafers for transmission IR spectroscopy are sometimes difficult to prepare but, above all, because a high pressure as applied for producing wafers or KBr pellets may partly or even entirely destroy the structure of non-rigid porous materials. Thus, Geidel and Lechert [162] provided unambiguous evidence for the complete destruction of mesoporous structures (MCM-41) under a pressure usually used for preparation of IR transparent wafers (about $3 \times 10^7 \text{ Nm}^{-2}$), in that they compared nitrogen sorption isotherms and distributions of pore radii of pressed and unpressed MCM-41. As a consequence of their results, Geidel and Lechert used exclusively DRIFT spectra to characterize the mesoporous samples and advised against using pressed samples of mesoporous materials for IR inspection (cf., e.g., Kosslick et al. [163], Hunger et al. [164], Katovic et al. [165]).

However, there is also an important drawback of DRIFT: Quantitative measurements are hardly possible since, different from the situation in UV-Vis DRS, no general standard sample is available. However, some researchers reported successful quantitative DRS measurements in the IR region (cf. [166–169]) of adsorbates on silica-alumina.

DRIFT spectra are displayed according to the Schuster-Kubelka-Munk remission function, Eq. (28):

$$F(R_\infty) = K/S = (1 - R_\infty)^2 / 2 R_\infty \quad (28)$$

where R_∞ stands for the reflectance of a very thick sample, i.e., a sample which does not exhibit any background reflectance [170–173]; K and S are parameters related to absorption and scattering of the sample, respectively. While K is dependent on the wavelength of the IR radiation, S is basically not. Thus, we can write

$$\log F(R_\infty) = \log K(\lambda) - \log S = \log K(\lambda) - \text{const} \quad (29)$$

and $\log F(R_\infty)$ describes the energy of absorption as a function of the wavelength. Insofar, a plot of $F(R_\infty)$ vs. the wavelength (or wavenumber) corresponds to the transmission spectrum of the investigated sample.

Accessories necessary for DRIFT measurements are described in the literature and in part are commercially available [174–176]). However, reflectance equipment may be also conveniently made in the laboratory using commercial lenses and mirrors [177]. An interesting new combination of DRIFT spectroscopy with the frequency response technique was recently developed and tested by Harkness et al. [178]. This enables one to measure simultaneously the dynamic responses of both the gas and adsorbate, which should be of great potential for the study of heterogeneous catalysis. A cell for fast response DRIFT spectroscopy is described in Ref. [178].

4.3

Photoacoustic IR Spectroscopy (PAS)

Photoacoustic IR spectroscopy is particularly recommended for investigation of opaque samples, i.e., samples showing very low transmittance. This technique is

based on the process of transformation of absorbed radiation energy into heat, occurring via radiationless deactivation of the previously excited absorbing species [179, 180]. The thus-produced heat diffuses to the surface of the sample which interacts with a filler gas and affects the gas pressure. The resulting variation of the pressure as a function of the wavelength of the absorbed monochromatized radiation is transformed into a signal using a microphone-like detector. In order to avoid disturbances by pressure changes due to effects other than radiation absorption, the intensity of the incident light is modulated by a chopper and amplified by a phase-sensitive amplifier. More details of instrumentation and procedures of photoacoustic spectroscopy are provided in, e.g., Ref. [181].

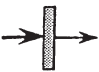



4.4

Fourier Transform Infrared Emission Spectroscopy (FT-IRES)

In an interesting article by Sullivan et al. [182], different IR spectroscopic techniques (except photoacoustic IR spectroscopy) were compared (cf. Table 3).

There was also described and discussed the relatively new Fourier transform infrared emission spectroscopy (IRES), its principle, an appropriate FT-IRES setup and applications. FT-IRES is unique in that it does not require an external radiation source, because the sample itself is the source. The radiation emitted from the sample is collected and sent to the detector. The ratio of the sample signal to that from a black body source represents the spectrum. However, appli-

Table 3. A comparison of infrared spectroscopic techniques for surface analysis (adopted from Ref. [182])

Method	Transmission	Diffuse reflectance	Reflection – absorption	Emission
				
Samples	thin wafers single crystals	powders	metal foils or	metal powders
Range [cm ⁻¹]	4000–1000	8000–1000 400–<10	4000–<10	2500–ca. 100 at 475 K (dependent on T)
Advantages	simple well-proven	surface sensitivity gas-solid contact less scattering losses	possibility of using metals	sample versatility spatial resolution
Dis-advantages	limited to semi-transparent materials, pressing of wafers required	lower re-producibility dilution	smooth samples required long signal pathway	low signal to noise ratio background radiation

cations in zeolite research are, so far, rather scarce. The above work provides results obtained with a ZSM-5 sample ($n_{\text{Si}}/n_{\text{Al}}=300$).

4.5

Raman Spectroscopy

In Raman spectroscopy (cf., e.g., [183–187]), the straylight spectrum is recorded of a sample which is irradiated with monochromatic light (produced, e.g., by a laser). A schematic representation of the Raman scattering experiment is shown in Fig. 10.

The spectrum of the strayed light contains, besides the signal of the exciting light at $\tilde{\nu}_0$, weaker so-called Raman lines appearing at wavenumbers $\tilde{\nu}_{\text{Ra}} = \tilde{\nu}_0 - \tilde{\nu}_s$ (Stokes lines, red-shifted) and (with even lower intensities) $\tilde{\nu}_{\text{Ra}} = \tilde{\nu}_0 + \tilde{\nu}_s$ (anti-Stokes lines, blue-shifted). They result from vibrations and rotations of the scattering species. Stokes lines in the Raman spectrum are due to those species which, after excitation, do not return into the ground state but into a vibration state of higher energy level. Anti-Stokes lines originate from species which were in a thermally excited vibration state when interacting with the incident radiation of wavenumber $\tilde{\nu}_0$ and then returned into the ground state. Raman rotation lines usually occur in the Raman spectra of gases causing the fine structure of the spectra. The rotational shifts are much smaller than those in which vibrations are involved.

In fact, the experimental pioneering work of Raman spectroscopy in zeolite research, viz. of hydrated microporous materials, was published by Angell [187] as early as 1973. Since that time the interest in utilizing this technique for mole-

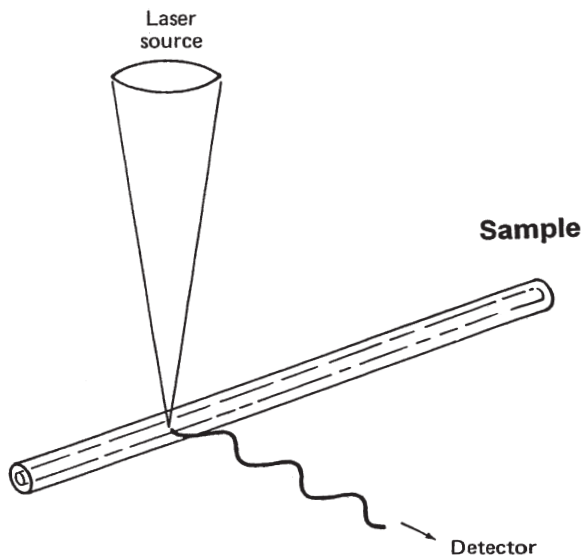


Fig. 10. Schematic representation of the Raman scattering experiment (adopted from [186])

cular sieve characterization has been growing, but nevertheless Raman spectroscopy has, compared to IR spectroscopy, played only a minor role in zeolite research. The probable reasons were (i) the intense Raman background [188, 189] and/or (ii) severe fluorescence problems under laser excitation in the visible region [190]. Several attempts have been made to “burn off” the fluorescence, for example, by high-temperature treatment under oxygen, but a prerequisite for a substantial progress in this field was the development of the near-infrared Fourier transform (NIR-FT) and ultraviolet (UV-FT) Raman techniques [191, 192]. These Raman techniques offer two substantial advantages. First, the fluorescence arising from impurities can be avoided by excitation with lasers emitting radiation in the near-infrared or ultraviolet range. Secondly, the FT technique facilitates a rapid accumulation of spectra, in particular useful if only weak scattering processes occur as in the case of zeolite frameworks. Today, Raman scattering provides a very valuable alternative or additional technique with respect to IR spectroscopy, which is still extensively used in zeolite research (cf., e.g., the review article by Knops-Gerrits et al. [193]).

There are, indeed, several convincing reasons to choose Raman spectroscopy for special fields of molecular sieve science. The principal difference between IR and Raman spectroscopy is that modes are IR-active if there are changes in the dipole moment as the vibration proceeds, whereas the Raman activity requires a change of the polarizability. Hence, different selection rules apply. If modes are both IR- and Raman-active, there are usually large differences in intensities between the corresponding bands in the two spectra. For these reasons, IR and Raman spectra provide complementary rather than redundant information, and it is desirable to use the two techniques in combination. The second fundamental difference between the two complementary techniques is that the Raman effect originates from a scattering rather than from an absorption process (*vide supra*). Framework vibrations of zeolites are generally characterized by low-scattering cross sections, and this property may be criticized as making Raman spectroscopy unsuitable for zeolite research. On the other hand, organic molecules, usually being strong scatterers, give rise to intense Raman spectra. This feature makes Raman spectroscopy a powerful tool for investigations of adsorbed molecules and templates. In the Raman spectra of sorbed systems, the contribution of the host lattice is apparently eliminated giving access to modes of the guest molecule normally hidden by the strong framework absorption in the IR spectra. Moreover, for guest species at low coverage the sensitivity can be considerably enhanced by resonance Raman spectroscopy which uses an excitation wavelength coinciding with an electronic transition of the molecule or by surface-enhanced Raman scattering. Gas phase Raman frequencies due to bonds, which may typically occur in adsorbate species, are collected in Table 4.

As large single crystals are frequently unavailable for synthetic zeolites, most of the Raman spectra have been taken from powdered samples without polarization. Minimum sample sizes of about 1 mm are required for conventional Raman techniques.

One more advantage of Raman spectroscopy is due to the fact that the Raman spectrum of water exhibits only a few signals of low intensity. Thus, careful dehydration of zeolites, which is crucial in many IR experiments, does not play the

Table 4. Gas phase Raman frequencies of selected bonds of possible adsorbates on zeolites

Bond	$\tilde{\nu}$ (cm ⁻¹)	Bond	$\tilde{\nu}$ (cm ⁻¹)	Bond	$\tilde{\nu}$ (cm ⁻¹)	Bond	$\tilde{\nu}$ (cm ⁻¹)
C–C	800–860	C–O	820–880	C–N	880–930	C–H aliphatic	2930
C=C	1600–1650	C=O	1710–1750	C=N	1650	C–H aromatic	3050
C≡C	2100–2250	C≡O	2160	C≡N	2150	–NO ₂	1310

same significant role in Raman spectroscopy. Exceptions occur, of course, when not only the pure zeolite but also adsorbed species should be studied: in such a case, pre-adsorbed H₂O molecules possibly poison the respective zeolitic adsorption sites and, thus, disturb the Raman experiment. Furthermore, Raman spectra may be obtained from samples enclosed in cells made from glass.

However, a detailed discussion of the progress in Raman studies of adsorbed molecules is beyond the scope of this chapter, and we therefore refer to previous extended reviews [194, 195]. In subsequent sections we will focus on some selected studies dealing with Raman spectroscopy. Fundamentals of Raman spectroscopy especially in surface research including zeolites are treated, e.g., in Refs. [183, 185]. Examples of application of Raman spectroscopy in zeolite research are provided, for instance, in Sects. 5.2 (frameworks), 5.3 (extra-framework cations), 5.5.2.7 (adsorption of complex molecules) and 5.6.2 (zeolite synthesis and crystallization).

4.6

Inelastic Neutron Scattering Spectroscopy (INS)

Unlike the scattering of electromagnetic radiation, neutron scattering can either be a coherent or an incoherent process, depending on the nature of the nuclei. While for almost all the atoms coherent scattering is dominant, neutron scattering by hydrogen atoms is predominantly incoherent due to spin effects. This means that, when utilizing neutrons in structural analysis, deuterated samples are preferable, whereas hydrogen or hydrogen-containing probes are best suited for dynamic measurements. In principle, neutron scattering is due to interactions with all degrees of freedom. The rotational and translational dynamics of molecules can be studied by incoherent quasielastic neutron scattering (IQNS), while inelastic neutron scattering (INS) gives information about vibrational modes (for typical applications in vibrational spectroscopy of molecules see, e.g., [196]). The application of various neutron-based techniques in zeolite research has convincingly been summarized in some reviews [197–199], and only some aspects of INS spectroscopy will be presented here.

Whilst with techniques of optical spectroscopies the dynamics of nuclei is monitored indirectly by changes of the electron distribution during the normal mode (reflected via changes of dipole moments or polarizabilities), the inelastic neutron scattering follows the nuclear motion directly. As com-

pared with optical spectroscopic methods, the INS technique provides several advantages.

- (1) INS is not governed by any selection rules, thus giving access to modes which are forbidden by symmetry in the optical spectra.
- (2) The proton incoherent cross-section is more than 10 times that of any other nucleus. Consequently, vibrational modes involving hydrogen displacements give rise to INS bands with much higher intensities than those of other modes. This effect is known as the so-called “hydrogen selection rule” of INS, but it should be treated with some caution for strongly bonded hydrogen atoms which “follow” the motions of their next-nearest neighbor atoms.
- (3) Modes at lower wavenumbers give more intense bands than modes in the high-frequency region. This makes INS useful for identifying vibrations in the energy range below 600 cm^{-1} which is often difficult to obtain by optical spectroscopies.
- (4) Due to the good penetration of neutrons into most materials, INS is well-suited to investigate adsorbed and intercalated species.

Of course, some problems in handling INS have to be mentioned as well.

- (a) There are only a few spectrometers in the world which are able to produce spectra with a resolution comparable to that of a routine infrared or Raman spectrometer.
- (b) In order to get reasonable signals, several grams of the sample are needed. A good-quality spectrum can be recorded if up to 25% of the incident beam is scattered, which often requires large amounts (20–30 g) of zeolite powder [198].
- (c) INS spectra are complicated by overtone and combination bands which are more intense than in the corresponding optical spectra. This leads to additional difficulties in the interpretation of INS spectra [200]. To reduce the multiphonon contributions, the samples are usually cooled to liquid-helium temperature.

5

Information Available from IR, Raman and Inelastic Neutron Scattering Spectroscopy

5.1

Introductory Remarks

Early applications of IR spectroscopy in zeolite research go back to studies by Szymanski et al. [201], Bertsch and Habgood [202], Tsitsishvili [203], Watanabe and Habgood [204] and especially the pioneering works of Uytterhoeven, Christner and Hall [205] and Cant and Hall [206] who, in particular, investigated the formation of OH groups on the external and internal surface of Y-type zeolites as, somewhat later, Ward [207] also did. Hall's group also studied the adsorption of small molecules such as ammonia [205] and ethylene [208–210] and employed pyridine as a probe to discriminate Brønsted and Lewis acid sites (cf.

[208, 210]; see also Sects. 5.3 and 5.4). These latter studies profited from earlier ones by Richardson and Benson [211] and Parry [212] on amorphous silica-alumina. For a long time, investigation of hydroxy groups and similar functional groups attached to zeolite frameworks or extra-framework species in zeolitic void volumes remained the domain of IR spectroscopy. Similarly, acidity of and adsorption onto zeolites were extensively studied with small molecules such as H₂O on X-type zeolites [202] or K-L [203], NH₃ [205], CO [213], CO₂ [202, 214–216], diatomic molecules at low temperatures [214–217], amines [218], paraffinic hydrocarbons [219, 220], boranes [221], nitriles [222], etc. as adsorbates (see also Sect. 5.5). These studies were frequently closely related to problems of catalysis on and gas separation through zeolites. Later on, IR spectroscopic investigations of zeolite systems were extended to more complex adsorbate (guest)/zeolite (host) systems (cf., e.g., Sect. 5.5.2.7).

It is worthy to note that IR spectroscopy was also relatively early employed to identify and investigate framework vibrations (vide supra, cf. [112, 114] and Sect. 5.2). In these experiments, usually the so-called KBr-technique was used (cf. Sects. 2.5, 4.2). Relationships between the vibration modes and, e.g., the $n_{\text{Si}}/n_{\text{Al}}$ ratio of the zeolite framework were disclosed and discussed.

Furthermore, with the advent of improved instrumentation and experimental techniques interesting in-situ investigations became possible which were related, for instance, to the synthesis of and heterogeneous catalysis on zeolites, catalyst deactivation, diffusion or solid-state ion exchange as well as other post-synthesis modifications. Combinations of IR spectroscopy with various characterization techniques such as, e.g., temperature-programmed desorption of probe molecules (TPD/IR, cf. [223, 224]), electron spin resonance spectroscopy (ESR/IR, cf. [225, 226]), UV-Vis spectroscopy [227, 228], etc. were developed.

Application of Raman spectroscopy to zeolite research was, for a long time, hampered by severe problems due to fluorescence phenomena. These could be overcome during the recent past (cf. Sect. 4.4 and [229]). Meanwhile, IR and Raman results of zeolite investigation, as reported in the literature are so numerous that an exhaustive overview would be beyond the frame of the present chapter {compare, therefore, also earlier reviews such as those by Yates [230], Ward [231], Baker et al. [232] (especially for Fourier transform far-infrared spectroscopy), Foerster [233] and Karge et al. [234]}. However, in the following subsections many examples will be provided which are meant to demonstrate the high potential of IR, Raman spectroscopy and INS for the characterization of zeolites and related systems.

5.2

Framework Modes

5.2.1

Pioneering Work

As mentioned already in Sect. 2.5, in 1971 Flanigen et al. [112] presented a study on IR bands observed with pure zeolite powders embedded in KBr or CsI pellets. Spectra were obtained in the wavenumber range below 1200 cm⁻¹ (or in some

cases below 1300 cm^{-1}), where the transmittance of the zeolite materials is already rather low. The results presented in Refs. [112, 114] were frequently used in the practice of zeolite characterization, especially the reported correlations between band positions and $n_{\text{Si}}/n_{\text{Al}}$ ratios of the zeolite samples. Therefore, this study by Flanigen et al. [112] on framework vibrations will be briefly reviewed here. From a theoretical point of view, the authors' interpretation of their findings is, however, questionable, as discussed in Sect. 2.5.

Flanigen et al. [112], published spectra of a series of zeolites, viz., X, Y (FAU), A (LTA), gismondine, P1 (GIS), mordenite (MOR), L (LTL), Omega (MAZ), and zeolites W {philillipsite-related, D, G, R, S, T (for the three-letter acronyms, cf. [235] and for the other abbreviations [236])}. They interpreted the framework vibration bands in terms of internal and external lattice vibration modes.

Internal modes were visualized as related to T-O vibrations (T=Si or Al) of isolated $\text{TO}_{4/2}$ tetrahedra of the framework, whereas external modes were seen as vibrations involving links of adjacent tetrahedra. Regarding this classification of zeolite framework vibrations, there exists, besides the theoretical problems (vide supra), a minor problem of terminology which is, nevertheless, worth mentioning: In solid-state vibration spectroscopy, the term "external" vibration is used to designate translational (and/or rotational or librational) modes of, e.g., cation vibrations against the framework (cf. Sect. 5.3), in contrast to "internal" vibrations which originate from (predominantly) covalent structures such as, for instance, bridging OH groups. Therefore, van Santen and co-workers [237] proposed, with respect to framework vibrations of zeolites, to replace the terms internal and external by "intra-tetrahedral" and "inter-tetrahedral" vibrations, respectively. This terminology will be used in what follows.

The suggestions of band assignments to framework vibrations advanced in Refs. [112, 114] were based on earlier IR investigations of silica and non-zeolitic aluminosilicate frameworks [238, 239]. These assignments are illustrated in Fig. 11.

The two main categories of bands observed in mid infrared, i.e., intra-tetrahedral and inter-tetrahedral vibrations, are indicated by (1) solid and (2) broken lines, respectively.

The most prominent bands ascribed to intra-tetrahedral modes were assumed to occur in the ranges from (i_1) 1250 to 950 cm^{-1} , (i_2) 790 to 650 cm^{-1} , and (i_3) 500 to 420 cm^{-1} . Proposed assignments were as follows (cf. also Table 1; T=framework cation, e.g., Si or Al):

- (i_1) asymmetric stretching modes, $\nu_{\text{as}} (\leftarrow \text{OT} \rightarrow \leftarrow \text{O})$;
- (i_2) symmetric stretching modes, $\nu_{\text{s}} (\leftarrow \text{OTO} \rightarrow)$, and
- (i_3) bending modes, $\delta (\text{O-T-O})$.

In a similar way, bands between 650 and 500 cm^{-1} were attributed to inter-tetrahedral vibrations of double four-membered rings (D4R, as, e.g., in A-type zeolites) or double six-membered rings (D6R as, e.g., in X- and Y-type faujasite). Again, it must be stressed that the assignment of inter-tetrahedral modes to ring vibrations (e_1, e_2 ; see Table 1) soon became a matter of debate and deviating interpretations were advanced (cf. Sect. 2.5 and Refs. [113, 240]). The intra-tetrahedral vibrations were shown to be essentially structure-insensitive. This became evi-

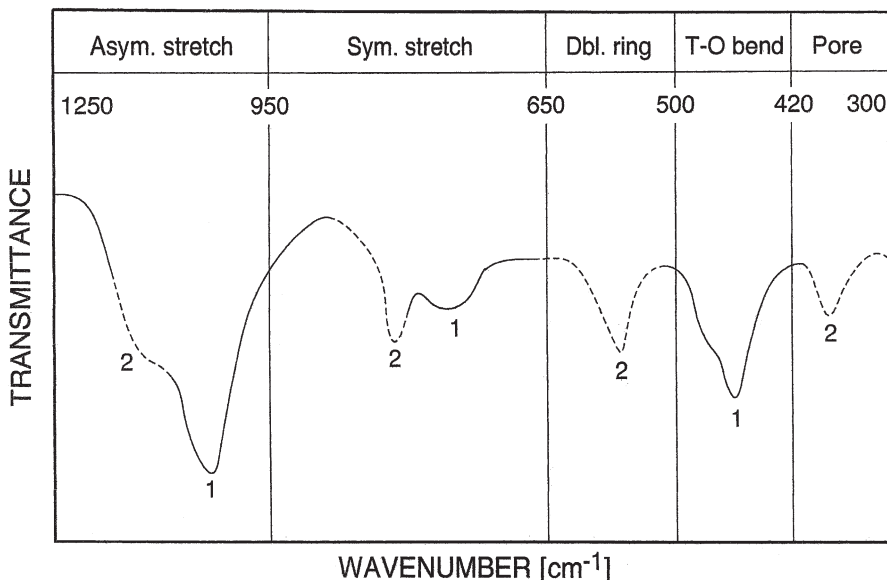


Fig. 11. Zeolite framework vibrations according to the interpretation of Flanigen et al. (adopted from [112]); 1, solid lines: intra-tetrahedral vibrations; 2, broken lines: inter-tetrahedral vibrations

dent when the spectral features of significantly different structures were compared. Moreover, the structure-insensitivity of intra-tetrahedral vibrations was, *inter alia*, confirmed by the observation that the respective bands, (i_1 – i_3 ; cf. Table 1) were little affected when the zeolite structure was progressively destroyed through thermal treatment. In contrast, bands originating from inter-tetrahedral modes were, by the same treatment, weakened and finally disappeared upon collapse of the structure.

As can be realized from Fig. 12, the wavenumbers of, e.g., the asymmetric (ν_{as}) and symmetric (ν_s) stretching modes were found to be linearly correlated to the mole fraction, $n_{Al}/(n_{Si}+n_{Al})$, of the frameworks of a homologous series of faujasite-type zeolites.

In fact, Beyer and colleagues [241, 242] as well as many other researchers used such relationships to determine the n_{Si}/n_{Al} ratio in zeolite frameworks (*vide infra*). This was particularly valuable before the ^{29}Si MAS NMR technique (cf. [243–245] and Chapter 3 of this volume) became generally accessible.

In the following paragraphs, more recent contributions are arranged with respect to the IR and Raman spectroscopic framework investigations of the various molecular sieves (Sect. 5.2.2), the effects on framework vibrations by cation-loading (Sect. 5.2.3), adsorption (Sect. 5.2.4), dealumination or n_{Si}/n_{Al} ratio (Sect. 5.2.5) and isomorphous substitution (Sect. 5.2.6). Furthermore, IR and Raman spectroscopic investigations were also conducted to monitor the product crystallinity during and/or after zeolite synthesis and crystallization (cf. Sect. 5.6.2).

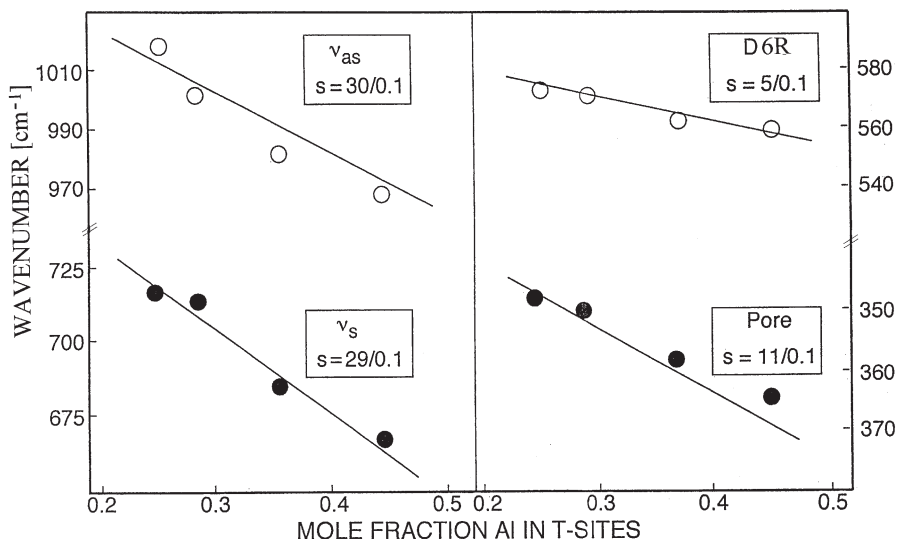


Fig. 12. Wavenumbers of various framework vibrations as a function of the mole fraction of aluminum in tetrahedral (T) sites of the zeolite framework; s indicates the slope, i.e., the decrease of the wavenumber (cm^{-1}) per 0.1 atom fraction of Al ion substitution (adopted from [112]). D6R means double six-membered ring, ν_s and ν_{as} stand for symmetric and asymmetric stretching modes, respectively (cf. text and list of abbreviations)

5.2.2

More Recent Investigations of Various Molecular Sieves

5.2.2.1

Faujasite-Type Zeolites (FAU)

Since the pioneering work by Flanigen et al. [112], many other studies of zeolite frameworks have appeared which used the IR/KBr technique, and frequently the interpretation of the obtained spectra was in line with or analogous to that given by Flanigen et al. [112] and Flanigen [114]. In many cases, the IR or Raman spectroscopic experiments were undertaken in order to complement a general characterization of the molecular sieves under study by, e.g., NIR, UV-Visible, XRD, MAS NMR spectroscopies or adsorption measurements.

The experimental results of IR and Raman studies on framework vibrations of *faujasite-type* Na-X by Miecznikowski and Hanuza [246] and Geidel [240, 248] and Geidel et al. [113], respectively, were compared by Geidel et al. [113]. The band positions and assignments proposed by Geidel et al. [113] are summarized and compared in Table 5.

Also, the IR and Raman spectra of Al-free faujasite structures were compared. The spectra show bands in the asymmetric ($1200\text{--}1000\text{ cm}^{-1}$) and symmetric ($850\text{--}700\text{ cm}^{-1}$) stretching regions of the framework vibrations; however, they contain a lower number of bands than predicted as IR- and Raman-active. Strong Raman bands around 500 cm^{-1} were ascribed by Geidel

Table 5. Approximate assignments of observed lattice vibrational frequencies of Na-X zeolite [246] based on calculations [113]

Observed bands [cm ⁻¹]		Calculated [cm ⁻¹]	Assignment
IR	Raman		
1078 sh	1082 m	1095–1065	ν_{bas} (SiO, AlO)
975 vs	985 m	936–901	
752 m	800 w	812–791	ν_{bas} (AlO)
700 m		744–692	$\nu_{\text{b,s}}$ (SiO, AlO)
612 vw		609–604	$\nu_{\text{T,s}}$ (AlO)
562 m		569	double ring mode
	510 vs	507–494	δ_{bbs} (OTO)
461 s			δ (OTO)
408 w			
364 m	375 m	365–260	pore opening mode

sh: shoulder, w: weak, vw: very weak; s: strong, vs: very strong, b: displacement of bridging tetrahedron; T: displacement of total tetrahedron.

[240, 248] and Geidel et al. [113] to bending motions of bridging tetrahedra, δ_{bs} (OTO), whereas Dutta et al. [249] interpreted them as being due to mixed stretching and bending modes strongly dependent on the TOT angles of the structure. Thus, Raman bands at 488 and 510 cm⁻¹ of the Al-free faujasite structure were supposed to correspond to the TOT angles of 141° and 147°, respectively. Comparison with the spectrum of Al-containing faujasite reveals a broadening of these bands upon incorporation of increasing amounts of Al³⁺ cations into the framework. Simultaneously, the band positions shift to lower wavenumbers, basically in agreement with the observations by Flanigen et al. (cf. [112, 114] and Fig. 12).

Falabella et al. [250] included IR framework spectra in their report on structural and acidity properties of RE-Y (where RE=La, Nd, Sm, Gd, Dy). Ballivet et al. [251] obtained IR spectra of La, Na-Y zeolites in the region of framework vibrations as well as in the OH stretching region (cf. Sect. 5.4.1.1) and used the spectral features in the range 1300–400 cm⁻¹ in dependence on the activation temperature for structural and stability determinations.

Yu et al. [252] successfully employed UV Raman laser spectroscopy for the characterization of the framework vibration range of zeolites A, X, Y, MOR, L, and Beta. UV Raman laser spectroscopy proved to be advantageous in that it was much less disturbed by fluorescence than the conventional Raman laser technique. The authors claimed that x-membered rings (xMR) in the structures were manifested by absorptions in the wavenumber ranges (in cm⁻¹) 470–530 (4MR), 370–430 (5MR), 290–410 (6MR) and 220–280 (8MR). The method was also used for the characterization of TS-1, [Fe]ZSM-5, [V]MCM-41 and in synthesis studies (vide infra).

In their combined FTIR /INS investigation of H-Y, Jacobs et al. [253] found framework T-O vibrations bands at 1130, 765, 565, 319 cm⁻¹ and assigned them to the asymmetric stretching, ν_{as} , the symmetric stretching ν_{s} , the D6R vibration (shoulder) and the pore opening vibration, respectively, essentially in line with

the approach by Flanigen et al. [112] and Flanigen [114]; a feature at 470 cm^{-1} was attributed to an O-T-O mode.

A series of partially amorphitized H-Y samples was investigated in the range of framework vibrations ($1100\text{--}500\text{ cm}^{-1}$) by the FTIR/KBr pellet technique and, concomitantly, in the $\nu(\text{OH})$ range ($3800\text{--}3400\text{ cm}^{-1}$) by FTIR spectroscopy of self-supporting wafers. This was done in the contribution of Cairon et al. [254], who determined the content of extra-framework aluminum and the degree of crystallinity of these materials. Note that the interpretation of the framework spectra again followed the approach of Flanigen et al. (cf. Sects. 2.5 and 5.2). However, the authors obtained consistent results and found the structure-sensitive double 6-ring band around 600 cm^{-1} , named ν_3 by the authors, most appropriate for quantitative analysis of the extra-framework aluminum content and evaluation of the crystallinity.

5.2.2.2

Zeolite A (LTA)

Huang and Jiang [255] reported on the IR and Raman vibration spectra of completely *siliceous zeolite A*. Their band assignment was analogous to the approach of Flanigen et al. [112, 114]. The authors found some evidence for a reduction of the average T-O-T angle in all-silica zeolite A in comparison with Al-containing A-type zeolite ZK-4 ($n_{\text{Si}}/n_{\text{Al}}=4.4$). In a study of the vibrational structure of zeolite A, undertaken in the group of Calzaferri [256], experimental and calculated IR and Raman spectra of zeolite A were reported. Their correlation allowed them to assign group frequencies to Al fundamental modes (for zeolite A see also [252]).

5.2.2.3

Sodalite (SOD)

An interesting contribution to infrared investigations of frameworks is contained in the review article by Stein and Ozin [257] on *sodalite* superlattices. These authors determined the effect of the number of Na_4Br clusters on the far-infrared spectra of dehydrated sodalites of the type $\text{Na}_{8-p}\text{Br}_{2-p}\{\ \}_p$, where $\{\ \}$ stands for an anion-free sodalite cage and p runs from 2 to 0.

5.2.2.4

Clinoptilolite (Heulandite-Like Structure, HEU)

DRIFT studies of the *clinoptilolite* framework were carried out by Elizalde-González et al. [258], who observed bands at $1633, 1417, 1018\text{ cm}^{-1}$ ($\nu_{\text{as}}[\text{T-O-T}]$) and a shoulder at 1200 cm^{-1} (assigned to inter-tetrahedral vibrations). The influence of the treatment temperature and the Sanderson electronegativity of exchange cations ($\text{Na}^+, \text{K}^+, \text{Mg}^{2+}, \text{Ca}^{2+}$) on the framework vibrations of natural clinoptilolite was studied by Rodríguez-Fuentes et al. [259] and interpreted in close analogy to the FKS correlation [112, 114].

5.2.2.5

Erionite (ERI), Offretite (OFF)

IR framework spectra were used as a diagnostic tool by Occelli et al. [260] in detecting the presence of *offretite* (via a band at 600–610 cm^{-1}) and *erionite* (bands at 410–425, 550–610, 655–685 cm^{-1}) in mixtures of these two structures. Roessner et al. [261] considered, in their IR spectroscopic work on the cation distribution in dehydrated calcium-exchanged erionite, also the framework vibrations of Ca-erionite besides OD vibrations, CO adsorption and DRIFT spectroscopy in the NIR region. They were able to show that the Ca^{2+} cations were selectively located in the supercages in front of the six-membered rings. Similar to the features encountered with Y-type zeolites and mordenite (vide supra), also with offretite a sufficiently linear relationship was found between the wavenumbers of the asymmetric and symmetric T-O vibrations and the number of framework Al atoms per unit cell [262].

5.2.2.6

Zeolite L (LTL)

Framework spectra of *zeolite K-L* were reported by Tsitsishvili [203] and related to the data of Flanigen et al. [112]. Also, IR spectroscopic features of water adsorbed on K-L (vide infra) were included in Ref. [203] (see also [252]). Dealumination of zeolite L via various methods was also studied (cf., e.g., Sect. 5.4.1.2.2)

5.5.2.7

Zeolite Beta (BEA)

Samples of *zeolite Beta* with various degrees of dealumination were prepared via various treatments by Yang and Xu [263]. These authors provided framework spectra of their samples, obtained in the region 1400–400 cm^{-1} through the conventional FTIR/KBr pellet technique. A band at about 950 cm^{-1} was attributed to Si-O vibrations in structural vacancies (cf. also [264]) and monitored in dependence on the treatment.

5.2.2.8

Ferrierite (FER)

The T-O-T vibrations of cobalt-exchanged *ferrierites* were monitored by the FTIR/KBr-technique in a work by Sobalík et al. [265] who attempted to evaluate quantitatively the intensity of the main band at 1070 cm^{-1} and, thus, to determine the number of Co^{2+} ions at cationic sites.

5.2.2.9

Chabazite (CHA)

A study on vibrational spectra of the frameworks of natural *chabazite* by Raman scattering and infrared reflection spectroscopy was conducted by Pechar and

Rykl [266]. The experiments provided information about the symmetry and the dynamics of the framework and the nature and strength of bond-types in the structure. Also, in investigations of natural zeolites such as natural chabazite the method of Flanigen et al. [112] was adopted [267].

5.2.2.10

ZSM-5 (MFI), ZSM-11 (MEL), MCM-22 (MWW), ZSM-35 (FER), ZSM-57 (MFS)

Miecznikowski and Hanuza [268] extended IR and Raman spectroscopic investigations of ZSM-5 framework vibrations to samples with different $n_{\text{Si}}/n_{\text{Al}}$ ratios including silicalite-1 and attempted to relate the data to the crystal structures. With the help of reflection/absorption vibrational spectroscopy of the framework region, Mihailova et al. [269] monitored the growth of silicalite-1 films on a gold-covered silicon support (cf. also [270]). Skeletal vibrations of ZSM-11 samples diluted with finely powdered KBr were studied by Kubelková et al. [271] via DRS in the range 1300–400 cm^{-1} . In addition, the region of OH vibrations (4000–2000 cm^{-1}) of pure powdered H-Y, Ce, Na-Y and dealuminated Ce, Na-Y was also investigated by DRS (vide infra). Infrared spectra of framework modes of MCM-22 were provided by Corma and colleagues [272, 273] together with results of synthesis, structure, acidity (IR spectroscopy of the OH groups), adsorption and catalysis studies. As a part of their work on characterization and catalytic properties of MCM-22, Ravishankar et al. [274] provided framework spectra, which they interpreted on the basis of Flanigen's studies [112, 114]. In particular, these authors deduced from the occurrence of a weak band at 406 cm^{-1} that the spectrum indicated the presence of 12-membered pore openings in the MCM-22 structure.

Using the IR/KBr pellet technique, Ernst and Weitkamp [275] obtained framework vibration spectra of ZSM-35 (cf. also [276]) and, for the first time, ZSM-57 (MFS). Both zeolites have two characteristic absorbances around 1230 cm^{-1} , which were assigned to vibrations of five-membered rings. While ZSM-5 exhibited a single band at about 600 cm^{-1} , ZSM-57 showed a doublet. The additional band was attributed to the presence of four-membered rings in the structure of ZSM-57.

5.2.2.11

AIPO₄s, SAPOs, MeAPOs

A whole series of partially well-known (SOD, LTA, FAU) and partially less common molecular sieves [Fe]-SOD, [Zn]-SOD, AlPO₄-20, SAPO-20, SAPO-37 with TMA occlusions was subjected to Raman spectroscopic determination of T-O-T vibrations in their frameworks in a contribution by Hong [277]. The author suggested that Raman spectroscopy may be helpful in proving the substitution of heteroatoms other than Al or Si into the structure of molecular sieves. Modeling of vibrational spectra of AlPO₄-5 and its silica analogs together with a comparison of experimental results was reported by de Man et al. [278]. Finally, IR and Raman vibrational spectroscopy of three-membered rings in molecular sieves such as VPI-7, ZSM-18 and zeolitic silica polymorphs have attracted attention, in

fact, in combination with MAS NMR experiments and theoretical treatments [279, 280].

Sinha et al. [281] investigated the framework vibrations of silicoaluminophosphate SAPO-39 and of magnesium aluminophosphate MAPO-39 by DRIFT spectroscopy and interpreted them according to the approach of Flanigen et al. [112]. The OH stretching region was studied by FTIR transmission spectroscopy (vide infra, Sect. 5.4.1).

5.2.2.12

Miscellaneous

A combination of Raman and ^{29}Si MAS NMR spectroscopy was employed by Annen and Davis [280] for a structure investigation of framework materials containing three-membered rings (3MR) including molecular sieves such as *lovdarite*, *ZSM-18* and *VPI-8*. However, it turned out that Raman spectroscopy is not useful for the identification of three-membered rings in framework materials.

An interesting composite material, viz., “Dallas amorphous material-1 (DAM-1)”, was described and characterized via FTIR in a publication by Coutinho et al. [282]. DAM-1 is a novel hexagonal mesoporous-microporous silica material, which exhibits simultaneously properties like MCM-41 and MFI structures and shows asymmetric as well as symmetric Si-O-Si stretching modes with $\nu_{\text{as}}=1087\text{ cm}^{-1}$, shoulders at 1143 and 1203 cm^{-1} , $\nu_{\text{s}}=800\text{ cm}^{-1}$, a bending mode of $\delta(\text{Si-O-Si})$ at 444 cm^{-1} and, finally, Si-OH vibrations due to defects and giving rise to a band at 952 cm^{-1} .

Infrared and Raman spectroscopic investigations of framework vibrations were also carried out with layered structures such as, e.g., *kanemite* [283]. Huang et al. [283] associated a strong Raman band around 465 cm^{-1} in the kanemite spectrum with six-membered rings of tetrahedra and another one at 1060 cm^{-1} with vibrations of Q^3 units. A broad band around 1015 cm^{-1} was assigned to Q^3 units involved in hydrogen bonding and, similarly, a broad band centered at 3463 cm^{-1} was supposed to be related to the stretching vibration of a hydrogen-bonded OH group.

A new family of crystalline microporous GeO_2 materials was synthesized and, inter alia, characterized with respect to their structure via IR spectra of their frameworks in a study of Li et al. [284]. Tentative assignments of the bands observed to Ge-O and Ge-O-Ge vibrations and four-, five- and six-fold coordinations of Ge with oxygen were proposed.

5.2.3

Effect of Cation-Loading on Framework Vibrations

The influence of exchangeable cations on zeolite framework vibrations was investigated by Maxwell and Baks [285], and, similar to the studies of Flanigen et al. [112], they derived linear relationships between the reciprocal of the sum of the cation radii and oxygen anion radius, $1/(r_{\text{cation}}+r_{\text{O}^{2-}})$ and the wavenumbers of framework vibrations of zeolites A and X.

5.2.4

Effect of Adsorption on Framework Vibrations

Already in the study by Flanigen et al. [112], it was shown that the positions of the bands of some of the framework vibrations sensitively respond to adsorption and desorption of water when a migration of multivalent cations was involved. In the case of *faujasite-type* zeolites containing Ca^{2+} or La^{3+} as charge-compensating cations, such a migration occurs from inside the sodalite cages to the centers of the double six-rings upon dehydration and vice versa on H_2O adsorption, which effects a distortion of the framework. This in turn changes the symmetry of the D6R, which results in a shift of the related (inter-tetrahedral) e_1 -band from 570 to 635 cm^{-1} .

Recently, Cheetham and co-workers [286, 287] studied the adsorption of hydrohalocarbons in faujasites by combining INS and NIR-FT Raman spectroscopy. For chloroform, the presence of hydrogen bonding to the framework oxygen was deduced from the observed red-shift of the C-H stretching mode (Raman) and the simultaneous blue-shift of the corresponding bending mode (INS). In addition, substantial van der Waals interactions between chlorine and framework oxygen atoms and electrostatic interactions between chlorine atoms and cations were found to be involved in the host/guest interaction. It was outlined that utilization of rather polar molecules may alter the INS band intensities of the sorption complexes relative to those of the empty zeolite. Thus, new framework bands at 527 and 463 cm^{-1} were observed in the INS spectrum upon chloroform adsorption. Obviously, these bands derive their enhanced intensity from coupling with normal modes of the strongly adsorbed probe molecules which involve large amplitudes of H atom displacements.

As recently demonstrated by Huang et al. [288, 289], FT-Raman spectroscopy is also a useful tool to investigate phase transitions that many zeolite frameworks undergo upon adsorption of certain organic molecules at higher loadings.

5.2.5

Effect of Dealumination and $n_{\text{Si}}/n_{\text{Al}}$ Ratio on Framework Vibrations

As already shown with a few examples, Raman scattering techniques provide an alternative to the extensively used IR spectroscopy for obtaining information about the dynamics of zeolite systems. In the following, we will focus on some selected studies dealing with Raman spectroscopy of bare zeolite frameworks.

As a typical application of considerable interest, the dependence of the Raman spectra on the $n_{\text{Si}}/n_{\text{Al}}$ ratio and the influence of cations has been investigated in several studies, e.g., [246, 247, 290, 291] and [292–296], respectively. Fig. 13 shows the FT-Raman spectra of two *faujasites* in the framework region in dependence on the $n_{\text{Si}}/n_{\text{Al}}$ ratio and Fig. 14 on varying extra-framework cations.

The spectra were taken from the hydrated samples without any chemical treatment. For excitation an Nd-YAG laser was used at 1064 nm with a laser power of 450 mW . As a general feature of all Raman spectra of zeolites, the stretching modes above 600 cm^{-1} are of lower intensities and give less structured bands than the bending modes in the range below 600 cm^{-1} . As in the corresponding infrared

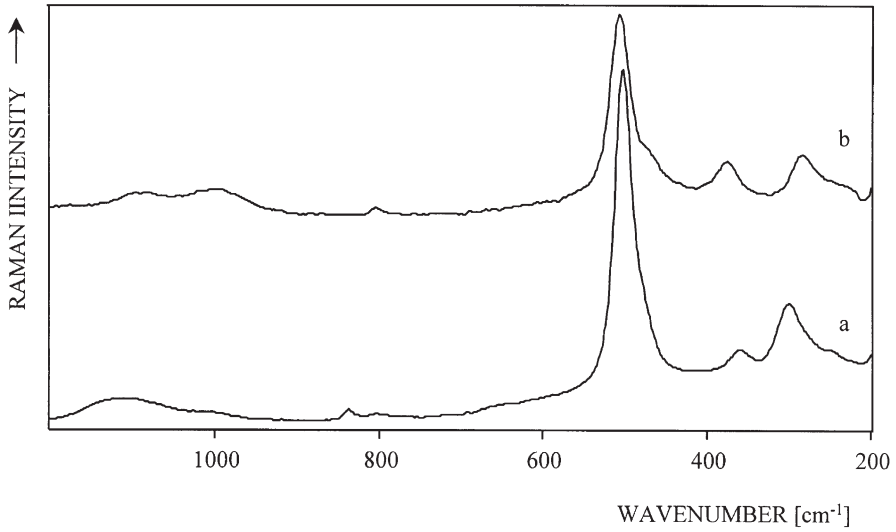


Fig. 13. Raman spectra of zeolites (a) Na-Y ($n_{\text{Si}}/n_{\text{Al}} = 2.6$) and (b) Na-X ($n_{\text{Si}}/n_{\text{Al}} = 1.18$)

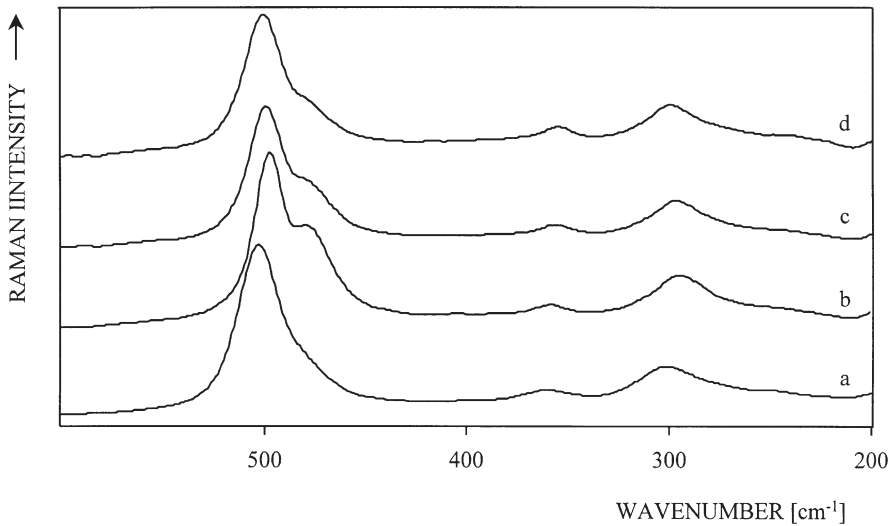


Fig. 14. Raman spectra of ion-exchanged Y-type zeolites ($n_{\text{Si}}/n_{\text{Al}} = 2.6$), viz. (a) Na-Y, (b) K-Y, (c) Rb-Y, (d) Cs-Y

spectra, the frequencies of stretching modes increase with increasing $n_{\text{Si}}/n_{\text{Al}}$ ratio. The generally low Raman intensity of the stretching modes in silicate and aluminosilicate frameworks opens the spectral range above 900 cm^{-1} for studies of isomorphous substitution [297] and lattice defects [298]. The most intense line appears in all the recorded Raman spectra of faujasites at about 500 cm^{-1} . Due to its dominant intensity, this band should be attributed to a highly symmetric motion. In analogy to SiO_2 phases [299], the vibrational behavior may be interpreted as a motion of the bridging oxygen atoms perpendicular towards the bisecting line connecting the two T atoms of a T-O-T bridge. This interpretation is in line with the approximate assignments of framework modes presented in the sections dealing with the theoretical background. It can be seen in Fig. 13 that, in contrast to the stretching modes, a slight downward shift is observed with increasing $n_{\text{Si}}/n_{\text{Al}}$ ratio of the isostructural faujasites.

Attempts have been made to correlate this behavior with the ring sizes and average T-O-T angles present in zeolites of different topologies [300]. However, the observed frequency dependencies were not fairly uniform. In particular, for *A-type zeolites* a trend reversed to that for faujasites has been observed by changing the $n_{\text{Si}}/n_{\text{Al}}$ ratio systematically [290]. Hence, the frequency shifts obviously arise from different effects of structural changes, altered nature of normal modes, and electron density distribution and from combinations of these effects. Instead of the band shift observed for aluminum-rich samples, for highly dealuminated faujasites the band width of the most prominent peak was discovered to reflect the aluminum content at low levels [295].

The effect of rare earth loading of Y-type zeolite on its dealumination during thermal treatment was monitored in a study by Roelofsen et al. [301], who found the band at 790 cm^{-1} to be most appropriate for the determination of the $n_{\text{Si}}/n_{\text{Al}}$ ratio, since the other structure-sensitive bands were too much affected by the cation amount, crystallinity and water content.

DRIFT spectra of *mordenites* with various $n_{\text{Si}}/n_{\text{Al}}$ ratios, which have been achieved via leaching of the parent material (Zeolon 900 Na from PQ Corp., $n_{\text{Si}}/n_{\text{Al}}=5$) with HCl, were recorded by Park et al. [302]. These authors found that the intensities of bands at 630 and 730 cm^{-1} , which were assigned to Al-O bonds, decreased with increasing $n_{\text{Si}}/n_{\text{Al}}$ ratios. Musa et al. [303] used the mid-infrared investigation of framework vibrations among a variety of other techniques to describe the effect of progressive dealumination ($n_{\text{Si}}/n_{\text{Al}}=6.3\text{--}82.5$) on synthetic mordenite. Similarly, Lutz et al. [304] carried out IR spectroscopic investigations of the hydrothermal stability and resistance against alkaline media of high-silica Y-type zeolite samples, DAY. These were obtained via various dealumination methods yielding $n_{\text{Si}}/n_{\text{Al}}$ ratios up to 150. Earlier observations of the stabilizing effect of extra-framework aluminum-containing species were confirmed. However, Lutz et al. [305] suggested for the case of steamed and leached faujasite-type zeolites a particular calibration procedure. This was required in order to account for the effect of extra-framework Si- and/or Al-containing species on the position of that band (in the range $1000\text{--}1060\text{ cm}^{-1}$), which is indicating the asymmetric vibration $\nu_{\text{as}}(\text{T-O-T})$. The IR (and XRD and NMR) data were calibrated through a determination of the framework and extra-framework $[\text{SiO}_2]$ - and/or $[\text{AlO}_2]$ -species by chemical analysis.

The FTIR/KBr method was, inter alia, applied by Maache et al. [306] for the characterization of various samples of *H-Beta* dealuminated by acid leaching. In the case of framework vibrations of *zeolite Beta*, a good linear correlation was found between the wavenumber of the asymmetric O-T-O vibration, $\nu_{as(O-T-O)}$, and the aluminum mole fraction, $n_{Al}/(n_{Si}+n_{Al})$ [263]. Ponthieu et al. [307] attempted to find a correlation between the wavenumbers of framework vibrations of *offretite* and *zeolite Omega* and the degree of dealumination (aluminum mole fraction) similar to those observed with faujasites and mordenites. However, linear correlations were hardly obtained.

5.2.6

Effect of Isomorphous Substitution on Framework Vibrations

Similar effects as found upon incorporation of Al into the faujasite framework (vide supra) were observed when heteroatoms isomorphously substituted Si framework cations of silicalite-1 (i.e., Al-free MFI structure, [Si]MFI) or siliceous sodalite ([Si]SOD): In fact, the band shifts may be not very dramatic, since usually only small degrees of isomorphous substitution of Si by introduction of Al or, similarly, B, Ti, V, Ga, Fe and V are considered.

Isomorphous substitution of *boron* into the MFI structure to produce [B]ZSM-5 was carried out and investigated via FTIR micro-spectroscopy (“infrared microscopy”) of single crystals by Jansen et al. [308]. Typical bands were observed at 1380 and 905 cm^{-1} . The integrated band intensity of the 905 cm^{-1} band was used as a quantitative measure of the boron content, and the boron distribution in the single crystals was shown to be homogeneous.

Incorporation of *titanium* into silicalite-1 yielding TS-1, i.e., [Si,Ti]MFI [309], gives rise to a prominent IR band around 960 cm^{-1} as a “fingerprint” in the IR and Raman spectra, as reported, e.g., in Refs. [297, 310, 311] and [312], respectively (cf. also [252] and references therein). Raman and IR spectra of the region of framework vibrations in two titanium-containing silicates, viz. ETS-4 (supposed to be related to *zorite*) and ETS-10 were reported by Mihailova et al. [313] (regarding ETS-4 and ETS-10 see also [314–316]).

A framework investigation of TS-1 by the IR/KBr pellet technique, including the observation of the 960 cm^{-1} band, was reported by Tuel and colleagues [317, 318]. Also, Bengoa et al. [319] considered the 960 cm^{-1} band as an indication of Ti-incorporation into the framework of silicalite-1. Gao et al. [320] reported that they have found a linear relationship between the intensity of that IR band and the titanium content in TS-1. An investigation of TS-1 by UV Raman laser spectroscopy was described in Ref. [321]. A band at about 979 cm^{-1} was observed by Das et al. [322] upon IR spectroscopic characterization of Ti-containing ETS-10, which they had prepared in testing choline chloride or hexaethylidiquat-5 bromide as templates.

There are, however, conflicting interpretations advanced in the literature regarding the appearance of these bands in the IR spectra (cf. [323–327]; see also Volume 1, Chapter 7, pages 198–199, of the present series). The situation is even more complicated by the fact that so-called hydroxyl nests in the silicalite-1 structure, $[(\text{O})_3\text{Si-OH}]_4$, give rise to an IR band around 960 cm^{-1} as well. There-

fore, Scarano et al. [324] have ascribed the 960 cm^{-1} band in [Si,Ti]MFI to a superposition of stretching vibrations of those $(-\text{O})_3\text{Si}-\text{OH}$ species and a mode sensitive to the presence of Ti in the framework. At variance with this interpretation, Astorino et al. [325] and, similarly, Boccuti et al. [326] considered the 960 cm^{-1} band as being due to an antisymmetric stretching vibration, $\nu_{\text{as,SiOTi}}$, i.e., a vibration of a bridging Si-O-Ti fragment of the structure. According to Zecchina et al. [327], the most probable assignment seems to be that the 960 cm^{-1} band is caused by an effect on the vibration of an adjacent $\text{SiO}_{4/2}$ tetrahedron exerted by the presence of a neighboring Ti with a higher polarity of the Ti-O bond.

Vibrational spectra of the Ti-substituted orthorhombic MFI structure were calculated by Smirnov and van de Graaf [328] via the method of molecular dynamics. A band at 935 cm^{-1} was obtained in good agreement with the experimental value reported in the literature (vide supra). It was interpreted as being due to a localized SiO^- vibration of defects in Si-O-T bridges consistent with the assignment given by Boccuti [326] and Cambor et al. [329]. This interpretation was adopted by, e.g., Das et al. [322]. Interestingly, a band around 970 cm^{-1} was also observed in a Raman spectroscopic study by Deo et al. [330] of titania silicate samples, in which Ti occurred as finely dispersed TiO_x [below $n_{\text{Ti}}/(n_{\text{Si}}+n_{\text{Ti}})=1.6\text{ mol}\%$] or TiO_2 [anatase, above $n_{\text{Ti}}/(n_{\text{Si}}+n_{\text{Ti}})=1.6\text{ mol}\%$]. Infrared features (OH bands, Brønsted and Lewis acidity) and catalytic properties of these materials were also reported. Deo et al. attributed the 970 cm^{-1} band to the Si-O stretching vibration of an $\text{SiO}_{4/2}$ tetrahedron with one non-bridging oxygen atom. However, in this context it is worthy to note that Marra et al. [331] detected by IR spectroscopy a band at 960 cm^{-1} and by Raman spectroscopy one at 976 cm^{-1} even in the case of heteroatom-free orthorhombic silicalite-1. In fact, this absorbance was absent with the monoclinic form.

Tetrahedral coordination of Ti in the TS-1 framework is maintained in the absence of certain adsorbates. Exposure to H_2O , LiOH , NH_3 or CH_3OH resulted in a more ionic character of hexa-coordinated Ti exhibiting Lewis acidity and a broadening to the point of disappearance of the 960 cm^{-1} band [327, 332, 333].

Ahedi et al. [334] found typical IR bands around 969 cm^{-1} upon crystallization of the Ti-derivative of NU-1 zeolite as well as other framework vibration modes. The latter were interpreted in line with the suggestions made by Flanigen et al. [112]. A new titanium-containing silico-aluminophosphate, TAPSO-37, was synthesized and characterized, inter alia, through the IR/KBr pellet technique, by Jappar et al. [335], who also observed a band around 960 cm^{-1} . However, the interpretation was complicated, since this band appeared in the IR spectrum of titanium-free SAPO-37 as well, although with somewhat lower intensity. But their SAPO-37 sample possessed also SiO^- defects (cf. [326, 327]). Therefore, the authors concluded that both the SiO^- defects occurring independently of Ti incorporation (as in SAPO-37) and those being induced by Ti incorporation (as in the case of TAPSO-37) contributed to the peak at 960 cm^{-1} .

Similar effects were reported for isomorphous substitution of Si in MFI structures by iron to [Si,Fe]MFI or vanadium to [Si,V]MFI. Anunziata et al. [336] prepared Ti-, V- and Fe-containing zeolites, viz., [Si,Ti]MFI (TS-1), [Si,Ti]MFE (TS-2), [Si,Ti]BEA, [Si,Ti]NCL-1 (for the synthesis and characterization of the latter new, large pore silica-rich zeolite compare the work by Kumar et al. [337]),

[Si,V]MFI (VS-1), and [Si,Fe]BEA. They characterized these materials, inter alia, by FTIR spectroscopy. With all Ti- and V-containing samples they observed a sharp band at 967.8 cm^{-1} , suggesting titanium and vanadium incorporation into the frameworks. Moreover, from the spectra it could be concluded that all samples had good crystallinity, and from the relative intensities of the bands at 967.8 and 800 cm^{-1} their $n_{\text{Si}}/n_{\text{Ti}}$ ratios were derived. Similarly, Higashimoto et al. [338] characterized VS-1, inter alia, via FTIR and observed a band at 960 cm^{-1} , which these authors ascribed to a perturbed V=O vibration due to the network structure including neighboring Si-OH groups.

Replacement of Si by Fe in silicalite-1, resulting in [Si,Fe]MFI, gave rise to an IR-active mode at 1015 cm^{-1} and a Raman-active mode at 1020 cm^{-1} (cf. Ref. [324] and Volume 1, Chapter 7, page 220, of the present series). These modes were assigned to vibrations of $(-\text{O}-)_3\text{Si-OH}$ entities polarized by adjacent Fe^{3+} in the structure in analogy with what was discussed for the appearance of the 960 cm^{-1} band in [Si,Ti]MFI (vide supra). The region of framework vibrations of [Fe]ZSM-5 was also investigated by UV Raman laser spectroscopy (cf. Yu et al., [339]).

Similar to Ti-containing molecular sieves, an IR band at ca. 960 cm^{-1} was also reported for [Si,V]MFI structures (cf., e.g., [340] and Volume 1, Chapter 7, pages 208–209, of the present series and references therein). Thus, Hongbin Du et al. [341] observed by the FTIR/KBr technique in synthesized large pore V-containing zeolite Beta a band at 960 cm^{-1} and took the appearance of this signal as an indication of vanadium incorporation into the framework to produce H-[Si,Al,V]Beta.

In their contribution to synthesis and characterization of a *tantalum* silicalite-1 molecular sieve with MFI structure, Ko and Ahn [342] regarded the occurrence of an IR band at 965 cm^{-1} as an indication of tantalum incorporation into the framework. Their interpretation followed that given in [326, 327]. The intensity of the 965 cm^{-1} band increased with increasing Ta content, and the material exhibited strong Brønsted acidity. However, a corresponding band around 960 cm^{-1} was not detected after isomorphous substitution of Al by Fe into, for instance, mordenite [343].

In analogy to the above discussed case of Ti-containing MFI structures, Mostowicz et al. [344] considered the appearance of an IR absorption at $1060\text{--}1010\text{ cm}^{-1}$ in the spectrum of *cobalt*-containing ZSM-5 to be an evidence for Co-O-Si linkages in the framework. After Xu et al. [345], highly dispersed ZnO clusters were produced in ZnO/Na-ZSM-5 mixtures through calcination at 1073 K , and the occurrence of new bands at $900\text{--}1000\text{ cm}^{-1}$ was interpreted as an indication of *zinc* incorporation into the framework.

Chromium incorporation into MFI structures was also claimed on the basis of IR spectroscopic evidence, i.e., based on the observation of a band around 960 cm^{-1} [346, 347]. The authors of Ref. [347] provided the whole spectrum of the framework vibrations ($1500\text{--}450\text{ cm}^{-1}$), which they interpreted in line with the work by Flanigen et al. [112].

Finally, it should be noted that IR absorption bands of Ga- and Ge-substituted frameworks of bromide sodalite were reported by Johnson and Weller [348]. These bands were seen in the range $1000\text{--}500\text{ cm}^{-1}$ ($\nu_{\text{as}}[\text{T-O-T}]$ and $\nu_{\text{s}}[\text{T-O-T}]$).

Isomorphous substitution was also reported for mesoporous materials. In a study on properties of Ti-containing MCM-41 by Corma and co-workers [349], it was reported that diffuse reflectance spectroscopy also with this material provided a band at 960 cm^{-1} .

Laha and Kumar [350] carried out IR spectroscopic investigations of [Si]MCM-41, where they observed bands at 1090 cm^{-1} ($\nu_{\text{as}}[\text{Si-O-Si}]$) and 962 cm^{-1} ($\nu[\text{Si-OH}]$). Similar results were obtained with [Al,Si]MCM-41, [Si,Ti]MCM-41 and [Si,V]MCM-41. Incorporation of vanadium into MCM-41 structures and their characterization by UV Raman laser spectroscopy was reported by Yu et al. [351]. Morey et al. (cf. [352], and references 13, 23 and 24 therein) succeeded in synthesizing an [Si,Ti]MCM-48 mesoporous molecular sieve and assumed that the incorporation of Ti is associated with the origin of a band (shoulder) near 960 cm^{-1} . A novel material containing structural features of both Ti-containing silicalite-1, TS-1, and MCM-41, designated as [Ti]MMM-1 and reported to exhibit bands at 550 and 960 cm^{-1} was described by Poladi et al. [353]. When UO_2^{2+} was exchanged into MCM-48, bands at 902 and 906 cm^{-1} appeared as was reported by Vidya et al. in Ref. [354].

Studies on isomorphously substituted molecular sieves will be also encountered in Sects. 5.4 and 5.5, which deal with zeolitic hydroxy groups and selected zeolite/adsorbate systems.

5.3

Cation Vibrations

5.3.1

Cation Vibrations in Pure Zeolites

The presence of charge-compensating cations located inside the channels and cages of zeolites significantly affects the chemical and physical properties of these microporous materials. Especially in the hydrated form are these non-framework cations rather mobile giving zeolites their unique property as ion-exchangers (cf. Volume 3, Chapter 1 of the present series). This is of substantial commercial importance, and hence the ion-exchange properties of zeolites have been explored extensively. Furthermore, these cations essentially represent centers of interaction with incorporated guest molecules forming a basis for applications of zeolites as catalysts and adsorbents. A detailed understanding of these processes at the microscopic level demands information about the location of cations with respect to the framework. Among other experimental methods like solid-state MAS NMR and XRD, vibrational spectroscopic techniques have proved to be very useful tools for detecting charge-balancing cations. Non-framework cations undergo frustrated translational motions with respect to the lattice, and these vibrations manifest themselves by transitions in the far-infrared range. Utilizing the throughput advantage of the FTIR technique in conjunction with highly sensitive liquid helium-cooled bolometers as detectors makes the FIR region routinely accessible. More experimental efforts are required to obtain high-quality low-frequency Raman spectra. For very low frequencies the dispersive technique using a monochannel triple monochromator operating in the

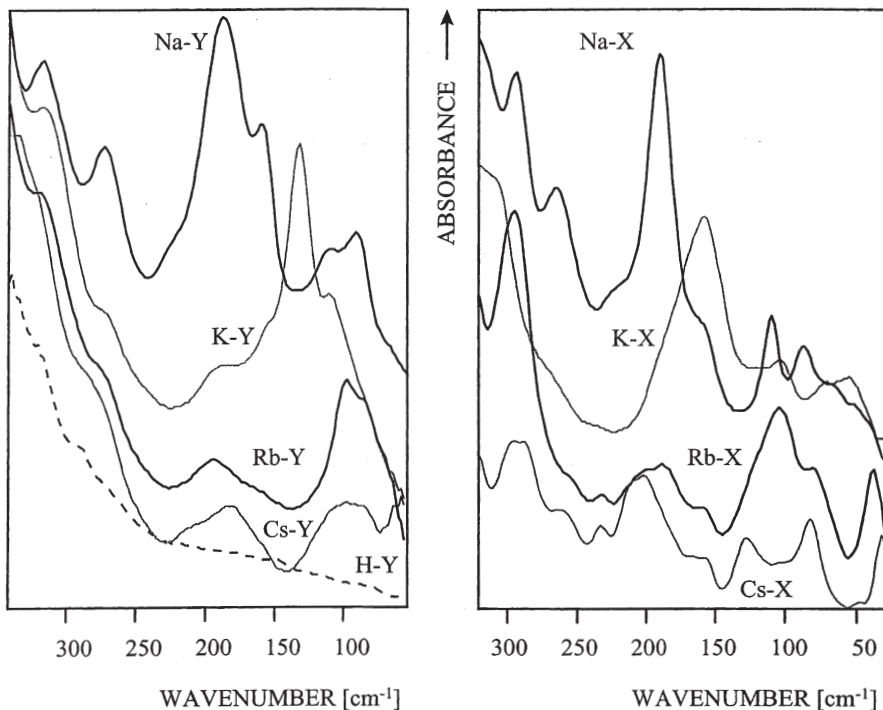


Fig. 15. Far-infrared (FIR) spectra of alkali-metal cation-exchanged faujasites and H-Y zeolite

visible region is preferred, and narrow slit widths are necessary for recording the spectra. Details of the experimental conditions and the problems related to the measurement of Raman spectra of zeolites in the far-IR region have been outlined by Brémard and Le Maire [295].

Fig. 15 shows typical far-infrared spectra of alkali metal-exchanged zeolites Y ($n_{\text{Si}}/n_{\text{Al}}=2.6$) and X ($n_{\text{Si}}/n_{\text{Al}}=1.18$).

The samples were prepared via solid-state ion exchange by thermal treatment of solid mixtures of the parent ammonium zeolite with the respective alkali metal chloride. Systematic studies concerning this kind of ion exchange have been summarized in previous reviews (cf. [355, 356] and Volume 3, Chapter 2 of the present series). It is well known that especially for $\text{NH}_4\text{-Y}$ high degrees of ion exchange are attainable [357]. For spectroscopic studies, solid-state ion exchange is clearly preferable due to the following advantages.

- (1) The degree of ion exchange is more complete.
- (2) With conventional ion exchange in aqueous solution of the in-going cation (usually starting with the sodium form as the parent sample), residual sodium ions always remain in the sample. This yields additional bands in the spectra which are avoidable by solid-state ion exchange.
- (3) The post-synthetic modification in aqueous phase requires the use of larger amounts of salt solutions which may result in a considerable contamination

of waste water. Furthermore, the liquid-state ion exchange necessitates an intensive drying of the sample before the infrared spectra can be recorded.

It can be seen in Fig. 15 that within the series of alkali-metal cation-exchanged faujasites the bands are shifted to lower wavenumbers with increasing cation mass. This phenomenon was recognized very early by Brodskii et al. [358, 359]. In an attempt to correlate the observed band positions with physical characteristics of the cations they found the relation

$$\tilde{\nu} = C_B m^{-1/2} r^{-3/2} \quad (24)$$

where $\tilde{\nu}$ is the wavenumber of the cation vibration in a particular site, m is the cation mass, r is the cation radius, and C_B represents the so-called Brodskii constant. Eq. (24) has been derived assuming a simple Coulomb-type interaction between the cation and the lattice which has been treated as rigid. In spite of its simplicity, this relation holds well for frequency shifts observed for several cations and zeolite types. Significant progress has been made by a more sophisticated model proposed by Ozin and co-workers [232, 360]. The authors recorded and compared a very large number of far-infrared spectra, including spectra of alkali, alkaline earth and transition metal-exchanged zeolites of types X, Y, A, and ZSM-5. Based on these experimental results and assisted by local molecule NMA calculations (clusters consisting of a cation plus the surrounding oxygen atoms) in combination with a transition-bond dipole moment approximation, an assignment for far-infrared spectra of zeolites has been derived. The assignment relies on the assumption that for most zeolite types the cation dynamics is dominated by local interactions at the cation-binding site [361]. On the basis of this model, each observed band has been assigned to cation modes at specific sites, and site locations and occupancies have been explored. The resulting assignment is illustrated for the FIR spectrum of zeolite Na-Y together with the site numbering in Fig. 16.

However, further investigations are necessary to prove unequivocally the validity of two approximations made:

- (1) the existence of persistent bonds between cations and surrounding oxygen atoms, and
- (2) the absence of the coupling of the cation motions to the framework vibrations, i.e., the interpretation of vibrational frequencies in terms of local harmonic oscillators.

To verify the correlation between site occupancies and far-infrared (FIR) bands, at first we have to distinguish between bands arising from cations and those originating from framework modes. This can be achieved by isotope substitution techniques. Labeling of ZSM-5 zeolites with the isotopes ^{17}O and ^{18}O yielded significant red-shifts of the bands at 380, 360, and 290 cm^{-1} in the infrared and Raman spectra [362]. In contrast, no dependence on isotope exchange was detectable for the bands below 290 cm^{-1} in the FIR spectra of Na-ZSM-5 [363]. The same effect has been revealed in the FIR spectra of faujasites upon ^{18}O isotope substitution: the bands at 320 and 270 cm^{-1} show distinct downward-shifts,

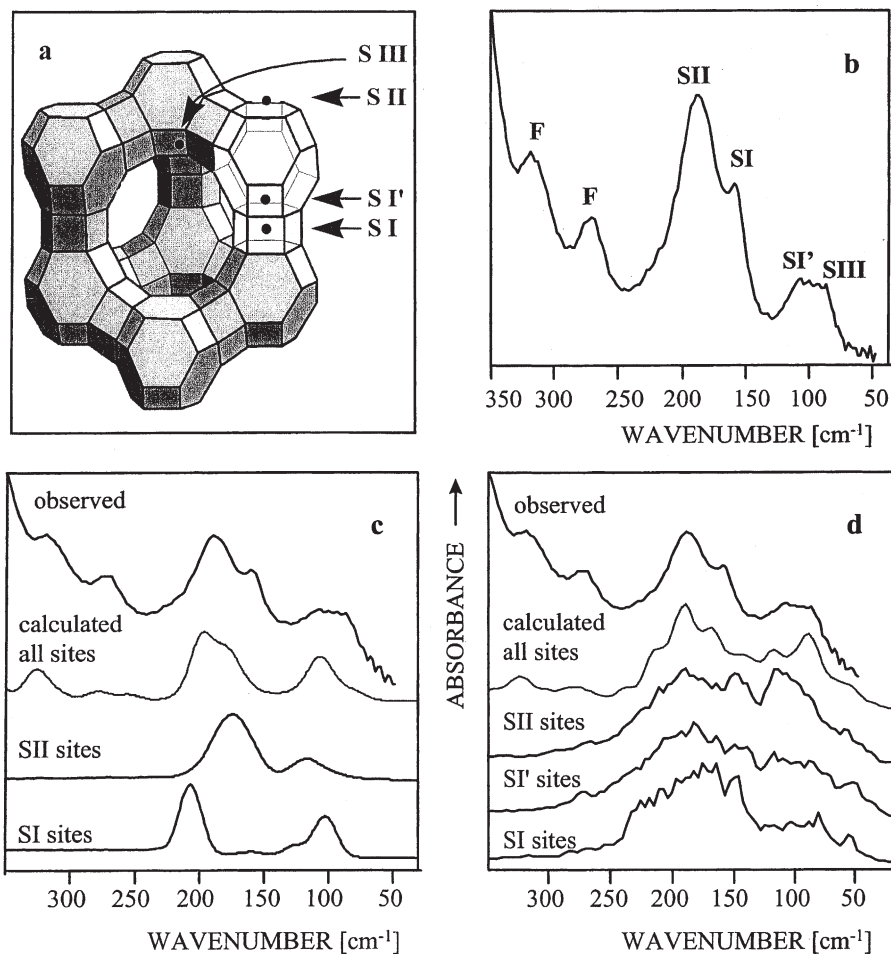


Fig. 16. (a) Extra-framework cation sites in X- and Y-type zeolites. (b) Far-infrared spectrum of Na-Y with band assignments to cation sites according to [232]. (c) Experimental IR spectrum in comparison to simulated spectra calculated according to the shell model and occupancy of different cation sites. (d) Experimental spectrum in comparison to power spectra simulated by MD at occupancy of different cation sites (parts c and d from [79] with permission)

whereas the bands below 270 cm^{-1} remain unaltered [24]. This clearly indicates that the bands above 270 cm^{-1} have to be assigned to framework modes. Such an assignment is further confirmed by the vanishing contributions of sodium ions in the KED in this spectral range (cf. Fig. 4d). On the other hand, one may conclude from the “empty” spectrum of H-Y below 250 cm^{-1} (Fig. 15) that framework modes obviously do not give rise to absorptions in this spectral range. So far, the approximate division into framework and cation vibrations is in agreement with the suggestions made by Ozin et al. [360, 361]. However, it should be emphasized that in general large amplitude vibrations of the framework such as torsional

motions or modes due to motions of larger building units against each other have to be expected in the frequency range below 250 cm^{-1} . Such motions involve large-amplitude atomic displacements that lead to considerable changes in the polarizability of the system and thus should be more Raman- than infrared-active. In fact, weak Raman bands were observed around 100 cm^{-1} in the spectrum of zeolites H-Y [295] and H-EMT [296]. One peak around 100 cm^{-1} also appears persistently in the Raman spectra of cation-exchanged A [77], X, Y [295], and EMT zeolites [296], and the frequency seems to be relatively invariant to the nature of the extra-framework cations. On the basis of MD simulations, this peak has been assigned to window fluctuations, i.e., breathing motions of 8-membered rings in zeolite A [76], of 12-membered rings in zeolite Y [64, 72], and of the two kinds of windows connecting adjacent cages in zeolite EMT [296]. The effect of cations on fluctuations of the window aperture has been interpreted as a consequence of the fact that extra-framework cations follow the motion of the framework atoms, i.e., as a consequence of mode couplings [76]. The assignment of the peak around 100 cm^{-1} in the Raman spectra to a framework mode is further corroborated by the KED of sodium ions in Na-Y which shows a distinct minimum of about 10–20% exactly in the range of $120\text{--}100\text{ cm}^{-1}$ (cf. Fig. 4d).

To further verify the validity of the “site-concept” for cation dynamics in zeolites, a comparative computer modeling study has been carried out for cation-exchanged zeolites Na-Y and K-Y [79]. Due to the above-mentioned substantial couplings between framework and cation motions [77], the lattice has been treated as flexible in the calculations performed on the basis of both energy minimization (EM) and MD techniques [79]. An $n_{\text{Si}}/n_{\text{Al}}$ ratio of 2.5 has been chosen to check the influence of correlation effects for more densely packed cations. In a first step, spectra were calculated for models in which cations occupy separately the relevant crystallographic positions. The far-infrared spectra calculated for Na-Y by the EM method using a shell-model potential are presented in Fig. 16 (c). The corresponding power spectra for cations using the MD technique are given in Fig. 16 (d). From the spectra calculated by the EM method, it is evident that at least two well-separated bands correspond to each cation site. The vibrational density of states calculated by MD are spread over the range between 250 and 30 cm^{-1} for each cation position. The results of both techniques indicate in good agreement that no band can be attributed exclusively to cations at one crystallographic position. This result coincides very well with the conclusion drawn in MD studies of zeolite A [77]. In a second step, spectra were calculated with the cations distributed at all sites according to crystallographic data. As can be taken from Figs. 16 (c) and (d), a very good overall agreement with the experimental far-infrared spectrum has been achieved in this case with both methods. All observed spectral absorptions have counterparts in the computed spectra. The conclusion that a good reproduction of the experiment can only be reached if all cation sites are taken into account in the calculations clearly indicates that the far-infrared spectra reflect the occupation of different cation positions. With this thought in mind, one expects vibrational spectroscopic techniques in the far-infrared region to be well-suited for qualitative studies of the occupation of different cation sites in zeolites. On the other hand, the results also show unambiguously that no particular band can be assigned to a cation mode in one

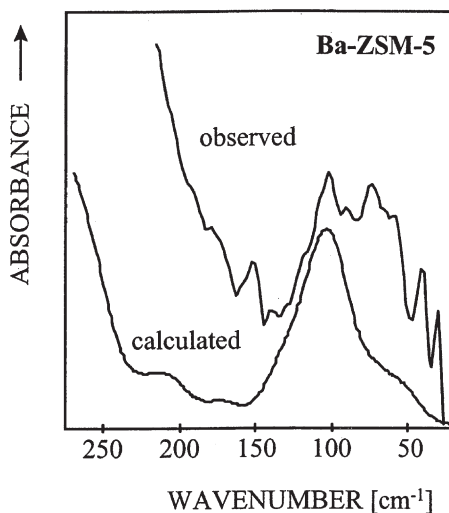


Fig. 17. Calculated and experimental FIR spectrum of Ba-ZSM-5 ($n_{\text{Si}}/n_{\text{Al}} = 13$), adopted from [363] with permission

specific position. In so far, the “site-concept” presently has to be considered as an oversimplification. Furthermore, from the calculated spectra shown in Figs. 16 (c) and (d) it follows that the entire spectrum cannot be conceived as a simple superposition of the contributions of separate sites. This points to dynamic interactions between cations at different sites.

Far-infrared spectra of zeolites with well-dispersed cations, which are compared to A-, X- and Y-type zeolites rich in silicon, would be of special interest. However, they are distinctly more difficult to record, because the low cation concentration gives rather low IR intensities. To our own experience, high-quality spectra can be recorded for divalent alkaline earth cation-exchanged MFI-type zeolites up to a silicon-to-aluminum ratio of around fifteen. This corresponds only to about three cations per unit cell. Figure 17 shows the far-infrared spectrum of a Ba-exchanged zeolite ZSM-5 with $n_{\text{Si}}/n_{\text{Al}}=13$ as an example [363].

As can be seen, two bands at 102 and 73 cm^{-1} arise. However, a reliable interpretation of this spectrum is quite difficult. The key problem in interpreting far-infrared spectra of silicon-rich zeolites such as ZSM-5 is connected with the fact that, due to the low cation concentration, structural information about cation sites are so far rather scarce. Under the mentioned conditions it would certainly be a substantial progress if the vibrational assignment in the far-infrared region could be assisted by other suitable cation-sensitive techniques which provide additional information. One way, as chosen in Ref. [363], is to start from X-ray absorption spectroscopy (XAS) giving access to the local environment of the cations and their coordination spheres. For the dehydrated Ba-ZSM-5 sample a six-fold oxygen coordination at a distance of 2.75 Å was obtained for Ba^{2+} ions by EXAFS analysis of the XAS spectrum. In a second step, positions in the unit cell of ZSM-5, which fulfill these criteria, were searched by computer simulation

techniques. By this procedure four equivalent sites located inside a cage consisting of two interconnected five-rings were found. These sites are surrounded by two sinusoidal and two straight channels, the latter being accessible via six-ring windows. Finally, the found Ba-ZSM-5 structure matching the EXAFS data has been taken to simulate the far-infrared spectrum using a shell model. The result of the calculation is given in Fig. 17 in comparison with the experimental spectrum. Two bands were calculated at 104 and 57 cm^{-1} , in good agreement with the experiment. As the results in the far-infrared region are very sensitive to cation positions, the close resemblance between the observed and the calculated spectrum can be taken as a confirmation of the cation site deduced from the EXAFS experiments.

Cation exchange with synthesized and calcined M-FAU and M-EMT samples ($M = \text{NH}_4, \text{Li}, \text{Na}, \text{K}, \text{Rb}, \text{Cs}, \text{Tl}$) was studied by means of far-infrared and low-frequency Raman spectroscopy in the contribution of Brémard et al. [364]. The IR and Raman spectra of the calcined M-EMT samples resembled those of the corresponding silica-rich cubic FAU materials. Bands attributed to motions of extra-framework cations changed in position and intensity depending on the nature of the cations. However, it turned out that it was impossible to assign any band to any particular site, and the translational motions of the cations were probably coupled with the deformation vibrations of the zeolite framework, thus confirming the above remarks on the “site-concept” and results reported in [77, 79]. A shifting and splitting of IR bands due to framework vibrations upon exchange of Zn^{2+} into zeolite A was observed by Wark et al. [365], in contrast to the IR results obtained on the exchange of other bivalent cations ($\text{Ca}^{2+}, \text{Mg}^{2+}, \text{Co}^{2+}, \text{Ni}^{2+}, \text{Cd}^{2+}$) into Na-A, Na-X and Na-Y. The observed effect of Zn^{2+} -introduction, which corresponded to XRD measurements, was explained by the formation of side-products such as $\text{Zn}(\text{OH})^+$, $\text{Zn}(\text{OH})_2$ or Zn-oxide particles during the exchange process, reducing the “local” symmetry of the framework tetrahedra.

Another interesting point is connected with the question whether there is any dependence of the most prominent Raman band, which generally occurs between 600 and 300 cm^{-1} in the spectra of zeolites, on the kind of the extra-framework cation. A first inspection of Fig. 14 reveals changes in position, intensity, and splitting of the line at about 500 cm^{-1} upon cation exchange. With respect to the spectrum of the Na-Y sample, a slight red-shift may be deduced with increasing cation radius, but this trend is not generally unequivocal. Even if the observed frequency shifts clearly indicate structural changes upon cation exchange, such effects should not be overestimated in the Raman spectra. One should be aware that, in particular for larger cations, no complete ion exchange can be reached with conventional exchange methods. In addition to the shift of the dominant Raman line upon cation exchange an additional shoulder has been observed at lower wavenumbers in the spectra of K-Y, Rb-Y, and (less pronounced) Cs-Y (Fig. 14d). The origin of this line splitting is at present not well understood. Attempts to reproduce the splitting adequately by MD simulations of the Raman spectra failed, even though both structural and force field parameters were varied considerably [74]. Hence, the effect is not, as often suggested, explicable by structural changes alone. One possible explanation may be sought in the influence of the different electrostatic fields of the cations requiring an explicit con-

sideration of long-range interactions. Alternatively, (i) longitudinal optic (LO) - transversal optic (TO) splitting or (ii) Fermi resonance have been proposed as conceivable explanations [296]. Both processes are not considered in the simulations: process (i) because of the restriction of MD simulations with periodic boundary conditions to the zero-wavevector modes of the simulation box (no LO modes) and process (ii) because of the classical model used in the calculations.

In the region between 500 and 200 cm^{-1} the Raman spectra are characterized by two weaker bands at about 370 and 300 cm^{-1} , slightly shifted in dependence on the kind of cation. These bands have to be assigned to faujasite framework modes. Their exact positions have been observed to be dependent on the hydration level of the sample [295].

In summary, the Raman spectra in the framework region are determined by three parameters: the $n_{\text{Si}}/n_{\text{Al}}$ ratio of the framework, the kind of cations occupying extra-framework sites, and the degree of water content of the individual sample.

5.3.2

Cation Vibrations Affected by Adsorption

It has been well-known for a long time that besides their cation sensitivity, far-infrared spectra of microporous materials can undergo remarkable changes upon adsorption of probe molecules [366]. Disregarding the far-infrared normal modes of the adsorbed molecules themselves, the expectations with respect to this spectral region are twofold.

On the one hand, one can expect to observe external modes which become hindered translations and rotations upon adsorption. Altogether, six degrees of freedom (three translational and three rotational) of the adsorbate are transformed into frustrated translations and rotations by adsorption, and the corresponding modes should be most sensitive to the nature and strength of host/guest interactions. Unfortunately, the direct observation of these modes by means of optical spectroscopy is extremely difficult and therefore limited to a few examples [367]. The most serious difficulties are certainly due to surface heterogeneity and anharmonic motions giving rise to broad and less intense bands hidden by strong absorptions of the host. Rather, the observation of external motions of trapped species seems to be a domain of neutron spectroscopy. For example, frequencies of external modes have been observed for benzene in Na-Y [368] and for methane in Na-A [369] zeolites by neutron spectroscopy. For methane in zeolite Na-A two peaks were observed at 178 and 69 cm^{-1} which were attributed to the libration and translation modes of the trapped molecules, respectively.

On the other hand, the interaction with adsorbed molecules is indicated by frequency shifts of the cation modes. In most of the earlier studies downward-shifts of the cation bands were observed and explained by both the delocalization of the framework charge and the increase of the effective mass of the oscillator by solvent interaction upon adsorption. Nevertheless, an unambiguous interpretation of the adsorption-induced changes in the far-infrared spectra is not straightforward due to at least three reasons:

- (1) Since cation modes and external modes are situated in the same energy range, a strong coupling between these motions might be expected. Such a coupling has recently been revealed for benzene adsorbed in Na-Y [370].
- (2) Especially in the case of polar guest molecules it is a well-known phenomenon that, upon adsorption, the cations can remarkably change their positions. Naturally, cation migration affects the far-infrared spectra emphatically. The repercussion of migration effects on the spectrum is not strictly evident, taking into account that no band can be assigned to modes at specific sites.
- (3) If probe molecules as reactive as CO₂ or aromatics are considered, one has to ensure that no chemical conversion takes place. In such cases it is recommended to record the spectra at low temperature instead of room temperature as usually done.

To illustrate the changes in the far-infrared spectra upon adsorption, Fig. 18 shows in an exemplary way the spectra of zeolites Na-Y and K-Y before and after adsorption of the N-heterocycles pyrrole [371] and pyrrolidine [372].

At a first glance, the spectra before and after adsorption look quite similar. A closer inspection, however, reveals that nearly all bands are entangled into interaction either by frequency shifts, changes in intensity, or by band broadenings. As can be seen, the shoulders at 159 (Na-Y) and 107 cm⁻¹ (K-Y), originally assigned to cation modes at SI sites (cf. Fig. 16b), are most remarkably influenced upon adsorption of both N-heterocyclic compounds. This again points to the insufficiency of the “site-concept”, since cations located inside the hexagonal prisms are not accessible by the probe molecules under study due to their large size. Looking at dependencies of the observed band shifts on the kind of cation shows that the shifts are slightly enhanced with increasing strength of the Lewis acidity of the cation. This can be taken as an indication of an increase of the interaction strength following the order Na⁺>K⁺. No additional bands due to external modes could be observed for the interaction with either of the probe molecules (cf. also Sect. 5.5.2.6). Only for the pyrrolidine/Na-Y system did a small additional shoulder at 65 cm⁻¹ appear, but from a comparison with the spectrum of pyrrolidine in the gas phase this band had to be assigned to the large amplitude ring-puckering motion (pseudorotation) of the molecule [372]. In contrast, the spectrum of pyrrole is free of bands below 400 cm⁻¹. This may be considered as an advantage of pyrrole as a probe molecule for investigations of adsorption-induced changes of cation modes [371].

The framework vibrations of AlPO₄-5 and the isostructural SSZ-24 as well as the effect of protonation and cation exchange on framework vibrations upon reammoniation of H-Y and dehydration of Ni-Y were demonstrated by Jacobs et al. [373] via in-situ IR experiments and, at the same time, related to theoretical studies of the correspondingly relaxed structures, using a valence force field model.

In summary, the far-infrared region reveals valuable information about host/guest interactions in molecular sieves, but many of the results reported so far should presently be considered as in an initial stage. We have mentioned some aspects from which we suggest to look very carefully at the interpretation of adsorption-induced changes, especially in this spectral range. In particular, a

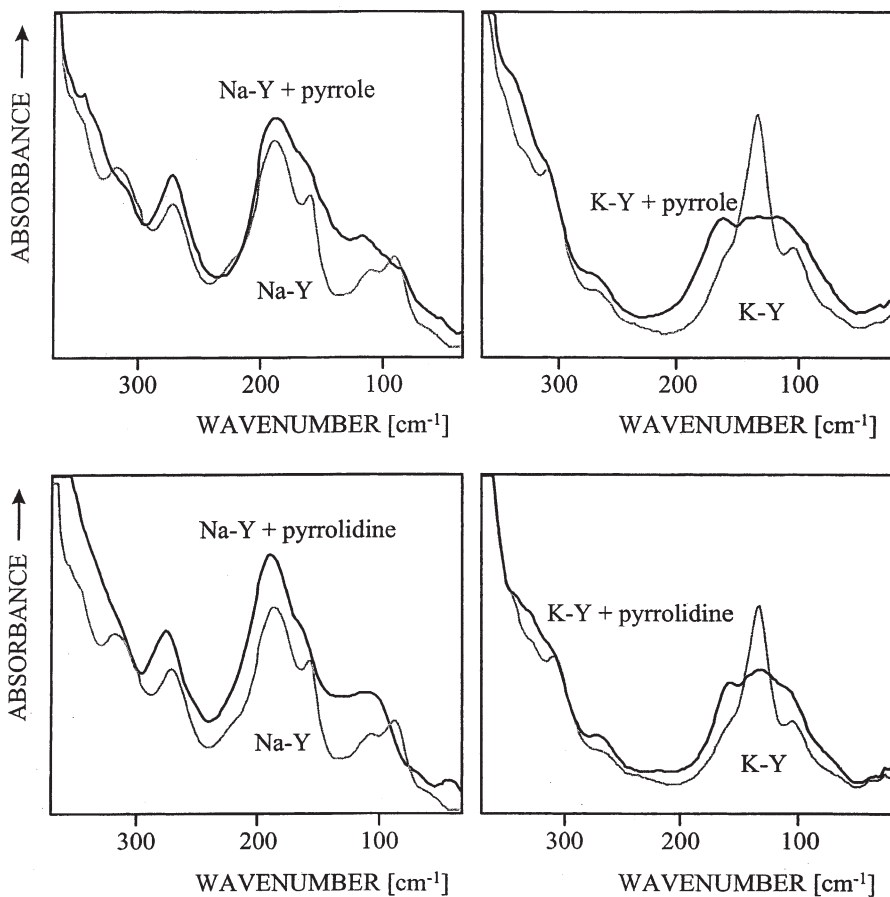


Fig. 18. Comparison of far-infrared spectra of zeolites Na-Y and K-Y before and after adsorption of pyrrole [371] and pyrrolidine (from [372] with permission)

reliable interpretation of the shift of only a single specific band seems to be impossible. Furthermore, we prefer to accompany FIR studies by other experimental and modeling techniques to provide a deeper insight into the adsorption behavior and dynamics of molecules in porous materials.

5.4

Hydroxy Groups

5.4.1

Hydroxy Groups of Zeolites Characterized by IR Fundamental Stretching Bands

From the very beginning of the application of infrared spectroscopy in zeolite science, problems of formation, characterization and properties of surface OH groups attracted the interest of researchers (cf. [214]), especially as far as acid

OH groups, so-called Brønsted acid sites, were regarded. This interest was particularly stimulated by the close relationship which was suspected to exist between (Brønsted and/or Lewis) acidity and the catalytic behavior of zeolites.

5.4.1.1

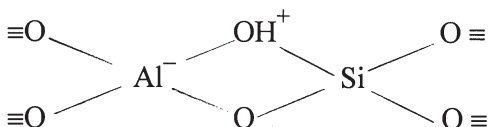
Faujasite-Type Zeolites (FAU)

5.4.1.1.1

Non-Modified Faujasite-Type Zeolites

Stimulated by the enormous interest in applications of faujasite-type zeolites (X- and Y-type zeolites) in catalysis, the pioneering IR spectroscopic work was first almost exclusively carried out with synthetic faujasites.

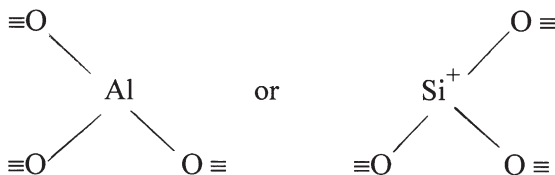
Early discussions on OH groups detected by IR of cationic (sodium or calcium) forms of zeolites, especially after interaction with water, were reported by Frohnsdorf and Kington [374], Carter et al. [375], Habgood [376], and Zhdanov et al. [377]. In fact, Frohnsdorf and Kington used zeolite A containing Na^+ cations as adsorbent for water, whereas the other authors employed X-type zeolite in its sodium form or loaded with the whole series of alkaline cations [377]. Even though the experimental techniques for IR spectroscopy on such materials like zeolites were not yet well-developed, these pioneering workers arrived at interesting and still valid results. Thus, already Szymanski et al. [201] observed bands at 3550 cm^{-1} indicative of hydroxy groups after interaction of water with Na-X zeolite and after heat treatment of (partially exchanged) $\text{NH}_4\text{Na-X}$. The band intensity was low in the first case and more pronounced in the latter. The authors essentially correctly interpreted the appearance of the bands as a result of replacement of Na^+ by H_3O^+ or H^+ during synthesis and, respectively, deammoniation of $\text{NH}_4\text{Na-X}$, followed by proton attack of the anionic framework. First, regarding the findings with Na-X and in view of later studies, water dissociation caused by interaction of H_2O with traces of contaminating Ca^{2+} could certainly not be excluded (*vide infra*). Secondly, the mechanism of OH formation via deammoniation of $\text{NH}_4\text{Na-X}$ was confirmed by monitoring the disappearance of the respective NH vibration modes (indicated by bands around 3150 and 1385 cm^{-1}) upon removal of NH_3 . The authors also suggested the formation of *bridging OH groups (Brønsted acid-type sites)* as a result of deammoniation or the above-mentioned replacement of Na^+ by H_3O^+ and subsequent elimination of H_2O . They also represented this type of surface species by the structure of Scheme 1.



Scheme 1

Finally, Szymanski et al. even advanced the idea of formation of only three-fold coordinated Al (or Si) through combination of two bridging OH groups under

elimination of H_2O upon thermal treatment at elevated temperatures giving rise to *Lewis acid-type sites*, as sketched in Scheme 2.



Scheme 2

In 1965, Uytterhoeven et al. published their classic paper, where they investigated by IR the development of acid OH groups via deammoniation of the ammonium form of Y-type zeolites [205]. In-situ deammoniation of faujasite-type $\text{NH}_4\text{-Y}$ at elevated temperatures generated bands of hydroxy groups at about 3740 , 3670 and 3580 cm^{-1} (cf. Fig. 19).

The two prominent bands at 3670 and 3580 cm^{-1} were ascribed to acid OH groups, now usually called “bridging OH groups or hydroxy groups” and visualized as *Brønsted acid centers*, since they were able to react with neutralizing bases such as NH_3 (reversing deammoniation) or pyridine (cf. Sect. 5.5.2.6.2). The

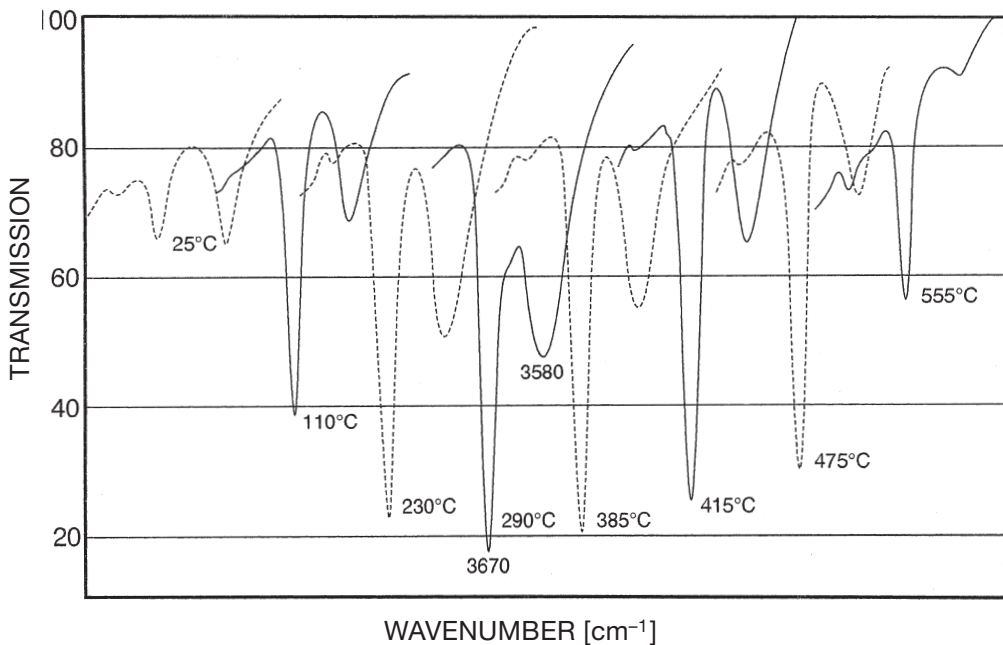


Fig. 19. Development of the low-frequency (3580 cm^{-1}) and high-frequency (3670 cm^{-1}) bands on deammoniation of zeolite $\text{NH}_4\text{-Y}$ in high vacuum at increasing temperatures leading to dehydroxylation above about $400 \text{ }^\circ\text{C}$ (675 K) (adopted from [205])

bands of bridging hydroxy groups in H-Y are usually observed at somewhat lower frequencies, viz. at about 3640 and 3550 cm^{-1} (cf., e.g., [206, 207]). Such differences are frequently encountered, especially in earlier IR studies, and may be due to differences in experimental conditions (spectrometer setting, sample composition and pretreatment, observation temperature, etc.). With further increasing temperature these bands started to decrease in intensity as a result of dehydroxylation (*vide infra*). Somewhat later, similar IR results obtained with $\text{NH}_4\text{-Y}$ and $\text{Mg}_2\text{NH}_4\text{-Y}$ and the effect of the calcination temperature were reported by Ward [207], who observed bands at 3742 , 3643 and 3540 cm^{-1} . The existence of two well-separated bands of acid OH groups in faujasite-type zeolites was first tentatively explained by a mutual interaction of a fraction of the hydroxy groups, i.e., it was assumed that adjacent OH groups with suitably low distance could form hydrogen bonds to each other [378] or to oxygen atoms of the framework [379]. However, no direct experimental proof for hydrogen bonding could be obtained from the far-infrared spectra (cf. Fig. 15). Based on systematic studies, Jacobs and Uytterhoeven suggested that the duplicity of OH stretching modes in the case of deammoniated $\text{NH}_4\text{-Y}$, i.e., H-Y, is due to differences in the crystallographic positions of the involved framework oxygens [380]. Thus, the high-frequency band (HF band at $3640\text{--}3680\text{ cm}^{-1}$) was ascribed to OH oscillators generated by proton attachment to O_1 -oxygens (cf. Fig. 20). These OH oscillators point into the large cavities, whereas the low-frequency band (LF band around 3550 cm^{-1}) was thought to be indicative of OH groups directing into the small cavities and correlated to O_2 -, O_3 - and O_4 -oxygens of the framework.

Jacobs and Uytterhoeven [380] confirmed in a systematic study the assignment of the HF band to O_1H groups suggested by earlier reports [379, 381–384].

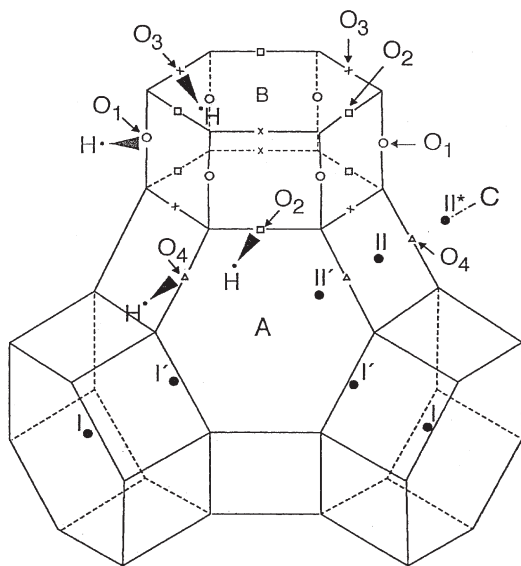


Fig. 20. Fragment of the faujasite-type structure indicating the four crystallographically different oxygen atoms (O_1 , O_2 , O_3 , O_4) and the corresponding OH groups (O_1H , O_2H , O_3H , O_4H)

However, depending on the degree of exchange of Na^+ by H^+ they found a maximum of up to three components contributing to the LF band. They attributed the main fraction to O_3H vibrations, and about 10% of the total acid OH groups were identified as O_2H and O_4H and also assumed to be involved in the LF band. Smaller band components around 3626 and 3450 cm^{-1} were ascribed to OH groups on aluminum-deficient sites in the lattice and artefacts, respectively; in fact, the 3450 cm^{-1} component of the decomposed LF band was absent in some samples used in the study of Ref. [380]. Czjzek et al. [385] reconsidered these assignments and showed via inelastic neutron scattering that the HF band mainly originates from O_1H and the LF band from O_3H vibrations. The concentration of O_2H was found to be distinctly lower and, at some variance to Ref. [380], the O_4 sites essentially non-populated by protons. These results are in good agreement with the predictions made by calculations using the lattice energy minimization technique [47].

The difference in the wavenumbers of the IR stretching bands of H-Y corresponds to the difference in their chemical shifts in ^1H MAS NMR spectra ([386–388]; cf. also Volume 4, Chapter 2 of this series), in that the IR-HF band is related to the ^1H MAS NMR signal (so-called line b) at δ (TMS)=3.9–4.6 and the IR-LF band to δ (TMS)=4.8–5.6 ppm (line c), referenced to tetramethylsilane, TMS.

Brunner [389] showed by ^1H MAS NMR that, in complete agreement with the findings of Czjzek et al. [385], the ratio of the concentration of the bridging hydroxy groups pointing into the large cavities (line b, HF band) to those vibrating into the six-membered rings (line c, LF band) is 0.9 ± 0.1 .

The higher value of the chemical shift (lower frequency) was explained as the consequence of an additional interaction of the respective OH groups with adjacent oxygen atoms in the small cavities [390, 391]. An earlier assumption of differences in the acid strength of the two types of hydroxy groups [392] was abandoned, in agreement with IR/TPD measurements using partially dealuminated H-Y samples, where both types of acid OH groups became accessible for the basic probe molecule pyridine ([393]; cf. also Sect. 5.5.2.6.2, and a subsequent chapter in a later volume on acidity in this series). Furthermore, a relationship between the decrease of the wavenumber of the OH stretching mode and the narrowness of the proton-containing oxygen rings of the zeolite structure was suggested [394]. A general consideration of the conditions under which the position of an OH stretching band in the IR spectrum of a zeolite structure (and the corresponding chemical shift in the MAS NMR spectrum) may indicate a measure of the acid strength of the respective OH groups is dealt with in Ref. [391].

It was observed that the exact wavenumber of bands indicating acid OH groups in zeolites was influenced by the $n_{\text{Si}}/n_{\text{Al}}$ ratio of the framework. Generally, the bands were found to shift to higher frequencies when the silicon content increased. This was first studied systematically by Barthomeuf [395, 396] (see also Sect. 5.4.1.2). Thus, the band observed at the highest frequency, i.e., at 3745 cm^{-1} (vide infra) is the only one in the case of completely dealuminated Y-type zeolite or other siliceous frameworks (such as silicalite-1, cf. Sect. 5.4.2) and coincides with the band well-known from pure, i.e., aluminum-free, non-acid, amorphous silica. In fact, it is indicative of a third type of OH groups of deammoniated

$\text{NH}_4\text{-Y}$ which are frequently called *silanol groups*. In the case of H-Y, the corresponding band at $3740\text{--}3745\text{ cm}^{-1}$ is usually rather small (see Fig. 19), which means that the density of silanol sites is relatively low. Actually, high intensities of the bands of internal silanol groups of hydrogen faujasites can be taken as an indication of lattice defects provided the activation of the samples was carried out under “shallow-bed” conditions, i.e., under exclusion of “self-steaming” (vide infra). This type of OH groups turned out to be non-acidic or at least much less acidic than the above-discussed centers indicated by the HF and LF bands. The hydroxy groups related to the $3740\text{--}3745\text{ cm}^{-1}$ band {and to the chemical shift of $\delta(\text{TMS})=1.8\text{ ppm}$; so-called line a (cf., e.g., [387, 389])}, were originally visualized as the only lattice-terminating OH groups on the external surface of the zeolite structure [205]. This was, inter alia, supported by a rough estimation of their number per gram zeolite via hydrogen-deuterium exchange and an estimation of the external surface based on sizes of $0.1\text{--}1.0\text{ mm}$ or an average size of $0.3\text{ }\mu\text{m}$ of the primary zeolite particles [205]. However, later on it was shown that on the one hand OH groups of similar properties exist in the interior of the zeolite crystallites {e.g., in the form of so-called hydroxy nests or defect sites, ([397]; vide infra)} and, on the other hand, acid OH groups also occur on the external zeolite surface [398]. Jacobs and Uytterhoeven [380, 399] advanced arguments to relate a 3727 cm^{-1} band to hydroxy groups associated with aluminum-deficient sites in the zeolite framework (internal silanols). At sufficiently high resolution of the spectrometer, this band can be well separated from the band at $3735\text{--}3740\text{ cm}^{-1}$ of external, crystallite-terminating silanol groups.

As an example of isomorphously substituted faujasite-type zeolite, Poncelet et al. [400] described properties of an X-type zeolite, where the silicon is completely substituted by germanium, i.e., H, Na-[Ge]X with $n_{\text{Ge}}/n_{\text{Al}}=1$. It was reported that H, Na-[Ge]X contained OH groups in the supercage, which gave rise to a stretching band around 3650 cm^{-1} . It appeared that the average acidity strength of the OH groups in the faujasite-type zeolites follows the sequence H, Na-[Ge]X ($n_{\text{Ge}}/n_{\text{Al}}=1.0$, $n_{\text{H}}/n_{\text{Al}}=0.2$) < H, Na-[Si]X ($n_{\text{Si}}/n_{\text{Al}}=1.25$, $n_{\text{H}}/n_{\text{Al}}=0.5$) < H, Na-[Si]Y ($n_{\text{Si}}/n_{\text{Al}}=2.5$, $n_{\text{H}}/n_{\text{Al}}=0.7$) < (dealuminated) H, Na-[Si]Y ($n_{\text{Si}}/n_{\text{Al}}\approx 4.7$, $n_{\text{H}}/n_{\text{Al}}=0.7$), where [Si]X and [Si]Y designate the materials with only silicon (besides aluminum) in the framework. However, it should be noted that the degree of exchange of H for Na increased in the same sequence (cf. $n_{\text{H}}/n_{\text{Al}}$).

5.4.1.1.2

Dealuminated Faujasite-Type Zeolites

Since the thermal stability of hydrogen forms of faujasite-type zeolites turned out to be crucial in their important industrial application as cracking catalysts [401, 402], techniques were developed for stability improvement, as for instance the treatment via “steaming” of the catalysts [403–406]. This procedure of treatment of $\text{NH}_4\text{-}$ or H-forms of faujasite-type catalysts requires the presence of water vapor at elevated temperatures [404–407]. It proved to reduce the density of strong Brønsted sites (indicated by the bands at ca. 3640 and 3550 cm^{-1}), to increase the concentration of non-acid silanol groups (i.e., the intensity of the 3740 cm^{-1} -band) and to generate additional OH groups different from those

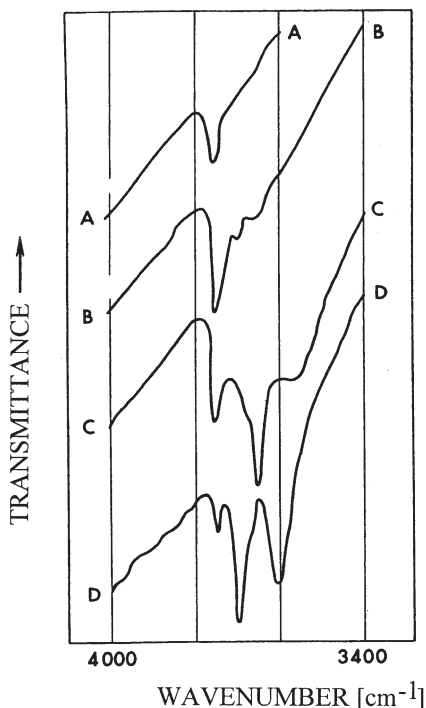


Fig. 21. Infrared spectra in the OH stretching region of Y-type zeolite after dealumination via steam treatment. Calcined in A: moist air at 813 K; B: self-steam at 813 K; C: moist air at 1033 K; D: self-steam at 1033 K [411]

discussed so far (Fig. 21; cf. [402, 408–412]). They were, however, detected by IR as well, and their wavenumbers were observed around 3600 and 3670–3690 cm^{-1} .

It was shown that the latter were due to non-acid hydroxy groups [399, 409]. Since stabilization of the hydrogen form was essentially due to dealumination [397, 407], the hydroxy groups newly formed upon steaming and indicated by the 3670–3690 cm^{-1} band were ascribed to OHs attached to extra-framework Al-containing species, i.e., Al-OH species [408, 410, 413; (cf. also [414, 417, 419])].

Breck and Skeels [407] removed via treatment with NaCl or KF solutions a significant fraction of aluminum atoms per unit cell from samples, which had been steamed at increasingly higher temperatures. The products obtained at each step (i.e., at a certain steaming temperature followed by extraction) were investigated IR spectroscopically prior to and after adsorption of ammonia and benzene (cf. Sects. 5.5.2.6.2 and 5.5.2.7). From the spectra of the OH region, both the acidity/non-acidity and accessibility/inaccessibility of the respective OH groups were deduced. Based on the spectroscopic results and chemical analysis of the extracts, the authors concluded that steaming possibly produced extra-framework species in the form of m-trioxotri-aluminum cations, $(\text{Al}_3\text{O}_3)^{3+}$, located in the sodalite cages and stabilizing the structure. A band at 3600 cm^{-1} observed after

steaming at 773 K was assumed to originate from (largely inaccessible) OH groups associated with these cations, another band at 3695 cm^{-1} assigned to (accessible) hydroxy groups at defect sites in the framework.

As a band around 3740 cm^{-1} indicating terminating silanol-like hydroxy groups was ubiquitous in IR spectra of zeolites, bands at about $3660\text{--}3680\text{ cm}^{-1}$ were also frequently observed with many different zeolite types, in particular when the materials were subjected to heat-treatment or other procedures which may cause dealumination. In contrast to the above interpretation (cf. [410, 413, 414]), sometimes different assignments were suggested. Thus, Ballivet and Barthomeuf [415] ascribed a band at 3680 cm^{-1} detected in the IR spectrum of zeolite L to non-acid OH groups associated with the cation (K^+). In the present context, the work by Wichterlová et al. [416] should be mentioned, who compared via IR spectroscopy dehydroxylated, steam-stabilized and Al-ion exchanged Y-type zeolites. The state of Al in these differently prepared materials was shown to be significantly different. Lutz et al. [408], in their investigation of hydrothermally dealuminated H-ZSM-5, assigned a band at 3665 cm^{-1} to proton-compensating AlO_4 tetrahedra, where the aluminum atom is still partly bonded to the zeolite framework. Another band at 3780 cm^{-1} , however, was ascribed to weakly acid OH groups of extra-framework aluminum-containing species such as $\text{O}=\text{Al}-\text{OH}$. However, generally the interpretation of the bands at $3660\text{--}3680\text{ cm}^{-1}$ as being due to OH groups of non-framework Al is accepted, the more so as this is supported by MAS NMR investigations (see also Refs. [418, 419]). Lohse et al. [419] reported (besides a band at 3606 cm^{-1} for acidic hydroxy groups) an IR band at 3693 cm^{-1} and an ^1H MAS NMR line at δ (TMS)=2.6 ppm for Al-OH groups in dealuminated H-Y. Also, Ward [420] interpreted an IR band at $3660\text{--}3670\text{ cm}^{-1}$ as representing Al-OH groups, possibly due to $\text{Al}(\text{OH})_3$, $\text{Al}(\text{OH})_2^+$, or $\text{Al}(\text{OH})^{2+}$.

In agreement with Refs. [380, 399], however, Loeffler et al. [417] advanced arguments to relate the 3727 cm^{-1} band to hydroxy groups associated with aluminum-deficient sites in the zeolite lattice.

The (fundamental) hydroxy region of ultrastable Y-type zeolite (US-Y) was also analyzed via FTIR in the study by Makarova and Dwyer [421]. These authors combined FTIR spectroscopy with a step-wise desorption of pre-adsorbed ammonia. This permitted a better resolution of the overlapping OH bands indicating OH groups of different strength. It was suggested that bands observed at 3599 and 3525 cm^{-1} originated from two types of superacidic hydroxy groups accommodated in the supercages and β -cages, respectively. The generation of superacidity was ascribed to a perturbation of the OH groups through Lewis sites (cf. also [422]). More recently, Datka et al. [423] determined the distribution of acid strengths in steamed H-Y after removal of extra-framework Al-containing species via treatment with EDTA, using a combination of IR, ^{27}Al MAS NMR and ^{29}Si MAS NMR spectroscopic experiments. A subsequent analysis of OH and OD spectra of severely dealuminated H-Y ($n_{\text{Si}}/n_{\text{Al}}\approx 100$) by Datka and co-workers [424] revealed that the remaining strongly acidic [$\equiv\text{Si}-(\text{O}_1\text{H})-\text{Al}\equiv$] groups were homogeneous in strength. This was explained by the assumption that after severe dealumination only [$(\text{OSi})_3\equiv\text{Si}-(\text{O}_1\text{H})-\text{Al}\equiv(\text{SiO})_3$] configurations were left, whereas, for instance, for the parent H-Y zeolite with $n_{\text{Si}}/n_{\text{Al}}=2.56$ three different

configurations and correspondingly three types of differently acidic OH groups were assumed.

Jia et al. [425] studied by IR spectroscopy the OH vibration region of dealuminated Y-type zeolites, designated as D-H-Y and D-La,H-Y, which were prepared by a combination of deep-bed calcination and acid leaching. HF-OH groups were detected at 3625 cm^{-1} (D-H-Y, D-La,H-Y), whereas the LF-OH bands appeared at 3540 (D-H-Y) and 3550 (D-La,H-Y). The effects of adsorption of probe molecules such as NH_3 , pyridine, butadiene, C_6D_6 (deuterium/hydrogen exchange) were extensively investigated (see Sect. 5.5.2.6.2)

A combined FTIR and INS study was conducted by Jacobs et al. [253] on the vibrational properties of H-Y zeolite, including the stretching and bending modes (see below) of the acid hydroxy groups and the proton-coupled framework vibrations (vide supra) as well as the effect of dealumination on these features. Similarly, the OH stretching region was investigated by IR spectroscopy in the work of Ray et al. [426] and Patzelová et al. [427]. Ray et al. found via IR several types of Si-OH moieties in dealuminated Y-type zeolites. The authors of Ref. [427] observed OH bands in the range of $3643\text{--}3625\text{ cm}^{-1}$, the wavenumbers of which decreased with increasing $n_{\text{Si}}/n_{\text{Al}}$ ratios (3.2–5.4). The DRIFT technique (for near infrared) as well as the transmission FTIR (for mid infrared) spectroscopy of thin wafers was employed by Hanke and Moeller [428] when monitoring the dealumination of H, Na-Y. The same study dealt also with the formation of OH groups upon interaction of water with and desorption of water from Na-A, Na-X, Na,Cs-X, K-X, Na-Y, and H-Y (vide supra, Sect. 5.4.1.1) and the deammoniation of NH_4 , Na-Y. The authors combined the results of IR spectroscopy in the regions of fundamental, combination and overtone modes.

In Sect. 5.2.2.10, the work by Kubelková et al. [271] on H-Y, Ce, Na-Y and dealuminated Ce, Na-Y was already mentioned, which was carried out employing the DRS/KBr pellet technique. These authors, however, obtained also DRS spectra of the powdered materials and compared their results with those of the conventional IR transmission spectroscopy of self-supporting wafers. They found that some of the OH bands observed by DRS were shifted to lower wavenumbers and attributed this effect to the higher temperature produced by the DRS beam in the powdered samples. In an investigation of hydrothermally treated and, thus, dealuminated H-ZSM-5 Martin et al. [429] observed by the pyridine/IR technique an elimination of Brønsted sites accompanied by a condensation of extra-framework Al-containing species (Lewis centers).

Y-type zeolite samples, which were dealuminated and stabilized by a second method, viz via the SiCl_4 technique (cf. Volume 3, Chapter 3 of the present series), were investigated by transmission IR spectroscopy in the work by Anderson and Klinowski [136]. These authors attempted to determine the concentration (more precisely the ratio of Brønsted to Lewis site concentrations, $c_{\text{B}}/c_{\text{L}}$), location and strength of the Brønsted and Lewis acid sites. They used extinction coefficients, ϵ_{v} (in $\text{cm}^2\ \mu\text{mol}^{-1}$), according to Eq. (24). Interestingly, they observed $c_{\text{B}}/c_{\text{L}}=0.9$ for the parent sample of H-Y, but a decreasing level of Lewis centers (extra-framework aluminum) and an increasing accessibility of acid sites inside the sodalite cages for, e.g., pyridine with progressive dealumination by SiCl_4 treatment (cf. [430] and vide infra, Sect. 5.5.2.6.2). The effect of this method of dea-

lumination on Na-Y was also studied by combined IR and NMR experiments by Grobet et al. [431].

Several authors compared via IR spectroscopy zeolites with systematically varied $n_{\text{Si}}/n_{\text{Al}}$ ratios, which were prepared by different dealumination techniques (cf. also Volume 3, Chapter 3 of this series). Thus, already Skeels and Breck [432], who developed the $(\text{NH}_4)_2\text{SiF}_6$ -method, followed dealumination through $(\text{NH}_4)_2\text{SiF}_6$ treatment via IR spectroscopy in both the framework and OH stretching region. Triantafillidis et al. [433] dealuminated zeolites with the help of EDTA, $(\text{NH}_4)_2\text{SiF}_6$, SiCl_4 or hydrothermal treatment and studied, inter alia IR spectroscopically, the effect on the OH stretching region. They showed that isomorphic substitution of silicon for aluminum can be achieved with SiCl_4 , $(\text{NH}_4)_2\text{SiF}_6$ or appropriate hydrothermal treatment, but not with EDTA. However, when substitution occurred, extra-framework aluminum-containing species were generated. The acidity of dealuminated Y-type zeolites and especially the effect of removal of extra-framework Al on the differences in adsorption of ammonia from the gas phase and aqueous solution was studied by Stockenhuber and Lercher [434], who employed various methods for characterization, including to a large extent FTIR spectroscopy. Leaching of extra-framework aluminum in solution enhanced considerably the adsorption capacity.

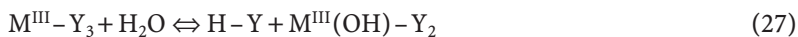
5.4.1.1.3

Cation-Exchanged Faujasite-Type Zeolites

Another method to produce more stable cracking catalysts is the introduction of polyvalent cations into, e.g., Na-Y, in particular La^{3+} or rare earth (RE) cations [435, 436]. Hirschler [437] and Plank [438] independently suggested that formation of OH groups via introduction of polyvalent cations is due to the following chemistry (which is nowadays generally referred to as the Hirschler-Plank mechanism), illustrated here with two selected examples using chlorides of two- or three-valent cations, M^{II} and M^{III} , respectively:



or



M^{II} may designate, e.g., Mg^{2+} , Ca^{2+} or Sr^{2+} and M^{III} may stand for La^{3+} or RE^{3+} ; Y represents here a monovalent, negatively charged fragment of the Y-type structure (see also [439–442]). The reactions are shifted the more to the right side the higher the polarizing effect of the cation is, i.e., the higher is its Coulomb field determined by the quotient q/r , where q stands for the charge and r for the radius of the cation [443, 444]. This is illustrated in Fig. 22 (taken from Ref. [443]) which shows (in fact, not for faujasites but for mordenites, MOR) an increasing absorbance of the band of Brønsted acid OH groups at around 3610 cm^{-1} with increasing q/r ($\text{Ba}^{2+} \rightarrow \text{Be}^{2+}$).

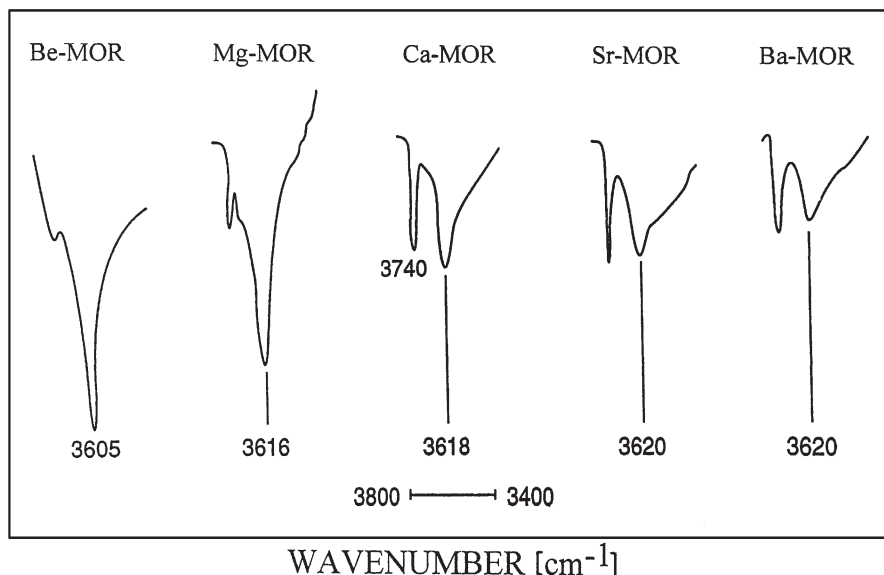


Fig. 22. Wavenumbers and intensities of the OH stretching bands of a homologous series of zeolites, viz. mordenites ion-exchanged with alkaline earth cations [443]

Similar reactions proceed with salt solutions of other cations (Cu^{2+} , Fe^{3+} , etc.) as well (cf., e.g., [445, 446]) and produce unavoidably OH groups which, in certain applications, may be undesired and have to be removed, for instance, by subsequent solid-state reaction (cf. Volume 3, Chapter 2 of this series) or via reaction with NaN_3 [447, 448].

Dzwigaj et al. [449] re-interpreted the HF OH-band generally appearing in the mid IR spectra of Y-type zeolites. They offered evidence for their suggestion that the HF-OH band of, e.g., H,Na-Y or H,Mg-Y is composed of two components with wavenumbers of 3648 and 3660 cm^{-1} originating from two different kinds of OH groups. This result was supported by pyridine adsorption experiments, which showed the appearance of two pairs of pyridinium ion bands, viz. at 1543/1627 and 1552/1636 cm^{-1} (cf. Sect. 5.5.2.6.2).

Spectra of Ce, Na-X obtained after activation at various temperatures were provided by Hoser et al. [450]. The spectra exhibited bands at about 3640 cm^{-1} (indicating acid OH groups in the supercages) and around 3520 cm^{-1} (presumably due to OH groups associated with Ce^{3+} cations). An FTIR study of RE-Y zeolites (RE=La, Nd, Sm, Gd, Dy) was carried out by Falabella Sousa-Aguiar et al. [250]. It showed that there were no significant changes in the framework region after incorporation of the RE cations (cf. Sect. 5.2). However, the band indicating the OH groups attached to the RE cations [cf. Eqs. (26) and (27)] shifted from 3530 (Gd) to 3556 cm^{-1} (La) as the cation radius increased. Surprisingly after pyridine adsorption (vide infra, Sect. 5.5.2.6.2), the intensity of the pyridinium ion bands (1540 and 1630 cm^{-1}) was reported to increase with decreasing r_{cation} .

Similar results were obtained upon interaction with 2,6-lutidine, which was claimed to be more selective with respect to Brønsted acid sites.

The Brønsted and Lewis acidity of La, Na-Y zeolites with various degrees of exchange was studied via IR spectroscopy of the OH stretching region, after adsorption of pyridine as a probe, after dehydroxylation and rehydration by Ballivet et al. [251]. Rehydration after dehydroxylation restored to a limited extent the OH groups (cf. also Sect. 5.6.3, especially [888]).

An extended re-investigation of the dehydration, deammoniation and reammoniation by in-situ FTIR was undertaken by van Santen and co-workers [451] in the whole range of 40–4000 cm^{-1} , including not only $\text{NH}_4\text{-Y}$ but also M-Y with M=Li, Na, K, Cs, Ca, Cu, Co and Ni. Thus, the OH stretching and bending modes (vide infra) as well as framework and cation vibrations (Sects. 5.2 and 5.3) were systematically studied. By the way, one interesting finding was a strong effect of heating on the framework modes in the case of exchange with the divalent cations Cu^{2+} , Co^{2+} and Ni^{2+} , which was explained by a relaxation of the flexible framework structure (cf. Sect. 5.2.3).

According to the Hirschler-Plank mechanism [cf. Eqs. (25–27)], however, not only the catalytically active Brønsted acid sites (H-Y) are generated, but also non-active OH groups of the M(OH) or M(OH)_2 complexes. While the acid OH groups formed through the above mechanism give rise to stretching frequencies similar to those discussed for deammoniated $\text{NH}_4\text{-Y}$, the OH groups attached to the metal cations M^{II} or M^{III} are apparently non-acid and, moreover, usually difficult to detect by IR. The latter is possibly due to low extinction coefficients and/or high thermal instability. Frequencies related to the Me(OH) or M(OH)_2 complexes are reported for several cases to occur around 3530 and 3680 cm^{-1} [442, 446, 452].

Later on, analogous experiments were carried out with H_2S . Here, the dissociation occurred even in the Coulomb field of monovalent cations such as Na^+ producing protons and SH^- groups which were attached to the cations [453–454]. The reaction took place according to



Both the Brønsted acid sites (H-X), generated via proton attack of the framework (bands around 3650 and 3580 cm^{-1}) and the SH groups (band around 2560 cm^{-1}) were detected by IR. As could be shown via quantitative evaluation of these bands, their intensities – and this means the density of the OH and SH groups – were correlated to the population of the SIII sites of the faujasite structure by Na^+ cations ([454, 455]; see Fig. 23).

5.4.1.2

Other Zeolites

Indeed, the faujasite-type zeolites (X and Y) attracted, from the beginning of research in zeolite catalysis and then for a long subsequent period, predominant interest of IR spectroscopists working in this field. However, already in the 1970s some similar studies were carried out with other zeolites. In fact, in that period

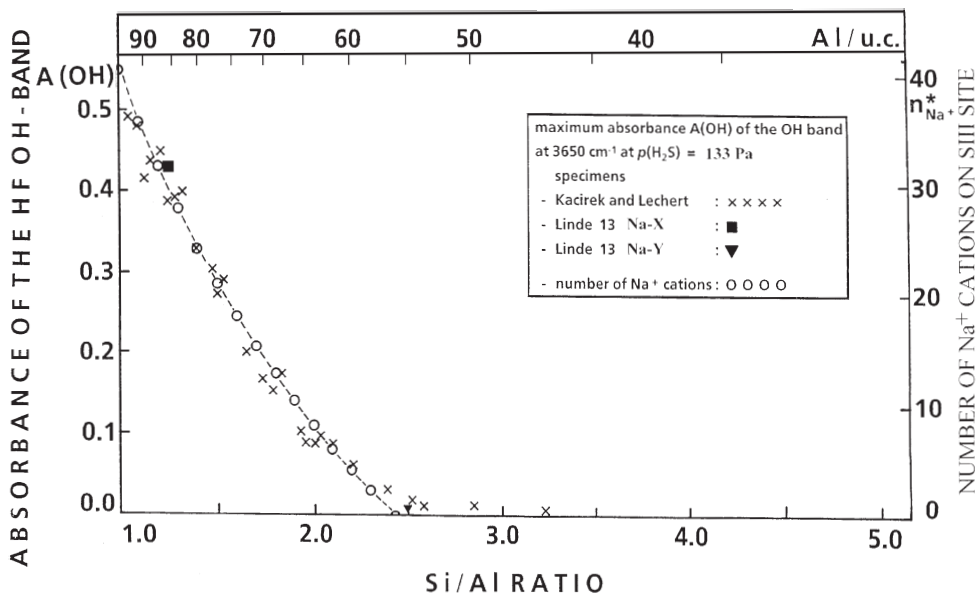


Fig. 23. Correlation between the absorbance of the OH stretching band produced on sorption of H_2S into faujasite-type zeolites and the population of the SIII sites (cf. Fig. 16a) by Na^+ cations [454]

only a few synthetic and/or natural zeolites other than faujasite-type ones, were available and suitable for such experiments. This situation changed only after the development of new synthesis methods and particularly after the advent of the synthetic zeolite ZSM-5 (MFI structure, cf. the “Atlas of Zeolite Framework Types” [235]).

5.4.1.2.1

Zeolite A (LTA)

Zeolite A, was first synthesized by Union Carbide Corp in 1956 [456–458] and then produced on a large scale and commercially applied as an adsorbent in separation processes and as an ion exchanger (very importantly, for instance, as a so-called builder in laundry detergents, cf. e.g., [459]). *Zeolite A* proved to be not a suitable material for IR investigation of zeolite hydroxy groups: This was due to the fact that the hydrogen form of zeolite A (obtained via deammoniation of the ammonium form) was rather unstable and suffered from lattice collapse [460–464]. This phenomenon of instability is related to the $n_{\text{Si}}/n_{\text{Al}}$ ratio of this zeolite (ideally $n_{\text{Si}}/n_{\text{Al}}=1$). Similar observations were made with NH_4 , Na-X zeolite with low $n_{\text{Si}}/n_{\text{Al}}$ ratios (of 1 to 1.2) and a high degree of exchange, i.e., replacement of Na^+ by NH_4^+ . In the case of hydrogen forms of zeolites having a very low $n_{\text{Si}}/n_{\text{Al}}$ ratio, intracrystalline acid solutions are generated on usually unavoidable contact with water vapor. These acid solutions, in turn, can easily attack the aluminum-rich framework, extract aluminum and, thus, destroy the lattice

[465, 466]. This is different, for instance, with highly siliceous zeolites such as mordenite, clinoptilolite, ZSM-5, etc. (vide infra).

5.4.1.2.2

Zeolite L (LTL)

An IR spectrum of *zeolite L (LTL)* was published as early as 1971 by Ward in his review article on infrared studies with zeolites [383] which dealt predominantly with faujasite-type materials (vide supra). He observed in deammoniated samples of NH_4 -L sharp bands at 3740 and 3630 cm^{-1} and a broad band centered around 3200 cm^{-1} . After evacuation at 813 K, only the 3740 cm^{-1} band remained. Similarly, Weeks and Bolton [467] found on deammoniation of NH_4 ,K-L, besides the absorbance at 3740 cm^{-1} , a single weak band at 3630 cm^{-1} . Major changes occurred in the framework region.

Dealumination of L-type zeolites through various methods, viz. steaming, treatment with $(\text{NH}_4)_2\text{SiF}_6$ and SiCl_4 was investigated by Bartl and Hoelderich [468] using XRD, ^{29}Si MAS NMR and FTIR spectroscopy of zeolite/KBr pellets. They monitored by the latter method changes in the framework vibrations and interpreted these in line with Flanigen's approach [114]. The dealumination via SiCl_4 treatment proved to be most efficient. It was, however, associated with a loss of adsorption capacity due to pore blockage by deposition of amorphous extra-framework silica and/or alumina.

5.4.1.2.3

Mordenite (MOR)

Hydrogen *mordenite* (H-MOR) was, because of its higher stability, in the first group of zeolites other than faujasite-type materials investigated in the hydrogen form by IR using the wafer technique. Early papers by Cannings [469] and Lefrançois and Malbois [470], however, did not report on direct investigations of the OH groups of mordenite, rather these authors observed the behavior of mordenite samples after adsorption of a basic probe, viz. pyridine, and respective results will be mentioned in Sect. 5.5.2.6.2. The difficulty in studying directly the OH stretching bands of H-MOR was due to the very low transmittance of the mordenite material in the respective spectral region; it was less than 1% compared to 25–40% of an NH_4 -Y (or H-Y) sample of equal "thickness", i.e., ca. 10 mg per cm^2 . Karge [466, 471, 472] was the first to succeed in obtaining IR spectra of H-MOR produced either by treatment of Na-MOR with mineral acids (Zeolon from Norton Comp., Worcester, Massachusetts) [466, 471, 472] or by deammoniation of NH_4 -MOR prepared via ion exchange of synthetic Na-MOR or natural mordenite [471, 472]. He found an OH stretching band close to 3610 cm^{-1} originating from acid OH groups, and bands at about 3740 cm^{-1} stemming from silanols. The thermal, chemical and catalytic properties of the acid OH groups were systematically studied by IR. Combination of quantitative IR determinations and activity measurements in acid-catalyzed reactions showed for the first time unequivocally that the Brønsted-acid sites (rather than the Lewis-acid centers, vide supra) are the catalytically relevant loci of acid-catalyzed reactions [471,

473]. In [473] Brønsted acid centers in mordenites were generated according to the Hirschler-Plank mechanism via introduction of alkaline earth cations (Be^{2+} to Ba^{2+}) and lanthanum (La^{3+}). In the case of the very efficient Be^{2+} , it was shown that the density of the newly formed acid OH groups, measured through the absorbance of their typical OH band at 3605 cm^{-1} , increased with increasing Be^{2+} content in parallel with the activity of the Be, Na-mordenites in the alkylation of benzene by ethylene. Finally, it was shown that, upon steaming, OH bands developed around 3650 cm^{-1} , originating from non-acid OH groups which could be etherified through reactions with alcohols [466, 471].

Fejes et al. reported on frequencies, anharmonicities and dissociation energies of OH groups in hydrogen mordenite [474] and Mirodatos et al. [475] on the effect of various treatments on the OH stretching region and on the acid properties as, inter alia, characterized by the IR/pyridine adsorption technique. The thermal decomposition of hydroxylammonium and hydrazonium mordenite was investigated by Beyer et al. [476]. Coinciding with the finding of [466, 471], the appearance of OH bands at 3650 cm^{-1} and 3610 cm^{-1} was observed.

In agreement with IR spectroscopic results regarding the intensities of the band around 3600 cm^{-1} and TPD measurements, Alberti [477] localized via XRD the Brønsted acid sites in hydrogen mordenite on framework oxygens O_2 and O_7 heading toward the 12MR and on O_9 , pointing to the center of the eight-membered rings, 8MR, each with the same population (vide infra). Moreau et al. [478] determined the integrated absorbance of the OH bands of hydrogen mordenite as a function of the degree of exchange of H^+ by Na^+ . They found that H^+ in the side pockets (related to an OH band at $3583\text{--}3585\text{ cm}^{-1}$) are preferentially exchanged compared to H^+ in the main (12MR) channels (related to an OH band at $3608\text{--}3611\text{ cm}^{-1}$). The effect of dealumination on the acid hydroxy groups of H-MOR was studied in detail by Maache et al. [140], who gave the same assignment of the OH bands observed as Moreau et al., and determined especially the heterogeneity and accessibility (for pyridine) of the Brønsted acid sites depending on severity of dealumination via acid leaching and steaming.

5.4.1.2.4

Heulandite (HEU) and Clinoptilolite

Hydrated and partially dehydrated NH_4 -exchanged *heulandite* (HEU, isostructural with *clinoptilolite*) were investigated by micro-infrared spectroscopy [479]. Absorptions typical of NH_4^+ and structural water were observed.

Similarly, acid OH groups of clinoptilolite were detected by IR giving rise to a band at about 3600 cm^{-1} [466]. Detrekoy and Jacobs [480] and Detrekoy et al. [481] reported a somewhat higher wavenumber for the fundamental stretching vibration of the acid OH groups in clinoptilolite (3620 cm^{-1}) which is, however, in less good agreement with Barthomeuf's correlation between the wavenumbers of acid OH groups in zeolites and their $n_{\text{Si}}/n_{\text{Al}}$ ratios [395, 396].

5.4.1.2.5

Erionite (ERI) and Offretite (OFF)

With erionite, bands of acidic OH groups at 3612 and 3563 cm^{-1} were observed by Best et al. [482]. DRIFT spectroscopy in the near infrared and transmission IR spectroscopy in the region of OD stretching and deformation vibrations were employed by Roessner et al. [483, 484] in their early experiments on dehydration and partial hydrolysis of deuterated *Na,K-erionite*. The authors proposed a detailed assignment of the observed OH and OD bands of water and bridging hydroxy groups. Interestingly, Roessner et al. [485] reported in a study of cation distribution in Ca-exchanged erionite (ERI) that, in contrast to $\text{M}^{\text{II}}\text{-Y}$, H_2O dissociation does not occur in Ca-ERI, i.e., OH groups do not form according to the Hirschler-Plank mechanism, Eq. (25). This was explained as being due to a rather strong interaction between the cations and the framework, so that their positive charge was efficiently shielded and insufficient to dissociate H_2O molecules. In another study, Kalies et al. [486] investigated the OH stretching region of erionite by transmission IR spectroscopy and related their results to measurements of the activity of this zeolite in cracking of light paraffins. Stretching bands of OH groups were found at 3740 (from silanol groups), 3700 (stemming from contaminating phases), 3690, 3660 (from extra-framework aluminum, Al-OH), 3610 (from acid Brønsted groups) and 3550 cm^{-1} (due to perturbed acid OH groups). Also, the corresponding OD bands of deuterated erionite were reported.

Barthomeuf and colleagues [487] investigated the hydroxy groups of *offretite* (OFF) after decomposition of the tetramethylammonium ions, which were present according to the synthesis conditions, and of the NH_4^+ ions introduced by exchange for K^+ . They observed bands at 3740 (due to terminating silanols), 3610 and 3550 cm^{-1} (both due to acid OH groups) and finally a band at 3660 cm^{-1} , in general agreement with the findings of Wu et al. [488], who reported bands at 3745, 3600, 3550 and 3690 cm^{-1} . The acid OH groups indicated by the 3600–3610 cm^{-1} band were assumed to be located in the channels and gmelinite cages (at O_5 , cf. Figs. 24 and 25, Ref. [487]) and found to be easily accessible for oxygen and small hydrocarbon molecules such as propane. The other type of acid OH groups seem to be located in the cancrinite cages (at O_2 or O_4) and poorly accessible. Finally, the 3660 cm^{-1} band was interpreted as originating from O_6H , i.e., sited in the hexagonal prisms and non-reactive against NH_3 . However, it could well be that this band is related to extra-framework Al-OH (*vide supra*).

The formation of acid centers in (highly siliceous) offretite and zeolite Omega (cf. also below) was spectroscopically studied also by Tsitsishvili and coworkers [489]. At some variance with Barthomeuf and colleagues, Tsitsishvili et al. concluded that all types of OH groups observed by IR were acid as indicated on NH_3 adsorption except those (silanol groups) giving rise to the band at 3740 cm^{-1} .

5.4.1.2.6

Zeolite Beta (BEA)

Brønsted acidity of *zeolite H*, *Na-Beta* was investigated by, e.g., Yang and Xu [263], Maache et al. [306], Corma et al. [490], Chun et al. [491], Borade and Clearfield

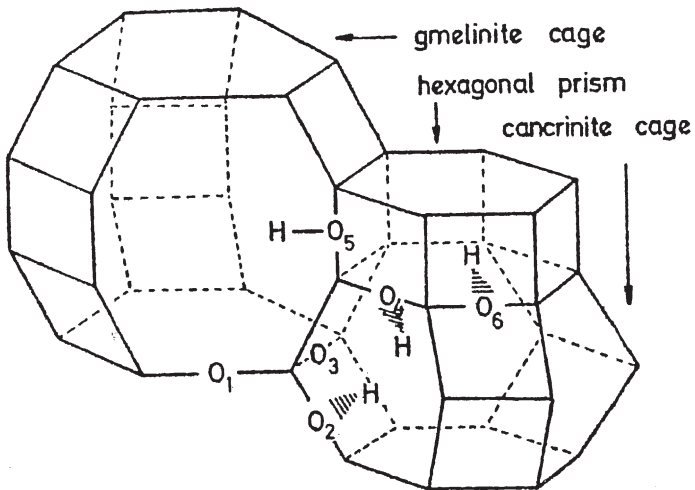


Fig. 24. Gmelinite cage, hexagonal prism and cancrinite cage of the offretite structure and indication of crystallographically different oxygen atoms and corresponding OH groups therein [487]

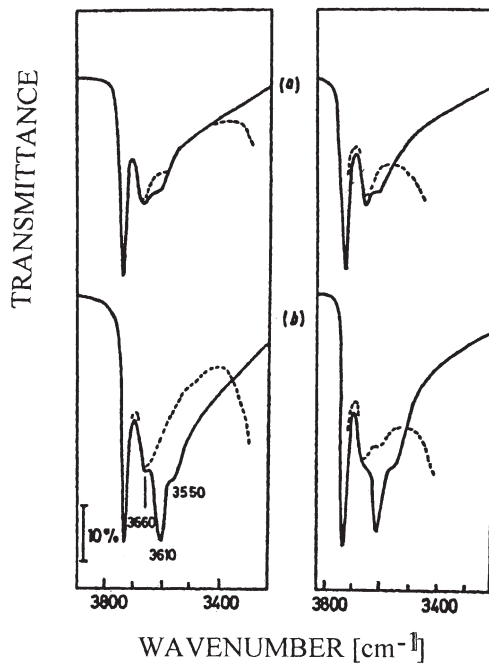


Fig. 25. Infrared bands of OH groups in hydrogen offretite (a: with 2.3 K⁺ cations per unit cell left after exchange; b: with 0.6 K⁺ cations per unit cell left after exchange): *Left*: before (full line) and after (dotted line) adsorption of pyridine. *Right*: before (full line) and after (dotted line) adsorption of ammonia [487]

[492], Kiricsi et al. [493], Katada et al. [494], and Su and Norberg [495]. The latter authors reported bands at 3789, 3745 and 3612 cm^{-1} and attributed them to O-H stretching vibrations of Al-OH, Si-OH and $[\equiv\text{Si}(\text{OH})-\text{Al}\equiv]$ species, respectively. All three types interacted with benzene (cf. Sects. 5.5.2.6.8 and 5.5.2.7). At some variance with the results reported in Ref. [495] were those of Hedge et al. [496], who investigated zeolite Beta both in the as-synthesized and calcined (H, Na-Beta) form by reflectance FTIR spectroscopy. They found, in good agreement with Refs. [263, 306, 493], with H, Na-Beta OH bands at 3740 (terminal or internal Si-OH), 3680 (without assignment, but most probably originating from OH groups attached to extra-framework Al-containing species (vide supra, cf., e.g., [408, 410, 413]), 3602 (Brønsted acid sites) and 3540 cm^{-1} (hydrogen-bonded OH species). These authors also provided detailed data about the acidity strength of their zeolite materials (cf. Sect. 5.5.2.6.2). Observations and interpretations similar to those by Hedge et al. [496] were provided in a publication of Lavalley's group [306] on properties of zeolite Beta which was dealuminated via acid leaching. These researchers investigated additionally framework vibrations (Sect. 5.2), Lewis acidity and acidity strength of the parent and acid-leached Beta samples, in particular as a function of the $n_{\text{Si}}/n_{\text{Al}}$ ratios. Finally, Yang and Xu [263] re-investigated in great detail the OH stretching region of differently prepared and dealuminated zeolite Beta samples, using FTIR spectroscopy of thin self-supporting wafers (and the KBr pellet technique for the study of the frameworks, vide supra, Sect. 5.2). Five OH bands were observed, viz. at about 3782, 3745, 3730–3738, 3660, and 3605 cm^{-1} , and assigned to vibrations of Al-OH in a “transient state” (when leaving the framework, i.e., $(\text{SiO})_2=\text{Al}-\text{OH}$), terminal Si-OH, internal Si-OH (at vacancies, forming simultaneously with Al-OH in the “transient state”), Al-OH of extra-framework species and bridging entities $[\equiv\text{Si}(\text{OH})-\text{Al}\equiv]$, respectively. These wavenumbers and assignments deviated slightly from those of Chun et al. [491].

A number of studies were devoted to the problem of re-alumination of zeolites. For instance, re-insertion of aluminum into dealuminated Y-type zeolites was, inter alia, investigated by Lutz et al. [304]. They found, as in the case of silicalite-1, surface alumination. Very recently, Oumi et al. [497] provided IR evidence for the reversibility of dealumination/re-alumination of zeolite Beta. The parent materials exhibited bands at (in cm^{-1}) 3782 (terminal OH groups at extra-framework species, e.g., AlOOH), 3740 (silanol groups), 3670 (OH groups attached to Al bound only by one or two bonds to the framework) and 3610 (acid bridging OH groups). The bands at 3782, 3670 and 3610 cm^{-1} were weakened or disappeared on dealumination, whereas the band of isolated silanol groups (3740 cm^{-1}) was intensified and a new broad band at 3500 cm^{-1} (hydrogen-bonded adjacent silanols, i.e., of hydroxy nests) developed. As an indication of re-insertion of Al into the hydroxy nests upon treatment of the dealuminated samples in aqueous solutions with controlled pH (pH=5.1, 7.1, 9.1), the bands at 3782 and 3610 cm^{-1} re-appeared and that at 3500 cm^{-1} vanished. By contrast, re-insertion of aluminum by acid treatment of dealuminated H-ZSM-5, which possessed extra-framework Al-containing species (band at 3667 cm^{-1}) as well as hydrogen-bonded Si-OH groups (band in the range 3550–3300 cm^{-1}), did not occur as shown by Omega et al. [498].

5.4.1.2.7

Ferrierite (FER)

In the case of *ferrierite* [499, 500], a relationship between the position of the OH stretching bands and the narrowness of the involved structure element (10MR, 8MR) hosting the OH groups was postulated [394], in that the OH groups residing in the larger 10-membered ring (10MR) channels exhibited a higher wavenumber (3640 cm^{-1}) than those probably located in the narrower 8-membered ring (8MR) channels (3600 cm^{-1}). The explanation is analogous to that given for the difference in the HF and LF bands of OH groups in the large and narrow cavities of H-Y, respectively (vide supra). Domokos et al. [500] reported for ferrierite OH bands at 3601 , 3591 and 3561 cm^{-1} assigned to bridging hydroxy groups in the channels of 10-membered rings, in cages of the channels with 8-membered rings and (tentatively) in the 6-membered rings pointing towards the larger channels.

5.4.1.2.8

Zeolites ZSM-5 (MFI) and ZSM-11 (MEL)

Among the many synthesized “second generation zeolites” [501], *zeolite* ZSM-5 [502–505] is probably the most widely studied material. Thus, a large body of literature exists of spectroscopic investigations of this zeolite, especially of studies by IR, MAS NMR and INS spectroscopy. Hatada et al. [506], and Jacobs and von Ballmoos [507] were the first to determine the position of the fundamental stretching band indicating the most important acid OH groups at about 3600 cm^{-1} (cf. also [508]). Besides this band at about 3600 cm^{-1} , the band of terminating silanol groups, which are generally present in zeolites, was observed at 3740 cm^{-1} . Additionally, a broad band centered around 3250 cm^{-1} was frequently reported (cf., e.g., [507]). This band was sometimes [509, 510] ascribed to hydrogen-bonded internal hydroxy groups or “bridging OH groups of type 2”. Upon adsorption of paraffins, CCl_4 , cyclohexane, CO_2 , etc., the band vanished and a new band at 3480 – 3530 cm^{-1} developed [511, 512]. Similarly, Brunner [513] and Brunner et al. [514] showed by MAS NMR studies that the corresponding line occurred at δ (TMS)=7.0 ppm, which was also observed by Beck et al. [515], as a proton signal originating from a second type of Brønsted sites. The signal was shifted upon adsorption of CO to the same position as the line (b) at δ (TMS)=4.2 corresponding to the IR band at 3600 cm^{-1} , namely to δ (TMS)=6.2 ppm. The explanation given by Brunner [513] was that the line at δ (TMS)=7.0 ppm and, correspondingly, the IR band at 3250 cm^{-1} were caused by acid bridging OH groups which, at variance with the acid OH groups indicated by signals at 3600 cm^{-1} and δ (TMS)=4.2 ppm, were not “free” OH groups but bound by interaction with adjacent framework oxygen atoms. These interactions were lifted upon adsorption of CO. Adsorption of tetrachloroethene had the same effect.

Brønsted (and Lewis) acidity of H,Na-ZSM-5 and H,Na-ZSM-11 was identified through FTIR spectroscopy of the OH stretching region also by Datka and Piwowska [516]. They observed for both zeolite structures a prominent OH band at 3609 cm^{-1} , exhibiting very strong Brønsted acidity. H,Na-ZSM-5 con-

tained significantly more silanol groups (band around 3740 cm^{-1}) than H, Na-ZSM-11. The authors amended their study by FTIR experiments using pyridine as a probe (cf. Sect. 5.5.2.6.2) and were able, after determining the respective extinction coefficient related to the 3609 cm^{-1} -band, to quantify their measurements. Dehydroxylation and poisoning experiments by Datka and Boczar [517] showed that the IR band at 3609 cm^{-1} observed with H,Na-ZSM-5 indicates hydroxy groups, which are heterogeneous in acid strength.

Martin et al. [429] used the IR/pyridine technique (cf. Sect. 5.5.2.6.2) to look at the elimination of Brønsted acid centers upon hydrothermal treatment of H-ZSM-5 zeolite and evidenced the condensation of extra-framework Al-containing species (Lewis sites).

A re-investigation into the nature of Brønsted and Lewis acid sites in H-ZSM-5 by FTIR, ^{27}Al -MAS NMR, ^{29}Si -MAS NMR and XRD led Woolery et al. [518] to the conclusion that, in fact through a special calcination process, a partial hydrolysis of Al-O bonds occurred, which generated a particular type of Lewis sites. These “atypical” sites were not due to extra-framework species but still belonged to the framework in specific T-sites, which allow for structural differences relative to the classical Brønsted sites.

In particular cases, an undesired formation of Brønsted acid hydroxy groups may be conveniently checked by FTIR, for instance in cases of ion exchange with bi- or polyvalent cations, where they may form according to the Hirschler-Plank hydrolysis mechanism (vide supra, Eqs. (25)–(27)). Thus, Marturano et al. [519] tested via IR spectra, whether the introduction of Fe^{3+} into cation sites of ZSM-5 was successful or not. While in all attempts with exchange in aqueous solutions OH bands appeared due to hydrolysis, only in the case of exchange through sublimation of FeCl_3 into H-ZSM-5 were these OH groups absent in the spectra of the exchanged material, suggesting that indeed Fe^{3+} cations were on cation sites.

Gosh and Kydd [520] reported on an infrared study of the effect of a mild treatment with hydrofluoric acid, HF, on the acidity of H-ZSM-5. A decrease of the concentration of Brønsted acid centers and an increase of the Lewis site density was observed. Due to results of parallel TPD experiments with pyridine as a probe, the authors attributed to these Lewis acid sites a higher strength than to the remaining Brønsted acid centers. Severe HF treatment removed all L-sites.

Silicates with MFI structure were synthesized in alkali- and template-free medium by Wallau et al. [521] and characterized, inter alia, via IR spectroscopy. The zeolites synthesized from template-containing gels showed almost exclusively Brønsted acidity, whereas the samples produced from template-free synthesis mixtures possessed a large number of Lewis acid sites.

The IR spectra of heteroatom-free MFI structures, i.e., orthorhombic and monoclinic silicalite-1 were published by Marra et al. [522]. These authors reported that the two modifications show differences both in the framework stretching ($1300\text{--}700\text{ cm}^{-1}$) and the OH stretching regions (cf. also Sect. 5.2):

- (i) Spectra of both silicalites exhibited bands in the $3800\text{--}3650\text{ cm}^{-1}$ range due to isolated terminal Si-OH groups. Their intensity was, however, three times higher in the case of the orthorhombic form.

- (ii) Only the orthorhombic structure had a significant absorption in the range 3650–3200 cm^{-1} with a maximum around 3450 cm^{-1} originating from O-H bonds, which interacted via hydrogen bonds of medium strength. The absorption of the monoclinic form was negligible in that range.

5.4.1.2.9

Miscellaneous: Zeolites MCM-22 (MWW), Chabazite (CHA), Omega (MAZ), ZSM-20 (EMT/FAU), ZSM-22 (TON)

IR spectroscopy combined with TPD of ammonia and ^{27}Al -MAS NMR was employed by Unverricht et al. [523] and Corma et al. [524] to characterize the acidity of zeolite MCM-22. Unverricht et al. found strongly and weakly acidic OH groups giving rise to bands centered at 3628 and 3670 cm^{-1} , respectively, and terminal silanol groups (band at 3750 cm^{-1}), whereas the latter authors observed two kinds of bridging hydroxy groups (indicated by bands at 3620 and 3575 cm^{-1} , both strongly acidic and accessible to pyridine) and also two kinds of internal silanol groups (manifested through bands at 3700 and 3500 cm^{-1}). The silanols producing the 3700 cm^{-1} -band were similar to those found in the case of H-Y and H-ZSM-5. Also, the framework vibrations with bands at 1245 and 550 cm^{-1} were found to be similar to those of H-ZSM-5 and interpreted in line with the approach of Flanigen et al. [112] (cf. Sects. 2.5 and 5.2). Dehydroxylation at 843 K led to extra-framework Al-containing Lewis-type species (as indicated by adsorbed pyridine with a band at 1450 cm^{-1} ; cf. Sect. 5.5.2.6.2). Another FTIR study on MCM-22 was conducted by Onida et al. [525]. These authors described the appearance of OH stretching bands at 3747, 3670 and 3626 cm^{-1} , the latter with the components 3628, 3618 and 3585 cm^{-1} , tentatively assigned them to hydroxy groups in supercages, 10-membered ring channels and 6-membered rings. Small amounts of true Lewis sites were always present. However, after dealumination extra-framework species occurred, which were coordinatively saturated by OH groups. Further experiments with the MCM-22 materials included adsorption of N_2 and CO at 77 K showing that the Brønsted acidity of MCM-22 was close to that of H-ZSM-5 (vide infra; cf. Sects. 5.5.2.1, 5.5.2.2 and 5.5.2.6.6). The acidity of MCM-22 (and MCM-58) was dealt with also in Refs. [526] and [527]. In the latter contribution, Cejka et al. used *p*-cymene and d_3 -acetonitrile as probes. They showed through FTIR spectroscopy that 50% of the bridging OH groups were reached by *p*-cymene, while the smaller d_3 -acetonitrile molecules had access to virtually all B- and L-sites.

Beyer et al. [528] studied by IR spectroscopy the thermal stability of NH_4 -chabazite. They observed two OH bands at 3630 and 3540 cm^{-1} , the behavior of which was related to that of the decreasing NH deformation bands at 1420 and 1460 cm^{-1} . The OH groups indicated by the 3540 cm^{-1} -band were thermally less stable than the other hydroxy groups.

Employing successfully a combination of X-ray photoelectron and infrared spectroscopy, Borade and Clearfield [492] studied the OH stretching region of a series of zeolites (H-Y, H-Mordenite, H-Beta (vide supra), H-Omega, H-ZSM-20, H-ZSM-22) and determined the nature of the acid sites present, their density and strength (cf. also Sect. 5.5.2.6.2).

Zeolite H-Omega was obtained via decomposition of NH₄-Omega [529], which produced OH stretching bands at around 3624 cm⁻¹, shifting to 3605 cm⁻¹ with increasing temperature of deammoniation.

5.4.1.2.10

Isomorphously Substituted Molecular Sieves

Investigation of hydroxy groups via FTIR was also carried out with isomorphously substituted zeolite frameworks. Thus, the hydroxy groups of the isomorphously substituted MFI materials H-[Fe]ZSM-5 and H-[Ga]ZSM-5 were determined via FTIR by Post et al. [530] and compared with those of H-[Al]ZSM-5. The wavenumbers of the acid bridging OH groups of H-[Fe]ZSM-5, H-[Ga]ZSM-5, H-[Al]ZSM-5 were determined as 3630, 3615 and 3610 cm⁻¹, respectively; their catalytic activity in *n*-hexane conversion increased in the same sequence.

Kubelková et al. [531] synthesized and characterized via IR spectroscopy hydrogen and copper forms of boron-substituted ZSM-5, i.e., H-[B]ZSM-5 and Cu,H-[B]ZSM-5, whereas Hedge et al. [532] discussed features in the OH stretching region of Ga-substituted zeolite Beta, i.e., H-[Ga]Beta and H-[Ga]ZSM-5. With H-[Ga]Beta, these authors observed four types of hydroxy groups, giving rise to bands at 3740, 3670, 3622, and 3540 cm⁻¹, which were assigned to terminal and internal Si-OH hydroxy groups associated with Ga, bridging [\equiv Si-(OH)-Al \equiv] species and hydrogen-bonded OH groups, respectively. A comparison with respect to the acid strength of related zeolites provided the sequence H-[Al]ZSM-5 > H-[Ga]ZSM-5 > H-[Al]Beta > H-[Ga]Beta > H-Y. Also, characterization of Brønsted and Lewis acidity by FTIR with the help of probe molecules (benzene and pyridine; cf. Sect. 5.5.2.6) as well as IR measurements of framework vibrations were reported. Hydroxy groups in H-[Si,Ga]Beta were also investigated by Chao et al. [533]. They evidenced incorporation of Ga into zeolite Beta through IR transmission spectroscopy. Bands of acid hydroxy groups were observed at 3619 cm⁻¹, originating from bridging [\equiv Si-(OH)-Ga \equiv] configurations, compared with the 3607 cm⁻¹-band in the case of bridging [\equiv Si-(OH)-Al \equiv] in H-[Si,Al]Beta.

In their work on synthesis and characterization of Beta molecular sieves, Borade and Clearfield [534] identified in H-[Fe,Al]Beta three types of OH groups giving rise to IR bands at 3740, 3670 and 3610 cm⁻¹, ascribed to silanol, acid [\equiv Si-(OH)-Fe \equiv] and [\equiv Si-(OH)-Al \equiv] groups, respectively. This assignment was supported by pyridine adsorption experiments. The strength of the Brønsted acidity of bridging OH groups in H-[Fe]Beta was shown by TPD of ammonia to be lower than in H-[Al]Beta.

5.4.1.2.11

SAPOs, MeAPOs and VPI-5

Characterization of the OH stretching region by DRIFT spectroscopy besides TPD measurements was reported by Chen et al. [535] for a series of SAPOs (SAPO-5, SAPO-17, SAPO-18 and SAPO-34), prepared by these authors. Besides

the P-OH ($\sim 3674\text{ cm}^{-1}$), Si-OH ($\sim 3742\text{ cm}^{-1}$), and two types of Al-OH vibrations (~ 3769 and 3793 cm^{-1}), SAPO-17, SAPO-18 and SAPO-34 exhibited two bands around 3620 and $3587\text{--}3601\text{ cm}^{-1}$, whereas SAPO-5 had only one absorption at 3626 cm^{-1} , but a weak additional one at lower frequency (3524 cm^{-1}), similar to SAPO-17 (3528 cm^{-1}). All of the latter OH-stretching modes were attributed to bridging [$\equiv\text{Si}(\text{OH})\text{-Al}\equiv$] groups, those with the higher wavenumbers supposed to reside in more spacious cages or channels, while those with lower wavenumbers were assumed to be located in smaller voids.

Attempts to incorporate zinc into the MFI structure were undertaken and controlled by FTIR spectroscopy in a recent work by Valange et al. [536]. The authors found that Zn is highly dispersed in the MFI matrix and possibly partly anchored to the zeolite framework (cf. also [345]). The presence of Zn produced a new type of acid OH groups, which were indicated by a medium-to-strong band at 3640 cm^{-1} , did not form ammonium ions with adsorbed ammonia (i.e., they were not true B-sites) but interacted with CO (cf. Sect. 5.5.2.6.6). Also, CO adsorption produced a band at 2200 cm^{-1} due to Lewis acid C-sites (Zn^{2+}).

FTIR transmission spectroscopy in the OH stretching region provided for SAPO-39 bands at $3780, 3740, 3618$ and 3540 cm^{-1} and for MAPO-39 at $3780, 3740, 3670$ and 3625 cm^{-1} [281]. These were attributed to P-OH, Si-OH, and two types of bridging hydroxy groups, respectively (cf. also the DRIFT experiments related to the framework vibrations). IR spectra in the OH stretching region of CoAPO-40 were provided by Lourenço et al. [537]. In the case of CoAPO-37, Costa et al. [538] detected OH stretching bands at $3677, 3610$ and a shoulder at 3546 cm^{-1} , which were attributed to terminal Al-OH or P-OH groups, Co-OH Brønsted acid sites in the large cages and the small ones, respectively. In particular, the band at 3610 cm^{-1} was taken as an indication of Co incorporation into the framework. The presence of Brønsted (and Lewis) acidity in CoAPO-37 was further confirmed by FTIR/pyridine experiments (cf. Sect. 5.5.2.6.2).

CoAPO-5 and CoAPO-11 were shown by Peeters et al. [539] via IR spectroscopy (using CD_3CN and CO as probes, vide infra, Sects. 5.5.2.6.4 and 5.5.2.6.6) to possess unusual Lewis acidity and redox properties (cf. also [540]).

Transmission IR spectra of aluminophosphates with 18-membered ring channels, VPI-5 and VPI-5 modified via introduction of silicon and manganese, designated as [Si]VPI-5 and [Mn]VPI-5, were provided in a contribution by Issakov et al. [541]. Pyridine adsorption on the modified materials revealed the presence of strong Brønsted acidity (cf. Sect. 5.5.2.6.2).

A selection of pertinent IR results related to fundamental stretching modes of OH groups of molecular sieves and reported in the literature together with the respective references are listed in Table 6 (see also [542]).

Table 6. Hydroxy stretching frequencies in hydrogen forms of zeolites and their proposed assignments

Zeolite ^a	OH frequency (cm ⁻¹)	Assignment	References ^c (selected)
FAU	3669 ^b , 3640 ^b	O ₁ -H in supercages	[380, 411]
	3584, 3550	O ₃ -H in sodalite cages 6MR, site I	[380, 411]
	3578	O ₂ -H, O ₄ -H in 6MR, site II	[380]
La-FAU	3628 ^b	O ₁ -H	[380]
	3530	OH-La	[383]
D-H-Y	3625 ^b	OH in supercages	[425]
	3540	OH in sodalite cages	[425]
D-La,H-Y	3625 ^b	OH in supercages	[425]
	3550	OH in sodalite cages	[425]
DAY	3670–3690	OH at Al-containing extra-framework species	[408, 410]
US-Y	3599	OH (superacidic?) in supercages	[421]
	3225	OH (superacidic?) in sodalite cages	[421]
HEU	3560	OH in 8MR pores	[481]
CLIN	3600, 3620	OH in pores	[466, 481]
CHA	3630 ^b	OH in 8MR	[528]
	3540	OH in 6MR	[528]
STI	3575	OH in 8MR	[476]
ERI	3612 ^b	OH in 8MR	[482]
	3563	OH in 6MR	[482]
MOR	3610 ^b	OH in pores, main channel,	[471, 472]
	3586	OH in side pockets	[478]
	3650	OH at Al-containing extra-framework species	[472]
MFI	3601 ^b	OH in channel intersections	[506, 507]
MEL	3609, 3605	OH in channel intersections	[516, 724]
MAZ	3624 ^b	OH in pores	[529]
LTL	3630 ^b	OH in pores	[383, 467]
BEA	3605	OH in [≡Si-(OH)-Al≡] bridges	[263]
[Ga]BEA	3622, 3219	OH in [≡Si-(OH)-Ga≡] bridges	[532, 533]
	3540	OH hydrogen-bonded	[532]
[Fe]BEA	3610	OH in [≡Si-(OH)-Al≡] bridges	[534]
	3670	OH in [≡Si-(OH)-Fe≡] bridges	[534]
FER	3640 ^b , 3612 ^b	OH in 10MR pores	[394, 499]
	3600	OH in 8MR pores	[394, 500]
OFF	3618 ^b	OH in pores?	[542]
RHO	3612 ^b	OH in 8MR pores	[542]
MCM-22	3620, 3626	OH in [≡Si-(OH)-Al≡] bridges,	[524, 525]
	3575, 3585	OH in [≡Si-(OH)-Al≡] bridges	[524, 525]
SAPO-5	3674	OH in P-OH	[535]
	3626 ^b	OH in supercages	[535]
	3524	OH in sodalite cages	[535]
SAPO-17	3620	OH in (≡Si-(OH)-Al≡) bridges	[535]
SAPO-18	3601–3587	OH in [≡Si-(OH)-Al≡] bridges	[535]
SAPO-34	3674	OH in P-OH	[535]
Si-OH	3720 ^d	OH of internal framework silanols, hydroxy nests	[724]
Si-OH	3720 ^d	OH of crystal termination	[476, 481]
Si-OH	3740 ^d	OH of external framework silanols	[471]

^a For three-letter codes cf. Ref. [235]. Note: A few abbreviations, as for instance CLIN, are not acronyms (three-letter codes) approved by the Structure Commission of the International Zeolite Association (IZA), but just convenient designations.

^b Frequency of stretching vibrations of OH groups vibrating in the largest pores and/or cages of the respective zeolites; abbreviated as “OH frequency”.

^c Ref. [411] reviews the observed IR frequencies of zeolites, in particular of faujasite-type ones, up to 1975.

^d Si-OH bands frequently observed with various zeolites.

5.4.2

Hydroxy Groups of Zeolites Characterized by Deformation, Overtone and Combination Bands

5.4.2.1

Characterization by Transmission IR Spectroscopy

Bending modes of OH groups are expected to absorb in the region of low transmittance (cf. $\delta(\text{OH})$ of H_2O , in liquid state or adsorbed on zeolites at $1640\text{--}1650\text{ cm}^{-1}$ [543]). According to calculations, the deformation band of bridging OH groups in H-Y, $\delta[\text{Si}(\text{OH})\text{Al}]$ should exist around 1200 cm^{-1} [544, 545]. Generally, such bands should occur in the region from 800 to 1200 cm^{-1} , i.e., in a range of the spectrum where zeolite materials are essentially IR-opaque, due to strong absorption of the IR light because of framework vibrations. Therefore, bands of bending modes of OH groups in zeolites are practically not available by direct measurements, but can only be indirectly estimated. Thus, the position of such deformation (δ) bands and, similarly, of framework vibrations (OTO, TO) may be derived from an (as precise as possible) determination via DRS of bands due to a combination of the respective deformation mode, δ , with the fundamental, ν , or overtone stretching mode, $\nu(0-2)\approx 2\nu$. In other words, one measures $(\tilde{\nu}+\delta)$ or $(2\tilde{\nu}+\delta)$ and ν ; the desired position of the deformation band is then simply obtained by subtraction of $\tilde{\nu}$ or $2\tilde{\nu}$. The result may be checked by comparison with theoretically computed band positions if available (cf. Table 7).

The IR range of combination and overtone modes lies above ca. 4000 cm^{-1} . It is also extremely difficult to investigate this region by transmission IR spectroscopy because of the weak intensities of the respective bands which usually are only 3 to 5% of that of the fundamentals. In this context one has to keep in mind that the absolute transmission of zeolite wafers in the region of fundamental OH stretching modes is sometimes only 1% or even less (vide supra, e.g., Sect. 5.4.1.2.3).

Table 7. Assignments of combination bands measured by DRIFT of H-ZSM-5 and derived assignments and lattice vibration modes (in cm^{-1}) [560] compared with computed frequencies [253]

Measured frequency (cm^{-1})	Assigned to combination vibrations	Derived		Computed frequency (cm^{-1})
		assignment	frequency (cm^{-1})	
3614 ^a	$\nu(\text{OH})$ of Si-OH-Al	–	–	–
4060	$\nu(\text{OH})+\delta(\text{OTO})$	$\delta(\text{OTO})$	446	470
4340	$\nu(\text{OH})+\nu_s(\text{TO})$	$\nu_s(\text{TO})$	726	765
4661	$\nu(\text{OH})+\delta(\text{OH})$	$\delta(\text{OH})$	1047	–
4760	$\nu(\text{OH})+\nu_{\text{as}}(\text{TO})$	$\nu_{\text{as}}(\text{TO})$	1146	1130
4800	$\nu(\text{OH})+\delta(\text{OTO})+\nu_s(\text{TO})$	$\delta(\text{OTO})+\nu_s(\text{TO})$	1186	1196
5700	$\nu(\text{OH})+2\delta(\text{OH})$	$\delta(\text{OH})$	1043	–

^a Frequency of the fundamental stretching vibration of the OH group in a Brønsted center, $\equiv\text{Si-OH-Al}\equiv$, of H-ZSM-5 zeolite.

5.4.2.2

Characterization by Diffuse Reflectance IR Spectroscopy

In view of the above-mentioned difficulties with transmission IR spectroscopy, the region of overtone and combination modes of zeolitic OH groups may be advantageously investigated by diffuse reflectance IR spectroscopy (DRS, see also Sect. 4.2), as was especially shown by Kazansky and coworkers in a series of pioneering papers [546–554]. The reason for the higher potential of DRS is due to the fact that a great number of reflections of the IR light occur when the electromagnetic waves interact with the zeolite powder particles. This is equivalent to an extended optical pathway. Simultaneously, the use of powder samples is in many cases advantageous because of difficulties in preparing self-supporting wafers. However, there is also a drawback with the DRS technique: quantitative measurements are hindered if not impossible and, furthermore, the band resolution is usually poorer than in the case of the transmission method.

Examples of successful experiments with diffuse reflectance spectroscopy on zeolites, leading to interesting results and interpretations were reported, for instance, by Kazansky and coworkers [546–554] and Staudte and colleagues [555–560]. Kazansky and his group studied a series of various zeolites including silica-rich ones. Spectra were obtained in the range from 3400 to 7000 cm^{-1} . As an example, Fig. 26 shows the spectrum of an H-ZSM-5 sample ($n_{\text{Si}}/n_{\text{Al}}=30$).

For the sake of comparison, the diffuse reflectance IR spectrum of amorphous silica was also studied. The latter showed bands at 3745, 4550 and 7325 cm^{-1} which were clearly indicative of the fundamental OH stretching vibration of silanol groups, i.e., $\nu[\text{Si}(\text{OH})]$, its combination with a bending OH mode, i.e.,

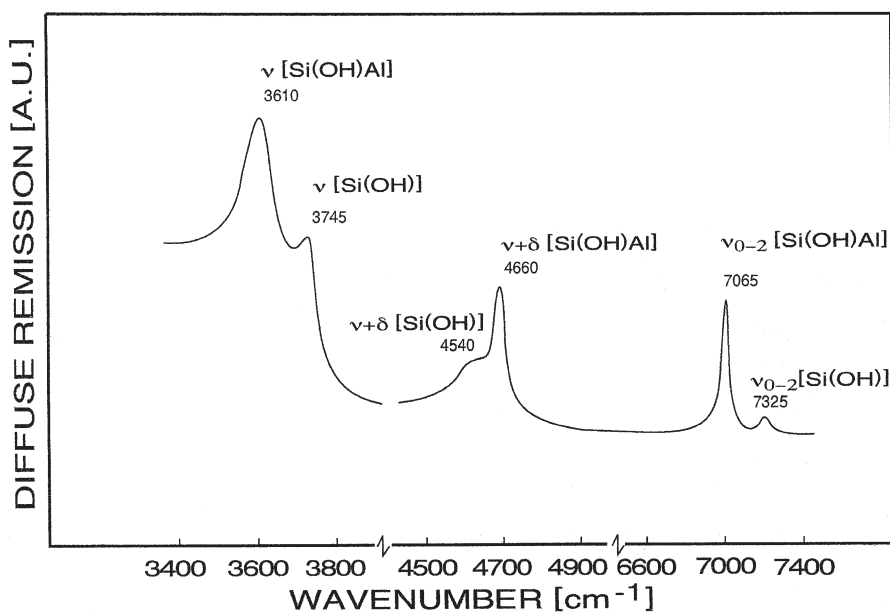


Fig. 26. Diffuse reflectance IR spectra of H-ZSM-5 (adopted from [546])

$(\tilde{\nu}+\delta)[\text{Si}(\text{OH})]$, and the overtone, i.e., $\tilde{\nu}(0-2)[\text{Si}(\text{OH})]$, respectively. Taking into account this silica spectrum and the well-established assignment of the fundamentals of H-ZSM-5 [506, 507], and mordenite [466, 471, 472], Kazansky et al. were able to interpret the complete DRS spectrum as reproduced in Fig. 26 and to give the band assignments as indicated in the figure. For instance, they obtained in the case of silanol groups of amorphous silica $\tilde{\nu} = 3745 \text{ cm}^{-1}$ for the fundamental stretching mode, $\tilde{\nu}[\text{Si}(\text{OH})]$, and ascribed the band at 4550 cm^{-1} to the combination of the fundamental stretching with a bending vibration, $(\tilde{\nu}+\delta)[\text{Si}(\text{OH})]$. The difference provides $\delta[\text{Si}(\text{OH})]=4550-3745=805 \text{ cm}^{-1}$. In the case of zeolites (cf. Fig. 26), the wavenumber of the bending mode for the silanol groups is the same, for the Brønsted sites, however, it is higher, viz. $\delta[\text{Si}(\text{OH})\text{Al}] = (\tilde{\nu}+\delta)[\text{Si}(\text{OH})\text{Al}] - \tilde{\nu}[\text{Si}(\text{OH})\text{Al}] = 4460 - 3610 = 1050 \text{ cm}^{-1}$ (see also Table 7). When hydrogen forms such as H-ZSM-5 are heat-treated, usually a new band appears around 3680 cm^{-1} (spectrum not shown here, but cf., e.g., Ref. [553]); this band is generally ascribed to OH groups attached to extra-framework aluminum-containing species, i.e., $\tilde{\nu}[\text{Al}(\text{OH})]$, originating from dealumination of the anion lattice [306, 555, 556] (see also above, Sect. 5.4.2.1).

Other interesting examples of pertinent studies of H-ZSM-5 by diffuse reflectance IR spectroscopy were reported by Staudte and colleagues [555–560] in the Leipzig group. These authors also investigated the region of overtone and combination vibrations ($4000\text{--}5600 \text{ cm}^{-1}$) of H-ZSM-5, Ca, Na-A and Mg, Na-A zeolites. They observed bands at 5130, 4055, 4555, and 4380 cm^{-1} and discussed their assignment to combination vibrations of hydroxy groups of adsorbed water, acid bridging OHs (acid Brønsted centers), silanol groups and extra-framework Al(OH) species, respectively. The spectra were scanned as a function of activation temperature (Fig. 27).

From analogous findings, Beck et al. [560] derived the positions of otherwise not accessible bands of OH bending modes of H-ZSM-5. For instance they obtained according to $\delta[\text{Si}(\text{OH})\text{Al}] = (\tilde{\nu}+\delta)[\text{Si}(\text{OH})\text{Al}] - \tilde{\nu}[\text{Si}(\text{OH})\text{Al}] = 4661 - 3614 = 1047 \text{ cm}^{-1}$, in good agreement with $\delta[\text{Si}(\text{OH})\text{Al}] = \{(\tilde{\nu}+2\delta)[\text{Si}(\text{OH})\text{Al}] - \tilde{\nu}[\text{Si}(\text{OH})\text{Al}]\} = (5700-3614)/2 = 1043 \text{ cm}^{-1}$ and also with the above results by Kazansky et al. The similarly derived lattice vibrations (OTO and TO) could be compared with theoretically computed band positions; again the agreement was quite satisfying (cf. Table 7).

Medin et al. [561] were able to elucidate through DRIFT experiments special features of the Lewis acidity of H-ZSM-5 zeolites, which were loaded with pre-adsorbed olefins. The authors used DRIFT and as probes CD_3CN and NH_3 (cf. also Sects. 5.5.2.6.2 and 5.5.2.6.4). On the basis of their experimental results they proposed a mechanism for the formation of strong Lewis sites, which includes breaking of Al-O bonds in framework fragments like $[\equiv\text{OAl-O-SiO}\equiv]$ by basic molecules and a positional inversion of the Al atom.

Various types of extra-framework Al-containing species in mildly dealuminated H-ZSM-5 samples were identified in DRIFT experiments carried out by Loeffler et al. [562]. Up to five different acid sites were distinguished. The species giving rise to bands in the OH stretching region were mainly hydroxylated fragments with strengths lower than that of the classical bridging OH groups (Brønsted acid centers). Bands assignments were given as follows: 3780 cm^{-1} : terminal

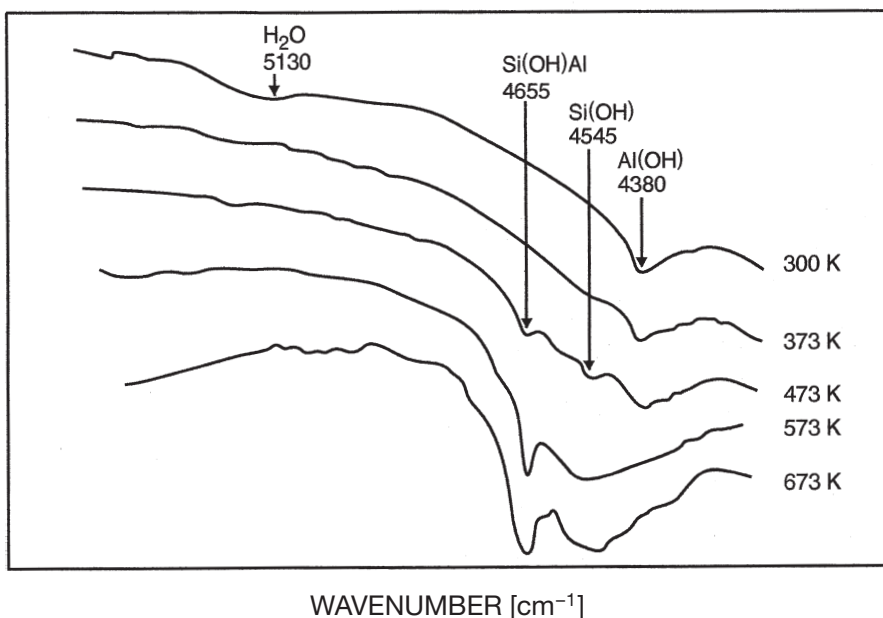


Fig. 27. Near-infrared spectra of H-ZSM-5 with combination bands, $\bar{\nu}(\text{OH})+\delta(\text{OH})$ on increasing activation temperatures (adopted from [557])

Al-OH; 3725 cm^{-1} : terminal Si-OH, the oxygen of which was assumed to interact with extra-framework Al-species; 3665 cm^{-1} : Al-OH still connected to the framework by one or two bonds; 3650 cm^{-1} : terminal Si-OH, the proton of which is interacting with extra-framework Al. The study is amended by DRIFT investigations of H_2 and C_3H_8 adsorption. For instance, H_2 adsorption on Lewis sites produced a typical band, $\bar{\nu}(\text{H}_2 \rightarrow \text{L})$, at 4080 cm^{-1} (cf. also Sects. 5.5.2.1 and 5.5.2.6.3).

Diffuse reflectance IR spectroscopy (DRIFT) was, furthermore, successfully employed in studying molecular sieves of the “new generation” [957] such as aluminophosphates (AlPOs) and silicoaluminophosphates (SAPOs). Thus, Zscherpel et al. and Loeffler et al. [563, 564] studied by DRIFT the range of fundamental OH stretching, OH deformation and framework vibrations of $\text{AlPO}_4\text{-18}$ (upon decomposition of the template, tetraethylammonium hydroxide), the fundamental and combination vibrations of hydroxy groups of SAPO-5 and SAPO-17 as well as the framework region of SAPO-34. In the latter case a comparison was made with the transmission spectrum.

ZSM-5 type boroaluminosilicates with MFI structure, SAPO-5, SAPO-11 and dealuminated H-Y were the subject of a combined ^1H -MAS NMR, ^{11}B -MAS NMR and DRIFT study by Brunner et al. [565]. Interesting results were that defect OH groups in SAPO-5 occurred adjacent to bridging hydroxy groups but were in no way related to an amorphous phase, bands at 4677 and 4608 cm^{-1} indicated OH groups with and without interaction with framework oxygen, $[\equiv\text{Si}(\text{OH})\text{-B}\equiv]$ groups gave rise to a band at 4655 cm^{-1} and were less acidic than $[\equiv\text{Si}(\text{OH})\text{-Al}\equiv]$ configurations and, finally, a band at 4385 cm^{-1} originated from non-acidic Al-

OH groups. DRIFT experiments with $\text{AlPO}_4\text{-5}$ and SAPO-5 samples were carried out by Hedge et al. [566], who determined the Brønsted acidity and Brønsted acid strength of these materials in comparison to hydrogen forms of other molecular sieves and arrived at the following sequence: $\text{H-ZSM-5} > \text{SAPO-5} > \text{H-Y} \gg \text{AlPO}_4\text{-5}$. Infrared measurements of the acidity of SAPO-37 in comparison to SAPO-5 and hydrogen forms of faujasites were also accomplished by Dzwigaj et al. [567]. These authors considered particularly the thermal stability and the acid strength of the respective hydroxy groups. The thermal stability was claimed to be higher than that of most zeolites. Also, pyridine was used as a probe, and these experiments showed that the strength of Lewis sites in SAPO-37 was similar to that of Lewis centers in H-Y (cf. also Sect. 5.5.2.6.2).

As was observed by Makarova et al. [568], the two bands exhibited by SAPO-37 at 3640 (HF-band due to OH groups in the large cages) and 3574 cm^{-1} (LF-band indicating OH groups in the small cavities) broadened with increasing silicon content, which showed an increasing heterogeneity of the respective bridging hydroxy groups. Furthermore, the authors reported that at $n_{\text{Si}}/(n_{\text{Si}}+n_{\text{Al}}+n_{\text{P}}) \leq 0.1$ each silicon atom generates one “isolated” Brønsted acid site associated with $\text{Si}(\text{Al})_4$ units. At $n_{\text{Si}}/(n_{\text{Si}}+n_{\text{Al}}+n_{\text{P}}) \geq 0.1$, at least up to 0.3, the number of Brønsted acid sites is not greatly dependent on the silicon content. In this range, $0.1 \leq n_{\text{Si}}/(n_{\text{Si}}+n_{\text{Al}}+n_{\text{P}}) \leq 0.3$, Brønsted acid sites are associated with “isolated” sites and with sites at the edges of siliceous domains.

IR spectroscopic inspection of SAPO-37 by Corma et al. [569] identified four bands in the OH stretching region at 3745, 3675, 3639 and 3570 cm^{-1} , which were assigned to Si-OH, external P-OH, HF- and LF-bridging hydroxy groups, respectively. The SAPO-37 samples possessed a higher total number of B-sites, but a lower amount of strong acid OH groups than US-Y samples with the same ratio $n_{\text{Si}}/n_{\text{Al}}=29$.

DRIFT spectroscopic investigation of silicon incorporation to produce SAPO-5, SAPO-31 and SAPO-34 was applied by Zibrowius et al. [570] in combination with multinuclear (^1H , ^{27}Al , ^{29}Si , ^{31}P) MAS NMR spectroscopy to reveal predominant incorporation into phosphorus T-sites. Two different types of acid hydroxy groups were identified, viz. OH groups giving rise to bands at 3625 and 3520 cm^{-1} or, in the case of small pore SAPO-34, at 3600 cm^{-1} . Masukawa et al. [571] proved through IR transmission spectroscopy that strong acid sites were generated in SAPO-5. Bands at 3745, 3676, 3626 and 3518 cm^{-1} were attributed to Si-OH, P-OH, $[\equiv\text{Si}(\text{OH})\text{-Al}\equiv]$ in 12MR and $[\equiv\text{Si}(\text{OH})\text{-Al}\equiv]$ in 6MR, respectively. Almost the same band positions and assignments were reported by Xu et al. [572].

Titanium silicoaluminophosphate with MFI-structure, designated as TAPSO, was prepared by Tuel [573], and characterized, inter alia, by transmission IR spectroscopy using the KBr technique. The author found OH stretching bands at 3745, 3670, 3620 and 3530 cm^{-1} similar to those observed with SAPO-5. Also, a band around 970 cm^{-1} was detected and related to the presence of Ti in the framework (cf. Sect. 5.2).

In an analogous way, the existence and properties of hydroxy groups of *mesoporous materials* were studied by transmission IR spectroscopy with and without the use of probe molecules such as pyridine (cf., e.g., in Sect. 5.5.2.6.2 [753, 754]) For the evaluation of experimental data reported (e.g., in [754]) of

Sect. 5.5.2.6.2), the molar extinction coefficients for bands of $\text{Py} \rightarrow \text{B}$ and $\text{Py} \rightarrow \text{L}$ were adopted from experiments with zeolites (cf., e.g., [144]), which is certainly problematic. Moreover, one has to keep in mind the serious warning referred to in [162]. In the case of a study by Llewellyn et al. [574], the IR spectra were, in fact, recorded with the help of an “IR microscope” (infrared microspectroscopy, cf. Sect. 4.1) from unpressed powder samples.

5.4.2.3

Characterization by Inelastic Neutron Scattering Spectroscopy

Due to its sensitivity to hydrogen displacements, INS spectroscopy proved to be a powerful tool in investigations of Brønsted acid sites in zeolites. As illustrated in Fig. 28, dynamics of bridging hydroxy groups is expected to involve three types of vibrations: O-H stretching, $\tilde{\nu}(\text{OH})$, OH in-plane bending, $\delta(\text{OH})$, and OH out-of-plane bending, $\gamma(\text{OH})$. Whereas the former can easily be identified by IR spectroscopy, the bending modes are hidden by intense framework absorptions in the infrared spectra. OH deformations are accessible in the IR spectra solely in an indirect way via their combination modes with O-H stretchings in the near infrared region (vide supra, e.g., [546, 554, 560]), but can directly be detected by INS.

The $\delta(\text{OH})$ modes have been identified in the INS spectra by intense peaks at 1090 cm^{-1} [575] and at 1060 cm^{-1} [576] for the acid forms of zeolites RHO and Y, respectively. The corresponding $\gamma(\text{OH})$ modes were observed at 360 cm^{-1} (H-RHO) and 420 cm^{-1} (H-Y). Figure 29 shows the INS spectrum (kindly provided by H. Jobic, Institut de Recherches sur la Catalyse, Villeurbanne, France) of an H-Y sample ($n_{\text{Si}}/n_{\text{Al}}=2.4$) in comparison with the power spectra of all atoms simulated in MD calculations of a unit cell of H-Y and D-Y with $n_{\text{Si}}/n_{\text{Al}}=2.3$ [577].

Utilizing INS and MD in combination with each other is especially convenient due to the direct relationship between the recorded spectrum and the calculated density of vibrational states. As can be seen, the most intense peak for H-Y is calculated at 1050 cm^{-1} and is in good agreement with the intense experimental peak at 1060 cm^{-1} which can clearly be attributed to the OH in-plane bending mode. The assignment of the observed peak at 420 cm^{-1} to the OH out-of-plane bending mode is less unequivocal. Although in the mentioned simulation a broad

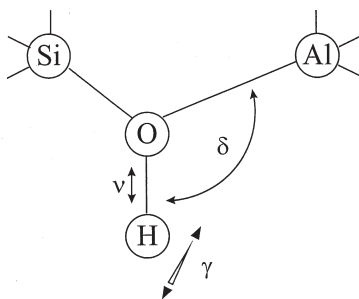


Fig. 28. The normal modes (ν : stretching, δ : in-plane, and γ : out-of-plane bending modes) of a bridging hydroxy group of a zeolite structure

band at 370 cm^{-1} is obtained, which is shifted to 260 cm^{-1} upon deuteration, the assignment of the $\gamma(\text{OH})$ mode is complicated due to strong coupling with framework modes [22]. However, it should also be mentioned that $\gamma(\text{OH})$ modes of bridging OH groups have been predicted in MD simulations for zeolite H-Y at wavenumbers as low as 221 cm^{-1} [81]. Even if the value of the $\gamma(\text{OH})$ force constant was close to the limit of the method, such a frequency may be plausible if the OH out-of-plane bending mode is considered as a hindered torsion of the proton around the Si-O bond. Such a hypothesis should be valid if quite different Si-O and Al-O force constants are assumed for Si-OH-Al bridges, namely 3.65×10^2 and $1.47 \times 10^2\text{ N m}^{-1}$ (3.65 and $1.47\text{ mdyne \AA}^{-1}$) [81]. A final decision can be only expected if INS spectra in the far-infrared region are available also for deuterated samples. But such spectra are extremely difficult to obtain and are, to our best knowledge, at present not reported in the literature, so that it is difficult to draw a definitive conclusion on this issue. Unfortunately, due to the low resolution no clear splitting could be observed in the INS spectra of H-Y zeolites for both OH bending peaks [576, 253] as it has to be expected from the appearance of HF- and LF-OH bands in the OH stretching range. Surprisingly, two $\gamma(\text{OH})$ modes were observed at 405 and 320 cm^{-1} in the INS spectrum of H-ZSM-5, for which only a single OH stretching mode is known in the infrared [578]. From analyses of IR combination modes of H-Y zeolites, Beck et al. [560] predicted two fundamentals for $\delta(\text{OH})$ at 1057 and 1028 cm^{-1} and for $\gamma(\text{OH})$ at 402 and 310 cm^{-1} , respectively. Nevertheless, a splitting into two sub-bands near 870 with a shoulder near 890 cm^{-1} could be observed in the infrared spectra after isotopic exchange with deuterium [20, 22]. Converting the bridging hydroxy groups into the deuterated analogues has the advantage that the corresponding $\delta(\text{OD})$ modes appear within the frequency gap between 920 and 850 cm^{-1} in the IR spectrum which is free of framework absorptions. The band positions observed in the IR spectra are in quite reasonable agreement with the peak at 890 cm^{-1} obtained in the vibrational density of states upon deuteration (cf. Fig. 29).

5.5

Characterization of Zeolite/Adsorbate Systems

5.5.1

Introductory Remarks

IR investigations of zeolite/adsorbate systems may have various aspects: They may

- (i) focus on the adsorbed molecules as such and on the changes of their properties caused by interaction with the zeolite lattice;
- (ii) monitor adsorption-induced effects on the adsorbent;
- (iii) use the adsorbate molecules as a probe.

These aspects are, however, not always clearly separated, in particular type (i)- and (iii)-studies frequently overlap.

Many examples of the first category are described in the literature, especially in Ward's early review [231], where IR results of the adsorption of H_2O , NH_3 , CO ,

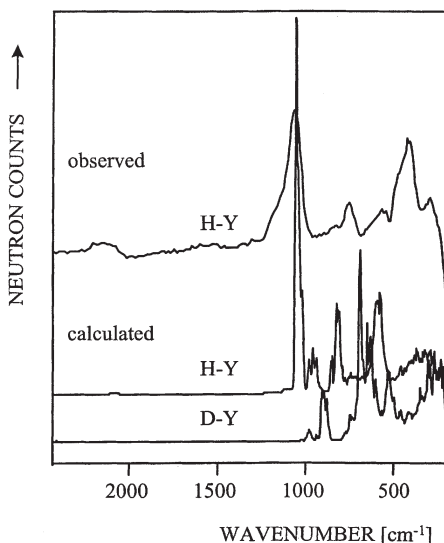


Fig. 29. Calculated power spectra of zeolites H-Y and D-Y in the mid-infrared framework region in comparison with the experimental INS spectrum of H-Y (from [577])

CO₂, NO_x, H₂S, SO₂, and many organic compounds such as olefins, aromatics, phenol, aniline, acetone, acetaldehyde, organic acids, nitriles and even triphenyl derivatives were collected. In Sect. 5.5.2 some selected systems will be dealt with and more recent developments reviewed. As examples of the second category the effects of adsorbates on the distribution of cations were already discussed (*vide supra*). A large number of IR investigations has been and continues to be devoted to testing and utilization of adsorbate molecules as probes, especially for Brønsted and Lewis acidity and/or basicity as well as of cations and metal particles in zeolites. This aspect will be discussed in Sect. 5.5.2.6. Characterization of the nature, density and strength of acid and basic sites, however, will be treated in even more detail in Volume VI of the present series, where not only IR spectroscopy but a great collection of techniques and methods will be described as being suitable to determine zeolite acidity and basicity. Furthermore, adsorption investigations related to processes such as zeolite-catalyzed model reactions and diffusion are dealt with, which will be treated in subsequent sections (*cf.* Sects. 5.6.2–5.6.5).

Also, INS spectroscopy is advantageously applied in studies of hydrogen-containing molecules adsorbed in microporous materials. The best studied adsorbates in zeolites are water, hydrocarbons, and methanol [579–581], but also the sorption states of aromatics like benzene [581, 582], furan [583, 584], and pyrrole [371, 585] have been investigated by INS. In the micropores of zeolites even small molecules “feel” the potential of large parts of the solid, and this is particularly true for bulkier molecules. This gives rise to several simultaneous interactions, and INS is especially suited to obtain information about the interactions via hydrogen atoms from the corresponding bending modes in the fingerprint region.

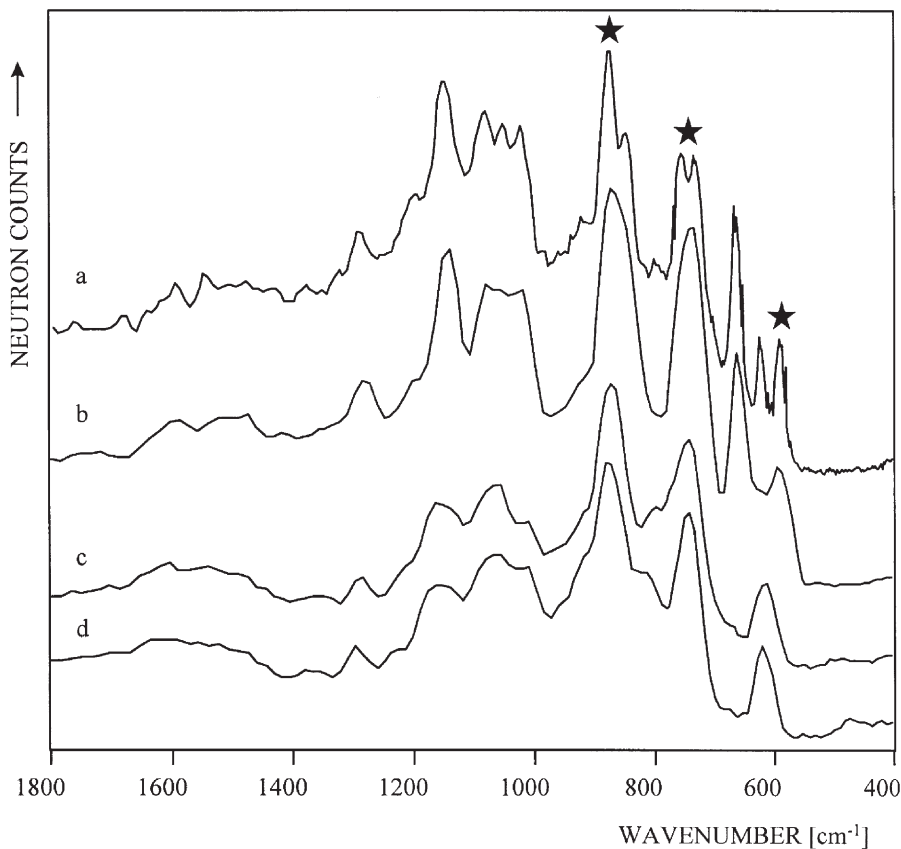


Fig. 30. INS spectra of bulk pyrrole obtained with the spectrometers (a) TFXA and (b) IN1BeF and of pyrrole adsorbed in (c) Na-Y and (d) Rb-Y; the asterisks indicate the most intense peaks, cf. text (from [585])

As an example, Fig. 30 shows the INS spectra of pyrrole in different states [585]. The INS spectra of bulk pyrrole were recorded at 5 K with the spectrometer IN1BeF at the Institut Laue-Langevin (Grenoble, France) and at improved resolution with the spectrometer TFXA at the Rutherford Appleton Laboratory (Oxford, UK).

As can be seen, below 1000 cm^{-1} the spectra are dominated by three intense peaks (indicated by asterisks in Fig. 30) at 862, 740, and 594 cm^{-1} . According to results of quantum mechanical calculations, these bands have to be assigned to out-of-plane bending modes of the hydrogen atoms [586], i.e., the peaks at 862 and 740 cm^{-1} to CH wagging modes and the peak at 594 cm^{-1} to the NH wagging mode. As a result of an improved resolution, a splitting of the two CH wagging peaks into two doublets was observed (cf. curve a in Fig. 30). To monitor changes in the INS spectra of pyrrole upon adsorption, the spectra of sorption complexes were ratioed against the background of the bare zeolite. This requires that the

framework modes remain essentially uninfluenced, an approximation valid only for not too polar adsorbates (cf., also, application of pyrrole as a probe for basicity, Sect. 5.5.2.6.10).

5.5.2

Selected Zeolite /Adsorbate Systems

5.5.2.1

Homonuclear Diatomic Molecules (N₂, H₂, D₂, O₂) as Adsorbates

Almost simultaneously and independently, two research groups started systematic IR spectroscopic work on the adsorption of homonuclear diatomic molecules in zeolites, viz. the groups of Foerster [587, 588] and Cohen de Lara [216, 589–593]. Their studies provided valuable information both about the properties of the sorbents, e.g., the internal electric fields; the sorbate molecules, e.g., their modes of motion and mobility; and the interaction between adsorbate and zeolite, e.g., the effect of adsorption on the molecular bonds. Mostly, A-type zeolites were employed as hosts. In fact, some early studies were also carried out with X- and Y-type zeolites [594, 595].

Under usual conditions, molecules such as *hydrogen, deuterium, nitrogen and oxygen* are IR-inactive, as with respect to their normal mode there does not occur a change in the dipole moment. However, upon adsorption, for instance at the walls of zeolitic channels and cavities, the symmetry of those molecules is disturbed and a dipole is induced by the local electric field. As a first example, Fig. 31 displays the spectra of D₂, N₂ and O₂ sorbed into zeolite Na₄Ca₄-A [587] at different pressures and (low) temperatures. Calculated geometries of the sorbate/sorbent complexes are displayed in subsequent figures (vide infra).

The most important aims of such IR studies were

- (i) characterization of the electric field inside the zeolite voids [587, 591, 596–600],
- (ii) determination of the mobility and energy barriers for intrazeolite motions of the adsorbed molecules [216, 588, 597–603] and
- (iii) comparison of the experimental with calculated spectroscopic data [590, 599, 604].

Thus, in many respects these simple diatomic molecules are suitable probes for zeolite research via IR spectroscopy [605]. In a similar sense, this also holds for small heteronuclear molecules such as CO, N₂O, CO₂, CH₄ (vide infra).

The IR experiments are mostly carried out at low temperatures in order to achieve a sufficiently strong interaction between sorbate and sorbent, i.e., usually at about 100 to 270 K (cf. [152], for low temperature cells see Sect. 4.1). In fact, a few related studies have been conducted earlier where, at room temperature and relatively high pressures (e.g., 2.6 kPa), weak bands of N₂ [606] and H₂ [607] after adsorption on nickel or porous glasses, respectively, were observed. For instance, a band of H₂ on porous glasses appeared at 4131 cm⁻¹ in good agreement with the Raman signal of gaseous H₂ at 4160 cm⁻¹.

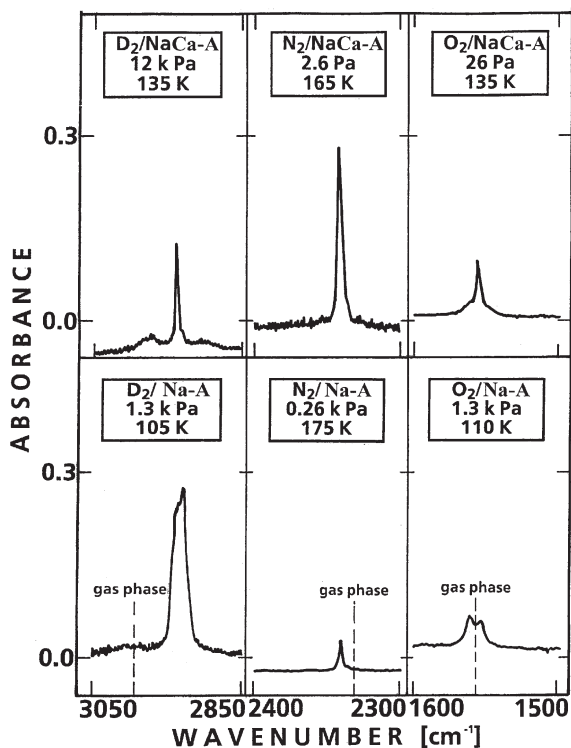


Fig. 31. Infrared fundamentals of molecular deuterium, nitrogen and oxygen adsorbed on A-type zeolites [587]

Much better IR spectra and more information were obtained by Foerster and Schuldt [587] upon adsorption on zeolites and measurement at low temperatures (105–175 K), even at low pressures down to 2.6 Pa in the case of N_2 on Na,Ca-A. (Here and subsequently, M_1, M_2 -Z designates a zeolite Z, e.g., zeolite A, containing two different cations, e.g., Na and Ca; usually, but not always, Na,Ca-A means Na_4Ca_4 -A).

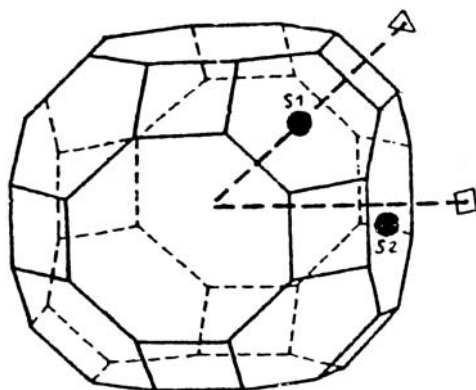
A field-induced fundamental stretching band of N_2 adsorbed on Na-A at 185 K and 16 kPa was also observed at 2239.5 cm^{-1} by Cohen de Lara and Delaval [591]. These authors identified as the most energetic adsorption sites the Na^+ cations in S3 positions and derived a field strength of 4.7 V nm^{-1} from the band intensities (vide infra) and 4.5 V nm^{-1} from calculations of the interaction potential. Furthermore, they found that the band intensity increased when the adsorption temperature decreased. This was explained by a decrease of the distance from the center of adsorption and a corresponding increase in the strength of interaction [216].

Spectra of D_2 , N_2 and O_2 (and CO, vide infra) adsorbed on Na-A ($Na_{12}[AlO_2]_{12}[SiO_2]_{12}$) or Na,Ca-A ($Na_4Ca_4[AlO_2]_{12}[SiO_2]_{12}$) as reproduced in Fig. 31 provided data which are presented in Table 8.

Table 8. Spectral data (given in cm^{-1}) of diatomic molecules adsorbed on A-type zeolites referenced to the gas phase frequencies, $\tilde{\nu}_g$

	Adsorbate	H ₂	D ₂	N ₂	O ₂	CO	
Na-A	$\tilde{\nu}_g$	4161,2	2993.6	2329.9	1556.4	2143.3	
	$\tilde{\nu}(Q)-\tilde{\nu}_g$	-80	-65	+11	+2	+22,+3	
Na-A	FWHH		-53	+8		-15,-28	
			25	40	2	15	6
				13	5		7
Na-A	$\tilde{\nu}_s-\tilde{\nu}(Q)$ sidebands	+90	+70	+23	± 4	± 160	
		+160	+40				
Na,Ca-A	$\tilde{\nu}(Q)-\tilde{\nu}_g$	-73	-54	+13	-1	+42	
			-30	+8		+25	
Na,Ca-A	FWHH	10	4	2	4	9	
			5	6	9	20	
Na,Ca-A	$\tilde{\nu}_s-\tilde{\nu}(Q)$ sidebands	+50	+35	+13	+23	± 7	
			+140	+23			
				+34			

All frequencies, frequency shifts and full-width at half-height (FWHH) in cm^{-1} ; $\tilde{\nu}_g$: gas phase frequency; $\tilde{\nu}(Q)$: frequency of pure vibrational transition; $\tilde{\nu}_s$: side band frequency; after Ref. [597].

**Fig. 32.** Supercage of zeolite A with the main cation positions and symmetry axes [588]

The authors of Ref. [588] suggested that the favored adsorption sites lie on a C_4 -axis in Na-A and on a C_3 -axis in Na,Ca-A (cf. Fig. 32)

Other interesting results of their study were that

- (i) the system O₂/Na-A showed a splitting of the main band due to a transition from a symmetrical librational state of the $v=0$ level to an m-split state in the $v=1$ level;
- (ii) D₂ on Na,Ca-A exhibited sidebands looking like envelopes of R and P branches and possibly indicating a relatively high degree of rotation, which might become more hindered at 115 K (cf. [588]). This interpretation, how-

- ever, was later on revised because of the results of calculations of potential wells, which led to the conclusion that a purely rotational origin of the sidebands should be ruled out [597]. Rather, excitation of a translational motion of the center-of-mass of the molecule perpendicular to the symmetry axis may be assumed (cf. [597, 600]). This was supported by the reasonable agreement between the experimentally observed shift of the sideband relative to the vibrational main band and the theoretically estimated magnitude of this shift [597] (vide infra);
- (iii) a large red-shift of D_2 on Na,Ca-A as well as on Na-A is due to the small mass of the molecule;
 - (iv) in contrast to D_2 , the spectra of N_2 on both adsorbents reveal a marked blue-shift, probably caused by the smaller quadrupole moment in the excited state (cf. [598]);
 - (v) the interaction of the molecules with the walls of Na,Ca-A cavities seemed to be stronger than with those of Na-A, since the shifts are larger and the asymmetry of the bands more pronounced than in the former case;
 - (vi) from the integrated absorbance, $A_{\text{int}} \propto \langle F_R \rangle^2$, of the bands of D_2 and N_2 adsorbed on Na, Ca-A a mean electrical field strength $\langle F_R \rangle$ in front of Ca^{2+} and Na^+ sites of 7 and $4.5 \text{ V} \cdot \text{nm}^{-1}$, respectively (cf. [587, 589, 591, 608]) was derived, in good agreement with theoretically estimated values of ca. 6 and $4.4\text{--}4.5 \text{ V} \cdot \text{nm}^{-1}$, respectively (cf. [591, 596, 608]);
 - (vii) from the spectrum of H_2 on Na,Ca-A at 130 K and $1.3 \times 10^3 \text{ Pa}$ it was inferred that the molecule was oriented parallel to the wall of the α -cage.

Adsorption of H_2 , HD and D_2 on Na-A was studied microgravimetrically, via neutron scattering and IR spectroscopy in a contribution by Cohen de Lara et al. [592], where in particular the composition of the fluid-like phase in the zeolite after co-adsorption could be determined IR spectroscopically. On adsorption, the bands of both H_2 and D_2 were shifted to lower wavenumbers with respect to the Raman data of the gas phase, viz. to 4075 and 2926 cm^{-1} , respectively.

Larin et al. [593] published calculations of the vibrational shifts of the diatomic molecules H_2 , N_2 and O_2 upon adsorption on zeolite Na-A. Most reliable results were obtained for H_2 , for which the required molecular constants were well known. The calculations led to relatively high values of the ionic charges of the zeolite, unlike most models commonly used. The O_2 and N_2 constants were less reliable than those of H_2 . Therefore, the calculated shifts were less accurate, but had nevertheless the right direction.

In a publication subsequent to Ref. [587], Foerster et al. [597, 616] provided more spectral data of H_2 , D_2 , N_2 , O_2 (and CO, vide infra) obtained after adsorption on Na-A and Na,Ca-A, viz. the pure vibrational frequencies compared to Raman gas phase data, the full-width at half-height of the bands, and satellite bands at low coverages (cf. Table 8).

While the narrow and intense bands were again ascribed to pure vibrational transitions, the satellites were now interpreted as modes of translational motions of the center-of-mass (of H_2 , D_2 on Na-A or Na,Ca-A) as already mentioned (vide supra). In the case of O_2 adsorbed on Na-A, a doublet of bands was observed (cf. Fig. 31 and [587, 597]). As an explanation it was suggested that the oxygen mol-

ecules were bound to sites, where nearly no dipole moment is induced, so that the spectrum would consist almost exclusively of the allowed translational side bands.

The spectrum of D_2 on Na_8Ca_2 -A and Na_4Ca_4 -A showed weak overtone bands at about 5760 cm^{-1} . Frequency shifts versus the frequency of the fundamental stretching mode in the gaseous state, ν_g , and full-width at half-height (FWHH) exhibited values roughly twice as large as those shown by the fundamental vibration bands [605]. From the overtone spectra the authors, therefore, concluded that

- (i) the interaction between the molecule and the zeolite host is linearly dependent on the vibrational state and
- (ii) the potential is not significantly affected by adsorption, i.e. the dissociation energy as well as the cation distribution do not appreciably change on interaction with the adsorbent.

Finally, it was found that the spectra of H_2 on Na,Ca-A revealed an *ortho-para* splitting of 4.5 cm^{-1} of the main band (cf. Fig. 33), in excellent agreement with the calculated splitting (4.4 cm^{-1}) reported in the same study.

The band with a lower frequency was ascribed to *o*- H_2 , because this band was more intense which obviously resulted from the higher population of the state in the case of *o*- H_2 . The decrease of the splitting compared to that of the free H_2 molecules point to a strong rotational hindrance occurring upon adsorption. Calculations for D_2 yielded a splitting of only 1.4 cm^{-1} which could not be experimentally resolved.

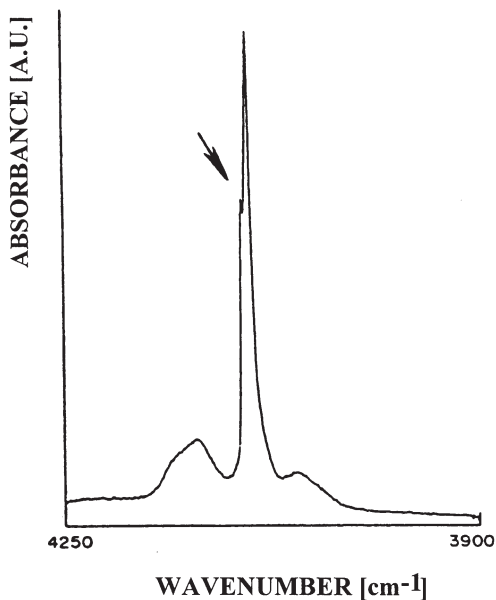


Fig. 33. Crystal field-induced splitting of the spectrum into *ortho*- and *para*-hydrogen bands on adsorption on Na_4Ca_4 -A at 90 K; the arrow indicates the *o*- H_2 /*p*- H_2 splitting (from [605])

Very recently, adsorption of dihydrogen as an IR probe was extended by Kazansky and coworkers to cation-containing zeolites as adsorbents [609–612]. The main aim of their studies was to localize the adsorption sites in these materials, especially the cations. This is especially difficult to achieve by other methods in the case of the catalytically important zeolites loaded with low amounts of transition metal cations. In the context of the pertinent investigations by Kazansky and coworkers, the dissociative adsorption of dihydrogen (and light paraffins) in cation-containing zeolites was dealt with, too.

By Raman spectroscopy of N_2 and O_2 adsorbed on zeolite A, Saperstein and Rein [613] observed bands at 2339 and 1555 cm^{-1} , respectively, in very good agreement with the IR results.

Adsorption of N_2 and CO (cf. also Sect. 5.5.2.2) on Cu-ZSM-5 was IR-spectroscopically studied by Broclawik et al. [614] in the context of the catalytic activity of the adsorbent in NO_x decomposition. The authors found three bands in the respective spectra originating from Cu^+N_2 and Cu^+CO adsorption complexes differing in bonding energies. The high frequency bands at 2297 (Cu^+N_2) and 2157 cm^{-1} (Cu^+CO) indicated the strongest Cu^+ adsorption sites.

5.5.2.2

Carbon Monoxide (CO) as an Adsorbate

Carbon monoxide molecules possess only a very small permanent dipole moment (0.112 debye). Therefore, the contribution of the term originating from the interaction of the dipole moment, μ , with the electric field, F_R , i.e., $\mu \cdot F_R \cdot \cos \Theta$ (Θ =angle between the molecular and the symmetry axis), to the total interaction potential is also small.

IR spectra of carbon monoxide adsorbed on zeolite A were studied by Felon and Rubalcava [594] and Foerster et al. [596, 597, 601, 604]. Felon and Rubalcava employed Na-A, Ca-A, Na-X and Ca-X zeolites, while Foerster used alkali- and alkaline earth-exchanged A-type sieves with systematically varied composition. The even earlier report by Angell and Schaffer [595] dealt with adsorption of CO on X- and Y-type zeolites, and their experiments were carried out at room temperature or, more precisely, at the temperature obtained by the sample in the IR beam. However, even though the CO molecule has a rather simple structure, the IR spectra of carbon monoxide adsorbed on zeolites appear to be relatively complex, especially when obtained at low temperature. They provide a wealth of information which to some extent may be lost at higher scanning temperatures. Moreover, since CO is, at room temperature, only weakly adsorbed on zeolites containing solely alkali- and/or alkaline earth cations, the intensities of the generated bands are rather low.

All of the IR investigations devoted to CO adsorption on zeolites suggest that the molecules were preferentially sited close to the cations. For X- and Y-type zeolites containing multivalent cations, Angell and Schaffer showed that the highest frequencies are due to molecules adsorbed on those cations. The uptake of carbon monoxide into zeolite A at room temperature was strongly affected by the ratio q/r , where q represents the cation charge and r the cation radius. It increased with q/r of the dominating cation in the sequence $Na^+ < Li^+ < Ca^{2+} < Mg^{2+}$ [608].

Consideration of the interaction potentials showed, however, that sites of large field gradients rather than those of high field strengths should be preferred for CO adsorption, e.g., sites in front of cations in S3 positions (cf. [608] and see below).

Boese and Foerster [596] found pronounced similarities in the adsorption behavior and IR spectroscopic features of isoelectronic molecules such as N₂ and CO (or CO₂ and N₂O, vide infra). For calculations, an electrostatic interaction model was used. As mentioned above, the cations were identified as the centers of adsorption, since the main potential wells were found in front of them. Also, the geometry of the adsorption complexes was shown to be similar (cf. Fig. 34).

Upon adsorption, the main bands of N₂ and CO were shifted to higher frequencies compared to the gas phase frequency, $\tilde{\nu}_g(Q)$. The agreement between the calculated and measured frequency shifts, $\tilde{\nu}_g(Q) - \tilde{\nu}$, was satisfying (Table 8). At variance with the spectra of N₂ on zeolite A, with CO an additional, downscale-shifted peak appeared already at low coverages, corresponding to a second potential different by 9 kJ mol⁻¹ from the first one. This finding was explained in view of two possible arrangements, viz. M-CO and M-OC (M=Na⁺, Mg²⁺, Ca²⁺; where divalent cations were the preferred sites). Furthermore, the field strengths calculated from the intensity measurements of the main IR bands of N₂ and CO on Na₄Ca₄-A zeolite were similar and amounted to about 7.3 V nm⁻¹ in front of Ca²⁺ in Na₄Ca₄-A and 4.5 V nm⁻¹ in front of Na⁺ in the case of Na₁₂-A, in accord with the calculated values of 8 and 4 V nm⁻¹, respectively (cf. [591, 596, 608]).

Already in the early study by Angell and Schaffer [595] on CO adsorption on X- and Y-type zeolites, it was observed that besides the main band (at 2168 cm⁻¹ for 13X, i.e., shifted from the Raman signal of the gaseous CO by +44 cm⁻¹) always one or even two more weaker bands appeared. Although these bands looked like the envelope of R- and P-branch rotational features, Angell and Schaffer did not assign them accordingly, because their intensities did not change with temperature and pressure as predicted by theory for a free rotor. Therefore, these authors tentatively attributed the additional bands to pure vibrational transitions of CO molecules bound to the adsorption centers in two different ways. However, this problem remained a matter of debate.

Thus, Fenelon and Rubalcava [594] attempted in their IR low-temperature study (at 150 K) on adsorption of isotopes, ¹³C¹⁶O and ¹²C¹⁶O, on Na-A, Na-X, Ca-A and Ca-X to distinguish between the following two possibilities:

- (i) pure vibrational transitions of CO adsorbed on two different sites or on one type of site, but in two different ways of adsorption and
- (ii) origin of the extra-peaks in the IR spectrum from vibrational-rotational transitions.

The evaluation of their spectra led Fenelon and Rubalcava to the conclusion that indeed in Na-A the CO molecules behave as almost free rotors, which seemed to be understandable in view of the effective diameter of a rotating carbon monoxide molecule and the diameter of the a-cage, viz. 0.45 nm and 1.14 nm, respectively. Good agreement was reported for the calculated and observed separations, (R-Q, Q-P), of the maxima assigned to the branches in the spectra of ¹²CO and

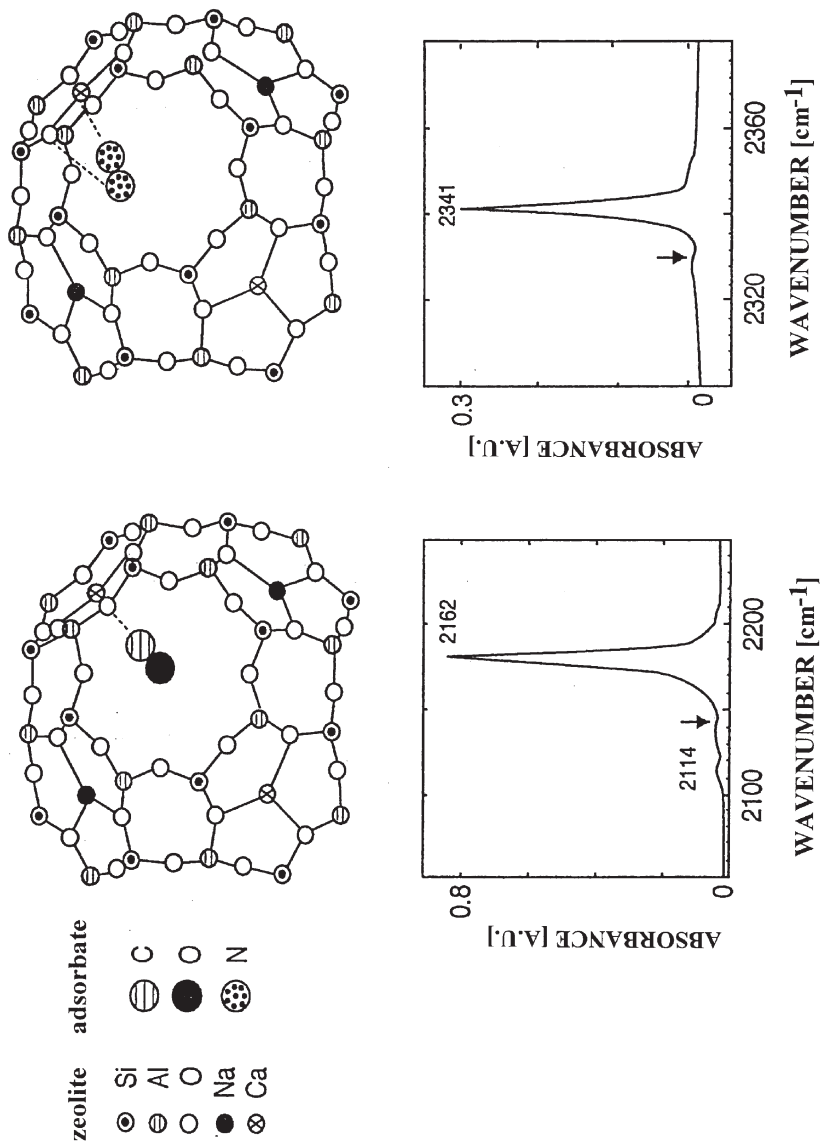


Fig. 34. Calculated adsorbate geometries and observed IR spectra of CO and N₂ in zeolite Na₄Ca₄-A; gas phase wavenumbers indicated by arrows (adopted from [596])

¹³CO. The alternative assumption (i) did not lead to such a coincidence of calculated and measured isotopic separations. A comparison of the band profiles observed with CO on the calcium forms (asymmetric profile) and on sodium forms (symmetric profile) of the zeolites suggested that in the case of calcium-exchanged A- and X-type zeolites the rotation of the CO molecules is significantly hindered, which resulted in the observed one strong band and two shoulders on both sides. Thus, the three absorptions in the case of CO/Na-A were interpreted as indicating the R, Q and P branches, i.e., free rotation. The spectrum of

CO/Na,Ca-A with one strong band and two weak shoulders was explained by hindered rotation.

The problem of motion and interaction of CO molecules inside A-type zeolites was re-investigated by Foerster and coworkers under improved experimental conditions [597, 601]. There were several facts which casted some doubt on the above conclusions drawn by Fenelon and Rubalcava:

- (i) Estimated barriers to rotation even in the case of D_2 /Na-A excluded the performance of the molecule as a free rotor (*vide infra*); in the case of CO in Na-A, however, this barrier must be markedly higher, i.e., of the order of 1000 cm^{-1} , due to the stronger interaction of CO with the wall of Na-A.
- (ii) The ratio of frequency shifts of about 20 as reported by Fenelon and Rubalcava for CO/Na-A and CO/Na,Ca-A appeared much too high, since usually these shifts show the same order of magnitude.
- (iii) The assumption in Ref. [594] that under the pressure applied the coverage was only one molecule per unit cell contradicted the results of adsorption isotherm measurements.
- (iv) There was no explanation provided for the anomalously high intensity ratio of 6:1 between the absorptions of the pretended R and P branches.

In the study by Foerster et al., the four bands reported in Ref. [594] for the system CO/Na-A were essentially reproduced at 2165, 2146, 2128 and 2115 cm^{-1} (cf. Fig. 35), as well as the bands given in Ref. [594] for the system $^{13}\text{CO}/\text{Na-A}$.

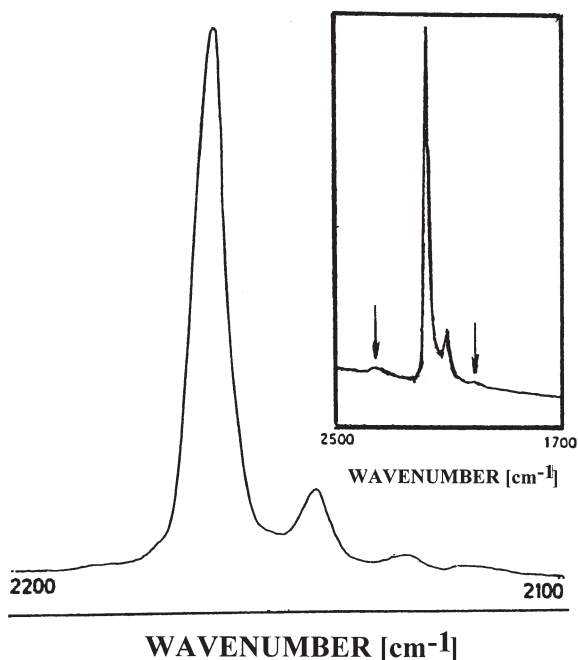


Fig. 35. Infrared spectrum of CO adsorbed on Na-A at 130 K exhibiting four bands; the arrows in the upper insert indicate the satellites, (see text, from [597])

The positions of the main band at 2165 cm^{-1} and the 2115 cm^{-1} band changed slightly with temperature and coverage. Additionally, two satellites were observed at 2320 and 2005 cm^{-1} . The shifts of these satellites by $\pm 160\text{ cm}^{-1}$ from the main band compared well with the intensity ratios between the $Q(v=1)$, $Q(v=2)$ and $Q(v=3)$ bands. For a fundamental libration frequency of 160 cm^{-1} an intensity ratio of 1:45 was calculated for the sideband R and the main band (cf. [615, 616]). This was in good agreement with the observed ratio of 1:40. In view of this agreement and since (i) the shifts of $\pm 160\text{ cm}^{-1}$ were too large to be explained by translational effects and (ii) free rotation could be ruled out because of the high potential barrier (vide supra), Foerster and coworkers proposed librational motions of the CO molecules inside the cavities of Na-A zeolite [597, 601]). Thus, the two satellites were ascribed to librational transitions between the levels with the librational quantum numbers $n=0$ and $n=1$.

CO adsorption on Na,Ca-A resulted, as reported in Ref. [601], in spectra significantly different from those which were obtained with CO/Na-A. Main bands were observed at 2180 and 2130 cm^{-1} for ^{12}CO and ^{13}CO , respectively, and a strong effect of coverage was found.

Foerster and coworkers [608] used zeolite A samples with systematically varied exchange of Ca^{2+} for Na^{+} of the parent zeolite, $\text{Na}_{12}\text{-A}$, resulting in $\text{Na}_{12-x}\text{Ca}_x\text{-A}$, as adsorbents for ^{12}CO and ^{13}CO . On the basis of these experiments, the authors were able to establish a more detailed assignment of the bands observed at 2165 , 2146 , 2129 , 2119 and 2098 cm^{-1} for ^{12}CO (see above); the corresponding bands with ^{13}CO appeared at 2117 , 2098 , 2082 , 2066 and 2047 cm^{-1} , and the intensities of both series of bands decreased in the sequence of decreasing frequencies. In addition, the above-discussed satellites were detected at 2317 , 2008 (^{12}CO) and 2265 , $-$ (^{13}CO) cm^{-1} ; the second satellite band was not observed with ^{13}CO .

The most intense band at 2165 cm^{-1} , which showed a large upscale shift of 22 cm^{-1} compared to the gaseous CO, could be assigned to ^{12}CO in front of Na^{+} in S1 sites ($\text{Na}^{+}\text{-CO}$), whereas the band at 2146 cm^{-1} was attributed to ^{12}CO close to Na^{+} in S2 or S3 sites. The band at 2129 cm^{-1} was ascribed to the reversed arrangement ($\text{Na}^{+}\text{-OC}$, vide supra). These assignments were in agreement with earlier experimental work and theoretical considerations [615, 616]. Finally, the weak absorptions at 2119 and 2098 cm^{-1} (not shown in Fig. 35) were suggested to originate from one or two more different species, which were not specified by the authors.

In the case of ^{12}CO adsorption on Na,Ca-A, particularly bands at 2185 cm^{-1} (strong) and 2115 cm^{-1} (weak) were assigned to carbon monoxide molecules residing in S1 sites. The corresponding pair of bands of ^{13}CO on Na,Ca-A were observed at 2134 and 2068 cm^{-1} . Both bands of the pairs (2185 and 2115 or 2134 and 2068 cm^{-1}) indicated the same adsorbate species, since they grew in parallel with CO coverage and the Ca^{2+} content. The same held for the satellites (vide supra), which appeared with ^{12}CO on Na,Ca-A at 2365 and 2002 cm^{-1} , i.e., about $\pm 180\text{ cm}^{-1}$ apart from the main band.

Bands of ^{12}CO on Na-A ($\text{Na}_{12}\text{-A}$), Na,Li-A ($\text{Na}_{1.3}\text{Li}_{10.7}\text{-A}$), Na,Ca-A ($\text{Na}_{4.2}\text{Ca}_{3.9}\text{-A}$, $\text{Na}_{1.2}\text{Ca}_{5.4}\text{-A}$) and Na,Mg-A ($\text{Na}_4\text{Mg}_4\text{-A}$) were also observed at ambient temperature and compared to those reported by Angell and Schaffer [595] for X-

and Y-type zeolites. The band shifts with respect to the purely vibrational transitions of the gaseous molecules were linearly related to the polarizing power of the cations ($\text{Na}^+ < \text{Li}^+ < \text{Ca}^{2+} < \text{Mg}^{2+}$). They were, however, smaller than those observed by Angell and Schaffer, which indicated an effect of structure and $n_{\text{Si}}/n_{\text{Al}}$ ratio.

In a further study by Foerster and coworkers [617], adsorption of CO on Ca- and Ni-exchanged zeolite A was compared. Even though similar experimental shifts of the fundamental CO vibration occurred (CO/Ca-A: 39 cm^{-1} ; CO/Ni-A: 47 cm^{-1}), MO calculations indicated that different mechanisms were operative: In the case of Ca-CO the main contribution originated from a strengthening of the CO bond, whereas for the spectrum of CO on Ni-exchanged zeolite A a coupling between Ni-C and C-O vibrations was predominant. This is due to the higher strength of the Ni-C bond compared with Ca-C, which is reflected in the estimated force constants: $F(\text{Ni-C}) \approx 200 \text{ N m}^{-1}$ vs. $F(\text{Ca-C}) \approx 70 \text{ N m}^{-1}$. In Ref. [617] the studies on zeolite A exchanged with transition metal cations were extended to experiments of CO adsorption on Co-, Mn- and Zn-exchanged materials and conducted at a low temperature (80 K).

Adsorption of CO and CH_4 (cf. Sect. 5.5.2.4) on zeolite Omega (MAZ) was studied through FTIR spectroscopy and adsorption measurements as a function of pore size and temperature in the work by Yamazaki et al. [618]. CO was preferentially adsorbed in the smaller pores consisting of 8-membered rings. Three signals were observed in the decomposed spectrum obtained at 273 K and 6.0 kPa CO pressure, viz. a weak and a large peak at the high-frequency and a broad peak at the low-frequency side of the band of gaseous CO (2143 cm^{-1}). The first and second peaks were attributed to an $[\text{M} \cdots \text{C} \equiv \text{O}]$, the third one to an $[\text{M} \cdots \text{O} \equiv \text{C}]$ arrangement (M=cation, not specified).

The formation of Ru(I)(CO)_3 after activation of $[\text{Ru}(\text{NH}_3)_6]^{3+}$ in mordenite or in a deep-bed calcined La-Y zeolite under CO atmosphere at $T < 373 \text{ K}$ was suggested through transmission FTIR spectroscopy in a contribution to this field of research by Schoonheydt et al. [619]. These authors observed bands at 2055, 2005 and 1960 cm^{-1} , which were ascribable to Ru(I)(CO)_3 . However, they did not exclude the possibility that the spectral features could originate from a mixture of monocarbonyls (2005 and 1960 cm^{-1}) and dicarbonyls (2055 cm^{-1}).

Extensive IR spectroscopic work was also carried out on adsorption of CO on metal clusters prepared in cavities of zeolites (cf. Volume 3, Chapter 4 of the present series). Such IR investigations are interesting (i) in view of cluster preparation via decomposition of metal carbonyls sorbed into zeolites and (ii) in view of possible reactions of CO catalyzed (perhaps shape-selectively) by metal clusters inside the cavities of a zeolite structure. Examples of IR observation of sorption of metal carbonyls, e.g., $\text{Fe}(\text{CO})_5$, $\text{Mo}(\text{CO})_6$, $\text{Ru}_3(\text{CO})_{12}$, etc. into Na-Y or H-Y, were provided in Refs. [620] and [621-623]. For instance, it was shown that, on adsorption of the carbonyl, the ν_1 mode of CO became IR active. During heating of the carbonyl/zeolite sample under vacuum, the intensities of the CO bands in the rather complex carbonyl spectra continuously disappeared, but intermittently multinuclear intermediates with bridged CO absorbing below 1900 cm^{-1} were formed. Similarly, $\text{Mo}(\text{CO})_6$, $\text{Re}_2(\text{CO})_{10}$ and $\text{Ru}_3(\text{CO})_{12}$ were adsorbed into H-Y, and the adsorption and progressive decomposition at increased temperatures

monitored by FTIR spectroscopy through the changes in the intensities and positions of the CO bands [621]. As could be demonstrated by Gallezot et al. [621], on partial decomposition Mo and Re complexes were displaced and bonded to the framework as indicated, for instance, by an Mo-O vibration band at about 920 cm^{-1} . The total decomposition of metal carbonyls adsorbed into zeolites was proposed as a valuable method to generate highly dispersed metal species.

Wrabetz et al. [624] and Wrabetz [625] studied adsorption of CO on ruthenium clusters obtained via ion exchange of Na-Y with aqueous solutions of $[\text{Ru}(\text{NH}_3)_6]\text{Cl}_3$, followed by drying and subsequent autoreduction. Fig. 36 displays the spectra obtained after adsorption of CO (130 Pa) on an autoreduced sample in the range from 75 to 298 K.

The spectrum at 298 K showed two bands due to $\text{Ru}(\text{CO})_3$ (at 2154 and 2086 cm^{-1} , the latter accompanied by a weak shoulder at 2098 cm^{-1}). A dicarbonyl species is indicated by the band at 2054 cm^{-1} and a linear species of CO adsorbed on Ru-clusters by the band at 2017 cm^{-1} . The intensities of the $\text{Ru}(\text{CO})_3$ bands decreased as the adsorption temperature was lowered to 185 K. The most dominant band appeared then around 2060 cm^{-1} with a shoulder at 2093 cm^{-1} indicating $\text{Ru}(\text{CO})_2$. Bridged CO exhibiting a band at about 1855 cm^{-1} was formed on cooling to 175 K. Bands between 2200 and 2100 cm^{-1} observed in this study were assigned to CO adsorbed on true Lewis acid sites (2174 cm^{-1}) and physisorbed CO forming $\text{SiOH}^{\delta+}\cdots\delta-\text{CO}$ (2160 cm^{-1}).

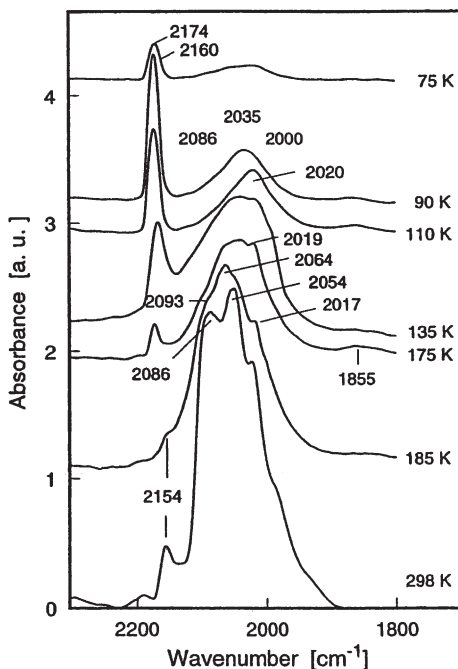


Fig. 36. IR spectra of CO adsorbed at 0.13 mbar on autoreduced Ru, Na-Y in the temperature range 75–298 K [624]

Important work by Sachtler and his group was devoted to the formation, characterization and application of platinum metal clusters in zeolites. These researchers also employed to a great deal FTIR spectroscopy. In particular, the outstanding review article by Sachtler and Zhang [626] should be referred to. The same subject attracted the attention of many other workers as well (cf. Gallezot's Chapter 4 in Volume 3 of the present series). Thus, to mention just a few of more recent contributions, the formation of Pt⁰ clusters through decomposition of the Pt-tetrammine complex, [Pt(NH₃)₄]²⁺, in both M-X and M-Y (M=Li, Na, K, Cs) and the subsequent autoreduction were monitored via in-situ FTIR in the work by Nováková et al. [627]. Also, the intermediate surface species were, inter alia, characterized and the reaction of CO+NO on the final Pt⁰-clusters studied by IR spectroscopy. Gucci and coworkers [628] investigated platinum carbonyl clusters (Chini clusters) encapsulated in cages of Na-Y through monitoring the CO vibrations by FTIR transmission spectroscopy and listed the most relevant infrared frequencies and band assignments in the range 1800–2200 cm⁻¹ obtained from their own work as well as from the literature. A linear correlation between the frequencies of terminal CO vibrations and the charge of the platinum was observed.

Rhodium carbonyl clusters in Y-type zeolite were generated from Rh(III)-Y and CO, and characterized by IR in the contribution of LeFebvre et al. [629], who identified monovalent rhodium dicarbonyl, Rh(I)(CO)₂ as well as polynuclear carbonyls, Rh₄(CO)₁₂ and the most stable Rh₆(CO)₁₆. The latter exhibited a pronounced activity for and selectivity to formation of alcohols and C₂-C₅ hydrocarbons.

Rhodium clusters entrapped in Na-Y and H-Y zeolites and their interaction with CO were also studied via transmission IR spectroscopy by Gelin et al. [630], whereas more recently Kazansky et al. [631] employed diffuse reflectance IR spectroscopy for their investigation of the Pt-C bond of CO adsorbed onto small platinum particles of 1–2 nm in size in (powdered) Na-Y zeolite. At lowest coverages, bands at 2045 and 1970 cm⁻¹ were observed, which were ascribed to two different kinds of CO adsorption. The lower CO stretching frequency was attributed to linearly bonded CO on negatively charged platinum clusters, whereas the higher frequency band was assigned to CO adsorbed on larger particles. The wavenumber of the metal-carbon stretching vibration was derived from the combination band ($\tilde{\nu}_{C-O} + \tilde{\nu}_{Pt-C}$) at about 2500 cm⁻¹ and found to be with 515 cm⁻¹ about 60 cm⁻¹ higher than in the case of larger platinum particles or bulk materials. This effect was ascribed to a higher back donation of electrons from the negatively charged, unusually small Pt clusters to the adsorbed CO molecules resulting in a stronger Pt-C bond and, correspondingly, a lower CO stretching frequency.

Formation of bimetallic alloy clusters from M, Na-Y (M=Pt, Ir, Rh, Ru) after partial ion exchange with CuSO₄ solution, oxygen treatment and subsequent reduction in flowing hydrogen was evidenced by the shift of the band position of adsorbed CO from 2090 cm⁻¹ by about 50 cm⁻¹ to lower wavenumbers [632]. Similar experiments were carried out with silicalite-1 or ZSM-5 as supports.

Reduction of reducible metal cations in exchanged zeolites with hydrogen resulted in the formation of structural OH groups (Brønsted acid centers), which

can be identified by IR. An early example was provided by Beyer and Jacobs [633] on reduction of Ag-Y:



where Z^- stands for a monovalent negatively charged zeolite fragment, Z. A corresponding IR result was reported by Naccache et al. [634] in their study of hydrogen and carbon monoxide interactions with Pd-Y zeolite by ESR and IR spectroscopy, where these authors monitored the development of OH stretching bands on the reduction of Pd^{2+} -Y with H_2 .

Investigation of metal clusters in zeolites by Fourier transform far-infrared spectroscopy is treated in the review article by Baker [232] as mentioned in Sect. 5.3.

5.5.2.3

Linear Triatomic Molecules (N_2O , CO_2) as Adsorbates

Carbon dioxide adsorption on Li-X, Na-X and K-X was investigated via IR already in 1963 by Bertsch and Habgood [202]. N_2O and CO_2 are also isoelectronic compounds. Moreover, the molecules of both compounds are linear, have a similar shape and identical mass; the dipole moment of N_2O is small (0.167 debye), that of CO_2 is zero; the three fundamentals of their internal vibrations fall in the same range of wavenumbers [636–638] (cf. also [640]). However, due to the lower symmetry, nitrous oxide molecules possess more possibilities of orientation [596].

The three fundamentals of N_2O are schematically sketched in Fig. 37.

In the gas phase, the corresponding wavenumbers are $\tilde{\nu}_1 = 1285$, $\tilde{\nu}_2 = 589$ and $\tilde{\nu}_3 = 2224$. Since N_2O and CO are molecules of lower symmetry compared to CO_2 and N_2 , more pronounced frequency shifts and larger band widths would be expected on adsorption of the former pair of species. After adsorption of N_2O on Na-A, bands due to the modes ν_1 and ν_3 were observed. The $\tilde{\nu}_1$ band is split as a consequence of two possible orientations of the molecule. Slightly above room temperature (310 K), the split bands appear at 1303 ($\Delta\tilde{\nu} = +18 \text{ cm}^{-1}$, more intense) and (with lower intensity) at 1264 cm^{-1} ($\Delta\tilde{\nu} = -21 \text{ cm}^{-1}$). The third vibration mode, ν_3 , gives rise to a band at 2260 cm^{-1} with a shift of $\Delta\tilde{\nu} = +36 \text{ cm}^{-1}$.

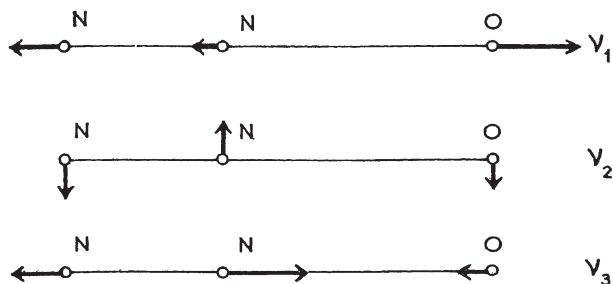


Fig. 37. Schematic representation of the fundamental vibrations of nitrous oxide, N_2O

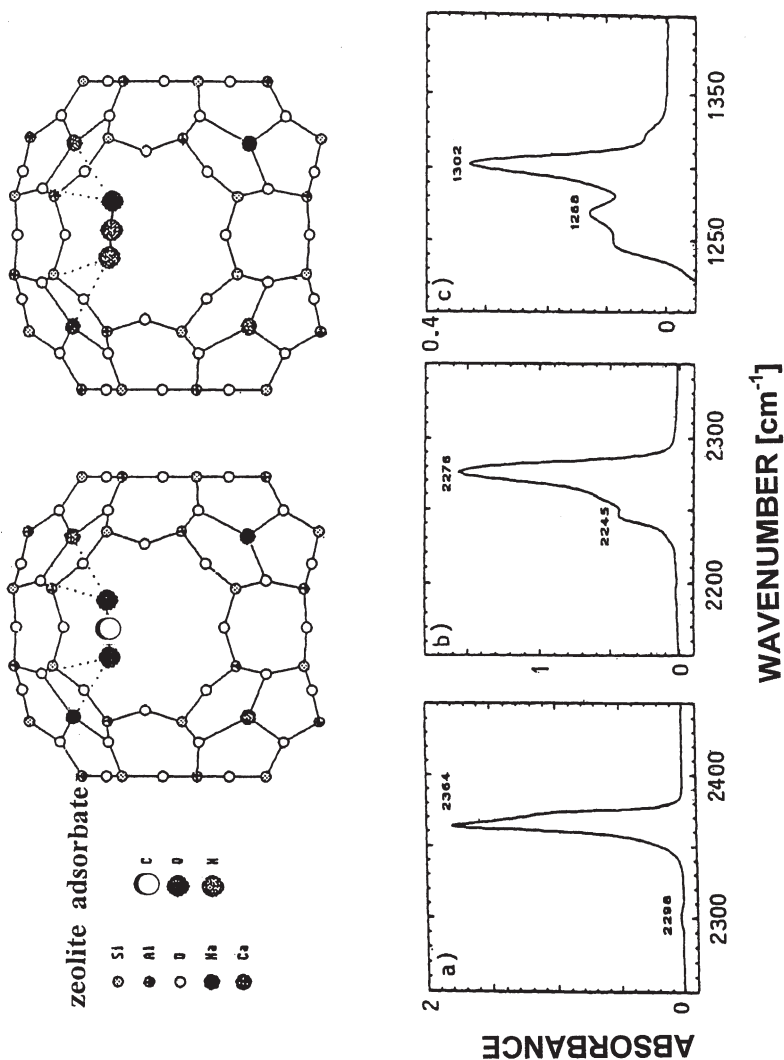


Fig. 38. Top: Sorption geometries of (a) CO₂ and (b) N₂O in zeolite Na₄Ca₄-A. Bottom: Observed fundamental vibrations ν_3 (a) of CO₂ and ν_3 (b) and ν_1 (c) of N₂O in zeolite Na₄Ca₄-A (adopted from [596])

Finally, a weak band occurring around 2600 cm⁻¹ was ascribed to the overtone $2\tilde{\nu}_1$ [635]. After adsorption at lower temperature (223 K), the bands were shifted to higher frequencies, viz. 1305, 1266 and 2272 cm⁻¹ (by Boese and Foerster [596] observed at 1302, 1268 and 2276 cm⁻¹, cf. Fig. 38).

This shifting was explained by the fact that the distance of the N₂O molecule to the cation in the adsorption site decreases with decreasing temperature and, thus, the interaction becomes more intense and the vibration more strongly affected. A calculation of the potential energies of the adsorbed N₂O molecule

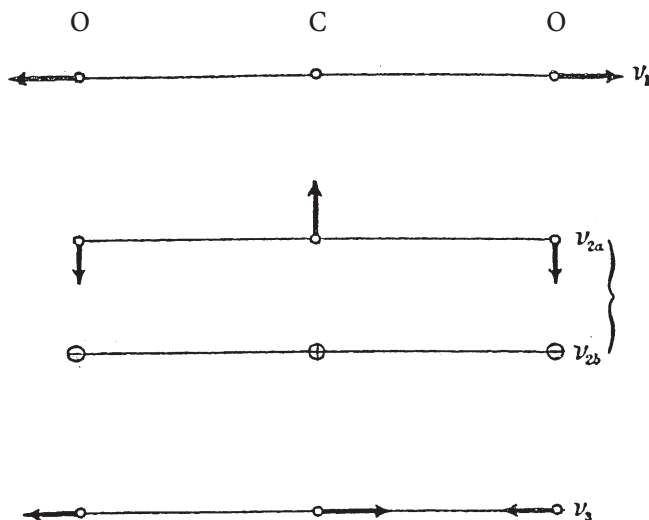


Fig. 39. Schematic representation of the fundamental vibrations of carbon dioxide, CO_2 ; the mode ν_2 is twofold degenerated (ν_{2a}, ν_{2b})

inside the Na-A structure yielded high barriers to translation and rotation. Therefore, N_2O molecules in Na-A perform translational oscillations ($\tilde{\nu}_T = 66 \text{ cm}^{-1}$) and librations ($\tilde{\nu}_L = 58 \text{ cm}^{-1}$), where an angular potential is involved [638]. In fact, a broad band at somewhat higher wavenumbers (60 to 140 cm^{-1}) could be observed in spite of experimental difficulties, but no indication of any rotation was found. The profile of the $\tilde{\nu}_3$ band was affected by translational vibrations, slowly modulating the internal vibration, which resulted in a distribution of frequencies. The band profile can thus be related to the potential distribution inside the α -cage [216].

In Fig. 39 the fundamental vibrations of CO_2 are schematically depicted.

In the gas phase, the symmetric stretching vibration is IR inactive but Raman allowed and then occurs in Fermi resonance with $2\tilde{\nu}_2$ (at about 1285 and 1388 cm^{-1}). At 667 cm^{-1} a weak band appears originating from the bending mode. Finally, the asymmetric stretching vibration produces a strong band at $\tilde{\nu}_3 = 2349 \text{ cm}^{-1}$. On sorption of CO_2 into Na-A, the $\tilde{\nu}_2$ band is shifted by -18 cm^{-1} to 649 cm^{-1} . A band observed at 1382 and 1383 cm^{-1} by Foerster and Schuldt [600] and Delaval and Cohen de Lara [639], respectively, was assigned to the (in gaseous state) IR-forbidden ν_1 mode and visualized as induced by adsorption and interaction with the zeolite walls. A band at 1247 cm^{-1} was ascribed to $2\tilde{\nu}_2$, but due to Fermi resonance it seemed to be lowered with respect to $2 \times 649 = 1298$. Finally, the band of the asymmetric stretching vibration was seen at 2360 – 2364 cm^{-1} , exhibiting a positive (blue-) shift to higher wavenumbers by $\Delta\tilde{\nu} = 11 \text{ cm}^{-1}$. Additionally, the authors observed combination bands of adsorbed CO_2 , viz. $\tilde{\nu}_3 + \tilde{\nu}_1$ and $\tilde{\nu}_3 + 2\tilde{\nu}_2$ in Fermi resonance, at 3712 and 3602 cm^{-1} , respectively, i.e., slightly shifted compared with the gas phase frequencies. The profile

of the $\tilde{\nu}_3$ band changed with temperature, the peak shifted to higher frequencies, and shoulders appeared. These features were ascribed to the occurrence of different types of adsorbate states due to different environments.

For both nitrous oxide and carbon dioxide molecules adsorbed into Na₄Ca₄-A, energy minima were found by calculation of the interaction potentials to occur between adjacent cations in the α -cage [596]. This suggested a tendency to a two-center adsorption (see Fig. 38). Assignment of the IR bands and characteristics of the adsorption complexes were confirmed by MO calculations and normal coordinate analyses [640].

Chemisorption of CO₂ leads to carbonate structures. Carbonate formation is accelerated by preadsorbed water (cf. also [543]). According to Boese et al. [608], the assignment of the corresponding bands is difficult because of band overlap. However, the authors tentatively attributed a band pair found with CO₂ on Na_{1.3}Li_{10.7}-A at 1660 and 1365 cm⁻¹ to a bidentate structure and a second one at 1588 and 1421 cm⁻¹ to a monodentate structure (cf. [543, 641]). From alkali ion-exchanged zeolites, carbonates could be removed by pumping at elevated temperatures, which was, however, not possible in the case of alkaline earth-exchanged zeolites.

5.5.2.4

Methane (CH₄) as an Adsorbate

Methane molecules do not possess a permanent dipole moment, and also the quadrupole moment is zero. CH₄ exhibits four fundamental vibration modes, the modes ν_1 and ν_2 , which are in the gas phase IR-forbidden and only Raman-allowed, and the IR- and Raman-active ν_3 and ν_4 modes. The corresponding wavenumbers are $\tilde{\nu}_1, \tilde{\nu}_2, \tilde{\nu}_3$ and $\tilde{\nu}_4$, i.e., 2914, 1526, 3020 and 1306 cm⁻¹, respectively. In fact, $\tilde{\nu}_2$ of adsorbed CH₄ was never observed, most probably because the intensity is too low. The spectra after adsorption on Na-A shown in Fig. 40 were taken at 203–273 K (cf. [216, 642]).

On interaction with the adsorbent, a dipole moment is induced, and a band due to the ν_1 mode, which is forbidden in IR for the gaseous state, appeared at 2892 and 2884 cm⁻¹ at 273 and 213 K, respectively [599, 603, 642]. The frequency shift of the induced bands, ($\tilde{\nu}_{\text{gas}} - \tilde{\nu}_{\text{ads}}$), increased with decreasing temperature (compare findings with, e.g., N₂O, vide supra). The collisional diameter of CH₄ is of the order of 0.4 nm, which should be compared with the diameter of the α -cage of 1.14 nm. From neutron scattering experiments it is known that CH₄ molecules are delocalized in the large cavity at 300 K and close to the internal surface at 200 K. Therefore, at 300 K the intensity of the $\tilde{\nu}_1$ band must be an average over all the positions of the CH₄ molecules in the α -cage. However, at 200 K the intensity is due to an intense interaction with the adsorption center. Thus, the field strength determined as 0.7 V nm⁻¹ from the absorbance measured at the higher temperature must be visualized as a mean value, whereas that determined from the intensity at 200 K as 1.7 V nm⁻¹ gives the field strength close to the Na⁺ cation in S₃ sites. The $\tilde{\nu}_3$ band shows a relatively broad profile, which presumably indicates that CH₄ retains a certain degree of rotational freedom inside the α -cage. The rotational motion of the adsorbed molecules is, however, more

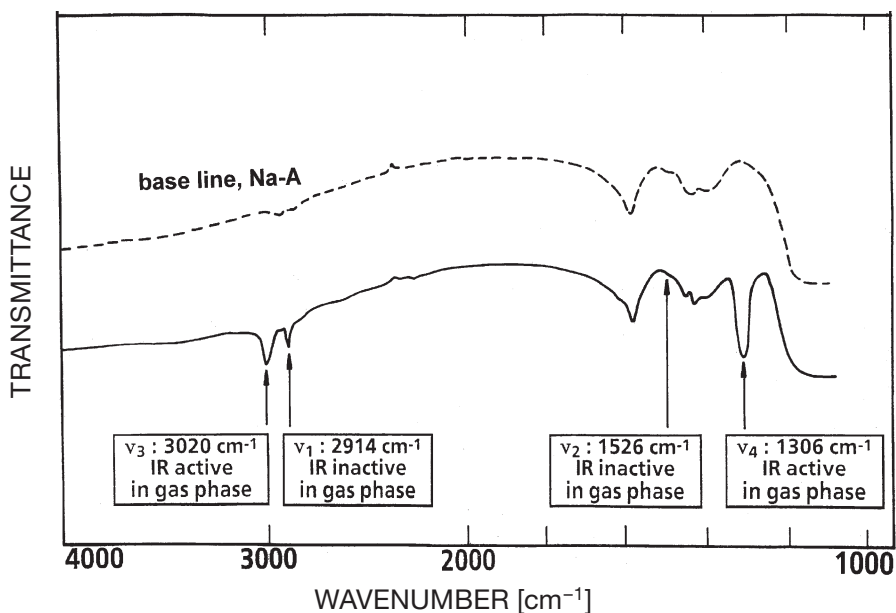


Fig. 40. Infrared spectra of methane, CH_4 , adsorbed on Na-A; the spectra obtained at 10^{-4} and 10^{-5} mbar (adopted from [599])

hindered than in the liquid state of CH_4 , since the heat of adsorption is about 26 kJ mol^{-1} , and the energy barrier for rotation is significant, certainly higher than 8 kJ mol^{-1} .

A molecular-dynamics study of methane (and ethane, propane, ethene as well as ethyne) adsorbed in silicalite-1 and (purely siliceous) zeolite A was performed by Dumont and Bougeard [643] using flexible molecules in rigid frameworks. The reproduction of the experimental IR and Raman features was satisfactory. The agreement was good in the case of silicalite-1, whereas some discrepancies appeared with zeolite A as the adsorbent, due to the role of the cations in the experimentally used, Al-containing zeolite A.

Adsorption of CH_4 on zeolite Omega (MAZ) was investigated by Yamazaki et al. [618], who employed volumetric adsorption measurements and FTIR spectroscopy and found that methane was scarcely adsorbed in the smaller pores consisting of 8-membered rings as long as the adsorption temperature was lower than 214 K, where the adsorbate molecules preferred the larger pores with 12-membered oxygen rings as windows. At temperatures above 250 K, however, most of the CH_4 molecules were distributed inside the small pores.

A combined NMR and DRIFT study of adsorption of CH_4 and trimethylgallium on H-Y was conducted by Seidel et al. [644]. In the IR spectra of adsorbed CH_4 , besides the IR-allowed ν_3 (3007 cm^{-1}) and ν_4 modes the forbidden ν_1 transition appeared and, furthermore, after adsorption of trimethylgallium a corresponding band at 3005 cm^{-1} , suggesting the formation of methane.

5.5.2.5

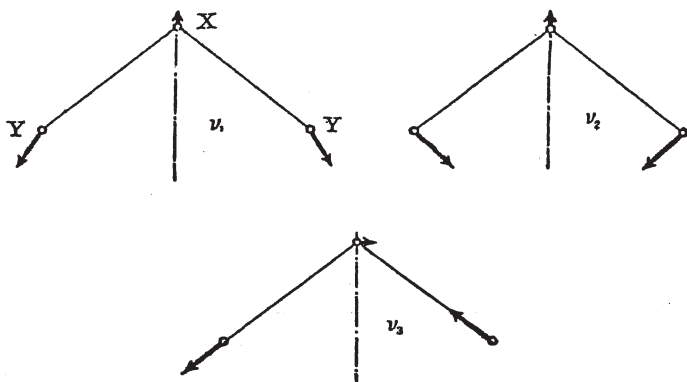
Bent Triatomic Molecules (SO_2 , H_2S , H_2O) as Adsorbates

As important examples, IR investigations on SO_2 , H_2S and H_2O molecules adsorbed on zeolites should be mentioned. All three of them proved to be non-linear, exhibiting the fundamental modes displayed in Fig. 41 (cf. [645]).

Sulfur dioxide, SO_2 , adsorbed on zeolites was first investigated by Deo et al. [646] and Foerster and Seelemann [649]. Deo et al. used as adsorbents Na-Y and H-Y zeolites, and their investigations were related to the modified Claus reaction which occurs according to the overall reaction formula of Eq. (29). Also, studies by Karge et al. [227, 228], using combined IR and UV-Vis spectroscopy for measurements of SO_2 adsorption on faujasite-type zeolites, were related to the modified Claus reaction:



Deo et al. observed a weak combination band, $\tilde{\nu}_1 + \tilde{\nu}_3$, at 2470 cm^{-1} and the more intense asymmetric stretching band with $\tilde{\nu}_3 = 1330\text{ cm}^{-1}$, shifted by $\Delta(\tilde{\nu}_1 + \tilde{\nu}_3) = -42$ and $\Delta\tilde{\nu}_3 = -31\text{ cm}^{-1}$ with respect to the gas phase wavenumbers ($\tilde{\nu}_1 + \tilde{\nu}_3 = 2512$, $\tilde{\nu}_3 = 1361\text{ cm}^{-1}$), respectively. No further band appeared, in particular no $\tilde{\nu}_2$ and no overtone band $2\nu_1$. On admission of H_2S to the SO_2 -loaded Y-zeolite sample, a band around $\delta_{\text{H}_2\text{O}} = 1650\text{ cm}^{-1}$ developed originating from the deformation mode of H_2O , which had formed according to Eq. (29).



(1) : SO_2 , X = S, Y = O

(2) : H_2S , X = S, Y = H

(3) : H_2O , X = O, Y = H

Fig. 41. Schematic representation of the fundamental vibrations of the bent triatomic molecules of sulfur dioxide, SO_2 , hydrogen sulfide, H_2S , and water, H_2O

Foerster and Seelemann employed A-type zeolites, viz. Na-A and Na,Ca-A. Similar to the above results obtained with Y-type zeolites, they did not see the overtone band of $2\tilde{\nu}_1$ either. The bands due to the combination mode $\tilde{\nu}_1 + \tilde{\nu}_3$ were slightly more shifted than those found with Y-type zeolites, viz. to 2460 cm^{-1} . Likewise, the $\tilde{\nu}_3$ band appeared at $1315\text{--}1320$ (type I) with Na-A or, with Na, Ca-A, at 1280 cm^{-1} (type II). The relative intensities depended on the SO_2 coverage. Since SO_2 cannot enter the sodalite cages, only sorption sites in the large cavities of both Na-A and Na,Ca-A came into consideration. On the basis of the adsorption and desorption behavior and literature data, absorption of type I was ascribed to physisorbed, relatively loosely bound SO_2 molecules, whereas type II absorption was assigned to SO_2 molecules, which were simultaneously bound through their S atoms to framework oxygens and via the polarized O atoms to the exchange cations (Na^+ or Ca^{2+}).

Hydrogen sulfide, H_2S , adsorbed on Y-type zeolites produced, according to Deo et al. [646], a $\tilde{\nu}_3$ band at 2525 cm^{-1} and, in the case of H-Y as adsorbent, an additional band around 3200 cm^{-1} indicating hydrogen bonding of H_2S . Foerster and Schuldt [647], who used Na-A and Na,Ca-A as zeolite adsorbents, reported that the same asymmetric stretching mode gave rise to adsorbate bands shifted to $2480\text{--}2520\text{ cm}^{-1}$ (on Na-A) and 2540 cm^{-1} (on Na,Ca-A). These shifts were the largest ones of the $\tilde{\nu}_3$ band of H_2S reported so far. Like Deo et al., the authors failed to detect bands due to the bending mode ν_2 , most probably because of the strong framework absorption in the range of the corresponding adsorbate band. A weak additional band at 2585 cm^{-1} was ascribed to a small fraction of more strongly held H_2S [647], presumably chemisorbed via dissociation. This assumption was confirmed by Karge and Raskó [454] in their investigation of dissociative H_2S adsorption on faujasite-type zeolites with $n_{\text{Si}}/n_{\text{Al}} \leq 2.5$ (Na-Y), where additionally the corresponding formation of OH groups as a consequence of the attack of framework oxygen by the remaining proton was measured (vide supra, Eq. (28) and [227, 468, 650]). Later IR experiments carried out by Sugioka et al. [651] confirmed the non-dissociative adsorption of H_2S on Na-Y ($n_{\text{Si}}/n_{\text{Al}} \geq 2.5$).

Adsorption of hydrogen sulfide on H-ZSM-5 and Na-ZSM-5 was investigated by Garcia and Lercher [652], who used a more sophisticated technique of adsorption under low adsorbate pressure of 10^{-2} to 50 Pa (see also below, adsorption of water and methanol vapors and NH_3). In the case of H-ZSM-5, they observed a decrease in the intensity of the 3610 cm^{-1} band of free acid OH groups, a band at 3100 cm^{-1} of perturbed acid OH groups and a band at 2560 cm^{-1} due to adsorbed H_2S , increasing with H_2S pressure. With Na-ZSM-5, bands appeared at $2566\text{--}2596\text{ cm}^{-1}$ due to S-H stretching vibrations, increasing in frequency and intensity with increasing coverage. Furthermore, these authors found that H_2S adsorbed on bridging OH groups of H-ZSM-5 in two different orientations, viz. (i) linearly hydrogen bonded and (ii) cyclically bonded with the S atom directed to the proton of the Brønsted OH and through one H atom interacting with an adjacent framework oxygen atom. In the case of Na-ZSM-5 bonding occurred through the lone electron pair of the sulfur atom to the alkali cation. No dissociative adsorption was observed, in agreement with the finding of Karge and Raskó that dissociation of H_2S took place on low-shielded cations in zeolites with low $n_{\text{Si}}/n_{\text{Al}}$ ratios [454].

Water vapor, H_2O , adsorbed on zeolites, was studied already in the very beginning of IR research on zeolites (cf., e.g., [374–376, 653]). According to Ref. [645], the wavenumbers of the fundamental vibration modes are $\tilde{\nu}_1 = 3654.5$ (Raman active), $\tilde{\nu}_2 = 1595.0$ (IR active) and $\tilde{\nu}_3 = 3755.8 \text{ cm}^{-1}$ (IR active). In zeolite research, usually the (shifted) $\tilde{\nu}_2$ deformation band of adsorbed H_2O is used, which appears around $1640\text{--}1650 \text{ cm}^{-1}$. The bands in the OH stretching region are usually very broad due to hydrogen bonding. Thus, the absence of the $\tilde{\nu}_2$ band is often taken as an indication of sufficient dehydration of a zeolite sample, which is important in many experiments with these highly hydrophilic materials. Similarly, the appearance of this band frequently shows that a reaction has occurred on the zeolite surface under formation of water. The intensity of the band is sometimes even used for quantitative determination of the adsorbed H_2O , although the band is shallow and broad.

For a number of bent triatomic molecules (SO_2 , H_2S , D_2S , H_2O) as well as linear ones (N_2O , CO_2), Foerster and Schuldt [654] found an interesting relationship between the band shape (full-width at half-height, FWHH or $\Delta\tilde{\nu}_{1/2}$) and the respective band shifts, $\Delta\tilde{\nu}$. In the case of the ν_3 modes, a linear correlation was observed between the absolute value of the shifts, $|\Delta\tilde{\nu}|$ and the widths, $\Delta\tilde{\nu}_{1/2}$ (cf. also [620]).

However, much more informative IR results can be obtained here and in other cases of adsorption on zeolites, if the spectra are not produced under rather high adsorbate pressures but at very low coverages. This technique was excellently developed in Lercher's group (cf. also H_2S adsorption, *vide supra* and methanol/ NH_3 interaction, Sect. 5.5.2.7). Thus, Fig. 42 displays a set of spectra of water vapor adsorbed under extremely low pressures adjusted by an ultrahigh vacuum leakage valve [127, 220].

The spectra shown in Fig. 42 are difference spectra, i.e., the spectrum of the activated, water-free adsorbent (H-ZSM-5) is subtracted from the adsorbate (H_2O)/zeolite spectrum. The spectrum of activated H-ZSM-5 exhibits bands at 3745 (silanol Si-OH groups), 3726 (defect sites) and 3610 cm^{-1} (Brønsted acid, bridging OH groups, i.e., $[\equiv\text{Si}(\text{OH})\text{-Al}\equiv]$). On contact with water vapor of low pressure (10^{-3} to 10^{-2} Pa), the bands at 3726 and 3610 cm^{-1} were slightly reduced and bands of unperturbed (3666 and 3668 cm^{-1}) and perturbed (3315 and 3338 cm^{-1}) OH groups appeared. Thus, under very low pressures the H_2O molecules preferentially adsorb onto defect sites which leads to the observed decrease in the intensity of the 3726 cm^{-1} band. Above 10^{-2} Pa of water vapor pressure, new bands of perturbed OH groups developed at 2904 and 2460 cm^{-1} , reaching their maximum in intensity under 10 Pa. On further increasing the H_2O pressure, the bands at 3726 and 3610 cm^{-1} were continuously reduced in intensity, while those at 3666 and 1630 cm^{-1} were enhanced. At higher water vapor pressures, the H_2O bending band around 1630 became relatively broad, and new bands of the perturbed OH groups at 3315 and 3222 cm^{-1} appeared. At about 1 Pa H_2O pressure, an equilibrium adsorption of 1 H_2O molecule per 1 Brønsted acid site (indicated by the 3610 cm^{-1} band) was reached. The authors assumed that in this situation hydroxonium ions were formed: They ascribed a band observed at 3695 cm^{-1} to the vibration of the free OH group, but the bands at 2885 and 2460 cm^{-1} to the antisymmetric and symmetric OH stretching vibrations of the hydroxonium ion,

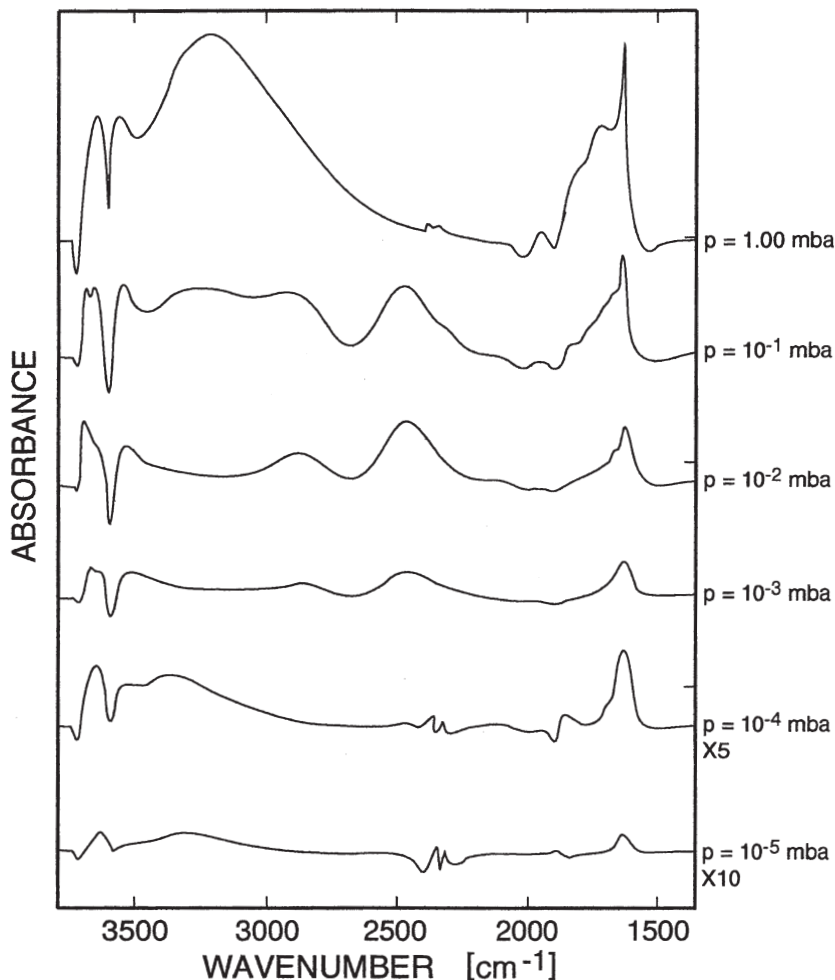


Fig. 42. Infrared spectra of water vapor adsorbed on H-ZSM-5 at low pressures (10^{-5} –1 mbar); the spectra obtained at 10^{-4} and 10^{-5} mbar were expanded by the factors 5 and 10, respectively (adopted from [127])

respectively. At pressures above 10 Pa, clusters of hydrated H_3O^+ were supposed to form.

Similar experiments of H_2O adsorption were carried out with M-ZSM-5 (M=Li, Na, K, Rb, and Cs, cf. [127]) and under co-adsorption of H_2O and *n*-hexane [220].

Later on, the hypothesis of H_3O^+ formation was questioned, since ab-initio quantum mechanical calculations by Krossner and Sauer [655] on H_2O adsorbed on zeolitic [$\equiv\text{Si}(\text{OH})\text{-Al}\equiv$] groups have shown that an (unsolvated) hydroxonium ion H_3O^+ would not be a stable entity (cf. also [656]). Rather, on the respective potential energy surface (PES) an H_3O^+ ion would be located on a saddle

point separating the energy minima of the two possible configurations of a neutral adsorption complex (cf. Fig. 43).

The saddle point energy lies only about 10 kJ mol⁻¹ higher than the minima of the two neutral complexes I and II [656]. Therefore, the hydroxonium ion was visualized only as a transition structure between those complexes.

On the basis of the quantum chemical calculations, the observed H₂O/zeolite spectrum with the three bands at 1630, 2460 and 2885 cm⁻¹ (A-B-C pattern) was interpreted as follows [655]: The in-plane (δ_{OH}) and out-of-plane (γ_{OH}) bending vibrations of the zeolitic bridging OH group [$\equiv\text{Si}-(\text{OH})-\text{Al}\equiv$], which were predicted by the MP2 calculations at 1317 and 1022 cm⁻¹, were blue-shifted on H₂O adsorption by about 270 and 700 cm⁻¹ and involved also in generating the 1630 cm⁻¹ band. In contrast, the OH stretching mode of that zeolitic OH group is, due to perturbation, strongly red-shifted to 2740–2850 cm⁻¹. Fermi resonance of the OH bending overtones with the strongly perturbed OH stretching mode produces the bands at 2460 and 2885 cm⁻¹ (cf. also [657]).

The interpretation of the above IR results of the H₂O/zeolite system was supported by inelastic neutron scattering (INS) studies by Jobic et al. [658] of H₂O adsorbed on hydrogen mordenite. These experiments were carried out in the range below 2000 cm⁻¹. Activated and water-free H-mordenite gave INS bands at 320 and 1060 cm⁻¹. On the basis of quantum mechanical calculations, these were assigned to the out-of-plane (γ_{OH}) and in-plane (δ_{OH}) deformation vibrations of the zeolitic OH groups, since these were predicted at 322 and 1047 cm⁻¹. On

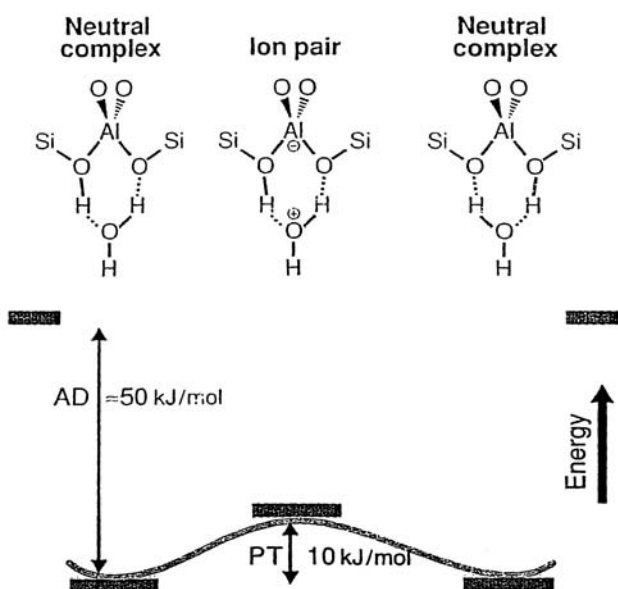


Fig. 43. Calculated potential energy surface for the adsorption of a single water molecule on a zeolitic Brønsted site (bridging OH group); AD: adsorption energy, PT: proton transfer energy (in kJ mol⁻¹), showing the hydroxonium ion as a transition structure and not in an energy minimum [655, 656]

adsorption of water vapor, peaks appeared at 340, 1060, 1385 and 1670 cm^{-1} . The bands observed at 1060 and 1385 cm^{-1} were identified as the shifted zeolitic γ_{OH} and δ_{OH} modes which were, for the neutral $\text{H}_2\text{O}/[\equiv\text{Si}(\text{OH})\text{-Al}\equiv]$ complex, predicted at 1064 and 1372 cm^{-1} . The H-O-H deformation mode (δ_{HOH}) and the out-of-plane deformation mode of the free proton of an adsorbed water molecule were predicted to occur at 1578 and 325 cm^{-1} , respectively. Therefore, the observed 1670 and 340 cm^{-1} bands were attributed to these two modes. The hypothesis of a hydroxonium ion existing on the charged zeolitic framework fragment, $[\equiv\text{Si}(\text{O}^-)\text{-Al}\equiv]$, which was advanced by Jobic et al., would in fact lead to the prediction of three peaks above 1200 cm^{-1} , viz. at 1335, 1435 and 1584/1612 cm^{-1} . However, only two bands were detected (*vide supra*), i.e., no peak corresponding to $\tilde{\nu} = 1435 \text{ cm}^{-1}$ was found. Furthermore, the ion-pair model would not provide any explanation for the bands found at 340 and 1060 cm^{-1} . Again, the conclusion was that the assumption of a neutral complex formed by an adsorbed H_2O molecule and the zeolitic $[\equiv\text{Si}(\text{OH})\text{-Al}\equiv]$ group is much more likely than ion-pair formation involving a hydroxonium ion. By a similar reasoning, the assumption was rejected that on methanol adsorption on a Brønsted acid site, $[\equiv\text{Si}(\text{OH})\text{-Al}\equiv]$ a methoxonium ion, CH_3OH_2^+ would form (*vide infra* and cf. [659, 660]).

In the case of higher coverages, i.e., for a ratio of, e.g., 2 molecules H_2O per Brønsted acid site, $[\equiv\text{Si}(\text{OH})\text{-Al}\equiv]$, the formation of a hydroxonium ion cannot be excluded by quantum mechanical arguments, the hydroxonium ion could then be stabilized through solvation [655]. This is shown by Fig. 44.

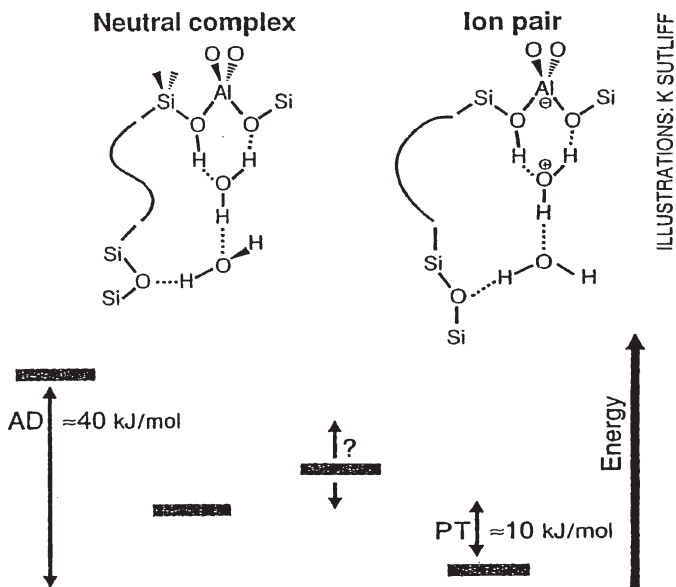


Fig. 44. Hydroxonium ion on a zeolite surface stabilized by a second water molecule where both surface species, $(\text{H}_2\text{O})_2$ and $(\text{H}_3\text{O}^+\cdot\text{H}_2\text{O})$ become stable [655, 656]. For the meaning of AD and PT see caption of Fig. 43 or list of abbreviations

In the present context, it should be mentioned that in the work of Fraissard and coworkers [661, 662] adsorption of water on acid zeolites was proposed to characterize the strength of Brønsted acidity. These authors also claimed that hydroxonium ions form via H_2O interaction with zeolitic acid OH groups. They attempted to determine the concentration of those hydroxonium ions through wide-line and high-resolution ^1H -NMR measurements and to establish a scale of acid strength similar to the pH concept of acid solutions. This approach by Fraissard et al. is dealt with in Ref. [663] and will be discussed in more detail in Volume 6 (Acidity and Basicity) of the present series.

Bibby and coworkers [664] reported on an interesting FTIR spectroscopic observation of an interaction between an excess of H_2O and Brønsted acid OH groups of H-Y. They found that at temperatures as low as 298 and 353 K this interaction and subsequent water desorption resulted in a partial breaking of Al-framework bonds under formation of Al-OH and Si-OH species and finally in a collapse of the framework (cf. [472]). In another series of experiments, Bibby and coworkers [665] found out by IR spectroscopy that H_2O and D_2O on D-ZSM-5 and H-ZSM-5 experienced at 353 K only a slow H/D exchange. Since approximately one water molecule was adsorbed per framework Al, the authors proposed that the adsorbed water was only partially protonated but also interacted with the zeolite framework.

5.5.2.6

Adsorption of Probe Molecules for the Characterization of Zeolitic Acidity and Basicity

5.5.2.6.1

Introductory Remarks

In the preceding Sects. 5.5.2.1–5.5.2.4, adsorption of simple molecules such as H_2 , D_2 , N_2 , CO, CH_4 , N_2O and CO_2 was discussed which are, inter alia, suitable for probing the local electric fields in zeolite voids.

However, the most important applications of probes in IR investigation of zeolites are certainly aimed at the characterization of zeolitic acidity and basicity. The above-mentioned molecules were also employed for that purpose. For example, the interactions of O_2 and N_2 (but also of He, Ar and Xe) with the hydroxy groups in H-Y were used by Wakabayashi et al. [666] to characterize via FTIR spectroscopy the acid properties of this zeolite in comparison with those of H-MOR and H-ZSM-5. Similarly, Bordiga et al. [667] investigated the spectral changes induced by adsorption of H_2 , N_2 , CO and NO on H-, Li-, Na- and K-exchanged ferrierite to characterize the local fields and the Brønsted and cationic Lewis acidity. In the case of H-FER the shift of the OH band at 3605 cm^{-1} suggested that the acid strength of the respective Brønsted acid sites was similar to that of H-ZSM-5, H-MOR or H-Beta.

Formation of hydrogen bonding upon interaction of probes with zeolites was studied in detail by Parker et al. [668], who, in particular, distinguished three classes of hydrogen bonding occurring upon adsorption of probes with H-ZSM-5. These classes were differentiated by the type of interaction, i.e., through (i) the zeolitic hydroxy groups according to the proton affinity of the probes, (ii) π -electrons of the probe molecules and (iii) lone electron pairs of oxygen or nitrogen atoms.

In spite of the importance of zeolite acidity and basicity, however, this topic will be discussed here only in a condensed overview, since it will be dealt with in greater detail in the frame of a later chapter especially devoted to acidity and basicity (cf. Volume 6 of the present series).

Furthermore, rather recent reviews appeared by Lercher et al. [669, 670], providing very valuable information about methods for characterizing acidity and basicity of oxides and zeolites. In [670] the authors provided a table listing frequently used probe molecules, indicating the types of sites, which these molecules may probe, and including some comments on the potentials and limitations of the respective probes. Janin and colleagues published a screening of various probes of various basic strengths (*alcohols, ethers, sulfides, thiols and hydrocarbons*) for determining Brønsted acid sites [671] and used particularly *hydrogen sulfide* and *ethene* for several series of dealuminated H-Y zeolites; the latter probe was adsorbed at 210 K to avoid polymerization [672]. More recently, Kazansky and coworkers [672a, 672b] suggested to characterize the strength of acid (active) sites not through the shift of, e.g., OH group bands upon interaction with probe molecules but by the intensities of the correlated bands.

5.5.2.6.2

Pyridine, Ammonia and Amines as Probes for Acid Sites

Pyridine was probably the first probe molecule which has been and continues to be extensively used in IR investigations of surface acidity of solids such as alumina, amorphous silica-alumina and zeolites [208, 211, 212]. In studying acidity of solids and particularly zeolites, one encounters three questions, i.e., what is (i) the *nature*, (ii) the *density* (or *concentration*) and (iii) the *strength* (or *strength distribution*) of the acid sites? Within certain limitations (vide infra), pyridine is a suitable probe to study these three aspects of zeolite acidity. Regarding the nature of the acid sites in zeolites, adsorbed pyridine allows to distinguish between Brønsted (B) acid sites [205, 211, 379, 673], “true” Lewis (L) acid sites (Al-containing extra-framework species, cf. [379, 674, 675]) and Lewis acid cation (C) sites [676–678]. This is possible through the respective typical bands of adsorbed pyridine (cf. Fig. 45), viz. at ca. 1540 (B-sites), ca. 1450 (L-sites) and 1430–1450 cm^{-1} (C-sites). In fact, some other bands may be used as well, e.g., the bands at 1632 cm^{-1} (B-sites) and 1620 cm^{-1} (B- and L-sites) [679]. A band at ca. 1490 cm^{-1} also produced via pyridine adsorption is non-specific; it appears on interaction of pyridine with all of the above-mentioned sites and also through hydrogen bonding.

The bands of pyridine adsorbed on zeolites are relatively narrow and, therefore, well-suited for a determination of the density of the sites, i.e., the amount of pyridinium ions generated through interaction with acid OH groups or the amount of pyridine molecules coordinatively bound to L- or C-sites. In fact, for a determination of the absolute concentrations of sites the knowledge of the extinction coefficients is required (cf. Sect. 3.2).

Using the FTIR/pyridine technique, Janin et al. [680] also investigated silanol groups and extra-framework Al-containing debris in dealuminated H-Y zeolites. A band at 3747–3749 cm^{-1} was sensitive to pyridine adsorption and ascribed to

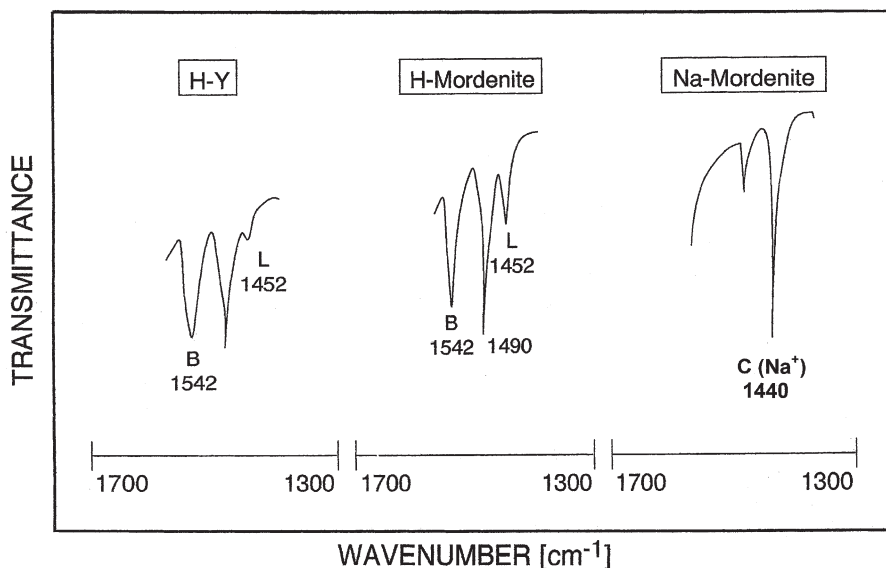


Fig. 45. IR bands of pyridine (n_{19b} mode, [679]) adsorbed on Brønsted acid sites (B-sites), “true” Lewis sites (L-sites) and cations (C-sites) in hydrogen faujasite-type zeolite H-Y (H-FAU), hydrogen mordenite (H-MOR) and sodium mordenite (Na-MOR); see text

silanols attached to silica/alumina debris (for the utilization of pyridine see below). A second band at $3744\text{--}3746\text{ cm}^{-1}$ was not affected by pyridine and suggested to originate from OH groups connected with silica-rich extra-framework debris. Finally, a band at 3738 cm^{-1} was attributed to terminal SiOH, which did not interact with the probe either.

A combination of X-ray photoelectron and infrared spectroscopy, where both techniques employed pyridine as a probe, was used by Borade and Clearfield [492] when they tested the acidity of a series of zeolites. All of their samples contained strong Brønsted sites, weak Brønsted sites and Lewis sites. With respect to the Brønsted acid strength of the hydrogen forms these authors arrived at the following sequence: H-Omega > H-Beta > H-ZSM-22 > H-mordenite > H-Y.

The effect of the synthesis medium (OH^- - or F^- -containing) on the acidity of [Si,Al]ZSM-5 was investigated by IR spectroscopy with and without pyridine as a probe in the work by Joly et al. [681]. These authors found in the case of H-MFI synthesized in the presence of OH^- only Brønsted acid sites, indicated by the OH band at 3600 and the pyridinium band at 1545 cm^{-1} , whereas synthesis in F^- -containing media resulted in materials with more Lewis acid sites (Py \rightarrow L bands at 1622 and 1455 cm^{-1}), depending on the $n_{\text{Si}}/n_{\text{Al}}$ ratio.

In the case of pyridine attached to cations, it was shown by Ward [678] that the band position linearly depends on the electrostatic Coulomb field, q/r , which is often useful for the identification of the cation (cf. Fig. 46).

Brønsted and Lewis acidity of ZSM-5 zeolites loaded with transition metal ions (Co, Fe) via impregnation were investigated by Rhee et al. [682–684] using the IR/pyridine adsorption technique with thin sample wafers.

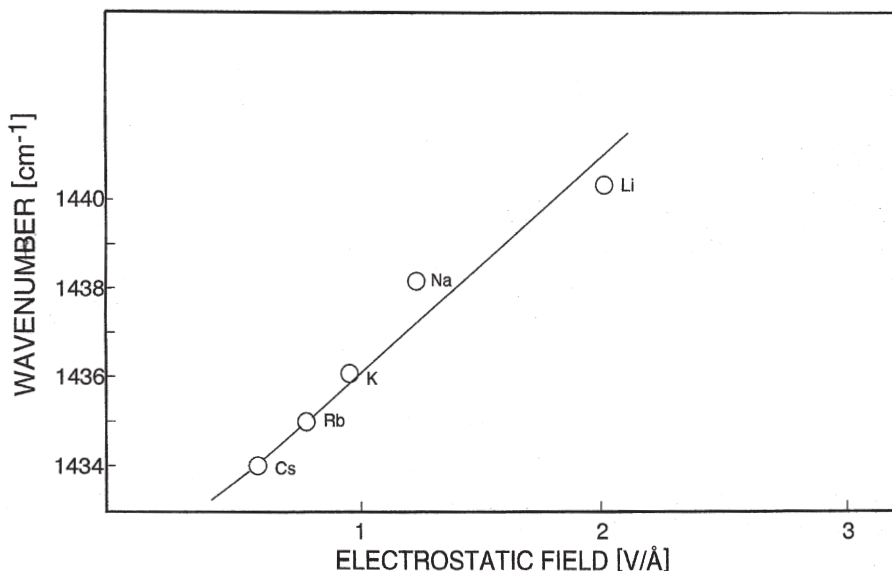


Fig. 46. Wavenumber of pyridine adsorbed on monovalent cations (C-sites) as a function of the electrostatic Coulomb field of the cations determined by the cation charge and radius; see text (adopted from [677])

In a similar way as described for microporous aluminosilicates, the acidity of AlPO_4 s, SAPOs and metal-substituted AlPO_4 -5 was also studied employing probe molecules and IR spectroscopy. Thus, Mueller et al. [685, 686] investigated AlPO_4 -5, SAPO-5, BeAPO-5, CoAPO-5, and MgAPO-5 via monitoring the adsorption of pyridine, ammonia and benzene (see below) by IR-micro-spectroscopy (using an “IR microscope”, cf. Sect. 4.1). The FTIR/pyridine technique was also employed, for instance, by Akolekar [687, 688] for the characterization of acidity in silicon-containing aluminophosphates such as the MAPSO-36, which exhibited framework-incorporated magnesium. In a similar way, FTIR spectroscopy of pyridine adsorbed on MgAlPO-5 indicated incorporation of magnesium into the molecular sieve and the corresponding formation of Brønsted acid sites, evidenced by a band at 1545 cm^{-1} , as reported by Concepción et al. [689]. Their strength was similar to that of high-silica zeolites: a TPD peak of NH_3 appeared at about 793 K. Adsorption of pyridine on CoAPO-37 revealed the presence of Brønsted as well as Lewis acid sites (vide supra, Sect. 5.4.1.2.11). Similarly, the acidities of AlPO_4 -31 and materials derived therefrom, CoAPO-31 and MnAPO-31, were determined by Tusar et al. [690] by FTIR using pyridine and ammonia as probe molecules. Both B- and L-sites were identified (cf. also [764] in Sect. 5.5.2.6.2).

One drawback of pyridine as a probe is the rather large size of the pyridine molecules relative to the openings of the zeolite cavities and channels. Thus, it is not capable of indicating acid centers in sodalite cages, channels of clinoptilolite, side pockets of mordenite [126], in the 8-membered ring pores of ferrierite [691]

etc. In this respect, the smaller molecules of *ammonia*, also frequently used as a probe, are more advantageous.

As an example, the IR spectroscopic investigation of H, Na-MOR as a function of the degree of exchange of H^+ for Na^+ by Datka et al. [141] (cf. also [134]) should be mentioned. These authors provided data of absolute concentrations on the basis of their determination of extinction coefficients (according to Eq. (24): $\epsilon_B=0.147 \text{ cm}^2 \mu\text{mol}^{-1}$ for NH_3 on Brønsted sites, i.e., $NH_4^+ \rightarrow Z^-$, and $\epsilon_L=0.022 \text{ cm}^2 \mu\text{mol}^{-1}$ for NH_3 attached to Lewis sites, $NH_3 \rightarrow L$). Up to 80% replacement of Na^+ , the concentration of Brønsted sites (band at 1460 cm^{-1}) corresponded to the Al content of the framework. At higher exchange degrees, some dehydroxylation and formation of Lewis sites (band at 1622 cm^{-1}) occurred.

However, the resulting IR bands of adsorbed NH_3 , e.g., around 1445 cm^{-1} (B-sites indicated by ammonium ions), 1620 cm^{-1} (L-sites, indicated by coordinatively bound NH_3) and $1600\text{--}1650 \text{ cm}^{-1}$ (C-sites) are usually rather broad and less suitable than those of pyridine for quantitative measurements.

Proton transfer from acid B-sites to ammonia to form NH_4^+ , which is then adsorbed with one or two hydrogen bonds to the zeolite and possibly co-adsorbed with another NH_3 molecule was theoretically treated by Teunissen et al. [692], and the calculated spectra were compared with experimentally observed ones of H-Y, H-mordenite, H-Beta and H-erionite.

In the application of NH_3 as a probe, however, there is one important point one has to be aware of. Under certain conditions, NH_3 is capable of reacting with hydroxy groups to form $-NH_2$ groups (manifested through bands at 1530 , about 3280 and 3330 cm^{-1} , i.e., the zeolite undergoes a so-called amination. This may occur with bridging OH groups in $[=Si(OH)-Al=]$ configurations even more easily, i.e., at lower temperatures, than with silanol groups, Si-OH. This was shown in the IR spectroscopic work by Schweckendiek [223] as well as by Fink and Datka [142]. Nevertheless, combined application of both probes (pyridine and ammonia) may enable us to discriminate between different types of acid sites. Thus, Datka and coworkers succeeded in distinguishing quantitatively between Brønsted acid sites located in the main channels of hydrogen mordenite (accessible for pyridine as well as for ammonia) and those in the side pockets (accessible for ammonia only). In fact, using the respective extinction coefficients, these authors could show that the amounts of both types of Brønsted acid sites are almost equal (cf. [134] and [471]).

Similarly, Karge et al. [398] employed pyridine and 2,6-di-*tert*-butylpyridine to differentiate between internal and external acid sites of zeolite crystallites. In this respect, another possibility is the use of lutidine [139] or quinoline. The latter probe was employed by Corma et al. [693] for the determination of external Brønsted and Lewis acid sites of H, Na-Y and Al, Na-Y zeolites (cf. also [694, 695]). For a characterization of the external Brønsted and Lewis acidity of ZSM-5 samples, Keskinen et al. [696] utilized as sufficiently bulky bases trimethylsilyldiethylamine and, like Karge et al. [398], 2,6-di-*tert*-butylpyridine. For the discrimination of external from internal acid sites of shape-selective H-ZSM-5 catalysts, Take et al. [135] utilized pyridine and a bulky trialkylamine (e.g., Et_3N , $n\text{-Pr}_3N$ and $n\text{-Bu}_3N$) as a pair of probes, with the former indicating the total amount of acid sites. For quantitative evaluation they determined the extinction

coefficients of $\text{Py} \rightarrow \text{B} (\text{PyH}^+)$ and $\text{Py} \rightarrow \text{L}$. The stronger trialkylamines were able to replace pyridine from (the external) Brønsted acid sites. Thus, the amount of external B-sites was determined from the decrease of the pyridinium ion band of pre-adsorbed pyridine upon dosing of, e.g., Et_3N . The amount of internal B-sites was determined from the integrated absorbance of the remaining pyridinium ion band at 1540 cm^{-1} .

Pyridine and especially ammonia are also widely used as probes in experiments designed to determine the strength of acid sites. This type of characterization is achieved by continuous or stepwise temperature-programmed desorption of the probe molecules which may be monitored not only by gas chromatography or mass spectrometry but through IR spectroscopy as well. In the latter case, the decrease in the intensity of the typical bands of the probe is measured [223, 224, 648, 697–699]. For instance, Zhang et al. [700] used this technique when studying the acidity of ultra-stabilized Y-type zeolite (US-Y), mordenite and ZSM-5 in that they monitored a stepwise temperature-programmed desorption of ammonia with FTIR transmission spectroscopy. This enabled them to discriminate between Brønsted and Lewis acid sites and to assign the IR bands to the corresponding TPD peaks, which characterized the strength of the respective centers. Similarly, Li et al. [701] carried out TPD of ammonia and pyridine from H-Y coupled with simultaneous FTIR spectroscopy, which enabled them to identify the sites from which the base molecules desorbed. The site strengths were characterized by the activation energies of desorption.

Selli and Forni [702] performed a detailed comparison of the determination of surface acidity by FTIR of pre-adsorbed pyridine on the one hand and temperature-programmed desorption of pyridine on the other, where the adsorbents were of Y-, Beta- or MOR-type. An important result of this study appears to be that the pyridine distribution between Brønsted and Lewis acid sites under equilibrium conditions (in FTIR) is not much different from that determined under kinetic control (in TPD).

Robb et al. [703] used transmission FTIR combined with stepwise TPD of NH_3 to study dealuminated zeolite Beta. Again, this method enabled the authors to qualitatively correlate the TPD peaks to the sites from which the probe molecules desorbed.

Acid properties of mazzite were revealed by FTIR transmission spectroscopy combined with TPD, using ammonia, pyridine and benzene (vide infra) as probes. Through this work by Guisnet et al. [138] it turned out that a broad OH band at 3600 cm^{-1} observed in the OH stretching region was composed of several submaxima with various positions and indicating different acid strengths. Quantitative results were obtained using extinction coefficients determined in an earlier study ($\epsilon_{\text{PyH}^+}^+ = 1.13 \text{ cm} \mu\text{mol}^{-1}$ and $\epsilon_{\text{PyL}} = 1.28 \text{ cm} \mu\text{mol}^{-1}$). Dealumination of mazzite to $n_{\text{Si}}/n_{\text{Al}} = 30$ increased the acid strength of the remaining OH groups (cf. [704]). Furthermore, Liepold et al. [315] reported in their work on characterization of the aluminum-containing microporous titanosilicate ETS-10 not only the FTIR spectrum of as-synthesized ETS-10; rather they obtained after pre-loading with NH_3 difference spectra in the range $1800\text{--}1600 \text{ cm}^{-1}$ as a function of desorption temperature. A band found after ammonia adsorption around 1680 cm^{-1} was suggested to be indicative of weak hydroxyl groups. Similarly, the

acid properties of NCL-1 zeolite, i.e., the presence of acid Brønsted as well as acid Lewis sites and their strengths, were determined by Sasidharan et al. [705] by FTIR and TPD of pyridine and ammonia. The zeolite NCL-1 was described as a high-silica, large-pore molecular sieve [706]. Finally, Taouli et al. [137] employed TPD of ammonia coupled with simultaneous FTIR spectroscopy to investigate the density and strength of B- and L-acidity in [Al]MCM-41 similar to the procedure used by Schweckendiek [223] or Karge and Schweckendiek [224] for zeolites. Since Taouli et al. have separately measured the integrated absorbance of the bands originating from NH_3 on B- and L-sites of [Al]MCM-41, they were able to quantify in short intervals the amounts of NH_3 desorbing from B- and L-sites of [Al]MCM-41 at increasing temperatures.

A more detailed description of zeolite characterization by temperature-programmed desorption of probe molecules will be presented in a special chapter of Volume 6 of the present series.

Probes such as pyridine and ammonia are rather strong bases. Accordingly, they may indicate even very weak acid sites. Since acidity studies are often related to the utilization of zeolites as catalysts, indication of such very weak, catalytically irrelevant sites may be misleading. Moreover, adsorption of very strong bases may affect and change the properties of the adsorbent. For instance, under the influence of strong bases protons may become mobile (cf. also Sect. 5.5.2.6.5). An example is the effect of piperidine which can interact with protons of OH groups usually not accessible by such a large molecule [379]. Also, the diffusivities of pyridine and similarly bulky probes in zeolites are often very low, so that rather long times and/or elevated temperatures are required for equilibration (cf. Sect. 5.6.4). In certain cases the acid (or base) sites or a particular fraction of them may be absolutely inaccessible for the probe molecules. This was, for instance, studied by Pieterse et al. [699] with the sorption of methyl-substituted pyridine derivatives (e.g., 2,6-lutidine, cf. [139]) and dibranched alkanes into zeolites FER and TON.

To avoid difficulties arising from too high a strength of basicity, catalytically relevant and weakly basic probes were proposed, for instance *light paraffins* [417, 546, 551, 699, 707–713, 718], *hydrogen* [417, 547–549, 551, 713–718], *benzene* [546, 711, 719–725], *toluene* [711], *o-xylene*, *p-xylene* [546, 711, 726], N_2O , CH_3I [727], deuterated [527, 657, 726, 728–730] and non-deuterated *acetonitrile* [222, 417, 657, 694, 731–735], *acetone* [733, 736, 737], *acetylacetone* [738, 739], *acetonitrile* vs. *p-cymene* and *adamantanecarbonitrile* [527, 694], *2,2-dimethylpropionitrile* [695], *halogenated hydrocarbons* [546, 711], *carbon monoxide* [735, 740–746] or phosphines [747].

5.5.2.6.3

Hydrogen (Deuterium), Light Paraffins and Nitrogen as Probes for Acid Sites

Kazansky and colleagues monitored the interaction of *dihydrogen*, H_2 , or *deuterium*, D_2 , and *light paraffins* with various zeolites (H-Y, H-MOR, H-ZSM-5) with the help of diffuse reflectance IR spectroscopy. An example is shown in Fig. 47 for the adsorption of H_2 on H-ZSM-5 at 77 K (cf. also Sect. 5.4.2.2, e.g., [562]).

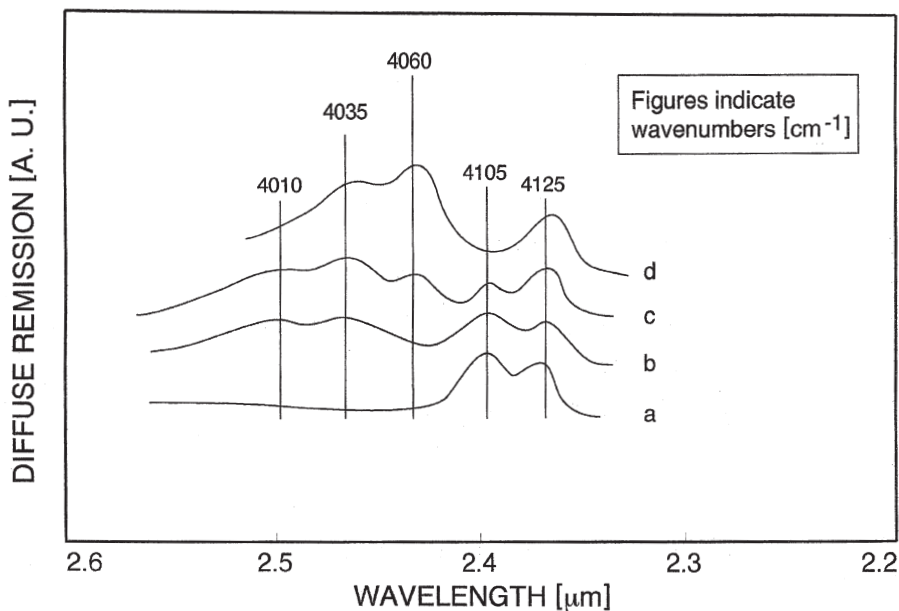


Fig. 47. Diffuse reflectance infrared spectra (DRIFT) of hydrogen adsorbed on H-ZSM-5 at 77 K; a, b, c after heat-pretreatment in high vacuum at 770, 970 and 1220 K, respectively; spectrum d after “deep-bed” treatment at 770 K; abscissa linear in wavelength; important bands indicated by wavenumbers in cm^{-1} (adopted from [713])

The bands were attributed as follows: In the case of the H-ZSM-5 sample activated at the usually employed temperature of 770 K two prominent peaks appeared after adsorption of H_2 , one around 4125, the other at 4105 cm^{-1} . Since a band at ca. 4125 cm^{-1} was also observed after adsorption of hydrogen on silica, the assignment to interaction of silanol groups of H-ZSM-5 with H_2 was obvious. The second band at 4105 cm^{-1} is then easily ascribed to a disturbance of the hydrogen molecule by acid OH groups, which, in the case of unloaded H-ZSM-5, gave rise to the fundamental OH stretching band at 3605 cm^{-1} (vide supra, Sect. 5.4.1.2.8). At higher pretreatment temperatures, dehydroxylation and formation of Lewis acid sites occurred [see Fig. 47, spectra b (970 K) and c (1220 K)]. H_2 perturbed via interaction with the thus-generated acid Lewis centers produced the bands at 4010, 4035 and 4060 cm^{-1} . The first two bands, produced by dehydroxylation at the lower temperature, were tentatively attributed to the interaction of H_2 with threefold coordinated aluminum, [$\equiv\text{Al}$], still connected with the framework. The 4060 cm^{-1} band, appearing only at more severe heat-treatment or “deep-bed” activation (spectrum d) and on the expense of the low-temperature band at 4010 cm^{-1} , was supposed to be due to “true” Lewis sites acting on H_2 molecules (extra-framework sites, such as $[\text{AlO}^+]$, cf. [674, 675]). Similar experiments to identify the nature of active sites using DRIFT and dihydrogen as a probe, were carried out by Kazansky and coworkers [718] on dehydrogenation catalysts, viz. H-ZSM-5 modified by ZnO or Ga_2O_3 . In another study, temperature-

programmed desorption of H₂ or D₂ from hydrogen forms of zeolites was monitored by diffuse reflectance IR and used to characterize the strength of the adsorption sites [748].

Similar studies with and without H₂ as a probe were conducted by Staudte and colleagues [749–752], Coluccia et al. [753] and Jentys et al. [754]. In fact, the latter authors [753, 754] investigated also mesoporous materials, using transmission spectroscopies as well, and applied N₂, CO and pyridine as probes. Beck et al. [755] investigated by the DRIFT technique the infrared spectra of hydrogen induced by the crystal fields of deep-bed treated sodium-containing zeolites (Na-ZSM-5, Na-MOR, Na-X, Na-A). They discussed the effect of H₂ coverage on the band shape as well as on the position of the bands due to fundamental and overtone modes. In the case of Na-Y it was observed that hydrogen molecules adsorbed on Na⁺ cations in SII positions gave rise to a pair of H₂ bands at 4123.3 and 4117.5 cm⁻¹ originating from *ortho-para* H₂ splitting. With the diffuse reflectance technique also overtone spectra were obtained, and a comparison with results of the IR transmission technique proved the higher sensitivity of DRIFT.

Wakabayashi and his group have shown that *dinitrogen*, N₂, is a suitable probe for acid sites in zeolites [756–759]. They studied N₂ molecules adsorbed on H-mordenite, H-Y or H-ZSM-5 by in situ FTIR spectroscopy at low temperatures (110–160 K) and observed two fundamental N-N stretching modes with bands at 2335 and 2352 cm⁻¹, which could be assigned to Brønsted and Lewis acid centers, respectively. The peak area of the band at 2335 cm⁻¹ was negatively correlated to that of the OH stretching band of H-mordenite at 3616 cm⁻¹ and positively correlated to a band at 3510 cm⁻¹ being due to hydrogen-bonded OH groups. An attempt was made and critically discussed to decide between two possible adsorption arrangements, viz. side-on and end-on adsorption of the N≡N molecule on the OH group, by the isotopic scrambling technique [760].

5.5.2.6.4

Nitriles as Probes for Acid Sites

Acetonitrile was employed by Angell and Howell [761], Geodokyan et al. [762] and Karge [222], and *deuterated acetonitrile* in combination with *adamantanecarbonitrile* by Areán et al. [694] to characterize zeolitic acidity. For the investigation of the acidity of a great variety of molecular sieves such as AlPO₄-5, MeAPO-5, (Me²⁺=Be²⁺, Mg²⁺, Ti²⁺, Fe²⁺, Co²⁺), SAPO-5, VPI-5 and Zr-containing pentasil structures, deuterated acetonitrile was employed in DRIFT experiments carried out by Bosacek and Kubelková [737]. In SAPO-5, two types of bridging hydroxy groups were accessible for the nitrile and interacted with, e.g., ethylene. Lewis sites, which were found in the metallophosphates and Zr-containing pentasils, did not interact with weak bases such as CO or H₂, but formed strong complexes with acetonitrile. In an investigation of the acid properties of metal-substituted aluminophosphates, MeAPOs, (Me²⁺=Mg²⁺, Mn²⁺, Co²⁺, Zn²⁺), Jaenchen et al. [763] showed via microcalorimetry and FTIR spectroscopy after adsorption of (deuterated) acetonitrile that the materials exhibited strong Lewis acidity indicated through IR bands around 2300 cm⁻¹. Related to the above-men-

tioned investigation of the acidity of $\text{AlPO}_4\text{-31}$ and MeAPO-31 by Tusar et al. [690], Ristic et al. [764] reported on the synthesis and characterization of triclinic and rhombohedral $\text{AlPO}_4\text{-34}$ and $\text{MeAPO}_4\text{-34}$ via FTIR (Me=Zn, Fe), where strong B-sites (band at 2174 cm^{-1} after CO adsorption) due to incorporation of Zn^{2+} and Fe^{2+} were detected. Also, with MeAlPO_4 a new band at 956 cm^{-1} was observed (cf. Sect. 5.2.6).

The interaction of deuterated and chlorinated acetonitrile, CD_3CN and CCl_3CN , respectively, with Brønsted acid sites of H-ZSM-5 and H,D-ZSM-5 and the thus-induced changes in the IR spectra were interpreted by Pelmenschikov et al. [657] in the frame of the resonance theory of the A-B-C triplet, developed for molecular H-complexes. The approach was similar to that of water adsorption (vide supra). Kotrla and Kubelková [729] discussed in great detail the spectral features observed on the adsorption of deuterated acetonitrile, designated as AN, (or acetone, vide infra) on a series of Brønsted acid zeolites (H, Na-X, H, Na-Y, H-Y, H-MOR, H-ZSM-5) and correlated especially the shift, $\Delta\tilde{\nu}$ (OH), of the (high-frequency) OH stretching bands to the acid strength (Sanderson's charge on the H atom). The shifted OH bands appeared as broad signals between 3025 ($\text{AN}\cdots\text{H-X}$) and 2540 cm^{-1} ($\text{AN}\cdots\text{H-ZSM-5}$) for the neutral complexes. Also, the in-plane, $\delta(\text{OH})$ and out-of-plane, $\gamma(\text{OH})$, bending vibrations were measured and compared with the results of Fermi resonance calculations. Interaction of d_3 -acetonitrile with NH_4^- , H, Na-, H-, and Co-Beta led to the detection of Brønsted and Lewis sites through the appearance of bands at 2297 and 2325 cm^{-1} , respectively. Na^+ and Co^{2+} were identified by bands at 2284 and 2308 cm^{-1} , respectively.

In particular, the combined application of acetonitrile and the bulkier adamantanecarbonitrile (diameter greater than 0.6 nm) in FTIR experiments proved to be suitable for discriminating internal from external acid sites of medium pore zeolite crystallites such as ZSM-5, chabazite, erionite and ferrierite. For the same purpose, Trombetta et al. [695] employed 2,2-dimethylpropionitrile (pivalonitrile, PN) instead of adamantanecarbonitrile. They studied B- and L-sites on the (external) surface of ferrierite and the total surface of [Si]MCM-41 and [Al]MCM-41. Upon adsorption of PN, the $\text{C}\equiv\text{N}$ band was shifted from 2236 to about 2250 cm^{-1} . The weak B-sites of [Al]MCM-41 interacted with pivalonitrile and were also associated with an OH band at 3745 cm^{-1} .

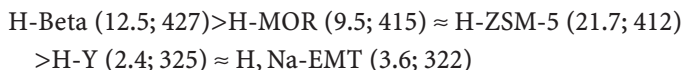
5.5.2.6.5

Halogenated Hydrocarbons and Phosphines as Probes for Acid Sites

Sachsenroeder et al. [765], Brunner et al. [766] and Sachsenroeder [767] could show that adsorption of *tetrachloroethylene* on free acid hydroxy groups of H-ZSM-5 and H, Na-Y zeolites caused a wavenumber shift, $\Delta\tilde{\nu}_{\text{OH}}$, which was linearly correlated with the analogously adsorption-induced shift of the $^1\text{H-MAS}$ NMR signal, $\Delta\delta$, so that the latter could be used for the calculation of deprotonation energies (cf. [767], where also reference is made to other probe molecules such as C_2F_4 and C_2Cl_6 , and their potential is shown to discriminate between external and internal OH groups of medium pore-sized zeolites).

Chloromethane was employed by Su and Jaumain [768] as an FTIR probe for Brønsted acidity and their relative strength in a number of hydrogen forms of

zeolites measured through the shifts of the IR stretching bands representing the accessible bridging OH groups [$\equiv\text{Si}-(\text{OH})-\text{Al}\equiv$]. The measurements resulted in the following sequence of Brønsted acid strengths, where the first figure in the parentheses gives the $n_{\text{Si}}/n_{\text{Al}}$ ratio and the second one the wavenumber shift, $\Delta\tilde{\nu}_{\text{OH}}$, in cm^{-1} :



in agreement with the results of catalytic tests.

Trimethylphosphine (TMP) and dimethylphosphine (DMP) were protonated by acid surface sites to give the corresponding phosphonium ions, which were observed, for instance, by Bein et al. [747], when they contacted the phosphine vapors with the acid H-Y zeolite. DMP is the weaker base and exhibited some advantages:

- (i) The adsorption is reversible at moderate temperatures (about 700 K).
- (ii) Independent determination of DMP and DMPH^+ is possible, since the adsorbed DMP is indicated by a strong P-H band at 2289 cm^{-1} , but the chemisorbed DMPH^+ gives rise to two new bands at 2495 and 2450 cm^{-1} , assigned to the antisymmetric and symmetric P-H stretching vibrations of the phosphonium ion.
- (iii) Only OH groups located in the supercages were involved; disappearance of the HF band at 3644 cm^{-1} indicated complete proton transfer in the supercages, whereas with TMP the situation is more complicated, i.e., the HF band could not be completely eliminated but, on the other hand, a fraction of the OH groups of the small cavities also reacted under the influence of the stronger base.

5.5.2.6.6

Carbon Monoxide as a Probe for Acid Sites

Carbon monoxide, CO, is another weakly basic probe molecule mentioned above as being appropriate for indicating acid centers in zeolites and characterizing their strength. In fact, it was frequently employed to probe *Brønsted acidity*, for instance by Wakabayashi et al. [756], Zecchina et al. [746], Kustov et al. [742] and Kubelková et al. [743]. The potential and applicability of this probe in a great variety of examples was reviewed by Mestl and Knoezinger [769]. Usually, carbon monoxide is adsorbed at low temperatures (e.g., 77 K) and low pressures. When interacting with acid hydroxy groups, the charge donation from an orbital on the carbon atom into an antibonding orbital of the O-H bond weakens the latter and causes a shift, $\Delta\tilde{\nu}(\text{OH})$, to lower wavenumbers. Fig. 48 demonstrates that with increasing doses of CO (spectra 2–6) the intensity of the high-frequency OH band of the adsorbent (H, Na-Y) decreases, and the absorbance of the shifted OH band around 3400 cm^{-1} is enhanced.

Quantitative FTIR measurements of Brønsted and Lewis acidity of hydrogen mordenites and Beta zeolites were carried out by Maache et al. [140, 306], who used both pyridine and CO as probes. To obtain quantitative data they first

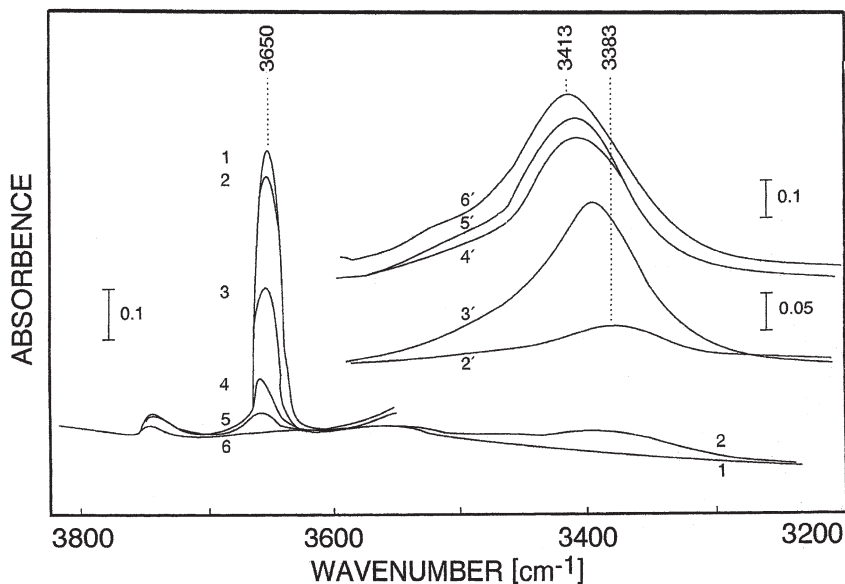
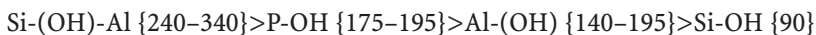


Fig. 48. IR spectra of OH groups of H, Na-Y before (1) and after (2–6) adsorption of increasing amounts of CO (adopted from [743])

determined with mordenite the extinction coefficients $\epsilon_B=1.8 \text{ cm } \mu\text{mol}^{-1}$, $\epsilon_L=1.5 \text{ cm } \mu\text{mol}^{-1}$ and $\epsilon_{CO}=2.7 \text{ cm } \mu\text{mol}^{-1}$, for pyridine after reaction with Brønsted sites, after interaction with Lewis sites and for CO after interaction with acid OH groups, respectively. The experiments revealed a heterogeneity of the B-sites in nature (two types were found with bands at 3612 cm^{-1} (due to OH groups in the main channels) and 3585 cm^{-1} (originating from OH groups in the side pockets) in agreement with results by Karge and Dondur [770] (cf. also the report by Datka et al. [711], vide infra). CO adsorption showed that the hydroxy groups in the side pockets are less acidic than those in the main channels (vide infra). A band at 3660 cm^{-1} was not interpreted as being due to OH attached to extra-framework species but was claimed to result from H_2O adsorption and subsequent protonation to H_3O^+ . This is at variance with earlier explanations (cf. [380, 426, 551, 771, 772]).

While the amount adsorbed (difference in integrated absorbance at 3650 cm^{-1} of, e.g., H,Na-Y or produced absorbance around 3400 cm^{-1}) may be taken as a measure of the density of the involved acid OH groups, the value of the shift, $\Delta\tilde{\nu}$ (OH), upon CO adsorption provides a measure of their strength. For a series of proton-containing molecular sieves, Kubelková et al. [743] obtained on the basis of the measured band shifts, $\Delta\tilde{\nu}$ (OH), the following ranking with respect to the acid strength (the respective wavenumber shifts, in cm^{-1} , are given in brackets):



FTIR studies of unusual OH groups in steamed H, Na-Y zeolites were carried out by Cairon et al. [773]. Their preparation of dealuminated samples resulted in large amounts of OH groups indicated by a band at 3700 cm^{-1} and exhibiting low acidic strength: on CO adsorption a shift of this band by only ($\Delta\tilde{\nu}(\text{OH}) = 145\text{ cm}^{-1}$) was measured, assumed to correspond to a Hammett value of $H_0 = -5$. This low acidity strength was suggested to prevent cracking and coke formation in reactions, which are catalyzed through acid OH groups but do not require strong acid sites. After leaching, the acid strength was somewhat increased as seen by the lowering of the band position to 3670 cm^{-1} and its shift on CO adsorption by $\Delta\tilde{\nu}(\text{OH}) = 185\text{ cm}^{-1}$ corresponding to $H_0 = -6$.

The shift of OH stretching bands, $\tilde{\nu}(\text{OH})$, upon adsorption of CO was measured for a series of zeolites (MOR, dealuminated MOR, dealuminated MAZ, TON, ZSM-5) in experiments carried out by Garrone et al. [744]. Similarly, Echoufi and Gelin [745] employed CO as a probe for the Brønsted acid strength of OH groups in H-Y samples with systematically varied $n_{\text{Si}}/n_{\text{Al}}$ ratios. These authors observed an increase of the acid strength up to $n_{\text{Si}}/n_{\text{Al}} = 9$, analogous to the increase of the chemical shift found in parallel ^1H -MAS NMR experiments. The heterogeneity of acid sites were related to coverage effects and viewed as a CO-induced rather than an intrinsic phenomenon.

Similarly, IR investigation of CO adsorption on molecular sieves was used to characterize *Lewis acidity of cations (C-sites)* and “*true*” *Lewis acidity (L-sites)* [740]. The interaction of CO with cations (acid C-sites) was dealt with already in Sect. 5.5.2.2. In particular, Angell and Schaffer [595] have carried out a detailed study of CO adsorption on a series of X- and Y-type zeolites containing monovalent and divalent cations of alkali, alkaline earth and transition metals. A linear relationship was found between the position of the IR stretching band of adsorbed CO and the Coulomb field, q/r , of the respective cationic adsorption center. This is similar to the observation made by Ward in the case of pyridine attached to cations (vide supra). It should be noted, however, that CO, like pyridine, is not capable of entering the sodalite cages and the hexagonal prisms of the faujasite structure, so that the cations located there are not detected by these probes.

Evaluation of IR spectra of CO adsorbed on Na,Al-ZSM-5 by Romotowski et al. [741] revealed that through ion exchange of Na-ZSM-5 in buffered aqueous AlCl_3 solution only a small fraction of Na^+ can be replaced by Al^{3+} . Most of the introduced aluminum occurred in the form of an extra-framework Al oxide (hydroxide) phase.

Through FTIR spectroscopy using carbon monoxide as a probe, Shigeishi et al. [704] proved for the first time that two types of OH groups in mazzite (indicated by OH stretching bands at 3626 and 3606 cm^{-1} and located in two types of channels of this zeolite) interacted with strong Lewis sites, which gave, at low coverages, rise to CO adsorption bands at 2229 and 2188 cm^{-1} . Since upon higher CO coverage the above-mentioned OH bands were shifted to 3247 and 3330 cm^{-1} , i.e. by $\Delta\tilde{\nu} = -379$ and $\Delta\tilde{\nu} = -276\text{ cm}^{-1}$, respectively, the authors concluded that the corresponding OH groups were superacid sites. Additionally, it was observed that at higher CO pressures the CO adsorption on a weaker acid Al-OH site (detected by an IR band at 3660 cm^{-1}) produced a wavenumber shift of $\tilde{\nu} = -210\text{ cm}^{-1}$ to

3450 cm^{-1} . The superacidity of bridging $[\equiv\text{Si}(\text{OH})\text{-Al}\equiv]$ groups in the hydrogen form of mazzite was related to a rate of *n*-butane conversion over this catalyst, which was much higher than over H-ZSM-5.

Garrone et al. [774] distinguished the acid strengths of the four different bridging $[\equiv\text{Si}(\text{OH})\text{-Al}\equiv]$ groups in SAPO-40, which were indicated by OH bands at 3637, 3626 (in twelve-membered ring channels) and at 3550, 3528 cm^{-1} (probably in smaller cavities (eight-membered ring channels and side pockets), by the shifts of these bands on CO adsorption).

A combination of DRIFT spectroscopy and TPD of CO adsorbed on faujasite-type zeolites, which have been exchanged with transition metal cations (Cu^{2+} , Fe^{2+} , Co^{2+} , Ni^{2+}), was employed by Rakic et al. [775]. Except on Cu, Na-Y, disproportionation of CO and carbon deposition occurred. The Lewis acid, charge-compensating sites were assumed to be the sites of adsorption.

IR spectroscopy of adsorbed CO probe molecules was employed by Manoilova et al. [776] to characterize silanol groups, acid bridging hydroxy groups (Brønsted acid sites) and coordinatively unsaturated aluminum and titanium atoms (Lewis acid sites) in Ti-containing zeolites (TS-1, Ti-Beta).

Bonelli et al. [777] used the CO adsorption monitored by FTIR also for the characterization of the acidity of [Al]MCM-41 samples, which were exchanged with alkali-metal cations. Lewis sites in the form of cations (C-sites) were detected by a hypsochromic shift of the band at 2143 cm^{-1} of gaseous CO, for instance to 2158 cm^{-1} in the case of a washed Cs-[Al]MCM-41 sample. No absorbance around 2220 cm^{-1} due to CO attached to Lewis sites in the form of Al-containing species was observed.

Acid properties were further detected by Romannikov et al. [778] via IR spectroscopy with and without CO adsorption in the case of zirconium-containing mesoporous materials, e.g., ZBS mesophases with texture characteristics close to those of MCM-41. However, the acidity was ascribed to terminal Zr-OH groups rather than to bridging hydroxy groups. But Lewis acid sites, which were moreover convertible by interaction with H_2O into bridging Brønsted acid hydroxy groups, were detected by, e.g., Viale et al. [779] in [Si,Al]MCM-41. These authors observed, besides silanol peaks, bands at around 3688 $[\equiv\text{Si}\text{-Al}(\text{OH})\text{-Si}\equiv]$, 3610 $[\equiv\text{Si}(\text{OH})\text{-Al}\equiv]$ and, after contact with NH_3 , at 1465 cm^{-1} (ammonium band).

5.5.2.6.7

Nitric Oxide as a Probe for Acid Sites

As was shown by Hadjiivanov [780], the adsorption of $\text{NO}+\text{O}_2$ leads to the formation of NO^+ , which can be used as a probe for the location of OH groups [781]. Thus, co-adsorption of NO and O_2 into mordenite produced two separate bands of NO^+ , a band at 2168 cm^{-1} due to the interaction with OH groups in the main channels and a second one at 2215 cm^{-1} , indicating the acid hydroxy groups in the side pockets. From the ratio of the intensities of these bands (2:1), the authors concluded that the population of the main channels with OH groups is twice as that in the side pockets (see, however, above and cf. [477]). When Na^+ cations were present in the mordenite structure, nitrate was formed and indicated by intense nitrate bands. The situation was more complicated when not only B-

and/or L-sites but cations (C-sites) were simultaneously present. For instance, Hadjiivanov and Dimitrov [782] carried out an IR study of both CO and NO_x adsorption on a Cu-[Zr]-HMS catalyst, using a hexagonal mesoporous silicate designated as [Zr]-HMS, which was prepared according to a recipe given in [783]. With Cu-[Zr]-HMS, CO was selectively adsorbed on Cu⁺ cations ($\tilde{\nu}(\text{CO}) = 2132 \text{ cm}^{-1}$), whereas NO adsorbed on Cu²⁺ ($\tilde{\nu}(\text{NO}) = 1888 \text{ cm}^{-1}$). Simultaneous adsorption of NO and CO on Cu-[Zr]-HMS resulted in the formation of N₂O₄ (exhibiting a band at 1740–1730 cm⁻¹) and N₂O₃ (indicated by bands at 1904 and 1540 cm⁻¹) as well as strongly bound nitrates (with a band at 1620–1540 cm⁻¹).

A similar IR study of CO and NO_x adsorption was carried out by Hadjiivanov [784] using Ag-ZSM-5 as an adsorbent. Stable Ag⁺-CO complexes characterized by a CO stretching mode at 2191–2189 cm⁻¹ were detected, which were under a CO gas phase at low temperatures converted into dicarbonyls with $\tilde{\nu}_s(\text{CO}) = 2189$ and $\tilde{\nu}_{as}(\text{CO}) = 2195 \text{ cm}^{-1}$.

Results of an FTIR investigation of NO adsorption on Co-ZSM-5 as a function of the Co-content was reported by Zhu et al. [785]. They observed dominant dinitrosyl bands at 1813 and 1896 cm⁻¹, whereas a band of the mononitrosyl form occurred at 1939–1941 cm⁻¹. Similarly, Ito et al. [786] carried out an infrared spectroscopic study of NO adsorption and NO/O₂ co-adsorption on cerium- and lanthanum-exchanged mordenites, Ce,Na-MOR and La,Na-MOR. NO adsorption led to the formation of NO₂ (indicated by a band at 2247 cm⁻¹), NO⁺ (nitrosonium ions producing a band at 2162 cm⁻¹) and NO_x⁻ (nitrito and/or nitrate species, bands in the range 1300–1500 cm⁻¹), whereas in the co-adsorption experiments bands of NO⁺ (2162 cm⁻¹) and NO₃⁻ (1515, 1488–1497 and 1333 cm⁻¹) were observed.

The reactivity of NO on Co²⁺/Co³⁺ redox sites in CoAPO-18 was studied by FTIR and UV-Vis spectroscopy in a contribution of Gianotti et al. to the 12th International Zeolite Conference [787]. Dinitrosyls were found absorbing at 1903 and 1834 cm⁻¹ when B-sites were involved, whereas bands at 1900 and 1813 cm⁻¹ appeared when the dinitrosyls were stabilized on structural Co²⁺ defects (C-sites). The adsorption of NO and NO+O₂ on Co-Y was investigated and compared with the adsorption on Co-ZSM-5 in a study by Ivanova et al. [788]. On Co-Y, they observed formation of Co²⁺(NO)₂ species with $\tilde{\nu}_{as} = 1900$ and $\tilde{\nu}_s = 1819 \text{ cm}^{-1}$, the stability of which was similar to that formed on Co-ZSM-5 with the corresponding bands at 1894 and 1819 cm⁻¹; they were, however, not involved in the selective catalytic reduction. While on Co-ZSM-5 monodentate nitrates appeared, indicated by a band at 1540 cm⁻¹, which easily interacted with hydrocarbons and, thus, seemed to be the key species in selective catalytic reduction (SCR), no such monodentates were detected on Co-Y.

NO adsorption was also investigated by FTIR with mesoporous materials as adsorbents, e.g., by Ziołek et al. [789, 790], who used Cu-[Al]MCM-41, Ni-[Al]MCM-41 and (for adsorption of sulfur-containing compounds) Nb- and Ti-modified MCM-41 materials. Adsorption of NO affected especially the IR features around 1600 cm⁻¹.

5.5.2.6.8

Benzene and Phenol as Probes for Acid Sites

In the literature, various other probe molecules were proposed to characterize the acidity of zeolites by IR inspection of their adsorption. Among them were, besides those already mentioned, *benzene*, (cf. Ref. [669]). The wavenumber shift of the band due to Brønsted acid OH groups, which occurs on benzene adsorption, is easily determined and provides, in a manner similar to CO, an approximate measure of the acid strength. An example is illustrated in Fig. 49.

Benzene adsorption into molecular sieves was extensively studied via IR spectroscopy by several workers. Karge et al. [791] used the prominent band at 1478 cm^{-1} to identify benzene adsorbed in zeolites. De Mallmann and Barthomeuf [792, 793] applied FTIR spectroscopy of benzene adsorbed on various faujasite-type zeolites (Na-X, Rb-X, Cs, Na-X Na-Y, Rb-Y, dealuminated Y) to determine the sites of adsorption and showed that the site preference depended on the balance between cation acidity and oxygen basicity. For a quantitative evaluation of the

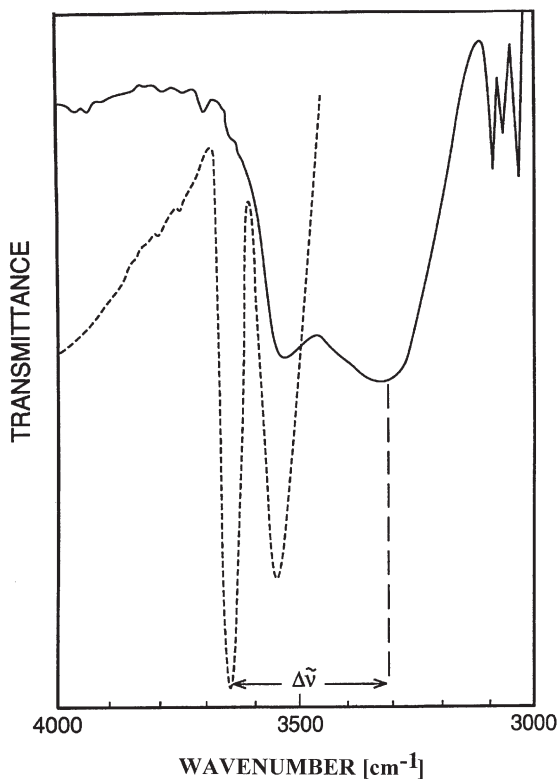


Fig. 49. Wavenumber shift, $\Delta\tilde{\nu}$, of the high-frequency OH band (at 3640 cm^{-1}) of H-Y on benzene adsorption; dotted-line spectrum: before, solid-line spectrum after adsorption of benzene (adopted from [724, 725])

IR results they determined the integrated absorbance of adsorbed benzene (cf. Sect. 3.2). Similarly, Su et al. [719] studied the location of benzene molecules and cations in Cs-exchanged EMT zeolite (Cs, Na-EMT). The Cs cations resided in the large cavities, and benzene interacted with both the cations and the 12-membered rings (12MR), in contrast to Na-EMT, where the benzene adsorption on 12MR windows was not favored. In the case of K-L zeolite, Su and Barthomeuf [721] derived from their IR spectroscopic results that, at low loadings ($p/p_0 = 10^{-4}$, where p is the actual partial pressure, p_0 the saturation pressure) about two benzene molecules interacted with cations, whereas at higher loadings simply pore filling occurred. The results were compared with those obtained on K-Y, Na-Y, Na-EMT, and Na-Beta.

In related studies, Norberg et al. [722] investigated the location and motion of benzene molecules in Na-EMT and K-L by in-situ FTIR spectroscopy and concluded that almost all benzene molecules were facially coordinated to cations residing in the large cages of the adsorbents.

In the case of H-ZSM-5 as an adsorbent for benzene, Jentys and Lercher [723] showed by IR spectroscopy that benzene interacted with H-ZSM-5 via four types of hydrogen bonding: one molecule on (i) [$\equiv\text{Si}(\text{OH})\text{-Al}\equiv$], (ii) Si-OH of hydroxy group nests, i.e., defect sites, (iii) free Si-OH and (iv) two molecules on [$\equiv\text{Si}(\text{OH})\text{-Al}\equiv$], where the strength of interaction decreased in the sequence (i) to (iv). For the activated, unloaded H-ZSM-5 samples, the three types of zeolitic OH groups producing the above hydrogen bondings (i), (ii), and (iii) were characterized by IR bands at 3610, 3726 and 3745 cm^{-1} , respectively. Upon benzene adsorption, the decrease of the 3610 cm^{-1} band was monitored and the appearance of a broad band at 3350–3250 cm^{-1} observed. A quantitative evaluation of the band at 1477 cm^{-1} typical of adsorbed benzene proved that, at low pressures (10^{-3} mbar), the stoichiometry was strictly one to one for all sites and samples. The thermal stability of the above hydrogen-bonded adsorption states was lower than that of adsorption complexes of benzene on Na^+ in Na-containing ZSM-5.

Jacobs et al. [724] introduced the FTIR measurement of the shift of the OH stretching band upon benzene adsorption as a measure of the acid strength of the hydroxy groups. Jacobs [725] also provided a theoretical reasoning for this effect. Similarly, O'Malley [794] developed an electrostatic model for predicting the shift of typical IR bands upon adsorption of aromatics on the respective zeolitic OH groups.

A heterogeneity of the acid strength of bridging OH groups in hydrogen forms of mordenite was claimed by Datka et al. [795] based on IR results of adsorption of both benzene and carbon monoxide (vide supra). These authors observed that the band of acid OH groups in H-MOR at 3610 cm^{-1} (cf. [466, 471]) was split upon adsorption of these probes. The submaxima of higher wavenumber shifts, viz. $\Delta\tilde{\nu}_{\text{OH}} = -360$ (benzene) and $\Delta\tilde{\nu}_{\text{OH}} = -300$ cm^{-1} (CO), were assigned to more acidic, those of lower shifts, viz. $\Delta\tilde{\nu}_{\text{OH}} = -240$ (benzene) and -206 cm^{-1} (CO) to less acidic Brønsted OH groups. The wavenumber shifts, $\Delta\tilde{\nu}_{\text{OH}}$, on adsorption of almost all of the probe molecules on various zeolites, employed to characterize the Brønsted acidity, were discussed and summarized in the contributions of Buzzoni et al. [796] and Garrone et al. [797].

In view of alkylation of benzene by *propene*, Flego et al. [798] investigated by UV-Vis and IR spectroscopy the adsorption and co-adsorption of these two hydrocarbons on H-Beta, which proved to be an efficient alkylation catalyst. It was claimed by the authors that isopropyl cations, which formed on the Brønsted acid sites were the key intermediates of the reaction (cf. also Janin et al. [671] and Macedo et al. [672]).

Datka et al. [711] applied besides benzene many of the above-listed probes (including toluene, *p*-xylene, fluoro- and chlorobenzene, and *n*-hexane) and concluded from the splitting of the shifted OH bands, resulting in four submaxima in the case of, e.g., *n*-hexane/H, Na-ZSM-5, that the acid OH groups are markedly heterogeneous, exhibiting different acid strengths.

Phenol adsorption on H-Y via the phenolic OH group at the acid hydroxy groups, (i.e., interaction of the acidic OH groups of H-Y with phenolic oxygen) and the orientation of the phenol ring perpendicular to the zeolite surface was derived by Li et al. [799] from their FTIR spectroscopic results.

5.5.2.6.9

Acetone and Acetylacetone as Probes for Acid Sites

Similar to the results of CO and benzene adsorption, Bosacek and Kubelková [737] found that the strength of interaction between *acetone* and framework OH groups increased with the acid strength of the protonic sites (cf. also [729]).

Adsorption of *acetylacetone* on H-ZSM-5 was IR spectroscopically investigated by Alexander et al. [738] in combination with ^{27}Al -MAS NMR and ^{13}C -MAS NMR. They showed that acetylacetone adsorption led to an increase of the signal of octahedrally coordinated Al not through producing $\text{Al}(\text{acac})_3$, but by forming a loosely bound adduct of acetylacetone to extra-framework Al-species. Acetylacetone proved to be more strongly held on Brønsted acid sites than on extra-framework aluminum.

Acetylacetone adsorption and interaction on the surface of layered silicates (montmorillonite) containing various cations (Li^+ , Na^+ , Ca^{2+} , Cu^{2+} , Co^{2+} , Ni^{2+} , Al^{3+} , and Fe^{3+}) were studied via IR spectroscopy in a contribution by Sohn and Lee [739]. These authors found that both the OH groups of the surface of the layers and of the cations interacted with the carbonyl group of the adsorbate and proposed a model for the orientation of the acetylacetonate complex between two layers of the montmorillonite.

5.5.2.6.10

Probes for Basic Sites

The number of probe molecules suitable for studying the basicity of zeolites by application of IR spectroscopy is much more limited than in the case of acidity. The sites of basicity are most likely oxygen atoms of the framework or basic extra-framework species such as Cs_2O or alkali metal clusters (cf. Volume 3, Chapters 5 and 6 of the present series).

Frequently proposed probes are *pyrrole* [371, 800–809], *carbon dioxide* [807, 810], *acetic acid* [811], *boric acid trimethyl ester* [812], other weak acids such as

acetylene or *acetylene derivatives* [807], and *halogenated light paraffins* [768]. Janin et al. [671] and Macedo et al. [672] listed a series of acid probes of different strengths and studied especially the suitability of *hydrogen sulfide*.

As an example of pyrrole application, Fig. 50 characterizes the basicity of X- and Y-type zeolites and the effect of the charge-compensating cations on the basicity of the adsorbent. As a measure of the base strength, the shift of the NH stretching band of the probe is used (cf. [803]).

Heidler et al. [806] investigated and discussed by a combination of the energy equalization method and results of the Monte Carlo technique the observed heterogeneity in the spectra of pyrrole adsorbed on basic faujasite-type zeolites (cf. also [804, 805]), arriving at the result that there is only *one* adsorption site for pyrrole but an effect of the n_{Si}/n_{Al} ratio on the orientation of the pyrrole molecule with respect to the six-membered rings.

Also, INS may be employed to study the effect of pyrrole adsorption on basic zeolites (cf. Sect. 5.5.1, Fig. 30). During adsorption of pyrrole, the peak of the NH wagging mode is shifted from 594 cm^{-1} to 613 cm^{-1} (pyrrole in Na-Y) and 620 cm^{-1} (pyrrole in Rb-Y). This clearly indicates the increasing strength of the hydrogen bond in comparison with solid pyrrole. The observed sequence of the shift, viz. Rb-Y > Na-Y is well correlated with the basic strength of the oxygen atoms of the zeolite lattice. Simultaneously, a blue-shift of the CH wagging modes with adsorption is perceptible from Fig. 30, increasing from Na-Y to Rb-Y. This effect should be interpreted as an additional interaction between the aromatic system of pyrrole with the cations [371]. Such information is difficult to obtain by optical spectroscopy.

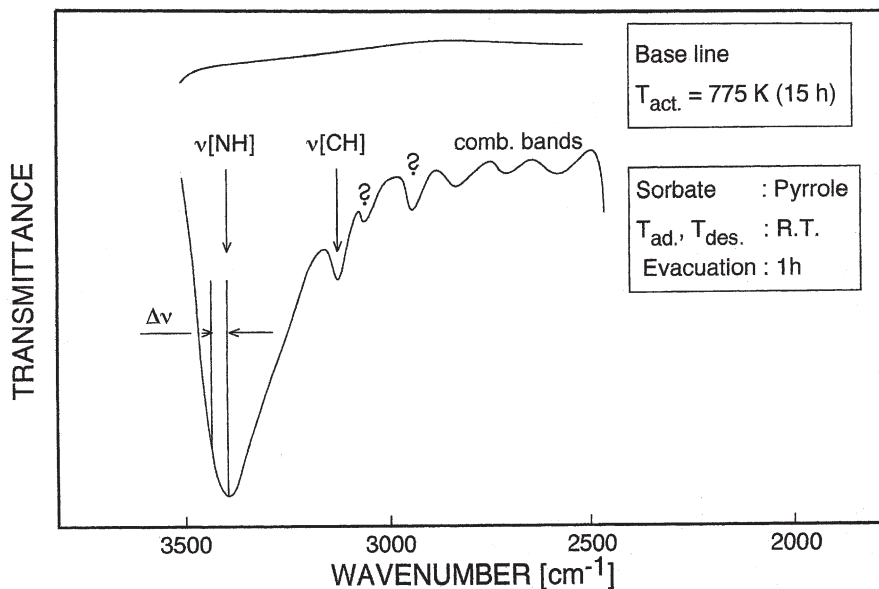


Fig. 50. Adsorption of pyrrole on zeolite K-LTL and the shift of the wavenumber of the NH-stretching band, $\Delta\tilde{\nu}$ (NH), as a measure of basicity (adopted from [802])

The existence of weak basic sites on mainly acid SAPO-5, MAPO-5 and MAPO-36 was claimed by Akolekar et al. [808] on the basis of their IR investigation of pyrrole adsorption on these materials. AlPO_4 -11 and MAPO-11 ($M=\text{Mg}$) were investigated via IR in a contribution by Fernandez et al. [809]. Bending vibrations, $\delta(\text{N-H})$, corresponding to wavenumbers 1589–1585 cm^{-1} and a band at 1608 cm^{-1} were observed, the latter originating from Brønsted OH groups, which were introduced through the Mg^{2+} cations incorporated into the framework and interacting with the template diisopropylamine.

The use of *carbon dioxide* as a probe is somewhat problematic because of possible chemisorption leading to various types of surface carbonates [608, 641, 803,]. Application of *acetylene* and similar compounds appeared to be more promising [807]. There are, however, only a very few pertinent reports so far, unfortunately not being in favor of these probes [807]. In a certain sense, also *dihydrogen* adsorption provides information about zeolite basicity, since it turned out that in H_2 interaction with cation-containing zeolites not only the Lewis acid cations but also the adjacent basic oxygen anions of the framework are involved, affecting the strength of the adsorption and, thus, the DRIFT spectra [717].

Base properties of faujasite-type zeolites (Na-X, Na-Y, H, Na-X, H, Na-Y) were also characterized in a study by Przystajko et al. [811]. These authors employed IR spectroscopy using both the KBr technique for studying the framework vibrations (cf. Sect. 5.2) and the adsorption of *acetic acid* for determining the concentration and strength of basic sites (hydroxy groups and oxygens of the framework), complemented by titration with benzoic acid in aprotic suspension and utilization of indicators. Surprisingly, the authors reported that both the hydrogen-sodium and the sodium form of X- and Y-type zeolites exhibited considerable basicity. The basicity strength was claimed to be higher in the case of the H, Na forms than with pure Na forms, because in the former case contributions to the basicity were suggested to originate from the (amphiprotic) hydroxy groups and the oxygens of $\text{Al}(\text{OH})_4^-$ tetrahedra of the framework, whereas in pure sodium forms only the latter species contributed. Basic sites in Y-type zeolites were characterized by Liu et al. [812] through the adsorption of *boric acid trimethyl ester (BATE)*, giving rise to typical bands at 1373 and 1320 cm^{-1} .

As Rymsa et al. [813] have shown, the utilization of *deuteriochloroform* as a probe is another possibility of characterizing the basicity of zeolitic systems by FTIR spectroscopy. The C-D stretching band of CDCl_3 was shifted to lower wavenumbers when the probe was adsorbed on basic materials such as M, Na-X, M, Na-Y ($M=\text{K, Rb, Cs}$), Cs-Beta, and the shift increased with increasing size of the cation exchanged into the zeolite.

5.5.2.7

Adsorption of Methanol, Benzene, Simple Benzene Derivatives, Light Alkanes, Boranes and Silanes

As was mentioned in the preceding section, methanol, benzene, simple benzene derivatives and alkanes were employed, to some extent, like other small-molecule compounds as probes for acidity and basicity of the adsorbents. However, IR

investigation of the adsorption of these compounds is interesting and selected here for a somewhat extended discussion, because these adsorbates are closely related to model reactions on and diffusion in zeolites (cf. Sects. 5.6.3 and 5.6.4)

Methanol plays an important role as an alkylating agent, for instance, in the methylation of toluene to form xylenes. Furthermore, the nature and behavior of the adsorption complex can be treated quantum mechanically, similar to the adsorption complex of water with Brønsted acid OH groups of the hydrogen form of zeolites (vide supra and Refs. [655, 656]). Adsorption of CH_3OH on H-ZSM-5, alkali-metal cation-exchanged ZSM-5, mordenite (MOR), faujasite (FAU) and erionite (ERI) was studied by Tvaruzkova et al. [728] and in great detail by Lercher and coworkers [814–820] using their technique of dosing low adsorbate pressures (cf. adsorption of H_2O , H_2S , NH_3 as described in Refs. [220, 434, 652, 816]) and, more recently, the picosecond infrared activation method [821]. As an example, a set of H-ZSM-5 spectra obtained after activation in high vacuum and under CH_3OH pressures of 0.1 to 100 Pa (0.001 to 1 mbar) is presented in Fig. 51.

After methanol adsorption on activated H-ZSM-5, the difference spectra exhibited a strong signal at 3610 cm^{-1} pointing to “negative” absorbance and thus indicating the interaction of CH_3OH with the acid OH groups of the zeolite. New bands appeared at 2993, 2958 and 2856 cm^{-1} (CH stretching modes) and at 3545, 2900, 2400 and 1687 cm^{-1} (OH stretching and deformation vibrations of protonated methanol molecules, i.e., methoxonium ions). However, on the basis of quantum chemical calculations and via a reasoning similar to that concerning H_2O adsorption on Brønsted acid sites (vide infra and [655, 656]), Haase and Sauer [822] could show that the formation of methoxonium ions, CH_3OH_2^+ , is rather unlikely at low loadings but may be expected for the adsorption of a second CH_3OH molecule on the same site (cf. also [823]). The adsorption of methanol on zeolites containing Lewis acid alkali metal cations was theoretically treated by Vayssilov et al. [819].

In the context of the zeolite-catalyzed reactions of methanol-to-gasoline (MTG process) and methanol-to-olefins (MTO process), the activation of CH_3OH on acid zeolite surfaces was particularly interesting. It was, for instance, studied in detail through the picosecond infrared technique (cf., e.g., [821]).

On adsorption of methanol on alkali metal-containing zeolites (M^+ -ZSM-5, M^+ -MOR, M^+ -FAU, M^+ =alkali metal cation), three types of local adsorption structures were discussed, viz. CH_3OH with (i) freely vibrating OH bonds, (ii) hydrogen bonds to the zeolite framework, and (iii) strong additional intermolecular hydrogen bonding [816, 818, 819]. Adsorbent zeolites such as M^+ -ZSM-5 ($\text{M}^+=\text{Li}^+, \text{Na}^+, \text{K}^+, \text{Cs}^+$), Na^+ -MOR, Na^+ -Y and M^+ -X ($\text{M}^+=\text{Na}^+, \text{K}^+, \text{Rb}^+, \text{Cs}^+$) were employed. Correlations were found between $\tilde{\nu}_{\text{OH}}$, $\tilde{\nu}_{\text{CH}}$, δ_{OH} and δ_{CH} of the adsorbed CH_3OH molecules and the intermediate Sanderson electronegativity, S_{int} , [822]. The wavenumbers of the stretching vibrations, $\tilde{\nu}_{\text{OH}}$, $\tilde{\nu}_{\text{CH}}$, and the Sanderson intermediate electronegativity S_{int} decreased, e.g., in the sequence $\text{Cs-X} > \text{Rb-X} > \text{K-X} > \text{Na-X}$.

In Refs. [814, 815, 817], it was shown by in-situ IR spectroscopy that the adsorption of methanol on small-pore zeolites is unequivocally affected by the nature of the adsorption centers involved. For instance, in single-component

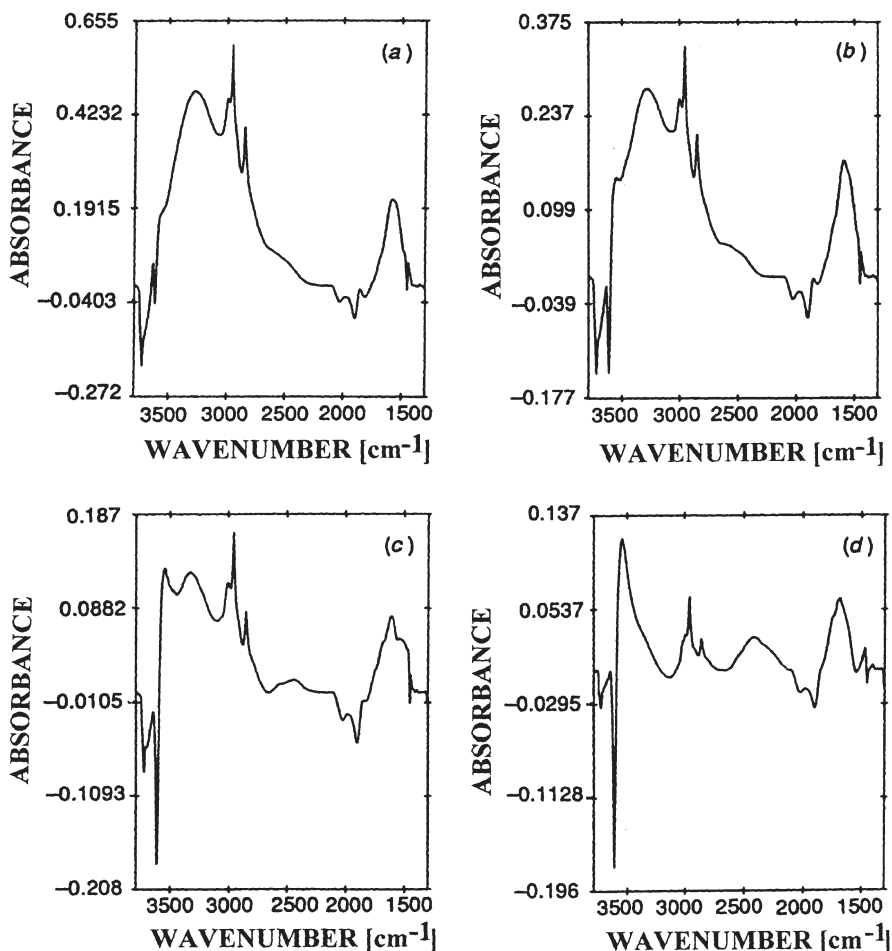


Fig. 51. Difference between the IR spectra of H-ZSM-5 loaded with methanol vapor at low pressures and the spectrum of the activated sample. (a) 1 mbar; (b) 10^{-1} mbar; (c) 10^{-2} mbar; (d) 10^{-3} mbar [820]

adsorption experiments with methanol and NH_3 both compounds were protonated by or strongly interacting with the Brønsted acid OH groups in, e.g., H-ZSM-5 or hydrogen erionite (H-ERI) and coordinatively bound to the cations in Na,K-ERI. In the case of co-adsorption, however, NH_3 displaced CH_3OH from the Brønsted acid OH groups. On H, Na,K-ERI, ammonia forms ammonium ions, whereas methanol interacts solely with Na^+ and K^+ cations. These studies were important in view of the selective synthesis of mono- and/or disubstituted amines via reaction between ammonia and methanol on zeolite catalysts (cf. Sect. 5.6.3, [817] and references therein).

Formation and reactivity of *methoxy groups* on CH_3OH adsorption on H-ZSM-5 was the subject of a time-resolved in-situ FTIR investigation by Jentys

et al. [824]. Wakabayashi et al. investigated by rapid-scanning FTIR spectroscopy the adsorption of methanol and water on H-ZSM-5 [825, 826] and observed that three types of methoxy groups could be discriminated by their IR bands (cf. also [814, 827]) in the order of decreasing reactivity: species A (2969 and 2856 cm^{-1}) formed on bridging OH groups (acid Brønsted sites); species B (2978 and 2868 cm^{-1}) generated on internal defect silanol groups; species C (2961 and 2857 cm^{-1}) originating from external silanol groups.

An ab initio quantum chemical model was proposed by Pelmenchikov et al. [828] to interpret IR data of methanol adsorption on zeolites. At variance with suggestions to assign bands at 2977 and 2871 cm^{-1} to methoxy groups, $[\equiv\text{Si}\cdots\text{O}(\text{CH}_3)\cdots\text{Al}\equiv]$, the authors claimed that the bands were due to strongly physically adsorbed methanol, stabilized on the bridging OH groups by two hydrogen bonds.

The properties of methoxy and ethoxy groups after reaction of methanol and *ethanol* with Na,H-X and Na,H-Y were recently studied by IR spectroscopy also in Datka's group [827]. IR spectra related to the synthesis of ethylenediamine from ethanolamine and ammonia over Brønsted acid mordenites were provided by Segawa et al. [829].

An FTIR spectroscopic study by Ziółek et al. [830] of the reaction between methanol and hydrogen sulfide over Na-X as a catalyst showed that both CH_3OH and H_2S were adsorbed on basic and/or cationic sites; methoxy groups as well as HS^- species were involved in the reaction. The effect of Brønsted acidity of faujasite-type zeolites on the sulfurization was studied by the same group [831].

Host/guest interactions of benzene, p-xylene, p-chlorotoluene and chlorocyclohexane with ZSM-5 were investigated by Huang et al. [832]. These authors used FT-Raman spectroscopy and utilized the excitation by an NIR laser ($\lambda=1064\text{ nm}$), which considerably reduced the fluorescence background. The effect of loading on the framework and OH stretching vibrations was determined as well as sorbate-induced phase transitions, conformational properties of the guest molecules, their location and sorbate/cation interactions.

As mentioned earlier, *benzene* adsorption into molecular sieves, especially into faujasite-type zeolites, was extensively studied via IR spectroscopy by Barthomeuf and colleagues [792, 793]. IR investigations of adsorption of benzene and especially simple benzene derivatives (*toluene, ethylbenzene, xylenes*) on zeolites were largely related to problems of diffusion (cf. Sect. 5.6.4) and catalytic reactions such as alkylation and isomerization (see Sect. 5.6.3).

The same holds mostly for IR spectroscopic work on adsorption of *alkanes* and unsaturated hydrocarbons such as *olefins* and *acetylenes* (isomerization, polymerization, coke formation) as will be indicated below. Examples were given, inter alia, in Refs. [473, 791, 833–838]. In the last reference, Howard et al. demonstrated that ethene interacted at low temperatures (295 K) via hydrogen bonding, and adsorption took place at three different hydroxy sites of H-ZSM-5. Datka [834] claimed on the basis of his IR spectroscopic observation of the interaction between ethene and OH groups of H, Na-A and H, Na-ZSM-5 that the strength of the acid hydroxy groups is homogeneous in the first, but heterogeneous in the second adsorbent zeolite. Foerster and Zakharijeva-Pencheva carried out a vibrational analysis of propene adsorbed in Y-type zeolites [839, 840]. Adsorption and

isomerization of butenes on Na,H-Y zeolites was investigated by Datka [791] and on zeolites containing transition metal cations by Foerster and Seelemann [841], who found a significant shift of the double bond stretching vibration to lower wavenumbers, depending on the charge-compensating cation.

Acetylene adsorption was IR spectroscopically studied by Howard and Kadir [833], who dealt with the uptake of this unsaturated compound into silver-exchanged zeolite A. They could evidence the formation of acetylides and the formation of two different adsorption complexes of π -bonded acetylene, indicated by bands at 1955 and 1912 cm^{-1} for C_2H_2 and 1740 and 1710 cm^{-1} for C_2D_2 under an adsorbate pressure of 13.3 kPa.

Recently, Cheetham and coworkers [286, 287] studied the adsorption of *hydrohalocarbons* in faujasites by combining INS and NIR FT-Raman spectroscopies. For chloroform, the presence of hydrogen bonding to the framework oxygen was deduced from the observed red-shift of the C-H stretching mode (Raman) and the simultaneous blue-shift of the corresponding bending mode (INS). In addition, substantial van der Waals effects between chlorine and framework oxygen atoms and electrostatic effects between chlorine atoms and cations were found to be involved in the host/guest interaction. It was outlined that using rather polar molecules may alter the INS band intensities of the sorption complexes relative to those of the empty zeolite. Thus, new framework bands at 527 and 463 cm^{-1} were observed in the INS spectrum upon chloroform adsorption. Obviously, these bands derive their enhanced intensity from coupling with normal modes of the strongly adsorbed probe molecules which involve large amplitudes of H atom displacements.

Adsorption of *boranes* and *silanes* on acid zeolites is frequently the initial step of a reaction of these molecules with the OH groups of the external and/or internal surface and aimed at a narrowing of the pore mouths or diameters. The respective processes can be conveniently monitored by IR spectroscopy. Thus, Masuda et al. [842] reacted under FTIR control methyl(diethoxy)silane with MFI-type zeolites to modify their pore sizes and determined the effect of the reaction temperature. Another example was provided in the contribution of Philippaerts et al. [221], where the implantation of boron-nitrogen compounds into mordenites was studied. The zeolite surface was first reacted with diborane, B_2H_6 , and subsequently treated with NH_3 , CH_3NH_2 or $\text{CH}_3\text{CH}_2\text{NH}_2$. The reactions were monitored by (photoacoustic) IR spectroscopy (PAS), in that the disappearance of the bands of the involved OH, BH and NH bonds were observed as well as the appearance of new B-O and B-N bands.

5.5.2.8

Adsorption of Large and Complex Molecules

Cavities of zeolites may accommodate even rather large entities with sizes close to the void dimensions. Such molecular guests may penetrate, possibly at higher temperatures or pressures, the narrower windows leading into the large cages or they may form inside the zeolite structures from smaller constituents. In any case, such large molecules residing in cavities of microporous or mesoporous materials are open to investigation by IR or Raman spectroscopy. Only a few

examples should be mentioned here. Thus, among the largest molecules taken up by faujasite-type zeolites are triphenylmethane derivatives. Introduction of, e.g., triphenylcarbinol, $(\text{C}_6\text{H}_5)_3\text{COH}$, triphenylchloromethane, $(\text{C}_6\text{H}_5)_3\text{CCl}$, and triphenylmethane itself, $(\text{C}_6\text{H}_5)_3\text{CH}$, into Na-Y and H-Y was carried out by Karge [222] and studied by transmission IR spectroscopy. The spectra provided evidence not only for the incorporation of those compounds, but, in the case of $(\text{C}_6\text{H}_5)_3\text{COH}$ and $(\text{C}_6\text{H}_5)_3\text{CCl}$, also for the formation of the respective carbenium ions, $(\text{C}_6\text{H}_5)_3\text{C}^+$, via interaction with Lewis sites of and stabilization by the zeolite matrix. The adsorption of 4,4'-bipyridine into $\text{Na}_x\text{-ZSM-5}$ ($x=0, 3.42, 6.62$) was studied by Raman spectroscopy, which provided insight into the location of the adsorbed molecules [843]. In the case of silicalite-1 ($x=0$), 4,4'-bipyridine was occluded in the straight channels in a twisted conformation. When Na^+ was present ($x=3.42, 6.62$), the molecules were in the straight channels but located in the vicinity of the sodium cations.

Examples of building up large molecules inside a zeolite structure via a reaction were frequently reported under the term "ship-in-the-bottle synthesis". For instance, very early Romanowski et al. [844] and, somewhat later, Schulz-Ekloff et al. [845] produced phthalocyanines in faujasite-type zeolites and investigated the products, inter alia, by IR spectroscopy. Cobalt-phthalocyanine encapsulated in zeolite EMT was prepared and, inter alia, characterized via IR spectroscopy by Ernst et al. (cf. [846] and references to related work therein). A number of typical bands of CoPc-EMT in the mid infrared ($1600\text{--}1200\text{ cm}^{-1}$) were observed and interpreted.

Balkus et al. [847] applied the IR/KBr pellet technique and reported on the characterization of Rh(III)-salen "ship-in-the-bottle" complexes encapsulated in zeolite X and Y zeolites. In their more recent, excellent review article on Raman spectroscopy on zeolite systems, de Vos et al. [848] made reference to the formation and Raman characterization of complexes such as Ru-2,2'-bipyridine (cf. also [849]) and related compounds as well as to zeolite-confined Schiff bases, e.g., $[\text{Mn}(\text{salen})\text{OH}]$, in Na-Y, (cf. also the IR study in Ref. [848]). IR spectra of Na(I)-salen and Pd(II)-salen complexes in zeolite Y were shown in [850].

Similarly, Zhan and Li [851] synthesized and characterized by Raman spectroscopy Mn(II)-1,10-phenanthroline complexes in Y-type zeolites. Selenium chains and rings confined in voids of various zeolites (zeolite A, zeolite X, mordenite, chabazite, and cancrinite) were studied by Raman spectroscopy in the range $300\text{--}100\text{ cm}^{-1}$ in the contribution of Poborchii [852].

Fourier transform Raman spectroscopy (FT-Raman) avoids a number of problems usually encountered with IR spectroscopy (such as disturbance by the presence of H_2O , broadening of signals due to hydrogen bonding, etc.). In the case of the salen complexes, sharp lines of the C=C and C=N stretching vibrations were well resolved between 1450 and 1650 cm^{-1} . The $\nu(\text{C}=\text{N})$ stretching mode of the zeolite-confined complexes was shifted to lower wavenumbers at about $1628\text{--}1630\text{ cm}^{-1}$ compared to the corresponding peak of the free protonated salen- H_2 at 1638 cm^{-1} . In some related experiments, a more advanced laser Raman technique (resonance Raman spectroscopy, "RR" technique) was employed. Here, the Raman intensities were significantly enhanced when the

laser light was in resonance with an electronic excitation of the chromophore of the molecule studied. A pertinent example for the application of RR spectroscopy is the investigation of $[\text{Ru}(\text{bpy})_3]^{2+}$ entrapped in faujasites [848]. Intrazeolite ferrous cyanide complexes in Y-type zeolite were prepared and IR spectroscopically characterized by Bresinska and Drago [853]. An IR band at 2050 cm^{-1} was proposed to be indicative of a water soluble, thermally stable complex located in the supercage, whereas a band around 2115 cm^{-1} was attributed to a less stable complex residing in the sodalite cage.

5.5.2.9

Infrared Micro-Spectroscopy of Molecules in Single Crystals or Powders of Zeolites

Phenomena of adsorption or incorporation of molecules into single crystals or powders of microporous materials can be advantageously investigated by infrared micro-spectroscopy (often simply but not entirely precisely called "IR microscopy"). Examples were already mentioned in the context of in-situ IR studies on adsorption into $\text{AlPO}_4\text{-5}$ -derived materials (vide supra and [854–856]). Very impressive studies in this field were undertaken by Schueth and colleagues. For example, the incorporation, ordering and orientation of nitroaniline and similar compounds into large single crystals of, e.g., ZSM-5 was observed by the IR microscope [857, 858]. Acid sites in single crystals of cloverite and the adsorptive behavior of this material against strong bases (ammonia, pyridine and trimethylamine) and alcohols (methanol, ethanol, propanol and butanols) were also studied [859, 860]. FTIR micro-spectroscopy was also successfully employed by Schueth et al. [861] for studying the adsorption of polar molecules such as *p*-xylene or *p*-nitroaniline into single crystals of silicalite-1, $\text{AlPO}_4\text{-5}$ or SAPO-5 using polarized infrared radiation. In general so-called IR microscopy proved to be a powerful tool to analyze the orientation of adsorbed molecules in molecular sieves.

Time-resolved in-situ micro-infrared spectroscopy was applied for the first time by Nowotny et al. [862] on a process occurring in a zeolite single crystal. These authors monitored the thermal decomposition of the template (tripropylamine, TPA) in single crystals of MFI materials with $n_{\text{Si}}/n_{\text{Al}}$ ratios below 1000 (silicalite-1), 122, and 31 (ZSM-5). Bands of the CH stretching modes at 2981, 2943, 2882 and 2746 cm^{-1} and of the CH bending vibrations at 1473 and 1458 cm^{-1} were observed. From the presence of the latter two bands the authors concluded that at ambient temperature TPA is rather immobile in the channels of the as-synthesized ZSM-5 crystals. From their measurements they arrived at the conclusions that

- (i) the mobility of TPA increased with increasing temperature,
- (ii) the decomposition of tetrapropylammonium ions at 613 K proceeded according to the Hoffmann elimination with subsequent β -elimination reactions to form tripropylamine at non-acid sites or tripropylammonium ions at acid Brønsted centers and
- (iii) the rate-determining step was the reaction producing dipropylamine or dipropylammonium ions.

Raman spectra of single crystals of ZSM-39 were obtained by Vergilov and Valtchev [863]. These spectra exhibited a highly polarized line at 3610 cm^{-1} , which was ascribed to a structure-bound hydroxy group. Also, vibrations of the framework and template cations (tetramethylammonium and trimethylammonium) were discussed.

Sorption of other compounds such as alkanes, benzene and simple benzene derivatives into single crystals of zeolites were treated in the context of catalytic and diffusion experiments as will be reviewed in the subsequent Sects. 5.6.3 and 5.6.4.

5.6

In-situ IR and Raman Spectroscopic Investigation of Processes in Zeolites

5.6.1

Introductory Remarks

Since the subjects of two of the subsequent sections, viz. catalysis on and diffusion in zeolites will be extensively treated in later volumes of the present series “Molecular Sieves – Science and Technology”, including the application of spectroscopic techniques in these fields, the reviews under Sects. 5.6.3 and 5.6.4 may be rather brief. They will just provide a few examples, where in-situ IR and Raman spectroscopy were employed with respect to problems of catalysis and diffusion.

5.6.2

Zeolite Synthesis and Crystallization

A scope of profitable applications of Raman spectroscopy is seen in studies of zeolite syntheses.

Results of IR and Raman investigations on synthesis solutions (sodium silicate and aluminate solutions) related to the solubility of zeolites and their formation were reported by, e.g., Beard [864] and Guth et al. [865]. A laser Raman study on the crystallization of A-, X- and Y-type zeolites was carried out already in 1983 by Roozeboom et al. [866]. As a result, they assumed that silica dissolved from the amorphous aluminosilicate gels, hydroxylated ions condensed with $\text{Al}(\text{OH})_4^-$ and formed a large variety of complex aggregates. These were identified as polymeric aluminosilicates, which may have been subsequently transformed into nuclei for crystal growth as centers of precipitation. When the precipitates consisted of crystallites large enough to be Raman- and X-ray-detectable, Raman and XRD signals showed up simultaneously in the course of crystallization. A mechanism for the formation of 4-membered and 6-membered rings versus the generation of 5-membered ring systems was proposed. Attenuated total reflection IR spectroscopy was employed by Groenen et al. [867] to characterize TMA^+ -double four-membered ring anions (D4R) in solution, with typical bands around 1000 and 1110 cm^{-1} . The authors suggested a relation to the role of silicate anions in zeolite synthesis.

IR spectra of suspensions of amorphous and crystalline colloidal silica aggregates were obtained by Mintova et al. [868]. These spectra revealed the presence of small (nano-sized) silicate units possibly containing D5R subunits. A complete transformation to crystalline particles of MEL-type zeolite was observed after an additional hydrothermal treatment of the aged precursor suspensions at 363 K for 68 h.

Furthermore, Raman spectra have been recorded during the formation and the crystal growth processes of mordenite [869], zeolite A [870], and zeolite Y [871]. The evolution of the spectra during the crystallization process in both the solid and the solution phases provided information about the formation of intermediate building blocks, agglomerations, and transformations at a molecular level. However, the interpretation of the spectra relies decisively on the assumption that specific Raman bands can be correlated with vibration modes of substructure building units of individual size. As already mentioned in Sect. 2.5, this should be treated with some caution, and hence reliable conclusions require a careful examination of the experimental material. Nevertheless, Raman spectra observed at different stages of formation are well suited for giving hints to the progress and mechanism of zeolite crystallization and aging. Thus, synthesis of zeolites A, X, Y, MOR, L and Beta was followed by UV laser Raman spectroscopy in the work of Yu et al. [252]. These authors suggested *inter alia* that in the course of crystallization of X-type zeolite 4MR units (indicated by a band at 510 cm^{-1}) were transformed into 6MR units (presumably of the β -cages), as was evidenced by the appearance of a band at 390 cm^{-1} .

Buge et al. [872] reported both on IR and Raman spectroscopic investigations devoted to the synthesis of ZSM-5 type zeolites and described a closed reactor using a special cell for Raman spectroscopic *in-situ* measurements under hydrothermal conditions up to about 470 K. There arose, however, experimental problems in obtaining exploitable Raman spectra because of increasing Raman background during hydrothermal treatment of the synthesis mixtures. Thus, the authors were unable to record *in situ* the changes of the Raman spectra during crystallization. Monitoring the progress of the syntheses was possible only by *ex-situ* Raman and IR spectroscopy, where the Raman spectra mainly reflected vibrations of the templates (tripropylammonium hydroxide, TPAOH; triethyl-2-hydroxyethylammonium hydroxide, TEHEAOH) and the IR spectra concerned the vibrations of the aluminosilicate species.

Decomposition of organic cations in offretite and ZSM-34 crystals was followed via FTIR spectroscopy by Occelli et al. [873] in that the decrease of the bands of the organic species and the concomitant appearance of the new bands in the OH stretching region was monitored. The protonic nature of the newly formed hydroxy groups was confirmed by their interaction with the probe pyridine and generation of the bands of pyridinium ions (cf. Sect. 5.5.2.6.2).

More recently, Schoeman and Regev [874] studied the crystallization of silicalite-1 *inter alia* by DRIFT spectroscopy. A band at 550 cm^{-1} was found to be typical of the presence of MFI-structured material.

The growth of silicalite-1 films on gold supports was monitored via scanning electron microscopy, X-ray diffraction and reflection/absorption infrared spectroscopy in the work by Engstroem et al. [875]. The development of peaks at 1229,

1117 and 1068 cm^{-1} was observed. The IR results suggested that during the growth of the films a gradual change in the puckering of the five-membered rings as building units of the MFI structure occurred. The support surface probably had initially a stronger influence on the vibrational modes of the larger-sized seeds, but after extended hydrothermal treatment (above, e.g., 24 h) the atomic arrangement during further film growth was independent of the initial seeding. Similarly, the crystallinity of as-synthesized Na-X and Na-X films deposited by pulsed laser on TiN-coated silicon wafers was compared by FTIR spectroscopy [876].

FTIR and Raman spectroscopic characterization and synthesis studies of ETS-10 were reported by Yang et al. [316] together with the analysis of framework vibrations (*vide supra*). The increasing crystallinity during synthesis of a SUZ-4 zeolite was followed via IR by Gujar and Price [877]. They detected 5MR, 6MR, 8MR and 10MR subunits.

Calabro et al. [878] demonstrated the great potential of in-situ attenuated reflectance FTIR spectroscopy in monitoring details of the formation of mesoporous silicate materials such as MCM-41.

The synthesis as well as the role of structure-directing molecules were studied with the help of Raman spectroscopy by Dutta [879] during the formation of a number of zeolites, viz. ZK-4, mordenite, ZSM-5 and ferrierite.

5.6.3

Chemical Reactions in Zeolites

There are several interesting attempts of in-situ studying chemical reactions in zeolites.

A reaction important in zeolite research, especially in view of the catalytically relevant acid OH groups, is the *hydrogen/deuterium exchange*. An interesting report was delivered by Heylen and Jacobs [880], who followed the H_2/D_2 exchange in La-X, La-Y and “deep-bed” calcined H-Y continuously via IR spectroscopy in the temperature range 473–673 K. These authors determined the reaction order and activation energy as a function of the nature of the cations, degree of cation exchange and presence of extra-framework aluminum, and they found the X-type samples to be the most active materials.

Another early report appeared by Ward on in-situ IR spectroscopic observation of *cumene cracking* on H-Y, unfortunately without a description of the IR reactor cell [881]. Usually, an appropriate reactor cell, which can be operated at higher temperatures and, if necessary, higher pressure is required. Several designs have been described (cf. Sect. 4.1). One of the early constructions was that by Gallei and Schadow [153]. For instance, Kredel used this high-temperature/high-pressure (and simultaneously vacuum-tight) IR cell, for in-situ monitoring the activation process of zeolite catalysts and subsequent catalysis of *1-hexene isomerization* [882]. Here, as in many other instances, the IR flow-reactor cell was connected to a gas chromatograph (or a mass spectrometer) to follow the conversion and analyze the product distribution. For further applications of IR spectroscopy on olefin adsorption and reaction see below.

Olefin reactions were, among other reactions, also studied in situ by DRIFT spectroscopy as described in a review article by Maroni et al. [883], where a cell was used similar to that mentioned in Sect. 4.2 (cf. [176]). Salzer et al. [884] described in-situ DRIFT experiments of activation of zeolite catalysts, for instance, NH_4 -erionite, where they also employed the commercially available, heatable DRIFT cell mentioned in Sect. 4.2.

The same type of cell as that developed by Gallei and Schadow [153] was used by Karge and Ladebeck [885] for an in-situ investigation of the *Claus reaction* [see Eq. (29)] on zeolites. However, since this reaction was also catalyzed by the stainless-steel walls of the cell, these walls had to be plated by an inert material (gold). The reaction was monitored by observing the H_2S , SO_2 and H_2O bands (vide supra) of the reactants and one of the products, and the degree of conversion was determined gas chromatographically. Oxidation of H_2S (and D_2S) on A-type zeolites (Na-A, Na,Ca-A) was investigated also via IR spectroscopy by Foerster and Schuldt [886].

Ethylbenzene disproportionation catalyzed by acid zeolites was studied by Karge et al. [887, 888] and recommended as a versatile test reaction for acid (monofunctional or bifunctional) catalysts such as acid zeolites or related materials and is frequently used for this purpose. Also, this reaction was studied in situ by IR spectroscopy in combination with gas chromatography for determination of conversion and selectivity [888]. In these experiments, a flow-reactor quartz glass cell as described in Ref. [152] was used, which could be operated under ultra-high vacuum during the pretreatment of the thin catalyst wafers of pressed zeolite powder at, e.g., 670–870 K and 10^{-4} Pa. After pretreatment, the cell was used as a differential fixed-bed micro-flow reactor (cf. also [152, 158]). Results are illustrated by Fig. 52.

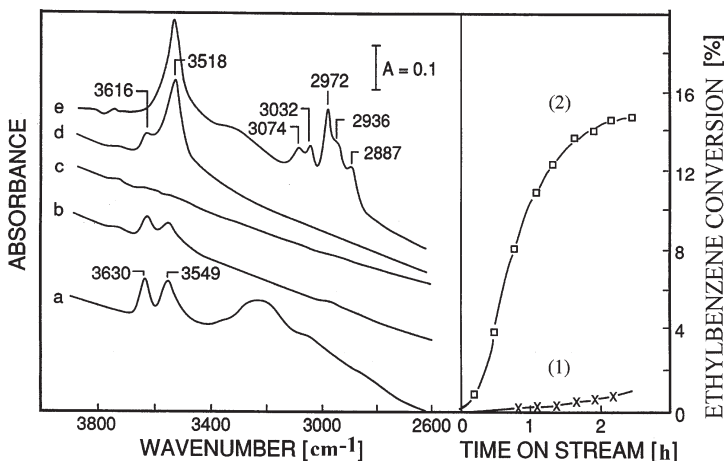


Fig. 52. Left: In situ IR spectra of $\text{LaCl}_3/\text{NH}_4\text{-Y}$ after heat-treatment in high vacuum at (a) 455, (b) 575, (c) 675 K, (d) rehydroxylation by 1 min contact with 0.1 kPa water vapor, (e) contact with feed stream of 1.3 vol.-% of ethylbenzene (EB) in dry helium, respectively. Right: (1), total EB conversion on a catalyst wafer characterized by spectrum c; (2), total EB conversion on a catalyst wafer characterized by spectra d and e (from [888])

It could be shown that (i) admission of water was necessary to generate acid and catalytically active OH groups (band at 3640 cm^{-1}) in the lanthanum-containing Y-type catalyst prepared via solid-state ion exchange (cf. Volume 3, Chapter 2 of the present series); (ii) ethylbenzene interacted with those acid OH groups (decrease in the intensity of the OH stretching band at 3640 cm^{-1}) and simultaneously the CH stretching bands of ethylbenzene appeared; (iii) the disproportionation of ethylbenzene immediately commenced after admission of ethylbenzene when in a preceding step the OH groups have been generated through intermittent interaction with small amounts of water vapor (without this intermittent admission of water vapor the zeolite catalyst remained inactive). The disproportionation of ethylbenzene yielded selectively benzene and diethylbenzenes in the molar ratio 1:1.

Alkylation of benzene with methanol over H, Na-Y via reaction with methoxy groups at 533 K was monitored through in-situ FTIR experiments carried out by Rakoczy and Romotowski [889].

Another instructive example of a reaction monitored in situ by transmission IR spectroscopy is the *alkylation of the toluene ring* by methanol reported by Lercher and coworkers [820, 890, 891]. This work was related to the investigation of adsorption and co-adsorption of toluene, methanol and ammonia on H-ZSM-5 and H, Na-ERI by the same group (vide supra and [127, 652, 814–821]). The authors used a continuously stirred tank reactor [892–895]. Some conclusions drawn by the authors from their results of combined IR spectroscopic and gas chromatographic experiments were reported as follows.

- (i) A co-adsorbate complex of methoxonium ion (vide supra) and toluene was indicated by a band at 3460 cm^{-1} ; its concentration and stability decreased with increasing reaction temperature.
- (ii) The products adsorbed in H-ZSM-5 were mainly slowly migrating m- and o-xylene and trimethylbenzenes, whereas in the temperature interval from 473 to 673 K the selectivity to the fast diffusing *p*-xylene increased, according to the GC measurements, from 30 to 55%.
- (iii) In the case of Na,K-ERI, methanol was found to adsorb coordinatively onto the alkali metal cations, while interacting with the protons in the case of H-erionite.
- (iv) Ammonia, however, was proved to displace adsorbed methanol from Brønsted acid sites, and the thus-generated NH_4^+ ions acted as adsorption centers for CH_3OH .
- (v) Formation of methoxy groups via reaction of CH_3OH with $[\equiv\text{Si}(\text{OH})\text{-Al}\equiv]$ groups of the framework was strongly suppressed by the presence of ammonia, which is important in view of the synthesis of mono- or di-substituted amines through the reaction of methanol and ammonia.

The *synthesis of alkylamines* was treated as a complex case study by Mirth and Lercher [892], viz. in their general discussion of strategies for the application of in-situ IR spectroscopy in developing catalysts and catalytic processes.

In-situ IR experiments and a kinetic analysis revealed that, during the synthesis of methylamine on Brønsted acid mordenites, all methylammonium ions were formed in the micropores of the catalyst via a bimolecular complex of

(methyl)ammonium on the Brønsted sites and hydrogen-bonded methanol. Their formation was, however, not the rate-determining step. Rather, desorption of the produced methylamines, facilitated by adsorbing ammonia molecules, was recognized as rate determining. Similarly, in the case of amination of methanol or ethanol by ammonia over Brønsted-acid mordenites it was also observed that the strength and location of the acid sites play a decisive role in the reaction [893–895]. The correlation between adsorption structures, reactivities and surface acidities with the kinetics and shape selectivities in the methylamine synthesis was dealt with in a contribution by Kogelbauer et al. [896]. The authors considered the reaction of ammonia and methanol over alkali-exchanged as well as Brønsted-acid mordenites and erionites. Their results suggested that amination proceeded via ammonolysis of chemisorbed methanol in the case of alkali-exchanged zeolites, whereas it occurred via methanolysis of chemisorbed ammonia over Brønsted acid forms.

Adsorption and *reaction of methanol and CO* on reduced iron-containing L-type zeolites, (prepared with and without potassium-doping, K,Fe/L and Fe/L, respectively) were investigated by IR spectroscopy in a study by Park et al. [897]. The reaction produced methyl formate. Accordingly, it was shown by the authors that over the same catalyst, K,Fe/L, when used for methanol synthesis via hydrogenation of CO₂, from the products CO and CH₃OH methyl formate was formed in a secondary reaction.

Examples of IR investigations of the type discussed earlier, i.e., of interactions of benzene derivatives with zeolite catalysts, where the aromatic ring of the reactants is involved, are also given by the studies of *xylene isomerization* [898, 899]. In fact, here are features of sorption and diffusion involved (cf. Sect. 5.6.4). Similarly, isomerization of *p*-ethyltoluene (band at 1515 cm⁻¹) to *m*-ethyltoluene (band at 1491 cm⁻¹) was observed via in-situ FTIR spectroscopy by Zikanova et al. [900].

However, another type of reactions of benzene derivatives was studied by in-situ IR spectroscopy as well, viz. the *side-chain alkylation* of alkylbenzenes, for instance of toluene, over basic zeolite catalysts such as M⁺-X zeolites (M=Na, K, Rb, Cs) [901, 902]. The intermediate conversion of methanol to formaldehyde turned out to be crucial for the side-chain alkylation as well as a strong polarization of the methyl group of toluene, the preferential adsorption of toluene, and a sufficient basicity, i.e., base strength of the catalyst. Related to these IR studies of side-chain alkylation of toluene were in-situ IR spectroscopic investigations of the *decomposition of methanol* over basic zeolites (M⁺-X, M⁺=Na⁺, K⁺, Rb⁺, Cs⁺; Na-ZSM-5 and Cs-ZSM-5 [903]). It was shown that over weakly basic zeolites (Na-ZSM-5, Cs-ZSM-5) dimethyl ether was formed from methanol, whereas over more strongly basic X-type zeolites formaldehyde was produced, which is an indispensable intermediate for the side-chain reaction (vide supra).

The *reaction of cyclohexene* over differently dealuminated H-Y samples at 370 K (isomerization to methylcyclopentene and hydroisomerization to methylcyclopentane, hydrogen transfer resulting in benzene and cyclohexane, cracking and coke formation) was monitored by Joly et al. [904] via in-situ IR spectroscopy in an IR flow-reactor cell coupled with a gas chromatograph. A good correlation was reported between the activity of the Brønsted acid sites and their strength

as measured through IR spectroscopy using 2,6-dimethylpyridine as a probe. The protonated probe molecules exhibited a typical band at 1630 cm^{-1} indicating the B-sites. The disappearance of the HF-OH and LF-OH bands was monitored as a function of time on stream and in dependence of the dealumination method.

In-situ IR spectroscopic investigation was extended to significantly more bulky reactants than those dealt with so far. For example, Neuber et al. [905] studied the reaction of 1- and 2-methylnaphthalene over zeolites with different pore widths, viz. H-ZSM-5 ($0.53 \times 0.56\text{ nm}$), H-ZSM-12 ($0.55 \times 0.59\text{ nm}$) and H-Y (0.74 nm) in a flow-type IR reactor cell connected with a gas chromatograph (cf. [152]). Both the OH bands of the zeolites and the respective CH bands of the feed and product molecules were monitored when the catalysts were working. At 575 K , isomerization and transalkylation proceeded well in large pore H-Y. The degrees of conversions of 1-methylnaphthalene in H-Y and H-ZSM-12 were comparable, but transalkylation was virtually absent in the case of the latter catalyst, because this reaction requires a bulky transition state or intermediate involving two feed molecules, which cannot be accommodated in the channels of H-ZSM-12. Hence, isomerization via monomolecular transition states is predominant in H-ZSM-12. From the IR spectra it was evident that the reactions, as far as they occurred, took place inside the zeolite structures. At 575 K , the uptake of the polynuclear feed molecules into H-ZSM-5 was still severely impeded, thus the overall conversion remained rather low. With the exception of H-ZSM-5, deposition of significant amounts of coke exhibiting aromatic constituents was observed by IR (vide infra).

Cyclodimerization of 1,3-butadiene over Cu-exchanged zeolites FAU and EMT was followed in situ by DRIFT in a study by Voskoboynikov et al. [906]. The reaction was Brønsted acid-catalyzed. Even though the deactivation was rather little, it could be also monitored in situ through the IR spectra showing the formation of polycyclic naphthenes, which then in part consecutively transformed into aromatics.

Formation of acetaldehyde via reaction of acetylene and water over Cd-exchanged phillipsite, mordenite, clinoptilolite, erionite, chabazite, and zeolites A, X and Y was investigated by the group of Kalló [907, 908], while acetaldehyde adsorption on H-ZSM-5 was studied via FTIR by Diaz et al. [909], which indicated proton transfer with formation of crotonaldehyde and subsequent dehydration. At pressures higher than 400 Pa oligomerization occurred.

As an example of *base-catalyzed* reactions over zeolites of different basicity (Cs, Na-Y, Cs, Na-X, CsOH/Cs, Na-Y), the *aldol condensation* of *n*-butyraldehyde was explored by Weitkamp et al. [910] using in-situ FTIR to monitor the conversion. During the reaction a band emerged at 1580 cm^{-1} , which could be ascribed to a COO^- stretching vibration of a carboxylate anion. These anions were suspected to poison the active basic sites and cause the catalyst deactivation.

Coke formation [911–915] is a very important phenomenon in most hydrocarbon conversions on zeolites. Also, *reactions of olefins* on zeolites (in particular isomerization and oligomerization) were frequently subject of in-situ IR experiments [916–919] and theoretical treatment [740, 920], in many cases because of the close relation to coke formation, for instance, during isomerization and alkylation reactions [835, 916, 917]. Further examples are presented in

Refs. [473, 837, 886, 921]. Kustov et al. [922] published an interesting DRIFT spectroscopic study on ethene oligomerization, including a discussion of the role of Lewis- and Brønsted-acid sites and ethoxy groups as intermediates of this reaction.

Due to the importance of coke formation for the application of zeolite catalysts in many hydrocarbon reactions, a large body of reports on this subject exists in the literature (cf., e.g., [912, 913] and references therein). Regarding IR spectroscopic investigations of coke formation, a particularly interesting feature is the appearance of the so-called coke band around 1600 cm^{-1} . Even though the composition of coke formed on zeolites during catalytic reactions of hydrocarbons is usually rather complex and strongly dependent on many factors [912, 913], this band is almost always indicative of the formation of carbonaceous deposits. The integrated absorbance of the coke band was even frequently used as a measure of the amount of coke deposited [912, 913, 923–925]. Interestingly, Haber et al. [915] reported on the formation of aromatic deposits upon reaction of olefins such as but-1-ene and dec-1-ene over H, Na-Y at relatively low temperatures, viz. 398 and 363 K, respectively. Datka [926] studied the oligomerization of but-1-ene over H, Na-Y and showed via IR spectroscopy that one proton was transferred from one OH group related to the HF-OH band to the oligomerizing butene molecules, giving rise to an alkyl carbocation. This quantitative evaluation was achieved using the previously determined extinction coefficient necessary to quantify the density of Brønsted sites via pyridine adsorption, viz. $\epsilon_B = 0.059\text{ cm}^2\ \mu\text{mol}^{-1}$. A determination of average extinction coefficients of the CH bands was also claimed to be possible: those of $\nu_{\text{as}}[\text{CH}_3]$, $\nu_{\text{s}}[\text{CH}_3]$ and $\nu[\text{CH}_2]$ of the oligomeric cation, *n*-hexane, and 2,2,3-trimethylpentane were reported to be 1.03, 0.63, and $0.65\text{ cm}^2\ \mu\text{mol}^{-1}$, respectively. The higher value in the case of the cationic oligomer was ascribed to the polarizing effect of the positive charge exerted on the CH bond. Decomposition of oligomers as coke precursors was also followed by IR in the above-mentioned experiments by Datka [926].

Coke formation on zeolite catalysts will be extensively reviewed in a particular chapter of a subsequent volume of the present series.

In-situ *decomposition of* (η^6 -benzene)tricarbonylchromium(0) and (η^6 -anisole)tricarbonylchromium(0) complexes on Na-X zeolite was studied via temperature-programmed reaction and DRIFT by Shirley and Scoville [927]. At increasing temperatures, the decomposition could be monitored, for instance, by the change from the band of complexed benzene (1452 cm^{-1}) to that of adsorbed benzene (1477 cm^{-1}). Similarly, the change from the spectrum of intact (η^6 -benzene)tricarbonylchromium(0) complex to that of a surface $\text{Cr}(\text{CO})_3$ complex with CO absorbances at 1917 and 1773 cm^{-1} was observed.

Particularly in view of environment protection, the *decomposition of chlorofluorocarbons* such as CCl_2F_2 and CHClF_2 upon interaction with zeolites (e.g., H-Y, H-MOR, H-ZSM-5) became an interesting topic. For example, results of an in-situ IR and multinuclear NMR spectroscopic study of this type of reactions were recently presented by Hannus et al. [928, 929]. The essential conclusion drawn from the experimental findings was, however, that in the case of the systems studied the zeolites did not play the role of catalysts but of reactants. They were more or less easily destroyed through a progressive dealumination of their frame-

works, which finally led to a collapse of the structures. Dealumination of zeolites can be performed via reaction with various agents (cf. Volume 3, Chapter 3 of the present series), among them CCl_4 and COCl_2 . In an MAS NMR and FTIR spectroscopic study, Hannus et al. [930] discovered that phosgene, COCl_2 , is formed as an intermediate in the reaction between zeolites and CCl_4 which was indicated through a Fermi resonance doublet at about 1715 and 1795 cm^{-1} . This surface-induced Fermi resonance, which does not occur in the gas phase of phosgene, is due to the fact that by adsorption on zeolites (Li-, Na-, K-, Rb-, and Cs-Y) the C=O stretching mode, ν_2 , (1827 cm^{-1} in the gas phase) experienced a red-shift and the overtone mode of the asymmetric stretching of C=Cl₂, $2\nu_4$, (1670 cm^{-1} in the gas phase) a blue-shift, so that the energy difference between both modes sufficiently decreased leading to their resonance. The authors proposed a mechanism of the dealumination by CCl_4 and interpreted their FTIR and ^{13}C -MAS NMR findings as a confirmation for their proposal.

The *formation of carbonyls and nitrosyls* via reaction of CO and NO with highly dispersed AuCl prepared in Na-Y or ZSM-5 ($n_{\text{Si}}/n_{\text{Al}}=1600$) was studied through in-situ FTIR by Qiu et al. [931]. Chemisorption of CO (under 0.67 kPa and at 293 K) produced a sharp IR band at 3184 and a much smaller one at 2137 cm^{-1} , whereas adsorbed NO (under 0.4–7.9 kPa and at 293 K) gave rise to an intense band 1820 cm^{-1} : the latter could be easily removed by evacuation. Au(I)-ZSM-5 formed by reductive carbonylation was shown to be catalytically active in NO reduction by CO.

On adsorption of NO into Cu^+ -containing zeolites, Wichterlová et al. [932] detected by FTIR spectroscopy mononitrosyl complexes ($\text{Cu}^+\text{NO}^{\delta-}$) (band at 1775–1799 cm^{-1} vs. 1909 cm^{-1} for $\text{Cu}^{2+}\text{NO}^{\delta-}$) in the case of zeolite Y and both mononitrosyl complexes (band at 1811 cm^{-1}) and dinitrosyl complexes, $\text{Cu}^+(\text{NO}^{\delta-})_2$, with bands at 1735 and 1826 cm^{-1} in the case of ZSM-5.

FTIR spectroscopy was employed by Brock et al. [933] to follow in situ the *decomposition of sodium azide* on FAU-type zeolites with different $n_{\text{Si}}/n_{\text{Al}}$ ratios. The main bands in the complex spectra occurred at 2072–2079 (Na-X) and at 2066–2079 cm^{-1} (Na-Y), depending on the $n_{\text{Si}}/n_{\text{Al}}$ ratio, and declined on progressive decomposition at increasing temperatures, which caused other bands intermediately to appear.

Hydrosulfurization of the C=C double bond over H- or M-exchanged zeolites A, X, Y, mordenite and clinoptilolite (M=Na, Ag, Ca, Zn, Cd, Cr, Mn, Fe, Co and Ni) was IR spectroscopically monitored by Kallo et al. [934]. The reaction of ethylene and propylene was best catalyzed over Cd-X, which simultaneously turned out to be the most stable catalyst.

Ziołek and Decyk [935] *decomposed ethanethiol and diethyl sulfide* over hydrogen and alkali forms of X, Y, and ZSM-5 zeolites, and attempted to identify the sites of the zeolites being active in these reactions and, also, to elucidate individual reaction steps with the help of IR spectroscopy. After ethanethiol adsorption on Na-Y or M, Na-Y (M=Cs, K, Li), bands at 2980, 2930, 2915 and 2850 cm^{-1} were observed due to C-H stretching vibrations, the intensity of which paralleled the catalytic activity. Depending on the various possible reaction pathways, either Brønsted-acid OH groups or alkali metal cations were viewed as the catalytically active centers.

The adsorption and *hydrodesulfurization* reaction of thiophene over hydrogen, nickel- and cobalt-exchanged forms of zeolite Y, MOR and ZSM-5 was investigated IR-spectroscopically by Korányi et al. [936]. On Ni,Na-Y thiophene reacted with the Na^+ cations, on MOR and ZSM-5 it was hydrogen-bonded to the strong Brønsted-acid OH groups, but not adsorbed on the unsulfided Co or Ni species, which were, however, indispensable for the hydrogenolysis of the C-S bond of partially saturated thiophene.

The generation of CdS clusters (e.g., Cd_4S_4 in zeolite Y) via sulfidation of Cd^{2+} -containing zeolites (LTA, FAU, ERI) was monitored by in-situ IR spectroscopy in the experiments of Tel'biz et al. [937] aimed at the preparation of photocatalytic clusters (cf. also [938] and, especially, Volume 3, Chapter 6 of the present series).

5.6.4

Diffusion in Zeolites

A new method for measuring diffusion coefficients by IR spectroscopy was developed by Karge and Niessen [158], Niessen [132] and Karge et al. [939]. The change in the intensities of bands typical of molecules migrating inside a zeolite structure during their uptake or desorption were measured by FTIR spectroscopy under high time-resolution as a function of small partial pressure jumps and at various temperatures. An appropriate method of evaluation of the time-resolved spectra was developed on the basis of solutions of Fick's second diffusion law provided by Crank [940]. As an example, Fig. 53 illustrates an uptake experiment with benzene (B) as the adsorbate and H-ZSM-5 as the adsorbent.

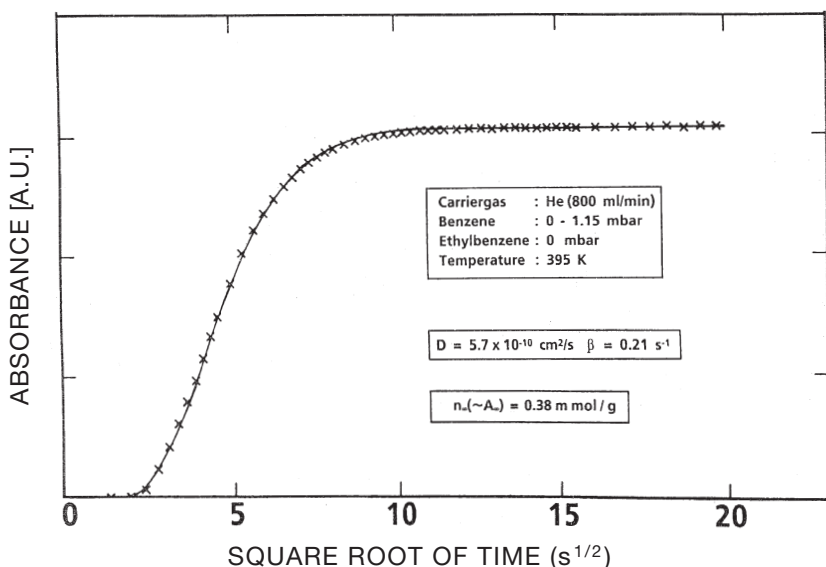


Fig. 53. Curve of uptake of benzene into H-ZSM-5 to evaluate the transport diffusion coefficient, D ; β is a parameter in the solution of the diffusion equation, related to the time lag (cf. abscissa); n_{∞} is the coverage at saturation, A_{∞} the corresponding absorbance [158]

The diffusivity (transport diffusion coefficient) was corrected for coverage dependence according to Darken's equation [941]. It amounted to $D(B) = 5.3 \times 10^{-10} \text{ cm}^2 \text{ s}^{-1}$ at 375 K and a coverage of 1.4 molecules per unit cell, in very good agreement with literature data (cf. [942]). Similarly, diffusivities of ethylbenzene (EB) and *p*-xylene (*p*-X) in H-ZSM-5 or silicalite-1 were determined [943]. Also, the technique enabled us for the first time to directly measure diffusion coefficients in the case of co-diffusion (B and EB, B and *p*-X) as well as for counter-diffusion (B vs. EB, EB vs. B, B vs. *p*-X, *p*-X vs. B, etc.) [152, 158, 943–945]. Moreover, the measurements were carried out under conditions close to those of catalytic experiments, for instance, with respect to reactant flow, elevated temperatures and feed composition. IR spectroscopic determination of diffusivities may be even carried out simultaneously with monitoring the formation of coke, thus studying in situ the effect of coke deposition on the reactant transport (vide supra, [939]). Using the same technique, pyridine diffusion in various zeolites was measured as well [946]. More recently, Roque-Malherbe and Ivanov [947] used the same method as developed by Karge and Niessen [158, 943] to investigate the diffusion and counter-diffusion of *para*- and *ortho*-xylene in H-SSZ-24 and H-ZSM-11 and determine diffusion coefficients.

FTIR experiments on diffusion were also carried out with single crystals of H-ZSM-5 as adsorbent and paraffin molecules (*n*-hexane, *n*-heptane, *n*-octane, neopentane, *n*-nonane) as diffusing species [944, 945]. In these experiments an "IR microscope" (cf. Sect. 4.1) was employed and a cell adopted from Lercher and coworkers [862, 894] after slight modifications.

Lercher et al., in their work on methylation of toluene and isomerization of xylenes, also attempted to extract diffusion coefficients of aromatics [toluene (T), xylenes (X)] from time-resolved FTIR spectroscopic measurements [815, 894]. This is an important subject in view of the subtle interdependence of rates of alkylation, isomerization and diffusion of the reactants and products with respect to selectivity in *p*-xylene formation. Data obtained for toluene diffusion in H-ZSM-5 single crystals at 320 K were $D(T) \approx (3.9\text{--}11) \times 10^{-10} \text{ cm}^2 \text{ s}^{-1}$ in reasonable agreement with related literature data determined by different techniques, whereas the diffusivities measured with polycrystalline H-ZSM-5 materials amounted only to $(1.5\text{--}1.9) \times 10^{-13} \text{ cm}^2 \text{ s}^{-1}$ (cf. also [815]). This value and the analogously derived diffusion coefficient for *p*-xylene, viz. $D(p\text{-X}) = 6 \times 10^{-12} \text{ cm}^2 \text{ s}^{-1}$ were certainly too small by two to three orders of magnitude. $D(p\text{-X})$ was found in other experiments under similar conditions to be equal to $1.5 \times 10^{-9} \text{ cm}^2 \text{ s}^{-1}$ [943], and should indeed be relatively close to that of benzene, $D(B) = 5.3 \times 10^{-10} \text{ cm}^2 \text{ s}^{-1}$ (cf. [942] and references therein) and close to or somewhat higher than that of *p*-diethylbenzene (DEB), i.e., $(p\text{-DEB}) = (1\text{--}3) \times 10^{-10} \text{ cm}^2 \text{ s}^{-1}$ [948]. It was observed that erroneously low diffusivities were sometimes due to so-called surface barriers. Uptake kinetics of *p*-xylene into single crystals of silicalite-1 and $\text{AlPO}_4\text{-5}$ were also monitored by Schueth et al. [861] using micro-infrared spectroscopy. From the uptake curves, a diffusion coefficient of $5 \times 10^{-8} \text{ cm}^2 \text{ s}^{-1}$ for *p*-xylene into silicalite-1 was derived, which was somewhat higher than the values reported in the literature. Reasons for the deviations (lower diffusion resistance in single crystals compared to pressed powders, cracks in the crystals) were discussed.

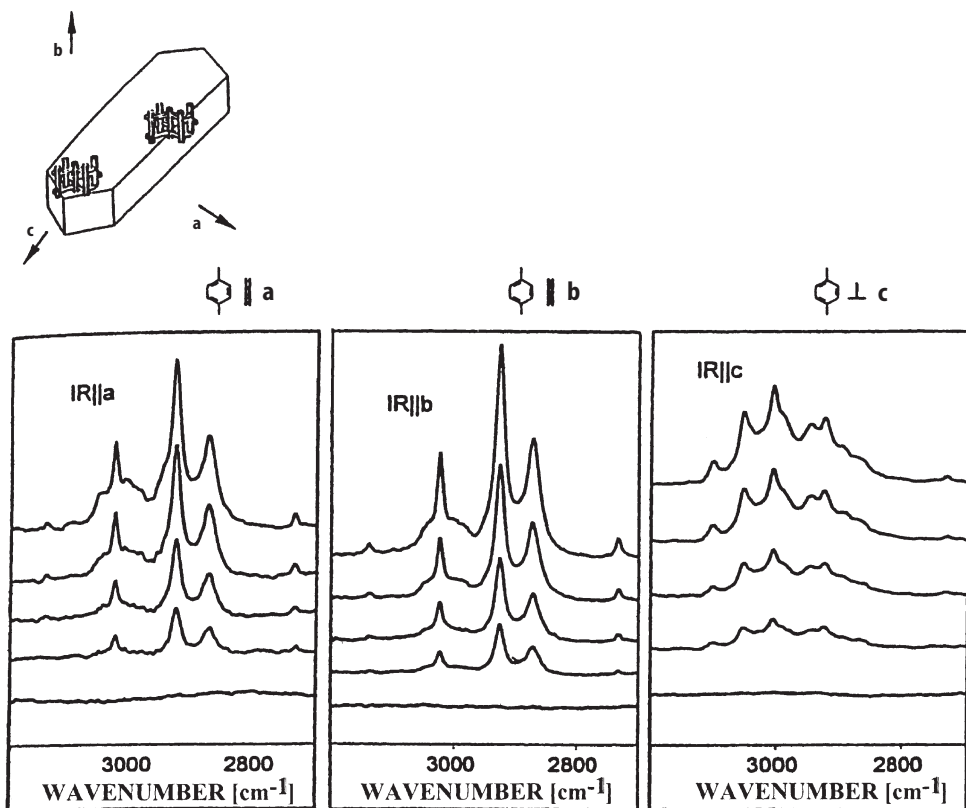


Fig. 54. Time-resolved FTIR spectra in polarized IR radiation of *p*-xylene sorption into silicalite-1 at 353 K. *From bottom to top*, the spectra correspond to the uptake of 0, 1, 2, 3 and 4 molecules of *p*-xylene per unit cell. The insert above the spectra shows schematically a silicalite-1 single crystal with the two types of straight and zigzag (or sinusoidal) channels (reproduced from [949]).

More recently, essentially the same technique as proposed by Hermann et al. [944, 945], viz. FTIR “microscopy” (Fourier transform micro-IR spectroscopy on single crystals), and by Mirth and Lercher [815], was successfully employed by Zhobolenko and Dwyer [949], who determined the transport diffusivities of a number of hydrocarbons (benzene, toluene, *p*-xylene, cyclohexane) in silicalite-1 in different crystallographic directions. No significant differences of the diffusivities in the straight and sinusoidal channels of the structure were found (cf. Fig. 54), at remarkable variance to results reported by Rees et al., who used the frequency response technique [950] and found significant differences for the diffusion coefficients in both types of channels, viz. one order of magnitude smaller ones for the sinusoidal than for the straight channels.

After all, the diffusion coefficients obtained by Zhobolenko and Dwyer were in rather good agreement with data arrived at by other authors and/or different

methods, including the determination of self-diffusion coefficients produced by NMR techniques. The method developed by Karge and co-workers was also employed for the investigation of diffusion and counter-diffusion in Corma's group [951, 952].

Hydrogen and deuterium spillover on a two-component system, viz. Pt-loaded Na-Y vs. Na-Y was investigated by Roland et al. [953], who also employed in-situ micro-FTIR spectroscopy. It could be shown that platinum is necessary to generate a hydrogen/deuterium exchange at room temperature, all zeolitic OH groups were involved in the exchange process, surface diffusion of the spilt-over deuterium species dominated and this surface diffusion as well as H/D exchange were rate-determining steps in the spillover process.

The uptake of hydrogen cyanide into protonic forms of synthetic zeolites Y, Beta, mordenite, as well as into naturally occurring clinoptilolite, ferrierite, stilbite and alumina-pillared clays were studied by Jamis et al. [954] using FTIR measurements of the $C\equiv N$ stretching vibration to characterize the binding of HCN to the various Brønsted-acid sites of the molecular sieve materials.

Diffusion processes in microporous and mesoporous materials, however, will be extensively and in more detail discussed in Volume 7 of the present series, where also the application and results not only of IR investigations but also of various other spectroscopic techniques will be included.

5.6.5

Kinetics of Solid-State Ion Exchange in Zeolites

It turned out that the kinetics of solid-state ion exchange like other reactions (cf. Sect. 5.6.3) can be monitored via time-resolved IR spectroscopy. However, to date this could be rendered possible only with the help of a probe. For instance, the exchange of Cu^+ for Na^+ in a Y-type zeolite or mordenite via solid-state reaction, proceeding in a solid mixture of $CuCl$ and Na-Y or Na-mordenite, was monitored through time-resolved FTIR in the presence of very low pressures of pyridine [955, 956]. The presence of pyridine resulted in the appearance of bands typical of pyridine attached to Na^+ ($Py \rightarrow Na^+$, bands at 1592 and 1442 cm^{-1}) and to Cu^+ ($Py \rightarrow Cu^+$, bands at 1604 and 1451 cm^{-1}). The kinetics could be described as determined by the diffusion of the in-going cation Cu^+ or the out-going cation Na^+ using the formalism of Fick's second law of diffusion. The solution of a suitable diffusion equation provided at 513 K formal diffusion coefficients for Cu^+ in Na-Y zeolite and Na-MOR of $D(Cu^+) \approx 2 \times 10^{-13}$ and $D(Cu^+) \approx 1 \times 10^{-13}$ $cm^2 s^{-1}$, respectively. However, the result that the kinetics of this example of solid-state ion exchange and similar ones could be satisfactorily described by a solution of the diffusion equation does not necessarily prove the diffusion of the exchanging cations to be the rate-determining step. More experimental work is certainly required to clarify the kinetics and mechanism of solid-state ion exchange (cf. Volume 3, Chapter 2 of the present series).

6

Concluding Remarks

This chapter has, hopefully, shown the great potential and vast applicability of vibrational spectroscopic techniques in the field of science and technology of microporous and mesoporous materials. The diversity of experimental and computational techniques in vibrational spectroscopy as well as the development of modern facilities and equipment allows us to tackle nowadays problems which seemed to be unsolvable only a short time ago. Thus, the number of reports in the field has increased immensely. Many applications became routine work. However, the prospects are still bright. The authors feel that the most promising progress in the role of vibrational spectroscopy in zeolite research will emerge from further development in computational methods, combination with various other techniques, continued access to the molecular level of processes in microporous and mesoporous materials and last but not least by the extension and perfection of in-situ observations of processes in zeolites such as synthesis, modification, diffusion, and catalytic reactions.

7

References

1. Wilson EB jr (1939) *J Chem Phys* 7:1047
2. Wilson EB jr (1941) *J Chem Phys* 9:76
3. El'jasevic MA (1940) *Dokl Acad Sci URSS* 28:605
4. Wilson EB jr, Decius JC, Cross PC (1955) *Molecular vibrations*, McGraw-Hill Book Company, Inc., New York
5. Levin IW, Pearce RAR (1975) Intramolecular force field calculations: methods and applications. In: Durig JR (ed) *Vibrational spectra and structure*, Vol 4, Elsevier, Amsterdam, p 101
6. Fadini A (1976) *Molekülkraftkonstanten*. Dr. Dietrich Steinkopff Verlag, Darmstadt
7. Blackwell CS (1979) *J Phys Chem* 83:3251, 3257
8. Pechar F (1985) *Zeolites* 5:139
9. Geidel E, Boehlig H, Peuker C, Pilz W (1988) *Z Chem* 28:155
10. Baertsch M, Bornhauser P, Calzaferri G, Imhof R (1994) *J Phys Chem* 98:2817
11. Geidel E, Boehlig H, Birner P (1991) *Z phys Chem* 171/I:121
12. Bornhauser P, Calzaferri G (1996) *J Phys Chem* 100:2035
13. No KT, Bae DH, Jhon MS (1986) *J Phys Chem* 90:1772
14. No KT, Seo BH, Jhon MS (1989) *Theoret Chim Acta* 75:307
15. Van Santen RA, Vogel DL (1989) Lattice dynamics of zeolites. In: Catlow CRA (ed), *Advances in Solid-State Chemistry*. Vol 1, JAI Press Inc., p 151
16. De Man AJM, van Santen RA (1992) *Zeolites* 12: 269,826
17. Creighton JA, Deckman HW, Newsam JM (1994) *J Phys Chem* 98:459
18. Boehlig H, Geidel E, Geiseler G (1986) *Z Chem* 26:389
19. Jacobs WPJH, van Wolput JHMC, van Santen RA (1993) *Zeolites* 13:170
20. Jacobs WPJH, van Wolput JHMC, van Santen RA (1993) *Chem Phys Lett* 210:32
21. Jacobs WPJH, van Wolput JHMC, van Santen RA (1993) *J Chem Soc, Faraday Trans* 89:1271
22. Jacobs WPJH, van Wolput JHMC, van Santen RA, Jobic H (1994) *Zeolites* 14:117
23. Bauer F, Geidel E, Peuker C, Pilz W (1996) *Zeolites* 17:278
24. Geidel E, Krause K, Foerster H, Bauer F (1997) *J Chem Soc, Faraday Trans* 93:1439
25. Gibbs GV, D'Arco P, Boisen MB jr (1987) *J Phys Chem* 91:5347

26. Etchepare J (1970) *Spectrochim Acta* 26A:2147
27. Lazarev AN (1972) *Vibrational spectra and structure of silicates*, Consultants Bureau, New York
28. Dowty E (1987) *Phys Chem Minerals* 14:67, 80 and 122
29. Bornhauser P, Calzaferri G (1990) *Spectrochim Acta* 46A:1045
30. Bornhauser P, Calzaferri G (1996) *J Phys Chem* 100:2035
31. Marcolli C, Laine P, Buehler R, Calzaferri G, Tomkinson J (1997) *J Phys Chem* 101B:1171
32. Badger RM (1934) *J Chem Phys* 2:128
33. Sauer J (1989) *Chem Rev* 89:199
34. Ermoshin VA, Smirnov KS, Bougeard D (1996) *Chem Phys* 209:41
35. Olson DH (1995) *Zeolites* 15:439
36. Geidel E, Bauer F, Boehlig H, Kudra M (1995) *Acta Chimica Hungarica – Models in Chem* 132:349
37. Bornhauser P, Bougeard D (1997) *Proceedings of the 9th German Zeolite Meeting (9. Deutsche Zeolithtagung)*, Halle, Germany, March 3–15, 1995, University of Halle, 1997, p 32
38. Bornhauser P, Bougeard D (2001) *J Phys Chem* 105B:36
39. Catlow CRA, Cormack AN (1987) *Int Rev Phys Chem* 6:227
40. Jackson RA, Catlow CRA (1988) *Molecular simulation* 1:207
41. Woodley SM, Battle PD, Gale JD, Catlow CRA (1999) *Phys Chem Chem Phys* 1:2535
42. De Man AJM, van Beest BWH, Leslie M, van Santen RA (1990) *J Phys Chem* 94:2524
43. Van Santen RA, van Beest BWH, de Man AJM (1990) In: *Guidelines for mastering the properties of molecular sieves*. NATO ASI 221, Plenum Press New York, p 201
44. Kramer GJ, Farragher NP, van Beest BWH, van Santen RA (1991) *Phys Rev B* 43:5068
45. Kramer GJ, de Man AJM, van Santen RA (1991) *J Am Chem Soc* 113:6435
46. Dick BG, Overhauser AW (1958) *Phys Rev* 112:90
47. Schroeder KP, Sauer J, Leslie M, Catlow CRA, Thomas JM (1992) *Chem Phys Lett* 188:320
48. Schroeder KP, Sauer J, Leslie M, Catlow CRA (1992) *Zeolites* 12:20
49. De Boer K, Jansen APJ, van Santen RA (1994) In: *Weitkamp J, Karge HG, Pfeifer H, Hoelderich W (eds) Zeolites and related microporous materials: State of the art 1994*, Proc 10th Int Zeolite Conf, Garmisch-Partenkirchen, Germany, July 17–22, 1994, Elsevier, Amsterdam, p 2083; *Stud Surf Sci Catal* 84:2083
50. De Boer K, Jansen APJ, van Santen RA (1994) *Chem Phys Lett* 223:46
51. Schroeder KP, Sauer J (1996) *J Phys Chem* 100:11043
52. Sierka M, Sauer J (1997) *Faraday Discuss* 106:41
53. Nachtigallova D, Nachtigall P, Sierka M, Sauer J (1999) *Phys Chem Chem Phys* 1:2019
54. Nicholas JB, Hopfinger AJ, Trouw FR, Iton LE (1991) *J Am Chem Soc* 113:4792
55. De Vos Burchart E, van Bekkum H, van de Graaf B (1992) *Collect Czech Chem Commun* 57:681
56. De Vos Burchart E, van Bekkum H, van de Graaf B, Vogt ETC (1992) *J Chem Soc, Faraday Trans* 88:2761
57. Hill J-R, Sauer J (1994) *J Phys Chem* 98:1238
58. Hill J-R, Sauer J (1995) *J Phys Chem* 99:9536
59. Maple JR, Hwang MJ, Stockfisch TP, Dinur U, Waldmann M, Ewig CS, Hagler AT (1994) *J Comput Chem* 15:162
60. Comba P, Hambley TW (1995) *Molecular modeling of inorganic compounds*, VCH Verlagsgesellschaft mbH, Weinheim
61. Allen MP, Tildesley DJ (1987) *Computer simulation of liquids*, Clarendon Press, Oxford
62. Demontis P, Suffritti GB (1992) *Molecular dynamics studies on zeolites*. In: Catlow CRA (ed), *Modelling of structure and reactivity in zeolites*, Academic Press Inc., San Diego, p 79
63. Demontis P, Suffritti GB (1997) *Chem Rev* 97:2845
64. Van de Graaf B, Njo SL, Smirnov KS (2000) *Introduction to zeolite modeling*. In: Lipkowitz KB, Boyd DB (eds) *Reviews in computational chemistry*. Vol 14, Wiley-VCH Publishers, New York, p 137

65. McQuarrie DA (1976) *Statistical mechanics*. Harper and Row, New York
66. Jobic H, Ghosh RE, Renouprez A (1981) *J Chem Phys* 75:4025
67. Berens PH, Wilson KR (1981) *J Chem Phys* 74:4872
68. Berens PH, White SR, Wilson KR (1981) *J Chem Phys* 75:515
69. Demontis P, Suffritti GB, Alberti A, Quartieri S, Fois ES, Gamba A (1986) *Gazz Chim Ital* 116:459
70. Demontis P, Suffritti GB, Quartieri S, Fois ES, Gamba A (1987) *Zeolites* 7:522
71. Demontis P, Suffritti GB, Quartieri S, Fois ES, Gamba A (1988) *J Phys Chem* 92:867
72. Schrimpf G, Schlenkrich M, Brickmann J, Bopp P (1992) *J Phys Chem* 96:7404
73. Demontis P, Suffritti GB, Bordiga S, Buzzoni R (1995) *J Chem Soc, Faraday Trans* 91: 525
74. Smirnov KS, Bougeard D (1993) *J Phys Chem* 97:9434
75. Smirnov KS, Bougeard D (1993) *J Raman Spectroscopy* 24:255
76. Smirnov KS, Bougeard D (1994) *Zeolites* 14:203
77. Smirnov KS, Le Maire M, Brémard CC, Bougeard D (1994) *Chem Phys* 179: 445
78. Smirnov KS, Bougeard D (1995) *J Mol Struct* 348:155
79. Krause K, Geidel E, Kindler J, Foerster H, Smirnov KS (1996) *Vibrational Spectroscopy* 12:45
80. Ermoshin VA, Smirnov KS, Bougeard D (1996) *Chem Phys* 202:53
81. Ermoshin VA, Smirnov KS, Bougeard D (1996) *Surf Sci* 368:147
82. Bougeard D, Smirnov KS, Geidel E (2000) *J Phys Chem* 104B:9210
83. Sauer J (1992) Quantum mechanical studies of zeolites. In: Catlow CRA (ed) *Modelling of structure and reactivity in zeolites*, Academic Press Inc., San Diego, p 183
84. Sauer J, Ugliengo P, Garrone E, Saunders VR (1994) *Chem Rev* 94:2095
85. *Ab initio and ab initio derived force fields: State of the science* (1997) *Spectrochim Acta* 53A: special issue
86. Hehre WJ, Radom L, Schleyer PvR, Pople JA (1986) *Ab initio molecular orbital theory*. Wiley, New York
87. Scott AO, Radom L (1996) *J Phys Chem* 100:16502
88. Blom CA, Altona C (1976) *Mol Phys* 31:1377
89. Pulay P, Fogarasi G, Pongor G, Boggs JE, Vargha A (1983) *J Am Chem Soc* 105:7037
90. Pulay P (1995) *J Mol Struct* 347:293
91. Baker J, Jarzecki AA, Pulay P (1998) *J Phys Chem* 102A:1412
92. Rauhut G, Pulay P (1995) *J Phys Chem* 99:3093
93. White JC, Hess AC (1993) *J Phys Chem* 97:6389, 8703
94. Nicholas JB, Hess AC (1994) *J Am Chem Soc* 116:5428
95. Anchell JL, White JC, Thompson MR, Hess AC (1994) *J Phys Chem* 98:4463
96. White JC, Nicholas JB, Hess AC (1997) *J Phys Chem* 101B:590
97. Zicovich-Wilson CM, Corma A (2000) *J Phys Chem* 104B:4134
98. Hess AC, McMillan PF, O'Keeffe M (1986) *J Phys Chem* 90:5661
99. Sauer J (1987) *J Phys Chem* 91:2315
100. Hess AC, McMillan PF, O'Keeffe M (1988) *J Phys Chem* 92:1785
101. Datka J, Geerlings P, Mortier W, Jacobs P (1985) *J Phys Chem* 89:3483
102. Sauer J, Hill J-R (1989) *Z phys Chem, Leipzig* 270:203
103. Nicholas JB, Winans RE, Harrison RJ, Iton LE, Curtiss LA, Hopfinger AJ (1992) *J Phys Chem* 96: 7958,10247
104. O'Keeffe M, McMillan PF, (1986) *J Phys Chem* 90:541
105. Lasaga AC, Gibbs GV (1987) 14:107
106. Lasaga AC, Gibbs GV (1988) 16:29
107. De Man AJM, Sauer J (1996) *J Phys Chem* 100:5025
108. Pereira JCG, Catlow CRA, Price GD (1999) *J Phys Chem* 103A:3252, 3268
109. Sierka M, Eichler U, Datka J, Sauer J (1998) *J Phys Chem* 102B:6397
110. Sauer J (1997) *Preprints Symp Adv and Appl Computational Chemistry Modeling*, San Francisco, USA, April 13–17, 1997, *Am Chem Soc, Washington DC*, 1997, 42:53
111. Eichler U, Braendle M, Sauer J (1997) *J Phys Chem* 101B:10035

112. Flanigen EM, Khatami H, Szymanski HA (1970) In: Flanigen EM, Sand LB (eds) 2nd Int Conf Molecular Sieves, Worcester, Mass, USA, Sept 8–11, 1970, Am Chem Soc, Washington, DC, 1971, p 201; Adv Chem Ser 101:201
113. Geidel E, Boehlig H, Peucker C, Pilz W (1991) In: Oehlmann G, Pfeifer H, Fricke R (eds) Catalysis and adsorption by zeolites. Proc Int Symp, ZEOCAT '90, Leipzig, Germany, August 20–23, 1990, Elsevier, Amsterdam, 1991, p 511; Stud Surf Sci Catal 65:511
114. Flanigen EM (1976) Structural analysis by infrared spectroscopy. In: Rabo JA (ed) Zeolite chemistry and catalysis, Am Chem Soc, Washington DC, 1976; ACS Monograph No 171, Chapter 2, p 80
115. Vimont A, Thibault-Starzyk F, Lavalley JC (2000) J Phys Chem 104B:286
116. Pichat P, Beaumont R, Barthomeuf D (1974) J Chem Soc, Faraday Trans I 70:1402
117. Krause K, Geidel E, Kindler J, Foerster H, Boehlig H (1995) J Chem Soc, Chem Commun 2481
118. Iyer KA, Singer SJ (1994) J Phys Chem 98:12670
119. Iyer KA, Singer SJ (1994) J Phys Chem 98:12679
120. Smirnov KS, Bougeard D (2001) Catal Today 70:243
121. Colthup NB (1950) J Opt Soc Am 40:398
122. Herzberg G (1945) Molecular spectra and molecular structure – II Infrared and Raman spectra of polyatomic molecules, van Nostrand Reinhold Comp, New York, p 196
123. Hair ML (1967) Infrared spectroscopy in surface chemistry. Marcel Dekker, New York, p 47
124. Hair ML (1967) Infrared spectroscopy in surface chemistry. Marcel Dekker, New York, p 292
125. Drago RS (1977) Physical methods in chemistry. WB Saunders Company, Philadelphia, London, Toronto, p 165
126. Karge H (1971) Z phys Chem, Neue Folge 76:133 (cf. especially pp 145 and 146)
127. Jentys A, Warecka G, Derewinski M, Lercher JA (1989) J Phys Chem 93:4837
128. Karge HG, Hunger M, Beyer HK (1999) In: Weitkamp J, Puppe L (eds) Catalysis and zeolites – fundamentals and applications. Springer Verlag, Berlin, Heidelberg, New York, p 203
129. Jacobs PA, Leeman HE, Uytterhoeven JB (1974) J Catal 33:17
130. Jacobs PA, Uytterhoeven JB (1972) J Catal 26:175
131. Khabtou S, Chevreau T, Lavalley JC (1994) Microporous Mater 3:133 (and references therein)
132. Niessen W, Dissertation (PhD thesis) University of Technology, Berlin, 1991
133. Wichterlová B, Zilkova N, Uvarova E, Cejka J, Priti S, Paganini C, Lercher JA (1999) Appl Catal A: General 182:297
134. Datka J, Gil B, Kubacka A (1996) Zeolites 17:428
135. Take J, Yamaguchi T, Miyamoto K, Ohyama H, Misono M (1986) In: Murakami Y, Iijima A, Ward JW (eds) New developments in zeolite science and technology. Proc 7th Int Zeolite Conf, Tokyo, Japan, August 17–22, 1986, Kodansha, Tokyo, Elsevier, Amsterdam, 1986, p 495; Stud Surf Sci Catal 28:495
136. Anderson MA, Klinowski J (1986) Zeolites 6:455
137. Taouli A, Klemm A, Breede M, Reschetilowski W (1999) In: Kiricsi I, Pál-Borbély G, Nagy JB, Karge HG (eds); Porous materials in environmentally friendly processes. Proc 1st Int FEZA Conf, Eger, Hungary, September 1–4, 1999, Elsevier, Amsterdam, 1999, p 307; Stud Surf Sci Catal 125:307
138. Guisnet M, Ayrault P, Datka J (1998) Microporous Mesoporous Mater 20:283
139. Benesi HA (1973) J Catal 28:176
140. Maache M, Janin A, Lavalley JC, Benazzi E (1995) Zeolites 15:507
141. Datka J, Gil B, Kubacka A (1995) Zeolites 15:501
142. Fink P, Datka J (1989) J Chem Soc, Faraday Trans I, 85:3079
143. Datka J (1981) Zeolites 1:113
144. Emeis CA (1993) J Catal 141:347
145. Bell AT (1980) In: Bell AT, Hair ML (eds) Vibrational spectroscopies for adsorbed species. ACS Symposium Series 137. American Chemical Society, Washington DC, p 13

146. Hair ML (1967) *Infrared spectroscopy in surface chemistry*. Marcel Dekker, New York, Chapter 2, p 19, and Chapter 3, p 53
147. Hair ML (1980) In: Bell AT, Hair ML (eds) *Vibrational spectroscopies for adsorbed species*. ACS Symposium Series 137. American Chemical Society, Washington DC, 1980, p 1
148. Drago RS (1977) *Physical methods in chemistry*. WB Saunders Company, Philadelphia, London, Toronto, p 133
149. Karge HG, Hunger M, Beyer HK (1999) In: Weitkamp J, Puppe L (eds) *Catalysis and zeolites – fundamentals and applications*. Springer-Verlag, Berlin, Heidelberg, New York, p 204
150. Guenzler H, Boeck H (1975) *IR-Spektroskopie – Eine Einfuehrung*. Verlag Chemie. Physik Verlag, Weinheim, (cf. especially p 287)
151. Hair ML (1967) *Infrared spectroscopy in surface chemistry*. Marcel Dekker, New York, p 72
152. Karge HG, Hunger M, Beyer HK (1999) In: Weitkamp J, Puppe L (eds) *Catalysis and zeolites – fundamentals and applications*. Springer Verlag, Berlin, Heidelberg, New York, p 208–211
153. Gallei E, Schadow E (1974) *Rev Sci Instruments* 45:1504
154. Cohen de Lara E, Delaval Y, Tsakiris J (1976) *J Chemie Physique* 73:387
155. Foerster H, Meyn V, Schuldt M (1978) *Rev Sci Instrum* 49:74
156. Mirth G, Eder F, Lercher JA (1994) *Appl Spectroscopy* 48:194
157. Mueller G, Narbeshuber T, Mirth G, Lercher JA (1994) *J Phys Chem* 98:7436
158. Karge HG, Niessen W (1991) *Catalysis Today* 8:451
159. Karge HG, Hunger M, Beyer HK (1999) In: Weitkamp J, Puppe L (eds) *Catalysis and zeolites – fundamentals and applications*. Springer-Verlag, Berlin, Heidelberg, New York, pp 210, 211
160. Klier K (1980) In: Bell AT, Hair ML (eds) *Vibrational spectroscopies for adsorbed species*. ACS Symposium Series 137. American Chemical Society, Washington DC, p 141
161. Karge HG, Hunger M, Beyer HK (1999) In: Weitkamp J, Puppe L (eds) *Catalysis and zeolites – fundamentals and applications*. Springer Verlag, Berlin, Heidelberg, New York, p 206
162. Geidel E, Lechert H, Doeblner J, Jobic H, Calzaferri G, Bauer F (2003) *Microporous Mesoporous Mater* (in press)
163. Kosslick H, Lischke G, Walther G, Storek W, Martin A, Fricke R (1997) *Microporous Mater* 9:13
164. Hunger M, Schenk U, Breuninger M, Glaeser R, Weitkamp J (1999) *Microporous Mesoporous Mater* 27:261
165. Katoric A, Giordano G, Bonelli B, Onida B, Garrone E, Lentz P, B-Nagy J (2001) *Microporous Mesoporous Mater* 44/45:275
166. Lucchesi PJ, Charter JL, Yates DJC (1962) *J Phys Chem* 66:1451
167. Shen JH, Klier K, Zettlemoyer AC (1973) *J Phys Chem* 77:1458
168. Shen JH, Klier K (1980) *J Colloid Interface Sci* 75:56
169. Klier K (1980) In: Bell AT, Hair ML (eds) *Vibrational spectroscopies for adsorbed species*, ACS Symposium Series 137. American Chemical Society, Washington DC, 1980, p 141
170. Schuster A (1905) *Astrophysics J* 21:1
171. Kubelka P (1948) *J Opt Soc Am* 38:448
172. Kubelka P, Munk F (1931) *Z Tech Phys* 12:593
173. Kortuem G (1969) *Reflexionsspektroskopie – Grundlagen, Methodik, Anwendungen*. Springer-Verlag, Berlin, Heidelberg, New York, S. 114; English edition: Springer-Verlag Berlin, Heidelberg, New York, 1969, p 111
174. Delgass WN, Haller GL, Kellermann R, Lunsford JH (1979) *Spectroscopy in catalysis*. Academic Press, New York, p 114
175. Klier K (1967) *Catalysis Reviews* 1:207
176. Harrick Scientific Corporation, 88 Broadway Ossining, NY
177. Kazansky VB, Borovkov VYu, Karge HG (1997) *J Chem Soc, Faraday Trans* 93:1843

178. Harkness IR, Cavers M, Rees LVC, Davidson JM, McDougall GS (1998) In: Treacy MMJ, Marcus BK, Bisher ME, Higgins JB (eds) Proceedings of the 12th Int Zeolite Conf. Baltimore, USA, July 5–10, Materials Research Society, Warrendale, Pa, USA, 1999, p 2615
179. Delgass WN, Haller GL, Kellermann R, Lunsford JH (1979) Spectroscopy in catalysis. Academic Press, New York, p 95
180. Karge HG, Hunger M, Beyer HK (1999) In: Weitkamp J, Puppe L (eds) Catalysis and zeolites – fundamentals and applications. Springer-Verlag, Berlin, Heidelberg, New York, p 207
181. Blank VB, Wakefield T (1979) Anal Chem 51:50
182. Sullivan DH, Conner WC, Harold MP (1992) Appl Spectroscopy 46:811 (and references therein)
183. Morrow BA (1980) In: Bell AT, Hair ML (eds) Vibrational spectroscopies for adsorbed species. ACS Symposium Series 137, American Chemical Society, Washington DC, p 119
184. Morrow BA (1977) J Phys Chem 81: 2663
185. Delgass WN, Haller GL, Kellermann R, Lunsford JH (1979) Spectroscopy in heterogeneous catalysis. Academic Press, New York, p 58
186. Drago RS (1977) Physical methods in chemistry. W B Saunders Comp, Philadelphia, p 146
187. Angell CL (1973) J Phys Chem 77: 222
188. Pilz W, Kriegsmann H (1987) Z phys Chem, Leipzig 268: 215
189. Pilz W (1990) Z phys Chem, Leipzig 271:219
190. Egerton TA, Hardin AH (1975) Catal Rev-Sci Eng 11: 71
191. Hendra PJ, Passingham C, Warnes GM, Burch R, Rawlence DJ (1989) Chem Phys Lett 164:178
192. Hendra PJ, Jones C, Warner G (1991), Fourier Transform Raman Spectroscopy, Instrumentation and Chemical Applications, Ellis Horwood, New York (cf. especially p 246)
193. Knops-Gerrits P-P, de Vos DE, Feijen EJP, Jacobs PA (1997) Microporous Mater 8:3
194. Burch R, Passingham C, Warnes GM, Rawlence DJ (1990) Spectrochim Acta 46A:243
195. Brémard C, Bougeard D (1995) Adv Mater 7:10
196. Hudson BS (2001) J Phys Chem 105A:3949
197. Cohen de Lara E, Kahn R (1992) In: Davies JED (ed), Spectroscopic and computational studies of supramolecular systems“ – Neutron scattering studies of zeolite complexes. Kluwer Academic Press, The Netherlands, Dordrecht, 1992, p 83
198. Jobic H (1992) Spectrochim Acta 48A:293
199. Trouw FR (1992) Spectrochim Acta 48A:455
200. Kearly GJ (1992) Spectrochim Acta 48A:349
201. Szymanski HA, Stamires DN, Lynch GR (1960) J Optical Soc Am 50:1323
202. Bertsch L, Habgood HW (1963) J Phys Chem 67:1621
203. Tsitsishvili GV (1973) In: Meier WM, Uytterhoeven JB (eds) Molecular Sieves, Proc 3rd Int Conf on Molecular Sieves, Sept 3–7, 1973, Zurich, Switzerland, Advances in Chemistry Series 121:291, Am Chem Soc, Washington, D.C., 1973, p 291
204. Watanabe Y, Habgood HW (1968) J Phys Chem 72:3066
205. Uytterhoeven JB, Christner LG, Hall WK (1965) J Phys Chem 69:2117
206. Cant NW, Hall WK (1968) Trans Faraday Soc 64:1093
207. Ward JW (1968) J Catal 11:251
208. Liengme BV, Hall WK (1966) Trans Faraday Soc 62:3229
209. Cant NW, Hall WK (1972) J Catal 25:161
210. Hall WK (1967) Chem Engng Progress, Symp Series 63:68
211. Richardson RL, Benson SW (1957) J Phys Chem 61:405
212. Parry EP (1963) J Catal 2:371
213. Angell CL, Schaffer PC (1966) J Phys Chem 70:1413
214. Yates DJC (1968) In: Molecular sieves, Soc Chem Industry, London, UK, p 334
215. Yates DJC (1969) Catal Rev 2:113
216. Cohen de Lara E (1980) In: Rees LVC (ed) Proc 5th Int Zeolite Conf, Naples, Italy, June 2–6, 1980, Heyden, London, p 414
217. Boese H, Foerster H, Frede W, Schumann M (1984) In: Olson D, Bisio A (eds) Proc 6th Int Zeolite Conf, Reno, Nevada, USA, July 10–15, 1983, Butterworths, Guildford, UK, p 201

218. Jacobs PA, Theng BKG, Uytterhoeven JB (1972) *J Catal* 26:191
219. Weeks TJ, Angell CL, Ledd JR, Bolton AP (1974) *J Catal* 33:256
220. Jentys A, Mirth G, Schwank J, Lercher JA (1989) In: Jacobs PA, van Santen RA (eds) *Zeolites: Facts, figures, future*, Proc 8th Int Zeolite Conf, Amsterdam, The Netherlands, July 10–14, 1989, Elsevier, Amsterdam, 1989, p 847; *Stud Surf Sci Catal* 49:847
221. Philippaerts J, Peeters G, Vansant EF, de Hulsters P, Verbiest J (1986) In: Murakami Y, Iijima A, Ward JW (eds) *New developments in zeolite science and technology*. Proc 7th Int Zeolite Conf, Tokyo, Japan, August 17–22, 1986, Kodansha, Tokyo, Elsevier, Amsterdam, 1986, p 319; *Stud Surf Sci Catal* 28:319
222. Karge HG (1973) *Surface Sci* 40:157
223. Schweckendiek J (1982) PhD Thesis, University of Bremen
224. Karge HG, Schweckendiek J (1983) In: Shopov D, Andreev A, Palazov A, Petrov L (eds) *Proc Vth Int Symp Heterogeneous Catalysis*, Varna, Bulgaria, Publishing House Bulgarian Acad Sci, Sofia, p 429
225. Karge HG, Trevizan de Suarez S, Dalla Lana IG (1984) *J Phys Chem* 88:1782
226. Karge HG, Zhang Y, Trevizan de Suarez S, Ziolk M (1984) In: Jacobs PA, Jaeger NI, Jiru P, Kazansky VB, Schulz-Ekloff G (eds) *Structure and reactivity of modified zeolites* Proc Int Conf, Prague, July 9–13, 1984, Elsevier, Amsterdam, 1984, p 49; *Stud Surf Sci Catal* 18:49
227. Karge HG, Ziolk M, Laniecki M (1987) *Zeolites* 7:197
228. Karge HG, Laniecki M, Ziolk M (1986) In: Murakami Y, Iijima A, Ward JW (eds) *New developments in zeolite science and technology*. Proc 7th Int Zeolite Conf, Tokyo, Japan, August 17–22, 1986, Kodansha, Tokyo, Elsevier, Amsterdam, 1986, p 617; *Stud Surf Sci Catal* 28:617
229. Morrow BA (1980) In: Bell AT, Hair ML (eds) *Vibrational spectroscopies of adsorbed species*, ACS Symp Ser 137, Am Chem Soc, Washington, DC, USA, 1980, pp 120–122
230. Yates DJC (1967) In: Soc Chem Industry (ed) *Molecular sieves*, Proc 1st Int Zeolite Conf, London, UK, April 4–6, 1967, Soc Chem Ind, London, 1968, p 334
231. Ward JW (1976) In: Rabo JA (ed) *Zeolite chemistry and catalysis*, ACS Monograph 171, Am Chem Soc, Washington DC, p 118
232. Baker MD, Ozin GA, Godber J (1985) *Catal Rev-Sci Eng* 27: 591
233. Foerster H (1992) In: Davis JE (ed) *Spectroscopic and computational studies of supramolecular systems, Infrared studies of zeolite complexes*, Kluwer Academic Publishers, Dordrecht, The Netherlands, 1992, p 29
234. Karge HG, Hunger M, Beyer HK (1999) In: Weitkamp J, Puppe L (eds) *Catalysis and zeolites – Fundamentals and applications*, Springer-Verlag, Berlin, Heidelberg, New York, 1999, p 198
235. Baerlocher C, Meier WM, Olson DH, (2001) *Atlas of zeolite framework types*, 5th edn, Elsevier, Amsterdam, 302 pp
236. Breck DW (1974) *Zeolite molecular sieves – Structure, chemistry, and use*, John Wiley & Sons, New York, pp 96, 175, 356, 358, 366, 316, 368
237. Jacobs WPJH, de Man AJM, van Wolput JHMC, van Santen RA (1992) In: von Ballmoos R, Higgins JB, Treacy MMJ (eds) *Proc 9th Int Zeolite Conf*, Montreal, Canada, July 5–10, 1992, Butterworth-Heinemann, Boston, 1993, Vol I, p 529
238. White WB, Roy R (1964) *Am Mineral* 49:1670
239. Dutz H (1969) *Ber Deutsche Keram Ges* 46:75 (and references therein)
240. Geidel E (1989) PhD Thesis, University of Leipzig, Germany
241. Beyer HK, Belenykaja IM, Hange F (1985) *J Chem Soc, Faraday Trans I* 81:2889
242. Kubelkova L, Seidl V, Borbely G, Beyer HK (1988) *J Chem Soc, Faraday Trans I* 84:1447
243. Engelhardt G, Lohse U, Samoson A, Maegi M, Tarmak M, Lippma E (1982) *Zeolites* 2:59
244. Engelhardt G, Michel D (1987) *High-resolution solid-state NMR of silicates and zeolites*. Wiley, Chichester, cf. especially Chapter IV.4, p 148
245. Fyfe CA (1983) *Solid state NMR for chemists*. CFC Press, Guelph, Canada, cf. especially Chapter 7.3, p 337
246. Miecznikowski A, Hanuza J (1985) *Zeolites* 5:188
247. Miecznikowski A, Hanuza J (1987) *Zeolites* 7:249 (cf. especially p 250)

248. Geidel E (1997) Habilitationsschrift (Habilitation Thesis), University of Hamburg
249. Dutta PK, Shieh DC, Puri M (1988) *Zeolites* 8:306 (cf. especially p 308)
250. Falabella Sousa-Aguiar E, Comorim LD, Zotin FMZ, Correira dos Santos RL (1998) *Microporous Mesoporous Mater* 25:25
251. Ballivet D, Pichat P, Barthomeuf D (1977) In: Katzer J (ed) *Molecular Sieves-II*, Proc 4th Int Zeolite Conf, Chicago, Ill, USA, April 18–22, 1977, p 469; ACS Symp Ser, Am Chem Soc, Washington DC, 1977, 40:469
252. Yu Y, Xiong G, Li C, Xiao F-S (2001) *Microporous Mesoporous Mater* 46:23
253. Jacobs WPJH, Jobic H, van Wolput JHMC, van Santen RA (1994) *Zeolites* 12:315
254. Cairon O, Khabtou S, Balanzat E, Janin A, Marzin M, Chambellan A, Lavalley JC, Chevreau T (1994) In: Weitkamp J, Karge HG, Pfeifer H, Hoelderich W (eds) *Zeolites and related microporous materials: State of the art 1994*. Proc 10th Int Zeolite Conf, Garmisch-Partenkirchen, Germany, July 17–22, 1994, Elsevier, Amsterdam, 1994, p 997; *Stud Surf Sci Catal* 84:997
255. Huang Y, Jiang Z (1997) *Microporous Mater* 12:341
256. Baertsch M, Bornhauser P, Calzaferrri G, Imhof R (1994) In: Weitkamp J, Karge HG, Pfeifer H, Hoelderich W (eds) *Zeolites and related microporous materials: State of the art 1994*, Proc 10th Int Zeolite Conf, Garmisch-Partenkirchen, Germany, July 17–22, 1994, Elsevier, Amsterdam, 1994, p 2089; *Stud Surf Sci Catal* 84:2089
257. Stein A, Ozin GA (1992) In: von Ballmoos R, Higgins JB, Treacy MMJ (eds) *Proc 9th Int Zeolite Conf*, Montreal, Canada, July 5–10, 1992, Butterworth-Heinemann, Boston, 1993 Vol I, p 93
258. Elizalde-González MP, Mattusch J, Wennrich R, Morgenstern (2001) *Microporous Mesoporous Mater* 46:277
259. Rodríguez-Fuentes G, Ruiz-Salvador AR, Mir M, Picazo O, Quintana G, Delgado M (1998) *Microporous Mesoporous Mater* 20:269
260. Occelli ML, Ritz GP, Iyer PS, Walker RD, Gerstein BC (1989) *Zeolites* 9:104
261. Roessner F, Steinberg K-H, Rudolf A, Staudte B (1989) *Zeolites* 9:371
262. Carvalho AP, Brotas de Carvalho M, Ramôa Ribeiro F, Fernandez C, B-Nagy J, Derouane EG, Guisnet M (1993) *Zeolites* 13:462
263. Yang C, Xu Q (1997) *Zeolites* 19:404
264. Fejes P, Hannus I, Kiricsi I (1984) *Zeolites* 4:73
265. Sobalík Z, Tvaruzková Z, Wichterlová B (1998) *Microporous Mesoporous Mater* 25:225
266. Pechar F, Rykl D (1983) *Zeolites* 3:329
267. Ciambelli P, Porcelli C, Valentino R (1980) In: Rees LVC (ed) *Proc 5th Int Zeolite Conf*, Naples, Italy, Heyden, London, p 119
268. Miecznikowski A, Hanuza J (1987) *Zeolites* 7: 249 (cf. especially p 251)
269. Mihailova B, Engstroem V, Hedlund J, Holmgren A, Sterte J (1999) *Microporous Mesoporous Mater* 32:297
270. Mihailova B, Engstroem V, Hedlund J, Holmgren A, Sterte J (1999) In: Kiricsi I, Pál-Borbély G, Nagy JB, Karge HG (eds); *Porous materials in environmentally friendly processes*. Proc 1st Int FEZA Conf, Eger, Hungary, September 1–4, 1999, Elsevier, Amsterdam, 1999, p 221; *Stud Surf Sci Catal* 125:221
271. Kubelková L, Hoser H, Riva A, Trifirò F (1983) *Zeolites* 3:244
272. Corma A, Corell C, Pérez-Pariente J (1995) *Zeolites* 15:2
273. Corma A, Corell C, Pérez-Pariente J, Guil JM, Guil-López R, Nicolopoulos S, Gonzales Calbet J, Vallet Regi M (1996) *Zeolites* 16:7
274. Ravishankar R, Bhattacharya D, Jacob NE, Sivasanker S (1995) *Microporous Mater* 4:83
275. Ernst S, Weitkamp J (1990) In: Oehlmann G, Pfeifer H, Fricke R (eds) *Catalysis and adsorption by zeolites*. Proc ZEOCAT '90, Leipzig, Germany, August 20–23, 1990, Elsevier, Amsterdam, 1991, p 645; *Stud Surf Sci Catal* 65:645
276. Coudurier G, Nacchache C, Vedrine JC (1982) *J Chem Soc, Chem Commun* 1413
277. Hong SB (1995) *Microporous Mesoporous Mater* 4:309
278. De Man AJM, Jacobs WPJH, Gilson JP, van Santen RA (1992) *Zeolites* 12:826
279. De Man AJM, Ueda S, Annen MJ, Davis ME, van Santen RA (1992) *Zeolites* 12:789

280. Annen MJ, Davis ME (1993) *Microporous Mater* 1:57
281. Sinha AK, Hegde SG, Jacob NE, Sivasanker S (1997) *Zeolites* 18:350
282. Coutinho D, Orozio-Tevan RA, Reidy RE, Balkus jr KJ (2002) *Microporous Mesoporous Mater* 54:229
283. Huang Y, Jiang Z, Schwieger W (1998) *Microporous Mesoporous Mater* 26:215
284. Li S, Xu R, Lu Y, Xu Y (1992) In: von Ballmoos R, Higgins JB, Treacy MMJ (eds) *Proc 9th Int Zeolite Conf, Montreal, Canada, July 5–10, 1992*, Butterworth-Heinemann, Boston, 1993, Vol I, p 345
285. Maxwell IE, Baks A (1973) In: Meier WM, Uytterhoeven JB (eds) *Molecular Sieves, Proc 3rd Int Zeolite Conf, Zurich, Switzerland, September 3–7, 1973*, *Advances in Chemistry Series* 121:87; Am Chem Soc, Washington, DC, 1973, p 87
286. Mellot CF, Davidson AM, Eckert J, Cheetham AK (1998) *J Phys Chem* 104 B:2530
287. Davidson AM, Mellot CF, Eckert J, Cheetham AK (2000) *J Phys Chem* 102 B:2530
288. Huang Y, Qiu P (1998) In: Treacy MMJ, Marcus BK, Bisher ME, Higgins JB (eds) *Proc 12th Int Zeolite Conf, Baltimore, USA, July 5–10, 1998*, Materials Research Society, Warrendale, Pa, USA, 1999, p 2431
289. Huang Y, Havenga EA (2000) *J Phys Chem* 104B:5084
290. Dutta PK, Del Barco B (1988) *J Phys Chem* 92:354
291. Dutta PK, Twu J (1991) *J Phys Chem* 95:2498
292. Pilz W, Peuker Ch, Moeller K, Oschuetz F, Kunath D, Lohse U, Buelow M, Samulevic VN (1983) *Z phys Chem, Leipzig* 264:217
293. Dutta PK, Del Barco B (1985) *J Phys Chem* 89:1861
294. Boulet H, Brémard C, Le Maire M (1992) *J Raman Spectroscopy* 23:421
295. Brémard C, Le Maire M (1993) *J Phys Chem* 97:9695
296. Bougeard D, Brémard C, Dumont D, Le Maire M, Manoli JM, Potvin C (1998) *J Phys Chem* 102B:10805
297. Pilz W, Peuker Ch, Tuan VA, Fricke R, Kosslick HZ (1993) *Ber Bunsenges Phys Chem* 97:1037
298. Scarano D, Zecchina A, Bordiga S, Geobaldo F, Spoto G, Petrini G, Leofanti G, Padovan M, Tozzola G (1993) *J Chem Soc, Faraday Trans* 89:4123 (cf. especially p 4125)
299. McMillan PF (1984) *Am Miner* 69:622
300. Dutta PK, Shieh DC, Puri M (1988) *Zeolites* 8:306 (cf. especially pp 306 and 307)
301. Roelofsen JW, Mathies H, de Groot RL, van Woerkom PCM (1986) In: Murakami Y, Iijima A, Ward JW (eds) *New developments in zeolite science and technology. Proc 7th Int Zeolite Conf, Tokyo, Japan, August 17–22, 1986*, Kodansha, Tokyo, Elsevier, Amsterdam, 1986, p 337; *Stud Surf Sci Catal* 28:337
302. Park GG, Chae HJ, Nam I-S, Choung JW, Choi KH (2001) *Microporous Mesoporous Mater* 48:337
303. Musa M, Tarina V, Sioica AD, Ivanov E, Plostinaru D, Pop E, Pop G, Ganea R, Birjega R, Muscà G, Paukshtis EA (1987) *Zeolites* 7:427
304. Lutz W, Zibrowius B, Loeffler E (1994) In: Weitkamp J, Karge HG, Pfeifer H, Hoelderich W (eds) *Zeolites and related microporous materials: State of the art 1994, Proc 10th Int Zeolite Conf, Garmisch-Partenkirchen, Germany, July 17–22, 1994*, Elsevier, Amsterdam, 1994, p 1005; *Stud Surf Sci Catal* 84:1005
305. Lutz W, Ruescher CH, Heidemann D (2002) *Microporous Mesoporous Mater* 55: 193 (and references therein)
306. Maache M, Janin A, Lavalley JC, Joly JF, Benazzi E (1993) *Zeolites* 13:419
307. Ponthieu E, Grange P, Joly J-F, Raatz F (1992) *Zeolites* 12:395
308. Jansen JC, de Ruiter R, Biron E, van Bekkum H, (1989) In: Jacobs PA, van Santen RA (eds) *Zeolites: Facts, figures, future, Proc 8th Int Zeolite Conf, Amsterdam, The Netherlands, July 10–14, 1989*, Elsevier, Amsterdam, 1989, p 679; *Stud Surf Sci Catal* 49:679
309. Perego G, Bellussi G, Corno C, Taramasso M, Buonomo F, Esposito A (1986) In: Murakami Y, Iijima A, Ward JW (eds) *New developments in zeolite science and technology. Proc 7th Int Zeolite Conf, Tokyo, Japan, August 17–22, 1986*, Kodansha, Tokyo, Elsevier, Amsterdam, 1986, p 129

310. Bellussi G, Fattore V (1991) In: Jacobs PA, Jaeger NI, Kubelková L, Wichterlová (eds) Zeolite chemistry and catalysis, Proc Int Symp, Prague, Czechoslovakia, Sept 8–13, 1991, Elsevier, Amsterdam, 1991, p 79; Stud Surf Sci Catal 69:79
311. Pirutko LV, Uriarte AK, Cheruyarsky VS, Kharitonov AS, Panov GI (2001) Microporous Mesoporous Mater 48:345
312. Deo G, Turek AM, Wachs IE, Huybrechts DRC, Jacobs PA (1993) Zeolites 13:365
313. Mihailova B, Valtchev V, Mintova S, Konstantinov L (1996) Zeolites 16:22
314. Kim WJ, Lee MC, Yoo JC, Hayhurst DT (2000) Microporous Mesoporous Mater 41:79
315. Liepold A, Roos K, Reschetilowski W, Lin Z, Rocha J, Philippou A, Anderson MW (1997) Microporous Mater 10:211
316. Yang X, Paillaud J-L, van Breukelen HFJ, Kessler H, Duprey E (2001) Microporous Mesoporous Mater 46:1
317. Goutier S, Tuel A (1996) Zeolites 16:18
318. Tuel A, Ben Taarit (1993) Microporous Mater 1:179 (and references therein)
319. Bengoa JF, Gallegos NG, Marchetti SG, Alvarez AM, Cagnoli MV, Yeramian AA (1998) Microporous Mesoporous Mater 24:163
320. Gao H, Lu W, Chen Q (2000) Microporous Mesoporous Mater 34:307
321. Li C, Xiong G, Xin Q, Liu J, Ying P, Feng Z, Li J, Yang W, Wang Y, Wang G, Liu X, Min E (2000) Angew Chem Int Ed 38:2220
322. Das TK, Chandwadkar AJ, Budhkar AP, Sivasanker S (1996) Microporous Mater 5:401
323. Bellussi G, Rigutto MS (2001) In: van Bekkum H, Flanigen EM, Jacobs PA, Jansen JC (eds) Introduction to zeolite science and practice, Elsevier, Amsterdam, 2001, p 911; Stud Surf Sci Catal 137:911
324. Scarano D, Zecchina A, Bordiga S, Geobaldo F, Spoto G, Petrini G, Leofanti G, Padovan M, Tozzola G (1993) J Chem Soc, Faraday Trans 89:4123
325. Astorino E, Peri JB, Willey RJ, Busca G (1995) J Catal 157:482
326. Boccuti M, Rao K, Zecchina A, Leofanti G, Petrini G (1989) In: Morterra C, Zecchina A, Costa G (eds) Structure and reactivity of surfaces, Proc European Conf, Trieste, Italy, Sept 13–16, 1988, Elsevier, Amsterdam, 1989 p 1; Stud Surf Sci Catal 48:1
327. Zecchina A, Spoto G, Bordiga S, Ferrero A, Petrini G, Leofanti G, Podovan M (1991) In: Jacobs PA, Jaeger NI, Kubelková L, Wichterlová B (eds) Zeolite chemistry and catalysis, Proc Int Symp, Prague, Czechoslovakia, Sept 8–13, 1991, Elsevier, Amsterdam, 1991, p 251; Stud Surf Sci Catal 69:251
328. Smirnov KS, van de Graaf B (1996) Microporous Mater 7:133
329. Cambor MA, Corma A, Pérez-Pariente J (1993) J Chem Soc, Chem Commun 557
330. Deo G, Turek AM, Wachs IE, Huybrechts DRC, Jacobs PA (1993) Zeolites 13:365
331. Marra GL, Tozzola G, Leofanti G, Padovan M, Petrini G, Genoni F, Venturelli B, Zecchina A, Bordiga S, Ricchiardi G (1994) In: Weitkamp J, Karge HG, Pfeifer H, Hoelderich W (eds) Zeolites and related microporous materials: State of the art 1994, Proc 10th Int Zeolite Conf, Garmisch-Partenkirchen, Germany, July 17–22, 1994, Elsevier, Amsterdam, 1994, p 559; Stud Surf Sci Catal 84:559 (and references therein)
332. Huybrechts DRC, Vaesen I, Li HX, Jacobs PA (1991) Catal Lett 8:237
333. Clerici MG, Ingallina P, Millini R (1992) In: von Ballmoos R, Higgins JB, Treacy MMJ (eds) Proc 9th Int Zeolite Conf, Montreal, Canada, July 5–10, 1992, Butterworth-Heinemann, Stoneham, MA, USA, 1993, Vol I, p 445
334. Ahedi RK, Shevade SS, Kotasthane AN (1997) Zeolites 18:361
335. Jappari N, Tanaka Y, Nakata S, Tatsumi T (1998) Microporous Mesoporous Mater 23:169 (and references therein)
336. Anunziata OA, Pierella LB, Beltramone AR (1999) In: Kiricsi I, Pál-Borbély G, Nagy JB, Karge HG (eds); Porous materials in environmentally friendly processes. Proc 1st Int FEZA Conf, Eger, Hungary, September 1–4, 1999, Elsevier, Amsterdam, 1999, p 523; Stud Surf Sci Catal 125:523
337. Kumar R, Reddy KR, Raj A, Ratnasamy P (1992) In: von Ballmoos R, Higgins JB, Treacy MMJ (eds) Proc 9th Int Zeolite Conf, Montreal, Canada, July 5–10, 1992, Butterworth-Heinemann, Stoneham, MA, USA, 1993, Vol I, p 189 (cf. especially pp 190, 195)

338. Higashimoto S, Matsuoka M, Zhang SG, Yamashita H, Kitao H, Anpo M (2001) *Microporous Mesoporous Mater* 48:329
339. Yu Y, Xiong G, Li C, Xiao F (2000) *J Catal* 194:487
340. Kornatowski J, Sychev M, Goncharuk V, Baur WH (1990) In: Oehlmann G, Pfeifer H, Fricke R (eds) *Catalysis and adsorption by zeolites. Proc ZEOCAT '90, Leipzig, Germany, August 20–23, 1990*, Elsevier, Amsterdam, 1991, p 581; *Stud Surf Sci Catal* 65:581
341. Hongbin Du, Min Fang, Yunling Liu, Shilun Qiu, Wenqin Pang (1997) *Zeolites* 18:334
342. Ko YS, Ahn WS (1999) *Microporous Mesoporous Mater* 30:283
343. Wu P, Komatsu T, Yashima T (1998) *Microporous Mesoporous Mater* 20:139
344. Mostowicz R, Dabrowski AJ, Jablonsli JM (1989) In: Jacobs PA, van Santen RA (eds) *Zeolites: Facts, figures, future, Proc 8th Int Zeolite Conf, Amsterdam, The Netherlands, July 10–14, 1989*, Elsevier, Amsterdam, 1989, p 249; *Stud Surf Sci Catal* 49:249
345. Xu B-Q, Yang M, Liang J, Sheng S-S (1992) In: von Ballmoos R, Higgins JB, Treacy MMJ (eds) *Proc 9th Int Zeolite Conf, Montreal, Canada, July 5-10, 1992*, Butterworth-Heinemann, Boston, 1993, Vol II, p 599
346. Chapus T, Tuel A, Ben Taarit Y, Naccache C (1994) *Zeolites* 14:349
347. Giannetto G, García L, Papa J, Yáñez F, Goldwasser MR, Linares C, Moronta D, Mendez B, Urbina de Navarro C, Monque R (1997) *Zeolites* 19:169
348. Johnson GM, Weller MT (1996) In: Chon H, Ihm S-K, Uh YS (eds) *Progress in zeolite and microporous materials, Proc 11th Int Zeolite Conf, Seoul, Korea, August 12–17, 1996*, Elsevier, Amsterdam, 1997, p 269; *Stud Surf Sci Catal* 105:269
349. Corma A, Navarro MT, Pérez-Pariente J, Sánchez F (1994) In: Weitkamp J, Karge HG, Pfeifer H, Hoelderich W (eds) *Zeolites and related microporous materials: State of the art 1994, Proc 10th Int Zeolite Conf, Garmisch-Partenkirchen, Germany, July 17–22, 1994*, Elsevier, Amsterdam, 1994, p 69; *Stud Surf Sci Catal* 84:69
350. Laha SC, Kumar R (2002) *Microporous Mesoporous Mater* 53:163
351. Yu Y, Xiong G, Li C, Li H, Xin Q, Feng Z (2000) *J Chem Soc, Chem Commun* 677:351
352. Morey M, Davidson A, Stucky G (1996) *Microporous Mesoporous Mater* 6:99
353. Poladi RHPR, Landry CC (2002) *Microporous Mesoporous Mater* 52:11
354. Vidya K, Dapurkar SE, Selvam P, Badamali SK, Gupta NM (2001) *Microporous Mesoporous Mater* 50:173
355. Karge HG (1992) In: Derouane EG, Lemos F, Naccache C, Ramôa Ribeiro F (eds) *Zeolite microporous solids: Synthesis, structure and reactivity*, Kluwer, Dordrecht, p 273
356. Karge HG (1996) In: Chon H, Ihm S-K, Uh YS (eds) *Progress in zeolite and microporous materials, Proc 11th Int Zeolite Conf, Seoul, Korea, August 12–17, 1996*, Elsevier, Amsterdam, 1997, p 1901; *Stud Surf Sci Catal* 105:1901
357. Foerster H, Esemann H (1995) *Z Phys Chem* 189: 263
358. Brodskii IA, Zhdanov SP, Stanevich AE (1971) *Opt Spectroskopie* 30: 58
359. Brodskii IA, Zhdanov SP (1980) In: Rees LVC (ed) *Proc 5th Int Zeolite Conf, Naples, Italy, 2–6 June, 1980*, Heyden, London, 1980 p 234
360. Ozin GA, Baker MD, Godber J, Gil CJ (1989) *J Phys Chem* 93: 2899
361. Ozin GA, Godber J, Baker MD (1988) In: Ward JW (ed) *Catalysis 1987*, Elsevier, Amsterdam, p 867
362. Bauer F, Ernst H, Geidel E, Peuker Ch, Pilz W (1996) In: Chon H, Ihm S-K, Uh YS (eds) *Progress in zeolite and microporous materials, Proc 11th Int Zeolite Conf, Seoul, Korea, August 12–17, 1996*, Elsevier, Amsterdam, 1997, p 487; *Stud Surf Sci Catal* 105:487
363. Esemann H, Foerster H, Geidel E, Krause K (1996) *Microporous Mater* 6: 321
364. Brémond C, Le Maire M, Manoli JM, Potvin C (1994) In: Weitkamp J, Karge HG, Pfeifer H, Hoelderich W (eds) *Zeolites and related microporous materials: State of the art 1994, Proc 10th Int Zeolite Conf, Garmisch-Partenkirchen, Germany, July 17–22, 1994*, Elsevier, Amsterdam, 1994, p 1027; *Stud Surf Sci Catal* 84:1027
365. Wark M, Lutz W, Loeffler E, Kessler H, Schulz-Ekloff G (1994) In: Weitkamp J, Karge HG, Pfeifer H, Hoelderich W (eds) *Zeolites and related microporous materials: State of the art 1994, Proc 10th Int Zeolite Conf, Garmisch-Partenkirchen, Germany, July 17–22, 1994*, Elsevier, Amsterdam, 1994, p 1043; *Stud Surf Sci Catal* 84:1043

366. Butler WM, Angell CL, McAllister W, Risen WM (1977) *J Phys Chem* 81: 2061
367. Davies JED, Foerster H (1996) In: Davies JED, Ripmeester JA (eds) *Comprehensive supramolecular chemistry; Vol 8. Physical methods in supramolecular chemistry*, Elsevier Science Ltd, Oxford, New York, Tokyo, 1996, p 33
368. Jobic H, Fitch AN (1996) In: Chon H, Ihm S-K, Uh YS (eds) *Progress in zeolite and microporous materials*, Proc 11th Int Zeolite Conf, Seoul, Korea, August 12–17, 1996, Elsevier, Amsterdam, 1997, p 559; *Stud Surf Sci Catal* 105:559
369. Kahn R, Mouche E, Cohen de Lara E (1990) *J Chem Soc, Faraday Trans* 86: 1905
370. Jousse F, Vercauteren DP, Auerbach SM (2000) *J Phys Chem* 104B: 8768
371. Foerster H, Fuess H, Geidel E, Hunger B, Jobic H, Kirschhock C, Klepel O, Krause K (1999) *Phys Chem Chem Phys* 1:593
372. Geidel E, Krause K, Kindler J, Foerster H (1996) In: Chon H, Ihm S-K, Uh YS (eds) *Progress in zeolite and microporous materials*, Proc 11th Int Zeolite Conf, Seoul, Korea, August 12–17, 1996, Elsevier, Amsterdam, 1997, p 575; *Stud Surf Sci Catal* 105:575
373. Jacobs WPJH, de Man AJM, van Wolput JHMC, van Santen RA (1992) In: von Ballmoos R, Higgins JB, Treacy MMJ (eds) *Proc 9th Int Zeolite Conf, Montreal, Canada, July 5–10, 1992*, Butterworth-Heinemann, Boston, 1993, Vol I, p 529 (cf. especially pp 530, 531)
374. Frohnsdorf GJC, Kington GL (1958) *Proc Royal Soc* 247:469
375. Carter JL, Lucchesi PJ, Yates DJC (1964) *J Phys Chem* 68:1385
376. Habgood HW (1965) *J Phys Chem* 69:1764
377. Zhdanov SP, Kiselev AV, Lygin VI, Titiva TI (1964) *Zh fiz Khim* 38:2408
378. Angell CL, Schaffer PC (1965) *J Phys Chem* 69:3463
379. Hughes TR, White HM (1967) *J Phys Chem* 71:2112
380. Jacobs PA, Uytterhoeven JB (1973) *J Chem Soc, Faraday Trans I* 69:359
381. Olson DH, Dempsey E (1969) *J Catal* 13:221
382. Uytterhoeven JB, Jacobs PA, Makay K, Schoonheydt R (1968) *J Phys Chem* 72:1768
383. Ward JW (1971) In: Flanigen EM, Sand LB (eds) *Molecular sieve zeolite – I*, Proc 2nd Int Zeolite Conf, Adv Chem Ser 101, Am Chem Soc, Washington, DC, p 380
384. Ward JW, Hansford RC (1969) *J Catal* 13:364
385. Czjzek M, Jobic H, Fitch AN, Vogt T (1992) *J Phys Chem* 96:1535
386. Freude D, Froehlich T, Hunger M, Pfeifer H, Scheler G (1983) *Chem Phys Lett* 98:263
387. Freude D, Hunger M, Pfeifer H, Scheler G, Hoffmann J, Schmitz W (1984) *Chem Phys Lett* 105:427
388. Engelhardt G, Michel D (1987) *High-resolution solid-state NMR of silicates and zeolites*. Wiley, Chichester, cf. especially Chapter IV.4, p 357
389. Brunner E (1993) *Microporous Mater* 1:431
390. Freude D, Hunger M, Pfeifer H, Schwieger W (1986) *Chem Phys Lett* 128:62
391. Brunner E (1995) *Habilitationsschrift (Habilitation Thesis) Universitaet Leipzig*, p 48
392. Freude D, Hunger M, Pfeifer H (1982) *Chem Phys Lett* 91:307
393. Neuber M, Dondur V, Karge HG, Pacheco L, Ernst S, Weitkamp J (1988) In: Grobet PJ, Mortier WJ, Vasant EF, Schulz-Ekloff G (eds), *Innovation in zeolite materials science*, Proc Int Symp, Elsevier, Amsterdam, 1988, p 461; *Stud Surf Sci Catal* 37:461 (cf. especially pp 464, 465)
394. Weitkamp J, Breuninger M, Karge HG, Hunger M (1999) In: Treacy MMJ, Marcus BK, Bisher ME, Higgins JB (eds) *Proc 12th Int Zeolite Conf, Baltimore, USA, July 5–10, 1998*, Materials Research Society, Warrendale, Pa, USA, 1999, p 2697
395. Barthomeuf D (1978) In: Fejes P (ed) *Proc Symp Zeolites, Szeged Hungary, Sept 11–14, 1978*; *Acta Universitatis Szegediensis, Acta Physica et Chemica, Nova Series*, 24:71
396. Barthomeuf D (1979) *J Phys Chem* 83:249
397. Beyer HK (2002) In: Karge HG, Weitkamp J (eds) *Molecular sieves – science and technology*, Springer-Verlag, Berlin, Heidelberg, New York, 3:205
398. Karge HG, Koesters H, Wada Y (1983) In: Olson DH, Bisio A (eds) *Proc 6th Int Zeolite Conf, Reno, Nevada, USA, July 10–15, 1983*, Butterworths, Guildford, UK, p 308
399. Jacobs PA, Uytterhoeven JB (1973) *J Chem Soc, Faraday Trans I* 69:373

400. Poncelet G, Dubru ML, Jacobs PA (1977) In: Katzer J (ed) *Molecular Sieves?II*, Proc 4th Int Zeolite Conf, Chicago, Ill, USA, April 18–22, 1977, p 606; ACS Symp Ser, Am Chem Soc, Washington DC, 1977, 40:606
401. McDaniel CV, Maher PK (1976) In: Rabo JA (ed) *Zeolite chemistry and catalysis*. Am Chem Soc, Washington DC, 1976, Chapter 4, especially p 322
402. Wojciechowski BW, Corma A (1986) *Catalytic cracking – catalysts, chemistry and kinetics*. Marcel Dekker, Inc, New York, 1986, Chapter 3, especially p 57
403. McDaniel CV, Maher PK (1968) In: *Molecular sieves*. Society of Chemical Industry, London, p 186
404. Kerr GT (1967) *J Phys Chem* 71:4155
405. Kerr GT (1969) *J Catal* 15:200
406. Beyer HK (2002) In: Karge HG, Weitkamp J (eds) *Molecular sieves – science and technology*, Springer-Verlag, Berlin, Heidelberg, New York, 3:205 (cf. especially p 213 and p 225)
407. Breck DW, Skeels GW (1977) In: Katzer J (ed) *Molecular Sieves, II*, Proc 4th Int Zeolite Conf, Chicago, Ill, USA, April 18–22, 1977, p 271; ACS Symp Ser, Am Chem Soc, Washington DC, 1977, 40:271
408. Lutz W, Loeffler E, Fechtelkord M, Schreier E, Bertram R (1996) In: Chon H, Ihm S-K, Uh YS (eds) *Progress in zeolite and microporous materials*, Proc 11th Int Zeolite Conf, Seoul, Korea, August 12–17, 1996, Elsevier, Amsterdam, 1997, p 439; *Stud Surf Sci Catal* 105:439
409. Ward JW (1976) In: Rabo JA (ed) *Zeolite chemistry and catalysis*, Am Chem Soc, Washington DC, ACS Monograph 171, pp 250–251
410. Beyer HK (2002) In: Karge HG, Weitkamp J (eds) *Molecular sieves – science and technology*, Springer-Verlag, Berlin Heidelberg, New York, 3:205 (cf. especially p 220)
411. Ward JW (1976) In: Rabo JA (ed) *Zeolite chemistry and catalysis*. ACS Monograph 171, Chapter 3, especially p165, Am Chem Soc, Washington DC, Chapter 3, p 118
412. Macedo A, Raatz F, Boulet R, Janin A, Lavalley JC (1987) In: Grobet PJ, Mortier WJ, Vansant EF, Schulz-Ekloff G (eds) *Innovation in zeolite materials science*; Proc Int Symp, Nieuwpoort, Belgium, Sept 13–17, 1987, Elsevier, Amsterdam, 1987, p 375; *Stud Surf Sci Catal* 37:375 (cf. especially pp 379, 380)
413. Patzelová V, Drahorodová E, Tvaruskova Z, Lohse U (1989) *Zeolites* 7:11
414. Grobet PJ, Geerts H, Tielen M, Martens JA, Jacobs PA (1988) In: Weitkamp J, Karge HG (eds) *Zeolites as catalysts, sorbents and detergent builders – applications and innovations*. Proc Int Symp, Wuerzburg, Germany, Sept 4–8, 1988, Elsevier, Amsterdam, 1989, p 721; *Stud Surf Sci Catal* 46:721
415. Ballivet D, Barthomeuf D (1977) *J Chem Soc, Faraday Trans I* 73:1581
416. Wichterlová B, Nováková J, Kubelková L, Jiru P (1980) In: Rees LVC (ed) Proc 5th Int Zeolite Conf, Naples, Italy, Heyden, London, p 373
417. Loeffler E, Kustov LM, Zhobolenko VL, Peuker Ch, Lohse U, Kazansky VB, Oehlmann G (1990) In: Oehlmann G, Pfeifer H, Fricke R (eds) *Catalysis and adsorption by zeolites*. Proc ZEOCAT '90, Leipzig, Germany, August 20–23, 1990, Elsevier, Amsterdam, 1991, p 425; *Stud Surf Sci Catal* 65:425
418. Jacobs PA, Uytterhoeven JB (1973) *J Chem Soc, Faraday Trans I* 69:359 (cf. especially p 368)
419. Lohse U, Loeffler E, Hunger M, Stoeckner J, Patzelová V (1987) *Zeolites* 7:11
420. Ward JW (1970) *J Catal* 18:348
421. Makarova MA, Dwyer J (1993) *J Phys Chem* 97:6337
422. Makarova MA, Garforth A, Zholobenko VL, Dwyer J, Earl GJ, Rawlence D (1994) In: Weitkamp J, Karge HG, Pfeifer H, Hoelderich W (eds) *Zeolites and related microporous materials: State of the art 1994*, Proc 10th Int Zeolite Conf, Garmisch-Partenkirchen, Germany, July 17–22, 1994, Elsevier, Amsterdam, 1994, p 365; *Stud Surf Sci Catal* 84:365
423. Datka J, Gil B, Fraissard J, Massiani P, Batamack P (1998) In: Treacy MMJ, Marcus BK, Bisher ME, Higgins JB (eds) Proc 12th Int Zeolite Conf., Baltimore, USA, July 5–10, 1998, Materials Research Society, Warrendale, Pa, USA, 1999, p 2595

424. Datka J, Gil B, Domagala T, Góra-Marek K (2001) *Microporous Mesoporous Mater* 47:61
425. Jia M, Lechert H, Foerster H, (1992) *Zeolites* 12:32
426. Ray GJ, Nerheim AG, Donohue JA (1988) *Zeolites* 8:458
427. Patzelová V, Drahorádová E, Traruzková Z, Lohse U (1989) *Zeolites* 9:74
428. Hanke W, Moeller K (1984) *Zeolites* 4:244
429. Martin A, Wolf U, Nowak S, Luecke B (1991) *Zeolites* 11:85
430. Neuber M, Dondur V, Karge HG, Pacheco L, Ernst S, Weitkamp J (1988) In: Grobet PJ, Mortier WJ, Vasant EF, Schulz-Ekloff G (eds), *Innovation in zeolite materials science, Proc Int Symp, Elsevier, Amsterdam, 1988, p 461; Stud Surf Sci Catal* 37:461
431. Grobet PJ, Jacobs PA, Beyer HK (1986) *Zeolites* 6:4
432. Skeels GW, Breck DW (1983) In: Olson D, Bisio A (eds) *Proc 6th Int Zeolite Conf, Reno, USA, 10–15 July, 1983, Butterworth, Guildford, UK, 1984, p 87*
433. Triantafyllidis CS, Vlessidis AG, Nalbandian L, Evmeridis NP (2001) *Microporous Mesoporous Mater* 47:369
434. Stockenhuber M, Lercher JA (1995) *Microporous Mater* 3:457
435. McDaniel CV, Maher PK (1968) In: *Molecular sieves. Society of Chemical Industry, London, p 186*
436. Wojciechowski BW, Corma A (1986) *Catalytic cracking – catalysts, chemistry and kinetics, Marcel Dekker, Inc, New York, 1986, Chapter 3 (especially p 68)*
437. Hirschler A (1963) *J Catal* 2:428
438. Plank CJ (1965) In: Sachtler WM, Schuit GCA, Zwietering P (eds), *Proc 3rd Int Congress on Catalysis, Amsterdam, The Netherlands, July 20–25, 1964, North-Holland Publishing Comp, Amsterdam p 272*
439. Ward JW (1968) *J Phys Chem* 72:4211
440. Rabo JA, Poutsma ML (1970) In: Flanigen EM, Sand LB (eds) *Molecular sieves – II, Proc 2nd Int Conf Zeolites, Worcester, Mass, USA, Sept 8–11, 1970, Adv Chem Series, Am Chem Soc, Washington DC, 1971, 102:284*
441. Ward JW (1968) *J Catal* 11:238
442. Ward JW (1971) *Trans Faraday Soc* 67:1489
443. Karge HG, Ladebeck J, Sarbak Z, Hatada K (1982) *Zeolites* 2:94 (especially p 99)
444. Karge HG, Hatada K, Zhang Y, Fiedorow R (1983) *Zeolites* 3:13 (especially pp 16-17)
445. Ermolenko NF, Tsybul'skaya YA, Malashevick LN (1973) *Kinet Catal* 14:904
446. Ward JW (1976) In: Rabo JA (ed) *Zeolite chemistry and catalysis, ACS Monograph 171, Am Chem Soc, Washington DC, p 132*
447. Fejes P, Hannus I, Kiricsi I, Varga K (1978) In: Fejes P (ed) *Proc Int Symp Zeolites, Szeged, Hungary, Sept 11–14, 1978; Acta Universitatis Szegediensis, Acta Physica et Chemica, Nova Series, Vol XXIV, Szeged Hungaria, 1978, p 119*
448. Kiricsi I, Hannus I, Kiss A, Fejes P (1982) *Zeolites* 2:247
449. Dzwigaj J, Haber J, Romotowski T (1983) *Zeolites* 3:134
450. Hoser H, Dabrowski A, Krzyanowski S (1977) In: Katzer J (ed) *Molecular Sieves-II, Proc 4th Int Zeolite Conf, Chicago, Ill, USA, April 18–22, 1977, p 572; ACS Symp Ser, Am Chem Soc, Washington DC, 1977, 40:572*
451. Jacobs WPJH, van Wolput JHMC, van Santen RA (1993) *Zeolites* 13:170 (cf. especially p 176)
452. Christner LG, Liengme BV, Hall WK (1968) *Trans Faraday Soc* 64:1679
453. Foerster H, Schuldt M (1975) *J Colloid Interface Sci* 52:380 (cf. especially p 383)
454. Karge HG, Raskó J (1978) *J Colloid Interface Sci* 64:522
455. Karge HG, Ziólek M, Laniecki M (1987) *Zeolites* 7:197
456. Breck DW, Eversole WG, Milton RM Reed TB, Thomas TL (1956) *J Am Chem Soc* 78:5963
457. Milton RM USP 2,882,243, Buffalo, NY, assignor to Union Carbide Corp (1959)
458. Milton RM USP 2,882,244, Buffalo, NY, assignor to Union Carbide Corp (1959)
459. Llenado RA (1983) In: Olson D, Bisio A (eds) *Proc 6th Int Zeolite Conf, Reno, USA, 10–15 July, 1983, Butterworth, Guildford, UK, 1984, p 940*
460. Zhdanov SP, Kiselev AV, Lygin VI, Ovepyan ME, Titova TI (1965) *Russ J Phys Chem* 39:1309
461. Ward JW (1967) *J Catal* 9:225

462. Kerr GT (1969) *J Phys Chem* 73:2780
463. Barrer RM, Makki MB (1964) *Canadian J Chem* 42:1481
464. Breck DW, Eversole WG, Milton RM, Reed TB, Thomas TL (1956) *J Am Chem Soc* 78:5963
465. Beyer H, Papp J, Kalló D (1975) *Acta Chim (Budapest)* 84:7
466. Karge HG (1975) *Z phys Chem Neue Folge* 95:241
467. Weeks TJ, Bolton AP (1975) *J Phys Chem* 79:1924
468. Bartl P, Hoelderich W (2000) *Microporous Mesoporous Mater* 38:279
469. Cannings FR (1968) *J Phys Chem* 72:4691
470. Lefrançois M, Malbois G (1971) *J Catal* 20:350
471. Karge H (1971) *Z phys Chem Neue Folge* 76:133 (cf. especially pp 139–141)
472. Karge HG (1980) *Z phys Chem Neue Folge* 122:103
473. Karge HG, (1977) In: Katzer J (ed) *Molecular Sieves, II, Proc 4th Int Zeolite Conf, Chicago, Ill, USA, April 18–22, 1977*, p 584; ACS Symp Ser, Am Chem Soc, Washington DC, 1977, 40:584
474. Fejes P, Foerster H, Kiricsi I, Seebode J (1982) *React Kinet Catal Lett* 20:241
475. Mirodatos C, Ha BH, Otsuka K, Barthomeuf D (1980) In: Rees LVC (ed) *Proc 5th Int Zeolite Conf, Naples, Italy, Heyden, London*, p 382
476. Beyer HK, Kiss A, Mihalyfi J, Jacobs PA (1980) *J Chem Soc, Faraday Trans I* 76:332
477. Alberti A (1997) *Zeolites* 19:411
478. Moreau F, Ayrault P, Gnep NS, Lacombe S, Merlen E, Guisnet M (2002) *Microporous Mesoporous Mater* 51:211
479. Sani A, Vezzolini G, Ciambelli P, Rapacciuolo MT (1999) *Microporous Mesoporous Mater* 31:263
480. Detrekoy EJ, Jacobs PA (1973) In: Uytterhoeven JB (ed) *Molecular Sieves, Proc 3rd Int Conf on Molecular Sieves, Sept 3–7, 1973, Zurich, Switzerland, Leuven University Press*, p 373
481. Detrekoy EJ, Jacobs PA, Kalló D, Uytterhoeven JB (1974) *J Catal* 32:442
482. Best DF, Larson RW, Angell CL (1973) *J Phys Chem* 77:2183
483. Roessner F, Rudolf A, Steinberg K-F (1988) *Z Chem* 28:228
484. Roessner F, Steinberg K-H, Freude D, Hunger M, Pfeifer H (1988) In: Karge HG, Weitkamp J (eds) *Zeolites as catalysts, sorbents and detergent builders – Applications and innovations, Proc Int Symp, Wuerzburg, Germany, Sept 4–8, 1988, Elsevier, Amsterdam, 1989*, p 421; *Stud Surf Sci Catal* 46:421
485. Roessner F, Steinberg K-H, Rudolf A, Staudte B (1989) *Zeolites* 9:371
486. Kalies H, Roessner F, Karge HG, Steinberg K-H (1991) In: Jacobs PA, Jaeger NI, Kubelková L, Wichterlová B (eds) *Zeolite chemistry and catalysis, Proc Int Symp, Prague, Czechoslovakia, Sept 8–13, 1991, Elsevier, Amsterdam*, p 425; *Stud Surf Sci Catal* 69:425
487. Mirodatos C, Abou-Kais A, Vedrine JC, Barthomeuf D (1978) *J Chem Soc, Faraday Trans I* 74:1786
488. Wu EL, Whyte Jr TE, Venuto PB (1971) *J Catal* 21:384
489. Tsitsishvili GV, Yakerson VI, Sidamondze SI, Iashvili II, Lafer LI (1980) In: Rees LVC (ed) *Proc 5th Int Zeolite Conf, Naples, Italy, June 2–6, 1980, Heyden, London*, p 394
490. Corma A, Fornes V, Melo F, Pérez-Pariente J (1987) *Prep Am Chem Soc Symp Div Petro Chem* p 632
491. Chun Y, Chen X, Yan A-Z, Xu Q-H (1994) In: Weitkamp J, Karge HG, Pfeifer H, Hoelderich W (eds) *Zeolites and related microporous materials: State of the art 1994, Proc 10th Int Zeolite Conf, Garmisch-Partenkirchen, Germany, July 17–22, 1994, Elsevier, Amsterdam, 1994*, p 1035; *Stud Surf Sci Catal* 84:1035
492. Borade RB, Clearfield A (1994) In: Weitkamp J, Karge HG, Pfeifer H, Hoelderich W (eds) *Zeolites and related microporous materials: State of the art 1994, Proc 10th Int Zeolite Conf, Garmisch-Partenkirchen, Germany, July 17–22, 1994, Elsevier, Amsterdam, 1994*, p 661; *Stud Surf Sci Catal* 84:661 (and references therein)
493. Kiricsi I, Flego C, Pazzuoni G, Parker Jr WO, Millini R, Perego C, Bellussi G (1994) *J Phys Chem* 98:4627
494. Katada N, Iijima S, Igi H, Niwa M (1996) In: Chon H, Ihm S-K, Uh YS (eds) *Progress in zeolite and microporous materials, Proc 11th Int Zeolite Conf, Seoul, Korea, August 12–17, 1996, Elsevier, Amsterdam, 1997*, p 1227; *Stud Surf Sci Catal* 105:1227

495. Su B-L, Norberg V (1997) *Zeolites* 19:65
496. Hedge SG, Kumar R, Bhat RN, Ratnasamy P (1989) *Zeolites* 9:231
497. Oumi Y, Mizuno R, Azuma K, Nawata S, Fukushima T, Uozumi T, Sano T (2001) *Microporous Mesoporous Mater* 49:103
498. Omegna A, Haonas M, Kogelbauer A, Prins R (2001) *Microporous Mesoporous Mater* 46:177
499. Gianetti JB, Perrotta AJ (1975) *Ind Eng Chem Proc Res Dev* 14:86
500. Domokos L, Lefferts L, Seshan K, Lercher JA (2000) *J Mol Catal A* 162:147
501. Flanigen EM (2001) In: van Bekkum H, Flanigen EM, Jacobs PA, Jansen JC (eds) *Introduction to zeolite science and practice*, 2nd edition, Elsevier, Amsterdam, 2001, pp 11 and 20; *Stud Surf Sci Catal* 137:11 (cf. especially p20)
502. Landolt GR (1972) US Patent 3702886, Assignee: Mobil Oil
503. Kokotailo GT, Lawton SL, Olson DH, Meier WM (1978) *Nature* 272:437
504. Flanigen EM, Bennett JM, Grose RW, Cohen JP, Patton RL, Kirchner RM, Smith JV (1978) *Nature* 271:512
505. Olson DH, Kokotailo GT, Lawton SL, Meier WM (1981) *J Phys Chem* 85:2238
506. Hatada K, Ono Y, Ushiki Y (1979) *Z phys Chem Neue Folge* 117:37
507. Jacobs PA, von Ballmoos R (1982) *J Phys Chem* 86:3050
508. Karge HG, Wada Y, Weitkamp J, Ernst S, Girschbach U, Beyer HK (1984) In: Kaliaguine S, Mahay A (eds) *Catalysis on the energy scene; Proc 9th Canadian Symp on Catalysis*, Québec, P.Q, Canada, Sept 30-Oct 3, 1984, Elsevier, Amsterdam, 1989, p 101; *Stud Surf Sci Catal* 19:101
509. Zholobenko VL, Kustov LM, Borovkov VYu, Kazansky VB (1988) *Zeolites* 8:175
510. Beck K, Brunner E, Staudte B (1995) *Z phys Chem* 190:1
511. Woolery GL, Alemany LB, Dessau RM, Chester AW (1986) *Zeolites* 6:14
512. Senchenya IN, Borovkov VYu (1990) In: Oehlmann G, Pfeifer H, Fricke R (eds) *Catalysis and adsorption by zeolites. Proc ZEOCAT '90*, Leipzig, Germany, August 20–23, 1990, Elsevier, Amsterdam, 1994, p 653; *Stud Surf Sci Catal* 65:653
513. Brunner E (1995) *Habilitationschrift (Habilitation Thesis) University of Leipzig*, pp 45, 70
514. Brunner E, Beck K, Koch M, Pfeifer H, Staudte B, Zscherpel D (1994) In: Weitkamp J, Karge HG, Pfeifer H, Hoelderich W (eds) *Zeolites and related microporous materials: State of the art 1994, Proc 10th Int Zeolite Conf, Garmisch-Partenkirchen, Germany, July 17–22, 1994*, Elsevier, Amsterdam, 1994, p 357; *Stud Surf Sci Catal* 84:357
515. Beck LW, White JL, Haw JF (1994) *J Chem Soc* 116:9657
516. Datka J, Piwowarska Z (1988) *Zeolites* 8:30
517. Datka J, Boczar M (1991) *Zeolites* 11:397
518. Woolery GL, Kuehl GH, Timken HC, Chester AW, Vartuli J (1997) *Zeolites* 19:288
519. Marturano P, Kogelbauer A, Prins R, (1999) In: Kiricsi I, Pál-Borbély G, Nagy JB, Karge HG (eds); *Porous materials in environmentally friendly processes. Proc 1st Int FEZA Conf*, Eger, Hungary, September 1–4, 1999, Elsevier, Amsterdam, 1999, p 619; *Stud Surf Sci Catal* 125:619
520. Gosh AK, Kydd RA (1990) *Zeolites* 10:766
521. Wallau M, Schueth F, Brenner A, Melson S, Spichtinger R, Unger K, Tissler A, Zibrowius B (1992) In: von Ballmoos R, Higgins JB, Treacy MMJ (eds) *Proc 9th Int Zeolite Conf*, Montreal, Canada, July 5–10, 1992, Butterworth-Heinemann, Boston, 1993, Vol I, p 643
522. Marra GL, Tozzola G, Leofanti G, Padovan M, Petrini G, Genoni F, Venturelli B, Zecchina A, Bordiga S, Ricchiardi G (1994) In: Weitkamp J, Karge HG, Pfeifer H, Hoelderich W (eds) *Zeolites and related microporous materials: State of the art 1994, Proc 10th Int Zeolite Conf, Garmisch-Partenkirchen, Germany, July 17–22, 1994*, Elsevier, Amsterdam, 1994, p 559; *Stud Surf Sci Catal* 84:559 (and references therein)
523. Unverricht S, Hunger M, Ernst S, Karge HG, Weitkamp J (1994) In: Weitkamp J, Karge HG, Pfeifer H, Hoelderich W (eds) *Zeolites and related microporous materials: State of the art 1994, Proc 10th Int Zeolite Conf, Garmisch-Partenkirchen, Germany, July 17–22, 1994*, Elsevier, Amsterdam, 1994, p 37; *Stud Surf Sci Catal* 84:37

524. Corma A, Corell C, Fornés V, Kolodziejski W, Pérez-Pariente J (1995) *Zeolites* 15:576
525. Onida B, Geobaldo F, Testa F, Crea F, Garrone E (1999) *Microporous Mesoporous Mater* 30:119
526. Balkus Jr KJ, Gbery G, Deng Z (2002) *Microporous Mesoporous Mater* 52:141
527. Cejka J, Krejčí A, Zilková N, Kotrla J, Ernst S, Weber A (2002) *Microporous Mesoporous Mater* 53:121
528. Beyer HK, Jacobs PA, Uytterhoeven JB, Till F (1977) *J Chem Soc, Faraday Trans I* 73:1111
529. Weeks TJ, Kimak DG, Bujalski RJ, Bolton AP (1976) *J Chem Soc, Faraday Trans I* 72:575
530. Post MFM, Huizinga T, Emeis CA, Nanne JM, Stork WHJ (1988) In: Karge HG, Weitkamp J (eds) *Zeolites as catalysts, sorbents and detergent builders – Applications and innovations*, Proc Int Symp, Wuerzburg, Germany, Sept 4–8, 1988, Elsevier, Amsterdam, 1989, p 365; *Stud Surf Sci Catal* 46:365
531. Kubelková L, Jirka I, Vylita J, Nováková J (1994) In.: Weitkamp J, Karge HG, Pfeifer H, Hoelderich W (eds) *Zeolites and related microporous materials: State of the art 1994*, Proc 10th Int Zeolite Conf, Garmisch-Partenkirchen, Germany, July 17–22, 1994, Elsevier, Amsterdam, 1994, p 1051; *Stud Surf Sci Catal* 84:1051
532. Hedge SG, Abdullah RA, Bhat RN, Ratnasamy P (1992) *Zeolites* 12:951
533. Chao KJ, Sheu SP, Lin L-H, Genet MJ, Feng MH (1997) *Zeolites* 18:18
534. Borade RB, Clearfield A, (1994) *Microporous Mater* 2:167
535. Chen J, Wright PA, Natarajan S, Thomas JM (1994) In.: Weitkamp J, Karge HG, Pfeifer H, Hoelderich W (eds) *Zeolites and related microporous materials: State of the art 1994*, Proc 10th Int Zeolite Conf, Garmisch-Partenkirchen, Germany, July 17–22, 1994, Elsevier, Amsterdam, 1994, p 1731; *Stud Surf Sci Catal* 84:1731
536. Valange V, Gabelica Z, Onida B, Garrone E (1998) In: Treacy MMJ, Marcus BK, Bisher ME, Higgins JB (eds) *Proc 12th Int Zeolite Conf*, Baltimore, USA, July 5–10, 1998, Materials Research Society, Warrendale, Pa, USA, 1999, p 2711
537. Lourenço JP, Ribeiro MF, Ramôa Ribeiro F, Rocha J, Onida B, Garrone E, Gabelica Z (1997) *Zeolites* 18:398
538. Costa CS, Lourenço JP, Henriques C, Antunes AP, Ribeiro FR, Ribeiro MF, Gabelica Z (1998) In: Treacy MMJ, Marcus BK, Bisher ME, Higgins JB (eds) *Proc 12th Int Zeolite Conf*, Baltimore, USA, July 5–10, 1998, Materials Research Society, Warrendale, Pa, USA, 1999, p 1771
539. Peeters MPJ, van Hooff JHC, Sheldon RA, Zholobenko VL, Kustov LM, Kazansky VB (1992) In: von Ballmoos R, Higgins JB, Treacy MMJ (eds) *Proc 9th Int Zeolite Conf*, Montreal, Canada, July 5–10, 1992, Butterworth-Heinemann, Boston, 1993, Vol I, p 651
540. Zholobenko VL, Kustov LM, Kazansky VB (1992) In: von Ballmoos R, Higgins JB, Treacy MMJ (eds) *Proc 9th Int Zeolite Conf*, Montreal, Canada, July 5–10, 1992, Butterworth-Heinemann, Boston, 1993, Vol II, p 299
541. Issakov J, Litvin E, Minachev C, Oehlmann G, Scharf V, Thome R, Tissler A, Unger B (1994) In: Weitkamp J, Karge HG, Pfeifer H, Hoelderich W (eds) *Zeolites and related microporous materials: State of the art 1994*. Proc 10th Int Zeolite Conf, Garmisch-Partenkirchen, Germany, July 17–22, 1994, Elsevier, Amsterdam, 1994, p 2005; *Stud Surf Sci Catal* 84:2005
542. Jacobs PA, Mortier WJ (1982) *Zeolites* 2:226
543. Hair ML (1967) *Infrared spectroscopy in surface chemistry*. Marcel Dekker, New York, pp 183, 190, 205
544. Sauer J (1989) In: Klinowski J, Barrie PJ (eds) *Recent advances in zeolite science*, Proc Meeting British Zeolite Association, Cambridge, UK, April 17–19, 1989, Elsevier, Amsterdam, 1989, p 73; *Stud Surf Sci Catal* 52:73 (and references therein)
545. Mix H, Sauer J, Schroeder K-P, Merkel A (1988) *Coll Czech Chem Comm* 53:2191
546. Kazansky VB, Kustov LM, Borovkov VYu (1983) *Zeolites* 3:77
547. Kazansky VB, Borovkov VYu, Kustov LM (1984) In: Dechema (ed) *Proc 8th Int Congress Catal*, Berlin, Germany, July 2–6, 1984, Verlag Chemie, Heidelberg, Vol III; p 3
548. Kustov LM, Borovkov VYu, Kazanskii VB (1984) *Kinetika i Kataliz* 25:471; *Engl Translat Kinetics and Catalysis* (1984) 25:393

549. Kazansky VB (1984) In: Jacobs PA, Jaeger NI, Jiru P, Kazansky VB, Schulz-Ekloff G (eds) Structure and reactivity of modified zeolites. Proc Int Conf, Prague, Czechoslovakia, July 9–13, 1984, Elsevier, Amsterdam, 1984, p 61; Stud Surf Sci Catal 18:61
550. Zhubolenko VL, Kustov LM, Kazansky VB, Loeffler E, Lohse U, Peuker Ch, Oehlmann G (1990) Zeolites 10:304
551. Loeffler E, Lohse U, Peuker Ch, Oehlmann G, Kustov LM, Zhubolenko VL, Kazansky VB (1990) Zeolites 10:266
552. Kustov LM, Kazansky VB (1991) J Chem Soc Faraday Trans 87:2675
553. Kazansky VB (1988), Catal Today 3:367
554. Kustov LM, Borovkov VYu, Kazansky VB (1981) J Catal 72:149
555. Mix H, Pfeifer H, Staudte B, Zscherpel U (1988) Experimentelle Technik der Physik 36:495
556. Mix H, Pfeifer H, Staudte B (1988) Chem Phys Lett 146:541 (and references therein)
557. Staudte B, Hunger M, Nimz M (1991) Zeolites 11:837
558. Pruski M, Ernst H, Pfeifer H, Staudte B (1985) Chem Phys Lett 119:412
559. Zscherpel U, Staudte B, Loeffler E, Peuker C, Jahn E (1989) Z phys Chem (Leipzig) 270:207 (cf. especially pp 208 and 209)
560. Beck K, Pfeifer H, Staudte B (1993) Microporous Mater 2:1 (cf. especially pp 4–5)
561. Medin AS, Borovkov VYu, Kazansky VB, Pelmentschikov AG, Zhidomirov GM (1990) Zeolites 10:668
562. Loeffler E, Lohse U, Peuker Ch, Oehlmann G, Kustov LM, Zhubolenko VL, Kazansky VB (1990) Zeolites 10:266
563. Loeffler E, Peuker Ch, Finger G, Girus I, Jahn E, Zubowa H-L (1990) Z Chem 30:255
564. Loeffler E, Peuker Ch, Zibrowius B, Zscherpel U, Schnabel K-H (1992) In: von Ballmoos R, Higgins JB, Treacy MMJ (eds) Proc 9th Int Zeolite Conf, Montreal, Canada, July 5–10, 1992, Butterworth-Heinemann, London, 1993 Vol I, p 521
565. Brunner E, Freude D, Hunger M, Pfeifer H, Staudte B (1984) In: Jacobs PA, Jaeger NI, Jiru P, Kazansky VB, Schulz-Ekloff G (eds) Structure and reactivity of modified zeolites Proc Int Conf, Prague, July 9–13, 1984, Elsevier, Amsterdam, 1984, p 453; Stud Surf Sci Catal 69:453
566. Hedge SG, Ratnasamy P, Kustov LM, Kazansky VB (1988) Zeolites 8:137.
567. Dzwigaj S, Briend M, Shikholeslami A, Peltre MJ, Barthomeuf D (1990) Zeolites 10:157
568. Makarova MA, Ojo AE, Al-Ghefaily KM, Dwyer J (1992) In: von Ballmoos R, Higgins JB, Treacy MMJ (eds) Proc 9th Int Zeolite Conf, Montreal, Canada, July 5–10, 1992, Butterworth-Heinemann, Boston, 1993, p Vol II, 259
569. Corma A, Fornes V, Franco MJ, Melo F, Pérez-Pariente J, Sastre E (1992) In: von Ballmoos R, Higgins JB, Treacy MMJ (eds) Proc 9th Int Zeolite Conf, Montreal, Canada, July 5–10, 1992, Butterworth-Heinemann, Boston, 1993, Vol II, p 343
570. Zibrowius B, Loeffler E, Hunger M (1992) Zeolites 12:167
571. Masukawa T, Komatsu T, Yashima T (1997) Zeolites 18:10
572. Xu Q, Yan A, Bao S, Xu K jun (1986) In: Murakami Y, Iijima A, Ward JW (eds) New developments in zeolite science and technology. Proc 7th Int Zeolite Conf, Tokyo, Japan, August 17–22, 1986, Kodansha, Tokyo, Elsevier, Amsterdam, 1986, p 835; Stud Surf Sci Catal 28:835
573. Tuel A (1995) Zeolites 15:228
574. Llewellyn PL, Ciesla U, Decher H, Stadler R, Schueth F, Unger KK (1994) In: Weitkamp J, Karge HG, Pfeifer H, Hoelderich W (eds) Zeolites and related microporous materials: State of the art 1994. Proc 10th Int Zeolite Conf, Garmisch-Partenkirchen, Germany, July 17–22, 1994, Elsevier, Amsterdam, 1994, p 2013; Stud Surf Sci Catal 84:2013
575. Wax MJ, Cavanagh RR, Rush JJ, Stucky GD, Abrams L, Corbin DR (1986) J Phys Chem 90:532
576. Jobic H (1991) J Catal 131:289
577. Koudriachova M, Geidel E (1998) In: Treacy MMJ, Marcus BK, Bisher ME, Higgins JB (eds) Proc 12th Int Zeolite Conf, Baltimore, USA, July 5–10, 1998, Materials Research Society, Warrendale, Pa, USA, 1999, p 423
578. Jobic H, Tuel A, Krossner M, Sauer J (1996) J Phys Chem 100:19545
579. Jobic H (1992) Spectrochimica Acta 48A:293

580. Trouw F, Iton LE, Davis ME (1994) In: Weitkamp J, Karge HG, Pfeifer H, Hoelderich W (eds) Zeolites and related microporous materials: State of the art 1994. Proc 10th Int Zeolite Conf, Garmisch-Partenkirchen, Germany, July 17–22, 1994, Elsevier, Amsterdam, 1994, p 851; Stud Surf Sci Catal 84:851
581. Jobic H, Renouprez A, Fitch AN, Lauter HJ (1987) J Chem Soc, Faraday Trans 83:3199
582. Jobic H, Fitch AN (1997) In: Chon H, Ihm S-K, Uh YS (eds) Progress in zeolite and microporous materials. Proc 11th Int Zeolite Conf, Seoul, Korea, August 12–17, 1996, Elsevier, Amsterdam 1997, p 559; Stud Surf Sci Catal 105:583
583. Beta IA, Boehlig H, Doebler J, Jobic H, Geidel E, Hunger B (2001) In: Galarneau A, di Renzo F, Fajula F, Vedrine J (eds) Zeolites and mesoporous materials at the dawn of the 21st century. Proc 13th Int Zeolite Conf, Montpellier, France, July 8–13, 2001, Elsevier, Amsterdam, 2001, p 1889; Stud Surf Sci Catal 135:1889
584. Beta I, Jobic H, Geidel E, Boehlig H, Hunger B (2001) Spectrochimica Acta 57A:55
585. Geidel E, Jobic H, Parker SF (1998) In: Treacy MMJ, Marcus BK, Bisher ME, Higgins JB (eds) Proc 12th Int Zeolite Conf, Baltimore, Maryland, USA, July 5–10, 1998, Materials Research Society, Warrendale, Pa, USA, 1999, p 2609
586. Geidel E, Billes F (2000) J Molecular Structure 507:75
587. Foerster H, Schuldt M (1977) J Chem Phys 66:5237
588. Foerster H, Schuldt M (1978) J Molecular Structure 47:339
589. Barrachin B, Cohen de Lara E (1986) J Chem Soc, Faraday Trans II 82:1953
590. Cohen de Lara E, Delaval Y (1977) In: Smith JV (ed) Proc 4th Int Conf Molecular Sieves, Recent Research Reports, Chicago, USA, April 18–22, 1977, University of Chicago Press, p 17
591. Cohen de Lara E, Delaval Y (1978) J Chem Soc, Faraday Trans II 74:790
592. Cohen de Lara E, Kahn R, Bouchaud JP, Ibnass H (1992) In: von Ballmoos R, Higgins JB, Treacy MMJ (eds) Proc 9th Int Zeolite Conf, Montreal, Canada, July 5–10, 1992, Butterworth-Heinemann, Boston, 1993, p Vol II, 55
593. Larin AV, Jousse F, Cohen de Lara E (1994) In: Weitkamp J, Karge HG, Pfeifer H, Hoelderich W (eds) Zeolites and related microporous materials: State of the art 1994. Proc 10th Int Zeolite Conf, Garmisch-Partenkirchen, Germany, July 17–22, 1994, Elsevier, Amsterdam, 1994, p 2147; Stud Surf Sci Catal 84:2147
594. Fenelon PJ, Rubalcava HE (1969) J Chem Phys 51:961
595. Angell CL, Schaffer PC (1966) J Phys Chem 70:1413 (cf. especially pp 1416 and 1417)
596. Boese H, Foerster H (1990) J Molecular Structure 218:393
597. Foerster H, Frede W, Schuldt M (1980) In: Rees LVC (ed) Proc 5th Int Conf Zeolites, Naples, Italy, June 2–6, 1980, Heyden, London, 1980, p 458
598. Zumofen G, Dressler K (1976) J Chem Phys 64:5198
599. Cohen de Lara E, Kahn R (1983) In: Olson D, Bisio A (eds) Proc 6th Int Zeolite Conf, Reno, USA, July 10–15, 1983, Butterworth, Guildford, UK, 1984, p 172
600. Foerster H, Schuldt M (1980) J Molecular Structure 61:361
601. Foerster H, Frede W, Schuldt M (1980) J Molecular Structure 61:75
602. Cohen de Lara, Kahn R (1990) In: Barthomeuf D, Derouane EG, Hoelderich W (eds) Guidelines for mastering the properties of molecular sieves – Relationship between the properties of zeolitic systems and their low dimensionality, NATO ASI Series B, Physics, Vol 221, Plenum Press, New York, p 169
603. Cohen de Lara E, Kahn R (1981) J Physique 42:1029
604. Foerster H, Frede W, Schuldt M (1982) J Molecular Structure 80:195
605. Foerster H, Frede W (1984) Infrared Physics 24:151
606. Sheppard N, Yates DJC (1957) Proc Roy Soc, London, Ser A 238:69
607. Eischens RP, Jacknow J (1965) In: Sachtler WMH, Schuit GCA, Zwietering P, Proc 3rd Int Congress Catal, Amsterdam, The Netherlands, July 20–25, 1964, North Holland Publ Comp, Amsterdam, 1965, p 627
608. Boese H, Foerster H, Frede W, Schumann M (1983) In: Olson D, Bisio A (eds) Proc 6th Int Zeolite Conf, Reno, USA, July 10–15, 1983, Butterworth, Guildford, UK, 1984, p 201

609. Borovkov VYu, Kustov LM, Kazansky VB, Viliams C (1991) *J Chem Soc, Faraday Trans* 87:2675
610. Borovkov VYu, Kustov LM, Kazansky VB, Viliams C (1992) *J Chem Soc, Faraday Trans* 88:3251
611. Kazansky VB (1999) *J Mol Catal A* 141:83
612. Kazansky VB, Borovkov VY, Serykh A, van Santen RA, Anderson BG (2000) *Catal Lett* 66:39
613. Saperstein DD, Rein AJ (1977) *J Phys Chem* 81:2134
614. Broclawik E, Datka J, Gil B (1999) In: Kiricsi I, Pál-Borbély G, Nagy JB, Karge HG (eds); *Porous materials in environmentally friendly processes. Proc 1st Int FEZA Conf, Eger, Hungary, September 1–4, 1999, Elsevier, Amsterdam, 1999, p 603; Stud Surf Sci Catal* 125:603
615. Schumann M, Grodzicki M, Boese H, Foerster H, Zakhariyeva-Pencheva O (1987) In: Shopov D, Andreev A, Palazov A, Petrov L (eds) *Proc 6th Int Symp Heterogeneous Catal, Sofia, Bulgaria, July 13–18, p 193*
616. Foerster H, Frede W, Peters G (1988) In: Karge HG, Weitkamp J (eds) *Zeolites as catalysts, sorbents and detergent builders – Applications and innovations. Proc Int Symp, Wuerzburg, Germany, Sept 4–8, 1988, Elsevier, Amsterdam, 1989, p 545; Stud Surf Sci Catal* 46:545
617. Foerster H, Witten U (1989) In: Jacobs PA, van Santen RA (eds) *Zeolites: Facts, figures, future, Proc 8th Int Zeolite Conf, Amsterdam, The Netherlands, July 10–14, 1989, Elsevier, Amsterdam, 1989, p 1053; Stud Surf Sci Catal* 49:1053
618. Yamazaki T, Nishimura H, Ozawa S (2000) *Miroporous Mesoporous Mater* 38:187.
619. Schoonheydt RA, Leeman H (1985) *Zeolites* 5:225
620. Gallezot P (2002) In: Karge HG, Weitkamp J (eds) *Molecular sieves – Science and technology, Springer-Verlag, Berlin, Heidelberg, New York, 3:257*
621. Gallezot P, Coudurier C, Primet M, Imelik B (1977) In: Katzer J (ed) *Molecular Sieves II, Proc 4th Int Zeolite Conf, Chicago, Ill, USA, April 18–22, 1977, p 144; ACS Symp Ser, Am Chem Soc, Washington DC, 1977, 40:144*
622. Jacobs PA (1986) In: Gates BC, Guzzi L, Knoezinger H (eds) *Metal clusters in catalysis; Stud Surf Sci Catal* 29:357, (cf. especially p 372)
623. Bein T, Jacobs PA, Schmidt F (1982) In: Jacobs PA, Jaeger NI, Jiru P, Schulz-Ekloff (eds) *Metal microstructures in zeolites – Preparation, properties, applications. Proc Workshop, Bremen, Germany, Sept 22–24, 1982, Elsevier, Amsterdam, 1982, p 111; Stud Surf Sci Catal* 12:111
624. Wrabetz S, Guntow U, Schloegl R, Karge HG (1996) In: Chon H, Ihm S-K, Uh YS (eds) *Progress in zeolite and microporous materials. Proc 11th Int Zeolite Conf, Seoul, Korea, August 12–17, 1996, Elsevier, Amsterdam 1997, p 583; Stud Surf Sci Catal* 105:583
625. Wrabetz S (1999) PhD Thesis, Technical University of Berlin
626. Sachtler WMH, Zhang Z (1993) *Adv Catal* 39:129
627. Nováková J, Kubelková L, Brabec L, Bastl Z, Jaeger N, Schulz-Ekloff G (1996) *Zeolites* 16:173
628. Dixit L, Lu G, Guzzi L (1994) *Zeolites* 14:588
629. LeFebvre F, Gelin P, Naccache C, Ben Taarit Y (1983) In: Olson D, Bisio A (eds) *Proc 6th Int Zeolite Conf, Reno, USA, 10–15 July, 1983, Butterworth, Guildford, UK, 1984, p 435*
630. Gelin P, Ben Taarit, Naccache C (1979) *J Catal* 59:357
631. Kazansky VB, Borovkov VYu, Sokolova N, Jaeger NI, Schulz-Ekloff G (1994) *Catal Lett* 23:263
632. Tebassi L, Sayari A, Ghorbel A, Dufaux M, Ben Taarit Y, Naccache C (1983) In: Olson D, Bisio A (eds) *Proc 6th Int Zeolite Conf, Reno, USA, 10–15 July, 1983, Butterworth, Guildford, UK, 1984, p 368*
633. Beyer HK, Jacobs PA (1977) In: Katzer J (ed) *Molecular Sieves II. Proc 4th Int Zeolite Conf, Chicago, Ill, USA, April 18–22, 1977, p 493; ACS Symp Ser, Am Chem Soc, Washington DC, 1977, 40:493*

634. Naccache C, Primet M, Mathieu MV (1973) In: Meier WM, Uytterhoeven JB (eds) *Molecular Sieves*, Proc 3rd Int Zeolite Conf, Zurich, Switzerland, September 3–7, 1973, Advances in Chemistry Series 121:266; Am Chem Soc, Washington, DC, 1973, p 266
635. Grodzicki M, Zakhariyeva-Pencheva O, Foerster H (1988) *Catalysis Today* 3:75
636. Hexter RM, Dows DA (1956) *J Chem Phys* 25:504
637. Cohen de Lara E (1972) *Molecular Physics* 23:555
638. Cohen de Lara E, Vincent-Geisse J (1976) *J Phys Chem* 80:1922
639. Delaval Y, Cohen de Lara (1981) *J Chem Soc, Faraday Trans I* 77:869
640. Grodzicki M, Zakhariyeva-Pencheva O, Foerster H (1988) *J Molecular Structure* 175:195
641. Ward JW, Habgood HW (1966) *J Phys Chem* 70:1178
642. Cohen de Lara E, Delaval Y, Tsakiris J (1976) *J Chimie Physique* 73:387
643. Dumont D, Bougeard D (1994) In: Weitkamp J, Karge HG, Pfeifer H, Hoelderich W (eds) *Zeolites and related microporous materials: State of the art 1994*. Proc 10th Int Zeolite Conf, Garmisch-Partenkirchen, Germany, July 17–22, 1994, Elsevier, Amsterdam, 1994, p 2131; *Stud Surf Sci Catal* 84:2131
644. Seidel U, Koch M, Brunner E, Staudte B, Pfeifer H (2000) *Microporous Mesoporous Mater* 35/36:341
645. Herzberg G (1945) *Molecular spectra and molecular structure – II Infrared and Raman spectra of polyatomic molecules*. Van Nostrand Reinhold Comp, New York, pp 66, 281, 283, 285
646. Deo AV, Dalla Lana IG, Habgood HW (1971) *J Catal* 21:270
647. Foerster H, Schuldt M (1975) *J Colloid Interface Sci* 52:380 (cf. especially p 384)
648. Hunger B, Miessner H, von Sombathely M, Geidel E (1996) *J Chem Soc, Faraday Trans* 92:499
649. Foerster H, Seelemann R (1976) *Ber Bunsengesellschaft* 80:153
650. Karge HG, Ladebeck J (1980) In: Sersale R, Colella C, Aiello R (eds), *Proc. of the 5th Int. Conf. on Zeolites*, Naples, Italy, June 2–6, 1980; Recent progress reports and discussion, Giannini, Naples, p. 180 (cf. especially pp 181 and 182)
651. Sugioka M, Amisawa M, Abe H, Sato K (1994) In: Weitkamp J, Karge HG, Pfeifer H, Hoelderich W (eds) *Zeolites and related microporous materials: State of the art 1994*. Proc 10th Int Zeolite Conf, Garmisch-Partenkirchen, Germany, July 17–22, 1994, Elsevier, Amsterdam, 1994, p 1603; *Stud Surf Sci Catal* 84:1603
652. Garcia CL, Lercher JA (1992) *J Phys Chem* 96:2230
653. Ward JW (1976) In: Rabo JA (ed) *Zeolite chemistry and catalysis*. ACS Monograph 171, Chapter 3, especially p 187, Am Chem Soc, Washington DC, 1976, Chapter 3, p 118
654. Foerster H, Schuldt M (1975) *Spectrochimica Acta* 31A:685
655. Krossner M, Sauer J (1996) *J Phys Chem* 100:6199
656. Sauer J (1996) *Science* 271:774
657. Pelenschikov AG, van Santen RA, Wolput JHMC, Jaenchen J (1994) In: Weitkamp J, Karge HG, Pfeifer H, Hoelderich W (eds) *Zeolites and related microporous materials: State of the art 1994*. Proc 10th Int Zeolite Conf, Garmisch-Partenkirchen, Germany, July 17–22, 1994, Elsevier, Amsterdam, 1994, p 2179; *Stud Surf Sci Catal* 84:2179
658. Jobic H, Tuel A, Krossner M, Sauer J (1996) *J Phys Chem* 100:19545
659. Haase F, Sauer J (1995) *J Am Chem Soc* 117:3780
660. Sauer J (1995) In: VCI (ed) *45 Jahre Fonds der Chemischen Industrie*, 1995, p 43
661. Batamack B, Dorémieux-Morin, Vincent R, Fraissard J (1991) *Chemical Physics Letters* 80:545
662. Batamack P, Dorémieux-Morin, Fraissard J, Freude D (1991) *J Phys Chem* 95:3790
663. Hunger M (2002) In: Karge HG, Weitkamp J (eds) *Molecular Sieves – Science and Technology*, Springer-Verlag, Berlin, Heidelberg, New York, 4:201
664. Parker LM, Bibby DM, Burns GR (1991) *Zeolites* 11:293
665. Parker LM, Bibby DM, Burns GR (1993) *Zeolites* 13:107
666. Wakabayashi F, Kondo JN, Domen K, Hirose C (1997) *Microporous Mater* 8:29
667. Bordiga S, Turnes Palomino G, Pazé C, Zecchina A (2000) *Microporous Mesoporous Mater* 34:67

668. Parker LM, Bibby DM, Burns GR (1989) In: Jacobs PA, van Santen RA (eds) *Zeolites: Facts, figures, future*. Proc 8th Int Zeolite Conf, Amsterdam, The Netherlands, July 10–14, 1989, Elsevier, Amsterdam, 1989, p 963; *Stud Surf Sci Catal* 49:963
669. Lercher JA, Gruendling C, Eder-Mirth G (1996) *Catalysis Today* 27:353 (and references therein)
670. Jentys A, Lercher JA (2001) In: van Bekkum H, Flanigen EM, Jacobs PA, Jansen JC (eds) *Introduction to zeolite science and practice*, 2nd edn. Elsevier, The Netherlands, Amsterdam, 2001, p 345; *Stud Surf Sci Catal* 137:345
671. Janin A, Lavalley JC, Macedo A, Raatz (1988) In: Flank WH, Whyte Jr TE (eds) *Perspectives in molecular sieve science*. ACS Symp Ser 368, Washington DC, 1988, p 117
672. Macedo A, Raatz F, Boulet R, Janin A, Lavalley JC (1987) In: Grobet PJ, Mortier WJ, Vansant EF, Schulz-Ekloff G (eds) *Innovation in zeolite materials science*. Proc Int Symp, Nieuwpoort, Belgium, Sept 13–17, 1987, Elsevier, Amsterdam, 1987, p 375; *Stud Surf Sci Catal* 37:375 (cf. especially p 376)
- 672a. Kazansky VB, Serykh AI, Semmer-Herledan V, Fraissard J (203) *Phys Chem Chem Phys* 5:966
- 672b. Subbotina IR, Kazanskii VB (2002) *Kinetics and Catalysis* 43:115 (Translated from *Kinetika i Kataliz* 43:125)
673. Ward JW (1967) *J Catal* 9:225
674. Kuehl GH (1973) In: Uytterhoeven JA (ed), *Proc 3rd Int Conf Molecular Sieves*, Zurich, Switzerland, Sept 3–7, 1973, University Leuven Press, p 227
675. Kuehl GH (1977) *Phys Chem Solids* 38:1259
676. Ward JW (1968) *J Catal* 10:34
677. Ward JW (1968) *J Colloid Interface Sci* 28:269
678. Ward JW (1976) In: Rabo JA (ed) *Zeolite chemistry and catalysis*. ACS Monograph 171, Chapter 3, especially p 227, Am Chem Soc, Washington DC, 1976, Chapter 3, p 118
679. Basila MR, Kantner TR, Rhee KH (1964) *J Phys Chem* 68:3197
680. Janin A, Maache M, Lavalley JC, Joly JE, Raatz F, Szydłowski N (1991) *Zeolites* 11:391
681. Joly JE, Auroux A, Lavalley JC, Janin A, Guth JL (1992) In: von Ballmoos R, Higgins JB, Treacy MMJ (eds) *Proc 9th Int Zeolite Conf*, Montreal, Canada, July 5–10, 1992, Butterworth-Heinemann, Boston, 1993, Vol II, p 235
682. Rhee KH, Rao VUS, Stencel JM, McIson GA, Crawford JE (1983) *Zeolites* 3:337
683. Rhee KH, Brown FR, Finseth DH, Stencel JM (1983) *Zeolites* 3:344
684. Rhee KH, Rao VUS, Stencel JM (1983) *Zeolites* 3:337
685. Mueller G, Bódís J, Eder-Wirth G, Kornatowski J, Lercher JA (1997) *J Molecular Structure* 410/411:173
686. Mueller G, Bodis E, Kornatowski J, Lercher JA (1999) *Phys Chem Chem Phys* 1:571
687. Akolekar DB (1993) *J Catal* 143:227
688. Akolekar DB (1996) *Zeolites* 17:283
689. Concepción P, López-Nieto JM, Mifsud A, Pérez-Pariente J (1996) *Zeolites* 16:56
690. Tusar NN, Mali G, Arčon I, Kaučič V, Ghambari-Siahkali A, Dwyer J (2002) *Microporous Mesoporous Mater* 55:203
691. Pieterse JAZ, Veefkind-Reyes S, Seshan K, Domokos L, Lercher JA (1999) *J Catal* 187:518
692. Teunissen EH, Jacobs WJH, Jansen APJ, van Santen RA (1992) In: von Ballmoos R, Higgins JB, Treacy MMJ (eds) *Proc 9th Int Zeolite Conf*, Montreal, Canada, July 5–10, 1992, Butterworth-Heinemann, Boston, 1993, Vol I, p 469
693. Corma A, Fornés V, Rey F (1993) *Zeolites* 13:56
694. Areán CO, Platero EE, Mentrut MP, Delgado MR, Llabrés i Xamena FX, García-Raso A, Morterra C (2000) *Microporous Mesoporous Mater* 34:55
695. Trombetta M, Busca G, Lenarda M, Storaro L, Pavan M (1999) *Appl Catal A* 182:225
696. Keskinen KM, Pakkanen TT, Raulo P, Ruotsalainen M, Sarv P, Tiitta M (1994) In: Weitkamp J, Karge HG, Pfeifer H, Hoelderich W (eds) *Zeolites and related microporous materials: State of the art 1994*. Proc 10th Int Zeolite Conf, Garmisch-Partenkirchen, Germany, July 17–22, 1994, Elsevier, Amsterdam, 1994, p 875; *Stud Surf Sci Catal* 84:875
697. Hunger B, Hoffmann J (1986) *Thermochimica Acta* 106:133

698. Topsøe N-Y, Pedersen K, Derouane EG (1981) *J Catal* 70:41
699. Pieterse JAZ, Veeffkind-Reyes S, Seshan K, Lercher JA (2000) *J Phys Chem B* 104:5715
700. Zhang W, Burckle EC, Smirniotis PG (1999) *Microporous Mesoporous Mater* 33:173
701. Li Q, Zhang R, Xue Z (1986) In: Murakami Y, Iijima A, Ward JW (eds) *New developments in zeolite science and technology. Proc 7th Int Zeolite Conf, Tokyo, Japan, August 17–22, 1986, Kodansha, Tokyo, Elsevier, Amsterdam, 1986, p 487; Stud Surf Sci Catal* 28:487
702. Selli E, Forni L (1999) *Microporous Mesoporous Mater* 31:129
703. Robb GM, Zhang W, Smirniotis PG (1998) *Microporous Mesoporous Mater* 20:307
704. Shigeishi RA, Chiche BH, Fajula F (2001) *Microporous Mesoporous Mater* 43:211
705. Sasidharan M, Hegde SG, Kumar R (1998) *Microporous Mesoporous Mater* 24:59
706. Kumar R, Reddy KR, Raj A, Ratnasamy P (1992) In: von Ballmoos R, Higgins JB, Treacy MMJ (eds) *Proc 9th Int Zeolite Conf, Montreal, Canada, July 5–10, 1992, Butterworth-Heinemann, Boston, 1993, Vol I, p 189 (cf. especially p 191)*
707. Datka J (1980) *J Chem Soc, Faraday Trans I* 76:705
708. Eder F, Stockenhuber M, Lercher JA (1997) *J Chem Phys B* 101:5415
709. Eder F, Lercher JA (1997) *J Phys Chem B* 101:1273
710. Eder F, He Y, Nivarthi G, Lercher JA (1996) *Recueil des Travaux Chimiques des Pays-Bas* 115:531
711. Datka J, Boczar M, Rymarowicz P (1988) *J Catal* 114:368
712. Kiricsi I, Tasi Gy, Foerster H, Fejes P (1994) *J Mol Structure* 317:33
713. Kazansky VB (1990) In: Oehlmann G, Pfeifer H, Fricke R (eds) *Catalysis and adsorption by zeolites. Proc ZEOCAT '90, Leipzig, Germany, August 20–23, 1990, Elsevier, Amsterdam, 1991, p 117; Stud Surf Sci Catal* 65:117
714. Khodakov AYu, Kustov LM, Kazansky VB, Williams C (1992) *J Chem Soc, Faraday Trans* 88:3251
715. Makarova MA, Zholobenko VL, Al-Ghefaily KM, Thompson NE, Dewing J, Dwyer J (1994) *J Chem Soc, Faraday Trans* 90:1047
716. Kazansky VB, Borovkov VYu, Serich A, Karge HG (1998) *Microporous Mesoporous Mater* 22:251
717. Kazansky VB, Jentoft FC, Karge HG (1998) *J Chem Soc, Faraday Trans* 94:1347
718. Kazansky VB, Kustov LM, Khodakov AYu (1989) In: Jacobs PA, van Santen RA (eds) *Zeolites: Facts, figures, future. Proc 8th Int Zeolite Conf, Amsterdam, The Netherlands, July 10–14, 1989, Elsevier, Amsterdam, 1989, p 1173; Stud Surf Sci Catal* 49:1173
719. Su B-L, Norberg V, Martens JA (1998) *Microporous Mesoporous Mater* 25:151
720. Kazansky VB, Borovkov VYu, Karge HG (1998) In: Treacy MMJ, Marcus BK, Bisher ME, Higgins JB (eds) *Proc 12th Int Zeolite Conf, Baltimore, Maryland, USA, July 5–10, 1998, Materials Research Society, Warrendale, Pa, USA, 1999, p 269*
721. Su B, Barthomeuf D (1995) *Zeolites* 15:470
722. Norberg V, Docquir F, Su B-L (1999) In: Kiricsi I, Pál-Borbély G, Nagy JB, Karge HG (eds); *Porous materials in environmentally friendly processes. Proc 1st Int FEZA Conf, Eger, Hungary, September 1–4, 1999, Elsevier, Amsterdam, 1999, p 253; Stud Surf Sci Catal* 125:253
723. Jentys A, Lercher JA (1988) In: Karge HG, Weitkamp J (eds) *Zeolites as catalysts, sorbents and detergent builders – Applications and innovations. Proc Int Symp, Wuerzburg, Germany, Sept 4–8, 1988, Elsevier, Amsterdam, 1989, p 585; Stud Surf Sci Catal* 46:585
724. Jacobs PA, Martens JA, Weitkamp J, Beyer HK (1981) *Faraday Discussions* 72:353
725. Jacobs PA (1982) *Catal Rev Sci Eng* 24:415
726. Datka J (1981) *J Chem Soc, Faraday Trans I* 77:511
727. Zubkov SA, Kustov LM, Kazansky VB, Girnus I, Fricke R (1991) *J Chem Soc, Faraday Trans* 87:897
728. Tvaruzkova Z, Tupa M, Jiru P, Nastro A, Giordano G, Trifiro F (1988) In: Karge HG, Weitkamp J (eds) *Zeolites as catalysts, sorbents and detergent builders – Applications and innovations. Proc Int Symp, Wuerzburg, Germany, Sept 4–8, 1988, Elsevier, Amsterdam, 1989, p 281; Stud Surf Sci Catal* 46:281

729. Kubelková L, Kotrla J, Florian J (1995) *J Phys Chem* 99:10285
730. Thibault-Starzyk F, Bettahar MM, Saussey J, Lavalley J-C (1996) In: Chon H, Ihm S-K, Uh YS (eds) *Progress in zeolite and microporous materials. Proc 11th Int Zeolite Conf, Seoul, Korea, August 12–17, 1996*, Elsevier, Amsterdam, 1997, p 925; *Stud Surf Sci Catal* 105:925
731. Šepa A, Gorte RJ, White D, Suits BH, Swaminathan VS (1998) In: Treacy MMJ, Marcus BK, Bisher ME, Higgins JB (eds) *Proc 12th Int Zeolite Conf, Baltimore, Maryland, USA, July 5–10, 1998*, Materials Research Society, Pa, USA, 1999, p 2287
732. Ratov AN, Kubasov AA, Topchieva KV, Rosolovskaya EN, Kalinin VP (1973) *Kinetics and Catal* 14:896
733. Kotrla J, Kubelková L (1995) In: HK Beyer, Karge HG, Kiricsi I, Nagy JB (eds) *Catalysis by microporous materials. Proc ZEOCAT '95, Szombathely, Hungary, July 9–13, 1995*, Elsevier, Amsterdam, 1995, p 509; *Stud Surf Sci Catal* 94:509
734. Meijer EL, van Santen RA, Jansen APJ (1996) *J Phys Chem* 100:9282
735. Kustov LM, Zubkov SA, Kazansky VB, Bondar LA (1991) In: Jacobs PA, Jaeger NI, Kubelková L, Wichterlová (eds) *Zeolite chemistry and catalysis. Proc Int Symp, Prague, Czechoslovakia, Sept 8–13, 1991*, Elsevier, Amsterdam, 1991, p 303; *Stud Surf Sci Catal* 69:303
736. Detrekoey E, Kalló D (1979) In: Shopov D, Andreev A, Palazov A, Petrov L (eds) *Proc 4th Int Symp Heterogeneous Catalysis, Varna, Bulgaria, October 2–5, 1979*, Publishing House Bulgarian Acad, Sofia, 1979, Part 2, p 437
737. Bosacek V, Kubelková L (1990) *Zeolites* 10:64
738. Alexander SM, Bibby DM, Howe RF, Meinhold RH (1993) *Zeolites* 13:441
739. Sohn JR, Lee SI (1996) In: Chon H, Ihm S-K, Uh YS (eds) *Progress in zeolite and microporous materials. Proc 11th Int Zeolite Conf, Seoul, Korea, August 12–17, 1996*, Elsevier, Amsterdam, 1997, p 1763; *Stud Surf Sci Catal* 105:1763
740. Paukshtis EA, Soltanov RI, Yurchenko EN (1982) *React Kinet Catal Lett* 19:105
741. Romotowski T, Komorek J, Paukshtis YA, Yurchenko EN (1991) *Zeolites* 11:497
742. Kustov LM, Kazansky VB, Beran S, Kubelková L, Jiru P (1987) *J Phys Chem* 91:5247
743. Kubelkova L, Beran S, Lercher JA (1989) *Zeolites* 9:539
744. Garrone E, Chiapetta R, Spoto G, Ugliengo P, Zecchina A, Fajula F (1992) In: von Ballmoos R, Higgins JB, Treacy MMJ (eds) *Proc 9th Int Zeolite Conf, Montreal, Canada, July 5–10, 1992*, Butterworth-Heinemann, Boston, 1993, Vol II, p 267
745. Echoufi N, Gelin P (1992) In: von Ballmoos R, Higgins JB, Treacy MMJ (eds) *Proc 9th Int Zeolite Conf, Montreal, Canada, July 5–10, 1992*, Butterworth-Heinemann, Boston, 1993, Vol II, p 275
746. Zecchina A, Spoto G, Bordiga S, Padovan M, Leofanti G, Petrini G (1990) In: Oehlmann G, Pfeifer H, Fricke R (eds) *Catalysis and adsorption by zeolites. Proc ZEOCAT '90, Leipzig, Germany, August 20–23, 1990*, Elsevier, Amsterdam, 1991, p 671; *Stud Surf Sci Catal* 65:671
747. Bein T, Chase DB, Farlee RD, Stucky GD (1986) In: Murakami Y, Iijima A, Ward JW (eds) *New developments in zeolite science and technology. Proc 7th Int Zeolite Conf, Tokyo, Japan, August 17–22, 1986*, Kodansha, Tokyo, Elsevier, Amsterdam, 1986, p 609; *Stud Surf Sci Catal* 28:311
748. Kazansky VB, Borovkov VYu, Karge HG (1999) *Z phys Chem* 211:1
749. Staudte B, Hunger M, Nimz M (1991) *Zeolites* 11:837 (cf. especially p 838)
750. Pruski M, Ernst H, Pfeifer H, Staudte B (1985) *Chem Phys Lett* 119:412 (cf. especially p 415)
751. Zscherpel U, Staudte B, Loeffler E, Peuker C, Jahn E (1989) *Z phys Chem (Leipzig)* 270:207 (cf. especially p 415)
752. Beck K, Pfeifer H, Staudte B (1993) *Microporous Mater* 2:1
753. Coluccia S, Marchese L, Martra G (1999) *Microporous Mesoporous Mater* 30:43
754. Jentys A, Kleestorfer K, Vinek H (1999) *Microporous Mesoporous Mater* 27:321
755. Beck K, Pfeifer H, Staudte B (1993) *J Chem Soc, Faraday Trans* 89:3995
756. Wakabayashi F, Kondo JN, Domen K, Hirose C (1997) *Microporous Mater* 8:29
757. Wakabayashi F, Kondo J, Wada A, Domen K, Hirose C (1993) *J Phys Chem* 97:10761

758. Wakabayashi F, Kondo J, Domen K, Hirose C (1993) *Catal Lett* 21:257
759. Wakabayashi F, Kondo J, Domen K, Hirose C (1993) *Microporous Mater* 2:35
760. Wakabayashi F, Kondo J, Domen K, Hirose C (1993) In: Hattori H, Misono M, Ono Y (eds) *Proc Int Symp on Acid-Base Catalysis II*, Sapporo, Japan, December 2–4, 1993, Elsevier, Amsterdam, 1993, p 157; *Stud Surf Sci Catal* 90:157
761. Angell CL, Howell MV (1969) *J Chem Phys* 73:2551
762. Geodokyan KT, Kiselev AV, Lygin VI (1967) *Russ J Phys Chem* 38:1480
763. Jaenchen J, Haanepen MJ, Peeters MPJ, van Wolput JHMC, Wolthuisen JB, van Hooff JHC (1994) In: Weitkamp J, Karge HG, Pfeifer H, Hoelderich W (eds) *Zeolites and related microporous materials: State of the art 1994. Proc 10th Int Zeolite Conf, Garmisch-Partenkirchen, Germany, July 17–22, 1994*, Elsevier, Amsterdam, 1994, p 373; *Stud Surf Sci Catal* 84:373
764. Ristić A, Tusar NN, Ačron I, Thibault-Starzyk F, Hanzel D, Czyzniewska J, Kaučič V (2002) *Microporous Mesoporous Mater* 56:303
765. Sachsenroeder H, Brunner E, Koch M, Pfeifer H, Staudte B (1996) *Microporous Mater* 6:341
766. Brunner E, Kaerger J, Koch M, Pfeifer H, Sachsenroeder H, Staudte B (1996) In: Chon H, Ihm S-K, Uh YS (eds) *Progress in zeolite and microporous materials. Proc 11th Int Zeolite Conf, Seoul, Korea, August 12–17, 1996*, Elsevier, Amsterdam, 1997, p 463; *Stud Surf Sci Catal* 105:463
767. Sachsenroeder H (1997) PhD Thesis, University of Leipzig
768. Su B-L, Jaumain D (1998) In: Treacy MMJ, Marcus BK, Bisher ME, Higgins JB (eds) *Proc 12th Int Zeolite Conf, Baltimore, USA, July 5–10, 1998*, Materials Research Society, Warrendale, Pa, USA, 1999, p 2689
769. Mestl G, Knoezinger H (1997) In: Ertl G, Knoezinger H, Weitkamp J (eds) *Handbook of catalysis*, VCH Verlagsgesellschaft, Germany, Weinheim, USA, New York, p 539
770. Karge HG, Dondur V (1990) *J Phys Chem* 94:765
771. Kogelbauer A, Lercher JA, Steinberg KH, Roessner F, Soellner A, Dinitriev RV (1989) *Zeolites* 9:224
772. Ha BH, Barthomeuf D (1979) *J Chem Soc, Faraday Trans I* 75:2366
773. Cairon O, Thomas K, Chevreau T (2001) *Microporous Mesoporous Mater* 46:327
774. Garrone E, Onida B, Gabelica Z, Derouane EG (1994) In: Karge HG, Weitkamp J (eds) *Zeolite science 1994: Recent progress and discussions. Supplementary materials to the 10 th Int Zeolite Conf, Garmisch-Partenkirchen, Germany, July 17–22, 1994*, Elsevier, Amsterdam, 1995, p 106, *Stud Surf Sci Catal* 98:106
775. Rakic VM, Hercigonja RV, Dondur VT (1999) *Microporous Mesoporous Mater* 27:27
776. Manoilova OV, Dakka J, Sheldon RA, Tsyganenko AA (1995) In: HK Beyer, Karge HG, Kiricsi I, Nagy JB (eds) *Catalysis by microporous materials. Proc ZEOCAT '95, Szombathely, Hungary, July 9–13, 1995*, Elsevier, Amsterdam, 1995, p 163; *Stud Surf Sci Catal* 94:163
777. Bonelli B, Ribeiro MF, Antunes AP, Valange S, Gabelica Z, Garrone E (2002) *Microporous Mesoporous Mater* 54:305
778. Romannikov VN, Fenelonov VB, Paukshtis EA, Derevyankin AYu, Zaikovskii VI (1998) *Microporous Mesoporous Mater* 21:411
779. Viale S, Garrone E, Di Renzo F, Chiche B, Fajula F (1996) In: Chon H, Ihm S-K, Uh YS (eds) *Progress in zeolite and microporous materials. Proc 11th Int Zeolite Conf, Seoul, Korea, August 12–17, 1996*, Elsevier, Amsterdam, 1997, p 533; *Stud Surf Sci Catal* 105:533
780. Hadjiivanov K (2000) *Catal Rev-Sci Engng* 42:71
781. Henriques C, Marie O, Thobault-Starzyk F, Lavalley J-C (2001) *Microporous Mesoporous Mater* 50:161
782. Hadjiivanov K, Dimitrov L (1999) *Microporous Mesoporous Mater* 27:49
783. Dimitrov L, Petrov L, Nikolov R (1998) *Bulg Chem Commun* 30 (1/2):583
784. Hadjiivanov (1998) *Microporous Mesoporous Mater* 24:41
785. Zhu CY, Lee CW, Chong PJ (1996) *Zeolites* 17:483
786. Ito E, Mergler YJ, Nieuwenhuys BE, van Bekkum H, van den Bleek CM (1995) *Microporous Mater* 4:455

787. Gianotti E, Marchese L, Martra G, Coluccia S (1998) In: Treacy MMJ, Marcus BK, Bisher ME, Higgins JB (eds) Proc 12th Int Zeolite Conf, Baltimore, USA, July 5–10, 1998, Materials Research Society, Warrendale, PA, USA, 1999, p 2775
788. Ivanova E, Hadjiivanov K, Klissurski D, Bevilacqua M, Armaroli T, Busca G (2001) *Microporous Mesoporous Mater* 46:299
789. Ziolk M, Sobczak I, Decyk P, Nowak I (1999) In: Kiricsi I, Pál-Borbély G, Nagy JB, Karge HG (eds); Porous materials in environmentally friendly processes. Proc 1st Int FEZA Conf, Eger, Hungary, September 1–4, 1999, Elsevier, Amsterdam, 1999, p 633; *Stud Surf Sci Catal* 125:633
790. Ziolk M, Nowak I, Poltorak H, Lewandowska A, Sobczak I (1999) In: Kiricsi I, Pál-Borbély G, Nagy JB, Karge HG (eds); Porous materials in environmentally friendly processes. Proc 1st Int FEZA Conf, Eger, Hungary, September 1–4, 1999, Elsevier, Amsterdam, 1999, p 691; *Stud Surf Sci Catal* 125:691
791. Karge HG, Ladebeck J, Sarbak Z, Hatada K (1982) *Zeolites* 2:94 (cf. especially p 97)
792. De Mallmann A, Barthomeuf D (1986) In: Murakami Y, Iijima A, Ward JW (eds) *New developments in zeolite science and technology*. Proc 7th Int Zeolite Conf, Tokyo, Japan, August 17–22, 1986, Kodansha, Tokyo, Elsevier, Amsterdam, 1986, p 609; *Stud Surf Sci Catal* 28:609
793. De Mallmann A, Barthomeuf D (1988) *Zeolites* 8:292
794. O'Malley PJ (1990) In: Oehlmann G, Pfeifer H, Fricke R (eds) *Catalysis and adsorption by zeolites*. Proc ZEOCAT '90, Leipzig, Germany, August 20–23, 1990, Elsevier, Amsterdam, 1991, p 689; *Stud Surf Sci Catal* 65:689
795. Datka J, Gil B, Weglarski J (1998) *Microporous Mesoporous Mater* 21:75
796. Buzzoni R, Bordiga S, Spoto G, Scarano D, Ricchiardi G, Lamberti C, Zecchina A (1994) In: Karge HG, Weitkamp J (eds) *Zeolite science 1994: Recent progress and discussions*. Supplementary materials to the 10 th Int Zeolite Conf, Garmisch-Partenkirchen, Germany, July 17–22, 1994, Elsevier, Amsterdam, 1995, p 104, *Stud Surf Sci Catal* 98:104
797. Garrone E, Onida B, Spanò G, Spoto G, Ugliengo P, Zecchina A (1994) In: Karge HG, Weitkamp J (eds) *Zeolite science 1994: Recent progress and discussions*. Supplementary materials to the 10 th int Zeolite Conf, Garmisch-Partenkirchen, Germany, July 17–22, 1994, Elsevier, Amsterdam, 1995, p 99, *Stud Surf Sci Catal* 98:99
798. Flego C, Kiricsi I, Perego C, Bellussi G (1995) In: Beyer HK, Karge HG, Kiricsi I, Nagy JB (eds) *Catalysis by microporous materials*. Proc ZEOCAT '95, Szombathely, Hungary, July 9–13, 1995, Elsevier, Amsterdam, 1995, p 405; *Stud Surf Sci Catal* 94:405
799. Li X-W, Su X, Liu X-Y (1998) In: Treacy MMJ, Marcus BK, Bisher ME, Higgins JB (eds) Proc 12th Int Zeolite Conf, Baltimore, USA, July 5–10, 1998, Materials Research Society, Warrendale, Pa, USA, 1999, p 2659
800. Scokart PO, Rouxhet PG (1980) *J Chem Soc, Faraday Trans I* 76:1476
801. Scokart PO, Rouxhet PG (1981) *Bull Soc Chim Belgique* 90:983
802. Barthomeuf D, de Mallmann A (1987) In: Grobet PJ, Mortier WJ, Vasant EF, Schulz-Ekloff G (eds) *Innovation in zeolite materials science*. Proc Int Symp, Nieuwpoort, Belgium, Sept 13–17, 1987, Elsevier, Amsterdam 1988, p 365; *Stud Surf Sci Catal* 37:365
803. Barthomeuf D (1990) In: Oehlmann G, Pfeifer H, Fricke R (eds) *Catalysis and adsorption by zeolites*. Proc ZEOCAT '90, Leipzig, Germany, August 20–23, 1990, Elsevier, Amsterdam, 1991, p 157; *Stud Surf Sci Catal* 65:157
804. Murphy D, Massiani P, Franck R, Barthomeuf D (1996) *J Phys Chem* 100:6731
805. Murphy D, Massiani P, Franck R, Barthomeuf D (1996) In: Chon H, Ihm S-K, Uh YS (eds) *Progress in zeolite and microporous materials*. Proc 11th Int Zeolite Conf, Seoul, Korea, August 12–17, 1996, Elsevier, Amsterdam, 1997, p 639; *Stud Surf Sci Catal* 105:639
806. Heidler R, Janssens GOA, Mortier WJ, Schoonheydt RA (1997) *Microporous Mater* 12:1
807. Garrone E, Marturano P, Onida B, Laspéras M, Di Renzo F (1998) In: Treacy MMJ, Marcus BK, Bisher ME, Higgins JB (eds) 12th Int Zeolite Conf, Baltimore, USA, July 5–10, 1998, Materials Research Society, Warrendale, Pa, USA, 1999, p 2705
808. Akolekar DB, Huang M, Kaliaguine S (1994) *Zeolites* 14:519
809. Fernandez R, Giotto MV, Pastore HO, Cordoso D (2002) *Microporous Mesoporous Mater* 53:135

810. Yagi F, Tsuji H, Hattore H (1997) *Microporous Mater* 9:237
811. Przystajko W, Fiedorow R, Dalla Lana IG (1987) *Zeolites* 7:477
812. Liu J, Ying P, Xin Q, Liu C (1997) *Zeolites* 19:197
813. Ryma U, Hunger M, Knoezinger H, Weitkamp J (1999) In: Kiricsi I, Pál-Borbély G, Nagy JB, Karge HG (eds); *Porous materials in environmentally friendly processes. Proc 1st Int FEZA Conf, Eger, Hungary, September 1–4, 1999*, Elsevier, Amsterdam, 1999, p 197; *Stud Surf Sci Catal* 125:197
814. Mirth G, Lercher JA (1991) In: Holmes et al. (eds) *Natural Gas Conversion*, Elsevier, Amsterdam, 1991, p 437
815. Mirth G, Lercher J (1991) *J Phys Chem* 95:3736
816. Rep M, Palomares AE, Eder-Mirth G, van Ommen JG, Roesch N, Lercher JA (2000) *J Phys Chem B* 104:8624
817. Kogelbauer A, Lercher JA (1992) *J Chem Soc, Faraday Trans* 88:2283
818. Rep M, Palomares AE, van Ommen JG, Lefferts L, Lercher JA (2000) In: Corma A, Melo FV, Mendioroz S, Fierro JLG (eds) *Proc 12th Int Congress Catal, Granada, Spain, July 9–14, 2000*, Elsevier, Amsterdam, 2000, p 2957; *Stud Surf Sci Catal* 130:2957
819. Vayssilov GN, Lercher JA, Roesch N (2000) *J Phys Chem B* 104:8614
820. Mirth G, Lercher JA, Anderson MW, Klinowski J (1990) *J Chem Soc, Faraday Trans* 86:3039
821. Bonn M, van Santen RA, Lercher JA, Kleyn AW, Bakker HJ (1997) *Chem Phys Lett* 278:213 (and references therein)
822. Haase F, Sauer J (1994) *J Phys Chem* 98:3083
823. Sauer J (1994) In: Weitkamp J, Karge HG, Pfeifer H, Hoelderich W (eds) *Zeolites and related microporous materials: State of the art 1994. Proc 10th Int Zeolite Conf, Garmisch-Partenkirchen, Germany, July 17–22, 1994*, Elsevier, Amsterdam, 1994, p 2039; *Stud Surf Sci Catal* 84:2039
824. Jentys A, Warecka G, Lercher JA (1989) *J Mol Catal* 51:309
825. Wakabayashi F, Kashitani M, Fujino T, Kondo JN, Domen K, Hirose C (1996) In: Chon H, Ihm S-K, Uh YS (eds) *Progress in zeolite and microporous materials. Proc 11th Int Zeolite Conf, Seoul, Korea, August 12–17, 1996*, Elsevier, Amsterdam, 1997, p 1739; *Stud Surf Sci Catal* 105:1739
826. Wakabayashi F, Kondo JN, Hirose C, Domen K (1998) In: Treacy MMJ, Marcus BK, Bisher ME, Higgins JB (eds) *Proc 12th Int Zeolite Conf, Baltimore, USA, July 5–10, 1998*, Materials Research Society, Warrendale, Pa, USA, 1999, p 2577
827. Datka J, Rakoczy J, Zadrozna G (1998) In: Treacy MMJ, Marcus BK, Bisher ME, Higgins JB (eds) *Proc 12th Int Zeolite Conf, Baltimore, USA, July 5–10, 1998*, Materials Research Society, Warrendale, PA, USA, 1999, p 2601
828. Pelenschikov AG, Morosi G, Gamba A (1992) In: von Ballmoos R, Higgins JB, Treacy MMJ (eds) *Proc 9th Int Zeolite Conf, Montreal, Canada, July 5–10, 1992*, Butterworth-Heinemann, Boston, 1993, Vol I, p 537
829. Segawa K, Mizuno S, Maruyama Y, Nakata S (1994) In: Weitkamp J, Karge HG, Pfeifer H, Hoelderich W (eds) *Zeolites and related microporous materials: State of the art 1994. Proc 10th Int Zeolite Conf, Garmisch-Partenkirchen, Germany, July 17–22, 1994*, Elsevier, Amsterdam, 1994, p 1943; *Stud Surf Sci Catal* 84:1943
830. Ziolek M, Czyzniewska J, Lamotte J, Lavalley JC (1996) *Zeolites* 16:42
831. Ziolek M, Czyzniewska J, Kujawa J, Travert A, Mauge F, Lavalley JC (1998) *Microporous Mesoporous Mater* 23:45
832. Huang Y, Leech JH, Havenga E, Poissant RR (2001) *Microporous Mesoporous Mater* 48:95
833. Howard J, Kadir ZA (1984) *Zeolites* 4:45
834. Datka J (1991) *Zeolites* 11:739
835. Becker KA, Karge HG, Streubel W-D (1973) *J Catal* 28:403
836. Yashima T, Nagata J-I, Shimazaki Y (1977) In: Katzer J (ed) *Molecular Sieves-II. Proc 4th Int Zeolite Conf, Chicago, Ill, USA, April 18–22, 1977*, p 626; *ACS Symp Ser, Am Chem Soc, Washington DC, 1977*, 40:626
837. Karge HG, Bolding EP (1988) *Catalysis Today* 3:379

838. Howard J, Lux PJ, Yarwood J (1988) *Zeolites* 8:427
839. Foerster H, Zakharijeva-Pencheva O (1986) *J Mol Structure* 145:149
840. Foerster H, Zakharijeva-Pencheva O (1990) *J Mol Structure* 218:399
841. Foerster H, Seelemann R (1979) In: Shopov D, Andreev A, Palazov A, Petrov L (eds) *Proc 4th Int Symp Heterogeneous Catalysis*, Varna, Bulgaria, October 2–5, 1979, Publishing House Bugarian Acad, Sofia, 1979, p 355
842. Masuda T, Fukumoto N, Kitamura M, Mukai SR, Hashimoto K, Tanaka T, Funabiki T (2001) *Microporous Mesoporous Mater* 48:239
843. Moissette A, Brémard C (2001) *Microporous Mesoporous Mater* 47:345
844. Romanowski BV (1984) In: Dechema (ed) *Proc 8th Int Congress Catal*, Berlin, Germany, July 2–9, 1984, Verlag Chemie, Heidelberg, Vol IV; p 657 (and references therein)
845. Schulz-Ekloff G, Woehrl D, Iliev V, Ignatzek E, Andreev A (1988) In: Weitkamp J, Karge HG (eds) *Zeolites as catalysts and detergent builders – applications and innovations. Proc Int Symp, Würzburg, Germany, Sept 4–8, 1988, Elsevier, Amsterdam, 1989, p 315; Stud Surf Sci Catal* 46:315
846. Ernst S, Traa Y, Deeg U (1994) In: Weitkamp J, Karge HG, Pfeifer H, Hoelderich W (eds) *Zeolites and related microporous materials: State of the art 1994. Proc 10th Int Zeolite Conf, Garmisch-Partenkirchen, Germany, July 17–22, 1994, Elsevier, Amsterdam, 1994, p 925; Stud Surf Sci Catal* 84:925
847. Balkus Jr KJ, Welch AA, Gnade BE (1990) *Zeolites* 10:722
848. De Vos DE, Knops-Gerrits PP, Vanoppen DL, Jacobs PA (1995) *Supramolecular Chemistry* 6:49
849. Knops-Gerrits PP, Toufar H, Jacobs PA (1996) In: Chon H, Ihm S-K, Uh YS (eds) *Progress in zeolite and microporous materials. Proc 11th Int Zeolite Conf, Seoul, Korea, August 12–17, 1996, Elsevier, Amsterdam, 1997, p 1109; Stud Surf Sci Catal* 105:1109
850. De Vos DE, Jacobs PA (1992) In: von Ballmoos R, Higgins JB, Treacy MMJ (eds) *Proc 9th Int Zeolite Conf, Montreal, Canada, July 5–10, 1992, Butterworth-Heinemann, Boston, 1993, Vol II, p 615*
851. Zhan B-Z, Li X-Y (1996) In: Chon H, Ihm S-K, Uh YS (eds) *Progress in zeolite and microporous materials. Proc 11th Int Zeolite Conf, Seoul, Korea, August 12–17, 1996, Elsevier, Amsterdam, 1997, p 615; Stud Surf Sci Catal* 105:615
852. Poborchii VV (1996) In: Chon H, Ihm S-K, Uh YS (eds) *Progress in zeolite and microporous materials. Proc 11th Int Zeolite Conf, Seoul, Korea, August 12–17, 1996, Elsevier, Amsterdam, 1997, p 631; Stud Surf Sci Catal* 105:631
853. Bresinska I, Drago RS (1990) In: Oehlmann G, Pfeifer H, Fricke R (eds) *Catalysis and adsorption by zeolites. Proc ZEOCAT'90, Leipzig, Germany, August 20–23, 1990, Elsevier, Amsterdam, 1991, p 101; Stud Surf Sci Catal* 65:101
854. Mueller G, Bódis J, Eder-Wirth G, Kornatowski J, Lercher JA (1997) *J Molecular Structure* 410/411:173
855. Mueller G, Bodis E, Kornatowski J, Lercher JA (1999) *Phys Chem Chem Phys* 1:571
856. Mueller G, Eder-Mirth G, Lercher JA (1995) In: Bonneviot L, Kaliaguine S (eds) *Zeolites: A refined tool for designing catalytic sites. Proc Int Symp, Québec, Canada, October 15–20, Elsevier, Amsterdam, 1995, p 71; Stud Surf Sci Catal* 97:71
857. Schueth F (1992) *J Phys Chem* 96:7493
858. Marlow F, Hoffmann K, Hill W, Kornatowski J, Caro J (1994) In: Weitkamp J, Karge HG, Pfeifer H, Hoelderich W (eds) *Zeolites and related microporous materials: State of the art 1994. Proc 10th Int Zeolite Conf, Garmisch-Partenkirchen, Germany, July 17–22, 1994, Elsevier, Amsterdam, 1994, p 2277; Stud Surf Sci Catal* 84:2277
859. Mueller G, Eder-Mirth, Kessler H, Lercher JA (1995) *J Phys Chem* 99:12327
860. Kalvachev Yu, Bezouhanova C, Lechert H (1991) *Zeolites* 11:73
861. Schueth F, Demuth D, Kallus S (1994) In: Weitkamp J, Karge HG, Pfeifer H, Hoelderich W (eds) *Zeolites and related microporous materials: State of the art 1994. Proc 10th Int Zeolite Conf, Garmisch-Partenkirchen, Germany, July 17–22, 1994, Elsevier, Amsterdam, 1994, p 1223; Stud Surf Sci Catal* 84:1223

862. Nowotny M, Lercher JA, Kessler H (1991) *Zeolites* 11:454
863. Vergilov I, Valtchev V (1991) *Zeolites* 11:387
864. Beard WC (1973) In: Meier WM, Uytterhoeven JB (eds) *Molecular Sieves, Proc 3rd Int Zeolite Conf, Zurich, Switzerland, September 3–7, 1973, Advances in Chemistry Series 121:162; Am Chem Soc, Washington DC, 1973, p 162*
865. Guth J-L, Caullet P, Wey R (1980) In: Rees LVC (ed) *Proc 5th Int Zeolite Conf, Naples, Italy, June 2–6, 1980, Heyden, London, p 30*
866. Roozeboom F, Robson HE, Chan SS (1983) *Zeolites* 3:321
867. Groenen EJJ, Emeis CA, van den Berg JP, de Jong-Versloot PC (1987) *Zeolites* 7:474
868. Mintova S, Petkov N, Karaghiosoff K, Bein T (2001) *Microporous Mesoporous Mater* 50:121
869. Tuw J, Dutta PK, Kresge CT (1991) *J Phys Chem* 95: 5267
870. Dutta PK, Shieh DC (1988) *J Phys Chem* 90:2331
871. Dutta PK, Shieh DC, Puri M (1987) *J Phys Chem* 91:2332
872. Buge H-G, Peuker Ch, Pilz W, Jahn E, Rademacher O (1990) *Z phys Chem (Leipzig)* 271:881
873. Occelli ML, Innes RA, Apple TM, Gerstein BC (1983) In: Olson D, Bisio A (eds) *Proc 6th Int Zeolite Conf, Reno, USA, 10–15 July, 1983, Butterworth, Guildford, UK, 1984, p 674*
874. Schoeman BJ, Regev O (1996) *Zeolites* 17:447
875. Engstroem V, Mihailova B, Hedlund J, Holmgren A, Sterte J (2000) *Microporous Mesoporous Mater* 38:51
876. Coutinho D, Balkus jr KJ (2002) *Microporous Mesoporous Mater* 52:79
877. Gujar AC, Price GL (2002) *Microporous Mesoporous Mater* 54:201
878. Calabro DC, Yalyocsik EW, Ryan FX (1996) *Microporous Mater* 7:243
879. Dutta PK (1992) In: von Ballmoos R, Higgins JB, Treacy MMJ (eds) *Proc 9th Int Zeolite Conf, Montreal, Canada, July 5–10, 1992, Butterworth-Heinemann, Boston, 1993, Vol I, p 181*
880. Heylen CF, Jacobs PA (1977) In: Katzer J (ed) *Molecular Sieves, II. Proc 4th Int Zeolite Conf, Chicago, Ill, USA, April 18–22, 1977, p 490; ACS Symp Ser, Am Chem Soc, Washington DC, 1977, 40:490*
881. Ward JW (1968) *J Catal* 11:259
882. Kredel P, PhD Thesis, Technische Hochschule Darmstadt, 1980
883. Maroni VA, Martin KA, Johnson SA (1988) In: Flank WH, Whyte TE Jr (eds) *Perspectives in molecular sieve science. ACS Symp Ser 368, Am Chem Soc, Washington DC, 1988, p 85*
884. Salzer R, Ehrhardt B, Dressler J, Steinberg K-H, Klæboe K (1990) In: Oehlmann G, Pfeifer H, Fricke R (eds) *Catalysis and adsorption by zeolites. Proc ZEOCAT '90, Leipzig, Germany, August 20–23, 1990, Elsevier, Amsterdam, 1991, p 663; Stud Surf Sci Catal* 65:663
885. Karge HG, Ladebeck J (1980) In: Sersale R, Colella C, Aiello R (eds), *Proc 5th Int Zeolite Conf, Naples, Italy, June 2–6, 1980; Recent progress reports and discussion, Giannini, Naples, 1980, p 180 (cf. especially p 183)*
886. Foerster H, Schuldt M (1975) *J Catal* 40:391
887. Karge HG, Hatada K, Zhang Y, Fiedorow R (1983) *Zeolites* 3:13 (especially p 15)
888. Karge HG, Borbély G, Beyer HK, Onyéstyk G (1988) In: Phillips MJ, Ternan M (eds) *Proc 9th Int Congress on Catalysis, Calgary, Canada, June26-July 1, 1988, Chemical Institute of Canada, Ottawa, 1988, p 396*
889. Rakoczy J, Romotowski T (1993) *Zeolites* 13:256 (cf. especially p 257)
890. Mirth G, Lercher JA (1991) *J Catal* 132:244
891. Eder-Mirth G, Wanzenboeck HD, Lercher JA (1995) In: Beyer HK, Karge HG, Kiricsi I, Nagy JB (1995) *Catalysis by microporous materials. Proc ZEOCAT'95, Szombathely, Hungary, July 9–13, 1995, Elsevier, Amsterdam, 1995; Stud Surf Sci Catal* 94:449
892. Lercher JA, Veeffkind VA, Fajerweg K (1999) *Vibrational Spectroscopy* 19:107
893. Gruendling C, Eder-Mirth G, Lercher JA (1996) *J Catal* 160:299 (and references therein)
894. Gruendling C, Veeffkind VA, Eder-Mirth G, Lercher JA (1996) In: Chon H, Ihm S-K, Uh YS (eds) *Progress in zeolite and microporous materials. Proc 11th Int Zeolite Conf, Seoul, Korea, August 12–17, 1996, Elsevier, Amsterdam, 1997, p 591; Stud Surf Sci Catal* 105:591
895. Veeffkind VA, Smidt ML, Lercher JA (2000) *Appl Catal A: General* 194/195:319

896. Kogelbauer A, Gruending C, Lercher JA (1994) In: Weitkamp J, Karge HG, Pfeifer H, Hoelderich W (eds) Zeolites and related microporous materials: State of the art 1994. Proc 10th Int Zeolite Conf, Garmisch-Partenkirchen, Germany, July 17–22, 1994, Elsevier, Amsterdam, 1994, p 1475; Stud Surf Sci Catal 84:1475
897. Park S-E, Shim EK, Lee K-W, Kim PS (1994) In: Weitkamp J, Karge HG, Pfeifer H, Hoelderich W (eds) Zeolites and related microporous materials: State of the art 1994. Proc 10th Int Zeolite Conf, Garmisch-Partenkirchen, Germany, July 17–22, 1994, Elsevier, Amsterdam, 1994, p 1595; Stud Surf Sci Catal 84:1595
898. Mirth G, Cejka J, Lercher JA (1993) J Catal 139:24
899. Mirth G, Cejka J, Nusterer E, Lercher JA (1994) In: Hattori T, Yashima T (eds) Zeolites and microporous crystals. Proc Int Symp Zeolites and Microporous Crystals, Nagoya, Japan, August 22–25, 1993, Elsevier, Amsterdam, Kodansha, Tokyo, 1994, p 287; Stud Surf Sci Catal 83:287
900. Zikanova A, Derewinski M, Krysciak J, Kociric M (1998) In: Treacy MMJ, Marcus BK, Bisher ME, Higgins JB (eds) Proc 12th Int Zeolite Conf, Baltimore, USA, July 5–10, 1998, Materials Research Society, Warrendale, Pa, USA, 1999, p 209
901. Palomares AE, Eder-Mirth G, Lercher JA (1997) Catal 168:442
902. Palomares AE, Eder-Mirth G, Rep M, Lercher JA (1998) J Catal 180:56
903. Rep M, van Ommen JG, Lefferts L, Lercher JA (2001) In: Galameau A, Di Renzo F, Fajula F, Vedrine J (eds) Zeolites and mesoporous materials at the dawn of the 21st century, Proc 13th Int Zeolite Conf, Montpellier, France, July 8–13, 2001, Elsevier, Amsterdam, 2001, p 316; Stud Surf Sci Catal 135:316
904. Jolly S, Saussey J, Lavalley JC, Zanier N, Benazzi E, Joly JF (1992) In: von Ballmoos R, Higgins JB, Treacy MMJ (eds) Proc 9th Int Zeolite Conf, Montreal, Canada, July 5–10, 1992, Butterworth-Heinemann, Boston, 1993, Vol II, p 319
905. Neuber M, Karge HG, Weitkamp J (1988) Catalysis Today 3:11
906. Voskoboinikov TV, Coq B, Fajula F, Brown R, McDougall G, Couturier JL (1998) Microporous Mesoporous Mater 24:89
907. Onestyák G, Papp J Jr, Kalló D (1988) In: Karge HG, Weitkamp J (eds) Zeolites as catalysts, sorbents and detergent builders – Applications and innovations. Proc Int Symp, Wuerzburg, Germany, Sept 4–8, 1988, Elsevier, Amsterdam, 1989, p 241; Stud Surf Sci Catal 46:241
908. Kalló D, Onestyák G (1996) Zeolites 17:489
909. Diaz CDC, Locatelli S, Gonzo EE (1992) Zeolites 12:851
910. Weitkamp J, Hunger M, Ryma U (2001) Microporous Mesoporous Mater 48:255
911. Karge HG, Boldingh EP (1988) Catalysis Today 3:53
912. Karge HG (2001) In: van Bekkum H, Flanigen EM, Jacobs PA, Jansen JC (eds) Introduction to zeolite science and practice, 2nd edn, Elsevier, Amsterdam, p 707; Stud Surf Sci Catal 137:707
913. Guisnet M (1999) In: Ertl G, Knoezinger H, Weitkamp J (eds) Handbook of heterogeneous catalysis, VCH Verlagsgesellschaft, Weinheim, Germany, p 626
914. Bauer F, Geidel E, Geyer W, Peuker Ch (1999) Microporous Mesoporous Mater 29:109
915. Haber J, Komorek J, Romotowski T (1989) In: Fejes P, Kalló D (eds) Proc Int Symp Zeolite Catal, Siófok, Hungary, May 13–16, 1985; Acta Physica et Chemica Szegediensis, Acta Physica et Chemica, Nova Series, Vol XXIV, Petoefi University, Kecskemét, 1985, p 671
916. Weeks TJ Jr, Bolton AP (1973) In: Uytterhoeven JA (ed), Proc 3rd Int Conf on Molecular Sieves, Zuerich, Switzerland, Sept 3–7, 1973, University Leuven Press, p 426
917. Rakoczy J, Romotowski T (1993) Zeolites 13:256
918. Foerster H, Seelemann R (1978) J Chem Soc, Faraday Trans I 74:1435
919. Kogelbauer A, Goodwin JG jr, Lercher JA (1995) J Phys Chem 99:8777
920. Foerster H, Zakharijeva-Pencheva O (1988) J Molecular Structure 175:189
921. Bodoardo S, Chiappetta R, Fajula F, Garrone E (1995) Microporous Mater 3:613
922. Kustov LM, Borovkov VYu, Kazansky VB (1984) In: Jacobs PA, Jaeger NI, Jiru P, Kazansky VB, Schulz-Ekloff G (eds) Structure and reactivity of modified zeolites. Proc Int Conf, Prague, Czechoslovakia, July 9–13, 1984, Elsevier, Amsterdam, 1984, p 241; Stud Surf Sci Catal 18:241

923. Kredel P, PhD Thesis, Technische Hochschule Darmstadt, 1980
924. Fetting F, Gallei E, Kredel P (1982) *Chem-Ing –Tech* 54:606
925. Fetting F, Gallei E, Kredel P (1984) *Ger Chem Engng* 7:32
926. Datka J (1981) *Zeolites* 1:145
927. Shirley WM, Scoville SP (2000) *Microporous Mesoporous Mater* 37:271
928. Hannus I, Kónya Z, Lentz P, B-Nagy J, Kiricsi I (1998) In: Treacy MMJ, Marcus BK, Bisher ME, Higgins JB (eds) *Proc 12th Int Zeolite Conf., Materials Research Society, Warrendale, Pa, USA, 199, p 2963*
929. Hannus I, Kónya Z, Kollár T, Kiyozumi Y, Mizukami F, Lentz P, Nagy JB, Kiricsi I (1999) In: Kiricsi I, Pál-Borbély G, Nagy JB, Karge HG (eds); *Porous materials in environmentally friendly processes. Proc 1st Int FEZA Conf, Eger, Hungary, September 1–4, 1999, Elsevier, Amsterdam, 1999, p 245; Stud Surf Sci Catal* 125:245
930. Hannus I, Ivanova II, Tasy Gy, Kiricsi I, Nagy JB (1994) In: Weitkamp J, Karge HG, Pfeifer H, Hoelderich W (eds) *Zeolites and related microporous materials: State of the art 1994. Proc 10th Int Zeolite Conf, Garmisch-Partenkirchen, Germany, July 17–22, 1994, Elsevier, Amsterdam, 1994, p 1123; Stud Surf Sci Catal* 84:1123
931. Qiu S, Pang W, Xu W, Xu R (1994) In: Weitkamp J, Karge HG, Pfeifer H, Hoelderich W (eds) *Zeolites and related microporous materials: State of the art 1994. Proc 10th Int Zeolite Conf, Garmisch-Partenkirchen, Germany, July 17–22, 1994, Elsevier, Amsterdam, 1994, p 1059; Stud Surf Sci Catal* 84:1059
932. Wichterlová B, Dedecek J, Tvaruzková Z (1994) In: Weitkamp J, Karge HG, Pfeifer H, Hoelderich W (eds) *Zeolites and related microporous materials: State of the art 1994. Proc 10th Int Zeolite Conf, Garmisch-Partenkirchen, Germany, July 17–22, 1994, Elsevier, Amsterdam, 1994, p 1555; Stud Surf Sci Catal* 84:1555
933. Brock M, Edwards C, Foerster H, Schroeder M (1994) In: Weitkamp J, Karge HG, Pfeifer H, Hoelderich W (eds) *Zeolites and related microporous materials: State of the art 1994. Proc 10th Int Zeolite Conf, Garmisch-Partenkirchen, Germany, July 17–22, 1994, Elsevier, Amsterdam, 1994, p 1515; Stud Surf Sci Catal* 84:1515
934. Kallo D, Onyestyak G, Papp jr J (1983) In: Olson D, Bisio A (eds) *Proc 6th Int Zeolite Conf, Reno, USA, 10–15 July, 1983, Butterworth, Guildford, UK, 1984, p 444*
935. Ziolk M, Decyk P (1994) In: Weitkamp J, Karge HG, Pfeifer H, Hoelderich W (eds) *Zeolites and related microporous materials: State of the art 1994. Proc 10th Int Zeolite Conf, Garmisch-Partenkirchen, Germany, July 17–22, 1994, Elsevier, Amsterdam, 1994, p 1579; Stud Surf Sci Catal* 84:1579
936. Korányi TI, Jentys A, Vinek H (1995) In: Beyer HK, Karge HG, Kiricsi I, Nagy JB (eds) *Catalysis by microporous materials. Proc of ZEOCAT '95, Szombathely, Hungary, July 9–13, 1995, Elsevier, Amsterdam, 1995, p 582; Stud Surf Sci Catal* 94:582
937. Tel'biz G, Shwets A, Gun'ko V, Stoch J, Tamulajtis G, Kukhtarev N (1994) In: Weitkamp J, Karge HG, Pfeifer H, Hoelderich W (eds) *Zeolites and related microporous materials: State of the art 1994. Proc 10th Int Zeolite Conf, Garmisch-Partenkirchen, Germany, July 17–22, 1994, Elsevier, Amsterdam, 1994, p 1099; Stud Surf Sci Catal* 84:1099
938. Qi, M, Xue Z, Zhang Y, Li Q (1994) In: Karge HG, Weitkamp J (eds) *Zeolite science 1994: Recent progress and discussions. Supplementary materials to the 10th Int Zeolite Conf, Garmisch-Partenkirchen, Germany, July 17–22, 1994, Elsevier, Amsterdam, 1995, p 87, Stud Surf Sci Catal* 98:87
939. Karge HG, Niessen W, Bludau H (1996) *Appl Catal A: General* 146:339
940. Crank J (1956) *Mathematics of Diffusion*. Oxford University Press, London, Chapter 6
941. Darken LS (1948) *Trans AIME* 175:184
942. Niessen W, Karge HG, Jozefowicz L (1992) In: Suzuki M (ed) *Proc 4th Int Conf on Fundamentals of Adsorption, Kyoto, Japan, May 17–22, 1992, Kodansha, Tokyo, 1993, p 475*
943. Niessen W, Karge HG (1993) *Microporous Mater* 1:1
944. Hermann M, Niessen W, Karge HG (1995) In: Beyer HK, Karge HG, Kiricsi I, Nagy JB (eds) *Catalysis by microporous materials. Proc of ZEOCAT,'95, Szombathely, Hungary, July 9–13, 1995, Elsevier, Amsterdam, 1995, p 131; Stud Surf Sci Catal* 94:131

945. Hermann M, Niessen W, Karge HG (1995) In: LeVan MD (ed) Proc 5th Int Conf on Fundamentals of Adsorption, Asilomar Pacific Grove, CA, 126.USA, May 13–18, 1995, Kluwer Acad Publ, Boston, Mass, USA, 1996, p 377
946. Bludau H, Karge HG, Niessen W (1998) *Microporous Mesoporous Mater* 22:297
947. Roque-Malherbe R, Ivanov V (2001) *Microporous Mesoporous Mater* 47:25 (and references therein)
948. Schumacher R, Karge HG (1999) *Microporous Mesoporous Mater* 30:307
949. Zhobolenko VL, Dwyer J (1998) In: Treacy MMJ, Marcus BK, Bisher ME, Higgins JB (eds) Proc 12th Int Zeolite Conf, Baltimore, Maryland, USA, July 5–10, 1998, Materials Research Society, Warrendale, Pa, USA, 1999, p 183
950. Rees LVC (1994) In: Weitkamp J, Karge HG, Pfeifer H, Hoelderich W (eds) Zeolites and related microporous materials: State of the art 1994. Proc 10th Int Zeolite Conf, Garmisch-Partenkirchen, Germany, July 17–22, 1994, Elsevier, Amsterdam, 1994, p 1133; *Stud Surf Sci Catal* 84:1133
951. Roque-Malherbe R, Wendelbo R, Mifsud A, Corma A (1995) *J Phys Chem* 99:14064
952. Wendelbo R, Roque-Malherbe R (1997) *Microporous Mater* 10:231
953. Roland U, Salzer R, Stolle S (1994) In: Weitkamp J, Karge HG, Pfeifer H, Hoelderich W (eds) Zeolites and related microporous material: State of the art 1994. Proc 10th Int Zeolite Conf, Garmisch-Partenkirchen, Germany, July 17–22, 1994, Elsevier, Amsterdam, 1994, p 1231; *Stud Surf Sci Catal* 84:1231
954. Jamis J, Smith TD, Kwak TAP, Dyer A (1994) In: Weitkamp J, Karge HG, Pfeifer H, Hoelderich W (eds) Zeolites and related microporous materials: State of the art 1994. Proc 10th Int Zeolite Conf, Garmisch-Partenkirchen, Germany, July 17–22, 1994, Elsevier, Amsterdam, 1994, p 1261; *Stud Surf Sci Catal* 84:1261
955. Jiang M, Karge HG (1995) *J Chem Soc, Faraday Trans* 91:1845
956. Jiang M, Koy J, Karge HG (1996) In: Occelli ML, Kessler H (eds) Synthesis of microporous materials-zeolites, clays and nanostructures. Proc 3rd Int Symp on Synthesis of Zeolites, Expanded Layer Compounds and other Crystalline Microporous or Mesoporous Solids; ACS Meeting, Anaheim, California, USA, April 2–7, 1995, Marcel Dekker Inc, New York, p 335
957. Flanigen EM, Lok BM, Patton RL, Wilson ST (1986) In: Murakami Y, Iijima A, Ward JW (eds) New developments in zeolite science and technology. Proc 7th Int Zeolite Conf, Tokyo, Japan, August 17–22, 1986, Kodansha, Tokyo, Elsevier, Amsterdam, 1986, p 103; *Stud Surf Sci Catal* 28:103

NMR Spectroscopy

Michael Hunger¹ · Eike Brunner²

¹ Institut für Technische Chemie I, Universität Stuttgart, 70550 Stuttgart, Germany

² Fakultät für Physik und Geowissenschaften, Universität Leipzig, 04103 Leipzig, Germany

1	Introduction	203
2	General Aspects of Solid-State NMR Spectroscopy	204
2.1	Line Broadening Mechanisms in Solids	204
2.1.1	Spin $I=1/2$ Nuclei	204
2.1.2	Quadrupole Nuclei	206
2.2	High-Resolution Solid-State NMR Spectroscopy	208
2.2.1	Multiple-Pulse Sequences	208
2.2.2	Magic Angle Spinning	209
2.2.3	Techniques for the Suppression of Second-Order Quadrupole Broadening	211
2.3	Double Resonance Techniques	212
2.3.1	Cross-Polarization	212
2.3.2	Dipolar-Dephasing Experiments	214
2.3.3	Spin-Echo Double Resonance	214
2.4	Two-Dimensional NMR Spectroscopy	215
3	NMR Spectroscopy of the Zeolite Framework	215
3.1	²⁹ Si MAS NMR Investigations of the Zeolite Framework	216
3.2	Solid-State ²⁷ Al NMR Spectroscopy on Zeolites	224
3.3	³¹ P MAS NMR of Aluminophosphate- and Gallophosphate-Type Zeolites	231
3.4	⁶⁹ Ga and ⁷¹ Ga NMR Spectroscopy of Gallium-Modified Zeolites and the Gallophosphate Cloverite	235
3.5	¹¹ B NMR Spectroscopy of Boron-Containing Zeolites	237
3.6	¹⁷ O NMR Studies of Zeolites and Zeolite-Like Materials	238
4	NMR Investigations on Extra-Framework Cations	238
4.1	Investigations of Cations in Hydrated Zeolites	239
4.2	Cesium Cations in Hydrated and Dehydrated Zeolites	240
4.3	Sodium Cations in Hydrated Faujasites	243
4.4	Sodium Cations in Dehydrated Faujasites	245
5	NMR Spectroscopy of Hydroxyl Protons in Zeolites	253
5.1	Formation of Hydroxyl Groups in Zeolites and Their Detection by ¹ H MAS NMR Spectroscopy	254

5.2	Local Structure of Bridging OH Groups	262
5.3	Mobility of Hydroxyl Protons in Zeolites	264
5.4	Investigations of Dipolar Coupled Hydroxyl Protons	266
5.5	Acidity and Location of Hydroxyl Protons Studied by Probe Molecules	269
6	Characterization of Zeolite Pore Architecture by ^{129}Xe NMR Spectroscopy	271
6.1	^{129}Xe NMR Shifts of Xenon Atoms Adsorbed in Zeolite Pores	272
6.2	Zeolites Exchanged with Diamagnetic and Paramagnetic Cations ..	273
6.3	Effects of Pore Blocking	276
6.4	Co-adsorption of Molecules	277
7	In Situ NMR Investigations of Chemical Reactions Catalyzed by Zeolites	279
7.1	Experimental Techniques	279
7.2	Assignment of In Situ NMR Spectra	281
7.3	Applications of In Situ NMR Spectroscopy	283
8	References	285

Abbreviations

2D	two-dimensional
Al ^f	framework aluminum
Al ^{nf}	non-framework aluminum
AlPO ₄	aluminophosphate
CAVERN	cryogenic adsorption vessel enabling rotor nestling
CAW	calcium tungstate aluminum sodalite
COSY	correlation spectroscopy
CP	cross-polarization
CRAMPS	combined rotation and multiple-pulse spectroscopy
DAS	dynamic-angle spinning
DOR	double-rotation
EFG	electric field gradient
F1	frequency domain 1 of a two-dimensional spectrum
F2	frequency domain 2 of a two-dimensional spectrum
FD	fixed delay
FID	free induction decay
FT	Fourier transform
INADEQUATE	incredible natural abundance double quantum transfer experiment
IR	infrared
LASER	light amplification by stimulated emission of radiation
MAS	magic angle spinning
MeOH	hydroxyl group attached to an extra-framework cation (Me)

MTG	methanol-to-gasoline
NMR	nuclear magnetic resonance
NOESY	nuclear Overhauser enhancement and exchange spectroscopy
QL	quadrupolar line
QP	quadrupolar pattern
REDOR	rotational-echo double resonance
rf	radio frequency
SAPO	silicoaluminophosphate
SEDOR	spin-echo double resonance
SI, SII ...	site I, site II ...
SiOH	silanol groups
SiOHAl	bridging hydroxyl groups
SP	single pulse
TEDOR	transferred-echo double resonance
TMS	tetramethylsilane
VT	variable temperature
WAHUHA	multiple-pulse sequence developed by Waugh, Huber, and Haeberlen
XRD	X-ray diffraction

1

Introduction

Solid-state NMR spectroscopy (nuclear magnetic resonance) now belongs to the most powerful techniques for the characterization of molecular sieves such as zeolites and related materials (see, e.g., [1–6]). The basis of this success was the invention of effective line narrowing techniques and two-dimensional experiments that make the detection of highly resolved solid-state NMR spectra and the separation of different spectral parameters possible. Solid-state NMR spectroscopy allows the direct investigation of the framework of zeolites and related materials, of extra-framework cations and of the different types of hydroxyl groups. The ^{129}Xe NMR spectroscopic investigation of adsorbed xenon atoms (described in more detail in Vol. 5 of this series) is a suitable method for the study of the pore architecture of molecular sieves. The catalytic behavior of porous catalysts can be investigated directly by *in situ* NMR spectroscopy.

Furthermore, it should be mentioned that NMR spectroscopic techniques have found numerous applications for the characterization of the acidity of zeolites and related materials (see Vol. 6 of this series) and for the investigation of the molecular diffusion in microporous materials (see Vol. 7 of this series).

2

General Aspects of Solid-State NMR Spectroscopy

2.1

Line Broadening Mechanisms in Solids

In general, liquids and gases exhibit narrow NMR signals since the influence of spatially anisotropic internal magnetic interactions on the linewidth is averaged to zero by thermal motions. In contrast, solids such as zeolite samples exhibit NMR signals that are strongly broadened by internal magnetic interactions. Important structural information can be obtained by the analysis of these broad-line solid-state NMR spectra which will be described briefly in this section.

2.1.1

Spin $I=1/2$ Nuclei

The dominating line broadening interactions of spin $I=1/2$ nuclei are described by the total Hamiltonian:

$$\hat{H} = \hat{H}_H + \hat{H}_{IS} + \hat{H}_{CSA} \quad (1)$$

where \hat{H}_H , \hat{H}_{IS} , and \hat{H}_{CSA} are the Hamiltonians of the homonuclear and the heteronuclear magnetic dipole-dipole interaction and the chemical shift anisotropy, respectively. Analytical expressions for these Hamiltonians are given, e.g., in [7–10]. The center of gravity, ν_{cg} , of the resulting broad-line solid-state NMR signal occurs at a frequency of:

$$\nu_{cg} = \int_0^{\infty} \nu f(\nu) d\nu \quad (2)$$

where ν denotes the frequency and $f(\nu)$ is the normalized line shape function. It is remarkable that ν_{cg} may deviate from the so-called Larmor frequency:

$$\nu_o = \frac{\gamma_I}{2\pi} B_o \quad (3)$$

which is the resonance frequency of an isolated and non-shielded nucleus with the magnetogyric ratio γ_I . B_o denotes the magnetic flux density of the external magnetic field. Assuming that the sample does not contain paramagnetic impurities and that other susceptibility effects can also be neglected, the interdependence between ν_{cg} and ν_o is given by:

$$\nu_{cg} = \nu_o (1 - \sigma) \quad (4)$$

σ denotes the shielding constant. The so-called isotropic chemical shift, δ , is defined as $\delta = \sigma_{ref} - \sigma$ where σ_{ref} denotes the shielding constant for a nucleus in a

reference substance. δ can be determined according to:

$$\delta = \frac{1}{3} (\delta_{11} + \delta_{22} + \delta_{33}) \quad (5)$$

where δ_{11} , δ_{22} , and δ_{33} denote the principal values of the chemical shift tensor, which are denoted such that the inequality $\delta_{11} \geq \delta_{22} \geq \delta_{33}$ is fulfilled.

The superposition of the different internal magnetic interactions often complicates the interpretation and calculation of the resulting normalized line shape function, $f(\nu)$. It is, therefore, advantageous to make use of the so-called second moment M_2 as a measure for the linewidth of the solid-state NMR signals. The full width at half maximum of an NMR signal in frequency units (further called static linewidth) amounts to:

$$\Delta\nu_{1/2} = \frac{1}{\pi} \sqrt{2 \ln 2} \sqrt{M_2} \quad (6)$$

for Gaussian lines. The second moment, M_2 , with respect to the center of gravity, ν_{cg} , of the signal is defined by:

$$M_2 = 4\pi^2 \int_0^{\infty} (\nu - \nu_{cg})^2 f(\nu) d\nu \quad (7)$$

In this chapter, second moments are generally given in units of the angular frequency.

The second moment of an NMR signal can be calculated (see, e.g., [7]) if the structure and the internal magnetic interactions of the system are known. For the total Hamiltonian given in Eq. (1) it follows that:

$$M_2 = M_2^I + M_2^{IS} + M_2^{CSA} \quad (8)$$

with

$$M_2^I = \frac{3}{5} \left(\frac{\mu_o}{4\pi} \right)^2 \gamma_I^4 \hbar^2 I(I+1) \frac{1}{N_I} \sum_{i \neq j}^{N_I} r_{ij}^{-6} \quad (9)$$

$$M_2^{IS} = \frac{4}{15} \left(\frac{\mu_o}{4\pi} \right)^2 \gamma_I^2 \gamma_S^2 \hbar^2 S(S+1) \frac{1}{N_I} \sum_{i \neq 1}^{N_I} r_{ij}^{-6} \quad (10)$$

$$M_2^{CSA} = \frac{4}{45} \gamma_I^2 B_o^2 \Delta\sigma^2 \left(1 + \frac{1}{3} \eta_{CSA}^2 \right) \quad (11)$$

\hbar denotes Planck's constant h divided by 2π and μ_o is the permeability of vacuum. I and S are the nuclear spins of the resonating I -spins and non-resonating S -spins, respectively. N_I and N_S denote the numbers of resonating and non-resonating nuclei in the sample; γ_S is the magnetogyric ratio of the non-resonating S -spins; and r_{ij} and r_{jk} are internuclear distances. The anisotropy,

$\Delta\sigma$, and the asymmetry parameter, η_{CSA} , of the chemical shift tensor are defined by:

$$\Delta\sigma = \frac{1}{2}(\delta_{11} + \delta_{22}) - \delta_{33} \quad (12)$$

and

$$\eta_{CSA} = \frac{3}{2} \cdot \frac{\delta_{11} - \delta_{22}}{\Delta\sigma} \quad (13)$$

Characteristic line shape functions can be observed in special cases as is shown in Fig. 1 by two examples. The so-called Pake doublet [11] is found for isolated spin pairs (see Fig. 1a). The spectrum shown in Fig. 1b is observed if an NMR signal is mainly broadened by the chemical shift anisotropy. The analysis of the line shape function, $f(\nu)$, allows the direct measurement of parameters like the internuclear distance, the chemical shift anisotropy, $\Delta\sigma$, or the asymmetry parameter, η_{CSA} , in these cases.

2.1.2

Quadrupole Nuclei

A further characteristic line broadening interaction occurs for nuclei with nuclear spins $I > 1/2$ in addition to the interactions discussed above [see Eq. (1)]. These nuclei exhibit an electric quadrupole moment that interacts with the electric field gradient at the site of the nucleus. The NMR spectrum of quadrupole nuclei with half-integer nuclear spins ($I=3/2, 5/2, \dots$) consists of the $\{+1/2 \leftrightarrow -1/2\}$ central transition and the so-called satellite transitions ($\{\pm 1/2 \leftrightarrow \pm 3/2\}$, $\{\pm 3/2 \leftrightarrow \pm 5/2\}$, ...). In the case of strong quadrupole interaction it is practically impossible to excite the whole spectrum non-selectively, i.e., the central transition is often selectively observed.

It is remarkable that the center of gravity, ν_{cg} , of the central transition is shifted by the so-called second-order quadrupole shift, ν_{qs} , which is given by [12]:

$$\nu_{qs} = \nu_{cg} - \nu_0(1 - \sigma) = -\frac{I(I+1) - 3/4}{30} \frac{\nu_Q^2}{\nu_0} \left(1 + \frac{1}{3} \eta_Q^2\right) \quad (14)$$

with respect to the line position given in Eq. (4). The quadrupole frequency is given by:

$$\nu_Q = \frac{3}{2I(2I-1)} C_Q \quad (15)$$

The so-called quadrupole coupling constant, C_Q , amounts to:

$$C_Q = \frac{V_{33} eQ}{h} \quad (16)$$

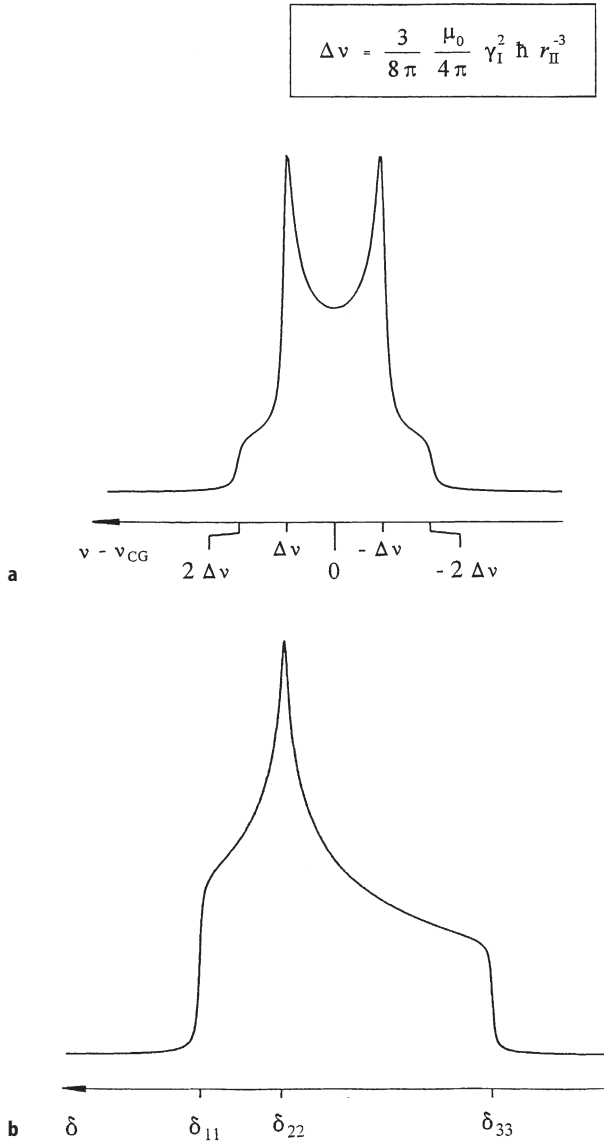


Fig. 1 a, b. Calculated line shape functions for special solid-state NMR signals of spin $I=1/2$ nuclei. Spin pairs with dominating intra-pair homonuclear magnetic dipolar interaction, r_{II} denotes the internuclear distance (a). Nearly isolated spins with dominating chemical shift anisotropy ($\eta_{CSA}=0.5$) (b)

and the asymmetry parameter, η_Q , of the electric field gradient tensor is defined by:

$$\eta_Q = \frac{V_{11} - V_{22}}{V_{33}} \quad (17)$$

eQ is the electric quadrupole moment. The principal values V_{11} , V_{22} , and V_{33} of the electric field gradient tensor at the site of the nucleus are denoted in such a manner that the inequality $|V_{11}| \leq |V_{22}| \leq |V_{33}|$ is fulfilled.

A characteristic broadening of the central transition can be observed in the case of strong quadrupole interaction (second-order quadrupole broadening). The second moment, M_2^{CT} , of the central transition with respect to its center of gravity is given by [12]:

$$M_2^{CT} = \frac{92 \pi^2}{7} v_{qs}^2 \quad (18)$$

2.2

High-Resolution Solid-State NMR Spectroscopy

The linewidth of typical solid-state NMR signals often strongly exceeds the chemical shift differences between the different signals in the spectra. The measurement of highly resolved solid-state NMR spectra, therefore, requires the application of special line narrowing techniques which will be described in the present section.

2.2.1

Multiple-Pulse Sequences

The principle of Fourier transform (FT) NMR spectroscopy is the observation of the so-called free induction decay (FID) after the application of radio frequency (rf) pulses to the resonating nuclei. The carrier frequency of the rf-pulses is the Larmor frequency. In many cases, the FID is observed after single-pulse (SP) excitation, e.g., after application of a so-called $\pi/2$ -pulse which rotates the magnetization by 90° from the direction of the external magnetic field (z-direction) into the x,y-plane. The characteristic time constant for the free induction decay is the transverse relaxation time, T_2 , which is given by $T_2 = (2/M_2)^{1/2} \approx 0.53 \cdot (\Delta\nu_{1/2})^{-1}$ for Gaussian lines. Fourier transformation of the FID yields the common absorption spectrum.

The influence of the line broadening interactions described above (see Sect. 2.1) can be suppressed at least partly by the application of special multiple-pulse sequences [8, 13–15]. A typical example is the so-called WAHUA (Waugh, Huber, Haerberlen) sequence [8] which consists of four $\pi/2$ -pulses with alternating phases: $[-\tau-(\pi/2)_x-2\tau-(\pi/2)_{-x}-\tau-(\pi/2)_y-2\tau-(\pi/2)_{-y}-]$. This pulse cycle which exhibits a cycle time of $t_c=6\tau$ is applied repeatedly to the resonating spins. Sampling the FID at multiples of t_c leads to a suppression of the influence of the homonuclear magnetic dipole-dipole interaction. It has, however, to be stated

that most of the multiple-pulse sequences do not lead to a simultaneous and complete suppression of all the line broadening interactions mentioned above.

2.2.2

Magic Angle Spinning

The principle of the magic angle spinning (MAS) technique [16] is based on a rapid rotation of the sample. The Hamiltonian \hat{H} [see Eq. (1)] can be replaced by the mean Hamiltonian $\langle \hat{H} \rangle_t$ for the limiting case of rapid sample spinning $\nu_{rot} \gg \Delta\nu_{1/2}$. In the first order of perturbation theory, $\langle \hat{H} \rangle_t$ is proportional to $(3\cos^2\theta - 1)$ where θ denotes the angle between the external magnetic field and the sample spinning axis. The maximum line narrowing effect is achieved for the magic angle $\theta_m = 54.74^\circ$ when $(3\cos^2\theta_m - 1)$ becomes zero. If a NMR signal is broadened by inhomogeneous interactions [17] such as the heteronuclear magnetic dipole-dipole interaction and the chemical shift anisotropy, magic angle spinning leads to a MAS NMR signal consisting of a narrow central line at the center of gravity, ν_{cg} , of the signal and spinning sidebands at the frequencies

$$\nu_k = \nu_{cg} + k \cdot \nu_{rot} \quad (19)$$

where $k = \pm 1, \pm 2, \dots$ denotes the order of the spinning sideband and ν_{rot} is the sample spinning rate. In the present work spinning sidebands will be denoted by (*) in all figures. The influence of the magic angle spinning technique on a typical solid-state NMR signal of a spin $I = 1/2$ nucleus is demonstrated in Fig. 2. The full width at half maximum of the central line of a MAS NMR signal is denoted as the residual linewidth, $\Delta\nu_{1/2}^{MAS}$. The central line as well as the spinning sidebands may exhibit a characteristic broadening in the presence of a homogeneous interaction such as the homonuclear magnetic dipole-dipole interaction between more than two nuclei (see, e.g., [17–20]). The residual linewidth is then approximately given by:

$$\Delta\nu_{1/2}^{MAS} = \frac{1}{A} \cdot \frac{(\Delta\nu_{II})^2}{\nu_{rot}} \quad (20)$$

with $10 \leq A \leq 40$ [19, 20]. $\Delta\nu_{II}$ denotes the so-called homonuclear linewidth that can be calculated from M_2^H according to Eq. (6) and the parameter A which depends on the spatial arrangement of the spins and the line shape of the central line [19]. The presence of other line-broadening interactions such as the heteronuclear magnetic dipole-dipole interaction and/or the chemical shift anisotropy in addition to the homonuclear magnetic dipole-dipole interaction can lead to a further increase in $\Delta\nu_{1/2}^{MAS}$ [18, 21, 22]. The influence of the homonuclear magnetic dipole-dipole interaction on $\Delta\nu_{1/2}^{MAS}$ can be reduced either by increasing the sample spinning rate, ν_{rot} , [see Eq. (20)] or by the application of the so-called CRAMPS technique (combined rotation and multiple-pulse spectroscopy [14, 23–26]).

Furthermore, $\Delta\nu_{1/2}^{MAS}$ may be affected by the following factors: (a) inhomogeneity of the external magnetic field, (b) misadjustment of the magic angle, (c)

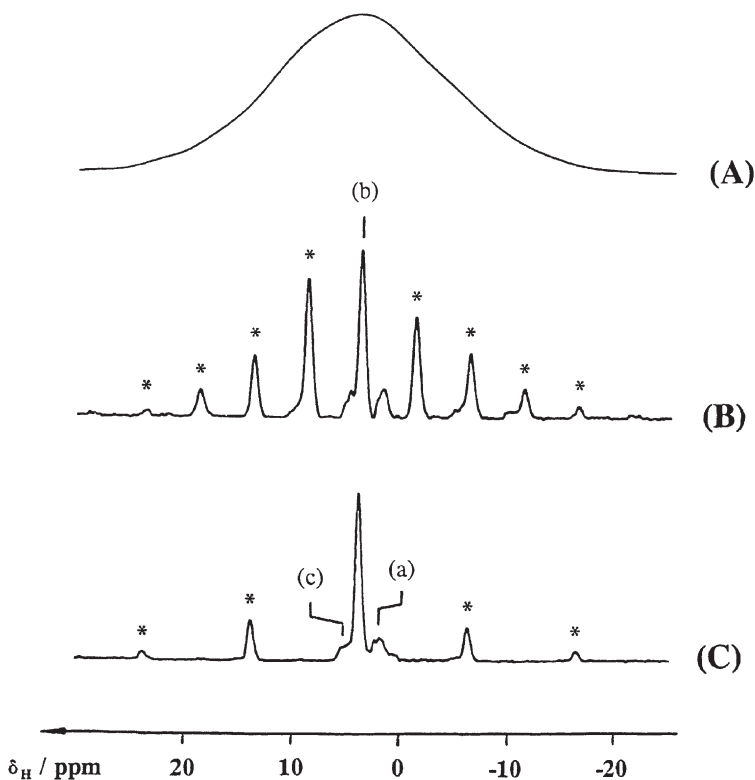


Fig. 2. Demonstration of the influence of the magic angle spinning technique on the ^1H NMR spectrum of an activated zeolite 30HNaY ($n_{\text{Si}}/n_{\text{Al}}=2.5$) measured at a resonance frequency of $\nu_0=500$ MHz ($B_0=11.74$ T). The spectra were recorded without magic angle spinning (A) and with magic angle spinning at sample spinning rates of 2.5 kHz (B) and 5 kHz (C). The intense signal at 3.9 ppm (line b) is due to bridging hydroxyl groups in the supercages. The relatively weak lines (a) and (c) at 2.0 ppm and 4.8 ppm are caused by SiOH groups and by bridging hydroxyl groups in the sodalite cages, respectively (see Sect. 5)

thermal motions and exchange processes [6, 27, 28], (d) heteronuclear magnetic dipole-dipole interaction with quadrupole nuclei [22, 29–32], (e) anisotropy of the magnetic susceptibility [33], and (f) distribution of the isotropic chemical shift [5, 21, 22].

The residual linewidth of the MAS NMR signals of quadrupole nuclei with half-integer nuclear spins is often determined by another effect. The second-order quadrupole broadening of the central transition described above is not completely suppressed by the magic angle spinning technique. Figure 3 shows the central transition of a half-integer spin calculated for the limit of rapid magic angle spinning, i.e., for $\nu_{\text{rot}} \gg (M_2^{\text{CT}})^{1/2}$. The second moment, $M_2^{\text{CT}, \text{MAS}}$, of the central transition under magic angle spinning conditions is given by [12]:

$$M_2^{\text{CT}, \text{MAS}} = \frac{7}{92} M_2^{\text{CT}} = \pi^2 \nu_q^2 \quad (21)$$

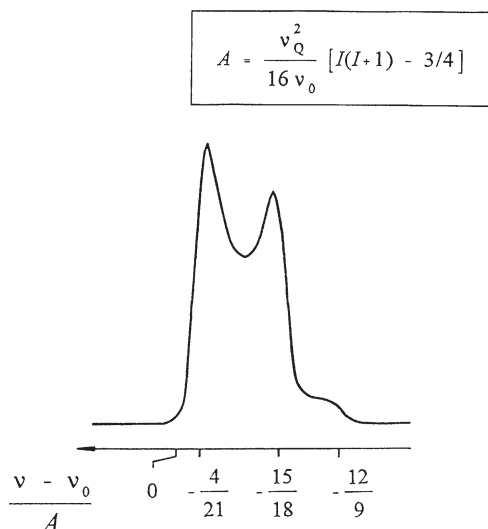


Fig. 3. Line shape function of the central transition of a quadrupole nucleus with a half-integer nuclear spin, calculated for $\eta_Q=0$ in the limiting case of rapid magic angle spinning assuming that the electric quadrupole interaction is the dominating line broadening interaction

and the position of the signal (center of gravity) is the same as in the static experiment [see Eq. (14)]. This means that the application of the MAS technique only leads to a reduction in the linewidth of the central transition by a factor of about 3.6 even at the limit of rapid sample spinning.

The analysis of the characteristic line shape of the central transition (see Fig. 3) often allows a direct measurement of ν_Q and η_Q . On the other hand, the resolution of the spectra is limited by this line-broadening effect. The resolution can be improved by increasing the external magnetic field, B_0 , because $M_2^{CT,MAS}$ strongly depends on ν_0 [see Eqs. (21) and (14)]. The maximum magnetic flux density of the external magnetic fields available on commercial NMR spectrometers presently amounts to 21.1 T. Common NMR spectrometers exhibit external magnetic fields between ca. 7 and 14 T. These magnetic flux densities are often insufficient for the complete suppression of second-order quadrupole broadening.

2.2.3

Techniques for the Suppression of Second-Order Quadrupole Broadening

The complete suppression of the influence of second-order quadrupole broadening requires the application of double rotation (DOR) [34–36] or dynamic angle spinning (DAS) [37–39] techniques.

In DOR experiments, the sample simultaneously rotates around two different axes. The corresponding device consists of an outer and an inner rotor [34]. The angle θ_1 between the external magnetic field and the rotational axis

of the outer rotor corresponds to the magic angle θ_m (vide supra), and the angle θ_2 between the rotational axes of the inner and the outer rotor amounts to 30.56° . The advantage of double rotation compared to magic angle spinning is the suppression of second-order quadrupole broadening. The minimum residual linewidth, $\Delta\nu_{1/2}^{\min}$, achievable under DOR conditions is determined by the distribution of the isotropic chemical shift, δ , and/or the quadrupole shift, ν_{qs} . In addition, the residual linewidth, $\Delta\nu_{1/2}^{DOR}$, of the DOR signals can exceed $\Delta\nu_{1/2}^{\min}$ considerably if the influence of the homonuclear magnetic dipole-dipole interaction is not completely suppressed by the rotation of the outer rotor [see Eq. (20)]. Roughly spoken, the influence of the homonuclear magnetic dipole-dipole interaction upon $\Delta\nu_{1/2}^{DOR}$ can only be neglected if the spinning rate of the outer rotor, ν_{rot} , is larger than the homonuclear linewidth, $\Delta\nu_{II}$. The maximum values of ν_{rot} achievable with recent DOR devices are lower than 1.5 kHz. Therefore, the minimum residual line width, $\Delta\nu_{1/2}^{\min}$, i.e., the maximum resolution, can only be observed for spin systems with a relatively weak homonuclear magnetic dipole-dipole interaction ($\Delta\nu_{II} \leq 1.5$ kHz). However, investigating aluminum atoms incorporated in zeolite frameworks has shown that the resolution of DOR NMR spectra is limited by the distribution of the NMR parameters discussed previously (see Sect. 3.2).

2.3

Double Resonance Techniques

In double resonance experiments, rf-pulses or pulse sequences are applied not only to the resonating *I*-spins, but also to the non-resonating *S*-spins. Magnetic interactions between the resonating and the non-resonating nuclei, especially the heteronuclear magnetic dipole-dipole interaction, can be studied selectively by double resonance techniques.

2.3.1

Cross-Polarization

Cross-polarization (CP) [40] is a typical double resonance technique which can be applied not only in static but also in magic angle spinning NMR experiments [41, 42]. The principle of this technique is demonstrated in Fig. 4. The experiment starts with a $\pi/2$ -pulse applied to the *S*-spins. Spin polarization is transferred from the *S*-spins to the *I*-spins during the contact period with a duration of τ_{CP} if the condition

$$\alpha_S \cdot \gamma_S \cdot B_{1S} = \alpha_I \cdot \gamma_I \cdot B_{1I} \quad (22)$$

is fulfilled [10]. The parameter α_S is equal to $[S(S+1)-m(m-1)]^{1/2}$ provided that the rf-pulse applied to the *S*-spins selectively induces transitions between the levels with the magnetic spin quantum numbers m and $m-1$. An analogous expression holds for α_I . The parameters α_S and α_I are equal to 1 for $I=S=1/2$, and Eq. (22) is then termed the Hartmann-Hahn condition [43]. B_{1I} and B_{1S}

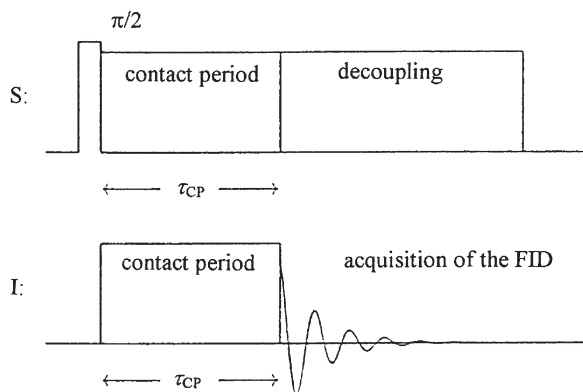


Fig. 4. Schematic representation of a cross-polarization experiment. The introduction of a time delay after the contact period leads to a dipolar dephasing of the resonating I -spins

denote the magnetic field amplitudes of the rf-pulses applied to the I - and S -spins, respectively. A free induction decay can be observed for the I -spins after the contact period. The intensity $I_{CP}(\tau_{CP})$ of the corresponding signal is given by [42, 44]:

$$I_{CP}(\tau_{CP}) \propto \left(1 - \frac{T_{CP}}{T_{1\rho}}\right)^{-1} \left(\exp\{-\tau_{CP}/T_{1\rho}\} - \exp\{-\tau_{CP}/T_{CP}\}\right) \quad (23)$$

$T_{1\rho}$ is the time constant for the decay of the S -spin magnetization under spin locking conditions. The so-called cross-polarization time constant, T_{CP} , is inversely proportional to M_2^I , i.e., the efficiency of the cross-polarization depends on the strength of the heteronuclear magnetic dipole-dipole interaction. It has to be mentioned, furthermore, that the maximum values of $I_{CP}(\tau_{CP})$ are obtained for rigid lattices, and that $I_{CP}(\tau_{CP})$ vanishes if the nuclei exhibit rapid thermal motions [45]. High-power decoupling of the S -spins during the acquisition of the I -spin FID leads to the suppression of the influence of the heteronuclear magnetic dipole-dipole interaction on the transverse relaxation time.

Cross-polarization experiments lead to an enhancement of the signal intensity for the I -spins if the S -spins exhibit a higher magnetogyric ratio and/or a higher concentration than the I -spins. The maximum signal enhancement achievable by CP experiments amounts to:

$$\frac{I_{CP}}{I_{SP}} = \frac{\gamma_S}{\gamma_I} \cdot \frac{1}{1 + \epsilon} \quad (24)$$

with

$$\epsilon = \frac{N_I}{N_S} \left(\frac{\alpha_I}{\alpha_S}\right)^2 \quad (25)$$

where I_{SP} denotes the intensity of the signal of the I -spins measured with single-pulse excitation.

2.3.2

Dipolar-Dephasing Experiments

Dipolar-dephasing experiments [46] can be used, e.g., to establish the existence of a heteronuclear magnetic dipole-dipole interaction. A simple modification of the cross-polarization experiment, namely, the introduction of a time delay, τ_D , after the contact period (i.e., before the acquisition of the FID, cf. Fig. 4) leads to a characteristic dipolar dephasing experiment. A decrease of the intensity of the NMR signals can be better observed with increasing values of τ_D . The decrease is more pronounced for signals caused by spins with a stronger heteronuclear magnetic dipole-dipole interaction than for signals due to spins with a weaker heteronuclear magnetic dipole-dipole interaction. The signal intensity completely vanishes for $\tau_D \gg (2/M_2^{IS})^{1/2}$.

2.3.3

Spin-Echo Double Resonance

The so-called SEDOR technique (spin-echo double resonance [9, 47, 48], see Fig. 5) allows the determination of internuclear distances, r_{IS} , for isolated spin pairs consisting of a resonating I -spin and a non-resonating S -spin. Hahn's echo [49] of the resonating I -spins is observed with a time between the $\pi/2$ -pulse and the π -pulse. A π -pulse applied to the S -spins after a variable time t_1 ($0 \leq t_1 \leq \tau$) leads to a characteristic damping of Hahn's echo of the resonating I -spins. The damped amplitude, $M(t_1)$, of Hahn's echo under SEDOR conditions is determined by:

$$M(t_1) \propto \int_0^\pi \cos(\omega(r_{IS}, \theta) t_1) \sin \theta d\theta \quad (26)$$

with

$$\omega(r_{IS}, \theta) = \frac{\mu_0}{4\pi} \gamma_I \gamma_S \hbar r_{IS}^{-3} (3 \cos^2 \theta - 1) \quad (27)$$

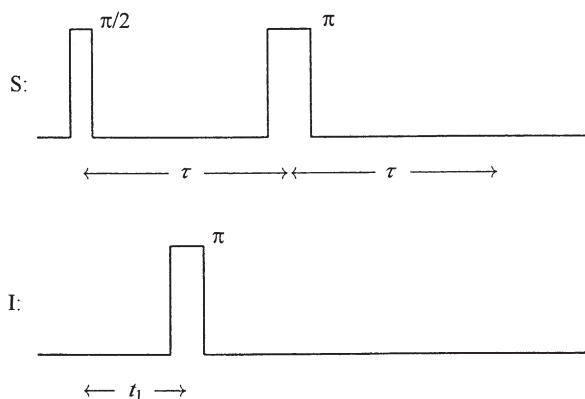


Fig. 5. Schematic representation of a SEDOR experiment. The pulse sequence applied to the resonating S -spins corresponds to the well-known Hahn's echo experiment

for a powder sample, where θ denotes the angle between the distance vector, r_{IS} , and the direction of the external magnetic field, B_0 . The advantage of this method is that the heteronuclear magnetic dipole-dipole interaction is separated from other line-broadening mechanisms.

The main problem is that the SEDOR experiment is carried out under static conditions, i.e., without magic angle spinning. Therefore, SEDOR measurements only yield average values for the internuclear distance if a sample contains two or more different types of *I-S*-spin pairs with different internuclear distances, r_{IS} . Typical double resonance experiments for the measurement of internuclear distances under magic angle spinning conditions are the REDOR (rotational-echo double resonance [50]) and the TEDOR (transferred-echo double resonance [51]) techniques.

2.4

Two-Dimensional NMR Spectroscopy

Considerable progress in solid-state NMR spectroscopy has been achieved by the introduction of two-dimensional (2D) NMR techniques (see [52]) and their application to zeolites. Typically, a 2D experiment starts with the preparation of the spin system (preparation period) by direct excitation or cross-polarization. In a subsequent period, t_1 , the spin ensemble evolves under the influence of the Hamiltonian of a selected interaction which may be the *J*-coupling, the dipole-dipole interaction, the quadrupole interaction, etc. The free induction decay of the resonating spins is acquired during the detection period, t_2 . The signal $G(t_1, t_2)$ consists of an array of free induction decays recorded for different evolution times, t_1 . The two-dimensional Fourier transformation of $G(t_1, t_2)$ yields the spectrum $F(\nu_1, \nu_2)$. In this 2D spectrum, the projection to the F1-dimension (ν_1) is determined by the interaction selected in the evolution period, t_1 , while the F2-projection (ν_2) corresponds to the spectrum obtained by a conventional one-dimensional experiment. The two-dimensional NMR experiments considered in Sects. 3.1, 3.3, 4.4, 5.2, 5.4, and 7.2 are useful to gain insight into framework connectivities, dipole-dipole couplings, the strength of quadrupole interactions, etc. In addition, the recently developed techniques of multiple-quantum MAS NMR spectroscopy (MQMAS) have to be mentioned as these have found an increasing application in the study of ^{17}O , ^{23}Na and ^{27}Al nuclei in zeolites [53–55].

3

NMR Spectroscopy of the Zeolite Framework

During the last decade a number of excellent reviews have been published summarizing the chemical and structural information and relationships of zeolite frameworks available through multi-nuclear solid-state NMR spectroscopy [1, 56–59]. Aluminosilicate-type zeolites consist of corner-sharing AlO_4 and SiO_4 tetrahedra and contain regular systems of intracrystalline cages and pores [60]. Since 1982 an entirely new family of porous solids has been synthesized, the aluminophosphate molecular sieves (AlPO_4), with structures consisting of alter-

nating AlO_4 and PO_4 tetrahedra [61]. Some of them have framework topologies already known from aluminosilicate-type zeolites, but many have new structure types (see [62]) and enable, therefore, new applications. The addition of a silicon source to an aluminophosphate gel results in the formation of silicoaluminophosphates (SAPO), and the additional incorporation of various metals, such as Mg, Mn, Fe, Co or Zn, gives the MeAPO or MeAPSO molecular sieves [63]. The most important metals that are introduced into the silicate-type frameworks are B, Ga, Ge, Ti, and Zn. The corresponding zeolite-like materials are denoted boro-, gallo-, germano-, titano-, and zincosilicates [64–66].

In principle, the four atomic constituents of the silicate-, aluminosilicate- and aluminophosphate- and silicoaluminophosphate-type zeolites are amenable to NMR spectroscopic investigations using their natural isotopes ^{29}Si , ^{27}Al , ^{31}P , and ^{17}O . The isotopes ^{29}Si and ^{31}P have natural abundances of 4.7% and 100%, respectively, and a nuclear spin of $I=1/2$ gives rise to narrow resonance lines. The isotope ^{27}Al ($I=5/2$) has a natural abundance of 100% but a large electric quadrupole moment which interacts with the electric field gradient (EFG) leading to a strong line broadening. This EFG is produced by non-spherically symmetric charge distributions around the aluminum nucleus. However, application of modern solid-state NMR techniques yields an insight into the coordination and local structure of framework aluminum atoms. In contrast, the ^{17}O isotope ($I=5/2$) has a very low abundance (0.037%) making ^{17}O NMR spectroscopy of the zeolite framework difficult. Most of the above-mentioned metal atoms, with the exception of ^{11}B , ^{69}Ga , and ^{71}Ga , are not accessible to NMR spectroscopy when introduced into zeolite frameworks.

3.1

^{29}Si MAS NMR Investigations of the Zeolite Framework

Silicon atoms in the zeolite framework are tetrahedrally coordinated (Q^4), resulting in five different silicon environments denoted as $\text{Si}(n\text{Al})$ units, where n corresponds to the number of aluminum atoms in the second coordination sphere. Each type of $\text{Si}(n\text{Al})$ unit ($n=0, 1, 2, 3$ or 4) yields ^{29}Si MAS NMR signals in a well-defined range of chemical shifts [1, 56–58]. These ranges are summarized for the various silicon units in Fig. 6. The ^{29}Si MAS NMR spectra of zeolites consisting of silicon atoms on crystallographically equivalent T-sites, e.g., zeolite X and Y, are only a function of framework composition (Fig. 7). Therefore, the framework $n_{\text{Si}}/n_{\text{Al}}$ ratio of these materials may be calculated directly from the ^{29}Si MAS NMR intensities using the formula:

$$n_{\text{Si}} / n_{\text{Al}} = \sum_{n=0}^4 I_{\text{Si}(n\text{Al})} / \sum_{n=0}^4 0.25 \cdot n \cdot I_{\text{Si}(n\text{Al})} \quad (28)$$

where the terms $I_{\text{Si}(n\text{Al})}$ are the intensities of the $\text{Si}(n\text{Al})$ lines. Moreover, by a comparison of the ^{29}Si MAS NMR-derived framework $n_{\text{Si}}/n_{\text{Al}}$ ratio with the bulk composition determined by chemical analysis, the amount of non-framework aluminum atoms can be calculated. However, in each zeolite, hydroxyl groups exist, bound to silicon atoms (Q^3 , Q^2) located at the outer surface of the zeolite

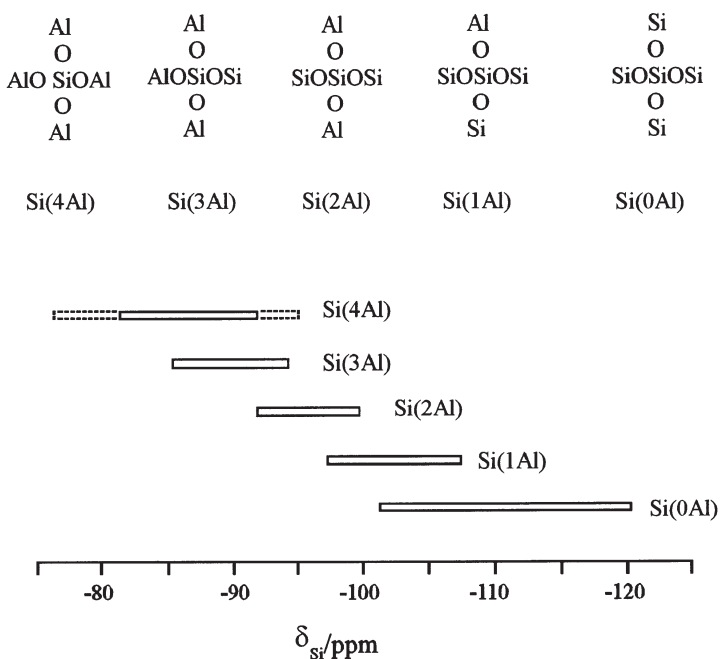


Fig. 6. ^{29}Si chemical shifts of $\text{Si}(n\text{Al})$ units in zeolite frameworks. The dotted lines for $\text{Si}(4\text{Al})$ designate the chemical shift range observed for 1:1 aluminosilicate sodalites with different cage fillings [1, 53, 56, 58, 71]

particles or at framework defects. It is important to note that the chemical shifts of $\text{Si}(1\text{Al})$ units (ca. -95 to -105 ppm) are in the same range as those of $\text{Si}(3\text{Si},\text{OH})$ units (ca. -100 to -103 ppm) [67]. Therefore, the number of SiOH groups limits the range of $n_{\text{Si}}/n_{\text{Al}}$ ratios which can be derived by ^{29}Si MAS NMR. In the same manner as described for ^{29}Si MAS NMR spectroscopy on aluminosilicate-type zeolites, the chemical compositions of zincosilicates and the gallium-modified ZSM-5 (Ga-MFI) were determined. The ^{29}Si MAS NMR spectra of zeolites VPI-7 and VPI-9, examined by Cambor and Davis [64], show signals of $\text{Si}(1\text{Zn})$ and $\text{Si}(2\text{Zn})$ units at resonance positions between -88.5 ppm and -95.6 ppm and between -77.9 ppm and -81.0 ppm, respectively. Using Eq. (28) with $\text{Si}(n\text{Zn})$ instead of $\text{Si}(n\text{Al})$, the authors calculated an $n_{\text{Si}}/n_{\text{Zn}}$ ratio of 3.5 for the VPI-7 samples under study. In the ^{29}Si MAS NMR spectra of H-Ga-MFI zeolites, Bradley and Howe [68] observed signals of $\text{Si}(0\text{Ga})$ and $\text{Si}(1\text{Ga})$ units at chemical shifts of ca. -112 ppm and -104 ppm, respectively. Comparing the bulk $n_{\text{Si}}/n_{\text{Ga}}$ ratios determined by elemental analysis with the framework $n_{\text{Si}}/n_{\text{Ga}}$ ratios derived by Eq. (28), with $\text{Si}(n\text{Ga})$ instead of $\text{Si}(n\text{Al})$, the numbers of gallium atoms in the framework and in non-framework species have been derived [68]. Investigating the titanosilicate ETS-10 and the titanoaluminosilicate ETAS-10, Rocha et al. [69] observed signals of $\text{Si}(0\text{Ti})$, $\text{Si}(1\text{Ti})$, and $\text{Si}(1\text{Al},1\text{Ti})$ units at ca. -103 ppm, in the range from -94 ppm to -97 ppm and ca. 4 ppm downfield shifted from the signal of $\text{Si}(1\text{Ti})$ units, respectively. A ^{29}Si MAS NMR signal ca. 1.5 ppm downfield

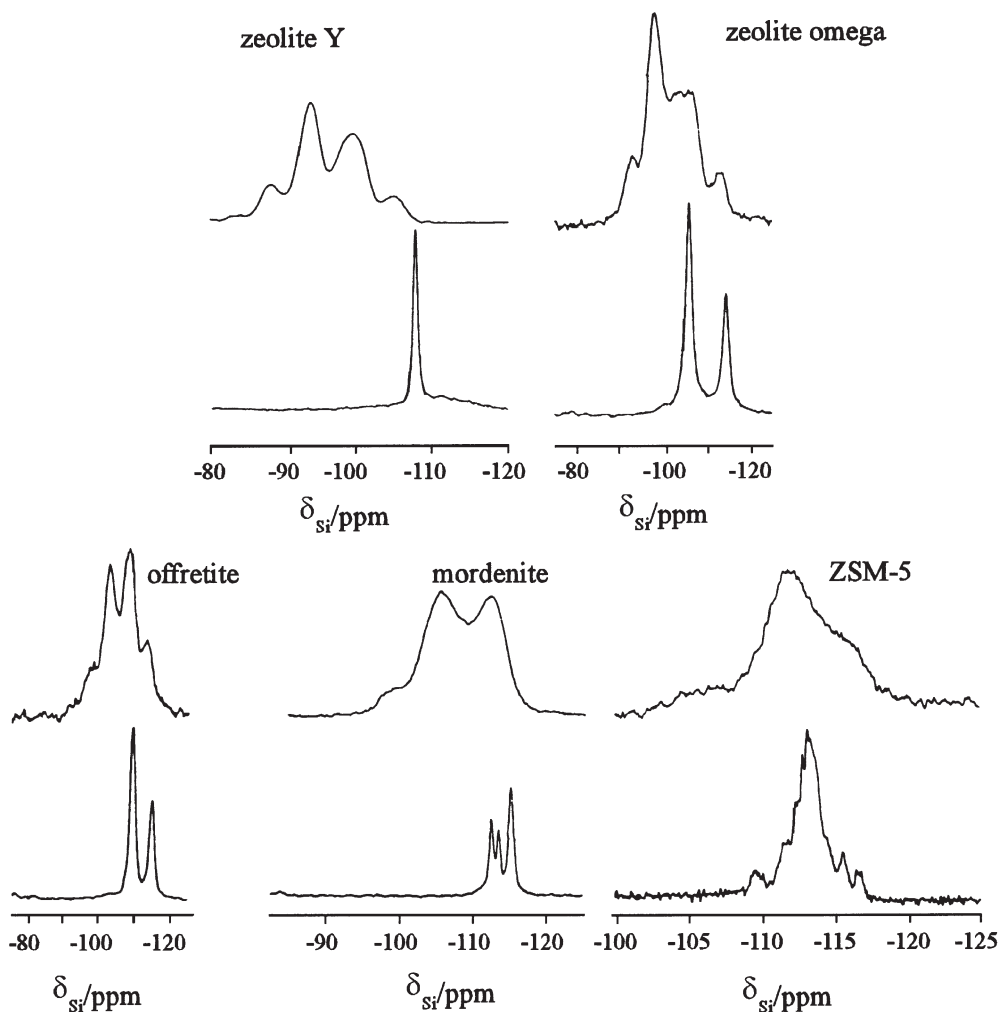


Fig. 7. ^{29}Si MAS NMR spectra of zeolites Y, omega, offretite, mordenite and ZSM-5 (*top*) and their dealuminated forms (*bottom*) [71]

from the Si(1Al,1Ti) resonance, observed in the spectrum of the titanogallosilicate ETGS-10, was assigned to Si(1Al,1Ti). Applying Eq. (28) with Si($n\text{Ga},m\text{Ti}$) instead of Si($n\text{Al}$), and setting the corresponding factors n and m in the denominator, the framework $n_{\text{Si}}/n_{\text{Ga}}$ and $n_{\text{Si}}/n_{\text{Ti}}$ ratios, respectively, were determined.

The order of silicon and aluminum atoms at framework T-sites has been investigated by comparing the relative Si($n\text{Al}$) populations obtained from ^{29}Si MAS NMR spectroscopy with those of models. For this approach models were used, derived from distribution patterns of the silicon and aluminum atoms in ordered subunits of the zeolite framework. By this method the silicon and aluminum order in zeolites X and Y and in several other structure types was investigated [1, 57, 70].

A number of the zeolite frameworks is characterized by crystallographically inequivalent T-sites with chemically equivalent environments which are responsible for a chemical shift distribution and/or a split of the ^{29}Si MAS NMR signals of framework silicon atoms. To investigate the local geometry of crystallographically inequivalent T-sites, it is advantageous to use high-silica zeolites consisting of Si(0Al) units only. If the ammonium form of zeolites is treated in the presence of water vapor at temperatures between 873 and 1073 K, a dealumination and ultrastabilization of the zeolite framework occurs, resulting in a dramatic decrease in the ^{29}Si MAS NMR linewidth [56, 71]. Figure 7 shows the spectra of several zeolites before (top) and after (bottom) dealumination and ultrastabilization. In agreement with the structure type (see [62]), the ^{29}Si MAS NMR spectrum of dealuminated zeolite Y consists only of one Si(0Al) line. In contrast, all other zeolites show ^{29}Si MAS NMR spectra with Si(0Al) signals of at least two crystallographically inequivalent T-sites. The intensity ratios of these lines, e.g., of 2 : 1 for zeolites omega and offretite, correspond to the population ratios of these T-sites. ^{29}Si chemical shift data of some selected zeolites are summarized in Table 1.

Differences in the ^{29}Si MAS NMR shifts of framework silicon atoms located on crystallographically inequivalent T-sites are mainly caused by different local geometries of SiO_4 tetrahedra. Empirical correlations and theoretical considerations yielded that the ^{29}Si NMR shifts, δ_{Si} , of Si($n\text{Al}$) units are linearly correlated with the mean value, $\bar{\alpha}$, of the four Si-O-T bond angles. With linear regression analysis, quantitative relationship between the values of δ_{Si} and $\bar{\alpha}$, $\sec \bar{\alpha}$, $\sin(\bar{\alpha}/2)$ and $\cos \bar{\alpha}/(\cos \bar{\alpha} - 1)$ have been found [1, 71–76]. For Si(4Al) units in sodalite,

Table 1. ^{29}Si chemical shifts of Si($n\text{Al}$) units (in ppm, referenced to TMS) of some selected zeolites

Zeolites	$n_{\text{Si}}/n_{\text{Al}}$	Sites	Si(4Al)	Si(3Al)	Si(2Al)	Si(1Al)	Si(0Al)	Ref
A	1.0	T	-89.6					165
	∞	T					-112.9	166
Y	2.5	T	-83.8	-89.2	-94.5	-100.0	-105.5	165
	∞	T					-107.8	167
Omega	3.1	T1		-89.1	-93.7	-98.8	-103.4	168
		T2	-89.1	-93.7	-98.8	-107.0	-112.0	
	∞	T1					-106.0	71
		T2					-114.4	
Offretite	2.9	T1		-93.5	-97.5	-101.9	-106.9	1
		T2		-97.5	-101.9	-106.9	-112.5	
	∞	T1					-109.7	71
		T2					-115.2	
Mordenite	5.0	T1 to T4			-100.1	-105.7	-112.1	169
	∞	T1					-112.2	71
		T4					-113.1	
		T2+T3					-115.0	
ZSM-5	20	T1 to T12				-106.0	-112.0	170

cancrinite, thomsonite and zeolites A, X, Y, ABW, Engelhardt et al. [75] obtained a correlation coefficient of 0.988 for the following relationship:

$$\delta_{Si}/\text{ppm} = -5.230 - 0.570 \cdot \bar{\alpha} \quad (29)$$

The correlation between δ_{Si} and $\overline{\cos \alpha / (\cos \alpha - 1)}$ was theoretically derived and led to [72]:

$$\delta_{Si}/\text{ppm} = -223.9 \overline{\cos \alpha / (\cos \alpha - 1)} + 5n - 7.2 \quad (30)$$

where n corresponds to the number of aluminum atoms in the second coordination sphere. Applying Eq. (30), the chemical shifts of silicon atoms at crystallographically inequivalent T-positions of the zeolite frameworks can be calculated from the Si-O-T bond angles that are obtained by XRD. This method allows the examination of structural models which are correct if the experimental ^{29}Si MAS NMR spectrum can be calculated using the structural data derived by XRD. Figure 8 shows the experimentally (top) and theoretically (bottom) derived ^{29}Si NMR signals of a monoclinic high-silica zeolite ZSM-5 [77]. The numbers at the top of the calculated spectrum assign the crystallographically inequivalent T-positions. As shown, there is a reasonable agreement in the line positions and intensities.

Fyfe et al. [78, 79] demonstrated that adsorption of organic molecules may induce a change in the zeolite framework geometry which can be detected by ^{29}Si MAS NMR spectroscopy. For instance, adsorption of p-xylene on dehydrated zeolite ZSM-5 induces a change of the monoclinic structure type with 24 crystallographically inequivalent T-sites to the orthorhombic structure type with 12 crystallographically inequivalent T-sites. The inverse transition was observed after heating the unloaded high-silica zeolite ZSM-5. Tuel et al. [80] used the temperature dependence of the transition from the monoclinic to the orthorhombic structure of titanosilicate TS-1 in order to determine the Ti content. TS-1 is a zeolite with the same structure type (MFI) as the zeolite ZSM-5; however, a number of silicon atoms are replaced by Ti atoms. The authors found that the transition temperature, observed by a change in the ^{29}Si MAS NMR line shape (appearance of shoulder at ca. -116 ppm), decreases linearly with increasing numbers of Ti atoms per unit cell.

In the same way that structural changes in MFI-type zeolites have been investigated by ^{29}Si MAS NMR spectroscopy, the migration of cations into the small cages of zeolite Y can be monitored [81, 82]. Local framework strains originating from multivalent cations located at position Si' in sodalite cages give rise to high-field shifts of the ^{29}Si MAS NMR signals due to $\text{Si}(n\text{Al})$ units located in six-membered oxygen rings close to the occupied cation sites. The spectra in Fig. 9 demonstrate the effect of lanthanum migration on the ^{29}Si MAS NMR signals of zeolites 30LaNaY and 60LaNaY (sodium exchange degrees of 30% and 60%, respectively) before (top) and after (bottom) calcination at 433 K and rehydration [82]. The spectra plotted at the top consist of lines at -89.2 ppm, -94.5 ppm, -100.5 ppm and -105.0 ppm due to $\text{Si}(3\text{Al})$, $\text{Si}(2\text{Al})$, $\text{Si}(1\text{Al})$ and $\text{Si}(0\text{Al})$ units, respectively. Calcination and rehydration result in an intensity

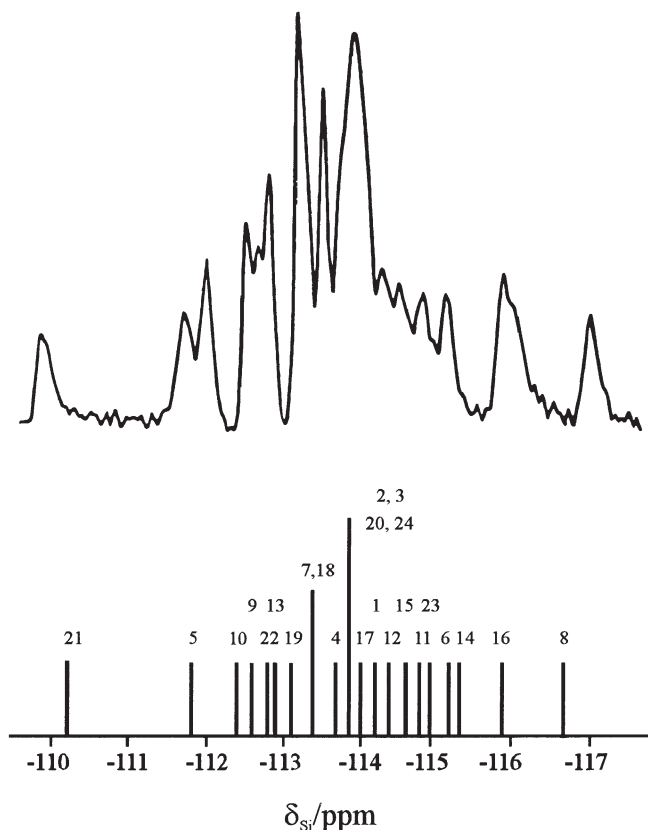


Fig. 8. Experimental (*top*) and calculated (*bottom*) ^{29}Si MAS NMR signals of silicon atoms at crystallographically inequivalent T-positions in the framework of monoclinic high-silica ZSM-5 [77]

decrease of the low-field lines and the appearance of a new peak at ca. -97 ppm (bottom of Fig. 9). A breakdown of these spectra showed that about 19% and 30% of the ^{29}Si MAS NMR signals caused by the calcined zeolites 30LaNaY and 60LaNaY, respectively, were shifted by about 3 ppm to a higher magnetic field (denoted $n=3'$, $2'$, and $1'$). Applying Eq. (29), this low-field shift corresponds to a variation in the mean Si-O-T bond angles of about 5° .

Three-dimensional connectivities between crystallographically inequivalent T-sites in zeolites ZSM-5, ZSM-12, ZSM-22, ZSM-23, ZSM-39, and DD3R have been investigated by Fyfe et al. [83–89] applying COSY (correlation spectroscopy) and INADEQUATE (incredible natural abundance double quantum transfer experiment) pulse sequences. The COSY experiment is based on the measurement of the J -coupling (direct bond couplings) within a molecular structure [84]. Figure 10a shows the pulse sequence consisting of: (i) the preparation of the spin system by magnetization transfer from the abundant S -spins (protons) to the dilute I -spins (silicons) by cross-polarization (CP), (ii) the evolution of the spin

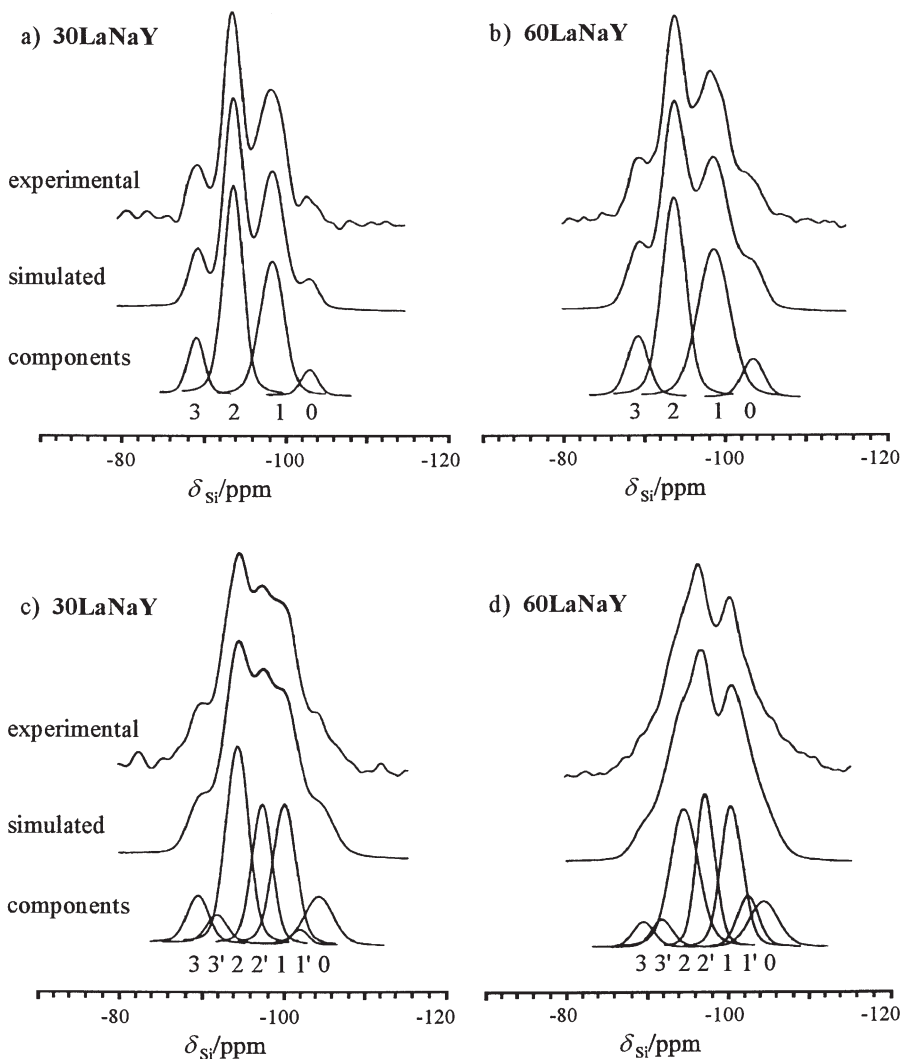


Fig. 9 a–d. ^{29}Si MAS NMR spectra of hydrated zeolites 30LaNaY (a, c) and 60LaNaY (b, d), recorded before (a, b) and after (c, d) thermal treatment at 433 K and rehydration. The figures at the bottom denote the signals of the undisturbed ($n=1, 2, 3$) and of the strained ($n=1', 2', 3'$) Si($n\text{Al}$) units [82]

system during the time period t_1 , (iii) a fixed delay (FD) before and after a $\pi/2$ pulse, and (iv) the acquisition of the free induction decay during the time period t_2 . The 2D spectrum of zeolite ZSM-39 depicted in Fig. 10c was recorded with 128 increments in t_1 and 64 scans for each t_1 . The contour plot in Fig. 10d shows diagonal peaks of silicon atoms located at T1, T2 and T3 and off-diagonal peaks (cross-peaks) originating from silicon atoms at T1 and T2 (cross-peak T1T2) and at T2 and T3 (cross-peak T2T3). Hence, the cross-peaks clearly indicate connec-

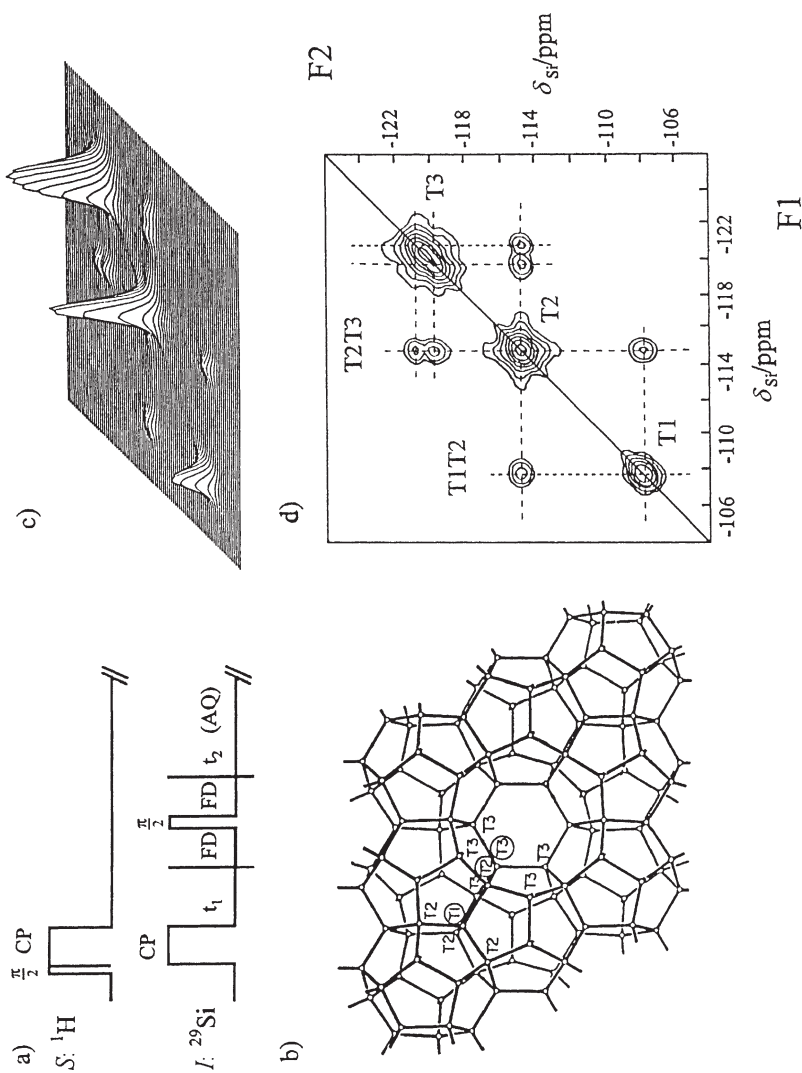


Fig. 10 a–d. Schematic representation of a modified COSY experiment (a), of the zeolite ZSM-39 framework (b), and the stacked plot (c) and the contour plot (d) of the two-dimensional ^{29}Si COSY MAS NMR spectrum of ZSM-39 recorded at 373 K with 128 experiments, 64 scans in each experiment, and a fixed delay of 5 ms. The total experimental time was about 23 h [84]

tivities between silicon atoms on T1 and T2 and between silicon atoms on T2 and T3. These results agree with the structure model of zeolite ZSM-39 depicted in Fig. 10b.

The more complex INADEQUATE pulse sequence has the following advantages [87–89]: (a) the diagonal peaks, i.e., the signals due to isolated spins, are suppressed, which improves the range of connectivities which is accessible for detection, and (b) a better signal-to-noise ratio can be reached. In addition, (c) any spinning rate may be used, as spinning sidebands will not appear after analysis of the data set. The main disadvantage of the technique is that the J -coupling has to be estimated in order to choose the correct pulse delays in the pulse

sequence. A description of experimental details and applications of INADEQUATE pulse sequences can be found in the literature [87–89].

3.2

Solid-State ^{27}Al NMR Spectroscopy on Zeolites

The ^{27}Al NMR spectra of zeolites are much simpler than their ^{29}Si NMR counterparts. According to Loewenstein's rule, the formation of Al-O-Al bondings is forbidden and only Al(4Si) units exist in the framework of aluminosilicates. Therefore, the ^{27}Al NMR spectra of hydrated zeolites consist, in general, of only one line of framework aluminum (Al^{f}) atoms in a relatively small range of chemical shifts of 55 ppm to 68 ppm [referenced to 0.1 M aqueous $\text{Al}(\text{NO}_3)_3$ solution]. In hydrated zeolites, there is only a small deviation from the tetrahedral symmetry of the AlO_4 units which results in a weak quadrupolar line broadening. Non-framework aluminum (Al^{nf}) species in hydrated zeolites, originating from dealumination by thermal treatment or acid leaching, are octahedrally coordinated (AlO_6) and cause a ^{27}Al NMR signal at about 0 ppm. If non-framework aluminum exists as polymeric aluminum oxide in zeolite cages or pores, strong quadrupolar line broadening may be observed owing to distortions of the octahedral symmetry of the AlO_6 units. A broad signal at 30–50 ppm may be caused by non-framework aluminum species in a disturbed tetrahedral coordination or a penta-coordinated state [90]. For the signals of tetrahedrally coordinated framework aluminum atoms, no definite relationships between the ^{27}Al chemical shift and the $n_{\text{Si}}/n_{\text{Al}}$ ratio or the silicon and aluminum order scheme of the zeolite framework was found. However, a linear relationship between the ^{27}Al NMR line positions and the mean Al-O-Si bond angles has been established [91]. An important prerequisite of a correlation is the careful correction of the experimentally derived shift data for the second-order quadrupolar shift (see Sect. 2.2.3). Using ^{27}Al and ^{29}Si MAS NMR spectroscopy on lithium and sodium halide aluminosilicate sodalites with high-speed spinning, Jacobsen et al. [92] found the following linear relationship between the ^{27}Al and ^{29}Si chemical shifts:

$$\delta_{\text{Al}}/\text{ppm} = 1.03 \cdot \delta_{\text{Si}}/\text{ppm} + 151.94 \quad (31)$$

For chemical shift data covering a range of 12 ppm a correlation coefficient of 0.9998 was calculated. This result suggests that accurate ^{27}Al chemical shifts allow the determination of mean Al-O-Si bond angles and the prediction of ^{29}Si chemical shifts of Si(0Al) units in high-silica zeolites. The ^{27}Al MAS NMR spectrum of zeolite omega ($n_{\text{Si}}/n_{\text{Al}}=4.6$), e.g., recorded at the resonance frequency of 104.3 MHz, consists of two signals of tetrahedrally coordinated framework aluminum at 61.5 ppm and 54.5 ppm caused by aluminum atoms of Al(4Si) units located at T1- and T2-sites, respectively [93, 94]. The ^{29}Si MAS NMR signals of silicon atoms of Si(0Al) units located at T1- and T2-sites appear at -106.0 ppm and -114.4 ppm, respectively (see Table 1 or [71]). The ^{27}Al MAS NMR spectrum of dealuminated zeolite MCM-22 ($n_{\text{Si}}/n_{\text{Al}}=20$) recorded at a resonance frequency of 195.4 MHz shows at least three peaks of framework aluminum atoms in the

chemical shift range from 49 ppm to 62 ppm [95]. No second-order quadrupolar shift was observed comparing the signals recorded at resonance frequencies of 104.2 MHz and 195.4 MHz. The ^{29}Si MAS NMR spectrum of the dealuminated zeolite MCM-22 consists of Si(OAl) signals covering a range from -104.0 ppm to -118.5 ppm [95]. Hence, the ratios of chemical shift ranges of framework silicon ($\Delta\delta_{\text{Si}}$) and aluminum ($\Delta\delta_{\text{Al}}$) atoms in zeolites omega and MCM-22 amount to $\Delta\delta_{\text{Si}}/\Delta\delta_{\text{Al}}=1.2$ and $\Delta\delta_{\text{Si}}/\Delta\delta_{\text{Al}}=1.1$, respectively, which is in reasonable agreement with Eq. (31).

A number of investigations published in the mid-1980s have demonstrated that quantitatively reliable ^{27}Al NMR spectra of dealuminated zeolites containing framework as well as non-framework aluminum atoms can only be obtained in high magnetic fields, with fast magic angle spinning and using short excitation pulses [96–99]. Dealuminated zeolites Y, mordenite and ZSM-5 have been extensively investigated by solid-state NMR spectroscopy [1, 67, 100–104]. ^{29}Si MAS NMR spectroscopy shows that, as a result of hydrothermal treatment or acid leaching, aluminum is removed from the zeolite framework while application of ^{27}Al NMR spectroscopy allows an insight into the formation of non-framework aluminum species. In order to elucidate the nature of the non-framework aluminum species, ^{27}Al MAS NMR and ^1H - ^{27}Al CP/MAS NMR investigations have been carried out on series of zeolites with an increasing degree of dealumination [90, 105]. In these investigations the Hartmann-Hahn condition was established on crystalline kaoline. Because only the central $\{+1/2 \leftrightarrow -1/2\}$ transition is observed, excitation in the ^1H - ^{27}Al CP/MAS NMR experiment is selective and, therefore, the Hartmann-Hahn condition [90] [cf. Eq. (22)] is:

$$3 \cdot \gamma_{\text{Al}} \cdot B_{1\text{Al}} = \gamma_{\text{H}} \cdot B_{1\text{H}} \quad (32)$$

As shown in Fig. 11, the decrease in the ^{27}Al MAS NMR signal of tetrahedrally coordinated framework aluminum at about 60 ppm is accompanied by the appearance of signals at about 0 ppm and 30 ppm. Furthermore, in the spectra recorded by the application of the cross-polarization technique (right-hand side), the intensities of the signals at 0 ppm and 30 ppm increase inversely to the intensity of the signal at 60 ppm. Therefore, the authors suggested that ^1H - ^{27}Al CP/MAS NMR experiments preferentially monitor non-framework aluminum atoms. In addition, this observation indicates that the 30-ppm line is an independent signal [90].

Broad-line ^{27}Al NMR spectroscopy was applied to investigate aluminum species in dehydrated zeolites [106–110]. These experiments were carried out using the phase-cycled selective echo sequence proposed by Kunwar et al. [111]. At a resonance frequency of 130.3 MHz, the full width of the signals varies from 24 kHz for dehydrated zeolite NaZSM-5 to 100 kHz for dehydrated zeolite HZSM-5. Therefore, application of the MAS technique is limited in this case as the presently achieved spinning rates do not exceed the second-order broadening of the central transition. Framework aluminum atoms in H-zeolites, whose negative charges are compensated by residual sodium cations, give rise to a narrow signal. Therefore, the static ^{27}Al NMR spectra of dehydrated zeolites consist of two sig-

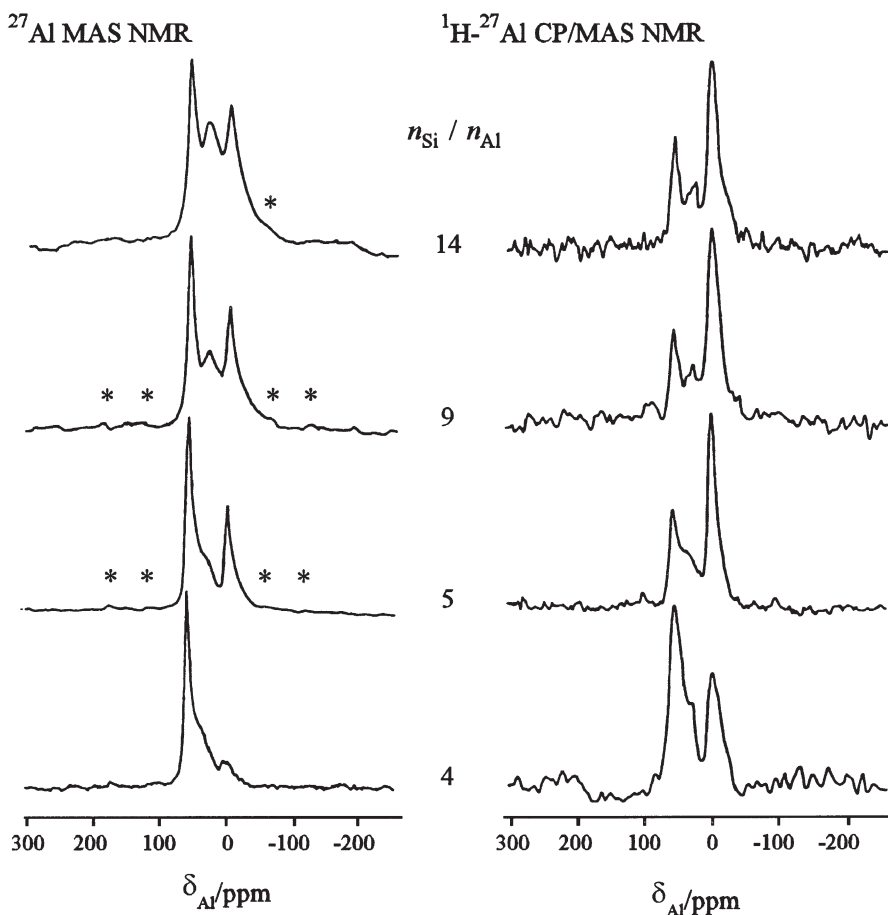


Fig. 11. ^{27}Al MAS NMR (left-hand side) and ^1H - ^{27}Al CP/MAS NMR spectra of increasingly dealuminated (from bottom to top) zeolite HY, recorded at a resonance frequency of 104.3 MHz and with a sample spinning rate of ca. 13 kHz (*: MAS sidebands) [90]

nals, a broad and a narrow one. The line shape analysis of the broad component QP (quadrupolar pattern) yielded coupling constants of $C_Q=12.7$ MHz for 92HY and $C_Q=16.0$ MHz for HZSM-5. The narrow component QL (quadrupolar line) corresponds to $C_Q=5.5$ MHz for NaY and $C_Q=4.7$ MHz for NaZSM-5. Dealuminated zeolite HZSM-5 was investigated after hydrothermal treatment at 810 K at water vapor pressures of 7, 13 and 93 kPa [107, 108]. The ^{27}Al NMR spectra of these samples consist of at least two signals. One component corresponds to QP, due to framework aluminum atoms ($C_Q=16$ MHz), while the other, which seems to be caused by an asymmetric electric field gradient tensor ($C_Q\approx 9$ MHz), was related to non-framework aluminum species [108].

In Fig. 12 the strong influence of the framework protonation on the ^{27}Al NMR spectra of a dehydrated zeolite ZSM-5 is demonstrated [109, 110]. The ^{27}Al NMR

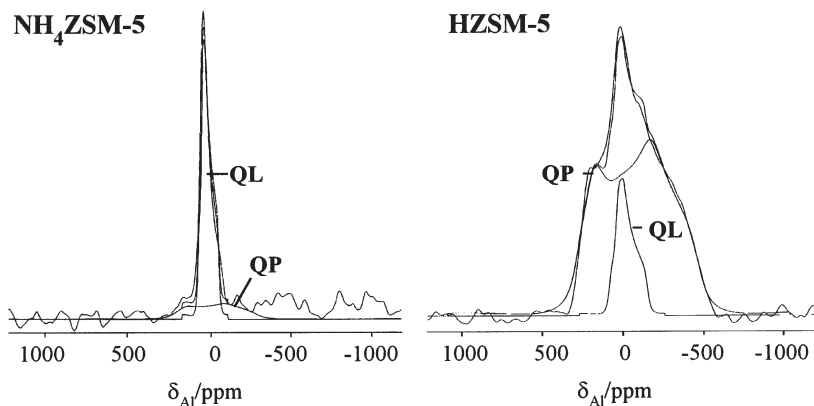


Fig. 12. Experimental and decomposed ^{27}Al NMR spectra of dehydrated zeolites $\text{NH}_4\text{ZSM-5}$ (left) and HZSM-5 (right) recorded at a resonance frequency of 104.3 MHz with a quadrupole-echo sequence [110]

parameters determined by decomposition and simulation of the ^{27}Al NMR signals of the dehydrated NH_4^- and H-forms of a zeolite Y ($n_{\text{Si}}/n_{\text{Al}}=2.6$), a dealuminated zeolite Y/de ($n_{\text{Si}}/n_{\text{Al}}=8.0$), a mordenite ($n_{\text{Si}}/n_{\text{Al}}=8.0$) and a zeolite ZSM-5 ($n_{\text{Si}}/n_{\text{Al}}=22.0$) are summarized in Table 2 [110]. Considering these data, the ^{27}Al NMR spectra of the dehydrated NH_4^- -form zeolites consist of a strong signal QL caused by AlO_4 tetrahedra of the non-protonated zeolite frameworks and a weak

Table 2. Aluminum quadrupole coupling constants, C_Q , asymmetry parameters, η_Q , and relative intensities, I_{rel} , derived by decomposition and simulation of ^{27}Al NMR spectra [110]

Zeolites	Signals	C_Q/MHz^a	η_Q	$I_{\text{rel}}/\%$
NH_4Y	QL	5.0	0.7	89
	QP	ca. 9.0	ca. 0.8	11
HY	QL	6.0	0.7	17
	QP	13.5	0.4	83
$\text{NH}_4\text{Y/de}$	QL	6.0	0.7	41
	QP	ca. 9.0	ca. 0.8	59
HY/de	QL	7.0	0.7	16
	QP	13.7	0.5	84
NH_4MOR	QL	5.0	0.7	100
HMOR	QL	6.8	0.7	14
	QP	15.0	0.35	86
$\text{NH}_4\text{ZSM-5}$	QL	7.0	0.7	81
	QP	ca. 9.0	ca. 0.8	19
HZSM-5	QL	7.3	0.7	21
	QP	15.5	0.5	79

^a Accuracy of 0.5 MHz.

signal QP that was, according to one report [108], attributed to non-framework aluminum. After deammoniation, the spectra of these samples are dominated by a strong signal QP, due to the AlO_4 tetrahedra of the protonated zeolites. Considering the quadrupole parameters given in Table 2, the framework protonation results in a significant increase in the ^{27}Al quadrupole coupling constant, C_Q , of the framework aluminum atoms. Investigating feldspars, Ghose and Tsang [112] observed a structural dependence of the quadrupole coupling constant of aluminum atoms in AlO_4 tetrahedra. For the quantitative description of the AlO_4 geometry, the authors used the so-called shear strain parameter [112] given by:

$$|\Psi| = \sum_{i=1}^6 |\tan(\Theta_i - \Theta_0)| \quad (33)$$

where the sum runs over the six individual O-Al-O bond angles Θ_i . The angle Θ_0 is the ideal bond angle of 109.5° . The geometries of AlO_4 tetrahedra given in the literature [112, 113] yielded a linear interdependence of $|\Psi|$ and C_Q with a gradient of 0.106 (see the bottom of Fig. 13). According to this gradient and the C_Q values given in Table 2, the protonation-induced increase in the aluminum quadrupole coupling constant of framework aluminum atoms may be explained by a shear strain of the AlO_4 tetrahedra which corresponds to a variation of the mean O-Al-O bond angles by about 8° [110]. Hence, the AlO_4 tetrahedra of the zeolite framework respond to the attack of the hydroxyl protons by a readjustment of their local geometry.

While the standard ^{27}Al MAS NMR technique reduces the second-order quadrupolar line broadening by a factor of about 3.6 (see Sect. 2.1.2), application of the double-rotation (DOR) technique causes a complete averaging of this solid-state interaction. Line narrowing of about two orders of magnitude may be achieved by DOR providing well-separated lines for framework atoms located at crystallographically inequivalent sites. Generally, the DOR central lines are accompanied by patterns of DOR sidebands, separated by the spinning frequency of the outer rotor. The central lines may be identified by spectra recorded at different spinning rates. Adopting the method published by Samoson and Lippmaa [35], rotor-synchronized single-pulse excitation suppresses the odd-numbered DOR sidebands. However, as mentioned in Sect. 2.2.3, a suitable resolution enhancement is only achieved if the line broadening is not caused by strong homonuclear dipole-dipole interaction, chemical shift distribution or distribution of quadrupolar parameters, e.g., due to a distribution of geometric parameters in the local structure of the investigated atoms. A significant line narrowing was observed in the ^{27}Al DOR NMR spectra of calcium tungstate aluminate sodalite (CAW) and sodium aluminosilicate sodalite [114], whose frameworks are built exclusively of AlO_4 tetrahedra and by alternating arrangements of AlO_4 and SiO_4 tetrahedra, respectively. The ^{27}Al DOR NMR spectra of CAW recorded with spinning rates of the outer DOR rotor in the range of 800–1150 Hz show seven sharp central lines caused by seven crystallographically inequivalent aluminum sites of the CAW framework.

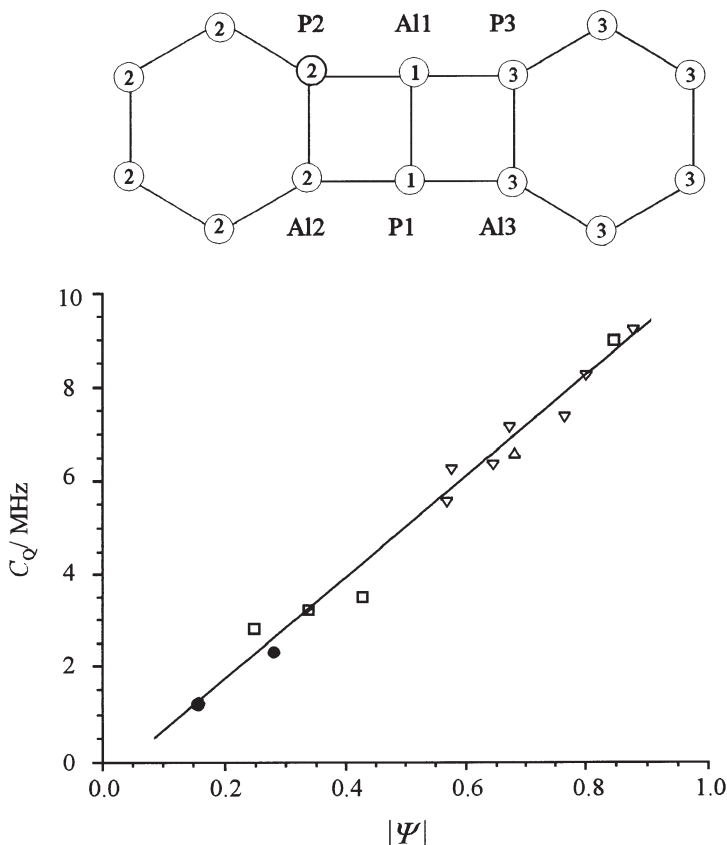


Fig. 13. Schematic drawing (*top*) of the VPI-5 structure and the plot (*bottom*) of the quadrupole coupling constants, C_Q , of ^{27}Al as a function of the shear strain parameter of AlO_4 tetrahedra in aluminates (\triangle, ∇), feldspars (\square), and VPI-5 (\bullet) [112, 113]

The frameworks of aluminophosphate-type zeolites are built of alternating AlO_4 and PO_4 tetrahedra and are characterized by a high degree of order. Therefore, the ^{27}Al DOR NMR spectra of these materials consist of narrow lines due to aluminum atoms on crystallographically inequivalent T-sites [115–119] or are caused by framework aluminum atoms interacting with probe molecules [120–123]. As an example, at the top of Fig. 14 the ^{27}Al DOR NMR spectrum of dehydrated VPI-5 is depicted. The two peaks at 36 ppm and 33 ppm with an intensity ratio of 2:1 were attributed to different tetrahedrally coordinated framework aluminum species [116]. According to the observed intensity ratio, the line at 36 ppm was assigned to aluminum sites in the six-membered oxygen rings and the line at 33 ppm to aluminum sites in double four-membered rings (see top of Fig. 13) [115]. The addition of water molecules dramatically alters the local bonding of the framework aluminum atoms of VPI-5, as reflected by the spectrum at the bottom of Fig. 14. The lines at 36 ppm and 33 ppm have disappeared

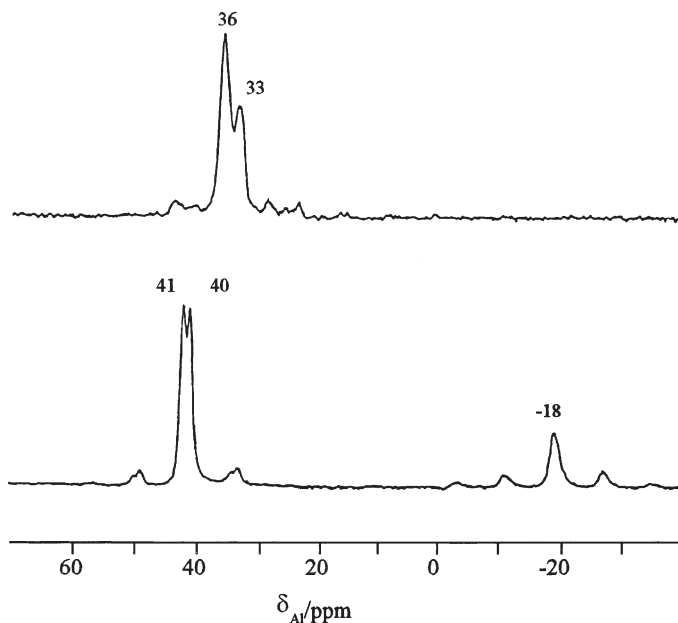


Fig. 14. ^{27}Al DOR NMR spectra of dehydrated (*top*) and hydrated (*bottom*) aluminophosphate VPI-5, recorded at 104.2 MHz with the rotation frequency of the outer DOR rotor of $\nu_{\text{rot}}=800$ Hz and rotor-synchronized pulses [116]

and two partially resolved signals associated with tetrahedrally coordinated framework aluminum atoms are present at 41 ppm and 40 ppm. In addition, a broader upfield line at -18 ppm in the range ascribed to octahedrally coordinated aluminum sites can be observed. The integrated intensities of these three lines occur in a 1:1:1 ratio. Spectra of hydrated VPI-5, recorded in different magnetic fields, consist of ^{27}Al DOR NMR signals that are shifted by second-order quadrupole interaction (see Sect. 2.1.2). By using Eq. (14), isotropic chemical shifts of 43.6, 41.6, and -10.4 ppm were determined. In the same way, quadrupole coupling constants of ca. 2 MHz for the first line and ca. 1 MHz for the second line were calculated [118]. A strong argument for the assignment of the two low-field peaks at 43.6 ppm and 41.6 ppm is based on the relationship between the strength of the quadrupole interaction of the framework aluminum atoms and the local geometry of the AlO_4 tetrahedra. As mentioned above, the local geometry of the AlO_4 tetrahedra can be described quantitatively by the shear strain parameter $|\psi|$. Using the structure data of VPI-5 [124] and applying Eq. (33), a shear strain parameter of $|\psi|=0.157$ for Al2 sites and of $|\psi|=0.280$ for Al3 sites was estimated. According to the correlation between $|\psi|$ and C_Q , shown at the bottom of Fig. 13, the low-field ^{27}Al DOR NMR signal at 43.6 ppm (C_Q ca. 2 MHz) is due to Al3 sites and the signal appearing at 41.6 ppm (C_Q ca. 1 MHz) has to be attributed to Al2 sites [113]. This example demonstrates that straightforward analysis of ^{27}Al quadrupole parameters is a suitable method for assigning experimental NMR signals and for deriving information on the local framework geometry.

3.3

³¹P MAS NMR of Aluminophosphate- and Gallophosphate-Type Zeolites

³¹P MAS NMR spectroscopy is a sensitive method for obtaining data on the local structures of aluminophosphate-, silicoaluminophosphate-, and gallophosphate-type zeolites. The first ³¹P NMR investigations on AlPO₄-5, AlPO₄-11, AlPO₄-17 and AlPO₄-31 were carried out by Blackwell and Patton [125]. Typically, the ³¹P MAS NMR signals of PO₄ tetrahedra in crystalline aluminophosphates cover a chemical shift range from -20 ppm to -33 ppm (referenced to 0.85 M H₃PO₄) [125–131]. As a result of ³¹P MAS NMR studies on crystalline AlPO₄ polymorphs and aluminophosphate-type zeolites, Mueller et al. [132] found a linear relationship between the resonance positions of tetrahedrally coordinated phosphorus atoms and their mean P-O-Al angles. The gradient was determined to be -0.61 ppm/deg with a correlation coefficient of 0.995. According to this relationship an increase in the mean P-O-Al angles causes a high-field shift of the ³¹P NMR signal.

As demonstrated by Barrie and Klinowski [133], the incorporation of metal atoms into the aluminophosphate framework (MeAPO) may affect the ³¹P MAS NMR line position. Investigating the magnesium aluminophosphate MgAPO-20, the authors observed ³¹P MAS NMR signals at chemical shifts of -14.0 ppm, -21.1 ppm, -28.0 ppm, and -34.9 ppm due to phosphorus atoms in P(1Al,3 Mg), P(2Al, 2 Mg), P(3Al,1 Mg), and P(4Al) units, respectively. The small chemical shift of the phosphorus atoms surrounded by four aluminum atoms [P(4Al)] was explained by the high P-O-Al bond angle of 160° (vide supra). The concentration of metal atoms incorporated into the framework of MeAPOs can be calculated from the ³¹P MAS NMR intensities in a manner similar to that used for the calculation of $n_{\text{Si}}/n_{\text{Al}}$ ratios from ²⁹Si MAS NMR spectra. With P(*n*Al) instead of Si(*n*Al) and using the integrated intensities $I_{P(n\text{Al})}$ of the P(*n*Al) signals, Eq. (28) yields the framework $n_{\text{P}}/n_{\text{Al}}$ ratio. The expression for the $n_{\text{P}}/n_{\text{Me}}$ ratio, and (since 50% of the T-sites are occupied by phosphorus) the fraction [*Me*] of T-sites occupied by the metal atom, Me, can be derived by [133]:

$$[\text{Me}] = \sum_{n=0}^4 (4-n) I_{P(n\text{Al})} / 8 \sum_{n=0}^4 I_{P(n\text{Al})} \quad (34)$$

Since the ³¹P MAS NMR spectra of the aluminophosphate VPI-5 are quite unusual, they must be considered here in the context of the structure of this material. As shown at the top of Fig. 13, the structure of VPI-5 consists of two phosphorus sites located in the six-membered oxygen rings and one belonging to two adjacent four-membered rings. Indeed, the ³¹P MAS NMR spectrum of dehydrated VPI-5 consists of two lines at about -26 ppm and -31 ppm with an intensity ratio close to 2:1 [134–136]. In contrast, the spectrum of hydrated VPI-5 reveals three lines of equal intensity at chemical shifts of ca. -23 ppm, -27 ppm, and -33 ppm [137–140]. A number of papers have been published [137–142] in regard to the assignment of these ³¹P MAS NMR signals to distinct phosphorus sites in VPI-5. In this context, van Eck and Veeman [140] investigated the spatial neighborhood of aluminum and phosphorus atoms in the framework

of VPI-5 by 2D NMR spectroscopy. The two-dimensional experiment used (Fig. 15a) enabled the correlation of two different nuclei via their heteronuclear dipole-dipole interaction. The preparation period of this experiment is a REDOR (rotational-echo double resonance) pulse sequence. During the evolution period (t_1) the S - and I -spins evolve under their chemical shifts and the dipolar coupling. Before the acquisition of the I -spin magnetization in t_2 , a second REDOR pulse sequence is applied. At the bottom of Fig. 15 the 2D ^{27}Al - ^{31}P MAS NMR correlation spectrum of dehydrated VPI-5 is depicted [140]. The cross-peaks observed in this spectrum indicate that each phosphorus atom is coupled in a dipolar fashion with tetrahedrally (43.6 ppm, 41.6 ppm) as well as octahedrally (-10.4 ppm) coordinated aluminum atoms. However, the intensities of the peaks differ. The

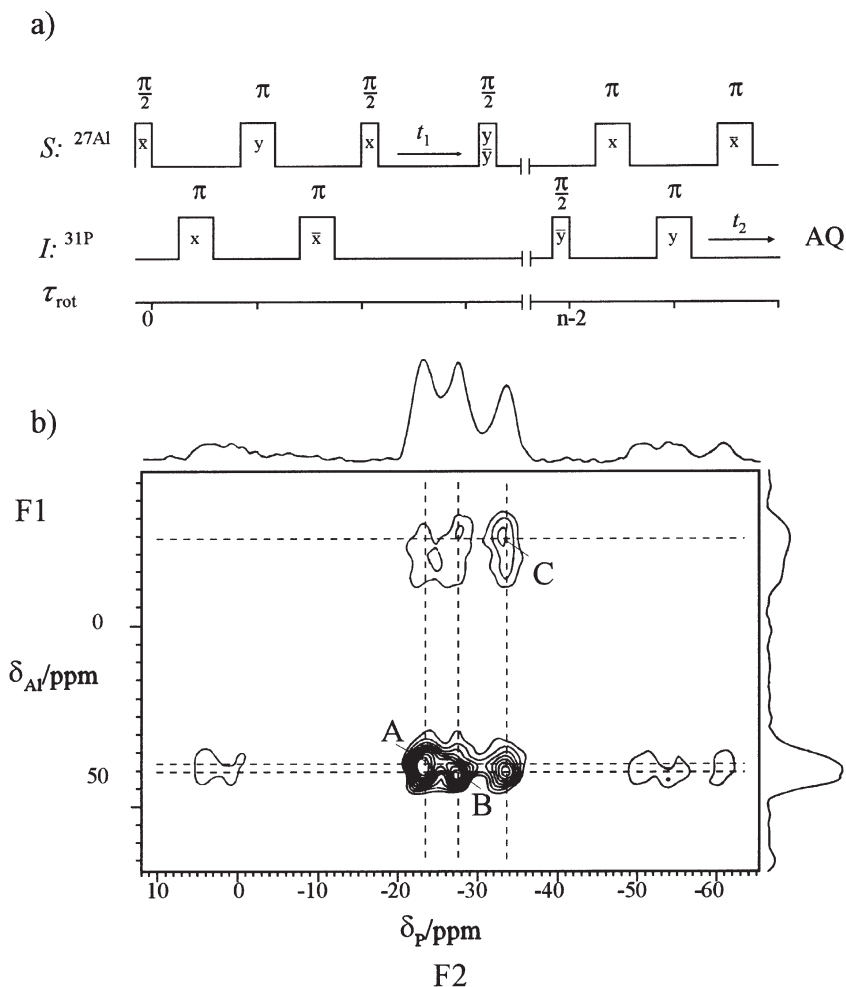


Fig. 15a, b. Pulse scheme of **a** the two-dimensional correlation experiment and **b** the contour plot and projections (F1: ^{27}Al , F2: ^{31}P) of the ^{27}Al - ^{31}P correlation spectrum of VPI-5 [140]

phosphorus atoms that are responsible for the three different ^{31}P MAS NMR signals have different aluminum neighbors (cf. top of Fig. 14). Considering the cross-peak intensities and the assignment of ^{27}Al NMR signals given above (Al1 at -10.4 ppm, Al2 at 41.6 ppm, and Al3 at 43.6 ppm [113]), the phosphorus atoms observed at -33 ppm are coupled in a dipolar fashion with 2Al1, Al2, and Al3; the phosphorus at -27 ppm with Al1, 2Al2, and Al3; and the phosphorus at -23 ppm with Al1, Al2, and 2Al3. Hence, the ^{31}P MAS NMR signals of hydrated VPI-5 observed at -33 ppm, -27 ppm, and -23 ppm were attributed to phosphorus atoms located at P1, P2, and P3, respectively [113, 140]. Fyfe et al. [143, 144] deduced the same signal assignment from two-dimensional TEDOR (transferred-echo double resonance) experiments.

The thermal stability of VPI-5 and its transformation to $\text{AlPO}_4\text{-8}$ have been extensively studied by multi-nuclear solid-state NMR spectroscopy [134, 138, 139, 145, 146]. Depending on the treatment conditions (vacuum, heating rate, final temperature), the structure of VPI-5 can be preserved up to a dehydration temperature of 673 K, as proved by ^{31}P MAS NMR spectroscopy. Under slightly elevated temperatures ($343\text{--}423$ K), VPI-5 undergoes a reversible dehydration and rehydration which results in a merging of the two low-field ^{31}P MAS NMR lines. The split occurs again after cooling down to ambient temperature [139, 145, 146]. Under more drastic conditions (unsealed samples, fast heating rates, high temperature), VPI-5 transforms to $\text{AlPO}_4\text{-8}$ that can be monitored by ^{31}P and ^{27}Al MAS NMR spectroscopy (Fig. 16) [134]. The ^{31}P MAS NMR spectrum of hydrated $\text{AlPO}_4\text{-8}$ at the bottom of Fig. 16 consists of three signals at about -21 ppm, -25 ppm, and -30 ppm with an intensity ratio of 1:2:6. Simultaneously, the center of gravity of the ^{27}Al MAS NMR signal is shifted from about 42 ppm (VPI-5) to about 37 ppm ($\text{AlPO}_4\text{-8}$).

Phosphorus atoms in gallophosphate frameworks are surrounded by four gallium atoms. In gallophosphate cloverite, these $\text{P}(4\text{Ga})$ units cause ^{31}P MAS NMR signals in the chemical shift range between -2 and -11 ppm (Fig. 17) [68, 147–149]. According to the structure of cloverite [150], five ^{31}P MAS NMR signals with an intensity ratio of 1:1:2:2:2 are to be expected. The phosphorus atom P3 (see scheme in Fig. 17) carries a hydroxyl group and has, therefore, a spectroscopic property that is characteristic for dipolar coupled spins. Since dipolar-dephasing experiments (see Sect. 2.3.2) lead to a disappearance of signals at ca. -2 ppm and -5 ppm, both lines were attributed to P3 sites [149]. In agreement with the dipolar-dephasing experiments, application of cross-polarization caused an enhancement of these low-field signals [149, 151]. Considering these results, the ^{31}P MAS NMR signals of cloverite were labeled as given in Fig. 17 [149]. According to their intensities, the lines 1 and 2 at ca. -2 ppm and -5 ppm, respectively, were assigned to P2 and P3 atoms. Lines 3 and 5 at ca. -9.5 ppm and -11.5 ppm, respectively, are due to P1 and P4 atoms that cannot be distinguished. Finally, line 4 at ca. -10.5 ppm is caused by P5 atoms. The intensity ratio of these lines of 1:1:2:2:2, derived by decomposition of the spectrum depicted in Fig. 17, agrees with the intensity ratio found by X-ray diffraction [150].

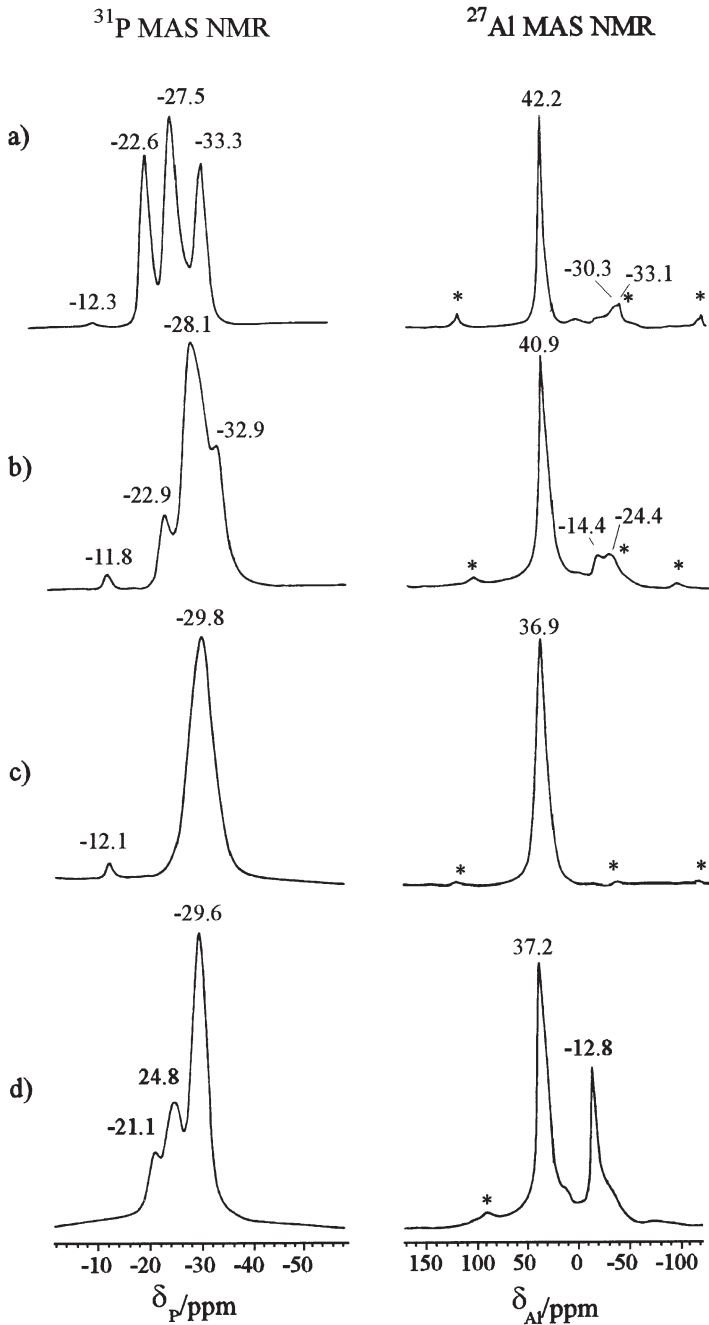


Fig. 16a–d. ^{31}P (left) and ^{27}Al MAS NMR (right) spectra of VPI-5 dried at 333 K overnight (a), VPI-5 evacuated at 327 K overnight and calcined at 523 K overnight (b), $\text{AlPO}_4\text{-8}$, transformed from VPI-5 by calcination at 673 K overnight (c) and hydrated $\text{AlPO}_4\text{-8}$ (d) [134]. The asterisks denote MAS sidebands

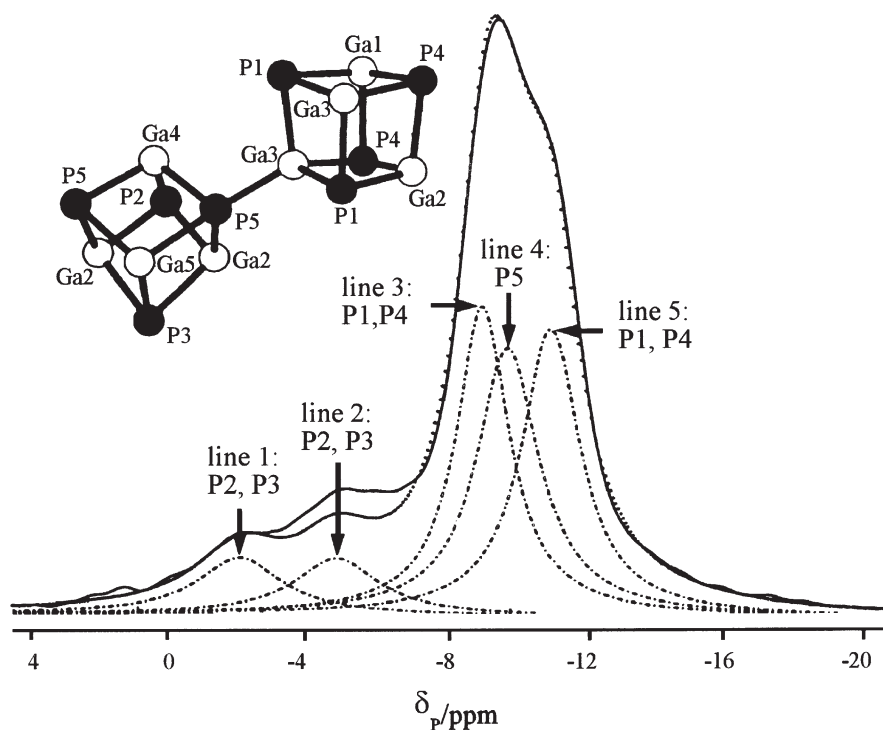


Fig. 17. ^{31}P MAS NMR spectrum of the gallophosphate cloverite (*solid line*) and its components (*dashed-dotted*) derived by decomposition [149]. At the top, a structural element of cloverite is shown

3.4

^{69}Ga and ^{71}Ga NMR Spectroscopy of Gallium-Modified Zeolites and the Gallophosphate Cloverite

The isotopes ^{69}Ga and ^{71}Ga with natural abundances of 60.4% and 39.6%, respectively, are both suitable candidates for solid-state NMR spectroscopy. Since the quadrupole moments of these isotopes have the same order as that of the aluminum nucleus, similar NMR line shapes can be expected for gallium and aluminum atoms incorporated at analogous framework sites. Moreover, Bradley et al. [152] found a linear relationship between the ^{71}Ga and ^{27}Al chemical shifts of a series of structurally analogous aluminum and gallium compounds with exclusively oxygen in the first coordination sphere:

$$\delta_{\text{Ga}}/\text{ppm} = 2.83 \cdot \delta_{\text{Al}}/\text{ppm} - 4.50 \quad (35)$$

The incorporation of gallium into the framework of zeolite ZSM-5 was studied by Bayense et al. [153] and Bedard et al. [154]. The samples used for these investigations were prepared by adding the gallium in the stage of gel formation. The

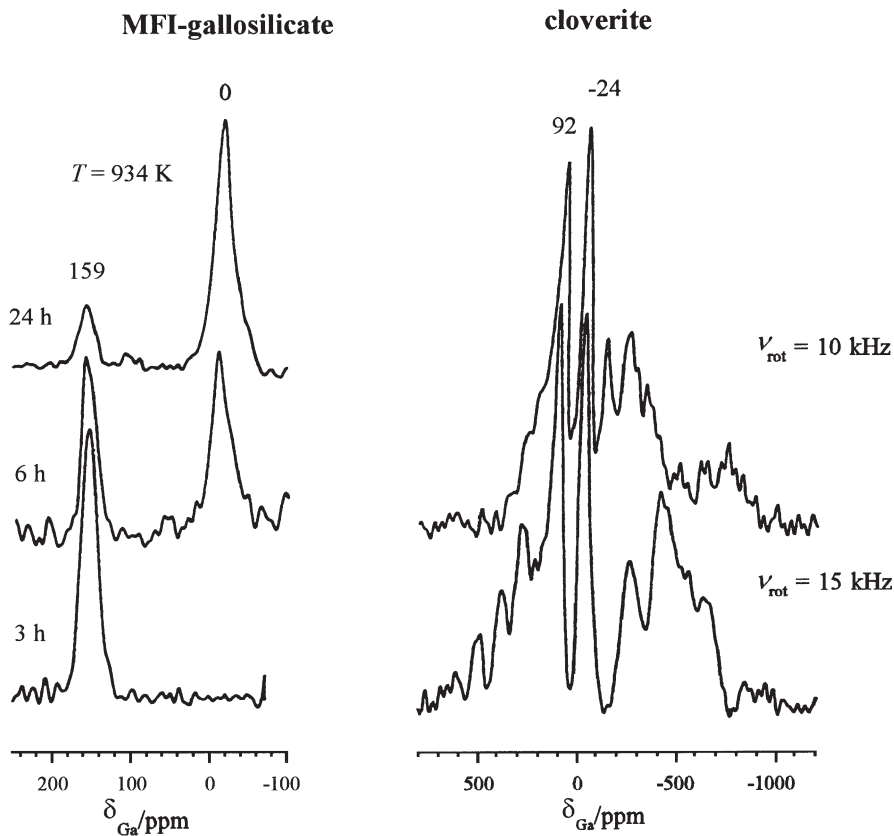


Fig. 18. ^{71}Ga MAS NMR spectra of an MFI-gallosilicate (left) after steaming for 3 h, 6 h, and 24 h at 934 K [153] and of as-synthesized cloverite (right) recorded with sample spinning rates of 10 kHz (top) and 15 kHz (bottom) [156]

^{71}Ga MAS NMR spectra shown on the left-hand side of Fig. 18 were recorded at a resonance frequency of 183.0 MHz and with a sample-spinning rate of ca. 8 kHz. In agreement with Eq. (35) the signal of tetrahedrally coordinated framework gallium appears at the resonance position of about 159 ppm [referenced to aqueous $\text{Ga}(\text{NO}_3)_3$ solution]. Extensive dehydration leads to a strong broadening and disappearance of this signal in the MAS NMR spectrum that agrees with the behavior of framework aluminum signals in ^{27}Al MAS NMR spectroscopy. Steaming of the gallium analogue zeolite ZSM-5 at 934 K for 3, 6, and 24 h results in the appearance of the signal of octahedral non-framework gallium species at about 0 ppm (Fig. 18). As demonstrated by the spectra depicted in Fig. 18, the intensity ratio of the lines at 159 ppm and 0 ppm strongly depends on the steaming time.

Kentgens et al. [155] utilized the different quadrupole moments of the two isotopes ^{69}Ga and ^{71}Ga to determine the quadrupole parameters of framework gallium atoms by their different second-order quadrupolar shifts [Eq. (14)]. In this way, quadrupole coupling constants of about 3.0 MHz for ^{69}Ga and 1.9 MHz

for ^{71}Ga located on tetrahedral framework positions in hydrated gallium-modified HZSM-5 have been calculated.

A number of groups have applied ^{71}Ga MAS NMR spectroscopy to investigate the gallophosphate cloverite [68, 147–149, 154, 156]. The right-hand side of Fig. 18 shows the ^{71}Ga MAS NMR spectra of an 'as-synthesized' cloverite sample [156]. Two types of resonances can be observed at chemical shifts of ca. 92 ppm and -24 ppm due to penta-coordinated and octahedrally coordinated gallium atoms, respectively. In both cases there is one fluoride ion in the first gallium coordination sphere. In addition, the octahedral gallium atoms are coordinated with one additional water molecule. Considering the chemical shift of 30 ppm for penta-coordinated aluminum atoms observed in the ^{27}Al MAS NMR spectra of aluminosilicate-type zeolites (vide supra), Eq. (35) yields a resonance position of penta-coordinated gallium atoms of ca. 80 ppm. This estimation is in good agreement with the experimentally derived ^{71}Ga MAS NMR shift of penta-coordinated gallium atoms in the cloverite framework (92 ppm). According to Zibrowius et al. [148], the misleading line shape of the ^{71}Ga MAS NMR spectra, which occurs also in the spectra recorded with sample-spinning rates of 10 kHz and 15 kHz (right-hand side of Fig. 18), may be explained by the extraordinarily strong quadrupolar coupling of framework gallium atoms. Using static ^{71}Ga NMR spectroscopy the quadrupole coupling constant of gallium atoms in cloverite was estimated to about 13 MHz [148].

3.5

^{11}B NMR Spectroscopy of Boron-Containing Zeolites

In boron-containing zeolites, boron may occur in tetrahedral BO_4 or trigonal BO_3 units. In magnetic fields of $B_0 \geq 7$ T and with application of the MAS technique, the tetrahedral BO_4 units yield a narrow ^{11}B MAS NMR signal with a symmetric line shape. As observed for framework aluminum atoms in hydrated aluminosilicate-type zeolites, the surroundings of tetrahedrally coordinated boron atoms in hydrated boron-containing zeolites is also characterized by an electric field gradient. Due to its strong quadrupolar interaction, the trigonal boron (BO_3) causes a broad quadrupolar pattern [157–160].

Scholle and Veeman [158] were the first to show for boron-substituted ZSM-5 the superposition of the narrow BO_4 signal and the broad BO_3 pattern. Usually, the narrow BO_4 line has a chemical shift of about -3 ppm (referenced to $\text{BF}_3 \cdot \text{OEt}_2$) and a line width of about 1 ppm in fully hydrated samples. At the resonance frequency of 96.2 MHz the singularities of the BO_3 pattern have a peak-peak distance of about 20 ppm [159]. In the spectra of dehydrated boron-containing zeolites, the broad BO_3 pattern predominates and is superimposed by the narrow signal of residual BO_4 units. Rehydration causes a partial reconstruction of the original spectrum consisting of a narrow BO_4 line [158–160]. Axon and Klinowski [161] utilized two-dimensional nutation MAS NMR spectroscopy to investigate boron atoms in zeolite ZSM-5. In this 2D experiment a high-power radio frequency pulse of length t_1 is applied to the resonating spins. In the 2D spectrum, the frequency ν_1 of the signal in the F1-dimension depends on the quadrupole frequency, ν_Q , of the resonating nuclei. Three different cases can be distinguished:

(1) ν_Q is small in comparison to the applied radio frequency, ν_{rf} i.e., $\nu_Q \ll \nu_{rf}$ and the signal appears at $\nu_1 = 1\nu_{rf}$; (2) $\nu_Q \gg \nu_{rf}$ leads to a nutation frequency of $\nu_1 = (I+1/2) \cdot \nu_{rf}$ i.e., ^{11}B nuclei with $I=3/2$ cause a signal at $\nu_1 = 2\nu_{rf}$; and (3) $\nu_Q \approx \nu_{rf}$ leads to signals in the range from $\nu_1 = 1\nu_{rf}$ to $\nu_1 = 2\nu_{rf}$. Applying this 2D experiment, Axon and Klinowski [161] found two signals of boron atoms in boron-modified zeolite ZSM-5 at $\nu_1 = 1\nu_{rf}$ due to tetrahedral boron ($\nu_Q \ll \nu_{rf}$) and at $\nu_1 = 2\nu_{rf}$ caused by trigonal boron ($\nu_Q \gg \nu_{rf}$). Hence, in agreement with the quadrupolar line broadening observed in the one-dimensional ^{11}B MAS NMR spectra, tetrahedral and trigonal boron atoms in boron-modified zeolite ZSM-5 are characterized by a negligibly weak and a strong quadrupole interaction, respectively.

3.6

^{17}O NMR Studies of Zeolites and Zeolite-Like Materials

Oxygen is the main constituent of the zeolite framework. However, ^{17}O NMR studies on zeolites have always been performed on isotopically enriched samples because of the low natural abundance of the isotope ^{17}O . Timken et al. [162, 163] carried out static ^{17}O NMR spectroscopic studies on zeolites NaA and NaY, on dealuminated Y-type zeolites and on gallosilicates and aluminophosphates. The spectra of aluminosilicate-type zeolites consist of broad quadrupolar patterns corresponding to quadrupole coupling constants, C_Q , of about 4.6–5.2 MHz and 3.1–3.2 MHz due to oxygen atoms in Si-O-Si bridges and Si-O-Al bridges, respectively. The asymmetry parameters, η_Q , are 0.1 for Si-O-Si and 0.2 for Si-O-Al arrangements. These values were verified by MAS and variable-angle spinning experiments in different magnetic fields. The isotropic chemical shifts, δ , amount to 44–57 ppm (referenced to H_2O) for Si-O-Si and 31–45 ppm for Si-O-Al [162]. ^{17}O NMR investigations on aluminophosphates and gallosilicates yielded the following quadrupole parameters: $C_Q = 5.6$ – 6.5 ppm, $\eta_Q \approx 0$ and $\delta = 61$ – 67 ppm for oxygen atoms in Al-O-P bridges and $C_Q = 4.0$ – 4.8 ppm, $\eta_Q \approx 0.3$ and $\delta = 28$ – 29 ppm for oxygen atoms in Si-O-Ga bridges [164].

Hence, ^{17}O NMR investigations on zeolites of different chemical compositions have demonstrated that the spectra of these materials consist of quadrupolar patterns characteristic of oxygen atoms in distinct T-O-T bridges (T=Si, Al, P, Ga). The presence of oxygens in more than one type of T-O-T bridges, e.g., in Si-O-Al and Si-O-Si bridges in zeolite Y, causes a superposition of quadrupolar patterns with intensities according to their relative numbers in the zeolite framework. The observed order of quadrupole coupling constants, C_Q , of oxygen atoms in different T-O-T bridges is: Al-O-P > Si-O-Si > Si-O-Ga > Si-O-Al, and that of isotropic chemical shifts, δ : Al-O-P > Si-O-Si > Si-O-Al > Si-O-Ga.

4

NMR Investigations on Extra-Framework Cations

Negative framework charges of zeolites, due to tetrahedrally coordinated aluminum atoms, are either compensated by hydroxyl protons of bridging OH groups or by exchangeable univalent or multivalent extra-framework cations. In

dehydrated zeolites, these cations are located on well-defined positions close to oxygen rings of the zeolite framework. Therefore, extra-framework cations influence, inter alia, the effective diameters of the zeolite pores. Moreover, cations act as adsorption sites and may activate and dissociate guest molecules due to their strong electrostatic fields.

With the implementation of sophisticated techniques (see Sect. 2.2.3), solid-state NMR spectroscopy has become a powerful method for elucidating the cation distribution in zeolites. Since all of the relevant cations exhibit a nuclear spin of $I > 1/2$, the quadrupole interaction between the electric quadrupole moment, eQ , and the z-component of the electric field gradient (EFG), eq , at the cation site is the dominant solid-state interaction. In hydrated zeolites, extra-framework cations are coordinated with the oxygens of water molecules forming the cationic hydration shells. Therefore, hydrated cations are characterized by a symmetric oxygen coordination and small quadrupole coupling constants, C_Q . Moreover, at ambient temperature, there is a rapid exchange of hydrated cations between different cation positions on the time scale of NMR spectroscopy. In contrast, cations in dehydrated zeolites are strongly coordinated to framework oxygens. Due to the EFG, these cations cause complex and often overlapping NMR line shapes. The corresponding spectra are difficult to analyze with respect to the quadrupole coupling constant, C_Q , the asymmetry parameter, η_Q , of the EFG, the isotropic chemical shift, δ , and the relative intensity, I_n . However, the progress achieved recently in the development of new experimental NMR techniques [34–36, 171, 172] and in the interpretation and quantitative evaluation of NMR spectra of quadrupolar nuclei has opened new routes for the application of solid-state NMR spectroscopy for detailed studies of cation migration and distribution in zeolites.

4.1

Investigations of Cations in Hydrated Zeolites

The study of lithium cations in zeolite structures is of great interest in view of their adsorption behavior and the formation of molecule-cation complexes. There are two lithium isotopes that are suitable for solid-state NMR spectroscopy, ^6Li and ^7Li . Both are quadrupole nuclei with nuclear spins of $I=1$ and $I=3/2$ and natural abundances of 7.4% and 92.6%, respectively. The first broad-line ^7Li NMR studies of lithium cations in dehydrated zeolite LiNaX were carried out by Lechert et al. [173]. Simulation of the spectra yielded a statistical distribution of lithium cations over all sites III near four-membered oxygen rings (see Fig. 19) in the apertures of the supercages. Schimiczek et al. [174] applied ^6Li NMR spectroscopy to investigate lithium-exchanged zeolite A. By a line shape analysis, the authors concluded that the lithium cations are located on the threefold symmetry axis normal to a six-membered oxygen ring. NMR spectroscopy of ^{205}Tl (natural abundance 70.5%) in hydrated zeolite A has been carried out by West [175]. Applying ^{139}La NMR spectroscopy to hydrated zeolites LaNaY, two broad and shapeless signals of lanthanum cations were found [82, 176, 177] corresponding to quadrupole coupling constants of ca. 30 MHz and 8 MHz. These signals are characteristic of hydrated lanthanum cations located in sodalite cages (30 MHz) and supercages (8 MHz). The change in the ^{139}La NMR intensities has been ana-

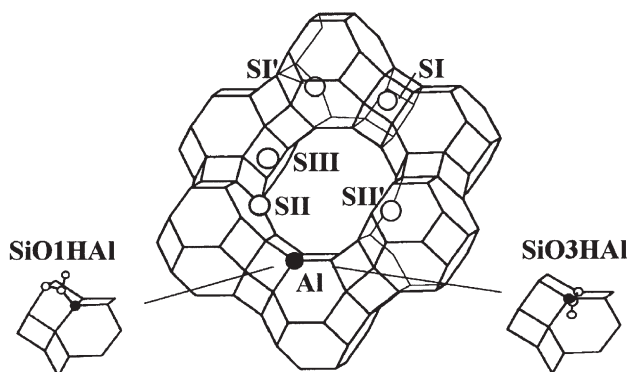


Fig. 19. Structure of faujasites with the cation positions SII and SIII in the supercages, SI' and SII' in the sodalite cages, SI in the hexagonal prisms, and bridging OH groups pointing into the supercage (SiO1HAL) and into the sodalite cages (SiO3HAL)

lyzed to gain insight into the migration of lanthanum cations in zeolite Y due to thermal treatment.

4.2

Cesium Cations in Hydrated and Dehydrated Zeolites

Cesium is an important promoter in heterogeneous catalysis used for the production of higher alcohols and base catalysis [178, 179]. The isotope ^{133}Cs has a natural abundance of 100%, a nuclear spin of $I=7/2$, and a weak quadrupole moment. Starting with the work of Chu et al. [180], static ^{133}Cs NMR and ^{133}Cs MAS NMR spectroscopy were applied to investigate the local structures of cesium cations in hydrated and dehydrated mordenite. The occupied cation positions in mordenite are labeled SII, SIV, and SVI, and have relative cesium occupancies of 3.78:1.86:1.75 [181]. Cesium cations on SII and SIV are located close to the center of eight-membered oxygen rings, while cesium cations on SVI are placed close to six-membered oxygen rings. The quadrupole coupling constant was determined by the peak-peak distance of the singularities of the $\{\pm 3/2 \leftrightarrow \pm 1/2\}$ satellite transitions and, additionally, by the simulation of MAS NMR line shapes [182]. In the ^{133}Cs MAS NMR spectrum of hydrated cesium-exchanged mordenite, a single line at the chemical shift of -64 ppm (referenced to saturated CsCl solution) with a quadrupole coupling constant of 210 kHz and an asymmetry parameter of zero was found. After dehydration, the ^{133}Cs MAS NMR spectrum consists of three components at isotropic chemical shifts of -157 ppm, -186 ppm, and -24 ppm, due to cesium cations located on positions SII, SIV and SVI, respectively. The quadrupole parameters were determined to be $C_Q=3.1$ MHz and $\eta_Q=0.6$ for cesium cations at SII and SIV and to $C_Q=3.2$ MHz and $\eta_Q=0.7$ for cesium cations at SVI. The NMR intensity ratio of cesium cations on positions SII, SIV, and SVI has been determined to be 2:1:1 which is in reasonable agreement with the values obtained by X-ray diffraction [181].

The example of cesium-exchanged mordenite has demonstrated that hydration of cations is connected with a strong variation in the solid-state ^{133}Cs NMR parameters and line shapes. By cooling the samples, the site-exchange of cations in hydrated zeolites can be significantly slowed. This results in line broadening, but the cations retain water molecules in their coordination shell. The resulting low-temperature spectra can be narrowed by use of variable-temperature (VT) MAS NMR spectroscopy. Ahn et al. [183, 184] and Tokuhiro et al. [185] have utilized this technique to study hydrated zeolites CsNaA and CsLiA ($3.8 \text{ Cs}^+/\text{u.c.}$). The ^{133}Cs MAS NMR spectra recorded at 294 K consist of only one signal at around -200 ppm (top of Fig. 20) caused by a rapid cesium exchange between six-ring and eight-ring sites in the large α -cages, whereas a temperature decrease down

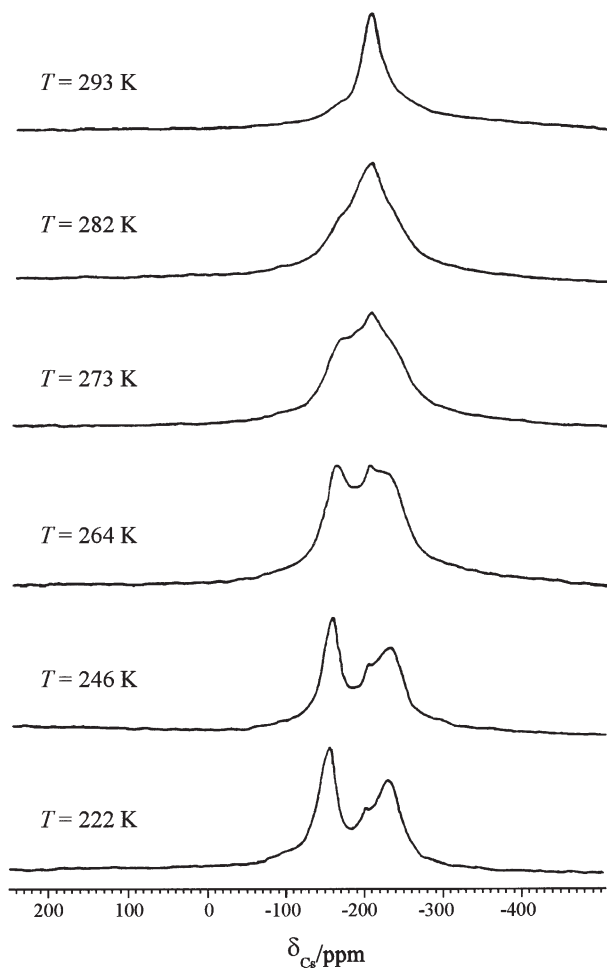


Fig. 20. ^{133}Cs MAS NMR spectra of a hydrated zeolite CsLiA ($3.8 \text{ Cs}^+/\text{u.c.}$). The spectra were recorded at temperatures between 222–293 K, at a resonance frequency of 39.8 MHz, and with a sample spinning rate of 2.5 kHz [185]

to 222 K yielded spectra consisting of three lines (bottom of Fig. 20). Two lines were readily assigned to cesium cations occupying sites in eight-membered (-226.8 m) of the α -cages. The third component at the chemical shift of -200.3 ppm was attributed to hydrated cesium cations located on sites in the large cages near four-membered oxygen rings interacting to a moderate degree with the framework. The analysis of the experimental line shapes using Bloch's equation [7, 184] yielded a lifetime of hydrated cesium cations at the sites in the eight-ring windows of $\tau=0.12$ ms. The activation energy for the site-exchange process of hydrated cesium cations was determined to be 44 kJ/mol. Subramanian and Seff [186] studied the location of cesium cations in zeolite CsNaA as a function of the exchange degree. They claimed that cesium cations in dehydrated zeolite CsNaA start to occupy positions close to the centers of six-ring windows inside the sodalite cages before they occupy positions in the α -cages. The chemical shifts of cesium cations located on equivalent positions inside and outside the sodalite cages are expected to be similar. However, considering the diameter of the six-ring windows, the site exchange of hydrated cesium cations between sites inside and outside the sodalite cages is too slow to cause one averaged signal at 293 K (top of Fig. 20). Therefore, Ahn et al. [184] proposed that cesium cations enter the sodalite cages first upon dehydration.

Koller et al. [187] investigated a homologous series of cesium-exchanged zeolites Y by solid-state NMR spectroscopy and X-ray powder diffraction. Rietveld refinement of the structure of 72% cesium-exchanged zeolite Y, dehydrated in vacuum at 623 K, revealed cesium cations at positions SII in the center of hexagonal prisms, at SI' close to the center of six-membered oxygen rings in sodalite cages, at SIII close to the center of six-ring windows in the supercages, and at SII close to four-membered oxygen rings in the supercages (see Fig. 19). Figure 21

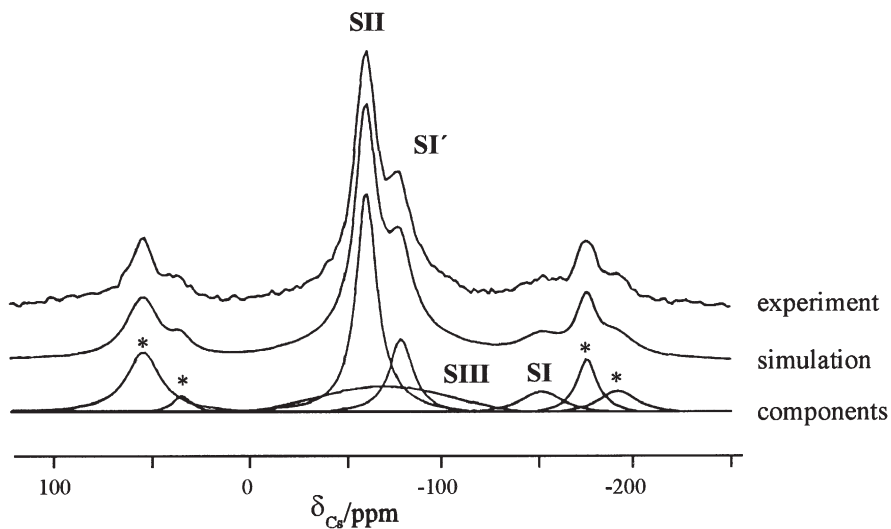


Fig. 21. ^{133}Cs MAS NMR spectrum of a dehydrated 72% cesium-exchanged zeolite Y (a), the simulated spectrum (b), the components (c), and spinning sidebands (*) [187]

shows the ^{133}Cs MAS NMR spectrum of this sample recorded at a resonance frequency of 52.4 MHz and with a sample-spinning rate of ca. 6 kHz. The spectrum is composed of four overlapping signals consisting of two narrow MAS central lines at -62 ppm and -79 ppm, a broad line at -71 ppm and a weak line at about -153 ppm. ^{133}Cs MAS NMR investigations carried out at resonance frequencies of 52.4 MHz and 26.2 MHz indicated a negligible quadrupole interaction of these cesium cations [187]. Therefore, the strong spinning sidebands of the signals at -62 ppm and -79 ppm are exclusively caused by chemical shift anisotropy. This makes the NMR properties of cesium cations in zeolite Y more reminiscent of a nuclei with spins $I=1/2$ than of quadrupolar nuclei. However, the large chemical shift range makes the line positions in the NMR spectra very sensitive to the coordination environment of cesium cations in zeolite cavities. The line at -62 ppm has the highest intensity and was, therefore, attributed to cesium cations located on position SII with the largest population. The signal at -79 ppm with a much smaller intensity, but a linewidth and MAS sideband pattern comparable to the first one, was assigned to cesium cations located on position SI'. Since both positions SII and SI' have equivalent site symmetries, cations located at these sites are characterized by similar NMR parameters. Because of the larger shielding of cesium cations by the higher number of oxygen atoms in the hexagonal prism, the high-field shifted line -153 ppm was attributed to cesium cations located on position SI and the remaining broad signal at about -71 ppm to cesium cations at SIII. From the NMR intensities of these signals, including the spinning sidebands, cation populations of 23.6 Cs⁺/u.c. on SII, 8.3 Cs⁺/u.c. on SI', 5.5 Cs⁺/u.c. on SIII, and 2.4 Cs⁺/u.c. on SI were determined which is in reasonable agreement with the values derived by XRD of 26.4 Cs⁺/u.c. on SII, 4.5 Cs⁺/u.c. on SI', 5.5 Cs⁺/u.c. on SIII, and 0.9 to 1.2 Cs⁺/u.c. on SI. Considering the free diameter of six-ring windows of 0.22–0.27 nm compared with the ionic diameter of cesium cations of 0.33–0.38 nm, migration of these cations into the sodalite cages and the hexagonal prisms seems to be improbable. However, as proven by solid-state NMR and XRD [187], cesium cations do migrate during thermal treatment (623 K) into the sodalite cages perhaps due to the flexibility of the zeolite framework.

4.3

Sodium Cations in Hydrated Faujasites

The natural abundance of 100% of ^{23}Na ($I=3/2$) combined with a moderate quadrupole moment makes this isotope a nucleus suitable for NMR spectroscopy. In a number of approaches [82, 177, 188–190], ammonium-, calcium- and lanthanum-exchanged zeolites Y have been investigated in their hydrated state before and after the first thermal treatment. The ^{23}Na MAS NMR spectra of hydrated lanthanum-exchanged zeolites Y consist of two lines at -9 ppm and -13 ppm, relative to solid NaCl (Fig. 22) [82]. While the first line is due to hydrated sodium cations located in supercages, the second signal is caused by hydrated sodium cations located in sodalite cages. Measurements carried out in different magnetic fields have shown that the signal at -13 ppm is a superposition of two components due to sodium cations in position SI in the hexagonal

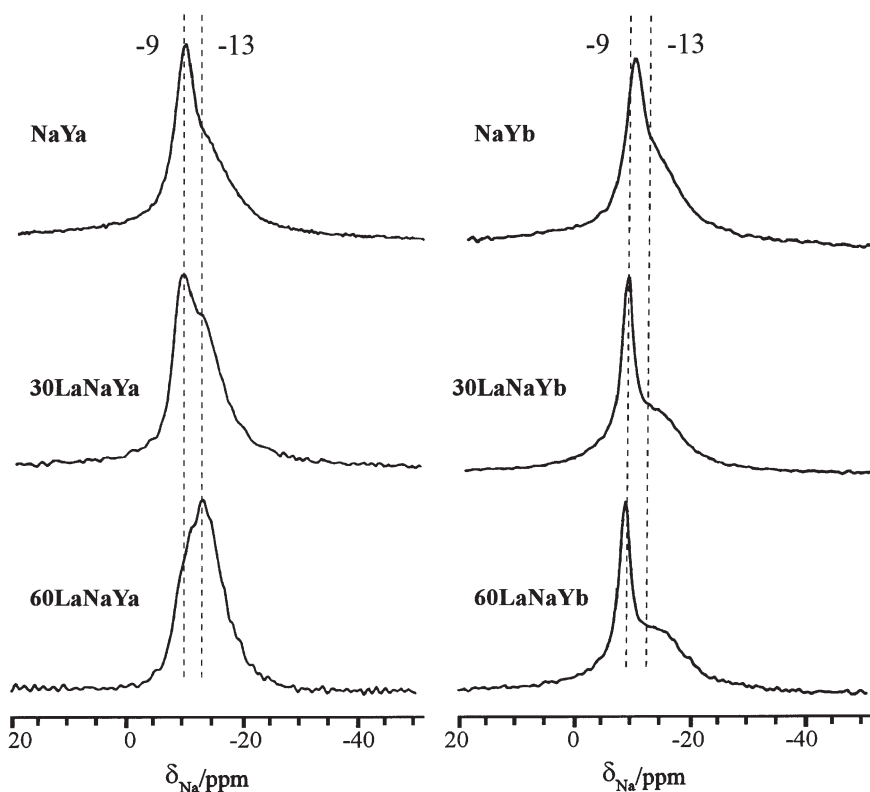


Fig. 22. ^{23}Na MAS NMR spectra of hydrated zeolites Y in the sodium form (NaY) and after exchange of 30% and 60% of the sodium cations by lanthanum (30LaNaY and 60LaNaY, respectively), recorded before (*left-hand side*, suffix a) and after (*right-hand side*, suffix b) thermal treatment at 433 K and rehydration [82]

prisms and hydrated sodium cations in sodalite cages [82]. In Fig. 22 the ^{23}Na MAS NMR spectra of a homologous series of hydrated lanthanum-exchanged zeolites Y are depicted, on the left-hand side before (suffix a) and on the right-hand side after (suffix b) the first thermal treatment at 433 K and rehydration. The notations 30LaNaY and 60LaNaY apply to zeolites after an exchange of 30% and 60%, respectively, of sodium cations by lanthanum cations.

The strong decrease in regard to the ^{23}Na MAS NMR intensity of the -9 ppm signal of zeolites 30LaNaYa and 60LaNaYa in relation to the parent zeolite NaY (*left-hand side* of Fig. 22) is indicative of an initial exchange of hydrated sodium cations in the large cavities. Hydrated lanthanum cations with a diameter of ca. 0.8 nm are too bulky to diffuse into the sodalite cages through the six-ring windows and, therefore, cannot exchange sodium cations located in these cavities. The thermal treatment at 433 K and rehydration of zeolites LaNaY (*right-hand side* of Fig. 22) results in a significant decrease in the ^{23}Na MAS NMR signal at -13 ppm while the signal at -9 ppm increases. This fact proves that the calcina-

tion-induced migration of lanthanum cations to positions in the sodalite cages (*vide supra*) is accompanied by a counter-migration of sodium cations from the sodalite cages into the supercages. A quantitative evaluation of the ^{23}Na MAS NMR spectroscopic data of hydrated lanthanum-exchanged zeolites Y is given in [82]. The effects observed in the ^{23}Na MAS NMR spectra of the ammonium- and calcium-exchanged series [188, 189] are similar to those mentioned above [82, 188].

The mobility of sodium cations in hydrated zeolites Y was studied by Challoner and Harris [191] and Lin and Chao [192]. Challoner and Harris [191] explained a broad hump in the statically recorded ^{23}Na NMR spectra of hydrated zeolite NaY by $\{\pm 1/2 \leftrightarrow \pm 3/2\}$ satellite transitions of sodium cations in a slow tumbling regime. However, a corresponding signal was not found in the spectra of cation-exchanged zeolites Y recorded with the MAS technique [82, 188–190]. Lin and Chao [192] applied 2D nutation NMR experiments to investigate the quadrupole parameters of hydrated sodium cations at low temperatures. In a more recent work [82], these experiments were combined with the application of the MAS technique that allowed the separation of different signals in the F2-dimension. As shown in Fig. 23, the 2D ^{23}Na nutation MAS NMR spectrum of the hydrated zeolite NaY recorded at 293 K (top) consists of one strong signal at $\nu_1 = \nu_{rf}$ in the F1-dimension and at -9 ppm in the F2-dimension (see Sect. 3.5). This signal corresponds to hydrated sodium cations in the large cavities which are mobile and, therefore, have a negligible quadrupole frequency ($\nu_q \ll \nu_{rf}$). The major signal in the nutation spectrum recorded at 150 K appears at $\nu_1 = 2\nu_{rf}$ in the F1-dimension and at -13 with a significant increase in the quadrupolar interaction ($\nu_q \gg \nu_{rf}$) and, therefore, with a high-field shift of the corresponding signal in the F2-dimension.

4.4

Sodium Cations in Dehydrated Faujasites

Cations in dehydrated zeolites are located on defined cation positions of the zeolite framework and are strongly coordinated with framework oxygens. Therefore, at ambient temperature, the site-exchange can be neglected on the time scale of NMR spectroscopy. In this case, the NMR line shapes of sodium cations are determined only by the strength of quadrupole interactions. The observed quadrupole coupling constant, C_Q , depends on the electric field gradients that, in a first approximation, are caused by a superposition of the electrostatic fields of the negatively charged framework oxygen atoms. Simply, C_Q is large for sodium cations that are non-spherically coordinated to oxygen atoms, e.g., for sodium cations close to the center of a six-membered oxygen ring as on position SII in zeolite Y, and is small for sodium cations in a spherical oxygen environment, e.g., octahedrally coordinated sodium cations on position SI in zeolite Y (see Fig. 19). Tijink et al. [193] investigated dehydrated zeolite NaA by static ^{23}Na NMR and determined the quadrupole parameters of $C_Q = 3.2$ MHz and $\eta_Q = 0.9$ for sodium cations located on four- and eight-membered oxygen rings and of $C_Q = 5.8$ MHz and $\eta_Q = 0$ for sodium cations located close to the centers of six-membered oxygen rings. In this case the assignment was found by the asymmetry parameter,

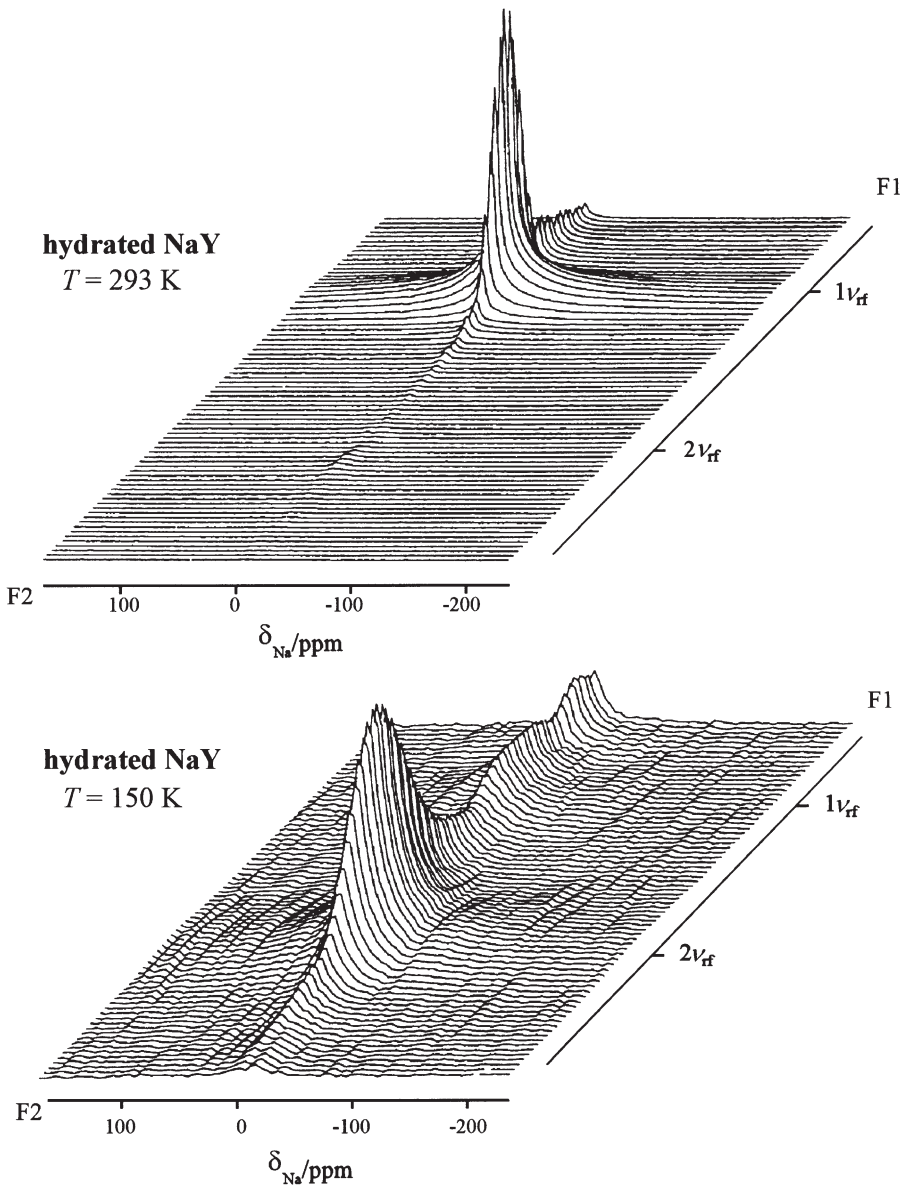


Fig. 23. Two-dimensional ^{23}Na nutation MAS NMR spectra of hydrated zeolite NaY recorded at 293 K (*top*) and 150 K (*bottom*), at the resonance frequency of 105.8 MHz and with a radio frequency field of $\nu_{\text{rf}}=125\text{ kHz}$ [82]

Table 3. Quadrupole coupling constants, C_Q , asymmetry parameters, η_Q , and isotropic chemical shifts, δ , (referenced to solid NaCl) of sodium cations in dehydrated zeolites NaY and NaX calculated by a point charge model (see text) and experimentally derived by solid-state ^{23}Na MAS NMR spectroscopy [194, 201, 203]

Zeolite/site	Calculation: C_Q/MHz	Experiment: C_Q/MHz	Experiment: η_Q	Experiment: δ/ppm
NaY				
SI	0.1–0.5	ca. 0.1	0	–12
SI'	4.6–5.6	4.8	0.2	–4
SII	3.4–4.2	4.2	0.2	–12
NaX				
SI	0.2	ca. 0.1	0	–6
SI'	3.6–5.2	5.2	0	–19
SII	4.4	4.6	0	–16
SIII	2.2–2.5	ca. 2.4	0.8	–14 to –30

η_Q , which should be small for sodium cations in the symmetric environment of six-membered oxygen rings.

However, more sophisticated approaches are often necessary to assign ^{23}Na NMR signals of sodium cations in dehydrated zeolites. One way of overcoming this problem is the theoretical estimation of quadrupole parameters using a point-charge model [194, 195]. Table 3 gives a summary of quadrupole parameters of sodium cations located on distinct positions in dehydrated zeolites NaY and NaX, calculated with oxygen charges between $-0.8 e^-$ and $-1.1 e^-$ and using the coordinates of oxygen atoms and sodium cations derived by X-ray diffraction. The characteristic values of the quadrupole coupling constants calculated for sodium cations located at different cation positions are useful for a rough interpretation of experimentally derived ^{23}Na NMR spectra. However, this assignment of the NMR signals should be supported by detailed studies on samples exchanged with various cations and/or by a comparison of the population numbers determined by XRD and solid-state NMR [194, 196]. ^{23}Na MAS NMR spectra of dehydrated zeolites Y in the sodium form (NaY) and after exchange of 52% and 83% of sodium cations by hydroxyl protons (HY) and barium cations (BaY), respectively, are depicted in Fig. 24. The low-field range of the spectra of dehydrated zeolites NaY and HY (left and middle) shows an isotropic line at about -13 ppm, while the high-field range of all spectra consists of a pattern with two singularities at about -32 ppm and -63 ppm [194]. The replacement of 52% of sodium cations by hydroxyl protons causes a strong decrease in relative intensity of the high-field pattern which is characteristic of cations initially located on positions SII and SI'. On the other hand, in the spectrum of the dehydrated zeolite BaY, the low-field line has completely disappeared which shows that this signal originates from sodium cations on position SI (see [197]). By application of two-dimensional ^{23}Na nutation MAS NMR spectroscopy, signals of sodium cations characterized by different quadrupole frequencies can be separated along the F1-dimension. In the 2D spectrum depicted at the top of Fig. 25, the high-field pattern of dehydrated zeolite NaY appears

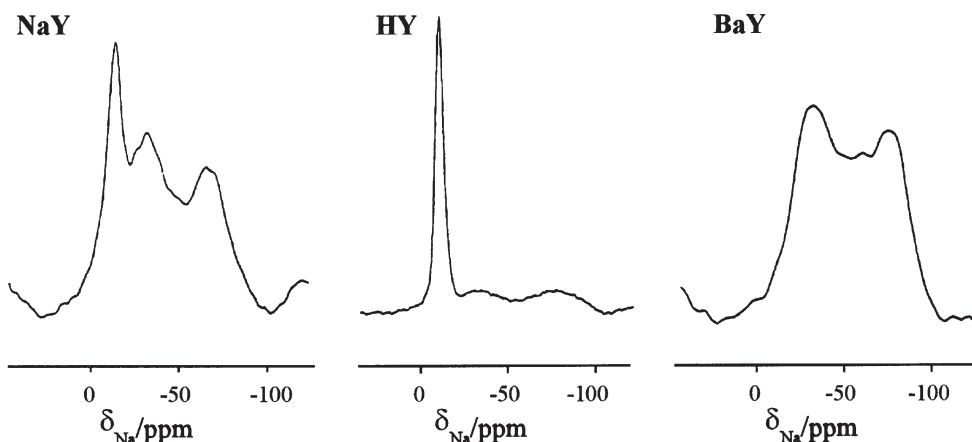


Fig. 24. ^{23}Na MAS NMR spectra of dehydrated (673 K) zeolites Y in the sodium form (NaY) and after exchange of 52% and 83% of the sodium cations by hydroxyl protons (HY) and by barium cations (BaY), respectively, recorded at a resonance frequency of 105.8 MHz [194]

at $\nu_1=2\nu_{rf}$ in the F1-dimension corresponding to a quadrupole frequency of $\nu_q \gg \nu_{rf}$ (see Sect. 3.5). In contrast, the low-field line shows small intensities in the range between $\nu_1=\nu_{rf}$ and $\nu_1=2\nu_{rf}$. Hence, this signal is caused by sodium cations with a quadrupole frequency of $\nu_q \approx \nu_{rf}$ ($\nu_{rf}=125$ kHz) [194]. As expected for dehydrated zeolite NaEMT, which has a negligible sodium population on position SI (low-field line) [198], the spectrum shown at the bottom of Fig. 25 consists of the high-field pattern at $\nu_1=2\nu_{rf}$, caused by sodium cations at SII and SI'.

As mentioned in Sect. 2.1.2, the observed center of gravity of the NMR signals caused by quadrupole nuclei is high-field shifted by the second-order quadrupolar shift, δ_q . This high-field shift is a function of the external magnetic field and the quadrupole parameters C_Q and η_Q . Therefore, the isotropic chemical shift, δ , can be calculated from the line positions δ_1 and δ_2 measured at different Larmor frequencies $\nu_{o,1}$ and $\nu_{o,2}$ [194]:

$$\delta = \frac{\delta_1 K_2 - \delta_2 K_1}{K_2 - K_1} \quad (36)$$

with

$$K_n = \frac{3 \cdot 10^6 [I(I+1) - 3/4]}{40 \cdot \nu_{o,n}^2 \cdot I^2 (2I-1)^2} \quad (37)$$

$I=3/2$ for ^{23}Na , $n=1, 2$, and the Larmor frequencies $\nu_{o,n}$ in MHz.

In addition, the quadrupole coupling constant $C_Q^* = C_Q \sqrt{(1+\eta_Q^2/3)}$ can be estimated by:

$$C_Q^* = \sqrt{\frac{\delta_1 - \delta_2}{K_2 - K_1}} \quad (38)$$

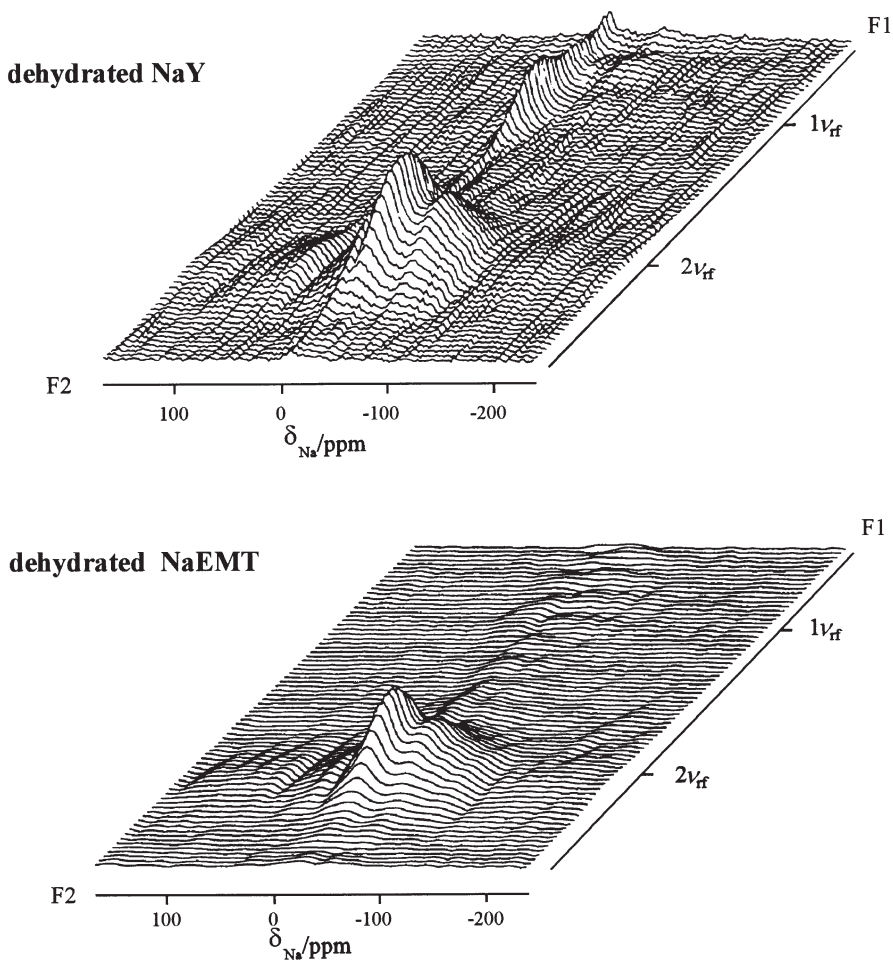


Fig. 25. Two-dimensional ^{23}Na nutation MAS NMR spectra of dehydrated (673 K) zeolites NaY (*top*) and NaEMT (*bottom*). The spectra were recorded at a resonance frequency of 105.8 MHz and with a radio frequency field of $\nu_{rf}=125$ kHz [194]

The values δ_n in Eqs. (36) and (38) correspond to the centers of gravity of the signals 1 and 2. One way of determining these centers of gravity is the application of DOR NMR spectroscopy. In DOR NMR spectra, the second-order quadrupolar broadening is averaged to zero and δ_n corresponds to the observed position of the DOR central line. Figure 26 shows the ^{23}Na DOR NMR spectra of dehydrated (673 K) zeolite NaY recorded at resonance frequencies of $\nu_{o,1}=79.4$ MHz and $\nu_{o,2}=105.8$ MHz, with rotor-synchronized pulse excitation and different rotation frequencies of the outer DOR rotor [194]. At least two DOR central lines can be observed, assigned by arrows, at chemical shifts of -13 ppm and -78 ppm in the spectra recorded at $\nu_{o,1}$ and of -13 ppm and -48 ppm in the spectra recorded

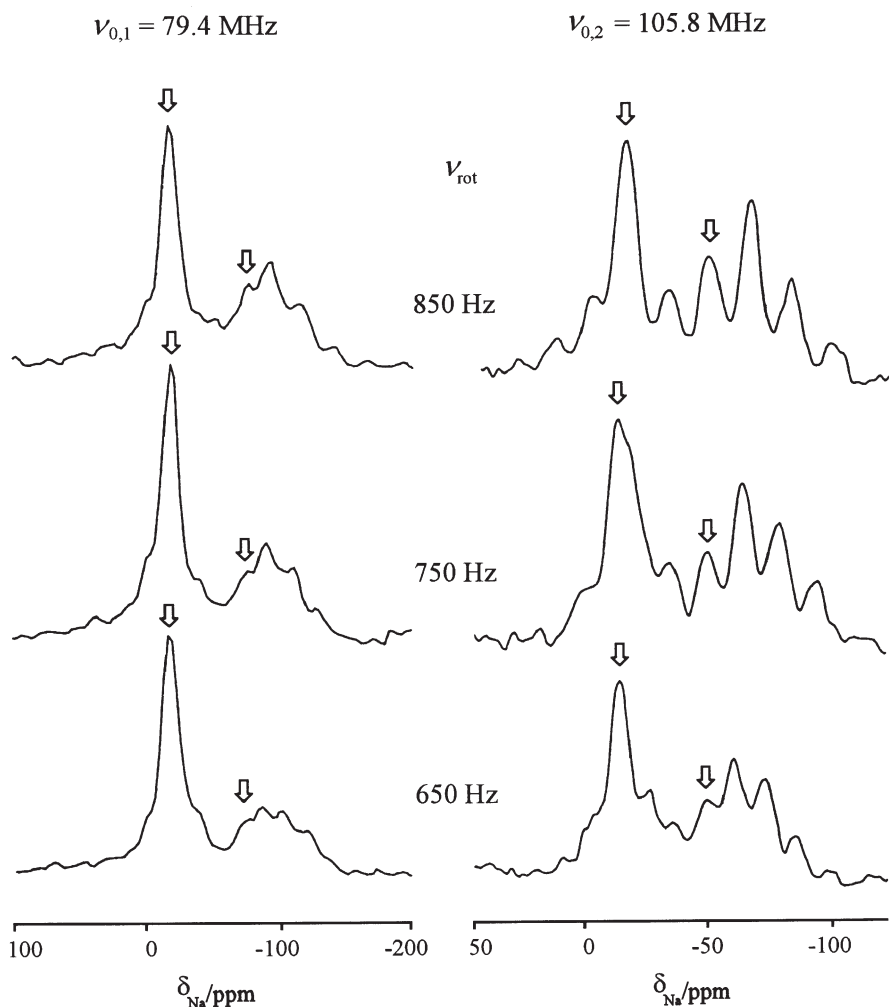


Fig. 26. ^{23}Na DOR NMR spectra of dehydrated (673 K) zeolite NaY recorded at resonance frequencies of 79.4 MHz (*left-hand side*) and 105.8 MHz (*right-hand side*) with rotor-synchronized pulse excitation and rotation frequencies of the outer DOR rotor between 650 Hz and 850 Hz [194]. The arrows assign the DOR central lines

at $\nu_{0,2}$. From these values isotropic chemical shifts of ca. -13 ppm and -9 ppm [Eq. (36)] and quadrupole coupling constants, C_Q^* , of about 0.1 MHz and 4.2 MHz [Eq. (38)] were calculated for the low-field line and the high-field pattern, respectively. These parameters are in reasonable agreement with the theoretically derived values given in Table 3 and with the results of the 2D nutation MAS NMR spectroscopy (*vide supra*).

^{23}Na MAS NMR investigations of dehydrated zeolite NaY carried out at resonance frequencies between 79.3 MHz and 198.4 MHz (Fig. 27), however, indicated

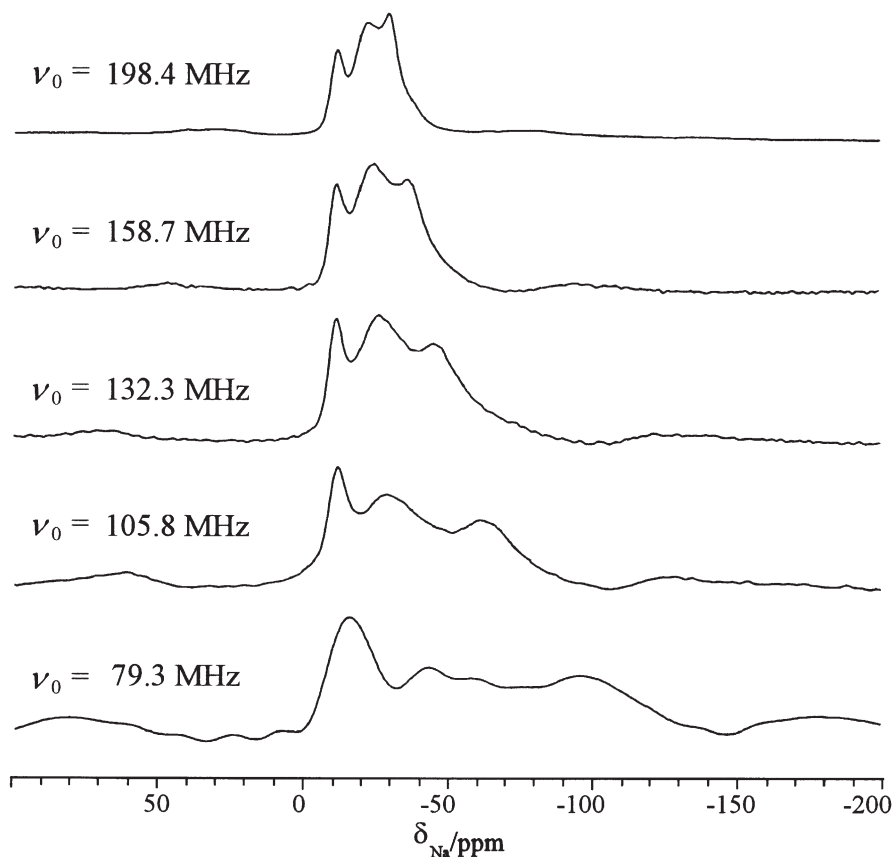


Fig. 27. Experimental ^{23}Na MAS NMR spectra of dehydrated (673 K) zeolite NaY recorded at resonance frequencies in the range between 79.3 MHz (*bottom*) and 198.4 MHz (*top*)

that more than two signals are necessary to produce the line shapes recorded in different external magnetic fields. Using the values derived by the point-charge model (see Table 3), the experimental ^{23}Na MAS NMR spectra were decomposed into a narrow low-field line with a C_Q of ca. 0.1 MHz due to sodium cations located on positions SI and two high-field patterns with C_Q values of 4.2 MHz and 4.8 MHz due to sodium cations at SII and SI', respectively. In general, selective excitation of the $\{+1/2 \leftrightarrow -1/2\}$ central transition is observed for nuclei involved in strong quadrupole interactions, while non-selective excitation of all transitions occurs for signals with vanishing quadrupole frequencies. For sodium nuclei with spin $I=3/2$, the central transition contains only 40% of the total intensity observed for non-selective excitation [12]. In addition, depending on the sample spinning rate, ν_{rot} , the Larmor frequency, ν_o , and the quadrupole parameters C_Q and η_Q , a certain portion of the MAS NMR intensity is distributed among the spinning sidebands. Using a method similar to that proposed by Massiot et al. [199], a correction of the experimentally derived intensities of the central tran-

Table 4. Sodium population in dehydrated (673 K) zeolites NaY ($n_{\text{Si}}/n_{\text{Al}}=2.6$) and NaX ($n_{\text{Si}}/n_{\text{Al}}=1.23$) derived by ^{23}Na MAS NMR spectroscopy (Fig. 29) and XRD (NaY: $n_{\text{Si}}/n_{\text{Al}}=2.37$ [202]; NaX: $n_{\text{Si}}/n_{\text{Al}}=1.18$ [204])

Zeolite/site	^{23}Na MAS NMR: Na ⁺ /u.c.	X-ray diffraction: Na ⁺ /u.c.
NaY		
SI	8	8
SI'	15	13
SII	30	30
NaX		
SI	3	3
SI'	26	29
SII	29	31
SIII	28	30

sitions as a function of C_Q , η_Q , ν_o , and ν_{rot} was carried out. In this way, the sodium populations of cation positions in dehydrated zeolite NaY have been determined by ^{23}Na MAS NMR and these are given in Table 4 in comparison with the values derived by XRD. Verhulst et al. [200] determined sodium populations of cation sites in dehydrated zeolite NaY by decomposition of the ^{23}Na DOR NMR spectra. However, strong overlap of DOR sidebands (cf. Fig. 26) complicates this approach.

Due to the large number of sodium cations in zeolite NaX, this material is a more complex system than zeolite NaY. However, application of the point-charge model and of all suitable solid-state NMR techniques, i.e., two-dimensional nutation MAS NMR, DOR NMR and MAS NMR spectroscopy in different magnetic fields, enables the separation and assignment of the ^{23}Na NMR signals of sodium cations located on at least five cation positions [201]. Figure 28 shows the ^{23}Na MAS NMR spectra of a dehydrated (673 K) zeolite NaX with the framework $n_{\text{Si}}/n_{\text{Al}}$ ratio of 1.2 recorded at Larmor frequencies of 105.8 MHz (bottom) and 158.7 MHz (top). The high-field range of the spectra consists of two patterns corresponding to C_Q values of ca. 4.6 MHz and 5.2 MHz which are caused by sodium cations located on positions SII and SI', respectively. In the low-field range a narrow line appears due to sodium cations located at SI. In contrast to the spectra recorded of dehydrated zeolite NaY, at least two additional signals of sodium cations located on positions SIII were found in the chemical shift range of -20 ppm and -30 ppm. Table 4 gives a summary of the population numbers of sodium cations derived by a decomposition, simulation and intensity correction of these spectra in comparison with values determined by X-ray diffraction [202]. The quadrupole parameters used to analyze the ^{23}Na MAS NMR spectra of dehydrated zeolites NaX and NaY with framework $n_{\text{Si}}/n_{\text{Al}}$ ratios between 1.1 and 4.0 correspond to those given in Table 3. With decreasing $n_{\text{Si}}/n_{\text{Al}}$ ratio, however, an increase in the quadrupole coupling constant, C_Q , up to 5.0 MHz for sodium cations located on position SII and up to 6.0 MHz for sodium cations at position SI' were found [201]. This fact is explained by the stronger electrostatic repulsion

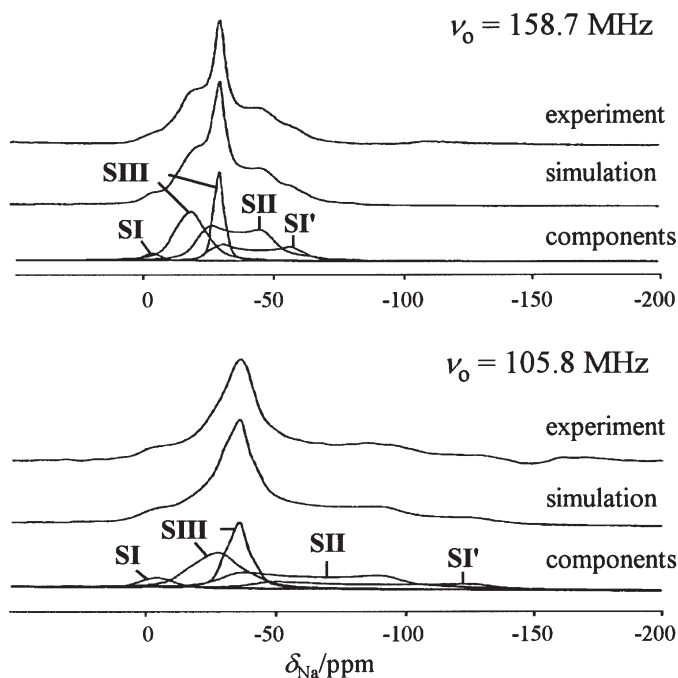


Fig. 28. Experimental and simulated ^{23}Na MAS NMR spectra of dehydrated (673 K) zeolite NaX ($n_{\text{Si}}/n_{\text{Al}}=1.23$) recorded at resonance frequencies of 105.8 MHz (*bottom*) and 158.7 MHz (*top*) [201]. The components are assigned by the labels of sites occupied by sodium cations

of sodium cations in zeolites with increasing cation populations that causes a shortening of the distances between the sodium cations and the framework oxygens. Figure 29 shows the population factors, P_{Na} , determined by ^{23}Na NMR and divided by the crystallographic multiplicity of the different cation positions (16 for SI, 32 for SI' and SII, and 96 for SIII) [201].

5

NMR Spectroscopy of Hydroxyl Protons in Zeolites

Surface hydroxyl groups in zeolites may act as proton donor sites (Brønsted acid sites) which are responsible for the ability of zeolites to catalyze chemical reactions [205–209]. The characterization of surface hydroxyl groups is, therefore, an important prerequisite for catalyst tailoring. The first ^1H MAS NMR investigations of dehydrated zeolites were carried out in a magnetic field with a magnetic flux density of $B_0=1.4$ T using single-pulse excitation yielding signals with residual line widths of about 1 kHz [210]. Application of external magnetic fields with magnetic flux densities of $B_0 \geq 7$ T and application of the CRAMPS [211, 212] or MAS technique with sample-spinning rates of $\nu_{\text{rot}} \geq 10$ kHz [5, 6] results in well-resolved ^1H MAS NMR spectra of dehydrated zeolites. However, such investiga-

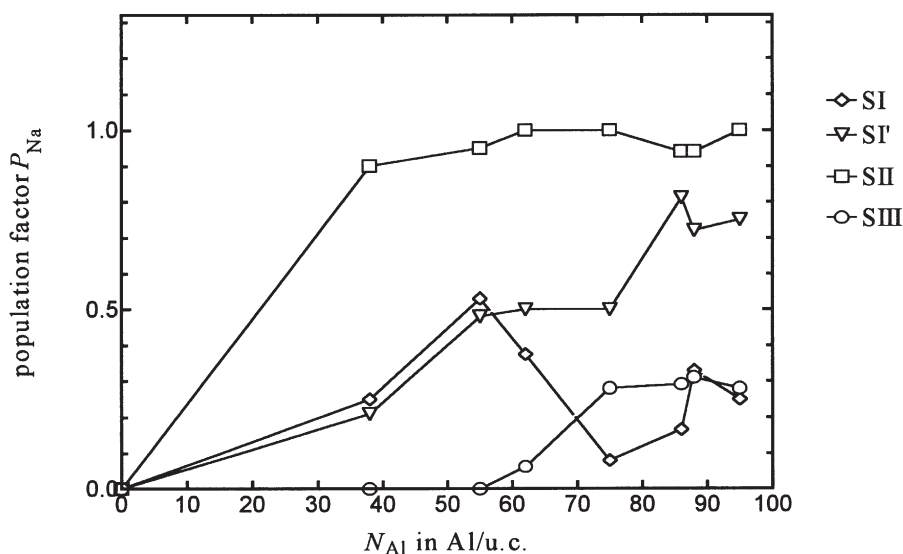


Fig. 29. Population factors, P_{Na} , of sodium cations in dehydrated (673 K) zeolites NaX and NaY as a function of the number of aluminum atoms per unit cell, N_{Al} , derived by solid-state ^{23}Na MAS NMR spectroscopy [201]

tions have to be carried out on carefully dehydrated samples, sealed in symmetrical glass ampoules or filled in gas-tight rotors [210, 211].

5.1

Formation of Hydroxyl Groups in Zeolites and Their Detection by 1H MAS NMR Spectroscopy

A suitable method often applied to form so-called bridging OH groups in zeolites is the exchange of charge-compensating cations such as Na^+ by ammonium ions and subsequent thermal treatment. Calcination of the ammonium-exchanged zeolites at temperatures of $T > 573$ K results in the removal of ammonia and formation of bridging hydroxyl groups (SiOHAl). Applying IR spectroscopy and neutron diffraction, Ward et al. [213, 214], Jirak et al. [215], and Czjzek et al. [216] investigated the occupation of the four crystallographically inequivalent proton sites SiO1Al, SiO2Al, SiO3Al, and SiO4Al in dehydrated zeolites HNaY. For a zeolite HNaY prepared by the exchange of 95% of the sodium cations by NH_4^+ ions and subsequent deammoniation, concentrations of 28.6 OH/u.c. for SiO1HAL groups in the supercages and of 24.5 OH/u.c. for SiO2HAL and SiO3HAL groups located in sodalite cages were found [216]. SiO4HAL groups in the supercages could not be detected. Figure 30 shows the 1H MAS NMR spectra of dehydrated zeolites HNaY ($n_{Si}/n_{Al}=2.56$) with sodium-exchange degrees of 36% (36HNaY), 52% (52HNaY), 71% (71HNaY) and 88% (88HNaY). Decomposition of these spectra was carried out using lines of (a) SiOH groups at 1.8 ppm, (b) SiO1HAL groups at 3.9 ppm, and (c) SiO3HAL and SiO2HAL groups at 4.8 ppm [6]. In Fig. 31

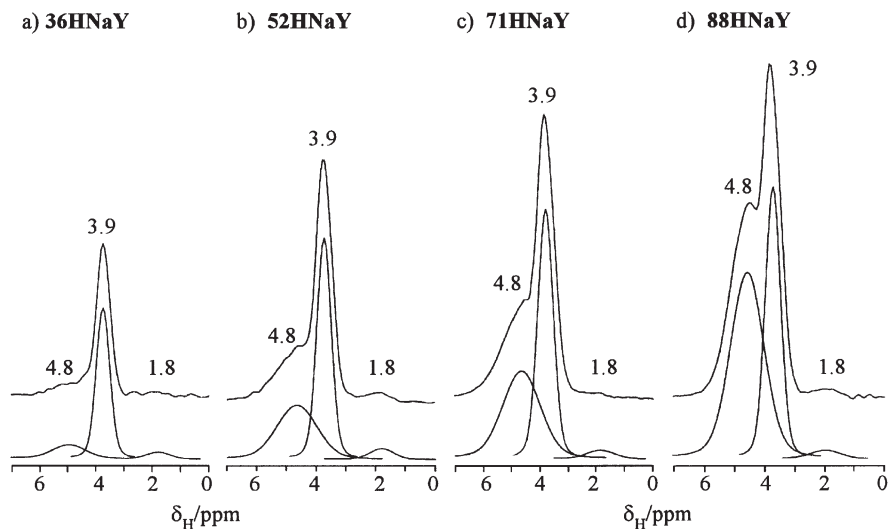


Fig. 30. ^1H MAS NMR spectra of calcined (673 K) zeolites HNaY ($n_{\text{Si}}/n_{\text{Al}}=2.6$) after exchange of 36% (a), 52% (b), 71% (c) and 88% (d) of sodium cations by ammonium ions [6]. The spectra were recorded at a resonance frequency of 400.13 MHz and with a sample-spinning rate of $\nu_{\text{rot}}=12$ kHz. The components are plotted at the bottom

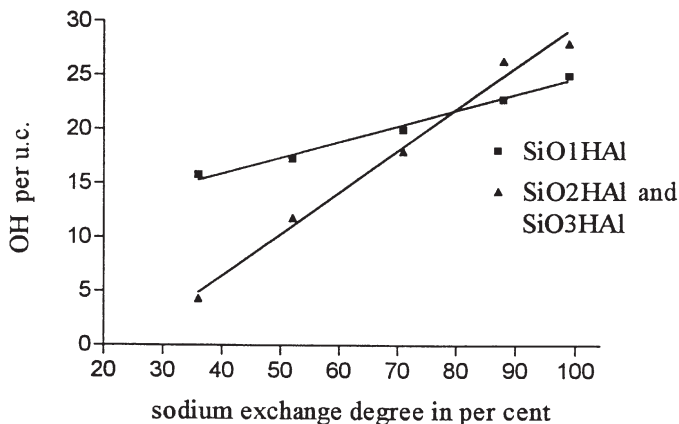


Fig. 31. The concentrations of bridging OH groups in the supercages (SiO1HAL) and the sodalite cages (SiO2HAL and SiO3HAL) of dehydrated zeolites HNaY as a function of the sodium-exchange degree. The values of zeolites 36HNaY, 52HNaY, 71HNaY and 88HNaY were determined by decomposition of the ^1H MAS NMR spectra depicted in Fig. 30. The values for zeolite 99HNaY were taken from [217]

the concentrations of bridging OH groups in the supercages (SiO1HAL) and in the sodalite cages (SiO2HAL and SiO3HAL) are plotted as a function of the sodium-exchange degree. Considering Fig. 31, exchange degrees of up to 25% of sodium cations cause an exclusive formation of SiO1HAL groups in the supercages of zeolite Y. For exchange degrees larger than 25% of the sodium cations, a linear increase in the concentration of the SiOHAL groups in the sodalite cages (SiO2HAL and SiO3HAL) was observed. The ratio between the concentration of bridging hydroxyl groups in the supercages and in the sodalite cages amounts to (0.9 ± 0.1) for a zeolite HNaY with a proton-exchange degree of more than 99% [217] which is in agreement with the results of neutron diffraction investigations [216]. It should be mentioned that line (a) is caused by terminal silanol groups (SiOH) located on the outer surface of zeolite particles or at internal framework defects.

The ^1H NMR shifts of free bridging OH groups in large zeolite cages and pores cover a range of 3.8–4.3 ppm and depend on the framework $n_{\text{Si}}/n_{\text{Al}}$ ratio [218, 219] and, therefore, on the mean electronegativity of the zeolite framework [220]. In Fig. 32, the chemical shift, δ_{H} , of free SiOHAL groups, i.e., of bridging OH groups which do not exhibit a hydrogen bond or an electrostatic interaction with the zeolite framework (column 6 of Table 5; [218, 220, 221]), is plotted as a function of the mean Sanderson electronegativity S^m [222] of the zeolite frameworks (column 5 of Table 5; [220]). S^m is defined as the geometric average of the atomic electronegativities, S_i , so that it follows for zeolites of composition $\text{HALO}_2(\text{SiO}_2)_n$

$$S^m = (S_{\text{H}} S_{\text{Al}} S_{\text{O}}^{2n+2} S_{\text{Si}}^n)^{1/(3n+4)} \quad (39)$$

with $S_{\text{Al}}=2.22$, $S_{\text{O}}=5.21$, $S_{\text{Si}}=2.84$, and $S_{\text{H}}=3.55$.

The results shown in Fig. 32 indicate an increase in the chemical shift, δ_{H} , with increasing mean electronegativity of the zeolite framework. However, the significant deviation of the chemical shift of bridging OH groups in zeolite 25HNaA is

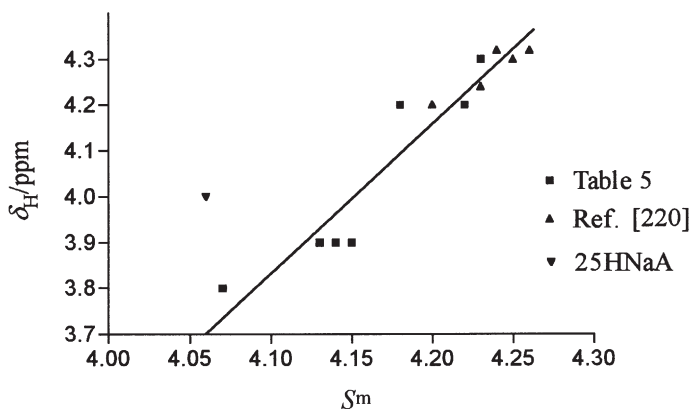


Fig. 32. ^1H NMR shifts, δ_{H} , of bridging OH groups in the supercages and channels of aluminosilicate type zeolites as a function of the mean Sanderson electronegativity S^m [222] given in columns 5 and 6 of Table 5 and in [220]

Table 5. Structural data [62], molar ratios of T-atoms [221], mean Sanderson electronegativities S^m [222] of aluminosilicate frameworks, chemical shifts (referenced to TMS) [221], δ_H , of bridging OH groups and H-Al distances [221], r_{HAl} , in the local structure of bridging OH groups derived by analysis of the ^1H MAS NMR sideband patterns

Zeolite	Structure type*	Oxygen rings*	$n_{\text{Si}}/n_{\text{Al}}^a$ $n_{\text{Si}}/n_{\text{Al+Si+P}}^b$	S^m	δ_H/ppm	$r_{\text{HAl}}/\text{nm}^{**}$
25HNaA	LTA	8-membered	1.0 ^a	4.06	4.0	0.238
50HNaX	FAU	12-membered	1.4 ^a	4.07	3.8	0.246
52HNaY	FAU	12-membered	2.6 ^a	4.13	3.9	0.250
90HNaY	FAU	12-membered	3.5 ^a	4.14	3.9	0.250
		6-membered			4.8	0.236
37HKERI	ERI	8-membered	2.9 ^a	4.15	3.9	0.246
HM	MOR	12-membered	7.1 ^a	4.18	4.2	0.248
HZSM-5/1	MFI	10-membered	15.0 ^a	4.22	4.2	0.250
HZSM-5/2	MFI	10-membered	26.0 ^a	4.23	4.3	0.246
SAPO-5	AFI	12-membered	0.036 ^b		3.8	0.252
		6-membered			4.8	0.236
SAPO-17	ERI	8-membered	0.021 ^b		3.7	0.242
		8-membered			4.0	0.240
SAPO-34	CHA	8-membered	0.114 ^b		3.8	0.242
SAPO-37	FAU	12-membered	0.121 ^b		3.8	0.250
		6-membered			4.3	0.234

* see Reference [62].

** accuracy of 0.002 nm.

noteworthy. This deviation may be caused by an additional electrostatic interaction with the zeolite framework since these bridging OH groups are located in eight-membered oxygen rings.

Since the ^1H NMR chemical shift of free surface hydroxyl groups was found to be correlated with S^m , it was suggested that δ_H could be used as a measure for the strength of gas-phase acidity, S_a [211, 212, 218–220]. This suggestion was confirmed by *ab initio* quantum-chemical calculations [223] which revealed a linear interdependence between δ_H and the deprotonation energy, ΔE_{DP} , of surface hydroxyl groups which are bound to T-atoms (Al, Si, P, or B) whose first coordination sphere consists of oxygen atoms only. This means that δ_H can be used to calculate ΔE_{DP} [5, 224].

In addition to the above-mentioned signals of free bridging OH groups, zeolites may exhibit signals due to bridging OH groups influenced by a hydrogen bond or an electrostatic interaction with the zeolite framework. An important example is line (c) at about 4.8 ppm in the ^1H MAS NMR spectra of dehydrated zeolites HY that could be assigned to bridging OH groups pointing into the centers of six-membered oxygen rings inside the sodalite cages (columns 3 and 6 of Table 5) [211, 212, 218, 225]. Similar phenomena have been found for other zeolites, e.g., for HZSM-5. Zholobenko et al. [226] detected a broad band at a position of ca. 3250 cm^{-1} in the diffuse reflectance IR spectrum of HZSM-5 with

$n_{\text{Si}}/n_{\text{Al}}$ ratios of 21 and 35 which was explained by a 'complex with a hydrogen bond between an acid OH group and a neighboring oxygen atom', i.e., a bridging hydroxyl group influenced by an additional electrostatic interaction with the zeolite framework. Furthermore, Woolery et al. [227] found a broad IR band at ca. 3500 cm^{-1} which especially occurs in highly siliceous zeolites HZSM-5 ($n_{\text{Si}}/n_{\text{Al}} > 100$). This band could be assigned to internal silanols, i.e., SiOH groups influenced by an electrostatic interaction with the zeolite framework. The correlation between the chemical shift, δ_{H} , and the wavenumber, ν_{OH} , of the IR stretching vibration is given by:

$$\delta_{\text{H}}/\text{ppm} = 57.1 - 0.0147 \cdot \nu_{\text{OH}}/\text{cm}^{-1} \quad (40)$$

for surface hydroxyl groups in zeolites and by

$$\delta_{\text{H}}/\text{ppm} = 37.9 - 0.0092 \cdot \nu_{\text{OH}}/\text{cm}^{-1} \quad (41)$$

for hydrogen bonded protons in various solids [228].

It has to be mentioned that OH groups located on cations such as, e.g., Mg^{2+} or Ca^{2+} significantly deviate from these equations. According to Eqs. (40) and (41) a wavenumber of ca. 3250 cm^{-1} should correspond to a chemical shift between 8.0 ppm and 9.3 ppm. A wavenumber of ca. 3500 cm^{-1} corresponds to a chemical shift of about 5.7 ppm. Engelhardt et al. [229] were the first to report the existence of a relatively broad shoulder at a chemical shift higher than that of line (b) at 4.2 ppm in HZSM-5. This shoulder was explained [220] by a broad component of line (b) and assigned to adjacent bridging hydroxyl groups on Al-O-Si-O-Si-O-Al sites. A well-resolved signal at a chemical shift of ca. 7 ppm (see Fig. 33) was

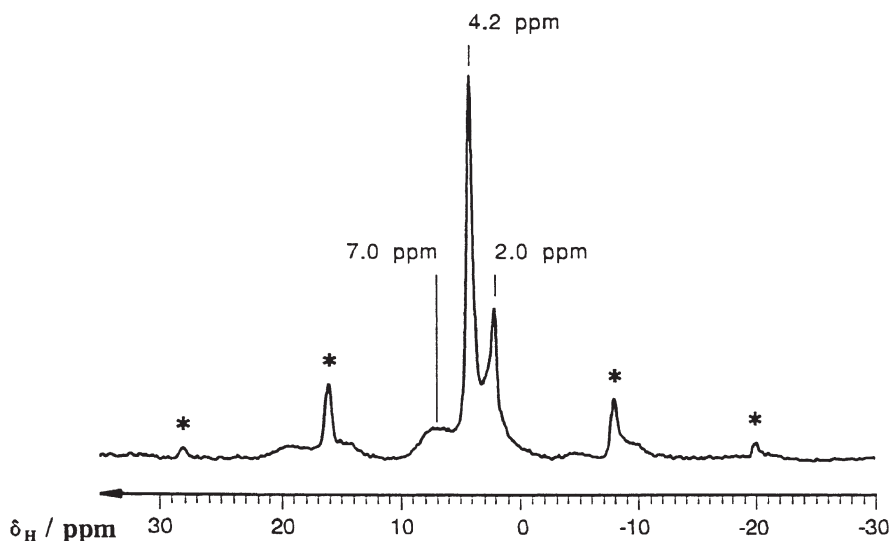
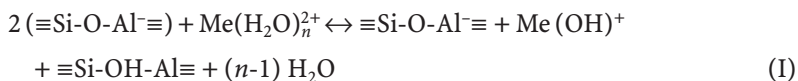


Fig. 33. ^1H MAS NMR spectrum of an activated (673 K) zeolite HZSM-5 measured at a resonance frequency of 500.1 MHz and a temperature of 123 K [230, 231]

observed in the low-temperature ^1H MAS NMR spectrum of zeolites HZSM-5 and was ascribed to bridging hydroxyl groups influenced by an additional electrostatic interaction with the zeolite framework [230, 231], as had been suggested by Zholobenko et al. [226]. Freude [232] pointed out that these protons could exchange between at least two of the four oxygen atoms around a framework aluminum atom. At one or more of these positions the proton exhibits an additional interaction with other framework oxygen atoms. The existence of a similar signal was also found for zeolite Beta [233]. It should also be mentioned that Koller et al. [234] provided evidence for the existence of hydrogen-bonded SiOH groups in highly siliceous HZSM-5.

Recently, Ernst et al. [106] and Freude et al. [107] suggested the quadrupole coupling constant, C_Q , of OD groups in zeolites as a scale of acid strength. The electric field gradient at the hydroxyl deuterons studied by ^2H NMR spectroscopy on deuterated samples describes the charge distribution in the closer spatial environment of OD groups in zeolites. Since it is known that both δ_H (vide supra) and the deuterium quadrupole coupling constant, C_Q , are strongly influenced by the presence of hydrogen bonds [235, 236], it has to be stated that the measurement of the acid strength via C_Q is complicated for surface hydroxyl groups which cannot be considered as free. For a general review of the various spectroscopic methods for the characterization of the acidity of zeolites the reader is referred to Vol. 6 of this series.

Zeolites exchanged with multivalent cations exhibit strong intracrystalline electric fields. The strength of this potential is proportional to the ratio of the charge and the radius of the cations. According to the mechanism suggested by Hirschler [237] and Plank [238], dissociation of water molecules upon adsorption on multivalent cations results in the formation of OH groups on the cations (further denoted by MeOH) and bridging OH groups. Hunger et al. [239] applied ^1H MAS NMR spectroscopy to investigate quantitatively the formation of hydroxyl protons due to water adsorption on dehydrated zeolites MgNaY and CaNaY. After adsorption, the samples were thermally treated at temperatures between 473–673 K. The ratio of the numbers of metal OH groups and bridging OH groups, derived by a quantitative analysis of the ^1H MAS NMR intensities of these hydroxyl groups, was found to be about 1:1 which can be explained by the formation of one MeOH group and one bridging OH group per dissociated water molecule according to Scheme (I).



After thermal treatment at temperatures of 473–673 K a simultaneous decrease in the ^1H MAS NMR intensities of MeOH and bridging OH groups was observed which indicates the reversibility of this mechanism. For zeolite LaNaY a maximum concentration of bridging OH groups occurs after dehydration at 450 K [240]. The hydrolysis of aluminum cations was studied on zeolite ZSM-5 exchanged with $\text{Al}(\text{NO}_3)_3$ [241]. Upon dehydration of zeolite AlZSM-5 at 473 K and subsequent water adsorption, a strong increase in the signal of AlOH groups

at a chemical shift of 2.8 ppm was found. As observed for zeolites MgNaY and CaNaY, dehydration of zeolite AlZSM-5 at temperatures between 473–673 K causes a simultaneous decrease of the concentrations of AlOH and bridging OH groups.

The lowest chemical shifts of hydroxyl protons in zeolites have been observed for MeOH, e.g., for OH groups on Mg^{2+} cations located on position SII in the supercages of zeolite Y. The corresponding signals appear at ca. 0 ppm (Fig. 34a) [239]. CaOH groups located in the sodalite cages of dehydrated zeolite CaNaY exhibit a low-field shift, $\Delta\delta_H$, of about 2.8 ppm with respect to the position of undisturbed MeOH groups (0 ppm) (Fig. 34b) [239]. Eckert et al. [242] devised an empirical formula to describe the interdependence between the O-O distance of hydrogen bonds (d_{OH-O}) and the 1H NMR chemical shift, δ_H , of OH groups in inorganic solids:

$$\delta_H/\text{ppm} = 79.05 - 0.255 d_{OH-O}/\text{pm} \quad (42)$$

Assuming the formation of hydrogen bonds, the low-field shift, $\Delta\delta_H$, of 2.8 ppm for CaOH groups in sodalite cages of zeolite CaY corresponds to a O-O distance of $d_{OH-O}=0.299$ nm [Eq. (42)]. XRD investigations on dehydrated zeolite CaY have shown that OH groups bonded to calcium cations, which are located at the position SI', exhibit an O-O distance to the next nearest framework oxygen atom of $d_{OH-O}=0.297$ nm [243]. This value is in reasonable agreement with the O-O distance derived by 1H MAS NMR. In zeolite LaNaY a low-field shift of the 1H NMR signal of LaOH groups of about $\Delta\delta_H=5.6$ ppm was found (Fig. 34c) [6]. Hence,

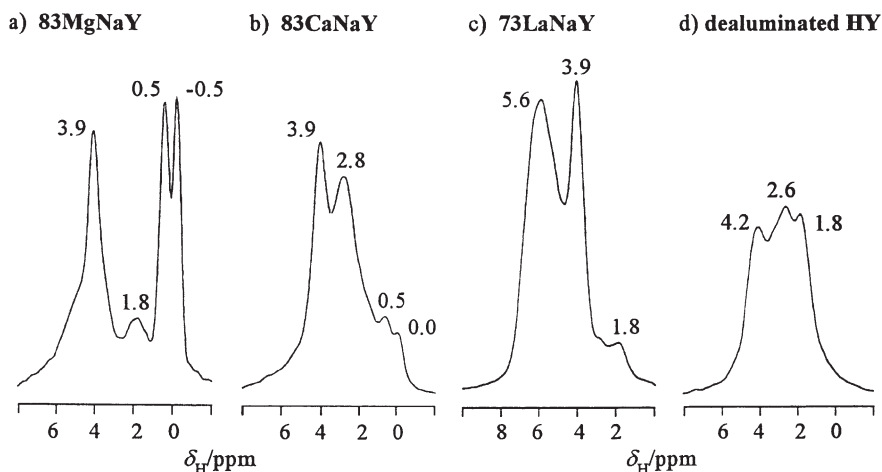


Fig. 34a–d. 1H MAS NMR spectra of zeolites 83MgNaY (a) [239], 83CaNaY (b) [239] and 73LaNaY (c) [6] calcined at 433 K and of dealuminated zeolite HY (d) [244] calcined at 673 K. The spectra depicted in a, b and d were recorded at a resonance frequency of 300.13 MHz and with a sample-spinning rate of $\nu_{rot}=3$ kHz. The spectrum plotted in c was measured at a resonance frequency of 400.13 MHz and with a sample-spinning rate of $\nu_{rot}=10$ kHz

depending on the location of non-acidic MeOH groups, their ^1H NMR chemical shift is in the range of 0–6 ppm. In the spectra of dealuminated zeolites HY (Fig. 34d) [244], H-mordenite [218] and HZSM-5 [103, 229], signals of hydroxyl protons on non-framework aluminum species appear at chemical shifts in the range 2.6–3.6 ppm. A comparison of these resonance positions with those of ALOH groups on the outer surface of aluminum oxides [245] indicates a low-field shift of about $\Delta\delta_{\text{H}}=3$ ppm. This behavior is a hint for the formation of hydrogen bonds between ALOH groups on non-framework aluminum species and adjacent oxygen atoms. A summary of ^1H NMR shifts of hydroxyl groups in dehydrated zeolites is given in Table 6.

Quantitative multi-nuclear solid-state NMR investigations of the dehydroxylation of zeolite HY have been published by Freude et al. [102]. Applying ^1H and ^{27}Al MAS NMR, the amounts of bridging OH groups and tetrahedrally coordinated framework aluminum atoms of a zeolite 88HNaY calcined at temperatures between 573–873 K were determined. In agreement with the dehydroxylation model proposed by Kuehl [246], the concentration of dehydroxylated bridging OH groups was found to be equal to the concentration of tetrahedrally coordinated aluminum atoms removed from the zeolite framework. This result contradicts the dehydroxylation model proposed by Uytterhoeven et al. [247] suggest-

Table 6. ^1H MAS NMR shifts (referenced to TMS) and assignments of hydroxyl groups in dehydrated zeolites

^1H NMR shift $\delta_{\text{H}}/\text{ppm}$	Abbreviation	Type of hydroxyl groups	Refs
–0.5–0.5	MeOH	OH groups attached to cations in large cavities or at the outer surface of zeolite particles	239, 245
1.3–2.2	SiOH	Silanol groups at the outer surface or at framework defects	211, 218, 221
2.6–3.6	ALOH	OH groups at non-framework aluminum species, hydrogen bonded	103, 218, 229, 241
2.8–6.2	MeOH	OH groups attached to cations which are located in sodalite cages of zeolite Y and in the channels of ZSM-5, hydrogen-bonded	6, 239, 240,
3.8–4.3	SiOHAl, SiO1HAl ^a	Bridging OH groups in large cages and channels of zeolites	109, 218, 221, 274
4.6–5.2	SiOHAl, SiO3HAl ^a	Bridging OH groups in small cages of zeolites, electrostatic interaction	218, 221
6.1–7.0	SiOHAl	Bridging OH groups in zeolites HZSM-5, HBeta, and HMCM-22, electrostatic interaction	95, 220, 231, 232, 233, 274

^a Assignment of bridging OH groups in faujasite-type zeolites.

ing that the dehydroxylation of two bridging OH groups leads to the formation of one trigonally coordinated framework aluminum atom. The second framework aluminum atom remains in a tetrahedral oxygen coordination in the zeolite framework.

^1H NMR studies on hydrothermally dealuminated zeolites HNaY, H-mordenite and HZSM-5 were published by Lohse et al. [244], Freude et al. [218] and Engelhardt et al. [229], respectively. Using a HZSM-5 ($n_{\text{Si}}/n_{\text{Al}}=15$), the interdependence between the treatment conditions and the n-hexane cracking activity was investigated [103, 248, 249]. After hydrothermal treatment carried out at 813 K with a water vapor pressure of 6.6 kPa, an increase in the reaction rate of n-hexane cracking by a factor of 2.7 in comparison with the parent samples was found. This remarkable effect, which was first observed by Lago et al. [250], was accompanied by a decrease in the ^1H MAS NMR signal of bridging OH groups and the appearance of the ^{27}Al MAS NMR signals of octahedrally and tetrahedrally coordinated non-framework aluminum species at ca. 0 ppm and 30 ppm, respectively. Considering these results, the enhanced n-hexane cracking activity was explained by an interaction between Brønsted acid sites and Lewis acid sites resulting in the formation of sites with an enhanced catalytic activity.

It is well known that the acidity of zeolites can be modified by dealumination and/or realumination of the zeolitic framework. ^1H MAS NMR studies of realuminated and rehydroxylated zeolite HNaY have been carried out on hydrothermally treated samples. This zeolite was dealuminated at 800 K, subsequently treated with an aqueous KOH solution, and ammonium-exchanged [251]. The ^1H MAS NMR spectra of the calcined (673 K) samples show an increase in the intensity of the signals due to bridging OH groups by a factor of about two compared with the dealuminated zeolite. This effect was explained by the reinsertion of a corresponding number of non-framework aluminum atoms into the zeolite framework. In agreement with the ^1H MAS NMR data, the ^{29}Si MAS NMR spectra of the KOH-treated samples showed a decrease in the framework $n_{\text{Si}}/n_{\text{Al}}$ ratio from 5.1 to 2.9 and a redistribution of framework aluminum atoms in comparison with the dealuminated sample [251]. The same result was obtained for hydrothermally dealuminated HZSM-5 treated with an aqueous NaOH solution [252].

5.2

Local Structure of Bridging OH Groups

The local structure of bridging OH groups in zeolites has been investigated in numerous quantum-chemical calculations [253–255]. Schroeder et al. [254] suggested local structures with H-Al distances of 0.239 nm and 0.233 nm for SiO_1HAl and SiO_3HAl groups in zeolite HY, respectively. Stevenson [256] measured the second moment, M_2^{HAl} , of the broad-line ^1H NMR signals of bridging OH groups in zeolite HY and determined an H-Al distance of $r_{\text{HAl}}=0.238$ nm. Freude et al. [257, 258] verified this value using the same method. Furthermore, an H-Al distance of $r_{\text{HAl}}=0.248$ nm was found for bridging OH groups in HZSM-5. Kenaston et al. [259] applied SEDOR pulse sequences (see Sect. 2.3.3) to determine the H-Al distance in bridging OH groups in HZSM-5 and obtained an H-Al distance of $r_{\text{HAl}}=0.243$ nm.

In a new approach, the second moments, M_2^{HAL} , due to the heteronuclear magnetic dipole-dipole interaction between the protons and the aluminum nuclei in the SiOHAl groups, and M_2^{CSA} , caused by the anisotropy of chemical shift, have been derived by an analysis of the spinning sideband patterns of the ^1H MAS NMR signals [220, 221, 260, 261]. An important advantage of this method is that the spinning sideband patterns of different signals can be analyzed separately. This means that the NMR parameters can be determined selectively, e.g., for bridging OH groups located in the 6- and the 12-membered oxygen rings occurring in zeolites HY, SAPO-5, and SAPO-37 [220, 221, 261].

The spinning sideband patterns of signals at different isotropic chemical shifts can be separated by a rotor-synchronized two-dimensional pulse experiment. In this experiment, the time t_1 after the $\pi/2$ -pulse excitation of the resonating spins amounts to multiples of the spinning period $\tau_{rot}=1/\nu_{rot}$, i.e., $t_1=n \cdot \tau_{rot}$ with $n=1, 2, \dots$, etc. Following the proposal of Aue et al. [262], a π -pulse was applied after t_1 . Acquisition of the signal as a function of t_2 was started immediately after the π -pulse. Two-dimensional Fourier transformation of the signal $G(t_1, t_2)$ yields a two-dimensional spectrum $F(\nu_1, \nu_2)$. The spinning sidebands are removed from the F1-dimension by this experiment (see top of Fig. 35), whereas the spinning sideband patterns of the different signals can be observed in the F2-dimension (see bottom of Fig. 35).

The simulation of the spinning sideband patterns of bridging OH groups was carried out according to the methods described in the literature [260, 261]. Table 5 gives a summary of the experimentally determined H-Al distances of bridging OH groups in various aluminosilicates and silicoaluminophosphates. The values of the chemical shift anisotropies, $\Delta\sigma_{OH}$, cover the range 13.5–17.5 ppm [221]. In Fig. 36 the H-Al distances of bridging OH groups are depicted as a function of the number of oxygen atoms in the oxygen rings where the hydroxyl protons are located (columns 3 and 7 of Table 5). The variation in these values suggests that the H-Al distances of bridging OH groups depend on the size of the oxygen rings. A difference of (0.015 ± 0.004) nm between the H-Al distance of SiOHAl groups in the supercages [$r_{HAL}=(0.250 \pm 0.002)$ nm] and in the sodalite cages [$r_{HAL}=(0.235 \pm 0.002)$ nm] of zeolites HY and SAPO-37 was determined by spinning sideband analysis. Values of $r_{HAL}=0.239$ nm and $r_{HAL}=0.233$ nm were determined by quantum-chemical investigations for SiO1HAL and SiO3HAL groups, respectively [253, 254]. The observation of shorter H-Al distances for SiOHAl groups in the sodalite cages is also in agreement with the results obtained by neutron diffraction analysis [216, 263].

Using spinning sideband analysis, Koch et al. [264] investigated the influence of carbon monoxide adsorption on the H-Al distance of bridging OH groups in HZSM-5. The same H-Al distance was found for unloaded and loaded (ca. one CO per SiOHAl) HZSM-5. However, the chemical shift anisotropy increases significantly from $\Delta\sigma_{OH}=14 \pm 2$ ppm to $\Delta\sigma_{OH}=22 \pm 2$ ppm after adsorption of carbon monoxide due to the formation of a linear adsorbate complex. At 123 K an equilibrium distance between the hydroxyl proton and the carbon atom of the probe molecule of $r_{HC}=0.20 \pm 0.02$ nm could be measured which is in reasonable agreement with the values derived by quantum-chemical calculations [265, 266] and ^{13}C NMR investigations [267].

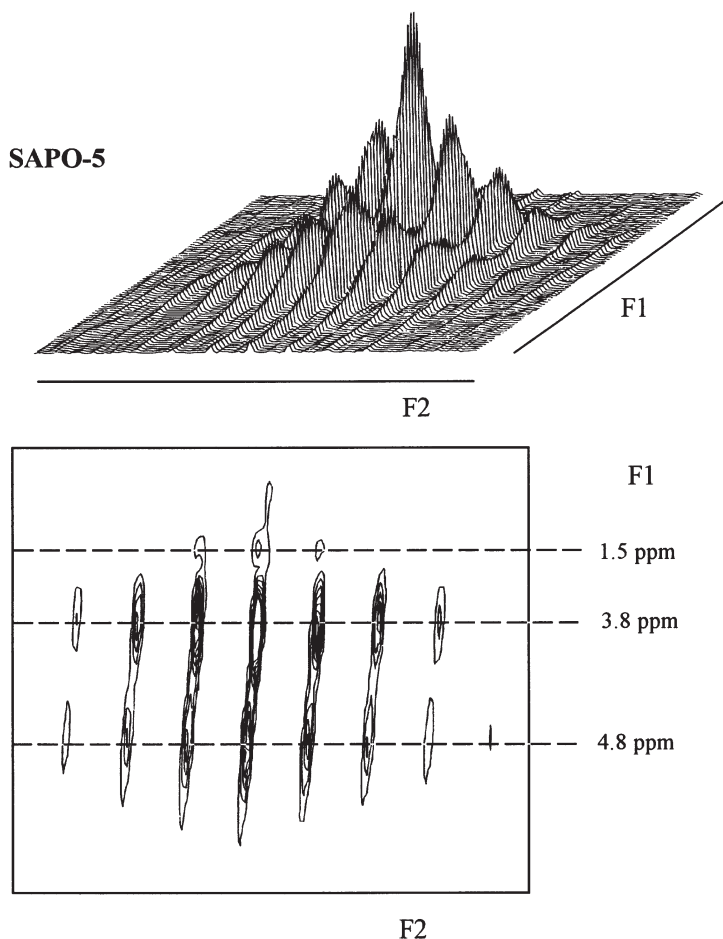


Fig. 35. Stacked plot (*top*) and contour plot (*bottom*) of the two-dimensional ^1H MAS NMR spectrum of dehydrated (673 K) silicoaluminophosphate SAPO-5 studied by Hunger et al. [221, 260]. The spectrum was recorded at a resonance frequency of 300.13 MHz with a sample-spinning rate of $\nu_{\text{rot}}=2$ kHz and a rotor-synchronized pulse sequence to eliminate MAS modulation in the F1-dimension [6]

5.3

Mobility of Hydroxyl Protons in Zeolites

The first investigations of the mobility of hydroxyl protons in H-zeolites were carried out in the mid-1970s by static ^1H NMR spectroscopy [268]. In recent papers it is shown that ^1H MAS NMR spectroscopy at elevated temperatures also allows the investigation of the proton mobility [6, 269, 270].

The ^1H MAS NMR spectra of dehydrated and unloaded zeolites consist of a narrow central line and sharp spinning sidebands at room temperature. Therefore, the correlation time of the hydroxyl protons must be large compared with the

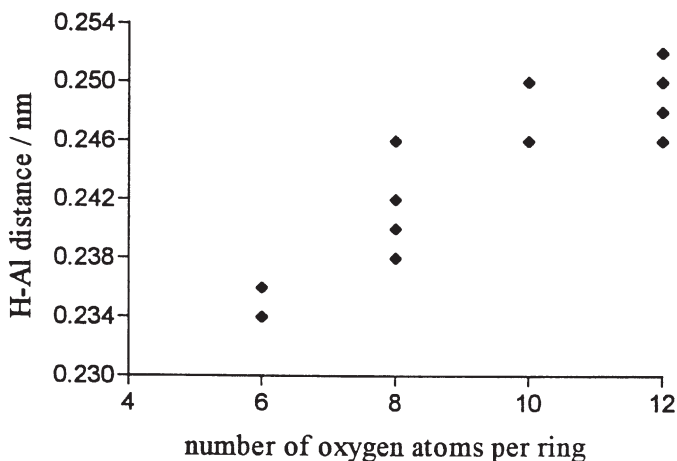


Fig. 36. Plot of the experimentally derived H-Al distances, r_{HAl} , of bridging OH groups as a function of the number of oxygen atoms per oxygen ring (columns 3 and 7 of Table 5) in which the hydroxyl protons are located

MAS spinning period $\tau_{\text{rot}}=1/\nu_{\text{rot}}$, where ν_{rot} denotes the sample-spinning rate. Assuming that the protons of bridging OH groups exhibit uncorrelated thermal motion (e.g., jumps), the envelope of the free induction decay is determined by the second moment, M_2^{HAl} , the correlation time, τ_c , of the protons at the framework oxygen atoms, and the sample-spinning rate, ν_{rot} . Figure 37a shows ^1H MAS NMR spectra of hydroxyl protons calculated according to the formalism reported in the literature [6, 27, 220, 271, 272] for $M_2^{\text{HAl}}=4.5\times 10^8\text{ s}^{-2}$, $\nu_{\text{rot}}=3\text{ Hz}$, and $10\text{ }\mu\text{s}\leq\tau_c\leq 10\text{ ms}$. The spinning sideband pattern consists of narrow lines for $\tau_c=10\text{ ms}$ (limiting case of rigid OH group). In contrast, the signals become significantly broader for correlation times in the order of $\tau_{\text{rot}}=1/\nu_{\text{rot}}$ and the sidebands disappear. Motional narrowing of the signal can be observed for $\tau_c\ll\tau_{\text{rot}}$, since the heteronuclear dipole-dipole interaction is then averaged to zero by isotropic thermal motions. The residual linewidths, $\Delta\nu_{1/2}^{\text{MAS}}$, of the spinning sidebands of first order (1.sb) and second order (2.sb) are plotted in Fig. 37b as a function of τ_c . The residual linewidth, $\Delta\nu_{1/2}^{\text{MAS}}$, calculated for the central line agrees well with the results published by Andrew and Jasinski [27]. The residual linewidths of the spinning sidebands, however, significantly exceed this value. In Fig. 38 the ^1H MAS NMR spectra of dehydrated (673 K) HZSM-5 ($n_{\text{Si}}/n_{\text{Al}}=18$) recorded at temperatures of 293 K (bottom) and 423 K (top) are depicted [6]. The spectrum measured at 293 K exhibits a narrow signal at 4.3 ppm and corresponding sidebands. Furthermore, a weak signal at 2 ppm due to SiOH groups occurs. A considerable increase in $\Delta\nu_{1/2}^{\text{MAS}}$ and a decrease in the relative intensity of the spinning sidebands were observed at 423 K. A simulation of the spectrum measured at 423 K yields a correlation time of $\tau_c=250\text{ }\mu\text{s}$ for the proton mobility [6]. This observation is in good agreement with the results published by Sarv et al. [270] who determined a correlation time of $\tau_c=35\text{ }\mu\text{s}$ at 500 K and a activation energy of 45 kJ/mol for hydroxyl protons in HZSM-5. These values correspond to $\tau_c=250\text{ }\mu\text{s}$ at 423 K. It was furthermore

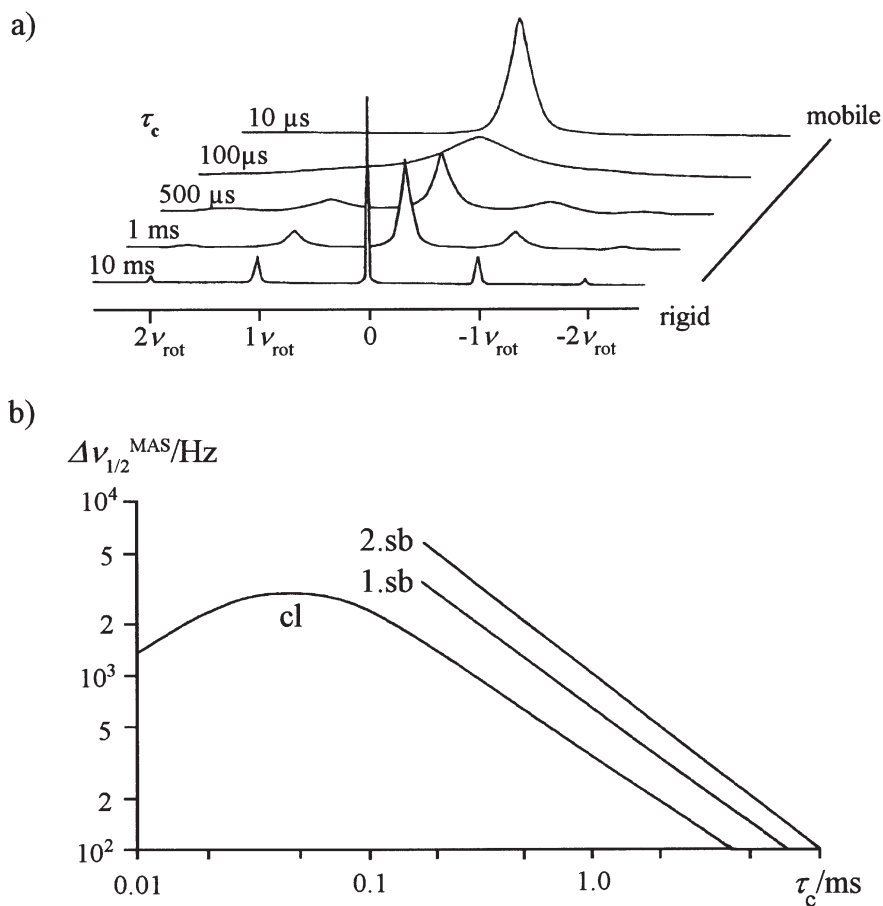


Fig. 37 a, b. ^1H MAS NMR spectra (a) of hydroxyl protons calculated for the following parameters: $M_2^{\text{HAL}} = 4.5 \times 10^8 \text{ s}^{-2}$, $\nu_{\text{rot}} = 3 \text{ kHz}$, and τ_c according to the values given on the left-hand side of the spectra. In (b) the residual ^1H MAS NMR linewidth, $\Delta\nu_{1/2}^{\text{MAS}}$, of the central line (cl), the first-order MAS sidebands (1.sb) and the second-order MAS sidebands (2.sb) are plotted as a function of the correlation time τ_c [6, 220]

pointed out [270] that the activation energy of ca. 45–60 kJ/mol for the thermal motions corresponds to the average proton affinity difference of the four oxygen atoms surrounding a framework aluminum atom. On the other hand, Baba et al. [269] have discovered a correlation between the framework aluminum concentration and the proton mobility in HZSM-5.

5.4 Investigations of Dipolar Coupled Hydroxyl Protons

The intensity of ^{29}Si MAS NMR signals of silicon atoms with protons in their closer spatial environment can be enhanced by the application of the cross-polar-

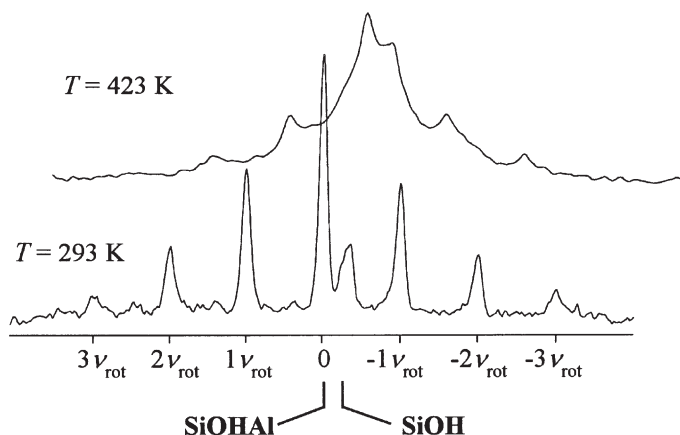


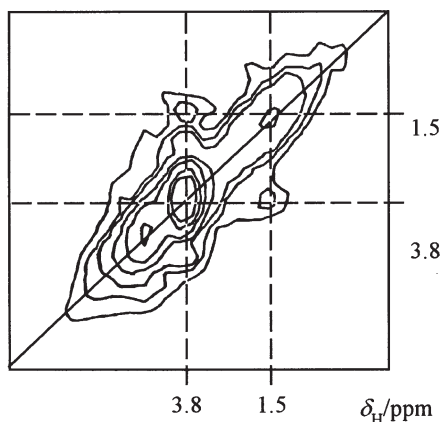
Fig. 38. ^1H MAS NMR spectra of dehydrated (673 K) zeolite HZSM-5 ($n_{\text{Si}}/n_{\text{Al}}=18$) recorded at a resonance frequency of 400.13 MHz, a sample-spinning rate of $\nu_{\text{rot}}=3$ kHz and at temperatures of $T=293$ K (bottom) and $T=423$ K (top) [6]

ization technique (CP, see Sect. 2.3). Hence, the application of this technique allows the selective investigation of $(\text{TO})_3\text{SiOH}$ and $(\text{TO})_2\text{Si}(\text{OH})_2$ groups giving rise to signals at ca. -100 ppm and -90 ppm, respectively [273]. Furthermore, the number of aluminum atoms in the second coordination sphere of the framework silicon atoms, contributing to the local structure of SiOHAl groups, can be determined [221]. In the ^{29}Si CP/MAS NMR spectra of zeolite 50HNaX ($n_{\text{Si}}/n_{\text{Al}}=1.4$), e.g., only the Si(4Al) signal is enhanced, while the lines due to Si(3Al) and Si(2Al) are absent [221]. For zeolite 37HK-erionite ($n_{\text{Si}}/n_{\text{Al}}=2.9$), which has two crystallographically inequivalent sites T1 and T2, the signal due to $\text{Si}_{\text{T1}}(2\text{Al})$ and $\text{Si}_{\text{T2}}(3\text{Al})$ is enhanced. This demonstrates that bridging OH groups in zeolites X and erionite are preferentially formed at oxygen atoms with a maximum number of framework aluminum atoms in the surroundings.

In recent solid-state NMR investigations, Beck et al. [233, 274] applied a dipolar-dephasing spin-echo ^1H MAS NMR sequence to HZSM-5 and zeolite HBeta in order to distinguish signals of hydroxyl protons with and without aluminum nuclei in their closer spatial environment. Using the same technique, Freude [232] recorded the ^1H dipolar-dephasing spin-echo MAS NMR spectra of a dehydrated HZSM-5 ($n_{\text{Si}}/n_{\text{Al}}=23$). An increase in the length of the dephasing pulses applied to the ^{27}Al spins results in a pronounced decrease in the NMR intensity of the signals at 4.3 ppm and ca. 7.0 ppm which shows that these hydroxyl groups exhibit a heteronuclear magnetic dipole-dipole interaction with aluminum nuclei.

^1H MAS NMR spectra of dehydrated aluminosilicates and silicoaluminophosphates may exhibit intense signals due to SiOH groups at about 2 ppm. Often the question arises as to whether these OH groups are located at defects on the outer surface of zeolite particles or inside the cages and pores. For an investigation of the location of SiOH groups their homonuclear magnetic dipole-dipole interaction with neighboring hydroxyl groups can be exploited by the application of two-dimensional homonuclear spin diffusion experiments [6, 275]

a) SAPO-5



b) HZSM-5

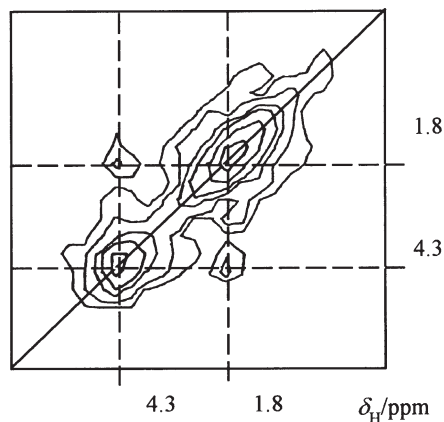
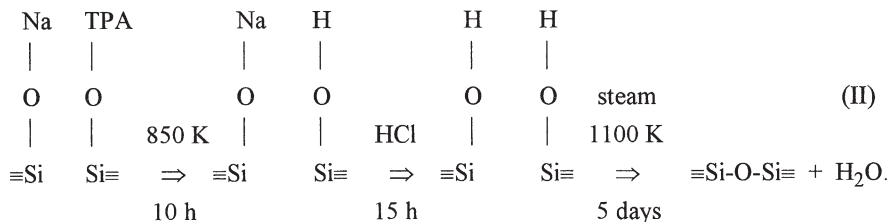


Fig. 39a, b. Contour plots of the two-dimensional ^1H NOESY MAS NMR spectra of hydroxyl protons in dehydrated (673 K) zeolites SAPO-5 (a) and HZSM-5 (b) recorded at a resonance frequency of 300.13 MHz, a sample-spinning rate of $\nu_{\text{rot}}=3$ kHz and using a mixing time of 50 ms. The dotted lines are drawn at the chemical shifts of SiOH groups at 1.5 ppm (a) and 1.8 ppm (b) and of bridging OH groups at 3.8 ppm (a) and 4.3 ppm (b) [6]

(NOESY: nuclear Overhauser enhancement and exchange spectroscopy [276]). The ^1H MAS NMR spectrum of silicoaluminophosphate SAPO-5 consists of signals at 1.5 ppm due to SiOH groups and at 3.8 ppm and 4.8 ppm caused by bridging OH groups in 12-ring pores and 6-membered oxygen rings, respectively [129, 221, 277]. The 2D NOESY cross-peaks caused by signals at 1.5 ppm and 3.8 ppm (Fig. 39a) indicate a homonuclear dipole-dipole interaction between SiOH groups and bridging OH groups. The latter species are located in the 12-ring pores of SAPO-5. Therefore, most of the SiOH groups must be located at framework defects inside the crystallites.

It is well known that synthesis of ZSM-5 with tetrapropylammonium iodide or bromide (TPA^+) as structure-directing agents yields zeolite particles with a high concentration of framework defects [170, 278–280]. Up to 8% of the framework silicon atoms in these zeolites are involved in defect SiOH groups. ^1H MAS NMR spectroscopic investigations of ZSM-5 [170, 278], after thermal decomposition of the template TPA^+ , acid leaching, and steaming, suggested Scheme (II) for the formation of SiOH in the ‘as-synthesized’ ZSM-5



(II)

This model was supported by the ^{29}Si CP/MAS NMR and FTIR investigations of Woolery et al. [227] and Groenen et al. [281]. The homonuclear 2D ^1H NOESY MAS NMR spectrum of hydroxyl protons in dehydrated HZSM-5 ($n_{\text{Si}}/n_{\text{Al}}=40$) is depicted in Fig. 39b. Cross-peaks due to spin exchange between the signals of SiOH groups at ca. 2 ppm and bridging OH groups at ca. 4 ppm indicate a homonuclear magnetic dipole-dipole interaction between the protons of SiOH and SiOHAl groups as in the case of SAPO-5. Since hydroxyl protons of free bridging OH groups point into the 10-ring pores of HZSM-5, most of the silanol groups at framework defects must be located inside the zeolite particles.

5.5

Acidity and Location of Hydroxyl Protons Studied by Probe Molecules

The acid strength and the location of hydroxyl groups in zeolites may be proven upon interaction with suitable probe molecules. These probe molecules may be strong, medium or weak bases such as pyridine and ammonia and even benzene, light paraffins or fluorinated compounds. Adsorption of the strongly basic pyridine molecule on dehydrated zeolites is useful in order to distinguish acidic and non-acidic OH groups [210, 218, 219]. Pyridinium ions are formed if pyridine interacts with strongly acidic hydroxyl groups. In contrast, the interaction between non-acidic hydroxyls such as SiOH groups and pyridine leads to the formation of strongly hydrogen-bonded complexes. ^1H NMR spectroscopy of organic acids dissolved in pyridine yields signals of protonated pyridine (PyH^+) at chemical shifts in the range 14–20 ppm [282]. In analogy, the interaction between SiOHAl groups and perdeuterated pyridine in zeolites HNaY [219] and HZSM-5 [218] causes signals at chemical shifts in the range 15.5–19.5 ppm (Fig. 40). Simultaneously, the signals of the acidic OH groups that are involved in this proton transfer from the zeolite framework to the probe molecules decrease. In contrast, interaction of pyridine with SiOH groups in HZSM-5 causes a shift of the ^1H MAS NMR signal from 2 ppm to ca. 10 ppm [283].

In a number of ^1H MAS NMR investigations of H-zeolites, ammonia was used as a probe molecule [129, 211, 212, 218, 284–286]. An important advantage of ammonia is its small size (vide infra), so that it can be employed in cases where the rather bulky pyridine fails. Narrow ^1H MAS NMR signals at a chemical shift between 6.8 ppm and 7.4 ppm indicate the existence of ammonium ions [102, 129, 211]. The intensity of the signals due to bridging hydroxyl groups decreases upon ammonia adsorption, while the signal of ammonium ions at about 7 ppm increases provided that $n < 1$, where n denotes the ratio of ammonia molecules and accessible bridging hydroxyl groups. The decrease in the line at 3.9 ppm observed for low loadings indicates a favored ammoniation of bridging OH groups in the supercages of zeolite HY. At $n=1$ the ^1H MAS NMR spectrum consists exclusively of ammonium signals in a shift range of 6.8 ppm to 7.4 ppm (Fig. 41b) while for $n > 1$ a high-field shift of the major signal occurs which originates from a rapid exchange of ammonium ions (about 7 ppm) and physisorbed ammonia molecules (about 3.2 ppm) [218, 284]. Two signals at 6.8 ppm and 5.3 ppm are not high-field shifted which was explained by ammonium ions and $\text{NH}_3\text{-NH}_4^+$ complexes, respectively, in sodalite cages which are not involved in the

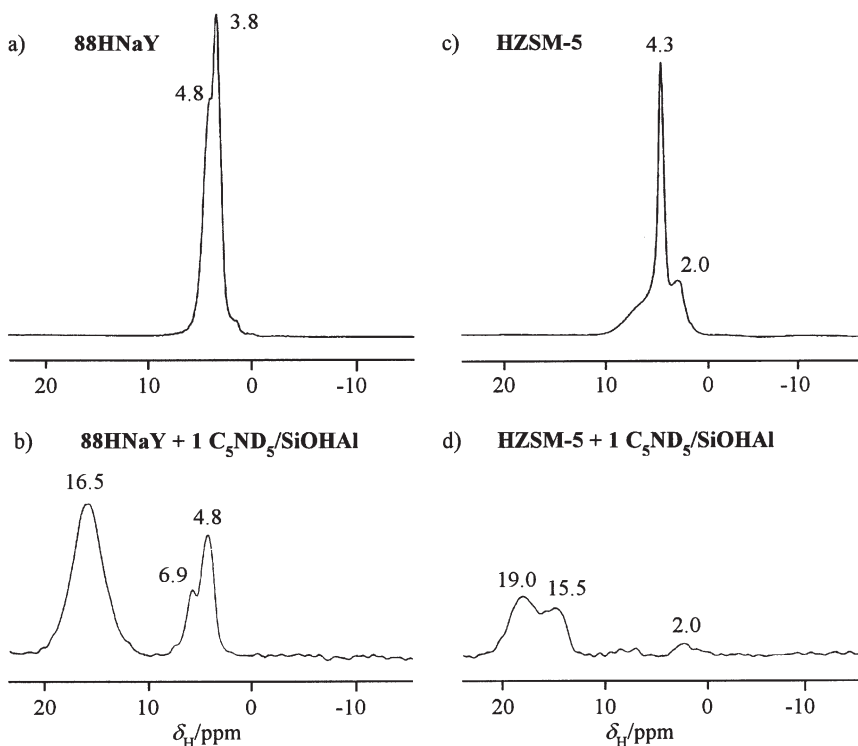


Fig. 40a–d. ^1H MAS NMR spectra of dehydrated (673 K) zeolites 88HNaY (a, b) and HZSM-5 (c, d), unloaded (a, c) and loaded (b, d) with one molecule of perdeuterated pyridine per bridging OH group. The spectra were recorded at a resonance frequency of 400.13 MHz and with a sample-spinning rate of $\nu_{\text{rot}}=8$ kHz [6]

rapid exchange process. Similar phenomena could not be observed for ammonia-loaded HZSM-5 [218, 284], SAPO-5 and SAPO-34 [129].

Furthermore, adsorption of probe molecules is a method suitable for investigating the location of hydroxyl groups in zeolites. Adsorption of deuterated cyclohexane (kinetic diameter: 0.6 nm [60]) on dehydrated SAPO-5, e.g., leads to a significant decrease in the ^1H NMR signal of bridging OH groups at 3.8 ppm which is explained by a H-D exchange between probe molecules and hydroxyl protons indicating a location of the corresponding hydroxyl protons in 12-ring pores [129] (free diameter: 0.73 nm [60]). After adsorption of pyridine on SAPO-34 no change in the signal of bridging OH groups at 3.8 ppm was observed [129]. In this case, the pyridine molecules cannot enter the 8-ring windows of the chabazite cages (free diameter: 0.38 nm [62]). However, ammoniation of dehydrated SAPO-34 gives rise to a ^1H MAS NMR signal of ammonium ions at 6.5 ppm [129] which proves the accessibility of bridging OH groups in chabazite for molecules with a size of 0.26 nm (kinetic diameter of ammonia [60]).

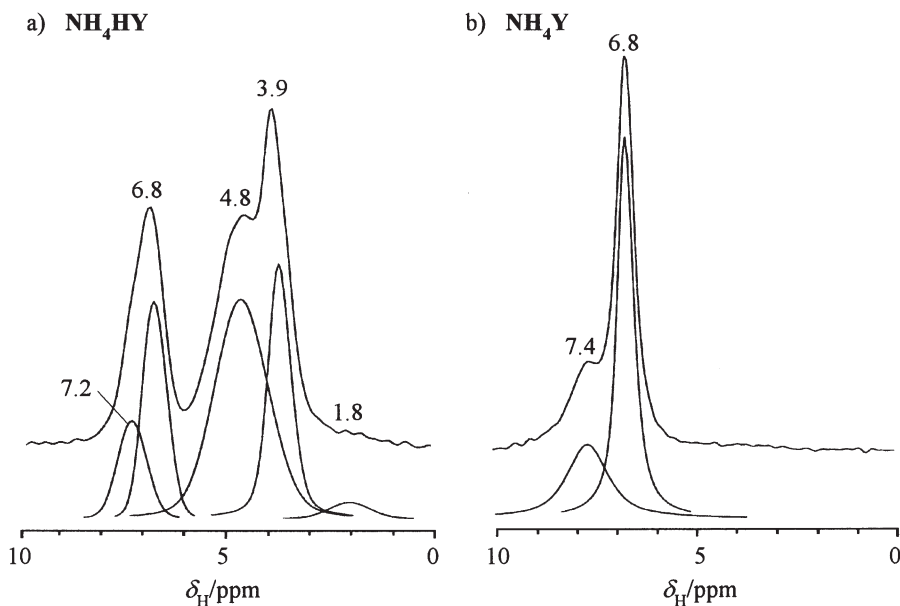


Fig. 41 a, b. ^1H MAS NMR spectra of zeolite HY reammoniated by adsorption of 5 molecules (a: NH_4HY) and 48 molecules (b: NH_4Y) of ammonia per unit cell, recorded at a resonance frequency of 400.13 MHz and with a sample-spinning rate of $\nu_{\text{rot}}=10$ kHz [6]

6

Characterization of Zeolite Pore Architecture by ^{129}Xe NMR Spectroscopy

The well-defined cages and pores of zeolites allow the application of these materials as molecular sieves and form-selective catalysts in heterogeneous catalysis. ^{129}Xe NMR spectroscopy of xenon atoms adsorbed on zeolites is a suitable method for the characterization of the zeolitic pore architecture. The isotope ^{129}Xe has a nuclear spin of $I=1/2$, a natural abundance of 26.4% and, adsorbed on zeolites, a T_1 relaxation time in the range between 10 ms and a few seconds.

In 1970 Jameson et al. [287] established a relationship between the ^{129}Xe NMR shift, δ , and the density, ρ , of pure xenon gas

$$\delta = \delta_0 + \delta_1 \rho + \delta^2 \cdot \rho^2 + \delta^3 \cdot \rho^3 \quad (43)$$

where δ_0 is the shift of the gaseous reference and $\delta_1 \rho$ describes the influence of two-body collisions of xenon atoms on the resonance position. The quadratic and cubic terms are due to more than two-body collisions occurring only at higher pressures. Assuming a fast exchange of xenon atoms adsorbed in zeolite pores, the ^{129}Xe NMR shift is described, similar to Eq. (43), by the following terms [288, 289]:

$$\delta = \delta_0 + \delta_S + \delta_E + \delta_M + \delta_{\text{Xe-Xe}} \cdot \rho_{\text{Xe}} \quad (44)$$

where δ_0 is the shift of the gaseous reference, δ_s is due to collisions between xenon atoms and the walls of the zeolite pores and cages, δ_E takes into account the electric field effect caused by exchangeable cations, and δ_M is a term to account for the presence of paramagnetic species. The term $\delta_{Xe-Xe} \cdot \rho_{Xe}$ arises from xenon-xenon collisions (two-body collisions) and disappears upon extrapolating the xenon density to zero. For aluminosilicate-type zeolites in the H-form or exchanged with alkali metal cations, and for $AlPO_4$ s also, the terms δ_E and δ_M can be neglected. In a number of ^{129}Xe NMR investigations, the empirical interdependence given in Eq. (44) was applied to characterize the void space and extra-framework species in zeolite particles. Reviews of ^{129}Xe NMR spectroscopy of xenon-loaded zeolites have been published [288–290].

6.1

^{129}Xe NMR Shifts of Xenon Atoms Adsorbed in Zeolite Pores

The characterization of zeolite pore architecture by ^{129}Xe NMR spectroscopy requires a discussion of the chemical shift of xenon atoms in dependence of the pore size. Demarquay and Fraissard [291] have shown that the chemical shift, δ_s , is inversely proportional to the mean free path, \bar{l} , of a single xenon atom in the zeolite pores. For an infinite cylinder, the mean free path is given by $\bar{l} = D_C - D_{Xe}$, where D_C is the diameter of the cylinder and D_{Xe} the diameter of the xenon atom (diameter: 0.44 nm [291]). In a similar way, $\bar{l} = 1/2 \cdot (D_S - D_{Xe})$ is derived for a sphere with the diameter D_S . Numerical values of the mean free path of xenon atoms in zeolite pores were calculated by a computer simulation of the random walk of single xenon atoms in different zeolite pores [291]. According to Johnson and Griffiths [292], δ_s depends on the time that the xenon atoms spend on the pore walls. Derouane and Nagy [293] discussed the influence of the van der Waals interaction of xenon atoms in zeolite pores on the ^{129}Xe NMR shift. They described the ^{129}Xe NMR shift of xenon atoms in zeolite pores by a curvature term that is a function of the pore radius. Although the above-mentioned methods allow only a rough estimation of the pore sizes, in certain cases ^{129}Xe NMR spectroscopy does provide valuable information, particularly when structural data are not available.

In zeolites X and Y with n_{Si}/n_{Al} ratios ranging from 1.2 to 50 and exchanged with univalent cations (Na^+ and Li^+) or H^+ , the interdependence of the ^{129}Xe NMR shift, δ , and the xenon coverage is approximately linear [294]. This is due to the term $\delta_{Xe-Xe} \cdot \rho_{Xe}$ in Eq. (44) arising from the two-body xenon-xenon-collisions and indicates that for these zeolites the terms δ_E and δ_M can be neglected. Furthermore, the experimentally derived chemical shifts of xenon atoms are independent of the framework composition. In Fig. 42 the ^{129}Xe NMR shifts of xenon atoms adsorbed on zeolites with different structure types are depicted. All curves show an increase in the chemical shifts, δ , with increasing xenon coverage $[Xe]$ that is, at least for low coverages, approximately linear. Extrapolation of the data to $[Xe]=0$ enables the determination of δ_s which covers a range of ca. 60 ppm for zeolite Y to 113 ppm for zeolite ZSM-5. The data given in columns 2 and 3 of Table 7 clearly demonstrate the relationship between δ_s and the pore size. The terms δ_s derived for xenon atoms adsorbed on aluminophosphates and silicoaluminophosphates are given in the literature [289, 295–297].

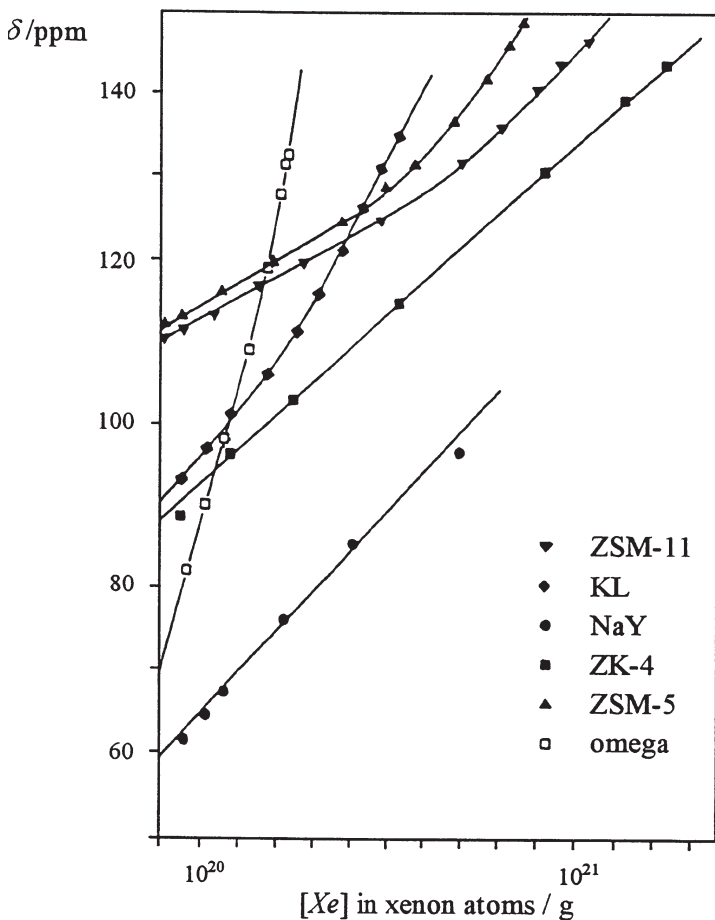


Fig. 42. ^{129}Xe NMR chemical shifts as a function of the number of xenon atoms per gram of powder material adsorbed on various zeolites [288]

6.2

Zeolites Exchanged with Diamagnetic and Paramagnetic Cations

Xenon atoms adsorbed on zeolites exchanged with divalent cations may show a parabola-like dependence of their ^{129}Xe NMR shift on the coverage. Cheung et al. [298] explained this effect in terms of a rapid exchange between strongly adsorbed xenon atoms and those remaining in the gas phase, i.e., in the void space of the zeolite pores. A xenon atom adsorbed on a divalent cation donates one of the 5p electrons to the empty s-orbital of the cation. The corresponding bond formation introduces excited electronic states that leads to a large paramagnetic contribution to the ^{129}Xe NMR shift [298].

Assuming the exchange rate between xenon atoms in the gaseous phase and strongly adsorbed xenon atoms to be much faster than the ^{129}Xe NMR relaxation

Table 7. Values of the term δ_s (referenced to the isolated xenon atom) determined for xenon atoms adsorbed in some selected zeolites and the cages and pore sizes of these zeolites (\emptyset , diameter of a cage or a pore) [288]

Zeolites	δ_s /ppm	Cages and pore sizes
X and Y	60	Spherical supercages with $\emptyset \approx 1.3$ nm
Omega	73	Unidimensional 12-ring pores with openings of 0.74 nm
A and ZK4	87	Spherical cages with $\emptyset \approx 1.14$ nm, six 8-ring openings with $\emptyset \approx 0.4$ –0.5 nm
L	90	Unidimensional 12-ring pores with openings of $\emptyset \approx 0.71$ nm, maximum $\emptyset \approx 0.9$ nm
ZSM-11	110	Three-dimensionally interconnecting 10-ring pores, 0.51×0.55 nm
Ferrierite	110	Pseudo-spherical cages with $\emptyset \approx 0.7$ nm, two 8-ring openings, 0.34×0.48 nm
	165	Bidimensionally interconnecting 10-ring pores, 0.43×0.55 nm
ZSM-5	113	Three-dimensionally interconnecting 10-ring pores, 0.51×0.55 nm and 0.54×0.56 nm
Rho	114	Three-dimensionally interconnecting pores forming spherical cages with $\emptyset \approx 1.0$ nm
	230	Prisms, 8-ring, 0.39×0.51 nm
Mordenite	115	Unidimensional 12-ring pores, 0.67×0.70 nm
	250	8-ring side-pockets, 0.29×0.57 nm

rate, Cheung et al. [298] found the following interdependence of the chemical shift $\delta(\rho)$:

$$\delta(\rho) = (n_s \cdot \delta_s + \zeta_g \cdot n_s^2) / \rho - 2 n_s \zeta_g + \zeta_g \cdot \rho \quad (45)$$

and the density, n_s , of the adsorption sites, where n_s is given by N_s/V with the number N_s of the adsorption sites and the free volume V of the cages. ζ_g is the chemical shift gradient in the gaseous phase while ρ is the xenon density. The $1/\rho$ dependence of the first term in Eq. (45) results in an initial decrease in the chemical shift $\delta(\rho)$ with increasing coverage before the third term, linear in ρ , begins to dominate.

Figure 43 shows experimentally derived ^{129}Xe NMR shifts observed for xenon atoms adsorbed on calcium- and magnesium-exchanged zeolites Y. The number before the cation gives the percentage of the sodium-exchange degree. At low exchange degrees (<55% exchange), the chemical shift, δ , increases linearly with the coverage. In these samples the divalent cations are located in the sodalite cages. However, at higher cation-exchange degrees, the divalent cations occupy positions in the supercages. Therefore, the parabola-like dependence of the chemical shift of xenon atoms adsorbed on these samples indicates an interaction of xenon atoms with these divalent cations. However, according to Gedeon et al. [299], the above-mentioned exchange model can be applied only to xenon atoms adsorbed on cations which exhibit an electron affinity comparable with

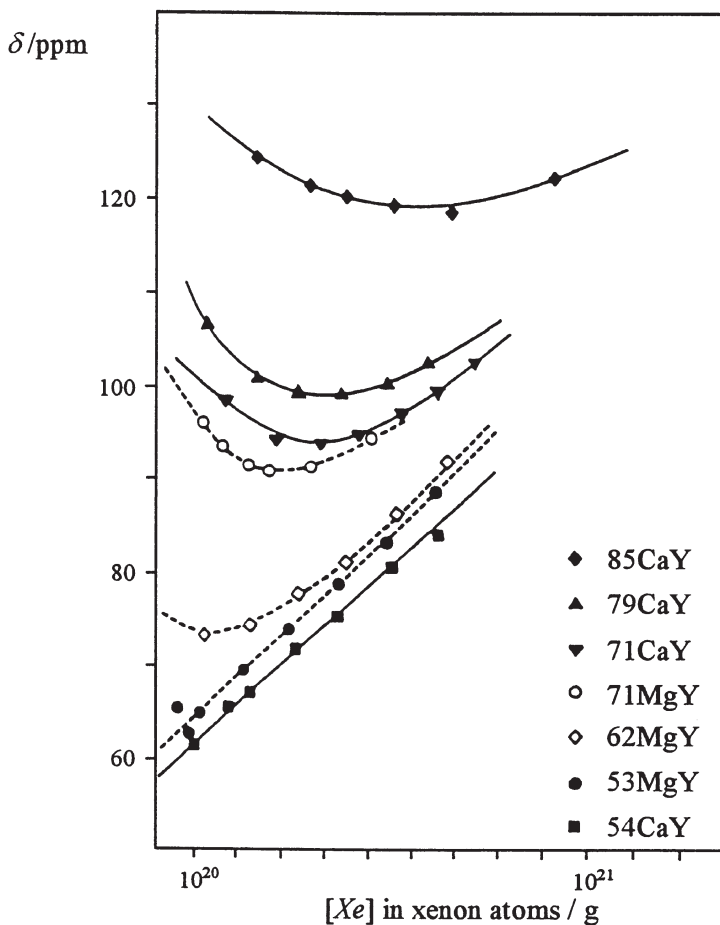


Fig. 43. ^{129}Xe NMR chemical shifts as a function of the number of xenon atoms per gram of powder material adsorbed on zeolites Y exchanged with various cations [288]

the xenon ionization potential. Liu et al. [300] explained the strong adsorption of xenon atoms in zeolites exchanged with divalent cations by a polarization of the interacting species.

In a number of studies, xenon atoms adsorbed on zeolites exchanged with Cd^{2+} , Zn^{2+} , Ce^{3+} , and La^{3+} [301–304] and loaded with metal particles (Ni, Rh, Ru, Pd, Ir, Pt) [288, 305–310] were investigated. The chemical shifts of xenon atoms adsorbed on these zeolites are, at least for low coverages, always greater than those of xenon atoms adsorbed on zeolites NaX and NaY. The sensitivity of the ^{129}Xe NMR spectroscopic data to the location of cations in zeolites was exploited by Scharpf et al. [305] to study the behavior of nickel in zeolite Y. For zeolites NiNaY with less than 14% nickel, Bansal and Dybowski [307] found that nickel occupies predominantly positions in the sodalite cages. With increasing nickel content, however, a paramagnetic shift arising from the term δ_M in Eq. (44) was

observed. Bonardet et al. [311] carried out studies of zeolites exchanged with Co^{2+} .

Gedeon et al. [299] found that xenon atoms adsorbed on dehydrated zeolites CuY are characterized by chemical shifts, δ , displaced to lower values. To date, only xenon atoms adsorbed on dehydrated silver- and copper-exchanged zeolites X and Y [301, 312–317] have shown these negative or, at least, small ^{129}Xe NMR shifts.

6.3

Effects of Pore Blocking

Fraissard and Ito [288] noted that ^{129}Xe NMR spectroscopy is a method suitable for investigating the crystallinity and the presence of intergrowths and non-framework species. The ^{129}Xe NMR signal intensity is not only proportional to the quantity of xenon atoms adsorbed per cage, but also to the number of cages. Consequently, if a sample consists of a mixture of different zeolites or of zeolites exchanged with different cations, the ^{129}Xe NMR spectrum is a direct measure of the composition of the sample. This was demonstrated by Springuel-Huet et al. [318] for a heterogeneous mixture of zeolites CaA and NaY. However, for this kind of investigation, the size of the zeolite particles has to be considered since it determines the diffusion of xenon atoms between different aggregates [319, 320].

Furthermore, ^{129}Xe NMR spectroscopy can be applied to investigate the blocking of pores. Smith et al. [321, 322] investigated the flexibility of the framework of zeolite Rho by ^{129}Xe NMR spectroscopy. The authors found that at a temperature of 160 K xenon is strongly adsorbed in the double eight-rings of zeolite Rho (see Table 7). Above 195 K, xenon is in rapid exchange between these sites and positions in the α -cages. According to Smith et al. [321, 322], this effect can be explained by destabilization of the adsorption sites in the double eight-rings relative to positions in the α -cages due to a change in the zeolite structure.

Bonardet et al. [323, 324] and Barrage et al. [325] applied ^{129}Xe NMR spectroscopy to monitor the formation of coke inside the zeolite cages. In this way, Barrage et al. [325] found that for coke deposits up to 10 wt.-%, only the supercages are filled with coke. Beyond 10 wt.-%, the coke forms deposits also on the external surface of the zeolite particles yielding microcavities between the crystallites [325]. Catalysts applied in fluid catalytic cracking have been studied by ^{129}Xe NMR spectroscopy at different stages of regeneration [324].

Bradley and Howe [326] investigated gallium-modified ZSM-5 with bulk $n_{\text{Si}}/n_{\text{Ga}}$ ratios between 11 and 210 by ^{129}Xe NMR spectroscopy. Parabola-like chemical shift curves were obtained for samples containing a high concentration of extra-framework gallium cations. Steaming of the zeolites led to a decrease of the parabola-like dependence of the ^{129}Xe NMR shift which was explained by a hydrolysis of the non-framework gallium cations forming uncharged oxides within the zeolite pores.

6.4

Co-adsorption of Molecules

The effect of the co-adsorption of organic molecules on the ^{129}Xe NMR spectra of xenon atoms adsorbed on zeolite NaY was studied by De Menorval et al. [327]. They found that the ^{129}Xe NMR shift depends on the kind of guest molecules, their concentration, and the density of xenon atoms inside the zeolite cages. The differences in the interaction of xenon atoms with aromatic molecules (benzene and trimethylbenzene) in comparison with saturated hydrocarbon chains like n-hexane were explained by an adsorption of the aromatic hydrocarbons parallel to the cage walls while the hydrocarbon chains are adsorbed perpendicular to the walls.

The local and macroscopic distribution of adsorbed benzene, 1,3,5-trimethylbenzene, and hexamethylbenzene (HMB) molecules among the intracrystalline cavities of zeolite NaY was investigated by Chmelka et al. [328]. Figure 44 shows

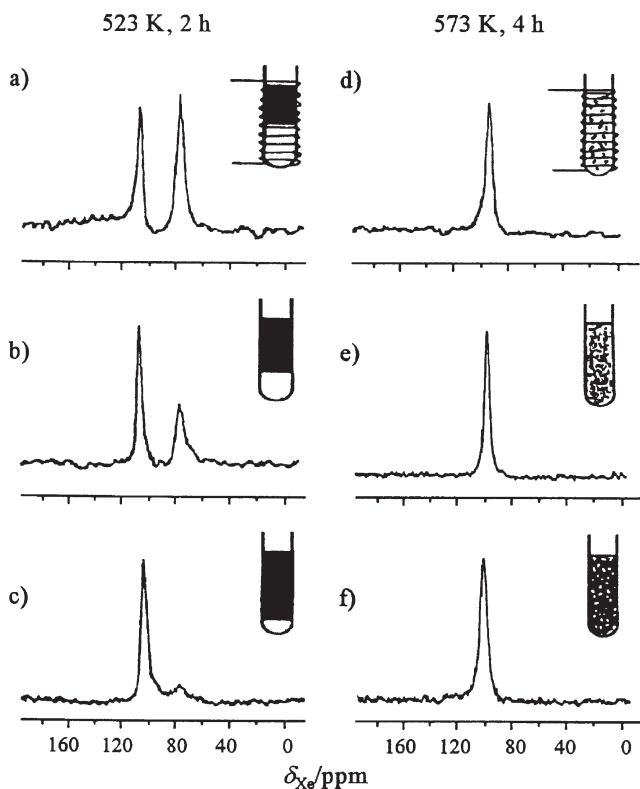


Fig. 44 a–f. ^{129}Xe NMR spectra of xenon (39 kPa equilibrium pressure) adsorbed on dehydrated zeolite NaY containing a 0.5, b 0.7, and c 0.9 hexamethylbenzene molecules per supercage [328]. The samples used for the spectra (a–c) on the left-hand side were all heated at 523 K for 2 h, the spectra (d–f) on the right-hand side were obtained after reheating the samples at 573 K for 4 h

the ^{129}Xe NMR spectra for different loadings of HMB on zeolite NaY at 523 K (left-hand side) and after redistribution of the adsorbate molecules at 573 K (right-hand side). The two peaks at 78 ppm and 109 ppm, shown in Fig. 44a, correspond to xenon atoms in distinct adsorption zones with and without HMB. The equal signal intensities indicate an equal number of xenon atoms adsorbed in these two zones. Spectra recorded after higher HMB loadings are shown in Fig. 44b and 44c. Upon heating these samples at 573 K for 4 h, the discrete lines collapse to single signals at a chemical shift of ca. 94 ppm which corresponds to a macroscopically uniform adsorbate distribution.

The equilibrium distribution of xenon atoms among the α -cages in zeolite A has been investigated by Jameson et al. [329–332] and Larsen et al. [333]. Figure 45 shows ^{129}Xe NMR spectra of xenon atoms adsorbed on dehydrated zeolite NaA at 296 K. The average numbers of xenon atoms per α -cage are given by the values $\langle n \rangle$. The distinct signals are due to clusters of xenon atoms of different size located in individual cages. With increasing numbers of xenon atoms per cage (Xe_1 to Xe_8), the signals are low-field shifted. The distribution of xenon atoms among the α -cages can be reproduced by grand canonical Monte Carlo simulations [329, 330]. Jameson et al. [334] have demonstrated that app-

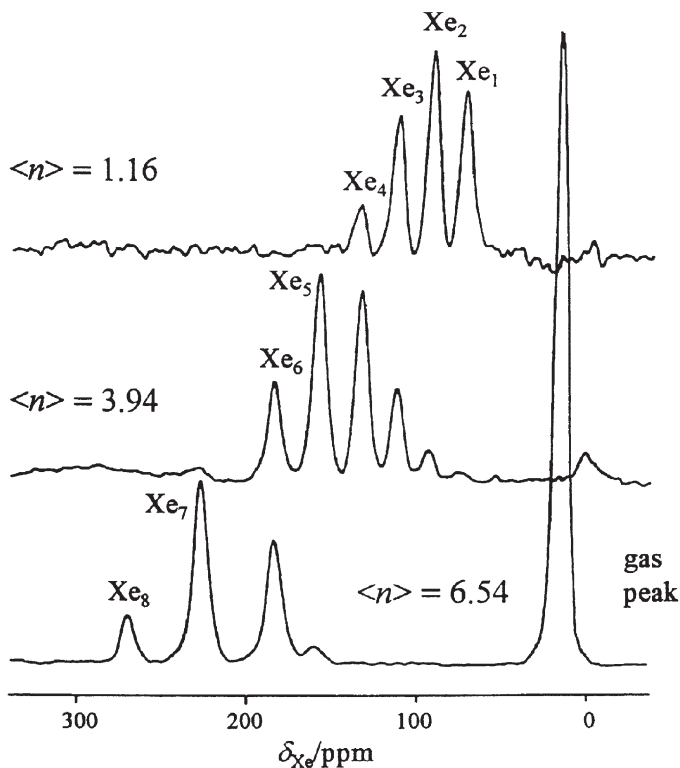


Fig. 45. ^{129}Xe NMR spectra obtained for sealed samples of xenon-loaded zeolite NaA recorded at 296 K [329]

lication of the MAS technique leads to a significant narrowing of the ^{129}Xe NMR signals of the different Xe_n clusters in the α -cages. Under MAS conditions, it is possible to observe upon addition of krypton the individual peaks corresponding to mixed Xe_nKr_m clusters inside the α -cages. Hence, this method allows the direct determination of the distribution of co-adsorbates in zeolite A [334].

7

In Situ NMR Investigations of Chemical Reactions Catalyzed by Zeolites

In the last decade, in situ NMR spectroscopy has found an increasing application for the investigation of chemical reactions heterogeneously catalyzed by acidic and basic zeolites. Using this method, it is possible to study the formation of adsorbate complexes, intermediates, and reaction products inside the zeolite crystals. An excellent review of in situ NMR spectroscopic studies of chemical reactions in zeolites is given by Haw [335]. Furthermore, the reader is referred to papers published by Klinowski [54, 58], Ivanova and Derouane [336], and Pfeifer and Ernst [4].

7.1

Experimental Techniques

In situ NMR investigations of chemical reactions catalyzed by zeolites may differ in the method of sample preparation. Often samples calcined in an external furnace, loaded with reactant molecules via a vacuum line, and sealed in glass ampoules have been used. These samples were studied at room temperature after a cyclic heating in an external furnace (method A) or during heating the samples to variable temperatures using a high-temperature NMR probe (method B). While the first in situ NMR investigations were carried out without application of high-resolution solid-state techniques [337], at the end of the 1980s the magic angle spinning technique was introduced which improved significantly the spectral resolution [338–343]. To open the way for studies of reactants that are converted on zeolite catalysts at room temperature, an equipment for the adsorption of reactant molecules at low temperatures was introduced [344–346]. In Fig. 46 the scheme of the CAVERN apparatus (cryogenic adsorption vessel enabling rotor nestling) is shown [335, 345]. This equipment is used to open the rotor under defined conditions to achieve an addition or removal of reactants according to a chosen protocol. The reactant molecules can be introduced into the CAVERN from a vacuum line and/or by crushing a small glass ampoule above the catalyst bed. High-temperature MAS NMR probes (method B) are built of ceramic parts in regions that are exposed to high temperatures. The MAS rotor is heated by variable-temperature gas (usually nitrogen) coming from a heater unit, e.g., situated on the top of the magnet bore [346]. Differing from this approach, Ernst et al. [347–350] and Ferguson et al. [351, 352] applied MAS NMR probes with a heating system consisting of a LASER. With these MAS NMR probes, the temperature inside the sample can be increased during the experi-

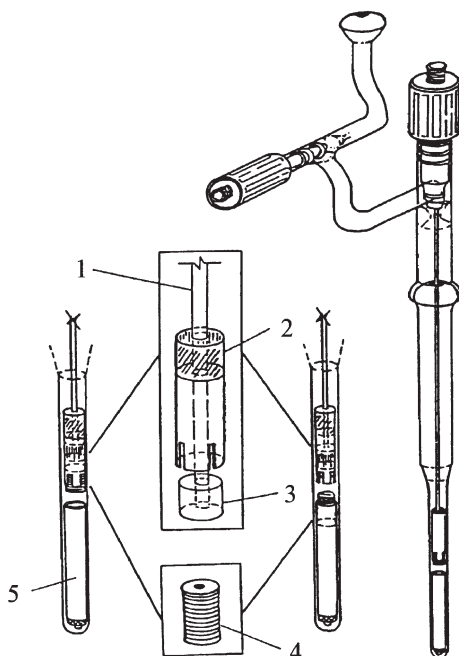


Fig. 46. Scheme of the CAVERN apparatus applied for the capping of rotors following adsorption of reactant and the capping and uncapping of rotors applied for the subsequent adsorption of different reactants onto the zeolitic catalyst. The expanded views show the capping procedure. Following parts are assigned: 1 aluminum rod; 2 Kel-F sleeve; 3 plunger; 4 Kel-F cap; 5 zirconia rotor [335]

ments from room temperature to about 500 K within a few seconds allowing time-resolved in situ NMR measurements.

In most cases, however, heterogeneously catalyzed reactions are carried out under continuous-flow conditions. The study of the steady state of these reactions requires a continuous reactant flow through the sample material. A simple approach is a sample cartridge that forms part of a flow reactor and is then transferred into a MAS NMR rotor after the reaction. The corresponding procedure is a version of the protocol in which a steady state is established before the NMR measurement (method A) [335]. In a new approach [353, 354], a carrier gas stream is injected into the rotating MAS NMR rotor through a fixed glass tube, placed in the rotor axis. Using a special tool, a cylindrical catalyst bed is formed at the inner rotor wall that is heated by the gas that bears the MAS rotor (Fig. 47a). A saturator is used to load the carrier gas with the reactant compounds. A flow controller or a rotameter is used to adjust the flow rate of the carrier gas (Fig. 47b). The gas stream flows inside the rotor from the bottom to the rotor cap and leaves the rotor via an annular gap in the cap. This equipment allows in situ MAS NMR investigations under continuous-flow conditions, at normal pressure and in a temperature range that is limited by the heating system of the MAS NMR probe.

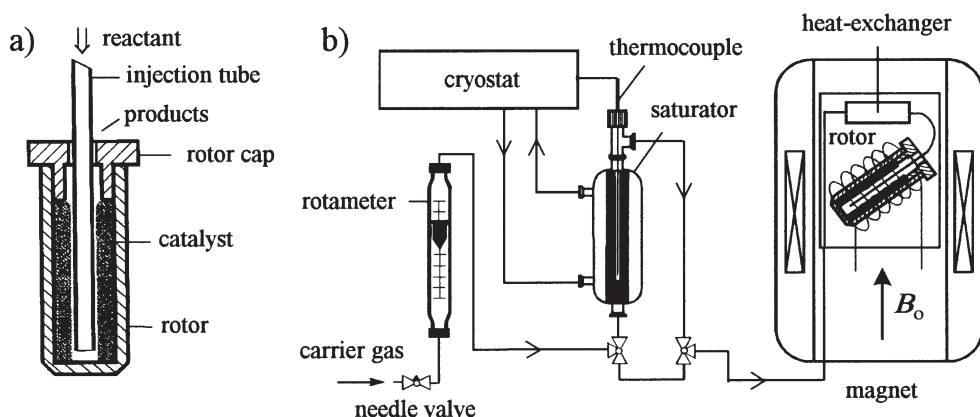


Fig. 47 a, b. Scheme of **a** the in situ MAS rotor and **b** the gas supply system which allows the passing of a carrier gas flow loaded with reactants through the MAS rotor [353, 354]

7.2

Assignment of In Situ NMR Spectra

Typically, molecules adsorbed on zeolites are characterized by a wide range of thermal correlation times reflecting the differences in their molecular mobilities. Some molecules or species reside in the gas phase or are involved in a rapid exchange with adsorbed molecules. Other species are strongly adsorbed on the zeolite surface or are entrapped in small cavities. In addition, the formation of coke results in large immobile complexes. Homonuclear (^1H - ^1H) and heteronuclear (^{13}C - ^1H) magnetic dipole-dipole interactions of immobile species are the main reasons for a line broadening of ^1H and ^{13}C NMR signals. Since the mobility of all of these species increases with increasing temperature, even without application of the MAS technique, narrow lines may be observed [337]. In addition, proton decoupling during the acquisition of ^{13}C NMR signals removes residual dipolar ^{13}C - ^1H interactions yielding solution-like conditions.

The high mobility of reactant molecules in zeolites and their variation have practical consequences on the application of the cross-polarization technique (see Sect. 2.3.1). The inefficiency of the CP technique for mobile compounds make the corresponding signals less intense than those of rigid species [42] resulting in only semiquantitative in situ ^1H - ^{13}C CP/MAS NMR spectra. On the other hand, CP is advantageous to avoid saturation by long ^{13}C -spin-lattice relaxation times of rigid compounds. The comparison of Bloch decay spectra and CP/MAS NMR spectra as well as the study of T_{CP} relaxation times is a method suitable for obtaining information useful for the signal assignment [335].

The most important parameter in ^{13}C MAS NMR spectroscopy is the isotropic chemical shift. While molecules that are strongly bonded to the zeolite framework have a residual ^{13}C MAS NMR line broadening of about 5 ppm, weakly adsorbed species have a line broadening of less than 1 ppm. Using an internal standard, e.g., methane, ^{13}C NMR shifts are derived with an accuracy of better

than 0.2 ppm. Typically, the ^{13}C NMR positions of adsorbates in zeolites are shifted 2–5 ppm downfield from their values in solution (see [355–357]). Therefore, it is useful to verify signal assignments by determining the ^{13}C NMR shifts of authentic compounds adsorbed in zeolites. This is particularly advisable if the adsorbate compound is protonated by acidic centers or if it is involved in the formation of surface complexes (see [358–360]). Data for protonation shifts of, e.g., amines [361, 362], phosphines [363], and phosphine oxides [364] are given in the literature.

Additional information which is useful for signal assignment can be derived by two-dimensional NMR experiments. One of these techniques is the 2D J -resolved ^{13}C MAS NMR which allows the separation of the $J(^{13}\text{C}-^1\text{H})$ coupling along the F1-dimension for signals at different isotropic chemical shifts in the F2-dimension [365, 366]. In 2D J -resolved spectra, the ^{13}C NMR signals of CH_n groups with particular values of n are gained by counting the number of lines ($n+1$) in the corresponding multiplet signal along the F1-dimension. Figure 48b shows the contour plot of the 2D J -resolved ^{13}C MAS NMR spectrum of ethylene converted on

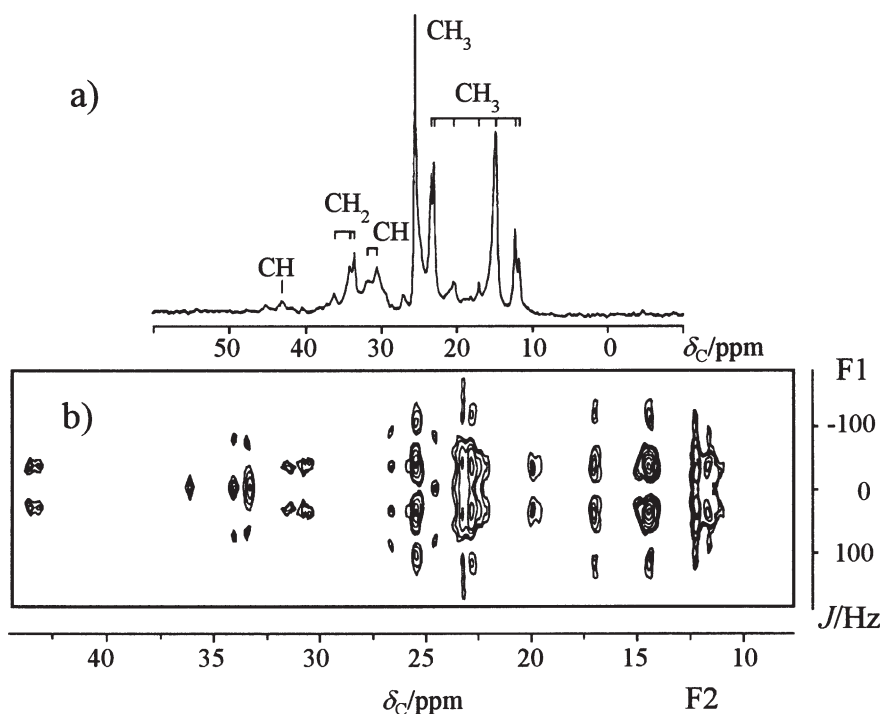


Fig. 48a, b. a One-dimensional ^{13}C MAS NMR spin-echo spectrum for the products of ethylene conversion on zeolite HZSM-5 at 373 K and b the contour plot of the 2D J -resolved solid-state ^{13}C MAS NMR spectrum of this sample [365]. Because of high power proton decoupling during the second half of the evolution time t_1 , the observed values of $J(^{13}\text{C}-^1\text{H})$ coupling constants are equal to half of the real $J(^{13}\text{C}-^1\text{H})$

HZSM-5 at 373 K [365]. The one-dimensional spin-echo spectrum of this sample is depicted in Fig. 48a. From the 2D spectrum it can be seen that all signals at chemical shifts between 11.7 ppm and 27.0 ppm are quartets (except the signal at 20.4 ppm) with a $J(^{13}\text{C}-^1\text{H})$ coupling of about 140 Hz corresponding to CH_3 groups. The signals at 30.6 ppm, 31.5 ppm, and 43.2 ppm are doublets and are due to CH groups. Finally, the triplet structure of the signals at 33.6 ppm and 34.1 ppm points to CH_2 signals.

7.3

Applications of In Situ NMR Spectroscopy

In the last decade a number of in situ NMR spectroscopic studies on chemical reactions catalyzed by zeolites have been reported. Surveys of the most important static in situ NMR [1] and in situ MAS NMR [4, 235] investigations have been published.

An interesting application of in situ NMR spectroscopy is the investigation of reaction mechanisms. As an example, a mechanistic work is demonstrated which is based on the incorporation of a suggested intermediate into a zeolite. For the MTG reaction (methanol-to-gasoline) a mechanism was proposed which involves CO as either an intermediate [341] or catalyst [367]. Since during the MTG reaction CO is often formed in low concentrations, the above-mentioned arguments were reasonable. Therefore, the role of CO was investigated after generating this molecule by thermal decomposition of formic acid in HZSM-5 [368]. Parallel in situ NMR investigations with and without CO yielded no catalytic effect. The in situ ^{13}C MAS NMR experiments shown in Fig. 49 were carried out to clarify the role of CO. The spectrum depicted in Fig. 49a was recorded after adsorption of ^{13}C -enriched methanol and ^{13}C -enriched formic acid adsorbed on HZSM-5. After heating the sample for 5 min at 523 K, formation of carbon monoxide (184 ppm) by decomposition of formic acid (165 ppm) can be observed (Fig. 49b). Methanol (51 ppm) and dimethyl ether (62 ppm) react to hydrocarbons while CO is partially converted to CO_2 (126 ppm) via the water-gas shift reaction. The integral intensity of CO and CO_2 was found to be constant. Hence, CO is not incorporated into the reaction products of the methanol conversion, which indicates that it does not act as an intermediate. The same result was derived by in situ NMR experiments on ^{13}C -enriched formic acid adsorbed on dehydrated HZSM-5 together with unlabeled methanol. The corresponding spectrum recorded at 523 K is depicted in Fig. 49e. It shows that no ^{13}C -labeled carbons were incorporated into the hydrocarbon products appearing at chemical shifts between -10 ppm and 50 ppm.

As an example for in situ NMR investigations carried out under continuous-flow conditions, the ^{13}C MAS NMR spectra of propan-2-ol conversion on zeolite Y at a temperature of 393 K are shown in Fig. 50 [354]. The catalyst used was a dehydrated zeolite 73LaNaY ($n_{\text{Si}}/n_{\text{Al}}=2.6$). Starting at the time $t=0$, a continuous flow of ^{13}C -enriched propan-2-ol with a modified residence time of $W/F_{\text{p-2-ol}}=450$ g h mol^{-1} was passed through the sample using the injection equipment depicted in Fig. 47. After a reaction time of 30 min (Fig. 50a), signals from the coke precursors emerged at chemical shifts between 20 ppm and 45 ppm. In addition, signals

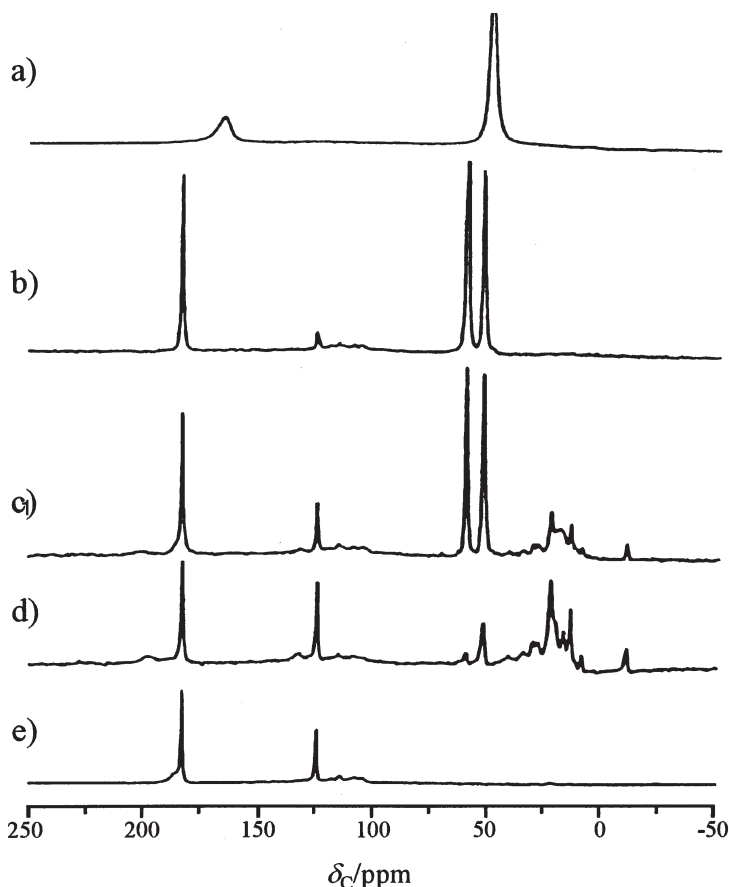


Fig. 49. In situ ^{13}C MAS NMR spectra of ^{13}C -enriched methanol and ^{13}C -enriched formic acid (a–d) and of unlabeled methanol and ^{13}C -enriched formic acid (e) adsorbed on zeolite HZSM-5, recorded at a 298 K, b after 5 min at 523 K, c after 150 min at 523 K, and d after 210 min at 523 K. e This spectrum corresponds to that in d, but was recorded with unlabelled methanol [368]

of propan-2-ol (65 ppm) with a shoulder of diisopropyl ether (70 ppm) and a line of acetone (220 ppm) were observed. The shoulder at 70 ppm indicates a preferential conversion of propan-2-ol to diisopropyl ether, while only a weak signal at 135 ppm indicates the formation of propene (Fig. 50b, c). The variation in the modified residence time from $W/F_{\text{p-2-ol}}=450 \text{ g h mol}^{-1}$ (Fig. 50c) to $W/F_{\text{p-2-ol}}=140 \text{ g h mol}^{-1}$ (Fig. 50d) resulted in an increase in the signal intensity of propan-2-ol and diisopropyl ether (65–70 ppm) while no change occurred in the signal of propene (135 ppm). In the spectrum recorded after purging the sample for 1 h with dry carrier gas (Fig. 50e), the ^{13}C MAS NMR signals of diisopropyl ether and propan-2-ol were absent, while the coke precursors could be observed with the same intensities as before indicating that these compounds were entrapped in zeolite cages. The signal at 220 ppm was decreased by a factor of two. Therefore,

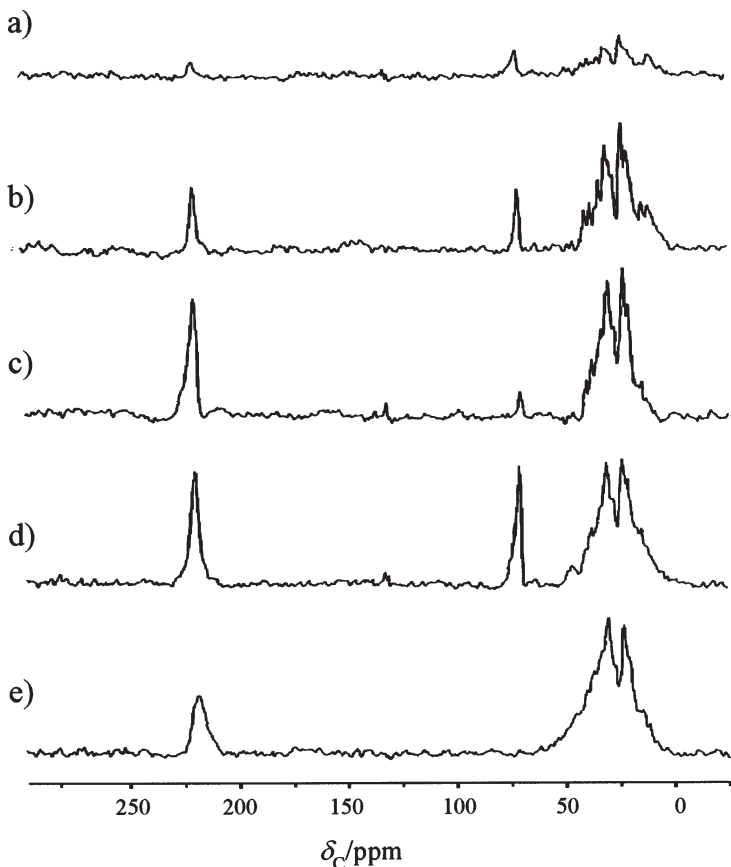


Fig. 50. In situ ^{13}C MAS NMR spectroscopy of zeolite LaNaY recorded at $T=393\text{ K}$ under a continuous flow of ^{13}C -enriched propan-2-ol with a modified residence time of $W/F_{\text{p-2-ol}}=450\text{ g h mol}^{-1}$ after reaction times of **a** 30 min, **b** 2.5 h, and **c** 7.0 h, with a modified residence time of $W/F_{\text{p-2-ol}}=140\text{ g h mol}^{-1}$ after a reaction time of **d** 1.0 h, and **e** after purging the sample with dry carrier gas for 1.0 h [354]

this signal was assigned to strongly surface-bonded acetone that slowly desorbed from the zeolite at 393 K (Fig. 50e) rendering its detection by chromatographic methods difficult.

8

References

1. Engelhardt G, Michel D (1987) High-resolution solid-state NMR of silicates and zeolites, Wiley, Chichester
2. Fyfe CA, Kokotailo GT (1994) Solid state NMR investigation of zeolites and related materials. In: Maciel GE (ed) Nuclear magnetic resonance in modern technology, NATO ASI series C, vol 447, Kluwer Academic Publishers, Dordrecht, Boston, London, p 447

3. Pfeifer H (1994) NMR of solid surfaces, NMR basic principles and progress, vol 31. Springer, Berlin, p 31
4. Pfeifer H, Ernst H (1994) *Annu Rep NMR Spectrosc* 28:91
5. Brunner E (1995) *J Mol Struct* 355:61
6. Hunger M (1996) *Solid State Nucl Magn Reson* 6:1
7. Abragam A (1962) *The principles of nuclear magnetism*. Clarendon Press, Oxford
8. Haeberlen U (1976) *High resolution NMR in solids*. Academic Press, New York
9. Slichter CP (1978) *Principles of magnetic resonance*, 2nd edn. Springer, Berlin
10. Mehring M (1983) *Principles of high-resolution NMR in solids*, 2nd edn. Springer, Berlin
11. Pake GE (1948) *J Chem Phys* 16:327
12. Freude D, Haase J (1993) *Quadrupole effects in solid-state nuclear magnetic resonance. NMR basic principles and progress*, vol 29. Springer, Berlin, p 1
13. Ostroff ED, Waugh JS (1966) *Phys Rev Lett* 16:1096
14. Haeberlen U, Waugh JS (1968) *Phys Rev* 175:453
15. Mansfield P, Ware D (1968) *Phys Rev* 168:318
16. Andrew ER, Bradbury A, Eades RG (1958) *Nature (London)* 182:1659
17. Maricq MM, Waugh JS (1979) *J Chem Phys* 70:3300
18. Brunner E, Freude D, Gerstein BC, Pfeifer H (1990) *J Magn Reson* 90:90
19. Brunner E, Fenzke D, Freude D, Pfeifer H (1990) *Chem Phys Lett* 169:591
20. Wind RA (1991), *Solid-state NMR of spin-1/2 nuclei*. In: Popov AI, Hallenga K (eds) *Modern NMR techniques and their application in chemistry*. Marcel Dekker, New York, p 125
21. Brunner E (1990) *J Chem Soc Faraday Trans* 86:3957
22. Brunner E (1993) *J Chem Soc Faraday Trans* 89:165
23. Schnabel B, Haubenreisser U, Scheler G, Müller R (1976) *Proc 19th Congr AMPERE, Heidelberg*, p 441
24. Pembleton RG, Ryan LM, Gerstein BC (1977) *Rev Sci Instrum* 48:1286
25. Ryan LM, Taylor RE, Paff AJ, Gerstein BC (1980) *J Chem Phys* 72:508
26. Scheler G, Haubenreisser U, Rosenberger H (1981) *J Magn Reson* 44:134
27. Andrew ER, Jasinski A (1971) *J Phys C: Solid St Phys* 4:391
28. Fenzke D, Gerstein BC, Pfeifer H (1992) *J Magn Reson* 98:469
29. Boehm J, Fenzke D, Pfeifer H (1983) *J Magn Reson* 55:197
30. Olivieri AC, Frydman L, Diaz LE (1987) *J Magn Reson* 75:50
31. Olivieri AC (1989) *J Magn Reson* 81:201
32. Olivieri AC (1993) *J Magn Reson A* 101:313
33. Alla M, Lippmaa E (1982) *Chem Phys Lett* 87:30
34. Samoson A, Lippmaa E, Pines A (1988) *Mol Phys* 65:1013
35. Samoson A, Lippmaa E (1989) *J Magn Reson* 84:410
36. Samoson A, Pines A (1989) *Rev Sci Instrum* 60:3239
37. Chmelka BF, Mueller KT, Pines A, Stebbins J, Wu Y, Zwanziger JW (1989) *Nature (London)* 42:339
38. Mueller KT, Sun BQ, Chingas GC, Zwanziger JW, Terao T, Pines A (1990) *J Magn Reson* 86:470
39. Mueller KT, Wooten EW, Pines A (1991) *J Magn Reson* 92:620
40. Pines A, Gibby MG, Waugh JS (1973) *J Chem Phys* 59:569
41. Schaefer J, Stejskal (1976) *J Am Chem Soc* 98:1031
42. Michel D, Engelke F (1994) *Cross-polarization, relaxation times and spin-diffusion in rotating solids. NMR basic principles and progress*, vol 32. Springer, Berlin, p 69
43. Hartmann SR, Hahn EL (1962) *Phys Rev* 128:2042
44. Fyfe CA, Mueller KT, Wong-Moon KC (1994) *Cross-polarization processes involving less common pairs of nuclei*. In: Maciel GE (ed) *Nuclear magnetic resonance in modern technology*, NATO ASI series C, vol 447. Kluwer Academic Publishers, Dordrecht, p 447
45. Schulze D, Ernst H, Fenzke D, Meiler W, Pfeifer H (1990) *J Phys Chem* 94:3499
46. Opella SJ, Frey MH (1979) *J Am Chem Soc* 101:5854
47. Kaplan DE, Hahn EL (1958) *J Phys Radium* 19:821

48. Wang P-K, Slichter CP, Sinfelt JH (1984) *Phys Rev Lett* 53:82
49. Hahn EL (1950) *Phys Rev* 80:580
50. Gullion T, Schaefer J (1989) *J Magn Reson* 81:196
51. Hing AW, Vega S, Schaefer J (1992) *J Magn Reson* 96:205
52. Ernst RR, Bodenhausen G, Wokaun A (1987) *Principles of nuclear magnetic resonance in one and two dimensions*. Clarendon Press, Oxford
53. Fernandez C, Amoureux JP, Chezeau JM, Delmotte L, Kessler H (1996) *Microporous Mater* 6:331
54. Rocha J, Lourenco JP, Ribeiro MF, Fernandez C, Amoureux JP (1997) *Zeolites* 19:156
55. Amoureux JP, Bauer F, Ernst H, Fernandez C, Freude D, Michel D, Pingel UT (1998) *Chem Phys Lett* 285:10
56. Klinowski J (1989) *Colloids Surf* 36:133
57. Engelhardt G, Koller H (1994) ²⁹Si NMR of inorganic solids. In: Diehl P, Fluck E, Günter H, Kosfeld R, Seelig J (eds) *Solid-state NMR II: inorganic matter*. Springer, Berlin, Heidelberg, New York, p 1
58. Klinowski J (1993) *Anal Chim Acta* 283:929
59. Stoecker M (1994) *Stud Surf Sci Catal* 85:429
60. Breck DW (1974) *Zeolite molecular sieves*. John Wiley, New York
61. Wilson ST, Lok BM, Messina CA, Cannan TR, Flannigen EM (1982) *J Am Chem Soc* 104:1146
62. Meier WM, Olson DH (1992) *Atlas of zeolite structure types*. Butterworths, Sevenoaks
63. Flanigen EM, Lok BM, Patton RL, Wilson ST (1986) *Pure Appl Chem* 58:1351
64. Cambor MA, Davis ME (1994) *J Phys Chem* 98:13151
65. Fricke R, Kosslick H, Tuan VA, Grohman I, Pilz W, Storek W, Walther G (1994) *Stud Surf Sci Catal* 83:57
66. Tuel A (1995) *Zeolites* 15:236
67. Engelhardt G, Lohse U, Samoson A, Maegi M, Tarmak M, Lippmaa E (1982) *Zeolites* 2:59
68. Bradley SM, Howe RT (1995) *Microporous Mater* 4:131
69. Rocha J, Lin Z, Ferreira A, Anderson MW (1995) *J Chem Soc Chem Commun* 867
70. Melchior MT, Vaughan DEW, Pictroski CF (1995) *J Phys Chem* 99:6128
71. Thomas JM, Klinowski J, Ramdas S, Hunter BK, Tennakoon DTB (1983) *Chem Phys Lett* 102:158
72. Radeaglia R, Engelhardt G (1985) *Chem Phys Lett* 114:28
73. Smith JV, Blachwell CS (1983) *Nature (London)* 303:223
74. Engelhardt G, Radeaglia R, Lohse U, Samoson A, Lippmaa E (1985) *Z Chem* 25:253
75. Engelhardt G, Luger S, Buhl JC, Felsche J (1989) *Zeolites* 9:182
76. Fyfe CA, Feng Y, Grondey H (1993) *Microporous Mater* 1:393
77. Engelhardt G, van Koningsveld H (1990) *Zeolites* 10:650
78. Fyfe CA, Kennedy GJ, DeSchutter CT, Kokotailo GT (1984) *J Chem Soc Chem Commun* 541
79. Fyfe CA, Strobl H, Kokotailo GT, Kennedy GJ (1988) *J Am Chem Soc* 110:3373
80. Tuel A, Ben Taarit Y (1992) *J Chem Soc Chem Commun* 1578
81. Chao KJ, Chern JY (1989) *J Phys Chem* 93:1401
82. Hunger M, Engelhardt G, Weitkamp J (1995) *Microporous Mater* 3:497
83. Fyfe CA, Gies H, Feng Y (1989) *J Chem Soc Chem Commun* 1240
84. Fyfe CA, Gies H, Feng Y (1989) *J Am Chem Soc* 111:7702
85. Fyfe CA, Feng Y, Gies H, Grondey H, Kokotailo GT (1990) *J Am Chem Soc* 112: 3264
86. Fyfe CA, Grondey H, Feng Y, Kokotailo (1990) *Chem Phys Lett* 173:211
87. Fyfe CA, Grondey H, Feng Y, Kokotailo (1990) *J Am Chem Soc* 112:8812
88. Fyfe CA, Gies H, Feng Y, Grondey H (1990) *Zeolites* 10:278
89. Fyfe CA, Grondey H, Feng Y, Kokotailo GT, Ernst S, Weitkamp J (1992) *Zeolites* 12:50
90. Rocha J, Carr SW, Klinowski J (1991) *Chem Phys Lett* 187:401
91. Lippmaa E, Samoson A, Maegi M (1986) *J Am Chem Soc* 108:1730
92. Jacobsen HS, Norby P, Bildsøe, Jakobsen HJ (1989) *Zeolites* 9:491
93. Klinowski J, Anderson MW, Thomas JM (1983) *J Chem Soc Chem Commun* 525

94. Massiani P, Fajula F, Figueras F (1988) *Zeolites* 8:332
95. Hunger M, Ernst S, Weitkamp J (1995) *Zeolites* 15:188
96. Samoson A, Lippmaa E (1983) *Phys Rev B* 28:6565
97. Samoson A, Lippmaa E (1983) *Chem Phys Lett* 100:205
98. Man PP (1986) *J Magn Reson* 76:78
99. Man PP, Klinowski J (1988) *J Magn Reson* 77:148
100. Klinowski J, Thomas JM, Fyfe CA, Gobbi GC (1982) *Nature (London)* 296:533
101. Maxwell IE, van Erp WA, Hays GR, Couperus T, Huis R, Clague DH (1982) *J Chem Soc Chem Commun* 523
102. Freude D, Froehlich T, Hunger M, Pfeifer H, Scheler G (1983) *Chem Phys Lett* 98: 263
103. Brunner E, Ernst H, Freude D, Hunger M, Krause CB, Prager D, Reschetilowski W, Schwieger W, Bergk KH (1989) *Zeolites* 9:282
104. Reschetilowski W, Einicke WD, Jusek M, Freude D, Hunger M, Klinowski J (1989) *Appl Catal* 56:L15
105. Rocha J, Klinowski J (1991) *J Chem Soc Chem Commun* 1121
106. Ernst H, Freude D, Wolf I (1993) *Chem Phys Lett* 212:588
107. Freude D, Ernst H, Wolf I (1994) *Solid State Nucl Magn Reson* 3:271
108. Ernst H, Freude D, Pfeifer H, Wolf I (1994) *Stud Surf Sci Catal* 84:381
109. Hunger M, Horvath T, Engelhardt G, Karge HG (1995) *Stud Surf Sci Catal* 94:756
110. Hunger M, Horvath T (1995) *Ber Bunsenges Phys Chem* 99:1316
111. Kunwar AC, Turner GL, Oldfield E (1986) *J Magn Reson* 69:124
112. Ghose S, Tsang T (1973) *Am Mineral* 58:748
113. Engelhardt G, Veeman W (1993) *J Chem Soc Chem Commun* 622
114. Engelhardt G, Koller H, Sieger P, Depmeier W, Samoson A (1992) *Solid State Nucl Magn Reson* 1:127
115. Wu Y, Chmelka BF, Pines A, Davis ME, Grobet PJ, Jacobs PA (1991) *Nature (London)* 346:550
116. Chmelka BF, Wu Y, Jelinek R, Davis ME, Pines A (1991) *Stud Surf Sci Catal* 69:435
117. Rocha J, Liu X, Klinowski J (1991) *Chem Phys Lett* 182:531
118. Grobet PJ, Samoson A, Gerts H, Martens JA, Jacobs PA (1991) *J Phys Chem* 95: 9620
119. Jelinek R, Chmelka BF, Wu Y, Davis ME, Ulan JG, Gronsky R, Pines A (1992) *Catal Lett* 15:65
120. Peeters MPJ, de Haan JW, van de Ven LJM, van Hooff JHC (1992) *J Chem Soc Chem Commun* 1560
121. Peeters MPJ, van de Ven LJM, de Haan JW, van Hooff JHC (1993) *J Phys Chem* 97: 8254
122. Peeters MPJ, de Haan JW, van de Ven LJM, van Hooff JHC (1993) *J Phys Chem* 97: 5363
123. Jaenchen J, Peeters MPJ, de Haan JW, van de Ven LJM, van Hooff JHC (1993) *J Phys Chem* 97:12042
124. McCusker LB, Baerlocher Ch (1991) *Zeolites* 11:308
125. Blackwell CS, Patton RL (1984) *J Phys Chem* 88:6135
126. Freude D, Ernst H, Hunger M, Pfeifer H (1988) *Chem Phys Lett* 143:477
127. Jahn E, Mueller D, Becker K (1990) *Zeolites* 10:151
128. Zibrowius B, Lohse U, Richter-Mendau J (1991) *J Chem Soc Faraday Trans* 87:1433
129. Zibrowius B, Loeffler E, Hunger M (1992) *Zeolites* 12:167
130. Zibrowius B, Lohse U (1992) *Solid State Nucl Magn Reson* 1:137
131. Borade RB, Clearfield A (1994) *J Mol Catal* 88:249
132. Mueller D, Jahn E, Ladwid G (1984) *Chem Phys Lett* 109:332
133. Barrie PJ, Klinowski J (1989) *J Phys Chem* 93:5972
134. Stoecker M, Akporiaye D, Lillerud KP (1991) *Appl Catal* 69:L7
135. Davis ME, Montes C, Hathaway PE, Garces J, Crowder C (1989) *Stud Surf Sci Catal* 69:199
136. Davis ME, Montes C, Hathaway PE, Arhancet JP, Hasha DL, Garces JM (1989) *J Am Chem Soc* 111:3919
137. Grobet PJ, Martens JA, Balakrishnan I, Mertens M, Jacobs PA (1989) *Appl Catal* 56:L21
138. Maistriau L, Gabelica Z, Derouane EG, Vogt ETC, van Oene J (1991) *Zeolites* 11: 583
139. Akporiaye D, Stoecker M (1992) *Zeolites* 12:351

140. van Eck ERH, Veeman WS (1993) *J Am Chem Soc* 115:1168
141. Derouane EG, Maistriau L, Gabilica Z, Tuel AB, Nagy J, Ballmoos R (1989) *Appl Catal* 51:L 13
142. Perez JO, Chu PJ, Clearfield A (1991) *J Phys Chem* 95:9994
143. Fyfe CA, Grondy H, Mueller KT, Wong-Moon KC, Markus T (1992) *J Am Chem Soc* 114:5876
144. Fyfe CA, Mueller KT, Grondy H, Wong-Moon KC (1993) *J Phys Chem* 97:13484
145. Rocha J, Kolodziejski W, He H, Klinowski J (1992) *J Am Chem Soc* 114:4884
146. He H, Kolodziejski W, Klinowski J (1992) *Chem Phys Lett* 200:83
147. Merrouche A, Patarin J, Kessler H, Soulard M, Delmotte L, Guth JL, Joly JF (1992) *Zeolites* 12:226
148. Zibrowius B, Anderson MW, Schmidt W, Schüth FF, Aliev AE, Harris KDM (1993) *Zeolites* 13:607
149. Meyer zu Altenschildesche H, Muhr HJ, Nesper R (1993) *Microporous Mater* 1:257
150. Estermann M, McCusker LB, Baerlocher C, Merrouche A, Kessler H (1991) *Nature (London)* 352:320
151. Barr TL, Klinowski J, He H, Alberti K, Mueller G, Lercher J (1993) *Nature (London)* 365:429
152. Bradley SM, How RF, Kydd RA (1993) *Magn Reson Chem* 31: 883
153. Bayense CR, van Hooff JHC, Kentgens APM, de Haan JW, van de Ven LJM (1989) *J Chem Soc Chem Commun* 1292
154. Bedard RL, Bowes CL, Coombs N, Holmes AJ, Jiang T, Kirkby SJ, Macdonald PM, Malek AM, Ozin GA, Petrov S, Plavac N, Ramik RA, Steele MR, Young D (1993) *J Am Chem Soc* 115:2300
155. Kentgens APM, Bayense CR, van Hooff JHC, de Haan JW, van de Ven LJM (1991) *Chem Phys Lett* 176:399
156. Bradley SM, Howe RF, Hanna JV (1993) *Solid State Nucl Magn Reson* 2:37
157. Gabelica Z, Nagy JB, Bodart P, Debras G (1984) *Chem Lett* 1059
158. Scholle KFMGJ, Veeman WS (1985) *Zeolites* 5:118
159. Brunner E, Freude D, Hunger M, Pfeifer H, Reschetilowski W, Unger B (1988) *Chem Phys Lett* 148:226
160. Kessler H, Chezeau JM, Guth JL, Strub H, Coudurier G (1987) *Zeolites* 7:360
161. Axon SA, Klinowski J (1994) *J Phys Chem* 98:1929
162. Timken HKC, Turner GL, Gilson JP, Welsh LB, Oldfield E (1986) *J Am Chem Soc* 108:7236
163. Timken HKC, Janes N, Turner GL, Lambert SL, Welsh LB, Oldfield E (1988) *J Magn Reson* 76:106
164. Kyung H, Timken C, Janes N, Turner GL, Lambert SL, Welsh LB, Oldfield E (1986) *J Am Chem Soc* 108:7236
165. Lippmaa E, Maegi M, Samoson A, Engelhardt G, Grimmer AR (1980) *J Am Chem Soc* 102:4889
166. Fyfe CA, Kennedy GJ, Kokotailo GT, DeSchutter CT (1984) *J Chem Soc Chem Commun* 1093
167. Engelhardt G, Lohse U, Lippmaa E, Tarmak M, Maegi M (1981) *Z Anorg Allg* 482: 49
168. Jarman RH, Jacobsen AJ, Melchior MT (1984) *J Phys Chem* 88:5748
169. Hays GR, van Erp WV, Alma NCM, Couperus PA, Huis R, Wilson AE (1984) *Zeolites* 4:377
170. Engelhardt G, Fahlke B, Maegi M, Lippmaa E (1985) *Z Phys Chem (Leipzig)* 266: 239
171. Samoson A, Lippmaa E (1988) *J Magn Reson* 79:255
172. Wu Y, Sun BQ, Pines A, Samoson A, Lippmaa E (1990) *J Magn Reson* 89:297
173. Lechert H, Basler WD, Henneke HW (1975) *Ber Bunsenges Phys Chem* 79:563
174. Schimiczek B, Greth R, Boddenberg B (1994) *Mol Phys* 82:369
175. West GW (1981) *Zeolites* 1:150
176. Herreros B, Man PP, Manoli JM, Fraissard J (1992) *J Chem Soc Chem Commun* 464
177. Hunger M, Engelhardt G, Weitkamp J (1994) *Stud Surf Sci Catal* 84:725
178. Kim JC, Li HX, Chen CY, Davis ME (1994) *Microporous Mater* 2:413
179. Hathaway PE, Davis ME (1989) *J Catal* 119:497
180. Chu PJ, Gerstein BC, Nunan J, Klier K (1987) *J Phys Chem* 91:3588

181. Schlenker JL, Pluth JJ, Smith JV (1979) *Mater Res Bull* 14:751
182. Torgeson DR, Barnes RG (1974) *J Chem Phys* 62:3968
183. Ahn MK, Iton LE (1989) *J Phys Chem* 93:4924
184. Ahn MK, Iton LE (1991) *J Phys Chem* 95:4496
185. Tokunishi T, Mattingly M, Iton LE, Ahn MK (1989) *J Phys Chem* 93:5584
186. Subramanian V, Seff K (1980) *J Phys Chem* 84:2928
187. Koller H, Burger B, Schneider AM, Engelhardt G, Weitkamp J (1995) *Microporous Mater* 5:219
188. Welsh LB, Lambert SL (1988) Analysis of cation position in ion-exchanged Y zeolites by ^{23}Na NMR. In: Flank WH, Whyte TE (eds) *Perspectives in molecular sieve science*, ACS Symp. Ser. 368. American Chemical Society, Washington DC, p 33
189. Welsh LB, Lambert SL (1989) Characterization of Y zeolites by ^{23}Na magic-angle-spinning NMR spectroscopy. In: Bradley SA, Gattuso MJ, Bertolacini RJ (eds) *Characterization and catalyst development – an interactive approach*, ACS Symp. Ser. 411. American Chemical Society, Washington DC, p 262
190. Beyer HK, Pál-Borbély G, Karge HG (1993) *Microporous Mater* 1:67
191. Challoner R, Harris RK (1991) *Zeolites* 11:265
192. Lin CF, Chao KJ (1991) *J Phys Chem* 95:9411
193. Tijink GA, Janssen R, Veeman WS (1987) *J Am Chem Soc* 109:7301
194. Hunger M, Engelhardt G, Koller H, Weitkamp J (1993) *Solid State Nucl Magn Reson* 2:111
195. Koller H, Engelhardt G, Kentgens APM, Sauer J (1994) *J Phys Chem* 98:1544
196. Jelinek R (1992) *J Am Chem Soc* 114:4907
197. Mortier WJ (1983) *Compilation of extra-framework sites in zeolites*. Butterworth, Guildford, p 26
198. Lievens JL, Verduijn JP, Bons AJ, Mortier WJ (1992) *Zeolites* 12:699
199. Massiot D, Bessada C, Coutures JP, Taulelle F (1990) *J Magn Reson* 90:231
200. Verhulst HAM, Welters WJJ, Vorbeck G, van de Ven LJM, de Beer VHJ, van Santen RA, de Haan JW (1994) *J Chem Soc Chem Commun* 639
201. Feuerstein M, Hunger M, Engelhardt G (1996) *Solid State Nucl Magn Reson* 7:95
202. Mortier WJ, Van den Bossche E, Uytterhoeven JB (1984) *Zeolites* 4:41
203. Engelhardt G, Hunger M, Koller H, Weitkamp J (1994) *Stud Surf Sci Catal* 84:421
204. Olson DH (1995) *Zeolites* 15:339
205. Rabo JA (1976) *Zeolite chemistry and catalysis*, ACS Monograph 171. Washington, DC
206. Rabo JA, Gajda GJ (1989–1990) *Catal Rev-Sci Eng* 31:385
207. Venuto PB, Habib ET (1978) *Fluid catalytic cracking with zeolite catalysts*. Marcel Dekker, Inc., New York
208. Venuto PB (1994) *Microporous Mater* 2:297
209. Chen NY, Garwood WE, Dwyer FG (1989) *Selective catalysis in industrial applications*. Marcel Dekker, Inc., New York
210. Freude D, Hunger M, Pfeifer H (1982) *Chem Phys Lett* 91:307
211. Freude D, Hunger M, Pfeifer H, Scheler G, Hoffmann J, Schmitz W (1984) *Chem Phys Lett* 105:427
212. Pfeifer H, Freude D, Hunger M (1985) *Zeolites* 5:274
213. Ward JW (1969) *J Catal* 9:225
214. Ward JW, Hansford RC (1969) *J Catal* 13:364
215. Jirak Z, Vratislav S, Bosacek V (1980) *J Phys Chem Solids* 41:1089
216. Czjzek M, Jobic H, Fitch AN, Voigt T (1992) *J Phys Chem* 96:1535
217. Brunner E (1993) *Microporous Mater* 1:431
218. Freude D, Hunger M, Pfeifer H (1987) *Z Phys Chem (NF)* 152:429
219. Freude D, Hunger M, Pfeifer H, Schwieger W (1986) *Chem Phys Lett* 128:62
220. Hunger M (1991) *Habilitation thesis*, Institute of Physics, University of Leipzig, Leipzig
221. Hunger M, Anderson MW, Ojo A, Pfeifer H (1993) *Microporous Mater* 1:17
222. Sanderson RT (1976) *Chemical bonds and bond energy*. Academic Press, New York
223. Fleischer U, Kutzelnigg W, Bleiber A, Sauer J (1993) *J Am Chem Soc* 115:7833
224. Brunner E, Pfeifer H (1995) *Z Phys Chem* 192:77

225. Makarova MA, Ojo AF, Karim K, Hunger M, Dwyer J (1994) *J Phys Chem* 98:3619
226. Zholobenko VL, Kustov LM, Borovkov VYu, Kazansky VB (1988) *Zeolites* 8:175
227. Woolery GL, Alemany LB, Dessau RM, Chester AW (1986) *Zeolites* 6:14
228. Brunner E, Karge HG, Pfeifer H (1992) *Z Phys Chem* 176:173
229. Engelhardt G, Jerschke HG, Lohse U, Sarv P, Samoson A, Lippmaa E (1987) *Zeolites* 7:291
230. Brunner E, Beck K, Koch M, Pfeifer H, Staudte B, Zscherpel D (1994) *Stud Surf Sci Catal* 84:357
231. Brunner E, Beck K, Heeribout L, Karge HG (1995) *Microporous Mater* 3:395
232. Freude D (1995) *Chem Phys Lett* 235:69
233. Beck LW, Haw JF (1995) *J Phys Chem* 99:1076
234. Koller H, Lobo RF, Burkett SL, Davis ME (1995) *J Phys Chem* 99:12588
235. Berglund B, Vaughan RW (1980) *J Chem Phys* 73:2037
236. Sternberg U, Brunner E (1994) *J Magn Reson A* 108:142
237. Hirschler AE (1963) *J Catal* 2:428
238. Plank CJ (1963), *Proc 3rd Int Congr Catal Amsterdam*, vol 1, p 727
239. Hunger M, Freude D, Pfeifer H, Prager D, Reschetilowski W (1989) *Chem Phys Lett* 163:221
240. Schlunk R (1994) Diploma thesis, Institute of Chemical Technology I, University of Stuttgart, Stuttgart
241. Staudte B, Hunger M, Nimz M (1991) *Zeolites* 11:837
242. Eckert H, Yesinowski JP, Silver LA, Stolper EM (1988) *J Phys Chem* 92:2055
243. Costenoble ML, Mortier WJ, Uytterhoeven JB (1978) *J Chem Soc Faraday Trans 1* 174:466, 477
244. Lohse U, Loeffler E, Hunger M, Stoeckner J, Patzelova V (1987) *Zeolites* 7:11
245. Mastikhin VM, Mudrakovsky IL, Nosov AV (1991) *Prog Nucl Magn Reson Spectrosc* 23:259
246. Kuehl GH (1973) *Proc 3rd Int Conf Molecular Sieves*, Leuven University Press, Leuven, p 227
247. Uytterhoeven JB, Christner LG, Hall WK (1965) *J Phys Chem* 69:2177
248. Brunner E, Ernst H, Freude D, Froehlich T, Hunger M, Pfeifer H (1989) *Stud Surf Sci Catal* 49:623
249. Brunner E, Ernst H, Freude D, Froehlich T, Hunger M, Pfeifer H (1991) *J Catal* 127:34
250. Lago RM, Haag WO, Mikovsky RJ, Olson DH, Hellring SD, Schmitt KD, Kerr GT (1986) *Stud Surf Sci Catal* 28:677
251. Klinowski J, Hamdan H, Corma A, Fornes V, Hunger M, Freude D (1989) *Catal Lett* 3:263
252. Reschetilowski W, Einicke WD, Jusek M, Schoellner R, Freude D, Hunger M, Klinowski J (1989) *Appl Catal* 56:L15
253. Sauer J (1994) *Stud Surf Sci Catal*, 84:2039
254. Schroeder KP, Sauer J, Leslie M, Catlow CRA, Thomas JM (1992) *Chem Phys Lett* 188:320
255. Curtiss LA, Brand H, Nicholas JB, Iton LE (1991) *Chem Phys Lett* 184:215
256. Stevenson RL (1971) *J Catal* 21:113
257. Freude D, Klinowski J, Hamdan H (1988) *Chem Phys Lett* 149:355
258. Freude D, Klinowski J (1988) *J Chem Soc Chem Commun* 1411
259. Kenaston NP, Bell AT, Reimer JA (1994) *J Phys Chem* 98:894
260. Fenzke D, Hunger M, Pfeifer H (1991) *J Magn Reson* 95:477
261. Hunger M, Freude D, Fenzke D, Pfeifer H (1992) *Chem Phys Lett* 191:391
262. Aue WP, Ruben DJ, Griffin RG (1981) *J Magn Reson* 43:472
263. Bull LM, Cheetham AK, Hopkins PD, Powell BM (1993) *J Chem Soc Chem Commun* 1196
264. Koch M, Brunner E, Fenzke D, Pfeifer H, Staudte B (1994) *Stud Surf Sci Catal* 84:709
265. Beran S (1983) *J Phys Chem* 87:55
266. Geerlings P, Tariel N, Botrel A, Lissilour R, Mortier WJ (1984) *J Phys Chem* 88:5752
267. Koch M, Brunner E, Pfeifer H, Zscherpel D (1994) *Chem Phys Lett* 228:501
268. Freude D, Oehme W, Schmiedel H, Staudte B (1974) *J Catal* 32:137; Mestdagh MM, Stone WEE, Fripiat JJ (1975) *J Catal* 38:358

269. Baba T, Inoue Y, Shoji H, Uematsu T, Ono Y (1995) *Microporous Mater* 3:647
270. Sarv P, Tuherm T, Lippmaa E, Keskinen K, Root A (1995) *J Phys Chem* 99:13763
271. Schaefer H (1987) Diploma thesis, University of Leipzig, Leipzig
272. Pfeifer H (1988) *J Chem Soc Faraday Trans 1* 84:3777
273. Engelhardt G, Lohse U, Samoson A, Maegi M, Tarmak M, Lippmaa E (1982) *Zeolites* 2:59
274. Beck LW, White JL, Haw JF (1994) *J Am Chem Soc* 116:9657
275. Brunner E, Freude D, Hunger M, Pfeifer H, Staudte B (1991) *Stud Surf Sci Catal* 69:453
276. Ernst RR (1987) *Chimia* 41:323
277. Freude D, Ernst H, Hunger M, Pfeifer H, Jahn E (1988) *Chem Phys Lett* 143:477
278. Schwieger W, Bergk KH, Freude D, Hunger M, Pfeifer H (1989) *ACS Symp Ser* 398:274
279. Hunger M, Kaerger J, Pfeifer H, Caro J, Zibrowius B, Buelow M, Mostowicz R (1987) *J Chem Soc Faraday Trans 1* 83:3459
280. Hunger M, Freude D, Pfeifer H, Schwieger W (1990) *Chem Phys Lett* 167:21
281. Groenen EJJ, Kortbeek AGTG, Mckay M, Sudmeijer O (1986) *Zeolites* 6:403
282. Ikenoue T, Yoshida N (1988) *J Phys Chem* 92:4883
283. Hunger M, Freude D, Froehlich T, Pfeifer H, Schwieger W (1987) *Zeolites* 7:108
284. Ernst H, Freude D, Hunger M, Pfeifer H, Seiffert B (1987) *Z Phys Chem (Leipzig)* 268:304
285. Jacobs WPJH, de Haan JW, van de Ven LJM, van Santen RA (1993) *J Phys Chem* 97: 10394
286. Roessner F, Steinberg KH, Freude D, Hunger M, Pfeifer H (1988) *Stud Surf Sci Catal* 46:421
287. Jameson AK, Jameson CJ, Gutowsky HS (1970) *J Chem Phys* 53:2310
288. Fraissard J, Ito T (1988) *Zeolites* 8:350
289. Barrie PJ, Klinowski J (1992) *Prog Nucl Magn Reson Spectrosc* 24:91
290. Ripmeester JA, Ratcliffe CI (1990) *J Phys Chem* 94:7652
291. Demarquay J, Fraissard J (1987) *Chem Phys Lett* 136:314
292. Johnson DW, Griffiths L (1987) *Zeolites* 7:484
293. Derouane EG, Nagy JB (1987) *Chem Phys Lett* 137:341
294. Ito T, Fraissard J (1982) *J Chem Phys* 76:5225
295. Davis ME, Saldarriaga C, Montes C, Hanson BE (1988) *J Phys Chem* 92:2557
296. Chen QJ, Fraissard J, Cauffriez, Guth JL (1991) *Zeolites* 11:534
297. Annen MJ, Davis ME, Hanson BE (1990) *Catal Lett* 6:331
298. Cheung TTP, Fu CM, Wharry S (1988) *J Phys Chem* 92:5170
299. Gedeon A, Bonardet JL, Lepetit C, Fraissard J (1995) *Solid State Nucl Magn Reson* 5:201
300. Liu SB, Fung BM, Yang TC, Hong EC, Chang CT, Shih PC, Tong FH, Chen TL (1994) *J Phys Chem* 98:4389
301. Gedeon A, Fraissard J (1994) *Chem Phys Lett* 219:440
302. Kim JG, Kompany T, Ryoo R, Ito T, Fraissard J (1994) *Zeolites* 14:427
303. Chen QJ, Ito T, Fraissard J (1991) *Zeolites* 11:239
304. Shy DS, Chen SH, Lievens J, Liu SB, Chao KJ (1991) *J Chem Soc Faraday Trans* 87:2855
305. Scharpf EW, Creceley RW, Gates BC, Dybowski C (1986) *J Phys Chem* 90:9
306. Shoemaker R, Apple T (1987) *J Phys Chem* 91:4024
307. Bansal N, Dybowski C (1988) *J Phys Chem* 92:2333
308. Ryoo R, Cho SJ, Pak C, Kim JG, Ihm SK, Lee JY (1992) *J Am Chem Soc* 114:76
310. Gedeon A, Bonardet JL, Ito T, Fraissard J (1989) *J Phys Chem* 93:2563
311. Bonardet JL, Gedeon A, Fraissard J (1995) *Stud Surf Sci Catal* 94:139
312. Grosse R, Burmeister R, Boddenberg B, Gedeon A, Fraissard J (1991) *J Phys Chem* 95:2443
313. Gedeon A, Burmeister R, Grosse R, Boddenberg B, Fraissard J (1991) *Chem Phys Lett* 79:191
314. Grosse R, Gedeon A, Watermann J, Fraissard J, Boddenberg B (1992) *Zeolites* 12:909
315. Gedeon A, Bonardet JL, Fraissard J (1993) *J Phys Chem* 97:4254
316. Hartmann M, Boddenberg B (1994) *Microporous Mater* 2:127
317. Boddenberg B, Hartmann M (1993) *Chem Phys Lett* 203:243
318. Springuel-Huet MA, Ito T, Fraissard J (1984) *Stud Surf Sci Catal* 18:13
319. Tway C, Apple T (1992) *J Catal* 133:42
320. Chen QJ, Fraissard J (1992) *J Phys Chem* 96:1814
321. Smith ML, Corbin DR, Abrams L, Dybowski C (1993) *J Phys Chem* 97:7793

322. Smith ML, Corbin DR, Dybowski C (1993) *J Phys Chem* 97:9045
323. Bonardet JL, Barrage MC, Fraissard J (1993) *Proc 9th Int Zeolite Conf Montreal*. Butterworth-Heinemann, Stoneham, p 475
324. Bonardet JL, Barrage MC, Fraissard J (1993) *Am Chem Soc Preprints* 38:628
325. Barrage MC, Bonardet JL, Fraissard J (1990) *Catal Lett* 5:143
326. Bradley SM, Howe RF (1995) *Microporous Mater* 4:131
327. De Menorval LC, Rafferty D, Liu SB, Takegoshi K, Ryoo R, Pines A (1990) *J Phys Chem* 94:27
328. Chmelka BF, Pearson JG, Liu SB, Ryoo R, de Menorval LC, Pines A (1991) *J Phys Chem* 95:303
329. Jameson CJ, Jameson AK, Baello BI, Lim HM (1994) *J Chem Phys* 100:5965
330. Jameson CJ, Jameson AK, Lim HM, Baello BI (1994) *J Chem Phys* 100:5977
331. Jameson CJ, Jameson AK, Gerald R II, de Dios AC (1992) *J Chem Phys* 96:1676
332. Jameson CJ, Jameson AK, Gerald R II, de Dios AC (1992) *J Chem Phys* 96:1690
333. Larsen RG, Shore J, Schmidt-Rohr K, Emsley L, Long H, Pines A (1993) *Chem Phys Lett* 214:220
334. Jameson AK, Jameson CJ, de Dios AC, Oldfield E, Gerald RE II, Turner GL (1995) *Solid State Nucl Magn Reson* 4:1
335. Haw JF (1994) *In situ NMR*. In: Bell AT, Pines A (eds) *NMR techniques in catalysis*. Marcel Dekker, Inc., New York, p 139
336. Ivanova II, Derouane EG (1994) *Stud Surf Sci Catal* 85:357
337. Michel D, Meiler W, Pfeifer H (1975/76) *J Mol Catal* 1:85
338. Anderson MW, Klinowski J (1989) *Nature (London)* 339:200
339. Aronso MT, Gorte RJ, Farneth WE, White D (1989) *J Am Chem Soc* 111:840
340. Anderson MW, Sulikowski B, Barrie PJ, Klinowski J (1990) *J Phys Chem* 94:2730
341. Anderson MW, Klinowski J (1990) *J Am Chem Soc* 112:10
342. Nosov AV, Mastikhin VM, Mashkina AV (1991) *J Mol Catal* 66:73
343. Ernst H, Pfeifer H (1992) *J Catal* 136:202
344. Haw JF, Richardson BR, Oshiro IS, Lazo ND, Speed JA (1989) *J Am Chem Soc* 111: 2052
345. Munson EJ, Murray DK, Haw JF (1993) *J Catal* 141:733
346. Oliver FG, Munson EJ, Haw JF (1992) *J Phys Chem* 96:8106
347. Ernst H, Freude D, Mildner T, Pfeifer H (1994) *Stud Surf Sci Catal* 84:1717
348. Ernst H, Freude D, Mildner T (1994) *Chem Phys Lett* 229:291
349. Ernst H, Freude D, Mildner T, Wolf I (1995) *Z Phys Chem* 189:221
350. Ernst H, Freude D, Mildner T, Wolf I (1995) *Stud Surf Sci Catal* 94:413
351. Ferguson DB, Krawietz TR, Haw JF (1994) *Chem Phys Lett* 229:71
352. Ferguson DB, Krawietz TR, Haw JF (1994) *J Magn Reson Ser A* 109:273
353. Hunger M, Horvath T (1995) *J Chem Soc Chem Commun* 1423
354. Hunger M, Horvath T (1997) *J Catal* 167:187.
355. Munson EJ, Kheir AA, Lazo ND, Haw JF (1992) *J Phys Chem* 96:7740
356. Munson EJ, Kheir AA, Haw JF (1993) *J Phys Chem* 97:7321
357. Murray DK, Chang JW, Haw JF (1993) *J Am Chem Soc* 115:4732
358. Xu T, Munson EJ, Haw JF (1994) *J Am Chem Soc* 116:1962
359. Bosacek V (1995) *Z Phys Chem* 189:241
360. Bosacek V (1993) *J Phys Chem* 97:10732
361. Maciel GE, Haw JF, Chuang IS, Hawkins BL, Early TE, McKay DR, Petrakis L (1983) *J Am Chem Soc* 105:5529
362. Haw JF, Chuang IS, Hawkins BL, Maciel GE (1983) *J Am Chem Soc* 105:7206
363. Lunsford JH, Rothwell WP, Shen W (1985) *J Am Chem Soc* 107:1540
364. Baltusis L, Frye JF, Maciel GE (1986) *J Am Chem Soc* 108:7119
365. Stepanow AG, Zudin VN, Zamaraev KI (1993) *Solid State Nucl Magn Reson* 2:89
366. Anderson MW, Klinowski J (1990) *Chem Phys Lett* 172:275
367. Jackson JE, Bertsch FM (1990) *J Am Chem Soc* 112:9085
368. Munson EJ, Lazo ND, Moellenhoff ME, Haw JF (1991) *J Am Chem Soc* 113:2783

Electron Spin Resonance Spectroscopy

Bert M. Weckhuysen¹ · Ralf Heidler² · Robert A. Schoonheydt²

¹ Departement Anorganische Chemie en Katalyse, Debye Instituut, Universiteit Utrecht, Sorbonnelaan 16, 3508 TB Utrecht, The Netherlands

² Centrum voor Oppervlaktechemie en Katalyse, Departement Interfasechemie, K.U. Leuven, Kasteelpark Arenberg 22, 3001 Heverlee, Belgium

Abstract. The theoretical principles of the ESR technique and its application in the field of molecular sieve science are reviewed. The first part of this chapter focuses on the basic principles and instrumentation of the ESR, ENDOR, ESE and ESEEM techniques. Special attention will be given to spectral simulation and quantitative analysis of ESR spectra. In the second part, the general features of the ESR spectra of transition metal ions and paramagnetic clusters in molecular sieves are presented and discussed. In addition, some remarks will be made about the use of paramagnetic molecules, such as NO.

1	Introduction	296
2	Principles and Practice of ESR	297
2.1	Basic Principles and Magnetic Interactions	297
2.2	Instrumentation and Signal Generation	300
2.3	Quantitative Analysis	304
2.4	Spectrum Simulation	306
2.5	Modern ESR-Related Techniques: ENDOR and Pulsed ESR	307
2.5.1	Electron Nuclear Double Resonance (ENDOR)	308
2.5.2	Electron Spin Echo Spectroscopy (ESE and ESEEM)	310
3	Application of ESR in Molecular Sieve Science	311
3.1	Transition Metal Ions	311
3.1.1	Cu ²⁺	311
3.1.2	Fe ³⁺	317
3.1.3	Cr ⁵⁺ and Cr ³⁺	318
3.1.4	V ⁴⁺	322
3.2	Paramagnetic Clusters and Metallic Particles	323
3.3	Paramagnetic Molecules	328
4	General Conclusions and Outlook	332
5	References	333

1

Introduction

Electron spin resonance (ESR) spectroscopy is a very powerful and sensitive method for the characterization of the electronic structures of materials with unpaired electrons. There is a variety of ESR techniques, each with its own advantages. In continuous wave ESR (CW-ESR), the sample is subjected to a continuous beam of microwave irradiation of fixed frequency and the magnetic field is swept. Different microwave frequencies may be used and they are denoted as S-band (3.5 GHz), X-band (9.25 GHz), K-band (20 GHz), Q-band (35 GHz) and W-band (95 GHz). Other techniques, such as electron nuclear double resonance (ENDOR) and electron spin echo envelope modulation (ESEEM) spectroscopies, record in essence the NMR spectra of paramagnetic species.

Electron spin resonance and related techniques have been applied in molecular sieve science for the characterization of transition metal ions that are present in the lattice and on the surface, coordinated to lattice oxygen atoms or to extra-lattice ligands. The technique is also applied to paramagnetic clusters, mainly of silver and alkaline metals and, in rare cases, to adsorbed paramagnetic molecules such as NO to probe defects and Lewis acidity. Because ESR spectra of transition metal ions are often characterized by interactions which are no longer small compared with the electron Zeeman interaction, one cannot use perturbation theory of the first order to evaluate the spectra. Therefore, extensive spectral simulation is required to extract physically meaningful ESR parameters. Such information is a necessity for a detailed description of the coordination geometry of zeolitic transition metal ions. ESR is also a very sensitive technique, but quantitative analysis can only be done with good standards within 10 to 20% accuracy.

This review deals with both the theoretical and practical aspects of the use of ESR spectroscopy in molecular sieve science. No attempt has been made to compile an exhaustive list of references to all the work that has been published so far. Rather, we have selected what, we feel, are the most important developments and also, where possible, we have drawn examples from our own work. In a first part, the ESR technique and its extensions such as ENDOR and ESEEM, will be highlighted with special emphasis on the principles of the techniques and the instrumental requirements. Attention will also be given to spectral simulation and to quantitative analysis. In a second part, the general features of ESR spectra of transition metal ions in molecular sieves are analyzed. In addition, some remarks will be made on paramagnetic metal clusters and on paramagnetic molecules. The chapter closes with general conclusions and an outlook into the future. For detailed explanations and discussions-in-depth, we refer to several excellent text books [1–9] and review papers [10–14].

2 Principles and Practice of ESR

2.1 Basic Principles and Magnetic Interactions

Electron spin resonance is a magnetic resonance technique, based on the interaction of unpaired electron spins with an external magnetic field. The essential aspects of ESR may be illustrated by considering the hypothetical case of a single isolated electron. This electron is characterized by the quantum number $S = 1/2$ and possesses a magnetic moment:

$$\vec{\mu}_e = -g_e \cdot \beta_e \cdot \vec{S} \quad (1)$$

with $g_e = 2.0023$, the electron g -factor or Landé-factor, $\beta_e = 9.42 \cdot 10^{-24} \text{ J}\cdot\text{T}^{-1}$, the electronic Bohr magneton and \vec{S} , the dimensionless electron spin vector. In a magnetic field, B_0 , there are two energy states for this electron, as illustrated in Fig. 1. This interaction, known as the Zeeman interaction, is expressed by the following Hamiltonian:

$$\bar{H}_{Z1} = -\mu_e \cdot \bar{B} = g_e \cdot \beta_e \cdot B_0 \cdot S_z \quad (2)$$

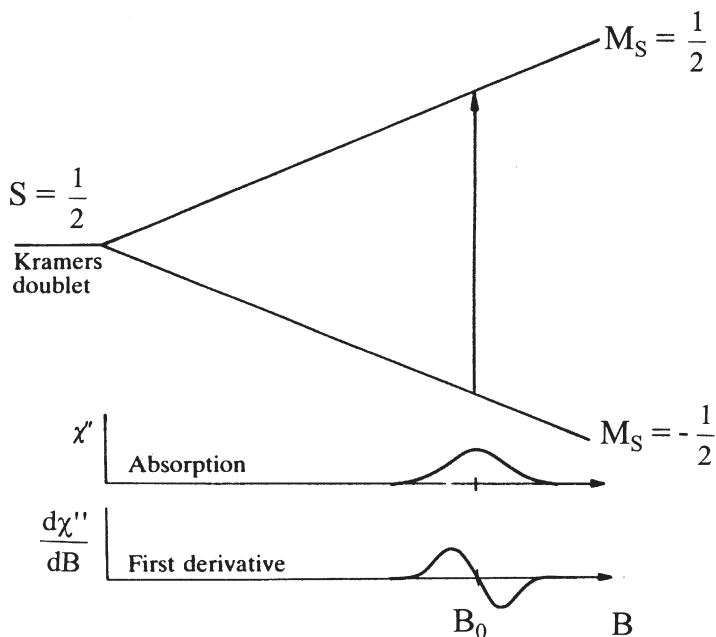


Fig. 1. Energy level diagram for an isolated electron in a magnetic field B and the corresponding absorption spectrum and first derivative ESR spectrum (reprinted from reference [2]. Copyright 1990 Oxford University Press)

Two energy levels evolve, viz. $E_{\beta} = -1/2 g_e \cdot \beta_e \cdot B_0$ and $E_{\alpha} = +1/2 g_e \cdot \beta_e \cdot B_0$, which are almost equally populated. In ESR spectroscopy, the magnetic component of a microwave energy, which is perpendicular to the magnetic field B_0 , induces microwave energy absorption subject to the resonance condition (3) and the selection rule $\Delta M_s = \pm 1$:

$$\Delta E = h \cdot \nu = g_e \cdot \beta_e \cdot B_0 \quad (3)$$

where ν is the microwave frequency.

In real chemical systems, the single unpaired electron is associated with at least one atom and the second contribution to paramagnetism stems from the electron motion in an orbital with orbital angular momentum L . This effect can be described by the following Hamiltonian:

$$\bar{H} = \beta_e \cdot \bar{B} (\bar{L} + g_e \cdot \bar{S}) + \lambda \cdot \bar{L} \cdot \bar{S} = \beta_e \cdot \bar{B} \cdot \bar{g} \cdot \bar{S} \quad (4)$$

with λ , the spin-orbit coupling constant and g , the effective g -value. The orbitals (atomic or molecular) have two effects: (1) spin-orbit coupling and (2) orbital-magnetic field interaction. These effects explain why g is no longer equal to 2.0023 ($=g_e$) and anisotropic. The anisotropy of the \bar{g} -tensor leads to orientation-dependent ESR-spectra for single crystals, but for disordered systems as in the case of molecular sieves, one observes the superposition of spectra of all possible orientations of the magnetic field. Idealized ESR patterns, together with their corresponding absorption profile, are given in Fig. 2. The anisotropy in g is classified into isotropic (one g -value), axial (two g -values) and rhombic (three g -values). The deviation of the principal g -values from the free electron value of 2.0023 carries information about the orbital angular momentum of the electron, i.e. information concerning the electronic structure of the atom or molecules.

The magnetic moment of the electron will also undergo additional interactions with local magnetic fields originating from non-zero nuclear spins. This coupling, known as the hyperfine interaction, is given by:

$$\bar{H}_{HF} = \bar{I} \cdot \bar{A} \cdot \bar{S} \quad (5)$$

with \bar{A} the hyperfine coupling tensor, characterized by three mutually orthogonal principal values A_{xx} , A_{yy} and A_{zz} . The point symmetry of the paramagnetic entity determines whether or not any of the principal axes of g and A are parallel to each other. The different possibilities and the relation with symmetry are summarized in Table 1, together with the generally accepted nomenclature for ESR behavior. The magnetic moment of the electron may also undergo interactions with the local magnetic fields originating from non-zero nuclear spins of atoms in the first coordination sphere around an atom with unpaired electron. This interaction, called superhyperfine splitting, is mostly weak and unresolved.

Some nuclei with nuclear spins $I \geq 1$ possess an electric quadrupole moment eQ because of the non-spherical charge distribution in the nucleus. The interaction with such nuclei may be expressed as:

$$\bar{H}_Q = \bar{I} \cdot \bar{Q} \cdot \bar{I} \quad (6)$$

with \bar{Q} the quadrupole coupling tensor.

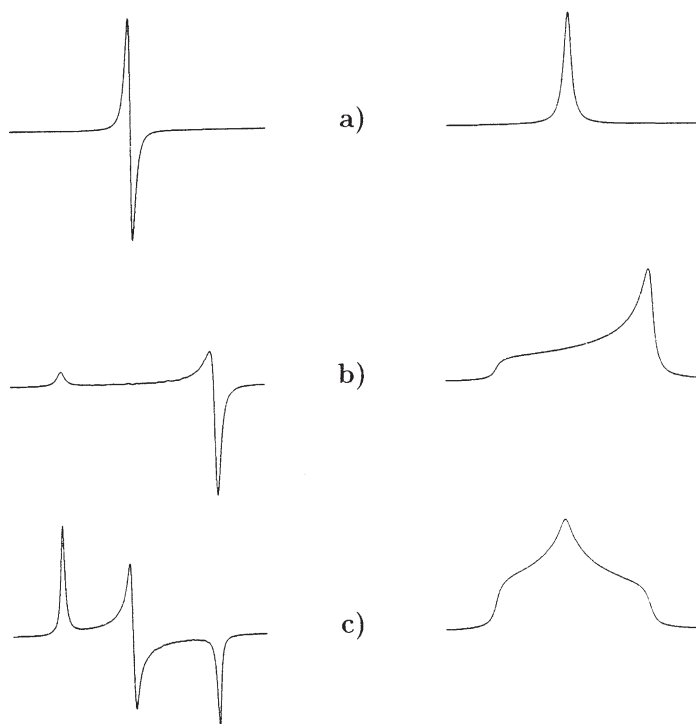


Fig. 2a–c. Idealized powder ESR patterns, together with their corresponding absorption profile: **a** isotropic; **b** axial and **c** rhombic

Table 1. Relationships between g and A tensors, ESR symmetry and the point symmetry of paramagnets

ESR symmetry	g and A tensors	Coincidence of tensor axes	Molecular point symmetry
Isotropic	$g_{xx}=g_{yy}=g_{zz}$ $A_{xx}=A_{yy}=A_{zz}$	all coincident	O_h, T_d, O, T_h, T
Axial	$g_{xx}=g_{yy}\neq g_{zz}$ $A_{xx}=A_{yy}\neq A_{zz}$	all coincident	$D_{4h}, C_{4v}, D_4, D_{2d}, D_{6h}, C_{6v}, D_6,$ $D_{3h}, D_{3d}, C_{3v}, D_3$
Rhombic	$g_{xx}\neq g_{yy}\neq g_{zz}$ $A_{xx}\neq A_{yy}\neq A_{zz}$	all coincident	D_{2h}, C_{2v}, D_2
Monoclinic	$g_{xx}\neq g_{yy}\neq g_{zz}$ $A_{xx}\neq A_{yy}\neq A_{zz}$	one axis of g and A coincident	C_{2h}, C_s, C_2
Triclinic	$g_{xx}\neq g_{yy}\neq g_{zz}$ $A_{xx}\neq A_{yy}\neq A_{zz}$	complete non-coincidence	C_1, C_i
Axial non-collinear	$g_{xx}\neq g_{yy}\neq g_{zz}$ $A_{xx}\neq A_{yy}\neq A_{zz}$	only g_{zz} and A_{zz} coincident	$C_3, S_6, C_4, S_4, C_{4h}, C_6, C_{3h}, C_{6h}$

As in the case of the magnetic moment of the electron, also the magnetic moment of the nucleus interacts with the magnetic field \vec{B} . This causes a further term in the spin Hamiltonian:

$$\bar{H}_{NZ} = -g_N \cdot \beta_N \cdot \vec{B} \cdot \vec{I} \quad (7)$$

with β_N the nuclear magneton and g_N the nuclear g -factor which is characteristic for each isotope. Usually this term is negligible in regular ESR, but important in ENDOR spectroscopy.

If two or more unpaired electrons are present, so that the total spin S of the electron system is greater than $1/2$, one has to take into account the interaction of the electrons with the electric field generated by the surrounding atoms (i.e. the crystal field or ligand field). This interaction causes a splitting of the more than twofold (Kramers-) degenerated ground state of the electron system even in the absence of an external magnetic field (i.e. zero field splitting). This interaction results in a line splitting in the ESR spectrum and this interaction can be described by the following Hamiltonian:

$$\bar{H}_{FS} = \bar{S} \cdot \bar{D} \cdot \bar{S} \quad (8)$$

with the fine structure tensor \bar{D} . The Hamiltonian becomes [2-5]:

$$\bar{H}_{FS} = D \left(\bar{S}_z^2 - \frac{S(S+1)}{3} \right) + E(\bar{S}_x^2 - \bar{S}_y^2) \quad (9)$$

Here D denotes the axial fine structure parameter, whereas E describes the orthorhombic fine structure parameter [5]. The influence of an axial (i.e. $D \neq 0$ and $E = 0$) and an orthorhombic fine structure splitting (i.e. $D \neq 0$ and $E \neq 0$) on a powder spectrum is shown in Fig. 3 for an isotropic g -tensor and for S equal to $3/2$ (e.g. Cr^{3+}).

Summarizing, four different magnetic interactions may occur, which influence the behavior of electrons in a magnetic field: (a) the Zeeman interaction, $\bar{H}_{Z\beta}$; (b) the nuclear hyperfine interaction, $\bar{H}_{HF\beta}$; (c) the electrostatic quadrupole interaction, \bar{H}_Q and (d) the zero-field splitting if $S > 1/2$, \bar{H}_{FS} . The sum of these interactions results in the total spin Hamiltonian, \bar{H}_T :

$$\bar{H}_T = \beta_e \cdot \vec{B} \cdot \vec{g} \cdot \vec{S} + \vec{I} \cdot \vec{A} \cdot \vec{S} + \vec{I} \cdot \vec{Q} \cdot \vec{I} + \vec{S} \cdot \vec{D} \cdot \vec{S} \quad (10)$$

2.2

Instrumentation and Signal Generation

The basic components of an ESR spectrometer are shown in Fig. 4 [15]. The microwave bridge supplies microwaves at a fixed frequency and chosen power, however, the microwave frequency is tuneable over a limited frequency range. The microwave source is a klystron or a gundiode. If one wishes to obtain ESR spectra at different frequencies, then a wide range of microwave sources need to be called in. The most commonly used and commercially available frequency is

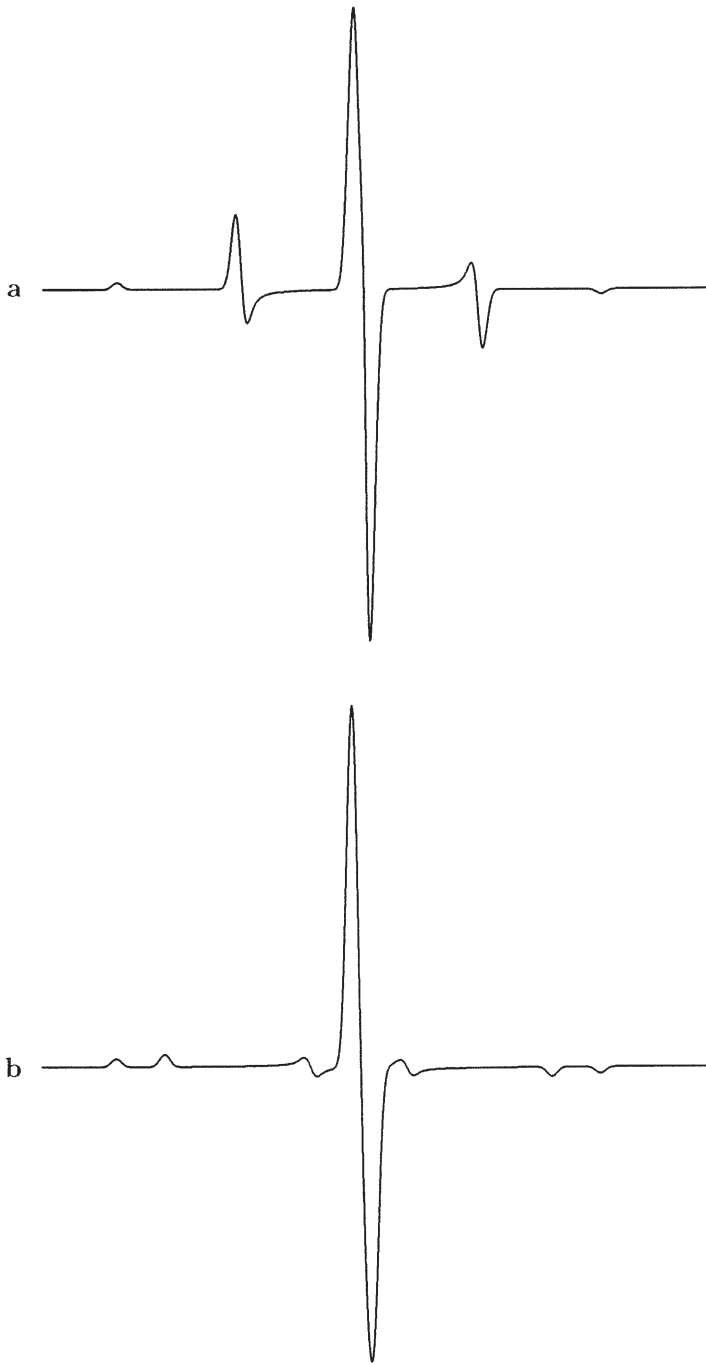


Fig. 3a, b. Influence of the zero field parameters D and E on a powder ESR spectrum with $S = 3/2$: **a** $D \neq 0$; $E = 0$ and **b** $D \neq E \neq 0$

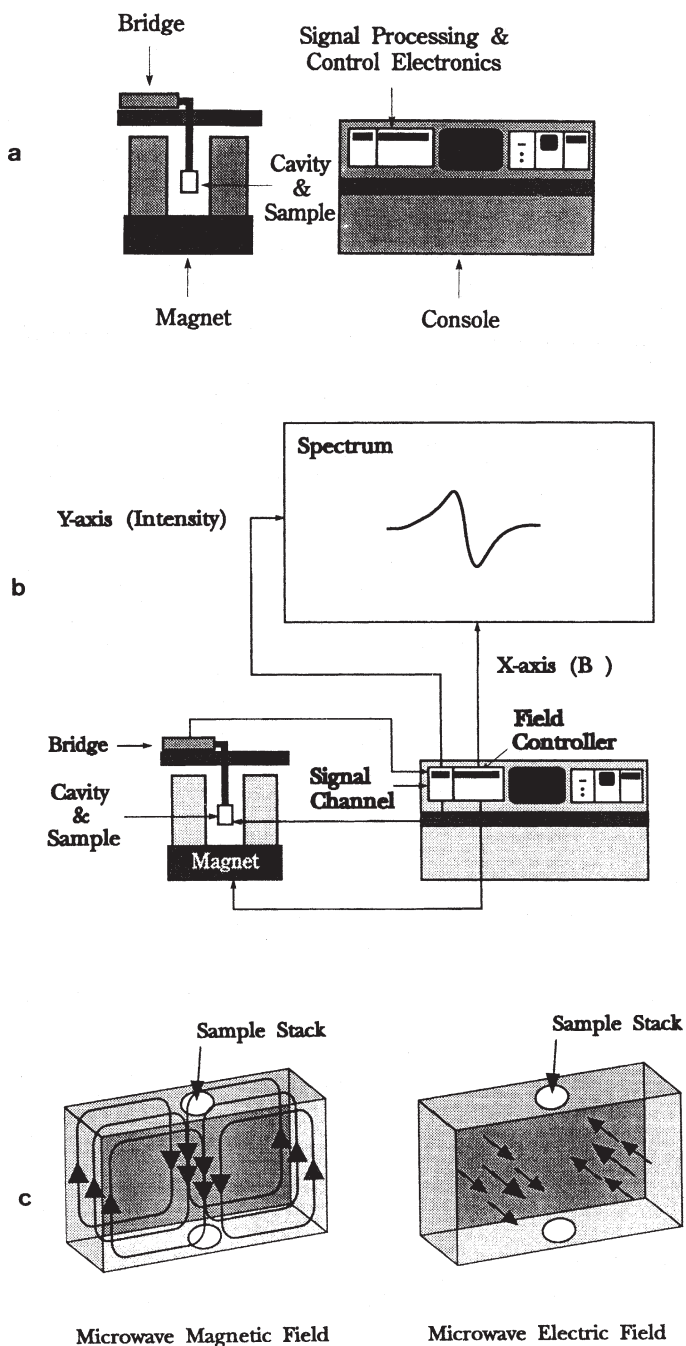


Fig. 4a-c. a General layout of an ESR spectrometer; b Block diagram of an ESR spectrometer and c Magnetic and electric field patterns in a standard ESR cavity (reprinted from reference [15]. Copyright 1992 Bruker Instruments, Inc.)

ca. 9.25 GHz (X-band) and the corresponding resonance field for $g=2$ is 0.3300 T. Q-band ESR, at ca. 35 GHz, is the next commonly used frequency, which gives transitions at 1.2500 T for $g=2.0$. More recently, a commercial W-band ESR spectrometer (ca. 90 GHz) became available and it is expected that it will add significantly to our understanding of zeolite materials. The microwaves are transmitted to a sample cavity via a waveguide. The sample cavity is a device in which the sample can be irradiated with the microwave energy, but which is also capable of being tuned so that microwave energy can be reflected back to a detector in the microwave bridge. The design of the cavity depends mainly on the applied microwave frequency because the dimensions of the cavity (and waveguide) must match the wavelength of the microwaves. The wavelength (and cavity dimensions) for X- and Q-band are 3.24 and 0.86 cm, respectively. It is also clear that these size limitations have a strong influence on the maximum amount of sample that a particular cavity will tolerate. For example, Q-band cavities permit only the use of very small amounts of samples. The sample cavity is then placed perpendicular to the applied magnetic field, B_0 , which can be varied in a controlled way. B_0 is generated by an electromagnet and should be as accurate and homogeneous as possible. In addition to the main magnetic field a controlled but smaller oscillating magnetic field is superimposed on the sample cavity via the modulation coils. Thus, the signal response from the cavity is modulated at the modulation frequency, and a first derivative ESR spectrum results. The ideal way to perform an ESR experiment would be to apply a fixed magnetic field and to vary the microwave frequency. However, as discussed above, microwave sources are tunable only over limited ranges. Therefore, the microwave frequency is kept constant and the applied magnetic field is varied over a field range in which microwave absorption is expected. This is called continuous wave electron spin resonance (CW-ESR). At the stage of microwave absorption, a change of the intensity of the reflected microwave energy is detected by a detector and the signal obtained is amplified, recorded and stored for further treatment.

The following parameters must be optimized to obtain a physically meaningful ESR spectrum:

- (i) magnetic field scan range: If you do not know much about your sample, it is advisable to scan the widest magnetic field range available, i.e. from zero up to the maximum. Afterwards, one may pick up the scan range of interest;
- (ii) modulation amplitude: An oscillating magnetic field at a fixed and stable frequency (mostly 100 kHz) is applied to the sample cavity via coils. The magnetic field is applied continuously throughout the experiment. The amplitude of this modulation is very important because high modulation amplitudes may distort the individual lines in a spectrum so that valuable information is lost. This is especially important when the lines are sharp and weak.
- (iii) sweep time: Short sweep times may significantly distort the ESR spectrum in that (a) the cross-over point of the first derivative spectrum may be shifted in the direction of the scan; (b) the spectrum becomes asymmetric or (c) the signal intensity reduces.

- (iv) sample temperature: Low concentrations of paramagnetic entities may become only visible at low measuring temperature. Furthermore, measurements of the signal intensity as a function of the sample temperature allow one to distinguish different types of magnetic behavior (i.e. paramagnetism, anti-ferromagnetism, etc.);
- (v) microwave power: At low values of the microwave power, the signal amplitude will increase in direct proportion to the square root of the microwave power received by the sample. This relationship, however, is only obeyed up to a certain power level, beyond which the signal intensity levels off or even decreases. This is known as microwave power saturation and no quantitative information can be extracted from saturated spectra. Saturation effects are also more pronounced at low temperatures.

If one wants to determine g -values from ESR spectra, one has to know both the field B_0 and the microwave frequency (Eq. 3). There are two possible methods: One can use a Gaussmeter and a frequency counter, both of which are relatively expensive instruments; the second method is based on the use of a standard with accurately known g -values. A double rectangular cavity (TE_{104}) is very convenient in that the standard (REF) is placed in one half of the cavity and the (unknown) sample (M) in the other. Only one cavity tuning operation is necessary for both measurements. With DPPH (diphenylpicrylhydrazine) as standard with $g_{REF} = 2.0036$, one has:

$$h \cdot \nu_{REF} = g_{REF} \cdot \beta \cdot B_{0,REF} \quad (11)$$

$$h \cdot \nu_M = g_{eff} \cdot \beta \cdot B_{0,M} \quad (12)$$

with

$$h \cdot \nu_{REF} = h \cdot \nu_M \quad (13)$$

or

$$g_{eff} = g_{REF} \cdot (B_{0,REF}/B_{0,M}) \quad (14)$$

The resonance fields $B_{0,REF}$ and $B_{0,M}$ are read directly from the ESR spectra.

2.3

Quantitative Analysis

The concentration, C , of a paramagnetic entity in a sample, subjected to an ESR experiment, is given by Eq. (15) [5]:

$$C = \frac{K \cdot I}{G \cdot P} \quad (15)$$

with K , a proportionality constant; I , the ESR line intensity; G , the amplifier gain of the spectrometer and P , the ESR transition probability [5]. The proportionality constant K is dependent on (a) the properties of the sample cavity, (b) the applied microwave power and (c) the applied modulation amplitude. The intensity I of the ESR signal must be obtained by working in the linear region of the microwave detectors and in the absence of microwave power saturation (i.e. low

paramagnetic concentrations). It is important to stress that an ESR signal consists of the first derivative of the absorption line and the ESR intensity must be related with the area under the absorption envelope. This is done by double integration of the recorded first derivative spectrum over a well-defined scan range.

If the number of spins in a standard is accurately known, its signal intensity can be used to determine the number of spins in the unknown sample. It is clear that K and P of Eq. (15) must be identical for the standard and the (unknown) sample. The related implications are that the conditions (a) to (c) should be identical for the paramagnetic sample and for the standard. Condition (a) means that the sample container, the volume of sample, the positioning in the sample cavity and the dielectric properties of both samples are identical. In addition, the standard should ideally have ESR properties (electronic structure, g -values, etc.) identical to those of the studied paramagnetic entity. Because this is almost impossible, one should choose a standard which is as close as possible to that of the unknown (e.g. Cu^{2+} (d^9) for Cr^{5+} (d^1) -quantification) [16].

If the ESR spectra of the paramagnetic entity in the unknown sample (M) and of the standard or reference compound (REF) have the same number of features spread over the same magnetic field range and if these spectra are integrated over the same scan range, then ESR allows the quantification of this paramagnetic entity according to Eq. 16:

$$N_M = N_{REF} \cdot \left(\frac{A_M}{A_{REF}} \right) \cdot \left(\frac{g_{REF}}{g_M} \right) \cdot \left(\frac{S_{REF} \cdot (S_{REF} + 1)}{S_M \cdot (S_M + 1)} \right) \quad (16)$$

with: N_M, N_{REF} = amount of spins of M and reference compound, respectively; A_M, A_{REF} = intensity of the ESR signal of M and reference compound obtained after double integration, respectively; g_M, g_{REF} = g -value of M and reference compound, respectively and S_M, S_{REF} = spin quantum number of M and reference compound, respectively. The last term in Eq. (16) corrects for the differences between the spin quantum number of the unknown and that of the reference compound.

Double integration of the ESR signal is not straightforward, especially in the case of transition metal ions with their spectra smeared out over a broad magnetic field range. The following parameters must be known or chosen:

- (i) Lineshape: This can be Gaussian, Lorentzian or a combination of both.
- (ii) Baseline: Integration is always very sensitive to baseline effects. A constant offset, for example, which means that the whole spectrum is shifted up or down from zero, results in a quadratic baseline in the doubly integrated spectrum. If integration is carried out over a wide range, such effect becomes large. This can be corrected by choosing a suitable baseline correction (cubic, linear, etc.).
- (iii) Integration width: Each spectrum must be integrated over the same scan range so that the same features are taken into account. Furthermore, large integration widths are recommended because tailing effects may cause important contributions to the overall spectrum.

It may be clear that a quantitative determination of paramagnetic species is rather complicated and requires a great deal of experimental care. Therefore, absolute determination of paramagnetic entities, especially transition metal ions, can only be done within 10 to 20% accuracy and explains why the number of quantitative ESR studies in molecular sieve science is rather limited [12,16].

2.4 Spectrum Simulation

For the simulation of ESR spectra one has to solve the spin Hamiltonian of Eq. (10). The easiest way to do this is to regard all the different terms in the spin Hamiltonian as small compared with the electron Zeeman interaction and to use perturbation theory of the first order. The Zeeman term can easily be solved within the eigensystem of the S_z operator (in the main axis system of the g -tensor or $\vec{S}_z = \vec{B}$ for isotropic cases), for instance in the isotropic case:

$$E^Z = g \cdot \beta \cdot B \cdot m_S \quad (17)$$

Unfortunately, in most cases this simplification is not applicable. Therefore, the use of perturbation theory of higher order is recommended, or in more complicated situations, the diagonalization of the spin Hamiltonian within the eigensystem of its spin operators.

Because the ESR experiment does not measure the energy spectrum for one fixed magnetic field by scanning the frequency of the microwave, but scans the magnetic field, it is necessary to calculate the energy levels for each magnitude of the magnetic field and to determine the resonance fields by comparing the differences of the energy levels with the applied microwave energy. Therefore, the spin Hamiltonian needs to be diagonalized very often and such calculations are time consuming. For the calculated resonance positions, it is easy to determine the appropriate intensities by evaluating the transition probabilities which can be calculated using the eigenfunctions of the spin Hamiltonian.

For disordered systems (e.g. powders), as usual in molecular sieve science, the contributions of all possible orientations of the magnetic field has to be taken into account. This is illustrated in Fig. 5. Thus, the above described calculations need to be summed up for all orientations (i.e. integration about φ in the axial case and about φ and ϑ in orthorhombic systems). Eventually the line shape has to be taken into account by convolution of the result with the appropriate line shape function (e.g. Gaussian or Lorentzian line with a suitable line width). There are a lot of simulation programs available in literature, either based on perturbation or matrix diagonalization methods: MAGRES (from the Department of Molecular Spectroscopy in Nijmegen, The Netherlands); MSPEN/MSGRA (from the group of Hüttermann in Hamburg, Germany); QPOW (from the group of Belford, University of Illinois, USA); EPR.FOR (from the group of Weil, University of Saskatchewan, Canada), Manchester program (from the group of Mabbs and Collison, Manchester University, UK) and Pilbrow program (from the group of Pilbrow, Monash University, Australia). Details about these programs can be found in the text book by Mabbs and Collison [5].

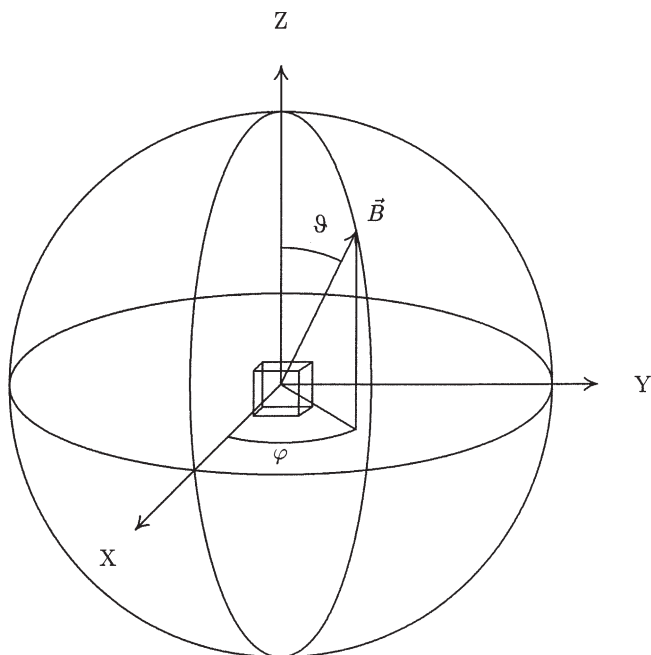


Fig. 5. Definition of the polar angles of the applied magnetic field, B_0 , with their respect to the principal axes

In practice one usually wishes to determine accurately the parameters of the spin Hamiltonian out of the measured spectrum. Therefore one has to estimate the parameters (g, D, E, A, Q , the line shape and the line width) to simulate the spectrum and to compare the result with the experimental spectrum, eventually followed by re-estimation of the parameters and simulation.

2.5

Modern ESR-Related Techniques: ENDOR and Pulsed ESR

The classic ESR technique, although very powerful, frequently suffers from inhomogeneous line broadening as a consequence of dipolar interactions and gives rise to poorly resolved ESR spectra. A considerable enhancement in resolution may be obtained by applying modern ESR-related techniques, which are capable of measuring nuclear magnetic transition frequencies in paramagnetic systems. In this paragraph two of these more advanced techniques will be discussed, i.e. electron nuclear double resonance (ENDOR) and a pulse variant of CW-ESR, electron spin echo spectroscopy (ESE). Detailed reviews on these techniques and their applications are available in the literature [17–24].

2.5.1

Electron Nuclear Double Resonance (ENDOR)

In ENDOR spectroscopy, one measures the NMR spectrum of nuclei which interact with a paramagnetic center. The principle of ENDOR spectroscopy is illustrated by Fig. 6 for a system with both S and I equal to $1/2$ (consider, e.g., a one electron – one proton two spin system, i.e. with one electron and one nuclear spin). The Hamiltonian operator, which is appropriate for this case ($I=1/2$, i.e. $eQ=0$; $S=1/2$, i.e. $D=0$; H_{NZ} non-negligible; see Eqs. (1), (2), (5), (7), (10)) is given by

$$\bar{H}_T = \beta_e \cdot \bar{B} \cdot \bar{g}_e \cdot \bar{S} + \bar{I} \cdot \bar{A} \cdot \bar{S} - g_N \cdot \beta_N \cdot \bar{B} \cdot \bar{I} \quad (18)$$

This operator has to be applied on the eigenfunctions of the spin system, (one electron-one proton two-spin system), i.e. on $\varphi_4=|\alpha_e \cdot \alpha_n\rangle$, $\varphi_3=|\alpha_e \cdot \beta_n\rangle$, $\varphi_2=|\beta_e \cdot \beta_n\rangle$, $\varphi_1=|\beta_e \cdot \alpha_n\rangle$; with $\alpha_e, \beta_e, \alpha_n, \beta_n$ indicating the eigenfunctions of the electron (e) spin or nuclear (n) spin with the eigenvalues $m_s=1/2, m_s=-1/2, m_I=+1/2$ and $m_I=-1/2$, respectively. This application provides the energy of levels 1 to 4 of Fig. 6 as follows (compare, e.g., Ref [23] or Ref. [24]):

$$\begin{aligned} E_4 &= \frac{1}{2} g_e \cdot \beta_e \cdot B + \frac{1}{4} a - \frac{1}{2} g_N \cdot \beta_N \cdot B \\ E_3 &= \frac{1}{2} g_e \beta_e \cdot B - \frac{1}{4} a + \frac{1}{2} g_N \cdot \beta_N \cdot B \\ E_2 &= -\frac{1}{2} g_e \cdot \beta_e \cdot B + \frac{1}{4} a + \frac{1}{2} g_N \cdot \beta_N \cdot B \\ E_1 &= -\frac{1}{2} g_e \cdot \beta_e \cdot B - \frac{1}{4} a - \frac{1}{2} g_N \cdot \beta_N \cdot B \end{aligned} \quad (19)$$

To detect an ENDOR signal one has to record the ESR spectrum and to choose an appropriate line which has to be (at least partially) saturated (vide infra).

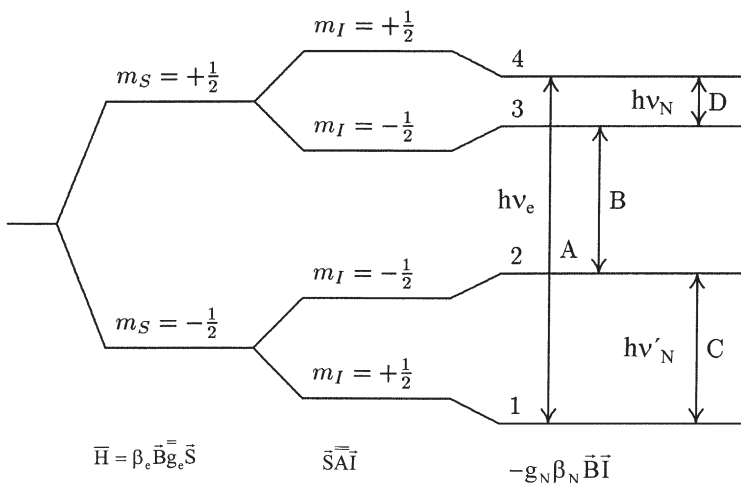


Fig. 6. Energy level scheme for ENDOR

For instance, the allowed ESR transition 1 ($1 \leftrightarrow 4$) can be saturated by application of a sufficiently high microwave power (vide infra) so that the levels 1 and 4 are equally populated and consequently no ESR signal is observed. Now, a strong radiofrequency field is applied with a frequency, ν_N , given by the energy difference between the levels 3 and 4, i.e.

$$h\nu_N = \frac{1}{2}a - g_N \cdot \beta_N \cdot B$$

Thus, NMR transitions *D* ($4 \leftrightarrow 3$) will be stimulated until the populations of levels 3 and 4 will be equalized. As a consequence, the population of level 4 will slightly decrease. This desaturation enables the ESR signal to re-appear.

Similarly, if a radiofrequency, ν_N , corresponding to the energy difference between levels 1 and 2, i.e.

$$h\nu_N = \frac{1}{2}a + g_N \cdot \beta_N \cdot B$$

were employed, NMR transitions *C* between these levels would be stimulated, again with the result of disturbing the equalized populations of levels 4 and 1, and thus, de-saturating of the electron resonance signal would again occur. In an experiment, where the electron resonance frequency, ν_e , is kept constant and the radiofrequency swept around $\nu_{rf} = \frac{1}{2h}$, the ESR signal will re-appear twice, viz. at

$$\nu_N = \frac{1}{h} \left(\frac{1}{2} - g_N \cdot \beta_N \cdot B \right)$$

$$\nu'_N = \frac{1}{h} \left(\frac{1}{2} + g_N \cdot \beta_N \cdot B \right)$$

From the ENDOR spectrum with these two lines, one can derive both the hyperfine splitting constant, *A*, and the nuclear factor, g_N (characteristic of given nucleus) with high accuracy.

Though the ENDOR method is a very powerful tool, there are several drawbacks to this method, which sometimes prohibits a successful application. For ENDOR spectroscopy in general an advanced equipment is necessary. Especially the generation of a sufficiently high radiofrequency power and the coils to generate the appropriate magnetic field on the sample are often problematic. Furthermore, the ENDOR effect is usually smaller than the ESR effect (mostly less than one tenth of the ESR intensity) and a sensitive ESR spectrometer is required. In addition, an ENDOR signal can only be detected if one is able to saturate the ESR line at least partially. This means that a low measurement temperature is recommended, usually using liquid helium (4.2 K). Furthermore, the nuclear relaxation time must not be too long to avoid saturation of the NMR transition. The last restrictions can sometimes be circumvented by using pulsed ESR techniques.

2.5.2

Electron Spin Echo Spectroscopy (ESE and ESEEM)

Electron spin echo spectroscopy (ESE) monitors the spontaneous generation of microwave energy as a function of the timing of a specific excitation scheme, i.e. two or more short resonant microwave pulses. This is illustrated in Fig. 7. In a typical two-pulse excitation, the initial $\pi/2$ pulse places the spin system in a coherent state. Subsequently, the spin packets, each characterized by their own Larmor precession frequency ω_i , start to dephase. A second π -pulse at time τ effectively reverses the time evolution of the spin packet magnetizations, i.e. the spin packets start to rephase, and an emission of microwave energy (the primary echo) occurs at time 2τ . The echo amplitude, as a function of τ , constitutes the ESE spectrum and relaxation processes lead to an irreversible loss of phase correlation. The characteristic time for the amplitude decay is called the phase memory time T_2^M . This decay is often accompanied by a modulation of the echo amplitude, which is due to weak electron-nuclear hyperfine interactions. The analysis of the modulation frequencies and amplitudes forms the basis of the electron spin echo envelope modulation spectroscopy (ESEEM).

The main limitation of the above described two-pulse experiment originates from phase relaxation processes. T_2^M may become too short with respect to the instrumental dead time (about 150 ns), resulting in an overlap with the ESE spectrum. This may be overcome by applying a three-pulse excitation scheme (Fig. 7), in which the second pulse of the two-pulse experiment is divided into two $\pi/2$

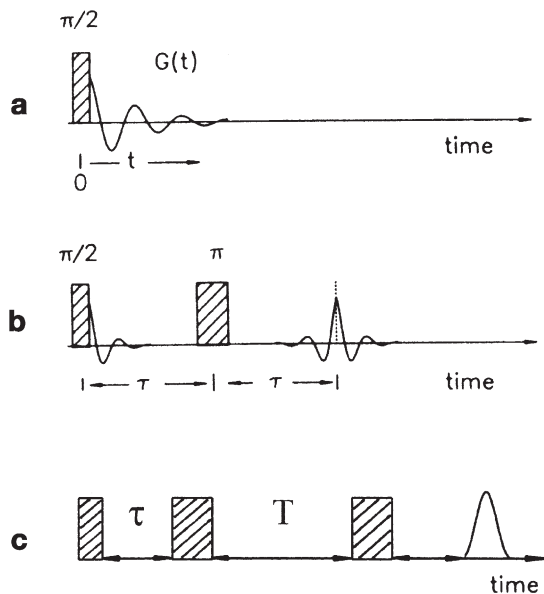


Fig. 7a–c. Pulse sequences for the pulsed ESR technique: **a** single pulse followed by a free induction decay; **b** two pulse sequence; **c** three pulse sequence (reprinted from reference [20]. Copyright 1987 R. Oldenbourg Verlag)

pulses. The echo can now be followed over a time of the order of magnitude $T_1 \gg T_2^M$. With the separation between the first and the second pulse denoted as τ and the one between the second and the third as T , the stimulated echo, occurring at $2\tau+T$, is monitored in the T -space. Thus, there are two experimentally controllable times τ and T . It is therefore possible to suppress one nuclear modulation frequency by appropriate selection of one of these times. The analysis of this modulation provides a way to measure the weak electron-nuclear hyperfine interactions. In addition, it is possible to determine both the number and the distance of magnetic nuclei, surrounding a paramagnetic center.

Three-pulse experiments are well suited for studying the interaction of adsorbed molecules with paramagnetic centers. For example, by selecting the appropriate pulse amplitude, it is possible to observe deuterium modulation, while suppressing proton modulation for adsorbed methanol. This is possible because of the difference in the nuclear frequencies of protons and deuterons. This allows the determination of the orientation of this adsorbed molecule with respect to a paramagnetic center by selective deuteration.

To extract detailed hyperfine information from an ESE spectrum, however, it is necessary to calculate the expected modulation pattern for a certain assumed nuclear geometry. By varying the assumed hyperfine interaction for a simulated modulation pattern until it fits the observed modulation pattern, the weak hyperfine parameters may be determined. The general analysis procedure is to analyze the ESE spectrum in terms of a number of equivalent nuclei located at an average distance from the paramagnetic center. The assumption is then that there is a small overlap of the unpaired electron wave function on the closest nuclei to give an isotropic hyperfine coupling constant A_{iso} .

3

Applications of ESR in Molecular Sieve Science

3.1

Transition Metal Ions

Transition metal ions (TMIs) coordinate to lattice oxygen atoms, form complexes inside the cages and/or channels or occupy framework sites. Classical ESR techniques as well as pulsed ESR, and in particular the analysis of the modulation of the echo envelope signal (ESEEM) has been used extensively to gather detailed information about the coordination environment of TMIs.

3.1.1

Cu^{2+}

In Fig. 8 typical high resolution spectra of Cu^{2+} in dehydrated zeolites are shown. The corresponding ESR parameters (Table 2) are obtained by simulation with an axial spin Hamiltonian, including the Zeeman, the hyperfine and quadrupole interactions, applying second order perturbation. The spectra of Cu-ZSM-5 were obtained from the literature [25–29] and the parameters obtained by visual

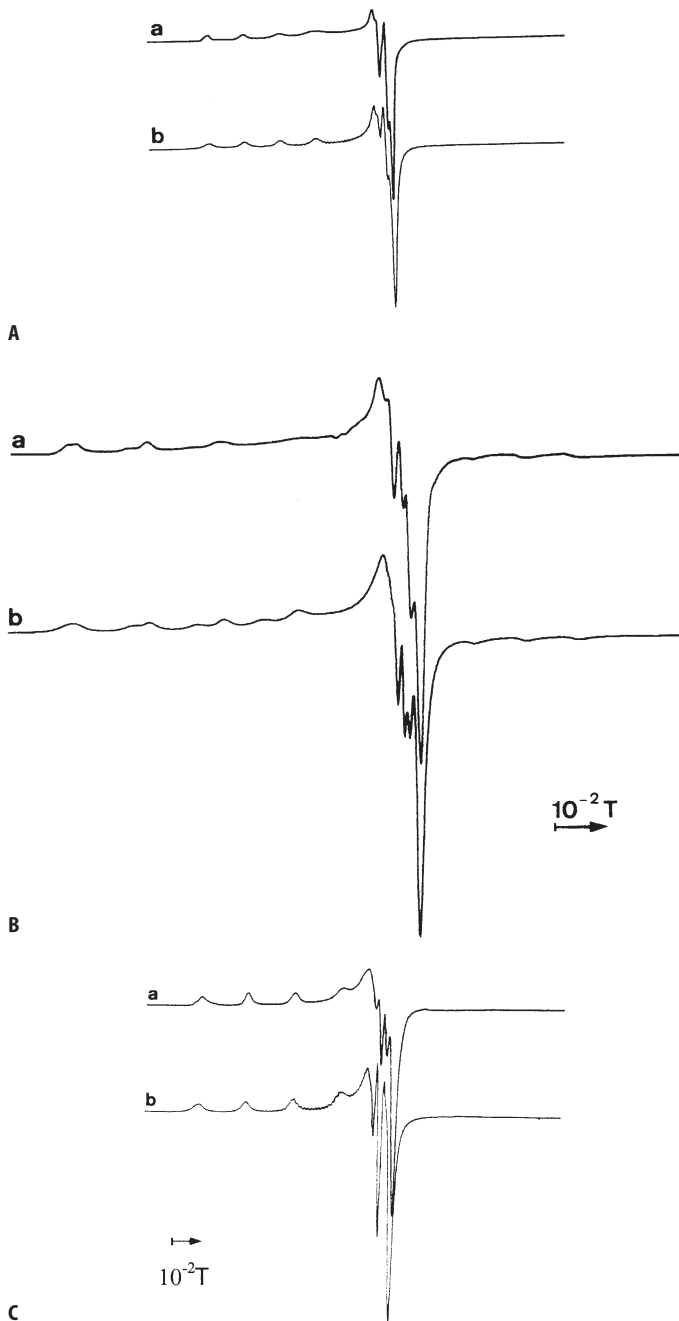


Fig. 8A-D. High resolution ESR spectra of Cu^{2+} in dehydrated zeolites : A zeolite A; B zeolite X; C Mordenite and D ZSM-5 (reprinted from reference [26]. Copyright 1993 Marcel Dekker, Inc and from reference [22]. Copyright 1995 American Chemical Society): *a* experimental and *b* theoretical

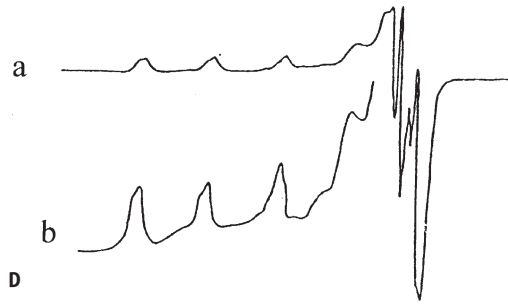


Fig. 8 (continued)

Table 2. ESR parameters of Cu^{2+} in dehydrated zeolites

Zeolite		g_{\parallel}	A_{\parallel} (mT)	g_{\perp}	A_{\perp} (mT)	Q (mT)	Assignment/Location
A		2.386	12.6	2.064	0.25	0.50	A
		2.386	12.6	2.063	1.57	0	re-simulated
X	(1)	2.384	12.7	2.074	1.20	0.33	II
		2.386	12.5	2.069	1.33	0.14	re-simulated
	(2)	2.354	14.3	2.068	1.50	0.35	III'
		2.353	14.4	2.064	1.64	0.00	re-simulated
Y	(1)	2.397	11.9	2.070	1.50	0.30	II
	(2)	2.328	15.5	2.065	1.90	0.32	I'
Mordenite	(1)	2.327	15.4	2.062	1.49	0.26	A
	(2)	2.277	16.8	2.057	1.19	0.28	E
ZSM-5	(1)	2.310	15.0–16.0	–	–	–	square pyramidal
	(2)	2.330	15.0–16.0	–	–	–	square pyramidal
	(3)	2.280	18.0	–	–	–	square planar

inspection. Similar spectra are obtained on Cu^{2+} -loaded SAPO's [30–35]. There are several remarks to be made about the spectra and their simulation:

- (1) While a very good guess of the parameters of the parallel region can be obtained from the spectra by visual inspection, this is certainly not the case for the perpendicular region. The reason is that in the parallel region forbidden transitions ($\Delta m_l = \pm 1, \pm 2$) do not contribute to the spectrum, while in the perpendicular region they come into play. They are negligibly small as long as the quadrupole coupling constant Q is small, but become important, as the ratio $|Q|/|A|$ increases. This is illustrated in Fig. 9, showing the perpendicular region of the Cu^{2+} -mordenite spectrum with $g_{\parallel} = 2.327$, $A_{\parallel} = 15.5$ mT, $g_{\perp} = 2.068$ and $A_{\perp} = 1.5$ mT. In the first case $Q = 0.2$ mT, in the second case $Q = 0.5$ mT. In the latter case, one notices the increased contribution of the $\Delta m_l = \pm 1$ and $\Delta m_l = \pm 2$ contributions between 0.32 and 0.33 T.

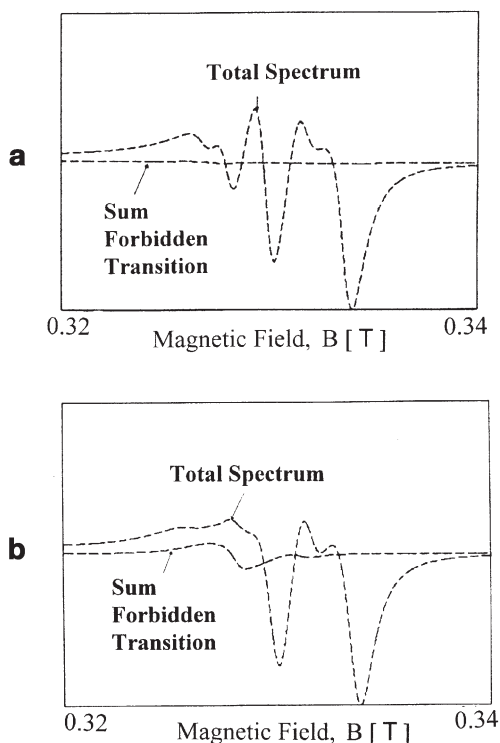


Fig. 9a, b. Effect of the quadrupole coupling constant Q on the ESR spectra of dehydrated Cu mordenite : a $|Q| = 0.2$ mT and b $|Q| = 0.5$ mT (reprinted from reference [36])

- (2) In powder spectra extra absorptions occur in the perpendicular regions due to significant contributions of paramagnetic centers resonating below 90° . This is illustrated with the absorption spectrum of Cu^{2+} -mordenite in Fig. 10.

The ESR parameters of Cu^{2+} in CuNaA and CuNaX, obtained by simulation with proper account of the forbidden transitions are given in Table 2 [36,37]. The differences are – as expected – more pronounced in the perpendicular region with smaller Q -values and somewhat larger A values. The new parameters are more in line with accepted Cu^{2+} ESR data [26].

We close this discussion by observing that ^{63}Cu and ^{65}Cu nuclei are usually not resolved in the ESR spectra of calcined Cu^{2+} -zeolites. Both nuclei have spin $I = 3/2$, have relative abundancies of respectively 69.2% and 30.8% and differ slightly in their nuclear Bohr magneton values and quadrupolar moment values. These values are respectively for ^{63}Cu and ^{65}Cu : $\beta_N(^{63}\text{Cu}) = 3.743 \times 10^{-27} \text{ J} \cdot \text{T}^{-1}$; $\beta_N(^{65}\text{Cu}) = 4.005 \times 10^{-27} \text{ J} \cdot \text{T}^{-1}$; $Q(^{63}\text{Cu}) = -0.222 \times 10^{-24} \text{ cm}^2$ and $Q(^{65}\text{Cu}) = -0.195 \times 10^{-24} \text{ cm}^2$. Such small differences are often not resolved in the broad powder spectra.

The assignment of the Cu^{2+} spectra to specific sites in dehydrated zeolites is a challenging subject [26]. It has been done with the aid of O_2 line broadening

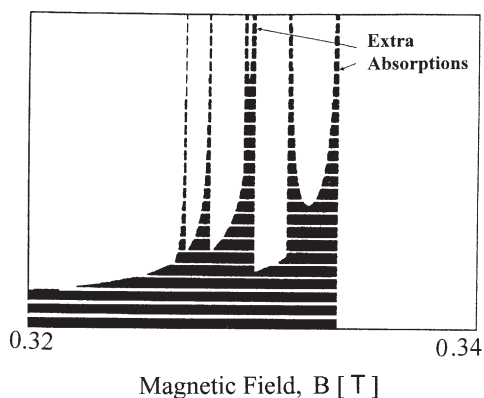


Fig. 10. Effect of the quadrupole coupling constant Q on the ESR spectra of dehydrated Cu mordenite: The perpendicular region in absorption mode shows four hyperfine lines and two extra-absorption lines (reprinted from reference [36])

experiments, with a study of the effect of co-cations on the relative signal intensities, by combination with a study of the d-d transitions and by model calculations in the frame of ligand field and angular model theories. The assignment is given in Table 2. Two remarks can be made here:

- (1) The distribution of Cu^{2+} over the sites in faujasite-type zeolites at the typical small loadings of the ESR investigations is not a simple straight line extrapolation from X-ray data (obtained at high loadings only). Common knowledge of zeolite chemistry should have led to the conclusion that at the small loadings of the ESR experiments all Cu^{2+} ions occupy site I. Instead, six-ring sites (I', II) are the preferred ones. There is a strong and short Cu^{2+} -O s-bond in six-ring sites, which cannot be realized in the hexagonal prisms and explains this site preference. An alternative explanation is that Cu^{2+} is asymmetrically located in the hexagonal prisms, i.e. coordinated to three oxygen atoms of one six-ring only, as suggested recently from theoretical calculations on Na^+ [38].
- (2) One might also wonder whether at the small loading of 0.25 Cu^{2+}/UC site assignment is possible after all. Do some or all the Cu^{2+} coordinate to the surface at some defect site such as silanol group ($>\text{Si-OH} + \text{Cu}^{2+} \rightarrow >\text{Si-O}^- - \text{Cu}^{2+} + \text{H}^+$) or others? This cannot be fully ruled out, but the consistency of the data point to real crystallographic Cu^{2+} -siting. Weak background signals, which are always present, might be due to traces of Cu^{2+} at such defects.

A more recent approach on the interpretations of Cu^{2+} spectra to specific cation sites in zeolites is based on the use of *ab initio* calculations [39–41]. The structure of appropriate model clusters of cation sites (e.g. six-ring and five-ring sites) are calculated and optimized with density functional theory. In a next step, the electronic spectra and g-values of the models are calculated. The first results of this approach look very promising and its rigorous application will certainly lead to a better insight into the coordination of transition metal ions in zeolites. An

important conclusions from these studies is that transition metal ions, in particularly Cu^{2+} and Co^{2+} , are able to distort the local environment of a cation site in order to increase their coordination number.

In some cases, especially that of zeolites with high Al content, superhyperfine interaction of Cu^{2+} with the ^{27}Al nucleus ($I=5/2$) has been observed. Here, ESEEM is particularly useful [42–44]. When Cu^{2+} is complexed with extra-lattice ligands such as H_2O , methanol, NH_3 , ethylenediamine or pyridine, its magnetic moment is effectively screened from the environment. Well resolved spectra can be obtained at much higher Cu^{2+} loadings than for dehydrated zeolites. The ESEEM technique has been pioneered by Kevan and co-workers to detect the weak magnetic interactions between transition metal ions and surrounding nuclei such as H, D and Al. For example, deuterated and ^{13}C -labelled adsorbates have been studied in H-, Na-, K- and Ca-ZSM-5 zeolites by ESR and ESEEM [42]. Simulation of the obtained signals show a fourfold methanol and ethanol coordination of Cu^{2+} in H-ZSM-5, whereas only a threefold coordination is observed in Cu^{2+} exchanged Na-, K- and Ca-ZSM-5. The use of deuterated molecules, such as D_2O and CD_3OH , was also useful in determining the location and structure of Cu^{2+} in zeolites as a function of the co-cation [43–44]. Recently, the technique has been extended to characterize Cu^{2+} complexes in mesoporous MCM-41 [45–46]. Surprisingly, Cu^{2+} was found to bind strongly with surface oxygen atoms and only 2 H_2O , 2 MeOH or 2 NH_3 could enter the coordination sphere, the larger molecules pyridine and benzene being excluded.

In specific cases, the exact composition of the first coordination sphere around Cu^{2+} can be derived from the superhyperfine splitting pattern in ESR. This is illustrated in Fig. 11 for a faujasite-type encaged $\text{bisCu}(\text{histidine})_2^+$ complex [47]. The axially symmetric ESR spectrum has a hyperfine splitting with values for g_{\parallel} , g_{\perp} and a_{\parallel} of around 2.27, 2.06 and 17 mT, respectively and a seven-line superhyperfine structure with an $A_{N\perp}$ value of 1.23 mT. The additional splitting is due to the presence of three nitrogen atoms ($2 \cdot I_N \cdot n_N + 1 = 7$ with I_N and n_N equal to 1 and 3, respectively) in the first coordination sphere of the Cu^{2+} -ion. This planar NNNO coordination environment was later on confirmed by detailed W-band pulsed ESR techniques [48]. It was also shown that the coordination geometry of

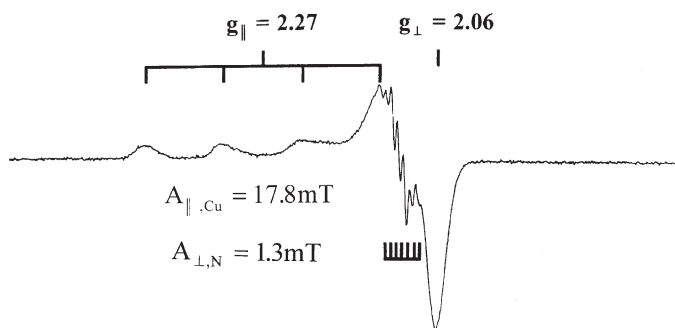


Fig. 11. ESR spectrum of zeolite encaged $\text{Cu}(\text{histidine})_2^{2+}$ (reprinted from reference [47]. Copyright 1995 VCH Verlagsgesellschaft)

these zeolite-encapsulated copper-histidine complexes depend on the Cu^{2+} -loading and, at low Cu^{2+} -loading, a mono $\text{Cu}(\text{his})^+$ complex could be formed inside the cages of zeolite Y. ESEEM indicates that this mono-complex is in close contact with the zeolite framework since strong ^{27}Al modulations were observed.

3.1.2

Fe^{3+}

The detection and characterization of Fe^{3+} in molecular sieves by ESR and Mössbauer spectroscopies is almost as old as spectroscopy of molecular sieves itself. Three signals are invariably reported [49–57]:

- a sharp line around $g=4.3$, interpreted as Fe^{3+} in a tetrahedral environment with strong rhombic distortion;
- a broad line around $g=2.3$ due to oxidic Fe species;
- a line around $g=2$, interpreted as Fe^{3+} in (distorted) octahedral environment.

The chemical interpretation of these signals is Fe^{3+} in the lattice, extra-framework Fe_2O_3 , Fe^{3+} at exchange sites, respectively. There are many reports in the literature that these interpretations, especially that of the $g=4.3$ signal and that of the $g=2.0$ signal, are not the only possible ones. An alternative interpretation was put forward by Lin et al. in that the three signals were assigned to three different types of framework sites in FAPO-5 [52]. This interpretation has become unlikely in the light of the results of Goldfarb et al. [53–54]. Their interpretation is that the signal at $g=4.3$ is due to Fe^{3+} at defect sites, e.g. silanol groups and that at $g=2.0$ to framework Fe^{3+} and/or Fe^{3+} in exchange sites. The latter signal is ascribed to the $|^{-1/2}\rangle \leftrightarrow |^{1/2}\rangle$ transition of tetrahedral Fe^{3+} . At the lowest substitution levels ($\text{Fe}/(\text{Fe}+\text{Al})=0.001$) the $g=2$ line is sharp and has a weak, broad side-band at low and high fields due to singularities of the other transitions $|^{-5/2}\rangle \leftrightarrow |^{-3/2}\rangle$, $|^{-3/2}\rangle \leftrightarrow |^{-1/2}\rangle$, $|^{1/2}\rangle \leftrightarrow |^{3/2}\rangle$, $|^{3/2}\rangle \leftrightarrow |^{5/2}\rangle$. If there is more than one crystallographical T site or if the Fe^{3+} content is slightly increased, the $g=2$ line broadens and the weak side bands are not observed anymore. When Fe-sodalite was synthesized with an Fe source enriched in ^{57}Fe , the ^{57}Fe hyperfine splitting constant of 28.7 MHz (10^{-3} T or 9.6×10^{-4} cm $^{-1}$) was determined by ENDOR.

Several other lines were also reported in the Fe^{3+} ESR spectra of molecular sieves. After solid-state ion exchange of FeCl_3 -HZSM-5 Kucherov and Slinkin observed up to 7 different signals in the low field region with g -values in the range 9.1–3.4 [55]. In a ferrisilicate three signals with $g=4.25$, 5.2 and 7.9 were observed. When FAPO-5 and ferrisilicalite are hydrothermally synthesized with very low Fe contents ($\text{Fe}/(\text{Al}+\text{P})=^{1/1000}-^{1/2000}$; $\text{Fe}/\text{Si}=^{1/200}-^{1/100}$) in order to avoid Fe^{3+} - Fe^{3+} interactions, the uptake of Fe in the solid, as measured by ESR matches the development of the crystallinity measured by XRD. Under these conditions at least 5 different signals were observed in X-band ESR and only the relative intensities of the signals vary upon reductive or oxidative treatments [56].

It is impossible to advance an interpretation for all these signals. Computer programs are now available which allow full matrix analysis of the ESR problem of Fe^{3+} instead of the usual perturbative approach. A set of theoretical spectra could be generated for comparison with experimental data [57]. On the other

hand, it is clear that the chemistry of Fe^{3+} in molecular sieves is extremely complicated, both in the synthesis mixtures and on ion exchange sites. We must strive towards very simple chemistry so as to obtain relatively simple spectra which are amenable to theoretical analysis or detailed spectroscopic analysis. Goldfarb et al. [53, 54] have shown the way.

3.1.3

Cr^{5+} and Cr^{3+}

Cr^{5+} (d^1) ESR signals have always axial or rhombic symmetry and typical g -values of zeolitic Cr^{5+} are given in Table 3. On this basis, the signals are assigned to square pyramidal and pseudo-tetrahedral chromyl cations on well-defined ion exchange sites [58–62]. Cr^{5+} in mordenite-type molecular sieves is an interesting example since it is characterized by a complex ESR spectrum (Fig. 12) possessing two rhombic signals with one exhibiting Al superhyperfine splitting (species B). The simulated spectrum, together with the individual components A and B, is also shown in Fig. 12, and is very close to the experimental one [63]. Species A is assigned to Cr^{5+} -ions present at the junction of the main channel and the side pocket, while species B is located near framework aluminum in the main channel of mordenite molecular sieves [64]. Such detailed level of understanding can only be obtained by using specific probe molecules, such as ammonia and pyridine, and also underlines the important role of spectrum simulations.

Three distinguished Cr^{3+} (d^3) ESR signals are observed in molecular sieves, independently of their type and composition [63–66]:

- a broad signal around $g_{\text{eff}}=2.0$, which follows the Curie-Weiss law, assigned to hexaquo Cr^{3+} complexes;

Table 3. ESR parameters of Cr^{5+} in chromium containing molecular sieve and their assignments

Zeolite	ESR signal	Assignment	Reference
Y	$g_{\parallel}=1.987; g_{\perp}=1.940$ $g_{\parallel}=1.980; g_{\perp}=1.915$	Y ₁ -signal : $[\text{Cr}=\text{O}]^{3+}$ -ion at site II (supercage) Y ₂ -signal : $[\text{Cr}=\text{O}]^{3+}$ -ion at site I' or II' (small cages)	58–60
Mordenite	$g_{xx}=1.9867; g_{yy}=1.9720;$ $g_{zz}=1.9110$ $g_{\parallel}=1.9947; g_{\perp}=1.9070$	A-signal : square pyramidal $[\text{Cr}=\text{O}]^{3+}$ -ion in the main channel B-signal : distorted tetrahedral $[\text{Cr}=\text{O}]^{3+}$ -ion at junction between main channel and the sidepocket	64
X	$g_{\parallel}=1.99; g_{\perp}=1.93$	$[\text{Cr}=\text{O}]^{3+}$ -ion	16
Silicalite	$g_{xx}=4.49; g_{yy}=2.71;$ $g_{zz}=1.66$ $g_{xx}=2.00; g_{yy}=1.67;$ $g_{zz}=1.66$	signal A (substitutional site) signal B (substitutional site)	66

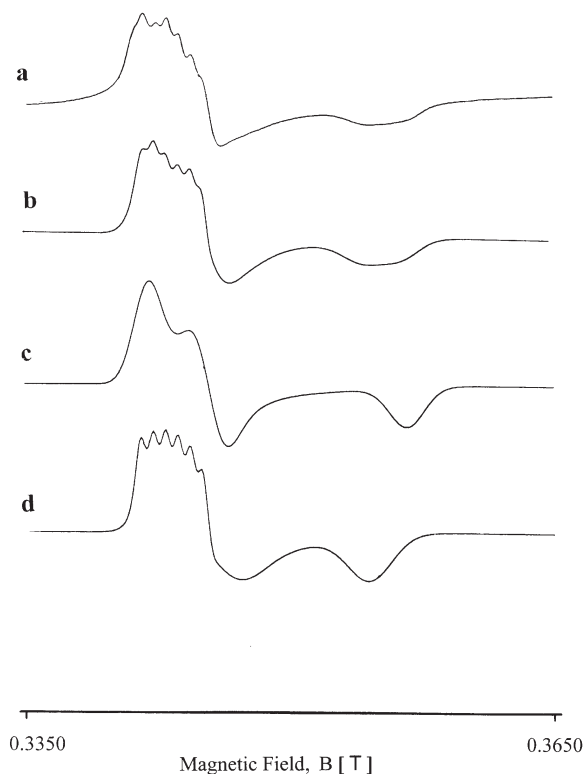


Fig. 12a-d. ESR spectrum of Cr^{5+} in mordenite: **a** experimental; **b** simulated spectrum obtained by an appropriate summation of the theoretical spectra of species A and B; **c** theoretical spectrum of species A and **d** theoretical spectrum of species B (reprinted from reference [63]. Copyright 1996 The Royal Society of Chemistry)

- a signal around $g_{\text{eff}}=2.0$, which broadens upon cooling, assigned to oxidic Cr^{3+} -clusters;
- a special signal with a broad and positive lobe in the region $g_{\text{eff}}=4.0-5.5$. The origin of this signal has only recently received attention. Detailed spectrum simulations of the Cr^{3+} -system have shown that zero-field parameters D and E need to be introduced into the simulation procedure to obtain spectra with positive lobes in the region $g_{\text{eff}}=4-5.5$. The effect of D and E on the ESR spectra of Cr^{3+} is illustrated in Fig. 13. For D and E equal to zero, only one transition is seen at $g_{\text{eff}}=2.0$. The introduction of small D values gives rise to several transitions at lower and higher g_{eff} -values, while with D equal to 0.5 cm^{-1} effective g -values in the x/y and z direction are obtained around 4.0 and 2.0, respectively. Only by introducing a zero field parameter E of 0.165 cm^{-1} , a clear positive lobe with $g_{\text{eff}}=4.0-5.5$ can be generated. The third signal must therefore be assigned to a strongly distorted Cr^{3+} -species [63]. Similar signals have been observed for Cr supported on amorphous supports and, consequently, they are not unique for zeolitic environments [67].

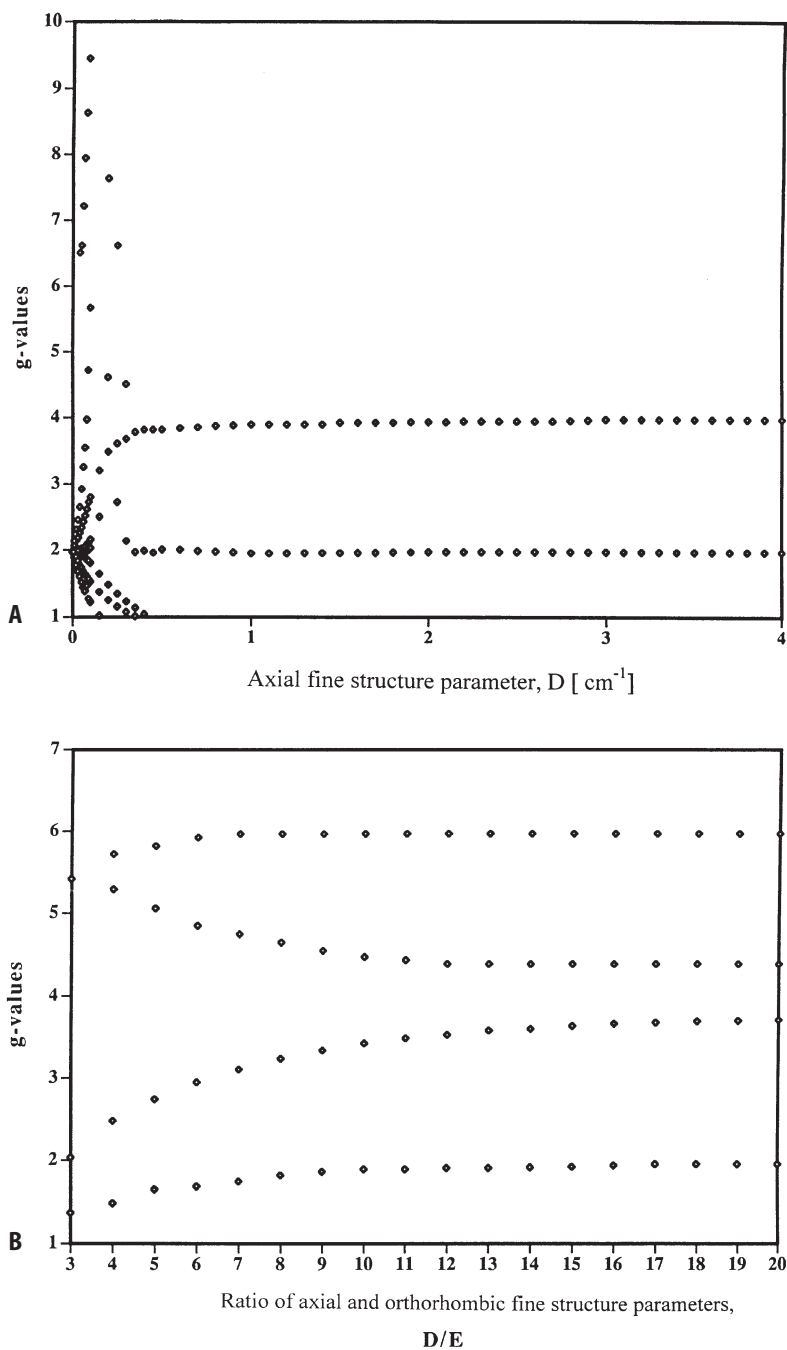


Fig. 13A–D. Influence of zero field parameters D and E on the effective g values of a Cr^{3+} -ion (reprinted from reference [63]. Copyright 1996 The Royal Society of Chemistry: A effective g -values as a function of D ; B effective g -values as a function of D and E)

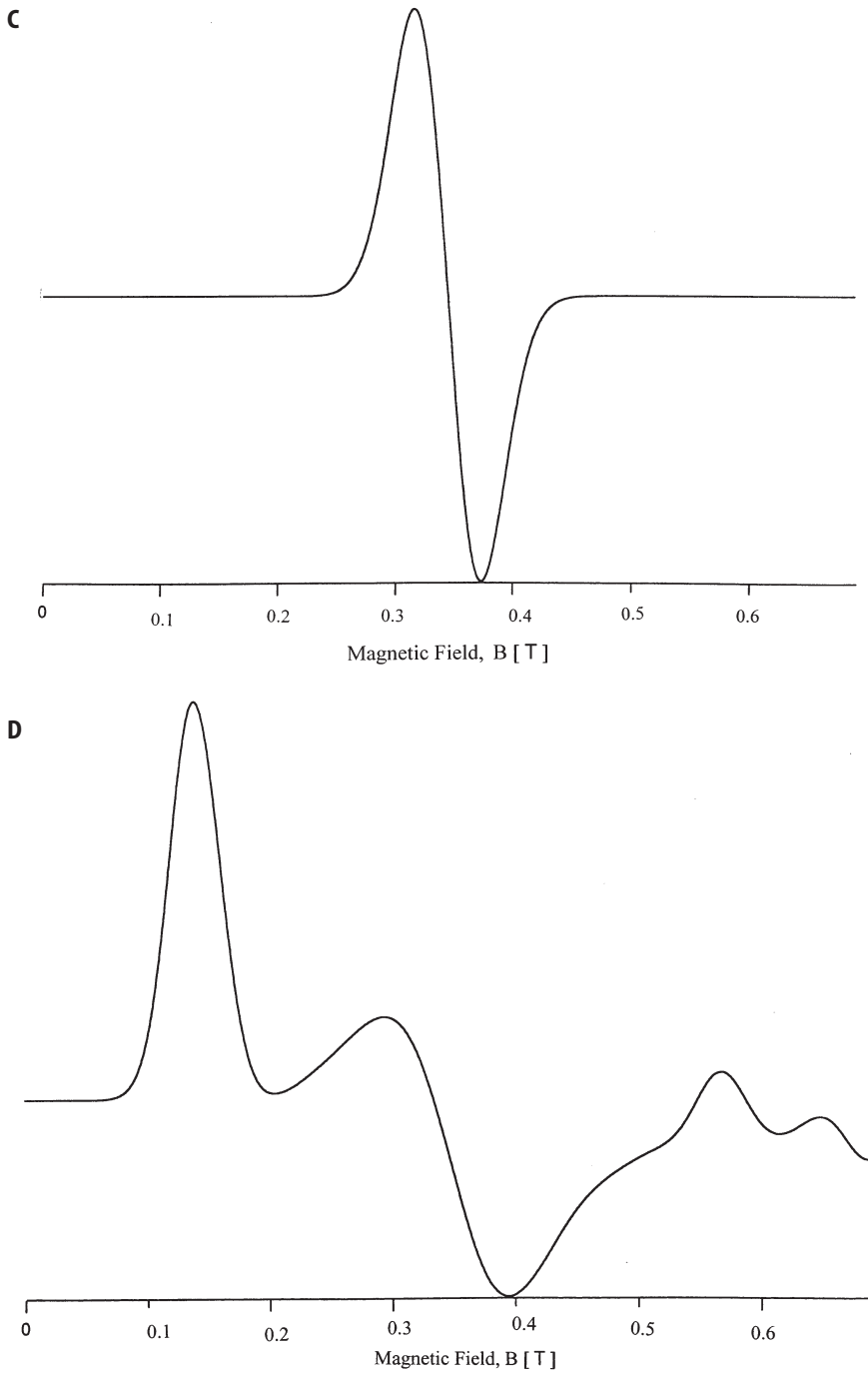


Fig. 13A–D (continued). **C** theoretical spectrum with $D = E = 0$ and **D** theoretical spectrum with $D = 0.5 \text{ cm}^{-1}$ and $E = 0.167 \text{ cm}^{-1}$

Table 4. ESR parameters of V^{4+} in vanadium containing molecular sieves

Zeolite		g-parameters	A-parameters (mT)	Reference
ZSM-5		$g_{ } = 1.925; g_{\perp} = 1.978$	$A_{ } = 18.15; A_{\perp} = 7.55$	70
Silicalite		$g_{ } = 1.932; g_{\perp} = 1.994$	$A_{ } = 18.3; A_{\perp} = 6.9$	70
AlPO-5	S_1 resimulation of S_1	$g_{ } = 1.939; g_{\perp} = \text{nd}$	$A_{ } = 18.9; A_{\perp} = \text{nd}$	73
		$g_{xx} = 1.977; g_{yy} = 1.993;$ $g_{zz} = 1.947$	$A_{xx} = 7.42; A_{yy} = 7.42; A_{zz} =$ 19.6	77
	S_2 resimulation of S_2	$g_{ } = 1.936; g_{\perp} = 1.996$	$A_{ } = 19.8; A_{\perp} = 7.3$	73
		$g_{xx} = 1.975; g_{yy} = 1.992;$ $g_{zz} = 1.930$	$A_{xx} = 7.4; A_{yy} = 7.4; A_{zz} = 19.5$	77
L	$g_{\text{eff}} = 2$		77	
Y		$g_{ } = 1.941; g_{\perp} = \text{nd}$	$A_{ } = 20.07; A_{\perp} = \text{nd}$	69

3.1.4

V^{4+}

V^{4+} (d^1)-exchanged faujasite type zeolites exhibit two distinguished ESR signals and the ESR parameters are summarized in Table 4. Signal A is usually assigned to a pseudo-octahedral V^{4+} -cation located at site III in the supercage, while the second signal is attributed to square-pyramidal V^{4+} coordinated to four lattice oxygen atoms in the supercage [68, 69].

Complex overlapping ESR spectra are observed in the case of hydrothermally synthesized molecular sieves [70–77]. This is shown in Fig. 14 for as-synthesized VAPO-5 molecular sieves as a function of the V-content [77]. At low vanadium content, the spectra are characterized by two signals with hyperfine splitting due to the ^{51}V nucleus ($I=7/2$). These signals, denoted as S_1 and S_2 , are usually considered as axially symmetric and possess slightly different g- and A-values as obtained by visual inspection of the spectra (Table 4). Furthermore, they represent only 10% of the total vanadium content [77]. At higher vanadium content, an additional broad signal (L) is formed with g_{eff} around 2.0. The L signal is due to clustered V^{4+} , while S_1 and S_2 must be due to magnetically isolated V^{4+} ions in distorted octahedral coordination. Tetrahedral coordination can be excluded because such species would have much lower A-values. There are two remarks to be made about this spectrum evaluation:

- (1) No good guess of the g- and A-values is possible by eye. This is because the allowed transitions in the x, y and z directions overlap in the central region of the spectra.
- (2) The relative intensities of the different allowed transitions strongly depend on the symmetry, resulting in complicated overlapping spectra.

Therefore, detailed values of g and A can only be obtained by simulation of the individual spectra S_1 and S_2 , followed by an appropriate summation of the theoretical spectra. This is shown in Fig. 15, and the obtained ESR parameters are

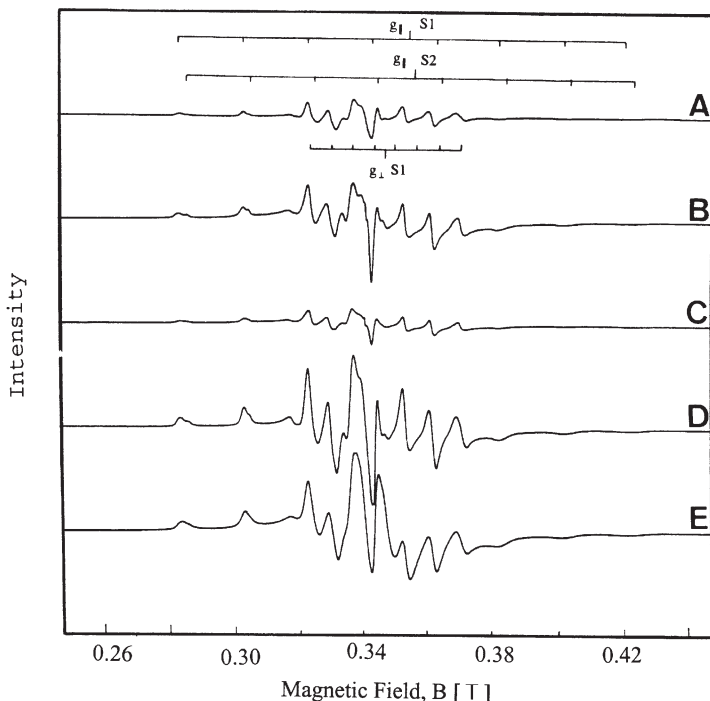


Fig. 14. ESR spectra of as-synthesised VAPO-5 molecular sieves as a function of the vanadium content (reprinted from reference [77]. Copyright 1995 Elsevier Science Publishers): gel composition $0.74\text{R} \cdot (\text{V}_x\text{Al}_y\text{P}_1)\text{O}_4 \cdot 16.7 \text{H}_2\text{O}$ with x equal to A 0.01; B 0.02 measured at 120 K; C 0.02 measured at 300 K; D 0.04 and E 0.08

included in Table 4. It is clear that S_1 and S_2 are slightly rhombic and that the theoretical spectrum nicely fits the experimental one [77].

3.2

Paramagnetic Clusters and Metallic Particles

Alkali metal and Ag clusters impart not only beautiful colors to zeolites, but also give characteristic ESR signals. The latter are due to paramagnetic ionic clusters, M_n^{x+} ($n < 6$) and metallic particles. This area has been pioneered by Kasai and Bishop [13]. There are several recent reviews [78, 79], which give detailed information on the preparation of these materials, the ESR signals and their interpretation. It suffices to state that the ionic clusters have been obtained in zeolites with a low Si:Al ratio and with cages: sodalite, A, X, Y, rho. Preparation methods are: (1) gamma- or X-ray irradiation [80] (2); H_2 reduction [81, 82]; (3) metal vapor adsorption [83–86]; (4) reduction with solvated electrons [87]; (5) in situ decomposition of azides [88–90]; and (6) reduction with organolithium compounds [91]. Here, attention is given to the ESR aspects of the ionic clusters and metal particles.

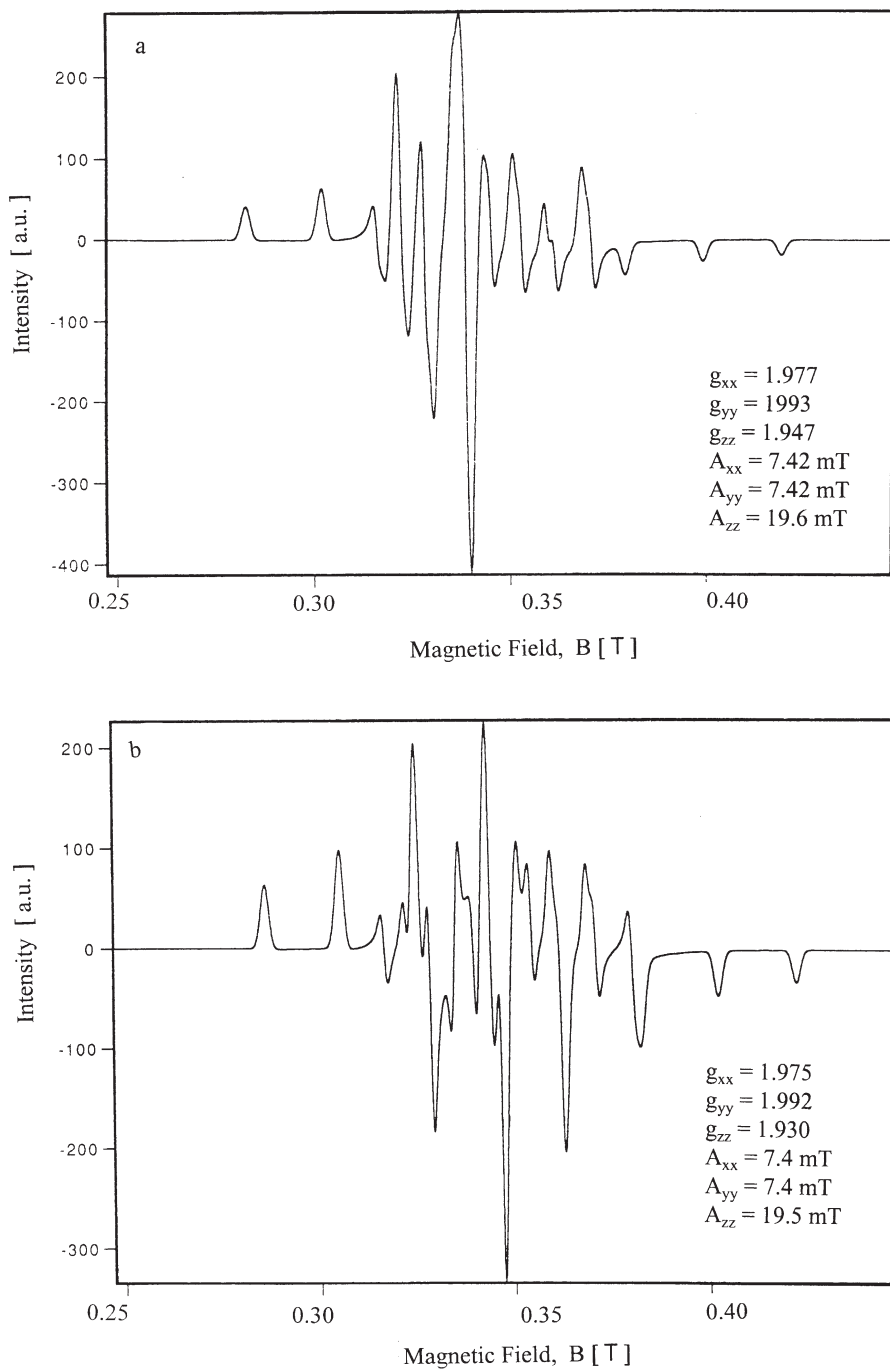


Fig. 15a-d. Simulation procedure of the ESR spectra of as-synthesised VAPO-5 molecular sieves: **a** theoretical spectrum of S_1 ; **b** theoretical spectrum of S_2

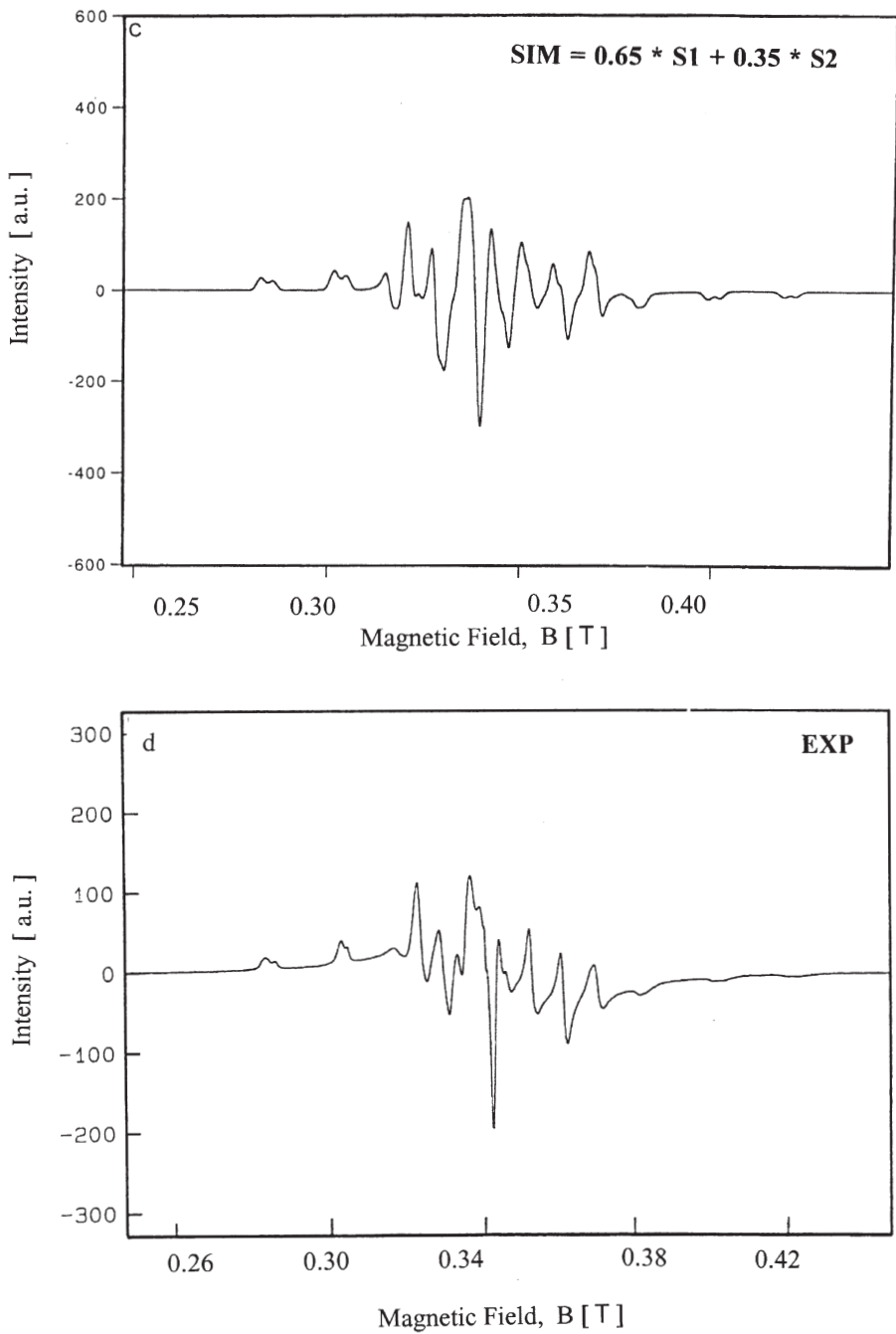


Fig. 15a-d (continued). **c** appropriate summation of the theoretical spectra of S_1 and S_2 and **d** experimental spectrum (reprinted from reference [77]. Copyright 1995 Elsevier Science Publishers)

Atoms and small nuclearity clusters, typically $n=2$ or 3 , are only stable at low temperatures and are usually produced by irradiation at 77 K. The ionic clusters obtained at room temperature have higher nuclearity, $n=4-6$. While n can be directly derived from the hyperfine structure of the ESR spectra, the charge of the clusters is unknown. Most authors prefer the highest possible charge, which is $3+$ for $n=4$ and $5+$ for $n=6$. Such highly charged clusters are not stable in vacuum. In the zeolite, both the negative charge of the framework and confinement in the cubo-octahedra are envisaged to be responsible for the stabilization. The ESR signals have isotropic g - and A -values, suggesting that the unpaired electron is equally distributed among the n nuclei. The ratio $(nA)/A_0$ with A_0 the hyperfine splitting constant of the atom in vacuum is a measure of the distribution of the electron density over the cluster. If this number is smaller than one, it indicates the extent of delocalisation of the electron over the environment of the clusters, i.e. the zeolite matrix and surrounding cations. Values of $(nA/A_0) \times 100$ are given in Table 5. For the Na clusters the A -value depends on the type of zeolite and the type of co-exchanged cation and, when possible, ranges are indicated. The ratio $(nA/A_0) \times 100$ is larger for Ag than for Na or K, indicating that in the former case the unpaired electron is more localized than in the Na and K case. Interaction among paramagnetic ionic clusters in neighboring cages is therefore more likely for Na and K than for Ag. This can be investigated in more detail with electron spin echo modulation [92]. Thus, in the case of Na_4^{3+} , Na_6^{5+} , K_3^{2+} , K_4^{3+} and Ag_6^{5+} interaction with framework Al is evident. In addition Ag clusters of smaller nuclearity can be stabilized in the presence of solvent molecules (H_2O , CH_3OH , $\text{C}_2\text{H}_5\text{OH}$) even in zeolites with channel structures such as SAPO-5 and SAPO-11.

A typical Ag_6^{x+} spectrum of zeolite A is shown in Fig. 16A. Simulation with Gaussian lines gives a somewhat better fit of the experimental spectrum than simulation with a Lorentzian line shape. The g and A values are in both cases equal (Table 5). When the spectrum becomes complex, as in the case of $I > 1/2$ nuclei, second derivative spectra are helpful in the assignment and the determination of the nuclearity (Fig. 16B).

Reduction does not stop at the ionic cluster level, but goes all the way to metallic particles. The latter is characterized by an isotropic conduction electron spin

Table 5. ESR parameters of alkali metal and silver clusters in zeolites

Cluster	Zeolite	g	A (mT)	$[nA/A_0] \cdot 100$ (%)	Reference
Na_4^{3+}	Y	2.0002	3.32	32–40	13, 79, 81, 83
Na_3^{2+}	X, A	2.0028	4.50	63–38	74, 81
Na_5^{4+}	X	2.0022	2.50	40	80, 83
Na_6^{5+}	X	2.0022	2.50	45	80, 83
Ag_6^{x+}	A	1.999	6.66	56	26
Ag_4^{x+}	rho	1.973	14.0	79	76
K_3^{2+}	A	1.9992	1.28	47	78, 81
Na_2^+	X	2.0063	8.5		74
	A	1.9983	10.0	64–46	74

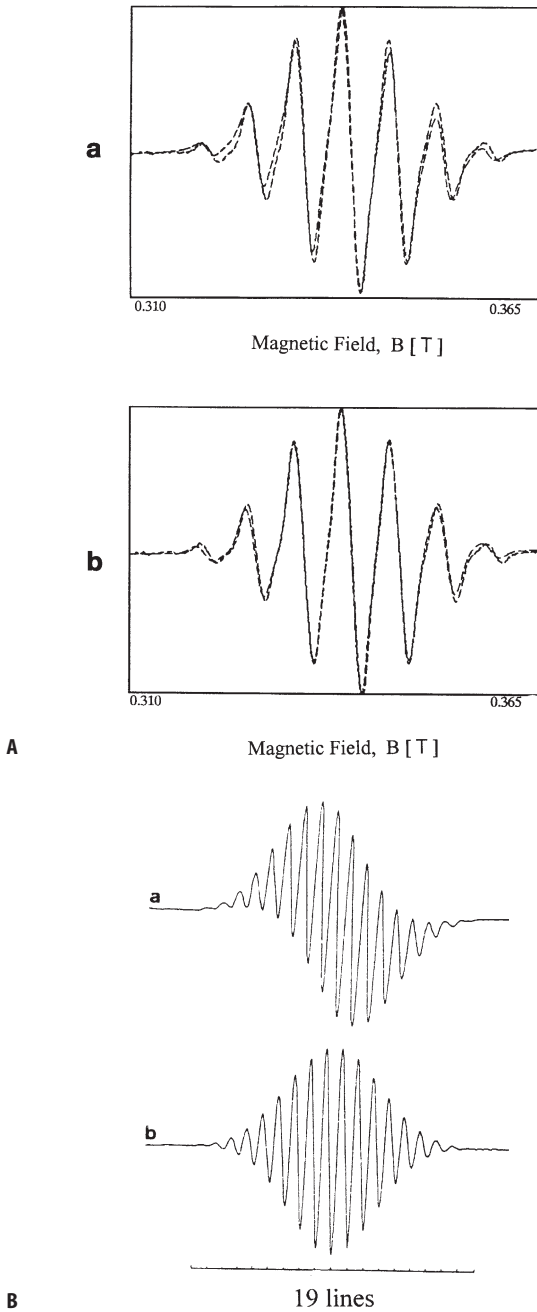


Fig. 16. A Experimental and theoretical spectra of Ag_6^{x+} clusters in zeolite A: *a* Lorentzian lineshape and *b* Gaussian lineshape (reprinted from reference [36]) and B theoretical spectra of Na_6^{5+} clusters in zeolite X : *a* first derivative and *b* second derivative (reprinted from reference [85]). Copyright 1995 VCH Verlagsgesellschaft)

resonance (cesr) line. In many cases this line overlaps with that of the ionic clusters. A quantitative separation of both lines is only possible by simulation. This is illustrated in Fig. 17 for the sodium case. The spectra are composed of Na_4^{3+} and the cesr signal of metallic Na particles. In one case the relative contribution of the isotropic signal is 47%, in the other case 17%. The g and A values are tabulated in Table 6. It is clear that such data can only be obtained by spectral simulation, as visual inspection of the experimental spectra hardly reveals any differences.

The interpretation of the cesr signals in terms of particle size has not been attempted. All the authors notice Curie-Weiss behavior, which is indicative of quantum-sized particles [87, 89]. One is tempted to locate these particles in the supercages. The maximum diameter is then around 1.2 nm, which corresponds to 630 Li, 252 Na, 88 K, 71 Rb or 48 Cs atoms in a closed packed spherical arrangement. The line width, increasing with the size of the atom, is qualitatively explained by this decrease of the number of atoms per cluster. The g values are equal to or somewhat lower than the free electron values. The deviation is explained by spin-orbit coupling effects and thus is more pronounced for the heavier elements (Table 6).

Edwards et al. have criticized the interpretation of the $g=2$ signal in terms of quantum-sized metallic particles [78, 79, 84]. The Na signal can also be generated by exchange coupling of unpaired electrons of Na_4^{3+} clusters in neighboring cubo-octahedra. This is not unreasonable in view of the small $[nA/A_0]$ values of Table 5. The $g=2$ signal is seen at a sodium loading below occupation of all cubo-octahedra with Na_4^{3+} , suggesting a clustering of Na_4^{3+} instead of random distribution over available cubo-octahedra. Even Li-atoms cannot freely migrate through a six-ring into the cubo-octahedra to form the paramagnetic ionic clusters [87]. Thus, formation of an ionic cluster requires electron transfer from an atom in the supercage via the zeolitic lattice to the cations in the sodalite cage. Secondly, there must be enough cations present in the cubo-octahedra to form the cluster. If the latter is not the case, cations must migrate to the sodalite cage and this cation migration will be the rate-determining step in the ionic cluster formation. Schoonheydt and Leeman found an activation energy of $47\text{--}63 \text{ kJ} \cdot \text{mol}^{-1}$ for Ag_6^{x+} formation in zeolite A [81]. Kuranova produced the same clusters by γ -irradiation and found a complex cluster formation mechanism with activation energies in the range $19\text{--}30 \text{ kJ} \cdot \text{mol}^{-1}$ and rate constants of $58\text{--}5300 \times 10^{-6} \text{ s}^{-1}$ at 293 K [91]. Because of the two different cluster production techniques the activation energies might not be comparable, but both point to cationic migration [93]. Clearly, research into the mechanism and kinetics of cluster formation is valuable and promising.

3.3

Paramagnetic Molecules

Molecular sieves can be used to isolate and to store stable paramagnetic molecules. These stable radicals can then be used to study Lewis acidity and exchangeable cations. We will limit our discussion to ESR studies of NO as a probe molecule. Details about the ESR results of other paramagnetic molecules, like NO_2 , NF_2 and ClO_2 can be found in a review of Kasai and Bishop [13].

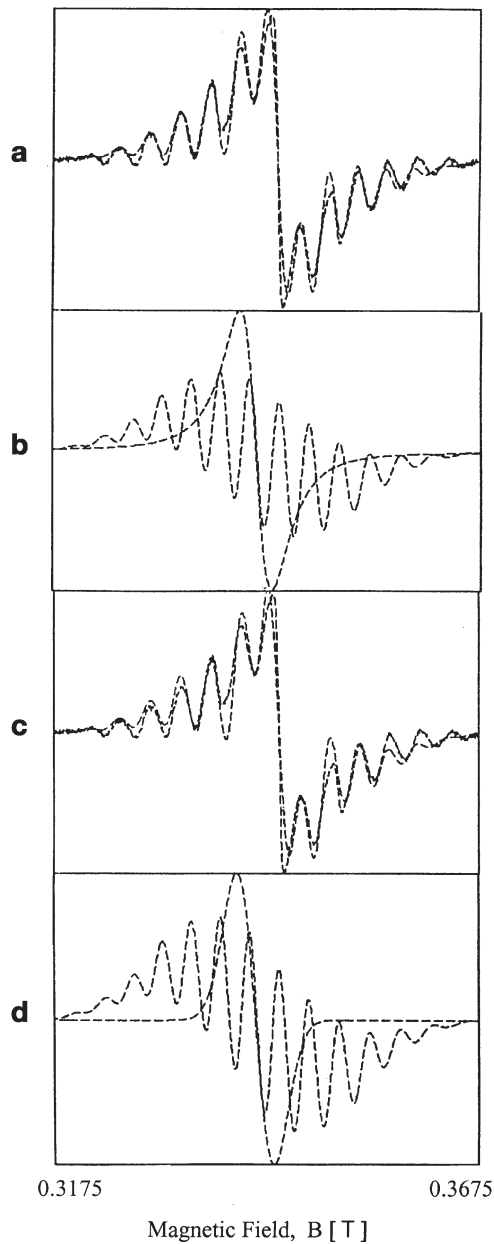


Fig. 17a–d. ESR spectra of zeolitic sodium clusters in zeolite Y: **a** experimental and theoretical spectrum obtained by a summation of the two signals of **(b)**; **b** the ionic cluster, characterized by a 13-line spectrum, is simulated using a Gaussian lineshape, whereas the metallic cluster with an isotropic signal has a Lorentzian lineshape; **c** experimental and theoretical spectrum obtained by a summation of the two signals of **(d)**; **d** the ionic cluster is simulated using a Gaussian lineshape, whereas the metallic cluster is now also simulated with a Gaussian lineshape (reprinted from reference [36])

Table 6. Conduction electron spin resonance signals in zeolite X and Y

Metal	Zeolite	g	Linewidth (mT)	Remark	Reference
Na	X	2.0016	0.43	NaN ₃	82
		2.0011		Na vapour	79
Na	Y	2.0002	0.82	NaN ₃	83
		2.0014		Na vapour	79
Na	A	2.0014		Na vapour	79
Na	A	2.0005		Na vapour	79
K	X	1.9997	0.58	KN ₃	82
Rb	X	1.9929	0.76	RbN ₃	82
Cs	X	1.9686	2.13	CsN ₃	82

NO is a stable paramagnetic molecule, which exhibits, in spite of its unpaired electron in the free molecule, no paramagnetism in its $^2p_{1/2}$ ground state. This is due to the degeneracy of the orbitals which leads to cancellation of the spin magnetic moment of the electron by its orbital magnetic moment. The ESR spectrum of this system should become observable if the orbital moment of the electron is quenched. Thus, the degeneracy among the p orbitals should be removed by its environment. This can be induced by the electric field associated with zeolitic cations. This is illustrated in Fig. 18. The z axis is identified with the N-O internuclear direction, and the zeolitic cation is placed in the y - x plane. The unpaired electron resides in the antibonding π_y^* orbital. One has to cool the zeolite sample down to low temperature to obtain the corresponding ESR spectrum. The spectrum originates from interaction of the unpaired electron of the NO molecule with the cation, while the observed hyperfine structure indicates the interaction of the unpaired electron with the ^{14}N atom with $I=1$. An example of such a spectrum is given in Fig. 19 for NO-treated Na-Y. The corresponding g tensors,

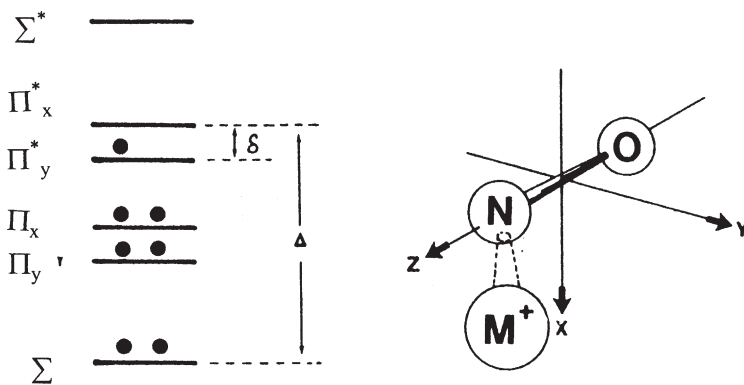


Fig. 18. Valence orbitals of NO adsorbed on a cation with a bent structure (reprinted from reference [13]. Copyright 1976 American Chemical Society)

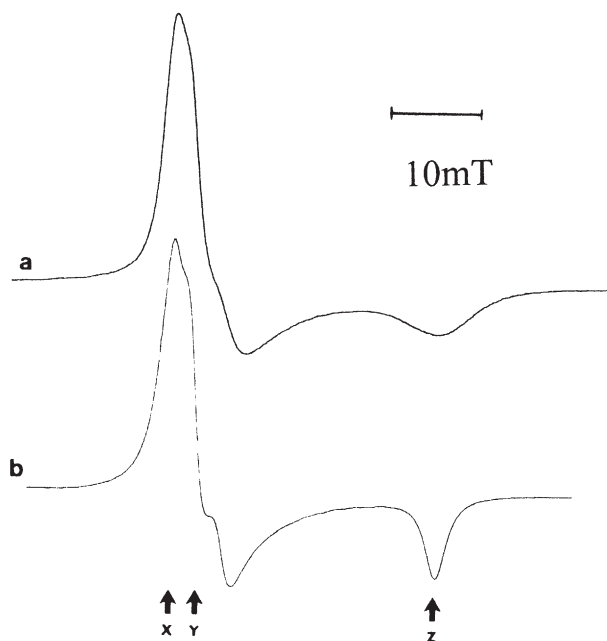


Fig. 19a, b. ESR spectrum of NO adsorbed on NO-treated NaY (reprinted from reference [13]. Copyright 1976 American Chemical Society): **a** experimental and **b** theoretical spectrum

the hyperfine coupling tensors A_N , and the π orbital separations (δ in Fig. 18) for a series of NO-treated Na-X, Na-Y and Ba-Y are given in Table 7.

An additional interaction is observed if aluminum containing extra-framework cations or Lewis acid sites are present. Due to the nuclear spin of Al ($I=5/2$), each nitrogen hyperfine line is split into six lines, some of which may overlap. An example of such interaction is shown in Fig. 20 for NO-treated H-ZSM-5. Witzel et al. have used this property to determine the density and acidity of Lewis sites in H-ZSM-5, H-Mordenite and H-Y zeolites [94–95]. The results obtained are in good agreement with those of more conventional methods and, consequently, ESR spectroscopy with NO as probe is a valuable tool for studying Lewis acidity in zeolites. It is important to stress that ESR spectroscopy of adsorbed NO is only

Table 7. The g tensors, the hyperfine coupling tensors A (mT) and the π orbital separations S (eV) in NO-treated X and Y zeolites (the z axis is parallel to the N-O bond, as shown in Fig. 18) [13]

Zeolite	g_{xx}	g_{yy}	g_{zz}	A_{xx}	A_{yy}/mT	A_{zz}	δ
NaX	1.970	1.970	1.790	0	2.9	0	0.09
NaY	1.999	1.995	1.830	0	3.4	0	0.12
BaY	2.000	1.998	1.890	0	3.0	0	0.18

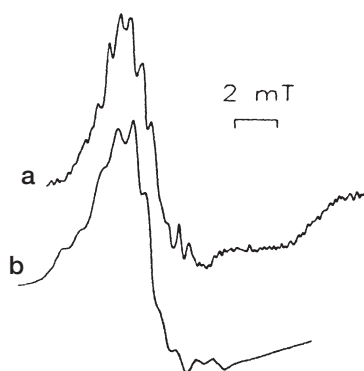


Fig. 20a, b. ESR spectrum of NO adsorbed on NO-treated H-ZSM-5 (reprinted from reference [94]. Copyright 1992 VDI Verlag): **a** experimental and **b** theoretical spectrum

probing the sites strong enough to quench the orbital magnetic moment of the NO molecule and other methods should be called in to give a more global picture of the Lewis acidity of a particular zeolite sample [96]. The ESR method, however, can provide an estimation of the strength of the detected Lewis acid sites, via the g_{zz} parameter. The stronger the electric field of the Lewis acid site, the smaller the difference $\Delta g_{zz} = g_e - g_{zz}$, where g_e is the free electron value (2.0023).

Paramagnetic molecules can also be generated inside the zeolite cavities by using ionizing γ - and X-ray radiation. The most studied molecules are O_2^- and Cl_2^- , but other anion radicals such as SO_2^- and CO_2^- can also be generated inside zeolites. The super-oxide ion O_2^- is obtained by interaction of O_2 with transition metal ions and their complexes in zeolites. While NO is a one electron system, O_2^- is a one hole system. Thus both molecules have similar ESR spectra with $g < 2.0023$ for NO and $g > 2.0023$ for O_2^- (see Tables 7 and 8). If the O_2^- is coordinated to transition metal ions such as Co^{2+} , typical hyperfine patterns are seen if the transition metal ion has a nuclear spin $I \neq 0$ [97].

4

General Conclusions and Outlook

Electron spin resonance is a very sensitive and powerful technique to probe the electronic structures of paramagnetic entities in molecular sieves. There is a vari-

Table 8. The g tensors and π orbital separations of δ (eV) O_2^- generated in zeolites by ionizing radiations (the z axis is parallel to the O-O bond) [13]

Zeolite	g_{xx}	g_{yy}	g_{zz}	δ (eV)
NaX	2.0000	2.0048	2.162	0.18
NaY	2.0016	2.0066	2.080	0.36
BaY	2.0046	2.0090	2.057	0.51

ety of ESR techniques available, each with their particular advantages and limitations. CW X-band ESR spectroscopy is the most popular technique because of its availability, although there is now an increasing use of more advanced techniques such as ENDOR and ESEEM. In addition, multi-frequency and high frequency ESR, such as CW W-band ESR, will be very useful in detailed analysis of coordination environments of transition metal ions.

The various ESR techniques can be applied at different levels of sophistication: from merely detecting the presence of paramagnetic species over the determination of the first coordination sphere around the paramagnetic center up to a detailed description of the electronic structure. Whatever level is being considered, it is important that the user realizes both the potential and the limitations of the particular technique. Over-interpretation should certainly be avoided. This holds equally so for under-interpretation, if with some extra effort (e.g. spectrum simulations), more physically meaningful information can be extracted from the experimental spectra. The systematic and intelligent application of ESR and its related techniques will therefore lead in the future to a better understanding of paramagnetic entities in molecular sieves.

Acknowledgments. BMW acknowledges the Fund for Scientific Research – Flanders (FWO-Flanders) for financial support over the past years. Part of the work reported was supported by the Concerted Research Action and by research grants from the FWO-Flanders.

5

References

1. Abragam A, Bleaney B (1970) *Electron paramagnetic resonance of transition metal ions*. Clarendon Press, Oxford
2. Pilbrow JR (1990) *Transition Ion Electron Paramagnetic Resonance*. Clarendon Press, Oxford
3. Atherton NM (1973) *Electron spin resonance, theory and applications*. Ellis Horwood, Chichester
4. Wertz JE, Bolton JR (1986) *Electron spin resonance, elementary theory and practical applications*. Chapman and Hall, New York
5. Mabbs FE, Collison D (1992) *Electron Paramagnetic Resonance of Transition Metal Compounds*. Elsevier, Amsterdam
6. Poole CP (1967) *Electron spin resonance: a comprehensive treatise on experimental techniques*. Interscience Publishers, a division of John Wiley, New York
7. Wilmshurst TH (1967) *Electron spin resonance spectrometers*. Hilger, London
8. Weckhuysen BM, Van Der Voort P, Catana G (eds) (2000) *Spectroscopy of transition metal ions on surfaces*. Leuven University Press, Leuven
9. Hyde JS, Froncisz W (1981) *Specialist Periodical Reports: Electron Spin Resonance*. Royal Society of Chemistry, Vol 10
10. Vedrine JC (1984) In: Delannay F (ed) *Characterization of Heterogeneous Catalysts*. Marcel Dekker, New York, p 161
11. Mabbs FE (1993) *Chem Soc Rev*: 314
12. Lunsford JH (1972) *Adv Catal* 22:265
13. Kasai PH., Bishop RJ (1976) In: Rabo JA (ed) *Zeolite Chemistry and Catalysis*. ACS Monograph 171, American Chemical Society, Washington, DC, p 350
14. McGarvey BR (1966) *Transit Metal Chem* 3:89
15. Weber RT (1992) *ESP 300 E EPR Spectrometer User's Manual*, Bruker Instruments, Inc, Billerica, Massachusetts, USA

16. Weckhuysen BM, Schoonheydt RA (1994) *Stud Surf Sci Catal* 84:965
17. Schweiger A (1991) *Angew Chem* 103:223
18. Mims WB (1972) In: Geschwind S (ed) *Electron Paramagnetic Resonance*. Plenum Press, New York 4:263
19. Heming M (1987) *Z Phys Chem Neue Folge* 151:35
20. Mehring M (1987) *Z Phys Chem Neue Folge* 151:1
21. Martini G (1990) *Colloids and Surfaces* 45:83
22. Kevan L, Bowman MK (1990) *Modern Pulsed and Continuous Wave Electron Spin Resonance*. Wiley, New York
23. Drago RA (1997) *Physical Methods in Chemistry*, E.B. Saunders Comp., Philadelphia, p 319
24. Ingram DJE (1956) *Free Radicals Studied by Electron Spin Resonance*. Butterworths, London, p 95
25. Dedecek J, Sobalik Z, Tvaruzkova Z, Kaucky D, Wichterlova B (1995) *J Phys Chem* 99: 16327
26. Schoonheydt RA (1993) *Catal Rev-Sci Eng* 35:129
27. Packet D (1987) PhD Thesis, Faculty of Applied Biological Sciences Nr 151, KULeuven
28. De Tavernier S (1989) PhD Thesis, Faculty of Applied Biological Sciences Nr 182, KULeuven
29. Schoonheydt RA (1989) *J Phys Chem Solids* 50:523
30. Chen X, Kevan L (1991) *J. Am. Chem. Soc.* 113:2861
31. Lee CW, Chen X, Kevan L (1992) *Catal Lett* 15:75
32. Lee CW, Chen X, Kevan L (1991) *J Phys Chem* 95:8626
33. Lee CW, Chen X, Kevan L (1992) *J Phys Chem* 96:358
34. Lee CW, Brouet G, Chen X, Kevan L (1993) *Zeolites* 13:565
35. Lee CW, Kevan L (1994) *Zeolites* 14:267
36. Uytterhoeven M (1989) *Optimalisatie van ESR poederspektra*, Master of Engineering thesis, KULeuven;
37. Uytterhoeven MG, Schoonheydt RA (1991) In: Jacobs PA, Jaeger NI, Kubelkov, L, Wichterlov B (eds) *Zeolite Chemistry and Catalysis*, Proc. Int. Symp., Prague, Szecho-Slovakia, Sept. 8–13, 1991 Elsevier, Amsterdam, 1991; *Stud Surf Sci Catal* 69:443
38. Heidler R, Janssens GOA, Mortier WJ, Schoonheydt RA (1996) *J Phys Chem* 100:19728
39. Pierloot K, Delabie A, Ribbing C, Verberckmoes AA, Schoonheydt RA (1998) *J Phys Chem* 102:10789
40. Delabie A, Pierloot K, Groothaert MH, Weckhuysen BM, Schoonheydt RA (2000) *Micropor Mesopor Mater* 37:209
41. Pierloot K, Delabie A, Groothaert MH, Schoonheydt RA (2001) *Phys Chem Chem Phys* 3:2174
42. Sass CE, Kevan L (1988) *J Phys Chem* 32:5192
43. Anderson MW, Kevan L (1987) *J Phys Chem* 91:2926
44. Brown DR, Kevan L (1988) *J Phys Chem* 92:1971
45. Poppl A, Baglioni P, Kevan L (1995) *J Phys Chem* 99:14156
46. Poppl A, Hartmann M, Kevan L (1995) *J Phys Chem* 99:17251
47. Weckhuysen BM, Verberckmoes AA, Vannijvel IP, Pelgrims JA, Buskens PL, Jacobs PA, Schoonheydt RA (1995) *Angew Chem Int Ed Engl* 34:2652; Weckhuysen BM, Verberckmoes AA, Fu L, Schoonheydt RA (1996) *J Phys Chem* 100:9456
48. Grommen R, Manikandan P, Gao Y, Shane T, Shane JJ, Schoonheydt RA, Weckhuysen BM, Goldfarb D (2000) *J Am Chem Soc* 122:11488
49. McNicol BD, Pott GT (1972) *J Catal* 25:223
50. Derouane EG, Mestdagh M, Vielvoye I (1974) *J Catal* 33:169
51. Ratnasami P, Kumar R (1991) *Catal Today* 9, 328
52. Lin DH, Coudurier G, Viedrine J (1989) In: Jacobs PA, van Santen, R (eds) *Zeolites: Facts, Figures and Future*, Proc 8th Int Zeolite Conf, Amsterdam, The Netherlands, July 10–14 1989 Elsevier, Amsterdam; *Stud Surf Sci Catal* 49:1431
53. Goldfarb D, Bernardo M, Strohmaier KG, Vaughan DEW, Thomann H (1994) *J Am Chem Soc* 116:6344

54. Goldfarb D, Bernardo M, Strohmaier KG, Vaughan DEW, Thomann H (1994) *Stud Surf Sci Catal* 84:403
55. Kucherov AV, Slinkin AA (1988) *Zeolites* 8:110
56. Catana G, Pelgrims J, Schoonheydt RA (1995) *Zeolites* 15:475
57. Uytterhoeven M (1995) PhD Thesis, Faculty of Applied Biological Sciences Nr 293, KU Leuven
58. Hemidy JF, Delavennat F, Cornet D (1973) *J Chim Phys* 11–12:1716
59. Hemidy JF, Goupil JM, Cornet D (1977) *J Chim Phys* 7:71
60. Hemidy JF, Cornet D (1974) *J Chim Phys* 5:739
61. Pearce JR, Sherwood DE, Hall MB, Lunsford JH (1980) *J Phys Chem* 84:3215
62. Kucherov AV, Slinkin AA (1994) *J Mol Catal* 90:323
63. Weckhuysen BM, Schoonheydt RA, Mabbs FE, Collison D (1996) *J Chem Soc Faraday Trans* 92:2431
64. Huang M, Deng Z, Wang Q (1990) *Zeolites* 10:272
65. Weckhuysen BM, Schoonheydt RA (1994) *Zeolites* 14:360
66. Nakumura O, Mambrim JS, Pastore HO, Vichi EJS, Gandra FG, Silva EC, Vargas H, Pelzi J (1992) *J Chem Soc Faraday Trans* 88:2071
67. Weckhuysen BM, Wachs IE, Schoonheydt RA (1996) *Chem Rev* 96:3327
68. Martini G, Ottaviani MF, Servavalli GL (1975) *J Phys Chem* 79:1716
69. Fricke R, Selenina M, Schnabel KH (1976) *Z Phys Chemie, Leipzig* Z57:968
70. Whittington BI, Anderson JR (1993) *J Phys Chem* 97:1032
71. Centi G, Perathorer S, Trifiro F, Aboukais A, Aissi CE, Guelton M (1992) *J Phys Chem* 96:2617
72. Petras M, Wichterlova B (1992) *J Phys Chem* 96:1805
73. Rigutto MS, van Bekkum H (1993) *J Mol Catal* 81:77
74. Montes C, Davis ME, Murray B, Naryana M (1990) *J Phys Chem* 94:6425
75. Jhung SH, Uh YS, Chon H (1990) *Appl Catal* 62:61
76. Rao PRHP, Ramaswamy AV, Ratnasamy P (1992) *J Catal* 137:225
77. Weckhuysen BM, Vannijvel IP, Schoonheydt RA (1995) *Zeolites* 15:482
78. Edwards PP, Woodall LJ, Anderson PA, Armstrong AR, Slaski M (1993) *Chem Soc Rev*:305
79. Edward PP, Anderson PA, Thomas JM (1996) *Acc Chem Res* 29:23
80. Liu X, Thomas JK (1992) *Chem Phys Lett* 192:555
81. Schoonheydt RA, Leeman H (1989) *J Phys Chem* 93:2048
82. Xu B, Kevan L (1991) *J Phys Chem* 95:1147
83. Anderson PA, Singer RJ, Edwards PP (1991) *J Chem Soc Chem Commun*: 914
84. Anderson PA, Edwards PP (1992) *J Am Chem Soc* 114:10608
85. Anderson PA, Edwards PP (1991) *J Chem Soc Chem Comm*:915
86. Anderson PA, Barr D, Edwards PP (1991) *Angew Chem* 103:1511
87. Xu B, Kevan L (1992) *J Phys Chem* 96:2642
88. Grobet PJ, Martens LRM, Vermeiren WJH, Huybrechts, DRC, Jacobs PA (1989) *Z Phys D – Atoms, Molecules, Clusters* 12:37
89. Blazey KW, Muller KA, Blatter F, Schumacher E (1987) *Europhysics Letters* 4:857
90. Yoon KB, Kochi JK (1988) *J Chem Soc Chem Comm*: 510
91. Kuranova GA (1990) *Russian J Phys Chem* 64:833
92. Michalik J, Wasowicz T, Sadlo J, Reijerse EJ, Kevan L (1995) *Radiat Phys Chem* 47:75
93. Mortier WJ, Schoonheydt RA (1985) *Progress Solid State Chem* 16:1
94. Witzel F, Karge HG, Gutsze A (1993) *Proc 9th Int Zeolite Conf, Montreal, Canada, July 5–10, 1992* (von Ballmoos R, Higgins JB, Treacy MMJ, eds) Butterworth-Heinemann, London, 283
95. Gutsze A, Plato M, Karge HG, Witzel F (1996) *J Chem Soc Faraday Trans* 92:2495
96. Catana G, Baetens D, Mommaerts T, Schoonheydt RA, Weckhuysen BM (2001) *J Phys Chem B* 105:4904
97. De Vos DE, Thibault-Starzyk F, Jacobs PA (1994) *Angew Chem* 106:447

UV/VIS Spectroscopy

H. Förster

Institute of Physical Chemistry, University of Hamburg, Bundesstraße 45, 20146 Hamburg, Germany

E-mail: foerster@chemie.uni-hamburg.de

1	Introduction. Electronic Spectroscopy: Ranges, Limits, Comparison with Related Methods	338
2	Theoretical Fundamentals and Principles	339
2.1	Physical Fundamentals and Basic Concepts of Electronic Spectroscopy	339
2.2	Selection Rules, Intensity	340
2.3	Fine Structure of Electronic Bands	343
2.4	Types of Electronic Transitions	345
2.4.1	Transitions of σ , π and n Electrons	345
2.4.2	d-d Transitions	348
2.4.2.1	Electrostatic Model	348
2.4.2.2	Molecular Orbital Model	354
2.4.3	Charge-Transfer Transitions	355
2.4.4	Electronic Transitions in Solids	357
2.5	UV/VIS Spectral Changes upon Interaction with the Surface	361
2.5.1	Band Shift	362
2.5.2	Change of Absorptivity	362
2.5.3	Change of Bandshape	364
2.6	Reasons for the Rare Application of Electronic Appearance of New Bands	364
2.6	Reasons for the Scarce Application of Electronic Spectroscopy	364
3	Experimental Techniques	365
3.1	Absorption/Reflection Spectroscopy	365
3.1.1	Dispersive vs. Nondispersive Spectrometry	365
3.1.2	Comparison Absorption vs. Reflection	367
3.2	Photoacoustic Spectroscopy	369
3.3	Luminescence Spectroscopy	372
4	Applications	373
4.1	Characterization of the Host	373
4.1.1	Optical Properties of Zeolites	373
4.1.2	Siting, Oxidation State, Coordination Sphere of Framework and Nonframework Cations	375

4.1.2.1	General Aspects of the Influence of the Environment on the Electronic and Optical Properties of Transition Metal Ions in Zeolites	377
4.1.2.2	Framework Cations	383
4.1.2.3	Nonframework Cations	386
4.1.3	Acid Strength of Zeolites	393
4.1.4	Polarity of Zeolites	394
4.2	Characterization of the Guest	397
4.2.1	Inorganic Compounds	397
4.2.2	Organic Compounds	398
4.2.3	Reactive Intermediates: Carbocations, Carbanions, Radicals	401
4.2.4	Polymerization in Zeolite Channels	406
4.2.5	Clusters of Metals, Metal Ions and Semiconductors in Zeolite Hosts	408
4.2.6	Zeolite-Hosted Oxides	414
4.2.7	Zeolite-Encapsulated Carbonyl, Metal Chelate Complexes and Dyes	415
4.3	Concluding Remarks	420
5	References	421

1

Introduction

Electronic Spectroscopy: Ranges, Limits, Comparison with Related Methods

In this chapter, ultraviolet(UV)-visible(VIS) spectroscopy of molecular sieves will be covered. This constitutes a major part of electronic spectroscopy but has to be discriminated from other techniques also summarized under this term like photoelectron, electron energy loss and X-ray absorption spectroscopy. In optical electronic spectroscopy or electronic spectroscopy in a narrow sense, the probing particle is a photon that excites an electronic transition without modification of the incoming radiation. Complementary methods are either emission, bringing the system back to its ground state, or reflectance, being a combination of both absorption and emission. Emission or luminescence is divided into fluorescence and phosphorescence, respectively, depending on being restricted to or exceeding the excitation period. In the case of coupling the incident radiation to an internal process, the outgoing photon has a different frequency.

The energy change of a quantized system is usually described in terms of:

$$\Delta E = h \nu = h c / \lambda = h c \tilde{\nu} \quad (1)$$

where ν is the frequency of the electromagnetic radiation, c is the speed of light in the vacuum, λ is the vacuum wavelength which is obtained by

$$\lambda = n \lambda_{\text{air}} \quad \text{and} \quad n \equiv c / c_{\text{air}} = \text{index of refraction} \quad (2)$$

Although in the UV-VIS region the radiation is more traditionally characterized by its wavelength λ in units of nm, it is more desirable to use its reciprocal, the wavenumber $\tilde{\nu}$ in the units cm^{-1} , which has the advantage of being proportional to the energy. Wavenumbers are always reported in vacuum wavenumbers.

The UV and VIS ranges are somewhat arbitrarily divided and overlap each other. It seems practical to take the actual or near UV range from 200–400 nm or 50,000–25,000 cm^{-1} and the VIS range from 400–800 nm or 25,000–12,500 cm^{-1} . Both are accessible by routine techniques, i.e., by commercial spectrometers. The neighboring spectral ranges are on the low-energy side at $\lambda > 800$ nm or $\tilde{\nu} < 12500$ cm^{-1} in which essentially vibrational overtones and combination modes as well as low-frequency electronic transitions are excited, and on the high-energy side at $\lambda < 200$ nm or $\tilde{\nu} > 50000$ cm^{-1} , the far or vacuum ultraviolet passing into the X-ray region where electronic transitions are excited from a core level into unoccupied bound states or continuum states. This then falls within the field of X-ray absorption spectroscopy (EXAFS, XANES) and is dealt with in a separate chapter (see Chap. 5, this Vol.).

In the frequency range 50,000–12,500 cm^{-1} information about the properties of the zeolite host can be obtained, e.g.:

- the band gap from transitions between the top of the valence band and the bottom of the conduction band,
- defects like electron-hole pairs,
- electronic transitions within the d orbitals of transition metal ions,
- charge transfer (CT) processes between cation and anion like transfer of electron density from a filled oxygen orbital to a partially occupied M^{n+} orbital or intervalence charge transfer (IVCT), i.e., movement of electron density between metal ions in different oxidation states.

On the other hand, information on the properties of the guest phase can be obtained provided:

- this phase contains chromophores giving rise to, e.g., $n \rightarrow \pi^*$ or $\pi \rightarrow \pi^*$ transitions, or
- transitions within the d orbital manifold of transition metal ions, or
- charge-transfer transitions, or
- transitions between electronic levels explained by the band theory of solids.

2

Theoretical Fundamentals and Principles

2.1

Physical Fundamentals and Basic Concepts of Electronic Spectroscopy

In this section only a breviary of the theory of UV-VIS spectroscopy will be given. For more detailed information the reader is referred to a selection of textbooks, e.g., [1–7].

In the case of isolated atoms purely electronic transitions can be obtained, while, in the more general case of molecules, rotational and vibrational motions

are also simultaneously excited, as illustrated in Fig. 1 by the electronic ground (") and excited states (') with their vibrational (v) and rotational levels (J). As the energies for excitations roughly follow the order $\Delta E_e > \Delta E_v > \Delta E_r \approx 10^3 > 10^2 \gg 1$, the position of a rotation-vibration-electronic transition is basically determined by the change in the electronic energy, while the respective changes of the other states only give rise to transitions nearby and determine the rotational and vibrational structures of the electronic bands. In the case of polyatomics, and especially with condensed matter and systems with strong interactions, the rotational fine structures cannot be resolved at all even with spectrometers of high resolution, and also a strong perturbation of the vibrational coarse structure has to be taken into account so that for UV-VIS spectra of zeolitic systems broad unstructured bands as the envelope are typical. However, in some rare cases, the vibrational structure of electronic bands indicates the superposition of vibrational on the electronic states.

The intensity of these bands are related to the concentration C and the path length l by the Bouguer-Lambert-Beer law:

$$A \equiv \log(I_0/I) = \epsilon C l \quad (3)$$

where A is the absorbance or extinction, I_0 and I are the intensities of the monochromatic light before and after the sample, respectively, and ϵ is the extinction coefficient.

2.2

Selection Rules, Intensity

The UV-VIS spectrum, usually an A or $\log A$ vs. $\tilde{\nu}$ plot, in a first approximation reflects the discrete electronic states as absorption maxima at different ν_{\max} positions which are correlated with the molecular structure and geometry. The extinction coefficient ϵ or more likely the integral absorption $\int \epsilon(\tilde{\nu}) d\tilde{\nu}$, which is approximately the product of ϵ_{\max} times the halfwidth $\Delta\tilde{\nu}_{1/2}$, gives information on the transition dipole moment R_{nm} or the Einstein coefficient of absorption or induced emission B_{nm} which are interrelated by

$$B_{nm} = (8 \pi^3 / 4 \pi \epsilon_0 3 h^2) |R_{nm}|^2 - \epsilon(\tilde{\nu}) \quad (4)$$

$\epsilon_0 =$ vacuum permittivity

where ϵ_0 is the vacuum permittivity.

The transition moment reflects the probability of a transition between two states ψ_n and ψ_m as the integral over the volume elements in the coordinates of all nuclei and electrons $d\tau$

$$R_{nm} = \int \psi_n^* \mu \psi_m d\tau \quad (5)$$

μ is the electric dipole moment operator with components $\sum e_i x_i$, $\sum e_i y_i$ and $\sum e_i z_i$ where e_i are the charges on the particles of coordinates x_i , y_i , z_i .

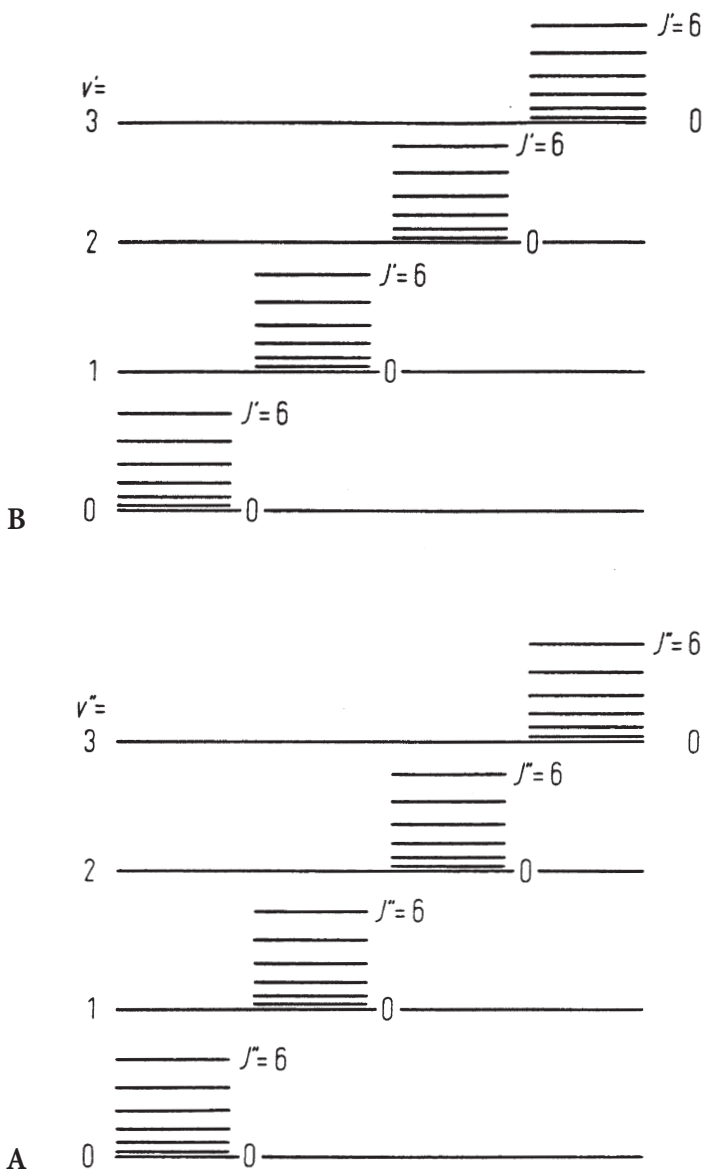


Fig. 1. Schematic representation of the vibrational and rotational sublevels of two electronic states of a molecule

The freedom of a possible transition is restricted by the selection rules, a kind of traffic regulations for spectroscopic transitions, which are based on Eq. (5). The transition moment being zero or nonzero predicts whether a transition is forbidden or allowed, i.e., that the intensity of a forbidden band is much lower in magnitude than that of an allowed band. In the case of an allowed transition, the integral must not vanish, i.e., the integrand must be an even or gerade function, or, in terms of symmetry, must be or contain the totally symmetric irreducible representation.

The first selection rule concerns the multiplicity of states: Since the components of μ are ungerade or odd, the integrand becomes gerade or even only provided the product of the two spin functions is ungerade, i.e., if their multiplicity or the total spin quantum number S does not change, or in other words if $\Delta S=0$. Thus singlet-triplet transitions are normally forbidden.

The second selection rule arises from the symmetry of the two states: Since the components of μ transform like the translations, the direct product of the interconnected wave functions must also transform like at least one of the translations in order to give the totally symmetric representation.

The third selection rule is valid for molecules with a center of symmetry: Only transitions changing the parity, i.e., where $g \leftrightarrow u$, are allowed (Laporte rule).

Although forbidden, such transitions are frequently observed as bands of finite intensity:

- in the case of many-electron excitation due to configurational interaction
- due to intramolecular or intermolecular perturbations by interaction with the surface of an adsorbent or by distortion of the molecular symmetry from simultaneously excited vibrations.

In order to quantify the intensity of an electronic band the oscillator strength f is used. This dimensionless quantity relates the observed integrated intensity to that of a calculated integrated intensity according to a simple model where the excited electron is attracted to the center of the molecule with a Hooke's law type force, i.e., using harmonic oscillator wave functions. f is the ratio of observed and calculated integrated intensities and amounts to

$$f = \int \epsilon(\tilde{\nu}) d\tilde{\nu}_{\text{obs}} / \int \epsilon(\tilde{\nu}) d\tilde{\nu}_{\text{calc}} = (4 \epsilon_0 m c^2 \ln 10 / N_L e^2) \int \epsilon(\tilde{\nu}) d\tilde{\nu}_{\text{obs}} \quad (6)$$

where m is the mass of the electron and N_L the Loschmidt number and should give a maximum value of 1. If $f \ll 1$ the transition is forbidden.

According to Eq. (1), electrons can be excited from the ground state S_0 , which is usually a singlet (S) state, into higher electronic states $S_1, S_2 \dots$ (Fig. 2). The return to S_0 can occur:

- by fluorescence, i.e., emission of radiation,
- by non-radiative transitions, i.e., internal conversion (IC),
- by consecutive intersystem crossing (ISC) steps under spin flip from the singlet to the triplet and back to the singlet states: $S_1 \rightarrow T_1 \rightarrow S_0$, or
- by phosphorescence which is a spin-forbidden radiative $T_1 \rightarrow S_0$ intercombination transition.

As transitions are possible between electronic, rotational and vibrational states, the system in a given electronic state can relax to lower rovibrational

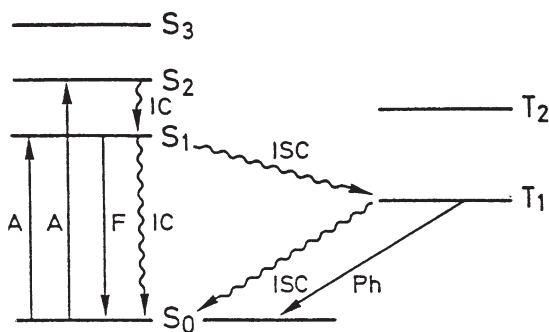


Fig. 2. Term diagram for electronic transitions. *A* Absorption; *F* fluorescence; *Ph* phosphorescence; *IC* internal conversion; *ISC* intersystem crossing. Reprinted from Hesse M, Meier H, Zeeh B (1995) *Spektroskopische Methoden in der organischen Chemie*, with kind permission of Georg Thieme Verlag, Stuttgart

states, so that the fluorescence transition is red-shifted compared to the excitation band.

2.3

Fine Structure of Electronic Bands

A change in the electronic state by ΔE_e would give rise to absorption or emission of one line. The simultaneous change ΔE_v of the vibrational states should result in a progression of so-called vibronic lines while the additional change ΔE_r of the rotational energies transforms it to a progression of rovibronic bands, which is a series of transitions, in the case of absorption with a common lower (v''), in the case of fluorescence or phosphorescence with a common upper (v') level. Figure 3 depicts the superposition of electronic with vibrational (and rotational) excitation for the case of internuclear distances in the two electronic states not significantly different from each other. As according to the Boltzmann expression

$$N_{v''}/N_{v''=0} = \exp [-(E_{v''} - E_{v''=0})/kT] \quad (7)$$

higher vibrational levels $v'' = 1, 2, \dots$ are also appreciably populated, additional and partly overlapping progressions arise from these hot v'' states.

Due to the fairly large energies the electronic transitions are accompanied by changes in the electronic structure reflected in alterations of the potential energy curves of the excited compared to the ground state (Fig. 4). For the former the equilibrium distances usually have increased as a result of bond weakening due to the electronic redistribution. On the changes of the vibrational states during electronic excitation there are no general restrictions, e.g., selection rules. The intensity distribution of the vibrational structure of an electronic band can be explained by the Franck-Condon principle: The electron jump takes place so rapidly in comparison to the vibrational motion that immediately afterwards the nuclei still have nearly the same relative position and velocity as before, i.e., the

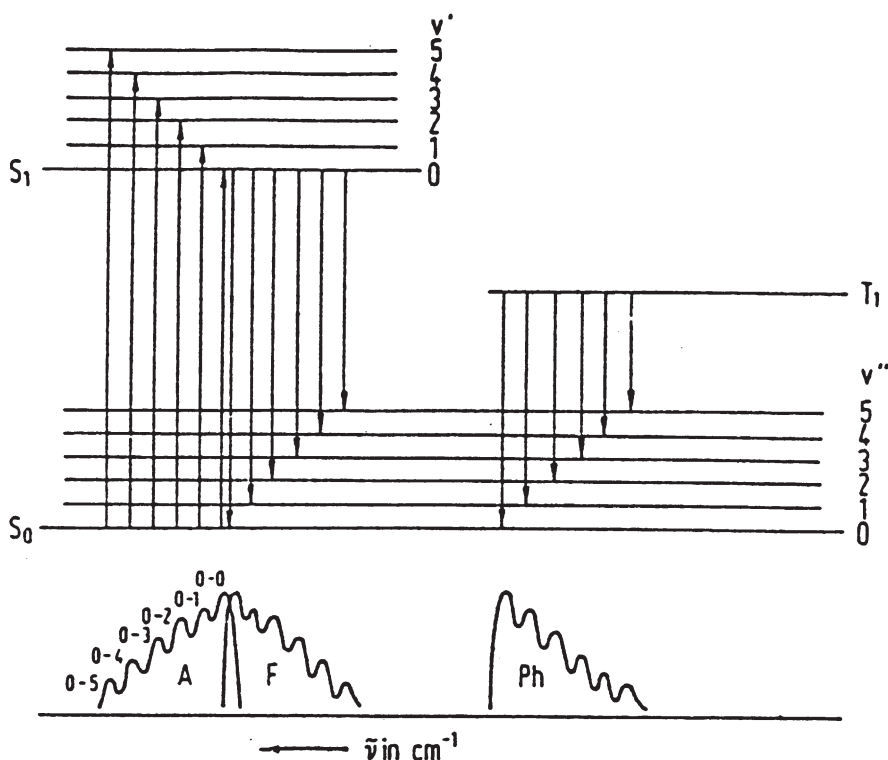


Fig. 3. Electronic excitation between singlet states superimposed by vibration giving rise to a vibrational progression for absorption (*A*), fluorescence (*F*) and phosphorescence (*Ph*). Reprinted from [7] with permission of Springer, Berlin Heidelberg New York. Copyright 1992

nuclei may be regarded as fixed during the transition. Taking into account the probability of being at a particular internuclear distance an electronic transition is most favored at a position such that it connects probable states of the system. In emission the most intense lines can be understood by vertical transitions starting from internuclear distances near the turning points of the oscillator. From quantum mechanical treatment the transition moment R_{ev} is given by

$$R_{ev} = \int \psi_e^* \mu_e \psi_{e'} d\tau_e \int \psi_{v'} \psi_{v''} d\tau_v = R_e \int \psi_{v'} \psi_{v''} d\tau_v \quad (8)$$

where μ_e is the part of the dipole moment depending on the electrons, τ_e and τ_v are the electronic and vibrational coordinates, respectively, and R_e is the electronic transition moment which for a given electronic transition is a constant. Thus, the second integral, the vibrational overlap integral, a measure of the overlap of the two corresponding vibrational wave functions, becomes important. Figure 4 shows the intensity distributions of vibrational progressions with increasing differences between the equilibrium nuclear distances in the electronically excited and ground state.

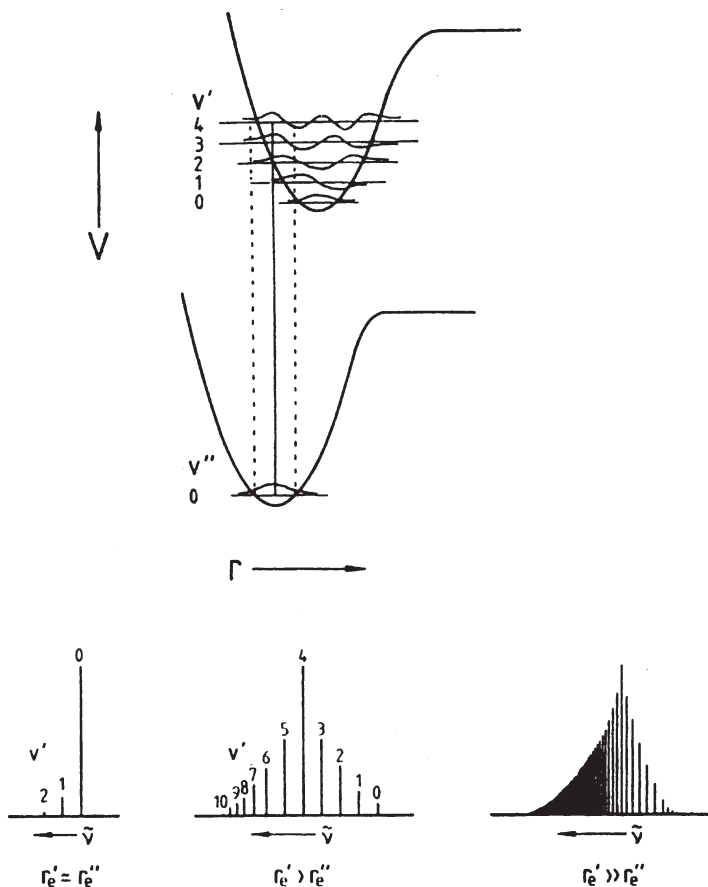


Fig. 4. Franck-Condon principle illustrated for the case $r_e' > r_e''$ and typical intensity distributions of vibrational progressions for the three cases indicated below. Reproduced from [6] with permission. Copyright John Wiley and Sons, Ltd

2.4

Types of Electronic Transitions

2.4.1

Transitions of σ , π and n Electrons

Analogous to the concept of group vibrations in IR spectroscopy, photon absorption in the UV-VIS range can be frequently traced back to the excitation of specific electrons in a particular group of the system, called a chromophore, that is responsible for the 'color' of the respective compound. Substituents that on their own do not confer color but increase (hyperchromic effect) or decrease (hypochromic effect) the coloring power of a chromophore are designated as auxochromes or *antiauxochromes*. Groups that shift the absorption maximum

to lower or higher wavenumbers are called bathochromic or hypsochromic groups.

Electrons in polyatomic systems, essentially s and p electrons, may occupy bonding, *antibonding* or nonbonding molecular orbitals (MOs). According to MO notation, bonding electrons are distinguished into σ or π electrons if their wave functions or charge densities are rotationally symmetric with respect to or contain a nodal plane through the valence axis. Electrons in the corresponding *antibonding* orbitals are labelled with asterisks and denoted σ^* or π^* electrons. Unshared or nonbonding electrons are called n electrons. The sequence of increasing electronic energy is usually in the order: $\sigma < \pi < n < \sigma^* < \pi^* < \text{Rydberg (R) states}$. The latter are highly excited states near the ionization limit.

To date there is no accepted standard notation for electronic transitions. Without going into detail some of the frequently used notations will be discussed shortly.

The first notation, introduced by Kasha, stems from MO representation. Normally, electrons are raised from bonding or nonbonding orbitals to empty *antibonding* orbitals. As transitions between π and σ orbitals are excluded by symmetry, in principle the following types remain: $\sigma \rightarrow \sigma^*$, $\pi \rightarrow \pi^*$, $n \rightarrow \pi^*$, and $n \rightarrow \sigma^*$. Both the arrows \rightarrow and \leftarrow are used at will so that the meanings of $\pi \rightarrow \pi^*$ and $\pi^* \leftarrow \pi$ are the same and, as the direction is indicated, there will be no confusion about the ground and the excited states; $n \rightarrow \pi^*$ transitions are also symmetry-forbidden, resulting in bands of very low intensity. The ranges of absorption for the above-mentioned transitions are outlined in Fig. 5.

The notations after Mulliken use different letters for denoting the ground and excited states, as shown in Table 1.

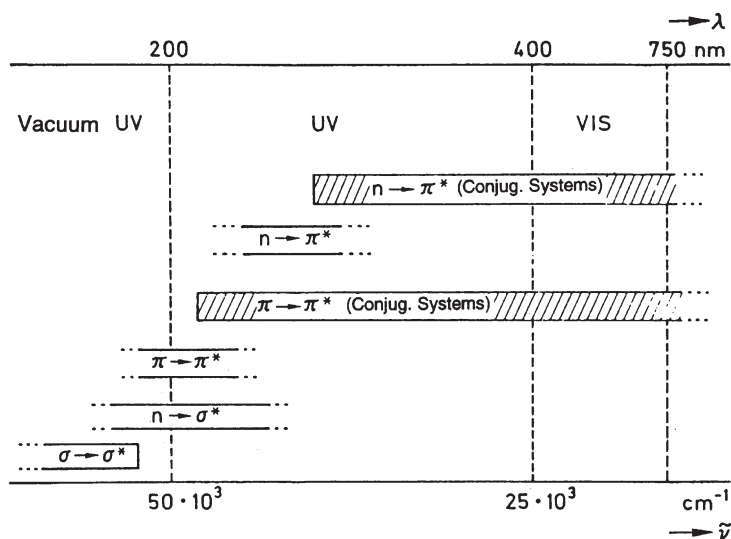


Fig. 5. Ranges of absorption for different electronic transitions. Reprinted from Hesse M, Meier H, Zeeh B (1995) *Spektroskopische Methoden in der organischen Chemie*, with kind permission of Georg Thieme Verlag, Stuttgart

Table 1. Different notations of electronic transitions

System	Symbols Ground state	Symbols Excited state	Examples	Correspondence
Kasha (MO representation)	σ, π, n	σ^*, π^*	$\sigma \rightarrow \sigma^*$ $\pi \rightarrow \pi^*$ $n \rightarrow \pi^*$ $n \rightarrow \sigma^*$	
Mulliken	N	Q, V, R	$V \leftarrow N$ $Q \leftarrow N$ $R \leftarrow N$	$\pi \rightarrow \pi^*$ or $\sigma \rightarrow \sigma^*$ $n \rightarrow \pi^*$ or $n \rightarrow \sigma^*$ Rydberg transition
Group theory	Irred. repr. incl. multiplicity	Irred. repr. incl. multiplicity	${}^1A_1 \leftarrow {}^1A_1$ ${}^1B_2 \leftarrow {}^1A_1$ ${}^1E_{1u} \leftarrow {}^1A_{1g}$	

Finally, the group theory notation classifies the states by the symmetry behavior of their electronic wave functions.

Let us consider ethylene as an example. From the twelve valence electrons ten are σ electrons while two occupy a bonding π MO, $\psi_b = 2p\pi_A + 2p\pi_B = \pi_u$ between the carbon atoms A and B. The corresponding *antibonding* combination is a $\psi_a = 2p\pi_A - 2p\pi_B = \pi_g^*$ MO. According to the D_{2h} point group these two orbitals belong to the b_{3u} and the b_{2g}^* irreducible representations. The ground state configuration is $\psi_b^2 = b_{3u}^2$ with paired spins due to the Pauli exclusion principle, i.e., forming a singlet. Configuration and state are characterized by the symmetry species of the corresponding point group using for distinction lower-case letters for the former and capital letters for the latter. Thus, the ground state is totally symmetric and, including multiplicity $2S+1$, denoted by 1A_g . Exciting one π electron into the *antibonding* MO leads to the configuration $\psi_b\psi_a = b_{3u}b_{2g}^*$ with either paired (singlet) or unpaired spins (triplet), the direct product of which gives the symmetry species ${}^1B_{1u}$ or ${}^3B_{1u}$, respectively. According to Hund's rule the triplet state has the lower energy. Raising both electrons into the π_g^* MO would give rise to the configuration $\psi_a^2 = b_{2g}^{*2}$ and thus again to a state 1A_g . From the ground and the three excited states three transitions should be expected, which in the different notations are shown in Table 2. The first is forbidden as a result of intersystem crossing. The second transition is allowed as the direct product of the interconnected wave functions. ${}^1A_g \otimes {}^1B_{1u} = {}^1B_{1u}$ belongs to the same representation as the z coordinate (and therefore is polarized in the z direction), resulting in a non-

Table 2. The three lowest electronic transitions of ethylene in different notations

Configuration	Kasha	Mulliken	Group theory	Selection rule
$\psi_b\psi_a \leftarrow \psi_b^2$	$\pi \rightarrow \pi^*$	$T \leftarrow N$	${}^3B_{1u}, \leftarrow {}^1A_g$	forbidden: $\Delta S \neq 0$
$\psi_b\psi_a \leftarrow \psi_b^2$	$\pi \rightarrow \pi^*$	$V \leftarrow N$	${}^1B_{1u} \leftarrow {}^1A_g$	allowed: ${}^1A_g \otimes {}^1B_{1u} = {}^1B_{1u}$
$\psi_a^2 \leftarrow \psi_b^2$	$\pi \rightarrow \pi^*$	$V \leftarrow N$	${}^1A_g \leftarrow {}^1A_g$	forbidden: $g \leftrightarrow g$

vanishing transition moment R_{nm} and thus in a strong band near 165 nm. The third ${}^1A_g \rightarrow {}^1A_g$ transition is parity-forbidden and only gives rise to a weak band around 210 nm.

According to the building-up principle in molecules, the MOs are occupied in a distinct order with increasing energy. The two so-called frontier orbitals, the highest occupied molecular orbital (HOMO) with energy E_n and the lowest unoccupied molecular orbital (LUMO) with energy E_{n+1} , play an important role in explaining the optical properties of these compounds. Upon exposure an electron is promoted from the HOMO into the LUMO. This so-called free electron molecular orbital model has been applied to molecules with conjugated double bonds and to aromatic hydrocarbons. On the basis of an electron-in-a-box approach the N -delocalized π electrons of the double bonds occupy in pairs the $n=N/2$ energy levels up to the HOMO. Thus, the frequency of the HOMO \rightarrow LUMO transition can be derived from:

$$\nu = (E_{n+1} - E_n)/h = (2n+1) h/8 m a^2 = (N+1) h/8 m a^2 \quad (9)$$

with m the electron mass and a the length of the conjugated system.

2.4.2

d-d Transitions

While in the preceding sections the discussion was mainly about s and p electrons, a second type of electronic transitions, typical of transition-metal compounds, concerns the excitation of d (or for rare earth elements f) electrons, especially in the presence of a ligand or crystal field. In the case of transition metals the ligand field partly removes the degeneracy of the d orbitals so that $d \rightarrow d$ transitions become feasible. This phenomenon can be explained either by (i) an electrostatic or (ii) a MO model. Here, only a brief introduction into the general features will be given. Further details can be found in the literature [e.g., 8–12].

2.4.2.1

Electrostatic Model

Here the environment is modelled by point charges. As the five d orbitals of the central ion are directed either along ($d_{x^2-y^2}$, d_{z^2}) or diagonally between the coordinate axes (d_{xy} , d_{yz} , d_{xz}), the approach of charges in a distinct arrangement with respect to the coordinates gives rise to a different perturbation of these orbitals and thus to a splitting caused by the environment. In a field of octahedral symmetry, the $d_{x^2-y^2}$ and d_{z^2} orbitals which belong to the e_g representation are raised by $3/5 \Delta_o$, while the d_{xy} , d_{yz} , and d_{xz} orbitals of t_{2g} symmetry are pushed down by $2/5 \Delta_o$, where Δ_o is the energy difference $e_g - t_{2g}$ increasing with the strength of the crystal field. In order to avoid fractions the definition $\Delta_o \equiv 10 Dq$ has been introduced where, according to Schlapp and Penney [8], Dq represents the field strength parameter. In this alternative notation, the e_g orbitals lie $6 Dq$ above and the t_{2g} orbitals $4 Dq$ below the average. In an octahedral surrounding the $d \rightarrow d$ transitions from t_{2g} to e_g are Laporte-forbidden and the respective bands in the VIS and NIR regions are weak in intensity.

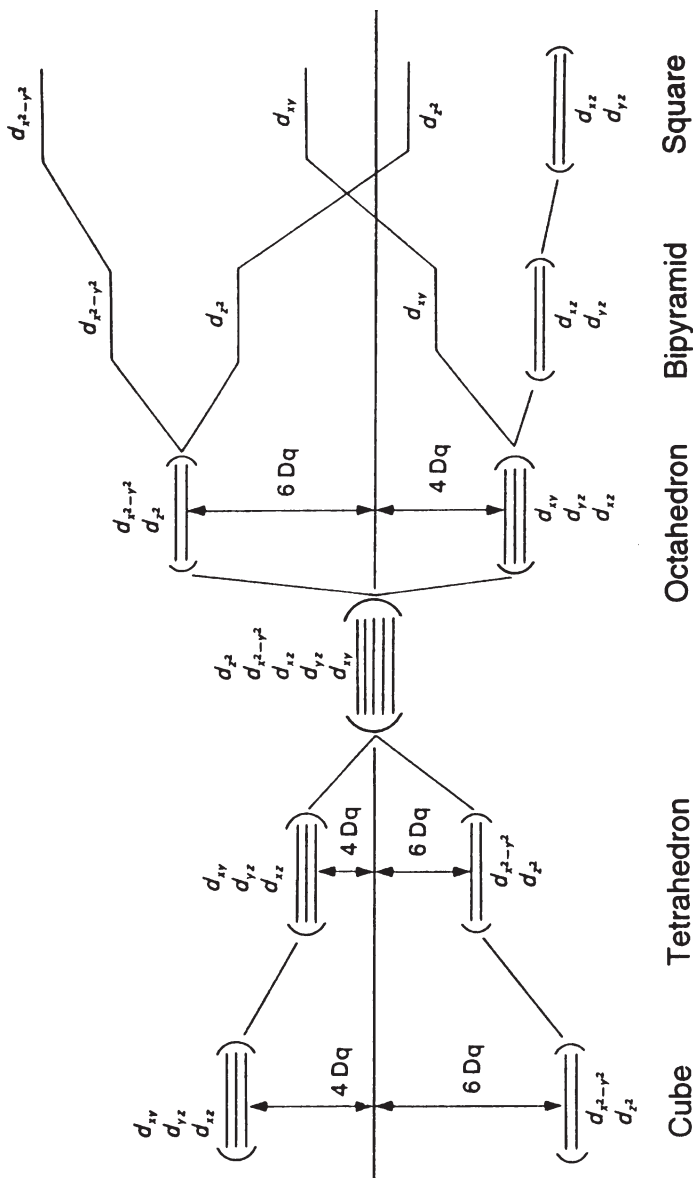


Fig. 6. d Orbital splitting in ligand fields of different symmetries

In tetrahedral environments the splitting becomes reversed: the former t_{2g} orbitals, now of t_2 symmetry, are lifted by $2/5 \Delta_t$ and the former e_g orbitals, now of e symmetry, are shifted downwards by $3/5 \Delta_t$, where $\Delta_t = E_{t_2} - E_{e_g} = 4/9 \Delta_o$ (see Fig. 6). Upon lowering the symmetry of the environment the residual degeneracy is removed further as shown, e.g., for a square planar field. As there is no center of inversion, the Laporte selection rule is no longer valid resulting in an increased intensity of the electronic bands.

So far only the interaction with the external field has been considered. But as a counterpart the electronic interaction also has to be taken into account. As known from textbooks, each electron configuration splits due to electrostatic (i.e., Coulomb) repulsive interaction into states ^{2S+1}L of different energies with multiplicity $2S+1$ that are $(2L+1)(2S+1)$ -fold degenerate, and some of these states are forbidden by the Pauli exclusion principle. From the remaining states, according to Hund's rules, the term with the greatest multiplicity and, for a given multiplicity, the term with the greatest L value, lies lowest in energy, i.e., forms the ground state.

A d^2 configuration, for example, splits into states of energetic order:

$${}^3F(21) < {}^1D(5) < {}^3P(9) < {}^1G(9) < {}^1S(1)$$

with degeneracies given in parentheses.

From quantum mechanical treatment of the term energies two types of integrals, the Coulomb integral J_{ij} and the exchange integral K_{ij} , have to be evaluated [8, 12]. Without going into detail, it has turned out to be advantageous to express these integrals in terms of parameters A , B and C , the so-called Racah parameters, which quantitatively express the meaning of Hund's rules. These parameters are positive quantities since they represent electron repulsion, the linear combination of which makes possible the calculation of the term energies using the following expressions:

$$\begin{aligned} E({}^1F) &= A - 8B, & E({}^3P) &= A + 7B, \\ E({}^1G) &= A + 4B + 2C, & E({}^1D) &= A - 3B + 2C \end{aligned} \quad (10)$$

and $E({}^1S) = A + 14B + 7C$.

As A is common to all terms, and if one is merely interested in relative energies, only the parameters B and C must be known. Further simplification can be achieved by the approximation $C \approx 4B$.

In the case of an octahedral field (see Fig. 6) the ligand field stabilization energy (LFSE), which is the net energy of a $(t_{2g})^x(e_g)^y$ configuration relative to the average energy of the orbitals, is obtained from:

$$\text{LFSE} = (-2/5 x + 3/5 y) \Delta_o \quad (11)$$

On the other hand, an electron which pairs with an electron already present in an orbital experiences a strong Coulomb repulsion, the so-called electron pairing energy P . So, the net energy gain upon occupying the orbitals at a given configuration is:

$$\text{LFSE} + P = (-2/5 x + 3/5 y) \Delta_o + P \quad (12)$$

and, therefore, dependent on Δ_o , i.e., on the ligand field strength. In the weak-field case, $\Delta_o < P$, occupation of the e_g orbital, in the strong-field case, $\Delta_o > P$, electron pairing is more favorable, giving rise to unambiguous configurations in the cases d^1-d^3 and d^8-d^{10} , but to two different high-spin and low-spin configurations in the cases d^4-d^7 , as shown in Fig. 7.

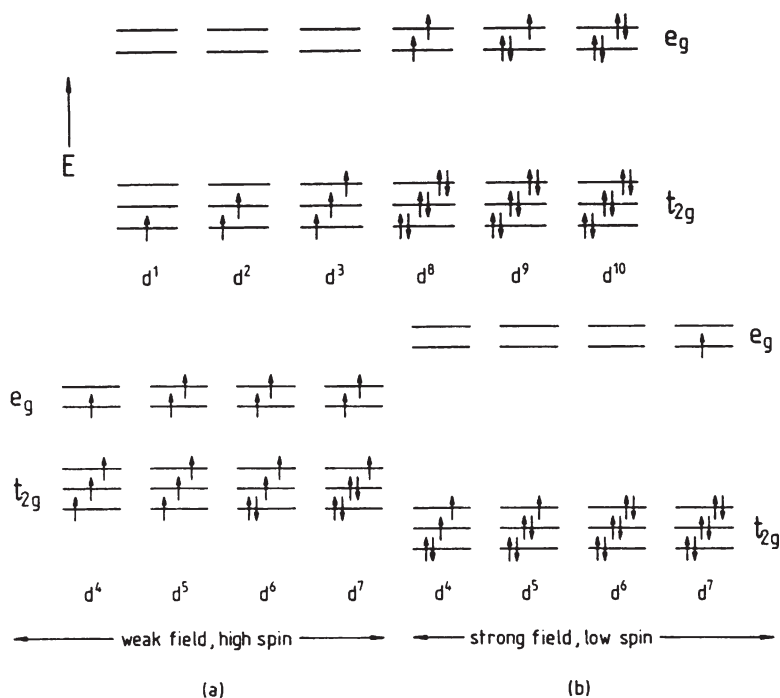
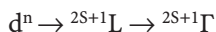


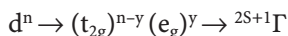
Fig. 7. Electron configurations in octahedral environments. Reproduced from [6] with permission. Copyright John Wiley and Sons, Ltd

For labelling the states of an electronic transition spectral term symbols are used in the form $^{2S+1}\Gamma$, where Γ is the upper-case version of the symmetry species of the overall orbital state and $2S+1$ the multiplicity. For the establishment of the spectral terms two extreme cases are considered:

- the weak-field limit in which only electronic repulsion is important



- the strong-field limit in which only the ligand field is determining



both meeting at the same intermediate case $^{2S+1}\Gamma$, which is obtained by drawing a correlation diagram (Fig. 8), exemplified for the d^2 configuration.

In the weak-field limit due to electron repulsion the d^2 configuration splits into a couple of states ${}^3F < {}^1D < {}^3P < {}^1G < {}^1S$, as shown before. The energy of the 3P state relative to the 3F ground state, expressed by means of the Racah parameters, is $15B$ according to Eq. (10). Switching on octahedral (O_h) field interaction, due to group theoretical considerations the 3F state correlates with ${}^3T_1 + {}^3T_2 + {}^3A_2$ and the 3P state with 3T_1 under conservation of the multiplicity.

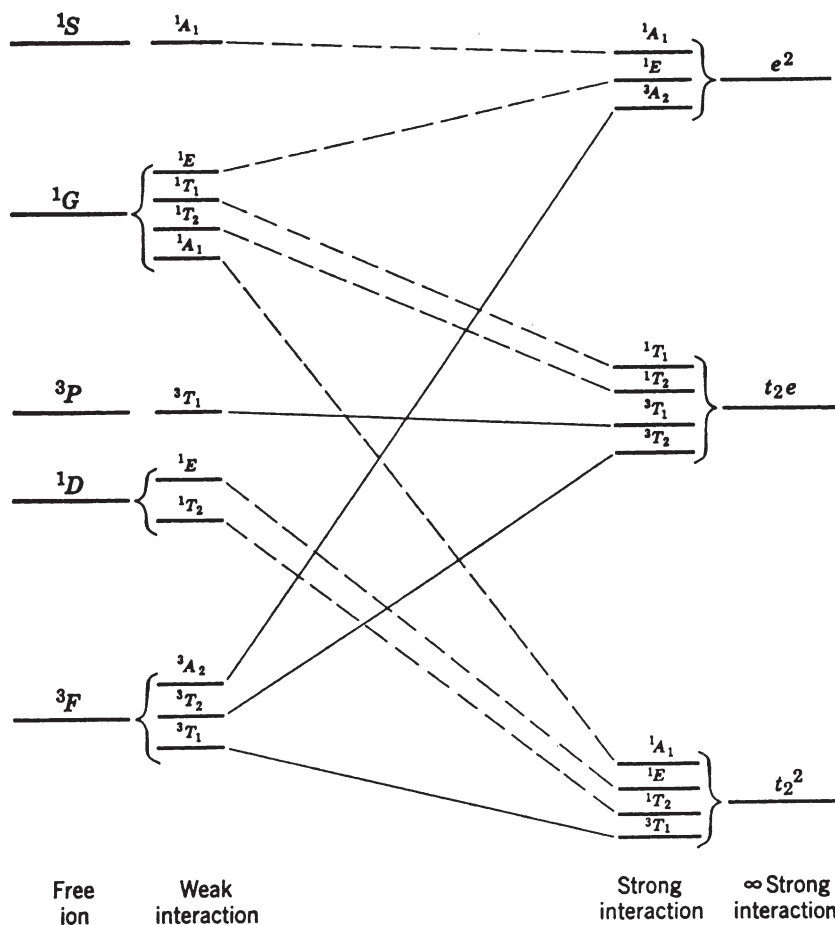


Fig. 8. Correlation diagram for d^2 ions in octahedral environment. The subscript g has been omitted as being common for all states and orbitals. Quoted from [9]. Copyright 1971 by John Wiley & Sons, Inc. Reprinted by permission of John Wiley & Sons, Inc

In the strong-field limit, a d^2 ion has the configurations:

$$(t_{2g})^2 < (t_{2g})^1 (e_g)^1 < (e_g)^2$$

According to Eq. (11), the relative energies of the $(t_{2g})^1 (e_g)^1$ and $(e_g)^2$ states with respect to $(t_{2g})^2$ are Δ_0 and $2\Delta_0$, respectively. The symmetries of the orbital states produced by electronic repulsion can be determined by taking the direct product and decomposing into ${}^3T_{1g} + {}^1T_{2g} + {}^1E_g + {}^1A_{1g}$ for t_{2g}^2 , into ${}^3T_{2g} + {}^3T_{1g} + {}^1T_{2g} + {}^1T_{1g}$ for $t_{2g}^1 e_g^1$ and into ${}^3A_{2g} + {}^1E_g + {}^1A_{1g}$ for e_g^2 .

A schematic overview of term splitting, starting from the strong-field limit (right) and from the weak-field limit (left), meeting at the actual case, i.e., taking

into consideration repulsion as well as field interaction, is given in Fig. 8. As ISC is forbidden and the ground term is a 3T_1 state, it is satisfactory to confine it to the triplet term from which transitions to 3T_2 , 3T_1 and 3A_2 can be expected. The energies of the intermediate cases with both ligand field and electron interaction involved are obtained by correlating both limiting cases which is now a standard problem in group theory. After evaluation of the symmetries of the split states, quantum mechanical calculations provide these energies as a function of the ligand field strength. The most frequently used graphs are the Tanabe-Sugano diagrams in which both energies E and the ligand field strength Δ are expressed in units of the Racah parameter B , and E/B is plotted vs. Δ/B taking the ground term energy of the free ion as zero (Fig. 9). From the analysis of these diagrams it becomes obvious that:

- the multiplicity does not change upon ligand field splitting,
- some of the lines are curved due to interaction of terms of the same symmetry which mix, as they obey the noncrossing rule of quantum mechanics, and diverge from each other,
- the diagrams become discontinuous when the ground term changes due to preference of electron pairing in strong ligand fields, and

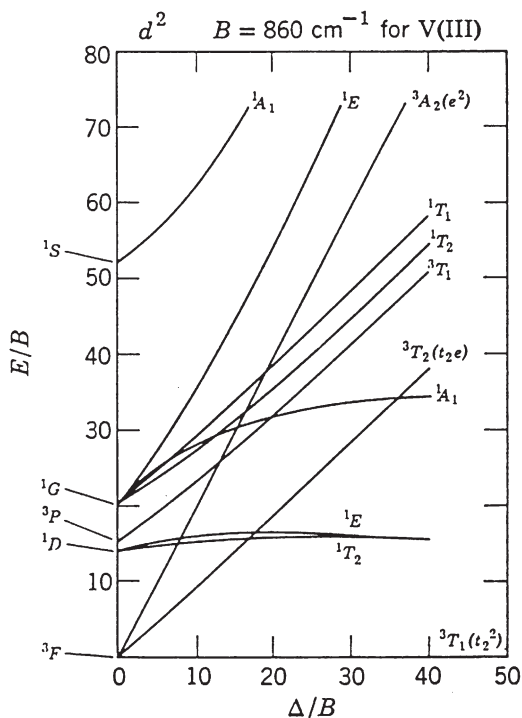


Fig. 9. Tanabe-Sugano diagram for the d^2 configuration. Quoted from [9]. Copyright 1971 John Wiley and Sons, Inc. Reprinted by permission of John Wiley and Sons, Inc

- the diagrams are in pairs qualitatively identical: those of the d^n systems in an octahedral field resemble those of the d^{10-n} systems in a tetrahedral field, and vice versa, explainable by the particle-hole formalism.

The electron repulsion in a free ion in the gas phase is always larger than that in a complex and can be expressed by the nephelauxetic parameter β as the ratio of their Racah parameters:

$$\beta = B(\text{complex})/B(\text{free ion}) < 1 \quad (13)$$

The term β depends on the ligand descending in the so-called nephelauxetic series:



in the sequence of increasing covalent character of the bonding between ion and ligand. Due to the overlap of the metal and ligand orbitals, the space of electron residence becomes enlarged, resulting in a lower electron-electron repulsion. The simple electrostatic model has proved inadequate to explain this series and thus the field splitting Δ .

2.4.2.2

Molecular Orbital Model

In the case of strong interaction between the central ion and ligands the crystal field approximation breaks down and for explanation the molecular orbital (MO) model is preferred. Within its frame the environment is no longer considered as an arrangement of point charges. Instead, bonding/*antibonding* molecular orbital pairs are formed in the usual way from the orbitals of the central ion and the σ and the π orbitals of the ligands provided they are of the same symmetry. This is schematically shown for transition metals of the fourth period in an octahedral environment neglecting the π electron interaction in Fig. 10. For the t_{2g} orbitals of the central ion there is no symmetry counterpart among the ligand σ orbitals (a_{1g} , t_{1u} and e_g in O_h symmetry), and so they are adopted as nonbonding orbitals into the MO scheme. Including the ligand π orbitals (t_{1g} , t_{2g} , t_{1u} and t_{2u} in O_h symmetry) gives rise to changes of the MO levels especially of the t_{2g} orbitals which, in this case, turn into bonding/*antibonding* orbitals, whereas now the ligand t_{1g} and t_{2u} orbitals have become nonbonding MOs due to the absence of symmetry counterparts among the metal ion orbitals. The MO model is more versatile in explaining the increase in the field splitting Δ by the formation of π bonds with suitable ligand orbitals. However, compared to the electrostatic model, the clarity of imagination is lost.

The Jahn-Teller theorem states that in nonlinear systems a degenerate ground electronic configuration is unstable and becomes stabilized by distortion of the O_h or T_d symmetries to lower, e.g., tetragonal or, as an extreme, to square planar symmetries, respectively, thus removing the degeneracy. In this way the energy separations between the ground and higher levels are increased and

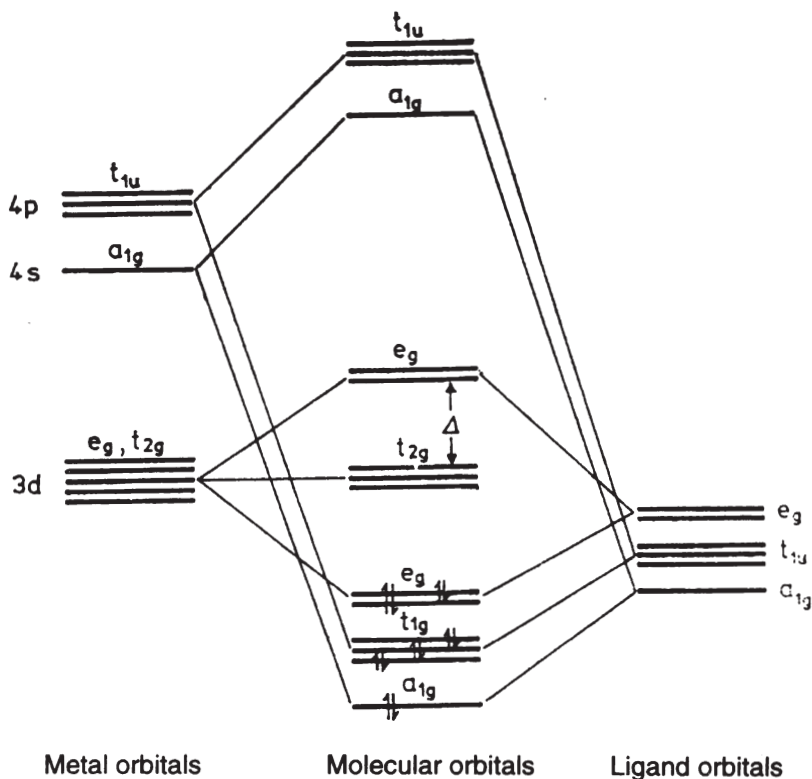


Fig. 10. MO diagram of octahedral complexes under neglect of π electron interaction

additional transitions become feasible. Typical cases are d^4 , d^7 and d^9 complexes with E_g and T_{1g} ground states. Jahn-Teller distortion is also valid for excited states.

The intensities of d-d bands are generally low as being forbidden by the parity and sometimes also by the multiplicity selection rules. Although forbidden, the observed intensities can be explained by relaxation of the selection rules by distortion, i.e., deviation from perfect centrosymmetry, vibronic interaction, configuration interaction or spin-orbit coupling, the details of which are beyond the scope of this article.

2.4.3

Charge-Transfer Transitions

Charge-transfer (CT) transitions take place in systems made up of two components, electron donor (D) and acceptor (A), correctly designated as donor-acceptor complexes. The binding strength between the two species extends from strong bonding, as with the transition metal-ligand complexes shown before, up to the other extreme, transitory contact CT complexes, which exist only during the

duration of collisions between donors and acceptors. It is suggested that donor-acceptor complexes are formed according to:



where DA and D^+A^- describe different resonance structures, the interaction of which is responsible for the resonance energy stabilization of the complex. The ground state may be expressed by its total wave function:

$$\psi_0 = \psi(DA) + \lambda \psi(D^+A^-) \quad (15)$$

where λ^2 determines the ionic contribution to the ground state. Electron excitation is connected with charge rearrangement involving charge transfer from one component to the other, expressed by the total wave function of the excited state:

$$\psi_1 = \psi(DA) + \lambda' \psi(D^+A^-) \quad (16)$$

and $\lambda' > \lambda$ indicates the excited state to be more ionic. Any endeavors to form a donor-acceptor complex and the energy change in the transition depend on (i) the ionization potential of the donor and (ii) the electron affinity of the acceptor.

There are several types of donor-acceptor interactions, the energy of which increases in the sequence: contact pairs $\pi-\sigma < \pi-\pi < n-\sigma < \text{Lewis acid-Lewis base}$.

In the case of transition-metal complexes one has to distinguish between (i) ligand-to-metal charge-transfer transitions (LMCT) and (ii) metal-to-ligand charge-transfer transitions (MLCT). For example, with the former, lone pair ligand π orbitals not directly involved in bonding are promoted into an empty orbital of predominant metal character. LMCT transitions require high-lying lone pair orbitals and low-lying empty metal orbitals, a prerequisite which is met in the case of high oxidation numbers of the metal equivalent to a low d-orbital population. MLCT transitions, on the other hand, are observed with metals of low oxidation numbers and empty low-energy π^* ligand orbitals. Examples of this are the spectra of complexes with aromatic, carbonyl and cyano ligands.

Upon dissolving of salts characteristic bands appear, which have to be attributed to charge-transfer-to-solvent transitions (CTTS) being dependent on the solvent polarity. As these are allowed by the selection rules in most cases, the intensity of CT bands is generally rather strong and depends on the extent of overlap of the ψ_0 and ψ_1 wave functions.

In luminescence experiments donor-acceptor complexes show the mirror image relationship between absorption and emission spectra. An interesting anomalous feature has been found with typical donor molecules in solutions of aromatics: A broad structureless emission band arises at the low-frequency side of the hydrocarbon band increasing in intensity with growing donor content at the expense of the former. This phenomenon has been explained by the formation of CT complexes in the excited state, so-called exciplexes. Exciplexes may be formed by interaction of excited acceptors with donors (A^*+D) or reverse (D^*+A).

2.4.4

Electronic Transitions in Solids

From the viewpoint of the tight-binding approximation, the electronic structure of a solid is characterized by delocalization of the valence electrons throughout the entire structure. The overlap of a large number of atomic orbitals (AOs) results in closely spaced molecular orbitals (MOs), so-called bands, designated as s -, p -, d -bands and so on, according to the angular momentum of the related atomic state. Depending on the separation of the AOs and on the strength of their interaction there may be a gap between them, a range of energies of zero density of states. This gap may be absent in the case of strong interaction where these bands overlap. The uppermost band is called the conduction band if its filling is incomplete, but it is called the valence band if it is full. In this case the conduction band is the empty band just above. With the band structure model the different properties of metals, semiconductors and insulators have been successfully explained. As far as radiative transitions are concerned, typical situations for photon absorption are indicated in Fig. 11: A conductor with a partially filled conduction band (a) shows excitations to nearby empty states in the same band or, surmounting the energy gap, to states in the uppermost empty band, reflected also by a gap in the spectrum. A conductor with superposition of the uppermost bands (b) thus shows a continuous absorption. In an insulator with a filled valence band (c) only transitions to the conduction band separated by a large gap are possible. Decrease of the gap would explain the behavior of semiconductors. The final example (d) describes the situation in the case of lattice defects, i.e.,

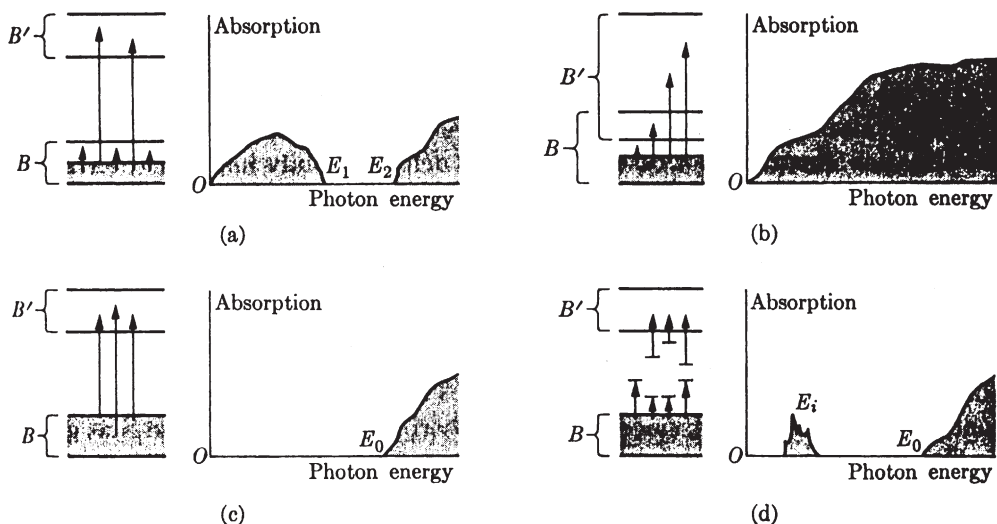


Fig. 11a-d. Radiative transitions in solids. Conductor **a** with incompletely filled conduction band; **b** with band overlap; **c** insulator or semiconductor depending on the width of the gap; and **d** insulator with lattice defects. From Alonso M, Finn EJ. *Fundamental University Physics*, vol VIII. Copyright Addison-Wesley Publishing Company. Reprinted by permission

imperfections of structure or composition, normally present in all solids as a consequence of equilibrium at nonzero temperatures predicted by thermodynamics. Intrinsic point defects are either vacancies or framework particles displaced into interstitial sites. Extrinsic point defects, on the other hand, are due to impurities. Intentionally introduced impurities are called dopants. Doping of solids with atoms of an element with more or fewer electrons gives rise to the formation of narrow donor or acceptor bands in the band gap and is responsible for n-type or p-type semiconductivity. In addition to the band gap crossing, much lower discrete energies, e.g., around E_i , are required for electron excitation. Provided these energies fall into the visible or near ultraviolet range, the respective point defects are called color centers.

The properties of color centers have been most thoroughly investigated with alkali halides. From the multitude of color centers the most frequently observed ones are the so-called F-centers (from German *Farbzentren*) obtained either (i) by thermal treatment of alkali halides in alkali metal or halogen vapor, (ii) by irradiation with UV light, X- and γ -rays as well as energy-rich protons, or (iii) by solid-state electrolysis. Only in case (i) is there a deviation from stoichiometry.

The F-center is equivalent to an electron trapped in an anion vacancy and, being nonlocalized, is extended over a space of more than the lattice constant. The electron spends more residence time near to all alkali atoms adjacent to the vacancy, forming temporarily a sodium atom.

Energetically, an F-center is equivalent to a number of discrete states localized in the gap between the valence and the conduction band. Optical absorptions are due to electronic transitions from the ground to excited states, the position of maximum absorption λ_{\max} being almost proportional to the square of the lattice constant.

Besides F-centers a number of further centers can be formed by thermal and optical treatment:

1. *Centers with trapped electrons.* The bands starting from the ground state to excited states are designated in the sequence of increasing energy as F-, K- and L-bands. In the case of the latter, promotion into the conduction band is possible. F'-centers are formed during bleaching the color caused by irradiation into the F-band and attributed to anion vacancies occupied by two electrons, which can also form by trapping of electrons from the conduction band in F-centers. The F'-band corresponds to the ionization of the second weakly bound electron. More complicated color centers are formed by aggregation. Their respective absorptions are named M-, R-, N- and O-bands.
2. *Centers with trapped holes.* For instance, bands due to Cl_2^- on anion lattice site absorbing at the high-frequency side of the F-band are called H- and V-bands.
3. *Exciton centers.* Excitons are mobile, excited electronic states connected with the formation of an electron-hole pair, equivalent to a positronium atom, which carry energy but no charge through the solid. Excitons can be considered as polarization waves spreading out in the crystal and can be described as lying between two limiting cases distinguished as (i) the Frenkel exciton (in alkali halides) and (ii) the Wannier-Mott exciton (in semiconductors).

The former is characterized by a radius small compared to the lattice parameters, and its energy of formation E_f in alkali halides is well reproduced by the empirical Hilsch-Pohl formula:

$$E_f = A - I + Me^2/a \quad (17)$$

where A is electron affinity of the halogen, I the ionization potential of the alkali atom, M the Madelung constant and a the nearest distance between the ions.

The latter is equivalent to an electron in the conduction band and a hole in the valence band, i.e., with a radius large compared to the lattice parameters. Therefore, bonding of the electron is weak similar to a positronium atom embedded in a dielectric with dielectric constant ϵ and an interaction potential approximated by $V(r) = -e^2/\epsilon r$. Such a system has energy states similar to the hydrogen atom following the formula:

$$E = E_g - 4\pi^2\mu e^4/2h^2\epsilon^2 n^2 \quad (18)$$

where E_g is the energy gap, μ is the reduced mass of an electron-hole pair and n the principal quantum number. According to Eq. (18), the exciton ground state with $n=1$ is $E_g - 4\pi^2\mu e^4/2h^2\epsilon^2$ above the valence band edge, and the excited states are bands located within the gap. Exciton transitions occur near the low-energy side of the band gap.

4. *Centers due to impurities.* Another type of color centers are impurity ions, the bands of which are caused by electronic transitions to neighboring ions of the host lattice (U -centers) or of electron defects trapped by impurities (F_Z -centers). In the case of high impurity concentrations colloidal segregations may form.

The process of luminescence in solids is also influenced by the band structure, as schematically outlined in Fig. 12. Figure 12a illustrates the promotion of an electron into the conduction band leaving behind a hole in the valence band. In Fig. 12b an electron of one of the impurity levels fills this hole while an electron of the conduction band may fall into an empty impurity level, which in Fig. 12c reduces its energy by transition into the impurity ground state, emitting radiation of lower frequency than the incident one. Instead, the electron may be trapped in a defect from which a radiative transition to the impurity ground state is forbidden (Fig. 12d). In this case, being a metastable state, the transition may be either delayed giving rise to phosphorescence or the electron may be liberated by excitation via the conduction band (Fig. 12e) and then go the way of normal fluorescence according to Fig. 12b and 12c.

In the case of metals their UV-VIS properties can be described by quantized plasma vibrations, so-called plasmons. Plasmons can be excited by inelastic scattering of electrons or reflection of electrons or photons on thin metal layers. More details are available in the literature [13].

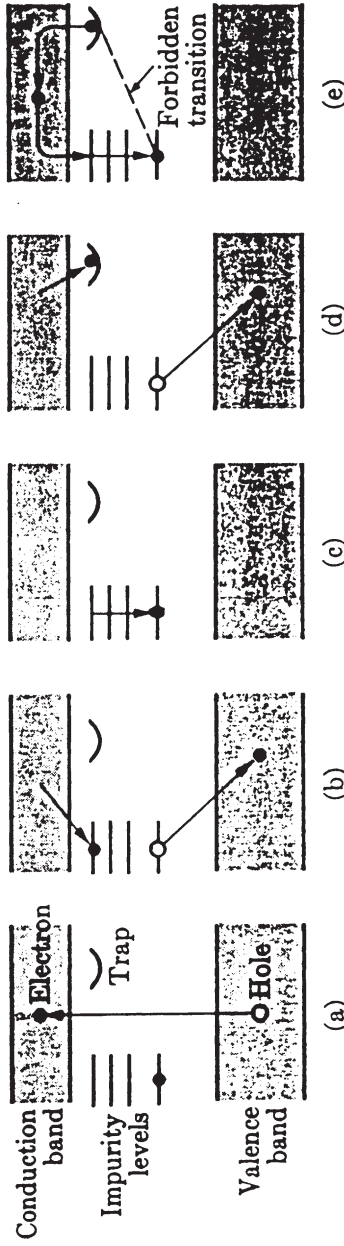


Fig. 12a-e. Mechanisms of luminescence in solids. From Alonso M, Finn EJ. Fundamental University Physics, vol VIII. Copyright Addison-Wesley Publishing Company. Reprinted by permission

2.5

UV/VIS Spectral Changes upon Interaction with the Surface

In this section the influence of molecular interaction on solid surfaces in general will be outlined; this topic has been reviewed in more detail in the literature [14–16]. There is a broad range of interactions reaching from weak to strong, placed between the extreme cases of physisorption and chemisorption and probably at best characterized by the magnitude of heat released during adsorption. Spectroscopy is of special interest as a tool for characterization as it is sensitive to all changes of the molecular properties due to interaction with the surface as well as lateral interaction with adjacent molecules. Furthermore, information about the nature of the active surface sites may be obtained.

UV-VIS spectroscopy in the first place is sensitive to alterations in the electronic structure. Studies of molecular interactions on solid surfaces started much later than those in solution. It is of historical interest that already in the early 1930s, UV-VIS spectroscopy was one of the first techniques applied to a zeolite, as shown in Fig. 13 for iodine adsorption on chabazite [17]. The figure shows the spectrum of iodine on chabazite compared to those of iodine as vapor, as a solid, dissolved in benzene and adsorbed on calcium fluoride. As illustrated by these examples, four main effects of interaction on the spectrum can be established [15, 16]:

1. shift of the band position,
2. change of the absorptivity,

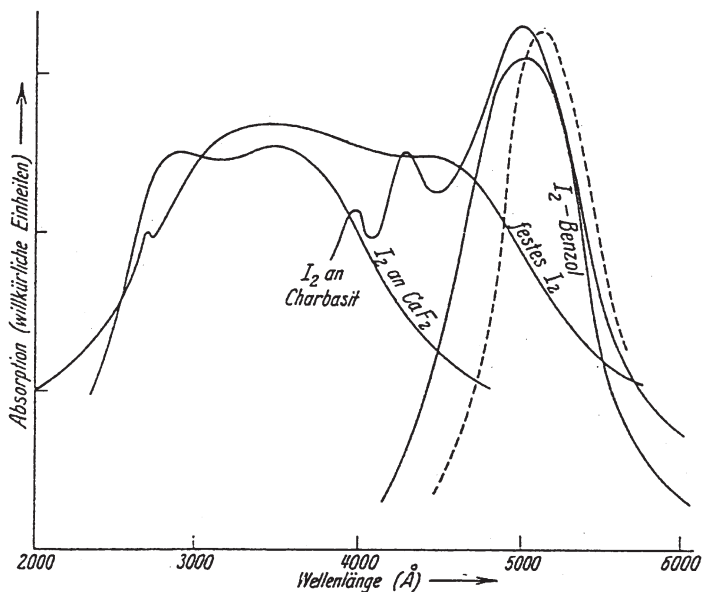


Fig. 13. Historical UV-VIS spectra of iodine adsorbed on chabazite and calcium fluoride compared to solid I₂, I₂ vapor (broken line) and I₂ dissolved in benzene. Reprinted from [17] with kind permission of R. Oldenbourg Verlag GmbH, München

3. change of the bandshape with respect to its vibrational structure, and
4. appearance of new bands.

2.5.1

Band Shift

The surfatochromic shift is characterized by magnitude and direction and is mostly related to the absorption maximum which, depending on the Franck-Condon factor, may not necessarily be the $0 \rightarrow 0$ but more likely a $0 \rightarrow \nu'$ transition. An explanation for both effects was given by de Boer [18] who, as shown in Fig. 14, used the concept of potential energy diagrams of a molecule A in the ground and the excited state A^* when approaching a solid surface together with the Franck-Condon principle: The energy $h\nu_g = ad$ necessary to promote an electron in the free molecule, i.e., far away from the surface, changes to that for the vertical transition in the adsorbed state $h\nu_a = be$ and can be related to the heats of adsorption $Q_A = -\Delta H$ in the ground and in the excited state Q'_{A^*} by:

$$h\nu_a - h\nu_g = Q_A - Q'_{A^*} \quad (19)$$

resulting in a frequency shift

$$\Delta\nu = \nu_a - \nu_g = (Q_A - Q'_{A^*})/h \quad (20)$$

which depends on the difference $Q_A - Q'_{A^*}$. Q'_{A^*} is not completely identical to the heat of adsorption of the excited state $Q_{A^*} > Q'_{A^*}$, but rather a hypothetical heat of adsorption which should be released provided the excited admolecule remains at the same distance from the surface as in the ground state. According to Eq. (20) three different cases must be distinguished:

1. $Q_A > Q'_{A^*}$ gives rise to a hypsochromic shift,
2. $Q_A < Q'_{A^*}$ leads to a bathochromic shift, while for
3. $Q_A = Q'_{A^*}$ the band position is unchanged.

From derivation it becomes clear that the frequency shift is not a measure of the absolute strength of interaction as it reflects only their differences in the excited and the ground state.

The two-dimensional treatment does not consider the change in the intramolecular nuclear distance in the two states which has been taken into account as a three-dimensional representation by de Boer and Custers [19].

2.5.2

Change of Absorptivity

Generally, upon adsorption, the intensity of UV-VIS bands is significantly altered caused by an increase or a decrease in the extinction coefficient ϵ . This effect depends mainly on the adsorption geometry, i.e., whether the electronic vector of the adsorbed species is parallel or perpendicular to the electrostatic surface field. In addition, ϵ may follow a direct or inverse variation with coverage θ , some-

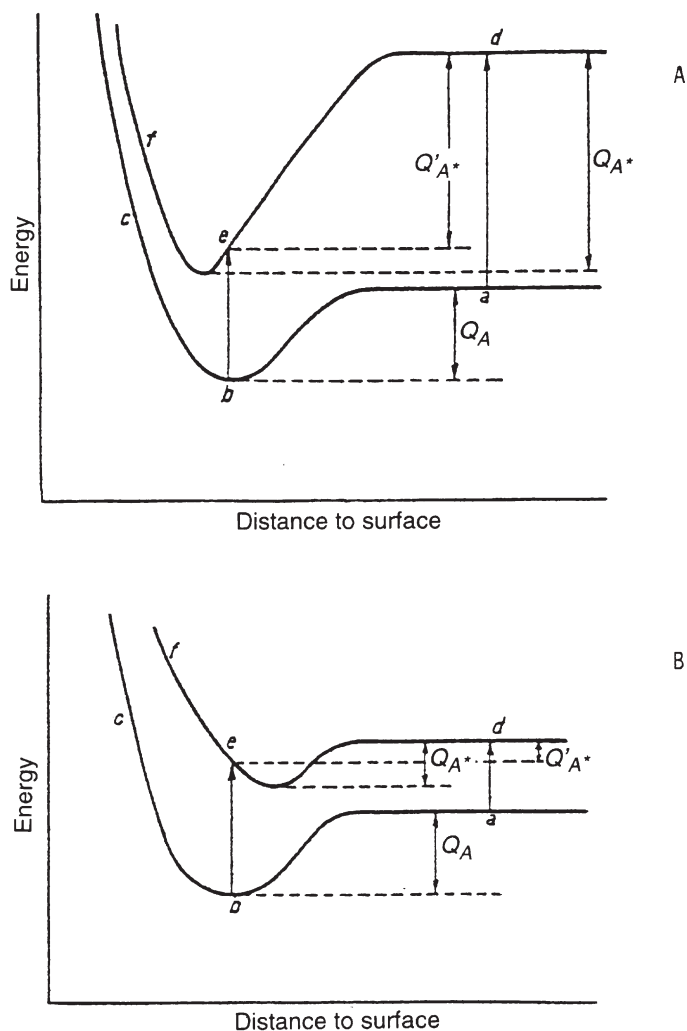


Fig. 14A, B. Potential energy curves of adsorbed molecules in the ground (*lower curve*) and the excited state (*upper curve*) for the explanation of bathochromic (A) and hypsochromic spectral shifts (B) according to de Boer. Reprinted from [18] with kind permission of R. Oldenbourg Verlag GmbH, München

times by several orders of magnitude, depending on both the adsorbate and the adsorbent. In the case of a heterogeneous surface this behavior parallels that of the dependence of the heat of adsorption on coverage: At low loading the perturbation of the admolecule is greatest due to interaction with the most active surface sites and then decreases when these sites are occupied. The resultant extinction coefficient of the adsorbed species is the average over all individual ones induced by the surface field.

2.5.3

Change of Bandshape

Information on interaction can also be derived from the vibrational structure of electronic bands which makes possible the evaluation of the symmetry change of the electron cloud. In those rare cases where this structure is preserved, it can be either displaced as a whole without alteration of the distances between the vibrational subbands or shows changes like the appearance of vibrational modes forbidden for the free molecule, induced by the unilateral surface field or suppressed in cases with motional components perpendicular to the surface. In addition, broadening and coalescence of the lines of a structured band due to a blurring of the rovibrational levels by concomitant enhancement of the averaged absorption can be observed.

2.5.4

Appearance of New Bands

The appearance of new bands, not observed with the adsorbent or with the gaseous adsorbate, indicates severe interference with the electronic structure of the admolecule by electron exchange with the active site or by bond scission which leads to the loss of its identity.

2.6

Reasons for the Rare Application of Electronic Spectroscopy

Compared with IR spectroscopy the development of UV-VIS surface studies was slower mainly (i) because of the complexity and inadequate development of the theory of electronic spectra and (ii) due to methodological difficulties.

UV-VIS spectra are complex as they contain the fine structure from rovibrational transitions. Upon adsorption this structure can only rarely be observed. Due to the blurring of the rovibrational levels mainly broad unresolved bands remain with the complete loss of structural information. The assignment of bands to certain electronic transitions is carried out in correspondence with the direction of the frequency shift or with the aid of semiempirical concepts. At present there is no strict theory relating the spectral changes to the nature of molecular interaction. New surface complexes and intermediate surface compounds have to be determined by comparison with the spectra of the same compounds in solution.

UV spectra are distinguished by their large extinction coefficients compared to the infrared. The methodological limitations are on one hand due to the fact that the UV bands of most organic compounds lie in the far ultraviolet and this region is not accessible using commercial spectrometers. On the other hand, strong scattering in the ultraviolet region by powders is a serious drawback, so that transmission experiments are frequently replaced by reflection studies. One way to improve the information is combination with other methods like IR spectroscopy in order to obtain information on the changes in the vibrational structure, or electron spin resonance (ESR), which is especially valuable in the case of radicals.

3 Experimental Techniques

3.1 Absorption/Reflection Spectroscopy

Spectroscopy of molecularly dispersed systems is routine both instrumentally and theoretically while that of heterogeneous systems like zeolites is still nonroutine. Thus, it requires much more effort and this will be concisely outlined in this section.

3.1.1 *Dispersive vs. Nondispersive Spectrometry*

Since the triumphant advance of interferometers in the infrared range, spectrometers are nowadays distinguished into interferometers or non-dispersive spectrometers and dispersive instruments. There are two main arguments for proving the superiority of interferometry over dispersive spectroscopy:

1. the throughput or Jacquinot advantage, i.e., the larger light gathering power due to the lack of slits resulting in larger signals, and
2. the multiplex or Fellgett advantage, i.e., the simultaneous recording of the optical signals giving rise to an improvement in the signal-to-noise ratio by the square root of the number of resolution elements.

However, the latter is cancelled out when the noise is dependent on the square root of the signal intensity (shot noise) as is the case with photomultiplier tubes (PMTs) or can be reversed into a multiplex disadvantage for those cases where the noise is directly proportional to the signal intensity (flicker noise). As the less structured broad bands in the UV-VIS, especially with adsorbed species, do not require the high resolution and the high wavelength accuracy (Connes advantage) achieved by interferometers, an inferiority of interferometry over dispersive spectroscopy has been theoretically predicted, which, however, has to be more carefully analyzed; this subject has been reviewed in more detail by Williams [20]. As a result, in the UV-VIS region mainly dispersive spectrometers are used while interferometers are only rarely applied to the solution of special nonroutine problems.

The basic components of dispersive spectrometers are a light source, a monochromator, a detector with subsequent amplifying circuit and a readout/recording device. The assembly of a traditional UV-VIS double-beam and, therefore, ratio-recording spectrometer is shown schematically in Fig. 15 [21, 22]. Different interchangeable light sources such as deuterium or tungsten-halogen lamps must be alternatively used for the ultraviolet and the visible range, respectively, while only one detector, the extremely sensitive PMT, is necessary. The light-dispersing part can be designed as a single or a double monochromator depending on whether one or two dispersing elements, today in general gratings, combined

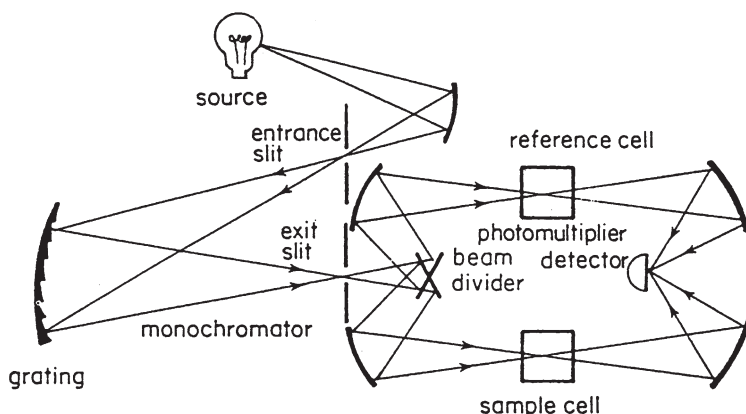


Fig. 15. Schematic representation of the optical layout of a double-beam ratio-recording spectrometer. Reprinted from [21]. Copyright John Wiley and Sons Ltd. Reproduced with permission

with two or three slits are mounted together. Double monochromators furnished with holographically ruled gratings ensure high resolution, light-gathering power, wavelength accuracy and low stray light.

An interesting alternative is the photodiode spectrometer shown schematically in Fig. 16. The monochromator, sometimes also called a polychromator, has only one entrance slit and no moving parts. The beam that is spatially resolved by a fixed grating falls upon a linear photodiode array thus making possible multichannel recording and fast electronic processing.

The advent of computers of reasonable price and their application to spectrometers, spurred by the rapid development of the Fourier transform technique, brought about a number of improvements that nowadays are integral parts of modern spectrometers, such as microprocessor control, self-checking routines, rapid scanning and visual display systems as well as opportunities for data manipulation and reduction, thus augmenting sensitivity, precision and fastness of data acquisition.

Data processing has evolved into an important procedure in modern spectroscopy. Baseline correction by polynomial fitting is one of the basic procedures. Sharpening of the bands can be achieved by deconvolution in the Fourier domain and signal-to-noise enhancement by digital filtering, least-squares polynomial or Fourier smoothing [7, 21]. Derivative spectroscopy, which has been reviewed in more detail elsewhere [23], facilitates the detection of overlapping bands, weak side bands, resolution of shoulders as well as their more precise localization [24] and can be carried out by computation, wavelength modulation or dual wavelength operation. Dual wavelength spectroscopy is a versatile technique [7, 25] that has also been successfully applied to zeolitic systems. In spite of the progress obtained by data processing it should be kept in mind that good spectra will be attained by a balanced application of an optimized parameter setting on the spectrometer and of data manipulation, “letting mathematics solve those problems

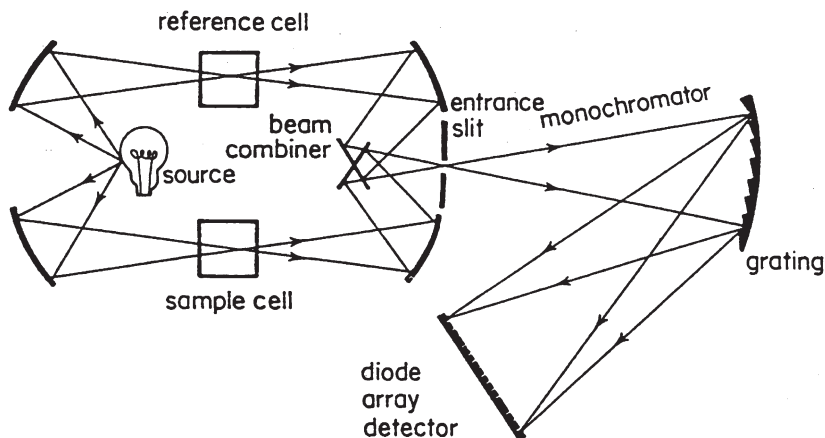


Fig. 16. Schematic representation of the optical layout of a diode array spectrometer. Reprinted from [21]. Copyright John Wiley and Sons Ltd. Reproduced with permission

that the optics cannot" [21]. For further information on spectroscopic instrumentation, the reader is referred to the literature [7, 22].

3.1.2

Comparison Absorption vs. Reflection

In ordinary electronic spectroscopy the transmission mode is predominantly applied, i.e., the absorbed light is measured as the absorbance given in Eq. (3) related to concentration and sample thickness provided the Bouguer-Lambert-Beer law holds over the entire range.

On powdered samples, however, the effects of reflection, refraction and diffraction, summarized into scattering, cause severe losses in transmittance. According to theory [26], the scattered intensity I_s from an incident beam with I_0 depends on the wavelength λ , the volume V and the number of particles per volume unit N and the relative refractive index n , derived for spherical particles is

$$I_s = I_0 24 \pi^3 (n^2 - 1/n^2 + 2)^2 N V^2 / \lambda^4 \quad (21)$$

Equation (21) is valid for Mie scattering, i.e., if the particle sizes are larger than the wavelength of light, as well as for the limiting case of Rayleigh scattering where the particle size is smaller compared to λ . On account of these accompanying processes, transmission experiments with powdered samples are termed as being carried out in "scattered transmission".

Since according to Eq. (21) the scattered light increases with the fourth power of the wavenumber, in the UV-VIS range it should be more advantageous to replace the transmission by the reflectance method. However, Sendoda et al. [27] compared both methods using nickel-exchanged X zeolite either packed as a layer of 3 mm thickness for the reflectance or as pressed self-supporting wafers

for the transmission experiments. Their general experience was a good agreement of the results obtained with both procedures, although the transmission method yielded more intense bands. Encouraged by these findings several groups decided to carry out their investigations in the transmission mode [28, 29]. The advantages of the transmission technique are (i) a demand for a lower sample amount, (ii) an easier sample handling concerning degassing and admission of adsorbate, (iii) no need for an extra diffuse reflectance accessory, and (iv) the omission of data conversion by means of the Schuster-Kubelka-Munk function. A typical experimental setup for transmission studies on zeolites is shown in Fig. 17 [30]. The zeolite powders are applied as self-supporting wafers with a thickness between 5–10 mg/cm² placed in a gold foil frame and inserted into a quartz cell fused to a Conflat flange and connected to a vacuum/dosage system. The heat treatment is achieved by surrounding the lower part of the cell by a tubular oven while the spectra are recorded at room temperature.

The vast majority of zeolite systems has been investigated applying reflectance spectroscopy. Diffuse reflection is caused by single, multiple and dependent scattering, the latter being a multiple scattering with phase coherence between the scattered photons. The reflectance R is defined as the ratio of the total intensity J_0 of light reflected from a sample to the total intensity I_0 incident

$$R = J_0/I_0 \quad (22)$$

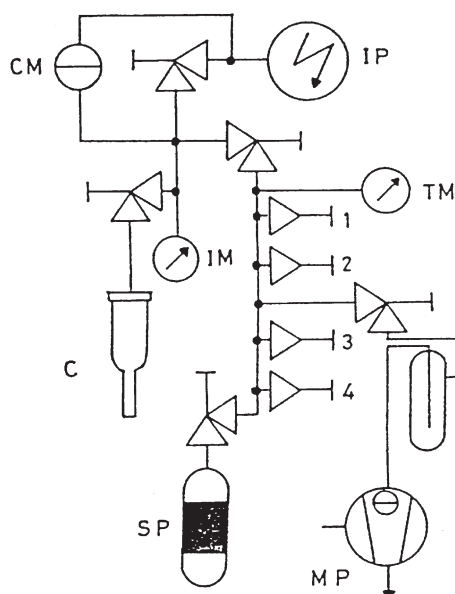


Fig. 17. Schematic representation of the experimental equipment for transmission UV-VIS studies on zeolites. *C* Quartz cuvette; *IM* ionization gauge; *CM* capacitance manometer; *IP* ion pump; *TM* thermal conductivity gauge; *SP* sorption pump; *MP* mechanical pump; *1-4* gas inlet valves. From [30] reproduced by permission of The Royal Society of Chemistry

In the case of both scattering and absorption the amount of light backscattered in a unit volume of the illuminated material is represented by the scattering coefficient $S(\lambda)$ and the part of light absorbed in the unit volume of the specimen by the absorption coefficient $K(\lambda)$. Both effects have been unified in the Schuster-Kubelka-Munk (SKM) equation:

$$F(R_{\infty}) = (1 - R_{\infty})^2 / 2 R_{\infty} = K/S \quad (23)$$

where R_{∞} is the reflectance of an “infinitely” thick sample. The SKM function replaces the Bouguer-Lambert-Beer law and enables the determination of the loss of absorbed radiation for strong scatterers. The theoretical background for the derivation of Eq. (23) can be found in the literature [7, 26, 31–34].

The schematic setup of a diffuse reflectance spectrometer which is obtained by supplying a normal UV-VIS spectrometer with a diffuse reflectance accessory is shown in Fig. 18. The core is an integrating sphere coated with a highly reflective material that collects the scattered radiation and leads it to the detector. The light remitted by the sample is compared with that of a white standard as the reference. Zeolite layers of ca. 5 mm depth are generally sufficient to meet the condition of infinite thickness. A typical sample cell furnished with an evacuated Infrasil double window and designed for temperature control and evacuation is depicted in the lower part of Fig. 18 [32]. Other cell constructions have been reported by Klier [31] and Schoonheydt [34].

3.2

Photoacoustic Spectroscopy

Photoacoustic spectroscopy (PAS) is based on the photoacoustic or optoacoustic effect: Provided modulated radiation impinges a solid in contact with a filler gas in a closed volume, the absorbed light is transferred via heat into mechanical energy as a sound wave registered by a highly sensitive microphone. This process consists of a sequence of steps as illustrated in Fig. 2: Light absorption promotes a system within 10^{-15} – 10^{-14} s into excited singlet states S_1, S_2, \dots . Radiationless deactivation from higher singlet states to S_1 occurs within 10^{-13} – 10^{-12} s and from S_1 to the ground state within 10^{-9} – 10^{-8} s under conversion into heat (IC). Undesired for PAS are some competing processes like (i) radiative deactivation within the singlet term system, (ii) intersystem crossing followed by phosphorescence, and (iii) photochemical reactions.

As shown in Fig. 19 for solid samples, monochromatic light, chopped at a frequency in the order of magnitude of 10–1000 cps which is low compared with the velocity of deactivation, strikes the solid sample contained in a sample holder. After excitation and relaxation the released heat diffuses to the surface, passes into the gas phase and acts as an acoustic piston which generates a pressure wave detected by the microphone and amplified by a phase-sensitive amplifier locked to the chopping frequency ω . Solution of the heat diffusion equation proves that after a distance x from their starting point the heat waves are damped by:

$$\exp(-x/\mu_s) \quad (24)$$

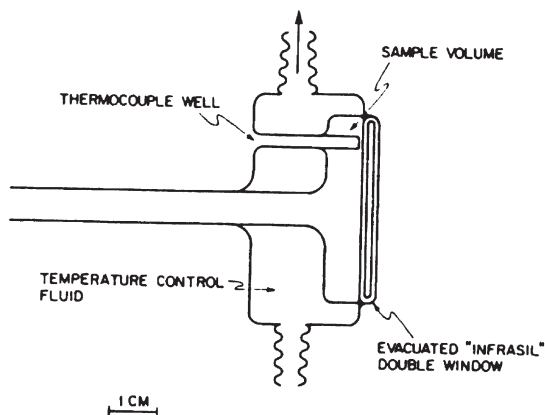
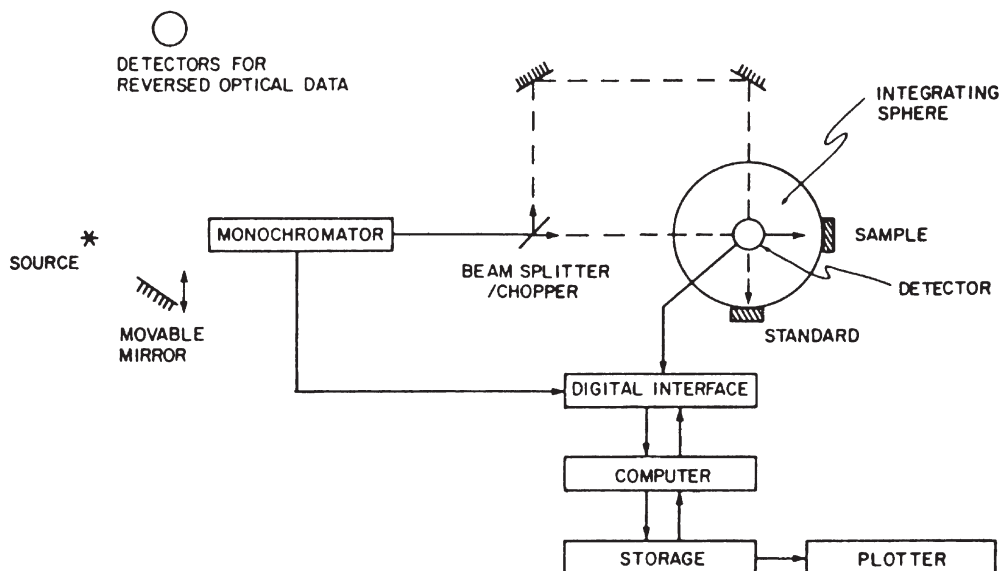


Fig. 18. A Schematic representation of a diffuse reflectance spectrometer. For (i) nondiffuse dispersed illumination the source at the left and the detector at the integrating sphere are used. For (ii) diffuse nondisperse illumination (in the case of fluorescent samples) a source directly attached to the sphere and the detectors on the left upper side are applied. B Temperature-regulated and evacuable diffuse reflectance sample cell according to [32]. Reprinted from [32] with permission of Academic Press, Inc

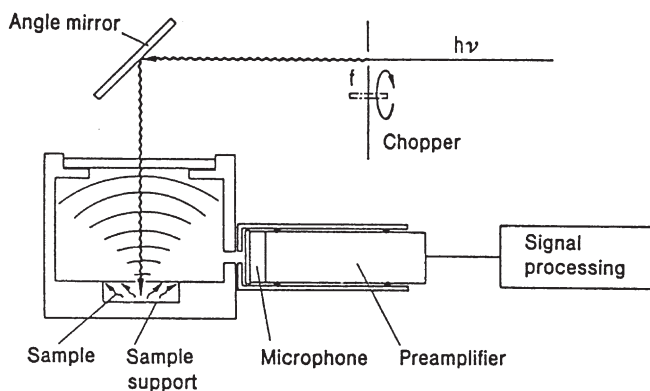


Fig. 19. Schematic representation of a photoacoustic cell for solid samples. Reprinted from [7]

with μ_s being the thermal diffusion length, i.e., the length within which the heat wave is diminished by $1/e$. μ_s is related to the thermal diffusivity α and the chopping frequency by:

$$\mu_s = \sqrt{2\alpha/\omega} \quad (25)$$

The PA signal is directly proportional to the absorption coefficient:

$$\beta = (1/d) \ln I_0/I \quad (26)$$

where d is the pathlength of the sample and thus is proportional to the number and energy of the photons. Therefore, this method is particularly suited for measurements in the UV-VIS region. The PA signal is usually normalized to that of a black body approximated by a carbon standard as the reference. For more details of the origin and interpretation of the complex PA signal the reader may consult the literature [7, 32] and the references given therein.

The advantages of this method against other techniques are:

1. PAS is well suited for the measurement of opaque materials.
2. As according to Eq. (25) the thermal diffusion length μ_s is inversely proportional to the square root of the chopping frequency ω , nondestructive depth profiling is possible.
3. There are minimal demands to sample preparation.
4. The detector is insensitive to light and therefore no interference with the emission of radiation by the sample will take place.

Comparison of the PAS technique with the diffuse reflectance spectroscopy (DRS) technique has been discussed [7, 32].

3.3 Luminescence Spectroscopy

In contrast to PAS this method makes use of the radiative deactivation upon excitation by fluorescence or phosphorescence, as illustrated in Fig. 3. According to the Kasha rule fluorescence starts from the first excited singlet state S_1 , while phosphorescence is the result of ISC followed by a spin-forbidden $T_1 \rightarrow S_0$ transition, both reflecting the vibrational structure of the electronic ground state.

As nonradiative deactivation also has to be taken into account for the fluorescence intensity F , the general expression of which is more complicated and can be found elsewhere, e.g., [7], the Bouguer-Lambert-Beer law does not always hold. In the simplified case of low concentrations c and extinction coefficients ϵ , F is directly proportional to c and ϵ . While the latter relates F to the absorption spectrum, the former gives rise to quantitative analytical application.

Luminescence spectroscopy is a tracer technique mostly applied to first-row transition metal and rare-earth ions. Its great advantage is the very high sensitivity that, for zeolites, facilitates the study of isomorphously substituted framework as well as exchangeable cations. However, the high sensitivity can also be a disadvantage, as spurious signals due to lattice defects may be observed. In addition, too high a concentration may give rise to concentration quenching, and the emission is dependent on the symmetry of the coordination sphere, so that for many applications luminescence is not quantitative.

The schematic layout of a luminescence spectrometer for recording of fluorescence, phosphorescence and excitation spectra is shown in Fig. 20. As excitation source a mercury vapor discharge lamp or, as a continuous source, a pulsed xenon flashlamp is used. Excitation spectra are obtained by setting monochromator b_2 at the maximum of the luminescence spectrum and varying by means of the monochromator b_1 the exciting wavenumber continuously over the whole absorption spectrum of the sample. The luminescence spectrum is corrected by diverting a portion of the incident light on a beamsplitter d to a quantum counter

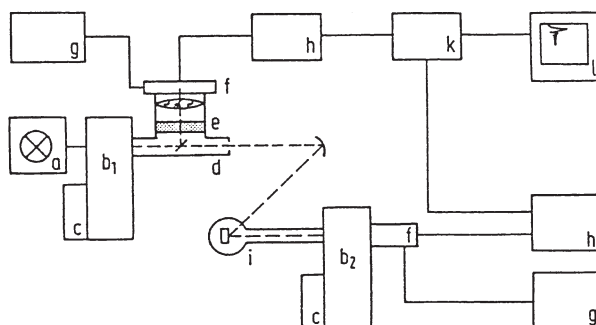


Fig. 20. Scheme of a fluorescence spectrometer for excitation and luminescence spectra. *a* Light source; *b* monochromator; *c* wavelength advance; *d* beam splitter; *e* quantum counter; *f* PMT; *g* high voltage supply; *h* amplifier; *i* cuvette compartment; *k* ratiometer; *l* recorder. Reprinted from [7] with permission of Springer, Berlin Heidelberg New York. Copyright 1992

e and dividing the amplified signals in the ratiometer k . The resultant luminescence excitation spectrum represents the corrected intensity recorded as a function of the excitation wavenumber. For a more detailed discussion the reader is referred to several books [7, 35, 36] that give an excellent overview of the state-of-the-art luminescence techniques, the latter two with special reference to solids.

Applying lasers as the excitation source and either a scanning monochromator connected to a boxcar integrator or, better, an optical multichannel analyzer for the experimental setup has given rise to the development of the laser-induced fluorescence technique which can be used for diagnostic purposes in many contexts [37]. Pulsed UV lasers like nitrogen, frequency-tripled Nd:YAG or excimer lasers serve as the light source.

Another luminescence-based method is luminescence lifetime measurement in which the decay of the excited states with time is followed [38]. Luminescence lifetime is the time required for the intensity to decrease to $1/e$ of its initial value. The most common technique is time-correlated single photon counting which uses a pulsed light source, one monochromator for the excitation and one for the emission side, a PMT with fast response as the detector, a time-to-amplitude converter and data storage in a multichannel analyzer.

Although earlier luminescence as a tool for probing catalysts and zeolites found only modest application, there is growing interest in this method, as has been documented in two reviews [39, 40].

4

Applications

Electronic spectroscopy has significantly contributed to the characterization of zeolites and of molecules adsorbed on their internal surface. A comprehensive review of UV-VIS spectroscopic investigations on zeolitic systems is too wide a scope to cover in this article. Instead different topics of application will be surveyed illustrated by selected examples taking into special account more recent work. As in zeolite science it has become fashionable to speak of host/guest chemistry, so first the host and later the guest will be discussed.

4.1

Characterization of the Host

4.1.1

Optical Properties of Zeolites

As SiO_2 , one of the parent materials of “classical” zeolites, is almost totally transparent over the whole range between $55,500\text{--}12,500\text{ cm}^{-1}$, porous silica should be expected to have similar optical properties. However, upon inspection of their diffuse reflectance spectra, the differently structured zeolites MFI, LTA, FAU and the mesoporous material MCM-41 revealed an onset of absorption near $35,000\text{ cm}^{-1}$ increasing in intensity to higher frequencies [41]. While the structure type and the Si/Al ratio had no effect, impurities like iron or residual template were decisive factors, the former due to a CT transition [42], the latter due to car-

bonaceous residues which, in insufficiently calcined samples, absorb up to 80% of the incident UV light. Furthermore, the crystal size is of major influence as, within the framework of the Schuster-Kubelka-Munk theory, the function $F(R_\infty)$ in Eq. (23) increases with growing particle size [26].

This absorption phenomenon observed for zeolites cannot be explained by band gap absorption. As thermal treatment results in a reduced reflectivity and a shift of the absorption onset to lower wavenumbers, it seems rather probable to assign it to structural defects. Such intrinsic defects have been observed in amorphous silicon dioxide by ESR as well as in crystalline silicalite by photothermal deflection spectroscopy [43]. Although the details are not yet fully understood, there are at present the following speculations: An oxygen atom may be set free from an -Si-O-Si- bond and forms an interstitial Frenkel defect. The remaining -Si-Si- bond is split and a hole trapped by one of the silicon atoms forming an E' center, which is a silicon dangling bond. This idea is supported by a paramagnetic line at $g=2$ in the ESR spectrum. The E' center may react with an oxygen molecule under formation of a dangling peroxide radical $-SiO_2^{\cdot}$ and/or a peroxide bridge -Si-O-O-Si- in the framework.

From this hypothesis the recipe for preparing zeolites highly transparent in the ultraviolet region should comprise both template-free synthesis and avoidance of calcination. In this way a ZSM-5 sample has been synthesized lacking absorption down to $50,000\text{ cm}^{-1}$. Zeolites with such optical properties are well-suited candidates for the development of luminophores. Luminescing guests like rare earth or other ions are excited by the lines of the mercury plasma in the ultraviolet region and emit radiation in the visible range; this phenomenon has been proved by Tb^{3+} and Ce^{3+} exchange into zeolite A [41]. Broadening and splitting of the emission bands indicate the occupation of different cation sites. In general, in addition to other properties, the exchange of the nonframework cations influences essentially the luminescence behavior of zeolites depending on the zeolite type, the reducing agent and the water content of the sample [44, 45].

In the last two decades there has been considerable progress in the synthesis of molecular sieve materials. One result of these efforts is cloverite, a large-pore gallophosphate molecular sieve with a 20 T-atom cloverleaf-shaped entrance into a supercage of about 30 Å diameter, which has attracted attention not only due to potential novel adsorption and catalytic properties and the uptake of bulky adsorbates, but also as a host for the preparation of semiconductor nanoclusters, as an example for the development of new advanced materials.

For this intention cloverite had to be thoroughly characterized by a host of analytical tools, among others by UV-VIS DRS in order to assess its optical properties and their change upon dehydration and calcination in oxygen at 400 °C [46]. As shown in Fig. 21, the spectra of the as-synthesized and slightly dehydrated samples reveal an $O^- \rightarrow Ga/P$ band-gap excitation near 250 nm. After heat treatment at 350 °C, four bands between 230 and 340 nm arise, somewhat blue-shifted upon treatment at 400 °C, which then merge into a broad intense absorption centered around 300 nm. For assigning these bands there are at present only speculations, the most probable of which attributes them to $\pi \rightarrow \pi^*$ transitions of occluded polycyclic aromatics originating from the pyrolysis of quinuclidine applied as template. A certain similarity to C_{60} buckminsterfullerene cannot be

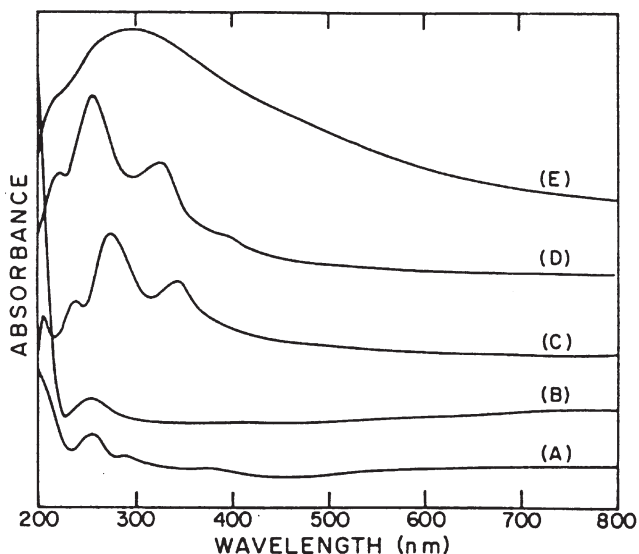


Fig. 21. UV-VIS spectra of cloverite samples. A As-synthesized; B dehydrated at 170°C; C 350°C; D 400°C; and E calcined at 400°C. Reprinted with permission from [46]. Copyright 1993 American Chemical Society

ignored. In this temperature range, the simultaneous depletion of cloverite from framework hydroxyls by condensation and residual template by cracking can be established.

4.1.2

Siting, Oxidation State, Coordination Sphere of Framework and Nonframework Cations

The properties of zeolites are decisively dependent on their cations, either on the framework cations introduced by replacement of Si or Al in the zeolite lattice or on the charge-compensating nonframework cations inserted by ion exchange in the solid state or from solutions. This opens possibilities for targeted modification of these materials in order to tailor their properties for specific applications.

The predominant importance of the cations in zeolites is that they form so-called active sites for selective interaction with guest molecules in sorption and catalytic processes. From the point of view of advanced material science [47] they play a significant role in the formation of quantum-sized clusters with novel optical or semiconducting properties. As they give rise to cationic conductivity, zeolites can be used as solid electrolytes, membranes in ion-selective electrodes and as host structures in solid-state batteries. Organometallic compounds and coordination complexes can be readily formed on these cations within the larger cages or channels and applied to gas separation, electron-transport relays and hybrid as well as shape-selective catalysis [48].

In the case of framework cations the T ions are isomorphously replaced by other ions which may be directly accessible due to the internal micropore surface.

However, they can also, if they are hidden, influence or change the overall properties of the zeolite framework.

The exchangeable nonframework cations are distributed over all potential sites such that the best charge balance is achieved and the energy of the unit cell becomes minimal. For detailed information the reader is referred to an atlas compiling among other things the extraframework sites of 36 structure types [49]. One principal difference to framework cations is that the former are mobile, which on the other hand means that one can never work on the assumption that the cations stick in fixed positions. On the contrary, they undergo a dynamic motion as in solution, jumping from site to site within the lattice. In addition an induced motion in the presence of ligands, other types of cations or hydroxyl groups, i.e., on all occasions that modify the charge distribution at the sites, has been established.

The crystallographic sites of nonframework cations in the structures of zeolite A (LTA) and zeolites X and Y (FAU) are indicated in Fig. 22 where their coordination to the framework is shown in the lower part. Their nomenclature, sites per unit cell, site symmetry and location are summarized in Table 3. Note that the SI position in LTA is equivalent to site SII in FAU and will be further designated as SIA.

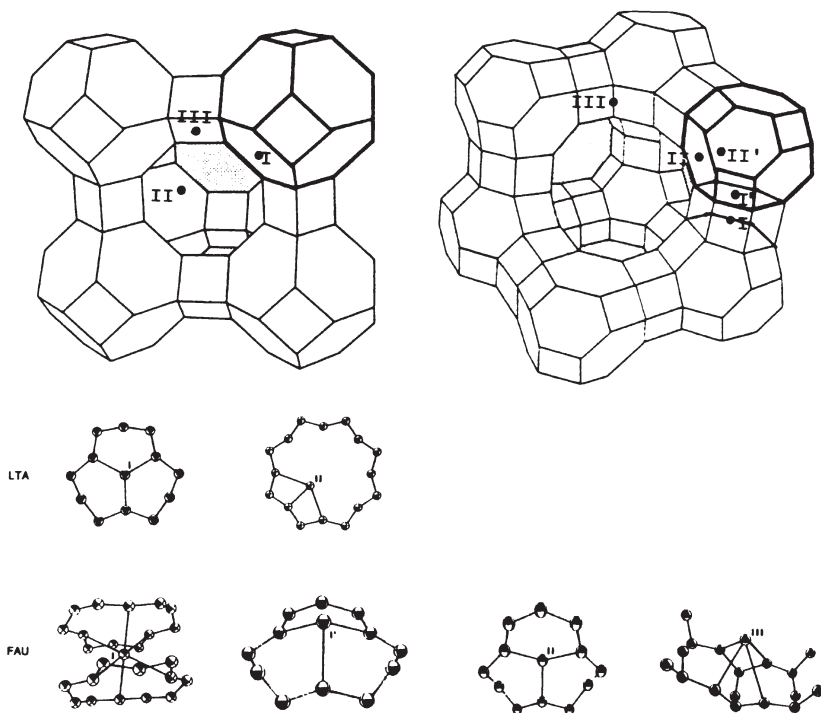


Fig. 22. Schematic representation of the structures of zeolite A (LTA) *left* and zeolites X and Y (FAU) *right* with indication of the cation sites. In the *lower part* the coordination of the cations to the framework is displayed. Reprinted from [58], p 133, by courtesy of Marcel Dekker, Inc

Table 3. Nomenclature, number per unit cell (u.c.), symmetry and location of nonframework cation sites in zeolites LTA and FAU

Zeolite	Site	Number of sites/u.c.	Site symmetry	Location
LTA	I	8	C_{3v}	6R, α cage
	II	3	C_1	8R, α cage
	III	12	$C_{2v}?$	4R, α cage
FAU	I	16	O_h	D6R, γ cage
	I'	32	C_{3v}	D6R, β cage
	II	32	C_{3v}	6R, α cage
	II'	32	C_{3v}	6R, β cage
	III	64	C_{4v}	4R, α cage

The considerable efforts that have been expended to discover location, coordination, ligancy, oxidation state, stability, and migration of the cations and the details of their interaction with guest molecules are documented by the vast number of publications. Different experimental methods have been used for this purpose, e.g., X-ray diffraction (XRD), extended X-ray absorption fine structure (EXAFS), IR, UV-VIS and ESR spectroscopy, calorimetry, thermogravimetry, differential thermal analysis, dielectric and magnetic measurements, to mention just a few, as well as their combined application. Nowadays, increasing support is given to them by theoretical methods such as quantum mechanical calculations, lattice energy and free energy minimization together with computer graphics [50]. Although from all these techniques XRD should be the method of choice, there are still some drawbacks, as sufficiently large single crystals are frequently not available and powder patterns are rather complicated so that Rietveld refinement is required. However, this does not alter the fact that, at low cation concentrations, this method becomes unreliable per se. In this case UV-VIS spectroscopy together with other techniques has contributed greatly to the enlightenment of this topic and has to be considered as its most important application. The results have been summarized in a number of review articles [31–34, 51–58].

4.1.2.1

General Aspects of the Influence of the Environment on the Electronic and Optical Properties of Transition Metal Ions in Zeolites

For investigations in the visible range, transition-metal ions (TMI) are excellent probes for the study of cation siting, coordination, ligancy, oxidation state and migration in zeolites. Knowledge of the introductory literature dealing with the theory of bonding in TMI complexes and with the theoretical interpretation of their spectra, e.g., [59, 60], seems to be appropriate for a better understanding.

With respect to the TMI the zeolite framework behaves like an anion, a solvent or a ligand. The ions are usually introduced from aqueous solution as hexaquo floating complexes $[M(OH_2)_6]^{n+}$. Upon partial dehydration they become stabilized as wall complexes bound in part to the framework and in part to remain-

ing water. Upon complete dehydration they become complexed as bare ions only to the framework. In zeolites A, X and Y the dominant site for trapping the cation is the distorted hexagonal oxygen window (6R) that is of D_{3h} site symmetry. Klier et al. [52, 56] have developed a theoretical model for this site. As shown in Fig. 23, the three basal ligands, L_1-L_3 , are formed by the three proximal oxygens of the 6R, while the fourth ligand L_4 represents either a sorbed guest molecule or the axial electric field from the zeolite framework charge. The ligand field for this model is of C_{3v} symmetry which reduces for $L_1=L_2=L_3, L_4=0$ and $\beta=90^\circ$ to D_{3h} and for $L_1=L_2=L_3=L_4$ and $\beta=109.48^\circ$ to T_d . The Hamiltonian for a generalized ligand field at a site of the symmetry group G has the form [52]:

$$H = \Sigma [-(\hbar^2/8\pi^2m) \nabla_i^2 - Z e^2/r_i + V_G(r_i, \theta_i, \varphi_i)] + \Sigma e^2/r_{ij} + H_{JT} + H_{LS} \quad (27)$$

where in the square brackets the first two are the kinetic energy and the nuclear-electron terms and V_G is the ligand field operator ($G=C_{3v}, D_{3h}, T_d$) representing the potential experienced by an electron on the central ion as a result of the repulsion by the ligands and H_{JT} and H_{LS} are the Jahn-Teller and spin-orbit coupling contributions. Taking at first only interelectronic repulsion $\Sigma e^2/r_{ij}$ and ligand field interaction into consideration, from diagonalization of their respective matrices the electronic energies and wavefunctions are obtained. While the electron repulsion matrix elements are evaluated in terms of the Racah parameters B and C , the matrix elements of V_G are evaluated in terms of two parameters, G_2 and G_4 , which account for distribution and strength of the ligand field G . G_2 and G_4 depend on each other, and for a given charge distribution G_2/G_4 is kept constant. Using G_2 and G_4 , the electronic wavefunctions are parameterized by selecting values that best fit the calculated to the spectroscopically observed electronic energies. For a D_{3h} complex, e.g., the splitting of the orbitals becomes:

$$\begin{aligned} \Delta_1 &= E(e'') - E(a_1') = \langle d_{xz} | V_{D_{3h}} | d_{xz} \rangle - \langle d_{z^2} | V_{D_{3h}} | d_{z^2} \rangle \\ &= (1/28)[6G_2 - 15G_4] \end{aligned} \quad (28)$$

and

$$\begin{aligned} \Delta_2 &= E(e') - E(a_1') = \langle d_{x^2-y^2} | V_{D_{3h}} | d_{x^2-y^2} \rangle - \langle d_{z^2} | V_{D_{3h}} | d_{z^2} \rangle \\ &= (1/28)[24G_2 - 15G_4/2] \end{aligned} \quad (29)$$

which for an assumed value of $G_2/G_4=10$ reduces to $\Delta_1=(45/28)G_4$ and $\Delta_2=(465/56)G_4$. These splittings are large compared to those familiar splittings in tetrahedral or octahedral fields $\Delta_t=(60/81)G_4$ and $\Delta_o=(5/3)G_4$.

The right hand side of Fig. 23 it is shown how the one-electron energies of a free TMI change when it is first brought into a spherical field and then fields of D_{3h} , C_{3v} and T_d symmetry are switched on. The transition from D_{3h} , through C_{3v} to T_d is accompanied by an increase of L_4 from 0 to 1 and of β from 90 to 109.48°, shown in the lower part of Fig. 23.

The energy term diagrams, i.e., energies of multi-electron states vs. parameter G_4 both in units of Racah parameter B , obtained for $d^{n+5}(d^n)$ ions in D_{3h} sites

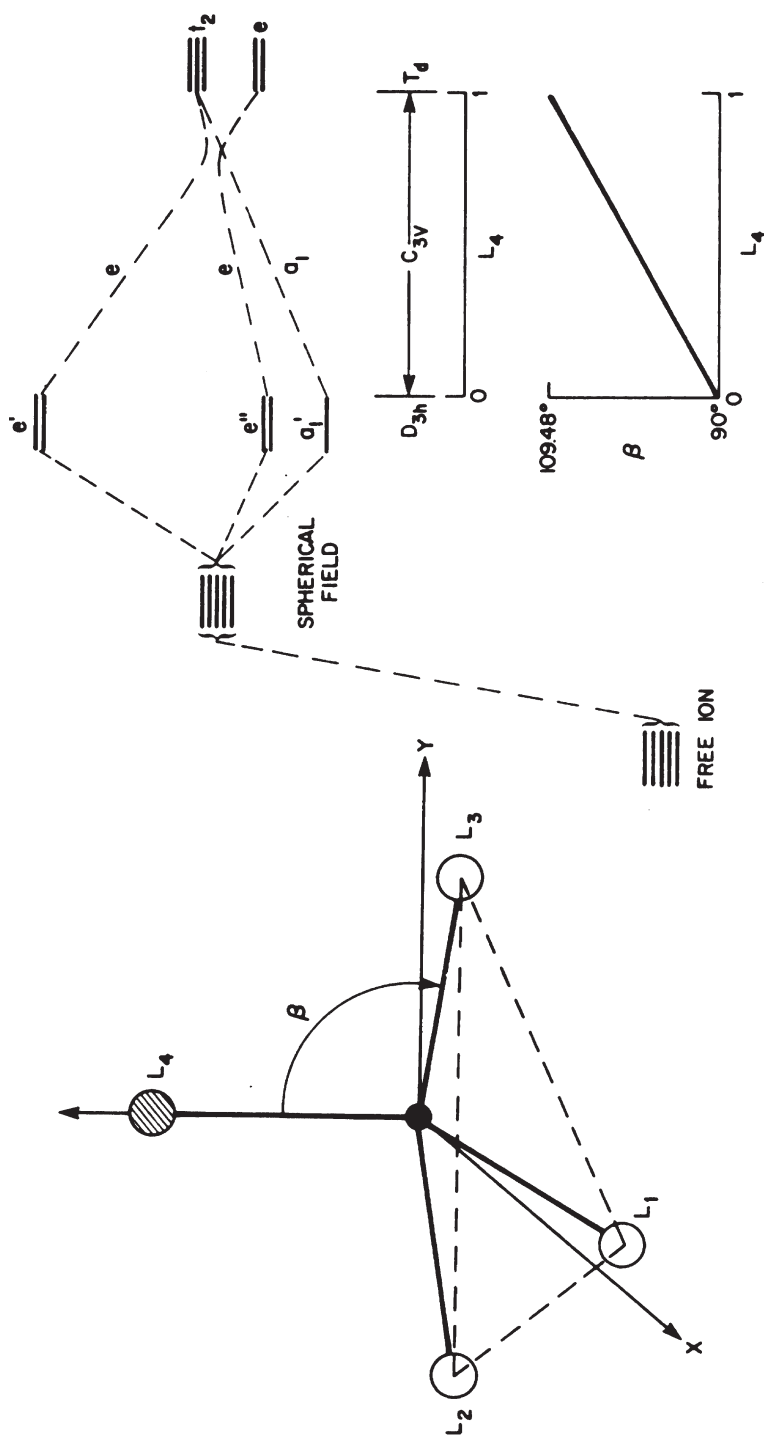


Fig. 23. C_{3v} ligand field model for intrazeolite transition-metal ion complexes (left). Changes of the one-electron energy levels starting from the free ion and switching on fields of spherical, D_{3h} , C_{3v} and T_d symmetry (right). Reprinted from [32] with permission of Academic Press, Inc

($\beta=90^\circ$, $G_2/G_4=10$, $C/B=4$) [56] are shown in Fig. 24. These diagrams can be used for the assignment of the main transitions in UV/VIS spectra, as will be exemplified in Sect. 4.1.2.3. However, for a detailed interpretation of the fine structure, a refinement of the ion position and of the term splitting due to the Jahn-Teller effect and spin-orbit coupling is necessary.

The D_{3h} position of a TMI is a very stable one. Provided the ion moves along the trigonal axis under transition to C_{3v} symmetry, there will be no removal of degeneracies and only a small energy change upon increasing the angle β by 30° . This justifies the application of the D_{3h} ligand field also to near-planar complexes. Jahn-Teller distortion, on the other hand, arises from off-axial motions of the cation [56].

When the trigonal site is approached by a guest molecule (L_4 in Fig. 23) and the strength of interaction with L_4 is comparable to that with the proximal framework oxygens L_1-L_3 , there are considerable changes in the energy levels and triply degenerate states $T_1=A_2+E$ and $T_2=A_1+E$ of the T_d group will be formed which, in the case of symmetry lowering, will split into symmetrical triplets.

Furthermore, from these diagrams, a number of useful properties can be obtained, e.g.:

1. ligand field stabilization energies

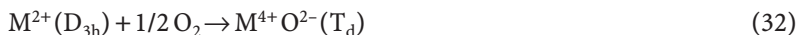
$$E_c = E_{gs}(G_4) - E_{gs}(G_4 = 0) \quad (30)$$

with E_{gs} the energy of the ground state,

2. one-electron oxidation potentials $\Delta E^{(1)}$ for oxidation processes of the kind



3. two-electron oxidation potentials $\Delta E^{(2)}$ for oxidations



4. reduction potentials $\Delta E^{(3)}$ for reduction to neutral atoms



and

5. reduction potentials $\Delta E^{(4)}$ for reduction to bulk metal according to

$$\Delta E^{(4)} = \Delta E^{(3)} - \Delta U_{coh} \quad (34)$$

with ΔU_{coh} the cohesive energy of the metal.

The quantities (1)–(5) have been calculated for $G_2/G_4=10$ and $G_4/B=3$; they are depicted in Fig. 25 and are given here without further discussion.

Other theoretical approaches for the analysis of spectroscopic data and the evaluation of the site preference are the angular overlap model (AOM) and the

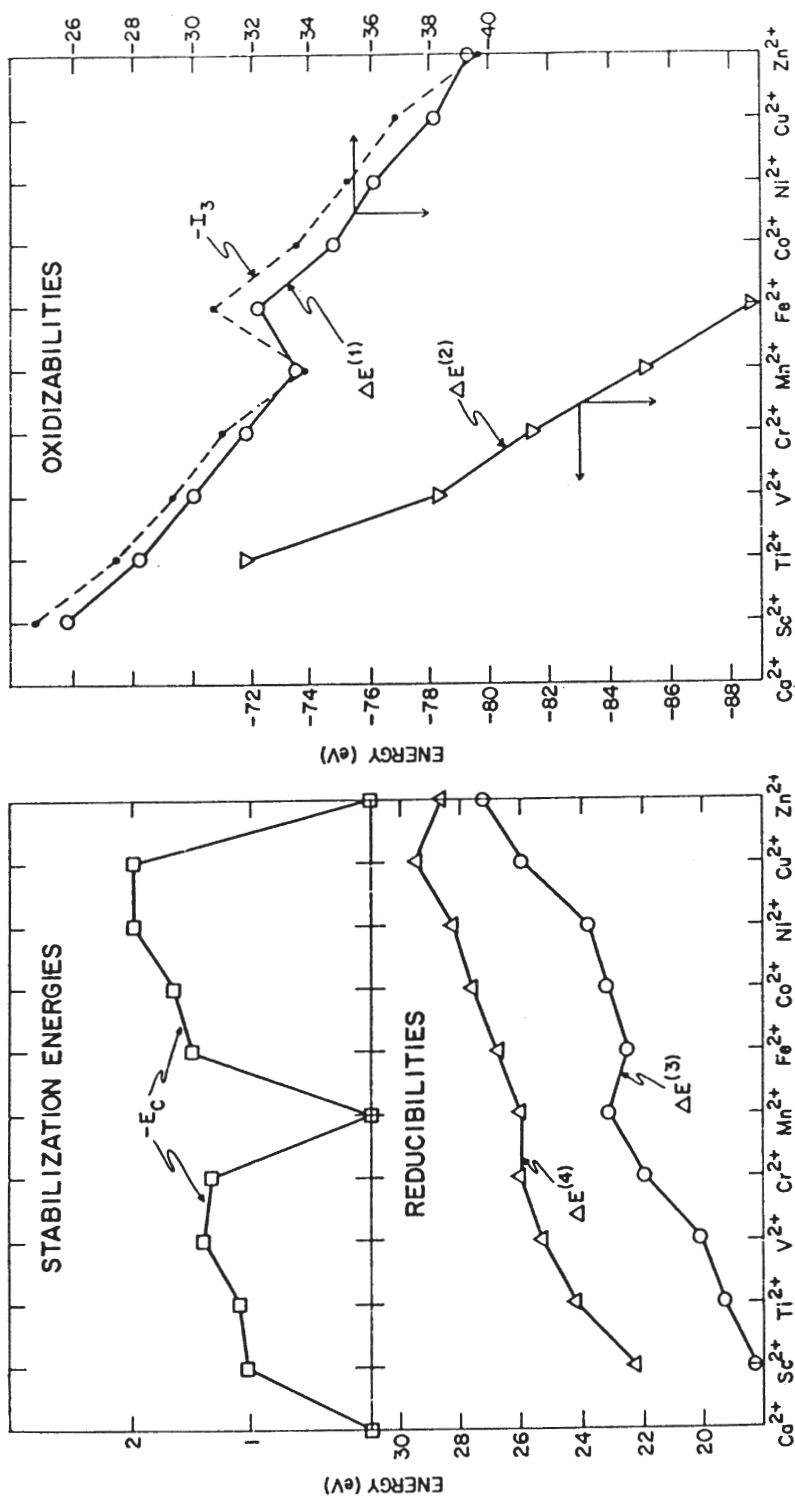


Fig. 25. Ligand field stabilization energies E_c , redox potentials to metal atoms $\Delta E^{(3)}$ and bulk metal $\Delta E^{(4)}$, one-electron $\Delta E^{(1)}$ and two-electron oxidizabilities $\Delta E^{(2)}$ for divalent ions of the first transition-metal series in sites of D_{3h} symmetry. Reprinted with permission from [56]. Copyright 1977 American Chemical Society

electronegativity equalization method (EEM). The basic ideas of these concepts may be inferred from [58]. For the details of calculation the original literature cited therein should be consulted.

A combination of mathematical and chemometrical techniques has been proposed by Verberckmoes et al. [61] for unravelling the contributions of differently coordinated TMI to DR spectra such as Co^{2+} in zeolite A. Subsequently to the decomposition of the spectra in Gaussian bands with the commercial software package Grams 386, the chemometrical methods PCA (Principal Component Analysis) and SIMPLISMA (SIMPLe-to-use Interactive Self-Modeling Analysis) were applied to receive the spectra and intensities of the pure components. In this way the DRS of CoA dehydrated at 400 °C was resolved into two components of trigonal and pseudo-tetrahedral symmetry.

4.1.2.2

Framework Cations

The first examples are devoted to zeolite synthesis (cf. also Vol. 1, Chap. 7 of this series “Molecular Sieves – Science and Technology”). Aluminophosphate-based molecular sieves (acronym AlPO_4) contain equimolar amounts of Al and P in lattice T sites that can both be replaced by other elements. In the case of Co insertion the acronym is changed to CoAPO or more generally to MeAPO. CoAPO is usually synthesized using Et_3N as template.

Isomorphously substituted tetrahedral cobalt can be proven by two triplets, one (542, 580, 624 nm) in the visible and another (1329, 1492, 1719 nm) in the NIR region and can be clearly distinguished from octahedral Co^{2+} (214, 304, 470 sh, 519 nm) [62]. Co^{2+} can be used as a sensitive probe for following its fate during synthesis from the gel to the final product. At low template concentration most of the Co^{2+} remains as octahedral $[\text{Co}(\text{H}_2\text{O})_6]^{2+}$ (519 nm) in solution with a small amount of an octahedral complex $[\text{CoO}_4(\text{H}_2\text{O})_2]$ (470 nm, sh) adsorbed on the surface of pseudoboehmite gel particles and leading to CoAPO-5 (AFI topology). At higher template concentrations tetrahedral surface complexes are formed giving rise to the formation of CoAPO-n with chabazite topology.

The distribution of cobalt within the CoAPO-44 crystallites has been investigated by photoacoustic spectroscopy making use of the depth-profiling capability of PAS [63]. The triplet between 500–650 nm in the spectra of the as-synthesized sample (Fig. 26, left), being due to a transition from ${}^4\text{A}_2$ to ${}^4\text{F}(\text{P})$, triply split by Jahn-Teller distortion of tetrahedrally coordinated Co^{2+} in framework positions, becomes less resolved due to band broadening with decreasing modulation frequency, i.e., increasing depth. In addition a band appears at 350 nm assigned to a CT transition of cobalt complexes with cyclohexylamine used as the template and obviously located in the inner part of the crystallite. The latter is also true for nonframework cobalt species of possible lower symmetry and responsible for spectral broadening at larger depths. On the contrary, after calcination the spectra are independent of the frequency (Fig. 26, right), i.e., the cobalt distribution has become more uniform.

Nonframework Co(II) in zeolites can only be partially oxidized. Substitution in aluminophosphates changes this property to a usual one [64]. Upon calcina-

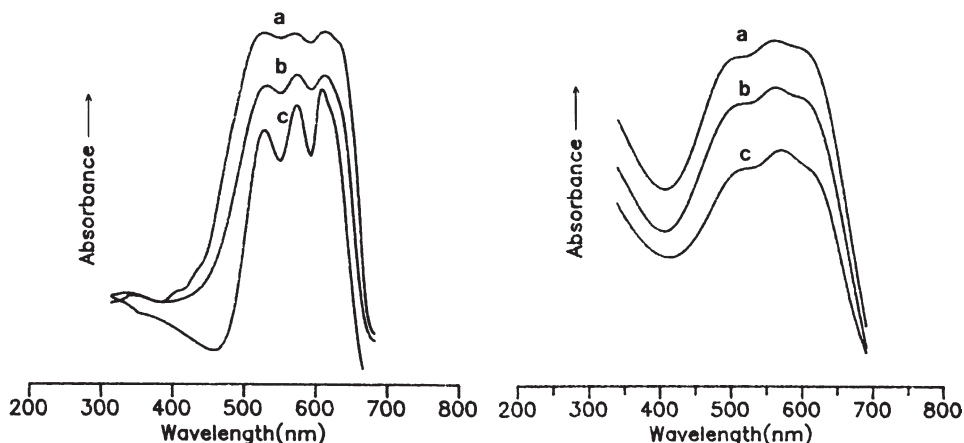


Fig. 26. Photoacoustic spectra of as-synthesized (*left*) and calcined CoAPO-44 at different modulation frequencies: *a* 25, *b* 200 and *c* 1600 Hz. Reprinted from [63] with kind permission of Elsevier Science NL, Sara Burgerhartstraat 25, 1055 KV Amsterdam, The Netherlands

tion of CoAPO in oxygen, the triplet mentioned above diminishes in favor of two new bands at 320 and 400 nm; the latter attributed to LMCT transition in Co^{3+} . However, the remainder of the triplet indicates that part of the Co(II) cannot be oxidized for which nonframework Co^{2+} , non-stoichiometric CoO or resistant framework species may be considered. Reduction with CO or H_2 reverses the spectral changes proving the reversibility of the redox reaction. Instead, water at elevated temperatures can also be used as reducing agent.

Recently, NO has proven to be a valuable molecular probe for siting of framework cobalt in CoAPO-18 [65]. From joint IR and UV-VIS investigations, the formation of nitrosyl complexes at two different sites could be distinguished: (i) Co^{2+} ions in the framework, associated with Brønsted acid sites as $[\text{Co}^{2+}(\text{OH})\text{P}]$ and (ii) structural defect Lewis acid Co^{2+} sites more slowly formed via activated processes possibly requiring the cleavage of some framework Co-O bonds. The change in the oxidation state of the cobalt ions was usually ascertained by DRS. While, as mentioned above, the absorptions in the visible (500–650 nm) and near-infrared (1000–2500 nm) regions are typical of tetrahedrally coordinated Co^{2+} ions, after admission of NO new bands appeared in the 220–500 nm range, dominated by an intense absorption at 260 nm, attributable to LMCT transitions of NO complexes on Co^{3+} ions. The latter are presumably formed from $[\text{Co}^{2+}(\text{OH})\text{P}]$ by oxidation with NO at room temperature.

Titanium has been introduced into zeolite frameworks in order to prepare catalysts which are both active and selective for oxidation of hydrocarbons with H_2O_2 . Catalysts of this type are suited for fine chemical production, as product waste will be minimized. Starting materials for Ti-modified zeolites were ZSM-5 (TS-1), ZSM-11 (TS-2), ZSM-48 and zeolite beta. Echchahed et al. [66] investigated the synthesis of TS-1 under variation of hydrothermal time and temperature. The change in the UV band with maximum at 208 nm, typical of tetrahedral Ti, which broadens with growing titanium incorporation, is explained by the

presence of two different framework Ti species: (i) open sites $[\text{Ti}(\equiv\text{SiO})_3\text{OH}]$ and (ii) closed sites $[\text{Ti}(\equiv\text{SiO})_4]$. An increasing number of the latter for higher loading cause strong local stress and crystal fragmentation, while the former, due to a bond rupture within the Si-O-Ti bridge, release the local tension.

Incorporating Ti into zeolite beta was carried out by hydrothermal synthesis and by post-synthesis modification with ammonium titanyl oxalate [67]. Evidence for isolated Ti(IV) most likely in a framework position was also given here by the strong 212 nm band. Post-synthesis treatment with nitrogen saturated with TiCl_4 vapor was also successful in isomorphous incorporation of Ti, enhanced by preceding acid leaching as revealed from the UV-VIS spectra [68]. Al-free Ti-beta preparation by dry gel conversion has been reported by Hari Prasad Rao et al. [69]. The intense band in the 205–225 nm region proves the incorporation of Ti into the framework. A weak band around 270 nm and the onset of absorption at 330 nm, however, suggest the presence of Ti at distorted positions or as extraframework titanium, e.g., as oligomeric hexacoordinated Ti species.

Corma et al. [70] attempted to insert Ti into the mesoporous structure MCM-41 by direct synthesis. The UV-VIS spectra revealed strong absorptions in the 190–300 nm range that confirm the absence of bulk anatase (330 nm) in agreement with Franke et al. [71]. However, the presence of isolated Ti atoms in octahedral coordination is proved by the LMCT transition near 225 nm which after dehydration shifts to 205 nm characteristic for tetraordinated Ti(IV) in TiO_4 and TiO_3OH environments. Additionally, a weak band around 270 nm points to hexacoordinated Ti-O-Ti species which probably belong to an extra-wall amorphous phase. The synthesized Ti-MCM-41 turned out to be a catalyst of good performance in oxidation of bulky olefins such as α -terpineol or norbornene. Using the same Ti source, a Ti-MCM-41 synthesis via an acidic route has been presented by Corma et al. [72] in which the samples obtained show a very narrow band of tetrahedrally coordinated Ti at 220 nm and missing higher-wavelength shoulders, as found in samples prepared under alkaline conditions, pointing to a more distorted environment.

Unfortunately, Ti(IV) forms hydroxides of low solubility. In order to avoid precipitation during the synthesis of Ti-MFI the admixture of complexing agents like acetylacetonone has been studied [73]. Due to the DR spectra acetylacetonone admission resulted in a higher amount of framework titanium (212 nm), again in the absence of anatase, and in a distinct reduction of extraframework Ti species, e.g., like octahedrally coordinated titanium (274 nm).

Successful application of DRS together with complementary methods like ESR, XRD, XAS, IR, SEM, NMR etc. for characterization of the synthesized microporous materials with respect to incorporation into the framework has been further reported for MFI-type vanadium silicalites [74, 75], for VAPO-5, MgAPO-5 and MgVAPO-5 [76], for MFI-type ferrisilicalite [77] and for insertion of chromium in a number of molecular sieves [78]. In the case of the latter, essentially nonframework species could be identified and even in Cr-silicalite and CrAPO-5 Cr^{3+} showed no tendency to change from octahedral to tetrahedral coordination.

4.1.2.3

Nonframework Cations

As mentioned above, chromium in hydrothermally synthesized Cr-silicalite and CrAPO-5 showed no motivation to change its coordination to tetrahedral which is the requirement for isomorphous substitution into the zeolite framework. Evidently, only a limited number of elements are able to form framework cations, whereas, for nonframework cations, there are theoretically a vast number of possibilities in various symmetries. Since nonframework cations are widely accessible they can form complexes with different guest molecules. Their electronic spectra are fingerprints of the electronic structure of these entities and give valuable hints to their identification. Distortions of the geometry and vibronic coupling give rise to a fine structure, and, from their interpretation, information on the stability of molecular species and, furthermore, on their reactivity can be obtained. First, siting, local geometry, oxidation state and migration of these ions in the absence of adsorbates will be considered. Water will be excepted since, due to its permanent availability and due to the hygroscopicity of zeolites, its presence must always be taken into account.

The classical investigations of TMI-exchanged zeolites, especially of the 3d elements, started on A-type zeolites exchanged with Ni^{2+} by Klier et al. [31] and were later extended to the cobalt and chromium forms, see, e.g., [51, 52, 54, 57]. As the optical spectroscopy of nonframework transition-metal ions has been reviewed in several contributions [16, 31, 34, 51, 52, 54, 55, 57, 58], only an outline will be given here and the main features will be considered briefly.

The optical spectra of fully hydrated zeolites largely match those of the hexaquo complexes, except the hypsochromic shifts of ca. 1500, 650 and 500 cm^{-1} in Cr(II)-, Co(II)- and Ni(II)-exchanged zeolites A [52]. These shifts might be explained by a greater ligand field of the zeolitic water which, compared to normal water, is more structured, but the influence of the framework cannot be excluded either. The similarity to the spectra in aqueous solutions indicates the presence of ions octahedrally coordinated by zeolitic water. These floating complexes are supposed to reside mainly in the large cages, although Seff reports hexaquo cobalt(II) located in the center of the smaller sodalite cage and forming twelve H-bonds to the framework of zeolite $\text{Co}_4\text{Na}_4\text{A}$ [53].

After complete dehydration, the transitions from the Cr(II) (d^4) ground state ${}^5E'$ to ${}^5E''$ and ${}^5A_1'$ excited states (12,300, 17,000 cm^{-1}), from the Co(II) (d^7) ground state ${}^4E''$ to ${}^4E'$, ${}^4A_1''$ (accidentally degenerate with ${}^4A_2''$) and ${}^4E''$ excited states (7000, 16,000, 25,000 cm^{-1}) and from the Ni(II) (d^8) ground state ${}^3A_2'$ (F) to ${}^3A_1''$ (accidentally degenerate with ${}^3A_2''$), ${}^3E''$ ($\sim {}^3E'$), ${}^3A_2'$ and ${}^3E'$ excited states (4500, 9090, 22,760, 36,000 cm^{-1}) prove trigonal coordination (D_{3h}) to the three proximal oxygens O_f of the 6R in site S1A of zeolite A as bare ion $[\text{M}(\text{O}_f)_3]^{2+}$ which can be assigned using the energy term diagrams in Fig. 24. Although, e.g., for nickel only the transitions to ${}^3A_1''$ and ${}^3E'$ are symmetry-allowed, the appearance of the other two indicate a breakdown of the electric dipole transition selection rule even for small deviations from planarity [52]. The spectral changes upon dehydration of Co(II)-exchanged zeolite A are shown in Fig. 27 [32]. The d-d band frequencies of some bare 3d TMI in zeolite LTA [52, 79]

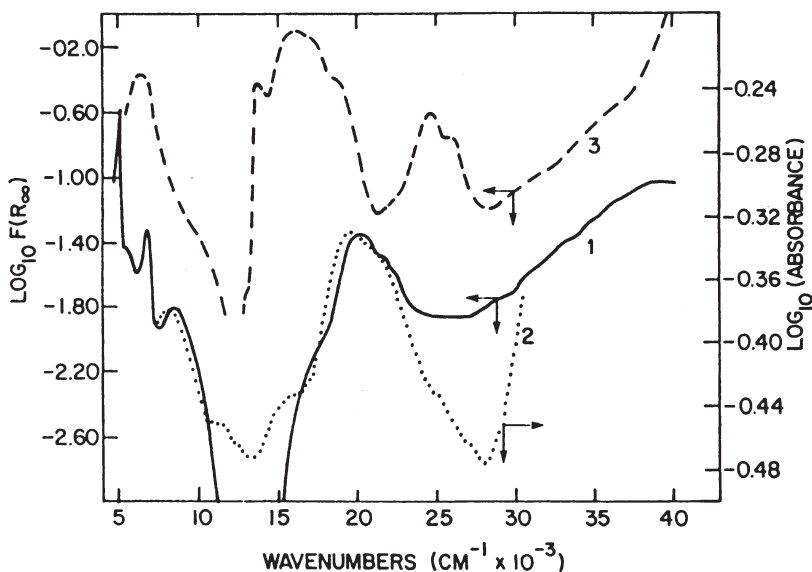


Fig. 27. DR spectrum of fully hydrated zeolite Co(II)A (1) compared to that of an aqueous Co(II) solution (2). Upon complete dehydration the spectrum drastically changes to (3) assigned to a Co(II) ion in trigonal planar D_{3h} coordination by the 6R. Reprinted from [32] with permission of Academic Press, Inc

and their ground and excited electronic states in D_{3h} ligand fields are compiled in Table 4.

Dehydration is accompanied by gradual migration of the ions into sites in which they become stabilized as wall complexes or bare ions. This process is strongly dependent on the zeolite type, on the ion and on the dehydration conditions. In zeolite CrNaY, e.g., it was shown by electronic spectroscopy that upon dehydration with increasing temperature the Cr(II) ions become localized first in SII sites, then in SII' or SI' sites and finally in O_h geometry in SI sites [57]. The red shift of this last complex ($14,300, 18,800 \text{ cm}^{-1}$) compared to the floating hexaquo complex ($16,400, 23,600 \text{ cm}^{-1}$) might be explained by the weaker ligand zeolitic oxygen compared to the oxygen of water.

Table 4. Sites, d-d band positions of some bare 3d TMIs in zeolite LTA and their ground and excited electronic states in D_{3h} ligand fields [52, 79]

3d TMI	Site	d-d Bands/ cm^{-1}	Ground state	Excited states
Cr ²⁺	I	12,300, 17,000	$^5E'$	$^5E'', ^5A_1'$
Co ²⁺	I	7000, 16,000, 25,000	$^4E''$	$^4E', ^4A_1'', ^4A_2'', ^4E''$
Ni ²⁺	I	4500, 9090, 22,760, 36,000	$^3A_2'$	$^3A_1'', ^3A_2'', ^3E'', ^3E', ^3A_2', ^3E''$
Cu ²⁺	I	10,400, 12,200, 15,000	$^2E'$	$^2E'', ^2A_1'$

Whereas the early investigations concentrated mainly on bare ion complexes in LTA and FAU, later more and more different types of zeolites, like chabazite, mordenite [80], MFI boralite [81] and nitrido zeolites [82], were investigated. The latter, e.g., P-N-sodalite with the general formula $M_{7-x}H_{2x}[P_{12}N_{24}]X_{2-y}$, where X stands for halogen and M for a 3d TMI, attracted attention as they represent a new class of zeolites with substitution of the anion substructure, in this case replacement of oxygen by nitrogen. Features of these sodalite-like materials are high thermal and chemical stability as well as intense coloration. Responsible for the color is a near-tetrahedral coordination more likely approximated by the complex $[MX(NH_3)_3]^+$ which gives rise to an electronic spectrum similar to that of $[MX_4]^{2-}$, however, taking into account symmetry lowering and LS coupling.

A study of the Cu(II) siting in dehydrated CHA and MOR by means of DRS assisted by ESR gave three d-d bands for CuNaCHA (10,700, 12,900, 14,800 cm^{-1}) accompanied by a LMCT transition at 40,000 cm^{-1} and for CuNaMOR (12,500, 13,700, 14,800 cm^{-1}) together with the corresponding LMCT transition around 42,000 cm^{-1} [58, 80]. The spectra of CuNaCHA are ascribed in analogy to those of CuNaFAU to Cu^{2+} ions essentially coordinated to the hexagonal rings, while those sited in the distorted hexagonal prisms do not significantly contribute due to the lower occupancy and the smaller extinction coefficient of pseudo-octahedral compared to trigonal complexes. The symmetry of the latter seems to be lower than C_{3v} , probably effected by LS coupling and Jahn-Teller distortion. According to the d-d transitions in CuNaMOR, a fourfold coordination either to site I (eight-membered ring) or to site IV (at the wall of the large channel) has to be assumed.

The positions of the d-d bands of bare Cu^{2+} ions in different zeolites and sites are summarized in Table 5. An overview indicates that they are site-dependent, e.g., the two types of six-rings at SI (LTA) and SII (FAU) can be discriminated from those at SI' (FAU, CHA). On the other hand, in a first approximation, they are independent of the structure type, the Si/Al ratio as well as ordering and the type of the co-cation [58]. The TMI "feels" only the first coordination sphere represented by the nearest oxygens.

After assignment of the bands the ligand field parameters such as splitting, Racah and nephelauxetic parameters can be determined from the frequencies. As an example, with fully hydrated Ni(II)X zeolite, five bands are observed at 5100, 6850, 8450, 14,700 and 24800 cm^{-1} from which the first two have to be attributed

Table 5. Electronic band positions of Cu(II) coordinated to lattice oxygens in different zeolites and sites, after [58], in brackets after [79]

Zeolite	Site	d-d Bands/ cm^{-1}		
LTA	I	10,400	12,200–12,800	15,000–15,400
FAU	II	10,400 (10,400)	12,400–13,000 (12,400)	14,700–15,100 (14,700)
FAU	I'	10,800 (10,700)	12,400–13,000 (12,900)	14,700–15,100 (14,800)
CHA	I'	10,700	12,900	14,800
MOR	I	12,500	13,700	14,800
MOR	VI		ill-defined	

to the $\nu_2 + \nu_3$ combination and the $2\nu_3$ overtone band of adsorbed water [27]. The latter three are due to the d-d transitions of hexaquo Ni^{2+} ions in O_h symmetry: ν_1 [${}^3A_{2g}(F) \rightarrow {}^3T_{2g}(F)$], ν_2 [${}^3A_{2g}(F) \rightarrow {}^3T_{1g}(F)$] and ν_3 [${}^3A_{2g}(F) \rightarrow {}^3T_{1g}(P)$], increasing in frequency in this order. In a similar way to that shown in Eq. (10), the term energies can be related to the splitting Dq and the Racah parameter B which for the frequencies lead to the expressions:

$$Dq = (1/10) \nu_1 \quad (35)$$

and

$$B = (1/15) (\nu_2 + \nu_3 - 3\nu_1) \quad (36)$$

The nephelauxetic parameter β is obtained from comparison of B (from Eq. 18) with B (free ion) which amounts to 1041 cm^{-1} in the case of Ni(II). The usual values of β fall in the range of 0.7–0.9, while its reduction indicates an increase of covalent character in the bonds. The results calculated from the frequencies mentioned above are $Dq = 845 \text{ cm}^{-1}$, $B = 943 \text{ cm}^{-1}$ and $\beta = 0.91$. These values proved to be somewhat dependent on the degree of Ni^{2+} ion exchange but changed dramatically upon dehydration. Dehydration at elevated temperature gave rise to a decrease of β to 0.30 and to an increase of Dq to 1110 cm^{-1} . The unusual value for the nephelauxetic parameter hints to a completely different environment in correspondence with a migration into SI sites and to a Ni-O bond with lattice oxygen being more covalent compared to water as the ligand.

However, it should be stressed that electronic spectroscopy, even when combined with complementary tools like ESR, does not unambiguously assign the TMI to a distinct site. Here the assistance of theoretical methods like AOM and EEM or others is indispensable. On the other hand, it gives reliable information on the accessibility of the ions to adsorbates, as will be shown below.

Exposure of TMI-exchanged zeolites to various guest molecules frequently gives rise to color changes which sensitively indicate spectral changes. They provide evidence of a competition between complexation to lattice oxygens and complexation to nonframework ligands. In this way, a large variety of sometimes rather unusual complexes can be formed in the zeolite interior; see Lunsford [54, 55] for reviews of the early efforts in this field.

What happens with the spectrum may be suspected from Fig. 27 in which the $25,000 \text{ cm}^{-1}$ band was indicative for a trigonal near-planar coordination of Co(II) to the proximal framework oxygens of the 6R in zeolite A. As shown in Fig. 28, admission of, e.g., nitric oxide leads to the disappearance of this unique band accompanied by the appearance of a strong band at $19,000 \text{ cm}^{-1}$ and the onset of a CT transition at $>31,000 \text{ cm}^{-1}$ [83]. The diminishing of this band assigned to the ${}^4E'' \rightarrow {}^4E''$ transition has already been observed earlier upon exposure to oxygen, CO, CO_2 , ethylene oxide, N_2O , H_2O , NH_3 , imidazole, cyclopropane and olefins like ethene, propene and the butene isomers [52, 84–87]. At higher degrees of cobalt exchange with *trans*-butene this band did not completely disappear indicating that not all Co(II) ions were coordinated by the hydrocarbons [87].

The explanation for the spectral changes is, in a first approach, the change from near D_{3h} to C_{3v} or near T_d symmetry effected by the adsorbed guest. Finer details concerning orientation and rotational behavior of the guest can be

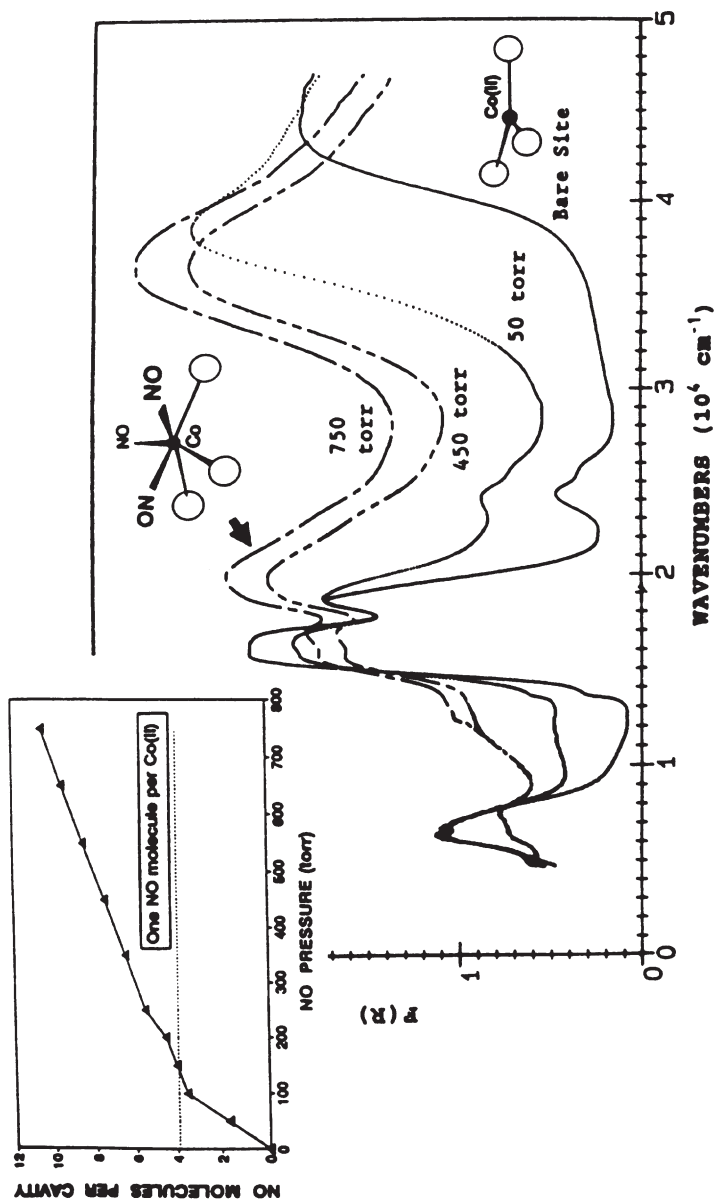


Fig. 28. Electronic spectra of fully dehydrated Co(II)A zeolite (3.9 Co²⁺/unit cell) and upon exposure to NO in increasing steps of pressure. The inset relates NO pressure to the occupation per cavity. Reprinted from [83] with kind permission of Elsevier Science NL, Sara Burgerhartstraat 25, 1055 KV Amsterdam, The Netherlands

inferred from the fine structure of the bands. The spectrum of a tetrahedral Co(II) complex corresponds to transitions from the ${}^4A_2(F)$ ground state to the triply degenerate ${}^4T_1(F)$ and ${}^4T_1(P)$ excited states. A dynamic Jahn-Teller effect should lift the degeneracy resulting in a symmetrical splitting, as shown on the left-hand side of the vertical dotted line in Fig. 29. But in the case of coordinated unsaturated hydrocarbons an unsymmetrical splitting of the 7000 and 17,300

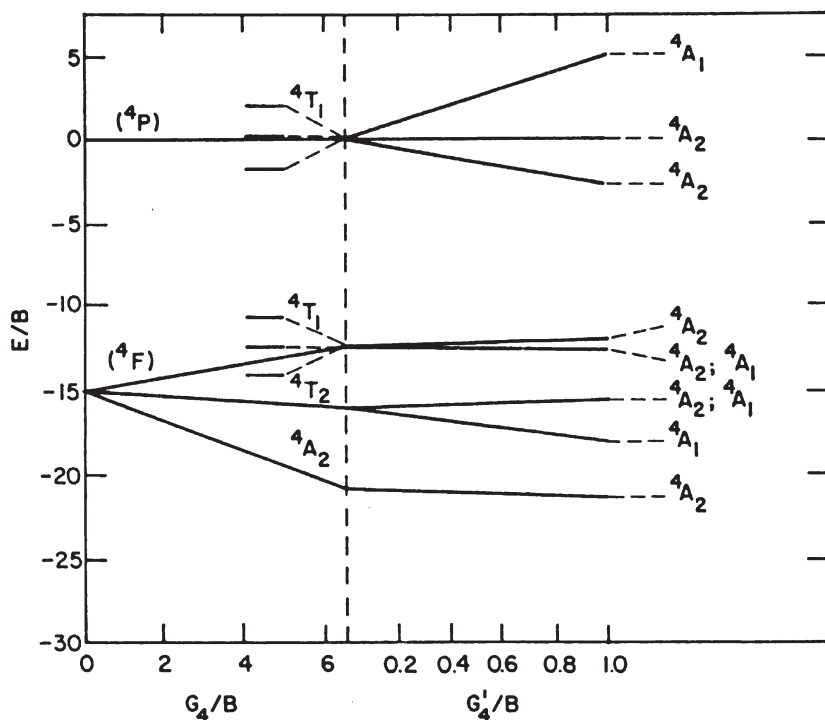


Fig. 29. Term diagram of a Co(II) ion (i) in a T_d environment with degeneracy lifting of the 4T_1 states by a dynamic Jahn-Teller effect indicated as a symmetric term splitting (left-hand side of the vertical dotted line); (ii) in an environment of lower symmetry (e.g., C_1) with removal of the degeneracy (right-hand side of the vertical dotted line). The best fit for Co(II)-ethylene is obtained for $G_4/B=6.6$ (vertical dotted line). Reprinted from [32] with permission of Academic Press, Inc

cm^{-1} bands is observed which must be accounted for by a static symmetry perturbation arising from the charge distribution of the ligand. The off-z-axis components of the charge distribution give rise to a C_{2v} perturbation that lowers the complex symmetry to C_1 or C_{1v} resulting in an unsymmetrical splitting into 4A_1 and 4A_2 states on the right-hand side of the vertical dotted line in Fig. 29. Prerequisite is an approach of the naked Co(II) ion by the ligand in π geometry, i.e., the hydrocarbon molecular axis is transverse to the threefold z-axis of the trigonal complex. While on the basis of theoretical considerations ethylene behaves like a freely rotating ligand, decreasing ability to split the $17,300 \text{ cm}^{-1}$ band follows steric hindrance increasing in the order ethene < propene < *cis*-butene < *trans*-butene [52]. Further examples of coordination of transition-metal ions with mono-, bi- and polydentate ligands have been reported recently [79]. While the identification of sites is not always unambiguous, optical spectra provide reliable data on the accessibility of the ions.

The nonframework ions, especially the TMI, frequently form the so-called active sites responsible for the catalytic properties of zeolites. In these cases, coor-

dination and polarization, in the case of protons protonation, of the guest is followed by transformation to a different compound as has been proven, e.g., by the isomerization of cyclopropane and n-butenes over A-zeolites [87, 88].

Nowadays, NO decomposition is of great importance from an environmental point of view. Investigating the suitability of zeolite CoA as a catalyst for this reaction, electronic spectroscopy turned out to be a valuable tool for the determination of surface intermediates and strength of adsorption. As shown in Fig. 28, starting from the bare site, sequential increase of the NO pressure yielded spectra assigned to complexes with multiple NO coordination which upon evacuation could be converted into the near tetrahedral mononitrosyl Co(II) complex. NO adsorption proved to be strong but reversible [83].

Complementary to reflectance and transmission spectroscopy, luminescence experiments are very useful for the study of TMI siting, resonance energy transfer and photocatalytic decomposition, especially in the case of Cu-containing zeolites. Basic investigations on the redox chemistry of Cu(II) ions in zeolite Y by Strome and Klier proved after dehydration a preferred location of Cu²⁺ ions in SI' sites while those in SI sites, being a center of inversion, only contributed slightly to the DR spectrum [89]. Upon hydrogen admission, Cu(II) was readily reduced to Cu(I). As inferred from the DR spectra shown in Fig. 30, the Gaussian-

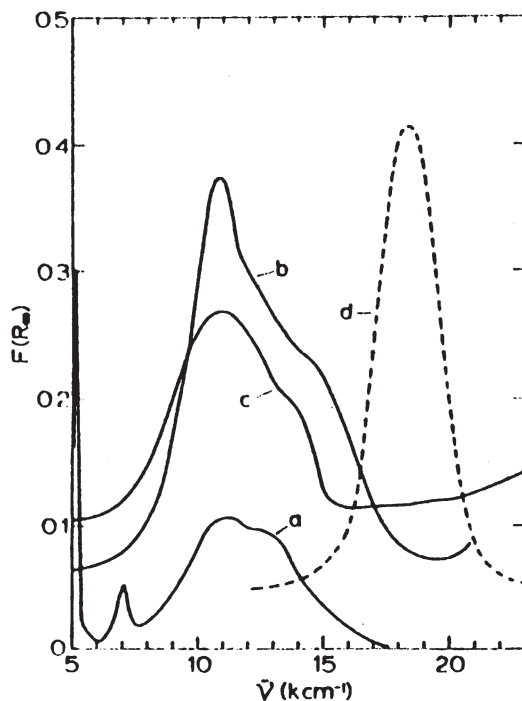


Fig. 30. DR spectra of hydrated Cu(II)Y (a), dehydrated Cu(II)Y (b) and the product of admitting oxygen to Cu(I)Y, forming a Cu(II)(O_p)₃O₂⁻ complex on SII sites (c). The 18400 cm⁻¹ photoemission of Cu(I)Y is shown as spectrum d. Reprinted with permission from [89]. Copyright 1980 American Chemical Society

shaped emission spectrum of Cu(I)Y centered at $18,400\text{ cm}^{-1}$ (spectrum d) has been assigned to the spin-forbidden ${}^3E({}^3D_3, 3d^94s) \rightarrow {}^1A({}^1S_0, 3d^{10})$ transition in a C_{3v} ligand field. When Cu(I)Y was exposed to oxygen in order to be reoxidized, the reflectance spectrum was different to that of Cu(II)Y (spectrum c in Fig. 30) and the emission was quenched resulting in a decrease in intensity and reduction of decay time in favor of a competing radiationless process. As shown in Fig. 30 (spectra c and d), the emission band overlaps with the absorption band of the product of oxygen interaction identified as a near-tetrahedral $\text{Cu(II)(O}_7\text{)}_3\text{O}_2^-$ complex in SII sites with an O_2^- ligand in π geometry. For the formation of this complex, the Cu(I) cations had to move out of SI and SI' positions to SII sites. This overlap indicates an efficient resonance energy transfer between Cu(I) as emitter center and $\text{Cu(II)(O}_7\text{)}_3\text{O}_2^-$ as absorber, i.e., between sodalite unit and supercage.

Cu(II)-containing high-silica ZSM-5 has attracted substantial attention as an active catalyst for the removal of nitrogen oxides. Ebitani et al. proposed that excitation of Cu(I) ions around 300 nm causes the photocatalytic decomposition of N_2O [90]. The excitation of this band gave rise to an emission centered at about 540 nm which was assigned to the radiative decay of an excited Cu(I) dimer, $(\text{Cu}^+-\text{Cu}^+)^*$, to its ground state. N_2O admission efficiently quenched the luminescence, so that an electronic interaction between $(\text{Cu}^+-\text{Cu}^+)^*$ and the *anti*-bonding MO of N_2O had to be assumed which releases the decomposition of N_2O into N_2 and O_2 . Furthermore, Cu^+ luminescence after deconvolution has been used for a semiquantitative determination of Cu coordination controlled by the $(-\text{Al}-\text{O}-(\text{Si}-\text{O})_n-\text{Al}-)$ sequence [91]. Of four possible sites, the most active in NO decomposition proved to be the one adjacent to a single Al atom.

As they are relatively cheap and are produced in the form of almost ultraviolet-transparent materials, rare-earth-doped zeolites have attracted growing interest as substitutes for more expensive phosphors which, applied in fluorescent lamps, should be able to efficiently convert UV into visible light. As shown by Borgmann et al. [92], Eu^{3+} -doped zeolite X excited with 254-nm radiation gave only weak emission. Additional insertion of molybdate caused absorption of UV radiation and subsequent transfer from the excited metalate LMCT state to the $\text{Eu}^{3+} {}^5D$ level increasing the quantum yield up to 7%. Upon thermal treatment at $1000\text{ }^\circ\text{C}$ a dense phase of the composition $\text{Eu}_4\text{Si}_4\text{Al}_8\text{O}_{24}(\text{MoO}_4)_2$ was formed, mainly consisting of a rare earth sodalite with 25% quantum yield, as shown by the emission spectra in Fig. 31; the quantum yield was improved to 38% upon isomorphous substitution of Eu^{3+} by Y^{3+} . Finally, the direct synthesis of sodalites from oxides gave a maximum quantum yield of 55% for the composition $(\text{Eu}_{0.4}\text{Y}_{0.6})_4\text{Si}_4\text{Al}_8\text{O}_{24}(\text{MoO}_4)_2$ due to the absence of any by-products.

4.1.3

Acid Strength of Zeolites

One of the outstanding properties of zeolites is their acidity. This is usually divided into Brønsted and Lewis acidity that make them capable of being applied in, e.g., cracking and shape-selective catalysis. Characterization of zeolite acidity comprises the determination of its nature, amount and strength and is com-

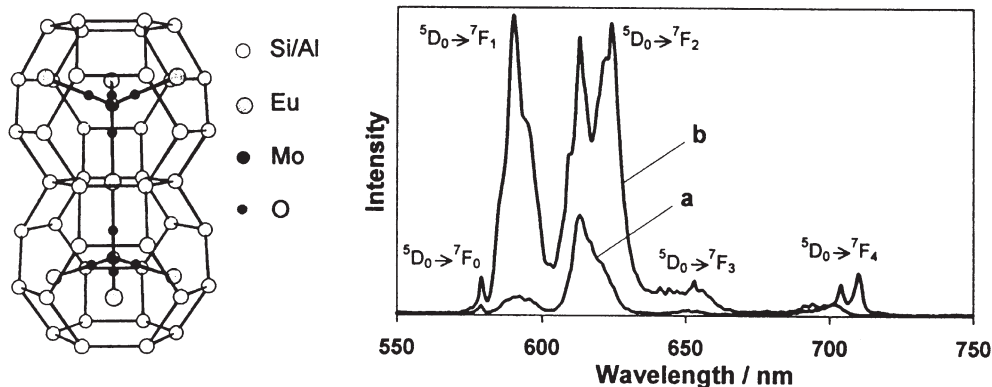


Fig. 31. *Left* Part of the structure of $\text{Eu}_4\text{Si}_4\text{Al}_8\text{O}_{24}(\text{MoO}_4)_2$ sodalite. *Right* Emission spectra of Eu^{3+} -doped zeolite X treated with 10 wt.% $(\text{NH}_4)_2\text{MoO}_4$ at 500 °C (a) and of sodalite $\text{Eu}_4\text{Si}_4\text{Al}_8\text{O}_{24}(\text{MoO}_4)_2$ obtained from the former by phase transformation at 1000 °C (b). The f-f transitions of Eu^{3+} are indicated. Reprinted from [92] with kind permission of the Materials Research Society, Warrendale

monly accomplished using a number of techniques such as titration, adsorption, IR spectroscopy of OH groups and basic probe molecules, TPD and NMR, and, to a lesser extent, electronic spectroscopy. Nevertheless, aromatic hydrocarbons, for example, can be readily ring-protonated under formation of carbocations that are known to give characteristic absorptions in the UV-VIS region. As the ease of protonation depends on both the acid strength of the host and the basic strength of the guest, electronic spectra with probes of decreasing basicity should allow determination of the acid strength.

As an example, the H-forms of ZSM-5, FAU, USY, MOR, dealuminated MOR (DEAMOR) and rare earth ion-exchanged zeolite Y (REY) have been probed with the vapors of – in order of increasing basicity – toluene, *p*-xylene, *m*-xylene, 1,2,4- and 1,3,5-trimethylbenzene [93]. The formation of the corresponding cyclohexadienyl cations of 1,2,4- and 1,3,5-trimethylbenzene on HMOR samples with decreasing Al content (HM, HM D-1...HM D-3) is shown in Fig. 32. The differences in intensities can be explained by the different basicities of the probes from which the former is protonated by strong and medium, the latter in addition also by weak Brønsted sites, i.e., 1,3,5-trimethylbenzene grasps the total acidity. As a result, dealumination of HMOR decreases the total number, but increases the number of strong Brønsted sites. From semiquantitative evaluation the relative strength of Brønsted acidity was determined and this increases in the order $\text{HNaY} < \text{REY} < \text{USHY} = \text{HMOR} < \text{DEAHMOR}$, HZSM-5.

4.1.4

Polarity of Zeolites

The functions of zeolites are versatile: they may behave as an anion, as a ligand or as a solvent. As a consequence of the latter zeolites should have solvent-like

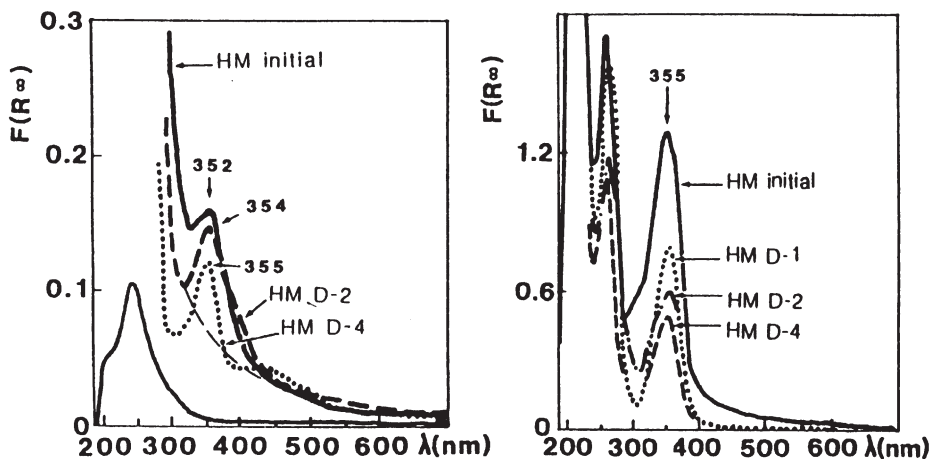


Fig. 32. DR spectra of 1,2,4- (left) and 1,3,5-trimethylbenzene (right) on HMOR samples. Reprinted from [93] with kind permission of Elsevier Science NL, Sara Burgerhartstraat 25, 1055 KV Amsterdam, The Netherlands

properties like, e.g., polarity, dipole moment, dielectric constant, etc. Since polarity is a characteristic of a bulk phase, micropolarity should be the more suitable term for this property when the extension of the phase is restricted to the nanometer scale as in the case of zeolite voids. This property does not have precisely the same meaning as in solution but reflects the electric field within the zeolite interior that is essentially provided by the cations. There have been some attempts to probe this property by means of photophysical techniques applying condensed benzenoid hydrocarbons, either making use of the intensity change of vibronic bands (Ham effect), of the shift of the emission maximum or of the changes in lifetimes in the fluorescence spectrum [94, 95]. As shown in Fig. 33 by the emission spectrum of pyrene in zeolites KX and CsX, the intensity ratio of higher transitions to that of the 0-0 transition of a vibronic progression might serve as a measure of the environmental polarity. Compared to solvents the polarities of the faujasite supercages are similar to those of methanol or acetonitrile.

As with solvents the intracavity formation of ionic CT complexes has been exploited to give a description of the supercage polarity. The contact ion pair methylviologen monoiodide undergoes a solvatochromic shift in acetonitrile/water mixtures due to the decrease in the energy gap between the ground and the excited state with decreasing polarity, i.e., with decreasing water content [96]. From comparison of the λ_{\max} position to that obtained at 362 nm in zeolite Y the polarity of its supercage was estimated to be equivalent to that of a 50% aqueous acetonitrile solvent.

Zeolites can also be considered as solid electrolytic solvents with a donor-acceptor interaction between the framework and the counter cation. The color of iodine is due to a $\pi^* \rightarrow \sigma^*$ transition in the visible range and is known to be largely sensitive to the solvent [3]. Because of a donor-acceptor interaction between iodine and the solvents the σ^* orbital is perturbed and shifted to higher

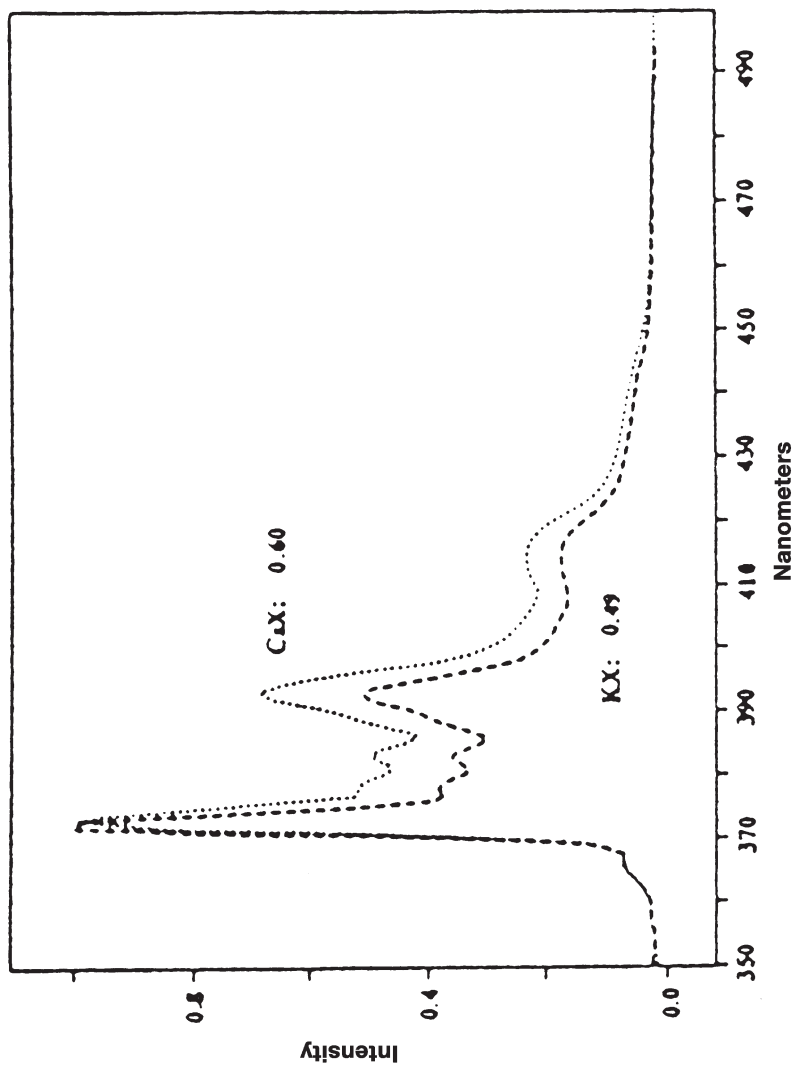


Fig. 33. Emission spectra of pyrene in KX and CsX zeolites. The intensity ratio of the monomer fluorescence at 392 vs. 372 nm amounts to 0.49 and 0.60 as indicated on the spectra. Reprinted from [94] with permission of Elsevier Science, Inc

energies with increasing donor strength of the solvent resulting in a hypsochromic shift of the corresponding band. Therefore, iodine should also be suitable for probing the donor strength, i.e., the basicity of zeolites. This idea has been proposed by Choi et al., who systematically investigated the frequency shift of the visible band in zeolites LTA, FAU, ZSM-5, LTL MAZ and MOR [97]. Upon adsorption of iodine vapor at room temperature, a broad unstructured band was observed, the maximum of which was shifted to shorter wavelengths compared to iodine in CCl_4 solution dependent on the zeolite type, the Si/Al ratio, the counter cation and residual moisture. The probe does not adsorb on the cations but forms a CT complex with the negatively charged framework oxygen atoms.

Moisture prevents iodine from a direct interaction and gives rise to a restricted blue shift. For alkali-exchanged faujasites a linear negative correlation of the absorption energy with the ionization potentials of the counter ions and the Si/Al ratio, respectively, could be established. Due to the larger hypsochromic shift it must be concluded that the FAU framework has a higher donor strength than LTA.

4.2

Characterization of the Guest

As already shown in the last section, electronic spectroscopy offers two possibilities of characterizing a guest molecule encapsulated in the zeolite cage either (i) an indirect one by following the changes of the host spectrum upon admission of an adsorbate or (ii) a direct one by observing the spectrum of the guest. For this case the adsorbate molecule must be capable of absorbing radiation in the UV-VIS region accessible with commercial spectrometers. The latter will be in the narrow sense the topic of the following section.

4.2.1

Inorganic Compounds

A number of simple inorganic compounds exhibit electronic spectra mainly arising from $n \rightarrow \pi^*$, $\pi \rightarrow \pi^*$, $\pi^* \rightarrow \sigma^*$ and CT transitions in the UV range. From sulfur-containing compounds, sulfur dioxide as an example shows a less intense band at 360 nm and a stronger band at 290 nm due to singlet-triplet and singlet-singlet $n \rightarrow \pi^*$ transitions [3]. SO_2 is one of the source materials for the production of elemental sulfur, accomplished by the modified Claus process in which it reacts with H_2S over alumina or bauxite [98, 99]. Although at present zeolites will not replace these materials in the industrial process, they can serve as useful model catalysts [100]. Adsorbed on zeolite NaX, SO_2 exhibits three bands at 215, 250 and 280 nm which, supported by IR investigations, are assigned to chemisorbed HSO_3^- , $\text{S}_2\text{O}_5^{2-}$ and physisorbed SO_2 , respectively [101]. The second reactant, H_2S , adsorbed on the same adsorbent, gives rise to one band that shifts with increasing coverage from 235 to 250 nm [102]. This electronic spectrum is, again combined with IR experiments, explained at low H_2S concentrations by a complete dissociation of H_2S into H^+ and S^{2-} on strong centers of interaction. Increasing the coverage, formation of SH^- ions on weaker centers and finally nondissociatively physisorbed H_2S species were identified. For the elucidation of the elementary steps of the Claus reaction both reactants must be brought together. After preadsorption of H_2S on NaX at room temperature the UV-VIS band mentioned above appeared (Fig. 34, spectrum 1). Treating the sample in the IR beam (spectrum 2) yielded SH^- species perceptible from the 2560 cm^{-1} band shown as trace A in the inset of Fig. 34. After exposure to SO_2 and subsequent heating in the IR beam, the SH^- species disappeared (see inset, trace A') evidencing their involvement in the reaction with SO_2 together with the appearance of new bands in the 250–500 nm region (spectra 3 and 4) attributed to S^{2-} (250 nm), S_2 (295 nm), $\text{S}_2\text{O}_4^{2-}$, c- S_8 (320 nm) and S_2^{2-} (385 nm) species. They were largely removed after evacuation at 573 K or transformed into chain molecules

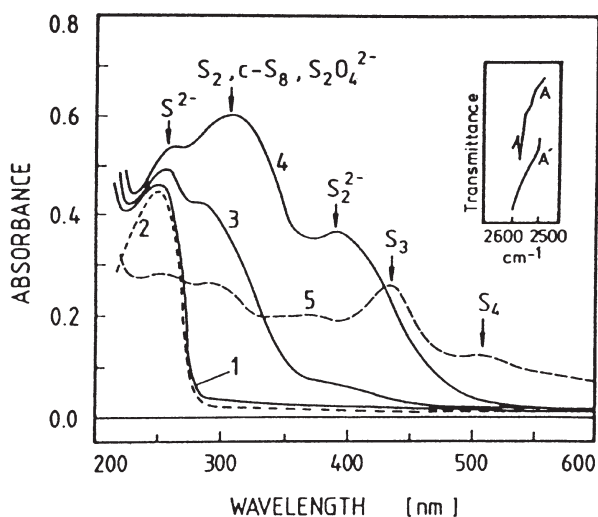


Fig. 34. Transmission UV-VIS spectra of reactive interaction of H_2S and SO_2 over zeolite NaX. After adsorption of H_2S at room temperature (1); after treatment in the IR beam for 1.5 h (2), giving rise to the IR spectrum A (see inset); after admission of SO_2 at room temperature (3); after treatment in the IR beam for 1 h (4) resulting in the IR spectrum A' (see inset); after evacuation for 3 h at 573 K. Reprinted from [100] with permission of Academic Press, Inc

like S_3 and S_4 (spectrum 5). On the other hand, S^{2-} species proved to be inactive in the Claus reaction. In conclusion, combined transmission UV-VIS and IR spectroscopy is a suitable tool for the study of the details of the Claus reaction over zeolite catalysts.

4.2.2

Organic Compounds

For simple organic molecules with a single chromophore there are a number of possibilities for electronic excitation. Saturated compounds with single bonds allow only $\sigma \rightarrow \sigma^*$ transitions occurring in the far UV region close to the Rydberg transitions. In the case of lone-pair electrons, e.g., on heteroatoms, the generally weaker $n \rightarrow \sigma^*$ and $n \rightarrow \pi^*$ transitions are possible at lower wavelengths. At last π -bonding in chromophores gives rise to $\pi \rightarrow \pi^*$ transitions. Benzene, e.g., exhibits three bands around 180 ($A_{1g} \rightarrow E_{1u}$, β), 200 ($A_{1g} \rightarrow B_{1u}$, p) and 260 nm ($A_{1g} \rightarrow B_{2u}$, α) that in the nomenclature of Clar are denoted as β , p and α bands [3]. Hückel MO treatment yields six wave functions, as shown in Fig. 35 [6, 9]. Their symmetries, given in brackets, are irreducible representations of point group D_{6h} . The ground electronic state is given by $(a_{2u})^2(e_{1g})^2(e_{1g})^2$ which belongs to the totally symmetric species ${}^1A_{1g}$. The lowest excited state has the electronic structure $(a_{2u})^2(e_{1g})^2(e_{1g})(e_{2u})$. According to group theory, the symmetry species of the orbital part of this electronic wave function are obtained from the direct product $\Gamma = e_{1g} \otimes e_{2u} = B_{2u} + B_{1u} + E_{1u}$. Taking electron repulsion into account the term

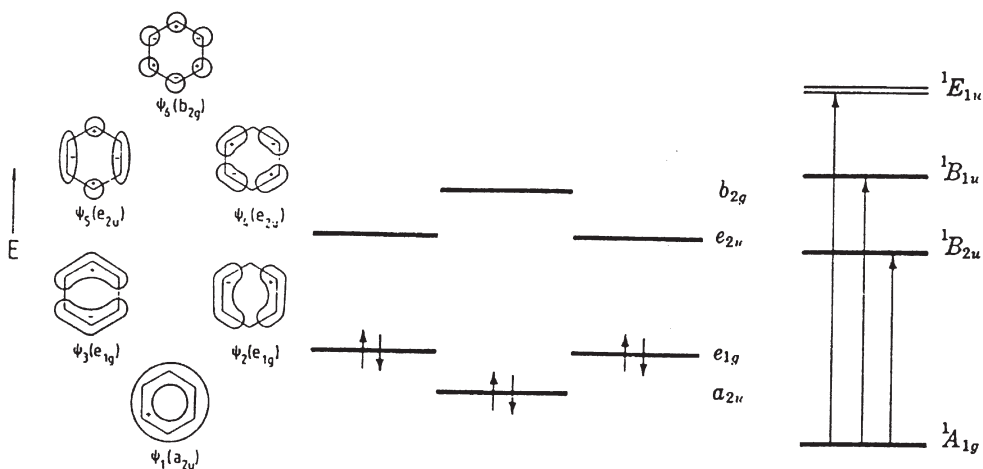


Fig. 35. The π molecular orbitals according to Hückel MO calculations (left), energy level diagram (center) and term diagram of benzene with electronic transitions indicated (right). Quoted from [6]. Copyright John Wiley and Sons, Ltd. Reproduced with permission. The other parts are taken from Chang R (1971) Basic principles of spectroscopy. McGraw-Hill Kogakushi, Ltd, Tokyo. Reproduced with permission of the McGraw-Hill Companies

level diagram is as shown on the right-hand side of Fig. 35 with the transitions indicated by arrows. The α band, although symmetry-forbidden, appears with a vibrational fine structure due to the distortion of the benzene ring by a bending vibration which allows it to borrow intensity from the β band [3]. Indeed the $0 \rightarrow 0$ vibrational transition is not observed which becomes allowed upon symmetry lowering by substitution of the aromatic ring or by interaction with solid surfaces [103]. Early investigations on aromatic systems adsorbed on zeolites have been carried out by Russian workers, e.g., [104, 105]. Some of the most important results have been reviewed [16, 106]. Benzene shows molecular adsorption with small band shifts to higher wavelengths. The larger displacements in the case of amine derivatives are explained by respective changes in the levels responsible for the $n \rightarrow \pi^*$ transitions as the result of participation of the lone-pair electrons of the substituent in the interaction. Comparing the frequency shifts of different alkali metal ion-exchanged zeolites X this shift could be correlated with the electrostatic potential of the nonframework cation expressed by the charge/radius ratio, as shown in Fig. 36. Triphenylcarbinol and anthraquinone on NaY proved only molecular adsorption [16]. The same is true with benzene, toluene and cumene on CaX. However, with aniline, diphenylamine, triphenyl methane and triphenylcarbinol, new bands appeared which must be assigned to carbocations.

Aromatic systems have always attracted considerable attention. Eremenko et al. [107, 108], choosing naphthalene and naphthylamine as probe molecules in alkali metal and alkaline earth ion-exchanged faujasites, investigated the formation of donor-acceptor complexes and the oxidation of naphthalene using luminescence and DR spectra. Naphthalene adsorbed from hexane solution in

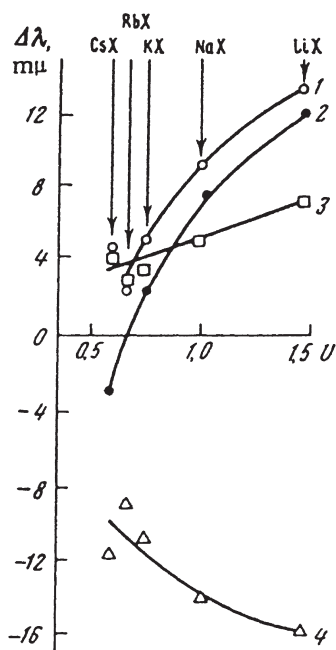


Fig. 36. Wavelength shift $\Delta\lambda$ of the electronic band of aniline (1), p-phenylenediamine (2), pyridine (3) and nitrobenzene (4) adsorbed on zeolites LiX, NaX, KX, RbX and CsX as a function of the electrostatic potential $U=e/r$ (Å) of the respective nonframework cation. Reprinted with permission from [106]. Copyright 1971 American Chemical Society

zeolite NaX exhibits both fluorescence (310–350 nm) and phosphorescence (470–540 nm) indicating monomer physisorption on different sites in the zeolite cages. An additional intermediate unstructured band with a maximum at 400 nm has been attributed to a naphthalene excimer, i.e., an excited dimer. Loading the zeolite from the vapor phase resulted in a broad unresolved luminescence of CT complexes and dimers on the outer zeolite surface. Coadsorption of water promotes the splitting of the dimers and migration into the zeolite interior. Adsorbed oxygen in the presence of water vapor caused oxidation of naphthalene to α -naphthoquinone in the case of sodium ions and to an α -naphthoquinone/ β -naphthol mixture in the case of alkaline earth ions. Similar behavior was observed for naphthalene in zeolite NaY where as well as weakly bound monomers chemisorbed donor-acceptor CT complexes but no exciplexes or excimers were evidenced [108]. As electron-acceptor sites coordinatively unsaturated silicon and aluminium ions are suggested.

These last considerations take this topic into the realm of electron- and charge-transfer reactions; of those a vast number have been investigated in zeolites, recently reviewed by Yoon [109]. The reader is referred to this article for further information.

4.2.3

Reactive Intermediates: Carbocations, Carbanions, Radicals

In the discussion of reaction mechanisms of multi-step reactions the so-called reactive intermediates like carbocations, radicals, carbanions and carbenes play an essential role as they function in a way as relay stations in consecutive reactions. Due to their mostly short lifetimes and/or low concentrations their presence is easier postulated than proved. Concerning carbocations and reviewing the hitherto obtained results by means of optical spectroscopy, electronic spectroscopy seems to be superior to vibrational spectroscopy due to (i) the considerably larger absorptivity and (ii) the lack of obscuring adjacent bands, provided there is not much interference with bands of the host, e.g., with d-d transitions in the case of TMI-exchanged zeolites or with CT bands. Although the electronic spectrum basically contains the overall information on the rotational, vibrational and electronic degrees of molecular freedom, those of the two former cannot be readily extracted, as the rovibrational fine structure frequently remains unresolved. Therefore, it must be considered as a substantial drawback that no structural evidence is given by electronic spectroscopy so that additional vibrational spectroscopic studies are necessary resulting in a mutual support.

On the zeolite surface the Brønsted acid sites are responsible for the generation of (i) carbonium ions from paraffins, (ii) alkyl carbenium ions from olefins, and (iii) alkenyl carbenium ions from dienes by protonation, while on Lewis acid sites (i) alkyl carbenium ions from paraffins and (ii) alkenyl carbenium ions from olefins are formed by hydride ion abstraction.

In carbocations formed on solid surfaces chromophores must be present with transitions in the near UV or VIS region, i.e., in a spectral range accessible to commercial spectrometers. This excludes alkyl carbocations from spectral proof because they have no absorptions above 210 nm [110]. Unsaturated compounds show π - π^* transitions in the far UV region which upon insertion of alkyl groups undergo a bathochromic shift due to hyperconjugation. Conjugation of olefinic double bonds gives rise to a lowering of the π orbitals accompanied by a reduction of the HOMO-LUMO gap resulting in a red shift together with an increase in intensity. This forms the basis for the detection of alkenyl carbenium ions by UV-VIS spectroscopy.

Early IR and UV-VIS spectroscopic studies on the formation of carbonium ions from triphenyl methyl compounds on zeolites, titania and alumina were carried out by Karge [111]. In 1979, upon interaction of olefins like ethene and propene with zeolites CoNaY, NiCaNaY, PdNaY and HY, the appearance of electronic bands between 230 and 700 nm was observed by Garbowski and Praliaud and attributed to an allylic carbenium ion which upon thermal treatment transforms into polyenyl carbenium ions and/or aromatic compounds [112]. These findings were corroborated and extended by studies of the interaction of propene, cyclopropane and *trans*-butene on zeolites NaCoY and HM [30]. In spite of the obscuration of the spectrum in the range between 450 and 700 nm by the threefold split d-d band of tetrahedrally coordinated Co(II) ions in the case of zeolite NaCoY, the development of bands near 330, 385 and 415 nm was assigned to unsaturated carbocations.

Systematic transmission spectroscopic studies of the transformations were carried out on the systems allene, propene, cyclopropane, *isopropanol* and acetone over NaM, HM and NaHM [113–117], 1-butene over NaHY [117, 118], allene, propene and cyclopropene over NaHY and NaHZSM-5 [116, 117, 119–122], neopentane over NaY, NaHY, NaHM and NaHZSM-5 [119, 123, 124], cyclohexene over HZSM-5 [119], 1-hexene, cyclohexane, cyclohexene, cyclohexadiene and benzene over NaHY and NaHZSM-5 [117, 125], allyl alcohol, acrolein and allene over HZSM-5 [126], allene and propyne over nonacidic zeolites NaA, CoNaA, CoNaX, NaY and NaHY [121] and benzene, toluene, ethylbenzene, and cumene over HZSM-5 [127].

The spectral features observed are in general quite similar to those shown in Fig. 37 with zeolite NaHY exposed to propene as an example [119]: Shortly after adsorbate admission a band around 300 nm emerges, increasing in intensity and shifting to higher wavelengths with time (a-d) accompanied by the development of bands around 370 and 450 nm enhanced by thermal treatment. Upon evacuation at higher temperatures, λ_{\max} is displaced to shorter wavelengths (e, f). This triad of bands is attributed to the π - π^* transitions of mono-, di- and tri-alkenyl carbenium ions. Basically, alkenyl carbenium ions can form by (i) protonation of dienes, (ii) hydride ion abstraction from olefins on Lewis acid

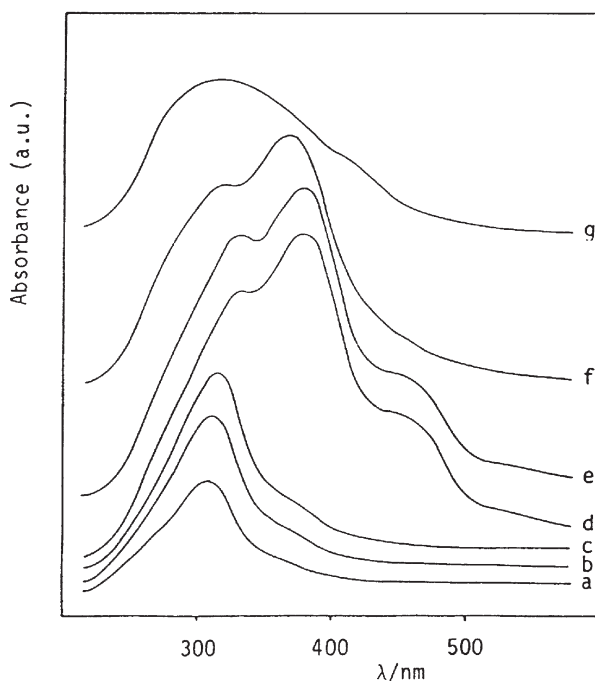


Fig. 37. Transmission electronic spectra of zeolite NaHY loaded with 1.33 kPa propene at room temperature after 5 min (a), 1 h (b), 2 h (c); at 320 K after 1 h (d); after evacuation for 1 h at room temperature (e), at 400 K (f) and at 570 K (g). Reprinted from [119] with kind permission of Elsevier Science NL, Sara Burgerhartstraat 25, 1055 KV Amsterdam, The Netherlands

sites, (iii) intermolecular hydride ion abstraction from olefins by alkyl carbenium ions, (iv) conjunct oligomerization, or (v) cracking of oligomers [128]. Mono-, di- and trialkenyl carbenium ions must contain at least 3, 5 or 7 C atoms, respectively.

The most important results from electronic spectra are briefly summarized as follows:

- The capability for alkenyl ion formation from different hydrocarbons and their derivatives follows the same sequence as observed in superacid solutions: dienes > olefins > alcohols > paraffins. Decreasing the Brønsted and the overall acidity has the consequence of slowing down the formation of alkenyl carbenium ions. Thus, protonation and hydride ion abstraction are the triggering steps.
- The wavelengths of the band maximum λ_{\max} characteristic for alkenyl carbenium ions formed in zeolites agree approximately with those calculated from the Sorensen equation

$$\lambda_{\max} = (319.5 + 76.5 n) \quad (37)$$

describing in superacid solutions the frequency dependence of polyenylic carbenium ions of the type



as a function of the number of conjugated double bonds.

- λ_{\max} is sensitive to structural changes of the carbenium ion; e.g.:
 1. insertion of an additional double bond gives rise to a wavelength jump of ca. 60 nm, while
 2. extension of the carbon chain or formation of branched oligomers results in a smooth upscale wavelength shift accomplished by consecutive reactions.

Therefore, only information on the degree of unsaturation, i.e., number of double bonds, is available while the structure remains uncertain.

Starting, e.g., from propene (as shown in Fig. 37), the consecutive reaction with itself gives rise to an equilibrium mixture of various monoenyl carbenium ions the common feature of which is a C₆ backbone. This explains the different wavelengths or the broad wavelength ranges observed in the spectra. Increasing the temperature enhances further oligomerization via alkyl and alkenyl cations. Upon protonation cyclic hydrocarbons undergo ring opening to olefins. Following the temporal development of the peak heights the induction period observed with dienyli ions points to their consecutive formation from monoenyl ions.

The higher the amount of Brønsted acid sites, the more pronounced the oligomerization of olefins and, consequently, the formation of alkenyl carbenium ions absorbing at higher wavelengths. It is assumed that a decrease in the number of Brønsted acid sites is related to an increase in the acid strength, thus promoting the stability of the respective carbenium ion.

The explanation of the upscale frequency shift linked with increasing temperature might be cracking and/or desorption, so that the remaining ions are of shorter carbon chain type, thus absorbing at higher frequencies.

Complementary aid is given by combined IR experiments from which bands at 1535 and 1505 cm^{-1} have to be assigned to the C-C-C stretching modes of mono- and dienyl carbenium ions, respectively. At low temperatures there is no indication of aromatics. After evacuation sometimes a band at 1585 cm^{-1} remains which must be attributed to coke.

Quantum chemical methods are valuable tools for assisting spectroscopic studies. Semiempirically calculated lowest vertical singlet excitation energies (LVSEE) prove the red shift of the bands with growing carbon chain length and methyl substitution [122]. Increased methyl substitution increases the stability of the ion as shown from the standard heat of formation ΔH_f . ΔH_f on the other hand slightly decreases in the sequence mono->di->trienyl carbenium ions. Their ease of formation as well as stability depends on zeolite acidity, i.e., on their environment that may be approximated by the relative permittivity from an MNDO effective charge model correlated with the heat of solvation, ΔH_{solv} , paralleling the stability of the alkenyl carbenium ion. From quantum chemical studies also a hint to the site of H^+ attack and thus to the kind of carbocation intermediate can be given, as shown for the protonation of allyl alcohol. The results of the quantum chemical calculations prove once more that the assignment of a given UV-VIS band to a well-defined alkenyl carbenium ion is rather difficult; only a group of such ions may be indicated.

There are a number of processes for which a carbenium ion mechanism has been proposed, and UV-VIS spectroscopy has proved to be a very attractive technique in these cases. However, interpretation of the spectra is rather difficult due to the overlapping bands from simultaneous formation of several carbocations and the shift of the peak position effected by the adsorbent, so that comparison with the bands observed in superacid solution is hampered. This technique was used to explore the formation of aromatics from methanol over zeolite HZSM-5 [129]. Cyclization of dienyl to cyclopentenyl cations (absorbing at 280 nm) and their structural rearrangement into cyclohexenyl carbenium ions (~300 nm) as well as further generation of polyalkylaromatics and polyaromatics (260, 280, 330, 420, 500, 600 nm) were observed. Although no coking in the zeolite channels during the experiment was detected, polyalkylaromatics and polyaromatics are considered to be the precursors for coking which obviously in this case takes place on the outer zeolite surface.

An interesting variant of the spectroscopic experiment is in situ investigations under catalytic conditions. For this purpose a special reactor cell has been designed equipped with quartz windows which allows the monitoring of the course of the reaction on the catalyst wafer. As an example, the transformation of ethene over HZSM-5 was studied up to 573 K using a scattered transmission accessory in which the sample is placed directly in front of the multiplier, so that the forward-scattered light almost completely impinges the detector [130]. At lower temperatures no substantial differences could be established between the carbocation spectra obtained in situ and ex situ. The spectroscopic discrepancies in the peak positions above 548 K are tentatively explained by the different

stability of carbocations at room temperature compared with higher temperatures.

Coke represents undesired carbonaceous residues leading to catalyst deactivation necessitating a burning off of used catalysts, e.g., in the FCC process. Karge et al. [29, 131] carried out systematic studies on coke formation in zeolites. Transmission electronic spectroscopy enabled these authors to distinguish between different stages of coke formation, low- and high-temperature coke, as can be seen from Fig. 38 in which the difference spectra of a methanol-loaded ZSM-5 catalyst are displayed obtained upon subsequent heating to the indicated temperatures in a closed cell. While at temperatures lower than 550 K essentially bands of mono- and dienylic carbocations near 300 and 360–370 nm appear, the high-temperature range is dominated by absorptions around 430 and above 500 nm of small aromatic carbocations and polyaromatics, respectively. The nature of the different forms of coke thus formed turned out to be dependent not only on the temperature but also on the acidity, morphology and crystallite size of the zeolites. Generation, characterization and transformations of unsaturated carbenium ions in zeolites have been comprehensively reviewed recently [132].

Carbanions as intermediates have been suggested in the base-catalyzed isomerization of unsaturated nitriles. As long as zeolites with anion-exchange properties are not available, basic centers must be introduced by exchange of the non-framework ions by alkali metal ions or of silicon by germanium, by precipitation

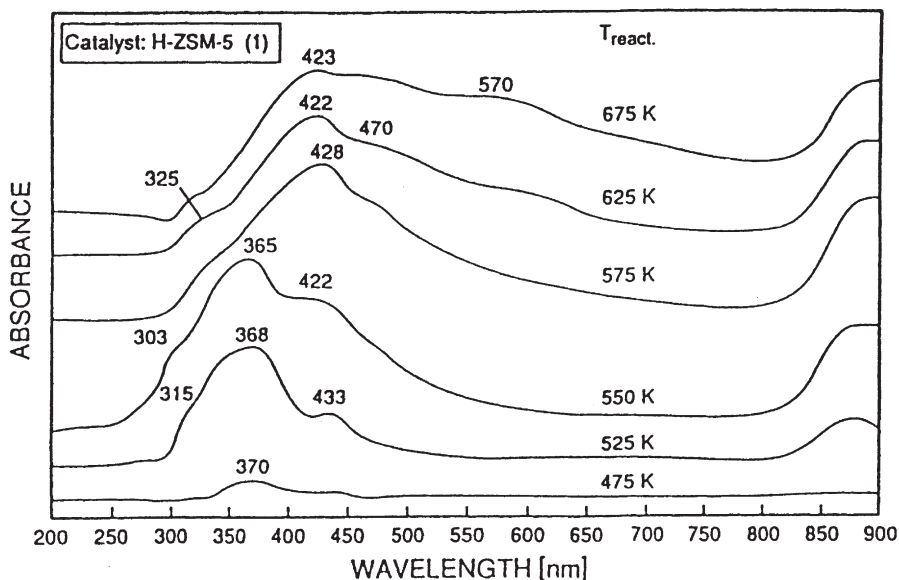


Fig. 38. UV-VIS difference spectra of carbonaceous deposits after reaction of methanol on HZSM-5 obtained from thermal treatment of the system at the indicated temperatures. Reprinted from [131] with kind permission of Elsevier Science NL, Sara Burgerhartstraat 25, 1055 KV Amsterdam, The Netherlands

of basic oxides within the zeolite interior or by generation of ionic alkali metal clusters, e.g., by impregnation with sodium azide followed by controlled decomposition. Applying the latter procedure to NaY, a modified basic faujasite was obtained which, exposed to allyl cyanide, readily catalyzed its isomerization to crotonitrile, proven by IR spectroscopy [133]. In the literature the electronic bands of carbanions are reported to appear in the 350–550 nm range. The UV-VIS spectra recorded during transformation showed only one broad band around 400 nm that increased in intensity and shifted to higher wavelengths with increasing time of contact and/or temperature. As it did not show the characteristic spectral behavior reported for unsaturated carbenium ions, it is assumed to be due to a π - π^* transition of the carbanion formed by interaction of allyl cyanide with basic sites.

Radicals are very reactive and therefore short-lived species with one or more unpaired electrons and may be neutral or charged as radical cations and anions. Neutral radicals often result from homolytic cleavage of a covalent bond to which the necessary dissociation energy is frequently supplied by heat or radiation. Therefore, early spectroscopic studies of radical formation on zeolites were carried out with molecules adsorbed in zeolites under UV irradiation; these have already been comprehensively reviewed in the literature [15, 16, 105, 106]. Benzene, e.g., in zeolite NaX, did not reveal spectral changes upon irradiation, while adsorbed in zeolites CaX and HX two bands at 460 and 565 nm were formed from which the former was assigned to the cyclohexadienyl cation and the latter to the radical cation $C_6H_7^+$. Similar results were obtained with cumene and anthraquinone. There are many studies of free-radical reactions in zeolites, in particular upon photolysis of molecules yielding fragments which react according to the cage effect [134]. Photoexcitation of the CT band of donor-acceptor precursor complexes by lasers leads to the formation of transient CT ion pairs composed of radical ion pairs which are stabilized in the zeolite cages by retardation of the back electron transfer and can be proved by UV-VIS spectroscopy [109]. Also, radical formation without irradiation is reported in the recent literature. Loading zeolite NaY and its protonated forms with bi- and terthiophene gave rise to bands in the 400–800 nm range attributed to bi-, ter- and hexathiophene radical cations [135].

4.2.4

Polymerization in Zeolite Channels

Zeolites provide novel hosts for preparation of conductive polymeric materials within their channels [136]. Provided the synthesis and the alignment of conjugated polymers are carefully controlled the formation of oriented molecular wires for microelectronic applications such as signal processing and information storage is feasible. As already outlined in the last section, acid groups in the zeolite are responsible for the generation of thiophene oligomers [135].

As another example, the protonated forms of zeolites M, omega, L, Y, beta, ZSM-5 and SAPO-5 have served as media for the alignment and packaging of incarcerated methylacetylene in order to explore the concepts for the production of tailored polymers with possible useful nonlinear optical properties [137].

Upon irreversible uptake the formation of yellow to brown products was the result of initial protonation to produce a vinyl cation followed by oligomerization. Several broad bands between 300–600 nm tailing out to 750–850 nm were observed, as shown for methylacetylene/HZSM-5 in spectrum b of Fig. 39, and these were assigned to conjugated oligomers pointing to similar mixtures of products in all zeolites under investigation. The conjugated species seemed to be a small portion of the total, as the spectrum of longer conjugated chains would be more extended to the long-wavelength range.

Oxidative doping enhances conductivity in conjugated polymers. Using iodine as oxidant in the case of methylacetylene/HZSM-5 gave UV-VIS spectra that essentially look like a superposition of the separate spectra of I₂ and methylacetylene in HZSM-5 (Fig. 39) and confirm that, as electron-deficient entities, the cationic species will not be readily oxidized further.

A more detailed description of the extent of branching and cyclization is not available from the spectra, as no obvious differences are obtained even using zeolites with different spatial restraints.

An interesting variant of the formation of nanometer-sized conductive strands is pyrolysis of intrazeolite polymers such as polyacrylonitrile in zeolite NaY, the color of which turns from white to grey-black [136]. The electronic spectrum of the extracted material is practically structureless with a feature at about 350 nm and resembles that of graphite. In this way graphite-like chains with conductivity in the order of 10⁻⁵ S cm⁻¹ can be prepared.

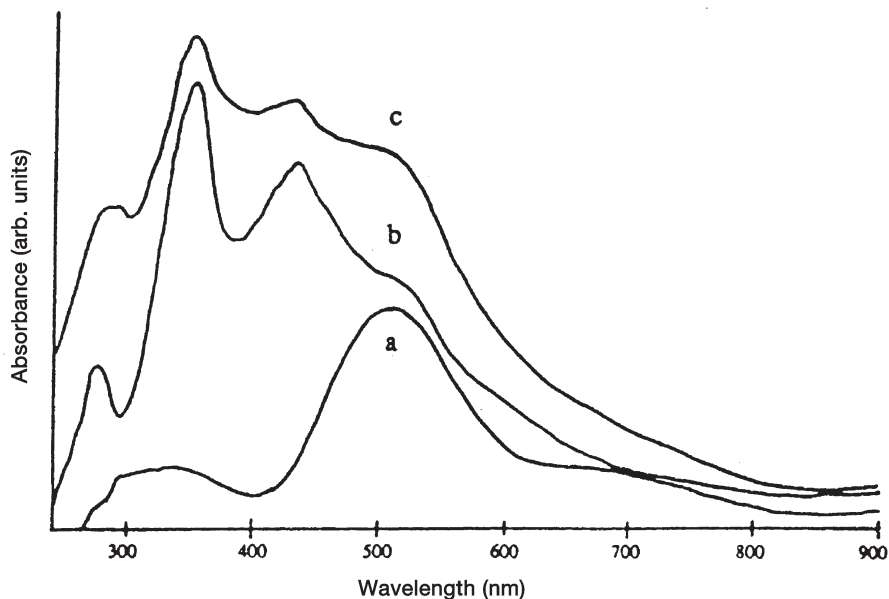


Fig. 39. Diffuse reflectance UV-VIS spectra of iodine in HZSM-5 (a), methylacetylene in HZSM-5 (b) and coadsorbed iodine and methylacetylene in HZSM-5 (c). Reprinted with permission from [137]. Copyright 1991 American Chemical Society

4.2.5

Clusters of Metals, Metal Ions and Semiconductors in Zeolite Hosts

Currently, there is a trend towards ever-decreasing electronic devices [138, 139]. The reduction in size of a solid leads to clusters with novel properties which have to be placed somewhere between those of the bulk phase and those of molecules or atoms. Changes in color are indicative for such quantum size effects. For these small clusters, with respect to their size also called nanoclusters, the description of the electron motion in a periodic structure by energy bands becomes replaced by the image of discrete energy levels similar to the particle-in-a-box behavior. One of the approaches to produce highly dispersed materials in a well-defined way is their preparation within the porous structure of zeolites that are known to stabilize unusual molecular species. Candidates of potential application of such nanoscale particles might be composite superconductors, new magnetic materials, effective catalysts in the case of metal and metal ion clusters and light switches, photocatalysts, reversible image capture/storage devices, solid-state batteries, electrochromic devices, sensors and solar cells in the case of semiconductor clusters. The preparation occurs either (i) by direct incorporation from the melt or the vapor or (ii) by in situ creation such as ion exchange followed by chemical reactions (reduction, sulfidation), thermal decomposition of inorganic as well as organometallic precursors or γ -irradiation of zeolites. Electronic spectroscopy is also a sensitive tool for the characterization of the electronic structure of these clusters.

The state of the art of silver clusters in zeolites, their structure and chemistry, complex formation and application have been reviewed by Sun and Seff [140]. Water cleavage is among others one of the most desirable processes for storage of solar energy. Upon illumination with light near 400 nm of silver-loaded zeolites in aqueous dispersion, Ag^+ ions become reduced by simultaneous evolution of oxygen [141]. This process is accompanied by self-sensitization, i.e., in the course of this reaction the sensitivity bathochromically shifts from the near UV to the visible region. This process can be rationalized as LMCT transition from the oxygen lone pair to the 5s level of zeolite-embedded Ag^+ ions. The lifetime of the holes hopping between the zeolite oxygens is long enough for their accumulation and reaction with water. The self-sensitization can be explained by the formation of partially reduced silver clusters absorbing at lower energies. Coupling of the oxidative step to a transition-metal complex forces the reduction of water under evolution of hydrogen via a MLCT transition. There is still little information on the details of the silver species produced which seem to be stronger reductants compared to bulk silver. A study on silver cluster stabilization in zeolites of different pore sizes and composition while also estimating the cluster size by comparison of the results from DRS, electron microscopy and small-angle X-ray scattering was carried out by Bogdanchikova et al. [142].

In contrast to zeolites X, Y and erionite, the amount of clusters formed in mordenite was rather large, i.e., the cage structure of the latter proves to be ideal for silver cluster stabilization. In the electronic spectra of AgM upon reduction with hydrogen at different temperatures (Fig. 40), two intense bands at 320 and 285 nm dominate beside two weak bands at 410 and 235 nm as well as shoulders at 350,

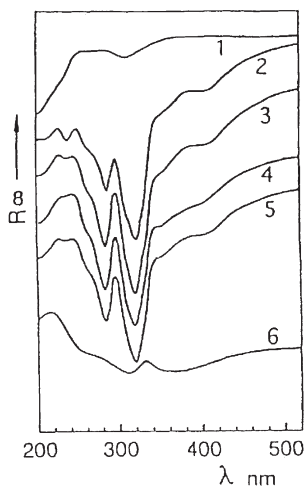


Fig. 40. Diffuse reflectance UV-VIS spectra of silver mordenite (Si/Al=15) reduced by hydrogen at room temperature (1), 323 K (2), 373 K (3), 473 K (4), 573 K (5) and 773 K (6). Reprinted from [142] with kind permission of Elsevier Science NL, Sara Burgerhartstraat 25, 1055 KV Amsterdam, The Netherlands

310 and 260 nm. The assignment takes its cue from that of Henglein et al. [143] for silver particles in aqueous solution, although some caution is advised as the band position depends on the environment and differs somewhat, e.g., for noble-gas matrices, liquid and frozen solutions and zeolites. Larger colloidal silver particles are discernible by the narrow surface plasmon band of the electron gas at 380 nm indicating metallic properties. This band becomes broadened and displaced to 360 nm in the case of quasi-metallic particles with agglomeration numbers around 10. Sharp bands below 360 nm are attributed to nonmetallic oligomeric species, called clusters. From smaller species Ag^0 absorbs at 360 nm, Ag_2^+ at 310 nm and Ag_4^{2+} at 275 nm. With respect to AgM the band at 410 nm corresponds to metallic silver, the 320 nm absorption to silver clusters of 0.7 nm size and those at 310, 285, and 235 nm to Ag_2^+ , Ag_n^+ and Ag^+ species, respectively. Reduction at 773 K shows agglomeration of the 320 nm clusters to larger particles absorbing at 360 nm, while the Ag_2^+ dimers at 310 nm are stabilized and not reduced even at this temperature.

DRS has also been successfully applied to follow the kinetics of silver-cluster formation in AgX monitoring the intensity changes of the 410 nm band which is assumed to originate from Ag_3^{2+} clusters in the SI'-SI-SI' position of the hexagonal prisms [144]; The rate-determining step has been rationalized by a model of diffusion into a sphere.

So far in addition to uncharged metal clusters, charged species have also been present. Prototypes of the latter are the alkali metal ion clusters which can be formed in zeolites by exposure to high-energy radiation, by alkali metal doping or by introduction of molecular electron donors [109, 134]. These seemingly very different procedures can be brought down to the common denominator of dis-

solution of surplus electrons in traps formed by the counterions of the zeolite framework. As mentioned earlier, the zeolite takes the role of a polar solid solvent and the widespread case of alkali metal doping, e.g., in faujasites, may be described as trapping of the released electron from the incoming alkali metal atom M among four equivalent sodium cations



In this way paramagnetic clusters of the type $M_n^{(n-1)+}$ with $n=2-6$ have been observed with sodium, although from MAS NMR and magnetic studies evidence on diamagnetic clusters M_n^{m+} with $n+m$ even has been reported. The main technique applied for identification of the cluster size is ESR. From the number of hyperfine lines predicted by the quantity $(2nI+1)$, where I is the nuclear spin, the number n of equivalent nuclei M^+ in the cluster can be evaluated. The most frequently observed species in the case of sodium are Na_4^{3+} perceptible from their 13 hyperfine line patterns. More complex ESR spectra with intensity ratios deviating from binomial distribution have sometimes been observed indicative of coexisting clusters of different nuclearity. For a more detailed discussion, which is beyond the scope of this article, the reader is referred to several reviews that represent the present state of alkali metal cluster research [140, 145–148].

The technique most frequently used next to ESR for the characterization of alkali metal ion clusters has been electronic spectroscopy. This seems understandable, as the trapped electron forms a color center quite similar to the F-centers in alkali halides (see Sect. 2.4.4). Both can be generated by exposure to γ -rays or UV light and can be bleached upon irradiation by intense white light, a photochromic behavior which gives rise to application as a read/write device. Unfortunately, the bands are broad and featureless without vibronic structure. As an example, the DRS of the sodium-doped sodium sodalite in Fig. 41 are dominated by a transition between the Stark effect broadened ground and first excited electronic states of the cluster in the range $15,500-18,000 \text{ cm}^{-1}$ accompanied by an UV band near $38,000 \text{ cm}^{-1}$. There have been several attempts to simulate the spectrum of the solvated electron in sodalite for a fixed and averaged orientation as shown on the right-hand side of Fig. 41 in comparison with the experimental spectrum at the lowest loading $\text{Na}_4^{3+}/\text{Na}_3^{3+}=1/50$ indicating reasonable agreement [145]. For another approach to the simulation of the electronic spectrum of the Na_4^{3+} color center in sodalite using 3-d wavepacket calculations, the reader is referred to an article by Blake and Stucky [147] and the references cited therein. These calculations reproduce the spectra well, support the observed linear relationship between λ_{max} of the guest band and the lattice constant of the host, and are in accordance with the distance of the color center to the nearest Na^+ neighbors deduced from ESR experiments. In the a_1 ground state the solvated electron is delocalized near the center of the $(\text{Na}^+)_4$ tetrahedron, while the excited state is a triply degenerate t_2 state. Upon excitation the resultant deshielding causes a vibrant breathing of the cluster that, apart from other effects, is jointly responsible for the breadth of the absorption band evidencing the sensitivity of the band to the Na^+-Na^+ distance in the cluster.

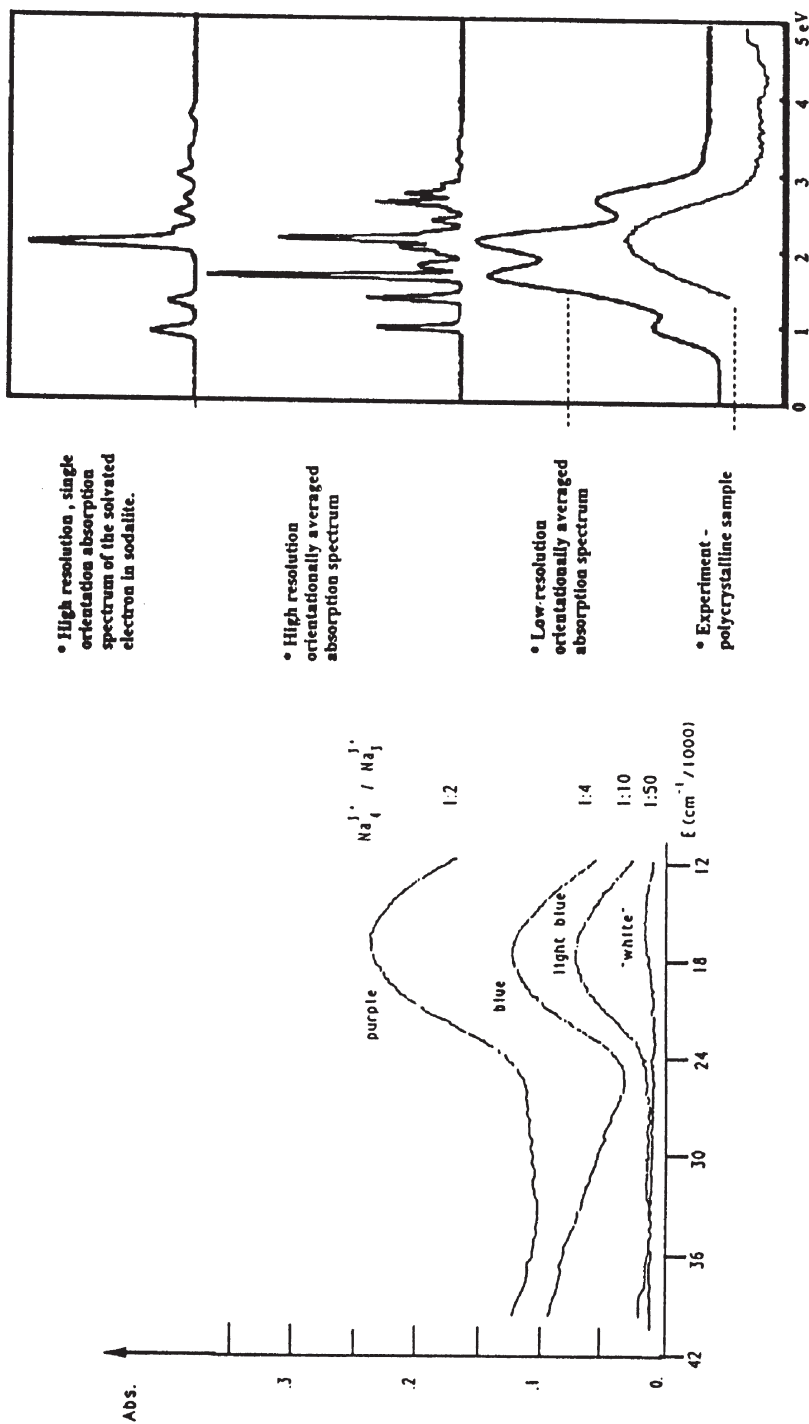


Fig. 41. Electronic spectra of Na_4^{3+} centers in sodium sodalite. *Left* Experimental spectra at $\text{Na}_4^{3+}/\text{Na}_3^{3+}$ loadings of 1:2, 4, 10 and 50. *Right* Calculated single-orientation spectrum and orientationally averaged spectra of a Na_4^{3+} cluster in a sodalite cage at high dilution with atomic charges of $\text{Si}=-1.5$, $\text{Al}=-0.85$, $\text{O}=0.84$ and $\text{Na}=+1$ (*top*). Blown-up experimental Na_4^{3+} spectrum at $\text{Na}_4^{3+}/\text{Na}_3^{3+}=1/50$ for comparison (*bottom*). Reprinted with permission from [145]. Copyright 1992 American Chemical Society

Attempting to summarize the hitherto existing literature on electronic spectroscopy of alkali metal ion clusters in zeolites [145–147, 149–168], it can be stated that the absorption of Na_4^{3+} clusters in zeolite NaY is correspondingly observed around 500 nm, while for X zeolites bands between 500 and 550 nm appear according to the method of preparation and the Si/Al ratio. Both absorptions were also proved for the first time after decomposition of sodium azide in faujasites [161, 162]. These bands are assigned to the $1s \rightarrow 1p$ transition of the electron trapped in the cluster. Contradictory are the data for Na_4^{3+} in sodalite with 560 nm [150] and 628 nm [146, 159] presumably due to the different type of synthesis. In zeolite NaA at low loading two bands are detected at 400 and 443 nm attributed to single-electron excitation of clusters containing one and more captured electrons, respectively, while the bands near 590, 886 and 1033 nm upon higher loading are assigned to an electron-hole pair formation and a surface plasmon transition, respectively.

At high amounts of doping the color of the sample turns black accompanied by a broadening of the absorption to a continuum with an onset at 1550 nm (0.8 eV). From these findings it must be concluded that the material has now become a semiconductor with a band gap of 0.8 eV. At this high level of alkali metal uptake an interaction of neighboring Na_4^{3+} clusters by overlap of their wave functions and coupling through exchange forces has to be assumed which results in the collapse of the ESR hyperfine structure to a singlet and raises hopes for achieving the insulator-metal transition at high excess electron concentrations, i.e., for the preparation of metallic conducting zeolites.

Light switching can be performed with semiconductors at their band edge by laser illumination which, due to the third-order non-linear optical properties, changes the refractive index and thus their state from opaque to translucent. As extreme speeds for processing are desired, the switching frequency must be increased by removal of the free carriers into defect (i.e., surface) sites which is simply achieved by increasing the surface/volume ratio, i.e., decreasing the particle size of the semiconductor. Making use of the zeolite pore structure, a number of different nanosized elemental and compound semiconductors have been prepared [139]. As an example of the latter, CdS clusters were generated by Cd^{2+} ion exchange followed by sulfidation. In zeolite Y distorted Cd_4S_4 cubes were formed in the sodalite unit where the Cd ions were octahedrally coordinated to three S and three O atoms of the zeolite 6R window [163, 164]. While bulk CdS is yellow-orange colored with a band gap of 2.42 eV (512 nm) [13] absorbing in the blue part of the visible range and increasing in absorption towards the ultraviolet, in zeolite Y at low concentrations the spectrum of the discrete cubes is displaced downscale with a shoulder at 280 nm corresponding to an edge shift of 230 nm. At a threshold of about 4 wt.% CdS, the population of adjacent sodalite cages becomes possible, and with increasing loading the spectral pattern shifts to the red with a distinct shoulder near 350 nm (see right-hand side of Fig. 42) which might be due to the exciton transition. Further increase of CdS concentration gives rise to a progression towards a semiconductor hyperlattice, as shown on the left-hand side of Fig. 42, with an intermediate behavior between the discrete cubes and the bulk. While at low amounts no emission was observed, above the threshold the interconnection brings about luminescence,

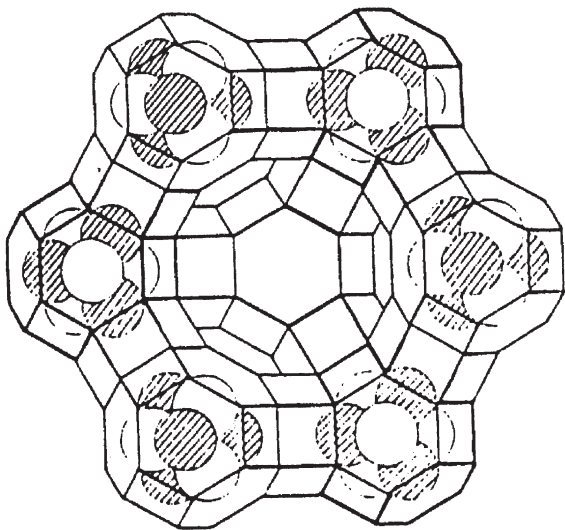
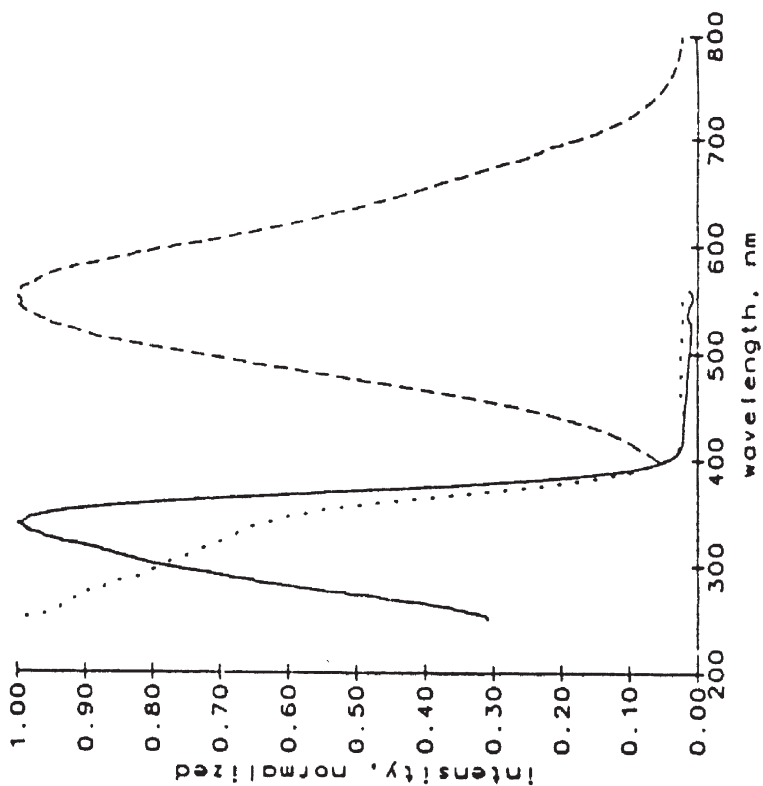


Fig. 42. *Left* Ultimate hyperlattice arrangement of $(\text{CdS}, \text{O})_4$ cubes in adjacent sodalite cages of zeolite Y (*hatched*=Cd, *open*=S, O omitted for clarity). *Right* Absorption (*dotted*), excitation (*solid*) and emission (*dashed*) spectra of 6.5 wt.% CdS occluded in zeolite Y. From [139] with kind permission from Kluwer Academic Publishers

as shown on the right-hand side of Fig. 42, with an excitation spectrum centered at the exciton shoulder. The properties of the semiconductor can be varied by application of different hosts. As revealed by electronic spectroscopy, the cluster-cluster interaction in CdS-loaded zeolite A is much weaker than in zeolite Y [163, 164].

4.2.6

Zeolite-Hosted Oxides

Synthesis of molecular sieves with T sites isomorphously substituted by other elements is frequently accompanied by the formation of more or less oxidic extraframework species as by-products (see Sect. 4.1.2.2). In this section the intended preparation of finely divided oxides or oxide clusters within the voids of the framework will be discussed.

Zeolite-stabilized oxides are of interest for catalytical application, due to their redox behavior as potential sensor materials and owing to the revealed quantum size effects for highly dispersed semiconductors.

Preparation of zeolite-hosted oxides can be carried out either (i) by chemical vapor deposition (CVD), i.e., loading the zeolite with volatile chlorides like TiCl_4 , VOCl_3 or SnCl_4 in a nitrogen carrier stream, followed by hydrolysis and calcination, or (ii) by impregnation with suitable compounds such as SnCl_4 or $\text{VO}(\text{acac})_2$ in aqueous or organic solution and subsequent calcination.

Due to their different appearance as

- isomorphously substituted ions in T positions,
- molecular oxidic species attached to the zeolite framework,
- quantum-sized particles, and
- oxides with bulk properties

there is considerable need for their reliable identification. This can be achieved from the maximum or the onset of absorption, i.e., the intersection of the tangent through the inflection point with the abscissa, or from both of the UV-VIS DR spectra. In the case of TiO_x -loaded faujasites it was possible to distinguish between TiO_x species double- or single-bonded to the framework and bulk TiO_2 (anatase) by their different maximum/onset at 240 nm/300–310 nm, 290 nm/330–340 nm and 328 nm/370 nm as well as the proof of tetrahedral Ti^{4+} from the onset at 250–260 nm [165].

Vanadium oxide particles in HZSM-5 prepared by CVD displayed CT bands at 210 and 250 nm typical of V in a distorted tetrahedral environment and one at 375 nm attributable to V in a distorted octahedral environment pointing to extraframework VO_x species enriched at the external surface according to XPS results [166]. Reversible reduction and oxidation was monitored by the decreasing or increasing reflectance at fixed wavelength (620 nm), due to the increasing or decreasing number of possible d-d transitions. Compared to VS-1, VZSM-5 is more sensitive to reduction/oxidation and shows a faster response to oxygen than to hydrogen.

Vanadium has also been incorporated into mesoporous MCM-41 materials by hydrothermal synthesis, impregnation and CVD [167]. UV-VIS DR spectra reveal predominantly mononuclear vanadium(V) oxide and oligomeric clusters

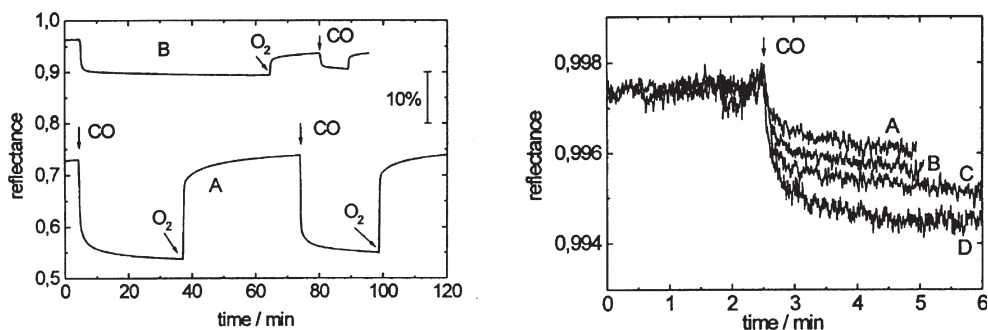


Fig. 43. *Left* Reversible reduction/oxidation cycles upon exposure to CO and O₂ of SnNaY loaded by impregnation (A) and bulk SnO₂ (B). *Right* Detection of small amounts of CO in air (A 250 ppm; B 500 ppm; C 1000 ppm; D 2000 ppm) by the decrease of the reflectance of SnNaY at 16200 cm⁻¹. Reprinted from [168] with kind permission of the Materials Research Society, Warrendale

both in more-or-less tetrahedral coordination inside the pore system. Both can be reduced by hydrogen, the latter with a steeper response. Irreducible vanadium is either buried in the framework or in nonporous by-products.

SnO_x particles in Y zeolites have been formed with diameters <1 nm using CVD and with diameters of 3–4 nm by impregnation indicating quantum size effects from the blue shift of the absorption onset in comparison to bulk SnO₂ [168]. While reduction of SnO₂ with hydrogen is irreversible, it becomes reversible with CO, leading to the formation of SnO_x particles (1 < x < 2). As the nanoparticles are located in the pores near the external zeolite surface they are highly accessible to gases. Figure 43 (left) shows reversible reduction/oxidation cycles of SnNaY prepared by impregnation compared to bulk SnO₂, monitored by the change of reflectance at fixed wavenumber (16,200 cm⁻¹) and demonstrate their application as sensors with optical detection. The detection of low amounts of CO down to 250 ppm is proved on the right-hand side of Fig. 43.

4.2.7

Zeolite-Encapsulated Carbonyl, Metal Chelate Complexes and Dyes

In this section, guests confined within the zeolite cavities will be discussed, i.e., guests of sizes larger than the portals formed by the pore aperture, so that they are unable to escape. Steric restrictions and the strong intrazeolitic electric fields affect the chemistry in these nanoreaction chambers and may cause structures and properties that are modified compared to those obtained in solution or on external surfaces. Furthermore, entrapping hinders interaction between the clusters and enhances their stability.

Different strategies for encapsulation of bulky entities in zeolite hollows have to be distinguished [79, 169]:

1. in situ preparation from the components,
2. flexible ligand method,

3. template synthesis method, and
4. zeolite synthesis method.

The topic of clusters confined to zeolite cages in general and of organometallic clusters in particular has been reviewed by several authors, e.g., [48, 79, 169–171]. In these articles the methods of synthesis have been described in detail, so that we can restrict ourselves to outlining their characterization which has profited greatly from electronic spectroscopy.

Prior to characterization encapsulation must be ensured and clusters formed outside the cavities must be ruled out. Only then can characterization be reliably carried out. A battery of techniques is available for this purpose, such as ^{13}C , Xe and metal NMR, EXAFS/XANES, XPS, IR and UV-VIS spectroscopy, electron microscopy, ESR, XRD, etc. Among these methods electronic spectroscopy plays an important role. The UV-VIS spectra reflect changes in the oxidation state of the metal as well as structural changes forced by incarceration and so serve as a valuable tool for the ascertainment of intrazeolite complexation. Although vibrational spectroscopy is most frequently applied, sometimes using the IR spectra as fingerprints for identification, it is inadequate to predict the exact structure of the clusters as these spectra may be different from those in solution or in the solid state due to interaction with the zeolite matrix. In any case, reliable characterization requires the combined application of complementary analytical methods.

The preparation of small metal clusters with narrow particle size distributions is of considerable interest from the catalytic point of view. One of the oldest routes is the thermal expulsion of CO from a metal carbonyl. As the direct synthesis is impractical for most of the d metals, the route often employed is reductive carbonylation, i.e., the reduction of a metal ion in the presence of CO. Thermal treatment of Pt^{2+} -exchanged faujasites, the properties of which were varied from acidic to basic by neutralization of their protons by Na^+ and Cs^+ ions, in the presence of CO at 373 K for several hours resulted in a red-purple coloring accompanied by the appearance of two bands at 445 and 730 nm in the UV-VIS spectrum in the case of the basic PtNaY sample [172]. Supported by IR spectroscopy and electron microscopy the carbonyl species formed were identified as Chini complexes [173] of the general formula $[\text{Pt}_3(\text{CO})_3(\mu_2\text{-CO})_3]_n^{2-}$, structured in a tinker toy construction, in line with $n=3$ and fitting into the supercage, while, in the case of the other basic zeolite CsNaX, the entrapped species are suggested to be extended through the 12R window in two adjacent supercages reaching $n=5$. The formation of these anionic platinum carbonyl complexes in zeolite PtNaX has been monitored in situ by combined electronic and IR spectroscopy [174]. The monomer $[\text{Pt}_3(\text{CO})_3(\mu_2\text{-CO})_3]^{2-}$ is distinguished by electronic bands at 318 and 456 nm remaining at their positions during reaction but growing with time, as shown in Fig. 44. The additional absorption at 230 nm has been attributed to small Pt particles. The shoulder on the right flank of the 456-nm band indicates the generation of oligomers with $n \geq 1$. These oligomers are more readily formed in PtNaY, perceptible from additional bands at 384, 512 and 725 nm, obviously due to the more acidic nature of this host.

Metal chelate complexes entrapped in zeolites have attracted increasing attention for application as oxygen carriers, enzyme mimics and catalysts [48,

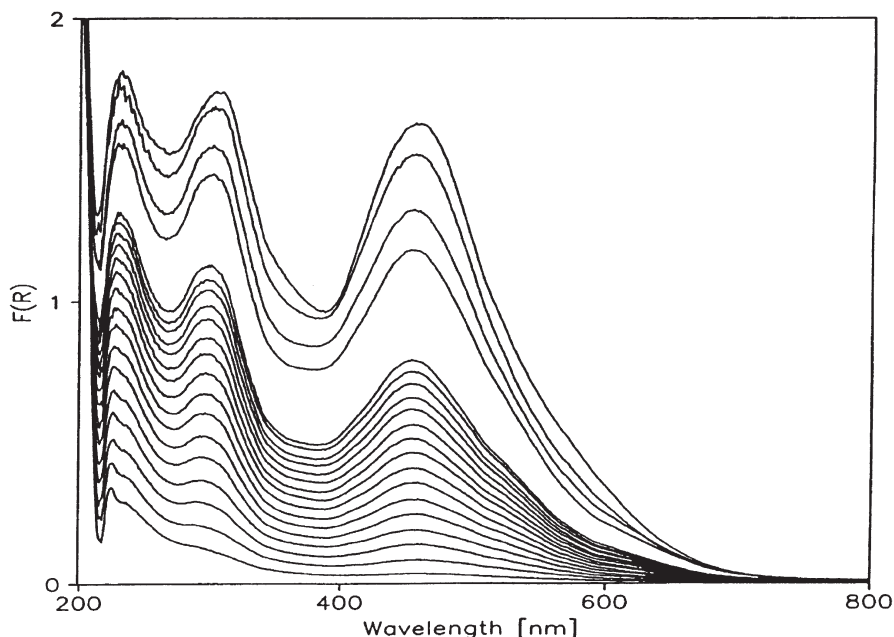


Fig. 44. DRS of reductive carbonylation of zeolite PtNaY at 363 K and $p=10^5$ Pa. In the *lower part* the sequence of recording is 15 min during the first 4 h and thereafter at 8, 24 and 48 h in the *upper part*. Reproduced from [174] by permission from Baltzer Science Publishers BV

175, 176]. Since 1977 several groups have succeeded in encapsulating transition metal phthalocyanines (Pc) in the supercages of zeolites A, X, Y and VPI-5 using one of the synthetic strategies mentioned before. The zeolite synthesis method, i.e., synthesis of the zeolite around FePc, CoPc and NiPc complexes, has been applied by Balkus Jr et al. [177]. For these ship-in-a-bottle species a strong Q band due to a $\pi \rightarrow \pi^*$ transition associated with the Pc ring in the range 600–900 nm is characteristic which, as shown in Fig. 45A for FePc/NaX, appears as a broad absorption around 630 nm [178]. After digestion of the sample in concentrated sulfuric acid the Q band near 790 nm proves that the FePc is still intact (Fig. 45B). The frequency of this band is sensitive to encapsulation and downscale shifted in comparison to the free complex. In contrast to the interpretation of IR, XPS and EXAFS results, a distortion from planarity of the MPC ligand could not be established by Raman and NMR spectroscopy. Thus, it seems probable to rationalize this shift by protonation of the MPC rather than by saddling as predicted by molecular modeling [169].

Pd complexes of the Schiff base salen (*N,N'*-bis-(salicylidene)-ethylenediamine) and its chiral derivative salen* (*R,R-N,N'*-bis-(3,5-di-*tert*-butylsalicylidene)-1,2-cyclohexanediamine) have been immobilized in the large cages of zeolites FAU and EMT, where the intracrystalline complex formation has been proved by UV-VIS spectroscopy [179]. These host/guest compounds are active catalysts for

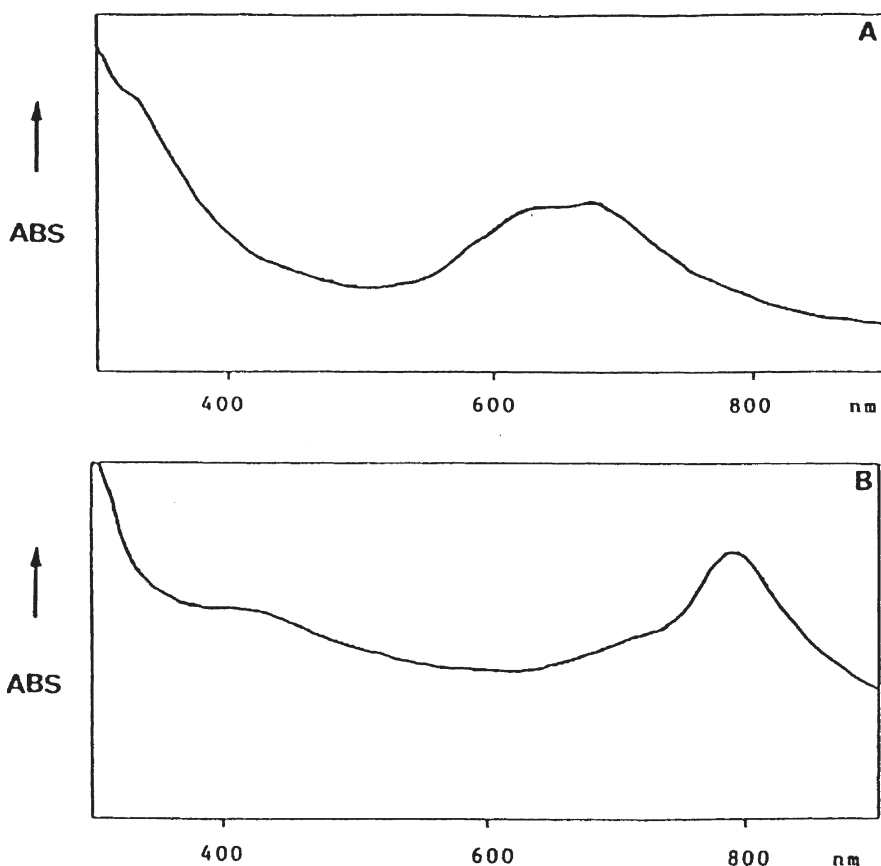


Fig. 45A, B. UV-VIS spectra of FePc inside zeolite NaX using A Nujol as mulling medium and B FePc/NaX dissolved in sulfuric acid. Reprinted with permission from [178]. Copyright 1992 American Chemical Society

hydrogenations, the salen* complex being a potential candidate for enantioselective hydrogenations.

A new family of hybrid organic-inorganic catalysts with dispersed active sites inside ordered *mesoporous* materials has been prepared by anchorage of transition-metal ligands of Schiff base-type and chiral amino alcohols like (1*R*,2*S*)-ephedrine on micelle-templated silicas [180]. Metalation of the grafted ligands with manganese was followed by UV-VIS spectroscopy.

Microwave-assisted growth of 50- μm large $\text{AlPO}_4\text{-5}$ single crystals monomolecularly loaded with dyes such as Rhodamine derivatives and Basic Yellow 40 has been reported by Braun et al. [181]. UV-VIS reflectance as well as fluorescence spectra revealed strong host/guest interaction resulting in distortion of the dye molecule, presumably in antiparallel orientation to the polar axis of the host, deviating from perfect alignment. While in the case of Rhodamine derivatives the concentration-quenched emission is red shifted with increasing dye loading, this

phenomenon is reversed for Basic Yellow 40 uptake >4 mmol/g pointing to distortions of the host structure by the chromophore.

Molecular sieve encaged dye molecules are aspirants for photochemical applications in the fields of information processing and storage as well as for novel pigments. As shown on the left-hand side of Fig. 46, e.g., thioindigo wrapped up by the framework of zeolite NaX resides in the center of the 12R aperture connecting two adjacent supercages, as revealed by Rietveld refinement of XRD patterns [182]. The DRS of NaX-incarcerated thioindigo is characterized by the strong $S_0 \rightarrow S_1$ transition near 530–560 nm (see Fig. 46, spectrum B) with a bandwidth somewhat broader than in solution (Fig. 46, spectrum A), while adsorption at the external surface gives rise to further broadening together with a bathochromic shift to 550 nm (Fig. 46, spectrum C) indicating stronger interac-

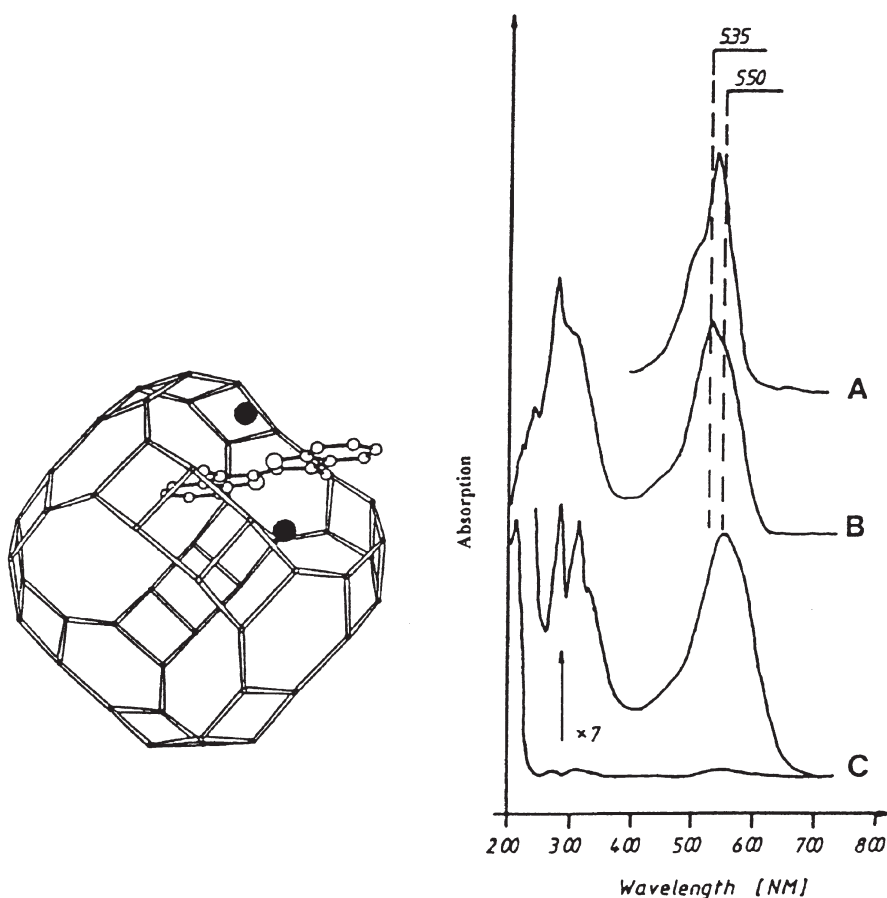


Fig. 46. *Left* Arrangement of *trans*-thioindigo between two supercages in zeolite NaX. The *dots* mark the positions of the Na^+ ions on SII* sites. *Right* UV-VIS spectra of thioindigo in toluene solution (A), encaged in zeolite NaX (B) and adsorbed at the external surface (C). Reprinted with permission from [182]. Copyright 1994 American Chemical Society

tion. The photoinduced *trans*-to-*cis* isomerization and the opposite thermal isomerization have been monitored by UV-VIS spectroscopy. The former is assumed to start from the triplet state of the excited *trans* conformer and occurs only provided the dye is not closely coordinated to the Na^+ ions. Otherwise it is prevented by strong interaction or by rapid quenching of the excited state. *cis*-to-*trans* Isomerization, on the other hand, is retarded due to an enhanced energy barrier for twisting.

In order to reduce the costs of photovoltaic devices for the conversion of light to electricity a high-efficiency solar cell has been developed based on the photosensitized electron injection into the empty states of nanosized semiconductors using charge-transfer dyes as sensitizers [183]. Dye-sensitized cells consist of electrodes based on an optically transparent film of titanium dioxide nanoparticles coated with a monolayer of the respective dye. This assembly can be mimicked in zeolites and related materials capable of hosting both semiconducting clusters and charge-transfer dyes. Wark et al. [184] started their investigations applying the mesoporous material MCM-41 as the host introducing Ti either by hydrothermal synthesis or by impregnation. Dispersion and coordination of the Ti could be inferred from the maxima and the onsets of absorption in the DR-UV/VIS spectra, as has been shown in the preceding section. By hydrothermal synthesis most of the titanium is tetrahedrally incorporated into the framework but restricted to about 2 wt.%. Higher loadings, up to 8 wt.%, predominantly in octahedral coordination are achieved by impregnation, where TiO_x is bound to two silanol groups at the same time. As the sensitizing dye zinc phthalocyanine and some of its derivatives are encapsulated either admixed with the surfactant during MCM synthesis or by impregnation. In the DR spectra the monomer M_{0-0} and M_{0-1} signals of the Q band are observed representing the transitions from the HOMO to the LUMO and its first overtone, pointing to the lack of aggregated ZnPc. Higher Ti loading and a closer contact between the Ti center and the dye enable the charge transfer from the latter to the former proved by the quenching of the fluorescence.

4.3

Concluding Remarks

Spectroscopic methods in general play an expanding role in characterization of host/guest systems like, e.g., zeolite systems. They provide valuable microscopic information on symmetry, structure and bonding in such associations, on the location and motion of the guest, on the nature of active sites for catalytic transformations, on the thus-formed intermediates and products, as well as on the detection of poisons.

UV/VIS spectroscopy in particular is suited for the determination of the local symmetry and the oxidation state of a TMI, but is not restricted to TMIs, and gives information on the perturbation of the excited and ground electronic states by host/guest interaction. There is a wide range of pressure and temperature in which the experiments can be carried out without interference from the gas or bulk solid phases, so that in situ as well as ex situ experiments are feasible.

UV/VIS spectroscopy has meanwhile become an established technique based upon safe theoretical foundations. The experimental techniques are straight-

forward, the instrumental requirements modest. The spectra of even strongly scattering samples can be readily interpreted and related to the properties of these systems.

UV/VIS spectroscopy has proved to be a powerful tool for the detection of stable as well as reactive guests monitoring their change of concentration with time of contact and temperature. By these means formation and further conversion of intermediates can be pursued. However, from UV/VIS spectroscopy alone detailed information on the species involved cannot be obtained. The combined application of UV/VIS and other spectroscopic techniques (IR/Raman, NMR, ESR) together with computer modeling and classical as well as quantum chemical calculations raises hopes on yielding a deeper insight into the microscopic world of host/guest systems.

5

References

1. Herzberg G (1966) *Molecular spectra and molecular structure. III. Electronic spectra and electronic structure of polyatomic molecules*. Van Nostrand Reinhold Company, New York
2. Jaffé HH, Orchin M (1970) *Theory and applications of ultraviolet spectroscopy*. Wiley, New York
3. Rao CNR (1975) *Ultra-violet and visible spectroscopy, chemical applications*. Butterworths, London
4. Lever ABP (1984) *Inorganic electronic spectroscopy*, 2nd edn. 2nd impression with corrections 1986. Elsevier, Amsterdam
5. Suzuki H (1967) *Electronic absorption spectra and geometry of organic molecules*. Academic Press, Inc., New York
6. Hollas JM (1987) *Modern spectroscopy*. Wiley, Chichester
7. Perkampus HH (1992) *UV-VIS spectroscopy and its applications*. Springer, Berlin Heidelberg New York
8. Schläfer HL, Gliemann G (1967) *Einführung in die Ligandenfeldtheorie*. Akademische Verlagsgesellschaft, Frankfurt am Main
9. Cotton FA (1971) *Chemical applications of group theory*. Wiley-Interscience, New York
10. Kober F (1979) *Grundlagen der Komplexchemie*. Salle+Sauerländer, Frankfurt am Main
11. Uhlemann E (1977) *Einführung in die Koordinationschemie*. VEB Deutscher Verlag der Wissenschaften, Berlin
12. Schuster P (1973) *Ligandenfeldtheorie*. Verlag Chemie, Weinheim
13. Kittel C (1973) *Einführung in die Festkörperphysik*. R. Oldenbourg, München
14. Leftin HP, Hobson MC Jr (1963) *Adv Catal* 14:115
15. Terenin A (1964) *Adv Catal* 15:227
16. Kiselev AV, Lygin VI (1975) *Infrared spectra of surface compounds*. Keter Publishing House Ltd., Jerusalem
17. Chilton D, Rabinowitsch E (1932) *Z Physik Chem* B19:107
18. de Boer JH (1932) *Z Physik Chem* B18:49
19. de Boer JH, Custers JFH (1933) *Z Physik Chem* B21:208
20. Williams R (1989) *Appl Spectrosc Rev* 25:63
21. Threlfall TL (1988) *Eur Spectros News* 78:8 and references cited therein
22. Knowles A, Burgess C (eds) (1984) *Practical absorption spectrometry*. Chapman and Hall, London
23. Dixit L, Ram S (1985) *Appl Spectrosc Rev* 21: 311
24. Talsky G (1994) *Derivative spectrophotometry low and high order*. VCH Verlagsgesellschaft GmbH, Weinheim

25. Shibata S (1976) *Angew Chem* 88:750
26. Kortüm G (1969) *Reflexionsspektroskopie*. Springer, Berlin Göttingen Heidelberg New York
27. Sendoda Y, Ono Y, Keii T (1975) *J Catal* 39:357
28. Förster H, Schumann M, Seelemann R (1980) *Stud Surf Sci Catal* 5:211
29. Karge HG, Łaniecki M, Ziołek M, Onyestyák G, Kiss A, Kleinschmit P, Siray M (1989) *Stud Surf Sci Catal* 49:1327
30. Förster H, Franke S, Seebode J (1983) *J Chem Soc Faraday Trans 1* 79:373
31. Klier K (1967) *Catal Rev* 1: 207
32. Kellerman R (1979) Diffuse reflectance and photoacoustic spectroscopies. In: Delgass WN, Haller GL, Kellerman R, Lunsford JH (eds) *Spectroscopy in heterogeneous catalysis*. Academic Press, New York, p 86
33. Klier K (1980) Investigations of adsorption centers, molecules, surface complexes, and interactions among catalyst components by diffuse reflectance spectroscopy. In: Bell AT, Hair ML (eds) *Vibrational spectroscopies for adsorbed species*. ACS Symp Ser 137:141. American Chemical Society, Washington
34. Schoonheydt RA (1984) Diffuse reflectance spectroscopy. In: Delannay F (ed) *Characterization of heterogeneous catalysts*. Marcel Dekker, Inc., New York, p 125
35. Hurtubise RJ (1981) *Solid surface luminescence analysis: theory, instrumentation, applications*. Marcel Dekker, New York
36. Vo-Dinh T (1984) *Room temperature phosphorimetry for chemical analysis*. Wiley, New York
37. Svanberg S (1992) *Atomic and molecular spectroscopy – basic aspects and practical applications*. Springer, Berlin Heidelberg New York London Paris Tokyo Hong Kong Barcelona Budapest, p 329
38. Demas JN (1983) *Excited state lifetime measurements*. Academic, New York
39. Pott GT, Stork WHJ (1976) *Catal Rev Sci Eng* 12:163
40. Tanguay JF, Suib SL (1987) *Catal Rev Sci Eng* 29:1
41. Engel S, Kynast U, Unger KK, Schüth F (1994) *Stud Surf Sci Catal* 84:477
42. Patarin J, Tulier MH, Durr J, Kessler H (1985) *Zeolites* 12:70
43. Leheny AR, Turro NJ, Drake JM (1992) *J Chem Phys* 97:3736
44. Beer R, Calzaferri G, Kamber I (1991) *J Chem Soc Chem Commun* 1489
45. Calzaferri G, Kunzmann A, Lainé P, Pfanner K (1995) *IS&T's 48th Ann Conf Proc*, Washington DC 1995, p 318
46. Bedard RL, Bowes CL, Coombs N, Holmes AJ, Jiang T, Kirkby SJ, Macdonald PM, Malek AM, Ozin GA, Petrov S, Plavac N, Ramik RA, Steele MR, Young D (1993) *J Am Chem Soc* 115:2300
47. Ozin GA, Kuperman A, Stein A (1989) *Angew Chem* 101:373
48. Ozin GA, Gil C (1989) *Chem Rev* 89:1749
49. Mortier WJ (1982) *Compilation of extra framework sites in zeolites*. Butterworth, Guildford
50. Catlow CRA (ed) (1992) *Modelling of structure and reactivity in zeolites*. Academic Press, London
51. Mikheikin ID, Zhidomirov GM, Kazansky VB (1972) *Russ Chem Rev* 41:468
52. Kellerman R, Klier K (1975) *Surface and Defect Properties of Solids* 4:1
53. Seff K (1976) *Acc Chem Res* 9:121
54. Lunsford JH (1976) *Catal Rev* 12:137
55. Lunsford JH (1977) *ACS Symp Ser* 40:473
56. Klier K, Hutta PJ, Kellerman R (1977) *ACS Symp Ser* 40:108
57. Atanasova VD, Shvets VA, Kazansky VB (1981) *Russ Chem Rev* 50:209
58. Schoonheydt RA (1993) *Catal Rev Sci Eng* 35:129
59. Sutton LE (1960) *J Chem Educ* 37:498
60. Carlin RL (1963) *J Chem Educ* 40:135
61. Verberckmoes AA, Weckhuysen BM, Schoonheydt RA (1997) *Stud Surf Sci Catal* 105:623

62. Uytterhoeven MG, Schoonheydt RA (1993) Probing the synthesis of CoAPO-n molecular sieves by analysis of wet precursor gels. In: von Ballmoos R, Higgins JB, Treacy MMJ (eds) Proceedings from the Ninth International Zeolite Conference. Butterworth-Heinemann, Boston London Oxford Singapore Sydney Toronto Wellington, vol I, p 329
63. Han H-S, Chon H (1994) Stud Surf Sci Catal 84:797
64. Peeters MPJ, van Hooff JHC, Sheldon RA, Zholobenko VL, Kustov LM, Kazansky VB (1993) Spectroscopic investigations of the redox properties of CoAPO molecular sieves. In: von Ballmoos R, Higgins JB, Treacy MMJ (eds) Proceedings from the Ninth International Zeolite Conference. Butterworth-Heinemann, Boston London Oxford Singapore Sydney Toronto Wellington, vol I, p 651
65. Gianotti E, Marchese L, Martra G, Coluccia S (1999) Reactivity of NO on Co²⁺/Co³⁺ redox sites in CoAPO-18. FTIR and UV-Vis-NIR studies. In: Treacy MMJ, Marcus BK, Bisher ME, Higgins JB (eds) Proceedings of the Twelfth International Zeolite Conference. Materials Research Society, Warrendale, vol IV, p 2775
66. Echchahed B, Trong On D, Beland F, Bonneviot L (1999) Incorporation level and nature of framework metal sites versus crystallization time and temperature in TS-1 and FES-1. In: Treacy MMJ, Marcus BK, Bisher ME, Higgins JB (eds) Proceedings of the Twelfth International Zeolite Conference. Materials Research Society, Warrendale, vol III, p 1877
67. Reddy JS, Sayari A (1995) Stud Surf Sci Catal 94:309
68. Guo X, Wang X, Wang G, Li G (1997) Stud Surf Sci Catal 105:607
69. Hari Prasad Rao PR, Ueyama K, Kikuchi E, Matsukata M (1999) Synthesis of pure silica beta and Al-free Ti-beta using TEOH and their characterization. In: Treacy MMJ, Marcus BK, Bisher ME, Higgins JB (eds) Proceedings of the Twelfth International Zeolite Conference. Materials Research Society, Warrendale, vol III, p 1515
70. Corma A, Navarro MT, Pérez-Pariente J, Sánchez F (1994) Stud Surf Sci Catal 84:69
71. Franke O, Rathousk? J, Schulz-Ekloff G, Stárek J, Zúkal A (1994) Stud Surf Sci Catal 84:77
72. Corma A, Jorda JL, Navarro MT, Pérez-Pariente J, Rey F (1999) Synthesis, characterization and catalytic activity of Ti-MCM-41 materials obtained under highly acidic media. In: Treacy MMJ, Marcus BK, Bisher ME, Higgins JB (eds) Proceedings of the Twelfth International Zeolite Conference. Materials Research Society, Warrendale, vol II, p 817
73. Kumar R, Raj A, Kumar SB, Ratnasamy P (1994) Stud Surf Sci Catal 84:109
74. Bhaumik A, Kumar R, Ratnasamy P (1994) Stud Surf Sci Catal 84:1883
75. Kornatowski J, Wichterlova B, Rozwadowski M, Baur WH (1994) Stud Surf Sci Catal 84: 117
76. Concepción P, López Nieto JM, Pérez-Pariente J (1995) Stud Surf Sci Catal 94:681
77. Patarin J, Tuilier MH, Durr J, Kessler H (1992) Zeolites 12:70
78. Weckhuysen BM, Schoonheydt RA (1994) Stud Surf Sci Catal 84:965
79. De Vos DE, Knops-Gerrits P, Parton RF, Weckhuysen BM, Jacobs PA, Schoonheydt RA (1995) Coordination chemistry in zeolites. In: Herron N, Corbin DR (eds) Inclusion chemistry with zeolites: nanoscale materials by design. Kluwer, Dordrecht, p 185
80. Packet D, Dehertogh W, Schoonheydt RA (1985) Stud Surf Sci Catal 24: 351
81. Kubelkova L, Jirka I, Vylita J, Novakova J (1994) Stud Surf Sci Catal 84:1051
82. Schnick W (1994) Stud Surf Sci Catal 84:2221
83. Klier K, Herman RG, Hou S (1994) Stud Surf Sci Catal 84:1507
84. Klier K (1971) Adv Chem Ser 101:480
85. Förster H, Thun K, Witten U (1983) Investigations on sorption and oxidation of carbon monoxide in transition metal ion-exchanged zeolites A. Proceedings of the Fifth International Symposium on Heterogeneous Catalysis, part 2, p 33
86. Förster H, Witten U (1987) Zeolites 7:517
87. Förster H, Schumann M, Seelemann R (1980) Stud Surf Sci Catal 5:211
88. Förster H, Seebode J (1983) Zeolites 3:63
89. Strome DH, Klier K (1980) ACS Symp Ser 135:155
90. Ebitani K, Morokuma M, Morikawa A (1994) Stud Surf Sci Catal 84:1501
91. Wichterlová B, Dedecek J, Sobalik Z (1995) Stud Surf Sci Catal 94:641

92. Borgmann C, Sauer J, Jüstel T, Kynast U, Schüth F (1999) The development of new luminescent materials from zeolite X. In: Treacy MMJ, Marcus BK, Bisher ME, Higgins JB (eds) Proceedings of the Twelfth International Zeolite Conference. Materials Research Society, Warrendale, vol III, p 2241
93. Naccache C, Chen FR, Coudurier G (1989) *Stud Surf Sci Catal* 49:661
94. Ramamurthy V, Eaton DF (1993) Dependence of the charge density and electric field within the cages of X and Y zeolites on the cation: photophysical probes. In: von Ballmoos R, Higgins JB, Treacy MMJ (eds) Proceedings from the Ninth International Zeolite Conference. Butterworth-Heinemann, Boston London Oxford Singapore Sydney Toronto Wellington, vol I, p 587
95. Ramamurthy V, Turro NJ (1995) Photochemistry of organic molecules within zeolites: role of cations. In: Herron N, Corbin DR (eds) Inclusion chemistry with zeolites: nanoscale materials by design. Kluwer, Dordrecht, p 239
96. Yoon KB, Kochi JK (1991) *J Phys Chem* 95:1348
97. Choi SY, Park YS, Yoon KB (1997) *Stud Surf Sci Catal* 105:671
98. Melsheimer J, Böhm MC, Lee JK, Schlögl R (1997) *Ber Bunsenges Phys Chem* 101:726
99. Melsheimer J, Schlögl R (1997) *Ber Bunsenges Phys Chem* 101:733
100. Karge HG, Łaniecki M, Ziołek M (1988) *J Catal* 109:252
101. Karge HG, Łaniecki M, Ziołek M (1986) Combined UV and IR spectroscopic studies on the adsorption of SO₂ onto faujasite-type zeolites. In: Iijima A, Ward JW (eds) New developments in zeolite science technology. Kondansha, Tokyo, p 617
102. Karge HG, Ziołek M, Łaniecki M (1987) *Zeolites* 7:197
103. Abramov VN, Kiselev AV, Lygin VI (1963) *Russ J Phys Chem* 37:1507
104. Kupcha LA, Lygin VI, Mineeva LV (1968) *Kinet Catal* 9:691
105. Kiselev AV, Kupcha LA, Lygin VI, Shatskii VG (1969) *Kinet Catal* 10:370
106. Lygin VI (1971) *Adv Chem Ser* 102:86
107. Eremenko AM, Ogenko VM, Chuiko AA (1995) *Stud Surf Sci Catal* 94:607
108. Ignatovich M, Ogenko V, Chuiko A (1995) *Stud Surf Sci Catal* 94:615
109. Yoon KB (1993) *Chem Rev* 93:321
110. Olah G, Pittman CU Jr, Symons MCR (1968) Electronic spectra. In: Olah G, Schleyer P (eds) Carbonium ions, vol I. Wiley-Interscience, New York, p 202
111. Karge HG (1973) *Surf Sci* 40:157
112. Garbowski ED, Praliud H (1979) *J Chim Phys Phys Chim Biol* 76:687
113. Fejes P, Förster H, Kiricsi I, Seebode J (1984) *Stud Surf Sci Catal* 18:91
114. Förster H, Seebode J (1985) Spectroscopic and kinetic studies on the cyclopropane isomerization over mordenites of different acidity. Proceedings of the International Symposium on Zeolite Catalysis, Siofok. *Acta Phys et Chem Szegediensis*. p 413
115. Förster H, Seebode J, Fejes P, Kiricsi I (1987) *J Chem Soc Faraday Trans 1* 83:1109
116. Förster H, Kiricsi I, Seebode J (1987) *Stud Surf Sci Catal* 37:435.
117. Kiricsi I, Tasi Gy, Förster H, Fejes P (1990) *J Mol Struct* 218:369
118. Förster H, Kiricsi I (1987) *Zeolites* 7:508
119. Förster H, Kiricsi I (1988) *Catalysis Today* 3:65
120. Kiricsi I, Förster H (1988) *J Chem Soc Faraday Trans 1* 84:491
121. Kiricsi I, Tasi Gy, Fejes P, Förster H (1990) *J Mol Catal* 62:215
122. Kiricsi I, Förster H, Tasi Gy, Fejes P (1991) *Stud Surf Sci Catal* 65:697
123. Kiricsi I, Förster H, Tasi Gy, Fejes P (1989) *J Catal* 115:597
124. Kiricsi I, Tasi Gy, Förster H, Fejes P (1993) *J Chem Soc Faraday Trans* 89:4221
125. Kiricsi I, Förster H, Tasi Gy (1988) *Stud Surf Sci Catal* 46:355
126. Kiricsi I, Tasi Gy, Molnar A, Förster H (1990) *J Mol Struct* 239:185
127. Förster H, Kiricsi I, Tasi Gy, Hannus I (1993) *J Mol Struct* 296:61
128. Kiricsi I, Förster H, Tasi Gy (1991) *J Mol Catal* 65:L29
129. Vedrine JC, Dejaive P, Garbowski ED, Derouane EG (1980) *Stud Surf Sci Catal* 5:29
130. Melsheimer J, Ziegler D (1992) *J Chem Soc Faraday Trans* 88:2101
131. Karge HG, Darmstadt H, Gutsze A, Vieth H-M, Buntkowsky G (1994) *Stud Surf Sci Catal* 84:1465

132. Kiricsi I, Förster H, Tasi Gy, Nagy JB (1999) *Chem Rev* 99:2085
133. Hannus I, Förster H, Tasi Gy, Kiricsi I, Molnar A (1995) *J Mol Struct* 348:345
134. Thomas JK (1993) *Chem Rev* 93:301
135. Enzel P, Bein T (1992) Synthesis of oligo- and polythiophenes in zeolite hosts. In: von Ballmoos R, Higgins JB, Treacy MM (eds) *Proceedings of the 9th International Zeolite Conference*. Butterworth-Heinemann, Boston London Oxford Singapore Sydney Toronto Wellington, vol II, p 177
136. Bein T (1992) *ACS Symp Ser* 499:274
137. Cox SD, Stucky GD (1991) *J Phys Chem* 95:710
138. Stein A, Ozin GA (1993) Sodalite supralattices: from molecules to clusters to expanded insulators, semiconductors and metals. In: von Ballmoos R, Higgins JB, Treacy MMJ (eds) *Proceedings from the Ninth International Zeolite Conference*. Butterworth-Heinemann, Boston London Oxford Singapore Sydney Toronto Wellington, vol I, p 93
139. Herron N (1995) Zeolites as hosts for novel optical and electronic materials. In: Herron N, Corbin DR (eds) *Inclusion chemistry with zeolites: nanoscale materials by design*. Kluwer, Dordrecht, p 283
140. Sun T, Seff K (1994) *Chem Rev* 94:857
141. Beer R, Calzaferri G, Li J, Waldeck B. (1991) *Coord Chem Rev* 111:193
142. Bogdanchikova NE, Dulin MN, Toktarev AV, Shevnina GB, Kolomiichuk VN, Zaikovskii VI, Petranovskii VP (1994) *Stud Surf Sci Catal* 84:1067
143. Linnert T, Mulvaney P, Henglein A, Weller H (1990) *J Am Chem Soc* 112:4657
144. Cvjeticanin ND, Petranovic NA (1994) *Zeolites* 14:35
145. Stucky GD, Srdanov VI, Harrison WTA, Gier TE, Keder NL, Moran KL, Haug K, Metiu HI (1992) *ACS Symp Ser* 499:294
146. Srdanov VI, Blake NP, Markgraber D, Metiu H, Stucky GD (1994) *Stud Surf Sci Catal* 85:115
147. Blake NP, Stucky GD (1995) Alkali-metal clusters as prototypes for electron solvation in zeolites. In: Herron N, Corbin DR (eds) *Inclusion chemistry with zeolites: nanoscale materials by design*. Kluwer, Dordrecht, p 299
148. Edwards PP, Anderson PA, Thomas JM (1996) *Acc Chem Res* 29:23
149. Kasai PH (1965) *J Chem Phys* 43:3322
150. Liu X, Iu K-K, Thomas JK (1994) *Chem Phys. Lett* 224:31
151. Liu X, Iu K-K, Thomas JK (1994) *J Phys Chem* 98:13720
152. Liu X, Thomas JK (1992) *Langmuir* 8:1750
153. Iu K, Liu X, Thomas JK (1993) *J Phys Chem* 97:8165
154. Westphal U, Geismar G (1984) *Z Anorg Allg Chem* 508:165
155. Breuer REH, de Boer E, Geismar G (1989) *Zeolites* 9:336
156. Kodaira T, Nozue Y, Ohwashi S, Goto T, Terasaki O (1993) *Phys Rev B* 48:12245
157. Park YS, Lee YS, Yoon KB (1993) *J Am Chem Soc* 115:12220
158. Park YS, Lee YS, Yoon KB (1994) *Stud Surf Sci Catal* 84:901
159. Srdanov VI, Haug K, Metiu H, Stucky GD (1992) *J Phys Chem* 96:9039
160. Goto T, Nozue Y, Kodaira T (1993) *Mat Sci Eng B* 19:48
161. Brock M, Edwards C, Förster H, Schröder M (1994) *Stud Surf Sci Catal* 84:1515
162. Schröder M (1996) PhD thesis, University of Hamburg
163. Wang Y, Herron N (1988) *J Phys Chem* 92:4988
164. Herron N, Wang Y, Eddy MM, Stucky GD, Cox DE, Möller K, Bein T (1989) *J Am Chem Soc* 111:530
165. Klaas J, Kulawik K, Schulz-Ekloff G, Jaeger NI (1994) *Stud Surf Sci Catal* 84:2261
166. Grubert G, Wark M, Grünert W, Koch M, Schulz-Ekloff G (1997) *Stud Surf Sci Catal* 105:1077
167. Grubert G, Grünert W, Rathousky J, Zukal A, Schulz-Ekloff G, Wark M (1999) Structure and redox properties of vanadium species in MCM-41. In: Treacy MMJ, Marcus BK, Bisher ME, Higgins JB (eds) *Proceedings of the Twelfth International Zeolite Conference*. Materials Research Society, Warrendale, vol II, p 825

168. Warnken M, Grubert G, Jaeger NI, Wark M (1999) Titanium and tin oxide-loaded zeolites as optical sensor materials for reductive atmospheres. In: Treacy MMJ, Marcus BK, Bisher ME, Higgins JB (eds) Proceedings of the Twelfth International Zeolite Conference. Materials Research Society, Warrendale, vol III, p 2249
169. Balkus KJ Jr, Gabrielov AG (1995) Zeolite encapsulated metal complexes. In: Herron N, Corbin DR (eds) Inclusion chemistry with zeolites: nanoscale materials by design. Kluwer, Dordrecht, p 159
170. Kawi S, Gates BC (1994) Clusters in cages. In: Schmid G (ed) Clusters and colloids from theory to applications. VCH, Weinheim, p 299
171. Ichikawa M (1992) Adv Catal 38:283
172. De Mallmann A, Barthomeuf D (1990) Catal Lett 5:293
173. Chini P (1980) J Organomet Chem 200:37
174. Schulz-Ekloff G, Lipski RJ, Jaeger NI, Hülstede P, Kubelkova L (1995) Catal Lett 30:65
175. Parton R, den Vos D, Jacobs PA (1992) Enzyme mimicking with zeolites. In: Derouane et al. (eds) Zeolites; zeolite microporous solids: synthesis, structure, and reactivity. Kluwer, Dordrecht, p 555
176. Herron N (1988) J Coord Chem 19:25
177. Balkus KJ Jr, Kowalak S, Ly KT, Hargis DC (1991) Stud Surf Sci Catal 69:93
178. Balkus KJ Jr, Hargis CD, Kowalak S (1992) ACS Symp Ser 499:347
179. Ernst S, Sauerbeck S, Yang X (1999) Preparation and catalytic properties of zeolite-encapsulated palladium-salen-complexes in the hydrogenation of selected unsaturated compounds. In: Treacy MMJ, Marcus BK, Bisher ME, Higgins JB (eds) Proceedings of the Twelfth International Zeolite Conference. Materials Research Society, Warrendale, vol III, p 2155
180. Sutra P, Bellocq N, Brunel D, Di Renzo F, Fajula F, Galarneau A, Lasperas M, Moreau P (1999) Design of well-defined catalysts supported on micelle-templated silicas. In: Treacy MMJ, Marcus BK, Bisher ME, Higgins JB (eds) Proceedings of the Twelfth International Zeolite Conference. Materials Research Society, Warrendale, vol I, p 675
181. Braun I, Schomburg C, Bockstette M, Schulz-Ekloff G, Wöhrle D (1999) Novel pigments via microwave-assisted crystallization inclusion of chromophores in $AlPO_4-5$ or ship-in-the-bottle synthesis of dyes in HY. In: Treacy MMJ, Marcus BK, Bisher ME, Higgins JB (eds) Proceedings of the Twelfth International Zeolite Conference. Materials Research Society, Warrendale, vol III, p 2233
182. Hoppe R, Schulz-Ekloff G, Wöhrle D, Kirschhock C, Fuess H (1994) Langmuir 10:1517
183. Hagfeldt A, Grätzel M (1995) Chem Rev 95:49
184. Wark M, Ortlam A, Ganschow M, Schulz-Ekloff G, Wöhrle D (1998) Ber Bunsenges Phys Chem 102:1548

XANES, EXAFS and Related Techniques

Peter Behrens

Institut für Anorganische Chemie, Universität Hannover, Callinstrasse 9, 30167 Hannover,
Germany

E-mail: Peter.Behrens@mbox.acb.uni-hannover.de

1	Introduction	429
2	Interaction of X-rays with Matter	432
3	Theory of X-ray Absorption Fine Structures	434
3.1	Theory of Extended X-ray Absorption Fine Structure (EXAFS)	434
3.2	Theory of X-ray Absorption Near Edge Structure (XANES)	439
3.2.1	XANES: Transitions into Unoccupied Electronic States	439
3.2.2	XANES: Multiple Scattering	440
4	Experimental and Data Analysis	441
4.1	Experimental	441
4.2	Data Analysis	443
5	Information from X-ray Absorption Fine Structure	447
5.1	Information from Extended X-ray Absorption Fine Structure (EXAFS)	447
5.1.1	MnK EXAFS Investigation of Manganese-Exchanged A and Y Zeolites	447
5.1.2	Local Environment of Cobalt in Cobalt Aluminophosphates	449
5.1.3	Mercury Iodide as a Guest Species in Porosils	450
5.1.4	Metal Sulfide Clusters in Zeolites	452
5.2	Information from XANES	453
5.2.1	Oxidation States of Non-framework Species	454
5.2.2	Coordination Geometries from Pre-edge Features	456
5.2.3	Structural Information from Multiple Scattering	457
6	Special Techniques and Applications	459
6.1	In Situ Applications and Time Resolution	459
6.2	Electron Energy Loss Spectroscopy	461
6.3	Resonant X-ray Diffraction	462
7	Concluding Remarks	462
8	References	464

Abbreviations

$Amp(k)$	amplitude term of the EXAFS formula
c	velocity of light
CHA	chabazite framework topology
d	thickness of the sample
DDR	framework topology of decadodecasil 3R
DEXAFS	dispersive EXAFS
ΔE_0	deviation of E_0 as obtained when an EXAFS spectrum is fitted as compared to the real value
$\Delta\mu d$	edge jump
$\Delta\sigma_j^2$	difference in σ_j^2 between reference compound and sample
E	energy
E_0	binding energy of an electron; position of an X-ray absorption edge
E_{kin}	kinetic energy of an excited electron
EELS	electron energy loss spectroscopy
EXAFS	extended X-ray absorption fine structure
$F(k)$	scattering amplitude
$F_j(k)$	scattering amplitude of the atoms in shell j
$ \bar{F}_j(k) $	absolute value of the scattering amplitude of the atoms in shell j
$ F(k) $	absolute value of the modified backscattering amplitude function
FAU	faujasite framework topology
FEFF	program for the calculation of scattering amplitude and phase-shift functions
FT	Fourier transform
h	Planck's constant
k	wavevector
I	intensity of the X-ray beam after passage through the sample
I_0	intensity of the original X-ray beam
λ	wavelength
$\lambda(k)$	mean free path of the excited photoelectron
l	quantum number
μ	linear absorption coefficient for X-rays
m_e	electron mass
MFI	framework topology of ZSM-5 (silicalite)
MS	multiple scattering
N	number of backscattering atoms
N_j	number of backscattering atoms in neighbor shell j
NEXAFS	near edge X-ray absorption fine structure
$\Phi_{ij}(k)$	total phase-shift function
$\Phi_i(k)$	individual phase-shift function of the absorbing atom i
$\Phi_j(k)$	individual phase-shift function of the scattering atom j
PXRD	powder X-ray diffraction
QEXAFS	quick-scanning EXAFS
R	interatomic distance
\tilde{R}	uncorrected interatomic distance as obtained from Fourier transforms

R_j	distance between shell j and the absorbing atom
σ_j^2	mean square displacement of the atoms of a pair of absorbing and backscattering atoms
S_0^2	amplitude reduction factor
SEXAFS	surface EXAFS
SOD	sodalite framework topology
T atoms	tetrahedrally coordinated framework atoms
UV-Vis	ultraviolet and visible
UWXAFS	a program for the evaluation of XAFS data
WinXAS	a program for the evaluation of XAFS data
$\chi(E)$	EXAFS as a function of the energy
$\chi(k)$	EXAFS as a function of the wavevector
$\chi_j(k)$	single-shell EXAFS as a function of the wavevector
XAFS	X-ray absorption fine structure
XANES	X-ray absorption near edge structures
XAS	X-ray absorption spectroscopy
XEOL	X-ray excited optical luminescence
X-FIT	a program for the evaluation of XAFS data
Z	atomic number

1

Introduction

The absorption of X-rays by matter as a function of their energy is characterized by a smoothly varying background absorption and by characteristic jumps of the absorption coefficient which are called absorption edges. The occurrence of these edges is caused by the ionization of electrons from atoms. These electrons stem from core-like electronic states, e.g., from the K shell or the L shell. Accordingly, these edges are designated as K or L_3, L_2 and L_1 , depending on the electronic level from where the ionization occurred. As the ionization energy depends on the nuclear charge of the atom hit by the incident X-rays, the energy positions E_0 of these edges are characteristic of each element.

Soon after the discovery of X-ray absorption edges and after their interpretation as being due to ionization from low-lying electronic states, the improving resolution of X-ray spectrometers showed that these edges exhibit fine structures. An interpretation correlating these features to the geometric and electronic structure of the sample under investigation was, however, possible only when synchrotron radiation became available at the beginning of the 1970s. Synchrotron radiation offers X-rays of very high intensity with a broad spectral distribution, ideally suited for X-ray absorption spectroscopy (XAS). In contrast, X-ray tubes only offer quasi-monochromatic characteristic X-ray wavelengths (e.g. $K\alpha$ or $K\beta$) of medium intensity and a polychromatic background ("bremsstrahlung") of weak intensity. With modern spectrometers at synchrotron facilities, high-resolution X-ray absorption spectra can be routinely measured. As an example, Fig. 1 shows the TiK edge spectrum of the titanosilicate mineral aenigmatite.

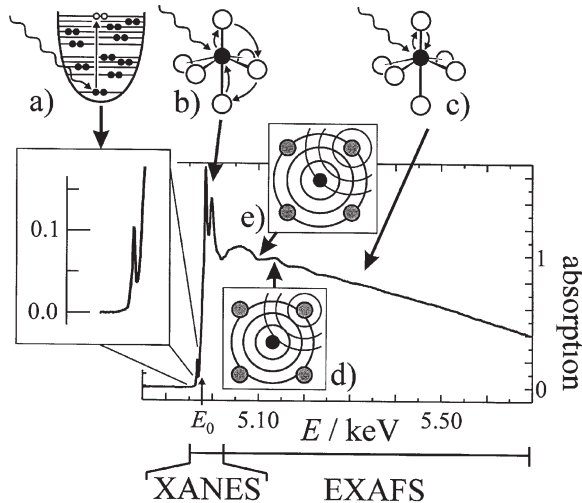


Fig. 1. TiK edge X-ray absorption spectrum of the (dense) titanosilicate mineral aenigmatite showing the partition into XANES and EXAFS regions. The physical processes leading to the different features in the spectrum are depicted schematically: *a* pre-edge absorption features (magnified in the inset), *b* multiple scattering features, *c* single scattering features which lead to minima and maxima in the spectrum in the cases of *d* constructive interference and *e* destructive interference

The X-ray absorption fine structure (XAFS) of a spectrum like the one depicted in Fig. 1 is divided into two components which differ in their physical origin. The X-ray absorption near-edge structure (XANES) comprises the regime from -10 eV below to about $+50$ eV above the edge energy E_0 . This regime is characterized by rather sharp variations of the absorption. It is subdivided further into the pre-edge region and the region directly above the edge. In the part from ca. $+50$ eV to ca. $+1000$ eV above E_0 , weak oscillations in the absorption occur. These are designated as extended X-ray absorption fine structure (EXAFS).

The features of the XANES region above the edge and those in the EXAFS regime are caused by the scattering of the electron, which has been ionized from the absorbing atom, by the surrounding atoms. In the XANES, multiple scattering (MS) of the electron can occur (Fig. 1b), and the theoretical description of this region is thus rather complex. Most of the features of the EXAFS region, however, can be explained quantitatively by single scattering of the excited electron (Fig. 1c). EXAFS thus allows the determination of interatomic distances and coordination numbers for several coordination shells around the absorbing atom. This is possible up to a distance of about 5 \AA , although the analysis of higher coordination shells is less reliable. EXAFS is, therefore, a method for the determination of local structures. It is element-selective and does not require the presence of long-range order, as diffraction methods do. As structural data from EXAFS analysis are usually less precise than those obtained from diffraction methods, the strength of this spectroscopic method appears whenever diffraction

methods are disturbed. Many EXAFS studies deal, for example, with liquids or glasses.

Features appearing in the pre-edge region can be traced back to electronic transitions from core levels into unoccupied electronic states located at the absorbing atom (Fig. 1a). Naturally, these features contain information about the electronic state of the absorbing atom. The simplest of these is the oxidation number, which also shows a relation to the edge position E_0 . Both the pre-edge peaks and the edge itself shift to higher energies as the oxidation number increases. The shape of the pre-edge features and their intensity contain further information on more detailed properties of the electronic and also on the geometric structure, for example, on the distortion of coordination environments.

Soon after the correct physical explanation for XAFS had been given and when more experimental stations with improving technical stability had been constructed at synchrotrons, the first applications of XAFS techniques to zeolites were reported. In fact, there are several good reasons to use the information content of XAFS in the characterization of zeolite-type solids (zeotypes).

Already the fact that many zeotype compounds can only be obtained as powders and not as single crystals, which are favored for diffraction investigations, makes EXAFS an attractive method. An even more important demand for this spectroscopic technique arises from the nature of zeotypes as host-guest compounds. Several of their properties and structural features, which are closely associated with this host-guest character, hamper the useful application of diffraction methods. The mere possibility to differentiate between a host and a guest component in zeotypes shows that we are dealing with two subsystems with different types of chemical bonding and different dynamical and order/disorder behavior. A typical application of EXAFS is thus the determination of the local environment of non-framework cations or the structure of larger guest species such as metal clusters or inorganic molecules. EXAFS is not routinely applied to organic molecules in zeolites containing only light atoms (C, H, O, N).

Another important application of EXAFS deals with disorder in the host framework. Tetrahedrally coordinated framework atoms (T atoms) such as Al, Si and P or less usual ones, such as Zn, Ga and Ge, are often disordered over the crystallographic sites of the framework, making it very difficult for diffraction methods to determine correct T–O bond lengths or even the type of coordination. EXAFS probes only the local environment of the atoms of a selected element; its analysis yields the interatomic distances and coordination numbers around these atoms. It cannot provide a full picture of the geometrical structure around the absorbing atom, as EXAFS is dominated by single-scattering events in which only two atoms are involved (the absorbing atom and the one scattering the electron), i.e., it can only probe pair correlations (i.e., interatomic distances), but not higher ones, for example, three-body correlations (i.e., interatomic angles). The XANES region above the edge, however, is determined by multiple scattering events of the excited electron and thus contains information on higher correlations. In principle, it is thus possible to extract, for example, bond angles from XANES spectra, but the quantitative analysis is much more difficult than for the single-scattering regime of the EXAFS. Therefore, qualitative

comparisons between reference compounds with known coordination geometry and the samples under investigation are often used.

As described above, the pre-edge region and the edge position E_0 contain interesting information on the local electronic structure at the absorbing atom. As the host lattice of most microporous compounds is electronically quite "inert", this type of information is most interesting for non-framework species.

This review aims to provide chemists working on porous materials with a basic understanding of XAS and related methods and to show them where the techniques might be of help in their research. After a short section on the basic physics of the interaction of X-rays with matter (Sect. 2), the basic physical processes and a theoretical description of XAFS are discussed (Sect. 3) in such a way that the method can be understood. Section 4 presents some experimental details and an example of a typical data analysis procedure. The next section is devoted to an explanation of the type of information contained in X-ray absorption spectra by using examples from zeolite chemistry (Sect. 5). Newer developments, especially with regard to time-resolved and in situ studies, as well as related techniques such as electron energy loss spectroscopy (EELS) and anomalous diffraction, are described in Sect. 6.

Several books and reviews on XAFS spectroscopy have appeared [1, 2], including a comprehensive volume edited by experts in catalysis [3] and one focusing on catalysis and surfaces [4]. Review articles about XAFS treating the subject in a less strictly scientific manner have appeared [5, 6]. Information about the International XAFS Society is also available via the Internet [7].

2

Interaction of X-rays with Matter

This topic, which is only described superficially here, is treated in more detail in the literature [1, 2].

When X-rays pass through matter, they inevitably lose intensity via interactions with the material. The loss in intensity is proportional to the original intensity and to the thickness d of the material inserted into the beam path. Thus, a Lambert-Beer-type law results:

$$\mu d = \ln(I_0/I) \quad (1)$$

Here, μ is the linear absorption coefficient. In measuring X-ray absorption spectra, we determine I_0 and I as functions of the wavelength λ or the energy E of the X-rays. In XAFS, we are interested only in the variations of the absorption with energy E , not in the thickness d of the sample. We can therefore use $\mu d(E)$ directly. The wavelength λ and the energy E are related by:

$$\lambda = hc/E \quad (2)$$

where c is the velocity of light.

The absorption we determine is a consequence of different processes, because X-rays interact with matter in a number of ways. These can be categorized into excitation of the matter an X-ray beam passes and into scattering with the medium. The excitation of an atom requires the absorption of an X-ray photon. Because the energy of X-rays is relatively large, the ionization occurs in the core-like electronic levels lying low in energy (core-level photoionization). By this process, an X-ray photon is annihilated, and the process is therefore called true absorption. To induce photoionization from a certain core level, the energy of the X-ray photon has to be larger than the binding energy of an electron in that level. This leads to the occurrence of edges in X-ray absorption spectra: X-rays with an energy E smaller than the threshold energy E_0 , i.e., the binding energy, experience no true absorption (but are scattered, see below); however, for those with $E \geq E_0$, the absorption becomes very large. Depending on the level from which the ionized electron stems, one differentiates between different types of edges:

- absorption by an electron from the $1s$ level corresponds to a K edge,
- absorption by an electron from the $2s$ level corresponds to a L_1 edge,
- absorption by an electron from the $2p_{1/2}$ level corresponds to a L_2 edge,
- absorption by an electron from the $2p_{3/2}$ level corresponds to a L_3 edge,

and so on. As the binding energies of electronic levels in atoms are directly related to the nuclear charge, their energy positions are characteristic of the elements.

The ionized atom will afterwards relax via one of the following routes:

- The filling of the inner shell vacancy left after photoionization by an outer shell electron produces a fluorescence X-ray photon. Again, the energies of fluorescent photons are characteristic of the elements, as they correspond to the differences of binding energies of electrons from different levels, which are different for different elements.
- The other major process that can follow photoionization is the Auger effect, where the core vacancy is filled by an electron dropping from a higher shell while the atom simultaneously ejects another electron, the so-called Auger electron. Again, the energy of the ejected electron is characteristic of an element. One can think of the Auger process as an autoionization process where a (hypothetical) fluorescent photon possesses enough energy to ionize another electron.
- X-ray fluorescent photons or Auger electrons emitted from an atom can eject electrons from the outer shells as they leave the atom, the so-called secondary electrons.

The quantity of both, fluorescent photons and Auger electrons, is directly related to the number of core holes created, i.e., to the absorption, and is thus a direct measure of the absorption. In cases where the usual X-ray absorption measurement in transmission is not feasible, determination of the intensity of X-ray fluorescence or of Auger electrons as a function of the energy of the primary X-ray beam will give absorption spectra.

In addition to photoionization leading to true absorption, X-rays become scattered in matter, i.e., they are deflected from their way of propagation by collisions

with other electrons or atoms. In this process the energy of the X-rays either stays constant or it becomes smaller, corresponding to elastic and inelastic scattering.

In measuring X-ray absorption spectra, we summarize the effects of true absorption and of scattering. The scattering is usually only a weak function of the atomic number Z and of the wavelength λ and can be described by the Victoreen formula:

$$\mu = C \lambda^3 + D \lambda^4 + E \quad (3)$$

where C , D and E are element-specific constants.

3 Theory of X-ray Absorption Fine Structures

For the measurement of an X-ray absorption spectrum, the energy E of the primary X-ray beam is usually increased stepwise. As soon as E becomes larger than the energy of the edge E_0 , the core-level electrons are ionized into unoccupied electronic states of the so-called continuum. These electrons then have a kinetic energy, E_{kin} , which is the difference between the energy E of the incoming X-ray beam and the bonding energy of the initial state E_0 :

$$E_{\text{kin}} = E - E_0 \quad (4)$$

The continuum, i.e., the density of unoccupied electronic states, is structured. The probabilities of the transitions of the electrons to unoccupied electronic states are governed by the transition dipole matrix elements, which also contain the basic quantum-mechanical selection rules. The absorption fine structures observed thus reflect the variations in the density of the unoccupied electronic states, selected by the transition dipole matrix elements. The structure of the unoccupied density of states can be obtained by considering scattering processes which the ionized electrons experience by the electrons of surrounding atoms. A full theoretical treatment of these scattering processes for electrons of varying energy E_{kin} would be extremely demanding. However, the basic features of this model can be rationalized by a rather simple picture and, on the basis of this picture, it is possible to understand the EXAFS formula.

3.1 Theory of Extended X-ray Absorption Fine Structure (EXAFS)

In the EXAFS region where E is larger than E_0 by at least roughly 50 eV, the fine structures of the absorption can in the main be described as a consequence of single-scattering processes (Fig. 1c): An excited electron leaves the absorbing atom with a kinetic excess energy $E_{\text{kin}} = E - E_0$. According to the wave-particle dualism this electron can be considered as a wave, the wavelength of which varies with E_{kin} and thus with E . This wave is scattered at the electrons of neighboring atoms. Interference then occurs between the outgoing and the scattered waves.

When there is constructive interference at the location of the absorbing atom, the absorption will be high (Fig. 1d); in the case of destructive interference, it will be low (Fig. 1e). As E_{kin} varies with E , the wavelength of the excited and scattered electron will also vary. Correspondingly, there will be a continuous change between constructive and destructive interference at the location of the absorbing atom and thus the absorption will show oscillations as a function of E . These are the so-called EXAFS oscillations. It is clear that the frequency of these oscillations is a function of the distance between the absorbing and the backscattering atoms and that their amplitude will depend on the number of backscattering atoms and on their backscattering power.

Based on this intuitive picture, a more quantitative treatment becomes accessible. The observed EXAFS $\chi(E)$ designates the deviations of the absorption $\mu d(E)$ from the absorption $\mu_0 d(E)$, which one would observe if the absorbing atom had no neighboring atoms:

$$\chi(E) = [\mu d(E) - \mu_0 d(E)] / \mu_0 d(E) = [\mu(E) - \mu_0(E)] / \mu_0(E) \quad (5)$$

The size of these deviations $\mu d(E)$ from the "atomic" absorption $\mu_0 d(E)$ amounts to roughly 10% of the edge jump $\Delta\mu d$, which describes the difference between the mean absorption at energies above the edge and below the edge. This 10% corresponds to the part of elastically backscattered electrons. The other part of the excited electrons experiences forward scattering or are lost by inelastic scattering processes. They do not contribute to variations in the absorption.

In order to obtain a mathematically simple connection between χ and structural parameters, it is of advantage to use the absolute value of the wave vector k of the excited electron instead of its energy E . Both are related to each other by the formula:

$$k = [2 m_e / \hbar^2 (E - E_0)]^{1/2} \quad (6)$$

where m_e is the mass of the electron and $\hbar = h/2\pi$ where h is Planck's constant. The EXAFS $\chi(E)$ is then transformed to $\chi(k)$.

An extensive derivation of the equation which describes the EXAFS is not possible here. This task has been accomplished in the literature several times, see for example Stern [8], Stern et al. [9], Lee and Pendry [10], Boland et al. [11] and Teo [1]; simpler and more heuristic derivations are given by Stern [12] and Brown et al. [13]. The EXAFS formula given below (Eq. 7) describes the EXAFS $\chi(k)$ on the basis of the assumption that the excited photoelectrons can be described as plane waves and that only single-scattering processes occur. As presented here, it is valid only for isotropic samples (polycrystalline powders, amorphous and liquid materials), because polarization and texture effects [14] have not been taken into account. As backscattering occurs from the electrons of all the atoms within a certain distance from the absorbing atoms, the neighboring atoms are partitioned into several "shells" of atoms within a similar distance to the absorbing atom. Each shell contributes to the total EXAFS $\chi(k)$ by its single-shell EXAFS $\chi_j(k)$, so that the measured EXAFS spectrum around an atom of type i is the convolution of these separate contributions j .

$$\begin{aligned}
 (-1)^l \chi(k) &= \sum \chi_j(k) \\
 &= 1/k S_0^2 \sum (N_j/R_j^2) |F_j(k)| \cdot \exp[-2k^2\sigma_j^2] \cdot \exp[-2R_j/\lambda_j(k)] \\
 &\quad \cdot \sin [2kR_j + \Phi_{ij}(k)]
 \end{aligned} \tag{7}$$

The term $(-1)^l$ reflects the different signs of the EXAFS of K and L_1 edges (initial state: $1s$ or $2s$, resp., $l=0$) versus L_2 and L_3 edges (initial state $2p_{1/2}$ or $2p_{3/2}$, resp., $l=1$). The other terms are:

- S_0^2 amplitude reduction factor;
- N_j number of backscattering atoms in neighbor shell j ;
- R_j distance between shell j and the absorbing atom;
- $|F_j(k)|$ absolute value of the scattering amplitude of the atoms in shell j ;
- σ_j^2 mean square displacement of the atoms of a pair of absorbing and backscattering atoms, induced by thermal and structural disorder;
- $\lambda_j(k)$ mean free path of the excited photoelectron; and
- $\Phi_{ij}(k)$ phase-shift function.

The amplitude reduction factor S_0^2 takes account of the fact that some of the electrons that have been excited cannot contribute to the EXAFS due to electronic processes taking place within the absorbing atom itself (e.g., so-called "shake-up" and "shake-down" processes [12]); thus, in principle, S_0^2 depends only on atom type i .

N_j and R_j are the most important structural data that can be determined in an EXAFS analysis. Another parameter that characterizes the local structure around the absorbing atom is the mean square displacement σ_j^2 that summarizes the deviations of individual interatomic distances from the mean distance R_j of this neighboring shell. These deviations can be caused by vibrations or by structural disorder. The simple correction term $\exp[-2k^2\sigma_j^2]$ is valid only in the case that the distribution of interatomic distances can be described by a Gaussian function, i.e., when a vibration or a pair distribution function is purely harmonic. For the correct description of non-Gaussian pair distribution functions or of anharmonic vibrations, different special models have been developed which lead to more complicated formulae [15–18]. This term, $\exp[-2k^2\sigma_j^2]$, is similar to the Debye-Waller factor correction used in X-ray diffraction; however, the term as used here relates to deviations from a mean interatomic distance, whereas the Debye-Waller factor of X-ray diffraction describes deviations from a mean atomic position.

The term $\exp[-2R_j/\lambda_j(k)]$ describes the attenuation of the EXAFS amplitude caused by inelastic scattering processes experienced by the excited electrons outside of the absorbing atom. The mean free path $\lambda_j(k)$ of electrons in condensed matter is rather small, typically between 5 and 10 Å. The k dependence of λ is often linear. Experimental $\lambda_j(k)$ curves are known for only very few substances.

With regard to the determination of the structural parameters N_j , R_j and σ_j , the knowledge of the scattering amplitude function $|F_j|$ (which depends only on the type of backscattering atoms) and of the phase shift function Φ_{ij} (which depends on both the absorbing and the backscattering atom) as functions of k are of prime importance.

The scattering amplitude function $|F_j(k)|$ is element-specific. Its value increases with the number of electrons of the backscattering atoms and generally drops as a function of k [19, 20]. In the case of heavier elements, however, the $|F_j(k)|$ curves show specific collapses that can be traced back to specific electronic resonances. As these so-called “Ramsauer-Townsend resonances” occur at characteristic k values, the curves can be used to obtain knowledge about the type of backscattering atoms. Provided the chemical composition of the sample is known and that no two elements with similar atomic numbers are present, the backscattering element can be identified. The term $Amp(k)$, i.e., the part of Eq. (7) describing the amplitude of the EXAFS oscillation, shows the same specific features as $|F(k)|$, as it is multiplied only by numbers and continuously varying functions:

$$Amp_j(k) = 1/k S_0^2 (N_j/R_j^2) \cdot |F_j(k)| \cdot \exp[-2k^2\sigma_j^2] \cdot \exp[-2R_j/\lambda_j(k)] \quad (8)$$

This term, which can be easily extracted from the measured data, can therefore be used to identify the type of backscatterer in a certain neighboring shell j even without a full analysis of the EXAFS data and without knowledge of N_j and R_j .

The sine term of Eq. (7) describes the frequency of the oscillations and thus contains information on the interatomic distances R_j . Part of this term is the function $\Phi_{ij}(k)$ that accounts for phase shifts the excited photoelectron experiences when leaving the absorbing atom, when being scattered by a neighboring atom and when returning to the absorbing atom. The term $\Phi_{ij}(k)$ is thus comprised by the individual phase shifts as follows:

$$\Phi_{ij}(k) = 2 \cdot \Phi_i(k) + \Phi_j(k) \quad (9)$$

These processes lead to a shift of the EXAFS oscillation on the k scale while leaving its frequency and its amplitude untouched.

As stated above, knowledge of the functions $F_j(k)$ and $\Phi_{ij}(k)$ [or $\Phi_i(k)$ and $\Phi_j(k)$, from which $\Phi_{ij}(k)$ can be easily calculated] is crucial for the evaluation of EXAFS data. Two different ways are currently used to retrieve these functions.

The experimental approach extracts the amplitude function $F_j(k)$ and the total phase-shift function $\Phi_{ij}(k)$ from the spectrum of a standard sample of known structure which should be as similar as possible to the sample under investigation. When N_j and R_j are known, a modified backscattering amplitude function can be derived from the measured EXAFS $\chi_j(k)$ of the standard sample:

$$|F_j(k)| = |\chi_j(k)| \cdot \exp(-2k^2\sigma_j^2) \cdot \exp(-2R_j/\lambda_j(k)) \quad (10)$$

Similarly, the total phase-shift function $\Phi_{ij}(k)$ can be extracted. These functions can then be used to analyze the EXAFS of the compound under investigation. If a standard compound is chosen so that its electronic and chemical properties are close to that of the compound under investigation, then the influence of some usually unknown factors, such as, e.g., S_0^2 or $\lambda_j(k)$, and of some simplifying assumptions made during the derivation of the EXAFS formula, such as, e.g., that of plane waves or that of a Gaussian distance distribution, is minimized. Instead of an absolute value of σ_j^2 , a relative value $\Delta\sigma_j^2$, describing the difference in devi-

ations from the mean interatomic distance in the standard sample and the sample under investigation, is derived.

The experimental way to derive the backscattering amplitude and the phase-shift functions is very intuitive. Its application is described in some detail in Sect. 4.

Another method for data evaluation relies on the quantum-mechanical calculation of the functions $F_i(k)$, $\Phi_i(k)$ and $\Phi_j(k)$. The first attempts to calculate such functions [19, 20] were important in establishing the general features of these relations, but were not of sufficient accuracy for the determination of reliable structural data [21]. This situation has changed over the years with the advent of more sophisticated calculation methods such as, for example, the FEFF code [22–25]. FEFF uses sophisticated approaches to describe the potentials acting on the ejected electron, but its most important feature is that it is based on curved-wave theory. Within this theoretical framework, the electron waves that are emitted and scattered are treated not as plane waves, a rather crude approximation which was used in the derivation of the simple EXAFS formula given above (Eq. 7), but as spherical waves. Within curved-wave theory, however, the amplitude and phase-shift functions become dependent on the interatomic distance. Therefore, before these functions can be used to describe an experimental EXAFS spectrum, a rough estimate of this interatomic distance must be known, and the functions must be calculated on the basis of this distance. The evaluation of EXAFS data using FEFF is becoming increasingly popular and substitutes the use of experimentally derived amplitude and phase functions. The FEFF code has been integrated into the UWXAFS program for the evaluation of XAFS data [26, 27]. Its results can be used directly in other user-friendly programs like WinXAS [28, 29] and X-FIT [30], too.

Several factors limit the EXAFS to extend only some 100 eV above the absorption edge: The damping exponential functions in Eq. (7), the backscattering amplitude function (the value of which usually decreases with k), and the $1/R_j^2$ term in Eq. (7). The resolution of different coordination shells and the accuracy in determining coordination numbers and interatomic distances are thus limited. The same is true with regard to the range of distances that give rise to distinct EXAFS functions. Reliable structural data can be obtained up to a maximum of ca. 4–6 Å around the absorbing atom.

For higher coordination shells, however, the evaluation of EXAFS data is further hampered by multiple scattering (MS). Such effects are most prominent in the XANES region (Sect. 3.2.2), but are also of importance in the EXAFS region [31, 32]. One case of MS is of special relevance. It is realized when three atoms are arranged in the linear geometry A–S1–S2. When the electron wave emanating from the absorbing atom A hits the scattering atom S1, part of the wave is scattered back giving rise to single scattering; another large part of the wave is scattered forward and then hits the atom S2, where it is in part backscattered. This wave then travels back to S1, where it is scattered forward again (Fig. 2). In total, the amplitude for the scattering from atom S2 is then much higher than would be expected on the basis of single scattering. This process is designated as the “focusing effect” [31, 32]. In principle, such MS effects allow the determination of three-particle correlations like bond angles, and this has been shown for sim-

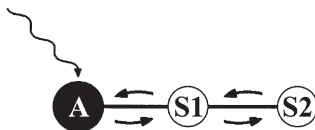


Fig. 2. Schematic display of the focusing effect

ple model systems [31, 32]. The amplitude and phase-shift functions cannot be derived experimentally and the calculations thus have to be performed using curved-wave theory. Multiple scattering events are included, for example, in the FEFF code [22–25]. Section 5.1.3 gives examples of focusing effects.

3.2

Theory of X-ray Absorption Near Edge Structure (XANES)

In the XANES region of the X-ray absorption spectrum, two physical processes play a significant role. These are electronic transitions into unoccupied electronic states and multiple scattering (MS) resonances.

3.2.1

XANES: Transitions into Unoccupied Electronic States

If an atom possesses quasi-local unoccupied electronic states, then increased absorption can occur already below the edge energy E_0 , in the so-called pre-edge region. The TiK edge spectrum of aenigmatite also shows such a pre-edge absorption (Fig. 1a) that corresponds to electronic transitions into unoccupied d states of the absorbing Ti^{4+} ions. The occurrence and the intensity of such pre-edge phenomena are governed – as are the other absorption processes – by quantum-mechanical selection rules. Dipole-allowed transitions, for example those from p orbitals into unoccupied d states, usually possess high intensities (examples will be given in Sect. 5.2.1). The pre-edge absorption in Fig. 1, however, is a $1s \rightarrow 3d$ transition, which is dipole-forbidden. The fact that such pre-edge peaks can nevertheless be observed is attributed to the hybridization of the $3d$ states with ligand p states (transitions from s to p states are dipole-allowed). It has also been suggested that these pre-edge absorptions are in fact quadrupole transitions [33, 34] or that the transitions become allowed by coupling to vibrations, similar to those that occur in optical spectroscopy. In any case, as the intensity and shape of such transitions depend on the symmetry of the coordination environment of the absorbing atom and on the type of bonding, they are of high diagnostic value in the determination of coordination geometries and electronic properties.

The exact positions of the pre-edge peak as well as of the edge itself reflect the effective charge of the absorbing atom which is determined mainly by its oxidation state and the number and electronegativity of its nearest neighbors. In a simple model, the energy required to excite an electron increases with increasing positive charge on the atom. The shifts in positions may amount to up to 10 eV

with a shift of 1–2 eV per oxidation state and of up to 0.5 eV for an additional ligand.

3.2.2

XANES: Multiple Scattering

When electrons from core electronic states are excited by X-rays of energies E which are only slightly larger (up to ca. 50 eV) than the edge energy E_0 , then the final states of these electronic transitions are located at the lowest part of the continuum of unoccupied electronic states. The XANES structures observed in this region reflect the dipole-selected unoccupied electronic density as projected onto the absorbing atom. The strong features of the absorption curve in this part of the spectrum show clearly that the continuum of unoccupied electronic states is structured. In the case of ordered solid-state structures these states can be determined by band-structure calculations.

Another approach to the interpretation of this part of the XANES is more general and can also be applied to non-crystalline materials. The features in this region can be explained by taking into account the possibility of multiple scattering (MS, Fig. 1b): Here, the kinetic energy $E_{\text{kin}}=E-E_0$ of the excited electrons is small. An electron with small kinetic energy is scattered not only forward or backwards, as is typical of the high-energy electrons of the EXAFS region, but with high probabilities also in other directions. When it then hits another atom, it will become scattered again, until finally it may return to the initial absorbing atom via a roundabout path, the MS path. As in the case of single scattering, each scattering path gives rise to an oscillation of the absorption coefficient. Of course, many different MS paths with different frequencies and amplitudes are possible, and all their signals overlap in the MS region. This region thus contains much valuable information on the geometrical arrangement, not only on interatomic distances and coordination numbers, but also on interparticle angles, of the coordination partners in the first and higher coordination shells. However, this information is very difficult to retrieve. In addition to the overlap of the different MS paths, there are other difficulties. For example, the scattering amplitude and the phase shift functions not only depend on k , but also on the scattering angle. They cannot be determined experimentally anymore, and their calculation is tedious.

Modern XAFS programs such as the FEFF code [22–25] allow such calculations. The analysis relies on iterative procedures. Plausible model structures of scattering centers around the absorbing atom are constructed; then, for each model structure, all relevant MS paths are calculated and their contributions to the total absorption are summed. The resulting absorption curves are then compared with the experimental spectrum. This process is repeated until an acceptable agreement is achieved. The difference between this complicated and time-consuming iterative procedure and the straightforward analysis of EXAFS oscillations is obvious; the length of the MS paths that have to be calculated is restricted by the free path of the excited electron, i.e., only MS paths which are shorter than the mean free electron path λ have to be included in the calculation. A cluster with a radius of that free path around the absorbing atom is thus a suf-

ficient structural characterization of the system under investigation. Such calculations have been performed for ZnS with zincblende structure and have shown that, in order to mimic the experimental XANES spectrum, scattering contributions from eight coordination shells around the central absorbing sulfur atom have to be included; this corresponds to a total number of 99 atoms [35]. In favorable cases with a mean free electron path of ca. 10 Å and average interatomic distances of ca. 2 Å, MS paths involving more than six scattering centers do not contribute significantly to the XANES curve. However, in non-metallic compounds, the mean free path may be considerably larger, and, for absorbing atoms with small atomic masses (including, e.g., Al and Si), some general problems arise in the calculations.

Because of the high information contents of the MS region and the difficulties encountered in the physical analysis, a more empirical approach has also been used to interpret these data. Within this approach, the MS curve of the sample under investigation is compared to compounds of known structure which are intuitively chosen so as to represent a series of gradual structural changes. An example of this approach is provided in Sect. 5.2.3.

4

Experimental and Data Analysis

These topics are extensively dealt with in reviews by Heald [36, 37], Heald and Tranquada [38], as well as Sayers and Bunker [39].

4.1

Experimental

The simplest way to measure an X-ray absorption spectrum is the transmission experiment shown in Fig. 3a. Although in principle the bremsstrahlung of a normal or a rotating anode X-ray tube can be used as a source, high-quality spectra are nowadays routinely measured at electron or positron storage rings, so-called synchrotrons. Apart from the high intensity, the continuous energy distribution of X-rays is the main advantage.

The primary X-ray beam is first monochromatized using a double-crystal monochromator, usually made of Si or Ge single crystals. The intensities I_0 and I_1 of the X-ray beam before and behind the sample are determined using ionization chambers. To detect instabilities in the energy scales of subsequent measurements, a reference sample that exhibits an edge in the scanned region can be measured simultaneously using a third ionization chamber.

For a transmission experiment, the sample should be of homogeneous thickness. In the case of powders, this can be achieved by grinding and pressing to a pellet, using in addition a matrix that only weakly absorbs X-rays, e.g., boron nitride or polyethylene. Fine powders can also be dusted onto adhesive tapes or precipitated from suspensions. The thickness of the sample must be adjusted so that the edge jump $\Delta\mu d$ amounts to 0.5–1.2. This is a reasonable compromise between the statistical validity of the data and the avoidance of so-called “thick-

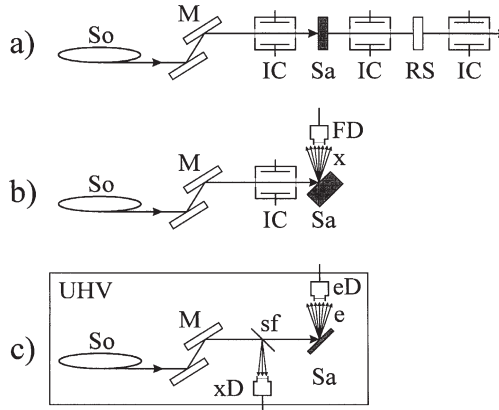


Fig. 3 a–c. Experimental set-ups for measuring X-ray absorption spectra. **a** Standard transmission experiment; **b** set-up for fluorescence yield measurements; **c** set-up for electron yield measurements placed in an ultra-high vacuum (UHV). *So* Synchrotron X-ray source, *M* double-crystal monochromator; *IC* ionization chamber; *Sa* sample; *RS* reference sample for energy calibration, *x* fluorescence X-rays; *FD* fluorescence detector (typically an energy-dispersive solid-state X-ray detector); *e* electrons emanated from the sample; *eD* detector for electrons (typically a scintillation counter); *sf* scattering foil which scatters a small part of the X-ray beams into the X-ray detector (*xD*), so that the intensity of the incoming beam can be measured

ness effects”, which can lead to errors in the amplitudes of an X-ray absorption spectrum [38, 40].

Apart from the detection of the transmitted X-ray beam, the corollaries of the absorption (see Sect. 2) can also be used for the registration of X-ray absorption spectra, for example, by detecting electrons (e.g., Auger electrons) or photons, either those emitted in the X-ray region (X-ray fluorescence) or those emitted in the visible or UV region (XEOL: X-ray excited optical luminescence). The production of fluorescence photons is proportional to the absorption; they are monochromatic and possess an energy that is characteristic for the absorbing element. Employing energy-dispersive X-ray detectors or by the clever choice of absorption filters before the detector, these photons can be counted selectively (Fig. 3b). This can be useful when the element under investigation is present only in very low concentration in the sample (concentrations of 1 atom per 100 to 100,000 atoms). With zeolite samples, this method can for example be of advantage when the local coordination of metal atoms substituted to a small degree into the host framework is to be investigated.

Electrons ejected after the core ionization can be measured either selectively by their energy as Auger electrons or unselected as the so-called total electron yield. Due to the small free path that electrons have in condensed matter, these electrons stem from a thin layer of the surface of the sample. Under these conditions, XAS becomes a surface-sensitive probe [41] known as SEXAFS (Surface EXAFS) and NEXAFS (Near Edge X-ray Absorption Fine Structure with the same meaning as XANES, but applied exclusively to near-edge spectra detected using surface-sensitive measurements). These methods have become very important

for the characterization of heterogeneous catalysts but are not so important for uniform catalysts as zeolites.

4.2

Data Analysis

In this section we describe the process of data analysis using the intuitive method of determining the backscattering amplitude and the phase-shift functions experimentally and then to use these functions to determine the structural parameters of the sample under investigation. Differences to data analysis using theoretical functions will be explained.

As an example we choose the investigation of the gallium coordination environment of the gallosilicate with the sodalite structure (SOD-GaSi) [42]. Apart from the model character of this compound, this study is at least of some academic interest because of the non-stoichiometry of the compound $\text{Na}_{7.9}[\text{Ga}_{5.9}\text{Si}_{6.1}\text{O}_{24}]\text{Cl}_2$. The gallium position is partially occupied by silicon atoms. Therefore, a direct determination of the Ga–O distance is not possible by diffraction techniques, as shown in powder X-ray [43] and neutron diffraction [44] studies (the compound is not available as single crystals). The EXAFS of the GaK edge, however, is a local probe and yields selective information on the Ga coordination.

ZnGa_2O_4 was chosen as a standard substance to determine experimental backscattering amplitude and phase-shift functions. In this compound with the normal spinel structure, gallium is coordinated octahedrally by oxygen atoms at a Ga–O distance of 1.99 Å.

Figure 4a, b shows the raw GaK edge X-ray absorption spectra of the model spinel compound and of SOD-GaSi. Also shown are Victoreen functions [see Eq. (3)] fitted to the pre-edge regions. These functions are subtracted from the whole spectra and then the edge jump is normalized to $\Delta\mu d=1$. At this stage, the XANES spectra can be compared visually and be analyzed further by fitting mathematical functions (Lorentzian, Gaussian or Voigtian functions for peaks, modified arcus-tangens functions to model the edge) to the curves in order to obtain quantitative data as intensities or peak widths of the characteristic features. The clear differences between the XANES spectra of both compounds shown in Fig. 4c are an expression of the different, octahedral and tetrahedral, coordination environments of the Ga atoms, which lead to different MS resonances.

To obtain pure EXAFS data, the edge energy E_0 is first determined and the energy coordinate is then transformed to the k scale according to Eq. (4). The data treated in this manner are shown in Fig. 4d, e (broken lines), together with fit functions (solid lines) that serve to describe the “atomic absorption background” $\mu_0 d$, i.e., the absorption curve that would be observed without neighboring atoms. Typical fit functions used are cubic spline functions or polynomials. These functions are then subtracted from $\mu d(k)$ to obtain the pure EXAFS functions $\chi(k)$ which are shown in Fig. 4f, g. In order to treat the data points at high k values, which are strongly damped, equivalently to those at low k and in order to obtain favorable conditions for the mathematical operation to follow

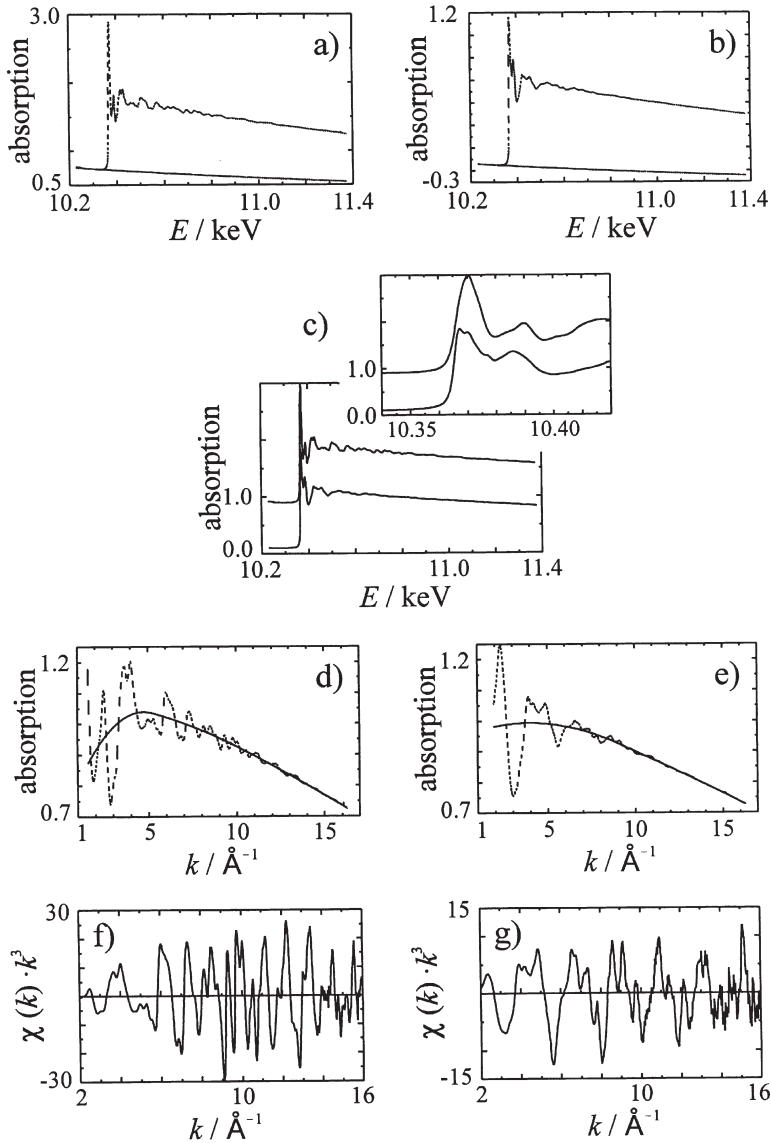


Fig. 4 a-i. Data analysis procedure for the evaluation of X-ray absorption spectra exemplified by the determination of structural parameters of the gallosilicate sodalite $\text{Na}_{7.9}[\text{Ga}_{5.9}\text{Si}_{6.1}\text{O}_{24}]\text{Cl}_2$ (SOD-GaSi) using backscattering amplitude and phase-shift functions derived experimentally from the spinel compound ZnGa_2O_4 . **a** Raw X-ray absorption spectrum of ZnGa_2O_4 ; **b** raw X-ray absorption spectrum of SOD-GaSi; for both spectra, a function fitted to the decay in absorption before the edge is included. **c** The spectra after background subtraction and normalization of the edge jump; *inset* comparison of the XANES spectra of both compounds (*top* ZnGa_2O_4 , *bottom* SOD-GaSi). **d** and **e** data (*broken lines*) after conversion to k scale, together with fit functions (*solid lines*) that describe the atomic absorption background μ_0 ; **d** shows the ZnGa_2O_4 data, **e** shows the SOD-GaSi data. **f** and **g** pure EXAFS functions $\chi(k)$ of ZnGa_2O_4 (**f**) and SOD-GaSi (**g**) weighted by k^3

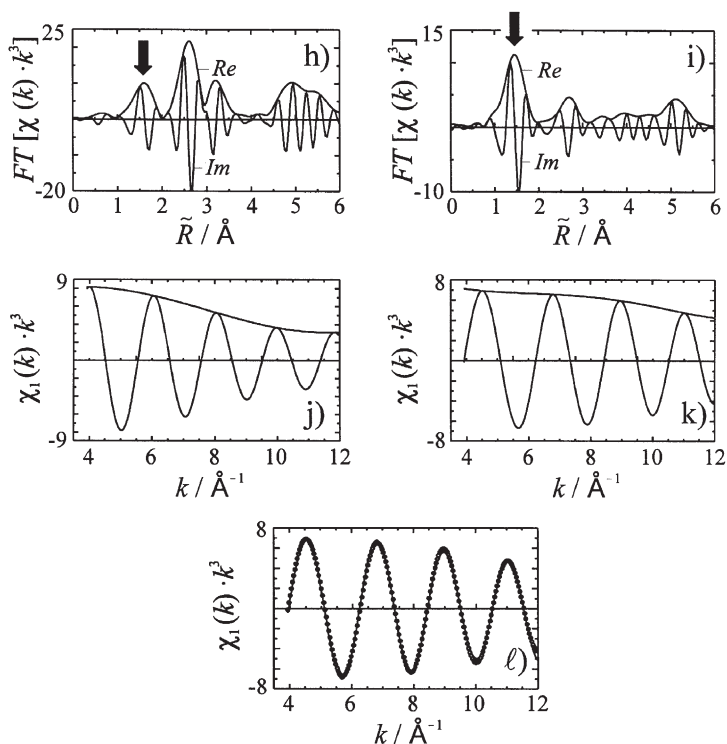


Fig. 4a-l. (continued) **h** and **i** Fourier transforms (FTs) of the EXAFS functions with real (*Re*) and imaginary (*Im*) parts; **h** ZnGa_2O_4 , **i** SOD-GaSi. **j** and **k** Backtransforms of the first peaks of the FTs, indicated by *arrows* in **h** and **i**, respectively, with their envelopes; **j** ZnGa_2O_4 , **k** SOD-GaSi. **l** Single-shell EXAFS of SOD-GaSi as shown in **k** fitted using backscattering amplitude functions and phase-shift functions determined on the single-shell EXAFS of ZnGa_2O_4 as shown in **j**

next, namely the Fourier transformation, the data are at this stage usually weighted with k^n ($n=1, 2, 3$).

The EXAFS oscillations from different coordination shells with differing distances R_j have different frequencies. By the Fourier transformation of the EXAFS data, these different frequencies are “sorted” and one obtains a radial distance distribution function as the real part (*Re*) of the Fourier transform (FT). The absorbing atoms are located at the zero-point of this radial distribution function (Fig. 4h,i). The distance scale \tilde{R} of this distribution is still shifted with respect to the true distance scale R because the phase shifts summarized in $\Phi_{ij}(k)$ have not yet been considered. Therefore we find, for example, the signal of the first oxygen coordination shell of ZnGa_2O_4 (which is indicated by an arrow in Fig. 4h) at an “uncorrected” distance of $\tilde{R} \approx 1.6 \text{ \AA}$ instead of $R=1.99 \text{ \AA}$, the distance determined by X-ray structural analysis. The height of the signals in the distance distributed EXAFS depends, of course, on those factors that determine the amplitude of the EXAFS function χ_j of the corresponding shell. However, for coordination shells

with rather similar distances to the absorbing atom, the χ_j functions will interfere in k space and will be diminished by mutual extinction, leading to decreased peak heights in the FT. This is a major weakness of the EXAFS method.

In order to obtain more precise structural information from EXAFS data, the peaks which are apparent in the FT are backtransformed individually. In this way one obtains the isolated scattering curves $\chi_j(k)$ of individual coordination shells. The envelope of $\chi_j(k)$ corresponds to the amplitude defined in Eq. (8); in this equation, only $|F_j(k)|$ can vary non-monotonically with k , and minima and maxima in the envelope yield information regarding the type of backscatterer (see Sect. 3.1). Figure 4j, k shows the EXAFS data $\chi_1(k)$, i.e., those corresponding to the first coordination shell of oxygen atoms, for the spinel and the sodalite, respectively. These curves were generated by backtransformation of the peaks that are indicated by arrows in Fig. 4h, i. Both functions do not show any specific extrema, a behavior expected of backscattering atoms with low atomic number, oxygen in this case. From the data relating to ZnGa_2O_4 , where N_1 and R_1 are known, the modified backscattering amplitude function $|F'_j(k)|$ [Eq. (10)] and the phase-shift function $\Phi_{\text{Ga,O}}(k)$ can be calculated. With the knowledge of these functions, it is then possible to fit the χ_1 function of the sodalite.

During the fit procedure, N_1 and R_1 as well as σ_1^2 are varied in an equation corresponding to a single-shell version of the EXAFS formula in Eq. (7). The disorder term then represents the disorder in the compound investigated as compared to the disorder in the model compound and thus corresponds to $\Delta\sigma_1^2$. In addition, the edge energy E_0 is varied, which influences directly the calculation of the k scale and which cannot be determined precisely enough *a priori*. The final fit is shown in Fig. 4l. The results are:

$$N_1: 4.1 \pm 0.4; R_1: 1.83 \pm 0.03 \text{ \AA}; \Delta\sigma_1^2: -2.7 \cdot 10^{-3} \text{ \AA}^2; \Delta E_0: -2.2 \text{ eV.}$$

The analysis shows, as do diffraction methods, that gallium is coordinated tetrahedrally by oxygen. In addition, the Ga–O bond length of 1.83 Å is obtained that cannot be determined directly from diffraction methods due to the partial occupation of the Ga sites by Si. As the negative value of $\Delta\sigma_1^2$ indicates, the deviations from the mean bond length are smaller in the sodalite than in the spinel compound. The parameter ΔE_0 bears no physical meaning, but $|E_0|$ values which are larger than some eV point to false results.

The alternative method of data evaluation employs amplitude functions and phase-shift functions calculated theoretically, e.g., using the program FEFF. These functions are then used in a similar fit procedure to the backtransformed single-shell EXAFS. This method gives an absolute value of σ_j^2 . For comparison, one or more reference compounds that have an absorbing atom with a similar coordination environment to that in the sample under investigation should be treated in the same way. This is also important for the determination of S_0^2 , a quantity that must be known in order to obtain reliable coordination numbers (when using backscattering amplitude and phase-shift functions determined experimentally, it is implicitly assumed that S_0^2 is the same for the sample being investigated and the model compound, see Sect. 3.1).

It should be noted that the analysis of EXAFS data is prone to mistakes and that it requires intensive training. This is true especially for fitting the $\mu_0 d$ func-

tion. Mistakes made in this step influence the whole further data evaluation and can lead to results that deviate drastically from the true values. When performed correctly, both ways of data evaluation yield typical errors of 1–3% for the determination of interatomic distances and up to 20% for the determination of coordination numbers (these errors may be larger when higher coordination shells are evaluated).

In another GaK edge study on a sodalite-type compound (galloibicchulite $\text{Ca}_8[\text{Ga}_8\text{Si}_4\text{O}_{24}](\text{OH})_8$), it was also possible, by special evaluation methods, to determine the type of next-nearest neighbors, i.e., the distribution of Ga and Si over the T sites in Ga–O–T [45]. GaK EXAFS has also been applied to the question of framework incorporation of Ga into MFI-type zeolites in dependence on the synthetic conditions [46].

The question of incorporation of metal atoms into zeolitic host frameworks is of course of importance for a wide variety of materials, and there have been many EXAFS studies concerned with this problem. Only some of these can be cited here as examples: Ti in titanium silicalite [47, 48], Zn and Mn in $\text{AlPO}_4\text{-34}$ [49], Zn in MFI [50], Zn, Mn and Co in MeAPO-34 (see Sect. 5.1.2) [51], Ti in ETS-10 [52], and Co in CoSAPO-34 [53]. In this context, it seems appropriate to also give an example of a misleading EXAFS study: From FeK edge data, the local environment of Fe atoms in as-synthesized iron-substituted ZSM-5 was evaluated and a description obtained containing no less than nine coordination shells around the absorbing atom, including even the atoms of the structure-directing agent [54]. This is a clear over-interpretation of the data and an over-estimation of the capabilities of the method.

5

Information from X-ray Absorption Fine Structure

The purpose of this section is to provide an impression of the information contents of XAFS, taking didactically chosen examples from the chemistry of porous materials.

5.1

Information from Extended X-ray Absorption Fine Structure (EXAFS)

As detailed in the sections above, EXAFS contains directly accessible information on interatomic distances and coordination numbers. Indirectly, such information can in favorable cases be used to speculate about particle sizes and morphologies (e.g., of zeolite-stabilized metal clusters).

5.1.1

MnK EXAFS Investigation of Manganese-Exchanged A and Y Zeolites

The following example, taken from one of the earliest reports of the application of XAFS to zeolites, deals with the coordination and location of ion-exchanged manganese ions in zeolite Y [55]. Figure 5 shows the FTs obtained on an aqueous solution of Mn^{2+} (Fig. 5a) as well as those obtained on the ion-exchanged zeolite

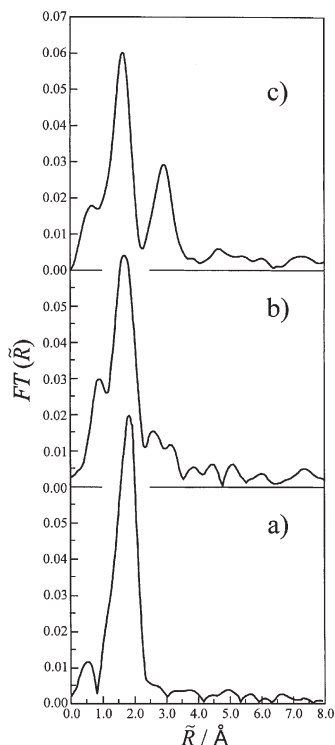


Fig. 5. Fourier transforms of the MnK edge EXAFS data of *a* an aqueous solution containing Mn^{2+} ions, *b* hydrated Mn^{2+} -exchanged zeolite Y, and *c* dehydrated Mn^{2+} -exchanged zeolite Y (after [55])

compound in the hydrated (Fig. 5b) and in the dehydrated state (Fig. 5c). Obviously, the environment of the Mn^{2+} ions in the hydrated zeolite is very similar to that in the solution, showing only one shell of coordinated atoms. Backtransformation of the corresponding peak in the radial distribution function and fitting the single-shell EXAFS show that this shell consists of six oxygen atoms at a distance of ca. 2.15 Å in both cases. Also for the zeolite-occluded Mn^{2+} ions, no contribution from further coordination shells are visible, ruling out a location near to the framework. In such a case, an additional coordination shell would appear at higher \tilde{R} values corresponding to the T atoms of the framework. In fact, such a coordination shell is apparent in the FT of the dehydrated sample. These results are consistent with a picture where the exchanged manganese cations exist as (partly) mobile aquo complexes in the hydrated zeolite, possibly located in the supercage of the FAU structure. Upon dehydration, they become attached to the framework where they are coordinated directly to framework oxygen atoms (first shell) and in addition possess well-defined distances to Al and Si atoms (second shell).

Also for Co^{2+} -exchanged [56, 57] Y-type zeolites, EXAFS analysis showed that these cations exist as sixfold coordinated aquo complexes in the large

voids of the zeolite structure when the sample is hydrated. More recently, the structure of dehydrated Ni^{2+} -exchanged zeolite Y was studied by a combination of Rietveld refinement of powder X-ray diffraction (PXRD) data, EXAFS and computer simulation [58, 59]. The results of the EXAFS analysis and of the PXRD investigation did not agree: The EXAFS analysis yielded a Ni–O bondlength of 2.02 Å, whereas the Rietveld analysis located the Ni^{2+} ions in the S_1 site, coordinated to six framework oxygen atoms at 2.28 Å. The site is occupied only to 75%. These findings were interpreted in the following way: PXRD detects a weighted average of S_1 site environments, i.e., from those sites occupied by Ni^{2+} ions and those that are not. Coordination numbers and distances from EXAFS, which, due to the element-selective character of XAFS reflect only the geometry of those sites occupied by the transition-metal ions, appear more reliable in this case [59]. The computational study verified the EXAFS results [58]. The contribution of the PXRD findings to the consistent structural model derived in these studies provides the evidence that the Ni^{2+} ions are in the S_1 sites, a fact that would have been very difficult to prove by EXAFS or computational methods.

5.1.2

Local Environment of Cobalt in Cobalt Aluminophosphates

The studies presented here deal with the coordination of cobalt atoms in cobalt aluminophosphates (CoAPOs). The compounds investigated include those of CHA topology (CoMnAPO-34) [51] and of SOD topology [42]. In the case of the CoMnAPO, a perfect fit to the filtered EXAFS function of the first coordination shell is obtained with four oxygen atoms at a distance $R_{\text{Co-O}}$ of 1.93 Å. This result is consistent with the presumed incorporation of the Co atoms into the aluminophosphate framework [51].

The situation is different for the SOD compound. The backtransformed EXAFS of the oxygen coordination cannot be fitted with a single O coordination. Instead, two shells with different Co–O distances have to be used (Fig. 6). Accord-

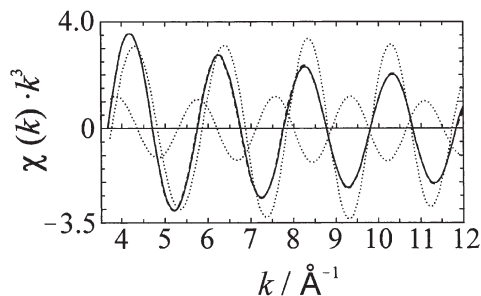


Fig. 6. Backtransformed CoK edge EXAFS data of the first coordination shell of Co in CoAPO-20 (*dashed line*) fitted using backscattering amplitude and phase-shift functions determined on cobalt acetate hydrate (*solid line*). Two different sub-shells of oxygen neighbors are necessary in order to obtain a satisfactory fit. Their individual EXAFS functions are shown by *dotted lines* [42]

ing to this two-shell fit, Co is, on average, coordinated to 3.5 ± 0.4 oxygen atoms at a distance of $1.99(3)$ Å and to 1.7 ± 0.4 oxygen atoms at a distance of $2.14(3)$ Å. When the shorter distance is ascribed to tetrahedrally and the longer one to octahedrally coordinated Co, then the coordination numbers give a ratio of ca. 80% fourfold and 20% sixfold coordination (compare the CoK XANES results in Sect. 5.2.2 [42]).

It should be noted that the synthesis of the CoAPO-20 compound dealt with here was not optimized and that the parent SOD compound of AlPO_4 composition is difficult to prepare. The CHA-type compound demonstrates that Co can be incorporated on fourfold coordinated sites into aluminophosphate frameworks [51].

5.1.3

Mercury Iodide as a Guest Species in Porosils

Mercury(II) halides can be inserted into porosils (crystalline microporous silicon dioxide modifications) via the vapor phase [60–63]. The guest molecules HgX_2 (X: Cl, Br, I) are disordered within the voids of the host and the positions of their atoms cannot be determined by diffraction methods. EXAFS as a local spectroscopic tool is well suited to gather information about the local structure of the guest species.

Figure 7 gives results calculated on the basis of HgL_3 and BrK edge EXAFS spectra obtained on a sample of HgBr_2 -loaden decadodecasil 3R (DDR). The DDR host contains isolated cages with an eight-membered ring window as maximum aperture. Figure 7a shows the FT of the HgL_3 edge data, which is dominated by a large peak at ca. 2.1 Å. The backtransform of this peak is shown in Fig. 7b as a solid line. The fit (dotted line) yields the following coordination parameters: $N=2$ and $R_{\text{Hg-Br}}=2.40(1)$ Å. Thus, mercury bromide is present as linear Br–Hg–Br molecules. Interestingly, the bond length is very close to that observed for such molecules in the vapor phase ($R_{\text{Hg-Br}}=2.38$ Å), whereas in solid pure mercury bromide, this distance is longer ($R_{\text{Hg-Br}}=2.46$ Å). Further investigations – Raman and UV-Vis spectroscopy [61, 62] – also point to the fact that porosil-inserted HgX_2 molecules are in a state which is very close to that of the vapor phase. This is not astonishing with regard to the weakness of the interactions between the neutral guest molecules and the neutral SiO_2 host framework, and this idea is further corroborated by the fact that the HgL_3 EXAFS does not provide any evidence for well-defined Hg–O contacts, ruling out the occurrence of preferred positions of the guest molecules within the porosil voids. The FT of the EXAFS (Fig. 7a) does, however, show another feature at $\tilde{R} \approx 4.3$ Å. This signal can be explained by multiple scattering within the HgX_2 molecules. Figure 7c shows the two relevant multiple scattering paths (one involving three scattering centers and one involving four) which, according to calculations using the FEFF code, cause the peak at $\tilde{R} \approx 4.3$ Å.

Figure 7d shows the FT of the BrK EXAFS of the inserted molecules and Fig. 7e its evaluation by a single-shell fit. The interatomic distance determined is $R_{\text{Br-Hg}}=2.38(1)$ Å, confirming the smaller value in the insertion compound as compared to the solid state. Interestingly, the FT again shows an additional

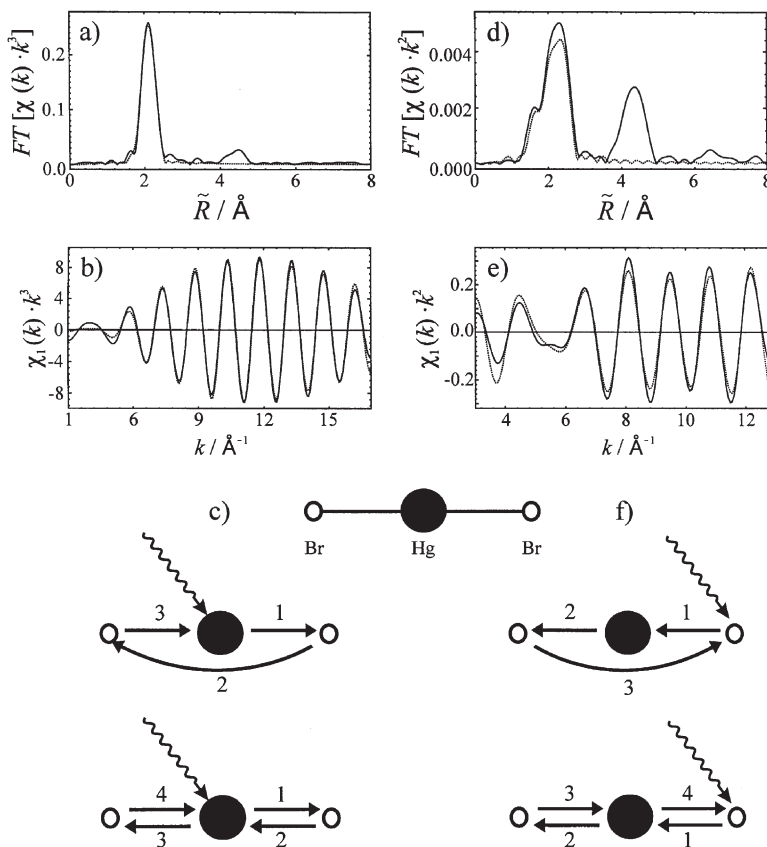


Fig. 7a-f. EXAFS investigation of HgBr₂ molecules inserted into the zeosil DDR. **a** Fourier transform (FT) of the EXAFS data at the HgL₃ edge. **b** Backtransform (solid line) of the first peak of the FT (at ca. 2.1 Å in **a**) with fit (dotted line) calculated using backscattering amplitude and phase-shift functions derived theoretically employing the FEFF program. **c** Multiple scattering paths giving rise to the second peak in the FT (at ca. 4.3 Å in **a**). **d** Fourier transform (FT) of the EXAFS data at the BrK edge. **e** Backtransform (solid line) of the first peak of the FT (at ca. 2.2 Å in **d**) with fit (dotted line) calculated using backscattering amplitude and phase-shift functions derived theoretically employing the FEFF program. **f** Multiple scattering paths giving rise to the second peak in the FT (at ca. 4.2 Å in **d**). After [60–63]

feature, this time at ca. 4.2 Å. This peak is also due to MS, based on the three- and four-atom paths shown in Fig. 7f.

In both backtransformed EXAFS functions, it can be seen that the envelope of the EXAFS does not drop continuously with k , as was observed with backscatterers of small atomic number (as oxygen, see Fig. 4j, k). Here, we have elements with higher atomic numbers as backscatterers, where Ramsauer-Townsend resonances introduce non-monotonic behavior into the backscattering amplitude functions (see Sect. 3.1).

5.1.4

Metal Sulfide Clusters in Zeolites

Zeolite-supported molybdenum sulfide catalysts promoted by nickel or cobalt have recently attracted considerable attention as hydrocracking catalysts. An important factor for the performance of these catalysts appears to be a high dispersion of the metal sulfide clusters that can also enhance synergy effects between the cobalt or nickel and molybdenum sulfides. Of the various methods used to prepare molybdenum sulfide clusters in zeolitic hosts – impregnation with aqueous heptamolybdate solution, solid-state reaction with MoCl_5 , ion exchange with $[\text{MoO}_2]^{2+}$ cations, adsorption of volatile $\text{Mo}(\text{CO})_6$ – the latter technique has been shown to yield highly dispersed and fully sulfided clusters after the sulfidation, which is generally carried out at slightly elevated temperatures using H_2S . The analysis of EXAFS data played an important role in these studies [64–66].

To demonstrate the application of EXAFS to this problem, we compare the FTs of the MoK edge of four different samples and a reference compound (Fig. 8):

- sample A Mo/S-zeolite Y prepared by impregnation;
- sample B Mo/S-zeolite Y prepared by loading with $\text{Mo}(\text{CO})_6$;
- sample C Fe/Mo/S-zeolite Y prepared by loading with $\text{Mo}(\text{CO})_6$ and $\text{Fe}(\text{CO})_5$;
- sample D Co/Mo/S-zeolite Y prepared by loading with $\text{Mo}(\text{CO})_6$ and $\text{Co}(\text{NO})(\text{CO})_3$;
- sample E polycrystalline MoS_2 .

Considering the FT peaks of all spectra, signals from three different environments can be discerned: Mo–O at $\tilde{R} \approx 1.3 \text{ \AA}$, Mo–S at $\tilde{R} \approx 1.9 \text{ \AA}$ and Mo–Mo at $\tilde{R} \approx 2.7 \text{ \AA}$. Only in sample A are molybdenum atoms partly surrounded by oxygen atoms (Fig. 8a). Obviously, the sulfidation process was not able to completely substitute Mo-bound oxygen atoms with sulfur atoms. With the help of other techniques (X-ray photoelectron spectroscopy and high-resolution transmission electron microscopy), this failure can be traced back to the fact that only some of the molybdenum oxide species present after impregnation are occluded and dispersed by the zeolite host. The remainder form agglomerated MoO_3 clusters on the external surface of the zeolite. These exterior clusters cannot be sulfided completely.

Samples B, C and D, where the molybdenum has been introduced via the carbonyl complex, do not show a distinct oxygen coordination shell. The Mo atoms are coordinated by sulfur (almost) exclusively. Mo–Mo contacts are also visible for these samples (Fig. 8b–d); however, they are much weaker than in pure MoS_2 (Fig. 8e). The “missing” Mo neighbors indicate a high dispersion of the Mo/S clusters in the zeolites [64, 65].

Most interesting is a comparison of the samples C and D, doped with Fe or Co atoms, respectively. For sample D, a Co coordination shell around Mo at $\tilde{R} \approx 2.4 \text{ \AA}$ is clearly visible (Fig. 8d). In contrast, no similar contacts appear in the FT of the iron-doped sample C (Fig. 8c), i.e., Fe and Mo atoms are not associated with each other [65].

The different structural environments of the molybdenum atoms are reflected in the catalytic properties of the materials. Sample B possesses a much higher

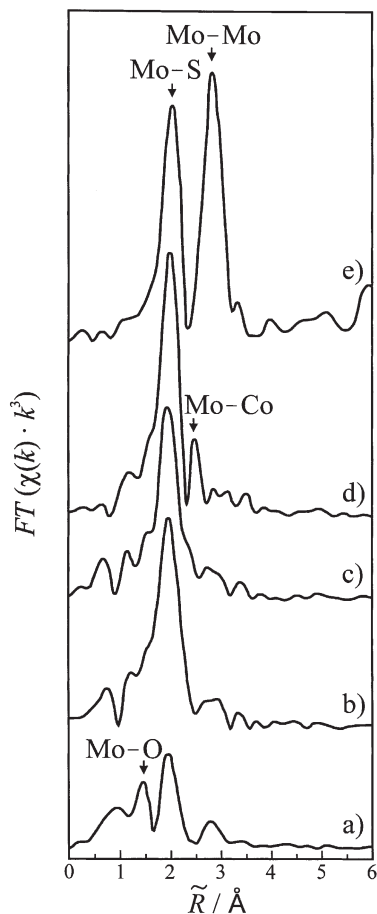


Fig. 8. Fourier transforms (FTs) of MoK edge EXAFS data of hydrodesulfurization catalysts and of a model compound. *a* Mo/S-zeolite Y prepared by impregnation; *b* Mo/S-zeolite Y prepared by loading with $\text{Mo}(\text{CO})_6$; *c* Fe/Mo/S-zeolite Y prepared by loading with $\text{Mo}(\text{CO})_6$ and $\text{Fe}(\text{CO})_5$; *d* Co/Mo/S-zeolite Y prepared by loading with $\text{Mo}(\text{CO})_6$ and $\text{Co}(\text{NO})(\text{CO})_3$; and *e* polycrystalline MoS_2 . After [64–66]

hydrodesulfurization activity than sample A. Doping with Co (sample C) further enhances the activity of the metal-complex-derived samples, obviously a synergistic effect [65, 66]. In contrast, Fe doping, which does not lead to composite Mo/Fe/S clusters, remarkably decreases the hydrodesulfurization activity [65].

5.2

Information from XANES

The XANES region contains information on the electronic state of the absorbing atom as well as on its coordination geometry. In general, three types of XANES features can be distinguished: Pre-edge peaks carrying information on coordi-

nation geometries and on oxidation states, the edge position E_0 which also reflects the oxidation state, and post-edge multiple scattering patterns influenced by the local environment of the absorbing atom.

5.2.1

Oxidation States of Non-framework Species

The energy necessary to ionize a core electron from an atom depends on the effective charge of the corresponding atom. The more positive this charge, the higher the ionization energy. A formal measure of the effective charge is the oxidation state and, therefore, the positions of pre-edge peaks and of the absorption edge itself shift to higher energies with increasing oxidation state. These shifts amount to 0.5–3 eV and thus are clearly above the spectral resolution and easily detectable.

These relationships are exemplified by the CuK edge spectra of elemental copper and of compounds with Cu in oxidation states +1, +2 and +3, shown in Fig. 9

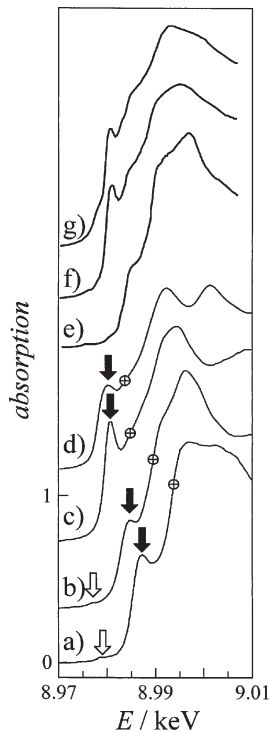


Fig. 9. CuK edge XANES spectra of (a to d) Cu in different oxidation states [6], and (e to g) Cu in zeolite Y [67]. a) Cu^{3+} in $\text{K}_5[\text{Cu}(\text{IO}_5\text{OH})_2] \cdot 12\text{H}_2\text{O}$, b) Cu^{2+} in CuO , c) Cu^+ in Cu_2O , d) Cu^0 in elemental Cu, e) zeolite Y ion-exchanged with $\text{Cu}(\text{NO}_3)_2$ solution, f) zeolite Y treated with gaseous CuCl , g) zeolite Y treated with gaseous CuCl and reduced using CO. For the spectra in a) to d), specific features have been depicted by the following symbols. \oplus : edge position E_0 , full arrow: $1s \rightarrow 4p$ transition, open arrow: $1s \rightarrow 3d$ transition

[6]. Shifts are observed for the edge position, a shoulder in the edge (which can be ascribed to a dipole allowed $1s \rightarrow 4p$ transition), and a pre-edge peak. The latter is ascribed to a $1s \rightarrow 3d$ transition. It is generally of weak intensity, as such a transition is dipole-forbidden (see also Sect. 5.2.2). This feature is absent in the spectra of elemental copper and of Cu_2O , as the $3d$ states are fully occupied in these samples.

In addition, Fig. 9 shows CuK edge spectra of differently treated Y zeolites loaded with copper species [67]. The spectrum of Fig. 9e was obtained on a sample of zeolite Y that had been ion-exchanged with $\text{Cu}(\text{NO}_3)_2$ solution. The positions of the three features clearly show that copper exists as Cu^{2+} ions in this sample. The spectrum in Fig. 9f was measured on a sample of zeolite Y in its protonic form treated with gaseous CuCl at elevated temperatures. Obviously, the oxidation state of the copper species in this sample is +1, possibly with minor traces of Cu^{2+} . Reduction of this sample with CO led to a substance that gave the spectrum depicted in Fig. 9g. The additional absorption in the pre-edge region is due to the formation of $\text{Cu}(0)$.

Na-Y zeolites containing gold species are of interest as heterogeneous catalysts [68]. They are prepared by physically mixing Na-Y zeolite with gold(III) chloride and subsequent thermal treatment of this mixture under vacuum. The generation of such samples has been followed by XAFS spectroscopy at the AuL_3 edge [69]. Figure 10 shows the XANES spectra of the reference compounds: metallic Au, AuCl , Au_2Cl_6 and Na-zeolite Y as well as e - g physical mixtures of Au_2Cl_6 and Na-zeolite Y treated at different temperatures: e 323 K; f 338 K; and g 353 K. After [69]

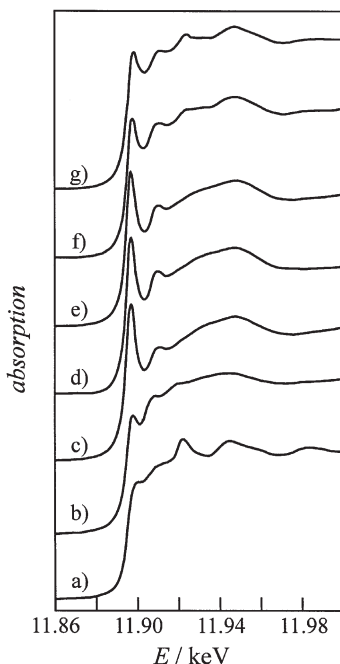


Fig. 10. AuL_3 XANES spectra of *a* metallic Au foil; *b* AuCl ; *c* Au_2Cl_6 ; *d* a physical mixture of Au_2Cl_6 and Na-zeolite Y as well as *e*-*g* physical mixtures of Au_2Cl_6 and Na-zeolite Y treated at different temperatures: *e* 323 K; *f* 338 K; and *g* 353 K. After [69]

AuCl and Au₂Cl₆, as well as those of zeolitic samples. It is obvious that the oxidation states 0, +1 and +3 of Au can be clearly distinguished by AuL₃ XANES. The most prominent feature of the spectra appears at approximately 11.89 keV, directly at the rising edge. It corresponds to $2p_{3/2} \rightarrow 5d$ electronic transitions. Note that these transitions are dipole-allowed, in contrast to the $s \rightarrow d$ pre-edge transitions seen in Fig. 9. It is practically absent for metallic gold where the $5d$ states are filled (Fig. 10a). Interestingly, a small peak appears for AuCl (Fig. 10b), although the $5d$ final states are formally filled in Au(I), too. However, it has been shown for the iso-electronic Ag(I), that the d states of the formal $4d^{10}$ sub-shell are partly depopulated [70]. In the case of the Au(III) compound Au₂Cl₆, the signal at 11.89 keV is very strong due to the open-shell configuration $5d^8$ (Fig. 10c).

The physical mixture of Au₂Cl₆ and the zeolite still contains Au(III), as expected (Fig. 10d); the oxidation state is not changed by heating the sample to 323 K (Fig. 10e). However, accompanying AuL₃ EXAFS investigations show that the Cl ligands of Au atoms have become partially exchanged against oxygen ligands. Further heating to 338 K results in partial reduction of the gold species. The spectrum in Fig. 10f strongly resembles that of AuCl. At still higher temperatures, metallic gold is formed, too. This is seen in Fig. 10g by the presence of a specific signature of the spectrum of metallic Au at ca. 11.92 keV [69].

This example shows nicely the ability of XANES to resolve subtle changes in the (mixed) oxidation states of the element under investigation. The application of additional analytical methods has led to the full characterization of the samples presented here [70].

5.2.2

Coordination Geometries from Pre-edge Features

K edge XANES spectra of transition-metal compounds often contain pre-edge features which are caused by dipole-forbidden $1s \rightarrow 3d$ transitions. These are of high diagnostic value, because the dipole rule holds strictly only when the coordination environment of the absorbing atom is centrosymmetric. Deviations from this high symmetry result in increasing intensity of the pre-edge absorption. This is exemplified by the CoK edge XANES spectra shown in Fig. 11. The intensity of the pre-edge absorption is minimal in the case of CoO with ideal octahedral coordination. A distorted octahedral coordination as in Co₂B₂O₅ already leads to an increase in the intensity of this peak. A stronger increase, however, appears in the case of tetrahedral coordination. This is shown by the spinel compounds CoGa₂O₄ and CoAl₂O₄ with 60% and 80% of the Co atoms in tetrahedral coordination, respectively. For a CoAPO-20 sample (the same as used in the EXAFS study presented in Sect. 5.1.2), the pre-edge peak indicates that ca. 60% of the Co is in a tetrahedral environment. This is in reasonable agreement with the result of the EXAFS study [42].

Similar investigations have been performed on a large number of zeotype compounds with transition-metal atoms (presumably) substituting in the framework. Often, the first derivatives of XANES spectra allow more detailed conclusions than the original spectra, as shown for example in a study on CoSAPO-34 [53].

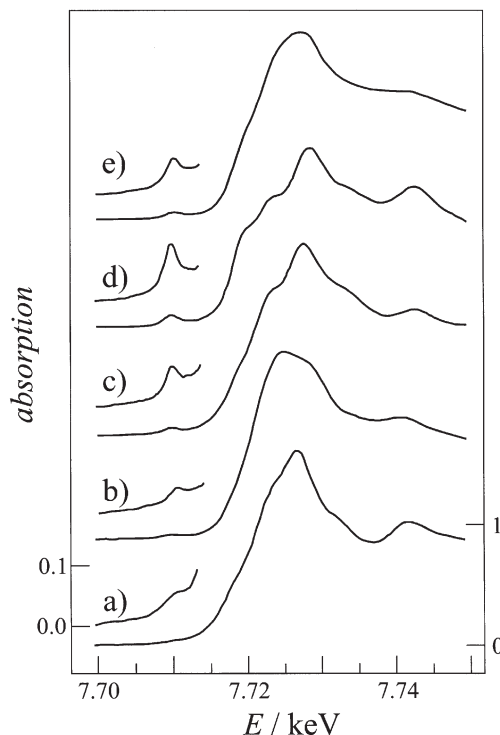


Fig. 11. CoK edge XANES spectra of *a–d* Co in different oxidic coordination environments and *e* of a sample of CoAPO-20. *Insets* represent enlarged pre-edge regions. *a* Co in a symmetrical octahedral environment in CoO; *b* Co in a strongly distorted octahedral environment in $\text{Co}_2\text{B}_2\text{O}_5$, *c* Co in the spinel CoGa_2O_4 with 60% of the Co in tetrahedral and 40% of the Co in octahedral coordination; *d* Co in the spinel CoAl_2O_4 with 80% of the Co in tetrahedral and 20% of the Co in octahedral coordination; and *e* Co in CoAPO-20; it can be estimated that ca. 60% of the Co in this sample is in tetrahedral coordination (after [42])

5.2.3

Structural Information from Multiple Scattering

As detailed in Sect. 3.2.2, a quantitative analysis of the multiple scattering (MS) region of the XANES is difficult. Here, an example is presented which relies on qualitative comparisons [62, 71].

Figure 12 shows a series of SiK edge XANES spectra. All spectra exhibit a strong absorption at the edge (feature A) and a broad hump at the end of the XANES region (feature C). Feature A is ascribed to a transition from the $1s$ states to the conduction band; feature C is typical of all compounds containing Si in a tetrahedral oxygen coordination. In the region in between (B), MS events determine the appearance of the spectra. It is not possible here to assign specific MS paths to the features appearing in region B. Nevertheless, some interesting information can be retrieved. Figure 12a, b shows the differences between crystalline

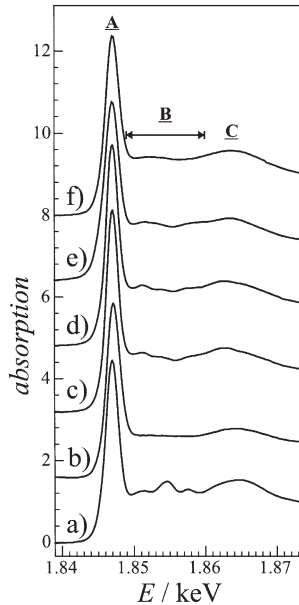


Fig. 12. SiK edge XANES spectra of silica modifications. *a* Quartz; *b* quartz glass; *c* as-synthesized ferrierite; *d* calcined ferrierite; *e* silicalite-1; and *f* calcined MCM-48

(quartz) and amorphous (fused quartz glass) samples. Whereas quartz exhibits strong and sharp variations of the absorption (due to well-defined MS paths in the crystalline structure), the glass shows an essentially flat *B* region (due to the amorphous nature, no specific MS paths are present). Figure 12c–e was obtained on zeolites, i.e., microporous silica modifications. All show distinct wiggles in region *B*, in correspondence to their crystalline nature. The features are less strong, however, than those of quartz because the structures of the zeolites are more complicated so that more different MS paths contribute to the signals in region *B*, leading to partial destructive interference between them. Noteworthy, the spectra of as-synthesized and calcined ferrierite (Fig. 12c, d) are very similar, showing that the presence of the molecules of the structure-directing agent are not involved in MS. The spectra of as-synthesized ferrierite and silicalite-1 (Fig. 12c, e), on the other hand, exhibit differences in region *B* due to their different structures. Finally, the spectrum in Fig. 12f was obtained on a mesoporous calcined MCM-48 sample. Only very weak features are observed in region *B*, but these are stronger than those of the glass. This indicates that the wall structure of mesoporous materials is not totally amorphous [72].

6 Special Techniques and Applications

6.1 In Situ Applications and Time Resolution

X-rays, at least those with energies higher than ca. 8 keV, can penetrate many materials consisting of elements with low atomic numbers (organic polymers, Teflon, beryllium, beryllium oxide). XAFS investigations can thus be carried out with a variety of different sample environments, reaching from high-temperature and high-pressure investigations to in situ studies. The latter are of course of special interest for the investigation of catalytically active systems [4]. In contrast to other heterogeneous catalysts, it is not necessary to apply special surface-sensitive experimental variants of XAS (SEXAFS) for the investigation of uniform catalysts as zeolites.

In situ studies using XAS are furthermore simplified by the high intensity of synchrotron radiation, allowing the collection of data with reasonable statistics even with small sample volumes or with short counting times. Thus, the development of X-ray methods providing spatial or temporal resolution is possible, in principle. The possibility of obtaining X-ray absorption spectra with spatial resolution (μm resolution can be achieved today) is of high interest for the characterization of surface heterogeneous catalysts and of interfaces, but is not so important for the investigation of uniform catalysts like microporous solids.

Two philosophies have been developed for the fast registration of X-ray absorption spectra [73–76]. One of these can be characterized as a brute-force variant of the normal transmission experiment, where the energy of the primary beam is increased stepwise. It takes about 20–30 min to take a full spectrum, and much of this time is used to perform corrections in the adjustment of the beam and to calm down mechanical vibrations and instabilities, which occur after every movement of the monochromator crystal. The QEXAFS (Quick-Scanning EXAFS) method [75, 76] uses a step-wise, rather than a continuous motion of the motors driving the movement of the crystals, so that such extra times are not necessary. If the counting times of the detectors are minimized as well, a full XAFS spectrum of sufficient quality can be obtained in a few seconds. Spectra with only minor losses in quality as compared to conventional step-by-step scanning can be obtained in a few minutes.

The DEXAFS (Dispersive EXAFS) method [73] uses a principally different approach. Using a bent monochromator crystal with a special curvature, the X-ray radiation of a certain energy range can be diffracted in such a way that the bundle of X-ray beams is focused at a small spot on the sample. Behind the sample, the beams of different wavelengths diverge again. Using a linear position-sensitive detector, the intensity distribution of the X-ray spectrum after passing the sample can be measured simultaneously. DEXAFS has the advantage that the whole spectrum is measured in one instant on a specific state of the sample. DEXAFS experiments can attain a time resolution in the millisecond regime. However, realistic measuring times for spectra with sufficient signal-to-noise ratio rather are in the range of several seconds and DEXAFS is experimentally

considerably more demanding than QEXAFS [74,76]. Therefore, it has been proposed that the installation of QEXAFS rather than DEXAFS beamlines at synchrotrons be encouraged [77].

Examples of recent *in situ* studies using conventional XAS scanning techniques have focused on the characterization of the local environment of non-framework metal cations (e.g., Pd in Na-zeolite Y [78], Rh/Pt clusters in Na-zeolite Y [79], Cu(I) in Cu-ZSM-5 [80]) or on the interaction of framework metal atoms with adsorbed species (e.g., the interaction of acetonitrile with cobalt aluminophosphates [81]).

An example for a QEXAFS study is given in Fig. 13 [82, 83]. It deals with the dehydration and subsequent decomposition of silver-exchanged zeolite A studied at the AgK edge. The XANES spectra taken at 298 K at normal pressure and under vacuum show that the application of the vacuum already induces changes in the sample, corresponding to its dehydration. Heating the sample then to 520 K does not produce any significant changes, indicating the stability of the dehydrated phase up to this temperature. However, the spectra taken subsequently

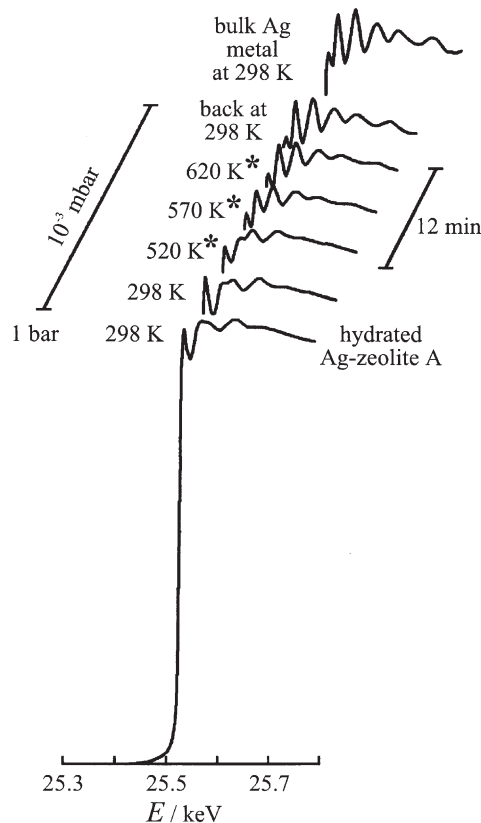


Fig. 13. AgK edge spectra documenting the dehydration and decomposition of Ag⁺-exchanged zeolite A. The spectra marked with asterisks were measured within 12 min using the QEXAFS technique

upon further heating show the formation of elemental silver. Note that these spectra were taken within 12 min. A comparison of the spectrum obtained after cooling the sample back to room temperature with that of a silver foil shows that bulk Ag has been formed. Correspondingly, an *ex situ* X-ray diffraction investigation of the sample after the QEXAFS measurements shows only lines of elemental Ag; the aluminosilicate framework of the zeolite has been destroyed by the heating procedure [82].

DEXAFS has, for example, been used to follow the dehydration of (Ni^{2+} , Na^+)-loaden zeolite Y [84]. In another study, the reactions of partially Cu-exchanged Na-zeolite Y with pure H_2 or with a mixture of $\text{H}_2/\text{H}_2\text{O}$ have been investigated [85]. Pure hydrogen leads to the reduction of Cu^{2+} to Cu^+ , but not to metallic copper due to the strong interaction of the Cu(I) cations with the aluminosilicate framework. After admission of additional water vapor, however, the Cu(I) cations become mobile and are reduced to Cu(0), forming small metallic copper clusters.

An interesting combination of X-ray based methods is the simultaneous application of XAS and powder XRD. This is because XAS yields information on the local environment, also of amorphous or liquid samples, whereas XRD reflects the long-range order of crystalline samples only. A typical experimental approach to the XAS-XRD combination applied *in situ* involves the use of QEXAFS to measure XAFS spectra and of a linear position-sensitive detector to assemble the XRD pattern [86]. Typically, XAFS and XRD patterns are measured in an alternating fashion, i.e., after scanning a XAFS spectrum the monochromator is adjusted to an energy below the edge probed and an XRD pattern is then registered using X-ray radiation of the corresponding wavelength (the XRD pattern should be measured with an X-ray energy below the absorption edge because otherwise strong fluorescent radiation will decrease the signal-to-noise ratio of the diffraction pattern). Such an approach has been used to investigate the high-temperature transformations of zeolites to dense ceramic materials (e.g., Mg-exchanged zeolite B \rightarrow cordierite [87] or Co-exchanged zeolite A \rightarrow cobalt aluminium spinel+nepheline [88, 89]). Two interesting studies use CoK XAFS and powder XRD as diagnostics for the chemical behavior of cobalt aluminophosphates. One probes the onset of crystallization of CoAPO-5. CoK XANES spectra show that, directly prior to the onset of crystallization (i.e., immediately before diffraction lines appear in the XRD pattern), the coordination of Co changes from octahedral to tetrahedral [90]. The other study compares the stabilities of pure CoAPO-44 and of CoAPSO-44. Only the latter is stable at temperatures of interest for catalytic reactions [91].

When heterogeneous catalysts are probed under *in situ* conditions, it is advisable to monitor also the product formation, e.g., by gas chromatography. Such complex experimental set-ups, consisting of XAS, XRD and chemical analysis methods, have been described [92, 93].

6.2

Electron Energy Loss Spectroscopy

High-energy electrons (40–400 keV) produced in a transmission electron microscope can also give rise to the core ionization processes that form the initial step

in X-ray absorption. The electrons lose energy in this process, i.e., they become inelastically scattered. Measuring the number of electrons that lose specific amounts of energy gives an energy loss spectrum. Such a spectrum contains edges and associated fine structures that are similar to XAFS spectra and can be evaluated in similar ways. This method is called electron energy loss spectroscopy (EELS) [94, 95]. The advantage of EELS lies mainly in the fact that the incident electron beam can be focused to sub-nanometer dimensions and thus gives very high spatial resolution which can be of interest for the study of, e.g., interfaces.

6.3

Resonant X-ray Diffraction

Close to the absorption edge of an element, its atomic form factor changes drastically, leading to strong differences in the intensities of X-ray diffraction intensities (anomalous dispersion). Different X-ray reflections react with different sensitivities to this change, according to the varying contributions of the corresponding element to the structure factors of these reflections. By comparing the diffraction data obtained using an X-ray wavelength which is far away from the X-ray absorption edges of the elements present (“off-edge” diffraction pattern) and those using a wavelength near to the absorption edge of a specific element in the sample (“near-edge” or resonance diffraction pattern), the atomic position(s) of the absorbing element can be determined more easily and more precisely. This method has been applied to determine the distribution of Zn^{2+} cations in a partly Zn-exchanged Na-zeolite Y. Two powder X-ray diffraction patterns were measured, one using X-rays of wavelength 0.799 \AA (“off-edge”) and one with X-rays of wavelength 1.286 \AA (“resonance”) [96]. In a similar manner, the Ni positions of a nickel aluminophosphate [97] and the locations of krypton sorbed in silicalite [98] were determined.

7

Concluding Remarks

The fine structures at X-ray absorption edges contain a manifold of information about the geometrical (EXAFS and XANES) and electronic (XANES) structure of matter. The main advantages of this method are:

- as only the local structure around the absorbing atom is probed, the sample does not need to have a high degree of structural order; in particular, no long-range order is required which is necessary for the application of diffraction methods;
- the method is element-selective and there are hardly any restrictions with regard to the elements to be investigated, in contrast, for example, to NMR and Mössbauer spectroscopy;
- XAFS can be applied using many different sample environments.

A major disadvantage of XAFS methods lies in the fact that the signals of all absorbing atoms of one type in the sample superimpose at the edge. When a sam-

ple contains an element in several different atomic environments, it becomes impossible to reconstruct the individual signals belonging to the different species (sometimes this is still possible in the XANES region, as, for example, a TiK edge study on a titanium silicalite-1 sample has shown [99]). This stands in contrast to other analytical tools, e.g., solid-state NMR or Mössbauer spectroscopy, where even very small differences in the environments lead to individual signals (or groups of signals). Another disadvantage of XAFS methods is the necessity to work at synchrotrons. Beam times are scarce and are scheduled months ahead.

Current XAFS research in the physical and theoretical area is devoted mainly to a better understanding of the XANES region in order to gain better access to the high content of information. Experimental improvements focus on improving time and spatial resolution. For in situ studies, the trend is to combine additional methods (XRD, gas chromatography, differential scanning calorimetry [100]) with XAFS in order to yield more comprehensive information about the state of the sample or about its catalytic activity.

Above, the fact that there are hardly any restrictions with regard to the choice of element was considered to be a major advantage of XAFS. In fact, there are two major restrictions, an inevitable and an experimental one:

- Organic molecules form a major part of many zeotype host-guest compounds, for example, as structure-directing agents or as reacting entities. The X-ray energies of the edges of elements of low atomic number, such as H, C, N, O, are very small. Thus, they are too soft to penetrate solid matter or even air. Therefore, XAFS studies on these elements must be performed under ultra-high vacuum conditions and are restricted to molecules adsorbed at the outer surface. Such SEXAFS investigations [41] are therefore of high interest for heterogeneous catalysts, but not for uniform catalysts such as zeolites.
- The *K* edges of the major framework elements of zeotypes (Al, Si, P) occur in an energy range from 1.5–2 keV. Most synchrotrons, however, focus either on the production of softer or of harder X-rays. In addition, the typical monochromator materials (silicon, germanium) cannot be used here. Only recently, a suitable material was found, the yttrium boride YB₆₆, which has high thermal and mechanical stability, can be grown as single crystals of sufficient size and possesses a crystallographic distance *d* large enough to diffract X-rays of the energy range mentioned above [101, 102]. The SiK edge spectra shown in Fig. 12 were obtained employing a YB₆₆ double crystal monochromator [71, 72].

Acknowledgements. The work of the author which is presented here was carried out at the synchrotron radiation sources in Hamburg, Germany (storage ring DORIS of the HASYLAB at DESY), at the SRS Daresbury (UK) and at the Stanford Synchrotron Radiation Laboratory (SSRL, USA). I thank these institutions for providing beam time and excellent experimental conditions. Thanks also go to Ronald Frahm (formerly at HASYLAB, now at the University of Wuppertal), Robert Bilsborrow (Daresbury) and Joe Wong (Lawrence Livermore National Laboratory). The help of Stefanie Assmann, Gianpietro van de Goor, Michael Fröba and Bernd Pillep in performing the measurements is acknowledged. Discussions with Michael Fröba, Bernd Pillep and Monika Hartl with regard to the interpretation of the spectra were extremely enlightening. This work was supported by the Fonds der Chemischen Industrie.

8

References

1. Teo BK (1986) EXAFS: Basic principles and data analysis. Inorganic chemistry concepts, vol 9. Springer, Berlin Heidelberg New York
2. Agarwal BK (1991) X-ray spectroscopy: an introduction. Springer series in optical sciences, vol 15. Springer, Berlin Heidelberg New York
3. Koningsberger DC, Prins R (eds) (1992) X-ray absorption. Chemical analysis, vol 92. Wiley, New York
4. Iwasawa Y (ed) (1996) X-ray absorption fine structure (XAFS for catalysts and surfaces) World Scientific, Singapore
5. Behrens P (1992) Trends Anal Chem 11:218
6. Behrens P (1992) Trends Anal Chem 11:237
7. Pages of the International XAFS Society on the WWW: <http://ixs.csrrri.iit.edu/IXS/index.html>
8. Stern EA (1974) Phys Rev B10:3027
9. Stern EA, Sayers DE, Lytle FW (1975) Phys Rev B11:4836
10. Lee PA, Pendry JB (1975) Phys Rev B11:2795
11. Boland JJ, Crane SE, Baldeschwieler JD (1982) J Chem Phys 77:142
12. Stern EA (1988) Theory of EXAFS. In: Koningsberger DC, Prins R (eds) X-ray absorption. Chemical analysis, vol 92. Wiley, New York, p 3
13. Brown GE, Calas G, Waychunas GA, Petiau J (1988) Rev Miner 18:431
14. Brouder C (1990) J Phys Condens Matter 2:701
15. Stern EA, Heald SM (1983) Basic principles and applications of EXAFS. In: Koch EE (ed) Handbook on synchrotron radiation, vol 1b. North Holland, New York, p 955
16. Bunker G (1983) Nucl Instrum Methods 207:437
17. Freund J, Ingalls R, Crozier ED (1989) Phys Rev B 39:12537
18. Magnan H, Chandesris D, Rossi G, Jezequel G, Hricovini K, Lecante J (1989) Phys Rev B40:9989
19. Teo BK, Lee PA (1979) J Am Chem Soc 101:2815
20. McKale AG, Veal BW, Paulikas AP, Chan S-K, Kanpp GS (1988) J Am Chem Soc 110:3763
21. Vaarkamp M, Dring I, Oldman RJ, Stern EA, Koningsberger DC (1994) Phys Rev B 50:7872
22. Rehr JJ, Albers RC (1990) Phys Rev B 41:8139
23. Mustre de Leon J, Rehr JJ, Zabinsky SI, Albers RC (1991) Phys Rev B 44:4146
24. Rehr JJ, Mustre de Leon J, Zabinsky SI, Albers RC (1991) J Am Chem Soc 113:14
25. Homepage of FEFf project on the WWW: <http://leonardo.phys.washington.edu/feff/>
26. Stern EA, Newville M, Ravel B, Yacoby Y, Haskel D (1995) Physica 208/209:117
27. Homepage of the UW XAFS program on the WWW: <http://leonardo.phys.washington.edu/uwxafs/>
28. Ressler T (1997) J Phys IV France 7:C2-269
29. Homepage of the WinXAS program on the WWW: http://ourworld.compuserve.com/homepages/t_ressler/
30. Homepage of the X-FIT program on the WWW: http://www.ansto.gov.au/natfac/asrp7_xfit.html
31. Teo BK (1981) J Am Chem Soc 103:3990
32. Filipponi A, Di Cicco A (1993) Synchr Radiation News 6:13
33. Uozomi T, Okada K, Kotani A, Durmeyer O, Kappler JP, Beaurepaire E, Parlebas JC (1992) Europhys Lett 18:85
34. Parlebas JC (1993) Phys Status Solidi B 178:9
35. Sainctavit P, Petiau J (1987) Physica B 158:347
36. Heald SM (1988) Design of an EXAFS experiment. In: Koningsberger DC, Prins R (eds) X-ray absorption. Chemical analysis, vol 92. Wiley, New York, p 87
37. Heald SM (1988) EXAFS with synchrotron radiation. In: Koningsberger DC, Prins R (eds) X-ray absorption. Chemical analysis, vol 92. Wiley, New York, p 119

38. Heald SM, Tranquada JM (1990) X-ray absorption spectroscopy: EXAFS and XANES. In: Rossiter BW, Hamilton JF (eds) *Physical methods of chemistry*, vol V. Determination of structural features of crystalline and amorphous solids, 2nd edn. Wiley, New York, p 189
39. Sayers DE, Bunker BA (1988) Data analysis. In: Koningsberger DC, Prins R (eds) *X-ray absorption. Chemical analysis*, vol 92. Wiley, New York, p 211
40. Heald SM, Stern EA (1977) *Phys Rev B* 16:5549
41. Stoehr J (1992) *NEXAFS spectroscopy*. Springer series in surface sciences, vol 25. Springer, Berlin Heidelberg New York
42. Behrens P, Felsche J, Niemann W (1991) *Catal Today* 8:479
43. McCusker LB, Meier WM, Suzuki K, Shin S (1986) *Zeolites* 6:388
44. Newsam JM, Jorgensen JD (1987) *Zeolites* 7:569
45. Pack MJ, Dann SE, Weller MT (1996) *Chem Commun* 1347
46. Behrens P, Kosslick H, Tuan VA, Fröba M, Neissendorfer F (1995) *Microporous Mater* 3: 433
47. Trong On D, Bonneviot L, Bittar A, Sayari A, Kaliaguine S (1992) *J Mol Catal* 74:233
48. Lopez A, Tuilier MH, Guth JL, Delmotte L, Popa JM (1993) *J Solid State Chem* 102:480
49. Novak Tusar N, Meden A, Arcon I, Kodre A, Kaucic V (1995) *Stud Surf Sci Catal* 94:232
50. Hagen A, Hallmeier K-H, Hennig C, Szargan R, Inui T, Roessner F (1995) In: Beyer HK, Karge HG, Kiricsi J, Nagy JB (eds) *Catalysis by microporous materials, Proc ZEOCAT '95, Sombathely, Hungary, July 9–13, 1995*, Elsevier, Amsterdam. *Stud Surf Sci Catal* 94:195
51. Tuel A, Arcon I, Novak Tusar N, Meden A, Kaucic V (1996) *Microporous Mater* 7:271
52. Sankar G, Bell RG, Thomas JM, Anderson MW, Wright PA, Rocha J (1996) *J Phys Chem* 100:449
53. Moen A, Nicholson DG, Ronning M, Lamble GM, Lee J-F, Emerich H (1997) *J Chem Soc Faraday Trans* 93:4071
54. Axon SA, Fox KK, Carr SW, Klinowski J (1992) *Chem Phys Lett* 189:1
55. Morrison TI, Iton LE, Shen GK, Stucky GD, Suib SL (1981) *J Chem Phys* 75:4086
56. Morrison TI, Reis AH, Gebert E, Iton LE, Stucky GD, Suib SL (1980) *J Chem Phys* 72:6276
57. Morrison TI, Iton LE, Shenoy GK, Stucky GD, Suib SL, Reis AH (1980) *J Chem Phys* 73:4705
58. Couves JW, Jones RH, Thomas JM, Smith BJ (1990) *Adv Mater* 2:181
59. George AR, Catlow CRA, Thomas JM (1991) *Catal Lett* 8:193
60. van de Goor G (1995) PhD thesis, Universität Konstanz, Germany
61. Wirnsberger G (1998) PhD thesis, Technische Universität Graz, Austria
62. Pillep B (1999) PhD thesis, Ludwig-Maximilians-Universität, München, Germany
63. Wirnsberger G, Pillep B, Knoll P, Popitsch A, van de Goor G, Behrens P (2002) *Chem Eur J* 8:3927
64. Okamoto Y, Katsuyama H, Yoshida K, Nakai K, Matsuo M, Sakamoto Y, Yu J, Terasaki O (1996) *J Chem Soc Faraday Trans* 96:4647
65. Okamoto Y (1996) Preparation and catalysis of highly dispersed metal sulfide catalysts for hydrodesulfurization. In: Absi-Halabi M (ed) *Catalysts in petroleum refining and petrochemical industries*. Elsevier, Amsterdam, p 77
66. Okamoto Y, Katsuyama H (1996) *Stud Surf Sci Catal* 101:503
67. Lamberti C, Spoto G, Scarano D, Paze C, Salvalaggio M, Bordiga S, Zecchina A, Turnes Palomino G, D'Apacito F (1997) *Chem Phys Lett* 269:500
68. Qiu S, Ohnishi R, Ichikawa M (1994) *J Phys Chem* 98:2719
69. Salama TM, Shido T, Ohnishi R, Ichikawa M (1996) *J Phys Chem* 100:3688
70. Behrens P (1992) *Solid State Commun* 81:235
71. Fröba M, Pillep B, Wong J, Behrens P, to be published
72. Fröba M, Behrens P, Wong J, Engelhardt G, Haggemüller C, van de Goor G, Rowen M, Tanaka T, Schwieger W (1995) *Mat Res Soc Symp Proc* 371:99
73. Fontaine A, Dartyge E, Itie JP, Jucha A, Polian A, Tolentino H, Tourillon G (1989) *Top Curr Chem* 151:179
74. Fontaine A, Baudet F, Dartyge E, Guay D, Tolentino H, Tourillon G (1992) Time-resolved X-ray absorption spectroscopy. In: Beswick A (ed) *Synchrotron radiation and dynamic phenomena*. AIP Conf Proc, vol 248, p 496

75. Frahm R (1988) *Nucl Instrum Methods A*270: 578–581
76. Frahm R, Wong J, Holt JB, Larson EM, Rupp B, Waide PA (1992) Solid combustion reactions characterized by time-resolved X-ray absorption spectroscopy. In: Beswick A (ed) *Synchrotron radiation and dynamic phenomena*, AIP Conf Proc, vol 248, p 615
77. Shido T, Prins R (1998) *Curr Opin Solid State Mater Sci* 3:330
78. Yamamoto Y, Matsuzaki T, Tanaka S, Nishihira K, Ohdan K, Nakamura A, Okamoto Y (1997) *J Chem Soc Faraday* 93:3721
79. Cimini F, Prins R (1997) *J Phys Chem B* 101:5285
80. Lamberti C, Bordiga S, Salvalaggio M, Spoto G, Zecchina A (1997) *J Phys Chem B* 101:344
81. Barrett PA, Sankar G, Jones RH, Catlow CRA, Thomas JM (1997) *J Phys Chem B* 101:9555
82. Behrens P, unpublished results
83. Behrens P, Aßmann S, Felsche J (1992) *HASYLAB Annual Report 1991*, HASYLAB/DESY, Hamburg, p 225
84. Couves JW, Thomas JM, Catlow CRA, Greaves GN, Baker G, Dent AJ (1990) *J Phys Chem* 94:17
85. Hagelstein M, Cunis S, Rabe P, Piffer R, Frahm R (1992) In: Beswick A (ed.) *AIP Conf Proc*, vol 258, p 575
86. Thomas JM, Greaves GN (1994) *Science* 265:1675
87. Sankar G, Wright PA, Natarajan S, Thomas JM, Greaves GN, Dent AJ, Dobson BR, Ramsdale CA, Jones RH (1993) *J Phys Chem* 97:9550
88. Colyer LM, Greaves GN, Dent AJ, Carr SW, Fox KK, Jones RH (1994) In: Weitkamp J, Karge HG, Pfeifer H, Hölderich W (eds) *Zeolites and related microporous materials: state of the art 1994*, Proc 10th Int Zeolite Conf, Garmisch-Partenkirchen, Germany, July 17–22, 1994, Elsevier, Amsterdam, 1994. *Stud Surf Sci Catal* 84:387
89. Colyer LM, Greaves GN, Dent AJ, Fox KK, Carr SW, Jones RH (1995) *Nucl Instrum Methods Phys Res B* 97:107
90. Sankar G, Thomas JM, Rey F, Greaves GN (1995) *J Chem Soc Chem Commun* 2549
91. Barrett PA, Sankar G, Catlow CRA, Thomas JM (1995) *J Phys Chem Solids* 56:1395
92. Clausen BS, Grabaek K, Steffensen G, Hansen PL, Topsoe H (1993) *Catal Lett* 20:23
93. Shannon U, Maschmeyer T, Sankar G, Thomas JM, Oldroyd RD, Sheehy M, Madill D, Waller AM, Townsend RP (1997) *Catal Lett* 44:23
94. Disko MM, Ahn CC, Fulz B (eds) (1992) *Transmission electron energy loss spectroscopy in materials science. The Minerals, Metals and Materials Society*, Warrendale, PA, USA
95. Egerton R (1997) *Phys World* 47
96. Wilkinson AP, Cheetham AK, Tang SC, Reppart WJ (1992) *J Chem Soc Chem Commun* 1485
97. Helliwell M, Gallois B, Kariuki BM, Kaucic V, Helliwell JR (1993) *Acta Cryst B* 49:420
98. Jones RH, Lightfoot P, Ormerod RM (1995) *J Phys Chem Solids* 56:1377
99. Behrens P, Felsche J, Vetter S, Schulz-Ekloff G, Jaeger NI, Niemann W (1991) *J Chem Soc Chem Commun* 678
100. Tröger L, Hilbrandt N, Epple M (1997) *Synchrotron Radiation News* 10:11
101. Wong J, Rek Z, Rowen M, Tanaka T, Schaeffers F, Mueller B, George GN, Pickering I, Via GH, DeVries B, Brown GE Jr, Fröba M (1995) *Physica B* 208/209:220
102. Wong J, Fröba M, Tamura E, Rowen M, Rek Z, Tanaka T (1997) *J Physique IV* 7:511

Photoelectron Spectroscopy of Zeolites

W. Grünert¹ · R. Schlögl²

¹ Lehrstuhl für Technische Chemie, Fakultät für Chemie, Ruhr-Universität Bochum,
Postfach 102148, 44780 Bochum, Germany

E-mail: w.gruenert@techem.ruhr-uni-bochum.de

² Fritz-Haber-Institut der Max-Planck-Gesellschaft, Abt. Anorganische Chemie, Faraday-
weg 4–6, 14195 Berlin, Germany. *E-mail: robert@graphite.RZ-Berlin.MPG.de*

Part I

1	Methodical Aspects	469
1.1	Introduction: the Basic Experiment	469
1.2	Surface Sensitivity and Information Depth	470
1.3	Instrumentation and Sample Handling	472
1.4	Sample Charging	474
1.5	Spectral Information	478
1.6	Accuracy of Chemical Shift Data	484
1.7	Interpretation of Chemical Shift Data	485

Part II

2	Case Studies	490
2.1	Constitutional Elements	491
2.1.1	Surface Composition	491
2.1.2	Acidity and Basicity	495
2.2	Ion Exchange	499
2.3	Isomorphous Substitution	504
2.4	Host-Guest Systems	506
2.4.1	Metals and Alloys	507
2.4.2	Other Guests	508
	References for Part I	509
	References for Part II	510

Abbreviations

Al ^{nf}	non-framework aluminium
B	Brønsted
BE	binding energy
CMA	cylindrical mirror analyzer
DTA	differential thermoanalysis
EELS	electron energy loss spectroscopy
EDTA	ethylenediaminetetraacetic acid

EPR	electron paramagnetic resonance
ESCA	electron spectroscopy for chemical analysis
EXAFS	extended X-ray absorption fine structure
FAT	fixed analyzer transition
FRR	fixed retardation ratio
HSA	hemispherical analyzer
IR	infrared
ISS	ion scattering spectroscopy
L	Lewis
MI	metal ion
MS	mass spectrometry
NMR	nuclear magnetic resonance
SIMS	secondary ion mass spectroscopy
TEM	transmission electron spectroscopy
TG	thermogravimetry
TPD	temperature-programmed desorption
TPR	temperature-programmed reduction
UHV	ultra-high vacuum
UPS	ultraviolet photoelectron spectroscopy
UV	ultraviolet
XAES	X-ray induced Auger electron spectroscopy
XANES	X-ray absorption near-edge spectroscopy
XPS	X-ray photoelectron spectroscopy
XRD	X-ray diffraction

Symbols

d	distance from the surface layer
E	energy
E_f	Fermi energy
ΔE^c	chemical shift of core level
I	integral intensity
I_o	intensity from surface layer
I	current
K^c	proportionality constant
q	valence charge
R	distance from central atom
U	potential
V	Madelung potential
λ	mean free path of photoelectrons

Part I

1

Methodical Aspects

1.1

Introduction: the Basic Experiment

A family of surface analytical techniques is designated “photoemission spectroscopies” according to their common mode of excitation. In these experiments a solid sample is excited by photons in the energy range from 20–1500 eV. Modern experiments use strongly monochromatic sources with linewidths between 0.005 and 0.3 eV or synchrotron sources. Most of the data in the literature were measured with analytical instruments using less monochromatic radiation with 0.8 eV linewidth. One effect of this irradiation is the photoemission of electrons with a wide range of kinetic energies. Selecting only those electrons that have characteristic sharp energy distributions allows the characteristic emissions from either core levels of atomic bound states or from the valence band to be recorded. These spectroscopic techniques are known as XPS – *X-ray induced photoelectron spectroscopy* (for core levels), or UPS – *ultraviolet induced photoelectron spectroscopy* (for the valence band), or among chemists under the historic designation [1] ESCA – *electron spectroscopy for chemical analysis*.

All experiments result in a spectrum which represents the energy distribution of photoelectrons convoluted with instrumental functions from the analyzer and the detector system. These functions are fundamentally different for the two common analyzer types; these are the cylindrical mirror analyzer (CMA) and the hemispherical analyzer (HSA). A description of the function of both devices can be found in the literature [2]. In commercial analytical instruments, the HSA is more common than the CMA and all further discussion is limited to this device.

The present text is devoted to the zeolite researcher who uses these methods as an analytical tool. It is organized into two independent sections dealing with the general aspects of the methods and with a selection of case studies. The general section is not a full description of the theory and instrumentation but focuses on specific points that are of relevance for the zeolite researcher. The case studies represent selected examples that are documented such that a meaningful interpretation of the data presented is possible. Unlike other applications of photoemission, the documentation of the data acquisition and data reduction is of extreme importance for reasons that will be discussed in the general section. For an in-depth treatment of photoemission the reader is referred to the textbooks of Briggs and Seah [2], Cardona and Ley [3], and Hüfner [4]. Many multi-method catalyst characterization textbooks also include illustrative sections on photoemission.

After their excitation from a bound state within an atom, the photoelectrons have to move through the other electron shells of the atom, through the lattice of a solid sample, through the surface barrier into the ultra-high vacuum (UHV) of the instrument and through the environment of the analyzer-detector device. The cross section of scattering processes with any matter is very large for elec-

trons with kinetic energies of 0–1500 eV. This necessitates the operation of the spectrometer in ultra-high vacuum to avoid collisions of the photoelectrons with gas molecules and adsorbates on the sample. In addition, the collision probability within the sample limits the depth from which the electrons can escape with little energetic modifications to a few monolayers, which causes the surface sensitivity of the method. The scattering cross sections vary in the energy range of interest over several orders of magnitude with the kinetic energy. The signal attenuation within the bulk of the sample may be defined as:

$$I = I_0 \exp(-d/\lambda) \quad (1)$$

where I_0 represents the spectral intensity from the surface layer, d the distance from the surface and λ the mean free pathlength which is a material constant.

1.2

Surface Sensitivity and Information Depth

The depth of information is considered as the depth from which an e -th part of the intensity I_0 emerges at the surface. It is a material constant and not an elemental constant as often inferred from the original literature. The reason for this is that the total attenuation is a convolution of the scattering of the photoelectron with other core electrons (element specific) and with the valence electrons (material specific). The scattering with valence electrons is a very efficient process [5] which reduces the mean free path in metals to a few monolayers for kinetic energies between 10 and 100 eV, whereas in ionic compounds the mean free path can be estimated to be ten times larger than in conducting materials. The determination of this important quantity is a difficult and controversial matter that has led to the definition of a “universal” curve for the surface sensitivity of all materials as a function of the kinetic energy. The curve is represented in Fig. 1. The data for a typical metal are contrasted with those for insulators [6]. The spread indicates the range of surface sensitivities that can be expected for different materials. The indicated area in the plot shows the parameters for useful XPS analysis occurring with zeolitic materials. The surface sensitivity is limited to about one crystallographic unit cell of these materials at energies useful for UV-excited valence band spectroscopy (UPS). Core level spectroscopy with typical kinetic energies of around 1000 eV for the silicon and aluminium main lines is slightly less surface-sensitive but will not be drastically different in its information depth relative to that of UPS.

The determination of the depth of information in zeolite materials is difficult as the termination of the oxidic surface is not equal to that of a bulk crystallographic unit cell. A film of strongly bound adsorbates (mostly water) and possible contamination from synthesis, catalytic application or ion exchange procedures (salts) will cover the zeolite surface and compensate for the significant polarity of the surface which is an unavoidable consequence of the termination of the crystal at its surface. In quantitative elemental analysis of zeolite materials, there will always be a significant excess of oxygen and carbon and often of alkali ions. This does not mean that these excess atoms are uniformly distributed

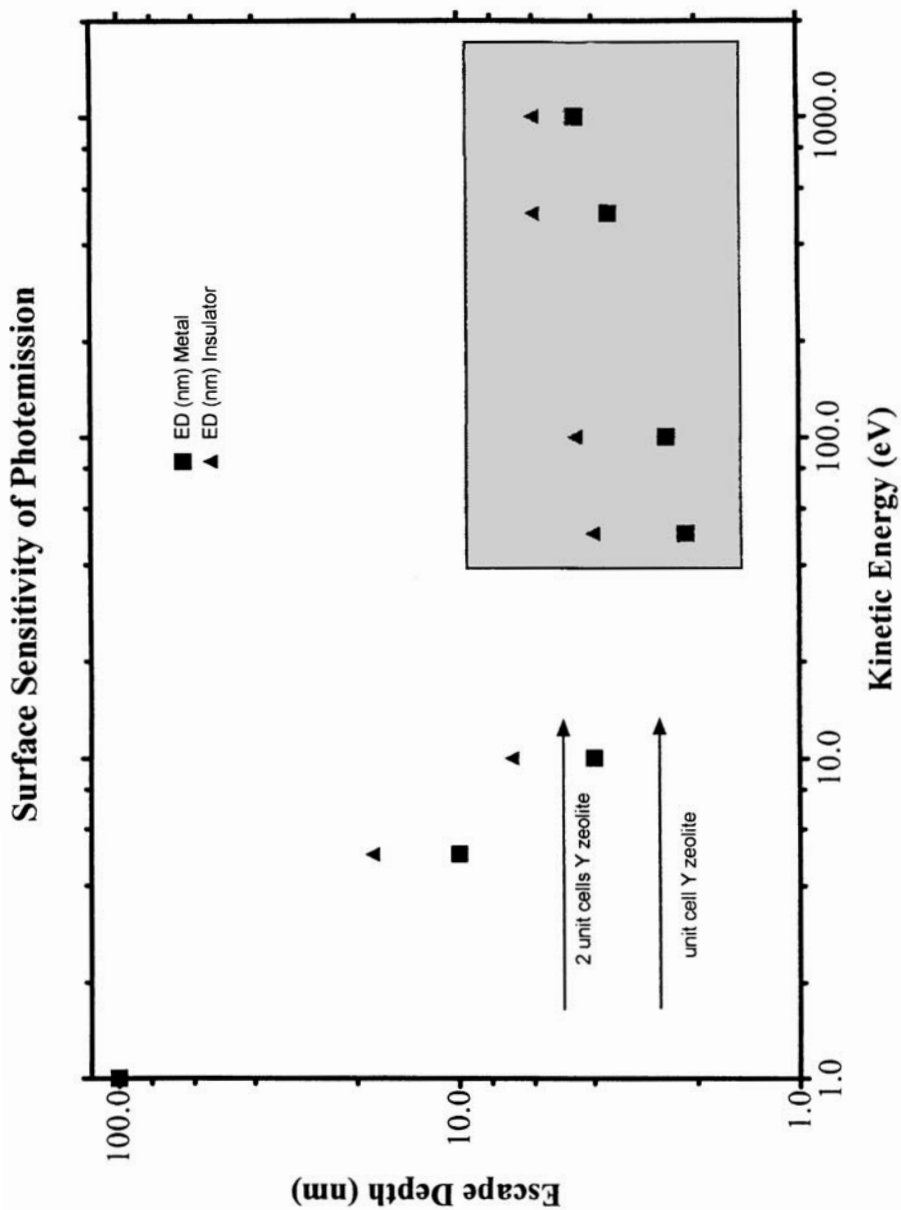


Fig. 1. “Universal” curve of escape depth of elastic photoelectrons from materials as a function of the electron’s kinetic energy (not of the “binding” energy of the emitting electronic level). The *arrows* indicate the coarse relationship between the curve and the crystallographic unit cell thickness of a typical zeolite. The *indicated area* depicts the range of parameters relevant for classical XPS analysis of zeolites

within the zeolite product. Discrepancies in bulk analytical data are to be expected and indicate the chemical heterogeneity of the outer surface that is accessible to XPS analysis relative to the inner surface which contributes only a fraction to the spectral information obtained by this technique. The determination of this difference in surface-to-bulk composition can be a useful application of XPS in conjunction with other analytical methods, as will be illustrated in Part II.

1.3

Instrumentation and Sample Handling

The main characteristics of a photoemission experiment are presented in Fig. 2. The simplest instrument consists of a UHV chamber with a light source, the sample and the analyzer with its detection unit.

The light source is a soft X-ray tube with Mg or Al as anode material. These two materials produce photons of 1253.6 and 1486.6 eV energy, respectively, with narrow line profiles of about 0.7 eV width. This narrow energy distribution is the main reason for selecting these anode materials that can, at typically 200–1000 W power loss, produce stable X-ray beams over several months of uninterrupted measurement time. In order to minimize the intensity of the diffuse radiation background and to protect the sample from heat and stray electrons, the light sources are covered with thin aluminium windows of 1–3 μm thickness which must be light-tight for reliable operation in particular with zeolitic samples. Details of the design and operation of such light sources can be found in the literature [3].

X-ray diffraction-focusing monochromators are used in modern instruments to remove the background from *Bremsstrahlung* and to sharpen the excitation line further to about 0.3 eV width. These measures overcompensate the severe loss of intensity caused by the non-perfect diffraction geometry in obtaining useful spectra; however, samples of high smoothness and well-defined surface geometry are needed, as the sample is part of the focusing geometry. Monochromated X-rays exhibit further the considerable advantage of complete suppression of the X-ray satellites arising from unwanted transitions within the excited anode materials. These satellite lines (see below) cause echo spectra of the main photoemission spectrum that can lead to severe problems with spectral interpretation (e.g., vanadium and platinum in zeolite materials, analysis of spectra of 3d- and 4d-transition metal ions in zeolites). Several mathematical procedures (known as “satellite subtraction”) have been developed for conventional light sources to remove these echo spectra which all rely on the assumption that the satellite intensity contribution to the whole spectrum is constant with time and energy.

Light sources for UPS are gas discharge lamps which use the light emission from a noble gas plasma operating in the pressure range of several mbar. Sophisticated collimation and differential pumping arrangements are required to keep the pressure in the analysis chamber within the UHV range and to avoid thermal loads on the sample. In zeolite research, these sources are rarely used.

The sample is introduced via an airlock-degassing stage into the UHV region. Significant attention has to be paid to zeolite samples as their internal pore system and the polar surface can bind large amounts of volatiles (water, solvents)

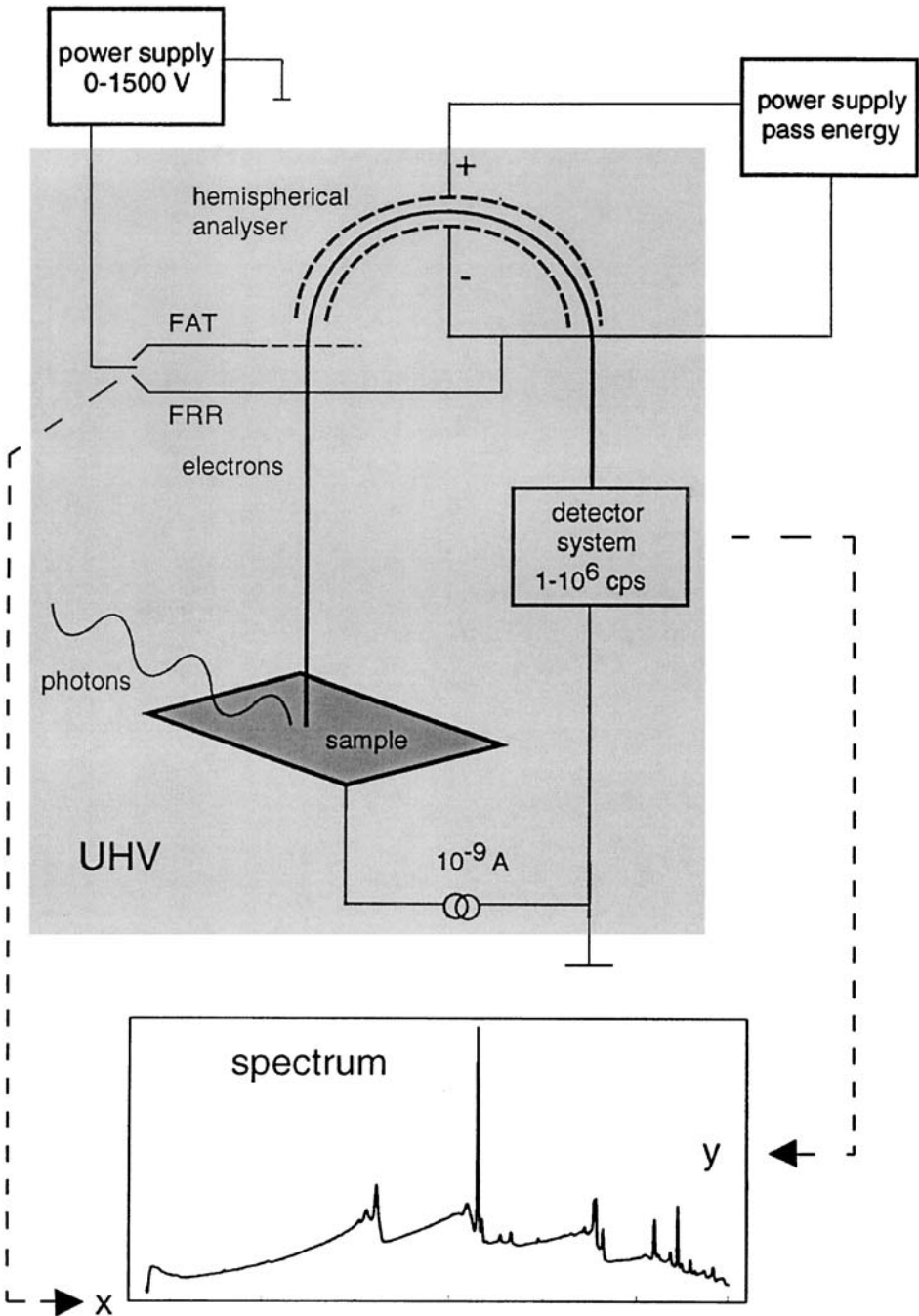


Fig. 2. The main constituents of a photoemission experiment. The relationships between the instrument and the resulting spectrum are indicated. *FAT* Fixed analyzer transmission; *FRR* fixed retardation ratio

which can interfere during their desorption with the analysis process. A pre-pumping and heating protocol to clean the surface prior to measurement is a very necessary step for generating reliable and internally consistent data sets.

The size of the sample is in conventional spectrometers about 0.5–1 cm² and must be uniform in thickness and compactness. Only then will a uniform electrostatic situation occur over the insulating surface which forms the basis of all spectral interpretation. The sample should be as thin as possible and must be supported on a conducting base material. Silver, gold and graphite are materials of choice depending on the analytical problem. The zeolite powder should be fixed preferably by drying a slurry of ultrasonically dispersed material in water or an inert organic solvent (alkanes, haloalkanes). The preparation should be optically non-dense in order to minimize the capacitance between the insulating surface and the powder-support interface. An alternative preparative technique is the mechanically solid connection of the powder to a conductor, e.g., indium foil or graphite powder in the form of a pellet. However, such samples are prone to massive charging effects during photoemission and need significant attention during data analysis. Absolutely unsuitable are techniques of sample preparation that use powder or pellets fixed with adhesive tape to a metallic substrate. These samples are contaminated and produce an ill-defined electrostatic situation at the surface leading to broad or even artificially split core level lines.

Only a few data are available on single crystals of zeolites which can either be studied as arrays of crystals or as single crystals in modern imaging spectrometers which allow the sample size to be reduced to the order of micrometers.

Great care must be taken not only to prevent contamination of the spectrometer by outgassing molecules from the zeolite sample, but also to prevent contamination of an activated zeolite by the residual gas from the spectrometer. In older spectrometers, hydrocarbon oil residues are common sources of contamination; in modern spectrometers, water and CO are sorbed by the sample which often exhibits a larger geometric surface area than the total surface of the analyzer chamber. The contamination interferes with the quantitative surface analysis, weakens the signal from the zeolite and can lead to serious problems when the zeolite is heated in situ. Coke formation and internal steaming (despite the UHV surrounding) can cause problems, in particular when poor base pressures in the 10⁻⁸-mbar pressure range are applied.

1.4

Sample Charging

The main problem with zeolites as samples for photoemission is their poor electrical conductivity. The equivalent of several nA is emitted from the irradiated sample. This is orders of magnitude larger than the current seen by the detector, which is due, for instance, to the limited collection angle of the analyzer, the dominating secondary electron current which is not usually analyzed and the transmission losses through the analyzer. The constant current out of the sample creates a significant potential through the dielectric resistance of the zeolite. The associated potential of the order of several hundred volts at the surface creates a retarding field for the photoelectrons and introduces an ill-defined energy scale

for the spectrum. The unavoidable and often characteristic local chemical heterogeneity of the zeolite (e.g., as metal-loaded or ion-exchanged material) will lead to local variations in the potential created by the photoelectron current. The resulting differential potential will create inhomogeneities in the retarding electrostatic field and create not one single shifted energy scale but a multitude of them with varying zero energies. Broadening and even splitting of core level lines are the consequences of this problem. The effects will be the more severe the more the sample is macroscopically or chemically heterogeneous (uneven distribution of metal clusters or coke deposits, extra-framework alumina in islands). Counterbalanced is this unavoidable effect by contamination of the sample. Most efficient here is strongly chemisorbed water leading to proton conductivity. Hydrocarbon contamination and coke will also reduce the sample potential. If the sources of contamination are unevenly distributed over the sample then their charge compensation effect will also be heterogeneous and again multiply referenced energy scales will result.

The charging phenomenon is depicted in Fig. 3. Chemical and macroscopic heterogeneity of the zeolite material on the metallic substrate is assumed. The electrical equivalent diagram (Fig. 3B) represents the effects. The resistivity of the sample across its surface does not permit equilibration of the local differences of the potentials arising from the photoemission current through the surface. The schematic energy level diagram (Fig. 3C) reveals the consequences of the local variation in surface potential. In practice, absolute and differential charging up to several eV (5–7 eV) can be observed. This range of artifacts in energy shifts is as large as the whole range of true chemical shifts. The chemical interpretation of binding energy data is thus fully affected by the charging phenomena which require the utmost care in their analysis. Zeolitic materials are especially susceptible to these phenomena as the powdered texture and the large internal inhomogeneity caused by the internal surface and its adsorbates create a wide variety of trajectories for electrical currents from the substrate to the outer surface with largely differing electrical resistivities which are not short-circuited by metallic conduction.

The technique to avoid charging by evaporating gold or other elements on the sample should never be used as the thin layer thicknesses required to “see” through the charge compensating layer will always lead to inhomogeneous distribution of the gold and thus cause the same effect as the inhomogeneous contamination layer.

With zeolites it is possible to compensate charging by heating the sample *in situ* to temperatures where either proton, cation or oxygen anion conductivity causes a complete breakdown of the insulating properties of the sample [7]. Inert sample holders, a well-outgassed sample and a very inert vacuum environment are required in addition to a field-free heating device for the successful application of this technique. It is limited to thermally stable zeolite samples, as temperatures of about 650 K are required for efficient compensation.

When samples with no chemically reducible constituents (guest species) are investigated, then the method of charge compensation can be applied by a flood of slow electrons generated in a “flood gun” (essentially a glowing filament with a small extraction potential accelerating electrons with about 50 eV onto the

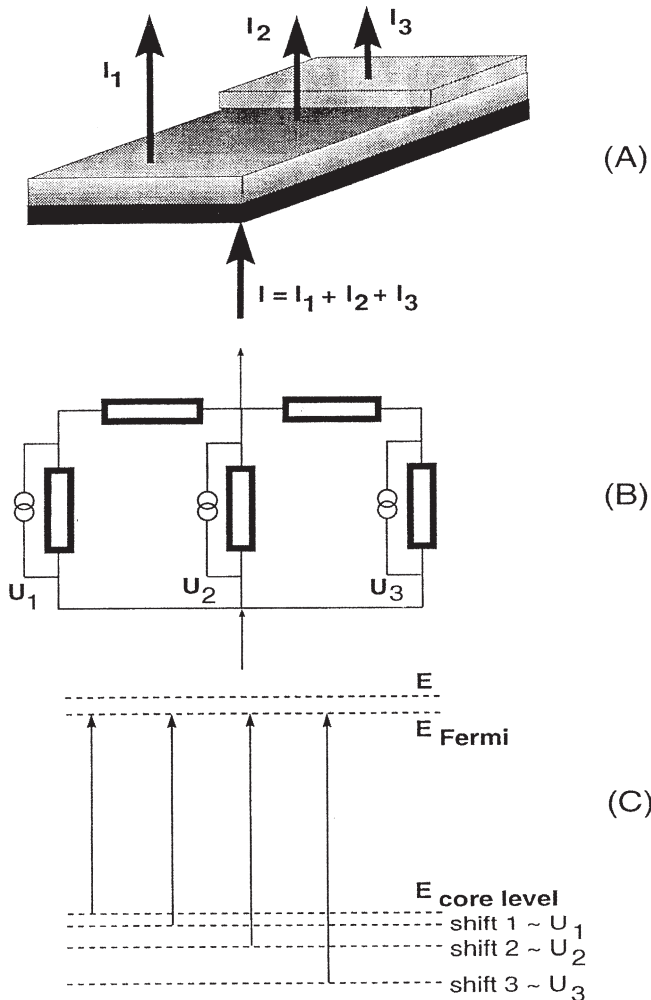


Fig. 3A–C. Representations of the differential-charging effect. **A** Heterogeneous sample consisting of conducting base (*black*) and a structured insulating surface (*grey*). The *arrows* depict schematically current trajectories for different spots of the sample denoted by the indices 1, 2, 3 (I_1, I_2, I_3 – emitted currents). Due to different resistance properties, different potentials U_1, U_2, U_3 arise. **B** Electrical equivalence diagram for a sample under constant irradiation. **C** Effect of differential charging on the position of the energy scale of the photoemission experiment

sample). In Fig. 4 an example is shown of determining the absolute value of the Si 2s chemical shifts in two zeolite materials. It is pointed out that in zeolites the application of the minimum kinetic energy of the flood-gun electrons is essential to obtain curves with a minimum that indicates charge compensation, as shown in the figure. Otherwise monotonous changes are observed of the binding energy with the electron current flowing over the sample. Several tests with

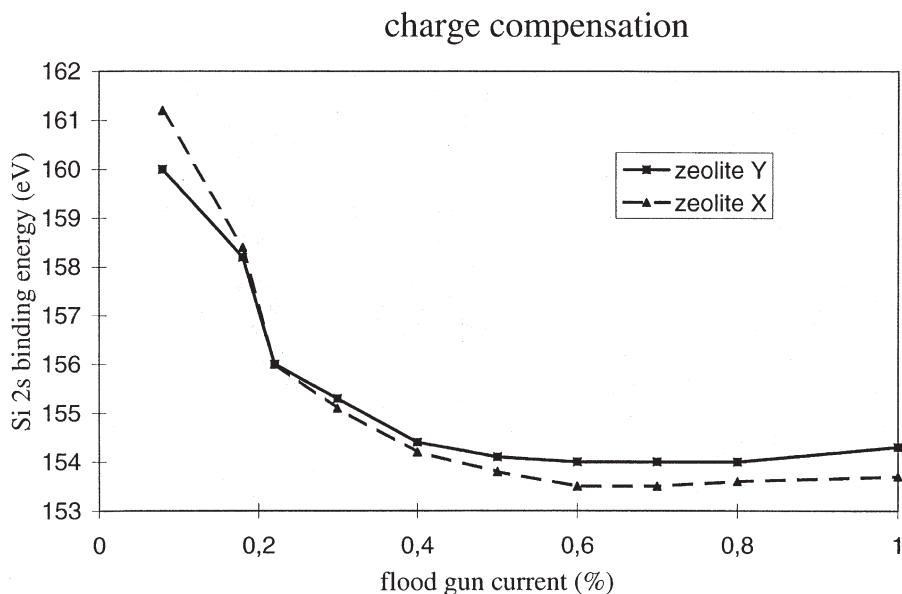


Fig. 4. Dependence of the position of the Si 2s XPS peak on the parameters of a flood-gun charge compensation device. A minimal emission of the flood-gun device (1% of the possible emission!) was useful to obtain the clear minimum of the uncharged binding energy. The difference in the absolute binding energy for the two zeolites is significant and is discussed in the text

varied flood-gun parameters have to be performed, as “intermediate” results can be obtained with erroneous minima leading to sample-independent but flood-gun dependent values of the apparent binding energies. For this reason the samples have to be clean and hydrocarbon-free in order to withstand several flood-gun tests without chemical modification by surface reductions. Clean cation-exchanged and dehydroxylated zeolites fulfill these conditions.

For more practical applications it is useful to determine internal standard chemical shifts (such as Si 2s) for reference zeolites and to use these values for numerical charge correction without a flood gun for the more sensitive samples. Care must be taken as these internal standards depend on the type of zeolite and cannot be used as universal values such as often done with the C 1s level. The data in Fig. 4 give an example of the spread of the position of standard lines. Several explanations have been given for these trends (cf. Part II). An interpretation based on a “Madelung shift” argument [8] has been recently substantiated by density-functional calculations [9] although the latter were undertaken on a basis that still includes some simplifications with respect to the true origins of chemical shifts (see below).

The use of the “adventitious” carbon with 285 eV as internal reference is the most commonly used method for correcting charging. The energy scale of the measured data set is shifted such that the maximum of the C 1s line occurs at 285.0 eV assuming that elemental carbon and/or hydrocarbons are the source of

the C 1s line. Despite its popularity it is a risky method for correction, as differential charging may be overlooked. An example is given in Fig. 5. A zeolite Y sample loaded with ruthenium clusters was measured in the as-prepared state in a good contamination-free UHV environment. The shape of the Si 2s signal shown in the inset indicates the presence of multiply referenced binding energy scales. Not only the split line but also the non-Lorentzian line profile indicates the presence of differential charging in an energy range of 0.3–4.8 eV. The shape of the uncharged carbon 1s line that is overlapping with the Ru 3d line doublet due to charging reveals the presence of carbon-hetero bonds. To account for this non-hydrocarbon fraction the reference carbon line was displaced from the arbitrary maximum at 285 eV, as shown in the figure. Chemical reduction with hydrogen using a sample preparation chamber and atmospheric pressure removed almost all carbon contamination. The clearly visible Ru 3d doublet occurs, however, at a much too high binding energy relative to the uncharged carbon. This is a clear example of differential charging between a zeolite surface covered with adventitious carbon and the ruthenium metal guest species located in the inner space of the zeolite with no electrical contact to the surface. The method of energy scale correction with the carbon “standard” is inapplicable to such a problem.

The problem can be solved by applying an external electric field between the sample surface and the entrance slit of the analyzer. This additional field either compensates or enhances the electrical field created by the specimen current on the surface. By changing polarity and field strength (via the applied voltage) all types of charging can be identified. Spectrum A in Fig. 5 was obtained with a negative polarity of the additional field (“tubus”), spectrum B with positive polarity. It seems that the adventitious carbon is not charged at all, as no shift was observed for the C 1s peak maximum. The Ru lines extended as in the spectrum without an external field, however, over an energy range larger than the spin-orbit splitting (4.1 eV) and the chemical shift range. This and the small peak at 280 eV in all spectra of the reduced sample indicated the existence of two Ru species, one with electrical contact to the carbon and one without this contact. Spectrum B with changed polarity of the applied external field revealed clearly the presence of the two species now with two well-resolved Ru 3d doublets. From the shifts of the Si 2s line with the external field and the knowledge of the Si 2s absolute binding energy (from a flood-gun experiment with Na-Y zeolite), the correct positions of all lines were established, as indicated in Fig. 5. It can be concluded that metallic Ru particles on the external surface of the zeolite coexist with intercalated clusters of electronic structure different from that of metallic Ru. As a result, the amount of surface carbon would have been overestimated by using the spectrum in the “as-reduced” state.

1.5

Spectral Information

The emitted photoelectrons are collected by an electron optical device from a solid angle significantly wider than defined by the entrance aperture of the analyzer. Modern instruments use sophisticated lens systems allowing the imaging of the sample by the photoelectrons. The hemispherical analyzer is an electro-

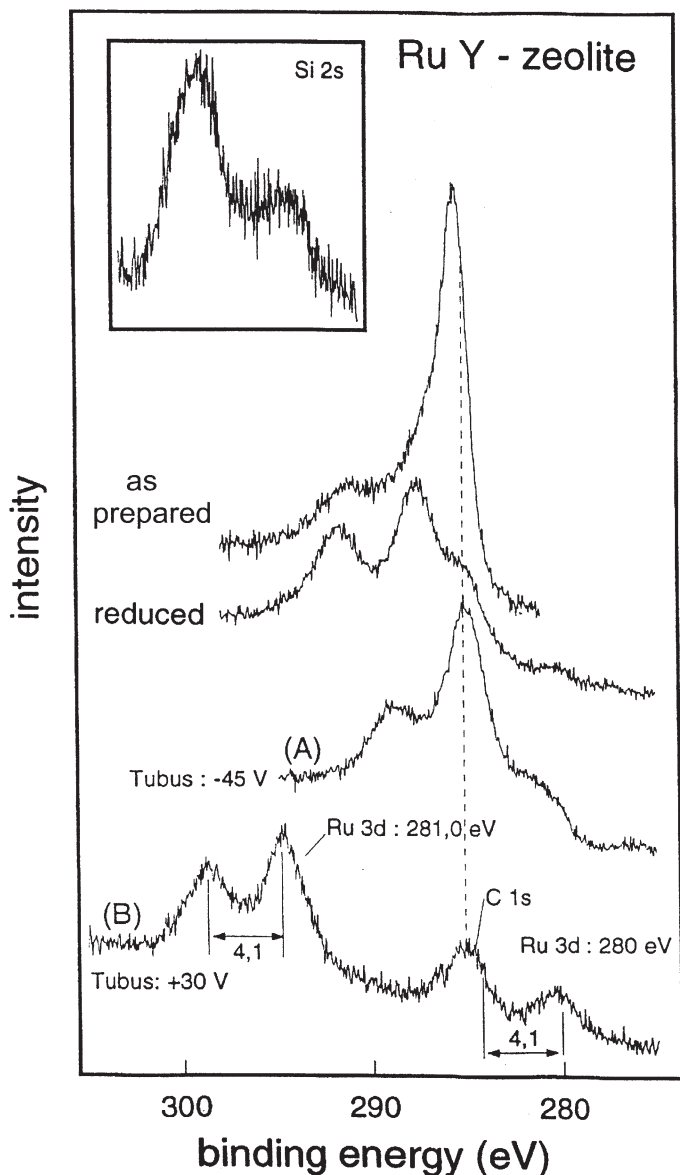


Fig. 5. Illustration of the effects of differential charging on the spectrum of a Ru Y zeolite sample. For a detailed discussion, see text. The term “tubus” in the figure designates the use of a magnetic field shielding tubus as electrode to apply an additional external electrostatic field superimposed on the field created by the charging of the sample surface. The two fields affect the kinetic energy of the photoelectrons moving in the space between the sample surface and the grounded entrance slit of the electron optical device collecting the electrons for the analyzer. **A** Spectrum of the reduced sample with negative polarity on the tubus; **B** spectrum with positive tubus polarity. The Ru 3d binding energies given are corrected for the shift caused by the extra field

static energy dispersion device [10] that images the entrance slit onto the detector for a small window of kinetic energies. These kinetic energies are either varied constantly during spectrum acquisition by changing the potential difference between the analyzer and the electric ground on which the sample is also fixed to (as shown in Fig. 2) or, alternatively, the analyzer is operated with a fixed potential difference between the electrodes (pass energy) and with respect to the sample, and the energy scan is accomplished by a variable retarding field. The difference in these two modes of operation lies in the strongly different convolution function [3, 11] by which the intensity distribution of the spectrum is modified. The convolution function is characteristic of each individual analyzer, of the spectrometer geometry, and of the operation mode. In the constant transmission mode or pass energy mode a fixed analyzer potential is selected which determines the resolution of the analyzer at fixed geometry and slit width. This FAT mode (fixed analyzer transmission) allows for a constant resolution over the entire spectral range. Its disadvantage is the sensitivity to background at low kinetic energies and the varying signal-to-noise ratio with decreasing kinetic energy. In the other mode, the electrons are decelerated by a constant ratio from their initial kinetic energy. The resolution varies with kinetic energy and is not constant for different spectral regions. The background suppression is very significant towards low kinetic energies and the signal-to-noise ratio is constant over the spectral range. This FRR (fixed retarding ratio) mode is preferentially used for wide scan spectra and for detection of weak peaks at low kinetic energies. It is not suitable for reliable quantification.

Quantitative spectra with optimized resolution are recorded in the FAT mode with optimized pass energies. Figure 6 exemplifies the drastic effects of the analyzer convolution function on a photoemission spectrum for a valence band UPS experiment on graphite. The spectra characterize the very same surface and are both recorded with HeI radiation. The characteristic differences of the two operation modes of the hemispherical analyzer (LH EA 200) can be clearly seen as well as the different suitability of the relevant spectra for qualitative and quantitative analysis. In XPS data, the same differences occur for the two modes of operation. The intrinsically more symmetric line profile of core level lines tends, however, to obscure the effects of the analyzer in narrow scan spectra.

A wide scan spectrum of a ZSM-5 sample in the FRR mode is shown in Fig. 7. Such a spectrum should always be recorded at the beginning of an XPS investigation in order to identify all elements present. In the figure the XPS and X-ray induced Auger lines of the sample are identified. The sample appears to be a sodium silicate with very little aluminium present (Si/Al ratio from elemental analysis: 62). At the low binding energy end of the spectrum the valence band region with the dominating O 2s signal at about 22 eV can be seen as a weak structure. The insulating character occurs from the zero emission at the Fermi edge as well as from the spike at the other end of the energy scale which is due to the electrical field from the charged sample which shifts the onset of the detector function into the visible spectral energy range.

Further typical of survey spectra are the strong features of step functions in the background which are proportional in their height to the integrated intensity of the characteristic emission lines. These step functions arise from the inelas-

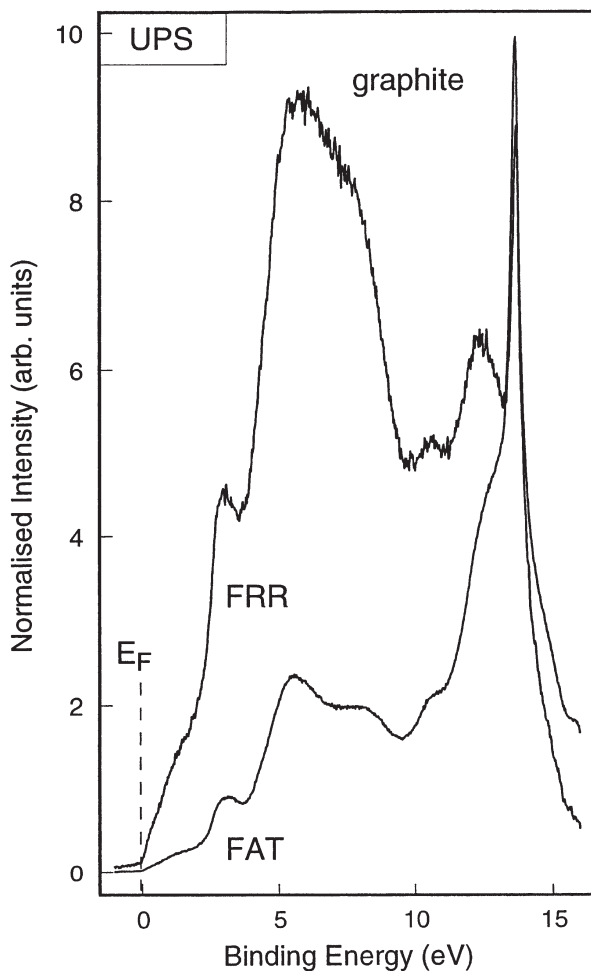


Fig. 6. Valence band HeI spectra of graphite recorded in two analyzer modes of a HSA device. *FAT* 12 12 eV fixed transmission energy; *FRR* 4 fixed retardation ratio at 4. The very different spectral shapes in *FRR* mode and *FAT* mode can be used to emphasize (Fermi edge) or de-emphasize (high energy background) spectral features of interest. There is no simple way to transform spectral shapes recorded in different analyzer modes. Great care must be taken when comparing shapes of literature spectra recorded in different modes with different analyzer equipments

tic losses of characteristic photoelectrons ejected from volumes of the sample deeper than the information depth. These backgrounds have to be removed very carefully before any quantification or even line profile analysis can be carried out. As all kinds of inelastic losses are convoluted into the background, the analytical description of the background function is difficult and is only possible with well-defined physical meaning for conductors. Very popular is the semiempirical “Shirley” background function [12], which approaches the loss function by an

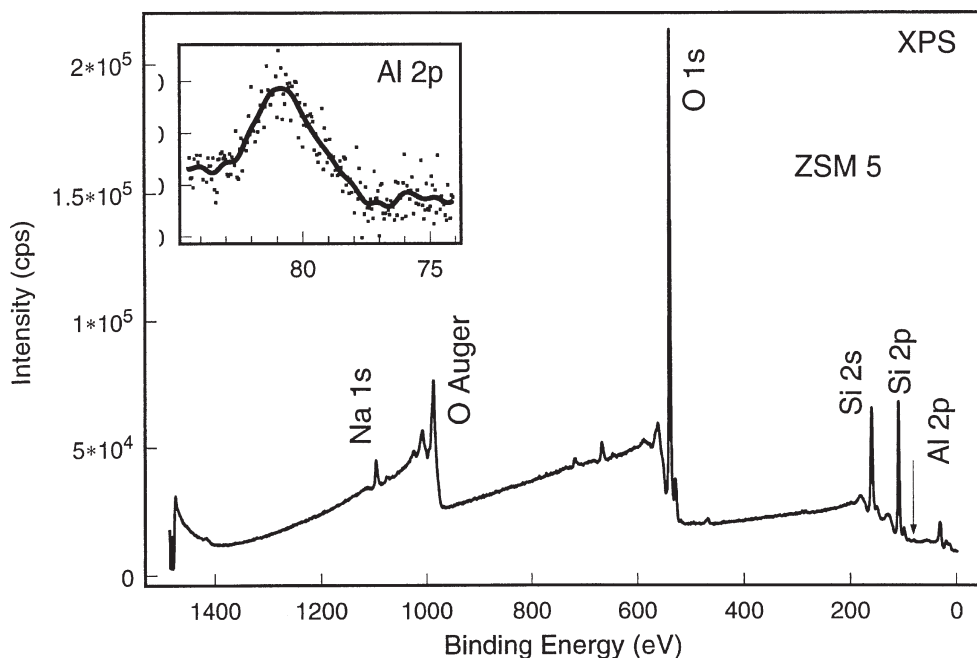


Fig. 7. Typical survey spectrum of a zeolite material recorded in the FRR mode (FRR 4) to suppress the background intensity. The *inset* shows an intensified and enlarged section of the Al 2p region indicated by the *arrow* in the main spectrum

iterative step function. A critical modification of this step function for multiple peak oxide spectra, which are also relevant for zeolites, is given in the literature [13]. The correct background subtraction is of high importance when accurate quantification is required, in particular when the peaks are of different width and largely different size (as for the Si/Al ratio determination in the ZSM-5 example). Great care has to be taken when different surface-to-bulk analytical values are reported, as in the case study section, where in some cases little attention has been given to the correct data analysis.

In the survey spectrum several additional wide and small lines can be seen which have not been identified. These lines can occur from one of the following origins and have to be considered in any case prior to any detailed examination of the spectrum:

- Sample holder peaks are frequently seen, such as in Fig. 7 for the gold spectrum.
- Collective excitation losses occur as broad features about 20 eV above the core level lines. If these features are neglected during Shirley background subtraction highly erroneous correction results are obtained.
- X-ray satellites occur from all photoemission lines (not from Auger lines) due to non-monochromatic excitation sources (except when monochromators or synchrotrons are used for excitation). These satellites should be removed as a first data reduction step. The most important satellites occur for Al excitation

at 9.6 eV and 11.5 eV to lower binding energies, with 7.8% and 3.3% intensity of the parent line, respectively, and for Mg radiation at 8.4 eV and 10.0 eV with 9.2% and 5.1% intensities, respectively.

- With imperfect anodes multiple excitation of photoemission lines occurs with simultaneous Al and Mg characteristic radiation. In this case two simultaneous spectra with a peak distance of 233.0 eV for each feature will occur.
- The sample surface is contaminated, e.g., with “adventitious” carbon (small signal in the figure with a height below the line thickness at 290 eV), with nitrogen compounds from templates, or with transition-metal impurities. Residual alkali ions from incomplete cation exchange or residual anions, e.g., from solid-state ion exchange, are other sources of unexpected elements in the sample.

Finally, it is noted that in zeolite research the analysis of plasmon losses has been used to gain additional information [14] on the chemical status of an element independent of the “chemical shift”.

The physics of the photoelectron emission for XPS is depicted schematically in Fig. 8. The figure assumes the most simple approximation to the excitation process known as the “sudden approximation” of an atom, which is in detail a quantum mechanical process described by the overlap integral between a bound atomic state and a series of final orbital states through which the electron is

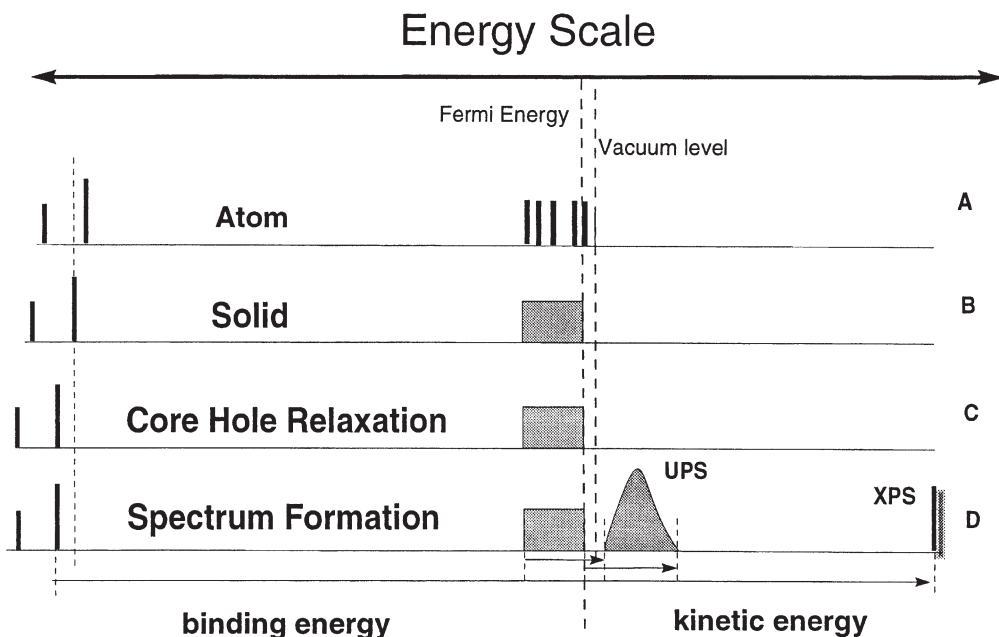


Fig. 8. Schematic representation of the physics of a photoemission process considering core levels and valence states. A A free atom in its ground state; B the atom in a solid; C effect of core-hole relaxation on the position of core level lines; and D the relationship of an observed spectrum and the position of the bound states from which the photoemission occurred

transported away from the atom. This distinction between the simple sudden approximation picture and the full quantum mechanical picture [3] is necessary to understand the rich phenomenology of “spectroscopic effects” which occur in spectra of heavy metal atoms. Practical examples of the complexity and usefulness of these spectral complications are given with the case studies. For the analysis of the main constituents of zeolites, viz. oxygen, aluminium, silicon, and for common guest species containing carbon and nitrogen, the sudden approximation is, however, sufficient to understand most of the spectral features.

1.6

Accuracy of Chemical Shift Data

The chemical shift in XPS is a small fraction of the measured binding energy. In zeolite research typical values are between 0.5 and 1.5 eV with binding energies of typically 100–600 eV. The accuracy in comparing binding energies between different sources and the problems of referencing the binding energies of insulator spectra to a consistent and reproducible standard are of paramount importance when spectral interpretations are based on a combination of literature studies (such as in the case studies) and own measurements. Round-robin analyses with conducting and zeolitic materials were made in order to know the reliability of small differences in binding energy and to be able to quantify the physical error bar on binding energies. The results [15, 16] of these studies can be summarized as follows.

- The absolute accuracy of binding energies between different instruments and laboratories varies even for noble metals significantly more than the numerical accuracy with which the peak position in a spectrum can be determined (more than the usually quoted 0.1 eV). This is independent of the method of spectrometer calibration and sample preparation.
- For insulators, the effect is significantly worse and the scatter reaches the range of the whole chemical shift (2.5 eV for Al 2p and 3 eV for Si 2p).
- The effect is not caused by calibration problems as the scatter is less than 0.5 eV for binding energy differences for core levels of the same element. Differences between lines of different elements are uncertain up to about 1 eV (Si 2p-O 1s, Al 2p-O1s).

As practical consequences for zeolite research it has to be accepted that only interpretations based on a consistent data set are meaningful. Each laboratory should measure its own set of spectra including frequently measured samples such as Na-Y and Na-A zeolite under exactly identical conditions of sample handling and sample preparation. Interpretations of series of spectra from one sample after different treatments are not so influenced by these effects as long as the sample does not change its physical status during the experiments and as long as no reference is made between own binding energies and literature data. Literature data can only be considered as trend indicators.

In no case should only absolute binding energy data be given in publications without reporting as accurately as possible all reference data, the method of charge correction, and without showing the adventitious C1s spectrum from at

least two differing cases. Only then can other investigators correctly use the reported data for their own work and much of the controversy reported in the case study section would be unnecessary.

An important consequence of the round-robin studies was the firm establishment of different binding energies for structurally different aluminosilicates. It was shown that, although the local chemical structure is always $\text{Si}^{4+}-\text{O}^{2-}$ and $\text{Al}^{3+}-\text{O}^{2-}$, there are significant long-range contributions to the chemical shift allowing a discrimination between zeolitic and non-zeolitic materials and even allowing a discrimination between octahedral and tetrahedral aluminium coordinations. Such a sensitivity to structure is untypical of photoelectron spectroscopy. The consequence is, of course, that none of the main constituent core levels should be used as “internal standard” for charge correction when different zeolite structures or zeolite-aluminosilicate samples are compared. This has not always been noted in the literature and can cause substantial errors when comparing binding energies referenced to, e.g., Si 2p.

1.7

Interpretation of Chemical Shift Data

The energy level diagrams of Fig. 8 illustrate the term “sudden approximation”. It is assumed that the creation of a photocation with a hole in a core level modifies instantaneously the electrostatic interaction between all remaining core states and the nucleus leading to a sudden (on the timescale of electronic motions of ca. 10^{-15} s) jump in the energy level diagram after the excitation process. This means that all measured core level energies are characteristic of electronically excited states and do not represent “binding energies” of the electronic ground state of the atom as they are accessible by quantum mechanical calculations. The difference in energy, which is termed “relaxation energy”, can be substantial and can reach some 10% of the total binding energy. Within the “sudden approximation” the difference between the ground state and the excited state is assumed to be constant for all core level lines and is assumed to be independent of the chemical environment of the atom under study.

As the rigorous treatment of chemical shifts in this model is rather complicated, a much simpler concept involving only ground state electronic configurations was developed and is used very frequently in chemical applications which do not seek quantitative understanding of the experimental binding energies. In zeolite research this model is adequate for analyzing trends in chemical shifts; phenomena of cation exchange and of lattice substitution by non-aluminium ions are found, however, to yield “unusual” shift parameters indicating the breakdown of the simple model.

The model predicts a chemical shift of a core level c in two compounds A and B with known valence charges q_A and q_B on the basis of a purely electrostatic interaction of charges with a positive nucleus of the atom and a cumulative repulsive interaction with all other electrons of the atom (not of the actually existing photocation!).

$$\Delta E^c(A, B) = K^c(q_A - q_B) + (V_A - V_B) \quad (2)$$

The first term in Eq. (2) describes the difference in electron–electron interaction between the (filled) core orbital c and the valence charges q . The proportionality factor K^c is the two-electron exchange integral between core and valence electron. It is approximated by a harmonic potential, which allows one to estimate a coupling constant of about 14 eV per unit charge and core orbital radii of 0.1 nm. The second term describes the chemical environment of the atom in a purely electrostatic interaction. In a point charge approximation the “Madelung” potentials V_A and V_B are obtained as sums over potentials arising from ionic charges q_j centered at positions R_{ij} relative to the atom in question i .

$$V_i = \sum_{j \neq i} \frac{q_j}{R_{ij}} \quad (3)$$

The advantage of this oversimplified empirical relationship [Eq. (2)] is that chemical quantities such as Pauling electronegativities or results from extended Hückel calculations can be used to determine the q_j parameter. The relationship is applicable to a wide variety of systems [17] including zeolites with different ion-exchanged cations. It contains, however, only a heuristic principle for sorting data and gives no quantum chemical description of the experimental binding energies.

On the basis of this crude picture a set of useful chemical shift data has been compiled as self-consistent data [18] which can be used for a qualitative first-sight interpretation of zeolitic materials. The list is given relative to a charge correction of adventitious carbon of C 1s=285.0 eV (Table 1).

The data in this table and of similar data sets provided by other authors (see Part II) have been interpreted with several degrees of sophistication in the simple model of electrostatic chemical shift. When the data base is, however, extended to wide ranges of silica-to-alumina ratios, to other cations and to other microporous materials, the picture is less clear which is either due to inconsistent data acquisition (no single data source available) and/or to the breakdown of the simple shift analysis.

The chemical shift range of oxygen 1s in oxides has been reviewed [19] for a large family of relevant compounds. As a general rule it should be noted that the

Table 1. Trends in chemical shifts for zeolite-related materials

Sample	Binding energy of Si 2p (eV)	Binding energy of Al 2p (eV)
Silica	103.95	–
ZSM-5	103.5	74.88
Ca-Y	103.0	74.75
Na-Y	102.95	74.6
Ca-X	102.85	74.95
Na-X	102.35	74.3
Ca-A	102.0	74.1
Na-A	101.5	73.8
Kaolinite	102.85	74.7
Alumina	–	74.2

main line of the O 1s transition is in low-resolution analytical spectra always symmetric and can be used to deduce several chemically inequivalent species. A general problem with all oxides is, however, the interference of hydroxyl groups that are present on all samples irrespective of the pumping and pre-heating protocol. A contribution at a binding energy higher by 1.2–1.5 eV than that of the main line arises from the hydroxide species of any oxide. Chemisorbed molecular water appears as a characteristic broad feature at about 533 eV, with the details depending on the exact structure of the chemisorbed state, which is usually not unique in polycrystalline samples. In wet zeolite samples broad lines between 531 eV and 534 eV can be frequently observed, which preclude any analysis of the oxidic contributions in the range 530.5–532.5 eV.

For most elements, the range of chemical shifts (a few electron volts) is small compared to the uncertainties in the determination of the values. This emphasizes the need for consistent experimental procedures. In addition, chemical effects such as the radiation-induced partial reduction of oxides or thermally induced shifts of the Fermi level of semiconducting samples can reach the same order of magnitude as the “true” chemical shift. This is illustrated in a reference experiment shown in Fig. 9. A (111) single crystal of silicon was chemically oxidized yielding a 0.5-nm thick overlayer of silica. The top spectrum in Fig. 9 shows clearly the chemical shift between elemental silicon (peak 1) and silica (peak 2) which is free of charging phenomena due to the thin and homogeneous character of the overlayer. The binding energy of the silica with 104.2 eV is automatically referenced to the Fermi level due to the finite conductivity of the p-doped silicon substrate. It agrees fairly well with the value shown in Table 1, given the fact that these data were referenced with a binding energy scale correction to the energy zero of the adventitious carbon.

A complex variation of the energy positions of both peaks is observed when the silicon oxide overlayer is heated in situ to various temperatures, as given in Fig. 9. These variations are due to the loss of strongly chemisorbed water and likely to structural relaxation of the silicon-to-oxide interface. The data reveal how sensitively the binding energy of Si 2p reacts to the exact nature of the oxide. It also shows that surface structural details of zeolitic samples, which are widely unknown, can affect measured binding energies in the same order of magnitude to “electrostatic” effects of the exchangeable cations used in the interpretations in the literature. The data finally confirm the statement that silicon XPS is sensitive to local structural variations that are not described by an ionic picture of $\text{Si}^{4+}\text{-O}^{2-}$. The well-known chemical covalence of the silicon–oxygen bond with its details such as bond length and bond angle are reproduced by the “chemical shift” in XPS, which is conceptually based in its simple derivation (see Eqs. 2 and 3), however, on purely electrostatic arguments.

Any in-depth analysis of chemical shifts really should take into account a full quantum-chemical description of the emitting atom in the excited state of a partly covalent bonding situation. Then not only are the excited electronic states of the bare atom relevant for the photoemission spectrum, but also the reorganization effects of the hybridized electronic states of the ligand atoms around the photoemitter. The analysis of shake-up satellites, which arise from interactions of the ejected photoelectron with the ligand molecular orbitals, is a prominent

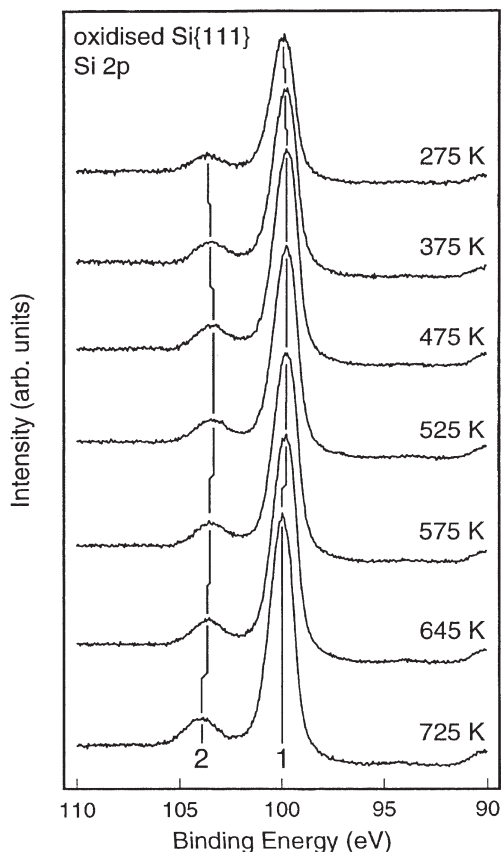


Fig. 9. Silicon 2p XPS raw data (Mg K α radiation, HSA, FAT 50 mode) of a silicon single crystal that was chemically oxidized and heated in situ to the temperatures given

example of the usefulness of a detailed understanding of the photoemission process for the elucidation of chemical information. Such a non-chemical-shift based analysis does not involve the general ambiguity of interpreting very small differences in measured binding energies. Practical examples in zeolite research are demonstrated in the case study section (Part II). The shake-up structures are prominent in spectra of covalently bound open-shell transition (copper oxides) and rare earth element (cerium oxide) spectra, where the total spectral intensity frequently exceeds 10% of the observed structure and needs to be accounted for in any analysis of the peak shape. In closed-shell electronic configurations these satellites are absent.

Another consequence of the strong interaction of the ejecting photoelectron with its surroundings is the occurrence of multiplet splitting, which is observed to be particularly prominent with shallow s core levels ("shallow" designates core levels close to the valence band, e.g. metal 3s states in first-row transition metals). The orbital from which a photoelectron is ejected retains one unpaired electron.

Table 2. Contributions to the observed binding energy of an electron in a solid

Contribution	Approx. weight (%)	Element specific	Compound specific
Core attraction	90	+	-
Valence attraction	10	+	+
Valence relaxation	5	-	+
Core relaxation	5	+	-
Extra-atomic relaxation	5	-	+
Condensation shift	5	-	+
Charge transfer	2	-	+

Its spin will interact with unpaired electrons in the valence orbitals and give rise to characteristic splitting of the single-line *s* core levels. The analysis of line shape and splitting of shallow core levels [20] in compounds, elements and alloys of many materials [21] has provided highly valuable information on chemical bonding in materials which again can be obtained without having to rely on chemical shifts.

The observation of shake-up and multiplet splitting as prominent features in XPS of many elements is a strong experimental justification to consider the whole palette of influences on the binding energy of an element in a given chemical environment and to be cautious with the simplistic ground-state electrostatic model. A tentative list of influences on a particular binding energy is given in Table 2. This list is extracted from the mentioned rigorous quantum chemical treatment [22] of the photoemission process.

The chemical shift, defined as the effect of the charge transfer between a central atom and its ligands (which is often treated as an integral part of the valence attraction term and does not even appear in many treatments), is a small contribution to the binding energy. Many other contributions that are compound- rather than element-specific interfere with the chemical shift. An illustrative example is the theoretical analysis [23] of the binding energies of Na 1*s* and Cl 2*s* in NaCl. In Table 3 the relevant quantities translated into the designations used in Table 2 are shown.

In this analysis of the binding energy of an ionic solid not all of the factors mentioned in Table 2 were explicitly taken into account. The data show, however,

Table 3. Analysis of the binding energies in NaCl

Contribution (eV)	Na 1 <i>s</i>	Cl 2 <i>s</i>
Core attraction	1079	281
Valence attraction+charge transfer	+9.2	-12.1
Extra-atomic attraction+relaxation ("Madelung term")	-8.9	+8.9
Polarization of ions	-2.5	-1.5
Theoretical binding energy	1076.8	276.3
Experimental value	1077.4	275.0

how well the compensation of several influences operates on the chemical shift. The ionization of atoms leads to “chemical shifts” in the intuitively expected direction but of much larger values than expected from measured binding energy shifts (almost zero for sodium in different chemical environments). The analysis further revealed that even in NaCl it is inadequate to use an electrostatic point charge model to calculate the electronic structure. The term “polarization of ions” had to be introduced which represents a correction for the covalent bonding interaction between sodium and chlorine in NaCl despite its classical treatment in the analysis.

The frequently assumed linear relationship between charge transfer and binding energy shift (thumb rule: 1 eV per formal charge or “oxidation state”) will be observed in the fortuitous case that all other influences listed in Table 2 compensate each other. As the signs of these effects are not clearly defined in a series of compounds, it is quite possible that this compensation will be operative. When, however, in any chemical interpretation of chemical shifts the so-called “unusual” valences have to be invoked in order to account for the observed binding energy, then great care must be exerted that none of the other factors that determine the binding energy changes such that the compensation of all factors is violated (see, e.g., the identification of “electron deficient” Ru clusters in Fig. 5). The more accurate the measurements are and the more data points are used in “chemical” correlations between binding energy and charge transfer, the more exceptions to the correlation will become apparent. For this reason it is strongly recommended that chemical bonding information is deduced at least in part from qualitative spectral interpretations and the discussion of “spectroscopic effects” and not by relying exclusively on binding energy shift arguments. It is pointed out that additional phenomena not mentioned here can give rise to characteristic energy losses of the primary photoelectron. Hence, additional types of satellites [24] that are of analytical value exist in the photoemission spectra of almost all elements. The discussion of case studies exemplifies the combined approach to a meaningful data analysis of photoemission data from zeolites.

Acknowledgements. One of the authors (R.S.) is grateful to H.G. Karge for introducing him to the subject. M. Wesemann and U. Wild provided data and carried out careful experiments used for the illustrations. U. Guntow, M. Keil and M. Schumacher prepared the samples for the experiments.

Part II

2

Case Studies

The application of photoemission techniques to zeolites is almost exclusively limited to XPS. It has recently been demonstrated that UP spectra may be measured with zeolites under special circumstances [1], and these have been used as complementary evidence to ISS and XPS data in a study of partially exchanged NaH faujasites [2]. UPS with zeolites provides characteristic shapes of the valence-

band signal which are probably related to the presence of ionic and covalent structural units (e.g., Si–O⁻–Al and Si–O–Si or Si–O–H). As a result of a recent quantum chemical study, these valence-band signals were reproduced by density-functional calculations [3]. UPS also provides signals of metal conduction bands if metal particles are present in the outmost surface region [1]. The field will require, however, more fundamental studies before a wider analytical application is feasible.

The most obvious use of XPS with zeolites is to establish coincidence or difference of properties between the external surface region and the overall crystallite. The latter have to be probed with bulk techniques such as elemental analysis, IR, NMR, XRD, EXAFS, and TPD, the results of which are not significantly affected by deviations in the thin photoemission sampling region. These studies are useful for the evaluation of zeolites after synthesis, modification and application as well as for the determination of the stability of intra-zeolite entities (ions, guests) towards segregation to the external surface. In addition, photoemission is often applied to study the chemistry of elements introduced into the zeolite (reduction, sulfidation, complexation, etc.). The results of such studies, although certainly useful, should be treated with some caution as they rely on the tacit assumption that the near-surface region with its higher degree of structural imperfection and its reduced intra-crystalline fields is nevertheless representative for the conditions in the interior crystallite.

2.1

Constitutional Elements

2.1.1

Surface Composition

Ever since the pioneering work of Tempere et al. [4], surface silicon-to-aluminium atomic ratios have been measured by XPS and related to the bulk ratios. In these studies, it was also observed that characteristic tendencies of all binding energies (BE) occur as the Si/Al ratio or the nature of the charge-balancing cation is varied [5–13]. The majority of studies report an almost linear decay of the O 1s and Si 2p binding energies with increasing Al concentration, while the Al 2p binding energy remains constant or decreases only slightly. At variance with these results is a recent study where the binding energies were found to go through maxima with varying Al content [14]. O 1s lines are symmetrical even when the presence of both OH groups and oxide ions is likely. Exchange of Na⁺ ions by protons leads to increasing O 1s, Si 2p, and Al 2p binding energies, while exchange by larger alkali cations has the opposite effect. These trends have been discussed both in terms of 'group shifts' that reflect varying covalency and ionicity of the lattice [7, 9] and on the basis of charge transfer assumed to occur in the zeolite framework [8, 13], while a possible influence of the Madelung potential was also suggested [8, 11].

Calculations with point-charge arrays representing zeolite unit cells have, indeed, confirmed that the BE trends described above are closely mirrored by the trends of the average Madelung potential felt by the emitting atom type (Si, O, Al,

Na) [12]. At the same time, an influence of final-state effects was ruled out in a first approximation by studying the behavior of the Auger parameters [15, 16] of the constituent elements. The Madelung potential of an atom type is averaged over atomic positions that experience quite different electrostatic potentials, which cannot, however, be resolved with the present XPS technique and leads to the considerable line widths observed with the constituent zeolite lines. Notably, a recent quantum chemical study by Vayssilov and Rösch [17], in which O 1s binding energies and basicity properties were evaluated by density-functional calculations of zeolite structural elements, has confirmed the view that the binding energies of zeolite elements are determined by the electrostatic potential at the emitting atom, with charge transfer rendering only minor correction terms. This study has also demonstrated that the correlations between oxygen basicity and O 1s binding energy, which have often been reported in the literature (see below), are mediated by the Madelung potential. The possibility of gauging intra-zeolite electrostatic potentials by XPS binding energies has also contributed to the development of a new view of metal-support interactions ([18, 19], see Sect. 2.4.1).

There are some reports on exceedingly high Si 2p and O 1s binding energies in dealuminated mordenites which served to justify the use of Si 2p as an internal BE standard [20, 21]. In H-Eu-1 (for zeolite nomenclature, see [22]), Si 2p was found even at 106–107 eV (with Al 2p=74–75 eV [23]). While the experimental problems encountered in the C 1s calibration (cf. Part 1) are well recognized, it is not obvious why C 1s, which was shown to provide a good alignment of the BE scale to the spectrometer Fermi level with fresh zeolites [1], should fail with dealuminated samples. Normal Si 2p binding energies of 102–103.5 eV have been reported by several groups for dealuminated Y, omega, and offretite [10, 24–26]. BE values exceeding this range may well indicate structural damage in the surface region (e.g., presence of differentially charged phases).

The analytical potential of XPS for the detection of deviating moduli between the external surface and the bulk rests mainly on the evaluation of line intensity ratios. In some cases, the underlying concentration gradients have been studied in more detail by combining Ar etching with XPS [23, 24, 26–28] or by mass-spectrometric techniques (SIMS [24, 29–31]).

In as-synthesized zeolites, coincidence of surface and bulk Si/Al ratios is often found, in particular for low-silica types, while for the surfaces of high-silica zeolites both depletion and enrichment of Al have been reported [7, 8, 32–36]. In dealuminated zeolites, the properties of the external surface region depend on the dealumination procedure applied [37]. It has been found by the combination of XPS with several bulk techniques that non-framework Al (Al^{nf}) remains in the zeolite cavities as long as thermal dealumination is performed under anhydrous conditions [38, 39]. In Y and MOR treated in moist media, the migration of the Al^{nf} to the external surface has been demonstrated as a consecutive step to dealumination by scanning a range of dealumination conditions [30, 38, 40]. The migration tendency of Al^{nf} appears to depend on the zeolite type: It was not observed in zeolite A [41], and it occurred in omega under conditions where it was absent in offretite [10]. With mordenites, the particle size was found to influence the extraction of Al^{nf} from the framework [42]. The external layer deposited

on steam dealumination was found to contain silicon even if far thicker than the photoemission sampling depth and was addressed, therefore, as a layer of amorphous aluminosilicate [25]. In dealuminated H-ZSM-5, Al^{nf} was found to cover a significant part of the remaining Brønsted acid sites, which were uncovered after extraction with acetic acid [43]. External Al^{nf} layers were easily removed from dealuminated Y and MOR by grinding, which exposed surfaces with properties close to those of the bulk crystallites [26, 44]. The surface composition approached that of the bulk also after acid leaching of steamed material [38, 39, 42, 43], but there is disagreement about Al depletion or enrichment in the resulting external zeolite surfaces [13, 43]. Dealumination by large molecules as EDTA or (NH₄)₂SiF₆ leads to preferential Al depletion of the external surface layers [25, 28, 45, 46].

Recently, it has been shown by a combination of XPS with other surface-analytical methods (UPS, ISS) that the Na⁺ distribution in partially exchanged NaH zeolites can give rise to another difference between surface and bulk properties [2]. After the typical thermal treatments used to obtain acidic protons (calcination of the NH₄ form, reduction of reducible cations; cf. also [47]), Na⁺ is depleted in the external surface layer. The effect was interpreted as resulting from an exchange of Na⁺ at near-surface sites by protons from deeper layers due to a difference in Madelung stabilization for Na ions and the less-charged protons between surface and bulk sites.

The question as to whether extra-framework Al species may be detected not only by their contribution to the Al signal intensity, but also on the basis of binding-energy data has long been discussed in the literature. Al 2p binding energies and Al Auger parameters have been shown to differ considerably between substances containing Al in octahedral (α -Al₂O₃ [48], amorphous aluminosilicates [49], layered aluminosilicates [20, 48, 50, 51]) and tetrahedral coordinations, i.e. zeolites [12, 48, 52, 53]). This question has been discussed in some detail [54]. Nevertheless, there are numerous studies on zeolite dealumination where no notice has been given of any peculiarity in the Al signal shapes.

In other studies, foreign phases and extra-framework Al species were detected by broadening of the Al 2p line or shoulder formation, mostly at the low-BE side [7, 20, 23, 34, 52, 55–57]. In one report [7], as many as four Al-containing species were assigned in the spectra of Na-ZSM-5 and of a silicalite with Si/Al \approx 100. In another report [56], the Al 2p signal of a minority analcime phase (Si/Al=2) appeared at higher BE than that of the majority beta phase (Si/Al=7.5), while one would expect the opposite from the Si/Al ratios if the origin of the BE scale was the same for both phases [7, 8, 12]. Under the latter condition, it should have been possible to resolve the Si 2p signals of these phases. As this was obviously not the case [56], differential charging may have influenced the measurement.

The analytical potential of the Auger parameter α_{Al} [15, 16] has been employed for the discrimination of Al species in the zeolite surface region. In a study of dealuminated mordenites [52], the Al KLL Auger signals were fitted by three components, which were combined with two Al 2p signals to describe 3 Al states with different Auger parameters (1460.9–1461.5 eV, 1459.8–1460.2 eV, and 1458.7–1459.3 eV, assigned to Al in octahedral and tetrahedral coordination, and tricoordinated Al, respectively; see Fig. 10). These assignments have been sub-

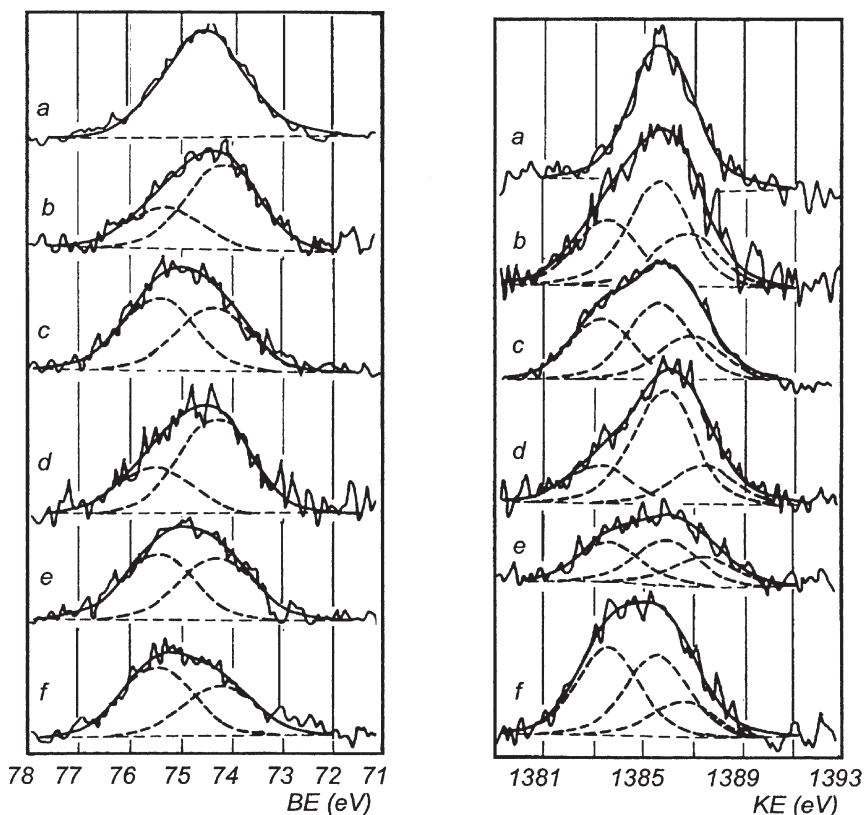


Fig. 10. Signals of Al 2p (left) and Al KLL (right) of mordenites dealuminated by different procedures (steaming-leaching combinations). $(Al/(Al+Si))_{bulk}=0.083$ (a), 0.025 (b), 0.014 (c), 0.013 (d), 0.011 (e), 0.009 (f). Taken from Remy MJ, Genet MJ, Notte PP, Lardinois PF, Poncelet G (1993) *Microporous Mater* 2:7, with kind permission from Elsevier Science NL, Sara Burgerhartstraat 25, 1055 KV Amsterdam, The Netherlands

stantiated on the basis of polarizability considerations [58]. Nevertheless, some doubt remains, in particular with respect to the signal with low α_{Al} . For instance, a decrease in α_{Al} to below 1459 eV was also reported for ZSM-5 in the Na form [12, 53], where the occurrence of tricoordinated Al is unlikely. Marschmeyer and Papp [43] assigned this signal, which they observed in dealuminated H-ZSM-5, to a species with Brønsted instead of Lewis acidity. Asymmetries in the Al KLL Auger signal assignable to a state with $\alpha_{Al}=1458.1-4$ eV were noted even in Na-MOR by Grünert et al. [12]. Al Auger signals providing $\alpha_{Al} < 1459$ seem to be a general feature of high-silica zeolites, and it has been proposed recently that they may originate from Al atoms adjacent to Si atoms bearing a surface silanol group [59].

In summary, there are situations in which extra-framework Al and foreign phases can be detected by particular XPS signals; however, the absence of the latter does not prove the absence of the former. The invisibility of these species may

be due not only to coincidence of their BE with that of the framework Al, but also to differences in the Fermi level in coexisting non-conducting phases. Despite some open questions, the use of the Al Auger parameter for the characterization of Al species in zeolite surfaces appears highly promising. However, there is another simple tool for the detection of extra-framework Al by XPS, which should not be overlooked: Re-exchange of the sample with Na⁺ ions and study of the Na/Al atomic ratio [41] should reveal the presence of any extra-framework Al in the surface region.

XPS may also be applied to characterize the effect of surface modification procedures. Such surface decoration is often performed to poison acidic sites of the external surface that would interfere with the shape selectivity of the pore system or to modify pore entrance sizes. XPS studies of such materials have been reviewed [13], including surface modification with trimethyl phosphite [60], SiCl₄ [61], silicon tetramethoxide [62] and germanium tetramethoxide [63]. In a recent study, the surfaces of US-Y zeolites have been modified by deposition of [Al₁₃O₄(OH)₂₄(H₂O)₁₂]⁷⁻ Keggin ions or alumoxane (by hydrolysis of triisobutylaluminium) to protect the zeolite against metal deposition in cracking applications. The Al overlayers were analyzed by XPS for their thickness and their structure on the basis of the Al Auger parameter [64].

2.1.2

Acidity and Basicity

Acid-base properties of zeolites are probed by studying their interactions with basic/acidic molecules by appropriate techniques (IR, NMR, calorimetry, TPD). For the external surface region, analogous methods based on XPS detection were developed following the pioneering work of Defossé and Canesson [65]. The probe molecules used are pyridine [55, 56, 66–72], ammonia [21, 43, 44, 73], and pyrrole and chloroform for basic sites [70, 74, 75]. Kaliaguine [59] has published a review of the results.

The interaction of acidic zeolites with pyridine results in broad N 1s signals which can be fitted by three states separated by 1.3–2 eV from each other (Fig. 11). According to Kaliaguine et al. [66–70], the binding energies of these states (referenced to Si 2p=103.3 eV) are 399.0±0.5 eV (signal I), 400.3±0.7 eV (II), and 401.7±0.2 eV (III). In later work by Borade et al. [56, 72], a fourth state at >403 eV was reported while signal I was missing. The signals were assigned on the basis of complementary information, e.g., their intensity trends upon pyridine desorption at increasing temperatures or after adsorption of pyridine onto previously dehydroxylated samples [transformation of Brønsted (B) into Lewis (L) sites]. As a result, signals III and IV were assigned to B sites of different strength, while signal I was attributed to L sites. On the basis of the factual material, signal II had to be assigned to strong L sites in H-Y and some other zeolite types [56, 68, 69, 72], but to weak B sites in H-ZSM-5 [56, 66], which is unfortunate as it prevents a priori usage of these assignments with other zeolite materials.

In most studies, ratios between B and L sites as obtained by XPS were compared with those measured by IR of adsorbed pyridine. While good agreement

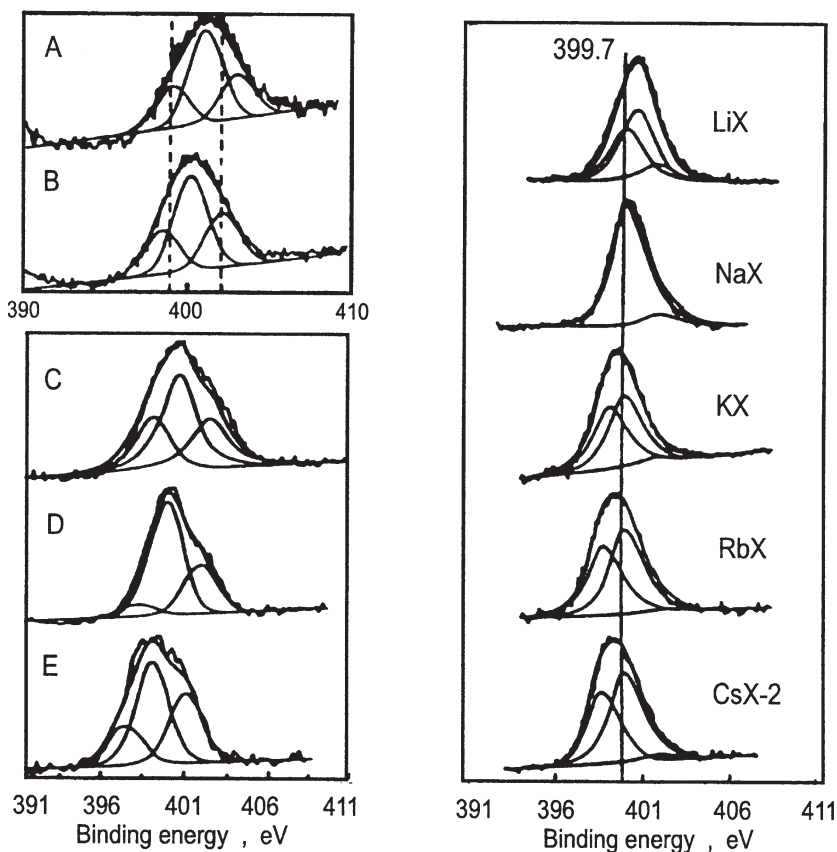


Fig. 11. Study of acidity and basicity with adsorbed probe molecules. *Left column* N 1s lines of pyridine chemisorbed on Al-ZSM-22 (A), Fe-ZSM-22 (B), Al-ZSM-5 (C), Fe-ZSM-5 (D), B-ZSM-5 (E); *right column* N 1s lines of pyrrole chemisorbed on alkali-exchanged X. Taken from Borade RB, Huang M, Adnot A, Sayari A, Kaliaguine S (1993) Acid-base properties of zeolites: an XPS approach using pyridine and pyrrole probe molecule. In: New frontiers in catalysis, Proc 10th Int Congr Catal, Budapest, Hungary 1992, p 1625, with kind permission from Elsevier Science NL, Sara Burgerhartstraat 25, 1055 KV Amsterdam, The Netherlands

was found in many cases, divergent results were interpreted to indicate differences in the type of acidity between the external surface and the bulk, e.g., after dehydroxylation of H-Y or after fluoridation of H-Beta [69, 76]. Relevant information was also obtained from the N/Al atomic ratio, which may reflect the presence of extra-framework Al [56] or the inaccessibility of sites, e.g., in H-Y [69]. With respect to the latter problem, comparison of N/Al ratios measured with pyridine and ammonia are most informative. In one report [44], it was concluded from such comparison that the sodalite cages of H-Y contain mostly strong B sites.

In some cases, trends in the BE of signals I–III were used to establish rankings in the acid strength of the corresponding sites. Such conclusions should be

treated with caution, as the Si 2p line is a safe charging reference only for high-silica zeolites. It was only in studies covering a broader Si/Al ratio [56, 72] that species IV was required to fit the experimental spectra. It would certainly be interesting to confirm this species, e.g., in a study with adsorbed NH_3 , which avoids complications with the C 1s reference due to adsorbate carbon.

Ammonia was used as a probe molecule in recent studies with H-Y [44] and dealuminated zeolites: MOR [21] and ZSM-5 [43]. As in the case of pyridine, the N 1s signal can be decomposed into three components, which were assigned to two B sites and one L site in two reports [21] and [44], but to three B sites in another [43]. Distributions of the acid site strength were derived for H-Y (fresh and steamed, the latter also after removing layers of extra-framework material) by following the relative N 1s intensity during NH_3 desorption at stepwise increased temperatures [44]. In the study with MOR, N/Al ratios in excess of 1 exhibited by some samples were attributed to NH_3 adsorbed on acidic Si-OH groups (signal II; IR band at 3740 cm^{-1}). There is disagreement in the assignment of the signal for Lewis sites (signal I [21]; signal II [44]). The interpretation of N 1s binding energies of adsorbed N bases (mainly NH_3) has recently been discussed by Johansson and Klier [73]. A correlation between the nitrogen charge evaluated by the extended Hückel method and the N 1s BE was demonstrated, which included pyridine on sulfated zirconia, and was discussed with the intention of establishing an acidity scale. Any attempt to extend this argument on binding energies of adsorbates at zeolite sites will have to consider also the influence of the intra-crystalline potentials.

XPS of adsorbed pyrrole was performed by Kaliaguine et al. [71, 74] to investigate the basic properties of alkali-exchanged Na-faujasites (exchange degree 35–70%, see Fig. 11). The BE scale was referenced with deposited gold and pyrrole carbon in this case. The N 1s lines contained contributions from two major species, which were attributed to pyrrole adsorbed on O atoms adjacent to the different alkali ions present. Their binding energies as well as the NH stretching frequency of the adsorbed pyrrole were correlated with partial charges derived from electronegativity considerations (cf. Fig. 12). It was, therefore, concluded that the N 1s BE reflects the strength of the basic sites. Minor N 1s signals were attributed to polymerized pyrrole (in Y) and to a weak basic site (in X; supported by IR evidence). A similar study with chloroform as a probe for basic sites in Na-X and Na-Y partially exchanged by other alkali ions has been published recently [75]. In these measurements (at liquid-nitrogen temperature), two states were again differentiated via their Cl 2p binding energy. It was shown that chloroform probes only strong basic sites and that the basicity may be ranked via the Cl 2p BE.

It has often been suggested that the O 1s binding energy may serve as a measure for the basic properties of oxygen in oxides including zeolites [13, 74, 77–82]. This expectation is based on proposals of Vinek and Noller [83, 84], which rely on the tacit assumption that the O 1s shifts are determined by variations in the partial charge. The calculations of Vayssilov and Röscher [17] imply rather that this correlation is mediated by the influence of the intra-crystalline potential: The same changes that give rise to decreasing O 1s binding energy (e.g., replacement of Si^{4+} by Al^{3+}) exert a stabilizing effect on the (partially) positive charge that

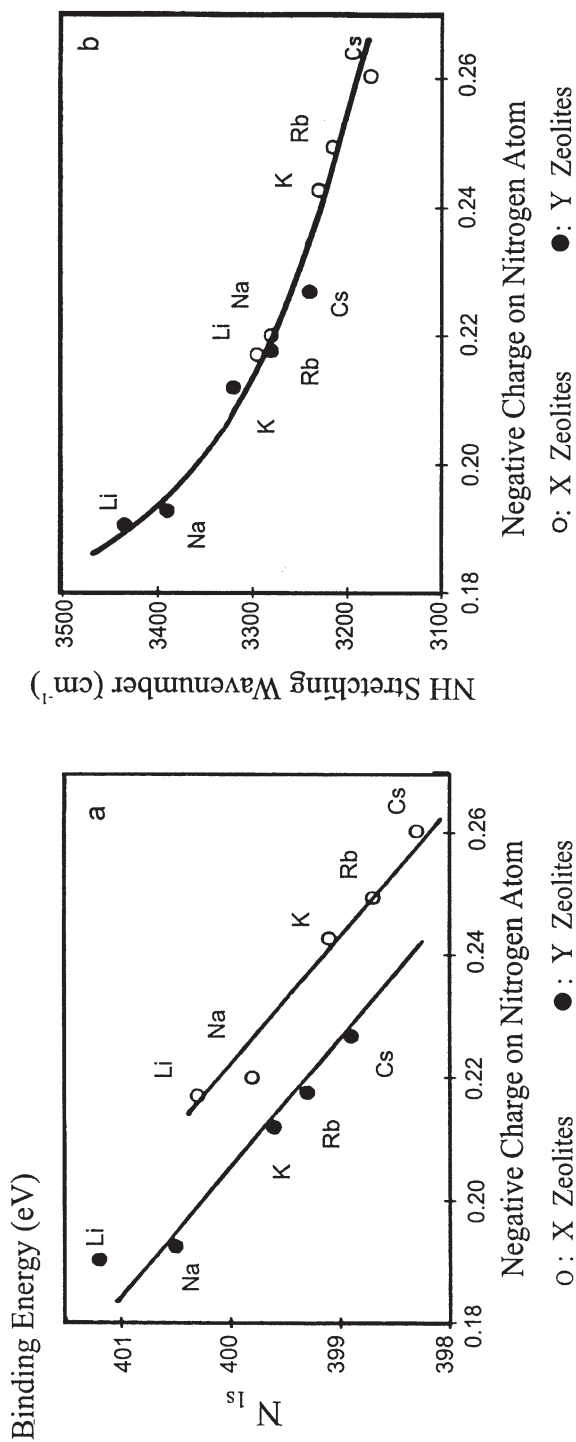


Fig. 12a, b. Evaluation of basicity by XPS and IR of adsorbed pyrrole: correlation between the partial charge on N as derived from the Sanderson electronegativity equalization principle and the (a) N 1s BE and (b) wavenumber of the NH vibration. Taken from Huang M, Adnot A, Kaliaguine S (1992) *J Am Chem Soc* 114:10005, with kind permission from the American Chemical Society

occurs on the basic oxygen in the interaction with an acid. In a general discussion of relations between physical properties and reactivity of oxide surfaces, Idriss and Barteau identified a similar influence of the Madelung potential on the O atoms and their performance in base catalysis [85].

From the publication of Vayssilov and Rösch [17] it is obvious that the basicity of oxygen atoms in zeolites depends strongly not only on their position (between Al and Si or Si and Si), but also on their distance to the alkali atoms and on the nature of the latter. Unfortunately, these differences cannot be resolved in the O 1s line shapes measured by XPS. On the other hand, probe molecules seem to be much better suited to differentiate basic sites by XPS, as demonstrated by Kaliaguine. For instance, no significant broadening of the O 1s line was observed in Y samples containing both Cs and Na (and exhibiting two distinct N 1s signals of adsorbed pyrrole), although the O 1s BE in the parent Na-Y, which should probe the basicity of the oxygens adjacent to Na⁺, differed from that in CsNa-Y by 0.7–1 eV [11, 74]. Hence, the N 1s binding energies in adsorbed pyrrole or Cl 2p in adsorbed chloroform, although probably also perturbed by Madelung effects, appear to provide a realistic chance to rank basic strengths of zeolite sites.

2.2

Ion Exchange

Photoemission techniques offer a variety of tools for the discrimination between extra- and intra-crystalline location of components introduced (e.g. metal ions, “MI”). Nevertheless, due to the specific limitations of these tools, detailed studies, preferably combining several of them, are often required to derive sound conclusions, in particular if both extra- and intra-zeolite species are present. Apart from quality assessment after ion-exchange steps, photoemission has been increasingly applied to describe mobility phenomena, e.g., the preparation of zeolite catalysts by solid-state reactions (solid-state ion exchange [86–89], reductive dispersion (Ga₂O₃ into H-ZSM-5 [90–93]), chemical transport [94–97]), the penetration of metal poisons (Ni, V) into FCC catalysts [98–101] and the redistribution of active catalytic components in zeolite crystals under reaction conditions [102–105]. Much of the earlier work in this field has been reviewed by Shpiro et al. [33, 35].

The well-known BE difference between XPS signals of metal ions in their oxides and in zeolites [33, 35] has frequently been used to prove the intra-zeolite location of species. Higher BE values observed with zeolites have been attributed to the influence of intra-crystalline potentials, in some cases also to final-state effects (La, Cu, *vide infra*). In view of the considerable variation in the Na 1s BE with the framework Al content [7–9, 11, 12] it may be expected that the binding energies of other metal ions will also depend on the Al/Si ratio. This has recently been confirmed for VO²⁺ ions [106], but a systematic study of this problem is not yet available. The BE of metal ions in zeolites are sometimes close to those in the corresponding hydroxides (e.g., Ni²⁺, Cu²⁺, Co²⁺), so that discrimination between extra- and intra-zeolite locations on the basis of XPS binding energies alone is not safe. Thus, it has been found that the Cu 2p BE of Cu(II) oxide species well

dispersed on the external surface of Na-ZSM-5 was close to that of intra-zeolite copper [107]. In this case, however, the two states could be discerned by their Auger parameter (*vide infra*).

Signal intensities are certainly valuable in the discussion of intra- or extra-zeolite location, but the ambiguities inherent in this information should be recognized. For well-dispersed MI, the MI/Si (or MI/Al) ratio found by XPS is near the bulk ratio, but the same may happen if large oxide particles are supported on the external surface. High MI/Si ratios indicate surface enrichment, but there are examples where a transition-metal component in highly surface-enriched material was partly or even totally intra-zeolite (Ni-Y [1], Cu-ZSM-5 [107, 108], V-ZSM-5 [106]). In studies of solid-state reactions with zeolites, increasing MI/Si ratios have been understood to prove the MI migration from the initial bulk crystallites into the zeolite matrix [88, 90, 91]. Such increases may, however, also result from the dispersion of the metal component over the *external* surface as recently found with CuCl/Na-ZSM-5 [96]. The migration of copper chloride species into the zeolite, which required significantly higher temperatures, was then accompanied by a *decreasing* Cu/Si ratio.

The importance of complementary information (in the latter case α_{Cu}) in particular with intensity considerations is well illustrated by this example, because the decreasing Cu/Si ratio could have also resulted from a clustering of the Cu compound on the external surface. In this situation, one might resort to depth profiling techniques using a combination of Ar (or He) ion sputtering and XPS intensity analysis as performed, e.g., in [90, 91, 109, 110] (in [110] with detection by AES). It should be noted, however, that highly preferential sputtering of Na ions was observed in Na zeolites, so that Na was detectable only with special experimental precautions [1, 2]. This preferential sputtering may be related to the cation mobility in zeolites. Hence, a thorough study of sputter yields in zeolite systems is required before depth profiling by sputtering can be recommended as a reliable tool for zeolite analysis. In some cases, useful information can be obtained already from “non-destructive depth profiling”, i.e., by studying the MI/Si ratio with two MI lines of strongly different photoelectron kinetic energy (e.g., Ga 2p, Ga 3d [92, 109]).

Recent work has drawn attention to other spectral features that may be used to discriminate extra-zeolite material from intra-zeolite species, among them the characteristic BE changes of the framework elements upon variation of the cation (alkali ions, H, RE ions [6–8, 11, 12]). These changes, which are most pronounced with low-silica zeolites, have been attributed to varying polarization of the framework charge by ions of varying electronegativity [8] or, more recently, to changing Madelung potentials as a result of a changing degree of covalency in the cation-framework bond [12]. Generally, the BE of the framework elements increase with the cation electronegativity. The introduction of Ag⁺ and Ni²⁺ into Na-zeolites (Ag into Y [2], Ni into Y, ZSM-5 [1, 111]) has been found to result in a significant decrease in the framework binding energies, which is not easily reconciled with current explanation patterns.

Satellite structure may be another spectral feature suited to demonstrate the intra-zeolite location of an element. Satellites arise from interactions between unoccupied atomic levels and the valence band in the final-state wave function.

Their shape and intensity should depend on the geometry of the coordination sphere between the cation and the anions forming the valence band and may therefore reflect the specific circumstances in zeolite environments. It has been shown that the shape of the La $3d_{5/2}$ line differs significantly between La in La_2O_3 and in faujasites [112] (Fig. 13). It underwent further modification upon heating of the zeolites, which is known to result in dehydration and site exchange between La in supercages and residual Na in sodalite cages. The sensitivity of satellite structure to intra-zeolite location was possibly encountered earlier with Fe-modified ZSM-5 [113, 114]. Fe 2p line shapes with broad, untypical satellites were interpreted to indicate the presence of Fe^{2+} , although Fe^{3+} should have been expected from the sample history. Fe 2p signals with similar properties were recently reported also for Fe-substituted LTL zeolite [115] and for Fe in Na-Beta [116], where only Fe^{3+} was found by Mössbauer spectroscopy. We believe that in all cases the XPS signals detected were those of Fe^{3+} with a satellite structure modified by the zeolite environment.

It can also be useful to study variations in the spin-orbit splitting (ΔE_{so}), which occur with the first-row transition elements due to multiplet splitting effects. In an early investigation, Wichterlova et al. [117] noted a low ΔE_{so} value for Cr^{3+} in zeolite Y (9.1–9.2 eV vs. 9.8 eV in Cr_2O_3). Such low values were also found for low-percentage Cr(III) on SiO_2 and Al_2O_3 [117, 118]. Thus, although reflecting the isolation of the MI rather than the specific zeolite environment, anomalous ΔE_{so}

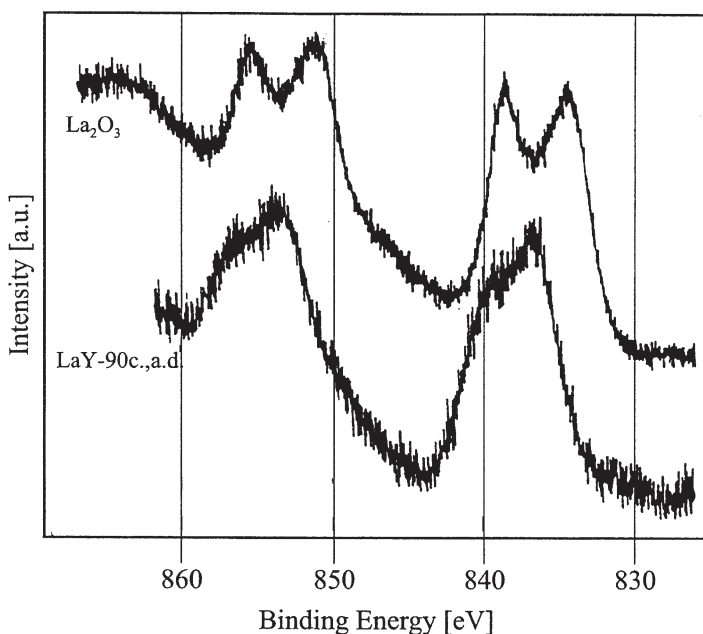


Fig. 13. La 3d line shape in La_2O_3 and La-Y. LaY-90 c./a.d.: La-Y, 90% exchange degree, air dried, calcined. Taken from Grünert W, Sauerlandt U, Schlögl R, Karge HG (1993) *J Phys Chem* 97:1413, with kind permission from the American Chemical Society

values could be another source of evidence for intra-zeolite location of the element of interest.

For copper-modified zeolites, the combination of XPS with XAES allows easy discrimination between intra- and extra-zeolite species. As first reported by Sexton et al. [119], intra-zeolite Cu(I) exhibits a very low CuLVV kinetic energy (ca. 913 eV as compared to 916.8 eV for Cu₂O), and similar shifts were found between intra-zeolite Cu²⁺ and bulk CuO [107] and intra-zeolite Cu(I) chloride species and bulk CuCl [96]. These Auger shifts combine with the XPS BE to give Cu Auger parameters significantly different between intra- and extra-zeolite locations. The effect was used to prove the intra-zeolite copper location in overexchanged Cu-ZSM-5, in which EXAFS had detected Cu-Cu coordinations typical of small oxide clusters [89, 108]. Figure 14 shows that intra- and extra-zeolite Cu is easily discerned in the Auger spectra even when coexisting. The origin of the strong shift in the Auger parameter is probably the localized character of the oxygen orbitals contributing to the final-state wave functions in zeolites (instead of the extended valence states in the crystalline compounds). Other possible reasons have been discussed [120]. An analogous approach has been used recently to analyze the state of copper in Cu-Beta [121]. Similar effects have not been demonstrated for other elements so far.

The influence of the zeolite on the redox chemistry of components dispersed in them is another topic studied by photoemission techniques [33, 35]. Numerous differences between the redox chemistry of transition elements in the bulk phase and in zeolites have been established, e.g., the stabilization of low (nonzero) valence states as Rh(I) [122–124], Pd(I) [125–127], Ni(I) [128]; a different stabilization of intermediate Cu(I) in Y and ZSM-5 or beta [108, 121, 129]; the stabilization of metal atoms in zeolites (Pd in H-Y [130], Pt, Ir in H-ZSM-5 [131]); the acceleration of the valence-state interchange $\text{Cu}^{2+} \rightleftharpoons \text{Cu}^+$ in overexchanged ZSM-5 and beta [89, 108, 121].

The influence of the zeolite environment on the XPS BE of dispersed ions (*vide supra*) means that reference compounds for this type of investigation are not easily available. This is not so much a problem for the starting material for which the highest oxidation state of the element is often plausible, but the identification of intermediate states, and sometimes of the final state of reduction, is not straightforward. As a first approximation, BE shifts known from bulk components (e.g., coordination compounds) are often used in the analysis of zeolite systems. Combination with bulk techniques sensitive to electronic structure can provide additional information notwithstanding possible differences between the conditions in the bulk crystallite and the surface layer. Thus, IR of adsorbed CO has been used to differentiate between Pt⁺ and Pt(0) atoms in H-ZSM-5 [131], EXAFS was able to detect very small intra-zeolite Cu(0) clusters formed from Cu⁺ with almost identical XPS/XAES signature [108], Mössbauer spectroscopy suggested the presence of Fe³⁺ in zeolites with doubtful Fe 2p satellites [116], and ESR was employed to support the occurrence of Pd⁺ in the reduction of intra-zeolite Pd(II) [126, 127].

The correlation of ESR with photoemission has sometimes led to debatable assignments of signals in XP spectra. The problem is that due to paramagnetic interaction of neighboring sites, the quantification of ESR becomes inaccurate in

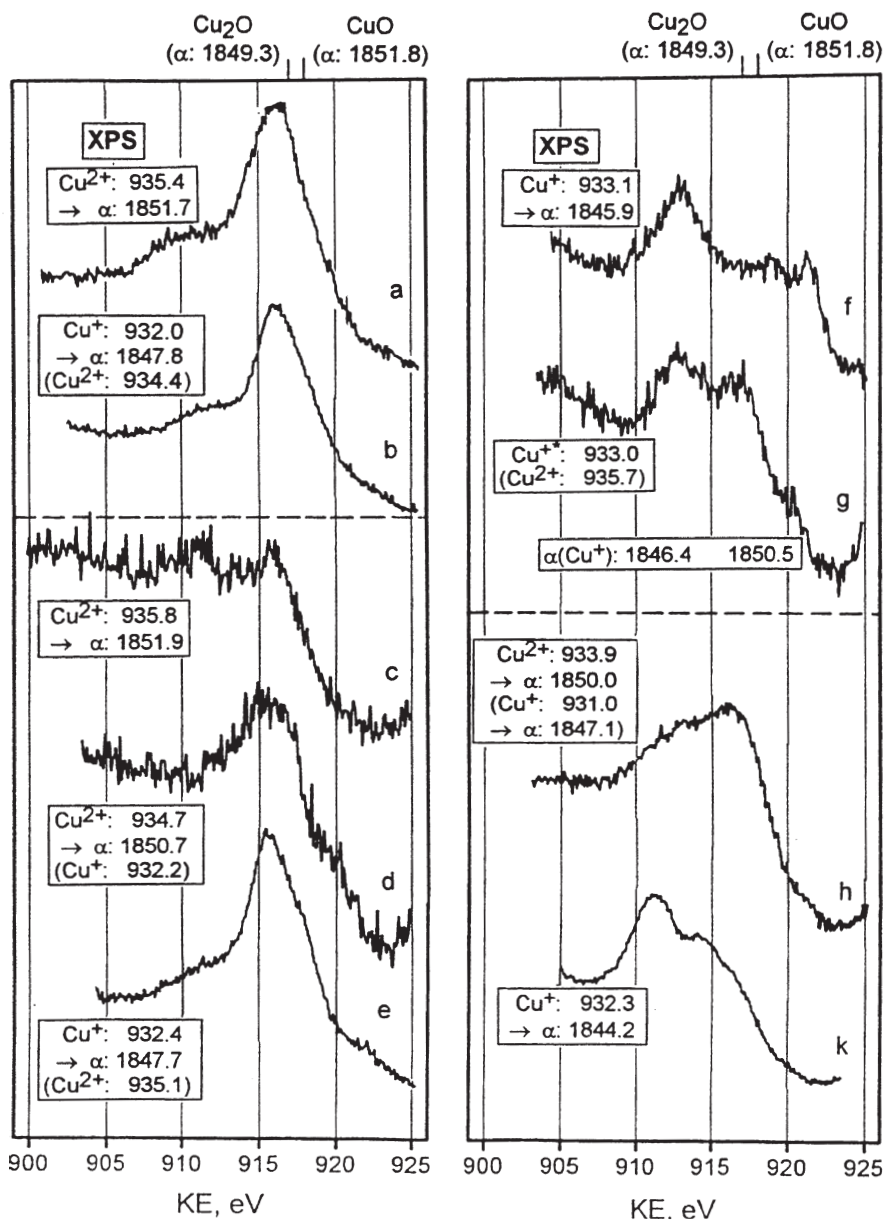


Fig. 14. Extra- and intra-zeolite Cu detected by CuL₃VV Auger spectroscopy. Chemical transport of CuCl_x into Na-ZSM-5. Insets Cu 2p XPS BE; α_{Cu}, eV. *a* bulk CuCl₂, *b* bulk CuCl, *c* CuCl₂/Na-ZSM-5 physical mixture, *d* (*c*) after microwave treatment, *e* (*c*) after N₂, 673 K, 24 h, *f* (*e*) after vacuum, 823 K, 1 h, *g* (*f*) after air, 673 K, 1 h; *h* CuCl/Na-ZSM-5 physical mixture, *k* (*h*) after N₂, 823 K, 4 h. Intra-zeolite Cu is indicated by the line at KE=911–913 eV (α_{Cu}=1844–1846 eV). Taken from Grünert W, Liese T, Schobel C (1997) Stud Surf Sci Catal 105:1517, with kind permission from Elsevier Science NL, Sara Burgerhartstraat 25, 1055 KV Amsterdam, The Netherlands

the concentration region covered by XPS. This leads to the acceptance of barely acceptable divergences in ion concentrations as supplied by the two methods (e.g., Ni⁺ in NiNa-X: 1% of total Ni by ESR vs. 30% by XPS [128]) just in the verification of a proposed assignment for an XPS signal. The reduction of Rh(III) in faujasites may serve as an example: The majority of the literature agrees upon the assignment of a signal between 308.2 and 308.8 eV to Rh(I) [122–124, 132] by analogy with Rh(I) in carbonyl complexes [133]. With this assignment, Rh(I) is the only reduction intermediate detected by XPS. Considering Rh(II) ESR signals observed under certain activation conditions, Goldfarb et al. [134] proposed a different assignment [Rh(II) at 308.8 eV, Rh(I) at 307.6 eV], which gave qualitative agreement between ESR and XPS at the expense of a large quantitative divergence [Rh(II): 4–0% of Rh by ESR, 35–58% by XPS] and implied that not even 10% of Rh in RhCa-X is reduced to Rh(0) in hydrogen at 770 K.

2.3

Isomorphous Substitution

XPS has also attracted attention as a tool for quality assessment of isomorphously substituted zeolites. The interest arises from the expectation that non-incorporated entities of the substitutional element are deposited near the external crystallite surface or form separate particles that should be detectable as well. The experimental basis for such quality assessment would be most reliable if BE differences allowed the substitutional element to be traced both in intra- and extra-framework positions. It appears now that such discrimination is possible for several elements (Ti [135–140], V [106, 141], Fe [142, 143], Co [144]) due to increased BE of the elements substituted in silica-rich lattices as compared to their oxides.

Ti-silicalite and related materials are the best-documented examples so far. Framework Ti has a typical Ti 2p_{3/2} BE of >459.5 eV (with C 1s=284.5 eV) [135–139], which is 1–1.5 eV higher than that of TiO₂ (anatase). Coexisting intra- and extra-framework Ti can be easily differentiated by fitting experimental Ti 2p signals [137, 138] (cf. Fig. 15). In well-synthesized Ti-substituted zeolites, Ti was depleted in the external surface region [137–139], while extra-framework titania was enriched at the external surface giving rise to a shoulder at the O 1s signal [139]. It should be noted, however, that quite opposite assignments were derived in a recent paper [140], where the Ti 2p BE of framework Ti was stated to be lower than that of extra-framework Ti (similarly for the Fe 2p BE of framework and extra-framework Fe). This discussion was based largely on the conclusions to be drawn from a calcination study of Ti- (and Fe-) substituted ZSM-5, where the assignment adopted resulted in the conclusion that Ti (and Fe) was ejected from the framework at higher temperatures, while the generally accepted assignment would have indicated an incorporation of the heteroatoms.

The high Ti 2p BE assigned to framework Ti by most groups is probably not linked either with the framework structure or with the tetrahedral Ti coordination: Similar values have been measured also with TiO₂-SiO₂ mixed oxides prepared by precipitation [145] or sol-gel techniques [146] and glasses [147, 148], and with Ti-Si minerals containing Ti in octahedral coordination [136, 139]. The

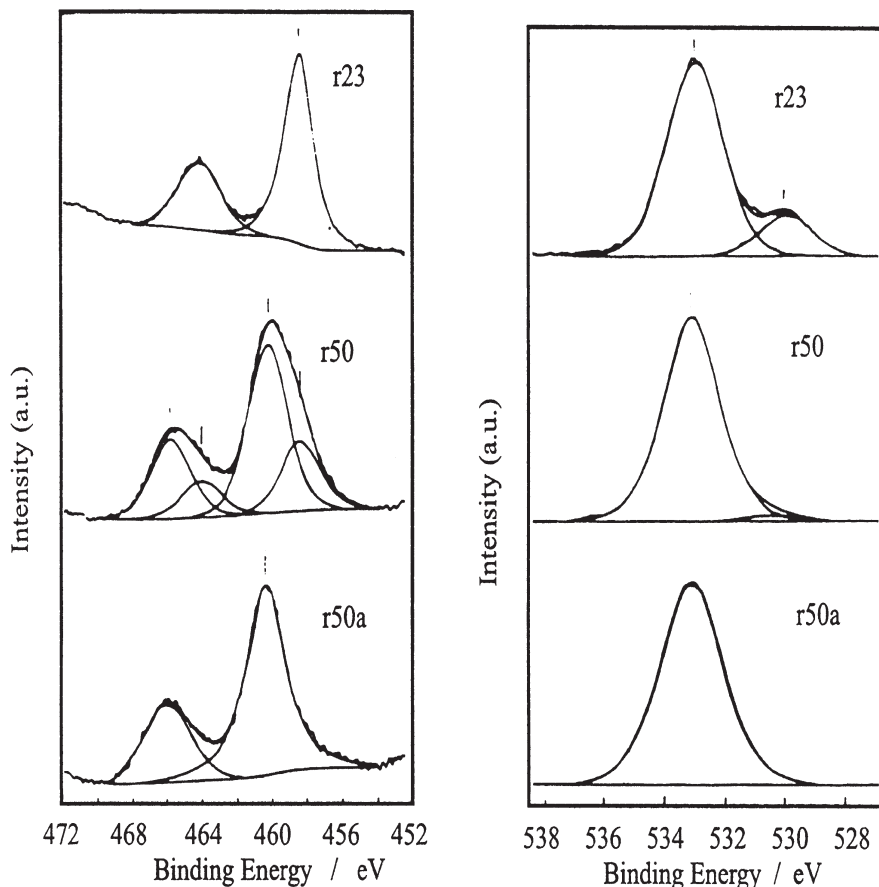


Fig. 15. Analysis of extra- and intra-framework Ti in Ti silicalites. *Left column* Ti 2p, *right column* O 1s. r23 (r50) – Si/Ti ratio in precursor gel – 23 (50); samples calcined (r23, r50) and acid leached (r50a). Taken from Grohmann I, Pilz W, Walther G, Kosslick H, Tuan VA (1994) *Surf Interface Anal* 22: 403, with kind permission from Wiley, Chichester

decisive property appears to be the population of the second coordination sphere of Ti by Si instead of Ti. This may prevent easy differentiation between intra- and extra-framework species if the latter are amorphous mixed-oxide clusters.

Recently, it has been shown that intra-framework V in V-silicalite can be discriminated from intra-zeolite vanadium oxide clusters and even from VO^{2+} ions exchanged into Na-ZSM-5 by its particularly high V 2p_{3/2} BE [106, 141]. Prerequisite for such analysis of weak V signals is a careful treatment of the X-ray satellites at the O 1s line, which mask the weak V 2p doublet. Problems with this superposition may be the reason for earlier reports of low V 2p BE for intra-zeolite vanadium [149].

Several groups found that intra-framework Fe(III) exhibits Fe 2p binding energies higher than Fe_2O_3 as well, although the situation is complicated as

cations are exchanged into the lattice ([135, 143], see, however, [140] as mentioned above). From a comparison between ferrisilicates with varying Si/Fe ratio, Fe(III)/H-(Al)ZSM-5, and Fe₂O₃-admixed H-ZSM-5, Yogo et al. [143] concluded that intra-framework Fe can be differentiated even from extra-framework but intra-zeolite iron species (BE: 712.1–5 and 711.4 eV, respectively, with Si 2p=103.3 eV). This may be true only for the H forms, because a clearly decreasing tendency of the Fe 2p BE upon exchange with alkali cations (Li, Na, and K; O 1s BE unchanged) was reported in another study [142]. Steaming of Na-(Fe)ZSM-5 produced extra-framework iron species discernible by a Fe 2p BE below 711 eV and a shoulder at the O 1s signal [142]. Such a shoulder at the O 1s line is strong evidence for the presence of impurities even if a high Fe 2p BE indicates the presence of some intra-framework iron as well [55, 150]. With increasing (Fe+Al) content of the zeolites, the diagnostic potential of the Fe 2p BE gets lost due to the superposition of various trends. Thus, in K-(Fe_xAl_{1-x})LTL, a Fe 2p BE below 711 eV has been found, although there was no other evidence for extra-zeolite iron [115].

The BE of intra-zeolite Ga has often been reported to exceed that found in Ga₂O₃ [90–93, 109, 152], but there seems to be insufficient BE variation to distinguish between intra-pore species (prepared, e.g., by impregnation) and intra-framework species [152]. However, Shpiro et al. [109] reported an increased binding energy of intra-framework as compared to intra-pore species for the 2p but not for the 3d level which is usually recorded. Reports of decreased Ga binding energies of intra-zeolite Ga species (relative to Ga₂O₃) [153] should be treated with caution because of the very low BE values given for the remaining elements.

Given the importance of AlPO₄ and SAPO molecular sieves, the number of surface studies with these materials is small. Barr et al. [154] have published a detailed investigation on alumophosphates, which confirms earlier work of Suib et al. [155]. Not unexpectedly, the Al 2p BE in AlPO₄ exceeds that in high-silica zeolites, while O 1s is in the same range as the latter. Similar trends were found for SAPO-5 [155], while Si 2p and O 1s binding energies lower than in aluminosilicate zeolites have also been reported [156]. The P 2p binding energies are well in the broad range known for phosphates but below that in P₂O₅ [154, 155]. The surface of AlPO₄ samples was found to be unstable upon prolonged X-ray irradiation [154].

2.4

Host-Guest Systems

Composites containing different types of guests (metal or alloy particles, oxides, sulfides, complexes, polymers) in the cavities of zeolite hosts are prepared for various applications in materials research and catalysis. Except for quality assessment by detection of extra-zeolite material after synthesis or thermal treatments, photoemission plays a largely auxiliary role in this area, cooperating with bulk techniques such as X-ray absorption, UV-Vis, IR of probe molecules, and temperature-programmed reduction. The attention drawn to the significance of intra-zeolite potentials by XPS studies [12] has, however, contributed to the elaboration of a new theory of metal-support interactions [18, 19].

2.4.1

Metals and Alloys

Zeolite matrices have been successfully applied to obtain dispersions of metal and alloy particles of small and fairly uniform dimensions [157, 158]. Under unsuitable conditions, the aggregate size increases by aggregation of particles in neighboring cages [157], by particle growth destroying the surrounding zeolite lattice [159] or after migration to the external zeolite surface. The latter mechanism has been often detected by photoemission [1, 33, 35, 103, 108, 125].

It is well known that the XPS lines of metals shift to higher BE as the particle dimension becomes very small. These shifts may contain contributions from initial-state and from final-state effects (band rehybridization and decreased core-hole shielding capacity, respectively). In zeolites, specific host-guest interactions may also be reflected in the initial state, and the intra-crystalline potentials affect the binding energies. With zeolite-hosted metals, positive shifts as large as 1.4–1.6 eV have been reported (Pt, Ir in Y [160], Pd in Y [130], Pt in H-ZSM-5 [131, 161], Ir in H-ZSM-5 [131, 162]), while shifts of 0.5–1 eV are found quite frequently [33, 35, 124, 131, 163–166]. Such shifts of the metal BE may lead to superposition of the signal with that of ionic species, e.g., Pt(I), Ir(I), and Pd(I) [130, 131] which cannot easily be resolved. Indeed, in the work of Shpiro et al. on the formation of isolated metal atoms in zeolites [131], the most convincing evidence for the zero valence state of the metal came from IR of adsorbed CO. In one report [130], a decrease of the Pd 3d line width served to prove the reduction of Pd(I) to Pd(0) atoms.

The decreased core-hole shielding capacity of very small particles has been found reflected in Auger parameters below that of the bulk metal (Pd(0) in Y [130], Cu(0) in ZSM-5 [108]). The BE shifts obtained with zeolite-encaged metal particles are, however, often larger than expected on the basis of final-state effects alone [167–169]. At comparable cluster size, stronger shifts are found with H-form matrices than with alkali-ion exchanged zeolites [124, 130, 131, 170]. In basic LTL zeolites, very small positive [131] and even strongly negative shifts of the metal BE were reported [170–172] and a correlation between binding energy and alkali content was established [170]. These tendencies have been interpreted to result from changes of the electrostatic potential exerted on the metal atoms by the neighboring ions, in particular oxygen ions [18]: A higher negative charge on oxygen arising from decreased acidity (or increased alkalinity) shifts the electronic states of the metal atoms to higher energy, i.e., decreases the XPS binding energies. The concomitant energetic shift of the conduction band and the modification of the internal potentials between the metal atoms are reflected in changes in CO and H₂ adsorption properties (as detected by IR and EXAFS) and shifts in particular X-ray absorption signals (“AXAFS”: atomic X-ray absorption fine structure), which are summarized elsewhere [18, 19]. This model of metal-support interaction gives a new basis for understanding the pronounced influence of zeolite (or support) acidity on reactions catalyzed by supported metals, e.g., hydrogenolysis [19, 170, 173, 174].

Zeolites have also been used to prepare and study highly dispersed alloy particles. The field has been comprehensively reviewed by Sachtler and Zhang [157].

Table 4. Zeolite-encaged alloys studied by photoemission techniques. For multitechnique studies, the major techniques have been underlined

Alloy	Host	Methods	Ref(s)
Pt-Mo	Y	IR (CO, NO), XANES, XPS, TEM	175
Pt-Cu	Y	TPR, XPS	129
Pt-Cu	ZSM-5	<u>EXAFS</u> , <u>IR (CO)</u> , XPS, XAES	131, 176
Pt-Ga	ZSM-5	<u>XPS</u> , TEM, IR (pyridine)	92, 151
Pt-Cr	ZSM-5	<u>EXAFS</u> , XPS, TEM	177–179
Pt-Co	Y	<u>XPS</u> , TPR, TPD	47, 180–182
Pt-Ir	Y	<u>NMR (Xe)</u> , IR (CO), XPS	183
Pt-In	Y	IR (CO), TPR, XPS	184
Pd-Ni	Y	XPS, XRD	102
RH-Fe	Y	<u>Mössbauer</u> , TPR, XPS	185
Ru-Co	X	XPS	186

Apart from the traditional applications of XPS (detection of extra-zeolite material, assessment of reduction degrees of alloy components), an attempt has been made to prove the formation of alloy particles by observation of alloy shifts with the signals of the metals involved [47]. For this purpose, however, EXAFS is by far superior.

Table 4 summarizes recent studies on zeolite-encaged alloy particles which involved photoemission work. In fact, XPS and related methods are not always used in studies of these materials, so Table 4 does not reflect the whole research activity in the field. The reader interested in such information is referred to [157] and [158].

2.4.2

Other Guests

Table 5 presents a survey of investigations in which materials containing non-metallic guests in zeolites have been studied by XPS. The hosts include sulfides, oxides, chlorides, carbonyl compounds, complexes, polymers, and halogen molecules. Among the applications of XPS are the detection of extra-zeolite material, the investigation of the guest stoichiometry (CdS_x [195], MoS_x [77, 79], NiS_x [193]) or of the degree to which metal ions or carbonyls originally introduced into the zeolite take part in the subsequent guest synthesis (phthalocyanines [200, 201], Chini complexes [192]), and the study of the decomposition chemistry of the guest ($\text{Mo}(\text{CO})_6/\text{Y}$ [77–79, 187], $\text{Pt}(\text{NH}_3)_4^{2-}$ [166]). For problems concerning bulk properties, XPS is often used as an auxiliary technique complementing studies with EXAFS [78, 189, 195–197], IR [78, 194, 196, 197, 203], and UV-Vis [141, 195–197, 203].

The presence or absence of extra-zeolite guest material has been frequently inferred by intensity data. Considerable BE increases of the guest cation in intra-zeolite locations, which have been reported with several host-guest systems (e.g., MoO_3 , WO_3 [196, 198], MoS_2 [77], $\text{Mo}(\text{CO})_6$ and other carbonyl compounds

Table 5. Non-metallic guests in zeolites studied by XPS

Guest type	Guest	Methods used together with XPS	Ref(s)
Carbonyls	Mo(CO) ₆		187, 188
	Mo carbonyls, subcarbonyls	TPD, IR, EXAFS	77–79, 189, 190
	Mo, Fe, Co carbonyls		191
	Fe(CO) ₅	Mössbauer	184
Sulfides	[Pt ₃ (CO) ₆] ₂ ²⁻	XANES, IR	192
	MoS _x	EXAFS, IR	77, 79, 189, 190
	NiS _x	IR	193
	Ni-Mo-sulfides	IR	194
	CdS	UV-Vis	195
Oxides	MoO _x , WO _x	EXAFS, NMR, UV-Vis, IR	196, 197
	Ni-Mo oxides	IR, EXAFS/XANES	198
	TiO ₂ , V ₂ O ₅	UV-Vis	141
Chlorides	CuCl	XAES	96
	AuCl ₃		94, 95
Carbon	“coke”	EELS, TPD, NMR	199
Complexes, dyes	Pt(NH ₃) ₄ ²⁺	TPD, IR	166
	phthalocyanines		200–202
	Co phthalocyanine	IR, UV-Vis, TG/DTA	203
	Rh salene	IR	204
	methylene blue		205
Halogens	iodine		206
Polymers	polypyrrole, -thiophene	IR	207

[191, 196, 197], N 1s in methylene blue or phthalocyanine complexes [195, 205]), may be more useful for the discrimination of intra- and extra-zeolite material. A shift to lower BE has been recently reported for Co 2p and N 1s in Co phthalocyanine encaged in Y [202].

For Cu-based systems (e.g., CuCl/Na-ZSM-5 [96]), the Cu Auger parameter (*vide supra*) is a powerful tool to prove intra-zeolite guest location. Special effects were reported for Co phthalocyanine, where an inequivalence of the N atoms, which is not observed in the XPS of solid phthalocyanine, can be detected when the molecule is dispersed in a zeolite [202]. With Ru and Os phthalocyanine (but not with the Co-, Ni-, and Fe-based complexes), the oxidation state of the metal and, consequently, its BE, has been reported to be higher in intra-zeolite locations than in the bulk solids [200, 202].

References for Part I

1. Hagström SBM, Nordling C, Siegbahn K (1964) Z Phys 178:433
2. Briggs D, Seah MP (eds) (1990) Practical surface analysis, vol 1. Wiley, Chichester New York
3. Cardona M, Ley L (eds) (1978) Photoemission in solids I. In: Topics in applied physics, vol 26. Springer, Berlin Heidelberg New York
4. Hüfner S (1996) Photoelectron spectroscopy: principles and applications, Solid-state sciences, vol. 82. Springer, Berlin Heidelberg New York

5. Seah MP, Dench WA (1974) *Surf Interface Anal* 1:2
6. Quinn JJ (1962) *Phys Rev* 126:1453
7. Grünert W, Schlögl R, Karge HG (1993) *J Phys Chem* 97:8638
8. Grünert W, Muhler M, Schröder K-P, Sauer J, Schlögl R (1994) *J Phys Chem* 98:10920
9. Vayssilov GN, Rösch N (1999) *J Catal* 186:423
10. Ray D, Carette JD (1972) *Topics Curr Phys* 4:13
11. Riviere JC (1990) In: Briggs D, Seah MP (eds) *Practical surface analysis*, vol 1. Wiley, Chichester New York, p 19
12. Shirley DA (1972) *Phys Rev B* 5:272
13. Bishop HE (1981) *Surf Interface Anal* 3:272
14. Barr TL (1983) *Appl Surf Sci* 15:1
15. Powell CJ, Erickson NE, Madey TE (1979) *J Electron Spectrosc Relat Phenom* 2:361
16. Madey TE, Wagner CD, Joshi A (1977) *J Electron Spectrosc Relat Phenom* 10:359
17. Shirley DA (1973) *Adv Chem Phys* 23:85
18. Barr TL, Lishka MA (1986) 108:3178
19. Johnsson O (1975) 8:162
20. Fadley CS (1978) Basic concepts of X-ray photoelectron spectroscopy. In: *Electron spectroscopy: theory, techniques and applications*, vol 2. Academic Press, London New York San Francisco, p 2
21. Hüfner S, Wertheim GK (1973) *Phys Rev B* 7:2333
22. Hedin L, Johansson A (1969) *Phys Rev B* 2:1336
23. Citrin PH, Thomas TD (1972) *J Chem Phys* 57:1446
24. Gadzuk JW, Sunjic M (1975) *Phys Rev B* 12:524

References for Part II

1. Grünert W, Schlögl R, Karge HG (1993) *J Phys Chem* 97:8638
2. Grünert W, Muhler M, Karge HG (1996) *J Chem Soc Faraday Trans* 92:701
3. Uzunova EL, Nikolov GS (2000) *J Phys Chem* 104:5302
4. Tempere JA, Delafosse D, Contour JP (1977) *ACS Symp Ser* 40:76
5. Wagner CD, Six HA, Jansen WJ, Taylor JA (1981) *Appl Surf Sci* 9:203
6. Barr TL (1983) *Appl Surf Sci* 15:1
7. Barr TL, Lishka MA (1986) *J Am Chem Soc* 108:3178
8. Okamoto Y, Ogawa M, Maezawa A, Imanaka T (1988) *J Catal* 112:427
9. Barr TL (1990) *Zeolites* 10:760
10. Ponthieu E, Grange P (1992) *Zeolites* 12:402
11. Huang M, Adnot A, Kaliaguine S (1992) *J Am Chem Soc* 114:10005
12. Grünert W, Muhler M, Schröder K-P, Sauer J, Schlögl R (1994) *J Phys Chem* 98:10920
13. Okamoto Y (1995) *Crit Rev Surf Chem* 5:249
14. Jirka I (1997) *J Phys Chem* 101:8133
15. Waddington SD (1990) Auger chemical shifts and the Auger parameter. In: Briggs D, Seah MP (eds) *Practical surface analysis*, vol 1. Wiley, Chichester New York, p 587
16. Moretti G (1997) Photoelectron and Auger spectroscopy. In: Ertl G, Knözinger H, Weitkamp J (eds) *Handbook of heterogeneous catalysis*, vol 2. Wiley-VCH, Weinheim, p 632
17. Vayssilov GN, Rösch N (1999) *J Catal* 186:423
18. Mojet BL, Miller JT, Ramaker DE, Koningsberger DC (1999) *J Catal* 186:373
19. Koningsberger DC, de Graaf J, Mojet BL, Ramaker DE, Miller JT (2000) *Appl Catal A* 101:205
20. Remy MJ, Genet MJ, Poncelet G, Lardinois PF, Notte PP (1992) *J Phys Chem* 96:2614
21. Remy MJ, Genet MJ, Lardinois PF, Notte PP, Poncelet G (1994) *Surf Interface Anal* 21:649
22. Meier WM, Olson DH, Baerlocher Ch (1996) *Atlas of zeolite structural types*, 4th edn. Elsevier, London
23. Rao GN, Kotasthane AN (1994) *Appl Catal A* 119:33

24. Corma A, Fornes V, Pallota O, Cruz JM, Ayerbe AJ (1986) *J Chem Soc Chem Commun* 4:333
25. Merlen E, Lynch J, Bisiaux M, Raatz F (1990) *Surf Interface Anal* 16:364
26. Guimon C, Zouiten A, Boreave A, Pfister-Guillouzo G, Schulz P, Fitoussi F, Quet C (1994) *J Chem Soc Faraday Trans* 90:3461
27. Goto M, Hidaka S, Takyuu T, Takeshita Y (1987) *X-Sen Bunseki no Shinpo* 18:127
28. Cruz JM, Corma A, Fornes V (1989) *Appl Catal* 50:287
29. Zhu K, Zhu H, Zhang X, Qiu X, Sheng S, Xu Y (1993) *Cuihua Xuebao* 14:127
30. Fleisch TH, Meyers BL, Ray GJ, Hall JB, Marshall CL (1986) *J Catal* 99:117
31. Dwyer J, Fitch FR, Quiz G, Vickerman JC (1982) *J Phys Chem* 86:4574
32. Minachev KM, Shpiro ES (1987) *React Kinet Catal Lett* 35:195
33. Minachev KM, Shpiro ES, Tkachenko OP, Antoshin GV (1984) *Izv Akad Nauk SSSR Ser Khim* 5
34. Kaushik VK, Bhat SGT, Corbin DR (1993) *Zeolites* 13:671
35. Shpiro ES, Minachev KM (1990) *Catalyst surface: physical methods of studying*, 1st edn. CRC Press, Boca Raton
36. Barr TL (1990) Applications of electron spectroscopy to heterogeneous catalysis. In: Briggs D, Seah MP (eds) *Practical surface analysis*, vol 1. Wiley, Chichester New York, p 357
37. Andera V, Kubelkova L, Novakova J, Wichterlova B, Bednarova S (1985) *Zeolites* 5:67
38. Meyers BL, Fleisch TH, Ray GJ, Miller JT, Hall JB (1988) *J Catal* 110:82
39. Meyers BL, Fleisch TH, Marshall CL (1986) *Appl Surf Sci* 26:503
40. Wang QL, Gianetto G, Torrealba M, Perot G, Kappenstein C, Guisnet M (1991) *J Catal* 130:459
41. Kaerger J, Pfeifer H, Seidel R, Staudte B, Gross T (1987) *Zeolites* 7:282
42. Moreno S, Poncelet G (1997) *Microporous Mater* 12:197
43. Marschmeyer S, Papp H (1997) *Surf Interface Anal* 25:660
44. Guimon C, Boreave A, Pfister-Guillouzo G (1994) *Surf Interface Anal* 22:407
45. Shyu JZ, Skopinski ET, Goodwin JG Jr, Sayari A (1985) *Appl Surf Sci* 21:297
46. Kubelkova L, Dudikova L, Bastl Z, Borbely G, Beyer HK (1987) *J Chem Soc Faraday Trans* 1 83:511
47. Zsoldos Z, Vass G, Lu G, Guzzi L (1994) *Appl Surf Sci* 78:467
48. Wagner CD (1990) Photoelectron and Auger energies and the Auger parameter: a data set. In: Briggs D, Seah MP (eds) *Practical surface analysis*, vol 1. Wiley, Chichester New York, p 595
49. Bicker R, Deger H, Herzog W, Rieser K, Pulm H, Hohneicher G, Freund H-J (1985) *J Catal* 94:69
50. He H, Barr TL, Klinowski J (1995) *Clay Miner* 30:201
51. Barr TL, Seal S, He H, Klinowski J (1995) *Vacuum* 46:1391
52. Remy MJ, Genet MJ, Notte PP, Lardiniois PF, Poncelet G (1993) *Microporous Mat* 2:7
53. Winiecki AM, Suib SL, Occelli ML (1988) *Langmuir* 4:512
54. Barr TL, Seal S, Wozniak K, Klinowski J (1997) *J Chem Soc Faraday Trans* 1 93:181
55. Borade RB, Adnot A, Kaliaguine S (1991) *Zeolites* 11:710
56. Borade RB, Clearfield A (1992) *J Phys Chem* 96:6729
57. Minachev KM, Shpiro ES (1986) *Kinet Katal* 27:824
58. Fillipone F, Moretti G (1998) *Appl Surf Sci* 135:150
59. Kaliaguine S (1996) *Stud Surf Sci Catal* 102:191
60. Corbin DR, Keane M, Abrams L, Farlee RD, Bierstedt PE, Bein T (1990) *J Catal* 124:268
61. Namba S, Inaoka A, Yashima T (1986) *Zeolites* 6:107
62. Niwa M, Kato S, Hattori T, Murakami Y (1984) *J Chem Soc Faraday Trans* 1 80:3135
63. Hibino T, Niwa M, Murakami Y, Sano M (1989) *J Chem Soc Faraday Trans* 1 85:2329
64. Catana G, Grünert W, Van der Voort P, Vansant EF, Schoonheydt RA, Weckhuysen BM (2000) *J Phys Chem* 104:9195
65. Defossé C, Canesson P (1976) *J Chem Soc Faraday Trans* 1 72:2565
66. Borade RB, Sayari A, Adnot A, Kaliaguine S (1990) *J Phys Chem* 94:5989
67. Borade RB, Adnot A, Kaliaguine S (1990) *J Mol Catal* 61:L7

68. Borade RB, Adnot A, Kaliaguine S (1990) *J Catal* 126:26
69. Borade RB, Adnot A, Kaliaguine S (1990) *J Chem Soc Faraday Trans* 86:3949
70. Borade RB, Huang M, Adnot A, Sayari A, Kaliaguine S (1993) *Stud Surf Sci Catal* 75: 1625
71. Huang M, Adnot A, Kaliaguine S (1993) *J Chem Soc Faraday Trans* 89:4231
72. Borade RB, Clearfield A (1994) *Stud Surf Sci Catal* 84:661
73. Johansson M, Klier K (1997) *Top Catal* 4:99
74. Huang M, Adnot A, Kaliaguine S (1992) *J Catal* 137:322
75. Xie JH, Huang MM, Kaliaguine S (1997) *Appl Surf Sci* 115:157
76. Borade RB, Clearfield A (1995) *J Chem Soc Faraday Trans* 91:539
77. Okamoto Y, Maezawa A, Kane H, Imanaka T (1989) *J Mol Catal* 52:337
78. Okamoto Y, Imanaka T, Asakura K, Iwasawa Y (1991) *J Phys Chem* 95:3700
79. Okamoto Y, Maezawa A, Kane H, Imanaka T (1988) In: Phillips MJ, Ternan M (eds) *Proc 9th Intern Congr Catalysis*, vol 1. The Chemical Institute of Canada, Ottawa, p 11
80. Barthomeuf D (1994) *NATO ASI Ser C (Acidity and basicity of solids)* 444:181
81. Barthomeuf D (1996) *Catal Rev-Sci Eng* 38:521
82. Auroux A, Huang M, Kaliaguine S (1995) *J Phys Chem* 99:9952
83. Vinek H, Noller H, Ebel M (1976) *Z Phys Chem NF* 13:325
84. Vinek H, Noller H, Ebel M, Schwarz K (1977) *J Chem Soc Faraday Trans* 1 73:734
85. Idriss H, Barteau MA (2000) *Adv Catal* 45:262
86. Wichterlova B, Beran S, Bednarova S, Nedomova K, Dudikova L, Jiru P (1988) *Stud Surf Sci Catal* 37:199
87. Jirka I, Wichterlova B, Maryska M (1991) *Stud Surf Sci Catal* 69:269
88. Wichterlova B, Sobalik Z, Petras M, Jirka I, Bosacek V (1993) *Stud Surf Sci Catal* 75:1649
89. Shpiro ES, Joyner RW, Grünert W, Hayes NW, Siddiqui MRH, Baeva GN (1994) *Stud Surf Sci Catal* 84:1483
90. Kanazirev V, Price GL, Dooley KM (1991) *Stud Surf Sci Catal* 69:277
91. Kanazirev V, Price GL, Tyuliev G (1992) *Zeolites* 12:846
92. Shpiro ES, Shevchenko DP, Tkachenko OP, Dmitriev RV (1994) *Appl Catal A* 107:147
93. Carli R, Bianchi CL, Giannantonio R, Ragaini V (1993) *J Mol Catal* 83:379
94. Qiu S, Ohnishi R, Ichikawa M (1994) *J Phys Chem* 98:2719
95. Salama TM, Shido T, Minagawa H, Ichikawa M (1995) *J Catal* 152:322
96. Grünert W, Liese T, Schobel C (1997) *Stud Surf Sci Catal* 105:1517
97. Liese T, Grünert W (1997) *J Catal* 172:34
98. Ocelli ML, Psaras D, Suib SL, Stencel JM (1986) *Appl Catal* 28:143
99. Torrealba M, Goldwasser MR, Perot G, Guisnet M (1992) *Appl Catal A* 90:35
100. Haas A, Suarez W, Young GW (1992) *AIChE Symp Ser* 291:133
101. Torrealba M, Goldwasser MR, Perot G, Guisnet M (1992) *Rev Soc Venez Catal* 6:89
102. Feeley JS, Stakheev AY, Cavalcanti FAP, Sachtler WMH (1992) *J Catal* 136:82
103. Haack LP, Hubbard CP, Shelef M (1995) *ACS Symp Ser* 587:166
104. Weckhuysen BM, Wang DJ, Rosynek MP, Lunsford JH (1998) *J Catal* 175:347
105. Koyano G, Yokoyama S, Misono M (1999) *Appl Catal A* 188:301
106. Wark M, Koch M, Grünert W (1998) *J Chem Soc Faraday Trans* 94:2033
107. Shpiro ES, Grünert W, Joyner RW, Baeva GN (1994) *Catal Lett* 24:159
108. Grünert W, Hayes NW, Joyner RW, Shpiro ES, Siddiqui MRH, Baeva GN (1994) *J Phys Chem* 98:10832
109. Minachev KM, Bragin OV, Vasina TV, Dergachev AA, Shpiro ES, Sitnik VP, Bondarenko TN, Tkachenko OP, Preobrazhenski AV (1989) *Dokl Akad Nauk SSSR* 304:1391
110. Simon MW, Nam SS, Xu WQ, Suib SL, O'Young JCE, Chin L (1992) *J Phys Chem* 96:6381
111. Xiao S, Meng Z (1994) *J Chem Soc Faraday Trans* 90:2591
112. Grünert W, Sauerlandt U, Schlögl R, Karge HG (1993) *J Phys Chem* 97:1413
113. Mahay A, Lemay G, Adnot A, Szöghy IM, Kaliaguine S (1987) *J Catal* 130:480
114. Simard F, Adnot A, Kaliaguine S (1989) *J Mol Catal* 50:81
115. Joshi PN, Awate SV, Shiralkar VP (1993) *J Phys Chem* 97:9749
116. Grünert W, Muhler M, Karge HG (1996) *DGMK-Ber* 9601:95

117. Wichterlova B, Krajcikova L, Beran Z, Tvaruzkova S (1984) *J Chem Soc Faraday Trans 1* 80:2639
118. Grünert W, Shpiro ES, Feldhaus R, Anders K, Antoshin GV, Minachev KM (1986) *J Catal* 100:138
119. Sexton BA, Smith TD, Sanders JV (1985) *J Electron Spectrosc Relat Phenom* 35:27
120. Moretti G (1994) *Zeolites* 14:469
121. Corma A, Palomares A, Marquez F (1997) *J Catal* 170:132
122. Okamoto Y, Ishida N, Imanaka T, Teranishi S (1979) *J Catal* 58:82
123. Wong TTT, Stakheev AY, Sachtler WMH (1992) *J Phys Chem* 96:7733
124. Busch F, Jaeger NI, Schulz-Ekloff G, Tkachenko OP, Shpiro ES (1996) *J Chem Soc Faraday Trans* 92:693
125. Minachev KM, Baeva GN, Shpiro ES, Antoshin GV, Fasman AB (1985) *Kinet Katal* 26:1265
126. Narayana M, Michalik J, Contarini S, Kevan L (1985) *J Phys Chem* 89:3895
127. Shpiro ES, Baeva GN, Sass A, Shvets VA, Fasman A, Kazanskii VB, Minachev KM (1987) *Kinet Katal* 28:1432
128. Contarini S, Michalik J, Narayana M, Kevan L (1986) *J Phys Chem* 90:4586
129. Moretti G, Sachtler WHM (1989) *J Catal* 115:205
130. Stakheev AY, Sachtler WHM (1991) *J Chem Soc Faraday Trans* 87:3703
131. Shpiro ES, Jaeger NI, Schulz-Ekloff G (1995) *Ber Bunsenges Phys Chem* 99:1321
132. Gol'dshleger NF, Azbel BI, Isakov YI, Shpiro ES, Minachev KM (1990) *Dokl Akad Nauk SSSR* 314:378
133. Frederick BG, Apai G, Rhodin TN (1987) *J Am Chem Soc* 109:4797
134. Goldfarb D, Contarini S, Kevan L (1988) *J Chem Soc Faraday Trans I* 84:2335
135. Trong OD, Bonneviou L, Bittar A, Sayari A, Kaliaguine S (1992) *J Mol Catal* 74:233
136. Blasco T, Cambor MA, Corma A, Perez-Pariente J (1993) *J Am Chem Soc* 115:11806
137. Grohmann I, Pilz W, Walther G, Kosslick H, Tuan VA (1994) *Surf Interface Anal* 22:403
138. Vetter S, Schulz-Ekloff G, Kulawik K, Jaeger NI (1994) *Chem Eng Technol* 17:348
139. Blasco T, Cambor MA, Fierro JLG, Perez-Pariente J (1994) *Microporous Mater* 3:259
140. Fejes P, Nagy JB, Halasz J, Oszko A (1998) *Appl Catal A* 175:89
141. Grubert G, Wark M, Grünert W, Koch M, Schulz-Ekloff G (1997) *Stud Surf Sci Catal* 7105:1077
142. Kan Q, Wu Z, Xu R, Wei Q, Peng S, Xiong G, Sheng S, Huang J (1991) *J Stud Surf Sci Catal* 69:241
143. Yogo K, Tanaka S, Ono T, Mikami T, Kikuchi E (1994) *Microporous Mater* 3:39
144. Rossin JA, Saldarriaga C, Davis ME (1987) *Zeolites* 7:295
145. Stakheev AY, Shpiro ES, Apijok J (1993) *J Phys Chem* 97:5668
146. Yamashita H, Kawasaki S, Ichihashi Y, Harada M, Takeuchi M, Anpo M, Steward G, Fox MA, Louis C, Che M (1998) *J Phys Chem B* 102:5870
147. Mukhopadhyay SM, Garofalini SH (1990) *J Non-Cryst Solids* 126:202
148. Yamashita H, Honda M, Harada M, Ichihashi Y, Anpo M, Hirao T, Itoh N, Iwamoto N (1998) *J Phys Chem B* 102:10707
149. Centi G, Perathoner S, Trifiro F, Aboukais A, Aissi CF, Guelton M (1992) *J Phys Chem* 96:2614
150. Borade RB, Clearfield A (1994) *Microporous Mater* 2:167
151. Shpiro ES, Shevchenko DP, Kharson MS, Dergachev AA, Minachev KM (1992) *Zeolites* 12:670
152. Chao KJ, Sheu SP, Lin LH, Genet MJ, Feng MH (1997) *Zeolites* 18:18
153. Lambert SL (1993) In: von Ballmoos R, Higgins JB, Treacy MMJ (eds) *Proc 9th Intern Zeolite Conf*, vol 1. Butterworth-Heinemann, Boston, p 223
154. He H, Alberti K, Barr TL, Klinowski J (1993) *J Phys Chem* 97:13703
155. Suib SL, Winiecki AM, Kostapapas A, (1987) *Langmuir* 3:483
156. Stoch J, Lercher J, Ceckiewicz S (1992) *Zeolites* 12:81
157. Sachtler WMH, Zhang Z (1993) *Adv Catal* 39:129
158. Stakheev AY, Kustov LM (1999) *Appl Catal A* 188:3
159. Exner D, Jaeger NI, Kleine A, Schulz-Ekloff G (1988) *J Chem Soc Faraday Trans 1* 84:1097

160. Vedrine JC, Dufaux M, Naccache C, Imelik B (1978) *J Chem Soc Faraday Trans 1* 74:440
161. Bragin OV, Shpiro ES, Preobrazhenskii AV, Isaev SA, Vasina TV, Dyusenbina BB, Antoshin GV, Minachev KM (1986) *Appl Catal* 27:219
162. Voskoboinikov TV, Shpiro ES, Landmesser H, Jaeger NI, Schulz-Ekloff G (1996) *J Mol Catal A* 104:299
163. Pedersen LE, Lunsford JH (1980) *J Catal* 61:39
164. Wellenbüscher J, Rosowski F, Klengler U, Muhler M, Ertl G (1994) *Stud Surf Sci Catal* 84:941
165. Voskoboinikov TV, Shpiro ES (1993) *Kinet Katal* 34:321
166. Bastl Z, Kubelkova L, Novakova J (1997) *Zeolites* 19:279
167. Mason MG (1983) *Phys Rev B* 27:748
168. DiCenzo SB, Wertheim GK (1987) *J Electron Spectrosc Relat Phenom* 43:C7
169. Parmigiani F, Kay E, Bagus PS, Nelin CJ (1985) *J Electron Spectrosc Relat Phenom* 36:257
170. Mojet BL, Kappers MJ, Muijsters JC, Niemantsverdriet JW, Miller JT, Modica FS, Koningsberger DC (1994) *Stud Surf Sci Catal* 84:909
171. Jiang X, Gao ZN, Ruan ZK, Sheng SS, Huang JS, Luo XH, Xu YD, Guo XX (1993) *Prepr-Am Chem Soc Div Pet Chem* 38:555
172. Sugimoto M, Katsuno H, Hayasaka T, Ishikawa N, Hirasawa K (1993) *Appl Catal* 102:167
173. Vaarkamp M, Miller JT, Modica FS, Lane GS, Koningsberger DC (1993) *Stud Surf Sci Catal* 75:809
174. Bremer H, Khue NG, Reshetilowski W, Wendlandt KP (1984) *Z Anorg Allg Chem* 508:12
175. Tri TM, Candy J-P, Gallezot P, Massardier J, Primet M, Vedrine JC, Imelik B (1983) *J Catal* 79:396
176. Shpiro ES, Tkachenko OP, Jaeger NI, Schulz-Ekloff G, Grünert W (1998) *J Phys Chem* 102:3798
177. Joyner RW, Minachev KM, Pudney PDA, Shpiro ES, Tuleouva G (1990) *Catal Lett* 5:257
178. Shpiro ES, Joyner RW, Tuleouva G, Preobrazhensky AV, Tkachenko OP, Vasina TV, Bragin OV, Minachev KM (1991) *Stud Surf Sci Catal* 65:357
179. Joyner RW, Shpiro ES, Johnston P, Tuleouva G (1993) *J Catal* 141:250
180. Lu G, Zsoldos Z, Koppány Z, Gucci L (1994) *Catal Lett* 24:15
181. Gucci L, Lu G, Zsoldos Z, Koppány Z (1994) *Stud Surf Sci Catal* 84:949
182. Boix A, Fierro JLG (1999) *Surf Interface Anal* 27:1107
183. Hwang IC, Woo SI (1994) *Stud Surf Sci Catal* 84:757
184. Meriaudeau P, Naccache C, Thangaraj A, Bianchi CL, Carli T, Narayanan S (1995) *J Catal* 152
185. Schuenemann V, Trevino H, Sachtler WMH, Fogash K, Dumesic JA (1995) *J Phys Chem* 99:1317
186. Huang W, Yin L-H, Wang C-Y (1994) *Stud Surf Sci Catal* 84:1633
187. Komatsu T, Namba S, Yashima T, Domen K, Onishi T (1985) *J Mol Catal* 33:345
188. Yong YS, Howe RF, Hughes AE, Jaeger H, Sexton BA (1987) *J Phys Chem* 91:6331
189. Okamoto Y, Katsuyama H, Yoshida K, Nakai K, Matsuo M, Sakamoto Y, Yu JH, Terasaki O (1996) *J Chem Soc Faraday Trans 1* 92:4647
190. Okamoto Y (1997) *Catal Today* 39:1997
191. Andersson SLT, Howe RF (1989) *J Phys Chem* 93:4913
192. Bastl Z, Beneke M, Brabec L, Jaeger NI, Hulstede P, Novakova J, Schulz-Ekloff G (2000) *PCCP* 2:3099
193. Mariscal R, Navarro RM, Pawelec B, Fierro JLG (2000) *Microporous Mesoporous Mater* 34:181
194. Ezzamarthy A, Catherine E, Cornet D, Hemidy JF, Janin A, Lavalley JC, Leglise J (1989) In: Jacobs PA, van Santen RA (eds) *Zeolites: facts figures, future*, Elsevier Science Publishers BV, Amsterdam, p 1025
195. Tkachenko OV, Shpiro ES, Wark M, Schulz-Ekloff G, Jaeger NI (1993) *J Chem Soc Faraday Trans* 89:3987
196. Ozin GA, Prokopowicz RA, Ozkar S (1992) *J Am Chem Soc* 114:8953
197. Ozkar S, Ozin GA, Prokopowicz RA (1992) *Chem Mater* 4:1380

198. Corma A, Vazquez MI, Bianconi A, Clozza A, Garcia J, Pallota U, Cruz JM (1988) *Zeolites* 8:464
199. Fleisch TH, Zajac GW, Meyers BL, Ray GJ, Miller JT (1988) In: Phillips MJ, Ternan M (eds) *Proc 9th Intern Congr Catalysis*, vol 1. The Chemical Institute of Canada, Ottawa, p 483
200. Shpiro ES, Antoshin GV, Tkachenko OP, Gudkov SV, Romanovsky BV, Minachev KM (1984) *Stud Surf Sci Catal* 18:31
201. Romanovsky BV, Gabrielov AG (1992) *Stud Surf Sci Catal* 72:443
202. Romanovsky BV, Gabrielov AG (1992) *J Mol Catal* 74:293
203. Paez-Mozo E, Gabriunas N, Lucaccioni F, Acosta DD, Patrono P, La Ginestra A, Ruiz P, Delmon B (1993) *J Phys Chem* 97:12819
204. Balkus KJ Jr, Welch AA, Gnade BE (1990) *Zeolites* 10:722
205. Hoppe R, Schulz-Ekloff G, Woehrle D, Shpiro ES, Tkachenko OV (1993) *Zeolites* 13:222
206. Rehakova M, Bastl Z, Finocchiaro P, Sopkova A (1995) *J Therm Anal* 45:511
207. Millar GJ, McCann GF, Hobbis CM, Bowmaker GA, Cooney RP (1994) *J Chem Soc Faraday Trans 1* 90:2579

Mössbauer Spectroscopy

Lovat V.C. Rees

Department of Chemistry, University of Edinburgh, King's Buildings, West Mains Road,
Edinburgh EH9 3JJ, UK. *E-mail:* Lovat.Rees@ed.ac.uk

1	The Mössbauer Effect	517
1.1	Hyperfine Interactions	521
1.1.1	Chemical Isomer Shift, δ	521
1.1.1.1	Second-Order Doppler Shift	522
1.1.2	Electric Quadrupole Interactions	522
1.1.3	Magnetic Hyperfine Interactions	523
1.2	Relative Intensities of Absorption Lines	523
2	Mössbauer Studies of Zeolites	525
2.1	Mössbauer Studies of Fe^{2+} and Fe^{3+} Cation Exchanged Zeolites	525
2.2	Ion Exchange	532
2.3	^{57}Co Emission Studies	533
2.4	Conversion Electron Mössbauer Spectroscopy	534
2.5	Tetrahedral Framework Fe(III)	535
2.6	Catalytic Studies	539
2.7	Encapsulation of Organometallic Complexes	539
2.8	Catalyst Preparation	541
2.9	Mesoporous Materials	541
3	Conclusions	541
4	References	542

1

The Mössbauer Effect

When a nucleus emits or absorbs a γ -photon without loss of energy from recoil of the nucleus or from thermal broadening effects, the phenomenon is referred to as the Mössbauer effect. The γ -photon is monochromatic to 1 part in 10^{10} – 10^{12} and this extremely well-defined electromagnetic radiation can be used to study the very small differences in the energy of interaction between a nucleus and its extra-nuclear electrons when a Mössbauer atom is sited in different chemical and physical environments.

Iron, tin, antimony, tellurium, iodine, xenon, europium, gold and neptunium are useful Mössbauer elements while nickel, ruthenium, tungsten and iridium can also be used but with greater difficulty. Much of the work reported in the lit-

erature involves iron and tin nuclei as these elements give good spectra at room and even higher temperatures. The other elements listed above are usually studied at much lower temperatures, e.g., 78 K, and in some cases temperatures down to 4 K need to be used.

If the excited state of a nucleus has a mean life-time, τ , there will be a spread of the γ -ray energy, E_γ , resulting from the decay of this nucleus, due to the Heisenberg uncertainty principle, of width, Γ_s , at half height;

$$\Gamma_s = \hbar/2\pi\tau = \hbar/\tau \quad (1)$$

where \hbar is Planck's constant.

For Fe(57), the half-life, $t_{1/2}$, is 97.7 ns. Therefore, $\Gamma_s[\text{Fe}(57)]$ is 4.67×10^{-9} eV. Since E_γ is 14.41 keV the Mössbauer radiation from Fe(57) is monochromatic to 3 parts in 10^{13} .

The probability of recoilless emission of a γ -ray from a nucleus is given by the recoil free fraction, f , where

$$f = \exp\left(\frac{-4\pi^2\langle x^2 \rangle}{\lambda^2}\right) = \exp\left(\frac{-E_\gamma^2(x^2)}{(\hbar c)^2}\right) \quad (2)$$

$\langle x^2 \rangle$ is the mean square vibrational amplitude of the emitting atom in the direction of the γ -ray of wave-length λ . The recoil free fraction, f , only becomes significant when $\langle x^2 \rangle \ll \lambda^2$ and E_γ is small. Thus an essential element in Mössbauer spectroscopy is that the emitting and absorbing nuclei must be tightly embedded in a *solid* lattice and E_γ has to be less than 150 keV.

The temperature dependence of f can be used to study lattice dynamics. However, a model has to be assumed for the vibrational modes. If one assumes an Einstein model (see, e.g., [1]) then:

$$f = \exp\left(\frac{-E_R}{\hbar\omega_E}\right) = \exp\left(\frac{-E_R}{k\theta_E}\right) \quad (3)$$

and for a Debye solid

$$f = \exp\left[\frac{-6E_R}{k\theta_D} \left\{ \frac{1}{4} + \left(\frac{T}{\theta_D}\right)^2 \int_0^{\theta_D/T} \frac{x dx}{e^x - 1} \right\}\right] \quad (4)$$

where ω_E and θ_E are the Einstein frequency and temperature, respectively, θ_D is the corresponding Debye temperature and E_R is the recoil kinetic energy given by $E_\gamma^2/2Mc^2$ where M is the mass of the vibration species and c is the velocity of light. θ_D varies from 88 K for Pb to 1000 K for Be.

Mössbauer experiments in the transmission mode (as shown in Fig. 1) usually use recoilless γ -rays emitted from a radioactive source followed by resonant recoilless reabsorption by a non-radioactive absorber. If the probability of recoilless emission from a source is f_s and the γ -photon has width Γ_s at half-height then the number of transitions $N(E)$ with energies between $(E_\gamma - E)$ and $(E_\gamma - E + dE)$ is given by:

$$N(E) \cdot dE = \frac{f_s \Gamma_s}{2\pi} \cdot \frac{dE}{(E - E_\gamma)^2 + (\Gamma_s/2)^2} \quad (5)$$

which is a Lorentzian distribution.

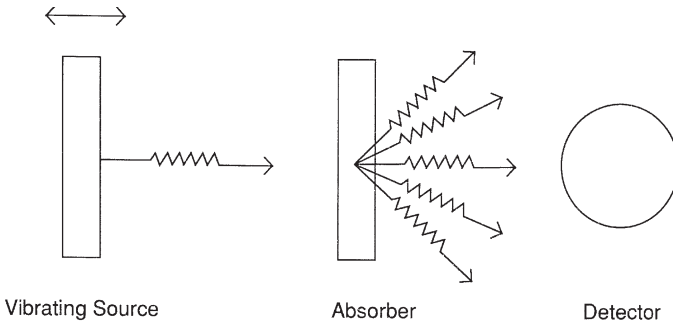


Fig. 1. Transition mode of Mössbauer spectroscopy

The resonant absorption cross-section $\sigma(E)$ is given by:

$$\sigma(E) = \sigma_0 \frac{(\Gamma_a/2)^2}{(E - E_\gamma) + (\Gamma_a/2)^2} \tag{6}$$

where Γ_a is Heisenberg width at half-height of the absorption profile and

$$\sigma_0 = 2\pi \lambda^2 \cdot \frac{2I_e + 1}{2I_g + 1} \cdot \frac{1}{1 + \alpha} \tag{7}$$

I_e and I_g are the respective nuclear spin quantum numbers of the excited and ground states of the nucleus and α is the internal conversion coefficient, i.e., α is the ratio of the number of conversion electrons to the number of γ -ray photons emitted from a Mössbauer atom. For σ_0 to be large we need E_γ and α to be small. σ_0 must also be large compared with the cross-section for other absorption processes, e.g., photoelectric.

If both source and absorber have the same line-width Γ (i.e., $\Gamma = \Gamma_s, \Gamma_a$) and the source and absorber have thicknesses tending to zero, the decrease in transmission with respect to ε , where ε is the energy displacement between source and absorber distribution maxima, is given by:

$$I(\varepsilon) = \frac{\Gamma_r}{2\pi} \frac{1}{(\varepsilon - E_\gamma) + (\Gamma_r/2)^2} \tag{8}$$

which is normalised such that:

$$\int_0^\infty I(E) d\varepsilon = 1$$

and $\Gamma_r = \Gamma_s + \Gamma_a = 2\Gamma$. This distribution is still Lorentzian. If the absorber has effective thickness $t = f_a n_a a_a \sigma_0 t_a$, the shape is still Lorentzian but broadened so that:

$$\frac{\Gamma_r}{\Gamma} = 2.0 + 0.27 t \quad \text{for } 0 < t \leq 5$$

and

$$\frac{\Gamma_r}{\Gamma} = 2.02 + 0.29t - 0.005t^2 \quad \text{for } 5 \leq t \leq 10$$

where n_a is the number of atoms of element concerned per cm^2 , a_a is the fractional abundance of the resonant isotope, and t_a is the thickness of the absorber (cm).

In Mössbauer spectroscopy the γ -rays from the source are passed through the absorber to a detector, as shown in Fig. 1. Transmission of the γ -rays is reduced because of resonant absorption in the absorber followed by re-emission over a 4π solid angle. When the Mössbauer active isotope in the source exists in a different chemical environment to the same isotopic species in the absorber then the energy of the γ -ray, E_γ , emitted by the source will differ from that required for resonant absorption by the absorber; E_γ can be modulated by moving the source or the absorber relative to the other. By applying an external Doppler energy, $\varepsilon = (v/c)E_\gamma$, where v is the Doppler velocity, the energy of the γ -ray, E_γ , can be adjusted to give resonant absorption. Thus, at a certain Doppler velocity, resonance will be a maximum and the count rate a minimum. At velocities above and below this optimum value resonance will decrease until it is effectively zero at velocities well removed from that at maximum resonance. A Mössbauer spectrum is usually presented as a plot of transmission against Doppler velocity. The Doppler velocities required to scan the line widths of various Mössbauer isotopes are quite small, e.g. Fe(57)=0.192 mm s^{-1} , Sn(119)=0.626 mm s^{-1} , Pt(195)=16 mm s^{-1} .

The normal experimental technique is to scan rapidly through the velocity range and repeat this scan many times until data of the required accuracy has been accumulated. The Doppler motion is provided by an electromechanical drive system controlled by a servo-amplifier. Usually, the source is attached to the drive shaft and driven either in a saw-tooth or a triangular constant acceleration wave form. The transducer is coupled to a multichannel analyser operating in the *multiscaler* mode, and the servo-amplifier is controlled by the channel advance frequency. The dwell time in each channel, corresponding to a specific velocity increment, is $\sim 100 \mu\text{s}$, and while the channel gate is open it accepts pulses from the detector.

The appropriate excited state of the resonant nucleus can be populated from (a) decay of a radioactive precursor, (b) nuclear reaction or (c) by excitation. Method (a) is most frequently employed because of its convenience. A typical example is shown in Fig. 2 for Co(57), which leads to the 14.41 keV first excited level of Fe(57) by electron capture. The internal conversion coefficient, α , for the 14.41 keV γ -ray is ~ 9.0 . Therefore, only $\sim 10\%$ of the nuclear decays originating from B produce the required 14.41 keV photon.

The thickness of the absorber required depends on numerous factors which tend to be specific to the isotope under consideration. For example, there is only 2.19% of the Fe(57) isotope in natural iron but the isotope has a large cross-section, α_0 , for 14.4 keV γ -rays of $2.57 \times 10^{-18} \text{ cm}^2$, and the optimum thickness for the absorber is found to be $\sim 10 \text{ mg}$ of total iron per cm^2 . One can readily obtain samples of iron enriched up to 90% in Fe(57). In such samples absorbers containing less than 1 mg of iron can give excellent spectra.

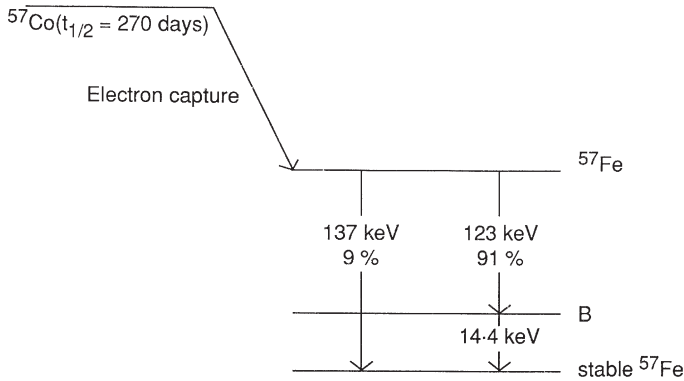


Fig. 2. Decay scheme of Co(57). The M1 decay from the 14.41 keV level is the Mössbauer active decay

1.1 Hyperfine Interactions

A Mössbauer spectrum can give information on three hyperfine interactions.

1.1.1 Chemical Isomer Shift, δ

The chemical isomer shift (IS) is given by:

$$\delta = \frac{2}{5} \pi Z e^2 \left\{ |\Psi_s(0)_A|^2 - |\Psi_s(0)_s|^2 \right\} \left\{ \langle R_e^2 \rangle - \langle R_g^2 \rangle \right\} \quad (9)$$

where $|\psi_s(0)|^2$ is the s-electron density at the nucleus and “A” and “S” refer to absorber and source, respectively. $\langle R^2 \rangle$ is the mean square radius and allows, therefore, for the quite common non-spherical shape of the nucleus. “e” and “g” refer to the excited and ground state of the nucleus. Equation (9) is a product of a chemical and nuclear term. The latter is constant for a given transition. For chemical applications we have, therefore:

$$\delta = \text{const} \cdot \left\{ |\Psi_s(0)_A|^2 - |\Psi_s(0)_s|^2 \right\} \quad (10)$$

The s-electron density at the nucleus is affected not only by the s-electron population, but also by the screening effects of p-, d-, and f-electrons and by covalency factors and bond formation.

In Fe(57) $R_g > R_e$ and a decrease in the IS therefore represents an increase in s-electron density on going from source to absorber. δ is usually quoted as a velocity, ν , in mm s^{-1} but can be converted to an energy from $\delta = (\nu/c)E_\gamma$.

1.1.1.1

Second-Order Doppler Shift

A relativistic temperature-dependent contribution to the IS exists. Since the emitting (or absorbing) atom vibrates on its lattice site, the emitted photon is affected by this Doppler motion. The observed frequency, ν' , of the photon compared with its frequency, ν , from a stationary source is given by

$$\nu' = \nu \left(1 - \frac{v}{c} \right) \left(1 + \frac{v^2}{2c^2} \right) \quad (11)$$

The first quotient is a function of the velocity, v , of the atom vibrating on its lattice site in the direction of the γ -ray and will average to zero over the lifetime of the excited state. The second term will not. It is referred to as a second-order Doppler shift given by:

$$\nu' = \nu \left(1 + \frac{\langle v^2 \rangle}{2c^2} \right) \quad (12)$$

which results in the Mössbauer line being shifted by:

$$\frac{dE_\gamma}{E_\gamma} = \frac{d\nu}{\nu} = - \frac{\langle v^2 \rangle}{2c^2} \quad (13)$$

Usually, if IS data are all obtained at the same low temperature, they may be directly compared as the respective zero-point and temperature-dependent terms largely cancel out.

1.1.2

Electric Quadrupole Interactions

The existence of an electric quadrupole interaction is one of the most useful features of Mössbauer spectroscopy. The energy levels in the presence of an electric field gradient (e.f.g.), q , are:

$$E_Q = \frac{eQ}{4I(2I-1)} \left[3m_I^2 - I(I+1) \right] \left(1 + \frac{\eta^2}{3} \right)^{1/2} \quad (14)$$

where eQ is the quadrupole moment of the nucleus of spin I . Further, $m_I = I, I-1, \dots, -I$, and η is the asymmetry parameter given by the second derivatives of the potential, V , with respect to the (Cartesian) coordinates x, y, z as follows:

$$\eta = \frac{V_{yy} - V_{xx}}{V_{zz}} \quad (15)$$

The axis system of the resonant atom is defined such that the maximum value of the e.f.g. is taken to be V_{zz} in the z -direction. The corresponding e.f.g.'s in the x and y directions are V_{xx} and V_{yy} , respectively.

For the case of Fe(57) $I_e=3/2$ and $I_g=1/2$. Thus the ground state has only one energy level in an e.f.g. but the excited state has two eigen values, $E_Q=eqQ/4$ and $E_Q=-eqQ/4$ for $m_I=\pm 3/2$ and $\pm 1/2$, respectively, when $\eta=0$, i.e. axial symmetry exists. Thus the spectrum consists of two lines of equal intensity if the sample is an isotropic powder with a quadrupole splitting (QS) of $1/2 eqQ$.

1.1.3

Magnetic Hyperfine Interactions

The third hyperfine interaction is the nuclear Zeeman effect which is found when a magnetic field exists at the nucleus. The energy levels obtained are:

$$E_m = -g\mu_N H m_I \quad (16)$$

where g is the nuclear g -factor, μ_N is the nuclear Bohr magneton and H is the magnetic field. There are $2I+1$ magnetic sub-levels equally spaced with a separation of $g\mu_N H$ between them. The nucleus experiences this interaction in both its excited and ground states but Δm_I is usually restricted by selection rules to $0, \pm 1$. The allowed transitions for the $3/2 \rightarrow 1/2$ Mössbauer transitions in Fe(57) produce a six-line spectrum in a randomly orientated, polycrystalline sample.

Figure 3 examples of spectra are given which demonstrate these three hyperfine interactions. Note in these spectra that at resonance the detector is observing a decrease in counts of up to 15%.

When both magnetic and quadrupole hyperfine interactions are present simultaneously the general interpretation of the spectrum can be quite complex. Since both interactions are direction-dependent it is necessary to know the angle between the principal axis of the e.f.g. tensor and the magnetic axis. Solutions are not too complicated if one interaction is weak and can be considered to be only a perturbation on the principal interaction. In many cases it is not possible to use such a simplified treatment and a complete analysis is required.

1.2

Relative Intensities of Absorption Lines

The probability of a γ -ray transition occurring depends on the product of an angular-independent term (the square of the appropriate *Clebsch-Gordan* coefficient, see Condon and Shortley "The Theory of Atomic Spectra" Cambridge University Press, 2nd edn 1953) and an angular-dependent term where θ is the angle between the direction of the γ -ray and the principal axis (z axis) of the magnetic field or e.f.g. tensor. The probabilities are listed in Table 1 for Fe(57) transitions.

When using a polycrystalline absorber, integration over all angles has to be made and the angular-independent probabilities are obtained.

The angular dependence of the intensities of a quadrupole-split spectrum from a single crystal absorber allows one to determine the line associated with the $\pm 3/2 \rightarrow \pm 1/2$ transition from the other line, and hence the sign of the princi-

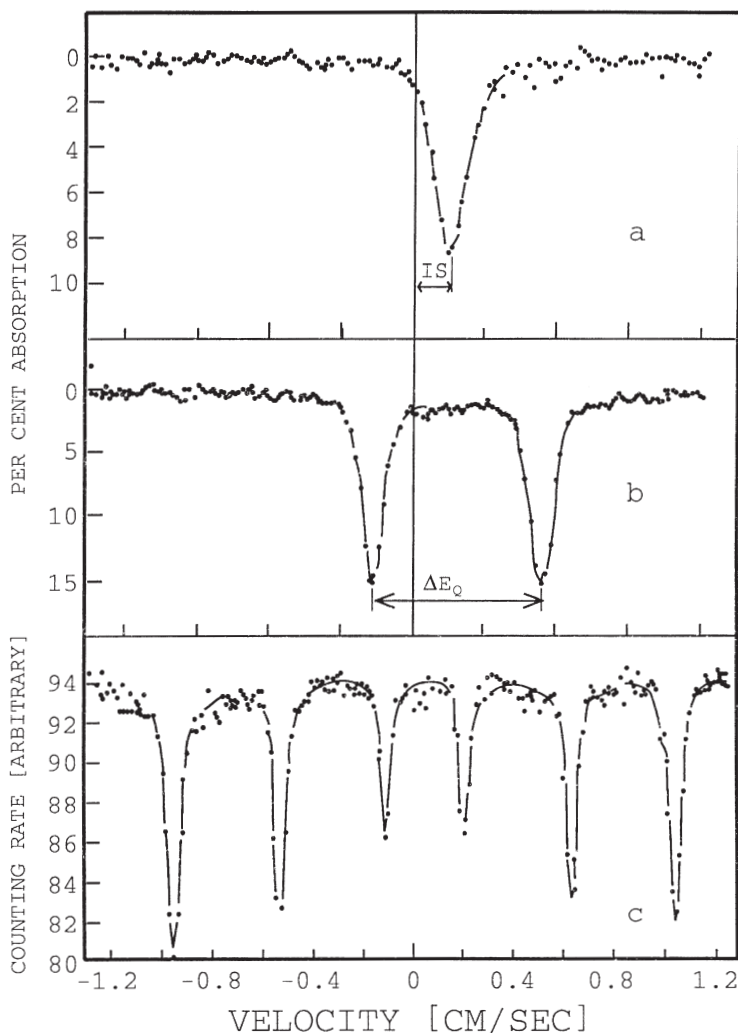


Fig. 3a-c. Spectra demonstrating the three hyperfine interactions of Fe(57). **a** Isomer shift; **b** quadrupole splitting; and **c** magnetic splitting

pal component of the e.f.g. tensor can be obtained. Analysis of magnetically split spectra derived from single crystal samples can also be used.

A number of excellent books have been published and these should be consulted when more extensive treatments of the theory of Mössbauer spectroscopy are required. (1) *Mössbauer Spectroscopy*, by N.N. Greenwood and T.C. Gibb, Chapman and Hall, 1971; (2) "Chemical Applications of Mössbauer Spectroscopy", V.I. Goldanskii and R.H. Herber (eds), Academic Press, 1968; and (3) "NMR, NQR, EPR and Mössbauer Spectroscopy in Inorganic Chemistry" by R.V. Parrish, Ellis Horwood, 1990.

Table 1. Relative probabilities for a dipole $3/2 \rightarrow 1/2$ transition

Magnetic spectra (M1)			Angular independent term			Angular dependent term	
m_1	m_2	$m_1 - m_2$		$\theta =$	90°	45°	0°
+3/2	+1/2	+1	3	$1 + \cos^2\theta$	3	4.5	6
+1/2	+1/2	0	2	$2 \sin^2\theta$	4	2	0
-1/2	+1/2	-1	1	$1 + \cos^2\theta$	1	1.5	2
-3/2	+1/2	-2	0	0	0	0	0
+3/2	-1/2	+2	0	0	0	0	0
+1/2	-1/2	+1	1	$1 + \cos^2\theta$	1	1.5	2
-1/2	-1/2	0	2	$2 \sin^2\theta$	4	2	0
-3/2	-1/2	-1	3	$1 + \cos^2\theta$	3	4.5	6

Quadrupole spectra(M1)		Angular independent term			Angular dependent term	
Transition			$\theta =$	90°	45°	0°
$\pm 1/2, \pm 1/2$		1	$2 + 3\sin^2\theta$	5	3.5	2
$\pm 3/2, \pm 1/2$		1	$3(1 + \cos^2\theta)$	3	4.5	6

2

Mössbauer Studies of Zeolites

2.1

Mössbauer Studies of Fe^{2+} and Fe^{3+} Cation Exchanged Zeolites

Mössbauer spectroscopy is a versatile technique for determining cation locations and coordination geometries in materials where the Mössbauer ions may be found in several sites. Such is the case in zeolites where the cations required to balance the negative charge of the aluminosilicate lattice can take up a number of different positions to produce a distribution with the lowest free energy. Mössbauer studies have been made on a number of zeolites, most interest being shown in the catalytically active Y-zeolites [2, 3]. Because of these catalytic properties the interaction between the cations in the zeolite and absorbed gases is also of interest and one that is particularly amenable to study by Mössbauer spectroscopy.

Unfortunately, in ferrous-Y after activation (in these samples only partial exchange of sodium-Y with ferrous ions has taken place), most of the ferrous ions occupy sites which are not accessible to organic sorbates. Essentially, the spectra of dehydrated ferrous-Y consist of two doublets; one with an isomer shift (IS) of 1.29 mm s^{-1} and a quadrupole splitting (QS) of 2.35 mm s^{-1} , and a smaller doublet with an IS of 0.91 mm s^{-1} and a QS of 0.62 mm s^{-1} [2–5]. The IS values are with respect to (w.r.t.) natural metallic iron as the standard. The ferrous ions producing the inner doublet are sited in the six-membered oxygen rings separating the supercage from the sodalite cages and are accessible to sorbates; however, they

produce less than 15% of the total Mössbauer absorbance. Thus, in the spectra of ferrous-Y after adsorption of various gases, the peaks due to the ferrous-sorbate complexes are not easily resolved. The changes to the parameters of the inner doublet due to the complexes being formed have to be deconvoluted from the much larger, unchanged outer doublet signal.

However, zeolite A has been extensively studied to overcome the problems encountered with zeolite Y. The zeolite A structure is similar to zeolite Y in a number of respects. Both zeolites contain sodalite cages as a basic structural unit. In zeolite Y these sodalite cages are joined to neighbouring sodalite cages through four of the eight six-membered oxygen rings which exist in a sodalite unit by oxygen bridges to give a tetrahedral array of sodalite units, whilst in zeolite A the six four-membered rings of the sodalite unit are used through oxygen bridges to give an octahedral array. In zeolite Y the sodalite units and hexagonal prisms contain cationic sites which are favoured on dehydration whereas in zeolite A cations are not sited in the sodalite cages and small cubic cages but prefer the six-membered oxygen rings between the sodalite and supercages. Although both zeolites contain this sodalite "window" site it is the preferred site for many divalent cations in the case of zeolite A.

However, zeolite A under normal synthetic conditions has a Si/Al ratio of 1 and is very unstable to acidic solutions. It is, therefore, quite difficult to ion-exchange Fe^{2+} ions into the zeolite without introducing spurious components into the Mössbauer spectra. Hydroxide species are precipitated on the external surfaces of the zeolite if reasonably high values of pH are used during the exchange while some degree of lattice collapse occurs on dehydration of the Fe^{2+} zeolite if lower values of pH are employed. It is essential, therefore, to establish the optimum conditions required to produce the maximum degree of Fe^{2+} exchange in zeolite A with a minimum degree of hydrolysis [6].

The optimum conditions were found to be as follows. H_2SO_4 (0.125 M) was added to a slurry of 0.5 g of the pure Na form of zeolite A in 45 ml of distilled water over a period of 20 min to give a final molarity of 0.0125 M H_2SO_4 . Solid $\text{FeSO}_4 \cdot 7\text{H}_2\text{O}$ (2 g) plus ascorbic acid (1 mg) were then added over a period of 5 min. Agitation was maintained by bubbling oxygen-free, nitrogen gas through the reactants for 1 h. The exchange was carried out in a glove box under an oxygen-free, nitrogen atmosphere. The unit cell formula of the optimum product was $\text{Na}_{3.67}\text{H}_{1.59}\text{Fe}_{3.37}[\text{Al}_{12}\text{Si}_{12}\text{O}_{48}]$. X-ray powder diffraction and oxygen sorption capacity at liquid nitrogen temperature confirmed that no structural breakdown had occurred.

The ferrous-exchanged zeolite was transferred as a slurry in distilled water into a Pyrex glass Mössbauer sample cell under oxygen-free, nitrogen gas. The cell had two very thin Pyrex windows separated by a 1 mm gap. The sample filled this gap after the excess water had been removed under vacuum. It is essential to keep the dry zeolite free from contact with air or oxygen as some immediate oxidation to the Fe^{3+} state can occur. The thin windows of the cell allowed some 40% transmission of the 14.4 keV γ -rays to occur. The Mössbauer spectrometer used and the complete experimental details are described in detail elsewhere [7].

The room temperature Mössbauer spectrum of the above sample shown in Fig. 4 consists of a broad doublet with IS of 1.20–1.22 mm s^{-1} , QS of

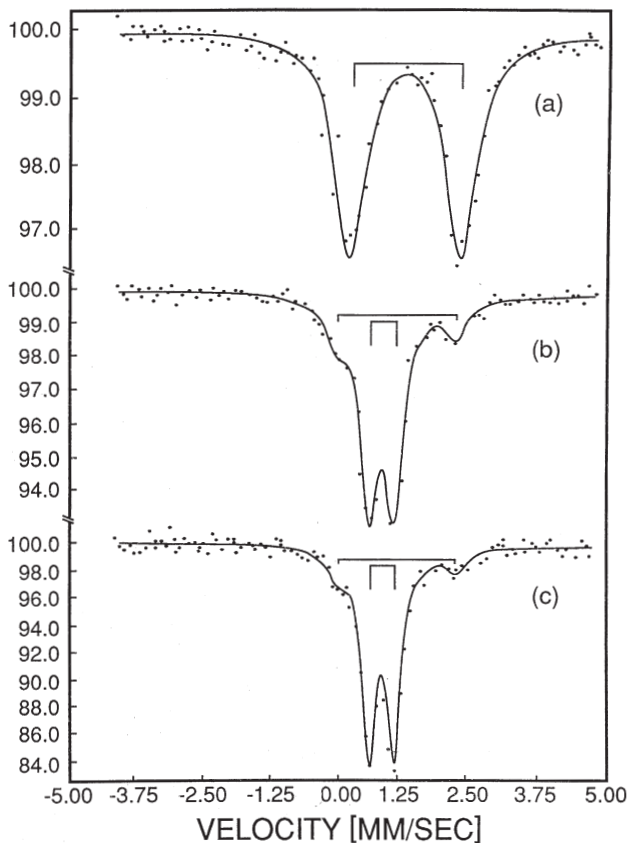


Fig. 4a-c. Room temperature Mössbauer spectra of (Fe,Na)-A zeolite. a Hydrated; b dehydrated at 373 K; and c dehydrated at 633 K

2.06–2.12 mm s^{-1} and line width, Γ , of 0.33–0.36 mm s^{-1} . Because of the high recoil free fraction, f , of this hydrated zeolite sample it was concluded that the Fe^{2+} ions were tightly bound on site I (six-membered window site) coordinated to three, nearest neighbour, framework oxygens of the six-ring and three water molecules in the supercage. There was no evidence of any other type of Fe^{2+} species being present which confirms that significant lattice collapse of zeolite A containing appreciable quantities of H^+ ions only occurs on dehydration at temperatures in excess of 373 K.

When the above sample is dehydrated under vacuum at 373 K the spectrum in Fig. 4 now exhibits two doublets arising from two different types of coordination around the Fe^{2+} ions. The parameters of the much weaker outer doublet ($\text{IS}=1.13\text{--}1.07 \text{ mm s}^{-1}$, $\text{QS}=2.30\text{--}2.12 \text{ mm s}^{-1}$) show a small decrease in IS and a small increase in QS compared with the parameters found above for the completely hydrated sample. These results are consistent with Fe^{2+} ions located in site I but now coordinated to three (or possibly fewer) water molecules in a more dis-

torted geometry than exists in the fully hydrated zeolite. However, this doublet could be produced by Fe^{2+} ions located in collapsed framework "sites". The intense low QS doublet is produced by Fe^{2+} located on site I trigonally coordinated to the three nearest neighbour framework oxygens. Thus, even after very mild dehydration at 373 K, some 70%–80% of the Fe^{2+} ions have no water ligands.

On dehydration at 633 K under vacuum for 24 h the spectrum in Fig. 4 shows that the area under the inner doublet increases slightly at the expense of the area under the outer doublet. When the dehydration was continued for a further 48 h to remove the last traces of water the area under the inner doublet increased again to a small extent at the expense of the outer doublet.

In all of the above dehydration spectra the parameters of the intense, inner doublet stayed sensibly constant at $\text{IS}=0.83\text{--}0.84\text{ mm s}^{-1}$, $\text{QS}=0.46\text{--}0.48\text{ mm s}^{-1}$ and line width of about 0.35 mm s^{-1} .

The temperature dependence of the inner doublet parameters were measured over the range 80–625 K. The QS area was found to be virtually independent of temperature decreasing only by 0.04 mm s^{-1} on increasing the temperature from 80 to 625 K. The IS showed a slight non-linear temperature dependence over this large temperature range decreasing from 0.89 mm s^{-1} at 80 K to 0.60 mm s^{-1} at 625 K. An IS of 0.83 mm s^{-1} at RT is very low for a high-spin ferrous ion but is consistent with a ferrous ion being located in a site of low coordination number. The very low, temperature-independent QS is also consistent with this low coordination. Simple crystal field theory indicates that the low QS arises from a near cancellation of the valence and lattice contributions to the electric field gradient at the ferrous nucleus. A value of 2.6 mm s^{-1} is calculated for the lattice contribution to the QS and between -2 and -3 mm s^{-1} for the valence contribution. As the ferrous ion site has threefold symmetry, the total QS is just the simple sum of these two contributions. Crystal field theory supports then the conclusion that the inner doublet arises from a ferrous ion in planar threefold coordination with framework oxygens, i.e. Fe^{2+} ions in site I have C_{3v} symmetry. The temperature independence of the QS arises from the large energy difference that exists between the d_z orbital and the next higher d_{xz} and d_{yz} orbitals.

The Fe^{2+} ions sited in site I of zeolite A are ideally suited for Mössbauer studies of the adsorption of adsorbates in this zeolite. When a sorbate molecule is sorbed on these Fe^{2+} ions, the symmetry around the Fe^{2+} ion changes from planar, threefold coordination of framework oxygens to a more symmetrical complex which has a distorted tetrahedral nature. In such a complex the Fe^{2+} ions are drawn out of the plane of the six-ring "window" and the lattice contribution to the QS is considerably reduced. The net result is that the QS increases on formation of the sorption complex to a value nearer the more normal value for Fe^{2+} ions in tetrahedral/octahedral complexes of greater than 2 mm s^{-1} . Such a large change in the QS (and also quite a significant change in the IS to values greater than 1 mm s^{-1}) is easy to observe and quantify. The sensitivity of such Fe^{2+} ions to the addition of sorbed species has been used in numerous studies. For example, the sorption, desorption of water [8–10] and ethanol [11] in zeolite A has been extensively studied.

The sorption of ethylene gave some very interesting results which are worth reporting in more detail [12]. The room temperature spectra of ferrous-A zeo-

lite containing increasing quantities of adsorbed ethylene are shown in Fig. 5. The spectra show no sign of a product doublet at loadings less than one ethylene molecule per Fe^{2+} cation (i.e. 1.5 mmol of ethylene g^{-1} of zeolite). Single doublets were fitted to the spectra and the IS, QS and areas under the doublets obtained from these fits are plotted in Fig. 6 as a function of ethylene loading. The area under the doublets shows a remarkable decrease and then an increase as the ethylene loading increases to a maximum value studied of ~ 5 molecules of ethylene per supercage. Both the QS and IS increase with loading until a loading of one molecule of ethylene per Fe^{2+} cation is achieved but then tend to flatten off. A sample at a loading of approximately one ethylene molecule per two Fe^{2+} cations was studied over the temperature range of RT down to 80 K. The spectra obtained are shown in Fig. 7 and clearly demonstrate the development of two doublets when the temperature is less than 200 K. At 80 K the parameters of the two doublets were accurately determined and found to be (a) an inner doublet

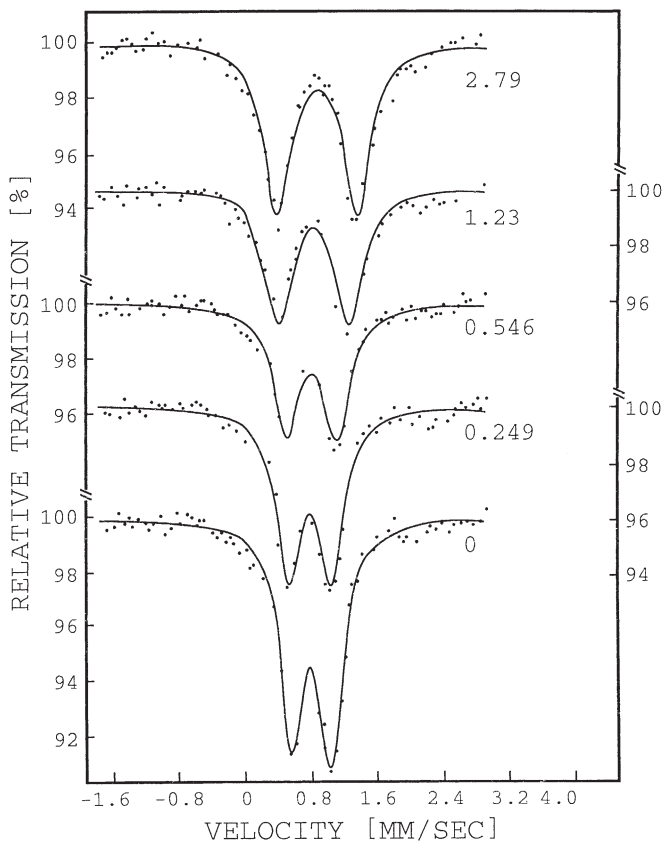


Fig. 5. Room temperature spectra of ferrous-A containing increasing quantities of adsorbed ethylene expressed as mmol g^{-1} of zeolite. Velocity scale w.r.t. natural metallic iron. (The continuous lines are computer fits of the experimental data)

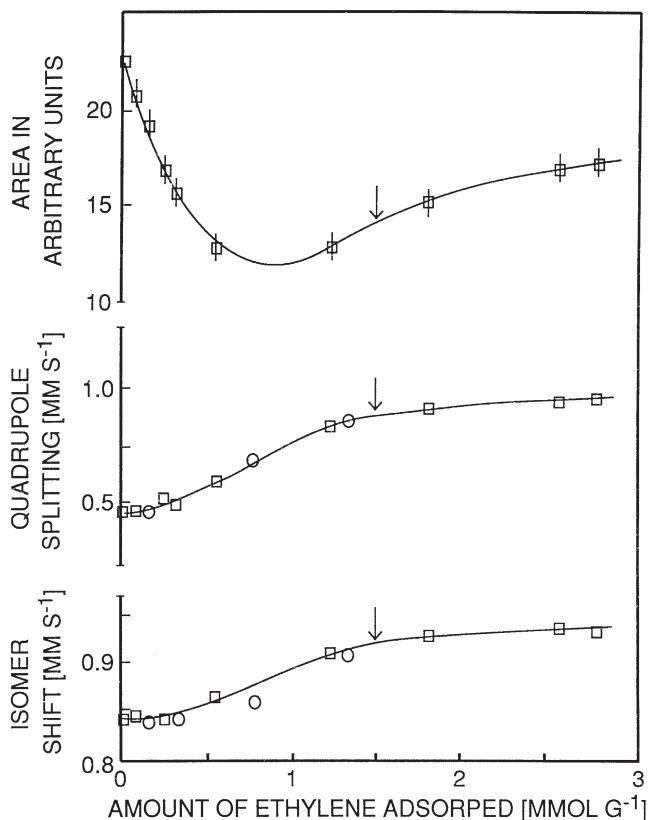


Fig. 6. Effect of adsorbed ethylene on the isomer shift, quadrupole splitting and absorption area of spectra taken at room temperature. Isomer shift w.r.t. natural metallic iron. The arrows indicate a loading of one ethylene molecule per Fe^{2+} cation

with parameters of the uncomplexed ferrous-A and (b) an outer doublet with parameters of the ferrous-ethylene complex.

If the heat of adsorption of ethylene in ferrous-A zeolite is assumed to be approximately 40 kJ mol^{-1} it is possible to calculate, if jump diffusion occurs with an activation energy approximately half the heat of adsorption, that the life-time of an ethylene-ferrous ion complex is $\sim 2 \times 10^{-11} \text{ s}$. The Mössbauer event time is $9.8 \times 10^{-8} \text{ s}$ during which time an ethylene molecule could make ~ 5000 jumps at RT.

The spectra in Fig. 7 can be readily interpreted from the mobility of the ethylene molecules. When an ethylene molecule is sorbed on a ferrous ion the ion is pulled out of the plane of the “window” and when the molecule jumps away the ion relaxes to its original position. Hence the ions are forced to oscillate perpendicularly to the plane of the window and the oscillation decreases the recoil free fraction which reduces the area under the doublet. As more ethylene is added the number of unoccupied ferrous sites decreases and the residence time of an ethylene molecule on any one site is increased. Hence the recoilless fraction

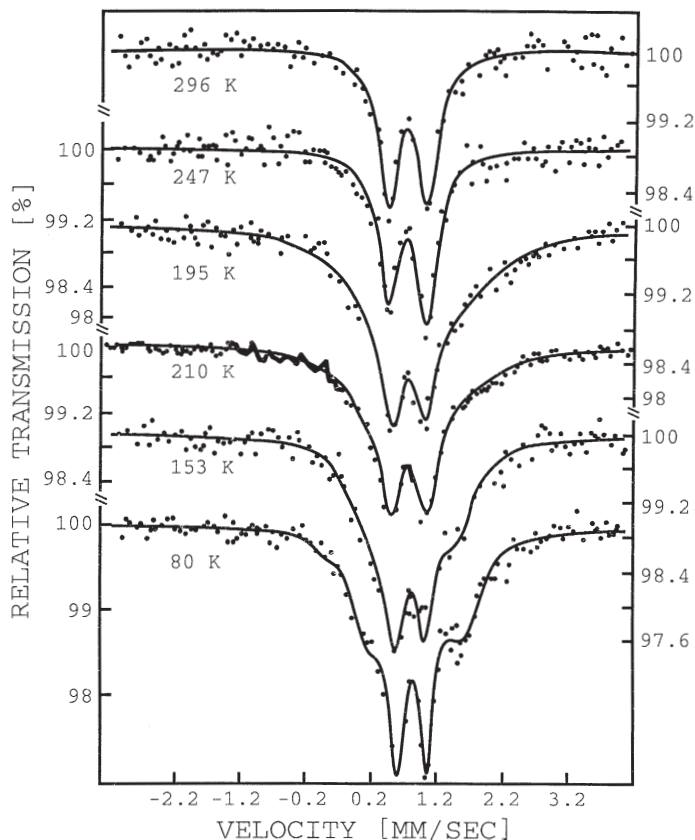


Fig. 7. Temperature dependence of the spectrum of ferrous-A zeolite containing 0.8 mmol of ethylene adsorbed per g of zeolite. Velocity scale w.r.t. natural metallic iron

should increase again as the sites are filled with a minimum absorption area occurring at 50% coverage of the ferrous ions. The experimental minimum occurs on a loading of one ethylene molecule to two ferrous ions indicating that ethylene molecules prefer ferrous ions to any other type of site.

The observation of mobile sorption through the effect of the sorbate molecules on the characteristics of the surface cations is a novel use of Mössbauer spectroscopy. There is obviously further scope to study the dynamic properties of ferrous-sorbate complexes in greater detail using this technique.

Further studies of ferrous-exchanged zeolite A with different degrees of hydrolysis (i.e. H^+ content of the unit cell) indicated that the area under the outer doublet found in samples on dehydration (see Fig. 4b,c) was closely correlated to the degree of hydrolysis [13]. This outer doublet would seem to be associated with Fe^{2+} ions contained in collapsed framework material.

Calcium ions are known to increase the thermal stability of zeolite A. Ferrous ions were, therefore, introduced into a zeolite A which had been partially

exchanged with calcium ions under conditions exactly analogous to those described above for the preparation of ferrous-exchanged samples from the pure Na form. The resulting zeolite had a unit cell composition of $\text{Fe}_{1.61}\text{Ca}_{2.65}\text{Na}_{2.30}\text{H}_{1.18}[\text{Al}_{12}\text{Si}_{12}\text{O}_{48}]$. On dehydration at 633 K for 24 h in vacuum a simple spectrum was obtained which only contained one doublet with IS of 0.82 mm s^{-1} and QS of 0.49 mm s^{-1} at RT, i.e. parameters very close to those of the inner doublet in the dehydrated Fe^{2+} , Na-A sample described above. The presence of Ca^{2+} ions in sites I of the supercage had little or no effect on the Fe^{2+} ions located in other sites I. The absence of an outer doublet confirms that this doublet does arise from ferrous ions sited in collapsed framework materials and provides further evidence of the increased stability of calcium-exchanged forms even in the presence of a reasonable concentration of H^+ ions.

Ferrous-exchanged Na- and Na,Ca-A zeolites could be readily oxidized in dry oxygen at 633 K and wet air at RT to give the ferric forms. High-spin Fe^{3+} ions located in site I of the fully hydrated zeolite were found to give an IS of $0.37\text{--}0.43 \text{ mm s}^{-1}$ and QS of $0.62\text{--}0.87 \text{ mm s}^{-1}$ at 298 K and IS of $0.47\text{--}0.51 \text{ mm s}^{-1}$ and QS of $0.78\text{--}0.90 \text{ mm s}^{-1}$ at 100 K. On dehydration the IS of the Fe^{3+} doublet decreased slightly but the QS increased significantly. The narrow QS doublet characteristic of Fe^{2+} ions in (dehydrated) site I appeared on dehydration at 633 K indicating that a small amount of the Fe^{3+} ion content of the samples was reduced to the Fe^{2+} state on dehydration. This ferrous doublet was removed reversibly on reoxidation of the sample on dry O_2 at 633 K. The Fe^{3+} doublet disappeared on reduction with hydrogen at 633 K for 4 h, to be replaced by two ferrous doublets with IS of 0.97 mm s^{-1} and QS of 1.78 mm s^{-1} and IS of 0.81 mm s^{-1} and QS of 0.46 mm s^{-1} at 298 K, respectively. No hyperfine lines of bulk metallic iron were ever found on such reductions.

2.2

Ion Exchange^a

Karge et al. [14–16] have studied solid-state ion exchange in zeolites in considerable depth. Generally, solid-state ion exchange occurs at relatively high temperatures (550–1000 K) in intimate mixtures of an H zeolite and metal halide or oxide. The process results in the formation of the respective metal zeolites and evolution of HCl and water. The method has been used to insert considerable amounts of ferrous ions into zeolite Y using intimate mixtures of $\text{NH}_4\text{-Y}$ and ferrous chloride. The changes of oxidation and coordination states of the iron cations during grinding of the mixtures in the presence of oxygen and upon successive heat treatments were investigated [17, 18] using X-ray diffraction, temperature-programmed evolution (TDE) of volatile products and Mössbauer spectroscopy at 300 K. Depending on the pretreatment temperature, two Fe(III) species with octahedral and trigonal coordination, respectively, and six Fe(II) species viz. $\text{FeCl}_2 \cdot x\text{H}_2\text{O}$; two types of iron(II) ions in tetrahedral and trigonal coordination respectively; and three Fe(II) species in various octahedral environments were found.

^a Cf. Vol. 3, Chaps. 1 and 2 of the present series “Molecular Sieves – Science and Technology”.

The large number of different iron species found was partially due to the method of preparation of the samples. Some 57% of the ferrous ions present in the $\text{FeCl}_2 \cdot 4\text{H}_2\text{O}$ starting material was oxidised to the trivalent state on grinding with the zeolite in air. However, the parameters obtained for ferrous ions in six-membered rings coordinately bound to three nearest neighbor oxygens (i.e., in SII sites) and in the SI hexagonal prism sites agreed with the parameters found for ferrous irons in these sites where the Fe^{2+} cations had been ion-exchanged into the zeolite by normal aqueous solution methods. A third Fe(II) species had parameters consistent with tetrahedrally coordinated Fe(II) located in the SI' site in the sodalite cage with one molecule of water involved in the coordination sphere. Fe(III) species located in the SII site were also found.

Autoreduction of a Fe(III) species occurred between 520 and 620 K while ammonium chloride was observed to be decomposed in the TPE experiments at 520 K. The resulting octahedrally coordinated Fe(II) species had Mössbauer parameters that were not typical of iron cations in faujasite. According to the authors this autoreduction reaction also involved oxidation of framework oxygen to molecular oxygen and the release of oxidic aluminium species.

The somewhat complicated results obtained in this study would, probably, be simplified by sample grinding and subsequent sample handling in an inert atmosphere.

A series of ultrastable zeolite Y samples containing Fe(III) ions were prepared by solid-state ion exchange of the ammonium forms of zeolite Y under deep-bed conditions at various temperatures [19]. The properties of these materials were compared with those of FeY samples prepared by conventional solid-state ion exchange using Mössbauer spectroscopy.

Zeolites, NaX and NaY, partially exchanged with 5 wt.-% Fe were reduced with sodium vapour produced by the thermal decomposition of sodium azide. The metallic iron particles produced had dimensions of a few nanometers, as revealed by Mössbauer spectroscopy and various other techniques [20].

The coordination properties of Eu^{3+} cations ion-exchanged into zeolites A, X and Y have been studied by Eu-151 Mössbauer spectroscopy [21]. In another study using Eu-151 Mössbauer spectroscopy [22] it was demonstrated that Eu^{3+} cations within the supercages of zeolite Y are partially reduced to Eu^{2+} by hydrogen.

2.3

^{57}Co Emission Studies

In all of the above studies a standard source, which in the case of iron has ^{57}Co atoms diffused into a cubic metal lattice, e.g. Pt, provides the recoil-free radiation. This radiation is then passed through an absorber containing ^{57}Fe atoms in the sample which is under investigation. It is possible to dope the sample of interest with ^{57}Co and use this sample as the source of the radiation. The radiation is passed through a standard absorber that is frequently 96% ^{57}Fe -enriched potassium ferrocyanide because it gives a simple line spectrum. Such Mössbauer emission studies have been carried out where $^{57}\text{Co}^{2+}$ ions have been exchanged into zeolite A [23, 24]. In such a study, as the zeolite is contained in a sorption bulb which is attached to a vacuum apparatus, the Doppler energy required to

scan the spectral energy range is imparted by vibrating the absorber rather than the source [7]. Only trace amounts of the Mössbauer active species are required in the zeolite phase, e.g. 1 Co^{2+} ion per 8700 unit cells of zeolite A. Similar spectra were obtained in these emission studies (although the spectra are the mirror images of those obtained when iron in the zeolite is in the absorber phase) demonstrating that even at these ppm concentrations of Co^{2+} ions the ions were located in the sodalite window site (site I) with trigonal coordination to lattice oxygens. The temperature dependence of the Mössbauer parameters of the dehydrated zeolite was measured in the range 77–573 K from which the Debye temperature and source recoil-free fractions, f_s , for Co^{2+} ions located in site I were calculated. These parameters gave useful information on the vibrational modes of the Co^{2+} ion located in site I of zeolite A.

The nature of the complexes formed between water, methanol and ethanol molecules and Co^{2+} cations was determined [24]. A large anomalous ferric component was observed in the spectra of the water-complexed sources but not with the alcohol-complexed sources. This ferric component arose from the radiolysis of the complexed water molecules in the electron capture decay process of ^{57}Co . Following the electron capture the water in the first coordination sphere of the Mössbauer atom is subjected to a flux of low energy Auger electrons and X-rays. This water is decomposed into H^\cdot and OH^\cdot radicals and it is the H^\cdot radicals that can oxidize the Fe^{2+} to Fe^{3+} . Interestingly, no anomalous Fe^{3+} component was observed when methanol or ethanol was the sorbate. Irradiation of alcohols does not lead to the production of alkoxide radicals.

Mössbauer emission spectroscopy revealed the effects of encapsulation on the 2,2'-bipyridine complex of Co^{2+} (57) synthesized in the supercages of zeolite Y [25]. The spectrum of this complex did not show the high spin state of the $\text{Fe}(\text{II})$ complex.

2.4

Conversion Electron Mössbauer Spectroscopy

^{57}Fe conversion electron Mössbauer spectroscopy (CEMS) is an interesting technique for studying reactions taking place on, or near, the surface of materials which contain iron in one form or another [9]. The decay processes following the resonant excitation of a ^{57}Fe nucleus are shown in Fig. 8. The number of photons and electrons produced following the capture of 100 resonant 14.4 keV recoil-free γ -ray photons is indicated in this figure.

In ^{57}Fe CEMS it is the 7.3 keV internally converted electrons which are normally detected but the 6.3 keV x-rays can also be used. The advantage of CEMS over normal Mössbauer studies is the nine-fold increase in the 7.3 keV electrons over the 14.4 keV γ -rays. Secondly, these electrons are rapidly attenuated within the solid which limits the probing depth of CEMS to ~ 300 nm from the surface. For surface studies the back-scatter method is employed and one detects the conversion electrons back-scattered from the surface of the sample under study. However, it is possible by this technique to measure the γ - and X-rays back-scattered following resonant absorption to increase probing depths to several microns.

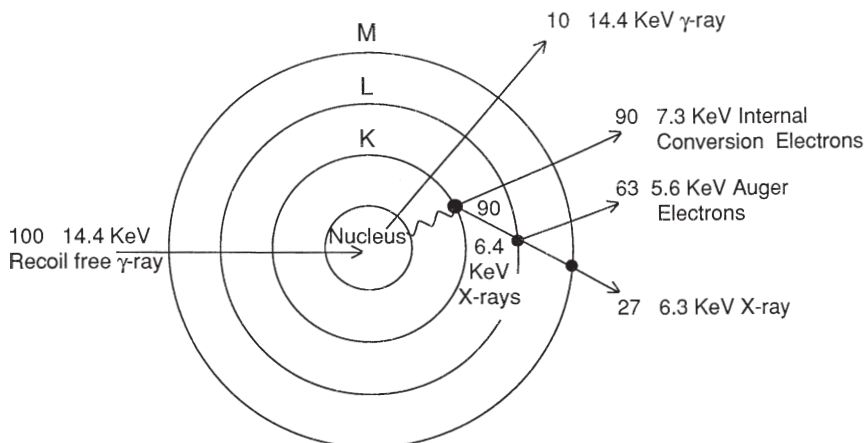


Fig. 8. Decay process following the resonant excitation of Fe(57) nuclei

In the back-scattering method maxima in the count rates are now observed at resonant energies as compared with the minima obtained in transmission experiments. The method has been used to study corrosion and oxidation of iron [26] and the austenitic content of the surface region of steels [27]. The method showed that the Fe_2O_3 particles formed from $\text{Fe}(\text{NO}_3)_3$ or $\text{Fe}(\text{CO})_5$ impregnation of SiO_2 support gave a Mössbauer spectral doublet at 300 K indicating superparamagnetic behaviour and an Fe_2O_3 particle size of <10 nm. Impregnation with FeCl_3 led to larger Fe_2O_3 particles since a six-line magnetically split spectrum was obtained at 300 K.

Although CEMS is a more difficult technique experimentally than normal Mössbauer spectroscopy it offers many exciting possibilities for the study of Mössbauer isotopes on or near the surface. It could be a useful technique to study the properties of bifunctional zeolite catalysts and metal-impregnated zeolite catalysts.

2.5

Tetrahedral Framework Fe(III)

Recently, there has been considerable interest in the isomorphous substitution of tetrahedral aluminium in zeolite frameworks with catalytically active elements such as iron, gallium and boron. These materials have acidities different from the corresponding aluminosilicates leading to altered activity, selectivity and stability. Mössbauer spectroscopy has been used to study the iron incorporated into zeolites during synthesis. Fe(III) can be present on tetrahedral framework sites; as Fe^{3+} cations acting as counterions; and as Fe(III) oxides precipitated in or on the zeolite crystals. The most common iron oxide is $\alpha\text{-Fe}_2\text{O}_3$ which contains iron only in octahedral coordination.

Secondly, when zeolites are hydrothermally treated, structural aluminium is known to be removed. The amount of dealumination depends on the duration

and severity of the hydrothermal treatment. Mössbauer spectroscopy is a very useful technique for following the fate of the tetrahedral framework Fe(III) when a ferrisilicate molecular sieve is subjected to various hydrothermal treatments.

The Mössbauer isomer shift can readily distinguish between iron in tetrahedral and octahedral coordination. At RT an IS ≤ 0.3 mm s⁻¹ is indicative of tetrahedral Fe(III) whereas octahedral ferric species give an IS > 0.3 mm s⁻¹ w.r.t. metallic iron at RT as the standard. The Doppler shift increases the IS as the temperature is lowered. A value of 0.35 mm s⁻¹ has been reported for tetrahedral ferric ions at 4.2 K [28] whereas octahedral ferric ions have a value of 0.47 mm s⁻¹ in α -Fe₂O₃ at 4.2 K [29]. It is possible that the occluded oxide phase contains iron in tetrahedral coordination, e.g. as in γ -Fe₂O₃. Fortunately, Mössbauer spectroscopy allows us, via the magnetic hyperfine interaction, to distinguish between tetrahedral iron present in (a) magnetically ordered iron oxide phases and (b) dilute, paramagnetic tetrahedral framework iron.

- (a) Magnetically ordered materials generally give a six-line ⁵⁷Fe spectrum with the splitting proportional to the hyperfine field B_{hf} . However, two complicating effects arise in the case of very small particles; (i) collective magnetic excitations [30] and (ii) superparamagnetism [31]. Collective magnetic excitations cause smaller values of B_{hf} in very small particles compared to bulk. Superparamagnetism leads to the collapse of the sextet to give a quadrupole doublet at a temperature referred to as the blocking temperature, T_B , which is below the magnetic-ordering temperature. For particles of a given structure, T_B often varies linearly with particle volume and this behaviour can be used to characterise small particles in catalyst systems.
- (b) Dilute paramagnetic ferric iron can give rise to six-line spectra at low temperatures because the electronic relaxation time is longer than the Mössbauer event time ($> 10^{-7}$ s). At higher temperatures and higher iron concentrations the six-line spectrum collapses into a broad singlet or unresolved doublet.

Thus, a problem can arise as these two very different cases can give rise to similar six-line spectra. However, one can differentiate between these two cases by application of a strong external magnetic field. Paramagnetic hyperfine split (PHS) spectra, unless already very sharp, become much sharper whereas the spectra of magnetically ordered iron oxides broaden or even double. Also in PHS spectra an increase in iron concentration leads to a reduction in the area under the sextet component to the benefit of the central singlet or doublet.

The study of these magnetic hyperfine interactions, however, do involve much more expensive spectrometry requiring cryostats which can cool the zeolite sample to 4.2 K and also require superconducting magnets which allow external magnetic fields to be applied to the sample.

Meagher et al. [32] have carried out an excellent Mössbauer study of ZSM-5 type ferrisilicates. Ferrisilicates having SiO₂/Fe₂O₃ ratios of 24, 51, 98 and 171 were studied. X-ray powder diffraction indicated that all samples were essentially 100% crystalline. SEM and EDX analyses showed no detectable secondary iron-containing phase. The as-synthesized samples were white in colour. K⁺ cation exchange capacities were used to measure the amount of framework-iron on syn-

thesis and after various calcination and steaming treatments. In the sample with the $\text{SiO}_2/\text{Fe}_2\text{O}_3$ ratio of 171 essentially all of the iron was present in tetrahedral framework sites on synthesis and after calcination at 773 K. However, after steaming at 823 K for 4 h the sample turned to a light brown colour and some 46% of the iron remained in the framework. The samples became decreasingly stable to calcination and steam treatments as the iron framework content increased until the sample with the $\text{SiO}_2/\text{Fe}_2\text{O}_3$ ratio of 24 showed little or zero framework iron after calcination and steaming, respectively. This latter sample was dark brown in colour.

The white colour of the as-synthesised samples indicated the absence of anti-ferromagnetic interactions due to Fe-O-Fe bonds arising from an iron oxide phase. The Mössbauer spectra of these samples at RT and 78 K were quite similar to each other and indicated that the iron was essentially all in the ferric state. The spectra displayed only a broad singlet at RT with an average IS of 0.25 mm s^{-1} indicative of iron tetrahedrally coordinated to oxygen. To obtain more information spectra were obtained at 4.2 K. The as-synthesised samples with $\text{SiO}_2/\text{Fe}_2\text{O}_3$ ratios of 171, 98 and 51 gave low IS of $0.35 \pm 0.01 \text{ mm s}^{-1}$ and relatively large hyperfine fields of $\sim 52 \text{ T}$. Once again this IS indicates tetrahedral iron. The data for these three samples suggests paramagnetic hyperfine splitting (i.e. iron in framework sites) since with increasing iron concentration the magnetically split component transforms to a central singlet or unresolved doublet. To confirm this interpretation a spectrum of the sample with lowest iron content was measured under an applied field of 8 T. The spectrum obtained was quite different from its low field analog with narrow line widths indicating paramagnetic hyperfine splitting. When the spectrum was fitted through a spin Hamiltonian simulation program the parameters selected confirmed that the majority, if not all, of the iron was present in tetrahedral framework sites.

The sample with a $\text{SiO}_2/\text{Fe}_2\text{O}_3$ ratio of 24 had an IS of 0.41 mm s^{-1} at 4.2 K which is intermediate between tetrahedral and octahedral iron indicating the presence of both in roughly equal quantities. There was no resolved hyperfine splitting indicating that none of the iron was present in well-isolated sites or in large clusters.

All of the hydrothermally treated samples were brown in colour indicating the presence of some iron oxide/hydroxide species. The Mössbauer spectra at RT and 78 K of these samples were all quite similar and indicated that essentially all of the iron in these samples was in the ferric state. The spectra consisted of a symmetric doublet with IS of 0.33 mm s^{-1} indicating iron in octahedral coordination while the QS of 0.84 mm s^{-1} is close to that for $\alpha\text{-Fe}_2\text{O}_3$ particles supported on silica [33].

Apart from the sample with the lowest iron content all other steamed samples gave similar spectra at 4.2 K. The common characteristics were large IS of $0.47 \pm 0.01 \text{ mm s}^{-1}$ and all of the absorption occurring as a six-line magnetic spectrum indicating that the superparamagnetic blocking temperature was above 4.2 K. The IS is typical of ferric iron in octahedral coordination. The magnitude of the hyperfine field varied between 48–51 T suggesting that the iron had been precipitated in different phases or as a single phase with varying particle size. When an 8 T field is applied parallel to the γ -direction at 4.2 K the spectra, espe-

cially for samples with high content of iron, indicate magnetically ordered particles and suggest that the particles contain several hundred iron ions in non-framework sites which must be located on the surface of the molecular sieve.

The calcined samples showed little or no iron oxide phases. The spectra at RT and 78 K of all samples were quite similar and indicated that the iron was in the ferric state. The RT spectra were somewhat asymmetric with an average IS of 0.29 mm s^{-1} which may indicate the presence of both octahedral and tetrahedral iron. The spectra could be deconvoluted into two doublets with one doublet for tetrahedral iron with an IS of 0.23 mm s^{-1} and the other doublet for octahedral iron with an IS of 0.33 mm s^{-1} .

From the as-synthesised and calcined samples one can conclude that the IS at RT for tetrahedral framework iron in ZSM-5 is $\sim 0.25 \text{ mm s}^{-1}$.

The spectrum of the calcined sample at 4.2 K with a $\text{SiO}_2/\text{Fe}_2\text{O}_3$ ratio of 171 is very similar to the as-synthesised samples, i.e. IS of 0.35 mm s^{-1} and large field of 51.1 T. Under an applied field of 8 T the iron is once again confirmed to be in the framework. The calcined samples with higher iron contents, i.e. $\text{SiO}_2/\text{Fe}_2\text{O}_3$ ratios of 98 and 51, have similar but complex spectra at 4.2 K. The spectra contain both magnetic sextet and quadrupole doublet components but resemble the as-synthesised samples more than the steamed samples. The occurrence of a quadrupole doublet at 4.2 K indicates that the non-framework iron is present as extremely small particles and could be in the pores of the zeolites. The calcined sample with a $\text{SiO}_2/\text{Fe}_2\text{O}_3$ ratio of 24 gives a 4.2 K spectrum which indicates that most of the iron is present as octahedral iron oxide phase in non-framework sites.

From the 4.2 K spectra with 8 T external field applied parallel to the γ -ray direction it is possible to estimate the amount of tetrahedral framework iron. Good agreement was obtained by this method with the K^+ exchange capacities. More simply it is possible to estimate the amount of tetrahedral iron from the 4.2 K IS data. A linear interpolation between the tetrahedral IS value of 0.35 mm s^{-1} and the octahedral value of 0.47 mm s^{-1} gives a fair indication of the tetrahedral iron content.

Iron in the framework of zeolite beta has been thoroughly characterised using RT and 4.2 K Mössbauer spectroscopy. An external applied field (4.13 T) was also applied at 4.2 K. The IS of 0.22 mm s^{-1} at RT and 0.32 mm s^{-1} at 4.2 K and the narrow, sharp hyperfine sextet at 4.2 K under the applied field demonstrated that most of the Fe^{3+} ions were present as tetrahedral iron in the framework [34].

The redox behaviour and Debye temperature of Fe-FER and Fe-MFI ferrisilicates have been studied using Mössbauer spectroscopy. Analysis and comparison of the data obtained support the conclusions that the redox centres are due to (Fe-framework)-O-(Fe-extra-framework) pairs [35].

Low iron content Fe-ZSM-5 has been synthesised and shown to contain well-separated Fe(III) ions in a tetrahedral environment which display paramagnetic behaviour [36]. Partial extraction of the framework iron occurs on hydrothermal treatment to generate nanosize iron oxide or oxyhydroxide ferrimagnetic particles with size $\sim 3 \text{ nm}$.

Samples of Na-A have been synthesised where some of the tetrahedral Al^{3+} is replaced by Fe^{3+} . The effect of the Fe^{3+} substitution on the Na(23), Al(27) and Si(29) magic angle spinning (MAS)-NMR spectra has been studied [37].

In conclusion, therefore, it has been shown that Mössbauer spectroscopy can identify the nature of the Fe(III) in ferrisilicate molecular series.

2.6

Catalytic Studies

Mössbauer spectroscopy of MFI ferrisilicates has been used to follow changes in the iron parameters under reducing and catalytic conditions [35, 38]. N_2O decomposition over Fe-ZSM-5 and Fe,H-ZSM-5 [39] and over Fe-BETA [40] has also been studied. Framework iron was found to be much more active than Fe^{3+} cations exchanged into the zeolites [39]. MFI ferrisilicates were characterised and the iron species were correlated with the catalytic properties for the conversion of toluene [41]. The state of the iron incorporated into H-MFI was correlated to the activity of the material in the aromatisation of ethane at 823 K [42]. Impregnated and framework iron H-ZSM-5 catalysts were compared for their activity in syngas conversion. The character of the iron species in these catalysts was determined by Mössbauer spectroscopy [43]. Cobalt sulphide particles dispersed in the micropores of zeolites have been found to have very high initial activities for the hydrodesulphurization of thiophene. The catalyst was characterised by Mössbauer emission spectroscopy using Co-57 [44].

Catalysts prepared by supporting tin and platinum in K-L zeolite exhibit high activity and selectivity for isobutane dehydrogenation and resistance to deactivation at 673–773 K. Tin Mössbauer spectroscopy was used to show that some of the tin interacts with the platinum to form Pt/Sn alloy particles in reduced Pt/Sn/K-L catalysts while the rest of the tin is present as Sn^{2+} [45].

Iron and tin Mössbauer spectroscopy was used to characterise supported zeolite catalysts [46].

2.7

Encapsulation of Organometallic Complexes

Studies of various complex molecules engaged inside zeolites have attracted much recent attention [47–50]. These complexes are usually larger in diameter than the diameter of the channels/windows interconnecting the cages containing the complexes and are thus trapped inside the zeolite framework. These complexes are commonly formed by introducing the Mössbauer active metal atom into the cage, where the complex molecule is then synthesised in situ. Mössbauer spectroscopy has been frequently used to study the complexes of iron ions with ligands such as bipyridyl, salen and phthalocyanine. These encapsulated complexes, which are important catalysts, resemble enzymes where the catalytic centre is the transition-metal ion and the stability and steric constraints are produced by the protein.

An important engaged complex is that of iron phthalocyanine [Fe(Pc)] which has been shown to have enhanced catalytic activity for the oxidation of hydrocarbons when the complex is engaged in the supercage of zeolite Y [51].

In an interesting study the Mössbauer spectra of non-engaged, solid-state Fe(Pc), engaged Fe(Pc)-Y and its pyridine adduct Fe(Pc)(Py)-Y were measured

at 77 and 300 K [52]. The characteristic Mössbauer data obtained are listed in Table 2.

Insertion of the complex into the zeolite cage has little effect on the IS and QS parameters. It is interesting to note that, although some distortion of the complex occurs on insertion into the zeolite Y supercage, this distortion does not result in any significant change in the QS which suggests that the plane of the nitrogens around the iron centre is not distorted to any significant degree. In contrast, complexing the Fe(Pc)-Y with pyridine results in a significant decrease in both the IS and QS values. These values are in good agreement with data reported for the Fe(Pc)(Py)₂ complex [53].

An apparent difference is observed in the relative intensities of the inner and outer doublets of the non-encaged and encaged samples of Fe(Pc) at 77 and 300 K, respectively. The intensity of the outer doublet of the encaged complex depends strongly on temperature whereas the corresponding intensity for the non-encaged sample is little affected, as shown in Table 2. Comparison of the A_{77}/A_{300} values for the non-encaged and encaged complexes suggests that the complex is more strongly bound to its environment when encaged. Secondly, a similar comparison of the Fe(III) component clearly shows that the Fe(III) ions are much more tightly bound to the zeolite lattice (N.B. It is highly probable that not all of the iron ions are complexed in the zeolite and some iron ions, therefore, remain naked in the zeolite).

Finally, spectra taken of the complex after treatment with oxygen and on subsequent reduction with argon/hydroquinone in an acetic acid medium indicated that the encaged complex was very stable.

Various other studies have used Mössbauer spectroscopy to gain insight into the properties of complexes encaged in zeolite cages [54–57]. The Mössbauer spectra of some ferrous complexes in zeolite Y supercages gave large quadrupole splittings for low-spin Fe(II) indicating that these complexes are distorted by the strong interactions with the zeolite framework atoms [58].

Table 2. Mössbauer parameters of iron-containing components in solid-state phthalocyaninato-iron complexes. IS isomer shift, related to metallic α -iron, mm/s; QS quadrupole splitting, mm/s; RI relative contribution to the spectrum, %; A spectral absorption, intensity/base line, %; A_{77}/A_{300} ratios of absorptions obtained from 77 K and 300 K spectra

Sample	Comp.	77 K				300 K				
		IS	QS	RI	A	IS	QS	RI	A	A_{77}/A_{300}
Fe(Pc)	Fe(II)(Pc)-1	0.52	2.77	12	6.74	0.40	2.66	48	2.81	234
	Fe(II)(Pc)-2	0.45	2.67	58		0.33	2.54	25		
	Fe(III)-1	0.52	0.89	22	2.85	0.47	1.00	9	1.06	267
	Fe(III)-2	0.25	0.81	7		0.25	0.81	18		
Fe(Pc)-Y	Fe(II)(Pc)	0.48	2.64	39	1.47	0.39	2.58	29	0.73	203
	Fe(III)	0.46	0.90	61	2.30	0.36	0.86	71	1.82	1.27
Fe(Pc)/Py-Y	Fe(II)(Pc)	0.30	1.94	35	1.23	0.25	2.00	21	0.58	214
	Fe(III)	0.40	0.84	65	2.27	0.36	0.81	79	2.15	1.06

The anisotropic molecular motion of $\text{Fe}(\text{C}_5\text{H}_5)_2$ and $\text{Co}(\text{C}_5\text{H}_5)\text{CO}_2$ molecules in the supercages of zeolite Y have been examined by NMR and Mössbauer spectroscopy [59]. The Mössbauer spectra of iron-glucose complexes in the cavities of natural clinoptilolite have also been reported [60].

2.8

Catalyst Preparation

Iron carbonyls have been used to prepare superparamagnetic iron zeolite catalysts [61, 62] and RhFe clusters in zeolites [63].

Cobalt ion exchanged zeolite Y has been reduced with hydrogen to produce cobalt clusters in the zeolite cages [64] and the stability of various CO/H₂ catalysts have been studied/characterised using Mössbauer spectroscopy [65].

2.9

Mesoporous Materials

Mesoporous (FeSi)MCM-41 has been synthesised [66, 67]. Mössbauer spectroscopy suggested that Fe(III) had been incorporated into the channel walls. The introduction of Fe(III) into the structure was found to improve the thermal and hydrothermal stability of SiMCM-41. A series of iron-containing mesoporous silicas with iron contents up to 5.7 wt.-% have been prepared at room temperature. The resulting tetrahedral Fe species are highly distorted with two long and two short Fe-O bond distances due to hydrogen-bonding interactions with the organic templates present. Subsequent calcination leads to, mainly, three-coordinated Fe species which are readily converted to four-coordinated species in the presence of water [68].

Fe-pillared clays have been prepared and characterised using Mössbauer spectroscopy [69].

The catalytic formation of carbon nanotubes on Fe-loaded zeolite supports with different pore sizes has been investigated [70]. Mössbauer spectroscopy showed that the Fe(II) species seemed to catalyse the formation of the carbon nanotubes. ¹²⁹I Mössbauer spectroscopy has been used to study the electronic state of iodine adsorbed in nanoporous graphite fibres with very high surface areas. The observed spectra consisted of five different quadrupole octets demonstrating the coexistence of I₃⁻ and I₂ molecules in the pores; this indicates that charge transfer from the graphite to the iodine had occurred [70].

3

Conclusions

This short review has clearly shown that Mössbauer spectroscopy can play an important role in characterising many aspects of zeolite chemistry. Although many elements are Mössbauer active the majority of studies have been concerned with spectroscopy involving Fe(57). However, there is a wealth of information available if researchers take the additional trouble and expense to work at temperatures down to 4 K.

4

References

1. Frauenfelder H (1963) *The Mössbauer effect*. Benjamin, New York
2. Morice JA, Rees LVC (1968) *Trans Faraday Soc* 64:1388
3. Delgass WN, Garten RL, Boudart M (1969) *J Chem Phys* 50:4603
4. Delgass WN, Garten RL, Boudart M (1969) *J Phys Chem* 73:2970
5. Dickson BL (1973) PhD thesis, University of London
6. Gao Zi, Rees LVC (1982) *Zeolites* 2:72
7. Fitch FR (1979) PhD thesis, University of London
8. Dickson BL, Rees LVC (1974) *J Chem Soc Faraday Trans I* 70:2038
9. Rees LVC (1980) Application of Mössbauer spectroscopy to surface chemistry. In: Fraissard JB, Resing HA (eds) *Magnetic resonance in colloid and interface science*. Reidel, Dordrecht, Holland, p 109
10. Rees LVC (1976) Mössbauer studies of ferrous-A zeolite. In: Resing HA, Wade CG (eds) *Magnetic resonance in colloid and interface science*. American Chemical Society, Washington DC, USA, p 301
11. Dickson BL, Rees LVC (1974) *J Chem Soc Faraday Trans I* 70:2060
12. Dickson BL, Rees LVC (1974) *J Chem Soc Faraday Trans I* 70:2051
13. Gao Zi, Rees LVC (1982) *Zeolites* 2:72
14. Pal-Borbely G, Beyer HK, Radics L, Sandor P, Karge HG (1989) *Zeolites* 9:428
15. Beyer HK, Pal-Borbely G, Karge HG (1994) *Zeolites* 14:512
16. Karge HG, Pal-Borbely G, Beyer HK, Onyestyak Gy (1988) In: Philips MJ, Ternan M (eds) *Proc 9th Int Cong Catal*. Chemical Institute of Canada Ottawa, p 396
17. Lazar K, Pal-Borbely G, Beyer HK, Karge HG (1994) *J Chem Soc Faraday Trans* 90:1329
18. Lazar K, Pal-Borbely G, Beyer HK, Karge HG (1995) *Stud Surf Sci Catal*, Elsevier, Amsterdam, vol 91, p 551
19. Hudec P, Smieskova A, Zidek Z, Jorik V, Miglierini M, Nagy JB (1997) *Stud Surf Sci Catal*, Elsevier, Amsterdam, vol 105, p 2043
20. Lazar K, Beyer HK, Onyestyak G, Jonsson BJ, Varga LK, Pronier S (1999) *Nanostructured Mater* 12:155
21. Liu X, Sun J (1994) *Zeolites* 14:600
22. Berry FJ, Marco JF, Steel AT (1994) *Zeolites* 14:344
23. Fitch FR, Rees LVC (1981) *Zeolites* 1:19
24. Fitch FR, Rees LVC (1981) *Zeolites* 1:75
25. Vanko G, Nagy S, Homonnay Z, Vertes A (2000) *Hyperfine Interactions* 126:163
26. Simmons GW, Kellerman E, Leidheiser H (1973) *Corrosion* 29:227
27. Swatzendruber, Bennett LH (1972) *Sempta Met* 6:737
28. Coey JMD (1984) In: Long GJ (ed) *Mössbauer spectroscopy applied to inorganic chemistry*. Plenum, New York, vol 1, chap 14
29. Amarasirwardena DD (1986) *Clays Clay Miner* 34:250
30. Morup S, Topsoe H (1976) *App Phys* 11:63
31. Dormann JL (1981) *Rev Phys Appl* 16:275
32. Meagher A, Nair V, Szostak R (1988) *Zeolites* 8:3
33. Yoshioka T, Koezuka J, Ikoma H (1990) *J Catal* 16:264
34. Kumar R, Date SK, Bill E, Trautwein A (1991) *Zeolites* 11:211
35. Lazar K, Kotasthane AN, Fejes P (1999) *Catal Lett* 57:171
36. Lopez A, Lazaro FJ, GarciaPalacios JL, Larrea A, Pankhurst QA, Martinez C, Corma A (1997) *J Mater Res* 12:1519
37. Kulshreshtha SK, Vijayalak R, Sudarsan V (1998) Recent advances in basic and applied aspects of industrial catalysis. 113:699
38. Lazar K, Fricke R, Kosslick H, Cejka J, Vorbeck G, Szeleczky AM (1995) *Stud Surf Sci Catal*. Elsevier, Amsterdam, vol 94, p 219
39. Chang YF, McCarty JG, Zhang YL (1995) *Catal Lett* 34:163

40. Coq B, Mauvezin M, Delahay G, Butet JB, Kieger S (2000) *Appl Catal B-Environmental* 27:193
41. Lazar K, Szelezcky AM, Vorbeck G, Fricke R, Vondrova A, Cejka J (1995) *J Radioanal Nucl Chem* 190:407
42. Hagen A, Roessner F, Weingart I, Spliethoff B (1995) *Zeolites* 15:270
43. Goldwasser MR, Navas F, Zurita MJP, Cubeiro ML, Lujano E, Franco C, Jimenez FG, Jaimes E, Moronta D (1993) *Appl Catal* 100:85
44. Van Santen RA, Vissenberg MJ, Vorbeck G, De Bont PW, Boellaard E, Van Der Kraan AM, De Beer VHJ (1995) *Stud Surf Sci Catal. Elsevier, Amsterdam*, vol 92, p 221
45. Cortright RD, Dumesic JA (1995) *Appl Catal* 129:101
46. Lazar K (1991) *Struct Chem* 2:245
47. Parton RF, Bezoukhanova CP, Thibault-Starazyk F, Reynders RA, Grobet PJ, Jacobs PA (1994) *Stud Surf Sci Catal. Elsevier, Amsterdam*, vol 84, p 813
48. Bedioui F, Roue L, Devynck J, Balkus KJ (1994) *Stud Surf Sci Catal. Elsevier, Amsterdam*, vol 84, p 917
49. Ernst S, Traa J, Deeg U (1994) *Stud Surf Sci Catal. Elsevier, Amsterdam*, vol 84, p 925
50. Knops-Gerrits PP, Thibault-Starzyk F, Jacobs PA (1994) *Stud Surf Sci Catal. Elsevier, Amsterdam*, vol 84, p 1411
51. Herron N, Stucky GD, Tolman CA (1986) *J Chem Soc Chem Comm* 1521
52. Lazar K, Szelezcky AM, Notheisz F, Zsigmond A (1995) *Stud Surf Sci Catal. Elsevier, Amsterdam*, vol 94, p 720
53. Tanaka M, Minai Y, Watanabe T, Tominaga T (1992) *J Radioanal Nucl Chem Lett* 164:255
54. Balkus KJ, Hargis CD, Kowalak S (1992) *ACS Symp Ser. American Chemical Society, Washington DC*, vol 499, p 347
55. Umemura Y, Minai Y, Tominaga T (1993) *J Chem Soc Chem Comm* 1822
56. Umemura Y, Minai Y, Tominaga T (1994) *J Radioanal Nucl Chem Lett* 186:213
57. Tanaka M, Minai Y, Watanabe T, Tominaga T (1994) *Appl Radiation Isotopes* 45:501
58. Umemura Y, Minai Y, Tominaga T (1999) *J Phys Chem B* 103:647
59. Overweg AR, Koller H, de Haan JW, van de Ven, van der Kraan AM, van Santen RA (1999) *J Phys Chem B* 103:4298
60. Concepcion-Rosabal B, Balmaceda-Era J, Rodriguez-Fuentes G (2000) *Microporous Mesoporous Mater* 38:161
61. Schunemann V, Winkler H, Butzlaff C, Trautwein AX (1994) *Hyperfine Interactions* 93:1427
62. Okamoto Y, Kikuta H, Ohto Y, Nasu S, Terasaki O (1997) *Progress in Zeolite and Microporous Mater* 105:2051
63. Schunemann V, Trevino H, Sachtler WMH, Fogash K, Dumesic JA (1995) *J Phys Chem* 99:1317
64. Ching JS, Yun HG, Koh DJ, Kim YG (1993) *J Mol Catal* 79:199
65. Gucci L, Lazar K (1991) *Catal Lett* 7:53
66. He NY, Bao SL, Xu QH (1997) *Progress in Zeolite and Microporous Mater* 105:85
67. He NY, Cao JM, Bao SL, Xu QH (1997) *Mater Lett* 31:133
68. Tuel A, Arcon I, Millet JMM (1998) *J Chem Soc Faraday Trans* 94:3501
69. Zurita MJP, Vitale G, de Goldwasser MR, Rojas D, Garcia JJ (1996) *J Mol Catal A* 107:175
70. He N, Kuang Y, Dai Q, Miao Y, Zhang A, Wang X, Song K, Lu Z, Yuan C (1999) *Mater Sci Eng C* 8/9:151

Subject Index

A

A-type zeolites

- adsorption of homonuclear diatomic molecules in - 106
- exchanged with Co^{2+} 386
- exchanged with Cr^{2+} ions 386
- exchanged with Ni^{2+} 386
- isomerization of cyclopropane over - 392
- isomerization of n-butenes over - 392
- optical spectroscopy 386

ab initio methods

- anharmonicity effects 25
- basis set deficiencies 25
- incorporation of electron correlation 25
- scaling procedures 25

absorbance

- integrated - 36
- maximal - 36

absorption edges

- by ionization of electrons 429
- core-like electronic states 429
- element characteristics 429
- fine structures 429

absorption/reflection spectroscopy of

- CdS occluded in zeolite Y 413
- heterogeneous systems 365

acetic acid

- probe for basic sites 147

acetone

- probe for acid strength 147
- strongly surface-bonded 285

acetonitrile, interaction with

- acid sites 139
- [Al]MCM-41 139
- chabazite 139
- erionite 139
- ferrierite 139
- NH_4^- , H, Na-, H-, and Co-Beta 139
- [Si]MCM-41 139
- ZSM-5 139

acetylacetone

- on H-ZSM-5 147

acetylene

- probe for basic sites 147, 149

acetylene adsorption

- IR spectroscopically studied 153

acetylene derivatives

- probes for basic sites 147

acid OH groups

- effect of $n_{\text{Si}}/n_{\text{Al}}$ ratios 87
- erionite 88
- offretite 88
- prominent bands 75
- via deammoniation of $\text{NH}_4\text{-Y}$ 75

acid strength

- OH in FAU-type zeolites 78
- probe molecules 269
- shift of the OH stretching band 146
- trends in binding energy, BE 496

acidity indicated by

- ammonia 495
- pyridine 495
- weakly basic probes 136
- XPS and probes

acidity of $\text{AlPO}_4\text{-5}$, SAPO-5, BeAPO-5, CoAPO-5, MgAPO-5

- adsorption of pyridine, ammonia and benzene 133

acidity of $\text{AlPO}_4\text{-31}$

- adsorption of pyridine 133

acidity of AlPO_4s , SAPOs and metal-substituted $\text{AlPO}_4\text{-5}$

- probe molecules and IR spectroscopy 133

acidity of CoAPO-31

- adsorption of pyridine 133

acidity of CoAPO-37

- adsorption of pyridine 133

acidity of H-Y, H-MOR, H-ZSM-5

- H_2 , D_2 , light paraffins and DRIFT 136

acidity of MgAlPO-5

- adsorption of pyridine 133

acidity of MnAPO-31

- adsorption of pyridine 133

- acidity of [Si,Al]ZSM-5
 - effect of the synthesis medium 132
 - IR with and without pyridine 132
- acidity of Si-containing aluminophosphates,
 - FTIR/pyridine technique 133
 - MAPSO-36 133
- acidity of zeolites
 - electronic spectroscopy 394
- acidity scale
 - correlation nitrogen charge vs. N 1s BE
- activation energy
 - thermal motions of protons in OH groups 265
- actual or near UV range
 - properties of zeolite host 339
 - properties of guest phase 339
- adsorbates in zeolites
 - signal assignments 282
- adsorption of 4,4'-bipyridine
 - into Na_x-ZSM-5 (x=0, 3.42, 6.62) 154
 - studied by Raman spectroscopy 154
- adsorption of a single water molecule on OH
 - calculated potential energy surface 128
 - hydroxonium ion as a transition structure 128
- adsorption of acetic acid
 - base properties of 149
 - concentration and strength of basic sites 149
- adsorption of alkanes, olefins and acetylenes
 - studied by IR spectroscopy 152
- adsorption of benzene and carbon monoxide
 - heterogeneity of acid strength 146
- adsorption of benzene derivatives
 - studied via IR spectroscopy 152
- adsorption of boranes and silanes
 - on acid zeolites monitored by IR 153
- adsorption of boric acid trimethyl ester (BATE)
 - basic sites in Y-type zeolites 149
- adsorption of CH₃OH
 - formation and reactivity of methoxy groups 151
 - Sanderson intermediate electronegativity, 150
- adsorption of CH₃OH on
 - alkali-metal cation-exchanged ZSM-5 150
 - erionite (ERI) 150
 - faujasite (FAU) 150
 - H-ZSM-5 150
 - Lewis-acid alkali metal cations 150
 - mordenite (MOR) 150
- adsorption of CH₄
 - FTIR spectroscopy 123
 - on zeolite Omega (MAZ) 123
 - volumetric adsorption measurements 123
- adsorption of CH₄ and trimethylgallium on H-Y
 - combined NMR and DRIFT 123
- adsorption of CO
 - decomposition of metal carbonyls 116
 - [M···C≡O] arrangement 116
 - [M···O≡C] arrangement 116
 - on metal clusters
 - on ruthenium clusters 117
 - on zeolite Omega (MAZ) 116
 - reactions of CO catalyzed by metal clusters 116
 - rotation of CO molecules 113
- adsorption of CO and CH₄
 - adsorption measurements 116
 - FTIR spectroscopy 116
- adsorption of CO₂
 - Fermi resonance 121
 - on Li-X, Na-X and K-X investigated via IR 119
 - on Na-A
 - vibration modes 121
- adsorption of deuteriochloroform
 - characterizing basicity 149
- adsorption of dihydrogen as an IR probe
 - cation-containing zeolites as adsorbents 111
 - dissociative adsorption 111
 - localization of adsorption sites 111
- adsorption of H₂, HD, D₂, N₂, O₂, CO on A-type zeolites
 - IR spectroscopy 109
 - microgravimetry 109
 - neutron scattering 109
- adsorption of hydrogen sulfide
 - different orientations 125
 - effect on OH groups 125
 - on H-ZSM-5 125
 - on Na-ZSM-5 125
- adsorption of hydrohalocarbons in faujasites
 - INS and NIR FT-Raman spectroscopies 153
 - new framework bands 153
- adsorption of large and complex molecules
 - investigation by IR or Raman spectroscopy 153
- adsorption of N₂ and CO
 - Cu⁺N₂ and Cu⁺CO adsorption complexes 111

- on zeolite Cu-ZSM-5 111
- adsorption of N₂O
 - on Na-A 119
- adsorption of N₂O and CO₂
 - confirmed by MO calculations 122
 - normal coordinate analyses 122
 - two-center adsorption 122
- adsorption of N₂O in Na-Y
 - calculation of potential energies 120
 - high barriers to translation and rotation 121
 - librations 121
 - translational oscillations 121
- adsorption of NO+O₂
 - probe for the location of OH groups 143, 270
- adsorption of probe molecules
 - hindered translations and rotations 71
 - location of hydroxyl groups 270
- adsorption of pyrrole on zeolite K-LTL
 - measure of basicity 148
- adsorption of SO₂
 - on Na-A 125
 - on Na,Ca-A 125
 - sorption sites in the large cavities 125
- adsorption of triphenylmethane derivatives
 - formation of carbenium ions 154
 - into Na-Y and H-Y 154
- adsorption of water on acid zeolites
 - assumption of hydroxonium ions 130
 - assumption of a neutral complex 129
 - equilibrium adsorption of 1 H₂O per 1 OH 126
 - excess of H₂O on acid OH of H-Y 130
 - H/D exchange 130
 - hydroxonium ion 126, 129
 - interpretation 129
 - IR spectroscopy 130
 - on H-ZSM-5 130
 - spectral features 129
- adsorption on zeolites at very low coverages
 - difference spectra 126
 - H₂S adsorption 126
 - methanol/NH₃ adsorption 126
 - water vapor adsorption 126
- adsorption onto zeolites
 - of boranes 49, 153
 - of CO 49, 109, 116
 - of CO₂ 49, 119, 121, 146
 - of H₂O 49, 126, 129, 130
 - of nitriles 49
 - of NH₃ 49, 495
 - of paraffinic hydrocarbons 49, 152
- Ag clusters
 - characteristic ESR signals 323
- Ag₆^{x+} formation in zeolite A
 - activation energy 328
- ²⁷Al and ²⁷Si chemical shifts
 - linear relationship 224
 - mean Al-O-Si bond angles 224
- ²⁷Al DOR NMR spectroscopy
 - assignment for VPI-5 230
 - calcium tungstate aluminate sodalite 228
 - local geometry of AlO₄ in VPI-5 230
 - of dehydrated VPI-5 229
 - significant line narrowing 228
 - sodium aluminosilicate sodalite 228
- ²⁷Al MAS NMR signals
 - of octahedrally and tetrahedrally coordinated Al^{IV} 262
 - of tetrahedrally coordinated framework Al 225
- ²⁷Al MAS NMR spectroscopy
 - Al(4Si) units in framework 224
 - Al^{IV} in disturbed tetrahedral coordination 224
 - aluminosilicate-type zeolites 237
 - dehydroxylation model 261
 - framework aluminum (Al^I) 224
 - increasingly dealuminated HY 226
 - non-framework aluminum (Al^{IV}) 224
 - of dealuminated zeolites 225
 - of dehydrated NH₄-zeolites 228
 - of dehydrated NH₄ZSM-5 and HZSM-5 227
 - penta-coordinated Al atoms 237
 - penta-coordinated state 224
 - quadrupolar line broadening 224
- ²⁷Al quadrupole parameters
 - analysis of – 230
 - local framework geometry 230
 - strong line broadening 216
- ²⁷Al-³¹P correlation spectrum
 - of VPI-5 232
- [Al]MCM-41
 - characterized by FTIR and TPD of pyridine and NH₃ 136
- alkali metal clusters
 - characteristic ESR signals 323
- alkali-metal cation-exchanged faujasites
 - band shift 66
 - Brodskii relation 66
- alkenyl carbenium ions
 - combined UV-Vis/IR experiments 404
 - on Brønsted acid sites 401
 - on Lewis acid sites 401

- alkenyl carbenium ions
 - via conjunct oligomerization 403
 - via cracking of oligomers 403
 - via hydride ion abstraction from olefins 402
 - via intermolecular hydride ion abstraction 403
 - via protonation of dienes 402
- alkyl carbenium ions
 - on Brønsted acid sites 401
 - on Lewis acid sites 401
- alloys in zeolites studied by XPS
 - alloy Pt-Co in Y 508
 - alloy Pt-Cr in ZSM-5 508
 - alloy Pt-Cu in Y 508
 - alloy Pt-Cu in ZSM-5 508
 - alloy Pt-Ga in ZSM-5 508
 - alloy Pt-In in Y 508
 - alloy Pt-Ir in Y 508
 - alloy Pt-Mo in Y 508
 - alloy Pt-Ni in Y 508
 - alloy RH-Fe in Y 508
 - alloy Ru-Co in X 508
- AlPO₄ molecular sieves
 - binding energies 506
 - XPS of – 506
- AlPO₄-5
 - A-parameters (ESR) 322
 - Brønsted acid strength 100
 - Brønsted acidity 100
 - DRIFT experiments 100
 - g-parameters (ESR) 322
 - ³¹P MAS NMR spectroscopy 231
- AlPO₅-5 single crystals
 - fluorescence spectra 418
 - loaded with Basic Yellow 418
 - loaded with dyes 418
 - loaded with Rhodamine derivatives 418
- AlPO₄-8
 - ²⁷Al MAS NMR spectrum of – 233, 234
 - ³¹P MAS NMR spectrum of – 233
- AlPO₄-11
 - mainly acid sites 149
 - ³¹P MAS NMR spectroscopy 231
 - weak basic sites 149
- AlPO₄-17
 - ³¹P MAS NMR spectroscopy 231
- AlPO₄-18
 - diffuse reflectance IR spectroscopy (DRIFT) 100
- AlPO₄-20
 - IR and Raman of framework vibrations 56
- AlPO₄-31
 - acidity of – 139
 - ³¹P MAS NMR spectroscopy 231
- AlPO₄-34
 - acidity of – 139
- alumina
 - binding energy of Al 2p 486
 - binding energy of Si 2p 486
- aluminophosphate VPI-5
 - ²⁷Al DOR NMR spectra 230
 - assignment of ³¹P MAS NMR signals 231
 - ³¹P MAS NMR spectra 231
- aluminophosphate-based molecular sieves
 - spectra in the NIR region 383
 - spectra in the visible region 383
- aluminophosphate-type zeolites
 - frameworks of – 229
- aluminophosphates (AlPOs), diffuse reflectance IR spectroscopy (DRIFT) 100
- aluminosilicates
 - H-Al distances of bridging OH groups 263
- amines
 - protonation shifts 282
- ammonia (cf. also NH₃)
 - bound to cations in Na,K-ERI 151
 - on H-ZSM-5 151
 - on hydrogen erionite (H-ERI) 151
 - strongly interacting acid OH groups 151
- ammonia as a probe (cf. also NH₃)
 - extinction coefficients 134
 - investigation of H, Na-MOR 134
 - possible formation of NH₂ groups 134
 - typical bands 134
- amplitude of EXAFS oscillations 437
- analysis by XPS
 - of extra- and intra-framework Ti 505
- analysis of vibrational spectra
 - by ab initio methods 25
- angular overlap model (AOM) 380
- aniline
 - adsorbed on LiX, NaX, KX, RbX and CsX 400
 - wavelength shift of the electronic band 400
- anisotropy of ESR g-values
 - axial (two K-values) 298
 - isotropic (one g-value) 298
 - three K-values 298
- application of the cross-polarization technique
 - ²⁹Si MAS NMR signal intensity 266
- appropriate excited state of the Mössbauer nucleus
 - populated by excitation 520
 - populated by nuclear reaction 520
 - populated from decay of a radioactive precursor 520

- assignment of Cu^{2+} ESR spectra
 - ab initio calculations 315
 - at small Cu^{2+} -loadings 315
 - in faujasite-type zeolites (six-ring sites) 315
 - to defect sites such as silanol groups 315
 - to specific sites in dehydrated zeolites 315
- assignment of particular bands in framework spectra
 - lack of general correlation 34
 - to specific ring or double-ring breathing modes 34
- assignment of vibrational bands
 - criterion for - 18
- assignment of vibrational transitions
 - force field and quantum mechanical methods 12
- assignments of ^1H MAS NMR shifts
 - in various types of hydroxyl groups 261
- assignments of zeolite framework bands
 - at progressive crystallization states 29
 - blue-shift of Si-O stretching modes 29
 - coupling within Si-O-Al bridges 29
 - coupling within the TO_4 tetrahedra 29
 - effect of the $n_{\text{Si}}/n_{\text{Al}}$ ratio 29
 - localized and delocalized modes 29
 - normal mode analyses 29
 - problems of - 29
 - red-shifts of the Al-O stretching modes 29
- asymmetry parameter, η_{CSA}
 - of the chemical shift tensor 206
- atomic displacements related to
 - eigenvalue problem 14
- attenuated reflectance FTIR spectroscopy
 - formation of mesoporous silicate (MCM-41) 158
- Auger Al KLL signals
 - of mordenites dealuminated by different procedures 494
 - assignments of Al signals 494
- Auger electrons
 - measure of the absorption 433
- Auger parameter α_{Al}
 - Al in octahedral coordination 493
 - Al in tetrahedral coordination 493
 - analytical potential 493
 - discrimination of Al species 493
 - tricoordinated Al 493
- Auger parameters
 - for decreasing particle size 507
- Auger process 433
- Auger shifts
 - discriminating intra- and extra-zeolite species 502
- autoreduction of a Fe(III) 533
- B**
- ^{11}B MAS NMR spectrum
 - of boron-containing zeolites 237
 - of tetrahedral BO_4 237
 - of trigonal BO_3 237
 - strong quadrupolar interaction 237
- B-matrix (and its transpose) 14
- backscattering amplitude functions
 - determined on single-shell EXAFS of ZnGa_2O_4 445
- band gap 357
- base-catalysis
 - isomerization of unsaturated nitriles 405
- basic centers
 - formation of - 405
 - ionic alkali metal clusters 406
 - isomerization of allyl cyanide 406
 - via basic oxides within the zeolite 406
 - via introduction of alkali metal ions 405
 - via introduction of germanium 405
- basic properties
 - O 1s binding energy 497
- basic site strength
 - N 1s binding energies 497
- basicity
 - by XPS and IR of adsorbed pyrrole 497, 498
 - FAU framework 397
 - hypsochromic shift of iodine 397
 - LTA framework 397
 - of M,Na-X; M,Na-Y (M=K, Rb, Cs) 149
 - of Cs-Beta 149
 - probed by chloroform 495
 - probed by pyrrole 495
- basicity of oxygen atoms
 - Cl 2p signal of adsorbed chloroform 499
 - distance to alkali atoms 499
 - N 1s signals of adsorbed pyrrole 499
- basicity of X- and Y-type zeolites
 - pyrrole adsorption 148
- basicity of zeolites (donor strength)
 - adsorption of iodine vapor as a probe of - 396, 397
- basicity strength
 - of X- and Y-type zeolites 149
- bathochromic groups 346
- Ba-ZSM5
 - cation site 70
 - EXAFS data 70

- Ba-ZSM5
- far-infrared spectrum 70
 - structure 70
- BE of the framework elements
- cation electronegativity 500
- bent triatomic molecules (SO₂, H₂S, D₂S, H₂O)
- band shape, $\Delta\bar{\nu}_{1/2}$, vs. band shifts, $\Delta\bar{\nu}$ 126
- benzene
- energy level diagram 399
 - π -molecular orbitals 399
 - term diagram 399
- benzene adsorption
- in H-ZSM-5 zeolite 146
 - in K-L zeolite 146
 - into dealuminated Y 145
 - into molecular sieves 152
 - into Na-X, Rb-X, Cs, Na-X, Na-Y, Rb-Y 145
 - studied via IR spectroscopy 152
 - via four types of hydrogen bonding 146
- Beta zeolite (BEA)
- Brønsted and Lewis acidity of - 140
 - dealumination of - 61
 - H-[Si,Al,V]Beta 63
- Bethe lattice approximation 16
- bimetallic alloy clusters from M,Na-Y (M=Pt, Ir, Rh, Ru) 118
- binding energies
- absolute accuracy 484
 - basicity properties 492
 - by density-functional calculations 492
 - chemisorbed molecular water 487
 - contribution from hydroxide species 487
 - dealuminated mordenites 492
 - in adsorbed probe molecules 496
 - in NaCl 489
 - interference of hydroxyl groups 487
 - intrazeolite electrostatic potentials 492
 - trends with Al concentration 491
 - trends with ion exchange 491
 - trends with Madelung potential trends 491
- binding energy differences
- of structurally different aluminosilicates 485
- binding energy shift
- on charge transfer 490
- Bloch's equation 242
- bonding between ion and ligand
- increasing covalent character of the - 354
- boric acid trimethyl ester
- probe for basic sites 147
- boroaluminosilicates with MFI structure
- combined ¹H-MAS NMR, ¹¹B-MAS NMR, DRIFT 100
- Bouguer-Lambert-Beer law 367, 372
- breathing motions
- of 8-membered rings in zeolite A 68
 - of 12-membered rings in zeolite Y 68
 - of windows connecting adjacent cages in EMT 68
- bridging hydroxy groups
- assignment to sites in faujasite-type zeolites 261
 - concentrations 255, 256
 - ¹H MAS NMR 262
 - H-Al distances 263, 265
 - in 6-membered oxygen rings 263
 - in 12-membered oxygen rings 263
 - in sodalite cages 255, 256
 - in supercages 255, 256
 - local structure 262
 - neutron diffraction investigations 256
 - of dehydrated zeolites HNaY 255
 - O-H stretching 102
 - OH in-plane bending 102
 - OH out-of-plane bending 102
- bridging OH groups in the supercages
- favored ammoniation of - 269
- broad-line ²⁷Al NMR spectroscopy
- Al species in dehydrated zeolites 225
- broad-line solid-state NMR signal
- frequency 204
- Brodskii relation 66
- Brønsted acid sites 75
- catalytic behavior in zeolites 74
 - catalytical relevance 86
 - different strength 495
 - in mordenites 86
 - shifts of IR stretching bands 140
 - undesired formation of - 92
 - via reduction of metal cations 118
 - via the Hirschler-Plank mechanism 87
- Brønsted acid sites in hydrogen mordenite
- effect of dealumination 87
 - function of the degree of exchange 87
 - heterogeneity and accessibility 87
 - localization 87
- Brønsted acidity
- of erionite (ERI) 88
 - of offretite (OFF) 88
 - of zeolite Beta (BEA)
- Buckingham term 19
- butanes
- on Na,H-Y zeolites 153
 - on zeolites containing transition-metal 153

C

- ¹³C MAS NMR spectroscopy
 - isotropic chemical shift 281
 - of adsorbates in zeolites 282
 - of coke precursors 284
 - of diisopropyl ether 284
- ¹³C-labelled adsorbates
 - studied by ESEEM 316
 - studied by ESR 316
- C₂Cl₆
 - adsorption-induced shift of the ¹H-MAS NMR signal 139
- C₂F₄
 - adsorption-induced shift of the ¹H-MAS NMR signal 139
- calculated NMR line shape functions 207
- calculated power spectrum of the pore-opening vibration
 - comparison with the simulated infrared and Raman spectrum 34
- calculations
 - effect of dehydration 27
 - of infrared and Raman intensities 18, 19
 - of vibrational frequencies
- calibration curve
 - extinction coefficient of benzene in H-ZSM-5 37
- carbanions
 - electronic bands of - 406
- cerium ions
 - effect of Brønsted acid sites 403
 - stability 403
- carbon dioxide (cf. also CO₂)
 - as a probe for basic sites 147
 - surface carbonates 149
- carbon monoxide (cf. also CO)
 - probing Brønsted acidity 140
 - weakly basic probe molecule 140
- carbonium ions
 - effect of Brønsted acid sites 401
- cation dynamics
 - couplings framework/cation motions 68
 - of cation-exchanged Na-Y and K-Y 68
 - site-concept 68
- cation migration and distribution in zeolites
 - NMR spectra of - 239
- cation modes and external modes
 - cation migration 72, 328
 - chemical conversion 72
 - strong coupling 72
- cation positions
 - in the structure of faujasites 240
 - studies of the occupation 68
- cation vibrations
 - affected by adsorption 71
 - coupled with framework vibrations 70
 - transitions in the far-infrared range 64
 - Raman spectra 64
 - vibrational spectroscopic techniques 64
- cations
 - assignment 245
 - in dehydrated zeolites 245
 - NMR line shapes of sodium cations 245
 - NMR spectra of - 239
- CAVERN apparatus 280
- Cd₄S₄ clusters
 - exciton transition 412
 - preparation of - 412
 - UV-VIS spectra of - 412
- (CdS,O)₄ cubes
 - in adjacent sodalite cages of Y 413
 - ultimate hyperlattice arrangement of - 413
- cells for transmission IR spectroscopy 41
- centers due to impurities 359
- centers with trapped electrons
 - F-, K- and L-bands 358
 - M-, R-, N- and O-bands 358
- centers with trapped holes 358
- central force field
 - for the simulation of infrared spectra 23
- cesium cations
 - in mordenite 240
- CH₃OH (cf. also methanol)
 - interaction with acid OH groups 150
- chabazite (CHA)
 - accessibility of bridging OH groups 270
 - framework vibrations 55
 - infrared reflection spectroscopy 55
 - OH bands 93
 - Raman scattering 55
 - thermal stability 93
- change in the ²⁹Si MAS NMR line shape of TS-1
 - Ti content 220
- change of UV-VIS bandshape
 - blurring of rovibrational levels 364
 - upon adsorption 364
- characterization by ESR of transition metal ions 296
 - coordinated to extra-lattice ligands 296
 - coordinated to lattice oxygen atoms 296
 - present in the lattice 296
 - present on the surface 296
- characterization of acid properties via FTIR
 - by adsorption of H₂, N₂, CO and NO 130
 - by adsorption of O₂, N₂, He, Ar and Xe on H-Y 130

- characterization of acid properties via FTIR
 – of H-, Li-, Na- and K-exchanged ferrierite 130
 characterization of zeolites
 – inelastic neutron scattering (INS) 12
 – infrared (IR) 12
 – Raman spectroscopy 12
 characterization of zeolitic acidity
 – by acetonitrile 138
 – by adamantane carbonitrile 138
 – by deuterated acetonitrile 138
 – in $\text{AlPO}_4\text{-5}$ 138
 – in MeAPO-5 ($\text{Me}^{2+}=\text{Be}^{2+}, \text{Mg}^{2+}, \text{Ti}^{2+}, \text{Fe}^{2+}, \text{Co}^{2+}$) 138
 – in SAPO-5 138
 – in VPI-5 138
 – in Zr-containing pentasil structures 138
 charge of clusters 326
 charge-transfer (CT) transitions
 – donor-acceptor complexes 355
 charged metal clusters in zeolites
 – formation of – 409
 chemical isomer shift (IS) 521
 chemical reactions
 – catalyzed by acidic and basic zeolites 279
 – in-situ NMR spectroscopic studies of – 279
 chemical shift, δ_{H} , in NMR
 – correlation with the IR wavenumber, ν_{OH} 258
 – of CaOH groups 260
 – observed for MeOH 260
 – of Si(1Al) units 217
 – of Si(3Si,OH) units 217
 chemical shift in NMR of ^{129}Xe atoms
 – effect of the pore size 272
 chemical shift in UPS and XPS of zeolites
 – consistent experimental procedures 487
 – discriminating octahedral and tetrahedral Al coordinations 485
 – discriminating zeolitic and non-zeolitic materials 485
 – long-range contributions to – 485
 – of oxygen 1s in oxides 486
 – quantum-chemical description 487
 – simple model of – 486
 – trends for zeolite-related materials 486
 – uncertainties 487
 chemical shift tensor in NMR 205
 – asymmetry parameter, η_{CSA} 206
 chemisorption of CO_2
 – bidentate structure 122
 – carbonate structures 122
 – monodentate structure 122
 chloroform
 – XPS of – 497
 chloromethane
 – FTIR probe for Brønsted acidity 139
 chromophore
 – hyperchromic effect 345
 – hypsochromic effect 345
cis-to-trans isomerization
 – monitored by UV-VIS spectroscopy 420
 Clar nomenclature 398
 Clebsch-Gordan coefficient 523
 clinoptilolite (heulandite-like structure, HEU)
 – DRIFT studies of framework 54
 – framework vibrations 54
 – influence of treatment temperature 54
 – micro-infrared spectroscopy of – 87
 – Sanderson electronegativity of exchange cations 54
 closely spaced molecular orbitals (MOs)
 – *s*-, *p*-, *d*-bands 357
 cloverite (gallophosphate)
 – ^{71}Ga MAS NMR spectroscopy of – 237
 – assignment of ^{31}P MAS NMR spectrum 233
 – band-gap excitation 374
 – decomposed ^{31}P MAS NMR spectrum of – 235
 – optical properties 374
 – penta-coordinated and octahedrally coordinated Ga 237
 – structural element of – 235
 – UV-VIS DRS spectroscopy 374, 375
 cluster Ag_4^{3+} in zeolite rho
 – ESR parameter *g* 326
 – ESR parameter *A* (mT) 326
 clusters $\text{Ag}_6^{5+}, \text{Ag}_6^{8+}, \text{K}_3^{2+}, \text{K}_4^{3+}, \text{Na}_4^{3+}, \text{Na}_6^{5+}, \text{Na}_4^{4+}, \text{Na}_5^{3+}, \text{Na}_5^{4+}$ 326
 – ESR parameter *A* (mT) 326
 – ESR parameter *g* 326
 – in zeolite *A* 326
 – in zeolite *X* 326
 – in zeolite *Y* 326
 – interaction with framework Al 326
 clusters of framework fragments 26
 – disadvantages of – 26
 – for spectroscopic investigations 26
 – mimicking zeolite frameworks 26
 clusters of metals
 – delocalisation of the electron 326
 – distribution of the electron density 326
 CO adsorption (cf. also carbon monoxide)
 – adsorption of isotopes, $^{13}\text{C}^{16}\text{O}$ and $^{12}\text{C}^{16}\text{O}$ 112

- affected by the ratio q/r 111
- as a probe for mesoporous materials 138
- band shifts vs. polarizing power of cations 116
- characterizing Lewis acidity of cations 142
- characterizing "true" Lewis acidity 142
- close to the cations 111
- different mechanisms of - 116
- diffuse reflectance IR of - 118
- force constants 116
- metal-carbon stretching vibration 118
- on Ca- and Ni-exchanged zeolite A 116
- on Co-, Mn- and Zn-exchanged materials 116
- on Na-A, Na-X, Ca-A and Ca-X 112
- on Na-Al-ZSM-5 142
- on sites in front of S3 cations 112
- on X- and Y-type zeolites 112, 116
- onto small platinum particles in Na-Y 118
- related to acidity strength 142
- revealing two types of OH groups in MAZ 142
- shift $\Delta\tilde{\nu}$ (OH) upon - 142
- two possible arrangements of CO 112
- ¹²CO adsorption on
 - Na₂Ca-A 115
 - Na₂Li-A 115
 - Na₁₂-A 115
 - Na₄Mg₄-A 115
- ¹²CO and ¹³CO adsorption
 - arrangement Na⁺-CO 115
 - arrangement Na⁺-OC 115
 - detailed assignment of the bands 115
 - in Na_{12-x}Ca_x-A 115
 - satellites 115
- CO and NO_x adsorption
 - on a Cu-[Zr]-HMS 144
 - on Ag-ZSM-5 144
 - on mesoporous silicate [Zr]-HMS 144
- CO molecules inside A-type zeolites
 - four bands essentially reproduced 114
 - re-investigated 114
- Co-aluminophosphates (CoAPOs)
 - combined XAFS (CoK edge) and XRD 461
- Co atoms in CoAPOs 449
- Co atoms in CoAPOs of CHA topology 449
- Co atoms in CoAPOs of SOD topology 449
- Co atoms in CoMnAPO-34 449
 - EXAFS data 449
- Co phthalocyanine in intra-zeolite locations
 - in [Si,Al]MCM-41 143
 - on coordinatively unsaturated Al and Ti 143
 - probing acid bridging hydroxy groups 143
 - probing acidity of [Al]MCM-31 143
 - probing acidity of Zr-containing mesoporous materials 143
 - probing Lewis acid sites in Ti-containing zeolites 143
 - probing silanol groups 143
 - XPS of - 509
- Co²⁺ cations
 - distortion of local environment of - 316
- Co-A zeolite
 - electronic spectra with adsorbates 389
- CoAPO
 - spectra in the NIR region 383
 - spectra in the visible region 383
- CoAPO-5
 - Brønsted and Lewis acidity in - 95
 - combined XAFS (CoK edge) and XRD 461
 - redox properties 95
 - unusual Lewis acidity 95
- CoAPO-11
 - redox properties 95
 - unusual Lewis acidity 95
- CoAPO-18
 - after admission of NO 384
 - change in the oxidation state of Co ions 384
 - NO at two different sites 384
 - UV-VIS spectra 384
- CoAPO-20
 - XANES spectra 456
- CoAPO-37
 - Brønsted and Lewis acidity 95
 - FTIR transmission spectroscopy 95
 - OH stretching region 95
- CoAPO-44
 - combined XAFS (CoK edge) and XRD 461
 - spectra in the visible region 383
 - UV-VIS spectra 384
- CoAPSO-44
 - combined XAFS (CoK edge) and XRD 461
- cobalt sulphide particles
 - for hydrodesulphurization 539
- coke
 - band around 1600 cm⁻¹ 163
 - formation of - 163, 281
 - IR spectroscopy of - 163

- color centers 358
- combined transmission UV-VIS and IR
 - Claus reaction 398
- CoMnAPO-3
 - EXAFS data 449
- complexes in Y-type zeolites
 - Mn(II)-1,10-phenanthroline 154
 - Se chains and rings in A, X, MOR, CHA, CAN 154
 - studied by Raman spectroscopy 154
- computer simulation
 - Ni²⁺-exchanged zeolite Y 449
- Co₄Na₄A
 - optical spectra 386
- concentration
 - of a paramagnetic entity by ESR 304
 - of OH by ¹H MAS NMR 77
 - of radiation absorbing species 35
- concept of the energy surface
 - ab initio calculations 25
 - harmonic approximation 25
 - harmonic force constants 25
- conduction band
 - partially filled excitations to nearby empty states 357
- conduction electron spin resonance signals
 - in zeolite A 330
 - in zeolite X 330
 - in zeolite Y 330
 - of Cs 330
 - of K 330
 - of Na 330
 - of Rb 330
- conductive polymeric materials
 - thiophene oligomers 406
 - within zeolite channels 406
- connectivities
 - between Si atoms on T1 and T2 and on T2 and T3 in ZSM-39 222
- Connes advantage
 - high resolution and wavelength accuracy 365
- continuous wave ESR (CW-ESR) 303
 - K-band (20 GHz) 296
 - Q-band (35 GHz) 296
 - S-band (3.5 GHz) 296
 - W-band (95 GHz) 296
 - X-band (9.25 GHz) 296
- conversion electron ⁵⁷Fe Mössbauer spectroscopy (CEMS) 534
 - bifunctional zeolite catalysts 535
 - corrosion and oxidation of iron 525
 - for studying reactions 534
 - metal-impregnated zeolite catalysts 535
- conversion of UV into visible light
 - by rare-earth doped zeolites 393
 - rare earth sodalite 393
- CoPc complexes 417
- core-level photoionization
 - true absorption 433
 - X-ray photon annihilation 433
- correlation diagram 351
 - for d² ions in octahedral environment 352
- correlation spectroscopy (COSY)
 - three-dimensional connectivities in ZSM-n (n = 5, 12, 22, 23, 39), DD3R 221
- Coulomb integral J_{ij} 350
- Cr³⁺ (d³) ESR signals
 - observed in molecular sieves 318
- Cr⁵⁺ (d¹) ESR signals
 - pseudo-tetrahedral chromyl cations 318
 - square pyramidal chromyl cations 318
- Cr⁵⁺ ion
 - theoretical ESR spectra 321
- Cr⁵⁺ mordenite
 - ESR spectrum 318
 - – simulations 318
 - superhyperfine splitting 318
- CrAPO-5
 - diffuse reflectance spectroscopy (DRS) 385
- CRAMPS technique 209
- cross-polarization (CP)
 - enhancement of NMR signal intensity 213
 - principle 212
 - schematic representation 213
- cross-polarization time constant 213
- crystal field
 - energy difference e_g-t_{2g} (Δ_o) 348
- crystallographically inequivalent T-positions in high-silica ZSM-5 221
 - exp. and calc. ²⁹Si MAS NMR signals 221
- ¹³³Cs MAS NMR spectroscopy
 - assignments 243
 - dehydrated Cs-exchanged zeolite Y 242
 - MAS sideband pattern 243
 - of hydrated zeolite CsLiA 241
- Cu²⁺ cations
 - distortion of local environment of site 316
- CuCl/Na-ZSM-5
 - Cu Auger parameter 509
- CuL₃VV Auger spectroscopy
 - extra- and intra-zeolite Cu detected by – 503

Curie-Weiss behavior

- conduction ESR signals of metallic Na 328
- indicative of quantum-sized particles 328

D

d-d band positions of

- Co²⁺-LTA 387
- Cr²⁺-LTA 387
- Cu²⁺-LTA 387
- Ni²⁺-LTA 387

d-d transitions of hexaquo Ni²⁺ ions

- zeolite Ni(II)X (fully hydrated) 389

d-Orbital splitting in ligand fields 349

Dallas amorphous material-1 (DAM-1)

- IR and Raman spectroscopy of - 57

Darken's equation

- correction of diffusivity for coverage dependence 166

data processing of UV-VIS spectroscopy 366

dealuminated H-Y

- combined ¹H-MAS NMR, ¹¹B-MAS NMR, DRIFT 100

dealuminated mordenite

- acid strength 142
- solid-state NMR spectroscopy 225

dealuminated Y-type zeolites

- by deep-bed calcinations and acid leaching 81
- effects of adsorption of probe molecules 81
- solid-state NMR spectroscopy 225

dealuminated ZSM-5

- solid-state NMR spectroscopy 225

dealumination

- ²⁷Al MAS NMR 225
- determination of the n_{Si}/n_{Al} ratio 60
- effect of rare earth loading 60
- ¹H-²⁷Al CP/MAS NMR 225
- investigation by XPS 493
- monitored by IR and Raman spectroscopy 60
- ²⁹Si MAS NMR 219

dealumination of zeolites by CCl₄

- MAS NMR and FTIR spectroscopic study 164
- mechanism of the - 164

dealuminted MAZ

- acid strength 142

deamination 254

- development of LF and HF OH bands 75
- formation of (bridging) OH groups 74

- of zeolite NH₄,Na-Y 81

- of zeolite NH₄-Y 75

decomposition of organic cations in offretite

- FTIR spectroscopy 157

decomposition of organic cations in ZSM-34

- FTIR spectroscopy 157

definition of polar angles of the field, B₀, in

ESR 307

dehydration

- effect on optical spectra 386
- migration of the ions 387

dehydroxylation 76

- of two bridging OHs 262

dehydroxylation of zeolite HY

- quantitative multi-nuclear solid NMR 261

derivation of MM force field

- ab initio calculations on molecular models 21
- for modeling zeolite frameworks 19
- interactions of organic molecules with frameworks 21
- representation of typical building units 21
- rigid ion model 19
- shell model 19
- with an anharmonic Morse potential 21

deuterium

- adsorption 106
 - sorbed into zeolite Na₄Ca₄-A 106
- DEXAFS (Dispersive EXAFS) method
- dehydration of (Ni²⁺, Na⁺)-loaden zeolite Y 461
 - reactions of partially Cu-exchanged Na-zeolite Y with pure H₂ 461
 - time resolution 459
 - whole spectrum measured in one instant 459

2,6-di-*tert*-butylpyridine

- on external Brønsted and Lewis acid sites 134

diffuse reflectance infrared spectra (DRIFT)

- advantages 42
- band assignments 137
- near infrared (NIR) 42
- of H-ZSM-5 99
- of hydrogen adsorbed on H-ZSM-5 137
- overtone and combination modes of vibrations 42

diffuse reflectance (DR) spectra

- trimethylbenzene on HMOR 395

diffuse reflectance spectrometer for UV-VIS

- schematic representation of a - 370

- diffuse reflectance spectroscopy (DR) in UV-VIS
- admission of oxygen to Cu(I)Y 392
 - assignment of bands 409
 - contributions of transition metal ions 383
 - formation of a Cu(II)(O_f)₃O₂⁻ complex 392
 - kinetics of silver-cluster formation in AgX 409
 - of coadsorbed iodine and methylacetylene in HZSM-5 407
 - of Co²⁺ in zeolite A 383
 - of CrAPO-5 385
 - of CuNaCHA 388
 - of CuNaMOR 388
 - of dehydrated Cu(II)Y 392
 - of hydrated Cu(II)Y 392
 - of iodine in HZSM-5 407
 - of methylacetylene in HZSM-5 407
 - of MFI-type ferrisilicalite 385
 - of MFI-type vanadium silicalites 385
 - of MgAPO-5 385
 - of MgVAPO-5 385
 - of NaX-incarcerated thioindigo 419
 - of silver mordenite 409
 - of VAPO-5 385
- diffusion (self-diffusion coefficients)
- by NMR techniques 168
- diffusion (transport diffusivities)
- by FT micro-IR spectroscopy on single crystals 167
 - hydrocarbons (benzene, toluene, *p*-xylene, cyclohexane) 167
 - in silicalite-1 in different crystallographic directions 167
- diffusion coefficients
- effect of coke deposition 166
 - co-diffusion (B, EB, *p*-X) 166
 - diffusion (B, EB, *p*-X) 166
 - measured by IR spectroscopy 165
 - of aromatics in H-ZSM-5 single crystals 166
 - of *p*-xylene in single crystals (silicalite-1, AlPO₄-5) 166
- diffusion in single crystals of H-ZSM-5
- *n*-heptane 166
 - *n*-hexane 166
 - *n*-nonane 166
 - *n*-octane 166
 - neopentane 166
 - surface barriers 166
 - toluene 166
 - xylenes 166
- diffusion of
- benzene 166
 - ethylbenzene 166
 - para-xylene 166
 - pyridine 166
- dihydrogen adsorption
- information about zeolite basicity 149
- dimensionless electron spin vector 297
- dimethylphosphine (DMP)
- on acid surface sites 140
- 2,2-dimethylpropionitrile (pivalonitrile, PN)
- on [Si]MCM-41 139
- dinitrogen, N₂, as a probe for acid sites
- in H-mordenite, H-Y or H-ZSM-5 138
- dipolar-dephasing experiments
- heteronuclear magnetic dipole-dipole interaction 214
- direct eigenvalue problem
- input and output for solving the - 14
- dispersive spectrometers
- in the UV-VIS region 365
- dissociation of H₂S
- detected by IR 84
 - quantitative evaluation 84
- distribution of xenon atoms
- simulations 278
- donor-acceptor complexes
- charge-transfer-to-solvent transitions (CTTS) 356
 - donor molecules in solutions of aromatics 356
- DOR NMR spectroscopy 249
- DOR sidebands 228
- double integration of an ESR signal
- baseline 305
 - integration width 305
 - lineshape 305
- double resonance techniques
- rf-pulses or pulse sequences 212
- double rotation (DOR)
- suppression of of 2nd order quadrupole line broadening 211
- double-rotation (DOR) technique
- averaging of 2nd order quadrupolar line broadening 228
- DRIFT spectroscopy
- accessories necessary for - 43
 - combination with frequency response technique 43
 - crystallization of silicalite-1 157
 - decomposition of (η⁶-anisole)tricarbonyl Cr (0) 163
 - decomposition of (η⁶-benzene)tricarbonyl Cr (0) 163
 - drawback of - 43
 - effect of progressive dealumination 60
 - mesoporous samples 43

- of mordenites 60
- of SAPO-5 101
- of SAPO-31 101
- of SAPO-34 100
- DRIFT technique (for near infrared)
 - monitoring dealumination of H,Na-Y 81
- dual wavelength spectroscopy in UV-VIS 366
- E
- \underline{E} -matrix (unit matrix) 15
- EELS (electron energy loss spectroscopy)
 - interfaces 462
 - similarity to XAFS spectra 462
 - sub-nanometer dimensions 462
- effect of quadrupole coupling constant Q
 - on ESR spectra of dehydrated Cu-MOR 315
 - perpendicular region in absorption mode 315
- effective g -value (g) 298
- efficiency of cross-polarization 213
 - strength of heteronuclear magnetic dipole-dipole interaction 213
- eigenvalue problem 14
- electric field gradient (EFG) 206
 - non-spherically sym. charge distributions 216
- electric field gradient tensor
 - asymmetry parameter, η_Q 208
 - Hamiltonian (\bar{H}_Q) 298
- electric quadrupole moment (eQ)
 - principal values V_{11} , V_{22} and V_{33} 208
- electron configurations
 - in octahedral environments 351
- electron energy loss spectroscopy (EELS) 432
- electron g -factor or Landé-factor (g_e) 297
- electron motion in an orbital
 - Hamiltonian (\bar{H}) 298
 - orbital angular momentum (L) 298
- electron nuclear double resonance spectroscopy (ENDOR) 296
- electron pairing energy
 - Coulomb repulsion energy difference e_g-t_g (Δ_o) 350
- electron spin echo envelope modulation (ESEEM)
 - analysis of modulation frequencies and amplitudes 310
- electron spin echo spectroscopy (ESE)
 - pulse sequences for pulsed ESR technique 310
 - short resonant microwave pulses 310
- electron spin resonance (ESR) 297, 303
 - resonance technique 297
 - unpaired electron spins/external magnetic field 297
- electronegativity equalization method (EEM) 383
- electronic band positions of Cu(II) in
 - CHA 388
 - FAU 388
 - LTA 388
 - MOR 388
- electronic Bohr magneton (β_e) 297
- electronic excitation between singlet states
 - superimposed by vibration 344
- electronic excited states 340
- electronic ground states 340
- electronic spectroscopy
 - accessibility of ions to adsorbates 389
 - alkali metal ion clusters 410
 - assignment of cations 389
 - calculated single-orientation spectrum 411
 - capability for alkenyl ion formation 403
 - clusters confined to zeolite cages 416
 - experimental spectra 411
 - guest molecules encapsulated in zeolite cages 397
 - in a narrow sense 338
 - modified Claus process 397
 - of alkali metal ion clusters in zeolites 412
 - of carbanions 401
 - of carbenes 401
 - of carbocations 401
 - of electronic structures of clusters 408
 - of Na_4^{3+} centers
 - of NO decomposition 392
 - of organometallic clusters in zeolite cages 416
 - of radicals 401
 - of reactive intermediates 401
 - of silver clusters 408
 - of sodium sodalite 411
 - of tetrahedral mononitrosyl Co(II) complex 392
 - orientationally averaged spectra 411
 - sulfur dioxide (SO_2) adsorbed on zeolite NaX 397
 - wavelengths of the band maximum λ_{max} 403
- electronic states
 - Co^{2+} -LTA 387
 - Cr^{2+} -LTA 387
 - Cu^{2+} -LTA 387
 - Ni^{2+} -LTA 387

- electronic transitions
 - frequently used notations 346
 - notations after Kasha 346
 - notations after Mulliken 346
- embedded cluster schemes
 - to calculate local force constants 27
 - to calculate vibrational frequencies 27
- emission spectra
 - CdS occluded in zeolite Y 413
- encapsulation of bulky entities
 - in zeolite hollows 415
- ENDOR spectroscopy 296
 - advanced equipment 309
 - drawbacks 309
 - energy level scheme for ENDOR 308
 - Fe-sodalite 317
 - low measurement temperature 309
 - NMR spectrum of nuclei interacting with paramagnetic centers 308
 - nuclear relaxation time 309
 - one electron-one proton/two-spin system 308
 - sensitive ESR spectrometer 309
- energies for excitations
 - order $\Delta E_e > \Delta E_v \gg \Delta E_r$ 340
- energy level diagram for an isolated electron
 - corresponding absorption spectrum 297
 - first derivative ESR spectrum 297
 - in a magnetic field B 297
- energy level diagram of benzene 399
- energy of the γ -ray, E_γ , emitted by a source 520
 - moving the source or the absorber 520
- energy term diagrams
 - for $d^{n+5}(d^n)$ ions in D_{3h} ligand field 381
 - non-framework cations 378
- enhanced catalytic activity
 - interaction Brønsted acid/Lewis acid sites 262
- erionite
 - bridging OH groups in 267
 - Ca-exchanged 88
 - DRIFT spectroscopy of – 88
 - OH and OD bands 88
 - transmission IR spectroscopy of – 88
- erionite (ERI), offretite (OFF)
 - framework vibrations 55
- ESEEM spectroscopy 296
 - adsorbed molecules 311
 - analysis of modulation frequencies and amplitudes 310
 - Cu^{2+} complexes in mesoporous MCM-41 316
 - distance of magnetic nuclei 311
 - number of magnetic nuclei 311
 - stimulated echo 311
 - superhyperfine interaction 316
 - weak electron-nuclear hyperfine interaction 311
- ESR (electron spin resonance) spectroscopy (cf. high-resolution ESR) 297, 300, 319
 - adsorbed paramagnetic molecules 296
 - alkali metal and silver clusters in zeolites 326
 - area under the absorption envelope 305
 - assignment/location of Cu^{2+} 313
 - assignments of parameters of Cr^{5+} 318
 - Cr-containing molecular sieve 318
 - Cu^{2+} complexes in mesoporous MCM-41 316
 - Cu^{2+} -mordenite 313
 - double integration 305
 - echo amplitude dependent on τ 310
 - effect of the quadrupole coupling constant Q 314
 - experimental study of Ag_6^{x+} clusters in A 327
 - Fe^{3+} in molecular sieves 317
 - g tensors 332
 - hyperfine information 311
 - hyperfine structure 330
 - interaction of unpaired NO electron with a cation 330
 - isotropic g - and A -values of clusters 326
 - Lewis acidity 296
 - NO as probe for Lewis acidity 331
 - O_2^- generated by ionizing radiations 332
 - of Ag_6^{x+} clusters in A 327
 - of calcined Cu^{2+} -zeolites 314
 - of ^{63}Cu and ^{65}Cu nuclei 314
 - of Cu^{2+} in dehydrated zeolites 314
 - of Cu^{2+} -loaded SAPO's 313
 - of CuNaA 314
 - of CuNaX 314
 - of dehydrated Cu mordenite 314
 - of Na_4^{3+} and metallic Na 328
 - of NO adsorbed on H-ZSM-5 332
 - of NO adsorbed on NaY 331
 - of NO treated H-ZSM-5 331
 - of paramagnetic ionic clusters 323
 - of sodium clusters in zeolite Y 329
 - of the parallel region of Cu^{2+} 313
 - of the perpendicular regions of Cu^{2+} 313, 314
 - of V^{4+} in V-containing molecular sieves 322
 - of zeolite encaged $\text{Cu}(\text{histidine})^{2+}$ 316
 - π orbital separations 332
 - orientation of an adsorbed molecule 311

- paramagnetic clusters 296
- phase memory time T_2^M 310
- quantitative analysis 296
- resonance condition 298
- sample cavity 303
- sensitivity 296
- signal intensity 305
- simulated modulation pattern 311
- single pulse followed by free induction decay 310
- spectral simulation 328
- spectrometer (block diagram) 302
- theoretical Fe^{3+} spectra 317
- theoretical study of Ag_6^{x+} clusters in A 327
- three pulse sequence 310
- two pulse sequence 310
- unpaired electrons distribution among nuclei 326
- with NO as a probe molecule 328
- ESR spectra of as-synthesised VAPO-5
 - as a function of the vanadium content 323
- ESR spectrum of Cr^{5+}
 - experimental 319
 - in mordenite 319
 - simulation 319
- ESR symmetry
 - axial 299
 - axial non-collinear 299
 - isotropic 299
 - monoclinic 299
 - of zeolites (ESR parameters) 313
 - rhombic 299
 - triclinic 299
- ESR-related techniques
 - electron nuclear double resonance (ENDOR) 307
 - electron spin echo spectroscopy (ESE) 307
 - enhancement in resolution 307
- estimation of the preferred zeolite geometry
 - minimum energy 19
 - molecular mechanics (MM) 19
- ethane
 - adsorbed in silicalite-1 123
 - adsorbed in purely siliceous zeolite A 123
- ethane aromatization
 - Mössbauer spectroscopy of the catalyst 539
- ethylbenzene disproportionation
 - in-situ IR spectroscopy/gas chromatography 159
- ethylenediamine, synthesis of - 152
- ethyne
 - adsorbed in silicalite-1 123
 - adsorbed in purely siliceous zeolite A 123
- ETS-4
 - IR spectra 61
 - Raman spectra 61
- ETS-10
 - IR spectra 61
 - Raman spectra 61
- Eu-151 Mössbauer spectroscopy 533
- EXAFS
 - constructive interference 435
 - coordination numbers 430
 - Cu-Cu coordinations in Cu-ZSM-5 502
 - destructive interference 435
 - disorder in the host framework 431
 - element-selectivity 430,462
 - Hg(II) halides in porosils 450
 - interatomic distances 430,431
 - interference outgoing and/scattering waves 434
 - local environment of non-framework cations 431
 - major methodical weakness 446
 - multiple scattering (MS) 430
 - probe pair correlations 431
 - role of long-range order 430,462
 - scattering of the electron 430
 - single scattering 430
 - structure of larger guest species 431
- EXAFS analysis
 - attenuation of the EXAFS amplitude 436
 - Co^{2+} -exchanged Y-type zeolites 448
 - coordination numbers 449
 - correction term $\exp[-2k^2\sigma_j^2]$ 436
 - most important structural data 436
 - N_j , number of backscattering atoms 436
 - R_j , distance shell j /absorbing atom 436
- EXAFS data analysis
 - amplitude 438
 - aqueous solution containing Mn^{2+} ions 448
 - backscattering amplitude 443
 - curved-wave theory 438
 - dehydrated Mn^{2+} -exchanged zeolite Y 448
 - determination of structural parameters 443
 - focussing effect 438
 - high dispersion of Mo/S clusters 452
- EXAFS data analysis
 - hydrated Mn^{2+} -exchanged zeolite Y 448
 - Mo atoms coordinated by sulfur 452
 - phase-shift functions 438,443

- EXAFS data evaluation
- zeolite-supported Mo sulfide catalysts 452
 - amplitude functions (theoretical) 446
 - calculation of $F_j(k)$, $\Phi_j(k)$ and $\Phi_j(k)$ 438
 - curved-electron-wave theory 438
 - edge energy E_0 of SOD-GaSi 446
 - FEFF code 438
 - for SOD-GaSi 446
 - framework incorporation of Ga into MFI 447
 - limitations of evaluation 438
 - multiple scattering (MS) 438
 - phase-shift functions (theoretical) 446
 - sodalite-type (galloboicichulite $\text{Ca}_8[\text{Ga}_8\text{Si}_4\text{O}_{24}](\text{OH})_8$) 447
 - total phase shift function $\Phi_{ij}(k)$ 437
- EXAFS formula
- distance shell l /absorbing atom 446
 - excited photoelectrons as plane waves 435
 - mean square displacement absorbing/backscattering atoms σ_l^2 446
 - number of backscattering atoms 446
 - single-scattering 435
 - single-shell version 446
- EXAFS function $\chi(E)$, $\chi(k)$ 435, 444
- elastically backscattered electrons 435
 - of SOD-GaSi 444
 - of $\text{Zn}_2\text{Ga}_2\text{O}_4$ 444
- EXAFS information on
- Co in CoAPO-20 449
 - data of hydrodesulfurization catalysts 453
 - morphologies 447
 - Mo/S-zeolite Y 453
 - Ni^{2+} -exchanged zeolite Y 449
 - particle sizes 447
 - zeolite-stabilized metal clusters 447
- EXAFS investigations
- Cl, O ligands of Au atoms 456
 - Co in CoSAPO-34 447
 - Ga coordination environment 443
 - in HgBr_2 molecules zeosil DDR 450, 451
 - metal atoms in frameworks 447
 - of a gallosilicate (SOD-GaSi) 443, 445
 - of Hg (II) halides in porosils 450
 - of SOD-GaSi (pure EXAFS data) 443
 - of SOD-GaSi (raw spectra) 443
 - Ti in ETS-10 447
 - Ti in titanium silicalite 447
 - victoreen functions of SOD-GaSi 443
 - Zn and Mn in AlPO_4 -34 447
 - ZnGa_2O_4 as a standard 443
 - Zn in MFI 447
 - Zn, Mn and Co in MeAPO-34 447
- EXAFS oscillation
- amplitude of - 437
 - backscattering power 435
 - distance absorbing/backscattering atoms 435
 - frequency of - 437
 - interatomic distances R_j 437
 - number of backscattering atoms 435
 - shift of the - on the k scale 437
 - type of backscatterer 437
 - use of a standard compound 437
- exchange integral K_{ij} 350
- exciplexes
- CT complexes in the excited state 356
- excitation of d (for RE: f) electrons 348
- d \rightarrow d transitions 348
- excitation spectra
- of CdS clusters in zeolites 412
 - of CdS occluded in zeolite Y 413
- excitation transitions
- near low-energy side of the band gap 359
- exciton centers
- formation of an electron-hole pair 358
 - Frenkel exciton 358
 - mobile excited electronic states 358
 - polarization of an electron-hole pair 358
 - Wannier-Mott exciton 358
- extended X-ray absorption fine structure (cf. EXAFS) 430
- external modes of frameworks
- sensitive to the structure 28
- extinction coefficient
- calibration curves 37
 - dependent on the concentration 36
 - determination of - 37
 - for pyridine adsorption 141, 163
 - of the CH bands 163
 - UV-VIS spectroscopy 340
- extinction coefficients 38, 39, 134, 135
- deviations between literature data 40
 - for CO 141
- extra-framework Al-containing species
- bands assignments in IR 99
 - binding-energy data 493, 495
 - broadening of the Al 2p line 493
 - identified in DRIFT experiments 99
 - leaching of - 82
 - XPS of - 493, 495
- extra-framework cations
- in X- and Y-type zeolites 67
 - motions of - 70
 - sites of - 67
- extra-framework Fe
- binding energy of - 506
 - XPS of - 506

F

- F-centers 358
- F-matrix 14, 15
- FAPO-5
 - ESR-spectra of – 317
- far infrared (FIR) spectroscopy
 - adsorption-induced changes 71
 - adsorption of pyrrole 72, 73
 - adsorption of pyrrolidine 72, 73
 - agreement with computed spectra 68
 - alkali, alkaline earth, transition metal zeolites 66
 - assignments of bands 66
 - band assignments to cation sites 67
 - calculated for Na-Y 68
 - comparison to simulated spectra 67
 - framework and cation vibrations 67
 - local molecule NMA calculations 66
 - M-FAU (M=NH₄, Li, Na, K, Rb, Cs, Tl) 70
 - M-PMT 70
 - of alkali-metal exchanged faujasites and H-Y 65
 - of types X, Y, A, and ZSM-5 66
 - of zeolites Na-Y and K-Y 67, 72
- far or vacuum ultraviolet 339
- FAU (faujasite-type zeolites)
 - base properties of – 149
 - cracking catalysts 78
 - four crystallographically different oxygens 76
 - hydrogen forms 78
 - IR and Raman of framework vibrations 52, 56
 - steaming 78
 - structure 78
 - V⁴⁺ (d¹)-exchanged – 322
- Fe³⁺ ESR spectra
 - chemical interpretation 317
- ⁵⁷Fe CEMS
 - back-scatter method 534
- Fe(57) Mössbauer spectroscopy
 - general interpretation of – 523
 - magnetic hyperfine interactions 523
 - quadrupole hyperfine interactions 523
 - quadrupole splitting (QS) 523
 - two lines of equal intensity 523
- [Fe]-SOD
 - IR and Raman of framework vibrations 56
- Fe-sodalite
 - ⁵⁷Fe hyperfine splitting 317
 - ENDOR 317
- Fe-ZSM-5
 - Fe(III) in tetrahedral environment 538
 - FePc complexes 417
- ferrierite (FER)
 - ¹²⁹Xe NMR spectroscopy on – 274
 - framework vibrations 55
 - OH stretching bands 91
- ferrisilicalite
 - ESR spectrum 317
- [Fe]ZSM-5
 - framework vibrations 63
 - UV Raman laser spectroscopy 63
- field strength parameter, D_q 348
- field-induced fundamental stretching band
 - adsorption sites 107
 - field strength 107
 - of N₂ adsorbed on Na-A 107
- fine structure tensor D 300
- FIR spectrum of Ba-ZSM-5
 - calculated and experimental 69
- FKS (Flanigen, Khatami, Szymanski) correlation 54
 - external modes 28
 - internal modes of the TO₄ tetrahedra 28
 - zeolite infrared assignments 28
- fluorescence 359
 - intensity 372
- fluorescence spectroscopy
 - excitation spectra 372
 - luminescence spectra 372
 - of AlPO₄-5 single crystals with dyes 418
 - spectrometer for – 372
- fluorescence technique
 - laser-induced 373
- fluorescent photons
 - measure of the absorption 433
- fluoro- and chlorobenzene
 - as a probe for acid strength 147
- focusing effect 438
 - amplitude 438
 - curved-wave theory 438
 - phase-shift functions 438
- forbidden ground state S₀ and return to S₀
 - by consecutive intersystem crossing (ISC) 342
 - by fluorescence 342
 - by non-radiative transitions 342
 - by phosphorescence 342
- forbidden transition 342
- force constants
 - harmonic 14
 - related to eigenvalue problem 14
- force field parameters
 - as a function of dehydration degree 27
 - by ab initio methods 25

- force field parameters
 - derived and treated as a “test particle setup” 27
 - for aluminosilicates 24
 - for OH groups in zeolites 24
 - for siliceous zeolites 24
- force field studies
 - mimic zeolite frameworks in – 26
- formation of a Cu(II)(O_i)₃ complex 392
 - kinetics of silver-cluster formation in AgX 409
 - of coadsorbed J₂ and methylacetylene in HZSM-5 407
 - of iodine in HZSM-5 407
 - of methylacetylene in HZSM-5 407
 - of silver mordenite 409
- formation of a donor-acceptor complex
 - electron affinity of the acceptor 356
 - ionization potential of the donor 356
- Fourier transform (FT) NMR spectroscopy
 - principle 208
- Fourier transform spectrometers
 - advantages 40
 - Connes’ advantage 41
 - Fellgett’s advantage 40
 - Jacquinet’s advantage 40
 - scheme of the principal design 41
- Fourier transformation
 - common absorption spectrum 208
 - of free induction decay (FID) 208
- framework aluminum atoms
 - interacting with probe molecules 229
- framework bands
 - red-shifts (increase of lattice parameters) 31
- framework defects
 - of ZSM-5 268
- framework modes
 - approximate classification of – 31
 - in Raman spectra 68
 - IR-bands of pure zeolite powders 49
 - of A-type zeolites 31, 60
- framework n_{Si}/n_{Al} ratio
 - from ²⁹Si MAS NMR intensities 216
- framework protonation
 - ²⁷Al quadrupole coupling constant 228
- framework spectra
 - dealumination of Beta 55
 - dealumination of zeolite L 55
 - of zeolite K-L 55
 - water absorbed on K-L 55
 - zeolite Beta 55
- framework Ti species 385
- framework vibrations
 - adsorption and desorption of water 58
 - adsorption of hydrohalocarbons 58
 - asymmetric stretching modes 50
 - band assignments 50
 - bending modes 50
 - content of extra-framework Al 54
 - correlations with n_{Si}/n_{Al} ratios 50
 - coupling of the cation motions to – 66
 - crystallinity 54
 - decoupling of modes 15
 - effects by adsorption 51
 - effects by cation loading 51
 - effects by crystallinity 51
 - effects by dealumination 51
 - effect of adsorption 58
 - effect of ammoniation of H-Y 72
 - effect of cation-loading 57
 - effect of dealumination 58
 - effect of dehydration of Ni-Y 72
 - effect of exchange 72
 - effect of isomorphous substitution 61
 - effect of n_{Si}/n_{Al} ratio 58
 - effect of protonation 72
 - in faujasites 50, 57, 58
 - influence of cations 58
 - INS and NIR-FT Raman 58
 - internal and external lattice vibration modes 50
 - isolated model cluster 15
 - isotope substitution techniques 66
 - mole fraction of Al in tetrahedral sites 52
 - of Dallas amorphous material-1, DAM-1 57
 - of faujasite-type Na-X 52
 - of gismondine P1 (GIS) 50
 - of H-Beta dealuminated by acid leaching 61
 - of L (LTL) 50
 - of MAPO-39 57
 - of mordenite (MOR) 50
 - of natural clinoptilolite 54
 - of offretite 61
 - of partially amorphitized H-Y 54
 - of SAPO-39 57
 - of zeolite A (LTA) 50, 57
 - of zeolite Beta 61
 - of zeolite gismondine, P1 50
 - of zeolite Omega (MAZ) 50, 61
 - symmetric stretching modes 50
 - terminology 50
- frameworks
 - of crystalline microporous GeO₂ 57
- frameworks containing 3-membered rings
 - ²⁹Si MAS NMR spectroscopy 57
 - Raman spectroscopy 57

- Franck-Condon principle 343, 345
 free electron molecular orbital model
 – electron from HOMO into LUMO 348
 free induction decay (FID)
 – after application of $\pi/2$ -pulse 208
 – after application of radio frequency (rf) pulses 208
 – after single-pulse (SP) excitation 208
 – characteristic time constant 208
 – transverse relaxation time, T_2 208
 frequency of microwave used in ESR 300
 frontier orbitals (HOMO) 348
 FT-Raman spectroscopy
 – of framework vibrations 58
 FTIR emission spectroscopy (FT-IRES) 44
 FTIR spectroscopy (for mid infrared) (cf. IR)
 – characterization and synthesis of ETS-10 158
 – crystallinity of Na-X and Na-X films 158
 – formation of acetaldehyde 162
 – monitoring the dealumination of H, Na-Y 81
 – of Brønsted and Lewis acidity 140
 – of diffusion 165
 – of *p*-xylene sorption into silicalite-1 167
 – of platinum carbonyl clusters (Chini clusters) 118
 – of [Si, Fe]BEA 63
 – of [Si, V]MFI (VS-1) 63
 – time-resolved in polarized IR radiation 167
 – uptake of hydrogen cyanide into alumina-pillared clays 168
 – uptake of hydrogen cyanide into zeolites 168
 – with pyridine and CO as probes 140
 FTIR/INS investigation of H-Y
 – assignment of framework vibrations 53
 fundamental vibrations
 – of bent triatomic molecules SO₂, H₂S, H₂O 124
 – of CO₂ 121
 – of CO₂ and N₂O in Na₄Ca₄-A 120
 – of nitrous oxide, N₂O 119
 fundamentals of Raman spectroscopy
 –, references of 47
- G**
- G-matrix 14
g-tensor 298
⁶⁹Ga and ⁷¹Ga isotopes
 – natural abundances 235
 – quadrupole moments 235
- ⁷¹Ga and ²⁷Al chemical shifts
 – linear relationship between – 235
⁷¹Ga MAS NMR spectroscopy
 – penta-coordinated Ga atoms 237
 – effect of dehydration 236
 – line shape 237
 – of MFI-gallosilicate 236
 – of as-synthesized cloverite 236
 – quadrupole coupling constant of Ga atoms 237
 – tetrahedrally coordinated Ga 236
 gallium-modified ZSM-5 (Ga-MFI) 217
 gallophosphate cloverite
 – ³¹P MAS NMR spectrum 233
 gallosilicate sodalite Na_{7,9}[Ga_{5,9}Si_{6,1}O₂₄]Cl₂
 – data analysis procedure 444, 445
 – EXAFS of the GaK edge 443
 – gallium coordination environment of – 443
 – non-stoichiometry of – 443
 – XANES spectra of – 443
 – X-ray absorption spectra 444, 445
 – ZnGa₂O₄, as a standard 444
 GF matrix method
 – computation of vibrational frequencies 13
 graphite-like chains
 – conductivity 407
 ground state
 – greatest multiplicity 350
 – lowest in energy 350
 – term with the greatest L value 350
 group frequencies 35
 gundiode 300
- H**
- ¹H dipolar-dephasing spin-echo MAS NMR
 – zeolite H-Beta 267
 – zeolite HZSM-5 267
¹H MAS NMR investigations
 – Brønsted acid sites 253
 – dehydrated zeolites 253
 – surface hydroxyl groups in zeolites 253
¹H MAS NMR shifts of
 – AlOH, (at non-framework aluminum) 261
 – MeOH, (in large cavities) 261
 – MeOH, (in sodalite cages) 261
 – SiOH, (at the outer surface) 261
¹H MAS NMR shifts of
 – SiOHAl, (bridging OH groups in HZSM-5, H-Beta, and H-MCM-22) 261
 – SiOHAl, (electrostatic interactions) 261
 – SiOHAl, SiO1HAL (in large cages) 261
 – SiOHAl, SiO3HAL (in small cages) 261

- ¹H MAS NMR spectra
 - application of CRAMPS 253
 - assignment 257
 - decomposition 254, 255
 - motional narrowing of hydroxyl protons 265
- ¹H MAS NMR spectra of
 - calcined zeolites HNaY 255
 - dealuminated zeolite HY 260
 - dehydrated aluminosilicates 267
 - dehydrated silicoaluminophosphates 267
 - dehydrated zeolite HNaY 254, 270
 - dehydrated zeolites 253
 - dehydrated zeolites HY 257
 - hydroxyl protons (calculated) 266
 - HZSM-5 257, 259, 270
 - zeolites MgNaY 259, 260
 - zeolite CaNaY 259, 260
 - zeolite HY (reammoniated) 271
 - zeolite LaNaY 260
 - zeolite loaded with perdeuterated pyridine 270
- ¹H MAS NMR spectroscopy of
 - activated zeolite HZSM-5 258
 - ammonium ions 269
 - dehydrated SAPO-5 (two-dimensional) 264
 - dehydroxylated bridging OH groups 261
 - formation of MeOH and bridging OH groups 259
 - Hirschler-Plank mechanism 259
 - physisorbed ammonia molecules 269
 - probes for acidity 269
 - realuminated zeolite HNaY 262
 - rehydroxylated zeolite HNaY 262
 - silicoaluminophosphate SAPO-5 268
- ¹H NEOSY MAS NMR
 - chemical shifts of bridging OH groups 268
 - chemical shifts of SiOH groups 268
 - of dehydrated SAPO-5 268
 - of dehydrated zeolite HZSM-5 268
- ¹H NMR chemical shift
 - affected by electrostatic interaction 257
 - correlated with S^m 257
 - in dehydrated zeolites 261
 - influenced by hydrogen bond 257
 - of dealuminated HY 261
 - of free bridging OH groups 256
 - of free surface hydroxyl groups 257
 - of H-mordenite 261
 - of hydroxyl protons 261
 - of HZSM-5 261
 - of non-acidic MeOH 261
 - related to deprotonation energy 257
 - related to mean Sanderson electro-negativity 256
 - related to strength of gas-phase acidity 257
 - related to the O-O distance 260
- ¹H NMR spectroscopy
 - influence of magic angle spinning 210
 - of activated zeolite 30HNaY 210
 - of H-mordenite 262
 - of HNaY 262
 - of HZSM-5 262
- ²H NMR spectroscopy
 - OD groups in zeolites 259
- H₂ as a probe
 - for mesoporous materials 138
 - for Na-ZSM-5, Na-MOR, Na-X, Na-A 138
- H-Al distance of bridging OH groups
 - by neutron diffraction analysis 263
 - by spinning sideband analysis 263
 - depending on size of oxygen rings 263
 - effect of carbon monoxide adsorption 263
- ¹H-²⁷Al CP/MAS NMR spectra
 - of dealuminated zeolites 225
 - of increasingly dealuminated HY 226
 - of non-framework aluminum 225
- ¹H-¹³C CP/MAS NMR spectra
 - comparison of Bloch decay spectra 281
 - of reactant molecules in zeolite 281
- H-Y zeolite
 - combined FTIR and INS study of - 81
 - effects of dealumination 81
 - vibrational properties of - 81
- H,Ga-ZSM-5 217
 - ²⁹Si MAS NMR spectra of - 217
- Hahn's echo 214
- halogenated light paraffins
 - as probes for basic sites 147
- harmonic approximation 15
- harmonic force constants 14
- Hartmann-Hahn condition 212, 225
- heterogeneously catalyzed reactions
 - by MAS NMR 280
 - under continuous-flow conditions 280
- heulandite (HEU)
 - micro-infrared spectroscopy of - 87
- HF-OH band of
 - H,Mg-Y 83
 - H,Na-Y 83
- high resolution ESR spectra of Cu²⁺
 - ESR parameters 311
 - in dehydrated zeolites 311, 312
 - in zeolite A 312
 - in zeolite mordenite 312

- in zeolite X 312
- in zeolite ZSM-5 312
- simulation 311
- highly dispersed materials
 - in the porous structure of zeolites 408
- Hilisch-Pohl formula 359
- Hirschler-Plank mechanism 82, 84
 - reversibility 259
- H₂O adsorption
 - co-adsorption of H₂O and *n*-hexane 127
 - on M-ZSM-5 (M=Li, Na, K, Rb, Cs) 127
 - on mordenite 128
- H₂O/zeolite spectrum
 - inelastic neutron scattering (INS) 128
 - interpretation 128
- HOMO→LUMO transition
 - frequency of 348
- homonuclear linewidth
 - calculated from M_2^{II} 209
- Hund's rule 347
- hybrid organic-inorganic catalysts 418
- hybrid organic-inorganic ligands 418
- hydrazonium mordenite 87
- hydride ion abstraction
 - Lewis acid sites 401
- hydrodesulphurization catalyst
 - characterized by Mössbauer spectroscopy 539
- hydrogen
 - adsorption 106
- hydrogen and deuterium spillover
 - on Pt-loaded Na-Y vs. Na-Y 168
- hydrogen form of zeolite A
 - instability 85
- hydrogen forms of zeolites
 - hydroxy stretching frequencies 96
 - assignments 96
- hydrogen mordenites
 - Brønsted and Lewis acidity 140
- hydrogen offretite
 - adsorption of ammonia 89
 - adsorption of pyridine 89
 - infrared bands of OH groups 89
- hydrogen sulfide
 - adsorbed on zeolites
 - adsorption into Na,Ca-A 125
 - as a probe for basic sites 147
 - dissociative adsorption 125
 - IR spectrum of - 125
 - non-dissociative adsorption 125
 - on faujasite-type zeolites 125
 - on H-Y 125
 - on H-ZSM-5 125
 - on Na-A 125
 - on Na-ZSM-5 125
- hydroxonium ion in zeolites
 - as a transition structure 128
 - stabilized by a second H₂O molecule 129
- hydroxy groups of zeolites
 - accessibility/inaccessibility 79
 - acidity/non-acidity 79
 - assignments of IR bands 80, 96
 - attached to extra-framework Al species 79
 - characterized by IR stretching bands 73
 - defection by ¹H MAS NMR 254
 - formation of - 254
 - in hydrogen forms of various zeolites 96
 - interpretation of IR bands 80
- hydroxy nests 78
 - IR bands around 960 cm⁻¹ 61
- hydroxyl protons in H-zeolites
 - mobility of - 264
- hydroxylammonium mordenite 87
- hyperfine interaction
 - Hamiltonian \bar{H}_{HF} 298
 - hyperfine coupling tensor 298
- hyperfine splitting constant
 - from ENDOR spectrum 309
- hypsochromic groups 346
- HZSM-5
 - additional electrostatic interaction of OH 258
 - chemical shifts 258
 - 2D ¹H NOESY MAS NMR spectrum 269
 - diffuse reflectance IR spectrum of 257
 - ¹H MAAS NMR spectra of - 257
 - hydrothermally dealuminated 80
 - internal silanols 258
 - interpretation of OH bands 80
- I**
- imperfections
 - due to dopants 358
 - due to extrinsic point defects 358
 - due to intrinsic point defects 358
- in situ ¹³C MAS NMR spectroscopy
 - of ¹³C-enriched formic acid 284
 - of ¹³C-enriched methanol 284
 - of LaNaY under flow of ¹³C-enriched propan-2-ol 285
 - under continuous-flow conditions 283
- in-situ MAS NMR investigations
 - investigation of reaction mechanisms 283
 - MTG reaction (methanol-to-gasoline) 283
 - of molecules adsorbed on zeolites 281

- in-situ MAS NMR investigations
 - of chemical reactions catalyzed by zeolites 279
 - under continuous-flow conditions 280
- in-situ MAS rotor 281
- INADEQUATE experiment
 - three-dimensional connectivities in zeolites 221
 - - in ZSM-5, ZSM-12, ZSM-22, ZSM-23, ZSM-39, DD3R 221
- INADEQUATE pulse sequence
 - advantages 223
- inelastic neutron scattering spectroscopy (INS)
 - coherent scattering 47
 - HF OH band 77
 - information about vibrational modes 47
 - incoherent scattering 47
 - LF OH band 77
 - nuclear motion 47
- information about the guest in zeolites by UV-VIS
 - charge-transfer transitions 339
 - chromophores 339
 - transitions between electronic levels 339
 - transitions within d orbital manifold 339
- information about the zeolite host
 - band gap from transitions top of valence band/bottom of conduction band 339
 - charge transfer (CT) processes 339
 - defects like electron-hole pairs 339
 - electronic transitions within d orbitals 339
- infrared flow-reactor cell
 - for in-situ measurements 42
- infrared micro-spectroscopy
 - adsorption into $\text{AlPO}_4\text{-5}$ -derived materials 155
 - decomposition of template 155
 - molecules in single crystals 155
 - nitroaniline and similar compounds in large single crystals of ZSM-5 155
 - *p*-xylene or *p*-nitroaniline in single crystals of
 - - silicalite-1 155
 - - $\text{AlPO}_4\text{-5}$ 155
 - - SAPO-5 155
 - single crystals of cloverite (adsorptive behavior) 155
 - using polarized infrared radiation 155
- infrared spectra in OH stretching region of Y-type
 - after dealumination 78
- infrared spectra of
 - deuterium adsorbed on A-type zeolites 107
 - methane adsorbed on Na-A 123
 - nitrogen adsorbed on A-type zeolites 107
 - oxygen adsorbed on A-type zeolites 107
- infrared spectra of ^{16}O -Na-Y zeolite
 - observed and calculated 30
- infrared spectra of water adsorbed on H-ZSM-5 127
- infrared spectroscopic techniques
 - a comparison of - 44
 - advantages 44
 - disadvantages 44
- infrared spectrum of CO
 - adsorbed on Na-A 114
 - satellites 114
- inhomogeneous ESR line broadening
 - dipolar interactions 307
- INS (inelastic neutron scattering spectroscopy)
 - adsorption of chloroform 58
 - advantages 48
 - at low wavenumbers 48
 - complication by overtone and combination bands 48
 - framework vibrations 58
 - hydrogen selection rule 48
 - information about the interactions via hydrogen atoms 104
 - information about vibrational modes 47
 - investigation of adsorbed and intercalated species 48
 - no selection rules 48
 - of adsorbed pyrrole 105
 - of benzene 104
 - of Brønsted acid sites in zeolites 102
 - of bulk pyrrole 105
 - of furan 104
 - of H-Y 103
 - of H-ZSM-5 103
 - of hydrocarbons 104
 - of hydrogen-containing molecules adsorbed 104
 - of methanol 104
 - of pyrrole 104
 - of water 104
 - peak assignment 105
 - proton incoherent cross-section 48
 - sensitivity to hydrogen displacements 102
- insertion of chromium 385
- in-situ DRIFT spectroscopy
 - activation of zeolite catalysts 159

- cyclodimerization of 1,3-butadiene 162
- olefin reactions 159
- in-situ IR and Raman spectroscopy
 - catalysis 156
 - diffusion 156
- in-situ IR spectroscopy
 - 1-hexene isomerization 158
 - activation process of zeolite catalysts 158
 - adsorption of NO into Cu⁺-containing zeolites 164
 - aldol condensation of *n*-butyraldehyde 162
 - alkylation of benzene with methanol 160
 - alkylation of the toluene ring by methanol 160
 - base-catalyzed reactions over zeolites 162
 - coke 162
 - coke formation 162
 - cumene cracking on H-Y 158
 - decomposition ethanethiol and diethyl sulfide 164
 - - over H and alkali forms of X, Y, and ZSM-5 164
 - decomposition of methanol over basic zeolites 161
 - decomposition of sodium azide 164
 - deposition of coke 162
 - ethylbenzene disproportionation 159
 - formation of carbonyls and nitrosyls 164
 - generation of CdS clusters 165
 - hydrosulfurization of the C=C double bond
 - over H- or metal-exchanged zeolites A, X, Y, MOR and clinoptilolite 164
 - isomerization of *p*-ethyltoluene 161
 - of LaCl₃/NH₄-Y
 - olefin adsorption and reaction 158
 - after heat-treatment 159
 - ethylbenzene conversion over - 159
 - rehydroxylation of - 159
 - oxidation of H₂S 159
 - reaction of 1- and 2-methylnaphthalene 162
 - reaction of cyclohexene over dealuminated H-Y 161
 - reaction of methanol and CO 161
 - reaction of olefins on zeolites 162
 - reaction with methoxy groups 160
 - side-chain alkylation of alkylbenzenes 161
 - sorption and diffusion 161
 - synthesis of alkylamines 160
 - xylene isomerization 161
- in-situ IR and multinuclear NMR spectroscopy
 - decomposition of chlorofluorocarbons 163
- in-situ micro-FTIR spectroscopy
 - of hydrogen and deuterium spillover 168
- integral absorbance
 - measure of the concentration of the absorbing species 37
- integral absorption
 - UV-VIS spectrum 340
- intensities of d-d bands
 - parity multiplicity selection rules 355
- intensity distributions
 - of vibrational progressions 344
- intensity of UV-VIS bands
 - extinction coefficient ϵ 362
 - upon adsorption 362
- interaction moment of the nucleus/magnetic field \vec{B}
 - additional Hamiltonian 300
 - importance in ENDOR 300
- interaction of CH₄ with the adsorption center
 - field strength 122
 - induced dipole moment 122
- interaction of electrons with the electric field
 - crystal field 300
 - ligand field 300
 - line splitting in ESR (Hamiltonian \bar{H}_{FS}) 300
 - of surrounding atoms 300
- interaction of probes with zeolites
 - formation of hydrogen bonding 130
- interaction of pyridine
 - with SiOH groups in HZSM-5 269
 - with SiOHAl groups 269
- interferogram 40
- interferometry
 - Fellgett advantage 365
 - Jacquinot advantage 365
 - the superiority of - 365
- intermediates
 - carbanions as - 405
- internal coordinates
 - transformatio of - 14
- internal valence force field (IVFF)
 - attempts of parameter reduction 17
 - general problem of missing experimental data 17
- internal vibrations
 - structure-insensitive 28

- inter-tetrahedral vibration modes
 - double six-membered rings 50
 - structure sensitive 51
 - vibrations of double four-membered rings 50
- intra- and extra-zeolite locations
 - discrimination by XPS/XAES 502
- intra-framework Fe
 - binding energy of - 506
 - XPS of - 506
- intra-tetrahedral vibration modes
 - asymmetric stretching modes 50
 - bending modes 50
 - structure-insensitivity 50
 - symmetric stretching modes 50
- intra-zeolite gallium
 - binding energy of - 506
 - XPS of - 506
- intra-zeolite location
 - sensitivity of XPS satellite structure 501
- intra-zeolite location of an element
 - XPS satellite structure 500
- intrazeolite transition-metal ion complexes
 - one-electron energy levels and site symmetry 379
 - ligand field model for (C_{3v}) - 379
- inverse eigenvalue problem
 - input and output for solving the - 14
- investigation of the acid properties
 - of MeAPOs, ($Me^{2+}=Mg^{2+}, Mn^{2+}, Co^{2+}, Zn^{2+}$) 138
 - via FTIR spectroscopy 138
 - via microcalorimetry 138
- iodine
 - CT complex with framework oxygen 396
- ionic cluster
 - electron transfer 328
 - ESR aspects of - 323
 - formation of - 328
- IR band around 960 m^{-1} 61
 - detection by ^1H MAS NMR 254
 - formation of - 254
 - in hydrogen forms of various zeolites 96
- IR bands
 - of N_2 and CO 112
 - of pyridine adsorbed on B-sites, "true" L-sites and cations in 132
 - , - hydrogen faujasite type zeolite H-Y (H-FAU) 132
 - , - hydrogen mordenite (H-MOR) 132
 - , - on Na_4Ca_4 -A zeolite 112
 - , - sodium mordenite (Na-MOR) 132
- IR data of methanol adsorption on zeolites
 - quantum chemical model 152
- IR experiments at low temperatures 106
- IR extinction coefficients
 - experimentally derived 38
 - of surface species of zeolites and adsorbates 38
- IR framework spectra
 - linear relationship wavenumbers/Al content 55
 - , - of La, Na-Y zeolites 53
 - , - of RE-Y (where RE=La, Nd, Sm, Gd, Dy) 53
 - , - offretite 55
 - , - of erionite 55
- IR investigations
 - of adsorbed SO_2 , H_2S and H_2O 124
 - of hydrogen sulfide (H_2S) adsorbed on zeolite NaX 397
 - of surface acidity of zeolites 131
 - of the modified Claus process 397
 - probe molecule pyridine 131
 - typical bands of adsorbed pyridine 131
- IR microscopy 41
- IR results of the H_2O /zeolite system 128
- IR spectrometers
 - dispersive instruments 40
 - non-dispersive (Fourier transform) instruments 40
- IR spectroscopic features of isoelectronic molecules
 - CO_2 and N_2O 112
 - calculated and measured frequency shifts 112
 - field strengths calculated from intensity 112
 - N_2 and CO 112
- IR spectroscopic investigations
 - of steamed and leached faujasite-type zeolites 60
 - of the hydrothermal stability 60
 - of Y-type zeolite 60
 - synthesis of ZSM-5 type zeolites 157
- IR spectroscopic/gas chromatographic experiments
 - alkylation of the toluene ring by methanol 160
- IR spectroscopy
 - adsorption of ammonia 48
 - catalyst deactivation 49
 - CO adsorbed on Y-type zeolites 111
 - CO adsorbed on zeolite
 - , - A 111
 - , - Ca-A 111
 - , - Ca-X 111
 - , - Na-A 111
 - , - Na-X 111
 - CO adsorbed on autoreduced Ru, Na-Y 117

- CO and N₂ in zeolite Na₄Ca₄-A 113
- , - calculated adsorbate geometries 113
- CO/Na,Ca-A 114
- , - explained by hindered rotation 114
- combined with electron spin resonance spectroscopy 49
- combined with temperature-programmed desorption 49
- combined with UV-Vis spectroscopy 49
- comparison experimental/calculated spectroscopic data 106
- decomposition of oligomers 163
- diffusion 49
- discrimination of Brønsted and Lewis sites 48
- electric field inside the zeolite voids 106
- ethylene adsorption 48
- formation of OH groups 48
- H₂/D₂ exchange in La-X, La-Y and calcined H-Y 158
- heterogeneous catalysis 49
- in-situ investigations 49
- identification of framework vibrations 49
- mobility and energy barriers 106
- of amorphous silica-alumina 49
- of decomposition of organic cations in OFF and ZSM-34 157
- of extra-framework species 49
- of homonuclear diatomic molecules 106
- of hydroxy groups 49
- of solid-state ion exchange 49
- , - kinetics of solid-state ion exchange 168
- of the framework of MCM-22 56
- of the framework of ZSM-5 56
- of the framework of ZSM 11 56
- of the framework of ZSM-35 56
- of the framework of ZSM-57 56
- of zeolites synthesis 49
- OH groups of H, Na-Y 141
- , - after adsorption of increasing amounts of CO 141
- pyridine adsorption 48
- requirement changes in the dipole moment 46
- time-resolved 168
- transformation to crystalline particles of MEL 157
- zeolites, qualitative interpretation 35
- IR spectroscopy coupled with gas chromatography
- correlation activity/strength of Brønsted acid sites 161
- IR vibration spectra
- band assignment 54
- of completely siliceous zeolite A 54
- of sodalite 54
- IR-experiments
- combined with other experimental techniques 42
- powder embedded in pressed KBr or CsI 42
- pressed powder 42
- single crystals 42
- wafers 42
- IR-spectroscopy of
- hydrodesulfurization reaction of thiophene 165
- , - over H-, Ni- and Co-exchanged Y, MOR and ZSM-5 165
- IR/pyridine technique
- extinction coefficient 92
- IR/TPD measurements
- acid strength hydroxy groups in H-Y 77
- isobutane dehydrogenation
- catalyst characterization by Mössbauer spectroscopy 539
- isomorphous substitution
- by germanium to H,Na-[Ge]X 78
- mesoporous materials 64
- of Si by introduction of Al, B, Ti, V, Ga, Fe and V 61, 82
- with iron to [Si,Fe]MFI 62
- with titanium to [Si,Ti]BEA 62
- with titanium to [Si,Ti]MFI (TS-1) 62
- with titanium to [Si,Ti]MFE (TS-2) 62
- with titanium to [Si,Ti]NCL-1 62
- with vanadium to [Si,V]MFI 62
- isomorphously substituted tetrahedral cobalt
- Jahn-Teller distortion of - 383
- spectra in the NIR region 383
- spectra in the visible region 383
- isotope ¹³³Cs in MAS NMR 240
- isotope exchange
- effect on framework vibrations 31
- isotropic chemical shift in MAS NMR 204, 248
- J**
- J-coupling
- direct bond couplings 221
- estimated for correct pulse delays 224
- Jahn-Teller distortion 380, 390
- Jahn-Teller distortion
- for excited states 355
- Jahn-Teller theorem
- energy separations ground level higher levels 354
- K**
- kanemite
- infrared and Raman spectroscopy of - 57

- kaolinite
 - binding energy of Al 2p 486
 - binding energy of Si 2p 486
- Kasha rule
 - fluorescence 372
 - phosphorescence 372
- KBr-technique
 - $n_{\text{Si}}/n_{\text{Al}}$ ratio of the zeolite framework 49
 - identification of framework vibrations 49
- kinetic energies
 - in terms of internal coordinates 13
- kinetic energy distribution (KED) of
 - aluminium atoms 32
 - oxygen atoms 32
 - silicon atoms 32
 - sodium atoms 32
 - sodium ions 31
- kinetic energy of electrons
 - bonding energy of the initial state E_0 434
 - energy E of the incoming X-ray beam 434
- kinetics of solid-state ion exchange in zeolites
 - monitored by time-resolved FTIR 168
- klystron 300
- L**
- L-matrix 14
- labeling the states of an electronic transition
 - spectral term symbols 351
- Lambert-Beer-Bouguer law 36
- LaNaY
 - ^{23}Na MAS NMR of – 244
- Laporte rule 342
- Laporte selection rule 349
- Larmor frequency 204
- lattice vibrational frequencies of Na-X zeolite
 - approximate assignments 53
- Lewis acid (L) sites 75
 - in H-mordenite 331
 - in H-Y zeolites 331
 - in H-ZSM-5 331
 - studied by XPS and probes 495
- LF OH-band in IR
 - decomposition of – 77
- ligand field
 - non-framework cations 378
- ligand field model (C_{3v})
 - intrazeolite transition-metal ion complexes 379
- ligand field stabilization energies 382
 - from transitions in UV-VIS 380
 - of transition metal ions in zeolites 380
- ligand field stabilization energy (LFSE)
 - Coulomb repulsion energy difference e_g-t_g (Δ_o) 350
- line-broadening in NMR
 - role of the external magnetic field 211
- line broadening interactions
 - application of special multiple-pulse sequences 208
- line broadening of ^{13}C NMR signals 281
- line narrowing techniques 208
- line shape function
 - of central transition of a quadrupole nucleus 211
- line shape function in NMR
 - asymmetry parameter, η_{CSA} 206
 - chemical shift anisotropy, $\Delta\sigma$ 206
 - internuclear distance 206
- line shapes
 - Gaussian 19
 - Lorentzian 19
- linear absorption coefficient in X-ray absorption 432
- linear triatomic molecules (N_2O , CO_2)
 - relationship band shape/respective band shifts 126
- local geometry of crystallographically inequivalent T-sites
 - high-silica zeolites consisting of Si(0Al) units 219
- local magnetic fields
 - additional interactions 298
 - originating from non-zero nuclear spins 298
- location of benzene molecules
 - in Cs-exchanged EMT zeolite 146
- location of hydroxy groups
 - studied by probe molecules 269
- lovdarite
 - ^{29}Si MAS NMR spectroscopy 57
 - Raman spectroscopy 57
- low-frequency electronic transitions 339
- low-frequency Raman spectroscopy
 - of M-FAU ($\text{M}=\text{NH}_4, \text{Li}, \text{Na}, \text{K}, \text{Rb}, \text{Cs}, \text{Tl}$) 70
 - of M-PMT 70
- lowest unoccupied molecular orbital (LUMO) 348
- LTA**
 - IR and Raman spectroscopy of framework vibrations 56
- luminescence experiments
 - lasers as the excitation source 373
 - lifetime measurement 373

- non-framework cations 374
- photocatalytic decomposition 392
- resonance energy transfer 392
- siting 392
- luminescence in solids 359
- luminescence spectrometer
 - excitation spectra 372
 - fluorescence spectra 372
 - phosphorescence spectra 372
- luminescence spectroscopy
 - applied to first-row transition metal and RE ions 372
 - study of exchangeable cations 372
 - study of isomorphously substituted framework 372
 - sensitivity 372
- luminophores 374
- lutidine
 - differentiation internal/external acid sites 134
- M**
- M(OH) or M(OH)₂ complexes
- M-matrix (and its inverse) 14
 - frequencies related to - 84
- magic angle spinning (MAS) technique
 - based on rapid rotation of the sample 209
 - magic angle $\theta_m=54.74^\circ$ 209
 - spinning sidebands 209
- magnetic and electric field patterns in ESR cavity 302
- magnetic field scan range (in ESR) 303
- magnetic field, B_0
 - first derivative ESR spectrum 303
 - modulation 303
- magnetic interactions of transition metal ions
 - with surrounding nuclei (H, D and Al) 316
- magnetogyric ratio of the non-resonating S-spins 205
- MAPO-5
 - IR investigation of pyrrole adsorption 149
 - weak basic sites 149
- MAPO-11 (M=Mg)
 - mainly acid property of - 149
- MAPO-36
 - IR investigation of pyrrole adsorption 149
 - weak basic sites 149
- MAPO-39
 - framework vibrations 57
 - FTIR transmission spectroscopy 95
- OH stretching region 95
- MAS NMR intensity
 - central transition 251
 - spinning sidebands 251
- maximum magnetic flux density of NMR spectrometers 211
- maximum resolution 212
- MCM-22 (MWW)
 - framework vibrations 56
- MCM-41
 - [Al,Si]MCM-41 64
 - diffuse UV-VIS reflectance spectra 373
 - IR spectroscopic investigations 64
 - mononuclear vanadium(V) oxide in - 414
 - oligomeric clusters of vanadium oxide in - 414
 - [Si]MCM-41 64
 - [Si,Ti]MCM-41 64
 - [Si,V]MCM-41 64
 - Ti-containing - 64
- MCM-48
 - XANES (SiK edge) spectra 458
- mean free path of electrons in condensed matter 436
- MeAPO-5 ($Me^{2+}=Be^{2+}, Mg^{2+}, Ti^{2+}, Fe^{2+}, Co^{2+}$)
 - acidity of - 138
- MeAPO-31
 - acidity of - 139
- MeAPO₄-34 (Me=Zn, Fe)
 - acidity of - 139
- MeAPOs ($Me^{2+}=Mg^{2+}, Mn^{2+}, Co^{2+}, Zn^{2+}$)
 - acidity of - 138
- measure of acidity strength
 - shift, Δv (OH), upon CO adsorption 141
- measure of the basicity strength
 - pyrrole adsorption 148
- mechanisms of luminescence in solids 360
- mesoporous material MCM-41 hosting Ti-oxide
 - as sensitizing dye zinc phthalocyanine 420
 - dispersion and coordination of TiO_x 420
 - photovoltaic devices 420
 - UV/VIS spectra 420
- mesoporous materials
 - extinction coefficients 101
 - hydroxy groups of - 101
 - Mössbauer spectroscopy 541
 - [Si,Ti]MCM-48 64
 - [Ti]MMM-1 64
 - UV Raman laser spectroscopy 64

- mesoporous MCM-41
 - loaded with Cu^{2+} complexes 316
 - , - studied by ESEEM 316
 - , - studied by ESR 316
- mesoporous structures (MCM-41)
 - destruction of - 43
 - DRIFT spectra of - 43
 - under pressure 43
- metal carbonyls ($\text{Fe}(\text{CO})_5$, $\text{Mo}(\text{CO})_6$, $\text{Re}_2(\text{CO})_{10}$, $\text{Ru}_3(\text{CO})_{12}$)
 - IR spectroscopy 116
 - progressive decomposition 116
- metal clusters in zeolites
 - Fourier transform far-infrared spectroscopy of - 119
- metal particles
 - ESR aspects of - 323
 - isotropic conduction electron spin resonance line 326
- metal sulfide clusters in zeolites
 - doped with Fe or Co atoms 452
- metallation of grafted ligands 418
- methane
 - adsorbed in purely siliceous zeolite A 123
 - adsorbed in silicalite-1 123
- methanol
 - absorbed on H-ZSM-5 151
 - absorbed on hydrogen erionite (H-ERI) 151
 - alkylating agent 150
 - bound to the cations 151
 - methylation of toluene 150
 - strongly interacting with acid OH groups 151
- methanol adsorption
 - methoxonium ion 129
- methanol-to-gasoline (MTG process)
 - activation of CH_3OH on acid zeolite 150
- methanol-to-olefins (MTO process)
 - activation of CH_3OH on acid zeolite 150
- methoxonium ion
 - quantum chemical calculations 150
- methoxy and ethoxy groups on Na,H-X and Na,H-Y
 - studied by IR spectroscopy 152
- methoxy groups
 - discriminated by their IR bands 152
 - formation and reactivity of methoxy groups 151
 - on H-ZSM-5
 - three types of - 152
- MFI structure (cf. ZSM-5, zeolite ZSM-5)
 - chromium incorporation 63
 - framework vibrations 56
 - incorporation of zinc into - 95
 - IR investigation of - 56
 - tantalum incorporation 63
- MFI-type ferrisilicalite
 - diffuse reflectance spectroscopy (DRS) 385
- MFI-type vanadium silicalites
 - diffuse reflectance spectroscopy (DRS) 385
- MgAPO-5
 - diffuse reflectance spectroscopy (DRS) 385
- MgVAPO-5
 - diffuse reflectance spectroscopy (DRS) 385
 - micro-infrared spectroscopy
 - of *p*-xylene diffusion into single crystals (silicalite-1, AlPO_4 -5) 166
- microwave bridge 300
- microwave frequency
 - tuning of - 303
- microwave power saturation 304
- migration of cations
 - effect on the ^{29}Si MAS NMR signals 220
- minimum residual line width in MAS NMR 212
- [Mn]VPI-5
 - Brønsted acidity of - 95
- MO diagram of octahedral complexes 355
- mobility of hydroxyl protons in zeolites
 - ^1H MAS NMR spectroscopy at elevated temperatures 264
- model of Si-OH formation
 - 2D ^1H NOESY MAS NMR spectrum 269
 - ^{29}Si CP/MAS NMR 269
 - FTIR 269
- model related to
 - eigenvalue problem 14
- modern UV-VIS-spectrometers 366
- modified COSY experiment
 - schematic representation of - 223
- modulation amplitude (in ESR) 303
- molecular dynamics (MD) simulations
 - Al-O-Si bending force constants 23
 - Al-O stretching force constants 23
 - angle bending terms 23
 - calculated structural parameters 24
 - calculated vibrational spectra 24
 - cation-oxygen interactions 23
 - comparison MD results with experimental spectra 22
 - empirical atom pair potential (central force field) 22
 - density of vibrational states 22

- force fields evaluated from NCA and MM studies for - 22
- framework-cation interactions 23
- of vibrational spectra of zeolites 24
- power spectrum 22
- Si-O-Si angle bending terms 23
- vibrational spectra 23
- with a simplified generalized valence force field (SGVFF) 23
- molecular orbital (MO) model
 - field splitting Δ 354
- π molecular orbitals of benzene (Hückel MOs) 399
- molecular sieve encaged dye molecules
 - aspirants for photochemical applications 419
 - photoinduced *trans*-to-*cis* isomerization 419
- molecular sieves
 - inelastic neutron scattering (INS) 12
 - infrared (IR) 12
- molecular wires for microelectronic applications 406
- molecular-dynamics study
 - of adsorbed methane, ethane, propane, ethane, ethyne 123
- molybdenum sulfide clusters in zeolitic hosts
 - EXAFS data analysis 452
 - preparation of - 452
- MoO₃ clusters
 - on the external surface of a zeolite 452
- mordenite (MOR)
 - band assignments 99
 - complete DRS spectrum 99
 - ¹²⁹Xe NMR spectroscopy on - 274
- mordenite, cesium-exchanged
 - solid-state ¹³³Cs NMR spectroscopy 241
- mordenite, dealuminated
 - XPS binding energies 492
- mordenites ion-exchanged with alkaline earth cations
 - wavenumbers and intensities of OH bands 83
- Mössbauer absorbance
 - spectra of ferrous-Y after adsorption of various gases 526
- Mössbauer data
 - ethylene molecule jumps 530
 - ferrous-ethylene complex 530
 - life-time of an ethylene-ferrous ion complex 530
 - uncomplexed ferrous cations 530
- Mössbauer effect
 - emission absorption of a γ -photon 517
 - , - without loss of energy from recoil 517
 - without thermal broadening effects 517
- Mössbauer elements
 - iron and tin nuclei (most frequently employed) 517
 - Sb, Te, J, Xe, Eu, Au, Np 517
- Mössbauer emission spectroscopy
 - 2,2'-bipyridine complex of Co²⁺(57) 534
- Mössbauer emission studies
 - ⁵⁷Co-zeolites 533
- Mössbauer emissions studies of Co²⁺
 - Co²⁺ coordination in zeolite A 534
 - Co²⁺ complex with ethanol 534
 - Co²⁺ complex with methanol 534
 - Co²⁺ complex with water 534
 - Co²⁺ siting in zeolite A 534
 - formation of H^{*} and OH^{*} radicals 534
- Mössbauer energy distribution
 - Lorentzian 519
- Mössbauer experiments
 - in the transmission mode 518
 - number of transitions *N(E)* 518
- Mössbauer line shape
 - Lorentzian 519
 - effect of the thickness 519
- Mössbauer line shift
 - second-order Doppler shift 522
- Mössbauer nucleus
 - mean life-time of excited state 518
 - tightly embedded in a solid lattice 518
- Mössbauer nucleus Fe(57)
 - half-life 518
 - Mössbauer radiation from Fe(57) 518
- Mössbauer parameters 530
 - absorption area 530
 - effect of adsorbed ethylene on - 530
 - introduction of Fe via solid-state ion exchange 533
 - isomer shift 530
 - of Fe-containing components in iron (Pc) complexes 540
 - of Fe(Pc) 540
 - of Fe(Pc)-Y 540
 - of Fe(Pc)/Py-Y 540
 - quadrupole splitting 530
- Mössbauer: recoil free fraction
 - temperature dependence of - 518
- Mössbauer spectra
 - of ZSM-5 type ferrisilicate 537
 - of (Fe²⁺, Na⁺) A-zeolite
 - , - after adsorption of water, ethanol, ethylene 528
 - , - after very mild dehydration 528
 - , - constant inner doublet upon dehydration 528

- Mössbauer spectra
- , - water ligands 528
 - dehydrated 527
 - Fe²⁺ coordination 527
 - Fe²⁺ siting 527
 - hydrated 527
- Mössbauer spectra of Fe(57)
- at temperatures lower than RT 528
 - demonstrating three hyperfine interactions 524
 - isomer shift 524
 - magnetic splitting 524
 - quadrupole splitting 524
- Mössbauer spectra of Fe²⁺-A
- increasing quantities of adsorbed ethylene 529
- Mössbauer spectroscopy
- absorber 519
 - application of Doppler energy 520
 - chemical isomer shift 521
 - cobalt clusters in zeolite cages 541
 - coordination 544
 - dealuminated Fe³⁺-containing zeolite Y 533
 - decay process after resonant excitation of Fe(57) 535
 - decay scheme of Co(57) 521
 - detector 519
 - effect of oxidation on Mössbauer parameters 532
 - Einstein model 518
 - electric field gradient (e.f.g.) 522
 - electric quadrupole interaction 522
 - experimental technique 520
 - experimental temperature 517
 - Fe³⁺ in molecular sieves 317
 - Fe-FER 538
 - Fe-MFI ferrisilicates 538
 - Fe-pillared clays 541
 - formation of carbon nanotubes catalyzed by Fe(II) 541
 - introduction of Fe²⁺, Fe³⁺ via solid-state ion exchange 533
 - introduction of ferrous ions 532
 - iron particles 533
 - isomorphous substitution of tetrahedral Al by Fe 535
 - lattice dynamics 518
 - magnetic hyperfine interactions 523
 - magnetic spectra 525
 - mesoporous (FeSi)MCM-41 541
 - model of a Debye solid 518
 - Mössbauer active decay 521
 - Mössbauer line shift 522
 - novel use for study of mobile sorption 531
 - nuclear Zeeman effect in the case of Fe(57) 523
 - of complexes of iron ions in zeolite 539
 - of complexes encaged in zeolite cages 540
 - of Fe(III) in ferrisilicate molecular sieves 539
 - of iron phthalocyanine [Fe(Pc)] 539
 - of molecular motion of Fe(C₅H₅)₂ and Co(C₅H₅)CO₂ 541
 - of zeolite Fe²⁺, Ca²⁺, Na⁺-A 532
 - oxidation of Fe²⁺, Ca²⁺, Na⁺-A 532
 - plot of transmission against Doppler velocity 520
 - population of the excited state 520
 - probability of a γ -ray transition 523
 - probability of recoilless emission 518
 - quadrupole hyperfine interactions 523
 - quadrupole spectra 525
 - relative probabilities for a dipole 3/2 \rightarrow 1/2 transition 525
 - relativistic T-dependent contribution to IS 522
 - resonant absorption at certain Doppler velocity 520
 - resonant absorption cross-section 519
 - RhFe clusters in zeolites 541
 - second-order Doppler shift 522
 - single crystal absorber 523
 - siting of Fe²⁺ cations 533
 - study of iron incorporated into zeolites 535
 - the asymmetry parameter 522
 - thickness of the absorber 520
 - three hyperfine interactions 521
 - transition mode of - 519
 - vibrating source 519
 - zeolite Eu-A 533
 - zeolite Eu-X 533
 - zeolite Eu-Y 533
- Mössbauer spectroscopy (⁵⁷Fe)
- application of strong external magnetic field 536
 - conversion electron Mössbauer spectroscopy (CEMS)
 - , - back-scatter method 534
 - conversion of toluene over ferrisilicates 539
 - of complexes of iron ions in zeolite 539
 - of dilute paramagnetic ferric iron 536
 - of dilute tetrahedral framework iron 536
 - of Fe in tetrahedral and octahedral coordination 536
 - of magnetically ordered materials 536
 - of MFI ferrisilicates
 - of N₂O decomposition over Fe-ZSM-5 539

- of N₂O decomposition over Fe,H-ZSM-5 539
- of N₂O decomposition over Fe-BETA 539
- of ZSM-5 type ferrisilicates 536
- under reducing and catalytic conditions 539
- Mössbauer spectroscopy with ¹²⁹I
 - I₂ adsorbed in nanoporous graphite fibres 541
- Mössbauer spectroscopy with Sn catalysts
 - isobutane dehydrogenation 539
 - supported zeolite catalysts 539
- Mössbauer spectrum
 - of zeolite Fe²⁺-A 526
 - , – mobile sorption 531
 - temperature dependence of – 531
- Mössbauer studies of Fe²⁺- and Fe³⁺-exchanged zeolites
 - coordination geometries 525
 - locations 525
 - Y-zeolites 525
- MTG reaction
 - in situ ¹³C MAS NMR 283
 - role of CO 283
- multi-nuclear solid-state NMR spectroscopy
 - aluminophosphate molecular sieves 216
 - MeAPO molecular sieves 216
 - MeAPSO molecular sieves 216
 - natural isotopes ²⁹Si, ²⁷Al, ³¹P, and ¹⁷O 216
 - silicoaluminophosphates (SAPO) 216
 - structural information and relationships of frameworks 215
- multiple scattering (MS)
 - in a series of SiK edge XANES spectra 457
- multiple-quantum MAS NMR spectroscopy (MQMAS) 215
- multiplicity of states 342, 347
 - conservation of – 351
 - first selection rule 342
- N**
- n*-hexane
 - as a probe for acid strength 147
- n*-type semiconductivity 358
- Na clusters
 - type of co-exchanged cation 326
 - type of zeolite 326
- Na₄³⁺ clusters
 - collapse of ESR hyperfine structure to a singlet 412
 - doping with 412
- ²³Na DOR NMR spectra
 - of dehydrated NaY 249, 250
 - sodium population in NaY 252
- ²³Na MAS NMR spectra
 - assignments 243, 244
 - counter-migration of sodium cations 245
 - decomposed 251
 - exchange of Na⁺ by Ba²⁺ 248
 - exchange of Na⁺ by protons 247, 248
 - hydrated La-exchanged zeolites 243
 - homologous series of La-exchanged Y 244
 - migration of La cations 245
 - of dehydrated zeolite NaX 253
 - of dehydrated zeolite NaY 251
 - of dehydrated zeolite Y 248
 - population factors, P_{Na} 253
 - sodium form (NaY) 248
- Na-Y zeolites containing gold species 455
- nanoscale particles in zeolites
 - possible applications 408
 - preparation within porous structure 408
- naphthalene
 - as probe molecule in exchanged faujasites 399
 - fluorescence 400
 - in zeolite NaX 400
 - in zeolite NaY 400
 - phosphorescence in NaX 400
- naphthalene excimer (excited dimer)
 - luminescence of CT complexes in NaX 400
- naphthylamine
 - as probe molecule in exchanged faujasites 399
- nature of radiation absorbing species 35
- NCL-1 zeolite
 - acid properties of – 136
 - characterized by FTIR and TPD of pyridine and NH₃ 136
- near-infrared spectra 100
 - of H-ZSM-5
- nephelauxetic parameter
 - nephelauxetic series 354
 - zeolite Ni(II)X, (fully hydrated) 389
- neutron spectroscopy
 - external motions of trapped species 71
- NEXAFS (Near Edge X-ray Absorption Fine Structure) 442
 - electrons stemming from a thin layer 442
- NH₄-Y
 - deammoniation of – 84
 - dehydration of – 84
 - reammoniation of – 84

- Ni-aluminophosphate
 - resonant X-ray diffraction 462
- NiPc complexes 417
- nitrido zeolites 388
 - electronic spectrum of - 388
- nitrobenzene
 - adsorbed on (M-X(M = Li, Na, K, Rb, Cs)) 400
 - wavelength shift of the electronic band 400
- nitrogen
 - adsorption 106
 - as a probe for mesoporous materials 138
 - sorbed into zeolite Na₄Ca₄-A 106
- NMR of chemical reactions catalyzed by zeolites
 - high-temperature NMR probe 279
 - low-temperature NMR probe 279
- NMR of quadrupole nuclei with $I=3/2, 5/2, \dots$
 - central transition 206
 - satellite transition 206
- NMR signal broadening
 - by chemical shift anisotropy 206
 - chemical shift anisotropy 209
 - heteronuclear magnetic dipole-dipole interaction 209
 - homonuclear magnetic dipole-dipole interaction 209
- NMR signals of liquids and gases
 - reason for narrowness of signals 204
- NMR signals of solids (zeolites)
 - broadening by internal magnetic interactions 204
- 2D NMR spectroscopy
 - of VPI-5 232
 - REDOR pulse sequence 232
- NMR/ESR technique
 - electron nuclear double resonance (ENDOR) 296
- NO adsorption
 - on Ce- and La-exchanged mordenites 144
 - on CoAPO-18 144
 - on Co-ZSM-5 144
 - on mesoporous materials (Cu-[Al]MCM-41 144
 - on Ni-[Al]MCM-41 144
- NO interaction
 - aluminum-containing extra-framework cations 331
 - Lewis acid sites 331
- non-framework Al (Al^{nf})
 - ²⁷Al NMR spectroscopy 225
 - AlOH groups 261
 - combination of XPS with bulk techniques 492
 - dealuminated zeolites HY 261
 - H-mordenite 261
 - ¹H-²⁷Al CP/MAS NMR 225
 - HZSM-5 261
 - migration 492
 - signals of hydroxyl protons on - 261
 - with hydrogen bonds 261
- non-framework cation complexes
 - electronic spectra 386
 - electronic structure of - 386
- non-framework cations
 - complexes with different guest molecules 386
 - coordination 377
 - in zeolites as catalysts and adsorbents 64
 - interaction with guest molecules 377
 - ion-exchangers 64
 - ligancy 377
 - location 377
 - migration 377
 - mobility 64
 - oxidation state 377
 - stability 377
 - UV-VIS spectroscopy of - 377
 - vibrational spectroscopy of - 64
- non-framework ions
 - active sites 391
 - catalytic properties of zeolites 391
- non-framework transition-metal ions
 - optical spectroscopy of - 386
- non-metallic guests in zeolites 509
- non-resonating S-spins 205
- nonbonding orbitals
 - in the MO scheme 354
- normal coordinate analyses (NCA)
 - computation vibrational frequencies 13
 - hot bands 18
 - overtones 18
- normal coordinates
 - transformation of - 14
- normal coordinates, Q 15
 - internal displacement coordinates, R 15
- normal mode analyses
 - additional approximations 15
 - of zeolites 16
 - problems and their present solutions 15, 16
 - symmetry theory 16
- normal modes
 - dependent on atomic masses 13
 - geometrical arrangement 13
 - kinetic energies 15

- of bridging hydroxy groups 102
- , - assignments 102
- potential energies 15
- potential energy surface 13
- utilizing INS and MD in combination 102
- notations of electronic transitions
 - ethylene as an example 347
 - group theory 347
 - Kasha notation (MO representation) 347
 - Mulliken notation 347
- NU-1 zeolite
 - Ti-derivative of - 62
- nuclear g -factor (g_N) 300
 - from ENDOR spectrum 309
- nuclear magneton (β_N) 300
- nuclear spins $I > 1/2$
 - electric quadrupole moment 206
 - line broadening interaction 206
- nuclear Zeeman effect
 - selection rules 523
- nuclearity of clusters
 - directly derived from ESR hyperfine structure 326
- 2D nutation MAS NMR spectroscopy
 - of dehydrated zeolite NaY 250
- O**
- offretite
 - acid centers in - 88
 - crystallographically different oxygen atoms 89
 - dealumination of - 61
 - decomposition of organic cations in - 157
 - OH groups 89
 - silanol groups 88
- OH deformation modes
 - directly detected by INS 102
- OH groups (cf. hydroxy groups)
 - diffuse reflectance IR spectroscopy (DRS) of - 98
 - formation via introduction of polyvalent cations 82
 - of H-[Al]ZSM-5 94
 - of H-[Fe]ZSM-5 94
 - of H-[Ga]ZSM-5 94
 - of zeolites ZSM-5 (MFI) 91
 - of ZSM-11 (MEL) 91
 - overtone and combination modes of - 98
 - removal by solid-state reaction 83
 - removal via reaction with NaN_3 83
- OH groups (HF OH-band)
 - re-interpretation 83
- OH groups attached to metal cations
 - non-acid 84
- OH groups in hydrogen mordenite
 - anharmonicities 87
 - dissociation energies 87
 - frequencies 87
- OH groups lattice-terminating 78
- OH groups of non-framework Al
 - IR band of - 80
- OH IR bands
 - of ferrierite (FER) 91
- OH stretching bands
 - of deammoniated $\text{NH}_4\text{-Y}$, i.e., H-Y -, - interpretation 76
 - of zeolite Beta -, - assignment of IR bands 90
 - on sorption of H_2S into faujasite-type zeolites 85
 - population of the SIII of Na-X sites by Na^+ cations 85
 - shift upon adsorption of CO 142
- Omega
 - ^{129}Xe NMR spectroscopy on - 274
 - dealumination of - 61
- one electron - one proton two-spin system
 - energy level scheme for ENDOR 308
- one electron oxidation potentials
 - from transitions in UV-VIS 380
 - of transition metal ions in zeolites 380
- optical absorptions
 - due to electronic transitions (ground to excited states) 358
- optical spectroscopy 338
 - of Co(II)-exchanged zeolite A 386
 - of coordination of transition-metal ions 391
 - , - mono-, bi- and polydentate ligands 391
 - of Cr(II)-exchanged zeolite A 386
 - of fully hydrated zeolites 386
 - of Ni(II)-exchanged zeolite A 386
- orbital-magnetic field interaction 298
- order of Si and Al at framework T-sites 218
- ortho-para H_2 splitting
 - pair of H_2 bands with H-ZSM-5 138
- orthorhombic and monoclinic silicalite-1
 - differences in framework and OH region 92
 - IR spectra of - 92
- Os phthalocyanine in intra-zeolite locations
 - XPS of - 509
- oscillator strength f
 - ratio observed/calculated integrated intensities 342

- oxidation number 431
oxidation of hydrocarbons
– in zeolite Y 539
– of iron phthalocyanine, [Fe(Pc)] 539
oxidation state
– absorption edge 454
– measure of the effective charge 454
– positions of pre-edge peaks 454
oxidizabilities 382
oxygen
– adsorption of – 106
– sorbed into zeolite Na₄Ca₄-A 106
- P**
³¹P MAS NMR intensities
– concentration of metal atoms in MeAPOs 231
– expression for the n_p/n_{Me} ratio 231
³¹P MAS NMR spectroscopy
– aluminophosphate-type zeolites 231
– gallophosphate-type zeolites 231
– metal atoms in MeAPO 231
– narrow resonance lines 216
– of dehydrated VPI-5 231
– of gallophosphate frameworks 233
– of hydrated VPI-5 231
– P-O-Al angles 231
– silicoaluminophosphate-type zeolites 231
p-phenylenediamine
– adsorbed on zeolites M-X, (M = Li, Na, K, Rb, Cs) 400
– wavelength shift of the electronic band 400
p-type semiconductivity 358
p-xylene
– as a probe for acid strength 147
paired spins (singlet) 347
Pake doublet
– for isolated spin pairs 206
paramagnetic clusters M_n⁽ⁿ⁻¹⁾⁺ (with n=2-6)
– electronic spectroscopy of – 410
– ESR spectroscopy of – 410
paramagnetic ionic clusters
– in neighboring cages 326
– interaction 326
paramagnetic molecules (O₂⁻, Cl₂⁻, SO₂⁻, CO₂⁻)
– ESR spectra of – 332
– generated inside the zeolite cavities 332
–, – by ionizing γ - and X-ray radiation 332
Pauli exclusion principle 347
Pd complexes
– of the Schiff base salen 417
permeability of vacuum 205
phase-shift functions
– via the single-shell EXAFS of ZnGa₂O₄ 445
phenol
– adsorption on H-Y 147
phosphine oxides
– protonation shifts 282
phosphines
– protonation shifts 282
phosphorescence 359
– radiative deactivation 372
photoacoustic cell for solid samples
– schematic representation of a – 371
photoacoustic IR spectroscopy
– instrumentation and procedures of – 43
– opaque samples 43
photoacoustic UV-VIS spectroscopy (PAS) 369
– black body approximation 371
– of CoAPO-44 384
– opaque materials 371
photoelectron (ejecting)
– strong interaction with its surrounding 488
photoelectron emission (for XPS)
– physics of the – 483
– sudden approximation 483, 485
photoelectron signals of Al
– assignments of Al signals 494
– of mordenites dealuminated by different procedures 494
photoelectron spectra
– shake-up structure 488
photoelectron spectroscopic study
– dehydroxylation of H-Y 496
– fluoridation of H-Beta 496
– of acidity and basicity with probe molecules 496
photoelectron spectroscopy
– analysis of shake-up satellites 487
– collective excitation 482
– combination with bulk techniques 502
– contamination of the spectrometer 474
– contaminations of the surface 483
– contamination of the zeolite sample 474
– contributions to binding energies 489
–, – charge transfer 489
–, – condensation shift 489
–, – core attraction 489
–, – core relaxation 489
–, – extra-atomic relaxation 489
–, – valence attraction 489
–, – valence relaxation 489
– correlations binding energy/charge transfer 490
– dealumination studied by – 493

- description of the background function 481
- line shape and splitting of shallow core levels 489
- main problem with zeolites 474
- multiple excitation 483
- of intra-framework Fe (III) 505
- of metals and alloys in zeolites 507
- of non-metallic guests in zeolites 509
- plasmon losses 483
- sample holder peaks 482
- Shirley background subtraction 482
- "Shirly" background function 481
- single crystals of zeolites 474
- survey spectrum 482
- X-ray satellites 482
- photoelectron spectroscopy of zeolites
 - "adventitious" carbon as internal reference 477
 - ammonia as a probe in XPS 497
 - application of an external electric field 478
 - assignment of N 1s signals after NH₃ adsorption 497
 - BE of metal ions 499
 - binding energy, BE 479
 - binding energies 485
 - charge compensation by a flood of slow electrons 475
 - charging phenomenon 475
 - coincidence or difference external surface/overall crystallite 491
 - compensation of charging by sample heating 475
 - dependence of the position of the Si 2s XPS peak 477
 - differential charging 478
 - effects of differential charging on Ru-Y 479
 - "flood gun" 475
 - flood gun current 477
 - internal standard chemical shifts 477
 - interpretations based on a consistent data set 484
 - local chemical heterogeneity of the zeolite 475
 - local variation in surface potential 475
 - multiply referenced binding energy scales 478
 - relaxation energy 485
 - UPS, ultraviolet-induced photoelectron spectroscopy 469, 491
 - use of literature data (deviations) 484
- photoelectrons (elastic)
 - "universal" curve of escape depth 471
- photoemission
 - migration of metals to external surface 507
 - mobility phenomena 499
 - penetration of metal poisons 499
 - reductive dispersion 499
 - , - Ga₂O₃ into H-ZSM-5) 499
 - solid-state ion exchange 499
 - solid-state reactions 499
 - studies on zeolite-encaged alloy particles 508
- photoemission experiment
 - additional field ("tubus") 478
 - analyzer 480
 - background from Bremsstrahlung 472
 - constant transmission mode 480
 - convolution function 480
 - fixed analyzer transmission, FAT 480
 - fixed retarding ratio, FRR 480
 - hemispherical analyzer 478
 - main characteristics of - 472
 - main constituents of a - 473
 - pass energy mode 480
 - representations of differential-charging effect 476
 - soft X-ray tube a source 472
 - UHV chamber 472
- photoemission from zeolites
 - main problem with zeolites 474
 - poor electrical conductivity 474
 - retarding field for the photoelectrons 474
- photoemission process
 - schematic representation of the physics of a - 483
- photoemission spectra
 - additional types of satellites 490
- photoemission spectroscopy
 - collective excitation 482
 - common mode of excitation 469
 - cylindrical mirror analyzer (CMA) 469
 - depth of information (material constant) 470
 - ESCA - electron spectroscopy for chemical analysis 469
 - hemispherical analyzer (HSA) 469
 - sample holder peaks 482
- photoemission spectroscopy
 - scattering cross sections 470
 - Shirley background subtraction 482
 - strongly monochromatic sources 469
 - surface sensitivity 470
 - survey spectrum 482
 - synchrotron sources 469
 - UPS - ultraviolet-induced photoelectron spectroscopy 469, 491

- X-ray satellites 482
- XPS - X-ray-induced photoelectron spectroscopy 469
- photoemission spectrum
 - correct background subtraction 482
 - echo spectra 472
 - effects of analyzer convolution function 480
 - FAT (fixed analyzer transmission) mode 481
 - FRR (fixed retarding ratio) mode 481
 - of a ZSM-5 sample in the FRR mode 480
 - of graphite 481
 - of ZSM-5 482
 - qualitative and quantitative analysis 480
 - satellite subtraction 472
 - XPS and X-ray induced Auger lines 480
- photoemission techniques
 - redox chemistry of components dispersed in zeolites 502
 - stabilization of low (non-zero) valence states 502
 - , - of Rh (I), Pd (I), Ni (I), Cu (I) 502
- photon absorption in the UV-VIS range
 - due to a particular group (chromophore) 345
- γ -photon (monochromatic)
 - extremely well-defined radiation 517
- picosecond infrared activation method
 - H-ZSM-5 spectra 150
- plasmon losses 483
- platinum carbonyl clusters (Chini clusters)
 - FTIR spectroscopy of - 118
- platinum metal clusters
 - FTIR spectroscopy of - 118
- polarity
 - of the electric field within the zeolite interior 395
 - intracavity formation of ionic CT complexes 395
- polarization of ions 490
- polyenylic carbenium ions
 - degree of unsaturation 403
 - number of double bonds 403
- pore size modification 153
 - by boranes 153
 - by silanes 153
 - monitored by photoacoustic IR spectroscopy 153
- porosil-inserted HgX_2 (X: Cl, Br, I) molecules
 - Raman and UV-VIS spectroscopy of - 450
- potential energies
 - in terms of internal coordinates 13
- potential energy curves
 - of the excited compared to the ground state 343
- potential energy curves of adsorbed molecules
 - in the ground and excited state 363
 - perturbation of the admolecule 363
- potential energy minimization
 - optimization of the geometry 19
- potential energy of a zeolite lattice
 - electrostatic interactions 19
 - harmonic angle bending potential 19
 - short-range interactions 19
- potential models
 - covalent character 20
 - high diversity 21
 - influence of the curvature of potential energy surface 21
 - prediction of vibrational spectra 20
 - terms of non-bonding interactions 20
- prediction of the HF-LF splitting in faujasites 27
- prediction of the vibrational frequencies 15
 - direct eigenvalue problem 13
 - inverse eigenvalue problem 13
- pre-edge region 430
 - electronic transitions core levels/unoccupied states 431
 - information about the electronic state 431
- probe molecules for 1H NMR spectroscopy 269
 - ammonia 269
 - benzene 269
 - pyridine 269
- probe molecules of different sizes
 - location of hydroxyl groups 270
- probes for acidity and basicity
 - alkanes 149
 - benzene 149
 - combined application of pyridine and ammonia 134
 - drawbacks of pyridine and ammonia 136
 - formation of hydrogen bonding 130
 - methanol 149
 - simple benzene derivatives 149
- probes for zeolite research via IR spectroscopy
 - characterization of zeolitic acidity and basicity 130
 - interactions of O_2 , N_2 , He, Ar and Xe with hydroxyl groups 130
 - simple diatomic molecules 106
 - small heteronuclear molecules 106

- probes of various basic strengths 131
 – for determining Brønsted acid sites 131
 –, – alcohols, ethers, sulfides, thiols, hydrocarbons 131
 probing local electric fields in zeolite voids
 – by adsorption of simple molecules 130
 –, – H₂, D₂, N₂, CO, CH₄, N₂O and CO₂ 130
 products of ethylene conversion 282
 propane
 – adsorbed in purely siliceous zeolite A 123
 – adsorbed in silicalite-1 123
 propene
 – adsorption on H-Beta 147
 proton population of O₁, O₂, O₃, O₄ sites in H-Y
 – predictions made by calculation 77
 pseudolattice method 16
 Pt-tetrammine complex, [Pt (NH₃)₄]²⁺
 – in M-X and M-Y (M=Li, Na, K, Cs) 118
 – monitored via in-situ FTIR 118
 pyridine
 – adsorbed on monovalent cations (C-sites) 133
 –, – wavenumber as a function of the electrostatic field 133
 – adsorbed on zeolites M-X (M=Li, Na, K, Rb, Cs) 400
 – as a probe for mesoporous materials 138
 – determination of the density of sites 131
 – extinction coefficients 131
 – probe for studying all aspects of zeolite acidity 131
 – probing Brønsted (B) acid sites 131
 – probing Lewis acid cation (C) sites 131
 – probing the nature of the acid sites 131
 – probing “true” Lewis (L) acid sites 131
 – typical bands of adsorbed pyridine 131
 – wavelength shift of electronic band 400
 pyridine and 2,6-di-*tert*-butylpyridine as probes
 – differentiating internal/external acid sites 134
 pyridine attached to cations
 – band position depending on electrostatic field, q/r 132
 pyridinium ion bands
 – two pairs – of 83
 pyrrole
 – adsorption-induced changes of cation modes 72
 – as a probe for basic sites 147
 – INS spectra of pyrrole adsorbed in Na-Y, Rb-Y 105
 – XPS of – 497
 pyrrole adsorption on basic zeolites
 – monitored by FTIR 148
 – monitored by INS 148
 pyrrolidine
 – adsorption-induced changes of cation modes 72
- Q**
 Q-band ESR (ca. 35 GHz)
 – wavelength and cavity dimensions 303
 QEXAFS (Quick-Scanning EXAFS) method
 – step-wise movement of the crystals 459
 QEXAFS AgK edge study
 – dehydration and decomposition of Ag⁺-A 460
 – silver-exchanged zeolite A 460
 quadrupole coupling constant 206, 248
 – characterization of zeolite acidity 259
 – effect on ESR spectra 314
 quadrupole coupling tensor 298
 quadrupole frequency 206
 quadrupole interactions 251
 quantification of an unknown paramagnetic entity 305
 quantitative determination of paramagnetic species
 – accuracy 306
 quantum chemical methods
 – assisting spectroscopic studies 404
 – related to vibrational spectroscopy 25
 quantum mechanical (QM) calculations
 – density functional methods (DFT) 25
 – for finite structural cutouts of the framework 26
 – Hartree-Fock theory (HF) 25
 – saturating dangling bonds 26
 – second-order Møller-Plesset perturbation theory (MP2) 25
 quantum mechanical ab initio calculations
 – of vibrational spectra 24
 quantum mechanical calculations
 – force constants 19
 quantum mechanical calculations
 – potential energy hypersurface 19
 – structure data 19
 – thermodynamic data 19
 – vibrational spectra 19
 quantum mechanical simulation
 – cations on extra-framework sites 27
 – frequencies of Brønsted acidic OH groups 27
 – spectra of zeolite frameworks 27
 – vibrational spectra 27

- quantum size effects
 – changes in color indicative of – 408
- quantum-sized metallic particles
 – interpretation of the $g=2$ ESR signal 328
- quasielastic neutron scattering (incoherent) (IQNS) 47
 – rotational and translational dynamics 47
- quinoline
 – differentiating internal/external acid sites 134
- R**
- Racah parameter 351
 – of zeolite Ni(II)X, (fully hydrated) 389
- Racah parameters 378
 – Hund's rules 350
 – represent electron repulsion 350
- radiative transitions in solids
 – depending on the width of the gap 357
 – in insulators with lattice defects 357
 – with band overlap 357
 – with incompletely filled conduction band 357
- radiative transitions in solids due to
 – continuous absorption 357
 – lattice defects 357
 – superposition of the uppermost bands 357
 – transitions to the conduction band 357
- radicals
 – formation on zeolites 406
 – UV-VIS spectroscopy of – 406
- Raman bands
 – of cation-exchanged A, X, Y and EMT zeolites 68
 – of zeolites H-Y and H-EMT 68
- Raman frequencies
 – of selected bonds of possible adsorbates 47
- Raman intensity
 – of modes in silicate and aluminosilicate frameworks 60
 – on isomorphous substitution 60
- Raman spectra
 – crystal growth processes of mordenite 157
 – interpretation of – 60
 – of faujasites 60
 – of ion-exchanged Y-type zeolites 59
 – of K-Y, Rb-Y, Cs-Y 70
 – of zeolite A 157
 – of zeolite Na-X 59
 – of zeolite Na-Y 59
 – of zeolite Y 157
 – of zeolites in the far-IR region 65
 – upon cation exchange 70
- Raman spectra and IR spectra
 – of ETS-4 61
 – of ETS-10 61
- Raman spectra in framework region
 – degree of water content 71
 – effect n_{Si}/n_{Al} ratio 71
- Raman spectra of ^{16}O -Na-Y zeolite
 – in comparison with those of ^{18}O -Na-Y zeolite 30
 – observed and calculated 30
- Raman spectra of zeolites
 – qualitative interpretation 35
- Raman spectra of zeolite frameworks
 – general feature of – 58
- Raman spectroscopy
 – advantage of – 46
 – anti-Stokes lines, blue-shifted 45
 – characterization and synthesis of ETS-10 158
 – fluorescence problems 46
 – formation of ZK-4, MOR, ZSM-5 and FER 158
 – from powdered samples 46
 – N_2 and O_2 adsorbed on zeolite A 111
 – near-infrared Fourier transform (NIR-FT) 46
 – of bare zeolite frameworks 58
 – of completely siliceous zeolite A 54
 – of crystallization of A-, X- and Y-type zeolites 156
 – of hydrated microporous materials 45
 – of the framework of MCM-22 56
 – of zeolite syntheses 156
 – for investigations of adsorbed molecules 46
 – Raman background 46
 – requires changes in the polarizability 46
 – schematic representation 45
 – Stokes lines, red-shifted 45
 – synthesis of zeolites A, X, Y, MOR, L and Beta 157
 – ultraviolet (UV-FT) Raman techniques 46
- Raman spectroscopy of T-O-T vibrations in frameworks of
 – $AlPO_4$ -20 56
 – FAU 56
 – [Fe]-SOD 56
 – LTA 56
 – SAPO-20 56
 – SAPO-37 56
 – SOD 56
 – VPI-7 56

- zeolitic silica polymorphs 56
- [Zn]-SOD 56
- ZSM-18 56
- Ramsauer-Townsend resonances 451
- backscattering amplitude functions 451
- ranges of absorption
- for different electronic transitions 346
- re-alumination of zeolites
- Y-type zeolites 90
- zeolite Beta 90
- RE-Y (RE = La, Nd, Sm, Gd, Dy)
- IR framework spectra 53
- reactant molecules in zeolites
- line broadening of ^1H NMR signals 281
- reaction methanol/hydrogen sulfide over Na-X
- FTIR spectroscopic study of - 152
- reasons for rare application of electronic spectroscopy 364
- broad unresolved bands 364
- REDOR pulse sequence
- applied to dehydrated VPI-5 232
- reducibilities of various cations to bulk metal 382
- reducibilities of various cations to metal atoms 382
- reduction of Ag-Y with H_2
- monitored by IR spectroscopy 119
- reduction of Pd^{2+} -Y with H_2
- monitored by ESR and IR spectroscopy 119
- reduction potentials for reduction to bulk metal
- from transitions in UV-VIS 380
- of transition metal ions in zeolites 380
- reduction potentials for reduction to neutral atoms 380
- reflectance spectroscopy
- vs. transmission spectroscopy in UV-VIS 368
- reflection/absorption infrared spectroscopy
- growth of silicalite-1 157
- reinsertion of non-framework aluminum 262
- effect on framework $n_{\text{Si}}/n_{\text{Al}}$ ratio 262
- ^1H MAS NMR 262
- in zeolite HNaY 262
- in dealuminated zeolite HZSM-5 262
- ^{29}Si MAS NMR 262
- relationships between g and A tensors, ESR symmetry, point symmetry
- coincidence of tensor axes 299
- ESR symmetry 299
- g and A tensors 299
- molecular point symmetry 299
- relative concentration
- by referencing to standard bands 35
- relaxation of the ionized atom
- core vacancy filled by electron from higher shell (Auger effect) 433
- emission of so-called secondary electrons 433
- filling of the inner shell vacancy 433
- fluorescence X-ray photon 433
- representation of the optical layout
- of a diode array spectrometer 367
- of a double-beam ratio-recording spectrometer 366
- residual linewidth
- affected by several factors 209
- of MAS NMR signals of quadrupole nuclei 210
- under DOR conditions 212
- resonance Raman spectroscopy, "RR" technique
- by Fourier transform Raman spectroscopy (FT-Raman) 154
- investigation of $[\text{Ru}(\text{bpy})_3]^{2+}$ entrapped in faujasites 155
- sensitivity of - 46
- resonance structures
- resonance energy stabilization of a complex 356
- resonant X-ray diffraction
- distribution of Zn^{2+} in Zn-exchanged Na-Y 462
- krypton sorbed in silicalite 462
- "near-edge" or resonance diffraction pattern 462
- Ni positions of a nickel aluminophosphate 462
- "off-edge" diffraction pattern 462
- resonating *I*-spins 205
- rhodium carbonyl clusters in Y-type zeolite
- characterized by IR 118
- rhodium clusters entrapped in Na-Y and H-Y zeolites
- studied via transmission IR spectroscopy 118
- rigid ion potential
- from ab initio calculations of clusters and ring structures 20
- rotational-echo double resonance (REDOR) 215
- rovibronic bands 343
- Ru phthalocyanine in intra-zeolite locations
- XPS of - 509

S

- s-electron density at the nucleus affected by
 - covalency factors and bond formation 521
 - s-electron population 521
 - screening effects of p-, d-, and f-electrons 521
- salen complexes
 - by Fourier transform Raman spectroscopy 154
 - candidate for enantioselective hydrogenations 418
- sample temperature (in ESR) 304
- Sanderson electronegativity 256
 - correlations with $\bar{\nu}_{\text{OH}}$, $\bar{\nu}_{\text{CH}}$, δ_{OH} and δ_{CH} of adsorbed CH_3OH 150
- SAPO molecular sieves
 - binding energies of – 506
 - XPS of – 506
- SAPO-5 (cf. also zeolite SAPO-5)
 - acid hydroxy groups 101
 - acidity of – 138
 - Ag clusters in – 326
 - ammonia-loaded 270
 - bridging OH groups 263
 - Brønsted acid strength of – 100
 - Brønsted acidity of – 100
 - combined ^1H -MAS NMR, ^{11}B -MAS NMR, DRIFT 100
 - diffuse reflectance IR spectroscopy (DRIFT) of – 100
 - DRIFT experiments 100
 - IR investigation of pyrrole adsorption in – 149
 - mainly acid character of – 149
 - NMR parameters, determined selectively 263
 - weak basic sites in – 149
- SAPO-11
 - Ag clusters in – 326
 - combined ^1H -MAS NMR, ^{11}B -MAS NMR, DRIFT 100
- SAPO-17 (cf. also zeolite SAPO-17)
 - diffuse reflectance IR spectroscopy (DRIFT) 100
- SAPO-20
 - IR and Raman spectroscopy of framework vibrations 56
- SAPO-31
 - acid hydroxy groups 101
- SAPO-34 (cf. also zeolite SAPO-34)
 - acid hydroxy groups 101
 - ammonia-loaded 270
 - diffuse reflectance IR spectroscopy (DRIFT) 100
- SAPO-37 (cf. also zeolite SAPO-37)
 - bridging OH groups 263
 - infrared measurements of – 101
 - IR and Raman spectroscopy of framework vibrations 56
 - NMR parameters, determined selectively 263
- SAPO-39
 - FTIR transmission spectroscopy 95
 - framework vibrations 57
 - OH stretching region 95
- SAPOs
 - diffuse reflectance IR spectroscopy (DRIFT) 100
 - OH stretching region by DRIFT spectroscopy of – 94
- SAPOs (Cu^{2+} -loaded)
 - ESR spectra of – 313
- scaled quantum mechanical (SQM) force field method
 - scaling applied to force constant matrix 26
- scattering amplitude function $|F_j(k)|$ 437
 - element-specific 437
 - number of electrons of the backscattering atoms 437
 - Ramsauer-Townsend resonances 437
- Schrödinger equation, time-independent 24
- Schuster-Kubelka-Munk (SKM) function $F(R_\infty)$ 368
 - absorption coefficient $K(\lambda)$ 369
 - relationship to particle size 374
 - scattering coefficient $S(\lambda)$ 369
- second moment M_2 of an NMR signal
 - calculation 205
 - measure for the linewidth of solid-state NMR signals 205
- second moment, M_2^{HAI} , approach
 - selective determination of NMR parameters 263
- second moment, $M_2^{\text{CT, MAS}}$, of the central transition
 - under magic angle spinning conditions 210
- second-order quadrupole broadening
 - strong quadrupole interaction 208
- second-order quadrupole shift, ν_{qs} 206
- secular determinant
 - related to vibrational frequencies 15
- secular equation
 - related to vibrational frequencies 15
- SEDOR experiment
 - heteronuclear magnetic dipole-dipole vs. other line-broadening mechanisms 215

- schematic representation of – 214
- selection rules
- forbidden or allowed transitions 342
- sequence of increasing electronic energy
- usually in the order:
 - $\sigma < \pi < n < \sigma^* < \pi^* < \text{Rydberg (R) states}$ 346
- severe interference with electronic structure of admolecules
- appearance of new bands 364
- SEXAFS (Surface EXAFS)
- electrons stemming from a thin layer 442
- less important for uniform catalysts as zeolites 459
- surface-sensitive variants of XAS 459
- “shake-up” and “shake-down” processes
- processes within the absorbing atom itself 436
- shear strain parameter 228, 230
- shear strain of the AlO_4 tetrahedra 228
- shell model
- ab initio calculations 20
- extension of the rigid ion model 20
- polarizability of oxygen anions 20
- predicting crystal structures 20
- polarizability of extra-framework cations 20
- simulating vibrational spectra 20
- shielding constant 204
- shift of wavenumber of the NH-stretching band, $\Delta\tilde{\nu}(\text{NH})$
- measure of basicity 148
- shifts in band positions
- upon adsorption 35
- shifts of OH bands on CO adsorption
- in SAPO-40 143
- ship-in-the-bottle synthesis
- characterized via IR spectroscopy 154
- in zeolite EMT 154
- $[\text{Mn}(\text{salen})\text{OH}]$ 154
- $\text{Na}(\text{I})\text{-salen}$ and $\text{Pd}(\text{II})\text{-salen}$ 154
- phthalocyanines in faujasite-type zeolites 154
- $\text{Rh}(\text{III})\text{-salen}$ complexes encapsulated in X and Y 154
- $\text{Ru-2,2}'\text{-bipyridine}$ 154
- ^{29}Si chemical shifts of $\text{Si}(n\text{Al})$ units
- correlation with Si-O-T bond angles 219
- in zeolite A 219
- in zeolite frameworks 217
- in zeolite mordenite 219
- in zeolite offretite 219
- in zeolite Omega 219
- in zeolite Y 219
- in zeolite ZSM-5 219
- ^{29}Si CP/MAS NMR spectra
- of zeolite 40HNaX 267
- ^{29}Si MAS NMR spectroscopy
- narrow resonance lines 216
- number of SiOH groups
- of hydrated LaNaY 222
- of zeolite offretite 218
- of zeolite mordenite 218
- of zeolite Omega 218
- of zeolite Y 218
- of zeolite ZSM-5 218
- titanogallosilicate ETGS-10 217
- Si-OH-Al bridges
- force constants 103
- $\text{Si}(n\text{Al})$ unit ($n=0, 1, 2, 3$ or 4)
- range of chemical shifts in ^{29}Si MAS NMR 216
- $[\text{Si,Fe}]\text{BEA}$
- crystallinity of – 63
- $n_{\text{Si}}/n_{\text{Tl}}$ ratios via FTIR 63
- $[\text{Si,Fe}]\text{MFI}$
- IR-active mode at 1015 cm^{-1} 63
- Raman-active mode at 1020 cm^{-1} 63
- $[\text{Si,V}]\text{MFI (VS-1)}$
- crystallinity 63
- $n_{\text{Si}}/n_{\text{Tl}}$ ratios via FTIR 63
- $[\text{Si}]\text{VPI-5}$
- Brønsted acidity of – 95
- signal assignment
- in 2D J -resolved ^{13}C MAS NMR 282
- of adsorbates in zeolites 282
- silanol groups
- band at $3740\text{--}3745\text{ cm}^{-1}$ 78
- external silanol groups 78
- internal silanol groups 78
- lattice defects 78
- of H-Y 78
- silica
- binding energy of Al 2p 486
- binding energy of Si 2p 486
- silicalite
- intrinsic defects 374
- XPS spectra of – 493
- silicalite-1
- incorporation of titanium 61
- isomorphous substitution of – 61
- XANES (SiK edge) spectra of – 458
- silicoaluminophosphates
- H-Al distances of bridging OH groups 263
- silicoaluminophosphates (SAPOs)
- diffuse reflectance IR spectroscopy (DRIFT) 100
- silicon atoms in zeolite frameworks
- $\text{Si}(n\text{Al})$ units 216

- silver clusters in zeolites
 - application 408
 - chemistry 408
 - complex formation 408
 - structure 408
- simulation of ESR spectra
 - diagonalization of the spin Hamiltonian 306
 - estimation of the parameters 307
 - , - *g, D, E, A, Q*, line shape, line width 307
 - perturbation theory of higher order 306
 - simulation programs available in literature 306
 - solving the spin Hamiltonian 306
 - transition probabilities 306
 - Zeeman term 306
- simulation procedure of ESR spectra
 - as-synthesised VAPO-5 molecular sieves 324
 - comparison with experimental spectrum 325
 - summation of theoretical spectra 325
 - VAPO-5 324
- simultaneous application of XAS and powder XRD - 461
 - high T transformations to dense ceramic materials 461
- single crystals of ZSM-39
 - Raman spectra 156
 - vibrations of framework and template cations 156
- singlet-triplet transitions
 - normally forbidden - 342
- SiOH groups
 - located at framework defects 268
- site-concept 72
 - oversimplification of - 69
- sites in
 - Co²⁺-LTA 387
 - Cr²⁺-LTA 387
 - Cu²⁺-LTA 387
 - Ni²⁺-LTA 387
- sites of Cu(II) in
 - CHA 388
 - FAU 388
 - LTA 388
 - MOR 388
- siting of framework cobalt 384
- small Pt particles
 - by combined electronic and IR spectroscopy 416
- SnO_x particles
 - formation of - 415
 - in zeolite NaY 415
- sensors with optical detection 415
- SOD (sodalite)
 - Ga- and Ge-substituted - 63
 - IR and Raman spectroscopy of framework vibrations of - 56
- sodalite ([Si]SOD)
 - framework vibrations 54
 - isomorphous substitution of - 61
 - , - by Al, B, Ti, V, Ga, Fe and V 61
- sodalite lattice
 - calculations with a GVFF 30
- sodalite-type Eu₄Si₄Al₈O₂₄(MoO₄)₂
 - structure of - 394
- sodium cations
 - asymmetry parameters 247
 - in dehydrated NaY and NaX 247
 - isotropic chemical shifts 247
 - quadrupole coupling constants 247
- solid-state ion exchange
 - advantages 65
 - coordination of Fe after - 533
 - ferrisilicate 317
 - in FeCl₂ · 4H₂O/NH₄-Y
 - large number of different iron species 533
 - of FeCl₃-HZSM-5 317
 - siting 533
- solid-state ²³Na MAS NMR spectroscopy
 - of sodium cations 247
- solid-state NMR spectroscopy
 - ⁶Li and ⁷Li isotopes 239
 - cation distribution in zeolites 239
- sorption geometries of CO₂ and N₂O
 - in zeolite Na₄Ca₄-A 120
- spectra in IR after adsorption of CH₄
 - on Na-A 122
- spectra in IR of H₂ on Na,Ca-A
 - ortho-para splitting 110
- spectra simulation
 - infrared and Raman intensities 18
- spectral changes
 - upon dehydration of Co(II)-exchanged A 386
 - upon dehydration of Cr(II)-exchanged A 386
 - upon dehydration of Ni(II)-exchanged A 386
- spectral data of diatomic molecules on A
 - band assignment 108
 - , - of H₂, D₂, N₂, O₂, CO 108
- spectral features of adsorbed deuterated acetonitrile
 - on a series of Brønsted acid zeolites 139
 - on H₃Na-X, H₃Na-Y, H-Y, H-MOR, H-ZSM-5) 139

- spectrum in traditional form
 - plot transmitted intensity vs. wavenumber 40
- spin-echo double resonance SEDOR
 - determination of internuclear distances 214
- spin-orbit coupling 298
- spinning sideband 209
- spinning sideband patterns
 - bridging OH groups 263
 - simulation of - 263
- splitting Dq
 - zeolite Ni(II)X₂ (fully hydrated) 389
- splitting of the spectrum into *o*-H₂ and *p*-H₂ bands
 - on Na₄Ca₄-A 110
 - crystal field-induced 110
- stabilization of cracking catalysts
 - via introduction of La³⁺ or rare earth cations 82
- stabilization of hydrogen form of zeolites
 - after dealumination 79
- standard (in ESR)
 - number of spins accurately known 305
 - with accurately known *g*-values 304
- static ²⁷Al NMR
 - framework aluminum atoms 226
 - non-framework aluminum species 226
 - of dehydrated zeolites 226
- static ¹³³Cs NMR vs. ¹³³Cs MAS NMR spectroscopy
 - Cs cations in hydrated and dehydrated mordenite 240
- static ¹⁷O NMR spectroscopy
 - of aluminophosphates 238
 - of dealuminated Y-type zeolites 238
 - of gallosilicates 238
 - of zeolite NaA 238
 - of zeolite NaY 238
 - of zeolite Y 238
 - of zeolites of different compositions 238
 - quadrupolar patterns 238
 - quadrupole coupling constant 238
 - quadrupole coupling constants, C_Q 238
 - , - of oxygen atoms in different T-O-T bridges 238
- static in-situ NMR spectroscopy
 - chemical reactions catalyzed by zeolites 283
- static linewidth
 - full width at half maximum of an NMR signal 205
- steaming
 - additional OH groups 78
- strength of acid sites
 - characterized by adsorption of ethane 152
 - continuous or stepwise TPD of probe molecules 135
 - FTIR combined with stepwise TPD of NH₃ 135
 - in dealuminated zeolite Beta 135
 - in mazzite 135
 - in microporous titanosilicate ETS-10 135
 - in zeolites of Y-, Beta- or MOR-type 135
 - monitored by stepwise TPD of NH₃ with FTIR transmission spectroscopy 135
 - ultra-stabilized Y-type zeolite (US-Y) 135
- stretching vibration modes
 - ammonium NH 35
 - aromatic CH 35
 - carbonylic CO 35
 - linearly correlated to n_{Al}/(n_{Si} + n_{Al}) of frameworks 51
 - paraffinic CH 35
 - zeolitic hydroxy groups OH 35
- strong interaction between the central ion and ligands
 - molecular orbital (MO) model 354
- strong-field limit
 - ligand field 351
- structure data of VPI-5
 - shear strain parameter of - 230
- sudden approximation 485
- sulfur dioxide, SO₂, adsorbed on zeolites
 - admission of H₂S 124
 - H-Y 124
 - IR and UV-Vis spectroscopy of - 124
 - IR spectrum 124
 - Na-Y 124
 - related to the modified Claus reaction 124
- superacid sites
 - suggested by CO adsorption 142
- superacidity
 - ultrastable Y-type zeolite (US-Y)
- superhyperfine interaction of Cu²⁺
 - in case of high Al content 316
 - with ²⁷Al nucleus 316
- superhyperfine splitting in ESR 298
- surface enrichment
 - by XPS of metal ion/Si ratios 500
- surface sensitivity
 - "universal" curve for all materials as a function of E_{kin} 470

- surfatochromic shift
 – bathochromic shift 362
 – concept of potential energy diagrams 362
 – depending on Franck-Condon factor 362
 – hypsochromic shift 362
 – transition in adsorbed state 362
 –, – resulting in a frequency shift 362
 – unchanged band position 362
 sweep time (in ESR) 303
 symmetry of the two electronic states
 – second selection rule 342
 synchrotron radiation 429
 synthesis of zeolites
 – IR and Raman investigations on – 156
- T**
- T-positions of zeolite frameworks
 – calculated from the Si-O-T bond angles 220
 Tanabe-Sugano diagrams
 – energies E and ligand field strength Δ
 – expressed in units of Racah parameters B 353
 – for the d^2 configuration 353
 TAPSO (Ti-silicoaluminophosphate with MFI-structure)
 – OH stretching bands of – 101
 – transmission IR spectroscopy of – 101
 TAPSO-37
 – Ti-containing silico-aluminophosphate 62
 temperature-programmed desorption (TPD) 138
 – characterization of strength of adsorption sites 138
 – monitored by diffuse reflectance IR 138
 – of H_2 or D_2 from H-forms of zeolites 138
 term diagram for electronic transitions
 – absorption 343
 – degeneracy lifting of 4T_1 states by Jahn-Teller effect 391
 – effect of olefin adsorption 391
 – fluorescence 343
 – internal conversion 343
 – intersystem crossing 343
 – of benzene with electronic transitions 399
 – of Co(II) ion in T_d environment 391
 – phosphorescence 343
 – with electronic transitions 399
 term splitting
 – starting from the strong-field limit 352
 – starting from the weak-field limit 352
- testing the acidity of a series of zeolites
 – by combination of XPS and IR using pyridine 132
 tetrachloroethylene
 – adsorption on free acid hydroxy groups 139
 – adsorption-induced shift of 1H -MAS NMR signal 139
 theoretical background of vibrational spectroscopy
 – symmetry theory 16
 theory of UV-VIS spectroscopy 339
 three-fold coordinated Al (or Si)
 – formation of – 74
 Ti-Beta
 – Lewis acid sites 143
 – preparation of – 385
 – UV-VIS spectra of – 385
 Ti-MCM-41
 – UV-VIS spectra of – 385
 – synthesis of – 385
 Ti-modified zeolite beta
 – change in the UV band 384
 Ti-modified zeolites 384
 Ti-modified ZSM-5 (TS-1)
 – change in the UV band 384
 Ti-modified ZSM-11 (TS-2)
 – change in the UV band 384
 Ti-modified ZSM-48
 – change in the UV band 384
 Ti-silicalite
 – XPS study of – 504
 tight-binding approximation
 – delocalization of valence electrons 357
 TiK edge X-ray absorption spectrum
 – of the (dense) titanosilicate mineral aenigmatite 430
 titanoaluminosilicate ETAS-10
 – ^{29}Si MAS NMR spectra of – 217
 titanosilicate ETS-10
 – ^{29}Si MAS NMR spectra of – 217
 titration with benzoic acid
 – concentration and strength of basic sites 149
 ^{205}Tl NMR spectroscopy 239
 toluene
 – as a probe for acid strength 147
 toluene conversion
 – catalyst characterized by Mössbauer spectroscopy 539
 TON (Theta-1)
 – acid strength 142
 total Hamiltonian
 – of spin $I=1/2$ 204

- total spin Hamiltonian (H_T) 300
- transferred-echo double resonance (TEDOR) 215
- transition dipole matrix elements
- basic quantum-mechanical selection rules 434
 - transitions of electrons to unoccupied states 434
- transition metal ions
- distortion of local environment of cation site 316
- transition metal phthalocyanines (Pc)
- encapsulating of - 417
 - in supercages of zeolites A, X, Y 417
 - ship-in-a-bottle species 417
- transition moment
- probability of a transition 340
 - R_{ev} 344
- transitions changing the parity
- third selection rule 342
- transitions of ethylene in electronic configurations
- in different notations 347
- transmission electronic spectroscopy
- of coke formation 405
 - of high-temperature coke 405
 - of low-temperature coke 405
- transmission FTIR spectroscopy
- formation of Ru(I)(CO)₃ 116
 - of sorption of metal carbonyls into Na-Y or H-Y 116
- transmission mode
- in ordinary electronic spectroscopy 367
- transmission UV-VIS studies
- of reactive interaction of H₂S and SO₂ over NaX 398
 - schemes of experimental equipment 368
- transmission vs. reflectance method
- advantages of transmission technique 368
 - more intense bands 368
- transmittance 36
- transport diffusion coefficient 165
- trialkylamines (Et₃N, *n*-Pr₃N and *n*-Bu₃N)
- characterization of external B- and L-acidity 134
- trimethylgallium
- adsorption of - into H-Y 123
- trimethylphosphine (TMP)
- on acid surface sites 140
- trimethylsilyldiethylamine
- characterization of external B- and L-acidity 134
- TS-1 (Ti-silicalite-1)
- Ti-content 220
 - titanosilicate TS-1 220
 - transition monoclinic to orthorhombic structure 220
- TS-1 (titanosilicalite-1)
- 960 cm⁻¹ band 61
 - bands in the IR spectra 61
 - calculated vibrational spectra 62
 - conflicting interpretation 61
 - exposure to H₂O, NH₃ or CH₃OH 62
 - framework 61
 - framework investigation of - 61
 - Lewis acid sites 143
 - [Si,Ti]MFI 61
 - UV Raman laser spectroscopy of - 61
- two-dimensional homonuclear spin diffusion
- location of SiOH 267
- two-dimensional ²³Na nutation MAS NMR spectra
- of hydrated zeolite NaY 246
- two-dimensional (2D) NMR techniques 215
- two-electron oxidation potentials
- from transitions in UV-VIS 380
 - of transition metal ions in zeolites 380
- types of donor-acceptor interactions
- ligand-to-metal CT transitions (LMCT) 356
 - metal-to-ligand CT transitions (MLCT) 356
- U**
- ultrastabilization of Y-type zeolite (US-Y)
- combined FTIR/step-wise desorption of NH₃ 80
 - hydroxy region of US-Y 80
 - ²⁹Si MAS NMR 219
 - superacidic hydroxy groups 80
- unpaired spins (triplet) 347
- unsaturated carbenium ions in zeolites 405
- UPS (ultraviolet photoelectron spectroscopy)
- gas discharge lamps 472
 - physics of the - 483
 - UPS binding energy data 484
 - -, - requirements for documentation 484
- UPS valence band experiment
- on graphite 480
 - qualitative and quantitative analysis 480
- uptake of benzene into H-ZSM-5 165
- UV Raman laser spectroscopy
- characterization of TS-1, [Fe]ZSM-5, [V]MCM-41 53
 - of framework vibrations 53
 - of zeolites A, X, Y, MOR, L, and Beta 53

- UV ranges
 - accessible by routine techniques 339
 - by commercial spectrometers 339
- UV spectra
 - combination with IR spectroscopy 364
 - combined with electron spin resonance (ESR) 364
 - large extinction coefficients compared to IR 364
 - reflection studies 364
 - strong scattering in ultraviolet region 364
- UV-VIS bands of finite intensity
 - although forbidden 342
 - by distortion of the molecular symmetry 342
 - due to perturbations 342
- UV-VIS difference spectra
 - of carbonaceous deposits after methanol reaction on HZSM-5 405
- UV-VIS diffuse reflectance spectra
 - TiO_x -loaded faujasites 414
 - vanadium oxide particles in H-ZSM-5 414
 - zeolite-hosted oxides 414
- UV-VIS properties
 - plasma vibrations 359
 - so-called plasmons 359
- UV-VIS spectra of
 - CoAPO-18 384
 - CoAPO-44 384
 - conjugated oligomers 307
 - encaged thioindigo in zeolite NaX and on external surface 419
 - intracrystalline complex formation 417
 - FePc inside zeolite NaX 418
 - methylacetylene/HZSM-5 307
 - reductive carbonylation of zeolite PtNaY 417
 - Ti-Beta 385
 - Ti-MCM-41 385
 - thioindigo in toluene 419
 - transition-metal phthalocyanines in A, X, Y 417
 - with broad unstructured bands 340
- UV-VIS spectroscopy
 - assignment of main transitions 380
 - carbenium ion mechanism studied by - 404
 - coking 404
 - cyclization of dienyl to cyclopentenyl cations 404
 - derivative spectra 266
 - effect of impurities 373
 - Einstein coefficient of absorption 340
 - generation of polyalkylaromatics and polyaromatics 404
 - historical UV-VIS spectra of iodine on CHA and CaF_2 361
 - induced emission B_{nm} 340
 - in-situ investigations 404
 - interaction of olefins with Ca-, Co-, Ni-, Pd-NaY/olefins 401
 - naphthylamine as probes 399
 - naphthalene as probes 399
 - of alkenyl carbenium on zeolites 401
 - of amine derivatives on zeolites 399
 - of anthraquinone on NaY 399
 - of carbonyl species formed in PtNaY/CO 416
 - of CdS clusters in zeolites 412
 - of Chini complexes 416
 - of CoNaY/olefins 401
 - of cyclohexenyl carbenium ions 404
 - of HY/olefins 401
 - of NiCaNaY/olefins 401
 - of precursors of coke 404
 - of preparation of small metal clusters 416
 - of radical formation 406
 - of triphenylcarbinol on NaY 399
 - of triphenyl methyl compounds on zeolites 401
 - on aromatic systems adsorbed in zeolites 399
 - PdNaY olefins 401
 - probe molecules in exchanged faujasites 399
 - reflectance method 367
 - scattered transmission 367
 - transition dipole moment R_{nm} 340
 - transition-metal ions (TMI) 377
 - under catalytic conditions 404
- UV-VIS spectroscopy (far UV region)
 - benzene 398
 - $n \rightarrow \sigma^*$ and $n \rightarrow \pi^*$ transitions (one-pair electrons) 398
 - π -bonding in chromophores 398
 - $\sigma \rightarrow \sigma^*$ transitions 398
- UV-VIS transmission electronic spectra
 - of zeolite NaHY loaded with propene 402
- V
 - V^{4+} in faujasite-type zeolite
 - ESR assignments 322
 - ESR parameters 322

- V-silicalite
- intra-framework V studied by XPS 505
- valence band 357
- valence force field 24
- valence orbitals of NO
- absorbed with a bent structure on a cation 330
- VAPO-5
- diffuse reflectance spectroscopy (DRS) 385
 - ESR spectra of - 322, 323
 - values of g and A obtained by simulation 322
- variation in the mean Si-O-T bond angles
- ^{29}Si MAS NMR signals with low-field shift 221
- vibrational analyses of zeolites
- ab initio techniques 17
 - Badger's rule (relationship between bond lengths (r) and force constants) 17
 - calculation of potential energy distributions (PED) 18
 - calculation of the kinetic energy distribution (KED) 18
 - characterization of normal modes 16
 - cluster models 16
 - effect of structure 16
 - force field methods 16
 - general problem of missing experimental data 17
 - idealized models 17
 - isotopic species 16
 - model force fields 16
 - normal modes 16
 - number of observable absorptions 17
 - problems and possible solutions 16
 - problem of asymmetry of primary building units 18
 - quantum mechanics 16
- vibrational and rotational sublevels of electronic states of 341
- vibrational frequencies $\tilde{\nu}_k$ 15
- vibrational frequencies related to
- eigenvalue problem 14
- vibrational levels $v'' = 1, 2$ appreciably populated
- hot v'' states 343
- vibrational overtones and combination modes
- information about properties of zeolite host 339
- vibrational spectra
- quantum mechanical (QM) calculations 24
 - vibrational spectroscopy of
 - carbanions 401
 - carbenes 401
 - carbocations 401
 - reactive intermediates 401
 - radicals 401
 - vibrations in frameworks of
 - all-silica faujasite 33
 - , - comparison with simulated IR and Raman spectra 33
 - sodalite 33
 - , - interpretation of - 33
 - zeolite A 33
- vibronic lines 343
- Victoreen formula 434
- VIS range
- by commercial spectrometers 339
- VO^{2+} in zeolite Na-ZSM-5 505
- intra-framework V studied by XPS
- VO_x -loaded MCM-41
- UV-VIS spectra of - 414
- VPI-5
- ^{27}Al MAS NMR spectrum of - 234
 - 2D ^{27}Al - ^{31}P MAS NMR of dehydrated - 232
 - ^{31}P MAS NMR spectrum of - 234
 - acidity of - 138
 - Brønsted acidity of - 95
 - quadrupole coupling constants, C_Q , of ^{27}Al 229
 - , - as a function of shear strain parameter of AlO_4 229
 - schematic drawing of - 229
 - structure
- VPI-5, hydrated
- assignment of ^{27}Al NMR signals 233
 - assignment of ^{31}P MAS NMR signals 233
 - dehydration monitored by ^{31}P MAS NMR 233
 - , - rehydration monitored by ^{31}P MAS NMR 233
 - thermal stability of - 233
 - transformation to AlPO_4 -8 233
 - , - monitored by ^{31}P and ^{27}Al MAS NMR 233
- VPI-7
- IR and Raman spectroscopy of framework vibrations 56
 - ^{29}Si MAS NMR spectra of - 217
- VPI-8
- Raman spectroscopy 57
 - ^{29}Si MAS NMR spectroscopy 57
- VPI-9
- ^{29}Si MAS NMR spectra of - 217

W

- W-band in ESR (ca. 90 GHz)
 - wavelength and cavity dimensions 303
- W-band pulsed ESR techniques
 - zeolite encaged Cu(histidine)²⁺ 316
- WAHUHA (Waugh, Huber, Haeberlen)
 - sequence
 - homonuclear magnetic dipole-dipole interaction 208
- water vapor adsorbed on zeolites
 - fundamental vibration modes 126
 - IR research of – 126
- wave vector k of excited electron 435
- waveguide in ESR 303
- wavenumber of bands of acid OH
 - influenced by the n_{Si}/n_{Al} ratio 77
- wavenumber shift, $\Delta\bar{\nu}$, of HF-band of OH in H-Y
 - on benzene adsorption 145
- weak-field limit
 - electronic repulsion 351
- weakly basic probes for acid sites in zeolites
 - acetone 136
 - acetonitrile 136
 - acetylacetone 136
 - benzene 136
 - carbon monoxide 136
 - CH₃I
 - hydrogen 136
 - light paraffins 136
 - N₂O 136
 - o-xylene 136
 - p-xylene 136
 - phosphines 136
 - toluene 136

X

- X-band (9.25 GHz)
 - resonance field for $g = 2$ (0.3300 T) 303
 - wavelength and cavity dimensions 303
- X-ray absorption fine structure (XAFS)
 - X-ray absorption near-edge structure (XANES) 430
- X-ray absorption spectra
 - experimental set-ups for measuring 442
 - occurrence of edges in – 433
- X-ray absorption spectra registration
 - at low concentrations 442
 - by detecting Auger electrons 442
 - by detecting electrons 442
 - by detecting photons in UV-VIS region 442

- X-ray absorption spectroscopy (XAS)
 - data analysis 443
 - of dehydrated Ba-ZSM-5 69
 - synchrotrons 441
 - transmission experiments 441
- X-ray scattering
 - elastic 434
 - inelastic 434
- X-rays interaction with matter
 - excitation of matter 433
 - scattering of X-rays 433
- X-type zeolites
 - adsorption of homonuclear diatomic molecules in – 106
- XAFS
 - monochromator materials (yttrium boride YB₆₆) 463
 - using $\mu d(E)$ directly 432
 - variations of the absorption with energy E 432
- XAFS (CoK edge) and powder XRD
 - of cobalt aluminophosphates 461
 - onset of crystallization of CoAPO-5 461
 - stabilities of pure CoAPO-44 and CoAPSO-44 461
- XAFS in-situ studies
 - high intensity of synchrotron radiation 459
 - investigation of catalytically active systems 459
- XAFS methods
 - disadvantages 462
- XAFS techniques
 - characterization of zeolite-type solids (zeotypes) 431
- XANES
 - ability to resolve subtle changes in oxidation states 456
 - bond angles 431
 - element-selective method 462
 - multiple scattering (MS) 430, 431
 - no long-range order required 462
 - scattering of the electron 430
- XANES (CuK edge) spectra
 - Y zeolites loaded with copper species 455
- XANES (multiple scattering)
 - roundabout path 440
- XANES (transitions into unoccupied electronic states)
 - diagnostic value 439
 - dipole-allowed transitions 439
 - dipole-forbidden transitions 439
- XANES calculations
 - for ZnS with zinblende structure 441
 - general problems 441

- XANES CoK edge spectra
 - of Co in different environments in CoAPO-20 457
- XANES CuK edge spectra
 - of Cu in different oxidation states 454
 - of Cu in zeolite Y 454
- XANES data analysis
 - backscattering amplitude 443
 - determination of structural parameters 443
 - phase-shift functions 443
- XANES MS (multiple scattering) curve
 - comparison to compounds of known structure 441
- XANES MS region
 - FEFF code calculations 440
 - valuable information on geometrical arrangements 440
- XANES pre-edge absorption
 - quantum-mechanical selection rules 439
- XANES pre-edge peak
 - electronegativity of nearest neighbors 439
 - number of nearest neighbors 439
 - oxidation state 439
 - position of the – 439
 - shift per oxidation state 440
- XANES region
 - coordination geometry 453
 - electronic state of the absorbing atom 453
 - electronic transitions into unoccupied states 439
 - multiple scattering (MS) resonances 439
- XANES scattering path
 - oscillation of the absorption coefficient 440
- XANES SiK edge spectra of
 - as-synthesized ferrierite 458
 - calcined ferrierite 458
 - silica modifications 458
 - silicalite-1 458
- XANES spectra of
 - CoAl_2O_4 with distorted octahedral coordination 456
 - CoGa_2O_4 456
 - CoS-APO-34 456
 - gallosilicate (SOD-GaSi) 443
 - $\text{Co}_2\text{B}_2\text{O}_5$ 456
 - Na-Y zeolites containing gold species 455
 - oxidation states 0, +1 and +3 of Au 456
 - physical mixtures of Au_2Cl_6 and Na-Y 455
- XANES spectra of transition-metal compounds
 - deviations from high symmetry 456
 - pre-edge features due to dipole-forbidden transitions 456
- XANES structures
 - band-structure calculations 440
 - continuum of unoccupied electronic states 440
- XAS (X-ray absorption spectroscopy)
 - high transformation to dense ceramic materials 461
 - Lambert-Beer-type law 432
 - simultaneous application with powder XRD – 461
- XAS in-situ studies
 - combined with in-situ XRD 461
 - of adsorbed species 460
 - of Cu(I) in Cu-ZSM-5 460
 - of Pd in Na-zeolite Y 460
 - of Rh/Pt clusters in Na-zeolite Y 460
- ^{129}Xe NMR chemical shifts
 - dependence on the coverage 272–275
 - exchanged zeolites 276
 - function of the pore radius 272
 - in zeolite pores 272
 - on a divalent cation 273
 - on Ag- and Cu-exchanged zeolites 276
 - on Ca- and Mg-exchanged zeolites X 274
 - on Co-exchanged zeolites 276
 - on various zeolites 273
 - on zeolites Y exchanged with various cations 275
 - parabola-like dependence 274
 - paramagnetic contribution 273
- ^{129}Xe NMR spectroscopy 277
 - aluminosilicate-type zeolites in the H-form 272
 - alkali metal-exchanged AlPO_4s 272
 - by MAS technique 279
 - cages and pore sizes of selected zeolites 274
 - catalysts regeneration 276
 - chemical shift, $\delta(\rho)$ formula 274
 - chemical shifts with selected zeolites 274
 - Cd^{2+} -, Zn^{2+} -, Ce^{3+} -, and La^{3+} -exchanged zeolites 275
- ^{129}Xe NMR spectroscopy
 - crystallinity 276
 - fast exchange of xenon atoms 271
 - formation of coke 276
 - line narrowing 279
 - loading with metal particles (Ni, Rh, Ru, Pd, Ir, Pt) 276
 - location of cations in zeolites 275
 - non-framework species 276
 - number of cages 276

- ¹²⁹Xe NMR spectroscopy
 - of aluminophosphates 272
 - of silicoaluminophosphates 272
 - presence of intergrowths 276
 - zeolite pore architecture by 271
- Xe_nKr_m clusters
 - inside α -cages 279
- XEOL (X-ray excited optical luminescence) 442
- XPS analysis
 - chemical heterogeneity of outer surface 472
 - difference in surface-to-bulk composition 472
 - limited penetration depth (about one u. c.) 470
 - zeolitic materials 470
- XPS binding energy data
 - requirements for documentation 484
- XPS detection
 - of ammonia 495
 - of chloroform 495
 - of pyridine 495
 - of pyrrole 495
- XPS discrimination intra-/extra-framework positions
 - for Ti, V, Fe, Co 504
- XPS intensity analysis
 - combination with Ar (or He) ion sputtering 500
- XPS lines of metal shifts
 - in alkali-ion exchanged zeolites 507
 - in basic LTL zeolites 507
 - in H-form matrices 507
- XPS lines of metals shift to higher BE
 - for decreasing particle size 507
- XPS of La 3d line shape
 - in La₂O₃ and La-Y 501
- XPS of Ru clusters on zeolite Y
 - existence of two Ru species 478
- XPS raw data (Si 2p)
 - of a silicon single crystal 488
- XPS signals of
 - extra-framework Al 494
 - foreign phases 494
- XPS spectra
 - absolute accuracy of binding energies 484
 - chemical shift in – 484
 - Co phthalocyanine 509
 - combination of Ar etching with depletion of Al 492
 - combination with mass-spectrometric techniques 492
 - discrimination of extra-zeolite intra-zeolite species 500
 - enrichment of Al 492
 - introduction of Ag⁺ and Ni²⁺ into Na-zeolites 500
 - measured binding energy 484
 - migration of non-framework Al^{nf} 492
 - Na⁺ distribution 493
 - paramagnetic interaction of neighboring sites 502
 - physics of the – 483
 - surface Si-to-Al atomic ratios 491
- XPS studies
 - new theory of metal-support interactions 506
 - of surface modification 495
- XPS/XAES combination
 - copper modified zeolites 502
 - discrimination between intra-/extra-zeolite species 502
- Y
- Y-type zeolites
 - accessibility of acid sites 81
 - Al-ion exchanged 80
 - Brønsted acid sites 81
 - dealumination by SiCl₄ 81
 - dehydroxylated 80
 - level of Lewis centers 81
 - Lewis acid sites 81
 - steam-stabilized 80
- Z
- Zeeman interaction
 - Hamiltonian (\bar{H}_{Z1}) 297
- zeolite A (cf. also zeolite LTA)
 - absorbent in separation processes 85
 - builder in laundry detergents 85
 - cations in the distorted hexagonal oxygen window (6R) 378
 - coordination of Co(II) in – 389
 - crystallographic sites of non-framework cations in – 376
 - diffuse reflectance spectrum of Co²⁺ in – 383
 - distribution of xenon atoms among the α -cages in – 278
 - effect of cation-loading on framework vibrations 57
 - electronic spectrum of – 388
 - ESR parameters of alkali and silver clusters in – 326
 - ESR parameters of Cu²⁺ in dehydrated – 313

- ferrous-exchanged - 526
- framework vibrations in - 54
- high-resolution ESR spectra of Cu^{2+} in - 312
- indication of the cation sites 376
- ion-exchange of Fe^{2+} ions into - 526
- ion exchanger 85
- ionic clusters in - 323
- ^6Li NMR spectroscopy of Li-exchanged - 239
- ligand fields in - 378
- lithium-exchanged
- migration of the Al^{IV} in - 492
- MD studies of - 68
- Mössbauer spectrum of ferrous exchanged - 526
- parameter A (mT) in ESR of - 326
- parameter g in ESR of - 326
- preparation of ferrous exchanged - 526
- SI position in LTA designated as SIA 376
- site model (theoretical) 378
- site symmetry 378
- structure of - 376
- supercage of - with main cation positions 108
- supercage symmetry axes of - 108
- Tb^{3+} and Ce^{3+} in - 374
- transition metal phthalocyanines in - 417
- ^{129}Xe NMR spectroscopy on - 274, 278
- zeolite AgX
 - kinetics of silver-cluster formation in AgX 408
- zeolite AlZSM-5
 - ^1H MAS NMR intensities 259
 - concentrations of AlOH and bridging OH groups 260
- zeolite BaY
 - ^{23}Na nutation MAS NMR spectroscopy 247
 - containing paramagnetic O_2^- species 332
- zeolite Beta 55
 - acidity strength 90
 - Brønsted acid sites 90
 - dealumination via acid leaching 90
 - framework vibrations 90
 - hydrogen-bonded OH 90
 - incarcerated methylacetylene 406
 - iron in the framework 538
 - Lewis acidity 90
 - Mössbauer spectroscopy of Fe-exchanged - 538
 - OH groups attached to Al^{IV} -containing species in - 90
 - reflectance FTIR spectroscopy of - 90
- zeolite Ca, Na-A
 - CaOH groups 260
 - overtone and combination vibrations 99
- zeolite Ca-A
 - binding energy of Al 2p 486
 - binding energy of Si 2p 486
- zeolite Ca-X
 - binding energy of Al 2p 486
 - binding energy of Si 2p 486
- zeolite Ca-Y
 - binding energy of Al 2p 486
 - binding energy of Si 2p 486
- zeolite Ca-ZSM-5
 - ^{13}C -labelled adsorbates on - 316
- zeolite catalysts
 - reaction between NH_4 and CH_3OH on - 151
- zeolite CaY, dehydrated
 - ^1H MAS NMR 260
 - IR spectra of - 83
 - XRD investigations 260
- zeolite Ce, Na-Y 81
 - dealumination of - 81
 - DRS spectra of 81
 - IR transmission spectroscopy of - 81
- zeolite chabazite
 - electronic spectrum of - 388
- zeolite ^{57}Co -A
 - ^{57}Co emission studies 533
- zeolite Co(II)A
 - DR spectrum of fully hydrated - 387
 - zeolite Co(II)A (fully dehydrated)
 - dynamic Jahn-Teller effect 390
 - electronic spectra of - 390
 - exposure to NO 390
- zeolite CoNaY
 - interaction of olefins with - 401
- zeolite CoY
 - EXAFS analysis of - 448
- zeolite Cr-Y
 - spin-orbit splitting (ΔE_{so}) in - 501
- zeolite CrNaY
 - migration of the ions in - 387
- zeolite crystallization
 - Raman spectra of - 157
- zeolite CsLiA
 - ^{133}Cs MAS NMR spectroscopy of - 241
- zeolite CsNa-X 416
- zeolite CsNa-Y 499
- zeolite CsNaA
 - ^{133}Cs MAS NMR spectrum of - 241, 242
 - simulated spectrum 242
 - spinning sidebands 242

- zeolite-CsX
 - emission spectrum of pyrene on - 395, 396
 - polarities of the faujasite supercages 395
- zeolite Cu⁺-Y
 - XPS of - 502
- zeolite Cu(I)Y
 - emission spectrum of - 393
 - migration of the Cu(I) cations in - 393
- zeolite Cu,Na-Y
 - DEXAFS study of - 461
- zeolite Cu⁺-Beta
 - XPS of - 502
- zeolite CuNa-CHA
 - electronic spectrum of - 388
 - siting of cations in - 388
- zeolite CuNa-MOR
 - electronic spectrum of - 388
 - siting of cations in - 388
- zeolite CuNa-X
 - ESR parameters of Cu²⁺ in - 314
 - zeolite KX 396
 - , - emission spectra of - 396
- zeolite CuNa-A
 - ESR parameters of Cu²⁺ in - 314
- zeolite Cu-Y
 - XANES spectra of - 454
- zeolite Cu-ZSM-5
 - high-resolution ESR spectra of - 311
 - metal ion/Si ratios by XPS of - 500
- zeolite D-Y (deuterated H-Y)
 - calculated power spectra 104
 - comparison with experimental INS spectrum 104
- zeolite DEAMOR (dealuminated mordenite)
 - probed with hydrocarbons of increasing basicity 394
- zeolite EMT
 - ²³Na MAS NMR spectroscopy on - 248
 - Pd-Salen complexes in - 417
- zeolite Eu-A
 - Eu-151 Mössbauer spectroscopy 533
- zeolite Eu-X
 - emission spectra of - 394
 - Eu-151 Mössbauer spectroscopy of - 533
- zeolite Eu-Y
 - Eu-151 Mössbauer spectroscopy of - 533
- zeolite faujasite (FAU)
 - basicity of - 396
 - diffuse UV-VIS reflectance spectra of - 373
 - electronic spectrum of - 388
 - location of sites in - 377
 - number of sites/u.c. 377
 - probed with hydrocarbons of increasing basicity 394
 - site symmetry in - 377
- zeolite Fe²⁺-A
 - Fe²⁺ coordination in - 527, 528
 - Fe²⁺ siting in - 527
 - increased stability after introduction of Ca 532
 - lattice collapse of - 527
 - Mössbauer data of - 528
 - Mössbauer parameter after adsorption 528
 - Mössbauer spectra of - 527
 - Mössbauer studies of the adsorption on - 528
 - oxidation of - 532
 - Pd-salen complexes in - 417
 - preparation of Fe,Ca,Na-A 532
 - sorption of ethylene into - 528
 - symmetry changes around Fe²⁺ ion 528
- zeolite Fe-FER (iron ferrierite)
 - Debye temperature of - 538
 - Mössbauer spectroscopy of - 538
 - redox centres of - 538
 - redox behaviour of - 538
- zeolite Fe-MFI
 - Debye temperature of - 538
 - Mössbauer spectroscopy of - 538
 - redox behaviour of - 538
 - redox centers of - 538
- zeolite Fe,Na-Beta
 - Fe 2p signals of - 501
- zeolite ferrierite (FER)
 - XANES (SiK edge) spectra of - 458
- zeolite ferrous-Y
 - locations of cations 525
- zeolite framework
 - adsorption-induced changes of - 220
 - adsorption of p-xylene on zeolite ZSM-5 220
- zeolite H,D-ZSM-5
 - interaction deuterated/chlorinated acetonitrile on - 139
- zeolite H,K-ERI
 - chemical shift of bridging OH groups 257
 - ¹H MAS NMR side-band patterns 257
 - H-Al distances 257
 - mean Sanderson electronegativity 257
- zeolite H,Na-A
 - chemical shift of bridging OH groups 257
 - ¹H MAS NMR side band patterns 257
 - H-Al distances 257

- mean Sanderson electronegativities 257
- molar ratios of T-atoms 257
- zeolite H,Na-Beta
 - Brønsted acidity of - 88
- zeolite H,NaX
 - chemical shift of bridging OH groups 257
 - ¹H MAS NMR side band patterns of - 257
 - H-Al distances 257
 - mean Sanderson electronegativities 257
 - molar ratios of T-atoms 257
- zeolite H,NaY
 - C₅ND₅/SiOHAl 270
 - chemical shift of bridging OH groups 257
 - ¹H MAS NMR side band patterns 257
 - H-Al distances 257
 - mean Sanderson electronegativities 257
 - molar ratios of T-atoms 257
 - perdeuterated pyridine in - 269
- zeolite H,NaY, dehydrated
 - occupation of four inequivalent proton sites 254
- zeolite H,Na-ZSM-5
 - Brønsted (B) and Lewis (L) acidity of - 91
 - dehydroxylation of - 92
 - extinction coefficient of - 92
 - FTIR spectroscopy of OH stretching region of - 91
 - FTIR experiments using pyridine 92
 - heterogeneity in acid strength 92
 - particular type of Lewis sites 92
 - re-investigation into nature of B- and L-sites 92
 - treatment with hydrofluoric acid 92
- zeolite H,Na-ZSM-11
 - Brønsted (B) and Lewis (L) acidity of - 91
 - dehydroxylation of - 92
 - extinction coefficient of - 92
 - FTIR spectroscopy of OH stretching region of - 91
 - FTIR experiments using pyridine 92
- zeolite H-[Ga]Beta
 - acid strength of - 94
 - hydroxy groups of - 94
- zeolite H-[Al]ZSM-5
 - acid strength of - 94
 - study of hydroxy groups via FTIR 94
- zeolite H-Beta
 - acid sites of - 93
 - ¹H dipolar-dephasing spin-echo MAS NMR spectra of 267
 - XPS and IR spectroscopy 93
- zeolite H-[B]ZSM-5
 - acid strength of - 94
 - hydroxy groups of - 94
- zeolite H-Eu-1
 - XPS binding energies 492
- zeolite H-[Fe,Al]Beta
 - OH groups of - 94
- zeolite H-[Fe]ZSM-5
 - study of hydroxy groups via FTIR 94
- zeolite H-[Ga,Si]Beta
 - IR transmission spectroscopy 94
- zeolite H-[Ga]ZSM-5
 - study of hydroxy groups via FTIR 94
- zeolite H-[Si,Al]Beta
 - IR transmission spectroscopy 94
- zeolite HM (cf. HMOR, H-mordenite)
 - characterized by Mössbauer emission 539
 - chemical shift of bridging OH groups 257
 - H-Al distances 257
 - interaction of olefins 401
 - ¹H MAS NMR sideband patterns 257
 - mean Sanderson electronegativity 257
 - systematic UV-VIS transmission spectroscopy of - 402
 - transformation of various organic compounds on - 402
- zeolite HMOR (HM, H-mordenite) 227
 - acid sites of - 93
 - aluminum quadrupole coupling constants 227
 - asymmetry parameters 227
 - relative intensities, *I*_{rel} 227
 - XPS and IR spectroscopy of - 93
- zeolite H-Omega
 - acid sites of - 93
 - deammoniation of - 94
 - X-ray photoelectron and infrared spectroscopy 93
- zeolite H-Y
 - acid sites 93
 - aluminum quadrupole coupling constants 227
 - ammonia as a probe in XPS of - 497
 - asymmetry parameters 227
- zeolite H-ZSM-5
 - bridging OH groups of - 263
 - calculated power spectra of - 104
 - comparison with experimental INS spectrum 104
 - dealumination of - 81
 - deformation band of bridging OH groups 97

- zeolite H-Y
 - desorption of water from - 81
 - distributions of the acid site strength in - 497
 - DRS spectra of - 81
 - favored ammoniation of - 269
 - interaction of olefins with 401
 - interaction of water with - 81
 - IR transmission spectroscopy of - 81
 - local structure of bridging OH groups 262
 - NMR parameters (selectively determined) 263
 - relative intensities of ^{27}Al MAS NMR signals 227
 - studied by XPS and IR 93
 - studied by XPS and probes 495
- zeolite H-Y/Pd
 - XPS of - 502
- zeolite H-ZSM-5 81, 262
 - activation energy for hydroxyl protons in - 265
 - aluminum quadrupole coupling constants 227
 - ammonia-loaded - 270
 - assignments of combination bands 97
 - asymmetry parameters 227
 - band assignments 99
 - ^{13}C -labelled adsorbates on - 316
 - $\text{C}_5\text{ND}_5/\text{SiO}_2\text{HAl}$ 270
 - carbon monoxide adsorption 263
 - chemical shift of bridging OH groups 257
 - combination bands 100
 - complete DRS spectrum of - 99
 - computed frequencies 97
 - 2D J -resolved solid-state ^{13}C MAS NMR 282
 - derived assignments 97
 - diffuse reflectance IR spectra of - 98
 - DRIFT with probes CD_3CN and NH_3 99
 - ESR of NO on - 331
 - formation of aromatics from methanol over - 404
 - ^1H dipolar-dephasing spin-echo MAS NMR of - 267
 - ^1H MAS NMR sideband patterns 257
 - H-Al distance of bridging OH groups 263
 - H-Al distances 257
 - interaction deuterated/chlorinated acetonitrile on 139
 - Ir in - 507
 - lattice vibration modes 97
 - lattice vibrations (OTO and TO) 99
 - Lewis acidity of 99
 - mean Sanderson electronegativity 257
 - non-framework Al 493
 - OH bending modes of - 99
 - photoelectron spectroscopy of - 495
 - products of ethylene conversion on - 282
 - Pt in - 507
 - region of overtone and combination vibrations 99
 - relative intensities of ^{27}Al MAS NMR signals 227
 - studied by XPS and probes 495
 - systematic UV-VIS transmission spectroscopy of - 402
 - theoretically computed band positions 99
 - transformation of ethene over - 404
 - transformations of various types of hydrocarbons 402
- zeolite H-ZSM-5 (dealuminated)
 - bands assignments 99
 - DRIFT investigations of H_2 and C_3H_8 adsorption 99
 - identified in DRIFT experiments 99
- zeolite H-ZSM-5 (dehydrated)
 - ^1H MAS NMR spectra of - 267
- zeolite H-ZSM-5 (loaded with methanol)
 - difference between IR spectra 151
- zeolite H-ZSM-5/Ir
 - XPS of - 502
- zeolite H-ZSM-5/Pt
 - XPS of - 502
- zeolite H-ZSM-20
 - acid sites of - 93
 - X-ray and IR spectroscopy of - 93
- zeolite H-ZSM-22
 - acid sites of - 93
 - XPS and IR spectroscopy of - 93
- zeolite infrared assignments
 - external linkages 28
 - internal tetrahedral linkages 28
- zeolite K-X
 - desorption of water from - 81
 - emission spectrum of pyrene on - 395, 396
 - interaction of water with - 81
 - polarities of the faujasite supercages 395
- zeolite K-ZSM-5
 - ^{13}C -labelled adsorbates on - 316
- zeolite L (LTL)
 - basicity of - 396
 - dealumination via SiCl_4 treatment 86
 - dealumination with $(\text{NH}_4)_2(\text{SiF}_6)$ 86

- deammoniation of - 86
- framework vibrations of - 55
- incarcerated methylacetylene 406
- IR spectrum of - 80, 86
- OH groups of - 80
- ^{129}Xe NMR spectroscopy on - 274
- zeolite La,Na-Y
 - Brønsted and Lewis acidity of - 84
 - dehydroxylation of - 84
 - rehydration of - 84
- zeolite LaNaY
 - bridging OH groups of - 259
 - ^{13}C MAS NMR spectra of propan-2-ol-conversion on - 283
 - ^1H MAS NMR intensities 259, 260
 - ^1H NMR signal of LaOH 260
 - ^{139}La NMR spectroscopy 239
- zeolite La-Y
 - La 3d line shape of - 501
- zeolite LiNaX
 - ^6Li NMR spectroscopy of - 239
- zeolite LTA (cf. also zeolite A)
 - diffuse UV-VIS reflectance spectra 373
 - location of sites in - 377
 - number of sites/u.c. 377
 - site symmetry 377
- zeolite M-A ($M = \text{Zn}^{2+}, \text{Cd}^{2+}, \text{Ca}^{2+}, \text{Mg}^{2+}, \text{Co}^{2+}, \text{Ni}^{2+}$) 70
- zeolite materials
 - depth of information by photoemission 470
- zeolite MAZ
 - basicity of - 396
- zeolite MCM-22
 - acidity of - 93
 - ^{27}Al MAS NMR spectrum of dealuminated - 225
 - d_3 -acetonitrile as probes 93
 - dehydroxylation of - 93
 - framework vibrations of - 93
 - IR spectroscopy combined with TPD of ammonia 93
 - *p*-cymene as a probe 93
 - ^{29}Si MAS NMR spectrum of dealuminated - 225
 - two kinds of bridging hydroxy groups 93
 - two kinds of internal silanol groups 93
- zeolite MCM-58
 - acidity of - 93
 - d_3 -acetonitrile as a probe 93
 - *p*-cymene as a probe 93
- zeolite MFI borasilite
 - electronic spectrum of - 388
- zeolite Mg,Na-A
 - region of overtone and combination vibrations 99
- zeolite M(I)X ($M(\text{I}) = \text{Li}, \text{Na}, \text{K}, \text{Rb}, \text{Cs}$)
 - nitrobenzene on - 400
 - pyridine on - 400
- zeolite modeling
 - force field calculations 12
 - simulation techniques 12
- zeolite MOR (cf. mordenite)
 - acid strength of - 142
 - basicity of - 396
 - non-framework Al in 493
 - probed with hydrocarbons of increasing basicity 394
- zeolite MOR (dealuminated)
 - ammonia as a probe in XPS 497
- zeolite mordenite (cf. also H-MOR, HM, H-mordenite)
 - assignment of ESR signals 318
 - Brønsted-acid sites 86
 - Cr^{5+} in - 318
 - electronic spectrum of - 388
 - ESR parameters of Cu^{2+} in dehydrated - 313
 - ESR signal 318
 - ESR spectrum 319
 - high-resolution ESR spectra of Cu^{2+} in - 312
 - hydrogen form of - 86
 - incarcerated methylacetylene 406
 - IR spectra of H-MOR 86
 - migration of Al^{nf} in 492
 - OH stretching bands of H-MOR 86
 - silver cluster stabilization 408
- zeolite M-Y ($M = \text{Li}, \text{Na}, \text{K}, \text{Cs}, \text{Ca}, \text{Cu}, \text{Co}$ and Ni)
 - deammoniation of $\text{NH}_4\text{-Y}$ 84
 - dehydration of - 84
 - re-ammoniation of - 84
- zeolite Na-A
 - adsorption of H_2 , HD and D_2 on - 109
 - adsorption of O_2 on - 108
 - binding energy of Al 2p 486
 - binding energy of Si 2p 486
 - blue-shift of N_2 on - 109
 - CO molecules inside - 115
- zeolite Na-A
 - dehydration of - 461
 - desorption of water from - 81
 - DEXAFS study of - 461
 - Fe(III) ions in a tetrahedral environment 538
 - interaction of water with - 81

- zeolite Na-A
 - librational motions in - 115
 - red-shift of D₂ on - 109
 - ¹²⁹Xe MR spectra of - 278
- zeolite Na,Ca-A
 - adsorption of D₂ on - 108
 - blue-shift of N₂ on - 109
 - CO molecules inside of - 115
 - red-shift of D₂ on - 109
 - spectrum of D₂ on - 109
 - spectrum of H₂ on - 109
 - spectrum of N₂ on - 109
- zeolite Na₄Ca₄-A
 - interaction molecule D₂/zeolite host 110
 - spectrum of D₂ on - 110
- zeolite Na₈Ca₂-A
 - interaction molecule D₂/zeolite host 110
 - spectrum of D₂ on - 110
- zeolite NaEMT, dehydrated
 - ²³Na MAS NMR spectroscopy of - 248
- zeolite NaHM
 - systematic UV-VIS transmission spectroscopy 402
 - transformations of various hydrocarbons on - 402
- zeolite NaHY
 - exposed to propene 402
 - systematic UV-VIS transmission spectroscopy studies 402
 - transformations of various hydrocarbons on - 402
- zeolite NaHZSM-5
 - systematic UV-VIS transmission spectroscopy 402
 - transformations of various hydrocarbons on - 402
- zeolite NaM
 - systematic UV-VIS transmission spectroscopy 402
 - transformations of various hydrocarbons on - 402
- zeolite NaX
 - absorption of Na₄³⁺ clusters in - 412
 - arrangement of *trans*-thioindigo in supercages of 419
 - assignment of ²³Na NMR signals 252
 - binding energy of Al 2p 486
 - binding energy of Si 2p 486
 - cation positions 247
 - desorption of water from - 81
 - DOR NMR spectroscopy of - 252
 - interaction of water with - 74
 - MAS NMR spectroscopy of - 252
 - ²³Na MAS NMR spectra 252
 - paramagnetic O₂⁻ species in - 332
 - population numbers 247
 - population numbers of sodium cations 252, 254
 - thioindigo wrapped up by the framework of - 419
 - two-dimensional nutation MAS NMR spectroscopy of - 252
 - UV-VIS of thioindigo in toluene for comparison - 419
- zeolite Na-X/Fe^o
 - Mössbauer spectroscopy of - 533
- zeolite Na-Y
 - absorption of Na₄³⁺ clusters in - 412
 - assignment of the NMR signals 247
 - binding energy of Al 2p 486
 - binding energy of Si 2p 486
 - cation positions 247
 - combined IR and NMR of - 82
 - containing paramagnetic species 332
 - dealumination of - 81, 82
 - dehydrated - 249, 252
 - dehydration of - 461
 - DEXAFS study of - 461
 - desorption of water from - 81
 - distribution in hexamethylbenzene in - 277
 - distribution of adsorbed benzene in - 277
 - distribution of 1,3,5-trimethylbenzene in - 277
 - DOR NMR spectra of dehydrated - 249
 - DRS spectra of - 81
 - guest molecules in - 277
 - INS spectra of pyrrole adsorbed in - 105
 - interaction of water with - 81
 - IR transmission spectroscopy of - 81
 - ²³Na MAS NMR spectra of dehydrated - 252
 - polyacrylonitrile in - 407
 - pyrolysis of intrazeolite polymers in - 407
 - Si 2s absolute binding energy 478
 - systematic UV-VIS transmission spectroscopy 402
 - transformation of various of organic compounds in - 402
 - two-dimensional ²³Na nutation MAS NMR 249
 - ¹²⁹Xe NMR of different loadings of hexamethylbenzene 278
 - ¹²⁹Xe NMR shift depending on - 277
 - ¹²⁹Xe NMR spectra of xenon 277

- zeolite NaY, dehydrated 244
 - 2D ^{23}Na nutation MAS NMR spectrum of dehydrated - 245
 - population factors of sodium cations in dehydrated - 254
- zeolite Na-Y/Fe^o
 - Mössbauer spectroscopy of - 533
- zeolite Na-ZSM-5 505
 - ^{13}C -labelled adsorbates on - 316
 - intra-framework V studied by XPS 505
 - VO²⁺ in 505
 - XPS spectra of - 493
- zeolite NH₄Na-X
 - deammoniation of - 74
- zeolite NH₄MOR
 - aluminum quadrupole coupling constants 227
 - asymmetry parameters 227
 - relative intensities of ^{27}Al MAS NMR signals 227
- zeolite NH₄Y
 - aluminum quadrupole coupling constants 227
 - aluminum quadrupole coupling constants of dehydrated - 227
 - asymmetry parameters 227
 - asymmetry parameters of dehydrated - 227
 - relative intensities of ^{27}Al MAS NMR signals 227
 - relative intensities of ^{27}Al MAS NMR signals of dehydrated - 227
- zeolite NH₄ZSM-5
 - aluminum quadrupole coupling constants 227
 - asymmetry parameters 227
 - relative intensities of ^{27}Al MAS NMR signals of - 227
- zeolite Ni(II)X (fully hydrated)
 - bands of - 388
 - ligand field parameters of - 388
- zeolite NiCaNaY
 - interaction of olefins with - 401
- zeolite NiY
 - computational study of - 449
 - coordination numbers of - 449
 - dehydration of - 461
 - DEXAFS study of - 461
 - distances from EXAFS 449
 - EXAFS analysis of - 449
 - PXRD investigation of - 449
 - XPS of metal ion/Si ratios 500
- zeolite offretite
 - migration of Al^{III} in - 492
 - population ratios of T-sites 219
 - XPS binding energies of - 492
- zeolite Omega
 - acid centers in - 88
 - ^{27}Al MAS NMR spectrum of - 224
 - incarcerated methylacetylene 406
 - migration of Al^{III} in - 492
 - population ratios of T-sites 219
 - silanol groups in - 88
 - XPS binding energies of - 492
- zeolite P-N-sodalite
 - electronic spectrum of - 388
- zeolite PdNaY
 - interaction of olefins on - 401
- zeolite PtNaY
 - combined electron and IR spectroscopy 416
 - carbonyl species formed in PtNaY/CO 416
- zeolite Rb-Y
 - INS spectra of pyrrole adsorbed in - 105
- zeolite RE-Y (RE=La, Nd, Sm, Gd, Dy) 83
- zeolite RHO
 - ESR parameters of alkali and silver clusters in - 326
 - framework of - 276
 - INS spectra of - 102
 - ionic clusters in - 323
 - ^{129}Xe NMR spectroscopy on - 274, 276
- zeolite Ru-Y
 - Ru 3d binding energies 479
- zeolite SAPO-5 (cf. also SAPO-5)
 - chemical shifts of bridging OH groups 257
 - H-Al distances in - 257
 - ^1H MAS NMR side band patterns 257
 - incarcerated methylacetylene 406
 - mean Sanderson electronegativity of - 257
- zeolite SAPO-17 (cf. also SAPO-17)
 - chemical shifts of bridging OH groups of - 257
 - ^1H MAS NMR side band patterns 257
 - H-Al distances in - 257
 - mean Sanderson electronegativity 257
- zeolite SAPO-34 (cf. also SAPO-34)
 - chemical shifts of bridging OH groups of - 257
 - H-Al distances in 257
 - ^1H MAS NMR side band patterns 257
 - mean Sanderson electronegativity 257
- zeolite SAPO-37 (cf. also SAPO-37)
 - chemical shifts of bridging OH groups 257
 - H-Al distances in - 257

- zeolite SAPO-37 (cf. also SAPO-37)
 - ^1H MAS NMR side band patterns 257
 - mean Sanderson electronegativity of - 257
- zeolite silicalite
 - A-parameters 322
 - assignment of ESR parameters of Cr^{5+} and V^{4+} in - 318, 322
 - ESR signals 318
 - g-parameters 322
 - loaded with Cr^{5+} and V^{4+} 318, 322, 505
- zeolite SnNaY
 - by impregnation 415
 - quantum size effects 415
 - reversible reduction/oxidation cycles with CO and O_2 415
- zeolite sodalite
 - ionic clusters in - 323
- zeolite sodium sodalite
 - Na^+ - Na^+ distance in the cluster 410
 - sodium-doped - 410
 - simulation of electronic spectrum 410
- zeolite US-Y
 - deposition of Keggin ions in - 495
 - probed with hydrocarbons of increasing basicity 394
- zeolite V-ZSM-5
 - characterized by XPS of metal ion/Si ratios 500
 - preparation of - 414
 - UV-VIS spectra of - 414
- zeolite X (FAU)
 - assignment of ESR parameters of Cr^{5+} and V^{4+} in - 318, 322
 - base properties of - 149
 - bridging OH groups in - 267
 - cations in distorted hexagonal window of - 378
 - charge compensation in photoemission 477
 - crystallographic sites of non-framework cations 376
 - effect of cations on framework vibrations 57
 - ESR parameters of alkali- and Ag-clusters in - 326
 - ESR parameters of Cu^{2+} in dehydrated - 313
 - ESR signals of Cr^{5+} in - 318
 - Eu^{3+} -doped - 393
 - exchanged with M ($\text{M} = \text{Zn}^{2+}, \text{Cd}^{2+}, \text{Ca}^{2+}, \text{Mg}^{2+}, \text{Co}^{2+}, \text{Ni}^{2+}$) 70
 - high-resolution ESR spectra of Cu^{2+} in - 312
 - indication of cation sites in - 376
 - ionic clusters in - 323
 - ligand field of a site in - 378
 - predicted frequencies 16
 - site model (theoretical) 378
 - site symmetry 378
 - structure of - 376
 - transition metal phthalocyanines in - 417
 - ^{129}Xe NMR spectroscopy of - 272, 274
- zeolite X, NO-treated
 - g tensors 331
 - hyperfine coupling tensors 331
 - π orbital separations 331
- zeolite Y (FAU)
 - A-parameters of Cr^{5+} and V^{4+} in - 322
 - application of XAFS 447
 - assignment of Cr^{5+} and V^{4+} in - 318, 322
 - base properties of - 149
 - ^{13}C MAS NMR of propan-2-ol-conversion on - 283
 - cations in the distorted hexagonal window of - 378
 - charge compensation in photoemission 477
 - containing Fe(III) ions 533
 - coordination/location of Mn ions in - 447
 - crystallographic sites of non-framework cations in - 376
 - distorted Cd_4S_4 cubes in - 412
 - ESR parameters of alkali and Ag-clusters in - 326
 - ESR signal of Cr^{5+} in - 318
 - ESR spectra of zeolitic sodium clusters in - 329
 - exchanged with M ($\text{M} = \text{Zn}^{2+}, \text{Cd}^{2+}, \text{Ca}^{2+}, \text{Mg}^{2+}, \text{Co}^{2+}, \text{Ni}^{2+}$) 70
 - g-parameters of Cr^{5+} and V^{4+} in - 318, 322
 - incarcerated methylacetylene in - 406
 - indication of the cation sites 376
 - INS spectra of - 102
 - introduction of Fe into - by solid-state ion exchange 533
 - introduction of ferrous ions into - 532
 - introduction of La 244
 - ionic clusters in - 323
 - ligand field of a site in - 378
 - loaded with ruthenium clusters 478
 - Mössbauer spectroscopy of Fe in - 533
 - Mössbauer studies of Fe^{2+} and Fe^{3+} in - 525
 - mobility of sodium cations in - 245

- ^{23}Na MAS NMR spectra of - 244, 245
- nickel in - 275
- non-framework Al in - 493
- Pd in - 507
- Pt, Ir in - 507
- quadrupole parameters of hydrated Na^+ in - 245
- rare earth ion-exchanged 394
- redox chemistry of Cu(II) ions in - 392
- site model (theoretical) of - 378
- site symmetry in - 378
- structure of - 376
- SnO_x particles in - 415
- transition metal phthalocyanines in - 417
- ^{129}Xe NMR spectroscopy of - 272, 274
- XAS in-situ studies of - 460
- XPS binding energies in - 492
- XPS of Ag^+ and Ni^{2+} in 500
- zeolite Y, NO-treated
 - g tensors of - 331
 - hyperfine coupling tensors of - 331
 - π orbital separations in - 331
- zeolite ZK4
 - ^{129}Xe NMR spectroscopy on - 274
- zeolite Zn, Na-Y
 - resonant X-ray diffraction 462
- zeolite ZSM-5 (MFI; cf. also ZSM-5)
 - A-parameters of V^{4+} in - 322
 - basicity of - 396
 - binding energy of Al 2p in - 486
 - binding energy of Si 2p in - 486
 - correct background subtraction in photoemission of - 482
 - Cu(0) in - 507
 - Cu(II)-containing - 393
 - ESR parameters of Cu^{2+} in dehydrated - 313
 - extra-framework gallium cations in - 276
 - Fe-containing - 539
 - , - aromatization of ethane 539
 - FT-Raman spectroscopy of - 152
 - g-parameters of V^{4+} in - 322
 - gallium-modified - 276
 - high-resolution ESR spectra of Cu^{2+} in - 312
 - host/guest interactions of organic molecules with - 152
 - interaction with benzene, p-xylene, p-chlorotoluene and chlorocyclohexane 152
 - incarcerated methylacetylene in - 406
 - incorporation of Ga into framework of - 235
 - photoemission spectrum of - 480, 482
 - probed with hydrocarbons of increasing basicity 394
 - removal of nitrogen oxides 393
 - studies by IR, MAS NMR and INS spectroscopy 91
 - without absorption down to $50,000\text{ cm}^{-1}$ 374
 - ^{129}Xe NMR spectroscopy on - 274, 276
 - XPS and X-ray induced Auger lines 480
 - XPS of Ni^{2+} in - 500
- zeolite ZSM-5 as-synthesized
 - formation of SiOH in - 268
- zeolite ZSM-5 (boron-modified)
 - ^{11}B MAS NMR spectra of - 237, 238
- zeolite ZSM-5 (dealuminated)
 - ammonia as a probe in XPS 497
- zeolite ZSM-5 (Fe-modified) 536-538
 - sensitivity of XPS satellite structure 501
- zeolite ZSM-11 (MEL; cf. also ZSM-11)
 - ^{129}Xe NMR spectroscopy on - 274
 - framework vibrations of - 56
- zeolite ZSM-39
 - 2D spectrum of - 222
 - COSY, MAS NMR spectrum of - 223
- zeolite/adsorbate systems
 - adsorbate molecules as probes 104
 - adsorption of
 - , - H_2O , NH_3 , CO , CO_2 , NO_x , H_2S , SO_2 , organic compounds 103
 - , - olefins 103
 - , - aromatics 103
 - , - phenol 104
 - , - aniline 104
 - , - acetone 104
 - , - acetaldehyde 104
 - , - organic acids 104
 - , - nitriles 104
 - , - triphenyl derivatives 104
 - distribution of cations 104
 - effects of adsorbates on - 104
 - IR investigations of - 103
- zeolite-encaged alloys
 - studied by photoemission techniques 508
- zeolite-hosted oxides
 - identification of - 414
 - preparation of - 414
- zeolites
 - binding energy of Al 2p 486
 - binding energy of Si 2p 486
 - charged and uncharged metal clusters in - 409
 - considered as solid electrolytic solvents 395

- zeolites
 - depth of information in photoemission spectroscopy 470
 - micropolarity of - 395
 - nitrido - 388
 - , - electronic spectrum of - 388
 - non-framework Co(II) in - 383
 - photoemission techniques (almost exclusively XPS) 490
 - rare-earth-doped - 393
 - silver-loaded - 408
 - trends in chemical shifts in UPS and XPS 486
 - UPS of - 490
 - , - analysis of - 470, 490
 - XPS of - 490
 - , - analysis of - 470, 490
- zeolites A, X, Y, MOR, L, Beta
 - UV Raman laser spectroscopy of framework vibrations 53
- zeolites containing
 - carbon studied by XPS 509
 - carbonyls studied by XPS 509
 - chlorides studied by XPS 509
 - halogens studied by XPS 509
 - oxides studied by XPS 509
 - polymers studied by XPS 509
 - sulfides studied by XPS 509
- zeolites with different structure types
 - introduction of Fe²⁺ 532
 - , - by solid-state ion exchange 532
 - , - Mössbauer spectroscopy of - 532
 - , - T-programmed evolution of volatile products 532
 - ¹²⁹Xe NMR spectroscopy of - 272
 - X-ray diffraction of - 532
- zeolitic silica polymorphs
 - IR and Raman spectroscopy of framework vibrations 56
- zeolitic water
 - of octahedrally coordinated ions 386
- Zeolon (Na-MOR) 86
- zero field parameters *D* and *E*
 - axial fine structure parameter, *D* 320
 - effect on a powder ESR spectrum 301
 - influence on the effective *g* values of a Cr³⁺-ion 320
 - ratio axial/orthorhombic fine structure parameters 320
- zincosilicates 217
 - [Zn]-SOD
 - IR and Raman spectroscopy of framework vibrations 56
- Zr-containing pentasil structures
 - acidity of - 138
- ZSM-5 (MFI; cf. also zeolite ZSM-5)
 - adic strength of 142
 - [B]ZSM-5 61
 - cobalt-containing ZSM-5 63
 - [Fe]ZSM-5 63
 - Raman spectroscopy of ZSM-5 framework vibrations 56
 - [Si,Ti]MFI 61
 - [Si,V]MFI 63
- ZSM-5 boron-substituted
 - BO₃ pattern 237
 - BO₄ line 237
 - rehydration 237
 - two-dimensional nutation MAS NMR spectroscopy 237
- ZSM-5 type ferrisilicates
 - after calcinations 537
 - after steaming 537
 - iron in tetrahedral framework sites of 537
 - Mössbauer spectra of - 536-538
 - white colour of the as-synthesise - 537
- ZSM-18
 - IR and Raman spectroscopy of framework vibrations 56, 57
 - ²⁹Si MAS NMR spectroscopy of - 57
- ZSM-35 (FER) (cf. also ferricrite)
 - framework vibrations of - 56
- ZSM-57 (MFS)
 - framework vibrations of - 56